CODEN: JASMAN

ISSN: 0001-4966

The Journal of the Acoustical Society of America

Vol. 110, No. 6 December 2001

(Continued)

THE JOURNAL OF THE ACOUSTICAL SOCIETY OF AMERICA VOL. 110, NO. 6, DECEMBER 2001

CONTENTS—*Continued from preceding page*

(Continued)

THE JOURNAL OF THE ACOUSTICAL SOCIETY OF AMERICA VOL. 110, NO. 6, DECEMBER 2001

CONTENTS—*Continued from preceding page*

(Continued)

THE JOURNAL OF THE ACOUSTICAL SOCIETY OF AMERICA VOL. 110, NO. 6, DECEMBER 2001

CONTENTS—*Continued from preceding page*

ACOUSTICAL NEWS—USA

Elaine Moran
Acoustical Society of America, Suite 1NO1, 2 Huntington Quadrangle, Melville, NY 11747-4502

Editor's Note: *Readers of this Journal are encouraged to submit news items on awards, appointments, and other activities about themselves or their colleagues. Deadline dates for news items and notices are 2 months prior to publication.*

New Fellow of the Acoustical Society of America

Rachel K. Clifton — For contributions to auditory perception and sound localization.

William A. Yost appointed to new position at Loyola University Chicago

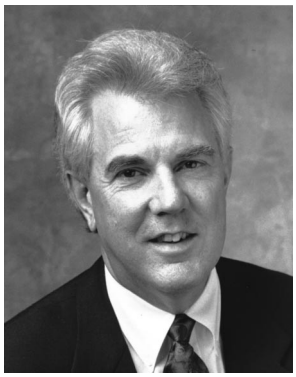

William A. Yost

William A. Yost has been appointed Associate Vice President for Research and Dean of the Graduate School. Dr. Yost was the Director of the Parmly Hearing Institute and the Interdisciplinary Neuroscience Minor at Loyola. He is a Fellow of the Acoustical Society of America and currently serves as ASA Vice President-Elect.

USA Meetings Calendar

Listed below is a summary of meetings related to acoustics to be held in the U.S. in the near future. The month/year notation refers to the issue in which a complete meeting announcement appeared.

2002

21–23 February	National Hearing Conservation Association Annual Conference, Dallas, TX [NHCA, 9101 E. Kenyon Ave., Ste. 3000, Denver, CO 80237; Tel.: 303-224-9022; Fax: 303-770-1812; E-mail: nhca@gwami.com; WWW: www.hearingconservation.org/index.html].
10–13 March	Annual Meeting of American Institute for Ultrasound in Medicine, Nashville, TN [American Institute for Ultrasound in Medicine, 14750 Sweitzer Lane, Suite 100, Laurel, MD 20707-5906; Tel.: 301-498-4100 or 800-638-5352; Fax: 301-498-4450; E-mail: conv_edu@aium.org; WWW: www.aium.org].
3–7 June	143rd Meeting of the Acoustical Society of America, Pittsburgh, PA [Acoustical Society of America, Suite 1NO1, 2 Huntington Quadrangle, Melville, NY 11747-4502; Tel.: 516-576-2360; Fax: 516-576-2377; E-mail: asa@aip.org; WWW: asa.aip.org]. Deadline for receipt of abstracts: 1 February 2002.
2–6 December	Joint Meeting: 144th Meeting of the Acoustical Society of America, 3rd Iberoamerican Congress of Acoustics, and 9th Mexican Congress on Acoustics, Cancun, Mexico [Acoustical Society of America, Suite 1NO1, 2 Huntington Quadrangle, Melville, NY 11747-4502; Tel.: 516-576-2360; Fax: 516-576-2377; E-mail: asa@aip.org; WWW: asa.aip.org/cancun.html]. Deadline for receipt of abstracts: 28 June 2002.

2003

28 April–2 May	144th Meeting of the Acoustical Society of America, Nashville, TN [Acoustical Society of America, Suite 1NO1, 2 Huntington Quadrangle, Melville, NY 11747-4502; Tel.: 516-576-2360; Fax: 516-576-2377; E-mail: asa@aip.org; WWW: asa.aip.org].
10–24 November	145th Meeting of the Acoustical Society of America, Austin, TX [Acoustical Society of America, Suite 1NO1, 2 Huntington Quadrangle, Melville, NY 11747-4502; Tel.: 516-576-2360; Fax: 516-576-2377; E-mail: asa@aip.org; WWW: asa.aip.org].

2004

17–21 May	75th Anniversary Meeting (145th Meeting) of the Acoustical Society of America, New York, NY [Acoustical Society of America, Suite 1NO1, 2 Huntington Quadrangle, Melville, NY 11747-4502; Tel.: 516-576-2360; Fax: 516-576-2377; E-mail: asa@aip.org; WWW: asa.aip.org].
29 Nov.–3 Dec.	146th Meeting of the Acoustical Society of America, San Diego, CA [Acoustical Society of America, Suite 1NO1, 2 Huntington Quadrangle, Melville, NY 11747-4502; Tel.: 516-576-2360; Fax: 516-576-2377; E-mail: asa@aip.org; WWW: asa.aip.org].

Cumulative Indexes to the *Journal of the Acoustical Society of America*

Ordering information: Orders must be paid by check or money order in U.S. funds drawn on a U.S. bank or by Mastercard, Visa, or American Express credit cards. Send orders to Circulation and Fulfillment Division, American Institute of Physics, Suite 1NO1, 2 Huntington Quadrangle, Melville, NY 11747-4502; Tel.: 516-576-2270. Non-U.S. orders add $11 per index.

Some indexes are out of print as noted below.

Volumes 1–10, 1929–1938: JASA and Contemporary Literature, 1937–1939. Classified by subject and indexed by author. Pp. 131. Price: ASA members $5; Nonmembers $10.

Volumes 11–20, 1939–1948: JASA, Contemporary Literature and Patents. Classified by subject and indexed by author and inventor. Pp. 395. Out of Print.

Volumes 21–30, 1949–1958: JASA, Contemporary Literature and Patents. Classified by subject and indexed by author and inventor. Pp. 952. Price: ASA members $20; Nonmembers $75.

Volumes 31–35, 1959–1963: JASA, Contemporary Literature and Patents. Classified by subject and indexed by author and inventor. Pp. 1140. Price: ASA members $20; Nonmembers $90.

Volumes 36–44, 1964–1968: JASA and Patents. Classified by subject and indexed by author and inventor. Pp. 485. Out of Print.

Volumes 36–44, 1964–1968: Contemporary Literature. Classified by subject and indexed by author. Pp. 1060. Out of Print.

Volumes 45–54, 1969–1973: JASA and Patents. Classified by subject and indexed by author and inventor. Pp. 540. Price: $20 (paperbound); ASA members $25 (clothbound); Nonmembers $60 (clothbound).

Volumes 55–64, 1974–1978: JASA and Patents. Classified by subject and indexed by author and inventor. Pp. 816. Price: $20 (paperbound); ASA members $25 (clothbound); Nonmembers $60 (clothbound).

Volumes 65–74, 1979–1983: JASA and Patents. Classified by subject and indexed by author and inventor. Pp. 624. Price: ASA members $25 (paperbound); Nonmembers $75 (clothbound).

Volumes 75–84, 1984–1988: JASA and Patents. Classified by subject and indexed by author and inventor. Pp. 625. Price: ASA members $30 (paperbound); Nonmembers $80 (clothbound).

Volumes 85–94, 1989–1993: JASA and Patents. Classified by subject and indexed by author and inventor. Pp. 736. Price: ASA members $30 (paperbound); Nonmembers $80 (clothbound).

Volumes 95–104, 1994–1998: JASA and Patents. Classified by subject and indexed by author and inventor. Pp. 632. Price: ASA members $40 (paperbound); Nonmembers $90 (clothbound).

ACOUSTICAL NEWS—INTERNATIONAL

Walter G. Mayer
Physics Department, Georgetown University, Washington, DC 20057

Acoustical Science and Technology (AST) has become available ONLINE

The Acoustical Society of Japan has been publishing its official English journal since 1980, and from the beginning of this century it has been an electronic online journal with the new title *Acoustical Science and Technology*. The journal is now available online through J-STAGE (http://ast.jstage.jst.go.jp/en/). The Acoustical Society of Japan hopes that the easy availability of AST will enhance the exchange of knowledge of acoustics worldwide. You are very welcome to contribute to *Acoustical Science and Technology*. (See ASJ home page: http://wwwsoc.nii.ac.jp/asj/index-e.html).

(This note was submitted by the Acoustical Society of Japan with the request that it be published in this column. Ed.)

International Meetings Calendar

Below are announcements of meetings to be held abroad. Entries preceded by an * are new or updated listings with full contact addresses given in parentheses. *Month/year* listings following other entries refer to meeting announcements, with full contact addresses, which were published in previous issues of the *Journal*.

February 2002

21–24 ***13th Interdisciplinary Phoniatrics Symposium**, Leipzig, Germany. (G. Loges, Department of ENT, University of Leipzig, Liebigstrasse 18a, 04103 Leipzig, Germany; Fax: +49 341 972 1709; e-mail: fuchsm@medizin.uni-leipzig.de)

March 2002

4–8 **German Acoustical Society Meeting (DAGA 2002)**, Bochum. (Web: www.ika.ruhr-uni-bochum.de) *10/00*

18–20 ***Spring Meeting of the Acoustical Society of Japan**, Kanagawa, Japan. (Acoustical Society of Japan, Nakaura 5th-Bldg., 2-18-20 Sotokanda, Chiyoda-ku, Tokyo 101-0021, Japan; Fax: +81 3 5256 1022; Web: http://wwwsoc.nacsis.ac.jp/asj/)

25–27 ***Institute of Acoustics Spring Conference**, Manchester, UK. (IoA, 77A St Peter's Street, St. Albans, Herts AL1 3BN, UK; Fax: +44 1727 850553; Web: http://www.ioa.org.uk)

April 2002

8–11 **6th Congress of the French Acoustical Society, joint with the Belgian Acoustical Society**, Lille. (Web: www.isen.fr/cfa2002) *8/01*

22–24 ***International Meeting on Acoustic Pollution in Cities**, Madrid, Spain. (Viajes, Princesa 47-4a Planta, 28008 Madrid, Spain; Fax: +34 1 559 74 11; e-mail: dccimad8@viajeseci.es)

May 2002

27–30 **Joint Meeting: Russian Acoustical Society and Conference on Ocean Acoustics**, Moscow. (Fax: +7 095 124 5983; Web: rav.sio.rssi.ru/Ixconf.html) *6/01*

29–1 **Nonlinear Waves in Microstructured Solids (Euromech 436)**, Tallinn. (Fax: +371 645 1805; e-mail: je@ioc.ee) *10/01*

30–1 ***2nd International Conference on Newborn Hearing Screening, Diagnosis, and Intervention**, Villa Erba/Como, Italy. (D. Hayes, The Children's Hospital, 1056 East 19th Ave. B030, Denver, CO 80218 USA; Fax: +1 303 764 8220; Web: http://www.biomed.polimi.it/nhs2002)

June 2002

4–6 **6th International Symposium on Transport Noise and Vibration**, St. Petersburg. (Fax: +7 812 127 9323; e-mail: noise@mail.rcom.ru) *2/01*

10–14 **Acoustics in Fisheries and Aquatic Ecology**, Montpellier. (Web: www.ices.dk/symposia/) *12/00*

24–27 **6th European Conference on Underwater Acoustics**, Gdańsk. (Fax: +48 58 347 1535; Web: www.ecua2002.gda.pl/) *10/01*

24–28 **11th Symposium of the International Society for Acoustic Remote Sensing**, Rome. (Fax: +39 06 20660291; Web: ISARS2002.ifa.rm.cnr.it/) *10/01*

July 2002

2–7 **ClarinetFest 2002**, Stockholm. (e-mail: kkoons@pegasus.cc.ucf.edu) *10/01*

15–17 **International Symposium on Active Control of Sound & Vibration (Active 2002)**, Southampton. (Fax: +44 23 8059 3190; Web: http://www.isvr.soton.ac.uk/active2002) *10/01*

August 2002

19–23 **16th International Symposium on Nonlinear Acoustics (ISNA16)**, Moscow. (Fax: +7 095 126 8411; Web: acs366b.phys.msu.su/isna16/) *12/00*

26–28 **2nd Biot Conference on Poromechanics**, Grenoble. (Web: geo.mhg.inpg.fr/biot2001) *8/01*

26–28 **Joint Baltic-Nordic Acoustical Meeting 2002**, Lyngby. (Fax: +45 45 88 05 77; Web: www.dat.dtu.dk) *10/01*

September 2002

11–13 ***10th International Meeting on Low Frequency Noise and Vibration**, York, UK. (W. Tempest, Multi-Science Co. Ltd., 5 Wates Way, Brentwood, Essex CM15 9TB, UK; Fax: +44 1277 223 453; Web: http://www.lowfrequency2002.org.uk)

16–21 **Forum Acusticum 2002 (Joint EAA-SEA-ASJ Meeting)**, Sevilla. (Fax: +34 91 411 7651; Web: www.cica.es/aliens/forum2002) *2/00*

26–28 ***Autumn Meeting of the Acoustical Society of Japan**, Akita, Japan. (Acoustical Society of Japan, Nakaura 5th-Bldg., 2-18-20 Sotokanda, Chiyoda-ku, Tokyo 101-0021, Japan; Fax: +81 3 5256 1022; Web: http://wwwsoc.nacsis.ac.jp/asj/)

November 2002

30–6 **Joint Meeting: 9th Mexican Congress on Acoustics, 144th Meeting of the Acoustical Society of America, and 3rd Iberoamerican Congress on Acoustics**. Cancún. (Web: asa.aip.org/cancun.html) *10/00*

April 2003

7–9 **WESPAC8**, Melbourne, Australia. (Web: www.wespac8.com) *10/01*

 0001-4966/2001/110(6)/2813/2/$18.00

June 2003

8–13 **XVIII International Evoked Response Audiometry Study Group Symposium**, Puerto de la Cruz. (Web: www.ierasg-2003.org) *8/01*

September 2003

1–4 **Eurospeech 2003**, Geneva. (Web: www.symporg.ch/eurospeech2003) *8/01*

April 2004

5–9 **18th International Congress on Acoustics (ICA2004)**, Kyoto. (Web: ica2004.or.jp) *4/01*

BOOK REVIEWS

P. L. Marston
Physics Department, Washington State University, Pullman, Washington 99164

These reviews of books and other forms of information express the opinions of the individual reviewers and are not necessarily endorsed by the Editorial Board of this Journal.

Editorial Policy: *If there is a negative review, the author of the book will be given a chance to respond to the review in this section of the Journal and the reviewer will be allowed to respond to the author's comments. [See "Book Reviews Editor's Note," J. Acoust. Soc. Am.* ***81****, 1651 (May 1987).]*

Emerging Cognitive Abilities in Early Infancy

Francisco Lacerda, Claes von Hofsten, and Mikael Heimann, Editors

Lawrence Erlbaum Associates, Mahwah, New Jersey, 2001. 263 pp. 264 pp. Price: $59.95 (hardcover) ($27.50 pb), ISBN: 0805826696 hc (080582670X pb).

Recently an international conference on infant cognition was held in a remote village in Sweden. Francisco Lacerda, Claes von Hofsten, and Mikael Heimann have edited a significant new volume of papers based on that conference as a contribution to the growing body of knowledge regarding early cognitive capabilities in humans. Overall, the book offers an extremely useful general introduction to empirical research and reasoning in this field. The book could be utilized effectively in graduate studies of child development and/or developmental cognitive and neurosciences, but may be a bit advanced for undergraduate use. The work covers a lot of ground, from perceptual illusions, to object permanence, to brain science, to speech perception, to parental input for language learning, to imitation, to concept formation, and more.

Perhaps the volume's strongest feature is that it introduces novel views in the study of cognition, views that posit infant capabilities that contrast importantly with the abilities of adults. These foundational capabilities are presumed to account for surprising cases of infant success in cognitive experiments. The new views distinguish themselves from widely publicized alternatives positing deep-seated and general innate capabilities to account for early infant successes in cognition experiments, and the new views also contrast with other well-known perspectives, especially those of Piaget. The reader is presented with a variety of positions, new and not so new, through contrasting interpretations and styles of experimentation from the various authors who clearly represent a gamut of opinion and direction in the study of cognition. The most recent approaches have a strongly developmental twist, while the more publicized innatist approaches tend to have a preformationist flavor, positing that abilities of infants must be present or largely preformed from the beginning of life in order to account for results showing success by infants on cognition tasks. The innatist approaches can be thought of as begging the question of where cognitive abilities come from. The new approaches provide at least tentative characterization for the process of change and growth.

A notable example of the new views is provided in Yuko Munakata's chapter wherein she attempts to account for ''task dependency'' in certain celebrated infant cognition experiments. She offers a reanalysis of infant successes in so-called ''object permanence'' investigations that utilize a violation-of-expectation model, contrasting these successes with failures at the same age on tasks originally reported by Piaget for retrieval of hidden objects. In the former case, for example, infants show surprise at a sort of magical event, by gazing especially long at a spot where an object ought to have reappeared from behind a screen after disappearance, given its prior trajectory. In retrieval experiments, on the other hand, infants of the same age fail to search for an object that has been hidden in a new location, B, after having previously found the object hidden at location A; the experiment reveals what has come to be known as the ''A not B error.'' In the violation-of-expectation case, the infant seems to know that an object exists (i.e., has permanence) even though it has disappeared, while in the retrieval case the infant seems not to know that an object exists even though it has been visibly hidden.

The story is complicated, but Munakata offers a theoretically rich alternative to the many proposed methodological accounts of this apparent discrepancy, accounts largely intended to preserve the generality of object permanence as an explanatory construct. In her alternative, infants succeed in the violation-of-expectation experiment, not because their cognitive system commands object permanence, but because, at a young age, they possess a precursor capability by which they are able to form expectations and make predictions about the appearance of objects given prior trajectories. This is not quite the same as object permanence, or knowing that an object exists during its period of disappearance. At a later age a full object permanence capability should emerge, according to the reasoning, founded upon the ability to form expectations such as those observed in the disappearing and reappearing object experiments. Munakata says that the ''principle'' of object permanence is not in place at the younger age but that a ''process'' of formation of expectations is in place. The ''process'' can account for success in the violation-of-expectation experiments, while at the same time providing no basis for success in the A-not-B task for infants of the younger age.

Davis and Lindblom similarly offer a new interpretation of early phonetic learning and adaptation. Contrasting both empirical results and theoretical considerations with Kuhl's prototype model, the authors illustrate that there is very substantial phonetic variation in the exemplars of speech (vowels, for example) presented to infants by adults, and they detail the reasons that such variation may be inevitable. Speech occurs in widely distinct contexts and there are phonetic variations that are heavily conditioned by those contexts. The unexpectedly large variation in parent speech to infants (given predictions of the prototype idea) can only be dealt with by the infant, the authors persuasively argue, if the infant's approach is based on a ''function'' for vowels or other segments rather than a ''point in phonetic space,'' a function that must be established and tuned through experience with speech in its multifarious contexts. The infant thus can be seen to begin with a very different set of capabilities from those of the adult. This view implies that the ''prototype'' model needs fundamental revision to account for the much more important role for adaptation in phonetic learning than Kuhl's model proposes. The theoretical sophistication and breadth of accommodation to existing literature in the Davis and Lindblom paper appears to forecast significant advancement of understanding in infant speech perception.

A general overall weakness of many of the papers in the volume is that they do not sufficiently acknowledge methodological limitations in the field of infancy. More skepticism is in order. The volume's papers tend to report infant experimentation results (not necessarily the interpretations, but the empirical results themselves) as well-documented fact, when the truth is that infant cognition experiments are extremely difficult to conduct, and that they are subject to many problems of interpretation, experimental noise, and potential experimenter bias, even though many precautions are routinely taken. Often the study of infancy is a bit like doing surgery with a sledge hammer. A lot may get done, but the precision of the outcome is questionable. Many of the results reported in this volume are based upon procedures that, like blunt-instrument surgery, are substantially open to question at the level of reliability of outcomes. Much research in this field fails to be published precisely because it fails to produce ''successful'' outcomes for infant performance in cognition or perception tasks. This failure to publish is worrisome, because it implies the literature may reflect more success on the part of infants than is veridical. The peer review process incorporates a natural conflict of interest with respect to the issue of publication of null results, and

 0001-4966/2001/110(6)/2815/2/$18.00

cannot resolve resulting conflicts of potential interpretation in the short run. Because there are so many variables involved in experimenting with infants, the methodological difficulties are particularly great in comparison with difficulties encountered in many other fields, and consequently it would appear that ambiguity of outcomes may persist as a perennial problem, and should be addressed more openly by the participants in the field.

The tendency to accept infant abilities as having been proven in experiments of the past 20 years or so appears to be heightened by the widespread ethic of the field, very much reflected in this volume, that has spurred so many attempts to show that infants are capable of much more elaborate actions and perceptions than was supposed in prior generations. In particular, Piaget's model has been the object of many experiments, the goals of which seem to have been much influenced by a wish to overthrow one or another tenet of the Piagetian approach. Investigators pursue the illustration that infants can imitate, perceive, and act in ways that are remarkable. Much of the excitement of the field has seemed to center around the ''gee whiz'' characteristic of outcomes that emphasizes infants' surprising abilities. Such an ethic may spur the development of data, but it is of concern in the absence of a genuine attempt to construct models of how infant capabilities emerge. Successful models require systematic demonstrations of what is both possible and impossible for infants, and even more precisely, what is easy and what is difficult. This volume provides a mix of ''gee whiz'' and serious modeling, and thus offers both useful data and hints at theoretical solutions to age-old problems of understanding what infants know.

So, there is a great deal that is interesting in the volume. New data and new models are being entertained, and there is reason for optimism that the trend will continue. The first chapter, by Kirsten Condry, W. Carter Smith, and Elizabeth Spelke, addresses perceptual organization, focusing on the abilities of infants to understand a variety of illusory displays, and seeking to address the general question of how infants perceive certain complex displays at birth and what features of that capability may last through to adulthood. Chapter 2 is the illuminating contribution by Munakata discussed above. Chapter 3 provides a neuroscience perspective on early cognition by Mark Johnson. Both physiological and simulated results from neural network research are considered. In Chapter 4 Claes von Hofsten reviews the exciting outcomes of research on early infant abilities to track, target, and often catch flying objects, abilities that provide considerable insights about both motoric/perceptual capabilities and the abstract knowledge that seems to underlie prediction. Francisco Lacerda and Ulla Sunberg take the opportunity in Chapter 5 to illustrate empirically that there may be an important bias in infant perceptual tendencies favoring high–low vowel contrasts, as opposed to front–back ones. In Chapter 6, Patricia Kuhl outlines her magnet or prototype model, and argues that parental input to children should conform to certain predictions of the model. Barbara Davis and Bjorn Lindblom offer a rich commentary on the prototype theory in Chapter 7. As noted above, both empirical and theoretical objections to the original model are raised, and a revised model is suggested. Chapter 8, by Peter Jusczyk, gives an expanding perspective on how speech perception results in infancy may be reaching the point of helping us to understand key foundations of lexical learning. There are multiple factors involved, Jusczyk argues, but he encourages us not to ignore the phonetic system in our enthusiasm for syntactic and lexical phenomena. Chapter 9 provides a view of the concept of animacy and its apparent domain specificity in early life. Maria Legerstee offers an elaborate review of information suggesting that animacy is not necessarily a unified concept early in life, but is bound by context sensitive constraining principles. Chapter 10, by Andrew Meltzoff and M. Keith Moore, provides insights that have interesting features in common with the perspective offered by Munakata. The model of ''numerical identity of objects'' that the authors propose is founded on the notion that infant and adult capabilities are different in type, and that the relationship between them can be characterized within the proposed model. The last chapter is by Mikael Heimann, who argues that neonatal imitation is ''fuzzy'' and subject to a variety of kinds of possible interference. The phenomenon is subcortical in Heimann's interpretation, and thus fundamentally different from later imitation in childhood.

The volume provides a fine addition to the literature on early cognition. It can be strongly recommended to any one interested in the nature of the development of the human mind.

D. KIMBROUGH OLLER
Professor and Chair
Department of Communication Sciences and Disorders
University of Maine

REVIEWS OF ACOUSTICAL PATENTS

Lloyd Rice
11222 Flatiron Drive, Lafayette, Colorado 80026

The purpose of these acoustical patent reviews is to provide enough information for a Journal reader to decide whether to seek more information from the patent itself. Any opinions expressed here are those of reviewers as individuals and are not legal opinions. Printed copies of United States Patents may be ordered at $3.00 each from the Commissioner of Patents and Trademarks, Washington, DC 20231. Patents are available via the Internet at http://www.uspto.gov.

Reviewers for this issue:

GEORGE L. AUGSPURGER, *Perception, Incorporated, Box 39536, Los Angeles, California 90039*
HASSAN NAMARVAR, *Department of Biomed Engineering, University of Southern California, Los Angeles, California 90089*
DANIEL RAICHEL, *2727 Moore Lane, Fort Collins, Colorado 80526*
KEVIN P. SHEPHERD, *M.S. 463, NASA Langley Research Center, Hampton, Virginia 23681*
WILLIAM THOMPSON, JR., *The Pennsylvania State University, University Park, Pennsylvania 16802*
ERIC E. UNGAR, *Acentech, Incorporated, 33 Moulton Street, Cambridge, Massachusetts 02138*

6,224,476

43.20.Mv SHOCK-WAVE FOOD PROCESSING WITH ACOUSTIC CONVERGING WAVE GUIDE

John B. Long and Richard A. Ayers, assignors to Hydrondyne, Incorporated
1 May 2001 (Class 452/141); filed 2 July 1999

This device takes advantage of the fact that meat can be tenderized and partially sterilized by shock waves that may be generated by, say, a chemically induced explosive charge or a capacitive discharge between two electrodes, as exemplified by John Long's prior United States Patents 5,273,766 and 5,328,403. In this new embodiment, the conduit walls are constructed of plastic or any other material that closely matches the acoustic impedance of water. The conduit is immersed in a water-filled tank. A shock-wave generator creates a shock wave via a capacitor discharge through electrodes. Because of the matched acoustic impedances, the shock passes through the conduit without substantial reflection. The shock wave tenderizes and sterilizes the meat. The plasma discharges are repeated long enough so that all of the meat passing through the conduit is treated.—DRR

6,229,761

43.30.Es ESTIMATING SHIP VELOCITY THROUGH THE WATER AND OVER THE GROUND

Kyrill V. Korolenko *et al.*, assignors to the United States of America as represented by the Secretary of the Navy
8 May 2001 (Class 367/91); filed 17 September 1999

An onboard ship sonar system is operated to generate sonar returns. Two returns originating from two different directions are selected. Each return includes both volume reverberation and bottom reverberation data. The Doppler shift in frequency for each of the two returns based on the volume reverberation data is used for estimating ship velocity relative to the water, while the Doppler shift based on bottom reverberation is used for estimating velocity relative to the ground.—WT

6,229,760

43.30.Ma INTEGRATED STREAMER ACOUSTIC POD

Loran Ambs, assignor to Western Geco
8 May 2001 (Class 367/16); filed 1 April 1999

Conventional marine seismic streamers consist of a tow/strength member to which a number of acoustic pods (containing transducer elements, electronics, and battery power supplies) have been attached. The exterior attachment of the pods results in an assembly which is difficult to retrieve and store as each pod must be removed from the streamer as it is withdrawn from the water. This patent discusses an assembly where the acoustic pods are, instead, mounted interior to and against the inner surface of a hollow tube streamer which also houses signal and power conducting wires, thereby eliminating the need for wet side batteries.—WT

6,215,734

43.30.Nb ELECTROHYDRAULIC PRESSURE WAVE PROJECTORS

William M. Moeny and Niels K. Winsor, assignors to Tetra Corporation
10 April 2001 (Class 367/147); filed 5 August 1996

The patent discusses electrohydraulic projectors, particularly those utilizing an electrical plasma in a liquid medium, to create acoustic pressure and/or shock waves. Methods for efficiently coupling the electrical current to the plasma are also discussed, as are many embodiments of the various components of the projectors and the use of multiple projectors in various arrays.—WT

6,222,794

43.30.Nb UNDERWATER NOISE GENERATOR ACTUATED BY MAGNETOINDUCTIVE/ACOUSTIC SIGNALS

Robert Woodall and Felipe Garcia, assignors to the United States of America as represented by the Secretary of the Navy
24 April 2001 (Class 367/1); filed 17 September 1999

An underwater noise source consists of a submerged container of a composition such as calcium carbonate that reacts with water to produce gas. The container also houses a receiver unit that is responsive to remotely generated acoustic or magnetoinductive signals in the extremely low frequency- or very low frequency ranges. Reception of an appropriate signal initiates an explosive squib that blows the lid off the container and also penetrates a protective covering over the composition, thus allowing water to flood in and react with the composition. The subsequent explosion of the resulting gas bubbles produces the radiated noise.—WT

6,226,227

43.30.Tg MANUAL SCAN IMAGING SONAR

Keith Lent and Kenneth Krueger, assignors to Board of Regents, The University of Texas System
1 May 2001 (Class 367/104); filed 25 March 1998

A manual scan sonar system comprises a transducer, orientation and motion sensors, power amplifier and preamplifier, and a microcomputer with display unit, all of which are contained within a compact waterproof housing. The user, either a diver or someone topside, scans the sonar across an area while the orientation and motion sensors monitor the user's motion to provide bearing information which is processed and stored in the microcomputer. The information provided by the sonar echoes is shown on the display unit. With a single-beam sonar, it is thus possible to generate wide sector views comparable to those of a multibeam sonar.—WT

6,192,006

43.30.Wi DEVICE FOR AND A METHOD OF DETERMINING THE ANGLE OF INCIDENCE OF A RECEIVED SIGNAL AND A SCANNING SONAR

Hiroshi Iino *et al.*, assignors to Furuno Electric Company Limited
20 February 2001 (Class 367/121); filed in Japan 30 January 1998

This transducer array is of general cylindrical shape, consisting of many elements arranged in multiple layers and columns (although the elements of adjacent layers may be circumferentially displaced from one another in brickwork fashion). A horizontal scan mode of operation is realized by forming a set of narrow horizontal beams from a phased subset of elements in each layer. A vertical scan mode is then realized by combining these horizontally focused beam signals, from one end of the array to the other, where the vertical angle of incidence is computed from the Doppler frequency shift associated with the sequential switching frequency at which these multiple horizontal beam signals are combined.—WT

6,201,764

43.30.Xm APPARATUS AND METHOD FOR CORRECTING FOR CAPACITANCE VARIATIONS IN HYDROPHONES

Charles Geoffrey Rice *et al.*, assignors to Input/Output, Incorporated
13 March 2001 (Class 367/21); filed 31 October 1997

In certain applications, the reverberation in a water column can be canceled by combining the outputs of adjacently positioned hydrophones and geophones. However, the low-frequency responses of these two types of sensors are fundamentally different. Therefore, to match the responses of the two types of sensors, the output of each hydrophone must be filtered. A procedure is described for *in situ* measurement of the capacitance of each hydrophone within an array which then allows adjustment of the frequency response characteristics of the individual filters associated with each hydrophone.—WT

6,208,584

43.30.Xm PLACE CALIBRATION OF SONAR RECEIVE ARRAY

Colin W. Skinner, assignor to L-3 Communications Corporation
27 March 2001 (Class 367/13); filed 16 September 1999

A system and methodology are described for the *in situ* calibration of each of the many hydrophones in a towed line array. Information about the relative amplitudes and phase angles of the receiving responses as well as the relative physical positions of the hydrophones can be computed.—WT

6,215,730

43.30.Yj SIDE-SCAN SONAR WITH SYNTHETIC ANTENNA

Marc Pinto, assignor to Thomson Marconi Sonar S.A.S.
10 April 2001 (Class 367/88); filed in France 10 December 1996

This side-scan, line-array sonar system has zeros in the transmission directivity pattern that are associated with a pair of transducers located at either end of the line array, and zeros of the reception directivity pattern that are associated with the entire line array. The system is implemented such that both sets of zeros coincide with alternate grating lobes of the directivity pattern of the synthetic antenna that is created when that actual antenna is towed through the water at some speed. This nulling of the grating lobes results in an increase in the range and hence the volume search rate of the sonar for a given speed.—WT

6,219,304

43.30.Yj DEVICE CAPABLE OF BEING SUBMERGED AND INCLUDING AN ACOUSTIC TRANSDUCER

Jean-Pierre Mignot and Paul Dinnissen, assignors to Asulab S.A.
17 April 2001 (Class 368/88); filed in Switzerland 28 August 1997

A method is described for mounting a tiny electroacoustic transducer within a diver's wristwatch case while maintaining waterproof integrity of the transducer and also providing an acoustical path to the surrounding water medium.—WT

6,221,038

43.35.Rw APPARATUS AND METHODS FOR VIBRATORY INTRALUMINAL THERAPY EMPLOYING MAGNETOSTRICTIVE TRANSDUCERS

Axel F. Brisken, assignor to Pharmasonics, Incorporated
24 April 2001 (Class 604/22); filed 9 August 1999

The patent covers an apparatus that is essentially an energy-transmitting catheter consisting of a catheter body with a vibrating assembly at its distal end. The vibrating assembly includes a magnetostrictive driver that is mechanically coupled to an interface member on the catheter for radiating energy into the surroundings at the distal end of the catheter body. The vibrating assembly usually also features a tail mass, an interface assembly, and a spring element which together constitute a resonant assembly for amplification of the displacement of the interface surface driven by the magnetostrictive driver. The catheter is said to be useful for treating luminal conditions, such as vascular clots and plaque. There is also an optional provision for delivering a therapeutic agent through the catheter before, during, or after application of the vibratory energy.—DRR

6,217,530

43.35.Wa ULTRASONIC APPLICATOR FOR MEDICAL APPLICATIONS

Roy W. Martin *et al.*, assignors to University of Washington
17 April 2001 (Class 601/2); filed 14 May 1999

Solid, tapered cones are mounted onto a preferably concave, spherically curved piezoelectric ultrasound transducer, which focuses and concentrates the ultrasonic energy into a narrow tip so that very high levels of therapeutic ultrasound can be delivered to the tissue in contact with the tip. The device can be used for presurgical and surgical procedures. The patent makes the argument that the contour of the tip provides improved ultrasonic coupling with the living tissue and that different configurations can be used to control the focusing of the ultrasonic signals. The materials of the cone can be selected for their respective acoustic impedances to accommodate passage of shear and longitudinal waves.—DRR

6,217,519

43.35.Yb DEVICE AND METHOD FOR OBSERVING VESSELS, SPECIALLY BLOOD VESSELS

Karl-Ernst Grund *et al.*, assignors to DWL Elektronische Systeme GmbH
17 April 2001 (Class 600/463); filed in Germany 25 March 1997

This apparatus for viewing blood vessels in body cavities and hollow organs consists of an ultrasonic transducer, which can be guided into a viewing position by an endoscope. The transducer is designed to detect an organ or fluid motion at a certain distance using a Doppler evaluation. The

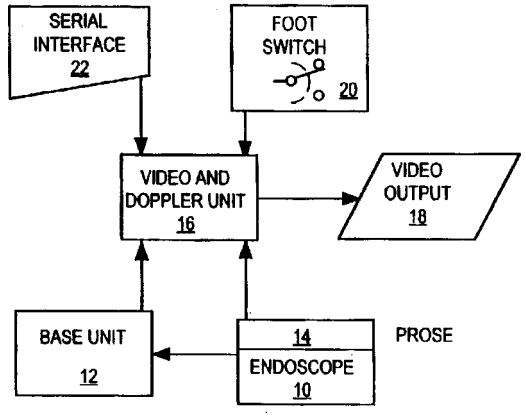

Doppler output signal is converted into a visual representation of the organ and/or fluid motion. A video output unit produces a combined overall image showing both an endoscopy image and a representation of the organ and/or fluid motion.—DRR

6,217,520

43.35.Yb DIAGNOSTIC MEDICAL ULTRASOUND SYSTEM AND METHOD FOR OBJECT OF INTEREST EXTRACTION

Anming He and Joan C. Main, assignors to Acuson Corporation
17 April 2001 (Class 600/467); filed 2 December 1998

This patent concerns a methodology said to be capable of delineating an object of interest without the necessity of manually tracing the borders of that object. A preferred embodiment operates with a diagnostic medical ultrasound system. The method consists of selecting a region of interest, selecting pixels to generate a binary ultrasound image, and performing one or more morphological operations on the image to extract the object of interest. Once an object has been extracted, operations such as contrast enhancement can be performed on that object.—DRR

6,160,894

43.38.Dv SPEAKER APPARATUS AND SOUND REPRODUCTION SYSTEM EMPLOYING SAME

Jun Kishigami *et al.*, assignors to Sony Corporation
12 December 2000 (Class 381/111); filed in Japan 28 May 1996

One of the first types of direct radiator loudspeakers produced commercially was the induction speaker. A fixed driving coil induces currents in a moving coil or directly in a conductive diaphragm. Induction speakers can be designed to handle high electrical power, but tend to be quite inefficient, especially at low frequencies. However, a multicoil, digitally driven induction speaker effectively transfers energy at a very high sampling frequency regardless of the frequency of its acoustic output. Possible designs for such a speaker, along with suitable driving circuitry, are disclosed in this patent.—GLA

6,211,601

43.38.Fx MULTI-TUNED ACOUSTIC CYLINDRICAL PROJECTOR

Robert J. Obara, assignor to the United States of America as represented by the Secretary of the Navy
3 April 2001 (Class 310/317); filed 4 March 1998

The invention is presumably intended for underwater sound generation, although the principles involved could be used in other applications. If piezoelectric transducers must operate over a substantial frequency range (''...broadband noise acoustic countermeasures''), then most of the current provided by the power amplifier is delivered to a highly reactive load. The patent describes a more efficient system employing two or more tuned power amplifiers, each connected to individual groups of ceramic cells.—GLA

6,215,881

43.38.Ja CEILING TILE LOUDSPEAKER

Henry Azima *et al.*, assignors to New Transducers Limited
10 April 2001 (Class 381/152); filed in the United Kingdom 2 September 1995

This is the latest in a series of patents relating to ''distributed mode'' panel-type loudspeakers. The practice of using an inertia transducer to drive a vibrating panel is at least 50 years old. Panel-type loudspeakers disguised as lay-in ceiling tiles have been commercially available for more than 10 years. But wait ... Using an inertia transducer to drive a ceiling tile loudspeaker apparently advances the art sufficiently to merit 11 patent claims.—GLA

6,226,927

43.38.Ja AUTOMOBILE VEHICLE DOOR PROVIDED WITH A MULTICOMPONENT MODULE A PART OF WHICH FORMS AN ACOUSTIC CAVITY

Carlo Bertolini and Laurent Arquevaux, assignors to Meritor Light Vehicle Systems, France
8 May 2001 (Class 49/502); filed in France 18 April 1997

A loudspeaker arrangement for an automobile vehicle door which includes a vented cavity, thus forming a ''bass reflex'' device with enhanced low-frequency performance.—KPS

6,219,431

43.38.Ja LOUDSPEAKER WITH IMPROVED COOLING STRUCTURE

Lucio Proni, Weston, Florida
17 April 2001 (Class 381/397); filed 29 October 1999

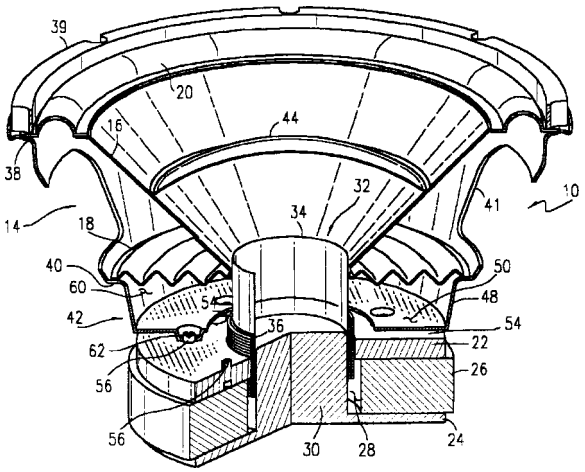

Speaker frame **48** has a flat bottom plate **50** which is spaced away from top plate **22**, forming a cavity **54** through which air is pumped by the motion of the ''spider'' **18**.—GLA

6,137,890

43.38.Ja LUMPED PARAMETER RESONATOR OF A PIEZOELECTRIC SPEAKER

Mitchell Markow, assignor to Compaq Computer Corporation
24 October 2000 (Class 381/330); filed 6 May 1997

Front plate **100** might be the screen of a laptop computer and rear plate **102** the case in which it is housed. Either or both may be driven by one or more piezoelectric transducers **118**. By controlling the resonance frequencies of the two panels and the mechanical coupling between them, extended low-frequency response can be obtained. Almost every conceivable variation is covered in the patent claims.—GLA

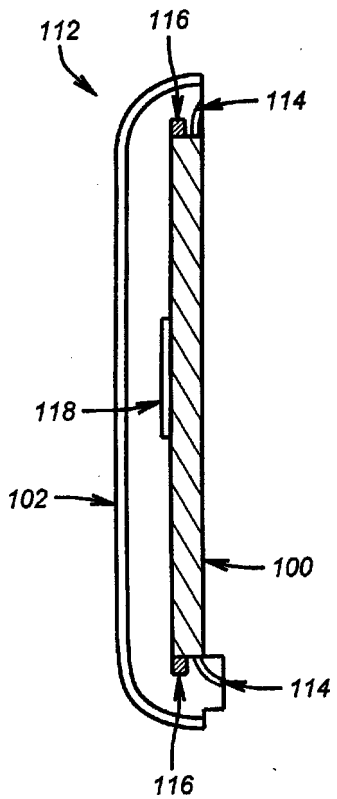

6,091,830

43.38.Kb TRANSMITTER STRUCTURE FOR LIMITING THE EFFECTS OF WIND NOISE ON A MICROPHONE

Nozomi Toki, assignor to NEC Corporation
18 July 2000 (Class 381/359); filed in Japan 19 July 1996

A small, simple microphone assembly includes a microphone element, a sound hole in the microphone case, and a slit filled with acoustically resistive material. The assembly is said to attenuate wind noise without the need for an external shield or special electronic circuitry.—GLA

6,147,787

43.38.Kb LASER MICROPHONE

James T. Veligdan, assignor to Brookhaven Science Associates; Brookhaven National Laboratory
14 November 2000 (Class 359/150); filed 12 December 1997

The invention is a practical, diaphragmless microphone intended for general use. It includes a laser resonator, a reference cell, and a sensing cell. Variations in air density produce sum and difference frequencies which are automatically heterodyned and detected by the sensing cell. According to the patent, ''Improved frequency response, dynamic range, and unlimited bandwidth are obtained. The objectionable popping 'P' sound is also eliminated.''—GLA

6,122,382

43.38.Vk SYSTEM FOR PROCESSING AUDIO SURROUND SIGNAL

Toshiyuki Iida and Tomohiro Mouri, assignors to Victor Company of Japan, Limited
19 September 2000 (Class 381/18); filed in Japan 11 October 1996

Most motion picture surround-sound recordings are transmitted or decoded as left, center, right, and surround channels. If such a recording is to be reproduced or re-recorded in the consumer two-channel stereo format, the required processing can range from simple panning to elaborate dynamic matrix techniques. The patent describes a method for sending derived left and right signals to left and right loudspeakers, plus deriving left rear and right rear signals and generating virtual rear sound sources from the same two loudspeakers.—GLA

6,215,879

43.38.Vk METHOD FOR INTRODUCING HARMONICS INTO AN AUDIO STREAM FOR IMPROVING THREE-DIMENSIONAL AUDIO POSITIONING

Morgan James Dempsey, assignor to Philips Semiconductors, Incorporated
10 April 2001 (Class 381/61); filed 19 November 1997

The idea of synthetically restoring upper harmonics that have been lost during the recording process is not new, but earlier patents were moslty concerned with analog recording and reproduction. Today we are involved with digital recording, and with using head-related transfer functions to create virtual sound sources. Some digital recordings, particularly sampled sounds, may have an upper-frequency cutoff as low as 5.6 kHz. The inventor argues that localization and subjective sound quality can both be improved by adding synthesized upper harmonic frequencies.—GLA

6,191,515

43.40.Tm COMBINED PASSIVE MAGNETIC BEARING ELEMENT AND VIBRATION DAMPER

Richard F. Post, assignor to The Regents of the University of California
20 February 2001 (Class 310/90.5); filed 3 September 1999

This patent pertains to a bearing system that employs arrangements of permanent magnets which act together to support a rotating element in a state of dynamic equilibrium. A piece of highly conductive nonmagnetic material, affixed to the nonrotating part of the bearing, serves to damp transverse vibrations of the rotor.—EEU

6,196,721

43.40.Tm SINUSOIDAL VISCOUS INTERFACE FOR ATTENUATION OF VIBRATION FOR BALL AND ROLLER BEARINGS

Stephen J. Farkaly, Indianapolis, Indiana
6 March 2001 (Class 384/99); filed 11 September 1998

The outer surface of the bearing race is constructed with an undulating surface, which mates with the inner surface of a mounting ring assembly. A viscous fluid between the mating surfaces provides damping to reduce the bearing vibrations within the race. Hydraulic ball valve systems maintain the predetermined fluid pressure.—EEU

6,199,801

43.40.Tm WHOLE-SPACECRAFT PASSIVE ISOLATION DEVICES

Paul S. Wilke and Conor D. Johnson, assignors to CSA Engineering, Incorporated
13 March 2001 (Class 244/170); filed 1 December 1997

A device for isolating a spacecraft from a launch vehicle must have high strength and long fatigue life, in addition to being compact. It must protect the spacecraft from high-frequency dynamic loads and be able to support it under high-G quasistatic accelerations with minimal movement. In addition, it must be completely linear, so that it can be taken into account computationally. The device described in this patent seeks to meet these requirements. It consists, in essence, of metal plate or beam elements that provide the necessary strength and linearity, with layers of viscoelastic material added to provide damping.—EEU

6,202,511

43.40.Tm VIBRATION DAMPED HAMMER

John C. Murray and David B. Scott, assignors to The Stanley Works
20 March 2001 (Class 81/22); filed 14 August 1998

Some isolation of the user's hand is achieved by use of a resilient material for the part of the hammer that is gripped. This material surrounds a metal element in the form of an I-beam, to which the hammer's head is attached. Longitudinal slots in the web of this element assist in providing good connection of this element to the grip.—EEU

6,202,961

43.40.Tm PASSIVE, MULTI-AXIS, HIGHLY DAMPED, SHOCK ISOLATION MOUNTS FOR SPACECRAFT

Paul S. Wilke *et al.*, assignors to CSA Engineering
20 March 2001 (Class 244/158 R); filed 21 March 2000

The isolation mount according to this patent consists, in essence, of a metal cylindrical shell, in which there is provided an array of partial circumferential slots, configured so that the remaining metal forms an array of stacked leaf springs. The outer and/or inner surface of the cylindrical element is covered with a layer of viscoelastic material, which is topped by a stiff constraining layer.—EEU

6,203,454

43.40.Tm MULTI-MODE VIBRATION ABSORBING DEVICE FOR IMPLEMENTS

Ahid D. Nashif and Gopichand Koganti, assignors to Roush Anatrol, Incorporated
20 March 2001 (Class 473/521); filed 28 December 1995

This patent pertains to a dynamic absorber (tuned damper) for use on hand-held implements, such as tennis rackets, golf clubs, and hammers. The absorber typically is placed at a location that constitutes an antinode of vibration in the lowest few modes of the implement. It consists, in essence, of a mass that is supported on an element made of a viscoelastic material, which provides both resilience and damping. The system consisting of the mass and its support element is configured to have natural frequencies that match the implement's natural frequencies which are to be suppressed.—EEU

6,196,528

43.40.Vn SPACECRAFT ANTENNA VIBRATION CONTROL DAMPER

Emil M. Shtarkman *et al.*, assignors to TRW, Incorporated
6 March 2001 (Class 267/140.14); filed 12 May 1998

The damper described in this patent is installed in a guideline cable that connects a point on the edge of an antenna dish to a relatively rigid support point on the spacecraft, so that the tension in the guideline is transmitted through the damper. The damper, in essence, consists of a flexible chamber that is filled with an electro-rheological or magneto-rheological fluid and surrounded by means for adjusting the electric or magnetic field that acts on the fluid. Strain sensors in the guideline and/or accelerometers at the antenna rim provide signals that are fed to a controller, which is programed to adjust the aforementioned electric or magnetic fields. Various embodiments include piezoelectric elements, mechanical springs, and foam pads.—EEU

6,196,529

43.40.Vn SPACECRAFT ANTENNA VIBRATION CONTROL DAMPER

Emil M. Shtarkman *et al.*, assignors to TRW, Incorporated
6 March 2001 (Class 267/140.14); filed 12 May 1998

The subject of this patent is the same as that of the foregoing one, except that the damper here is configured so as to include a rod that transmits the tension in the guideline. Extensional vibrations of the rod are suppressed by the action of magneto-rheological or electro-rheological fluid acting on a piston.—EEU

6,202,492

43.40.Vn ANTI-VIBRATION APPARATUS AND EXPOSURE APPARATUS

Tatsuya Ohsaki, assignor to Nikon Corporation
20 March 2001 (Class 73/662); filed in Japan 5 April 1996

This patent pertains predominantly to the control of vibrations in precision equipment, such as that used in the manufacture of microelectronics, in which a stage is moved stepwise in a horizontal plane between brief exposures to light or other radiation. The apparatus described here consists of a bed that is supported on air springs and provided with mechanical actuators. A control system that acts on the basis of signals from displacement sensors adjusts the pressure in the air springs to keep the bed horizontal. A second system, acting on the basis of signals derived from accelerometers, controls the actuators to suppress vibrations of the bed.—EEU

6,189,650

43.50.Gf MUFFLER STRUCTURE

Kazuhiro Inuzuka *et al.*, assignors to Futaba Industrial Company, Limited
20 February 2001 (Class 181/254); filed 23 August 1999

This is another in a series of automobile mufflers having a pressure-activated valve which creates a second flow path. A scheme is described

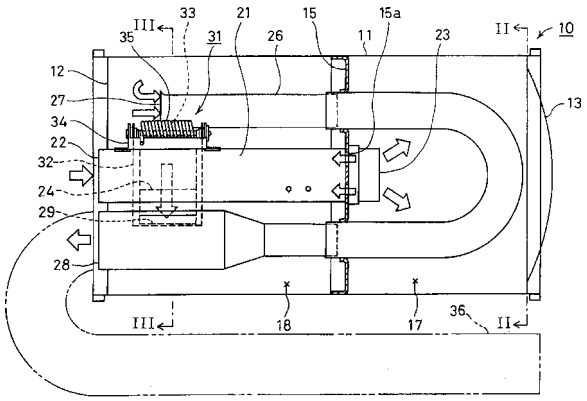

which aims to reduce chattering of the valve caused by exhaust gas pulsations.—KPS

6,196,351

43.50.Gf SILENCER CARTRIDGE

Neville Julian Clokey and George Christopher Frederick Balmer, assignors to Lancaster Glass Fibre Limited
6 March 2001 (Class 181/252); filed 4 June 1999

A silencer for incorporation into an automobile muffler is described in which an outer layer of needlemat **8** encloses sound-absorbent fibrous material **12**. The exhaust pipe (not shown) fits into the hollow core **4**. The

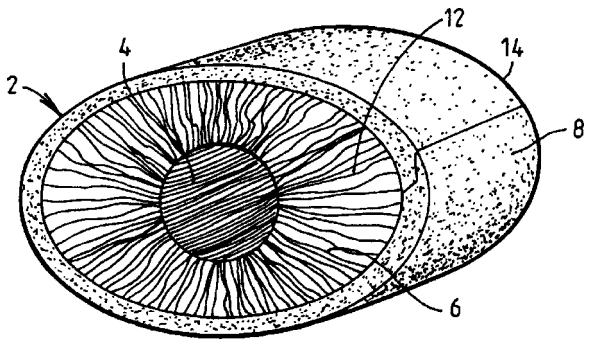

interesting aspect of this design is the arrangement of the fibers, all of which are substantially parallel to the flow direction of the exhaust. This arrangement is said to yield improved longevity of the acoustical performance of the muffler.—KPS

6,199,657

43.50.Gf MOTOR VEHICLE INTAKE MUFFLER DUCT

Kichiji Misawa *et al.*, assignors to Honda Giken Kogyo Kabushiki Kaisha; Tigers Polymer Corporation
13 March 2001 (Class 181/229); filed in Japan 14 October 1998

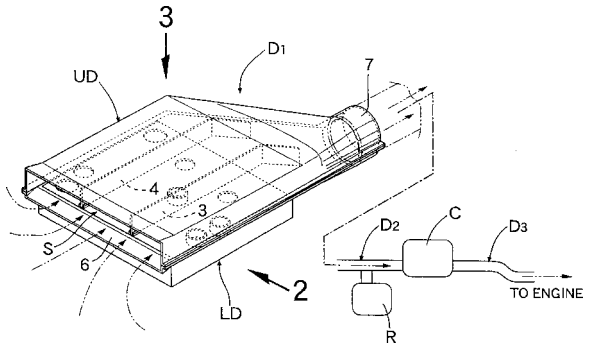

An air intake muffler for an automobile engine is described which consists of multiple flow paths and cavities. This compact device consists of only three components, making assembly easy and cost effective.—KPS

6,199,658

43.50.Gf MULTI-FOLD SIDE-BRANCH MUFFLER

Ronald G. Huff, assignor to JB Design, Incorporated
13 March 2001 (Class 181/265); filed 20 January 1998

A ''straight-through'' muffler intended for use in high-performance automobiles consists of a series of concentric cylinders forming multiple

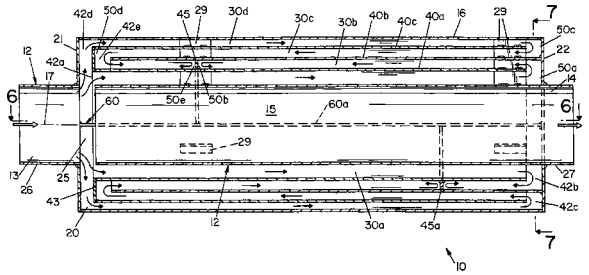

annular passages. Radial elements serve to tune the lengths of these multiple side-branch resonators to yield broadband sound attenuation. Various geometrical arrangements are described and acoustical performance is quantified.—KPS

6,202,702

43.50.GF ACOUSTIC DAMPING PIPE COVER

Yasuyuki Ohira and Mitsuo Hori, assignors to Shishiai-Kabushikigaisha
20 March 2001 (Class 138/149); filed 18 February 2000

This cover is intended for installation on water pipes and the like in buildings, in order to reduce the noise radiated from these pipes. The cover consists of a 4- to 10-mm-thick layer of foam in contact with the pipe, surrounded by a layer of rubber, which is topped by a layer of a dense material with a surface density between 1.5 and 5.0 kg per square meter. The outermost layer is covered by a sheet of a heat-contractile material, so that the assembly is ''shrink-wrapped'' onto a pipe when heat is applied to that sheet.—EEU

6,209,679

43.50.Gf AIRCRAFT ENGINE ACOUSTIC LINER AND METHOD OF MAKING SAME

William H. Hogeboom and Gerald W. Bielak, assignors to The Boeing Company
3 April 2001 (Class 181/286); filed 13 June 1996

An acoustic liner intended for use in aircraft engine nacelles is described. It consists of metal honeycomb sandwiched between a perforated face sheet and an impervious backing sheet. In contrast to conventional absorptive liners, the perforate in this design has a very high percentage of open area, yielding very low absorption. This liner configuration is alternated, axially, with areas of conventional absorptive liner. The idea is that the low-resistance liner scatters sound from low-order duct modes into higher-order modes which are more readily absorbed by the conventional higher-resistance liner segments. Methods to manufacture honeycomb liners of varying depths are also described.—KPS

6,213,251

43.50.Gf SELF-TUNING EXHAUST MUFFLER

Stephen H. Kesselring, Dothan, Alabama
10 April 2001 (Class 181/249); filed 24 September 1997

Exhaust gases from an internal combustion engine flow into inner pipe **24**. This pipe has a multitude of louvres which allows flow into the outer cavity formed by **24** and **30**. The gases exit from these concentric cavities at

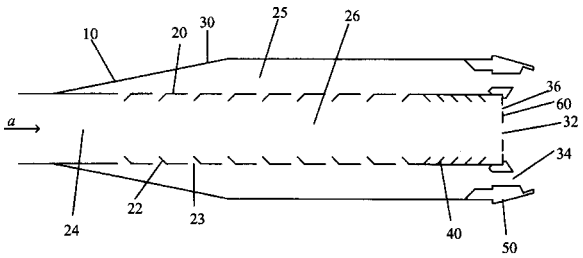

32 and **34**. The exit at annulus **34** contains a perforated disk and various geometric arrangements are described. The idea behind this design seems to be that high-frequency sound is attenuated in the outer cavity **34** and low-frequency sound by the inner one **32**.—KPS

6,220,387

43.50.Gf EXHAUST MUFFLER

Matthew S. Hoppes *et al.*, all of Phoenix, Arizona
24 April 2001 (Class 181/259); filed 21 October 1999

Exhaust gases enter the tapered inner tube **28** at **76**. The inner tube is surrounded by an outer tube **40** and the two are in fluid communication via elliptical holes **66**. The exhaust flow through the inner tube induces the

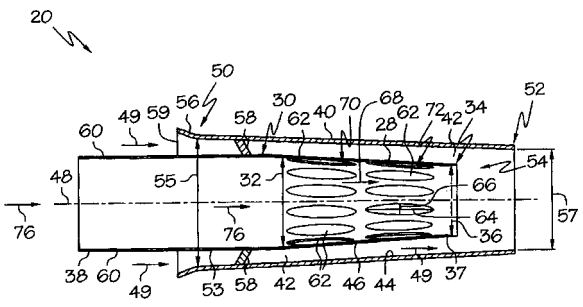

entrainment of ambient air which enters at **59**. The mixed flow exhaust exits at **54**. This mixing of hot exhaust gases with cool, ambient air is said to achieve effective noise attenuation.—KPS

6,205,765

43.50.Ki APPARATUS AND METHOD FOR ACTIVE CONTROL OF OSCILLATIONS IN GAS TURBINE COMBUSTORS

Robert J. Iasillo *et al.*, assignors to General Electric Company
27 March 2001 (Class 60/39.06); filed 6 October 1999

A method to control pressure oscillations in an industrial gas turbine combustor consists of a combination of passive (United States Patent 5,211,004) and active techniques. The active control system consists of a pressure transducer in the combustion chamber which provides a feedback control signal to the fuel system, rather than to actuators in the combustion chamber itself. The control signal is analyzed and control is achieved by modulation of the fuel flow.—KPS

6,195,608

43.50.Lj ACOUSTIC HIGHWAY MONITOR

Edward Fredrick Berliner *et al.*, assignors to Lucent Technologies, Incorporated
27 February 2001 (Class 701/118); filed 28 May 1993

A method for detecting the presence of vehicles on a roadway is described. An elevated microphone array is pointed at a region of the roadway and signal processing is used to sense the presence of a vehicle's acoustic emissions in the 3–8-kHz frequency range. This approach has advantages over the conventional detection method which requires an induction loop being buried within the road.—KPS

6,215,732

43.58.Dj EXPENDABLE DEVICE FOR MEASUREMENT OF SOUND VELOCITY PROFILE

David M. Nugent, assignor to the United States of America as represented by the Secretary of the Navy
10 April 2001 (Class 367/134); filed 17 September 1999

The system comprises an acoustic receiver mounted, for example, on a submarine and a source mounted on an expendable vehicle that moves throughout the water surrounding the submarine. Synchronized clocks are associated with both the source and the receiver. At predetermined times and transmitting locations, an acoustic signal is radiated from source to receiver. The sound velocity is computed from the measured propagation time and predetermined separation distance. A sound velocity profile is determined by using multiple transmitting locations.—WT

6,226,598

43.58.Dj METHOD OF MEASURING THE PROPAGATION TIME OF A SOUND SIGNAL IN A FLUID BY MEANS OF A ZERO-CROSSING OF SAID SOUND SIGNAL

Robert De Vanssay and Jérôme Juillard, assignors to Schlumberger Industries, S.A.
1 May 2001 (Class 702/48); filed in France 7 June 1996

This invention relates to a method of measuring the propagation time, and hence the speed of sound, between two transducers with a known separation distance by using a procedure for accurately determining the first zero-crossing time of the received signal.—WT

6,208,585

43.58.Vb ACOUSTIC LWD TOOL HAVING RECEIVER CALIBRATION CAPABILITIES

James W. Stroud, assignor to Halliburton Energy Services, Incorporated
27 March 2001 (Class 367/26); filed 26 June 1998

When drilling oil wells it is current practice to periodically check the qualities of the cement bonding to the bore by making an acoustic log. Such a test involves moving a transmitter and receiver through the length of the well bore. A novel feature of this invention, as compared with prior art, is a method of dynamically testing and calibrating the receiver unit during actual operation. ''Periodically, during normal logging service, the tool processor collects calibration data and sends the calibration data to the surface computer.''—GLA

6,236,025

43.60.Bf ACOUSTIC SENSING SYSTEM FOR BOIL-STATE DETECTION AND METHOD FOR DETERMINING BOIL STATE

Ertugrul Berkcan *et al.*, assignors to General Electric Company
22 May 2001 (Class 219/497); filed 19 March 1999

When water or another liquid is heated, it goes through a presimmer stage, characterized by a calm liquid, a simmer onset phase in which bubbles begin to appear, then a simmer phase characterized by bubbles appearing in jets, and finally a boil phase in which the bubbling of the liquid becomes more generalized, resulting in greater turbulence. The formation and collapse of bubbles during these phases generate an acoustic signature that changes with the size and number of bubbles, the rates of their formation and collapse, and the temperature gradients in the liquid. The acoustic response is also affected by the type of liquid undergoing the boiling process, type of cooking vessel, and the ingredients in the liquid. According to this patent, a cooking range is equipped with an acoustic sensing system for determining the boil state of the contents of a cooking utensil placed upon the cooking surface. The acoustic sensing system is designed to detect acoustic emissions in frequency ranges that are characteristic of boiling water or other liquids in a variety of cooking utensils. The sensing system can be interfaced with the cooktop control system, which provides for monitoring of the heating elements.—DRR

6,157,592

43.60.Dh ACOUSTIC POSITION DETERMINATION METHOD AND APPARATUS

J. Stanley Kriz and Patrick K. Garner, assignors to Resolution Displays, Incorporated
5 December 2000 (Class 367/127); filed 6 July 1998

In a virtual reality environment is is necessary to accurately and continuously locate the user, who may be moving fairly rapidly. Previously known methods utilize sonar techniques with at least three sequentially scanned transmitters and recievers. A number of trade-offs must be addressed which involve line of sight limitations, transit time, and susceptibility to external noise interference. This patent describes a method whereby receivers can quickly identify individual transmitters without signal demodulation. The invention is clearly described and will be of interest to anyone involved in the field.—GLA

6,226,605

43.60.Dh DIGITAL VOICE PROCESSING APPARATUS PROVIDING FREQUENCY CHARACTERISTIC PROCESSING AND/OR TIME SCALE EXPANSION

Yoshito Nejime *et al.*, assignors to Hitachi, Limited
1 May 2001 (Class 704/207); filed in Japan 23 August 1991

The proclaimed goal of the device is to assuage hearing function difficulties due to aging effects, partial sensorineural deafness, etc. The patent covers a digital acoustic signal-processing apparatus that can be applied in digital hearing aids and in ''appliances with sound output'' (e.g., television receivers, telephone sets, etc.). The apparatus consists of an acoustic signal memory, a filter, and a speech rate changer to reproduce the voice at lower

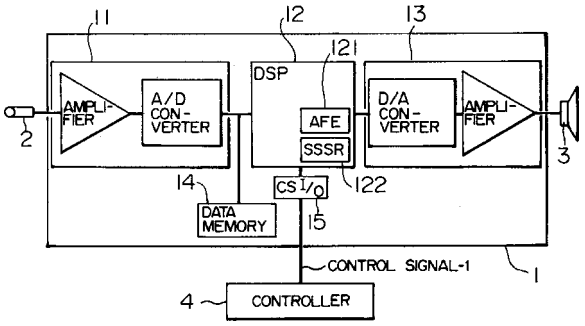

speed. In the example of a digital hearing aid, after the voice is stored in the memory and the time scale is expanded, the filtered speech signal (customized according to the user's hearing curve) is presented to the user at low speed. Also, a control system allows the user to repeat the voice playback.—DRR

6,230,130

43.60.Dh SCALABLE MIXING FOR SPEECH STREAMING

Paulo M. Castello da Costa *et al.*, assignors to U.S. Philips Corporation
8 May 2001 (Class 704/258); filed 18 May 1998

The patent describes a method and a system for processing audio signals, mixing concurrent streams of audio data. Mixing of speech streams is required at a receiver when multiple speech streams must be played out through a single audio device. Mixing of speech streams may be desired at an intermediate point in the transmission path (e.g., a server in a client/server architecture) when multiple speech streams are to be combined into a single stream for retransmission. According to this method, a subset of frames is selected from among the concurrent frames. The selected frames are decoded, mixed using optional stream-specific gains, and relayed to a receiver or set of receivers.—DRR

6,236,889

43.60.Dh METHOD AND APPARATUS FOR ACCOUSTICALLY COUPLING IMPLANTABLE MEDICAL DEVICE TELEMETRY DATA TO A TELEPHONIC CONNECTION

Orhan Soykan *et al.*, assignors to Medtronic, Incorporated
22 May 2001 (Class 607/30); filed 22 January 1999

The patent covers an apparatus and method for transmitting acoustic telemetry data produced by an implantable medical device over a commu-

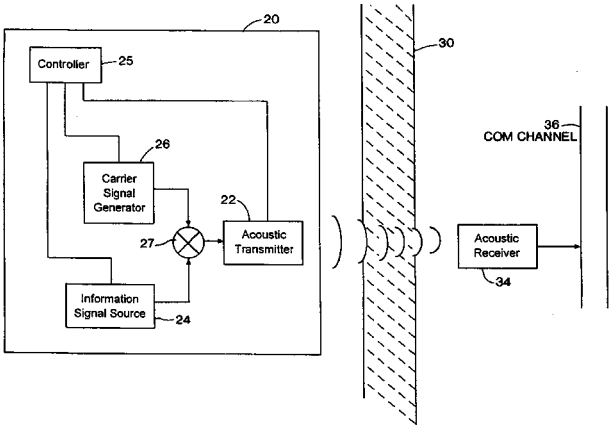

nication channel. The system includes a signal generator, a modulator, and an acoustic transmitter, each of which is provided in the implantable medical device. The modulator modulates a carrier signal with information acquired or produced by the implantable medical device. The modulated signal has a frequency range that is readily communicated through a public exchange channel, such as a conventional telephone system. The acoustic signal may contain digital telephonic tones, each having a frequency and format that conforms to one or more telephony standards. A number of different modulation techniques may be employed, including phase modulation, amplitude modulation, or frequency modulation. Examples of medical devices that may incorporate telephony circuitry of the present device include pacemakers, pacemaker/cardioverter/defibrillator (PCD) combinations, oxygen sensors, implantable hemodynamic monitor, and muscle- or nerve stimulation devices.—DRR

6,219,424

43.60.Qv ELECTRONIC STEREOPHONIC AMPLIFIER

Edward John Murphy, assignor to Hunter Area Health Service
17 April 2001 (Class 381/67); filed in Australia 4 May 1998

This device, essentially an amplified, stereo stethoscope, consists of two diaphragm-type sound accumulator chambers. A microphone is located in each chamber and is connected to an amplification stage. The amplified audio output signals may be sent to headphones, signal processors, or loudspeakers. The device is intended to provide a sense of directionality and spatiality that is lacking in current ''monaural'' stethoscopes.—DRR

6,199,036

43.72.Ar TONE DETECTION USING PITCH PERIOD

Masoud Ahmadi, assignor to Nortel Networks Limited
6 March 2001 (Class 704/207); filed 25 August 1999

Electronic speech communications systems typically use a variety of single and dual sinusoidal tones imposed upon the speech signal for transmitting various signal conditions. Such tones can be garbled by speech-processing algorithms, particularly echo cancellers, to the point that they fail to serve their original signaling purpose. This system detects such tones by running an autocorrelator in parallel with the normal speech-coding process. A peak detector applied to the autocorrelation output detects peaks which

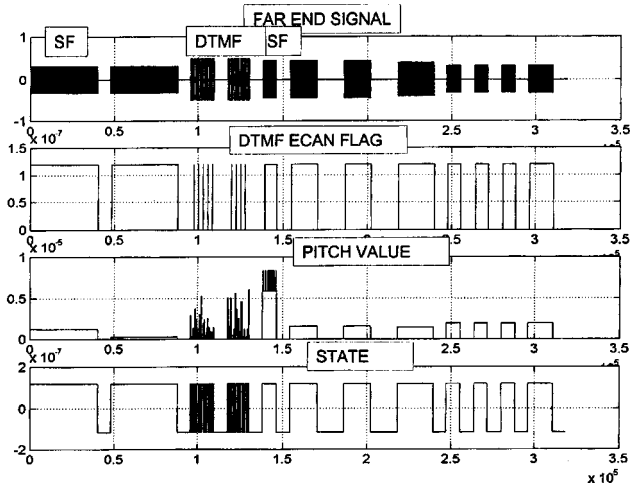

identify any tones present. Ideally, the peak detector will have access to a reference catalog of possible tones, making the tone identification faster and more accurate.—DLR

6,199,037

43.72.Ar JOINT QUANTIZATION OF SPEECH SUBFRAME VOICING METRICS AND FUNDAMENTAL FREQUENCIES

John C. Hardwick, assignor to Digital Voice Systems, Incorporated
6 March 2001 (Class 704/208); filed 4 December 1997

This speech compression system computes subframe values for both voicing and pitch parameters based on the previous frame values and differences between predicted and current subframe values. The basic coding model is the multiband excitation technique, in which individual frequency bands are assigned independent voicing and pitch values. For this model, it is important to minimize the number of bits used to code voicing and pitch information. Once the subframe residuals have been computed, then voicing and pitch values for the past and current frames are used to determine the most compact quantizations of these values for the current frame.—DLR

6,202,075

43.72.Ar SECOND ORDER LMS TAP UPDATE ALGORITHM WITH HIGH TRACKING CAPABILITY

Kameran Azadet, assignor to Lucent Technologies, Incorporated
13 March 2001 (Class 708/322); filed 7 December 1998

This device seems to be a hardware implementation of a well-known public domain adaptive filter algorithm. The finite impulse response (FIR) input signal is sent to a bank of adaptor circuits as well as to the filter input. Each adaptor circuit consists of a correlation multiplier, a loop filter, and an integrator, all connected in series. Each such circuit feeds the corresponding FIR filter tap, adjusting it so as to maintain a minimum value for the difference between the filter output and a reference signal.—DLR

6,205,422

43.72.Ar MORPHOLOGICAL PURE SPEECH DETECTION USING VALLEY PERCENTAGE

Chuang Gu *et al.*, assignors to Microsoft Corporation
20 March 2001 (Class 704/233); filed 30 November 1998

This speech-presence detector is primarily based on a feature known as the valley percentage (VP). The VP measure consists of the ratio of energy minimum to energy maximum within a narrow time window. The window is then advanced by one sample and a new ratio is computed. The resulting

ratio sequence is compared to a threshold, resulting in a sample-by-sample peakiness measure. This is smoothed by so-called morphological filters, which seem to function somewhat like median filters, but are also based on maximum and minimum sample values within a sliding window. The method is said to achieve accurate speech-start- and speech-ending epochs.—DLR

6,205,424

43.72.Fx TWO-STAGED COHORT SELECTION FOR SPEAKER VERIFICATION SYSTEM

William D. Goldenthal and Brian S. Eberman, assignors to Compaq Computer Corporation
20 March 2001 (Class 704/247); filed 31 July 1996

This speaker verification system uses two sets of precomputed coefficients to rate whether a given unknown speaker is who the person claimed to be. An initial training set consists of some minimum number of speakers. For this speaker set, ''self-comparison'' scores and all possible ''cohort-comparison'' scores are computed. When an unconfirmed speaker uses the system, a self-score is computed and cohort scores are computed for each registered user. The new self- and cohort scores are compared with the training scores to determine the identity of the test speaker.—DLR

6,195,640

43.72.Ja AUDIO READER

John Martin Mullaly and Winslow Scott Burleson, assignors to International Business Machines Corporation
27 February 2001 (Class 704/260); filed 29 January 1999

The device described here combines a text-to-speech synthesizer system with an eye-gaze tracker, used to locate the phrases or sentences to be spoken and triggering the audio output spoken from that written material. This allows the user to skip around through a body of text displayed on a computer screen.—DLR

6,202,048

43.72.Ja PHONEMIC UNIT DICTIONARY BASED ON SHIFTED PORTIONS OF SOURCE CODEBOOK VECTORS, FOR TEXT-TO-SPEECH SYNTHESIS

Katsumi Tsuchiya *et al.*, assignors to Kabushiki Kaisha Toshiba
13 March 2001 (Class 704/260); filed in Japan 30 January 1998

This speech synthesizer is based on a linear prediction (LP) codebook, such as used in an LP vocoder. The phonetic sequence to be synthesized is converted by dictionary look-up into a sequence of LP spectral and excitation codes, represented in the form of codebook entries. A gain value is produced for each code segment based on the desired prosodic structure. An additional shift parameter provides a wider choice of excitation signals. The code sequence is then processed by a typical vocoder synthesis filter to produce the speech output signal.—DLR

6,202,049

43.72.Ja IDENTIFICATION OF UNIT OVERLAP REGIONS FOR CONCATENATIVE SPEECH SYNTHESIS SYSTEM

Nicholas Kibre and Steve Pearson, assignors to Matsushita Electric Industrial Company, Limited
13 March 2001 (Class 704/267); filed 9 March 1999

Concatenative speech synthesis consists of a sequence of selected phonetic units of some specific coded type joined together either as waveform segments or, more typically, in some coded form which is then passed through a corresponding decoder. In this system, multiple training examples of each vowel are analyzed to produce Markov models which separately represent the nucleus and transition portions of the vowel. A method known as embedded reestimation is then used to compute optimal boundaries for the vowel portions. Such boundary markers are used to join particular coded speech segments from the original speech database to produce the synthetic output.—DLR

6,205,420

43.72.Ja METHOD AND DEVICE FOR INSTANTLY CHANGING THE SPEED OF A SPEECH

Tohru Takagi *et al.*, assignors to Nippon Hoso Kyokai
20 March 2001 (Class 704/211); filed in Japan 19 March 1997

This patent makes the argument that a person with hearing difficulties can sometimes understand speech better when it is spoken more slowly. In order to provide that capability for a person wearing a hearing aid, this device records live speech input, such as from the hearing aid pickup, and replays the material at a lower speech rate. Incoming speech material is analyzed by autocorrelation, zero crossings, power level, and pitch detection, and classified as voiced, voiceless, or silence. The input is then segmented into blocks for storage in memory, with the block length dependent on the classification. Voiced material is ideally stored in pitch–period–length blocks. During playback, blocks can be skipped or repeated according to the current rate setting.—DLR

6,201,960

43.72.Kb SPEECH QUALITY MEASUREMENT BASED ON RADIO LINK PARAMETERS AND OBJECTIVE MEASUREMENT OF RECEIVED SPEECH SIGNALS

Tor Björn Minde *et al.*, assignors to Telefonaktiebolaget LM Ericsson (publ)
13 March 2001 (Class 455/424); filed 24 June 1997

This patent describes a method of combining various objective and statistical measures of the quality of speech transmitted by a telecommunications system in order to better approximate a true perceptual evaluation of the received quality. Such a communication system may involve various speech coding systems, coding rates, and packet protocols, each contributing to the overall quality. The patented method considers measures such as bit

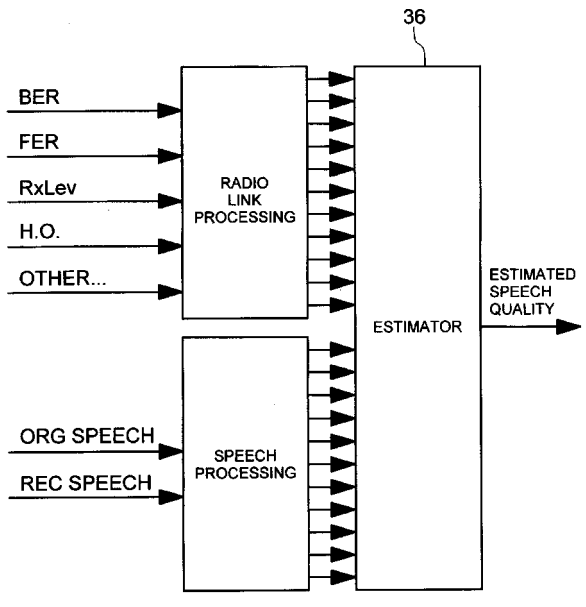

error rate, frame error rate, received level, and handover statistics. In addition, an evaluation is performed using an existing measure, such as the perceptual speech quality measure, as specified by ITU standards. The various measures are combined, either by linear weighting or by neural network, to derive a final speech quality measure.—DLR

6,202,046

43.72.Kb BACKGROUND NOISE/SPEECH CLASSIFICATION METHOD

Masahiro Oshikiri *et al.*, assignors to Kabushiki Kaisha Toshiba
13 March 2001 (Class 704/233); filed in Japan 23 January 1997

This speech frame classifier makes a three-way decision of voiced, unvoiced, or nonspeech for use by subsequent processing stages. The speech frame classification is based on a frame power measurement and a line spectral pairs analysis which includes a pitch period analysis. Estimates of

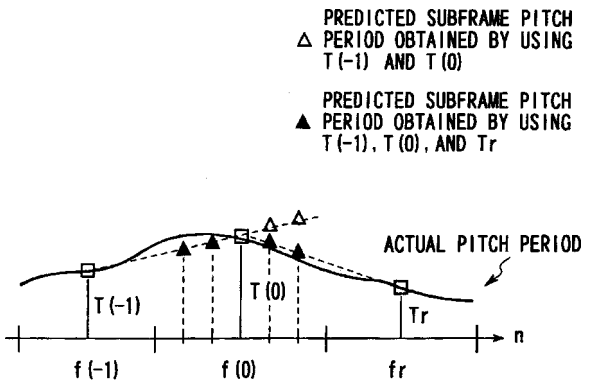

these measures based on the previous frame, especially the pitch period, are compared to the current values. Fluctuations of both power and spectral content indicate nonspeech. Otherwise, pitch continuity provides a voicing indication.—DLR

6,202,050

43.72.Kb WITHOUT LOSING WORDS OF VOICE ACTIVATE TRANSMITTING DEVICE FOR TWO-WAY RADIO

Stephen Chen, assignor to E. Lead Electronic Company, Limited
13 March 2001 (Class 704/275); filed 16 February 1999

This voice-activated, two-way radio device includes a digital memory unit used to introduce a delay in the transmitted signal when a voice activation event is detected. During nontransmit periods, the microphone signal is stored in a continuous loop manner in the memory and is also processed by the voice detector circuit. When a voice start event is detected, the microphone signal continues to be stored while previous memory contents are retrieved for transmission. The memory thus acts as a delay line inserted between the microphone and the transmitter.—DLR

6,195,638

43.72.Ne PATTERN RECOGNITION SYSTEM

Gabriel Ilan and Jacob Goldberger, assignors to Art-Advanced Recognition Technologies, Incorporated
27 February 2001 (Class 704/241); filed in Israel 30 March 1995

The patent describes in detail how to compute a constrained dynamic time-warping solution in which the traced path must, at all times, remain within a bounded region enclosing the diagonal line from start to finish. The method has been described thoroughly in speech recognition literature from the 1970s.—DLR

6,195,639

43.72.Ne MATCHING ALGORITHM FOR ISOLATED SPEECH RECOGNITION

Alberto Jimenez Feltström and Jim Rasmusson, assignors to Telefonaktiebolaget LM Ericsson (publ)
27 February 2001 (Class 704/252); filed 14 May 1999

As speech recognition designers struggle to put complete systems on a single chip, old speaker-dependent algorithms, which were deemed primitive in the 1980s as speaker-independent systems flourished, are now seeing something of a comeback, often with new optimizations. This system minimizes memory accesses for stored reference patterns, doing as much as possible with each retrieved pattern before going on to the next.—DLR

6,199,041

43.72.Ne SYSTEM AND METHOD FOR SAMPLING RATE TRANSFORMATION IN SPEECH RECOGNITION

Fu-Hua Liu and Michael A. Picheny, assignors to International Business Machines Corporation
6 March 2001 (Class 704/231); filed 20 November 1998

The sample rate referred to in the title of this patent seems to relate to the frequency structure of the cepstral vectors and is only indirectly related to the sample rate used for analog to digital conversion of the speech signal. It is of course true that a change in the frequency basis of the mel-scale filter structure would affect the usefulness of existing reference data and could, as a result, require full retraining. It is this the patented method seeks to avoid. The method involves forward- and reverse discrete cosine transforms applied to the existing cepstral data in order to make those data conform to a new mel-scale frequency structure.—DLR

6,199,043

43.72.Ne CONVERSATION MANAGEMENT IN SPEECH RECOGNITION INTERFACES

Alan J. Happ, assignor to International Business Machines Corporation
6 March 2001 (Class 704/272); filed 24 June 1997

This patent addresses some of the many problems involved in setting up a computer system to conduct an interview with a human participant. Just a few of those problems are the lack of facial cues or voice nuances from the computerized interviewer and the uncooperative nature of the recognition system due to misunderstandings, vocabulary limitations, and disregard for interruptions. The described approach uses multiple video displays in addition to the synthetic speech output to increase the amount of system information available to the human participant. A recorded human actor reading prepared phrases is shown on one channel, while a synthetically generated figure synchronized with the synthetic output speech is shown on the second channel.—DLR

6,202,047

43.72.Ne METHOD AND APPARATUS FOR SPEECH RECOGNITION USING SECOND ORDER STATISTICS AND LINEAR ESTIMATION OF CEPSTRAL COEFFICIENTS

Yariv Ephraim and Mazin G. Rahim, assignors to AT&T Corporation
13 March 2001 (Class 704/256); filed 30 March 1998

Various methods have been used in the past to adapt a hidden Markov model parameter set collected in noisy conditions for use in a recognition system under quiet conditions. This patent offers a new method for that

adaptation based on the second-order properties of the cepstral data. In one version, cepstral features are processed using a fixed, signal-independent diagonal matrix as the Markov covariance matrix. In another version, a new cepstral vector is generated from an explicit linear least-mean-square error estimate of the noisy speech signal. The patent includes a fairly detailed mathematical treatment of the described techniques.—DLR

6,205,425

43.72.Ne SYSTEM AND METHOD FOR SPEECH RECOGNITION BY AERODYNAMICS AND ACOUSTICS

Kit-Fun Ho, Shatin, Hong Kong Special Administrative Region of the People's Republic of China
20 March 2001 (Class 704/251); filed 22 September 1989

This speech recognition system is said to be able to achieve superior levels of accuracy by means of sensing oral air-flow patterns as well as

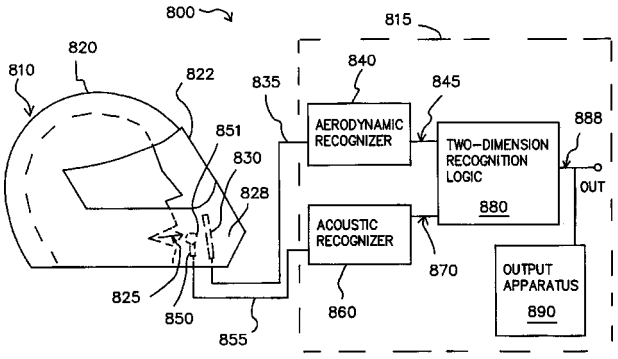

sampling the audio speech signal. An additional factor is the relative isolation of the speaker due to the helmet which contains the microphone and air-flow sensors.—DLR

6,195,641

43.72.Ne NETWORK UNIVERSAL SPOKEN LANGUAGE VOCABULARY

Keith Loring and Paratosh Patel, assignors to International Business Machines Corporation
27 February 2001 (Class 704/275); filed 27 March 1998

This multiuser speech recognition system maintains vocabulary lists both in the individual user stations and in the central server. Each client station has the ability to create new vocabulary items from user input if the needed item is not available either at the client station or from the server. New vocabulary items generated by any client user are transmitted back to the server, where they can be used as needed by any other client.—DLR

6,208,965

43.72.Pf METHOD AND APPARATUS FOR PERFORMING A NAME ACQUISITION BASED ON SPEECH RECOGNITION

Deborah W. Brown *et al.*, assignors to AT&T Corporation
27 March 2001 (Class 704/246); filed 20 November 1997

This patent describes a method for recognizing a user's ID, such as a name, an account number, or a password. This is done by matching the input ID with comparison IDs that are generated from the user's input ID. Rather than a prestored set of references IDs, the system requires that the user

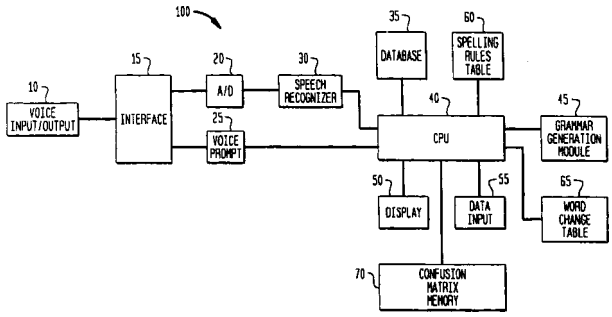

provide the input ID according to specific rules. The system then generates several comparison IDs and prompts the user to provide another ID in a different form. A confusion matrix **70** provides a high degree of accuracy in finding a match.—HHN

6,234,975

43.80.Qf NONINVASIVE METHOD OF PHYSIOLOGIC VIBRATION QUANTIFICATION

Kenneth J. McLeod *et al.*, assignors to Research Foundation of the State University of New York
22 May 2001 (Class 600/552); filed 5 August 1997

The patent describes a method of detecting the onset of osteoporosis, which entails measuring the vibrational response of the musculoskeletal system. Risk of bone fracture due to osteoporosis stems from three factors: muscle strength, bone mass, and postural stability. These three risk factors can be noninvasively determined by quantifying physiological vibration using a low-mass accelerometer placed at an appropriate muscle. Presence of vibrations below 5 Hz indicates postural instability. In addition, a specific frequency component (25–50 Hz) represents the contribution of fast-oxidative fibers, which correlates well to the bone mineral density of humans.—DRR

Transverse, normal modes of vibration of a cantilever Timoshenko beam with a mass elastically mounted at the free end (L)

C. A. Rossit[a] and P. A. A. Laura[a),b)]
Department of Engineering, Universidad Nacional del Sur, 8000-Bahía Blanca, Argentina

(Received 25 September 2000; accepted for publication 12 September 2001)

An exact solution for the title problem is obtained by means of the classical eigenfunction approach. The natural frequencies are computed for a wide range of the intervening mechanical and geometric parameters. Normal modes of transverse vibration are plotted for some cases of practical interest. The problem is technically important in several areas of applied science and technology. © *2001 Acoustical Society of America.* [DOI: 10.1121/1.1416908]

PACS numbers: 43.40.At [PJR]

I. INTRODUCTION

The problem of transverse vibrations of structural elements (beams and plates) carrying masses rigidly attached to the support structure is of great technological importance in several fields of engineering: from civil engineering situations to mechanical, naval and aerospace systems passing through electronic packages which operate under severe dynamic excitations. Several studies are available on the subject matter.[1–3]

When shear and rotatory inertia effects are taken into account the problem is considerably more complex and the number of investigations published in the open literature is considerably more scarce.[4] The situation is even more critical if the mass is elastically attached to the structural element.[5]

The present investigation deals with the determination of natural frequencies and normal modes of transverse vibration of the system shown in Fig. 1.

II. ANALYTICAL SOLUTION

When the system vibrates in one of its normal modes one expresses the transverse displacement, $v(x,t)$, and the angle of rotation due to flexure $\psi(x,t)$ in the following manner:

$$v(x,t)=V(x)e^{i\omega t}, \tag{1}$$

$$\psi(x,t)=\psi(x)e^{i\omega t}, \tag{2}$$

where ω is the natural, circular frequency.

The solution of the system of differential equations of the Timoshenko beam is well known and may be expressed in the form[4]

$$V(x)=C_1\sin\alpha x+C_2\cos\alpha x+C_3\sinh\beta x+C_4\cosh\beta x, \tag{3}$$

$$L\psi(x)=-C_1\left(\frac{\delta}{\alpha L}\right)\cos\alpha x+C_2\left(\frac{\delta}{\alpha L}\right)\sin\alpha x+C_3\left(\frac{\varepsilon}{\beta L}\right)\cosh\beta x+C_4\left(\frac{\varepsilon}{\beta L}\right)\sinh\beta x, \tag{4}$$

where

$$\alpha=\sqrt{(H+\sqrt{H^2-4F})/2}, \tag{5a}$$

$$\beta=\sqrt{(-H+\sqrt{H^2-4F})/2}, \tag{5b}$$

$$\delta=\Omega^2\eta\lambda-\alpha^2L^2, \tag{6a}$$

$$\varepsilon=\Omega^2\eta\lambda+\beta^2L^2, \tag{6b}$$

$$H=[(1+\lambda)\Omega^2\eta]/L^2, \tag{7a}$$

$$F=[\Omega^2(\Omega^2\eta^2\lambda-1)]/L^4, \tag{7b}$$

$$\lambda=[2(1+\upsilon)]/k, \tag{8a}$$

$$\eta=r^2/L^2=I/A_0L^2, \tag{8b}$$

$$\Omega^2=\omega^2L^4(\rho A_0/EI), \tag{8c}$$

where k is the shear factor.

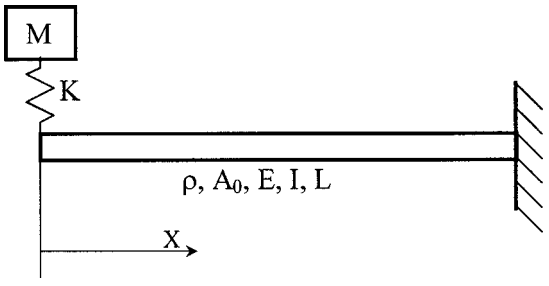

FIG. 1. Structural system under study.

[a)]Research scientist, CONICET.
[b)]Electronic mail: ima@criba.edu.ar

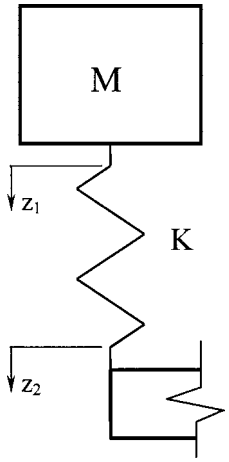

FIG. 2. Analysis of the discrete system attached to the beam tip.

The governing boundary conditions are

$$d\psi/dx|_{x=0}=0, \tag{9}$$

$$EA/\lambda\,[\psi(0)-|dV/dx|_{x=0}]=F_s, \tag{10}$$

$$V(L)=0, \tag{11}$$

$$\psi(L)=0, \tag{12}$$

where F_s is the force transmitted to the beam through the spring defined by its constant K.

Referring to Fig. 2 one determines F in the following fashion.[5] Let z_1 be the displacement of the mass M and z_2 the one corresponding to the other end of the spring. Accordingly one has

$$M(d^2z_1/dt^2)=K(z_2-z_1). \tag{13}$$

Defining

TABLE I. Values of frequency coefficients of the system shown in Fig. 1 for $r/L=0.01$.

K_1	m	Ω_1	Ω_2	Ω_3	Ω_4	Ω_5	Ω_6
⋯	0	⋯	3.512 65	21.8889	60.7409	117.516	191.18
0.1	0.2	0.695 153	3.571 3	21.898	60.7442	117.518	191.181
	0.5	0.439 825	3.569 91	21.898	60.7442	117.518	191.181
	1	0.311 043	3.569 46	21.898	60.7442	117.518	191.181
	2	0.219 939	3.569 24	21.898	60.7442	117.518	191.181
	3	0.179 611	3.569 16	21.898	60.7442	117.518	191.181
1	0.2	1.851 65	4.220 86	21.9808	60.7733	117.532	191.19
	0.5	1.205 22	4.101 43	21.9803	60.7732	117.532	191.19
	1	0.859 305	4.067 65	21.9801	60.7732	117.532	191.19
	2	0.610 001	4.0518	21.9800	60.7732	117.532	191.19
	3	0.498 694	4.046 66	21.9800	60.7732	117.532	191.19
10	0.2	2.528 59	9.3003	22.936	61.0723	117.681	191.279
	0.5	1.882 73	7.922 33	22.8719	61.0696	117.681	191.279
	1	1.418 75	7.440 48	22.8521	61.0687	117.681	191.279
	2	1.037 39	7.198 43	22.8425	61.0683	117.681	191.279
	3	0.856 732	7.117 89	22.8393	61.0681	117.681	191.279
∞	0.2	2.610 88	18.1103	52.8401	105.477	175.167	260.561
	0.5	2.015 08	16.8160	51.0214	103.425	172.997	258.340
	1	1.556 44	16.1700	50.2317	102.596	172.156	257.502
	2	1.157 60	15.7838	49.7918	102.149	171.710	257.062
	3	0.962 328	15.6438	49.6377	101.995	171.558	256.912

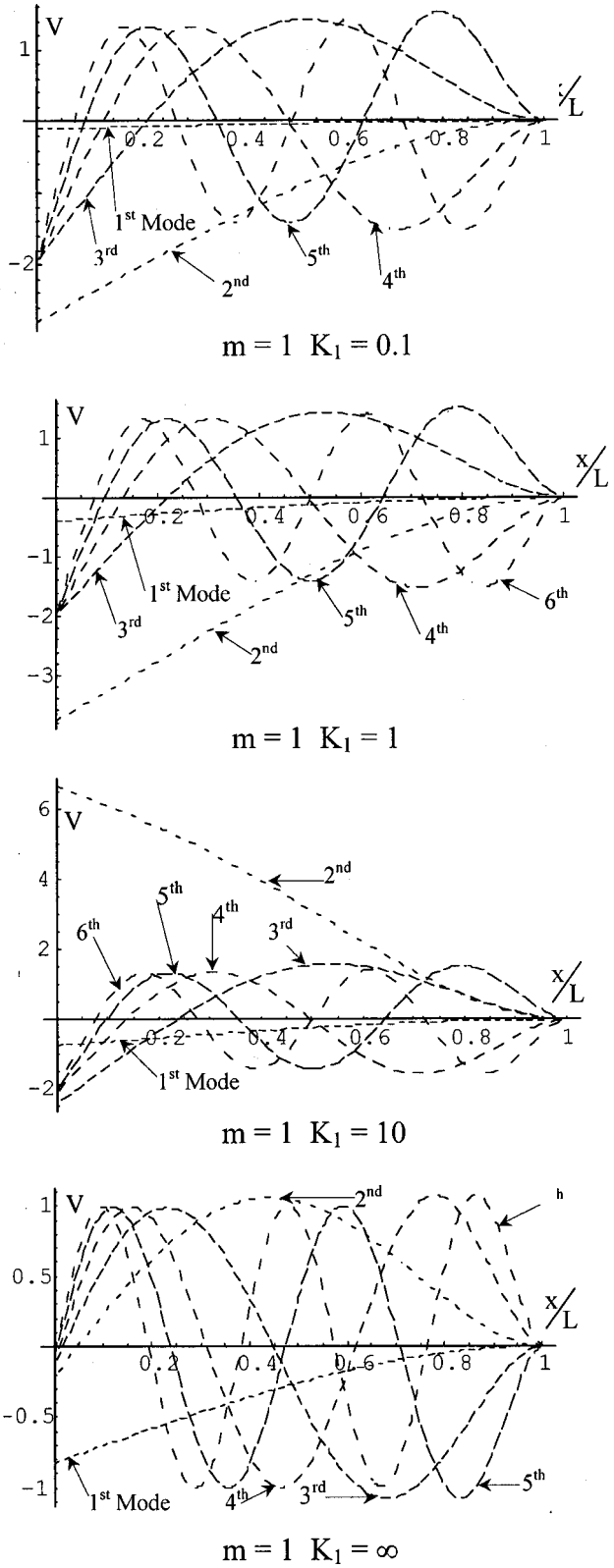

FIG. 3. Model shapes for $r/L=0.01$.

TABLE II. Values of frequency coefficients of the system shown in Fig. 1 for $r/L=0.05$.

K_1	m	Ω_1	Ω_2	Ω_3	Ω_4	Ω_5	Ω_6
⋯	0	⋯	3.435 27	19.1036	46.6031	78.9022	113.750
0.1	0.2	0.694 873	3.493 78	19.1124	46.6062	78.9037	113.751
	0.5	0.439 659	3.492 33	19.1124	46.6062	78.9037	113.751
	1	0.310 927	3.491 86	19.1124	46.6062	78.9037	113.751
	2	0.219 873	3.491 63	19.1124	46.6062	78.9037	113.751
	3	0.179 53	3.491 55	19.1124	46.6062	78.9037	113.751
1	0.2	1.841 62	4.147 18	19.1927	46.6337	78.9174	113.759
	0.5	1.200 78	4.022 87	19.192	46.6337	78.9174	113.759
	1	0.856 542	3.987 88	19.1917	46.6337	78.9174	113.759
	2	0.608 171	3.971 48	19.1916	46.6337	78.9174	113.759
	3	0.497 234	3.966 17	19.1916	46.6337	78.9174	113.759
10	0.2	2.490 03	9.140 84	20.1613	46.9218	79.0568	113.84
	0.5	1.8601	7.772 75	20.0759	46.9174	79.0561	113.839
	1	1.403 97	7.291 43	20.0501	46.9159	79.0558	113.839
	2	1.027 52	7.0492	20.0377	46.9152	79.0557	113.839
	3	0.848 861	6.968 55	20.0336	46.9149	79.0557	113.839
∞	0.2	2.567 34	16.1768	41.6733	72.9088	107.23	143.104
	0.5	1.986 35	15.1074	40.3738	71.6557	106.056	142.035
	1	1.536 36	14.5623	39.7905	71.1294	105.58	141.608
	2	1.143 65	14.2331	39.4607	70.8408	105.323	141.379
	3	0.951 041	14.1131	39.3444	70.7405	105.234	141.300

$$z=z_2-z_1 \tag{14}$$

and replacing in (13) one obtains

$$M(d^2z_2/dt^2)=Kz+M(d^2z/dt^2)\,, \tag{15}$$

and since

$$z_2=W(0)e^{i\omega t}, \tag{16}$$

substituting in (15) results in

$$M\,(d^2z/dt^2)+Kz=-\omega^2MW(0)e^{i\omega t}. \tag{17}$$

whose particular solutions is

$$z=[\,\omega^2MW(0)/\omega^2M-K]\,e^{i\omega t}. \tag{18}$$

Accordingly,

$$F_s=Kz=[\,\omega^2MW(0)/\omega^2M/K-1]\,e^{i\omega t}. \tag{19}$$

Substituting (3) and (4) in the governing boundary conditions and applying the nontriviality requirement to the resulting homogeneous system of equations,

$$\begin{vmatrix} 0 & \dfrac{\delta}{L^2} & 0 & \dfrac{\varepsilon}{L^2} \\ -\left(\dfrac{\delta}{\alpha L}+\alpha L\right) & -\dfrac{\Omega^2 m\,\eta\lambda}{1-\Omega^2 m/K_1} & \left(\dfrac{\varepsilon}{\beta L}-\beta L\right) & -\dfrac{\Omega^2 m\,\eta\lambda}{1-\Omega^2 m/K_1} \\ \sin\alpha L & \cos\alpha L & \sinh\beta L & \cosh\beta L \\ -\dfrac{\delta}{\alpha L}\cos\alpha L & \dfrac{\delta}{\alpha L}\sin\alpha L & \dfrac{\varepsilon}{\beta L}\cosh\beta L & \dfrac{\varepsilon}{\beta L}\sinh\beta L \end{vmatrix}=0, \tag{20}$$

where $m=M/\rho A_0L$ and $K_1=K/(EI/L^3)$.

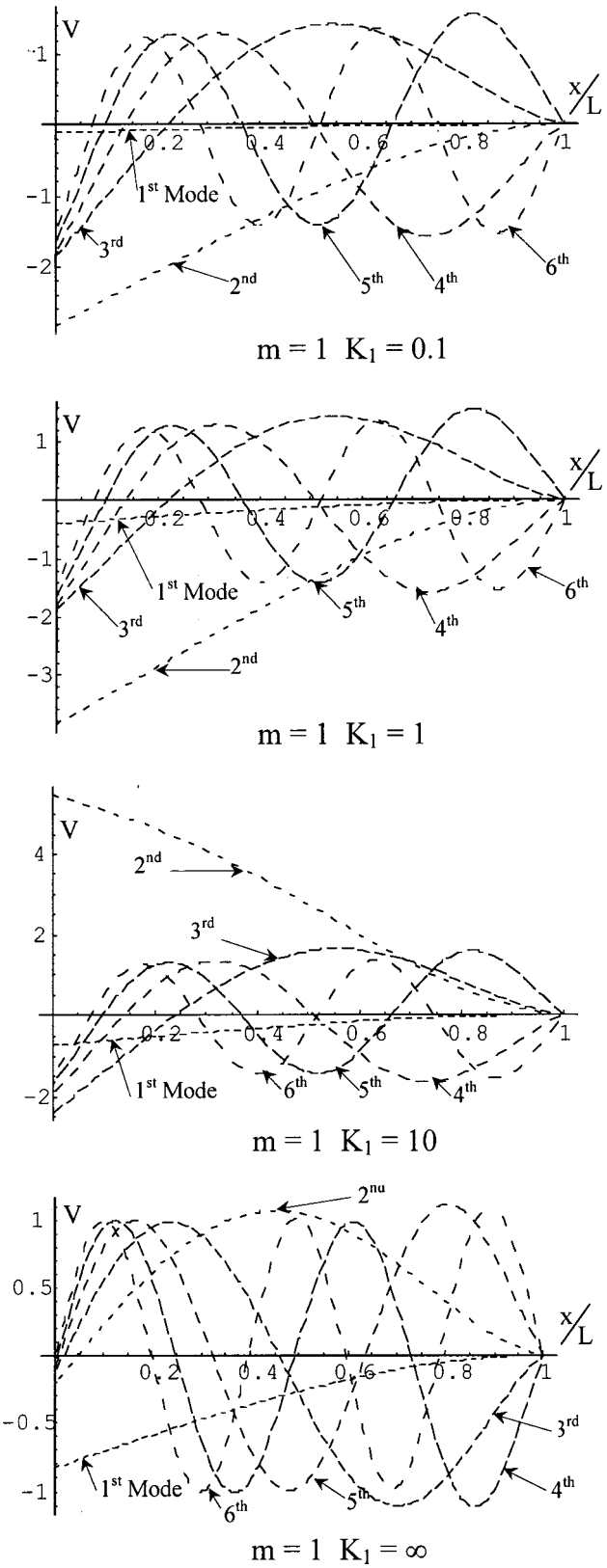

FIG. 4. Model shapes for $r/L=0.05$.

III. NUMERICAL RESULTS

The numerical determinations have been performed making Poisson's ratio (ν) equal to 0.3 and the shear factor (k) equal to $\frac{5}{6}$.

The frequency coefficients have been tabulated as a function of $K_1 = K/(EI/L^3)$ and $m = M/\rho A_0 L$.

Table I depicts values of Ω_i for $r/L = 0.01$ which corresponds to a rather thin beam. The case of $r/L = 0$ is obviously the Bernoulli–Euler situation and has been treated extensively in a previous publication.[6]

The first line of Table I corresponds to the vibrating bare beam (no spring–mass attached to the structural element). The values of Ω_i corresponding to $K_1 = 0.1$, 1, 10 and ∞ (rigidly attached) are depicted in the rest of the table for $m = 0.2$, 0.5, 1, 2, and 3. The lowest frequency determined for $K_1 = 0.1$, 1, and 10 is the frequency of the sprung system modified by the presence of the continuous structural element.

Table II shows values of Ω_i for a stiff beam ($r/L = 0.05$) and determined for the same values of K_1 and m which have been previously considered. As it was to be expected the frequencies corresponding to the spring–mass system experience minor change when compared with those obtained for $r/L = 0.01$.

Figures 3 and 4 depict the lower modal shapes of the system for $r/L = 0.01$ and 0.05, respectively.

One observes that for very small values of K_1 the beam exhibits, for both values of r/L, very small displacement amplitudes in correspondence with the first mode. On the other hand, the discrete system exhibits rather large vibration amplitudes.

ACKNOWLEDGMENTS

The present study has been sponsored by CONICET Research and Development Program and by Secretaría General de Ciencia y Tecnología of Universidad Nacional del Sur. The authors are indebted to Dr. P. J. Remington and two of the unknown referees for their cooperation and constructive criticism.

[1] T. W. Lee, "Vibration frequency for a uniform beam with one end spring-hinged and carrying a mass at the other free end," J. Appl. Mech. **95**, 813–815 (1973).

[2] P. A. A. Laura, J. L. Pombo, and E. A. Susemihl, "A note on the vibrations of a clamped-free beam with a mass at the free end," J. Sound Vib. **37**, 161–168 (1974).

[3] R. B. Bhat and H. Wagner, "Natural frequencies of a uniform cantilever with a tip mass slender in the axial direction," J. Sound Vib. **45**, 304–307 (1976).

[4] R. E. Rossi, P. A. A. Laura, D. R. Avalos, and H. A. Larrondo, "Free vibrations of Timoshenko beams carrying elastically mounted, concentrated masses," J. Sound Vib. **165**, 209–223 (1993).

[5] P. A. A. Laura, E. A. Susemihl, J. L. Pombo, L. E. Luisoni, and R. Gelos, "On the dynamic behavior of structural elements carrying elastically mounted concentrated masses" Appl. Acoust. **10**, 121–145 (1977).

[6] C. A. Rossit and P. A. A. Laura, "Free vibrations of a cantilever beam with a spring–mass system attached to the free end," Institute of Applied Mechanics, Publication 2000-24 (Bahía Blanca, Argentina, 2000).

Acoustical design of Benaroya Hall, Seattle (L)

Cyril M. Harris
Department of Electrical Engineering and the Graduate School of Architecture, Columbia University, New York, New York 10027

(Received 13 December 1999; revised 10 September 2001; accepted 11 September 2001)

Benaroya Hall in Seattle, Washington, was inaugurated on September 12, 1998. This 2500-seat concert hall has a rectangular plan, follows the traditional ''shoebox'' form, and has a volume of 680 000 ft^3 (19 244 m^3). To obtain excellent diffusion over a wide frequency range requires surface irregularities of different sizes and shapes; to obtain excellent diffusion at very low frequencies requires scattering surfaces of very large dimensions. These considerations were essential to the acoustical design of Benaroya Hall. The two principal reasons for providing a high degree of diffusion across the frequency range were (1) to increase the uniformity of the distribution of sound throughout the concert hall, and (2) to smooth out significant variations in the rate of growth and the rate of decay in the hall. The values of reverberation time, at all measured frequencies, for fully occupied Benaroya Hall are within 0.1 sec of the corresponding values in the Grossermusikvereinssaal in Vienna. Noise is inaudible throughout the auditorium, having a measured value of between NC-10 and NC-15 with air conditioning systems in operation. © *2001 Acoustical Society of America.* [DOI: 10.1121/1.1416199]

PACS numbers: 43.55.Fw, 43.55.Gx [JDQ]

I. INTRODUCTION

Benaroya Hall in Seattle, Washington, was inaugurated with a performance by the Seattle Symphony Orchestra on 12 September 1998 under the baton of its Music Director, Gerard Schwarz. This concert hall has a rectangular plan, illustrated in Fig. 1, that follows the traditional ''shoebox'' form of many concert halls of acoustical excellence. The design objective was to emulate the acoustical characteristics of the Grossermusikvereinssaal in Vienna, often cited as having the best acoustical properties in the world. Reviews of concerts at Benaroya Hall have been excellent. For example, the chief music critic of *The New York Times*, in his review on 15 September, 1998, had this to say: ''The place is a world-class establishment, a significant success. The Seattle Symphony is going to have to work hard to keep up with it.'' [1]

The hall's seating capacity is 2500: 1544 seats at orchestra level, 286 in the first tier, 286 in the second tier, and 384 in the third tier. As illustrated in Fig. 2, the side tiers of each balcony level are comprised of boxes that run along the side walls of the hall; boxes are also at the front of the rear-wall balconies. In the design of a concert hall, it is important that the space under each balcony have a depth which is relatively shallow and have an opening which is relatively high; these conditions promote the flow of sound from the auditorium into the space under the balcony. Ideally, for a concert hall, the depth of the balcony should not exceed the height of the opening—a condition that is met at Benaroya Hall.

The width of rectangular concert halls differs considerably, some excellent ones being relatively narrow, others wider. [For example, the Concertgebouw in Amsterdam, often ranked among the three best halls in the world in terms of acoustical quality, has a width of 91 ft (27.7 m).] At Benaroya Hall, the width of the hall itself varies because of its highly irregularly shaped side walls; the average width at orchestra level is 85 ft (25.9 m) and the minimum width between faces of opposite balconies is 65 ft (19.8 m). The distance from the stage to the rear wall is 114 ft (34.8 m), taken along the center line. The ceiling height is approximately 60 ft (18.3 m) above the auditorium floor. The floor is finished with $\frac{3}{4}$-in. (1.9 cm) oak strips, laid over a plywood subflooring of the same thickness that is supported by wood joists with an air space between the joists. The volume of Benaroya Hall is 680 000 ft^3 (19 244 m^3).

II. SOUND DIFFUSION

In traditional concert halls, the diffusion of sound throughout the hall primarily results from the scattering of sound from the hall's interior irregular surfaces, such as pilasters, niches, coffers, statues, balcony faces, and other surface ornamentation. Such irregularities and objects are especially effective in scattering sound when their dimensions are roughly between about a half-wavelength and the wavelength of the incident sound.[2,3] Therefore, to obtain excellent diffusion over a wide frequency range, the irregularities must be of different sizes and shapes. Excellent diffusion at very low frequencies requires scattering surfaces of very large dimensions. In general, such sizes are practical only when the diffusers become part of the overall architectural design of the concert hall. Fortunately, at Benaroya Hall the acoustical design and the basic architectural design went hand-in-hand as a result of an unusually close collaboration between the architect and the author.

The basic design of the hall included walls having irregularly shaped, engaged polyhedral columns as part of the wall treatment; one such column, in the first bay of the auditorium adjacent to the proscenium, is illustrated in Fig. 3. The bases of these columnar diffusers are as large as 16 ft (4.9 m) wide on the side walls and 24 ft (7.3 m) wide on the rear wall; they extend from the orchestra floor to the ceiling

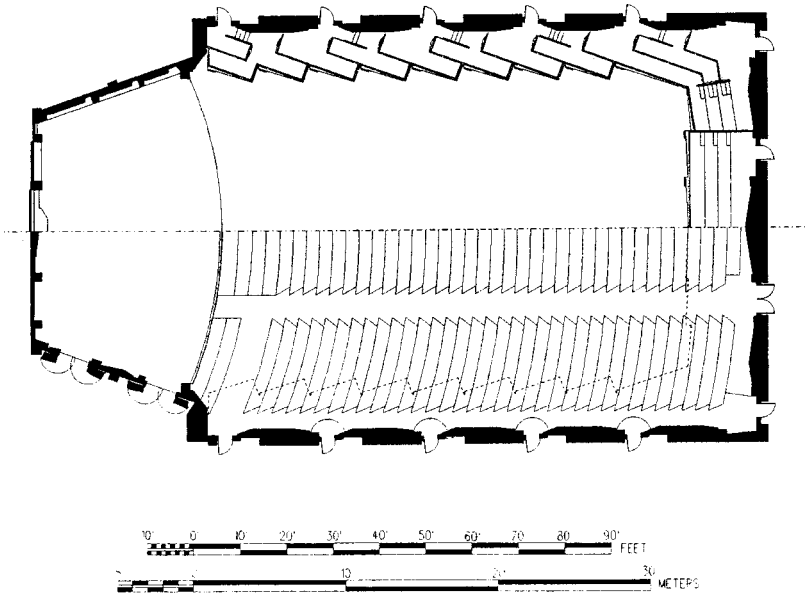

FIG. 1. Plan of Benaroya Hall showing the seating at orchestra and balcony levels.

and narrow with increasing height. On their surfaces are superposed smaller-scale flat-surface irregularities to provide additional scattering of sound in the middle-frequency range. The columnar diffusers project outward and irregularly from the walls into the concert hall by about 12 in. (0.3 m) to about 24 in. (0.6 m), depending on their location. The auditorium walls, including the columnar diffusers, are clad with an assemblage of 2500 wood panels 3/4 in.-(1.9 cm)-thick that are fastened to wood battens fixed to the cast-concrete wall structure. To ensure that the panels would fit tightly together when assembled, they were precision cut with a computer-controlled milling machine.

The ceiling is deeply coffered and has a plaster thickness of $1\frac{1}{2}$ in. (3.8 cm). It provides greater diffusion than coffered ceilings in earlier traditional rectangular halls, such as Symphony Hall in Boston, because an inverted, nonsymmetrical, four-sided plaster-on-metal-lath polyhedron was placed within each coffer. Each polyhedron projects downward into the auditorium about 14 in. (0.35 m) below its base.

The balcony faces are finished with 3/4-in. (1.9 cm)-thick plaster-on-metal-lath rhomboidal diffusers that vary in size; their geometry also varies with their position along the face of each side box and along the face of each rear balcony. These diffusers are horizontal in orientation, in contrast to the huge diffusers on the side walls where the orientation is primarily vertical.

The two principal reasons for providing such a high degree of diffusion across the entire frequency range were: (1) to increase the uniformity of the distribution of sound throughout the concert hall; and (2) to smooth out variations in the rate of growth and rate of decay in the hall.[4] The uniformity of sound distribution in Benaroya Hall has been noted by many listeners; for example, the music critic of the *Seattle Post-Intelligencer*, had this to say: ''One of the most remarkable aspects of Benaroya Hall is the evenness of sound throughout the hall. Two private concerts were given so symphony officials could hear music with an audience. I attended one and sat in five locations: two on the main floor and three above, including a side box and the very top of the house. Sound was extraordinarily consistent in every place.

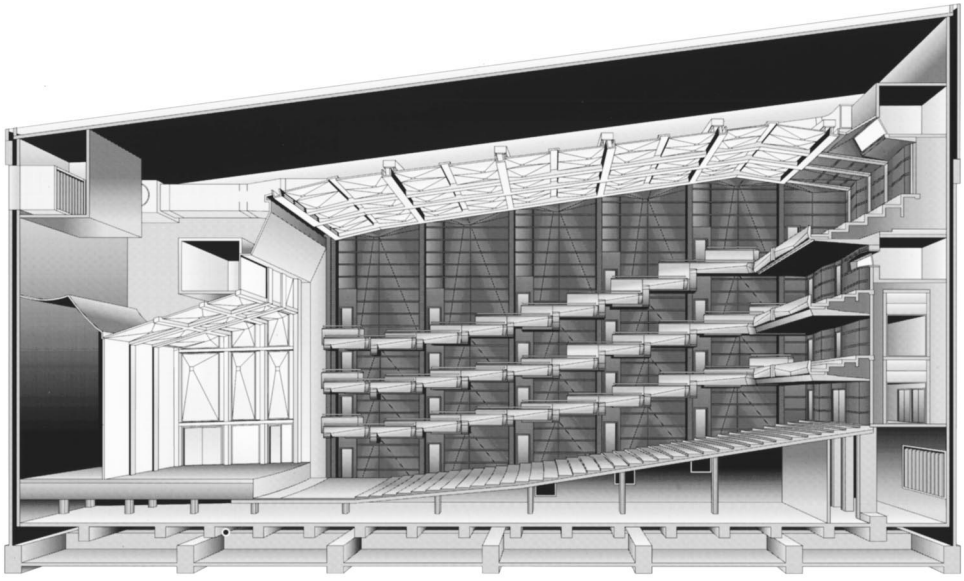

FIG. 2. View of side wall of Benaroya Hall from the center line of the hall. (*Courtesy of Jeff Neumann/Seattlel Times.*)

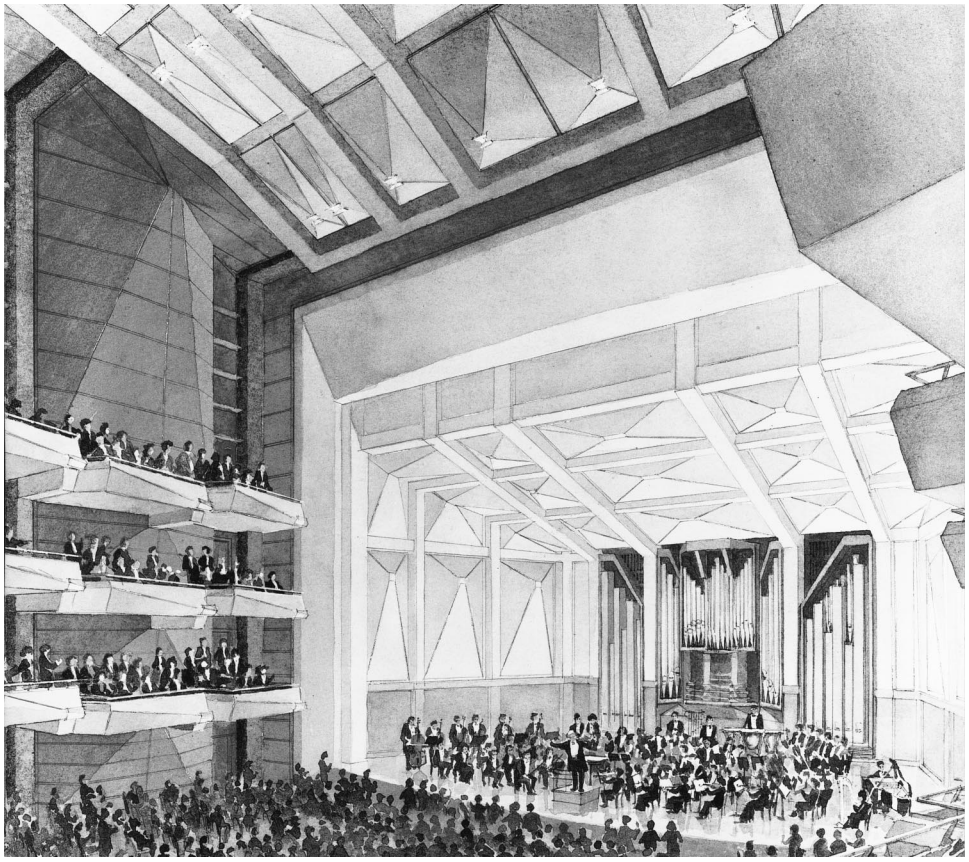

FIG. 3. Illustration of the stage, showing the coffers in the auditorium ceiling; an inverted polyhedron is set within each coffer to promote diffusion of sound within the hall. The organ façade is at the rear of the stage. To the left of the stage, in the first bay adjacent to the proscenium on stage right, is one of the series of huge engaged polyhedral columns along the walls. (Courtesy *W. G. Hook Architectural Drawings*.)

Always there was presence, clarity and responsiveness. Few halls can make that claim.'' [5]

III. REVERBERATION TIME

The measured values of reverberation time for fully occupied Benaroya Hall, given in Table I, are within 0.1 s of the values for the Grosssermusikvereinssaal at all measured frequencies. Both of these concert halls have reverberation times very close to those in fully occupied Orchestra Hall in Minneapolis, also a shoebox concert hall of quite different wall and ceiling construction. The reverberation times in all three halls are longer than the values in fully occupied Boston Symphony Hall. Like all traditional concert halls, Benaroya Hall has no provision for varying the hall's reverberation characteristics, either by electronic or mechanical means.

Reverberation times were measured in unoccupied Benaroya Hall using a cannon and blank 10-gauge shotgun shells as the sound source whose decay was measured. For the fully occupied hall, the values of reverberation time were determined from the magnetic tape recordings made during actual performances of the orchestra playing a fortissimo at the end of a movement in which the fortissimo was followed by silence. These tape recordings were made from a microphone placed at ear level in both the orchestra level and first tier level, and also above the heads of those seated at orchestra level. The decay rate (and hence the reverberation time) was determined from the slope of high-speed level recordings of these decays.

TABLE I. A comparison between reverberation times in Benaroya Hall when unoccupied with the hall when it is fully occupied (with the orchestra on stage).

	Frequency, in Hz					
	125	250	500	1000	2000	4000
Unoccupied	2.29	2.24	2.23	2.17	2.12	1.93
Fully occupied	2.20	2.10	2.04	1.90	1.87	1.67

IV. STAGE ENCLOSURE

The stage enclosure, illustrated in Fig. 3, has irregular side walls, a sloped ceiling, and an organ façade at the rear of the stage. Its lower side walls are finished with wood diffusers having a shape suggestive of the engaged columns on the side walls of the auditorium. The upper parts of these side walls are comprised of plaster-on-metal-lath polyhedrons. The sloped plaster ceiling above the stage is coffered; each coffer contains an inverted polyhedron similar to those in the coffers on the auditorium ceiling. The stage floor is $\frac{3}{4}$-in. (1.9 cm) tongue-and-groove oak boards, laid on a subflooring of plywood that rests on wood sleepers isolated from the concrete stage foundation by elastomeric pads. The surface of the stage floor is 42 in. (1.1 m) above the adjacent auditorium floor.

V. ORGAN

The organ, whose pipes form the façade of the rear wall of the stage, was designed and built by C. B. Fisk, Inc. of Gloucester, Massachusetts. It has three manual keyboards of

61 notes each, 83 stops, a pedal keyboard of 32 notes, and a total of 4485 pipes. Each key is mechanically linked to a valve controlling the supply of wind to a pipe. At the rear of the stage, the organ façade, with massive wood pipes, acts as a significant acoustical scattering surface.

VI. BACKGROUND NOISE

Noise from the air-conditioning system (as well as noise from any ancillary mechanical systems within the building) is inaudible throughout the auditorium and stage, having a measured value of between NC-10 and NC-15 with all systems in operation. With the HVAC system turned off, the typical noise level in the hall is somewhat lower. The principal external noise source (resulting from the occasional passage of railway cars through a railroad tunnel that runs diagonally below the site) is reduced well below the threshold of audibility and is sufficiently low in level to permit the hall to be used for high-quality digital recording. This was made possible primarily by the following measures: a box-within-a-box construction, in which the concert hall (the ''inner box'') is structurally isolated from, and independent of, the surrounding ancillary facilities (the ''outer box''); a massive layer of concrete, 6.5 ft (2 m) thick, above the railway tunnel, which acts as the first stage in the vibration isolation system; and 310 huge rubber pads that serve as vibration isolators which support a concrete slab on which the concert hall rests.

ACKNOWLEDGMENTS

The author worked closely with, and is especially indebted to, Gerard Schwarz, Music Director of The Seattle Symphony. The author collaborated closely with Mark Reddington, design partner of LMN, Architects. He is also grateful to the following individuals for their contributions to the design aspects of this project: James M. Brown, Project Architect, and James Cade, Project Manager at LMN. The Seattle Symphony: Deborah R. Card, Executive Director. Pipe Organ: Steven Dieck of C. B. Fisk, Inc. Structural Engineers: Brian Glover, Project Manager of Skilling Ward Magnusson Barkshire. Ground-borne vibration–isolation system: George Paul Wilson of Wilson, Ihrig & Associates. Noise control for mechanical and electrical systems: Robert M. Hoover of Hoover & Keith, Inc. (in consultation with Al Zuck). Public address system: J. Ashton Taylor of Hoover & Keith, Inc.

[1] B. Holland, *The New York Times*, 15 Sept. 1998. This review and numerous others, including many additional illustrations, are contained in a publication, *Inaugural Celebration of the Opening of Benaroya Hall*, published by the Seattle Symphony, which may be obtained without charge by writing The Seattle Symphony, Attention: Ms. Mary Langholz, P.O. Box 21906, Seattle, WA 98111-3906.
[2] P. M. Morse, *Vibration and Sound* (McGraw-Hill, New York, 1948), Chap. VII.
[3] P. M. Morse and K. U. Ingard, *Theoretical Acoustics* (McGraw-Hill, New York, 1968), Chap. 8.
[4] V. O. Knudsen and C. M. Harris, *Acoustical Designing in Architecture* (Wiley, New York, 1950), pp. 139, 399.
[5] R. M. Campbell, *Seattle Post-Intelligencer*, 14 September 1998.

Comparison of voice F_0 responses to pitch-shift onset and offset conditions (L)

Charles R. Larson,[a] Theresa A. Burnett,[b] Jay J. Bauer, and Swathi Kiran[c]
Department of Communication Sciences and Disorders, 2299 North Campus Drive, Northwestern University, Evanston, Illinois 60208

Timothy C. Hain
Departments of Otolaryngology, Neurology and Physical Therapy, Northwestern University Medical School, Chicago, Illinois 60611

(Received 27 April 2000; revised 14 September 2001; accepted 19 September 2001)

In order to maintain a steady voice fundamental frequency (F_0), it is assumed that people compare their auditory feedback pitch with an internal (memory) or external (acoustic) referent. In the present study we examined whether the internal referent is fixed or variable by comparing voice F_0 responses to incorrect auditory feedback in two timing conditions. In one condition, the incorrect pitch was introduced during vocalization (ON condition). In the second, the incorrect auditory feedback pitch was presented before vocal onset and then removed during vocalization (OFF condition). These conditions were examined with pitch-shift stimuli of ± 25, 100, and 200 cents. There were no differences in response latency or magnitude between the two timing conditions, indicating that for a sustained-pitch vocalization task, the internal referent is not fixed. Several alternative types of referencing are discussed, which include use of a pitch relative to that which existed at the onset of vocalization (a sample and hold strategy) and pitch velocity referencing.
 [DOI: 10.1121/1.1417527]

PACS numbers: 43.70.Aj [AL]

I. INTRODUCTION

One issue of concern in the study of voice fundamental frequency (F_0) control is how people maintain a steady voice F_0 level. Trained singers can hold their voice F_0 at a desired level in a steady manner, or they can deliberately modulate it around a desired level, such as in vibrato (Sundberg, 1987). It is also well known that auditory feedback is important for the accurate control of voice F_0 (Elliott and Niemoeller, 1970; Elman, 1981; Jones and Munhall, 2000; Ternström *et al.*, 1988) and that pitch memory is important in enabling singers to sing a specific note (Takeuchi and Hulse, 1993). We have proposed a model of voice F_0 control in which perceived pitch of auditory feedback is compared either with an internal referent (e.g., memory) or an external referent (e.g., piano note) (Hain *et al.*, 2000). A related issue is whether an internal referent is fixed or variable. It is well known that some people have ''perfect'' or absolute pitch, implying a fixed reference, while others are unable to reliably produce an accurate pitch without an external reference.

In the present study, we utilized the pitch-shifting paradigm in nontrained singers to determine whether the internal voice F_0 reference for comparison with auditory feedback is fixed or variable. Voice F_0 responses to altered voice pitch feedback were studied under two timing conditions. In the onset condition (ON), the pitch-shift stimulus was unexpectedly turned on shortly after the start of vocalization. In the offset condition (OFF), the pitch-shift processor was turned on prior to the initiation of vocalization and then unexpectedly turned off during vocalization. Thus under the OFF condition, the feedback pitch was returned to normal for the remainder of the vocalization. It was hypothesized that if the internal referent is fixed, subjects would respond to the onset of the pitch-shift stimulus (ON) but not the offset (OFF condition). The reason they would not respond in the OFF condition is because according to the *fixed* referent hypothesis, they would recognize the feedback as not being their own voice, and hence it would be irrelevant to their own production. However, if the internal referent is variable, subjects would respond to both conditions; any sudden change in voice pitch feedback would be recognized as an error, and the audio-vocal system would attempt to negate it. To test whether or not any effect depended on the magnitude of the pitch-shift stimulus or direction of pitch-shift modulation, six different stimulus magnitudes were employed across both timing conditions.

II. METHODS

A. Subjects

Thirty-three undergraduate students (26 females, 7 males, ages 18–22 years) served as subjects. All subjects passed a hearing screening at 20 dB HL (500–8 kHz), none reported any neurological or speech abnormalities, and none was trained as a professional singer or claimed to have perfect pitch.

[a]Electronic mail: clarson@northwestern.edu
[b]Laryngeal and speech section, NINDS, Bldg. 10, Rm 5D38, Bethesda, MD 20892-1416
[c]Department of Communication Sciences and Disorders, University of Texas, Austin, Texas 78712

B. Apparatus and procedures

The subjects' voices were transduced with an AKG boom-set microphone, amplified with a Mackie Mixer (model 1202), processed through an Eventide Ultraharmonizer (model H3000 SE) for pitch-shifting, mixed with 70 dB SPL pink masking noise and fed back over AKG earphones (model K 270 H/C). Subjects vocalized a vowel (ah) at a habitual pitch and at an intensity of 70 dB SPL, aided by observing a Dorrough Loudness Monitor, resulting in voice feedback loudness of about 80 dB SPL at the headphones. Subjects sat in a sound-treated room and were instructed to vocalize for 5 s, pause for a breath and repeat. They were instructed to hold voice pitch as steady as possible and to ignore any auditory feedback variations. At a random time (500–2500 ms) after vocalization onset, the pitch of the feedback signal was altered by a preset amount. Thirty consecutive vocalizations were recorded during each experimental block. During each block, 15 upward and 15 downward (pseudorandomly mixed) pitch shifts were presented. (For a more detailed description of the methodology see Burnett *et al.*, 1998; Hain *et al.*, 2001; Larson *et al.*, 2000.)

In this study two *timing*, three *magnitude*, and two stimulus *direction* experimental conditions were compared across six blocks of trials. In the ON timing condition, the pitch-shift stimulus (PSS) was presented during the vocalization. In the OFF timing condition, the pitch-shift stimulus was turned on before vocal onset and then removed during the vocalization. Thus, in the OFF condition, when subjects began vocalizing, they heard their voice pitch already shifted, and when it was removed, they heard their normal, unperturbed pitch feedback. Three pitch-shift stimulus magnitudes (25, 100, or 200 cents) (100 cents=one semitone) and two pitch-shift stimulus directions (upward and downward) were examined in addition to the timing conditions. The change in pitch feedback that occurred during the vocalization was maintained for the duration of the vocalization. Sixteen subjects were tested with PSS of ± 25 cents (13 females, 3 males), while the other 17 subjects were tested with ± 100 and ± 200 cent PSS (13 females, 4 males).

During the experiment, the voice signal, the feedback signal, and a TTL pulse (indicating time of change in the feedback signal) were digitized at 2 kHz on a laboratory computer. In offline analysis, a software algorithm was used to generate signals where voltage is proportional to the F_0 of the subject's voice (F_0 analog) and the feedback signals. These signals were then time aligned to the TTL pulse for each subject for each experimental condition and event-related averages were computed. From these averaged signals, the preshift mean F_0 was calculated. In the period following the pitch shift, a response was measured whenever the voltage of the averaged F_0 signal differed by more than two standard deviations from the preshift mean. Only deviations beginning at least 60 ms after onset of the pitch-shift stimulus and lasting for at least 60 ms were considered valid. Latency and amplitude measures from the averaged responses (hereafter, ''responses'' refers to averaged responses) were recorded (Burnett *et al.*, 1998; Hain *et al.*, 2000; Larson *et al.*, 2000).

Responses following the change in pitch feedback were tested with a modified $3\times(2\times2)$ repeated measures factorial MANOVA. Response latency and response magnitude were the dependent variable measurements. The within subjects (repeated) factors were *timing* and stimulus *direction* conditions, each with two levels. The between-subjects factor of PSS *magnitude* was modified to fit three levels, although it was derived from two separate subject groups. The first group ($N=16$) was tested only on PSS magnitude of 25 cents, while the second group ($N=17$) was tested on both PSS magnitudes of 100 and 200 cents. Differences were considered significant for p values less than 0.01. Significance of incidence of compensating versus ''following'' responses was done with a chi-square test.

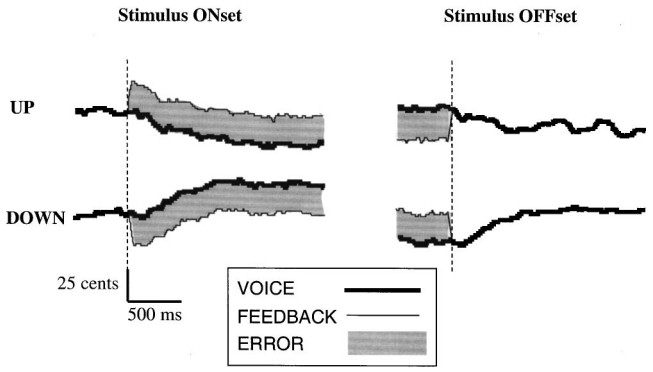

FIG. 1. Averaged response traces from a single subject illustrating typical behavior to 25-cent pitch-shift stimulus. In each set, the heavy line is voice F_0 and the light line is feedback pitch. The vertical dashed line indicates onset of pitch-shift stimulus (left) and offset of pitch shift stimulus (right). The top row shows responses to upward pitch-shifts, while the bottom row displays downward pitch shifts. Shaded areas represent error between feedback pitch and output F_0.

III. RESULTS

A total of 200 averaged responses were measured out of a total of 200 possible responses. For the 16 subjects receiving PSS of ± 25 cents, there were a total of 64 responses (1 magnitude$\times$2 direction$\times$2 timing conditions). For the 17 subjects receiving PSS of ± 100 and ± 200 cents, there were 136 responses (2 magnitude$\times$2 direction$\times$2 timing conditions). These totals translate to 100 ON and 100 OFF responses. Therefore responses were observed for all subjects under each experimental condition.

Representative data from one subject in Fig. 1 show traces representing voice F_0 and feedback pitch for the ON and OFF conditions. The left half of Fig. 1 illustrates a subject's responses to upward and downward pitch-shift stimuli for the ON condition. Before the onset of the PSS (vertical dashed line), the voice F_0 and feedback pitch are identical. After the onset of the PSS, there is a discrepancy (error) of 25 cents between the voice F_0 and the feedback pitch (shaded area) that is maintained throughout the remainder of the vocalization. A gradual change in voice F_0 (dark line) is apparent, which after about 500 ms, results in the voice F_0 reaching an asymptote and the feedback pitch (light line) approaching the baseline level that existed prior to the stimulus onset. The right-hand side of Fig. 1 shows responses to upward and downward pitch stimuli in the OFF condition. In

this case there is a discrepancy between feedback pitch and voice F_0 at the onset of vocalization (shaded area). When the stimulus is turned off (vertical dashed line), the feedback pitch (light line) matches that of voice F_0 (dark line). Subjects respond with a gradual change in F_0, which after approximately 500 ms, results in the feedback signal approaching the level that existed prior to the pitch shift. In both the ON and OFF conditions and regardless of pitch-shift direction, subjects respond to the change during vocalization such that the feedback pitch approaches the level that existed before the pitch shift was presented (compensatory response). It should be noted that at the end of the record, the feedback pitch does not always match the level that existed prior to the pitch-shift stimulus in either the ON or OFF condition.

There were no significant differences in response latency or magnitude as a function of the ON and OFF conditions (Wilk's Lambda 0.91, $df=2$, 46, $p=0.12$). Therefore subjects responded equally to ON and OFF timing conditions. The mean latency of the ON responses was 155 ms (SD 128) and that of the OFF responses was 170 ms (SD 109). The mean magnitude of the ON responses was 42 (SD 36) and the OFF responses was 33 (SD 30) cents. There was a main effect for the pitch-shift magnitude (Wilk's Lambda 0.432, $df=4$, 92, $p<0.001$). Post hoc Sheffé testing revealed that the latencies for the 25-cent pitch-shift stimuli (mean 246, SD 156 ms) were significantly longer than that for the 100 cent (mean 117, SD 60 ms) and 200 cent stimuli (mean 130, SD 80 ms). Although not significant, the response magnitudes for the 25-cent pitch-shift stimuli (mean 26, SD 8.4) were less than the 100-cent (mean 48, SD 39) and the 200-cent (mean 39, SD 39) pitch-shift stimuli. Furthermore, there were nonsignificant differences in latency and magnitude measures as a function of pitch-shift direction (up or down), as well as nonsignificant interactions.

One hundred eighty four responses were identified as compensatory and 16 as ''following'' responses. Of these 16 ''following'' responses 12 were elicited from downward stimuli, 11 from OFF stimuli, and 8 from DOWN-OFF experimental conditions. Chi-square comparisons of opposing versus ''following'' prevalence failed to reach significance ($p>0.05$). However, compensating responses were statistically larger in magnitude (39.7 cents) compared with ''following'' responses (16.7 cents) ($F=7.1$, $df=1$, $p<0.005$).

IV. DISCUSSION

Results of this study show that regardless of whether a pitch-shift stimulus is presented before or after vocalization onset, subjects respond equivalently. In both the ON and OFF conditions, a pitch-shift stimulus elicits a ''compensatory'' F_0 response that brings the feedback signal back toward the level (approximately) that existed before the stimulus. Thus, the comparison between auditory feedback and voice F_0 is not fixed, but is variable. If the comparison were fixed, then the vocalist would know that the altered feedback pitch in the OFF condition was not normal, and would not respond to the change when it was turned off during vocalization. Use of a variable, or relative reference implies one of several different strategies that will be discussed in the following.

The simplest possible organization of a system that maintains a steady F_0 is to compare the auditory feedback signal with a referent. We call this scheme *absolute* F_0 referencing. The referent might be external such as a piano note, or internal such as an efference copy of motor output, proprioceptive memory or a memory of a pitch (Sundberg, 1987). External references are intrinsically fixed, and an economical control design might also use fixed (absolute) internal references. However, in the present study, no differences in response magnitude or latency were observed as a function of the ON and OFF conditions and indicates that a relative F_0 reference strategy is used, at least in most subjects, for stabilization where there is no external reference available.

There are two potential relative (variable) referencing organizations that are consistent with our observations. First, subjects may be using changes in auditory feedback velocity to compensate for and null changes in F_0 (termed *velocity control*), rather than keeping F_0 set to a fixed internal reference. Velocity control could also stabilize a glissando by comparing intended and perceived F_0 velocity. An alternative to velocity control is a ''*sample and hold*'' strategy based on using a memory of initial perception of F_0 as a reference. Disparities between perceived F_0 and memory would invoke a corrective response similar to those observed in this experiment. However sample/hold would likely result in a longer latency compared to the velocity control strategy as it requires first storage of an auditory input followed by a comparison with the referent. In addition, sample/hold could not stabilize a glissando because there is no stable referent, but it might be more accurate than velocity control for stabilizing a steady-state F_0.

These several types of feedback referencing are not mutually exclusive and might all be used simultaneously. Certainly, some degree of absolute F_0 referencing is necessary for accurate tracking of an external reference. Individuals that have reliable internal absolute F_0 references (i.e., ''absolute or perfect pitch'') might select absolute internal F_0 referencing, velocity control, or sample/hold. Those without absolute pitch might use either velocity control or sample/hold relative referencing. Weightings for these control strategies that vary with behavioral goals, individual abilities, and the availability of references from the environment would likely be the most effective strategy.

These data also indicate that the mechanism for *detecting* the error is the same regardless of the magnitude of the F_0 disparity (25–200 cents). That is, subjects produce a compensatory response to both the ON and OFF stimuli for each stimulus magnitude. However, the ability of the system to *correct* for errors depends on the stimulus magnitude. In this and previous studies (Burnett *et al.*, 1998), it was shown that response magnitude rarely exceeded 50 cents even in the presence of stimulus magnitudes of 100 and 200 cents. This limitation in response magnitude may be present to prevent this reflexive low-level stabilization mechanism from interfering with or destabilizing higher level, more sophisticated tracking mechanisms, possibly using F_0 position references.

Analysis of numbers of ''compensatory'' and ''following'' responses show there was no significant difference in

the number of ''following'' responses with the ON or OFF stimuli, which further demonstrates that subjects did not try to match the feedback signal. Had there been more ''following'' responses with the OFF stimuli, it would have suggested that subjects treated it as an external reference. We have previously postulated that ''compensatory'' responses are made by comparing the feedback signal with an internal referent, and ''following'' responses made by comparison with an external referent (i.e., the feedback signal itself or musical accompaniment) (Burnett *et al.*, 1998; Hain *et al.*, 2000). Hence these conditions do not appear to influence whether a person would use an internal versus an external reference.

ACKNOWLEDGMENTS

This research was supported by NIH Grant No. DC02754-01. Portions of this study have been presented in abstract form at the Speech Motor Control Conference, Tucson, AZ, February, 1998. We wish to thank Danielle Lodewyck and Mary Kay Kenney for assistance with data analysis and Rokny Akhavein for help with computer programming.

Burnett, T. A., Freedland, M. B., Larson, C. R., and Hain, T. C. (**1998**). ''Voice $f0$ responses to manipulations in pitch feedback,'' J. Acoust. Soc. Am. **103**, 3153–3161.

Elliott, L., and Niemoeller, A. (**1970**). ''The role of hearing in controlling voice fundamental frequency,'' Int. Audiol. **IX**, 47–52.

Elman, J. L. (**1981**). ''Effects of frequency-shifted feedback on the pitch of vocal productions,'' J. Acoust. Soc. Am. **70**, 45–50.

Hain, T. C., Burnett, T. A., Larson, C. R., and Kiran, S. (**2001**). ''Effects of delayed auditory feedback (daf) on the pitch-shift reflex,'' J. Acoust. Soc. Am. **109**, 2146–2152.

Hain, T. C., Larson, C. R., Burnett, T. A., Kiran, S., and Singh, S. (**2000**). ''Instructing participants to make a voluntary response reveals the presence of two vocal responses to pitch-shift stimuli,'' Exp. Brain Res. **130**, 133–141.

Jones, J. A., and Munhall, K. G. (**2000**). ''Perceptual calibration of f_0 production: Evidence from feedback perturbation,'' J. Acoust. Soc. Am. **108**, 1246–1251.

Larson, C. R., Burnett, T. A., Kiran, S., and Hain, T. C. (**2000**). ''Effects of pitch-shift onset velocity on voice $f0$ responses,'' J. Acoust. Soc. Am. **107**, 559–564.

Sundberg, J. (**1987**). *The Science of the Singing Voice* (Northern Illinois University Press, Dekalb, IL).

Takeuchi, A. H., and Hulse, S. H. (**1993**). ''Absolute pitch,'' Psychol. Bull. **113**, 345–361.

Ternström, S., Sundberg, J., and Colldén, A. (**1988**). ''Articulatory $f0$ perturbations and auditory feedback,'' J. Speech Hear. Res. **31**, 187–192.

Generation of very high pressure pulses with 1-bit time reversal in a solid waveguide

Gabriel Montaldo
Laboratorio de Ultrasonido, Inst. De Fisica, Fac. De Ciencias, Montevideo, Uruguay and Laboratoire Ondes et Acoustique, ESPCI, Universite Paris 7, Paris, France

Phillippe Roux and Arnaud Derode
Laboratoire Ondes et Acoustique, ESPCI, Universite Paris 7, Paris, France

Carlos Negreira
Laboratorio de Ultrasonido, Inst. De Fisica, Fac. De Ciencias, Montevideo, Uruguay

Mathias Fink
Laboratoire Ondes et Acoustique, ESPCI, Universite Paris 7, Paris, France

(Received 28 March 2001; revised 28 August 2001; accepted 31 August 2001)

The use of piezoelectric transducer arrays has opened up the possibility of electronic steering and focusing of acoustic beams to track kidney stones. However, owing to the limited pressure delivered by each transducer (typically 10 bar), the number of transducers needed to reach an amplitude at the focus on the order of 1000 bars is typically of some hundreds of elements. We present here a new solution based on 1-bit time reversal in a solid waveguide to obtain, with a small number of transducers, a very high amplitude pulse in tissues located in front of the waveguide. The idea is to take advantage of the temporal dispersion in the waveguide to create, after time reversal, a temporally recompressed pulse with a stronger amplitude. The aim of this work is threefold: first, we experimentally demonstrate 1-bit time reversal between a point source in water and several transducers fastened to one section of a finite-length cylindrical waveguide. Second, we numerically and experimentally study the temporal and spatial focusing at the source as a function of the characteristics of the ''solid waveguide–time reversal mirror (TRM)'' system: length and diameter of the guide, number of transducers of the TRM. Last, we show that the instantaneous power delivered in water at the focus of the solid waveguide is much higher than the power directly transmitted into water from a classically focused transducer. The combination of 1-bit time reversal and a solid waveguide leads to shock wave lithotripsy with low-power electronics. [DOI: 10.1121/1.1413753]

PACS numbers: 43.20.Mv, 43.80.Vj [DEC]

I. INTRODUCTION

Today, extracorporeal shock-wave lithotripsy is by far the method of choice to treat kidney and gall stones. It involves the use of large amplitude acoustic shock waves that are generated extracorporeally and focused onto a stone within the body.[1] Lithotripters typically have a high focusing gain so that pressures are high at the stone but substantially lower in the surrounding tissue. The alignment of stone in the patient with the lithotripter focus is accomplished with fluoroscopy or ultrasonic imaging. Focusing is achieved geometrically, i.e., with ellipsoidal reflectors, concave focusing arrays of piezoelectric transducers, or acoustic lenses. Shock waves have amplitudes at the focus on the order of 1000 bar and a duration of a few microseconds. They are typically fired at a 1-s pulse repetition rate. The use of 2D arrays of piezoelectric transducers has opened the possibility of electronic steering and focusing the beam in biological tissues.[2] Tracking focusing procedures have also been studied. The feasibility of a piezoelectric shock-wave generator in which the focal zone is moved electronically to track the stone during a lithotripsy treatment using time-reversal technique has been implemented and tested.[3,4] In such techniques, however, the number of transducers needed to reach an amplitude of the order of 1000 bar at the focus is typically of some hundreds elements. This is mainly owed to the fact that today the piezoelectric transducer technology allows the delivery in front of a transducer of an amplitude limited to 10 bar. Despite the spatial gain due to the spatial focusing, the number of transducers cannot be reduced if the beam has to be steered in attenuating tissues. As in time reversal technology, each transducer has its own electronic in order to record the stone echo. The signal is time reversed, and it is retransmitted to the stone. The price of an electronic board of several hundred channels is very high and limits the commercial interest of such a lithotripter.

Our ambition is to propose a new elegant solution that combines the use of time reversal technology with a small number of piezoelectric transducers fastened to a solid waveguide. The idea is to take advantage of time reversal pulse recompression in a waveguide to obtain from a few transducers high-amplitude shock waves in a tissue or in a fluid located in front of the waveguide. Time reversal focusing has been previously studied in waveguides in the field of ultrasound[5,6] and in ocean acoustics.[7–9] This technique is based on the reversibility of acoustic propagation which implies that the time-reversed version of an incident pressure field naturally refocuses on its source whatever the heteroge-

neity of the propagation medium. More precisely, a time-reversal experiment consists in

(1) recording the incident field emitted from a pulsed acoustic source on one transducer or an array of transducers (called time reversal mirror);
(2) time reversing the signal and transmitting the time-reversed field from the time-reversal mirror (TRM) back into the propagation medium;
(3) receiving the time-reversed field at and around the initial acoustic source to quantify the spatial and temporal refocusing.

Derode *et al.* performed ultrasonic time reversal focusing through an unknown high-order multiple scattering medium.[10] Furthermore, Derode *et al.* recently investigated time reversal robustness by successfully running 1-bit time reversal experiments through multiple scatterers.[11] During a classical time reversal experiment, a time-domain version of the signal is time reversed, meaning that both the instantaneous phase and amplitude information of the received signal are sent back. During a 1-bit time reversal experiment, the amplitude of the time-reversed signal is set to ± 1 depending on the sign of the received signal. This means that the instantaneous phase information present in the zero crossing of the signal is time reversed while the instantaneous amplitude information is ignored. Through a higher-order multiple scattering medium, authors have shown that classical time reversal and 1-bit time reversal provide the same temporal and spatial focusing results.

Following this set of results, we investigate more precisely in this article 1-bit ultrasonic time-reversal in a solid waveguide. The aim of this work is threefold: first, we demonstrate 1-bit time reversal between a point source in water and several transducers fastened to one section of a finite-length cylindrical waveguide. Second, we study the temporal and spatial focusing on the source as a function of the characteristics of the ''solid waveguide–time reversal mirror (TRM)'' system: length and diameter of the guide, number of transducers of the TRM. Last, we show that 1-bit time reversal carried out with transducers fastened to a cylindrical waveguide section permits us to obtain high-intensity pulses in water. More precisely, we show that the instantaneous power delivered in water at the focus of the solid waveguide is much higher than the power directly transmitted into water from a classically focused transducer. The combination of 1-bit time reversal and a solid waveguide would then lead to shock-wave lithotripsy with low-power electronics.

This article is divided into four parts. In Sec. II, we describe the experimental setup, and we demonstrate time reversal focusing between a point source in water and several transducers attached to one section of a cylindrical metallic waveguide. Section III deals with a theoretical description of acoustic propagation in a solid waveguide. More particularly, a numerical simulation based on normal-mode theory is developed to describe time-reversal experiments in a cylindrical metallic waveguide. In Secs. IV and V, we take advantage of this simulation to investigate numerically and experimentally the temporal and spatial 1-bit time reversal focusing as a function of the characteristics of the system ''solid waveguide–TRM.'' We compare then the instantaneous power of the pulses transmitted onto the source in water by this system to the instantaneous power classically transmitted in water by the same transducers. We conclude with a final discussion on the application of the system ''1-bit time reversal–low power electronics–solid waveguide'' to shock wave lithotripsy.

II. EXPERIMENTAL SETUP AND FIRST RESULTS

In this part, we describe the experimental setup and the first results obtained after time reversal in a solid waveguide. In Fig. 1, a schematic of the experimental setup puts in evidence the characteristics of the experiment. Time reversal is performed between a point source in water (in S) and seven 8-mm-diam piezoelectric transducers (in A) attached to a section of a 3.2-cm-diam, 50-cm-long duraluminium cylinder. Both the source and the transducers are linear and reciprocal. The central frequency is 1 MHz with a 75% bandwidth, which corresponds to a 5-mm central wavelength for compressional wave in duraluminium. The bottom end of the metallic cylinder is immersed in water at a distance d from the source (d between 0 and 10 cm). Each transducer in A is connected to an electronic circuitry which consists of

(1) two 8-bit D/A and A/D converters having a 15-MHz sampling rate, to receive the incident signal and transmit the time-reversed signal;
(2) a memory which records the incident signal sent from the source;
(3) a processor which creates a time-reversed version of the incident signal.

According to these characteristics, classical time reversal is then 8-bit time reversal. On the other hand, during a 1-bit time reversal experiment, only the sign of the time-reversed signal is transmitted ($+V$ if $s(t)>0$, $-V$ if $s(t)<0$, where V is the maximum amplitude of the input signal).

Figure 1(b) represents the signal received on one transducer in A after transmission of a pulse from the source in S [Fig. 1(a)]. As expected, the signal spreads in time because of many reverberations on the interfaces of the solid waveguide. The signal lasts more than 2000 μs, i.e., around 1000 times the length of the initial pulse. In a duraluminium sample, 2 ms corresponds approximately for a longitudinal wave to a 10-m distance, to be compared to the 50-cm length of our cylinder. This means that many round trips inside the cylinder are present in the dispersed signal. In Fig. 1(c), we show a 100-μs window of the 1-bit time-reversed version of the incident signal. Figure 1(d) corresponds to the signal obtained at the source in water after back propagation through the solid guide with 1-bit time reversal. We observe a remarkable time compression on the initial source in S. This confirms that the instantaneous amplitude information which has been ignored with 1-bit time reversal is not necessary to successfully perform a time reversal experiment in a solid waveguide.

In Fig. 2, we compare the time-reversed signal at the source with 1- and 8-bit time reversal, respectively. The major difference between 1- and 8-bit time reversal lies in the

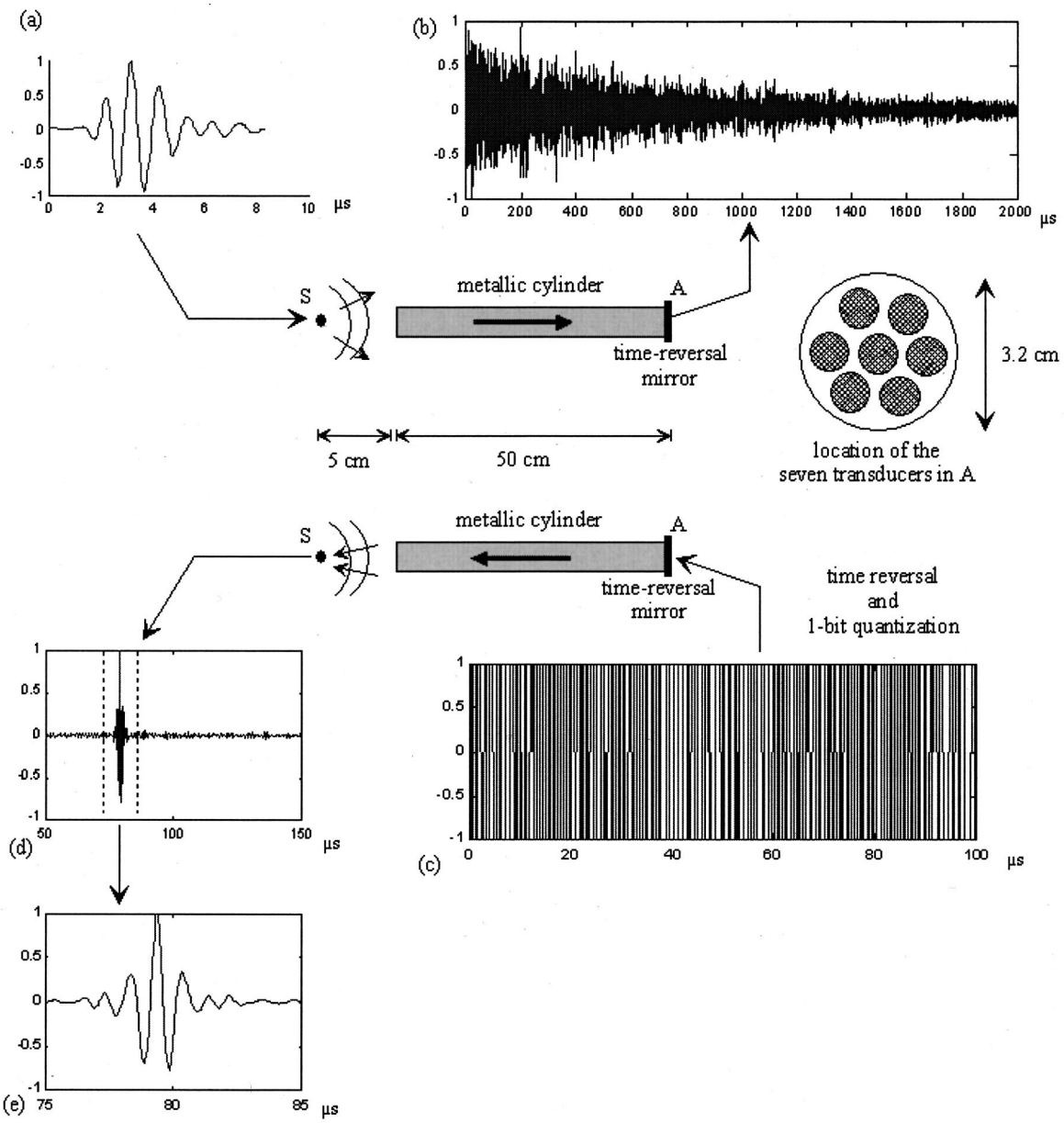

FIG. 1. Experimental demonstration of 1-bit time reversal in a metallic waveguide. (a) The acoustic source transmits a pulsed signal in water. (b) Normalized signal received on one of the seven transducers in A at the end of the 50-cm-long, 3.2-cm-diam metallic waveguide; the signal spreads over more than 2 ms. (c) The signal is time reversed, 1-bit quantized and retransmitted from the same transducer in A. For presentation reason, only the first 100 μs are plotted. (d) Normalized signal obtained in S after 1-bit time reversal from the seven transducers in A and back propagation through the guide. (e) Zoom of the time reversed signal between the dashed lines: the time-reversed signal (e) is similar to the source signal (a).

amplitude of the signal received in S. The instantaneous power obtained with 1-bit time reversal is nearly five times higher than the instantaneous power obtained with 8-bit time reversal, which is itself higher than the power transmitted into the water by the transducer without a waveguide.

The amplification of the instantaneous power delivered from one transducer after time reversal with or without a waveguide is the main point of this article. At first sight, the amplification obtained between 1- and 8-bit time reversal can be easily understood by comparing Figs. 1(b) and (c). More energy has been indeed delivered into the waveguide (and then to the source) with 1-bit time reversal because the natural decrease of the signal has been compensated. What happens now at the source? For a linear system characterized by its impulse response $h(t)$, the response $R(t)$ at an excitation $f(t)$ is

$$R(t)=h(t)\otimes f(t). \tag{1}$$

Time reversal uses as excitation the time-reversed version of the impulse response, which implies

$$R(t)=h(t)\otimes h(-t). \tag{2}$$

It is well known that $R(t)$ is then symmetrical in time with a maximum at $t=0$. Let us find out now what is the input signal $f(t)$, with the constraint $|f(t)|\leqslant 1$, that produces the maximum output amplitude at $t=0$. Writing Eq. (1) as an integral, we get

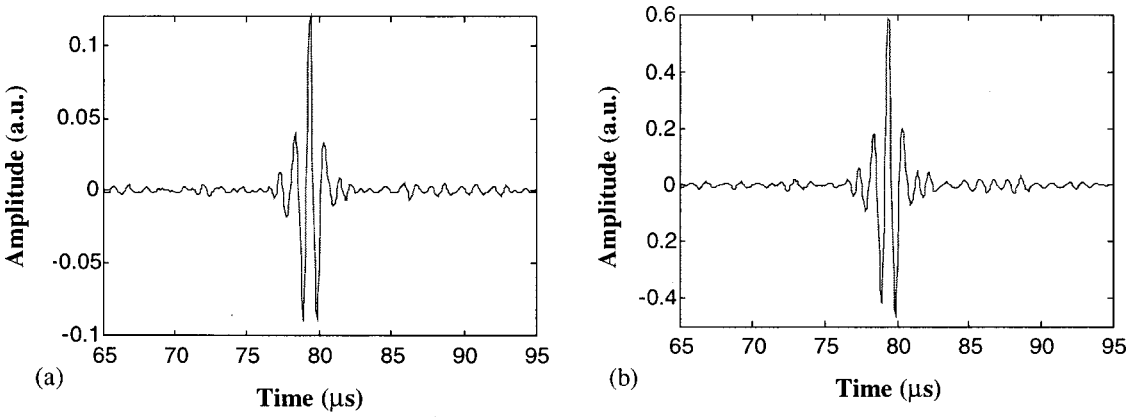

FIG. 2. Experimental comparison between (a) 8-bit time-reversal and (b) 1-bit time-reversal. Time reversal is performed by seven transducers fastened at one end of the guide (in A). The source is placed in water at 6 cm from the other end of the guide.

$$R(0)=\int f(\tau)h(-\tau)d\tau \leqslant \int |f(\tau)||h(-\tau)|d\tau. \tag{3}$$

As we suppose $|f(t)|\leqslant 1$, it follows

$$R(0)\leqslant \int |h(-\tau)|d\tau = \int \mathrm{sign}(h(-\tau))h(-\tau)d\tau. \tag{4}$$

In conclusion, we have proven that

$$R(0)\leqslant \mathrm{sign}(h(-t))\otimes h(t)\big|_{t=0}. \tag{5}$$

This result implies that the maximum amplitude of the output of a linear system is obtained using as input the sign of the time-reversed impulse response of the system. Thus, 1-bit time- reversal delivers at the source a higher maximum amplitude than 8-bit time-reversal. Furthermore, a 1-bit signal offers the advantage of being a binary signal which is electronically much easier to generate and process than an amplitude-modulated signal. On the other hand, Eq. (5) does not give any information about the signal-to-noise ratio obtained with 8- or 1-bit time reversal.

In the following, we carefully study theoretically, numerically, and experimentally the influence of the characteristics of the system ''solid wave guide–TRM'' (length and diameter of the guide, number of transducers of the TRM) on the amplification of the instantaneous power obtained on the source after 1-bit time reversal. More precisely, we will focus on the comparison between the instantaneous power transmitted at the source after 1-bit time reversal in a solid waveguide and the instantaneous power directly transmitted into the water by a transducer.

III. THEORETICAL APPROACH

The acoustic field that propagates along the z axis of a fluid waveguide is usually decomposed at a frequency ω as an addition of orthogonal modes

$$P(x,y,\omega)=\sum_n A_n P_n(x,y,\omega)e^{ik_n(\omega)z}, \tag{6}$$

where P_n is the shape of each mode and k_n is the wavenumber associated with mode number n. If we know the dispersion relationships $k_n(\omega)$ for each mode, we calculate the pressure in any plane z as

$$p(x,y,z,t)=\sum_n A_n P_n(x,y,\omega)e^{i(\omega t-k_n(\omega)z)}. \tag{7}$$

The normal modes follow an orthogonality relation

$$\int_s P_n V_m^* ds=\delta_{nm}, \tag{8}$$

where s is a section of the guide and V_m is the velocity induced by the acoustic pressure field P_m. Using the linear relation between pressure and velocity at a frequency ω, $P=ZV$ where Z is the acoustical impedance, we obtain for the amplitude coefficients A_n

$$A_n=Z\int_s VV_n ds. \tag{9}$$

We are now looking for a method which allows us to calculate, in a solid waveguide, the amplitudes A_n for a known excitation on one section of the guide.[12,13] In a solid, the stress tensor T and velocity V are not linearly related but fulfill the relation

$$\nabla\cdot T=i\omega V. \tag{10}$$

Considering a section of the solid waveguide, the orthogonality relation (8) is changed into the following equation,

$$\int_s (V_m^* T_n+V_n T_m^*)_z ds=-4\delta_{mn}, \tag{11}$$

where the subindex z indicates the z-component of a vector; the factor 4 corresponds to the normalization of the energy flux to -1 when $m=n$.

The stress tensor and velocity in any section of the guide follow a normal-mode decomposition

$$T=A_m T_m, \quad V=A_m V_m. \tag{12}$$

Using orthogonality relation (11) we obtain

$$\int_s (V_m^* T+VT_m^*)_z ds=-4A_m. \tag{13}$$

Equation (13) allows us to calculate the modal amplitudes A_m knowing the stress tensor T and velocity V on a section of the guide. When a transducer excites the end of the guide, the stress and the velocity are not independent. To calculate

the amplitudes A_n using only the velocity field V, we substitute Eq. (12) into Eq. (13),

$$\int_s (A_m T_m V_n^* + T_n^* V)_z ds = -4A_n. \tag{14}$$

Considering that $A_n = \delta_{nm} A_m$, we have

$$\left(4\delta_{mn} + \int_s (T_m V_n^*)_z ds\right) A_m = -\int_s (T_n^* V)_z ds. \tag{15}$$

This linear equation allows us to get the amplitude A_m from a knowledge of the velocity V on a section of the guide. Similarly, if we only know stress T, we obtain a similar equation of the following form:

$$\left(4\delta_{mn} + \int_s (T_n^* V_m)_z ds\right) A_m = -\int_s (T V_n^*)_z ds. \tag{16}$$

In order to apply the mode decomposition method, we need to know the dispersion relations and the mode shapes for the solid wave guide. In a cylindrical guide, three types of fundamental modes are present: compressional, torsional and flexural modes.[14] Using a longitudinal wave excitation placed symmetrically to the guide axis, the main excited modes will be the compressional ones. We reduce then our model to the study of the behavior of the compressional modes on the axis of the cylindrical waveguide.

For a guide of radius a, it is demonstrated that the axial and radial components of the velocity are given by

$$v_r = [pAJ_1(pr) + ikCJ_1(qr)]e^{i(\omega t - kz)} \tag{17}$$

$$v_z = [ikAJ_0(pr) + qCJ_0(qr)]e^{i(\omega t - kz)}, \tag{18}$$

where $p^2 = (\omega/V_l)^2 - k^2$, $q^2 = (\omega/V_t)^2 - k^2$ and V_l, V_t are the longitudinal and transverse wavespeeds in the material. The constants C and A are determined by boundary conditions. Imposing free boundary conditions on the surface of the guide, we obtain an implicit equation between k and ω of the form

$$\frac{2p}{a}(q^2+k^2)J_1(pa)J_1(qa) - (q^2-k^2)^2 J_0(pa)J_1(qa) - 4k^2 pqJ_1(pa)J_0(qa) = 0. \tag{19}$$

For a given frequency ω, this equation has an infinite number of roots, each one corresponding to a different mode of the guide. The solution of Eq. (19) gives the dispersion relations $\omega(k)$ for different values of ω.

In Fig. 3(a) the theoretical dispersion relations are shown. The frequency is normalized by the transverse velocity and the wavenumber by the guide radius. Notice that all the modes except the first one have a cut-off frequency. In order to visualize experimentally the dispersion curves, a hydrophone was slid along the lateral surface of the guide in order to record the spatial-temporal dependence of the impulse response $h(z,t)$ of the guide. Performing a spatial-temporal Fourier transform, we transform the (z,t) plan into the (k,ω) plan. Experimental dispersion relations are represented in Fig. 3(b).

These dispersion curves allow us to numerically calculate the pulse obtained after 8- and 1-bit time reversal on the

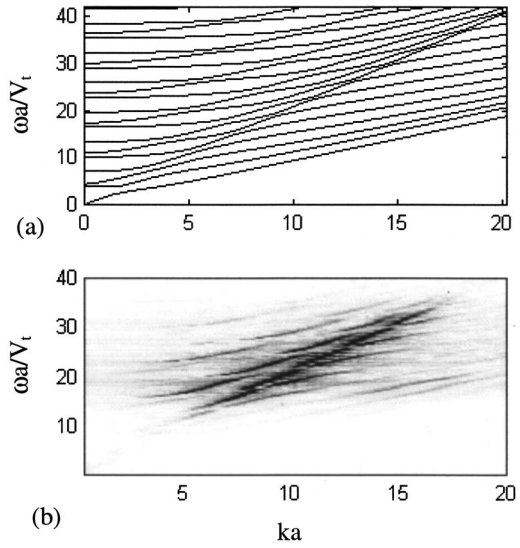

FIG. 3. Representation of the (a) theoretical and (b) experimental dispersion relations in the (k,ω) plane. Experiments have been performed with a 16-mm-diam duraluminium waveguide with a 75%-bandwidth, 0.9-MHz central frequency transducer.

axis of a 50-cm-long, 32-mm-diam duraluminium guide excited by seven 75%-bandwidth, 0.9-MHz center frequency transducers. Round trips inside the cylinder are of course taken into account. The sidelobe level is measured as the maximum amplitude of the time-reversed signal outside the main peak. The agreement between simulations and experimental results on the pulse shape, the pulse amplitude, and the sidelobe level is good (Fig. 4). For example, simulations confirm the amplitude gain of a factor of 5 between 8- and 1-bit time reversal. Table I summarizes the main characteristics of the pulses.

IV. POWER AMPLIFICATION VERSUS WAVEGUIDE CHARACTERISTICS

In this section, we show that the system ''solid waveguide–TRM'' acts as an acoustic resonator able to transmit very intense pulses with only a few transducers. The principle of this resonator is roughly the following: dispersion of a short pulse into a long low-amplitude signal, amplification, and finally recompression of the long signal into the initial, but now very intense, short pulse. The gain in amplitude depends on both the amplification factor and the duration of the long low-amplitude signal, i.e., the efficiency of the ''dispersion+recompression'' stage. In our case, amplification is limited by our low-power electronics. On the other hand, the ''dispersion+recompression'' is very efficient in our system. First, dispersion in the solid waveguide allows us to record signals whose duration is more than 1000 times the duration of the initial pulse. Second, time reversal is able to recompress all the acoustic energy into a short pulse.

The aim of this section is then to compare the amplitude of pulses obtained in water with our acoustic resonator with the amplitude of pulses generated by a classically focused transducer used as a reference. This reference transducer has the same diameter as the cylindrical solid waveguide and the same bandwidth as the transducers attached at A on one sec-

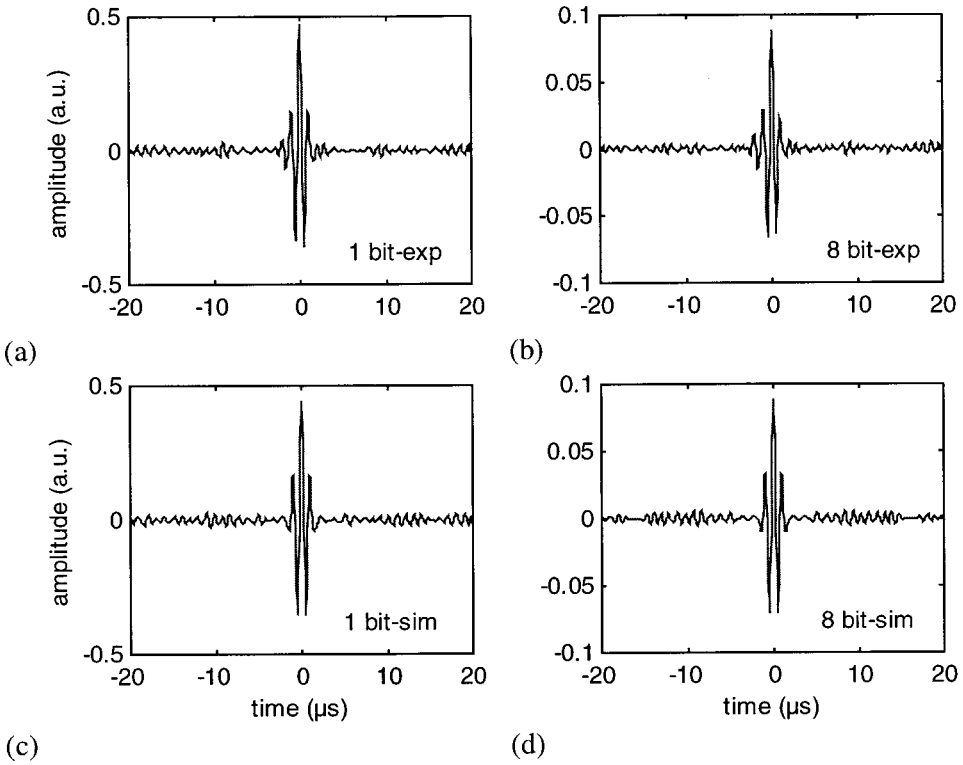

FIG. 4. Comparison between experimental and simulated signals obtained at the source after time reversal. Time reversal is performed from seven transducers fastened to one section of a 50-cm-long, 32-mm- diam duraluminium cylinder. The source is placed at 2 cm from the cylinder end. (a) Experimental 1-bit time reversal; (b) experimental 8-bit time reversal; (c) simulated 1-bit time reversal; and (d) simulated 8-bit time reversal.

tion of the guide. It is prefocused at $F=2$ cm. To compare things in a proper way, we have to pay careful attention to the following point: with our resonator, transducers transmit acoustic energy into the solid cylinder, whereas the reference transducer transmits energy directly into water. The difference of acoustical impedance between water and duraluminium implies that, for the same displacement, the power transmitted into the duraluminium is larger than the power transmitted into the water. We base our comparison on transducers that would transmit the same power whatever the acoustical impedance of the propagation medium. This means that we choose to transmit the same power from the resonator into the solid cylinder and from the reference transducer into the water. Our comparison criterion is then the pulse amplitude received after 1-bit time reversal at the focus $F=2$ cm in water. The ratio between the pulse amplitude obtained with the resonator and the reference transducer is the gain G of the resonator.

In the following, we numerically study the gain G as a function of the resonator characteristics, its length and diameter of the cylinder, and size of the transducers attached to the cylinder. Numerical results are obtained from the simulation described in Sec. III.

TABLE I. Comparison between experimental and simulated signals obtained at the source after time reversal.

Type of signal	Peak-peak amplitude (a.u.)	Signal/noise ratio (dB)
8-bit experimental	165	24.4
1-bit experimental	833	23.4
8-bit simulation	165[a]	22.7
1-bit simulation	784	24.3

[a]The 8-bit simulated signal has been normalized to provide the same amplitude as the 8-bit experimental signal.

In Fig. 5 we present the resonator gain versus cylinder length with a 3.2-cm-diam cylinder. Figure 6 shows the gain as a function of the cylinder diameter with a 50-cm-long cylinder and one 8-mm transducer fastened at the center of the cylinder section. These results demonstrate the resonator efficiency. Using 1-bit time reversal, a solid waveguide and one transducer, we show that we multiply up to a factor 20 the pulse amplitude generated by a classically focused transducer.

In Fig. 7, the gain of the resonator is plotted with respect to the size of the TRM transducers. The cylinder diameter is

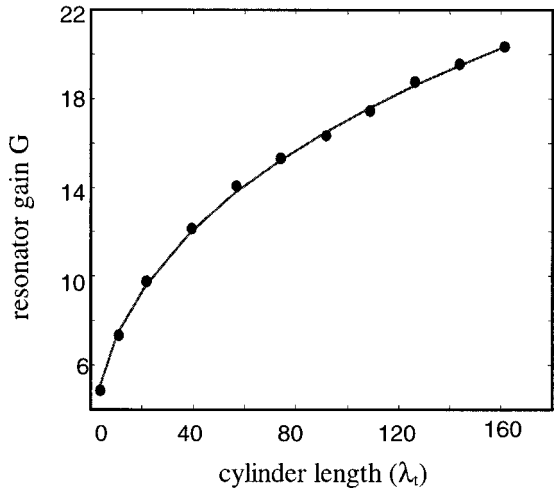

FIG. 5. Resonator gain as a function of cylinder length for a 3.2-cm-diam cylinder. The resonator is made of one 8-mm-diam transducer placed on the axis of the duraluminium cylinder. (*) correspond to simulations. Full line is a power-law fit whose coefficient is 0.37. Unit length is the transverse wavelength $\lambda_t = V_t / f_c = 3.1$ mm, where $V_t = 3100$ m/s is the transverse speed in duraluminium and $f_c = 1$ MHz is the transducers central frequency.

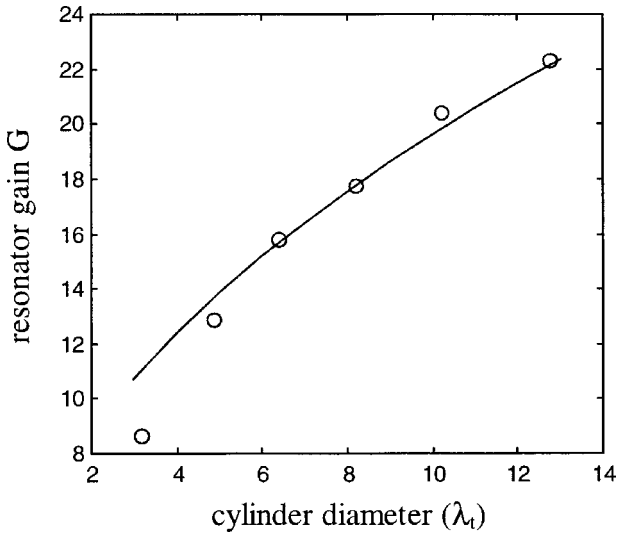

FIG. 6. Resonator gain as a function of cylinder diameter for a 50-cm length cylinder. The resonator is made of one 8-mm-diam transducer placed on the axis of the duraluminium cylinder. (○) correspond to simulation. Full line is a power-law fit whose coefficient is 0.5. Unit length is the transverse wavelength $\lambda_t = V_t / f_c = 3.1$ mm, where $V_t = 3100$ m/s is the transverse speed in duraluminium and $f_c = 1$ MHz is the transducers central frequency.

3.2 cm and its length is 50 cm. The resonator is now made of several limited-size transducers that cover all the cylinder section. We vary the size of the transducers fastened on this section which means that, decreasing the transducers size, we increase the number of transducers. We observe then that the larger the transducers, the smaller the gain. Indeed, if the TRM is made of one transducer that covers all the cylinder section, we excite only the first mode of the guide. If we cover the cylinder section with smaller transducers, this allows us to excite more modes, i.e., to disperse more efficiently the acoustic field and thus to increase the resonator gain. The optimal transducer size is a bit less than $\lambda_t/2$, which corresponds to the correlation length of the acoustic field received at the cylinder end on the TRM.

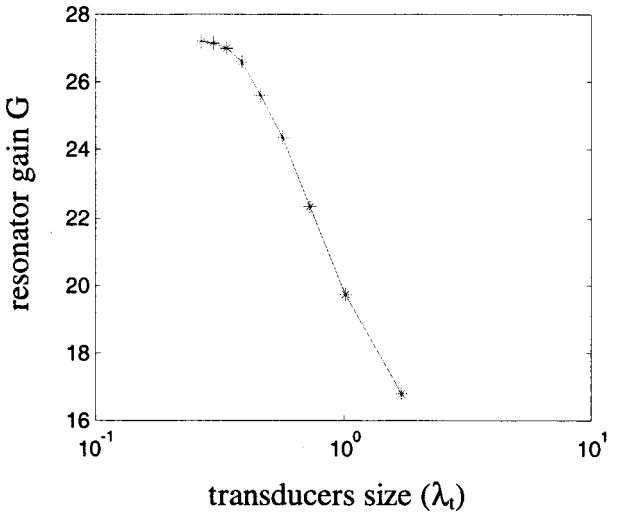

FIG. 7. Resonator gain versus transducers size for a 3.2-cm-diam, 50-cm-length cylinder. The TRM covers all the cylinder section. Unit length is the transverse wavelength $\lambda_t = V_t / f_c = 3.1$ mm, where $V_t = 3100$ m/s is the transverse speed in duraluminium and $f_c = 1$ MHz is the transducers central frequency.

Finally, we try to obtain an experimental demonstration of the pulse amplification obtained with the acoustic resonator with respect to a prefocused transducer whose diameter is the same as the cylinder diameter. The difficulty here is first to work with transducers that have the same bandwidth and, second, to work with the same input power in the two configurations. In the case of the resonator, transducers are fastened to a solid and the reference transducer is immersed in water. Because the electrical impedance of the two systems is different, the comparison is possible only if each electrical impedance matches as well as possible the 50-ohm output of the TRM. In this case we compare the pulse amplitude obtained at $F = 2$ cm with the acoustic resonator described in Fig. 1 and the reference transducer. We obtain experimentally a resonator gain of $G \sim 15$, which is a bit less than the theoretical gain of $G_{\text{theoretical}} \sim 18$ predicted in Fig. 7 with transducers of size λ.

V. EXPERIMENTAL RESULTS: SPATIAL FOCALIZATION

In Sec. IV, we have numerically demonstrated the power amplification at the output of our acoustic resonator. We have shown that the amplitude of the 1-bit time reversed signal at the source is much higher than the pulse amplitude generated by a classical focused transducer.

In this section, we study experimentally the spatial focusing properties of the acoustic resonator described in Fig. 1. The focal spot is obtained by measuring the pulse maximum amplitude at, and around, the focus. The main point is that the focal distance of this system is variable. Indeed, focal depth depends only on the position of the initial source that can vary from 0.5 cm up to 15 cm. Of course, a new set of signals has to be recorded for each focal depth before time reversal. This variable depth focusing is a big advantage compared to prefocused transducers.

Figure 8 presents experimental focal spots obtained with the ''solid waveguide–TRM'' device at $F = 2$, 4, 6, and 10 cm, respectively. Results are close to the theoretical limits given by focused tranducers whose diameters are the same as the cylinder diameter. However, the sidelobe level outside the focal spot is a bit higher. We will show in future articles that time reversal based on the inverse filter approach would allow us to reduce significantly the sidelobe level.[15]

Similarly, Fig. 9 shows the focal spot change when the source S is no longer on the axis of the cylinder. Once again, the big advantage of time reversal is the possibility to focus, whatever the position of the initial source. We observe that the focal spot size increases slowly and that the maximum amplitude of the pulse significantly decreases when the focus is off-axis. The cylinder symmetry naturally acts in favor of the cylinder axis.

Finally, Fig. 10 presents the pulse maximum amplitude as a function of focal distance. This shows that the ''solid waveguide–TRM'' system has an optimal focal distance of $F_{\max} = 2$ cm that depends mainly on the cylinder diameter. Simulations are in good agreement with experimental results.

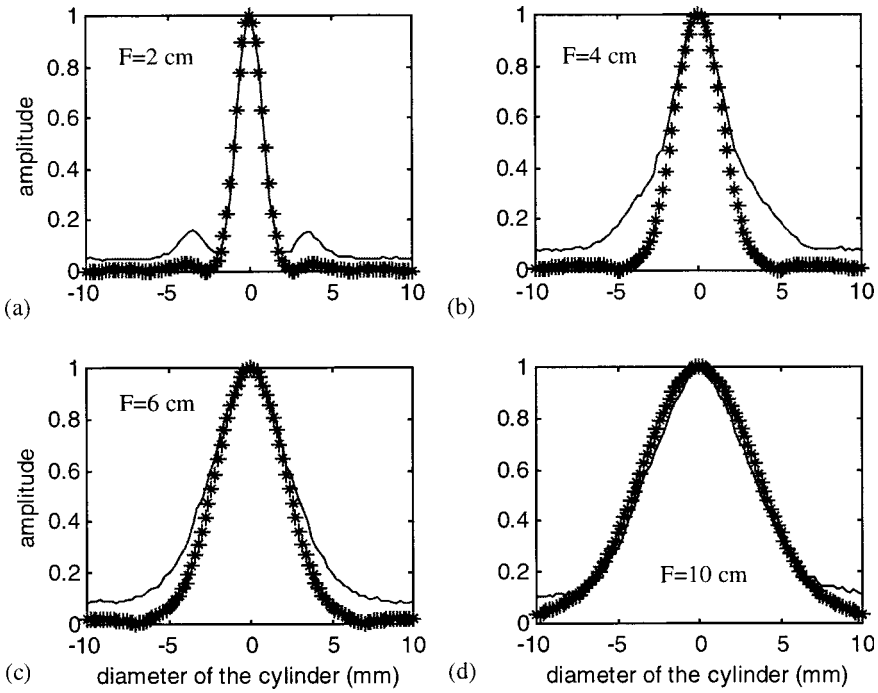

FIG. 8. Experimental focal spots obtained after 1-bit time reversal with the acoustic resonator described in Fig. 1 (full line). Stars correspond to the theoretical field generated at the focal F of a prefocused reference transducer. The reference transducer has the same diameter as the cylinder (3.2 cm) and the same bandwidth as the TRM transducers. (a) $F=2$ cm; (b) $F=4$ cm; (c) $F=6$ cm; (d) $F=10$ cm.

VI. CONCLUSION

In this work, we have demonstrated 1-bit time-reversal between a point source in water and a few transducers attached to one section of a cylindrical solid waveguide. We have shown that this system acts as an acoustic resonator which takes advantage of temporal and spatial dispersion in the solid to recompress and transmit into water a very intense pulse. We have achieved experiments with a resonator made of a 50-cm-long, 3.2-cm-diam cylinder and seven transducers centered around 0.9 MHz. The gain of the resonator, with respect to a classically focused transducer, is theoretically around 18 and experimentally around 15. Moreover, we have studied spatial focusing properties of this resonator. Experimental results show that this system is able to focus whatever the point source location in water. However, it appears, first, that the axis of the cylinder is a preferred direction and, second, that the resonator has an optimal focal distance of $F_{\max}=2$ cm.

One application of this acoustic resonator is lithotripsy. All experimental results presented here have been obtained in a linear regime for acoustic propagation. Our ambition is now to obtain high-intensity pulses in water with low-power (and therefore low-cost) electronics. For a low-voltage excitation (± 40 V), the maximum pressure obtained at $F=F_{\max}$ with our seven-transducer resonator could reach 650 bars. The next stage is to build an acoustic resonator made of a 10-cm-diam cylinder and 32 transducers. This new generation of lithotripter would combine several advantages. First, the cylinder diameter will be small compared to classical 30-cm-diam lithotripter. Second, the system will be able to

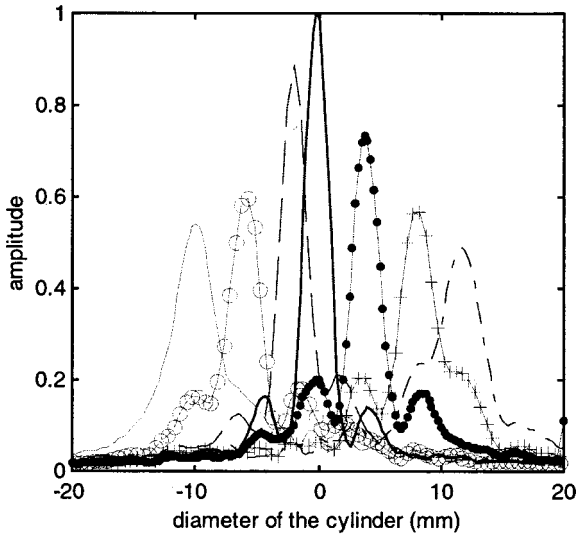

FIG. 9. Experimental focal spots obtained at $F=2$ cm while moving the focus of a distance d along a diameter of the cylinder: $d=0$ (axis of the cylinder), $d=-2$ mm, $d=4$ mm, $d=-6$ mm, $d=8$ mm, $d=-10$ mm and $d=12$ mm.

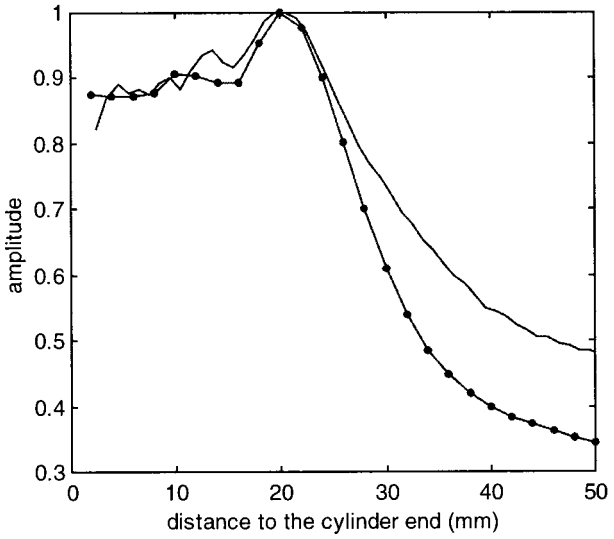

FIG. 10. Pulse maximum amplitude as a function of focus distance. Experimental results (full line) and simulation (dotted line).

focus anywhere in the body and not only at a predefined focus. Last, its price, in relation to the number of independent electronics, will be greatly reduced compared to a classical time reversal lithotripter made of more than 100 transducers. In future research, we will study the shock waves generated by our acoustic resonator and will perform *in vitro* as well as *in vivo* experiments related to lithotripsy applications.

ACKNOWLEDGMENTS

The authors would like to thank Christian Dorme for his contribution to the experimental setup and to the editor for proofreading the article.

[1] M. Delius ''Lithotripsy,'' Ultrasound Med. Biol. **26**, Suppl. 1, S55–S58 (2000).
[2] S. Nachef, D. Cathignol, and A. Birer, ''Piezoelectric electronically focused shock wave generator,'' J. Acoust. Soc. Am. **92**, 2292 (1992).
[3] M. Fink, C. Prada, F. Wu, and D. Cassereau, ''Self-focusing in inhomogeneous media with time-reversal acoustic mirrors,'' Proc. IEEE Ultrasonics Symposium, 1989, Vol. 2, pp. 681–686.
[4] J.-L. Thomas, F. Wu, and M. Fink, ''Time reversal mirror applied to lithotripsy,'' Ultrason. Imaging **18**, 106–121 (1996).
[5] P. Roux, B. Roman, and M. Fink, ''Time-reversal in an ultrasonic waveguide,'' Appl. Phys. Lett. **70**(14), 1811–1813 (1997).
[6] P. Roux and M. Fink, ''Time reversal in a waveguide: Study of the temporal and spatial focusing,'' J. Acoust. Soc. Am. **107**, 2418–2429 (2000).
[7] W. A. Kuperman, W. S. Hodgkiss, H. C. Song, T. Akal, C. Ferla, and D. R. Jackson, ''Phase conjugation in the ocean: Experimental demonstration of an acoustic time-reversal mirror,'' J. Acoust. Soc. Am. **103**, 25–40 (1998).
[8] W. S. Hodgkiss, H. C. Song, W. A. Kuperman, T. Akal, C. Ferla, and D. R. Jackson, ''A long-range and variable focus phase conjugation experiment in shallow water,'' J. Acoust. Soc. Am. **105**, 1597–1604 (1998).
[9] H. C. Song, W. A. Kuperman, and W. S. Hodgkiss, ''A time-reversal mirror with variable range focusing,'' J. Acoust. Soc. Am. **103**, 3234–3240 (1998).
[10] A. Derode, P. Roux, and M. Fink, ''Robust acoustic time-reversal with high-order multiple scattering,'' Phys. Rev. Lett. **75**(23), 4206–4209 (1995).
[11] A. Derode, A. Tourin, and M. Fink, ''Ultrasonic pulse compression with one-bit time reversal through multiple scattering,'' J. Appl. Phys. **85**(9), 6343–6352 (1999).
[12] G. Kino, *Acoustic Waves: Devices, Imaging, and Analog Signal Processing* (Prentice–Hall, Englewood Cliffs, NJ, 1987), pp. 569–573.
[13] B. A. Auld, *Acoustic Fields and Waves in Solids. Volume II* (Wiley, New York, 1973), pp. 155–159.
[14] D. Royer and E. Dieulesaint, *Elastic Waves in Solids* (Masson, Paris, 1996), pp. 289–297.
[15] M. Tanter, J. L. Thomas, and M. Fink, ''Time reversal and the inverse filter,'' J. Acoust. Soc. Am. **108**, 223–234 (2000).

Scattering from a ribbed finite cylindrical shell

Michel Tran-Van-Nhieu[a)]
Thomson Marconi Sonar, 7-9 rue des Mathurins, 92 221 Bagneux, France and Lab. Acoust. Ultrasonore et Electron. UPRESA CNRS 6068, 76 610 Le Havre, France

(Received 17 July 2001; accepted for publication 5 September 2001)

Scattering from a ribbed finite cylindrical shell is investigated with a theoretical formalism valid for long cylinders. An analytic expression is derived for the scattered pressure and it is shown that the scattered far field can be expressed as the sum of three components associated with specular reflection, scattering from helical waves, and Bloch–Floquet waves. Approximate solutions are proposed to reduce the computation load and resonance scattering is analyzed from the derived formulas leading to a relatively simple equation for the calculation of the Bloch–Floquet dispersion curves. Simple equations are proposed to determine the locations of the Bloch–Floquet waves for weak interactions of the ribs and the surface elastic waves. In the first Brillouin zone, it is found that the maximum level of Bloch–Floquet wave scattering depends only on the length of the cylinder as for the resonant modes of uniform cylindrical shells. Finally the relevancy of the method is examined by comparing numerical results to experimental data available in the published literature.
 [DOI: 10.1121/1.1413997]

PACS numbers: 43.20.Fn, 43.40.Ey [JGM]

I. INTRODUCTION

The scattering of sound waves by uniform finite cylindrical shells has been a subject of considerable interest because their resonance properties can be utilized to determine the elastic parameters of the body and also because the geometry of the object is sufficiently simple to permit the derivation of analytical methods.[1–5] The resonance scattering mechanism that involves phase matching to helical supersonic shear and compressional waves is well known and useful approximate equations have been derived to compute the dispersion curves of these elastic waves.[6] However as most of the ship hulls are stiffened by ribs, it is interesting to analyze the influence of a set of periodic rings on this scattering process and determine to what extent the ribs could modify the acoustic signature of this simple target.

In a series of papers, Photiadis *et al.* have published interesting results concerning scattering from ribbed cylindrical shells.[7–9] In these papers, the importance of scattering from Bloch or Floquet waves has been clearly displayed among other scattering mechanisms that occur on ribbed shells in the midfrequency range. These waves, which arise from multiple scattering of subsonic waves between the periodic rings along the surface of the cylindrical shell, would not radiate sound in this frequency range in the absence of the ribs. This is a new scattering mechanism involving subsonic flexural waves that of course does not exist on a uniform shell. Monostatic scattering measurements revealed strong highlights that occur when there is phase matching to the free elastic waves propagating on the surface of the ribbed shell, namely the helical shear and compressional waves and the Bloch–Floquet waves. Simple models have also been proposed to predict the dispersion curves which are useful for a qualitative interpretation of the experimental results but more complete methods are highly required to quantatively describe the interactions of the different surface waves with the motion of the ribs.

Most of the published papers concerning cylindrical shells have been devoted to the acoustic radiation from infinite cylinders with simply[10] or doubly[11] periodic ring supports and formal solutions are given by these authors to calculate the radiated far field. When the shell is finite, the problem becomes more complex and to our knowledge there is no analytical method that has been proposed in the published literature to deal with acoustic scattering from a ribbed finite shell. In this paper, a theoretical investigation of scattering from ribbed finite cylindrical shells is presented. The method is based upon the expansion of the solution near the surface of the shell in terms of the shape functions as defined by Miles[12] for finite periodic simply supported structures and on the description of the solution by a continuous distribution of elementary singularities that are used in our previous works on scattering from slender bodies or long cylindrical shells.[13,14]

In this article, the theoretical formalism is presented in Sec. II, where analytic expressions for the scattered pressure are derived under a certain number of assumptions. Approximate solutions for the scattered pressure are given in Sec. III in order to reduce the amount of calculation. Resonance scattering and equations leading to the determination of helical waves and Bloch–Floquet waves are discussed in Sec. IV and some simple formulas are derived to compute the dispersion curves. Section V presents analysis of numerical results and comparison to measured data. Finally a conclusion is given to summarize all the main results.

II. THEORETICAL ANALYSIS

Consider a harmonic plane wave p_i incident upon a thin cylindrical shell that is submerged in an acoustic medium of density ρ_f and velocity c_f and assume that the incident wave is parallel to the xOz plane. The origin O is located at the

a)Electronic mail: michel.tranvannhieu@fr.thalesgroup.com

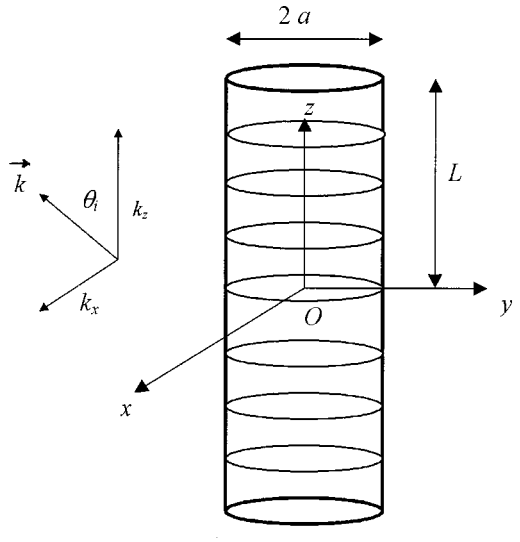

FIG. 1. Geometry of the ribbed cylindrical shell.

center of the shell as shown in Fig. 1. The interior of the cylinder is *in vacuo* and a set of periodically spaced rings are attached to the inside surface of the object (see Fig. 2).

The theoretical formalism was derived under the following assumptions:

(H1) the harmonic time dependence is in $e^{-i\omega t}$; for convenience, the term $e^{-i\omega t}$ will be dropped out of the equations,
(H2) the cylindrical shell is slender: $a/L \ll 1$,
(H3) the motions of the shell and the rings are described by thin shell theories,
(H4) only the normal component of the reactive force applied by the ring to the shell is considered,
(H5) the positions z_m of the rings on the z axis are given by $z_m = -(M-1)d:(M-1)d$ where $2M \gg 1$ is the number of periodic units $(2L = 2Md)$,
(H6) the ends of the shell are assumed to be simply supported,
(H7) the acoustic effects of the end sections are neglected.

The present approach is derived for a long cylinder (H2) and it is valid in the frequency range where the classical thin shell theories are available (H3). Assumption (H4) is rather restrictive as the other components of the reactive forces might considerably change the results;[15] this is not the case for assumption (H5) as it is believed that the exact locations of the rings are not significant for $M \gg 1$. Finally the last two assumptions limit the theory to aspect angles different from the cylinder axis.

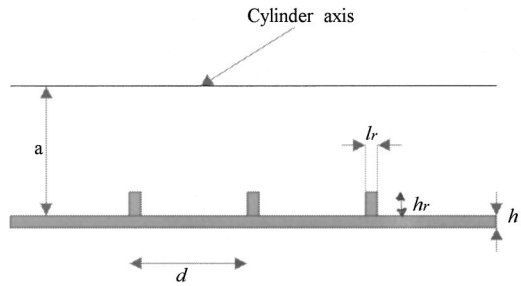

FIG. 2. Geometry of the ribs.

As for uniform cylindrical shells, the scattered pressure is split up into two components:

$$p_s = p_{\text{rig}} + p_{\text{res}}, \tag{1}$$

where p_{rig} is the pressure scattered by the cylinder considered as a perfectly rigid object and p_{res} consists of elastic resonances due to the elasticity of the material. For long cylinders p_{rig} and p_{res} are sought in the form of continuous distributions of sectorial spherical harmonics that were previously used to describe the acoustic field scattered by a slender body. It can be shown that p_{rig} can be expressed in cylindrical coordinates (r,φ,z) in the following form:[5]

$$p_{\text{rig}} = -\frac{k}{\pi}\sum_{n=0}^{\infty} \epsilon_n i^n \frac{\cos n\varphi}{\sin^n \theta_i}\left[\frac{J_n'}{H_n'}\right](k_x a) \times \int_{-L}^{L} h_n(k\rho)\left(\frac{r}{\rho}\right)^n e^{ik_z t}dt, \tag{2}$$

where $k = \omega/c$ is the acoustic wave number, $k_x = k\sin\theta_i$, and $k_z = k\cos\theta_i$. J_n is the cylindrical Bessel function of order n, H_n and h_n are, respectively, the cylindrical and spherical Hankel functions of order n of the first kind. The prime denotes the differentiation with respect to the argument, ϵ_n is the Neumann factor, $\epsilon_n = 1$ for $n = 0$ and $\epsilon_n = 2$ for $n > 0$ and $\rho = \sqrt{(t-z)^2 + r^2}$.

The resonant component p_{res} is sought in the form given by Eq. (3), which verifies the Helmholtz equation and the Sommerfeld condition at infinity

$$p_{\text{res}} = \frac{k}{\pi}\sum_{n,p,j} \epsilon_n i^n \cos n\varphi b_{npj} \int_{-L}^{L} h_n(k\rho)\left(\frac{r}{\rho}\right)^n \phi_{pj}(t)dt, \tag{3}$$

where the unknown coefficients b_{npj} are determined by the mechanical equations describing the vibrations of the ribbed shell, ϕ_{pj} are the shape functions for periodic, simply supported structures. In Eq. (3), as in the remainder of this paper, the symbol summation with indexes n, p, and j denotes a triple summation with the azimuthal mode number n varying between 0 and infinity, $0 \leqslant p \leqslant 2M$ and j is function of p as discussed in Sec. II A.

A. Shape functions

The shape function ϕ_{pj} was introduced by Miles[12] in his study of wave motion in finite periodic simply supported plates. In infinite periodic structures the solution is usually expanded in a series of space harmonics. When the structure is finite and its boundaries are simply supported, this series is replaced by sine functions. Indeed by an adaptation of this space-harmonics series that are used to analyze propagation of free waves in infinite periodic structures, he found that the solution can be expanded in terms of a specially ordered sine functions ϕ_{pj} of the form

$$\phi_{pj}(z) = \sin k_{pj}(z+L), \tag{4a}$$

where the axial wave numbers k_{pj} are defined as follows:

TABLE I. Values of $(p+4jM)$ for $2M=6$, $-2\leqslant j\leqslant 2$.

p	$j=-2$	$j=-1$	$j=0$	$j=1$	$j=2$
0				12	24
1	−23	−11	1	13	25
2	−22	−10	2	14	26
3	−21	−9	3	15	27
4	−20	−8	4	16	28
5	−19	−7	5	17	29
6			6	18	30

$$k_{pj}=\frac{\pi p}{2L}+\frac{2\pi j}{d}=\frac{\pi}{2L}(p+4jM) \quad p=0:2M. \tag{4b}$$

For these functions to be linearly independent and nonzero, it is required that

$$\begin{aligned} &j=1,N \quad \text{if } p=0,\\ &j=0,N \quad \text{if } p=2M,\\ &j=-N,N \quad \text{for } p\neq 0, \quad p\neq 2M. \end{aligned} \tag{5}$$

The number N determines the order of spatial resolution that may be obtained with these shape functions. The values of the arguments of k_{pj} for $M=3$ and $N=2$ are illustrated in Table I, which gives the number of half-waves associated with each function. As can be seen, it is a rearrangement of the arguments of the axial modes of the uniform cylindrical shell in order to make these sine functions unique. It has been shown that this sine series is well suited to structures having symmetric periodic units.[12]

B. Shell motion

The Donnell equations for the displacements of the cylindrical shell are[16]

$$\begin{aligned} &\frac{\partial^2 u}{\partial z^2}+\frac{\mu^-}{a^2}\frac{\partial^2 u}{\partial \varphi^2}+\frac{\mu^+}{a}\frac{\partial^2 v}{\partial z\partial\varphi}+\frac{\mu}{a}\frac{\partial w}{\partial z}+k_s^2 u=0,\\ &\frac{\mu^+}{a}\frac{\partial^2 u}{\partial z\partial\varphi}+\mu^-\frac{\partial^2 v}{\partial z^2}+\frac{1}{a^2}\frac{\partial^2 v}{\partial\varphi^2}+\frac{1}{a^2}\frac{\partial w}{\partial\varphi}+k_s^2 v=0,\\ &\frac{\mu}{a}\frac{\partial u}{\partial z}+\frac{1}{a^2}\frac{\partial v}{\partial\varphi}+\frac{w}{a^2}+\frac{h^2}{12}\left(\frac{\partial^2}{\partial z^2}+\frac{1}{a^2}\frac{\partial^2}{\partial\varphi^2}\right)^2 w-k_s^2 w\\ &\quad=-\frac{p_i+p_{\text{rig}}+p_{\text{res}}+p_r}{\rho_s c_s^2 h}, \end{aligned} \tag{6}$$

where (u,v,w) are the axial, circumferential, and radial components of the shell displacements and p_r denotes the pressure applied by the rings to the shell, $c_s=\sqrt{E_s/\rho_s(1-\mu^2)}$ is the longitudinal wave speed, μ is Poisson's constant, ρ_s is the shell density, E_s is the Young modulus of the shell material, h is the shell thickness, $\mu^{\pm}=(1\pm\mu)/2$, and $k_s=\omega/c_s$.

The components (u,v,w) are sought as expansions in the following form:

$$u(z,\varphi)=\sum_{n,p,j}\epsilon_n i^n\cos n\varphi\cos[k_{pj}(z+L)]u_{npj},$$

$$v(z,\varphi)=\sum_{n,p,j}\epsilon_n i^n\sin n\varphi\,\phi_{pj}(z)v_{npj}, \tag{7}$$

$$w(z,\varphi)=\sum_{n,p,j}\epsilon_n i^n\cos n\varphi\,\phi_{pj}(z)w_{npj},$$

where the coefficients $(u_{npj},v_{npj},w_{npj})$ are to be determined.

To proceed further the expansions of p_i, p_{rig}, p_{res}, and p_r are now calculated near the surface of the cylinder. First by inserting Eq. (A3) into Eq. (2), p_{rig} becomes

$$p_{\text{rig}}=-e^{ik_z z}\sum_{n=0}^{\infty}\epsilon_n i^n\cos n\varphi\left[\frac{J_n'}{H_n'}\right](k_x a)H_n(k_x r). \tag{8}$$

Using the classical expansion of plane wave with respect to cylindrical Bessel functions and applying the Wronskian identity of the Bessel functions $W(J_n(z),Y_n(z))=2/\pi z$, the following expression is obtained for $r=a$:

$$p_i+p_{\text{rig}}=\sum_{n,p,j}\epsilon_n i^n\cos n\varphi\,\phi_{pj}(z)P_{npj}, \tag{9}$$

where

$$P_{npj}=\frac{2}{\pi k_x a H_n'(k_x a)}F(k_z L,k_{pj}L). \tag{10}$$

In Eq. (10), the function F is defined as

$$F(x,y)=\frac{\sin(x+y)}{x+y}e^{iy}-\frac{\sin(x-y)}{x-y}e^{-iy}. \tag{11}$$

Next with Eqs. (3), (A1), and (A5), the resonant scattered pressure can be approximated near the surface of the cylinder by Eq. (12),

$$p_{\text{res}}(z,\varphi,r)=\sum_{n,p,j}\epsilon_n i^n B_{npj}\cos n\varphi H_n(\alpha_{pj}r)\phi_{pj}(z), \tag{12}$$

where α_{pj} is defined by Eq. (A6) and

$$B_{npj}=b_{npj}\left(\frac{\alpha_{pj}}{k}\right)^n. \tag{13}$$

From the condition of continuity of the radial displacement at the interface between the shell and fluid and with Eqs. (7)–(12), it is easy to find that

$$B_{npj}=\frac{\rho_f\omega^2}{\alpha_{pj}H_n'(\alpha_{pj}a)}w_{npj}. \tag{14}$$

Equations (9)–(14) give the expansions of p_i+p_{rig} and p_{res} on the surface of the cylinder. It remains now to find the expression of p_r which is induced by the ring motion.

C. Ring motion

It is assumed that p_r is of the form

$$p_r=\sum_{m=-M+1}^{M-1}p_m^r(\varphi)\,\delta(z-md), \tag{15}$$

where δ is the Dirac delta function. Therefore the mean pressure p_m applied by the shell to the ring located at $z=md$ is equal to

$$p_m=\frac{1}{l_r}\int_{z=md-l_r/2}^{z=md+l_r/2} p_r dz=\frac{p_m^r(\varphi)}{l_r}. \tag{16}$$

Considering each ring as a rod of circular curvature and neglecting inertia and rotary effects, the dynamical equations of motion for a rib are given by[17]

$$\frac{1}{a^2}\frac{\partial^2 V_m}{\partial\varphi^2}+\frac{1}{a^2}\frac{\partial W_m}{\partial\varphi}+\frac{\beta_r^2}{a^2}\left(\frac{\partial^2 V_m}{\partial\varphi^2}-\frac{\partial^3 W_m}{\partial\varphi^3}\right)+k_r^2 V_m=0,$$

$$\frac{1}{a^2}\frac{\partial V_m}{\partial\varphi}+\frac{W_m}{a^2}+\frac{\beta_r^2}{a^2}\left(\frac{\partial^4 W_m}{\partial\varphi^4}-\frac{\partial^3 V_m}{\partial\varphi^3}\right)-k_r^2 W_m=\frac{p_m^r(\varphi)}{\rho_r c_r^2 A_r}, \tag{17}$$

where (V_m, W_m) are the circumferential and radial components of the ring displacements, $\beta_r^2=h_r^2/12a^2$, $k_r=\omega/c_r$, $c_r=\sqrt{E_r/\rho_r}$, and $A_r=l_r h_r$ is the cross section of the ring (see Fig. 2).

Assuming expansions of (V_m, W_m, p_m^r) to be of the form

$$V_m(\varphi)=\sum_n \epsilon_n i^n \sin n\varphi V_n^m,$$

$$W_m(\varphi)=\sum_n \epsilon_n i^n \cos n\varphi W_n^m, \tag{18}$$

$$p_m^r(\varphi)=\sum_n \epsilon_n i^n \cos n\varphi P_n^m,$$

and inserting Eq. (18) into Eq. (17), it is easy to show that

$$Z_n^r W_n^m=P_n^m, \tag{19a}$$

where Z_n^r is given by

$$Z_n^r=\frac{\rho_r c_r^2 A_r}{a^2}\left[1-\Omega_r^2+\beta_r^2 n^4+\frac{n^2(1+\beta_r^2 n^2)^2}{\Omega_r^2-n^2(1+\beta_r^2)}\right];$$

$$\Omega_r=k_r a. \tag{19b}$$

From the expansion of the radial displacement of the shell given by Eq. (7) and with the definition of $W_m=w(md,\varphi)$, the coefficients W_n^m can be expressed in the form $W_n^m=\Sigma_{q,l}\phi_{ql}(md)w_{nql}$ and with Eqs. (15), (18), and (19) the reactive force applied by the rings to the shell takes the form

$$p_r=\sum_{m,n,q,l}\epsilon_n i^n \cos n\varphi Z_n^r w_{nql}\phi_{ql}(md)\,\delta(z-md). \tag{20}$$

D. Scattered pressure

Substituting the expansions of the shell displacements given by Eq. (7) into the Donnell equations describing the vibration of the shell and using the above-mentioned results and Eq. (B6), the following equation for w_{npj} is obtained after a little algebraic calculation:

$$w_{npj}+A_{npj}A_n^{r\,-1}\sum_{l=-N}^{N} w_{npl}=-\frac{A_{npj}P_{npj}}{\rho_f\omega^2 a}$$

$$\text{for } 2M>p>0, \tag{21a}$$

$$w_{npj}=-\frac{A_{npj}P_{npj}}{\rho_f\omega^2 a} \quad \text{for } p=0 \text{ or } =2M, \tag{21b}$$

where

$$A_{npj}=[Z_n^f(\alpha_{pj}a)-Z_n^s(k_{pj}a)]^{-1},$$

$$A_n^r=\left[\frac{Z_n^r}{\rho_f\omega^2 a d}\right]^{-1}, \quad Z_n^f(\alpha)=\frac{H_n(\alpha)}{\alpha H_n'(\alpha)}, \tag{22a}$$

$$Z_n^s(\alpha)=\frac{\rho_s h}{\rho_f a\Omega^2}\left\{\Omega^2-\beta_s^2(\alpha^2+n^2)^2-\frac{\Omega^4-\mu^-[\Omega^2 n^2+(2\mu+3)\Omega^2\alpha^2-4\mu^-\mu^+\alpha^4]}{[\mu^-(\alpha^2+n^2)-\Omega^2](\alpha^2+n^2-\Omega^2)}\right\}, \tag{22b}$$

where $\Omega=\omega a/c_s$.

Equation (21a) can be solved explicitly: indeed the term $\Sigma_{l=-N}^N w_{npl}$ may be computed by summing both members of Eq. (21a) from $j=-N$ to $j=N$. Then the coefficients B_{npj} are found by using Eq. (14),

$$B_{npj}=\frac{-A_{npj}}{\alpha_{pj}aH_n'(\alpha_{pj}a)}\left(P_{npj}-\delta_p\frac{\Sigma_{l=-N}^N A_{npl}P_{npl}}{A_n^r+\Sigma_{l=-N}^N A_{npl}}\right)$$

$$\text{for } p=0{:}2M, \tag{23}$$

where $\delta_p=0$ for $p=0$ or $p=2M$ and $\delta_p=1$ for $2M>p>0$.

The expression of the far field pressure scattered by the ribbed cylindrical shell is obtained by inserting the asymptotic expansion of spherical Hankel function h_n for large arguments[18] into Eqs. (2) and (3); this gives

$$p_s=\frac{e^{ik\rho_0}}{\rho_0}(D_{\text{rig}}+D_{\text{res}}), \tag{24}$$

where ρ_0 is the distance from the observation point to the origin O and

$$D_{\text{rig}}=\frac{2i}{\pi k}\frac{\sin[kL(\cos\theta_i-\cos\theta)]}{\cos\theta_i-\cos\theta}\sum_{n=0}^{\infty}\epsilon_n\cos n\varphi \times\left[\frac{J_n'}{H_n'}\right](k_x a)\left(\frac{\sin\theta}{\sin\theta_i}\right)^n, \tag{25}$$

whereas from Eqs. (10), (13), and (23) D_{res} becomes

$$D_{\text{res}}=\frac{2L}{\pi^2 k_x a^2}\sum_{n,p,j}\epsilon_n\cos n\varphi \times\left(\frac{k\sin\theta}{\alpha_{pj}}\right)^n\frac{F(-kL\cos\theta,k_{pj}L)A_{npj}}{H_n'(k_x a)\alpha_{pj}H_n'(\alpha_{pj}a)} \times\left(F(k_z L,k_{pj}L)-\delta_p\frac{\Sigma_{l=-N}^N A_{npl}F(k_z L,k_{pl}L)}{A_n^r+\Sigma_{l=-N}^N A_{npl}}\right). \tag{26}$$

With the definition of k_{pj} as discussed in Sec. II A and from Eq. (11) one has $F(x,-y)=-F(x,y)$ so that $F(-kL\cos\theta,k_{pj}L)F(k_zL,k_{pj}L)=F(-kL\cos\theta,|k_{pj}|L)F(k_zL,|k_{pj}|L)$.

Then the expression of $D_{\rm res}$ can be recast in the following form:

$$D_{\rm res}=D_{\rm res}^{\rm ucs}+D_{\rm res}^{r}, \tag{27a}$$

where

$$D_{\rm res}^{\rm ucs}=\frac{2L}{\pi^2k_xa^2}\sum_{n=0}^{\infty}\sum_{p=1}^{\infty}\epsilon_n\cos n\varphi\left(\frac{k\sin\theta}{\alpha_p}\right)^n \times\frac{F(-kL\cos\theta,k_pL)F(k_zL,k_pL)}{H_n'(k_xa)\alpha_pH_n'(\alpha_pa)(Z_n^f(\alpha_pa)-Z_n^s(k_pa))}, \tag{27b}$$

$$D_{\rm res}^{r}=-\frac{2L}{\pi^2k_xa^2}\sum_{n=0}^{\infty}\sum_{p=1}^{2M-1}\sum_{j=-N}^{N}\epsilon_n\cos n\varphi\left(\frac{k\sin\theta}{\alpha_{pj}}\right)^n \times\frac{F(-kL\cos\theta,k_{pj}L)A_{npj}}{H_n'(k_xa)\alpha_{pj}H_n'(\alpha_{pj}a)} \times\frac{\Sigma_{l=-N}^{N}A_{npl}F(k_zL,k_{pl}L)}{A_n^r+\Sigma_{l=-N}^{N}A_{npl}}. \tag{27c}$$

It can be seen with the present notation that $D_{\rm res}^{\rm ucs}$ given by Eq. (27b) corresponds to the expression previously derived for the resonant contribution of a uniform finite cylindrical shell.[2] When the shell has a set of rings periodically spaced, the reactive forces applied by the rings to the shell give rise to an extra term $D_{\rm res}^{r}$ in the scattered pressure the expression of which is described by Eq. (27c). Finally gathering all these results, the expression of the far field pressure scattered by a ribbed finite cylindrical shell is equal to

$$D_s=D_{\rm rig}+D_{\rm res}^{\rm ucs}+D_{\rm res}^{r}, \tag{28}$$

where $D_{\rm rig}$, $D_{\rm res}^{\rm ucs}$ and $D_{\rm res}^{r}$ are given by Eqs. (25), (27b), and (27c). Equation (28) is the main result of this paper: it provides an analytical expression to compute the pressure scattered by a ribbed finite cylindrical shell and it is expressed in a form that permits one to separate the different physical mechanisms involved in the scattering process. However the computation load remains relatively high for the determination of $D_{\rm res}^{r}$ so that further simplifications are necessary to reduce the amount of calculation.

III. APPROXIMATE EXPRESSIONS FOR THE SCATTERED PRESSURE

In order to simplify the above-mentioned expressions, we will now proceed to the following approximations. First we note that the function F given by Eq. (11) can be replaced by

$$|F(x,y)|\approx\frac{\sin(x\pm y)}{x\pm y}\quad\text{for}\quad|x\mp y|\gg1 \tag{29}$$

for large arguments so that at the first approximation, we shall restrict the summations to axial wave numbers k_{pj} verifying the condition

$$|k_z\pm k_{pj}|L<\pi. \tag{30}$$

If k_{pj} is of the form $k_{pj}=k\cos\theta_{ij}$ then for $kL\gg1$, we have $\theta_{ij}\approx\theta_i$ so that $\alpha_{pj}\approx k\sin\theta_i$. Furthermore as there is only one axial wave number k_{pj} meeting Eq. (30) for a given index p in Eq. (27c), the summation with index l reduces to one term equal to $D_{npj}F(k_zL,k_{pj}L)$. Therefore Eq. (27) becomes

$$D_{\rm res}^{\rm ucs}=\frac{2L}{(\pi k_xa)^2}\sum_{n=0}^{\infty}\sum_{p\in P_1}\epsilon_n\cos n\varphi\left(\frac{\sin\theta}{\sin\theta_i}\right)^n \times\frac{F(-kL\cos\theta,k_pL)F(k_zL,k_pL)}{[H_n'(k_xa)]^2(Z_n^f(\alpha_pa)-Z_n^s(k_pa))}, \tag{31a}$$

$$D_{\rm res}^{r}=\frac{-2L}{(\pi k_xa)^2}\sum_{n=0}^{\infty}\sum_{(p,j)\in P_2}\epsilon_n\cos n\varphi\left(\frac{\sin\theta}{\sin\theta_i}\right)^n \times\frac{F(-kL\cos\theta,k_{pj}L)F(k_zL,k_{pj}L)A_{npj}^2}{[H_n'(k_xa)]^2(A_n^r+\Sigma_{l=-N}^{N}A_{npl})}, \tag{31b}$$

where P_1 and P_2 are defined for $k_z>0$ as

$$P_1=\{p\geqslant1:|k_z-k_p|L<\pi\},\qquad P_2=\{2M-1\geqslant p\geqslant1;|j|\leqslant N:|k_z\pm k_{pj}|L<\pi\}. \tag{32}$$

The backscattered pressure D_s^m can be found by setting $\theta=\pi-\theta_i$; $\varphi=\pi$ in the above-mentioned equations; this yields

$$D_s^m=D_{\rm rig}^m+D_{\rm res}^{{\rm ucs},m}+D_{\rm res}^{r,m}, \tag{33a}$$

$$D_{\rm rig}^m=\frac{i}{\pi k}\frac{\sin(2kL\cos\theta_i)}{\cos\theta_i}\sum_{n=0}^{\infty}\epsilon_n(-1)^n\left[\frac{J_n'}{H_n'}\right](k_xa), \tag{33b}$$

$$D_{\rm res}^{{\rm ucs},m}=\frac{2L}{(\pi k_xa)^2}\sum_{n=0}^{\infty}\sum_{p\in P_1}\epsilon_n(-1)^n \times\frac{F^2(k_zL,k_pL)}{[H_n'(k_xa)]^2(Z_n^f(\alpha_pa)-Z_n^s(k_pa))}, \tag{33c}$$

$$D_{\rm res}^{r,m}=-\frac{2L}{(\pi k_xa)^2}\sum_{n=0}^{\infty}\sum_{(p,j)\in P_2}\epsilon_n(-1)^n \times\frac{F^2(k_zL,k_{pj}L)A_{npj}^2}{[H_n'(k_xa)]^2(A_n^r+\Sigma_{l=-N}^{N}A_{npl})}. \tag{33d}$$

IV. RESONANCE SCATTERING

It can be seen from Eqs. (27c) and (33d) that the amplitude of the term in the summation is enhanced when the amplitude of one of the two terms A_{npj}^{-1} or $A_n^r+\Sigma_{l=-N}^{N}A_{npl}$ is minimum.

A. Helical waves

It can be noted that Z_n^s is a real number according to Eq. (22b) so that

$$A_{npj}^{-1}=Z_n^f(\alpha_{pj}a)-Z_n^s(k_{pj}a)$$
$$=\{\mathrm{Real}(Z_n^f(\alpha_{pj}a))-Z_n^s(k_{pj}a)\}$$
$$+i\,\mathrm{Imag}(Z_n^f(\alpha_{pj}a)). \quad (34)$$

Therefore A_{npj}^{-1} is minimum when the real part of the left member of Eq. (34) vanishes,

$$\mathrm{Real}(Z_n^f(\alpha_{pj}a))-Z_n^s(k_{pj}a)=0, \quad (35)$$

which leads to the well-known resonance condition for the modes associated with compressional, shear, and flexural waves propagating on a uniform thin cylindrical shell. This equation was analyzed in Ref. 1 so that the reader could refer to this work for more details.

B. Bloch–Floquet waves

Consider now the expression $A_n^r+\Sigma_{l=-N}^N A_{npl}$. Indeed according to Eq. (22) A_n^r is a real number and in like manner as previously this expression is minimum when its real part is equal to 0,

$$R_{\mathrm{res}}^n=\mathrm{Real}\left(A_n^r+\sum_{l=-N}^{N}A_{npl}\right)$$
$$=\frac{\rho_f\omega^2 ad}{Z_n^r}+\sum_{l=-N}^{N}\mathrm{Real}\left(\frac{1}{Z_n^f(\alpha_{pl}a)-Z_n^s(k_{pl}a)}\right)=0, \quad (36)$$

which leads to the determination of the modes associated with Bloch–Floquet waves (BFW) that describe the propagation behavior of elastic waves on infinite periodic structures. As the number N defines the maximum of number of half-waves resolved by the shape functions ϕ_{pj}, Eq. (36) permits one to calculate the N first BFW. Because of its complexity, there is no attempt to solve Eq. (36) analytically in the present work; instead its solutions will be sought numerically. However some interesting results could be extracted from the above-mentioned derivation by the following considerations.

First it can be seen intuitively that a solution of Eq. (36) exists when one of the terms in the left member varies continuously from $-\infty$ (respectively, ∞) to ∞ (respectively, $-\infty$) near the root of

$$R(\overline{\chi_l})=Z_n^f(\sqrt{(ka)^2-\overline{\chi_l}^2})-Z_n^s(\overline{\chi_l})=0, \quad (37)$$

while the other terms remain finite. Then this solution could be approximated by the root of Eq. (37) provided that there is a change of sign of $R(x)$ when $x\to\overline{\chi_l^{\pm}}$. In Eq. (37), the variable $\overline{\chi_l}$ is defined as

$$\overline{\chi_l}=\overline{\chi}+\frac{2\pi la}{d}, \quad (38)$$

where l is an integer number and the unknown variable $\overline{\chi}=\overline{\chi}(n)$ is the Bloch–Floquet wave number of the periodic shell normalized by a^{-1} and associated with the azimuthal mode number n. Equation (37) has a solution only if Z_n^f is a real number and according to Eq. (22a) this condition is only met when the argument of Z_n^f is a pure imaginary number, i.e., when $\overline{\chi_l}$ is a subsonic mode $|\overline{\chi_l}|>ka$. For $\Omega\gg 1$ Eq. (22b) can be approximated by

$$Z_n^s(\alpha)\approx\frac{\rho_s h}{\rho_f a\Omega^2}\{\Omega^2-\beta_s^2(\alpha^2+n^2)^2\} \quad (39a)$$

and using uniform asymptotic expansions for large orders of Kelvin functions,[18] one has

$$Z_n^f(i\alpha)=\frac{K_n(\alpha)}{\alpha K_n'(\alpha)}=-\frac{1}{\sqrt{\alpha^2+n^2}}. \quad (39b)$$

Inserting Eq. (39) into Eq. (37) yields

$$\eta^2-1-\frac{\epsilon}{\tilde{\Omega}^{1/2}}\frac{1}{\sqrt{\eta-\tilde{\Omega}}}=0, \quad (40)$$

which is exactly the equation for a fluid-loaded plate.[19] In Eq. (40) $\epsilon=\rho_f c_s/\rho_s c_f\sqrt{12}$ denotes the intrinsic fluid-loading parameter, $\tilde{\Omega}=c_s h\omega/c_f^2\sqrt{12}$ is the radian frequency normalized by the coincidence frequency of the plate, and

$$\eta=\frac{\beta_s(\overline{\chi_l}^2+n^2)}{\Omega}. \quad (41)$$

An approximate solution to Eq. (40) can be easily obtained for $\epsilon\ll 1$; it is equal to

$$\eta=1+\frac{\epsilon}{2\tilde{\Omega}^{1/2}}\frac{1}{\sqrt{1-\tilde{\Omega}}}. \quad (42)$$

Then substituting Eqs. (41) and (42) into Eq. (38) gives

$$\overline{\chi}=\left[\frac{\Omega}{\beta_s}\left(1+\frac{\epsilon}{2\tilde{\Omega}^{1/2}}\frac{1}{\sqrt{1-\tilde{\Omega}}}\right)-n^2\right]^{1/2}-\frac{2\pi la}{d}. \quad (43a)$$

It can be easily checked that $R(x\to\overline{\chi_l^{\pm}})$ verifies the required condition of sign when the solution is given by Eqs. (38) and (43a) provided that $\tilde{\Omega}<1$. Equation (43a) reduces to

$$\chi=\overline{\chi}/a=k_f-\frac{2\pi l}{d} \quad (43b)$$

when the term of order ϵ is neglected and $n\ll\sqrt{\Omega/\beta_s}$. Equation (43b) is identical to the free wave dispersion equation that is proposed previously for a *crude* prediction of the flexural Bloch–Floquet wave number.[8] It should be emphasized here that the present derivation is only valid when the interactions of the ribs and BFW of different order are weak so that their corresponding terms in Eq. (36) remain finite near the root of Eq. (37); otherwise the results might change considerably as we will see later in the numerical applications.

Then consider the first Brillouin zone where the acoustic wave number verifies the relationship $k<\pi/d$. Indeed in this region there is only one supersonic mode meeting the spatial coincidence condition

$$k_z=k_{pj} \quad (44)$$

for a given value of p while the other axial modes k_{pl} are subsonic. At spatial coincidence aspect angle, the projection of the incident wave number vector in the direction of the shell axis is equal to the (p,j) axial wave number mode and according to Eq. (29) the amplitude of the function F is maximum and is of the order of unity. If Eqs. (36)–(44) are

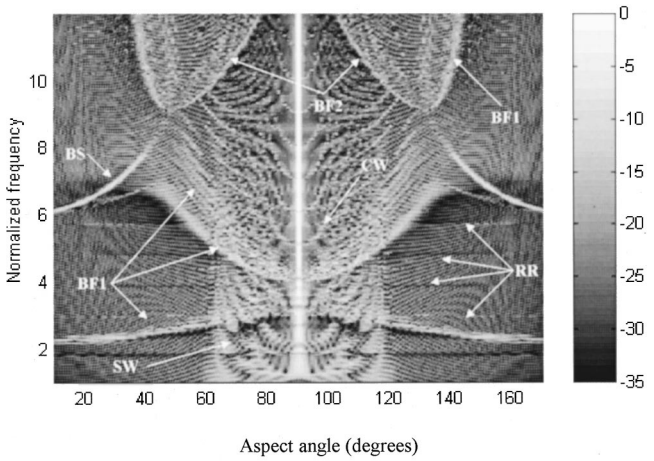

FIG. 3. Backscattering from a ribbed finite cylindrical shell. BFn: scattering of BFW of order n; BS: Bragg scattering; RR: rib resonance; SW: shear wave scattering; CW: compressional wave scattering.

fulfilled simultaneously and as Z_n^f is a real number for subsonic modes, the coefficients in the expansion of $D_{\rm res}^{r,m}$ become

$$(D_{\rm res}^{r,m})_{npj}=\frac{2iL}{(\pi k_x a)^2}\,\frac{\epsilon_n(-1)^n A_{npj}^2 F^2(k_zL,k_zL)}{[H_n'(k_xa)]^2\,{\rm Imag}(A_{npj})}, \tag{45}$$

where Imag(x) denotes the imaginary part of x. At spatial coincidence one has $\alpha_{pj}=k_x$ and

$${\rm Imag}(A_{npj})=-|A_{npj}|^2\,{\rm Imag}[Z_n^f(\alpha_{pj}a)], \tag{46a}$$

$${\rm Imag}[Z_n^f(x)]={\rm Imag}\left(\frac{H_n}{xH_n'}\right)=\frac{2}{\pi x^2|H_n'|^2}. \tag{46b}$$

Inserting the above-mentioned results into Eq. (45) yields

$$|D_{\rm res}^{r,m}|_{npj}=\frac{\epsilon_n L}{\pi}F^2(k_zL,k_zL)\approx\frac{\epsilon_n L}{\pi}, \tag{47}$$

which shows that the maximum resonance scattering level of BFW is equal to the total length of the shell divided by π for $n>0$ in the first Brillouin zone. This result is similar to the case of the resonant helical modes propagating on a uniform cylindrical shell.[1–3]

V. NUMERICAL APPLICATIONS

The ribbed cylinder used for the computations has approximately the same parameters as for the framed cylindrical shell investigated in Ref. 8: radius $a=6.92$ cm, a total length $2L=0.856$ m, shell thickness $h=0.635$ mm. The rings have length $l_r=0.533$ mm, thickness $h_r=5.7$ mm, and a rib spacing $d=1.05$ cm. The elastic parameters are that of nickel with $E_s=E_r=2.1\times10^{11}$ Pa, $\mu=0.3$, and $\rho_r=\rho_s=8800$ kg/m^3 while the external fluid is water with $c_f=1500$ m/s and $\rho_f=1000$ kg/m^3. Equation (33) was used to calculate the pressure backscattered by the ribbed cylindrical shell.

D_s^m is shown in Fig. 3 as a function of Ω and aspect angle. The computation was made at every degree for angle varying between 10° and 170° with a frequency increment $\Delta f=100$ Hz. The amplitude of the far field is presented in black and white colors and it ranges between -35 and 0 dB. This representation in the (angle, frequency) plane that was adopted in Refs. 3, 20, and 21 for displaying resonance scattering from uniform cylindrical shells, is now usually adopted to point out the importance of elastic scattering. As can be seen the calculation shows patches of high amplitudes corresponding to specular reflection at broadside and to nonspecular scattering of acoustic waves due to phase matching to the free elastic waves that propagate on the ribbed cylindrical shell in this frequency range. These waves are helical shear and compressional waves and Bloch–Floquet waves (BFW) of first and second order. Figure 3 also displays Bragg scattering of first order that occurs when the projection of the acoustic wave number on to the z axis is equal to an integer number of π/d: $k_z=\pi n/d$ $(n=1)$. The existence of these different scattering phenomena is confirmed by experiments and they were analyzed by using elementary modeling techniques.[7,8] The comparison of our computed results with measured backscattering (see Fig. 2 of Ref. 8) shows a good agreement at low and high frequencies for the prediction of the locations and the amplitudes of these different scattering mechanisms in the (angle, frequency) plane. Furthermore according to Eq. (47) the maximum amplitude of Bloch waves is equal to $20\log(0.856/\pi)=-11$ dB, which is consistent with the experimental results.

However only a partial agreement has been found in the frequency range $3<\Omega<8$ where the two highlight curves formed by the envelopes of the upper portions of the computed BFW of first order (BFW1) are less curved toward the x axis than the two more-or-less horizontal curves observed experimentally. It can be clearly seen that the upper parts of BFW1 depend significantly on the value of n and tend to form two distinct curves of high amplitude level associated with the low and high azimuthal mode numbers.

The effects of the ribs near the resonant frequencies which occur when $Z_n^r=0$ [see Eq. (19b)] close to $\Omega=n$ can also be observed: however according to Eq. (33d) $D_{\rm res}^{r,m}$ vanishes at these resonances. Therefore the present theory does not predict a high amplitude level in the scattering response at the rib resonances because the ribs/shell forces are minimized. Note that a calculation by finite elements method shows that the flexural vibration of individual ribs may give rise to highlights at certain frequencies corresponding to the resonances of an annular plate.[22] Indeed the ribs are considered as curved beams in the present approach so that formally thin shell theories do not hold when the ring thickness exceeds $\lambda_s/20$ where λ_s is the shear wavelength, i.e., when $f>2f_c$.

In order to analyze the distortions of BFW by the rib motion and the interference effects, the locations of BFW1 and BFW2 are obtained by calculating numerically the expression of $R_{\rm res}^{n^{-1}}$ where $R_{\rm res}^n$ is given by Eq. (36). The computation was made with $N=2$ in the (angle, frequency) plane and $k_{pj}=k\cos\theta$. The amplitude of $R_{\rm res}^{n^{-1}}$ is shown in relative dB levels in Fig. 4 for two azimuthal mode numbers at low $n=10$ and high $n=20$; the locations of the roots of Eq. (36) are represented in white color that is associated with the maximum amplitude level. The computations using Eq. (43a) with $l=1$ (respectively, $l=2$) for BFW1 (respectively,

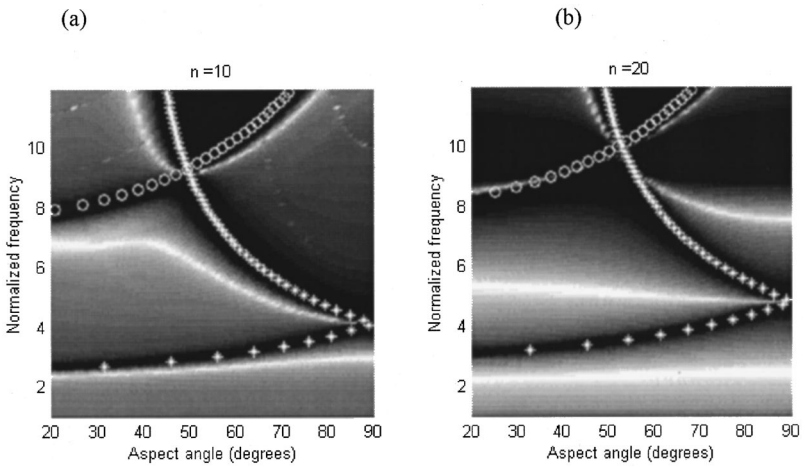

FIG. 4. Locations of Bloch–Floquet waves for (a) $n=10$ and (b) $n=20$. BFW of first order (+: BFW1) and second order (○: BFW2) computed using Eq. (43a).

BFW2) are overlaid to make the interpretation of the results easier. As can be seen in Fig. 4(a) there is a strong interference of the upper part of BFW1 with the lower part of BFW2 for the low azimuthal mode number in the frequency range $6<\Omega<9$ merging into two curves that are different than those predicted by Eq. (43a) in the frequency range $4<\Omega<8$. Finally in Fig. 4(b) two almost horizontal bands could be seen at low frequencies corresponding to the locations of the roots of Eq. (36) in the (angle, frequency) plane. In principle they should give rise to a high scattering level according to Eq. (47) but as in Eq. (33d) $H_n^{1\prime}(x)$ is very large for $n>x$, these high amplitudes occur in exponentially small regions that could not be detected in the calculation of the scattered pressure.

VI. CONCLUSIONS

The problem of scattering from a ribbed finite cylindrical shell has been investigated theoretically by applying a formalism that is valid for long cylinders. The solution is derived under a certain number of assumptions the most restrictive of which is that the ribs may be considered as thin curved rods and interact with the cylinder only through normal forces. As in the case of slender bodies, the scattered pressure is sought as a continuous distribution of sectorial spherical harmonics where their strengths are determined by the mechanical equations governing the motions of the cylindrical shell and the set of periodic rings. This is achieved by expanding the unknown variables in terms of angular harmonics and shape functions that are an adaptation of space-harmonics series to finite simply supported structures.

It has been shown that the expression of the far field scattered pressure is the sum of three terms: the first term is equal to the pressure scattered from a perfectly rigid long cylinder, the second term corresponds to the expression previously derived for the resonant contribution of a uniform cylindrical shell, whereas the last term is due to the reactive forces applied by the set of periodic rings to the shell. Approximate expressions to the last two terms have been proposed to reduce the computation load. Resonance scattering has been investigated and it has been demonstrated that the free waves propagating on the ribbed shell are the helical waves and the Bloch–Floquet waves; an equation has been derived for the computation of the Bloch–Floquet dispersion curves. When the interactions between Bloch–Floquet waves and ribs are weak, a simple approximate solution to the dispersion equation has been found. Furthermore, it has been shown that the maximum amplitude of Bloch–Floquet wave scattering depends only on the length of the cylindrical shell in the first Brillouin zone. Lastly the present theory does not predict a high scattering level at the rib resonances.

The validity of the method has been checked by comparing the computed backscattered far field pressure to monostatic scattering measurements carried out by Photiadis *et al.* Good agreement has been found at low and high frequencies whereas the complex structure in the central frequency range is only partially predicted. This might come from the modeling of the ribs which should be considered in this case as an annular plate rather than a circular rod.

APPENDIX A

Consider the expression

$$I_{npj}(r,z)=\frac{k}{\pi}\int_{-L}^{L}h_n(k\rho)\left(\frac{r}{\rho}\right)^n\phi_{pj}(t)dt. \tag{A1}$$

It can be shown (see Appendix B of Ref. 14) that for points of space located near the z axis but not at the end sections so that

$$\left|\frac{z-L}{r}\right|\gg 1,$$

the following integral

$$I_n(k_z,r,z)=\frac{k}{\pi}\int_{-L}^{L}h_n(k\rho)\left(\frac{r}{\rho}\right)^n e^{ik_z t}dt \tag{A2}$$

may be approximated by

$$I_n(k_z,r,z)=e^{ik_z z}H_n(\alpha r)\left(\frac{\alpha}{k}\right)^n, \tag{A3}$$

where

$$\alpha=\begin{cases}(k^2-k_z^2)^{1/2} & \text{if } k>|k_z|\\ i(k_z^2-k^2)^{1/2} & \text{if } k<|k_z|\end{cases} \tag{A4}$$

for any real number k_z. Then using Eqs. (A2)–(A4) and Eq. (4a), it is readily seen that for

$$\left|\frac{z\pm L}{r}\right| \gg 1,$$

I_{npj} can be replaced by

$$I_{npj}(r,z)=H_n(\alpha_{pj}r)\phi_{pj}(z)\left(\frac{\alpha_{pj}}{k}\right)^n, \tag{A5}$$

where α_{pj} is defined as

$$\alpha_{pj}=\begin{cases}[k^2-k_{pj}^2]^{1/2} & \text{if } k>|k_{pj}| \\ i[k_{pj}^2-k^2]^{1/2} & \text{if } k<|k_{pj}|\end{cases}. \tag{A6}$$

APPENDIX B

Let the summation S be defined as

$$S=\sum_{m=-M+1}^{M-1}\phi_{ql}(md)\phi_{pj}(md)$$

$$=\sum_{m=-M+1}^{M-1}\sin[k_{ql}(md+L)]\sin[k_{pj}(md+L)], \tag{B1}$$

where p and q are positive integers. From Eq. (4b) $k_{pj}d=\pi p/2M+2\pi j$; this gives

$$S=\sum_{m=1}^{2M-1}\sin m(k_{ql}d)\sin m(k_{pj}d)$$

$$=\sum_{m=1}^{2M-1}\sin m\frac{\pi p}{2M}\sin m\frac{\pi q}{2M}, \tag{B2}$$

which shows that S is independent of indices j and l. Applying classical trigonometrical relations, Eq. (B2) can be cast in the form

$$S=\frac{1}{2}\sum_{m=1}^{2M-1}\cos m\frac{\pi(p-q)}{2M}-\cos m\frac{\pi(p+q)}{2M}. \tag{B3}$$

From Eq. (B3), it can be noted that

$$S=0 \quad \text{for } p=q=0, \quad p=q=2M. \tag{B4}$$

Applying the following identity

$$\frac{1}{2}+\cos\alpha+\cos 2\alpha+\cdots+\cos n\alpha=\frac{\sin(n+1/2)\alpha}{2\sin(\alpha/2)} \tag{B5}$$

for $\alpha=\pi(p\pm q)/2M$ and $n=2M-1$, Eq. (B3) reduces to

$$S=\frac{\sin\left[(2M-1/2)\dfrac{\pi(p-q)}{2M}\right]}{4\sin\dfrac{\pi(p-q)}{4M}}$$

$$-\frac{\sin\left[(2M-1/2)\dfrac{\pi(p+q)}{2M}\right]}{4\sin\dfrac{\pi(p+q)}{4M}}. \tag{B6}$$

Then it can be readily seen from Eqs. (B4)–(B6) that

$$S=\begin{cases}0 & \text{if } p\neq q \\ 0 & \text{if } p=q=0 \text{ or } =2M. \\ M=L/d & \text{if } p=q\neq 0\end{cases} \tag{B7}$$

[1] V. V. Muzychenko and S. A. Rybak, "Low-frequency resonance scattering by finite cylindrical shells(review)," Sov. Phys. Acoust. **34**, 325–333 (1988).
[2] M. Tran-Van-Nhieu, "Scattering from a finite cylindrical shell," J. Acoust. Soc. Am. **91**, 670–679 (1992).
[3] M. L. Rumerman, "Contribution of membrane wave reradiation to scattering from finite cylindrical steel shells in water," J. Acoust. Soc. Am. **93**, 55–65 (1993).
[4] S. F. Morse and P. L. Marston, "High-frequency backscattering by thick finite cylindrical shells in water at oblique incidence: Experiments, interpretation and calculations," J. Acoust. Soc. Am. **103**, 785–794 (1998).
[5] M. Tran-Van-Nhieu, M. Gensane, A. Tesei, S. Fiovaranti, and A. Maguer, "Scattering by a fluid filled finite cylindrical shell: Comparison theory-experiments," Proceedings of the Fourth European Conference on Underwater Acoustics, 1998, Vol. 2, pp. 819–824.
[6] Y. P. Guo, "Approximate solutions of the dispersion equation for fluid-loaded cylindrical shells," J. Acoust. Soc. Am. **95**, 1435–1440 (1994).
[7] D. M. Photiadis, J. A. Bucaro, and B. H. Houston, "Scattering from flexural waves on a ribbed cylindrical shell," J. Acoust. Soc. Am. **96**, 2785–2790 (1994).
[8] B. H. Houston, J. A. Bucaro, and D. M. Photiadis, "Broadband acoustic scattering from a ribbed shell," J. Acoust. Soc. Am. **98**, 2851–2853 (1995).
[9] D. M. Photiadis, B. H. Houston, E. G. Williams, and J. A. Bucaro, "Resonant response of complex shell structures," J. Acoust. Soc. Am. **108**, 1027–1035 (2000).
[10] M. V. Bernblit, "Sound radiation from a ribbed cylindrical shell," Sov. Phys. Acoust. **21**, 518–521 (1976).
[11] C. B. Burroughs, "Acoustic radiation from fluid-loaded infinite circular cylinders with doubly periodic supports," J. Acoust. Soc. Am. **75**, 715–722 (1984).
[12] R. N. Miles, "An approximate method for modal analysis of finite periodic structures," J. Sound Vib. **134**, 165–174 (1989).
[13] M. Tran-Van-Nhieu, "A slender-body approximation in scattering theory," J. Acoust. Soc. Am. **85**, 1834–1840 (1989).
[14] M. Tran-Van-Nhieu, "An approximate solution to sound radiation from slender bodies," J. Acoust. Soc. Am. **96**, 1070–1079 (1994).
[15] Y. P. Guo, "Sound scattering by bulkheads in cylindrical shells," J. Acoust. Soc. Am. **95**, 2550–2559 (1994).
[16] M. C. Junger and D. Feit, *Sound, Structures and Their Interaction*, 2nd ed. (MIT, Cambridge, MA, 1986).
[17] K. F. Graff, *Wave Motion in Elastic Solids* (Dover, New York, 1975), see pp. 195–199.
[18] M. Abramowitz and I. A. Stegun, *Handbook of Mathematical Functions* (Dover, New York, 1970).
[19] D. G. Crighton, "The 1988 Rayleigh medal lecture: Fluid loading—the interaction between sound and vibration," J. Sound Vib. **133**, 1–27 (1989).
[20] M. L. Rumerman and S. C. Schreppler, "Scattering from cylindrical shells due to membrane waves," J. Acoust. Soc. Am. **90**, 2340 (1991).
[21] S. C. Schreppler and J. W. Maxwell, "Scattering by a finite baffled thin elastic cylindrical shell: Theory and experiment," J. Acoust. Soc. Am. **90**, 2341 (1991).
[22] M. H. Marcus and A. Dickinson, "Rib resonances present in the scattering response of a ribbed cylindrical shell," J. Acoust. Soc. Am. **103**, 1864–1866 (1998).

On the complex conjugate roots of the Rayleigh equation: The leaky surface wave

Christoph T. Schröder[a] and Waymond R. Scott, Jr.[b]
School of Electrical and Computer Engineering, Georgia Institute of Technology, Atlanta, Georgia 30332-0250

(Received 24 May 2001; accepted for publication 11 September 2001)

In recent experiments and numerical studies, a leaky surface wave has been observed at the surface of an isotropic homogeneous elastic solid. This paper gives a detailed description of this leaky surface wave and explains its origin from the fundamental differential equations. Theoretically, the leaky surface wave arises from the complex conjugate roots of the Rayleigh equation. The complex conjugate roots give rise to a wave that propagates along the surface and is coupled to a plane shear wave in the medium. Due to the coupling, the surface wave leaks energy into the medium and is highly inhomogeneous. Its particle motion at the surface is prograde in nature, distinguishing it from the well-known Rayleigh surface wave which causes a retrograde particle motion. © *2001 Acoustical Society of America.* [DOI: 10.1121/1.1419085]

PACS numbers: 43.20.Bi, 43.35.Pt, 68.35.Ja [ANN]

I. INTRODUCTION

Elastic surface waves have been the subject of extensive research, since Lord Rayleigh first discovered the existence of elastic waves confined to the superficial region of an infinite homogeneous isotropic solid more than a century ago.[1] Elastic surface waves play an important role in various fields. In seismology, surface waves have been found to carry the bulk of the energy among the waves excited by an earthquake. In electroacoustics, surface waves are utilized to make filters and resonators. In geoscience, the propagation characteristics of surface waves are used to obtain information about the physical properties of the ground. In this paper, the theory of elastic surface waves is revisited.

A point source placed on the surface of a homogeneous isotropic medium excites five different kinds of waves: a pressure wave and a shear wave propagating in the medium, a Rayleigh surface wave that is confined to the surface of the medium, a lateral wave that is induced by the pressure wave at the surface, and a leaky surface wave that travels along the surface with a wave speed smaller than the pressure wave but larger than the shear wave. The first four of these wave types are well-known and have been treated extensively in the literature. However, the existence and theoretical foundation of the leaky surface wave has not been discussed as much.

The leaky surface wave arises from the complex conjugate roots of the Rayleigh equation. The leaky surface wave is an inhomogeneous wave that propagates along the surface with a phase velocity larger than the shear wave but smaller than the pressure wave. It couples into a plane shear wave that propagates in the medium. Due to the coupling, the surface wave loses energy and, thus, decays in its propagation direction.

The leaky surface wave has been observed by various authors in experimental and numerical studies. For example, Roth *et al.* noticed a rapidly decaying seismic surface wave in an environment with a very high Poisson ratio that had a phase velocity larger than the Rayleigh wave, but smaller than the pressure wave.[2] Smith *et al.* identified prograde and retrograde surface wave modes in a geologic study conducted on the shore of the gulf of Mexico.[3] Glass and Maradudin found a leaky surface wave to exist in the flat-surface limit of a corrugated crystal surface.[4] And Phinney provides a theoretical study of the leaky surface wave, which he calls a *Pseudo-P* mode.[5] Although not all of these authors explicitly describe a leaky surface wave, their observations are consistent with the results presented in this paper.

In this paper, the theoretical derivation of the leaky surface wave is described in some detail. In Sec. II, the governing equations are briefly outlined, leading to the Rayleigh equation. In Sec. III, the various roots of the Rayleigh equation are discussed. It will be shown that for materials with a high Poisson ratio a leaky surface wave exists, due to the complex conjugate roots of the Rayleigh equation. In Sec. IV, the waves excited by a line source on the surface are derived analytically. The method of steepest descent is applied to obtain closed-form expressions for the various waves in the far field.

II. THE RAYLEIGH EQUATION

The elastic wave fields at the surface of a semi-infinite, isotropic, lossless, homogeneous half space are to be determined. The half-space is bounded at $z=0$ by a free-surface boundary. The fields are assumed to be invariant in the y-direction and nonzero only in the x-z plane (*plane-strain case*, $u_y=\partial/\partial y=0$). Thus, the originally three-dimensional problem reduces to a two-dimensional one. The elastic wave fields in a medium may be expressed in terms of their potential functions:[6]

$$\mathbf{u}=\nabla\Phi+\nabla\times\mathbf{H}, \tag{1}$$

where $\mathbf{u}$ is the displacement vector, Φ is a scalar potential describing the longitudinal pressure wave, and $\mathbf{H}$ is a vector

[a]Electronic mail: christoph.schroeder@ece.gatech.edu
[b]Electronic mail: waymond.scott@ece.gatech.edu

potential describing the transverse shear wave. The potentials satisfy the wave equations

$$\nabla^2\Phi = \frac{1}{c_P^2}\frac{\partial^2\Phi}{\partial t^2}, \tag{2}$$

$$\nabla^2\mathbf{H} = \frac{1}{c_S^2}\frac{\partial^2\mathbf{H}}{\partial t^2}, \tag{3}$$

for the pressure and shear wave, respectively, with their corresponding wave speeds, c_P and c_S. In the *plane-strain* case, the only nonzero vector potential component is H_y and the only nonzero displacement components are u_x and u_z. The only independent stress components are τ_{xx}, τ_{zz}, and τ_{xz}.

Assuming harmonic time-dependence, the plane wave solutions for Φ and H_y satisfying Eqs. (2) and (3) are given by

$$\Phi = Ae^{j\xi x + j\alpha z - j\omega t}, \tag{4}$$

$$H_y = Be^{j\xi x + j\beta z - j\omega t} \tag{5}$$

and the wave numbers are defined by

$$\alpha^2 = \omega^2/c_P^2 - \xi^2, \tag{6}$$

$$\beta^2 = \omega^2/c_S^2 - \xi^2, \tag{7}$$

$$\xi^2 = \omega^2/c^2. \tag{8}$$

Using the well-known differential equations, the displacement and stress components are obtained:

$$u_x = (j\xi\, Ae^{j\alpha z} - j\beta\, Be^{j\beta z})e^{j\xi x}, \tag{9}$$

$$u_z = (j\alpha\, Ae^{j\alpha z} + j\xi\, Be^{j\beta z})e^{j\xi x}, \tag{10}$$

$$\tau_{xx} = \mu((2\alpha^2 - \beta^2 - \xi^2)Ae^{j\alpha z} + 2\beta\xi\, Be^{j\beta z})e^{j\xi x}, \tag{11}$$

$$\tau_{zz} = \mu((\xi^2 - \beta^2 Ae^{j\alpha z} - 2\beta\xi\, Be^{j\beta z})e^{j\xi x}, \tag{12}$$

$$\tau_{xz} = \mu(-2\alpha\xi\, Ae^{j\alpha z} + (\beta^2 - \xi^2)Be^{j\beta z})e^{j\xi x}. \tag{13}$$

At the surface, the normal stress vanishes, and thus $\tau_{zz}|_{z=0} = \tau_{xz}|_{z=0} = 0$. Using this condition, the ratio of the coefficients is determined from Eqs. (12) and (13) to be

$$\frac{A}{B} = \frac{2\xi\beta}{\xi^2 - \beta^2} = -\frac{\xi^2 - \beta^2}{2\xi\alpha}. \tag{14}$$

Re-inserting the amplitude ratio into Eqs. (12) and (13), the characteristic equation is obtained:

$$(\xi^2 - \beta^2)^2 + 4\xi^2\alpha\beta = 0. \tag{15}$$

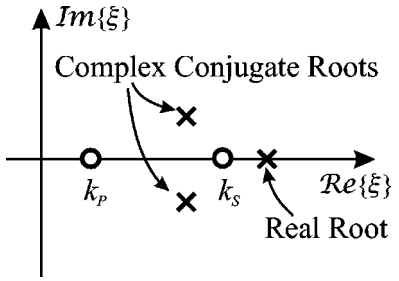

FIG. 1. Schematical arrangement of the roots in the complex ξ-plane.

Equation (15) is commonly called the *Rayleigh Equation*, because it gives rise to the well-known Rayleigh surface wave.

Using Eqs. (6)–(8), the characteristic equation can be rewritten in terms of the wave speeds:

$$\left(2 - \frac{c^2}{c_S^2}\right)^2 + 4\sqrt{\frac{c^2}{c_P^2} - 1}\sqrt{\frac{c^2}{c_S^2} - 1} = 0. \tag{16}$$

By rationalizing, this equation may be expressed as

$$\left(\frac{c}{c_S}\right)^2\left(\left(\frac{c}{c_S}\right)^6 - 8\left(\frac{c}{c_S}\right)^4 + (24 - 16(c_S/c_P)^2)\left(\frac{c}{c_S}\right)^2 - 16(1 - (c_S/c_P)^2)\right) = 0. \tag{17}$$

Equation (17) always has three solutions for c^2 (when neglecting the trivial solution). Dependent on the Poisson Ratio ν of a material, different kinds of roots arise. For $\nu < 0.263$, Eq. (17) has three real roots. For $\nu > 0.263$, Eq. (17) has one real root and two complex conjugate roots. In each case, the real root that is smallest in magnitude gives rise to the Rayleigh surface wave, which propagates along the surface and decays into the medium. The other roots have often been classified as erroneous or nonphysical roots of the Rayleigh equation.[6–8] However, it will be shown here that the complex conjugate roots of the Rayleigh equation in fact give rise to a *leaky surface wave*.

III. THE ROOTS OF THE RAYLEIGH EQUATION

Let the roots of Eq. (17) be denoted by c. In general, c will be complex:

$$c = c_r + jc_i, \tag{18}$$

TABLE I. Solutions to the Rayleigh equation.

(1)	$\xi_r > 0,\ \xi_i = 0$	$\alpha_r = 0, \alpha_i > 0$ $\Phi \sim e^{-\lvert\alpha_i\rvert z} e^{j\lvert\xi_r\rvert x}$	$\beta_r = 0, \beta_i > 0$ $H_z \sim e^{-\lvert\beta_i\rvert z} e^{j\lvert\xi_r\rvert x}$
(2)	$\xi_r > 0,\ \xi_i < 0$	$\alpha_r > 0, \alpha_i > 0$ $\Phi \sim e^{(j\lvert\alpha_r\rvert - \lvert\alpha_i\rvert)z} e^{(j\lvert\xi_r\rvert + \lvert\xi_i\rvert)x}$	$\beta_r < 0, \beta_i < 0$ $H_z \sim e^{(-j\lvert\beta_r\rvert + \lvert\beta_i\rvert)z} e^{(j\lvert\xi_r\rvert + \lvert\xi_i\rvert)x}$
(3)	$\xi_r > 0,\ \xi_i > 0$	$\alpha_r < 0, \alpha_i > 0$ $\Phi \sim e^{(-j\lvert\alpha_r\rvert - \lvert\alpha_i\rvert)z} e^{(j\lvert\xi_r\rvert - \lvert\xi_i\rvert)x}$	$\beta_r > 0, \beta_i < 0$ $H_z \sim e^{(j\lvert\beta_r\rvert + \lvert\beta_i\rvert)z} e^{(j\lvert\xi_r\rvert - \lvert\xi_i\rvert)x}$
(4)	$\xi_r > 0,\ \xi_i < 0$	$\alpha_r < 0, \alpha_i < 0$ $\Phi \sim e^{(-j\lvert\alpha_r\rvert + \lvert\alpha_i\rvert)z} e^{(j\lvert\xi_r\rvert + \lvert\xi_i\rvert)x}$	$\beta_r > 0, \beta_i > 0$ $H_z \sim e^{(j\lvert\beta_r\rvert - \lvert\beta_i\rvert)z} e^{(j\lvert\xi_r\rvert + \lvert\xi_i\rvert)x}$
(5)	$\xi_r > 0,\ \xi_i > 0$	$\alpha_r > 0, \alpha_i < 0$ $\Phi \sim e^{(j\lvert\alpha_r\rvert + \lvert\alpha_i\rvert)z} e^{(j\lvert\xi_r\rvert - \lvert\xi_i\rvert)x}$	$\beta_r < 0, \beta_i > 0$ $H_z \sim e^{(-j\lvert\beta_r\rvert - \lvert\beta_i\rvert)z} e^{(j\lvert\xi_r\rvert - \lvert\xi_i\rvert)x}$

TABLE II. Solutions to the Rayleigh equation.

	$\xi=$	$\alpha=$	$\beta=$
(1)	$2.5998k_P$	$j2.3997k_P$	$j0.8711k_P$
(2)	$(1.2184-j0.2526)k_P$	$(0.4030+j0.7636)k_P$	$(-2.1448-j0.1435)k_P$
(3)	$(1.2184+j0.2526)k_P$	$(-0.4030+j0.7636)k_P$	$(2.1448-j0.1435)k_P$
(4)	$(1.2184-j0.2526)k_P$	$(-0.4030-j0.7636)k_P$	$(2.1448+j0.1435)k_P$
(5)	$(1.2184+j0.2526)k_P$	$(0.4030-j0.7636)k_P$	$(-2.1448+j0.1435)k_P$

where c_r is the real part and c_i is the imaginary part of c. If c is purely real ($c=c_r$), ξ will be real [see Eq. (8)]. If additionally c is smaller than both the pressure wave speed and the shear wave speed, i.e., $c=c_r<c_S<c_P$, α and β will be purely imaginary. For the solution to be physical, $\mathrm{Im}\{\alpha\}=\alpha_i>0$ and $\mathrm{Im}\{\beta\}=\beta_i>0$, thus the waves described by these wave numbers *propagate* in the *x*-direction and *decay* in the *z*-direction. This solution represents the well-known Rayleigh surface wave, first explored by Lord Rayleigh more than a century ago.[1] A solution of this form always exists, independent of the Poisson ratio of a material.

For $\nu<0.263$, two more purely real roots of the Rayleigh equation exist. It can be shown that for these roots the wave speed is always larger than the pressure wave speed, c_P. These two roots describe the angles of incidence at which *complete mode conversion* occurs. In the case of complete mode conversion an incident shear wave, for example, is completely reflected as a pressure wave, without inducing a reflected shear wave component. Complete mode conversion is physically possible only for materials with a Poisson ratio smaller than 0.263 and occurs at two distinct angles of incidence, defined by the two roots of the Rayleigh equation (see also, for example, Graff[6]).

If $\nu>0.263$, one real root and two complex conjugate roots of the Rayleigh equation arise. The real root again gives rise to the Rayleigh surface wave. For the complex conjugate roots, the wave speed is complex, $c=c_r+jc_i$, and consequently also the wave numbers are complex: $\xi=\xi_r+j\xi_i$, $\alpha=\alpha_r+j\alpha_i$ and $\beta=\beta_r+j\beta_i$. It can be shown that for the complex conjugate roots the real part of the wave speed is always smaller than the pressure wave speed, but larger than the shear wave speed, $c_S<\mathrm{Re}\{c\}<c_P$.

Although c may be a solution to Eq. (17), it does not necessarily follow that also Eq. (15) is fulfilled. This is due to the manipulation of Eq. (15) to arrive at Eq. (17). In fact, the complex conjugate roots of Eq. (17) do not represent solutions to Eq. (16). It can be shown, however, that they do represent solutions to Eq. (15), if the signs of the wave numbers α and β are picked correctly. It may be recalled that according to Eqs. (6) and (7) the wave numbers α and β are functions of the square root of c^2,

$$\alpha=\pm\frac{\omega}{c}\sqrt{\frac{c^2}{c_P^2}-1}=\pm(\alpha_r+j\alpha_i), \tag{19}$$

$$\beta=\pm\frac{\omega}{c}\sqrt{\frac{c^2}{c_S^2}-1}=\pm(\beta_r+j\beta_i). \tag{20}$$

The sign in front of the square roots must be chosen according to physical and causal constraints of the underlying problem. To obtain Eq. (16), the positive sign has been assumed for both α and β. However, it turns out that Eq. (15) is only satisfied if, for the complex conjugate roots, both the real part and the imaginary part of α and β have opposite signs, i.e., $\mathrm{sign}(\alpha_r)\neq\mathrm{sign}(\beta_r)$ and $\mathrm{sign}(\alpha_i)\neq\mathrm{sign}(\beta_i)$.

Figure 1 shows schematically the arrangement of the roots in the complex ξ-plane. The possible solutions of the Rayleigh equation are summarized in Table I, giving all possible combinations of ξ, α and β. Only waves propagating in the positive *x*-direction are considered. Five possible solutions arise.

The first solution describes the Rayleigh surface wave. For the second solution, both the pressure wave potential and the shear wave potential, Φ and H_y, propagate and increase in the positive *x*-direction ($\xi_r>0$, $\xi_i<0$). However, Φ propagates and decays in the positive *z*-direction ($\alpha_r>0$, $\alpha_i>0$), whereas H_y propagates and decays in the negative *z*-direction ($\beta_r<0$, $\beta_i<0$). For the third solution, the potentials decay in the *x*-direction ($\xi_i>0$). Φ now propagates and increases in the negative *z*-direction ($\alpha_r<0$, $\alpha_i>0$), whereas H_y propagates and increases in the positive *z*-direction ($\beta_r>0$, $\beta_i<0$). For the fourth and fifth solution, the signs of α and β are reversed.

The behavior of the five possible solutions is best demonstrated by calculating the wave fields for a medium with a specific value of Poisson's ratio. Assuming Poisson's ratio to be $\nu=0.4$, the elastic wave fields are computed using Eqs. (9)–(13). The amplitude of the shear wave potential is chosen to be unity, and the amplitude of the pressure wave potential is computed with Eq. (14). For $\nu=0.4$, the pressure wave speed exceeds the shear wave speed by a factor of about 2.45: $c_P=2.4495c_S$. The roots of Eq. (17) in terms of the shear wave speed c_S are

$$c=\begin{cases}0.9422c_S\\(1.9276+j0.3996)c_S\\(1.9276-j0.3996)c_S.\end{cases} \tag{21}$$

The resulting wave numbers are shown in Table II. All wave numbers are expressed in terms of the longitudinal wave number, $k_P=\omega/c_P$.

In Fig. 2, the displacements according to the five solutions of the Rayleigh equation are plotted versus *x* and *z*. The distance on the axes is normalized to the wavelength of the Rayleigh surface wave, λ_R. The two columns show the horizontal and vertical displacements, u_x and u_z. Pseudo-color plots are used to display the wave fields, employing a logarithmic scale with a dynamic range of 50 dB. Superimposed with the horizontal displacement component is the real part

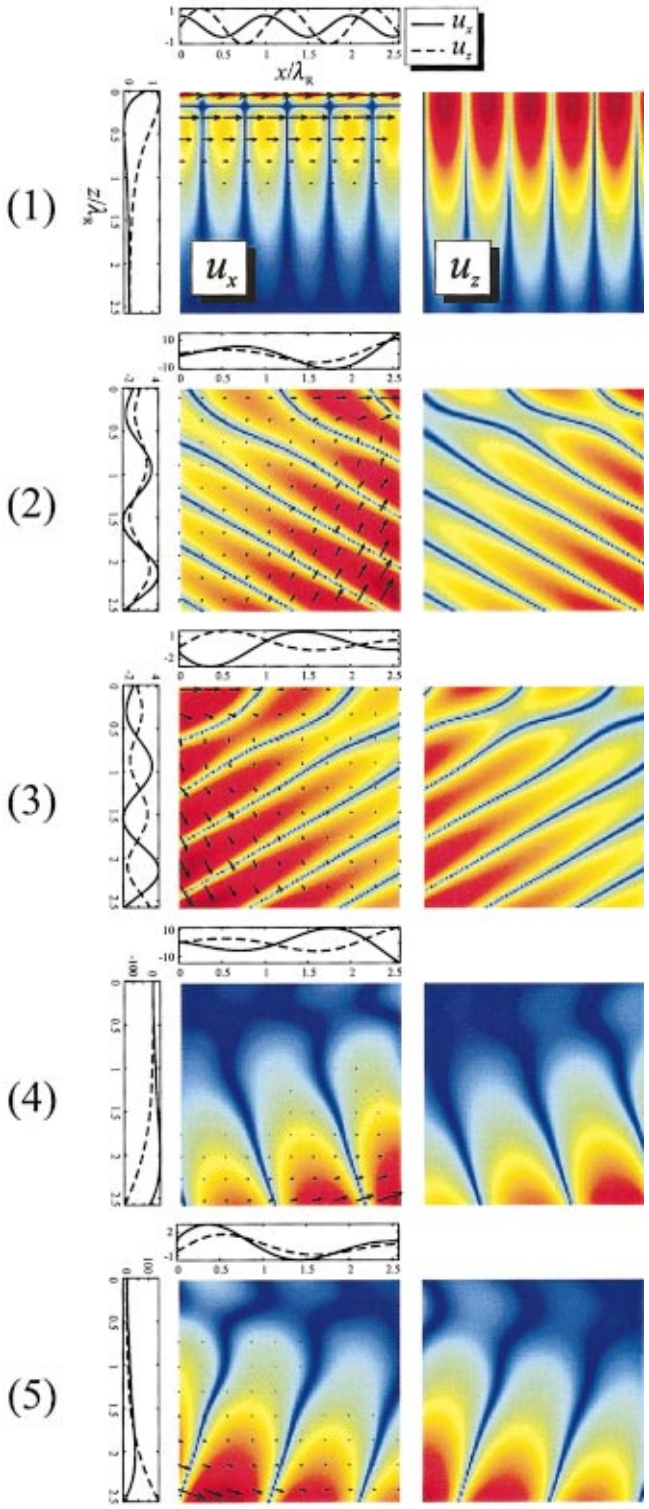

FIG. 2. Horizontal and vertical displacements according to the five solutions of the Rayleigh equation.

of the complex Poynting vector, thus indicating the direction of the energy flow. The upper edge of each plot corresponds to the free surface.

First, the Rayleigh surface wave is shown. For the Rayleigh surface wave, the energy flow is seen to be parallel to the surface. Both the horizontal and the vertical displacements decay away from the surface. The second solution describes a shear wave in which energy is carried toward the surface. Close to the surface, the energy flows parallel to the surface. The waves grow exponentially in the x- and z-direction. The third solution is the converse of the second one. This time, the energy flows from the surface into the medium, and the waves decay in the x-direction. Again, close to the surface the energy flow is parallel to the surface. The fourth and fifth solution are similar to the second and third. However, now a pressure wave propagates in the medium, and the energy flows at a different angle with respect to the surface. Also, the exponential growth is enhanced.

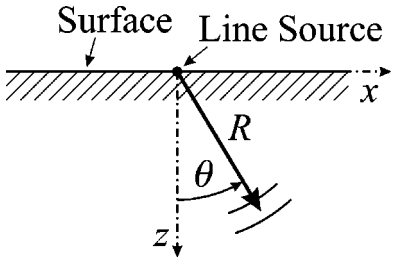

FIG. 3. Line source on the surface.

All of the five possible solutions described above can, in certain cases, represent physical solutions. For example, if a field distribution is created on the surface that matches the field distribution of Solution (5) on the surface, waves similar to the ones described by Solution (5) would be induced in the medium. If a field distribution is generated within the medium that is equal to the field distribution of Solution (2), waves propagating toward the surface would be excited that perfectly couple into a surface wave. Of course, the solutions as described here would require an infinite medium and wave fields of infinite extent that are nonzero at infinity, which violates physical as well as causal constraints. However, over a finite range all of these solutions can be excited with the appropriate field distributions.

IV. WAVES DUE TO A LINE SOURCE ON THE SURFACE

In the previous section, the solutions to the wave equation at a free-surface boundary have been described in a general form. In this section, the wave fields due to a specific excitation, a line source on the surface, are determined. The

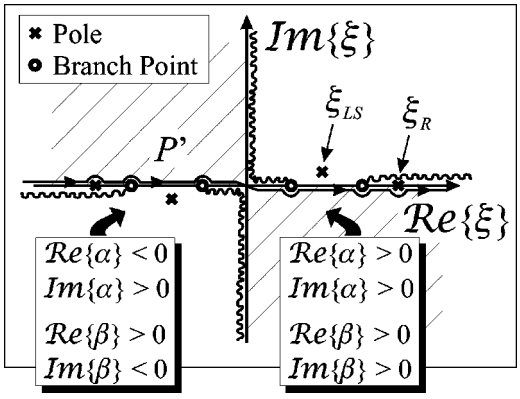

FIG. 4. Location of the poles and branch cuts in the complex ξ-plane for the line-source problem.

analysis presented here is largely based on the general mathematical description of Felsen and Marcuvitz.[9]

Figure 3 shows the underlying geometry. A line source is placed on the surface at $x=0$ and extends into the y-direction. The line source excites the normal stress component τ_{zz}. If harmonic time dependence is assumed, the displacement fields due to a line source can be written in form of an integral equation:[6]

$$u_x(x,z) = -\frac{j}{\mu\pi}\int_{P'}\frac{\xi}{F_0(\xi)} \times[-2\alpha\beta e^{j\beta z}+(\beta^2-\xi^2)e^{j\alpha z}]e^{j\xi x}\,d\xi, \quad (22)$$

$$u_z(x,z) = -\frac{j}{\mu\pi}\int_{P'}\frac{\alpha}{F_0(\xi)} \times[2\xi^2 e^{j\beta z}+(\beta^2-\xi^2)e^{j\alpha z}]e^{j\xi x}\,d\xi, \quad (23)$$

where

$$F_0(\xi) = (\xi^2-\beta^2)^2+4\xi^2\alpha\beta \quad (24)$$

is the Rayleigh equation. The amplitude of the excitation is assumed to be unity.

A. General considerations

The integrals in Eqs. (22) and (23) each represent an inverse Fourier transform from the wave number domain into the spatial domain. The integrands contain poles and branch points. The poles are due to the roots of the Rayleigh equation in the denominator. The branch points arise because of the square root dependence of α and β on ξ. They are located at the roots of α and β, at $k_P=\pm(\omega/c_P)^2$ and $k_S=\pm(\omega/c_S)^2$ [see Eqs. (6) and (7)].

To compute the integrals, contour integration in the complex ξ-plane must be applied. The integration must be performed along the real ξ-axis. Figure 4 shows the location of the poles and branch points in the complex ξ-plane. To determine the waves propagating in the positive x-direction, Eqs. (22) and (23) must be integrated along the path P'. The contour is closed at infinity. Only the poles and branch cuts for $\mathrm{Re}\{\xi\}>0$ are included in the integration contour (indicated by the indentations of P'), whereas the poles for $\mathrm{Re}\{\xi\}<0$ are excluded and, therefore, do not contribute to the integral.

Due to the branch points, the integrands are not single-valued. To make the integrands unique, a Riemann surface for the ξ-plane is necessary, with branch cuts providing the transition from one Riemann sheet to the other.[9] The location of the branch cuts in general is arbitrary, but defines the disposition of those regions in the complex ξ-plane in which for example $\mathrm{Re}\{\alpha\}>0$ or $\mathrm{Re}\{\alpha\}<0$. Figure 4 shows the top Riemann sheet for Eqs. (22) and (23). The signs of the wave numbers on the top Riemann sheet must be chosen according to physical and causal reasons. The integration along the real axis determines the shear and pressure waves excited by the line source. For the shear and the pressure waves to be causal, they must propagate away from the source and vanish at infinity. For this to be true, the wave numbers along the real axis must be chosen such that $\mathrm{Re}\{\alpha\}>0$, $\mathrm{Im}\{\alpha\}>0$, $\mathrm{Re}\{\beta\}>0$ and $\mathrm{Im}\{\beta\}>0$. It can be easily shown that in this case the wave numbers in the entire second and fourth quadrant must behave in the same way. In the first and third quadrant, the branch cuts must then be chosen such that $\mathrm{Re}\{\alpha\}<0$, $\mathrm{Im}\{\alpha\}>0$, $\mathrm{Re}\{\beta\}>0$ and $\mathrm{Im}\{\beta\}<0$. This is true because α and β must be continuous across the real axis. Thus, in the first and third quadrant, the pressure wave potential propagates and increases in the negative z-direction, whereas the shear wave potential propagates and increases in the positive z-direction. It is evident that in the first quadrant of the top Riemann sheet the wave numbers behave as described for Solution (3) of the Rayleigh equation as indicated in Table I. The poles on the top Riemann sheet correspond to physically existing waves and, therefore, the pole associated with Solution (3) of the Rayleigh equation represents a physical solution to the line-source problem. The pole in the third quadrant is the equivalent to the pole in the first quadrant, but describes a wave traveling in the negative x-direction. The two poles on the real ξ-axis are present on all sheets and, consequently, also represent physical waves. All other poles of the Rayleigh equation lie on different sheets and, thus, are nonphysical for the line-source case.

It can be seen in Fig. 4 that four poles and four branch cuts exist on the top Riemann sheet. The poles at $\pm\xi_R$ on the real ξ-axis give rise to the well-known Rayleigh surface wave. The complex poles at $\pm\xi_{\mathrm{LS}}$ in the first and third quadrant describe leaky surface waves propagating to the right and left, respectively. As described earlier, the leaky surface wave couples into a plane shear wave. Both the leaky surface wave and the shear wave that is fed from the surface wave are inhomogeneous, which is indicated by the pole being complex.

B. Steepest-descent approximation

To evaluate the integrals asymptotically in the far field, the method of steepest descent shall be applied. To simplify the procedure, the two terms of the integral are treated separately. Dividing the integrals each into a pressure wave term and a shear wave term, Eqs. (22) and (23) are rewritten as

$$u_x^S(x,z) = -\frac{j}{\mu\pi}\int_{P'}\frac{\xi}{F_0(\xi)}(-2\alpha\beta)e^{j\beta z}e^{j\xi x}\,d\xi, \quad (25)$$

$$u_x^P(x,z) = -\frac{j}{\mu\pi}\int_{P'}\frac{\xi}{F_0(\xi)}(\beta^2-\xi^2)e^{j\alpha z}e^{j\xi x}\,d\xi, \quad (26)$$

$$u_z^S(x,z) = -\frac{j}{\mu\pi}\int_{P'}\frac{\alpha}{F_0(\xi)}2\xi^2 e^{j\beta z}e^{j\xi x}\,d\xi, \quad (27)$$

$$u_z^P(x,z) = -\frac{j}{\mu\pi}\int_{P'}\frac{\alpha}{F_0(\xi)}(\beta^2-\xi^2)e^{j\alpha z}e^{j\xi x}\,d\xi. \quad (28)$$

The total displacements equal the superposition of the pressure wave component and the shear wave component:

$$u_x(x,z) = u_x^S(x,z)+u_x^P(x,z), \quad (29)$$

$$u_z(x,z) = u_z^S(x,z)+u_z^P(x,z). \quad (30)$$

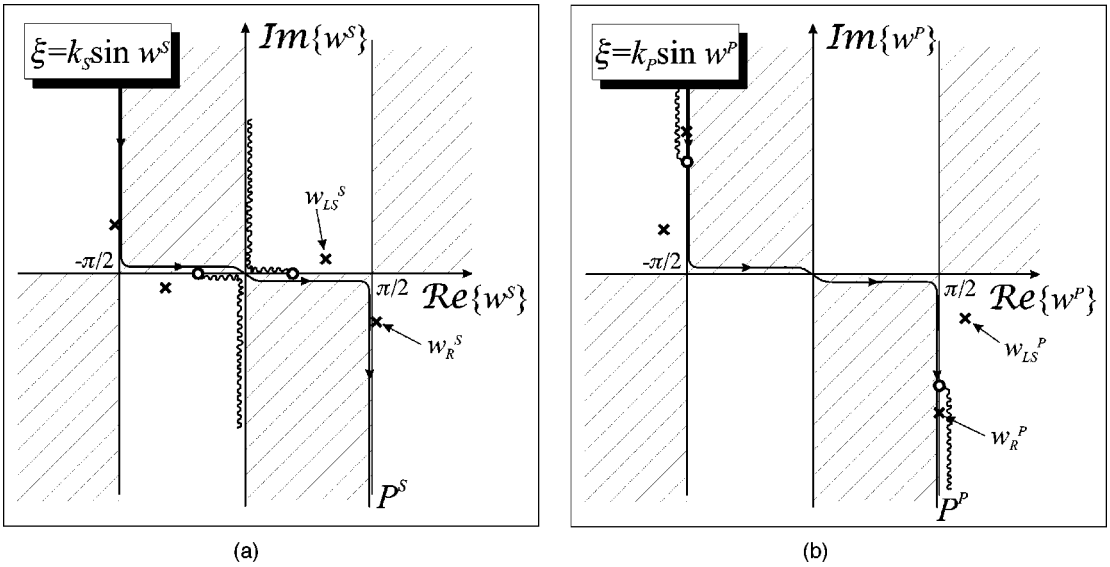

FIG. 5. Location of the poles and branch cuts (a) in the complex w^S-plane and (b) in the complex w^P-plane.

To facilitate the evaluation of the integrals, the complex ξ-plane is transformed into the complex w^S-plane for the two shear wave terms, and into the w^P-plane for the pressure wave terms:

$$\xi = k_S \sin w^S, \tag{31}$$

$$\xi = k_P \sin w^P. \tag{32}$$

These transformations are single-valued.[9] From the periodicity of $\sin w^S$ and $\sin w^P$ it is evident that multiple values for w^S and w^P correspond to a single value of ξ. Thus, the transformations can be used to map the entire ξ-plane with its multiple Riemann sheets into adjacent strips of width 2π in the w^S- or w^P-plane. The arrangement of the poles and branch cuts of the top Riemann sheet in the complex w^S-plane and w^P-plane are shown in Fig. 5. Here, the top Riemann sheet is mapped into a strip reaching from $-\pi$ to π in the complex w^S-plane for the shear wave terms, and similarly for the pressure wave terms in the complex w^P-plane. The positions of the transformed Rayleigh wave pole and the leaky surface wave pole in the complex w^S- and w^P-plane are indicated by w_R^S, w_{LS}^S, and w_R^P, w_{LS}^P, respectively. The transformed integration paths are denoted by P^S and P^P.

The separate transformations for the shear wave terms and the pressure wave terms become necessary, because, when the method of steepest descent is applied, the different terms will give rise to different steepest-descent paths. By applying the different transformations, the steepest-descent paths will have a rather simple shape for both the shear wave

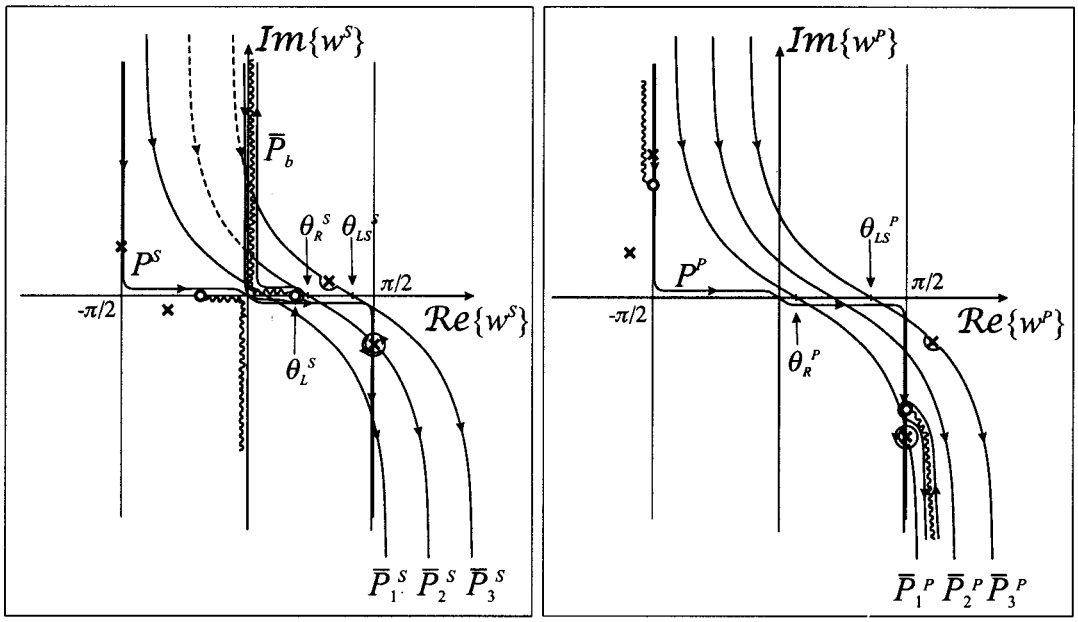

FIG. 6. Steepest-descent paths for (a) the shear wave terms in the complex w^S-plane and (b) the pressure wave terms in the complex w^P-plane.

terms and the pressure wave terms, thus, making the steepest-descent approximation considerably easier.

Applying the transformations, two of the branch cuts are eliminated in each of the integrals in Eqs. (25)–(28). For the shear wave terms the branch cuts at $\pm k_S$ vanish, whereas for the pressure wave terms the branch cuts at $\pm k_P$ are removed. For the shear wave terms, β then reduces to

$$\beta = k_S \cos w^S, \tag{33}$$

and for the pressure wave terms α becomes

$$\alpha = k_P \cos w^P. \tag{34}$$

Introducing polar coordinates,

$$x = R \sin \theta, \tag{35}$$

$$z = R \cos \theta, \tag{36}$$

Eqs. (25)–(28) are rewritten as integrals in the w^S- and w^P-plane:

$$u_x^S(x,z) = -\frac{j}{\mu\pi}\int_{P^S}\frac{\xi}{F_0(\xi)}(-2\alpha\beta) \times e^{jk_S R\cos(w^S-\theta)}\beta\, dw^S, \tag{37}$$

$$u_x^P(x,z) = -\frac{j}{\mu\pi}\int_{P^P}\frac{\xi}{F_0(\xi)}(\beta^2-\xi^2) \times e^{jk_P R\cos(w^P-\theta)}\alpha\, dw^P, \tag{38}$$

$$u_z^S(x,z) = -\frac{j}{\mu\pi}\int_{P^S}\frac{\alpha}{F_0(\xi)}2\xi^2 e^{jk_S R\cos(w^S-\theta)}\beta\, dw^S, \tag{39}$$

$$u_z^P(x,z) = -\frac{j}{\mu\pi}\int_{P^P}\frac{\alpha}{F_0(\xi)}(\beta^2-\xi^2) \times e^{jk_P R\cos(w^P-\theta)}\alpha\, dw^P, \tag{40}$$

where θ describes the polar angle measured from the surface normal toward the propagation direction (see Fig. 3). The wave numbers in terms of w^S are

$$\xi(w^S) = k_S \sin w^S, \tag{41}$$

$$\beta(w^S) = k_S \cos w^S, \tag{42}$$

$$\alpha(w^S) = \pm\sqrt{k_P^2 - \xi(w^S)^2}, \tag{43}$$

and in terms of w^P

$$\xi(w^P) = k_P \sin w^P, \tag{44}$$

$$\beta(w^P) = \pm\sqrt{k_S^2 - \xi(w^P)^2}, \tag{45}$$

$$\alpha(w^P) = k_P \cos w^P. \tag{46}$$

The signs of $\alpha(w^S)$ and $\beta(w^P)$ must be chosen as described earlier for the complex ξ-plane. Thus, in the shaded and nonshaded regions of Fig. 5, α behaves just as in the shaded and nonshaded regions of Fig. 4.

With the integrals transformed as described above, it is relatively straightforward to apply the method of steepest descent. For the method of steepest descent, the integration paths P^S and P^P are deformed into new paths, the *steepest-descent paths* $\overline{P^S}$ and $\overline{P^P}$, respectively. The new path is chosen such that the dominant contribution to the integral arises from only a small section of the path. To achieve this, the path is deformed such that it passes through the saddle point of the integrand. Away from the saddle point it follows the direction in which the integrand decays most rapidly. Along this path, the integrand will then be negligible everywhere but around the saddle point, and the integral can be approximated by the contribution from the integrand in the vicinity of the saddle point.

The path of steepest descent is a path of constant phase.[9] For integrals in the form of the ones in Eqs. (37)–(40), the steepest-descent path is given by

$$\mathrm{Re}\{w^{S,P}\} - \theta = \cos^{-1}(\mathrm{sech}(\mathrm{Im}\{w^{S,P}\})). \tag{47}$$

The procedure is the same for the shear wave terms and the pressure wave terms. In Fig. 6, three steepest-descent paths are shown each for the shear wave terms in the w^S-plane, $\overline{P_1^S}$, $\overline{P_2^S}$, $\overline{P_3^S}$, and for the pressure wave terms in the w^P-plane, $\overline{P_1^P}$, $\overline{P_2^P}$, $\overline{P_3^P}$. Each steepest descent path corresponds to a different propagation (polar) angle. The saddle point in each case is located at the intersection of the steepest-descent path with the real w^S- or w^P-axis, respectively. Physically, the contributions from the saddle points describe the pressure and the shear waves in the far field .

When the original integration path is deformed into the steepest-descent path, care has to be taken whether poles or branch cuts are crossed during the deformation. According to Cauchy's theorem, if a singularity is crossed during the deformation from one integration path into another, the contribution from the contour integral around the singularity must be included into the total integral. For example, when P^S in Fig. 6 is deformed into the steepest-descent path $\overline{P_1^S}$, no singularities are crossed during the deformation. However, for $\overline{P_2^S}$, the integrals around the branch cut, $\overline{P_b}$, and around the pole at w_R^S must be included. For $\overline{P_3^S}$, the branch cut integral as well as the integrals around the poles at w_R^S and w_{LS}^S contribute to the total integral.

The contour integrals around the singularities in both the w^S- and the w^P-plane give rise to different types of waves. The integral around the branch cut in the w^S-plane describes a lateral wave. The lateral wave is a plane shear wave induced by the pressure wave propagating along the surface. It appears only if the polar angle exceeds $\theta_L^S = \sin^{-1}(k_P/k_S)$, because, mathematically, the branch cut integral contributes to the total integral only for $\theta > \theta_L^S$. It can be shown that the integral around the branch cut in the w^P-plane is approximately zero and, thus, it does not contribute to the total integral. The integrals around the poles give rise to the Rayleigh surface wave and the leaky surface wave. They exist only for $\theta > \theta_R^S$ and $\theta > \theta_{\mathrm{LS}}^S$ in the w^S-plane, and for $\theta > \theta_R^P$ and $\theta > \theta_{\mathrm{LS}}^P$ in the w^P-plane. The total Rayleigh surface wave and the total leaky surface wave are comprised of the superposition of the contributions from the integrals around the singularities both in the w^S-plane and w^P-plane. The angles $\theta_R^{S,P}$ and $\theta_{\mathrm{LS}}^{S,P}$ are easily obtained by inserting $w_R^{S,P} = \sin^{-1}(\xi_R/k_{S,P})$ and $w_{\mathrm{LS}}^{S,P} = \sin^{-1}(\xi_{\mathrm{LS}}/k_{S,P})$ into Eq. (47).

The integrals are now approximately determined using the method of steepest-descent. Five separate wave types arise: the bulk shear wave, the bulk pressure wave, the Rayleigh surface wave, the leaky surface wave and the lateral wave. A detailed description of the steepest-descent method is given, for example, by Felsen and Marcuvitz.[9]

Using the method of steepest-descent, the shear wave in the far field comes out to be

$$u_x(R,\theta)|_{\text{Shear}} = \frac{j}{\mu\pi}\sqrt{\frac{2\pi}{k_S R}}\frac{e^{j(k_S R-\pi/4)}}{F_0(k_S \sin\theta)} \cdot 2\sqrt{k_P^2-k_S^2\sin^2\theta}\,k_S^3 \sin\theta\cos^2\theta, \quad (48)$$

$$u_z(R,\theta)|_{\text{Shear}} = \frac{-j}{\mu\pi}\sqrt{\frac{2\pi}{k_S R}}\frac{e^{j(k_S R-\pi/4)}}{F_0(k_S \sin\theta)} \cdot 2\sqrt{k_P^2-k_S^2\sin^2\theta}\,k_S^3 \sin^2\theta\cos\theta. \quad (49)$$

For the pressure wave,

$$u_x(R,\theta)|_{\text{Pressure}} = \frac{-j}{\mu\pi}\sqrt{\frac{2\pi}{k_P R}}\frac{e^{j(k_P R-\pi/4)}}{F_0(k_P \sin\theta)} \cdot [k_S^2-2k_P^2\sin^2\theta]k_P^2 \sin\theta\cos\theta, \quad (50)$$

$$u_z(R,\theta)|_{\text{Pressure}} = \frac{-j}{\mu\pi}\sqrt{\frac{2\pi}{k_P R}}\frac{e^{j(k_P R-\pi/4)}}{F_0(k_P \sin\theta)} \cdot [k_S^2-2k_P^2\sin^2\theta]k_P^2 \cos^2\theta. \quad (51)$$

The Rayleigh surface wave and the leaky surface wave are derived from the contour integral around the respective poles of the Rayleigh equation. Using contour integration, the Rayleigh wave is described by

$$u_x(R,\theta)|_{\text{Rayleigh}} = \frac{2\xi_R}{\mu F_0'|_{\xi_R}}[U(\theta-\theta_R^S) \cdot(-2\alpha_R\beta_R)e^{j\beta_R R\cos\theta} + U(\theta-\theta_R^P) \cdot(\beta_R^2-\xi_R^2)e^{j\alpha_R R\cos\theta}]\cdot e^{j\xi_R R\sin\theta}, \quad (52)$$

$$u_z(R,\theta)|_{\text{Rayleigh}} = \frac{2\alpha_R}{\mu F_0'|_{\xi_R}}[U(\theta-\theta_R^S)\cdot 2\xi_R^2 e^{j\beta_R R\cos\theta} + U(\theta-\theta_R^P)\cdot(\beta_R^2-\xi_R^2)e^{j\alpha_R R\cos\theta}] \cdot e^{j\xi_R R\sin\theta}, \quad (53)$$

where

$$F_0'|_{\xi_R} = 4\xi_R(\xi_R^2-\beta_R^2)+8\xi_R\beta_R\alpha_R-4\xi_R^3\left(\frac{\beta_R}{\alpha_R}+\frac{\alpha_R}{\beta_R}\right). \quad (54)$$

$F_0'|_{\xi_R}$ is the derivative of the Rayleigh equation with respect to ξ at $\xi=\xi_R$, and $U(\theta-\theta_R^{S,P})$ is the Heaviside unit step function; α_R, β_R, and ξ_R describe the wave numbers of the Rayleigh wave (see Table II). The result for the leaky surface wave is determined in exactly the same way and is obtained by simply replacing $\theta_R^{S,P}$, ξ_R, α_R and β_R by $\theta_{\text{LS}}^{S,P}$, ξ_{LS}, α_{LS} and β_{LS}, i.e., inserting the wave numbers for the leaky-wave pole instead of the Rayleigh wave pole.

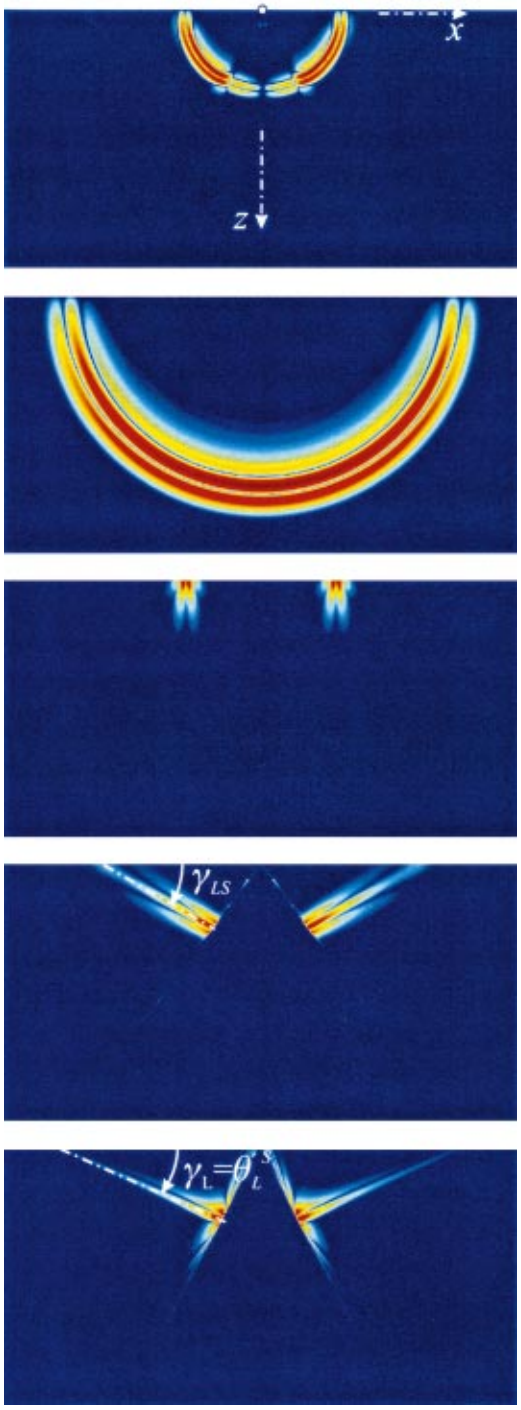

FIG. 7. Waves due to a point source on the surface. From top to bottom: shear wave, pressure wave, Rayleigh surface wave, leaky surface wave, lateral wave.

The lateral wave is defined by the integral around the branch cut, $\overline{P_b}$ in Fig. 6. Following Felsen and Marcuvitz,[9] the integral is asymptotically approximated to become

$$u_x(R,\theta)\big|_{\text{Lateral}} = U(\theta-\theta_L^S)\cdot\frac{-2^{3/2}/(\mu\sqrt{\pi})}{[k_S R|\sin(\theta-\theta_L^S)|]^{3/2}} \cdot\frac{(\sin\theta_L^S)^{3/2}(\cos\theta_L^S)^{5/2}}{(2\sin^2\theta_L^S-1)^2} \cdot e^{jk_S R\cos(\theta-\theta_L^S)+j3/4\pi}, \tag{55}$$

$$u_z(R,\theta)\big|_{\text{Lateral}} = U(\theta-\theta_L^S)\cdot\frac{2^{3/2}/(\mu\sqrt{\pi})}{[k_S R|\sin(\theta-\theta_L^S)|]^{3/2}} \cdot\frac{(\sin\theta_L^S)^{5/2}(\cos\theta_L^S)^{3/2}}{(2\sin^2\theta_L^S-1)^2} \cdot e^{jk_S R\cos(\theta-\theta_L^S)+j3/4\pi}. \tag{56}$$

C. Example

Equations (48)–(56) give the asymptotic far-field approximations for the wave fields excited by a harmonic line source on the surface. To determine the wave fields for a specific excitation in the time domain, the results must be transformed from the frequency domain into the time domain and convolved with the excitation function. The inverse-Fourier transform is given by

$$\hat{\mathbf{u}}(R,\theta,t) = \int_{\omega=-\infty}^{+\infty} G(\omega)\cdot\mathbf{u}(R,\theta,\omega)\cdot e^{-j\omega t}\,d\omega. \tag{57}$$

Here, $G(\omega)$ represents the Fourier transform of the excitation function. To obtain the particle velocity rather than the displacement, the displacement is differentiated with respect to time:

$$\hat{\mathbf{v}}(R,\theta,t) = \int_{\omega=-\infty}^{+\infty} G(\omega)\cdot\mathbf{u}(R,\theta,\omega)\cdot(-j\omega)e^{-j\omega t}\,d\omega. \tag{58}$$

In the following, a differentiated Gaussian pulse is used as excitation, with its Fourier transform

$$G(\omega) = -j\sqrt{2\pi}t_0^2\omega\cdot e^{0.5-0.5(\omega t_0)^2}, \tag{59}$$

where t_0 describes the width of the pulse. The particle velocity is determined here, because the analytical results are to be compared to numerical results, and the numerical finite-difference code that has been developed for this purpose computes the particle velocity rather than the particle displacement.

The wave fields excited by a differentiated Gaussian pulse are computed for a material with a Poisson ratio of $\nu = 0.4$. The wave fields are calculated according to Eqs. (48)–(56) and then transformed into the time domain using Eq. (58). In Fig. 7, the separate wave fields throughout the half

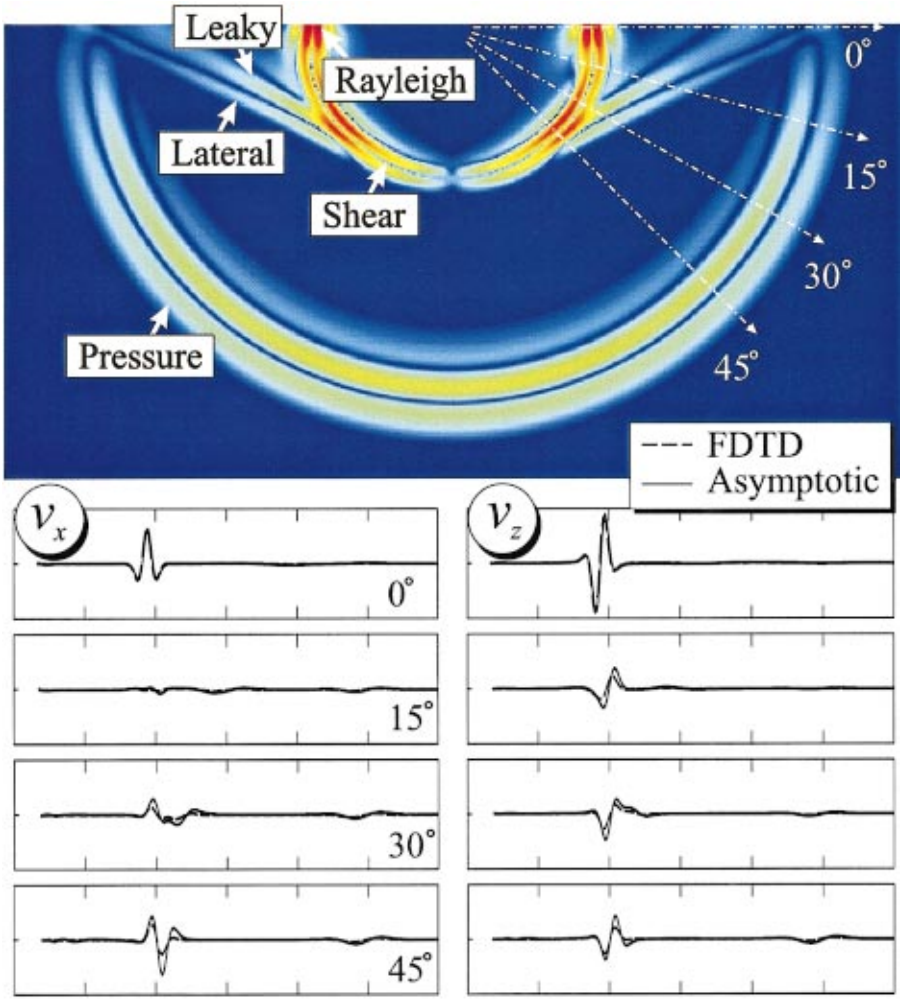

FIG. 8. Finite-difference results; comparison to asymptotic solution.

space are plotted for one instant in time, ten milliseconds after their excitation. The plots show, from top to bottom, the shear wave, the pressure wave, the Rayleigh surface wave, the leaky surface wave, and the lateral wave. A logarithmic color scale is used, ranging from dark red (0 dB) over yellow and green to blue (−40 dB). The top of each plot coincides with the surface of the medium. The source is located on the surface, at the center of each plot.

The shear wave and the pressure wave exhibit cylindrical wave fronts. They both vanish at the surface. The Rayleigh surface wave is confined to the surface and decays into the *z*-direction. The leaky surface wave propagates along the surface with a speed greater than the one of the shear wave, but smaller than the speed of the pressure wave. It feeds an inhomogeneous plane shear wave. The angle that the shear wave makes with the surface is approximately defined by

$$\gamma_{\mathrm{LS}} = \sin^{-1}(\mathrm{Re}\{\xi_{LS}\}/k_S). \tag{60}$$

Due to the coupling into the shear wave, the leaky wave ''leaks'' energy into the medium and decays in its propagation direction. The lateral wave propagates at an angle of approximately

$$\gamma_L = \theta_L^S = \sin^{-1}(k_P/k_S). \tag{61}$$

The artifacts that are especially visible for the lateral wave are due to the Fourier transform algorithm that is being used.

Figure 8 shows the wave fields due to a line source on the surface at one instant in time as determined numerically with the finite-difference time-domain (FDTD) algorithm. The wave fields are plotted at the top on a logarithmic color scale on a cross section through the half space and at the bottom on a linear scale along four radial lines, corresponding to four distinct propagation angles, as a function of the distance from the source. Again, a material with a Poisson ratio of 0.4 is assumed. With careful inspection, the five different wave types are distinguishable. The differences between the FDTD result and the asymptotic approximation are mainly due to the fact that the asymptotic approximation describes the waves in the far field, whereas the FDTD computations show the waves in the near field. Results essentially identical to the FDTD results have been obtained when integrating Eqs. (22) and (23) numerically rather than approximating the integrals asymptotically.[10]

To obtain a better picture of the behavior of the various waves at the surface, the particle motion due to the different surface waves is analyzed. For this, the wave fields of the Rayleigh surface wave, the leaky surface wave and the lateral wave are computed using Eqs. (52)–(56) for harmonic time-dependence, and hodograms of the particle motion at the surface are generated. In these hodograms, the vertical displacement along the surface is plotted versus the horizontal displacement. The hodograms are shown in Fig. 9. As it is well-known, the particle motion due to a Rayleigh surface wave is retrograde (counterclockwise) in nature [Fig. 9(a)]. This is caused by a phase shift between the horizontal and the vertical displacement component: the horizontal displacement is lacking 90 degrees in phase behind. The hodogram also indicates that the Rayleigh wave does not decay as it propagates along the surface. The particle motion

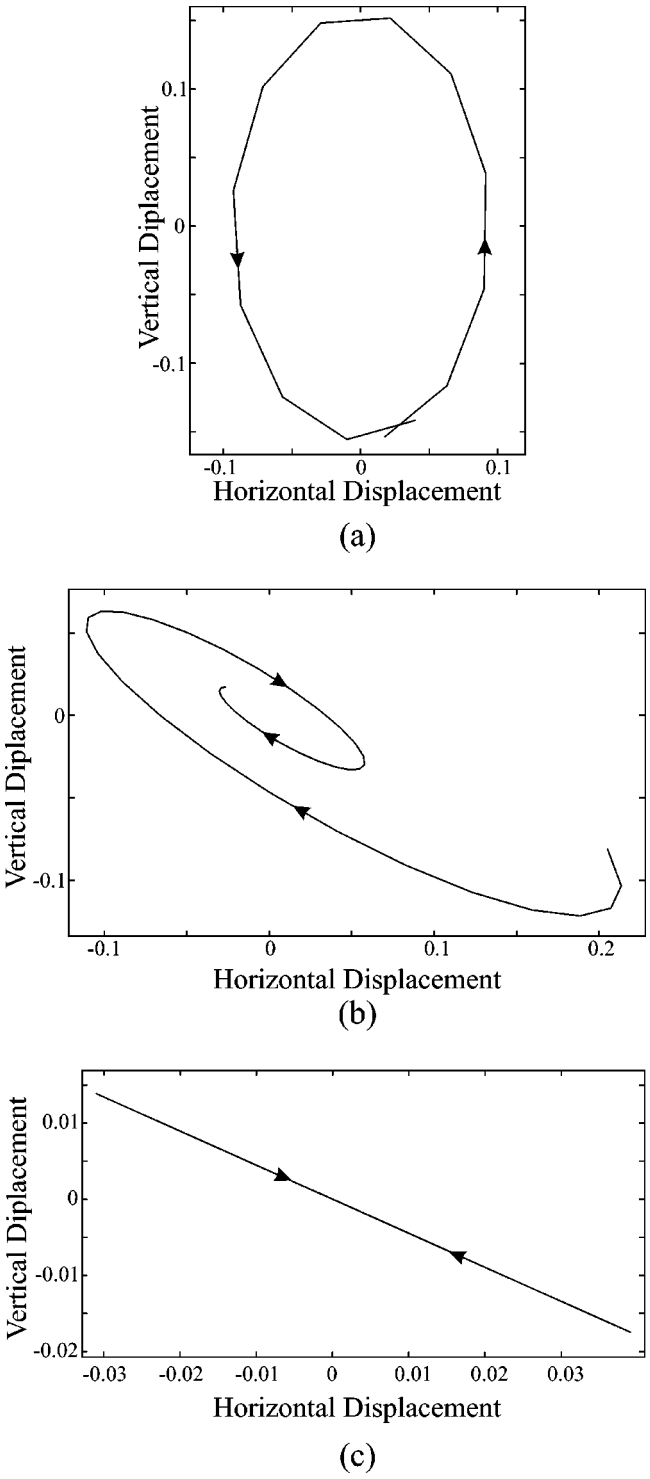

FIG. 9. Hodograms of the particle motion at the surface. Plots for the vertical displacement vs the horizontal displacement for (a) the Rayleigh surface wave, (b) the leaky surface wave, and (c) the lateral wave.

due to the leaky surface wave is prograde (clockwise), caused by the horizontal displacement being ahead in phase of the vertical displacement [Fig. 9(b)]. Clearly, the leaky surface wave decays as it travels along the surface. For the lateral wave, the displacement components are in phase, and the hodogram shows a diagonal line [Fig. 9(c)]. The lateral wave also decays as it propagates along the surface. The prograde and retrograde particle motions of surface waves

have also been observed experimentally by, for example, Smith *et al.*[3]

V. CONCLUSIONS

This paper gives a detailed theoretical description of the existence of a leaky surface wave in an isotropic homogeneous solid. The leaky surface wave is shown to arise from the complex conjugate roots of the Rayleigh equation. It exists only for materials with a Poisson ratio larger than about 0.263. The leaky surface wave propagates along the surface with a wave speed smaller than the pressure wave, but larger than the shear wave. Due to matching tangential wave vectors at the surface, it couples into a plane shear wave directed into the medium. Both the surface wave and the plane shear wave are, because of the coupling, inhomogeneous. It is demonstrated that a normal line source on the surface of an infinite half-space in fact excites the leaky surface wave. The far field expressions for the leaky surface wave are given and are compared to numerical results obtained by using the finite-difference time-domain method. The particle motion on the surface due to the leaky surface wave is prograde (clockwise), contrary to the well-known Rayleigh surface wave which induces a retrograde (counterclockwise) particle motion.

ACKNOWLEDGMENTS

The authors would like to thank Professor Glenn S. Smith, Professor Peter H. Rogers, Dr. Gregg D. Larson, and James S. Martin for their advice and consideration throughout this research and their help in obtaining support for this project. This work is supported in part under the OSD MURI program by the U.S. Army Research Office under Contract No. DAAH04-96-1-0448, and by a grant from the U.S. Office of Naval Research under Contract No. N00014-99-1-0995.

[1] J. W. S. Rayleigh, Proc. London Math. Soc. **17**, 4 (1887).
[2] M. Roth, R. Spitzer, and F. Nitsche, in *Proc. 12th Annu. Int. Meeting, Symp. Application of Geophysics to Engineering and Environmental Problems* (1999), pp. 49–55.
[3] E. Smith, P. S. Wilson, F. W. Bacon, J. F. Manning, J. A. Behrens, and T. G. Muir, J. Acoust. Soc. Am. **103**, 2333 (1998).
[4] N. E. Glass and A. A. Maradudin, J. Appl. Phys. **54**, 796 (1983).
[5] R. A. Phinney, Bull. Seismol. Soc. Am. **51**, 527 (1961).
[6] K. F. Graff, *Wave Motion in Elastic Solids* (Dover, New York, 1975).
[7] J. Miklowitz, *The Theory of Elastic Waves and Wave Guides* (North-Holland, New York, 1978).
[8] J. D. Achenbach, *Wave Propagation in Elastic Solids* (North-Holland, New York, 1973).
[9] L. B. Felsen and N. Marcuvitz, *Radiation and Scattering of Waves* (IEEE Press, 1994).
[10] C. T. Schröder and W. R. Scott, Jr., IEEE Trans. Geosci. Remote Sens. **38**, 1505 (2000).

Small-slope scattering from rough elastic ocean floors: General theory and computational algorithm

Robert F. Gragg,[a] Daniel Wurmser, and Roger C. Gauss
Naval Research Laboratory, Washington, D.C. 20375-5350

(Received 9 March 2001; revised 8 August 2001; accepted 23 August 2001)

In this article acoustic scattering by a random rough interface that separates a fluid incident medium from an underlying uniform scattering medium, either fluid or elastic solid, in cases for which the Bragg scale lies within the power-law tail of the roughness spectrum is dealt with. The physical foundation is an inherently reciprocity-preserving, local small-slope theory. A fully bistatic formulation is developed for the scattering strength, together with a robust numerical implementation that allows a wide range of spectral exponent values. The practical result for ocean acoustics is a significantly improved description of the interface component of sea floor scattering. Calculations are presented to demonstrate the advantage of this approach over perturbation theory, and to illustrate its dependence on frequency and environmental parameters as well as its operation in bistatic geometries. [DOI: 10.1121/1.1412444]

PACS numbers: 43.20.Fn, 43.30.Hw [DLB]

I. INTRODUCTION

Bottom scattering usually dominates the reverberation of active systems in shallow water. Although it is important for many practical purposes to have a quantitative assessment of the separate contributions from the principal sources of bottom scattering (the water/sediment interface, sub-bottom volume inhomogeneities, basement roughness), this can be extremely difficult to obtain. The basic reason (aside from a general lack of information about the values of operationally relevant geoacoustic parameters) is a scarcity of physics-based scattering models that are sufficiently comprehensive and flexible to make diagnostic predictions of this kind. In this article we provide such a model for what is often the most important component of bottom scattering—the contribution from the rough water/sea floor interface.

A. Background

As sampled by low-to-mid-frequency acoustic fields (20 Hz–10 kHz), most of the world's ocean floor is an effectively single-valued rough interface that separates the water from an acoustically fluid sedimentary bottom or from exposed rock that behaves as an elastic solid. In some places, sound can penetrate a relatively flat sediment cover and then scatter from a rough rock basement. In this article we address such scattering—from rough bottoms that remain effectively single valued down to the acoustic wavelength scale—which we consider to be a major contributor to the overall bottom-scattering problem. Of course, non-single-valued bottoms do occur (e.g., rocky bottoms with deep wavelength-scale hollows and fissures, and cobbled or gravelly bottoms ensonified at high frequency); however, the apparent interface scattering from them turns out to be a type of volume scattering that is properly modeled by other means (e.g., a theory developed by Jackson and Ivakin[1,2]), and such interface-generated effects should be distinguished from the competing phenomenon of true volume scattering by sub-bottom inhomogeneities.[3,4]

In the past, scattering from rough bottoms has been modeled using perturbation theory in the elastic case,[5] and using either the Kirchhoff approximation (for interfaces that vary slowly on the acoustic wavelength scale) or composite models (for interfaces with both slow and wavelength-scale variations) in the fluid case.[6,3] Although the underlying theories are not inherently restricted to backscatter, the published work, with certain notable exceptions such as Ref. 21, has dealt exclusively with that case.

Scattering from the air–sea interface is the simplest rough-surface scattering problem commonly found in underwater acoustics, and during the 1980's it was also the aspect of the problem of most immediate interest. Consequently, important innovations to the theory of acoustic scattering from rough surfaces emerged in this context. The genesis of the small-slope approximation counts among the most significant of these advances. This theory was originated by Voronovich[7,8] for the Dirichlet problem, and was later studied in the context of a new scattering formalism constructed by Dashen *et al.*[9–11] and by Berman and Dacol.[12] These studies demonstrated that the small-slope approximation improves on the composite model in a number of ways. It models the effects on scattering from both the wavelength scale and the larger scales, and furthermore seamlessly connects the two by correctly modeling the intermediate scales. Its derivation is systematic, in contrast to the composite model, for example, which requires an *ad hoc* choice for the boundary between large and small waves. It is also easier to implement than the composite model. In summary, the small-slope approximation, ''... in many respects, solves the problems of a unified description of wave scattering at rough surfaces in the framework of a single method and, in a sense, unifies the [method of small perturbations] and [tangent plane (Kirchhoff) approximation]....''[8] It is significant that Dashen's formalism makes it relatively simple to derive the small-slope

[a]Electronic mail: robert.gragg@nrl.navy.mil

formulation; however, this is true only for the lowest order, whereas Voronovich's original approach inherently points to a method for calculating higher orders.

In the early 1990's, Berman derived a small-slope scattering theory for the fluid–elastic interface.[13] Following the approach pioneered by Voronovich, he postulated a basic form for the scattering amplitude *T*, and then forced this form into order-by-order agreement with the corresponding perturbative result that he had developed earlier with Dacol.[14] Beyond the term that turns out to be numerically equivalent to the result that will be obtained in this paper (which we call the ''basic small slope'' or later simply the ''small slope''), Berman got a further term that is manifestly good to first order in the slope/curvature expansion. (The basic small slope is ostensibly good only to zeroth order in this expansion, but we will soon see that this is far too pessimistic.) In fact, Berman notes that the manifestly second-order correction term vanishes so that his results are actually valid all the way up to this order. The correction terms involve such nonlocal effects as diffraction, multiple scattering, and shadowing. His Monte Carlo numerical studies on the one-dimensional (1-D) problem demonstrate that shear is indeed important and that the basic small-slope approximation generally gives excellent results unless the incident field hits a very rough elastic surface at the Rayleigh angle. (That particular circumstance involves a resonant interaction with a leaky interface wave, which is not handled well by the basic small slope theory.)

Yang and Broschat extended Berman's result to stochastic rough surfaces,[15] obtaining a ''zeroth-order'' term for the cross section ($\sigma \propto \langle |T|^2 \rangle$) that once again corresponds to the basic small-slope result. They carried out a numerical analysis of this term for the 1-D problem, imposing both Gaussian and cutoff power-law spectra. They compared their small-slope results to first-order perturbation theory and to the Kirchhoff approximation (and also to the exact solution for the cutoff power law, which exists for this problem though not in two dimensions). Their results confirmed that the basic small-slope approximation indeed holds promise as a technique for calculating scattering from rough elastic surfaces.

Even though the basic small slope is sometimes called a ''zeroth-order'' theory, it, in fact, represents a higher-order correction to perturbation theory. Consider the deterministic scattering amplitude *T*. By construction, the basic small slope already subsumes first-order perturbation theory. By considering the consequences of a finite translation, one can demonstrate that it also includes the effect of the surface height alone to all orders.[16,17] Thus, the next term must be second order and must involve the slope (or a more generalized definition for the slope such as a difference between surface heights, which can be expanded into a Taylor series with the slope appearing in the lead term). In fact, since it can be shown that a manifestly reciprocal form for the scattering amplitude corresponding to a fluid–elastic interface exists,[17] an argument that has been applied to the formalism for Dirichlet boundary conditions (Ref. 18, Secs. I A and I B) can also be applied to the fluid–elastic case to show that the ''first-order'' correction to the basic small slope, in fact, goes as the *square* of the generalized slope. To compare the *stochastic* theory for the small-slope expansion to the stochastic perturbation theory expansion, consider the fact that the corrections in the scattering amplitude associated with slope/curvature begin at second order. The nonspecular contribution to stochastic theory must involve cross terms between the scattering amplitude and its complex conjugate, so the correction term associated with slope/curvature must begin at third order, as measured by perturbation theory. Finally, note that random rough surfaces are usually assumed to follow Gaussian statistics. For such surfaces, all expectation values of products involving odd powers of terms associated with the surface height vanish, so the ''zeroth-order'' small slope encompasses third-order perturbation theory and (most significantly) includes all orders that are purely in the surface height.

In 1997, Broschat and Thorsos carried[19] out a numerical analysis of the higher-order corrections to the basic small-slope approximation for the Dirichlet problem with a Gaussian interface. Under demanding conditions, they found the basic small slope approximation to be quite accurate in the forward direction, though somewhat less so in the backward direction. However, experience with the basic small slope in realistic problems such as backscatter from the air–sea interface indicates that it is very often quite adequate, even in backward directions.[20]

The starting point for the formalism developed below is an alternative form of the basic small slope derived by Wurmser.[17] The derivation is based on an expression for the change in the scattering amplitude that results from a change in the reference surface, $h(x,y) \rightarrow h(x,y) + \delta h(x,y)$. By considering the properties that must accompany a finite *translation*, this expression, which is initially only valid to first order in δh, is used to generate an expression good to infinite order in powers that involve only the surface height. The basic small slope then emerges when the formalism is applied to a quasiplanar rough surface and the reference surface is chosen to be its average plane. This approach is more transparent than the traditional derivation of the small-slope approximation, and it has one other advantage. The two must ultimately be equivalent, and both must somehow obey the reciprocity condition; however, Wurmser's version of the small slope manifestly exhibits the property while Berman's does not (as noted in Ref. 13). (We have verified that in the proper limit, the reciprocal small-slope approximation reduces to a perturbation theory that agrees numerically with the elastic-bottom perturbation formulation obtained by Essen,[5] although the equivalence of the analytic expressions is not readily apparent in this case either.) The manifestly reciprocal formulation has the advantages of simpler analytic form and easier numerical implementation.

In this article we perform a comprehensive study of the full bistatic theory formulated so that the inputs are a minimal set of geoacoustic parameters. Specifically, an azimuth-invariant spectrum with a power-law tail will be used for the rough bottom. The associated correlation function will be expanded, and that expansion will be truncated at an order where the expression for the scattering amplitude is sensitive to the tail of the spectrum but not the peak. This is significant because, although empirical descriptions of the tail have

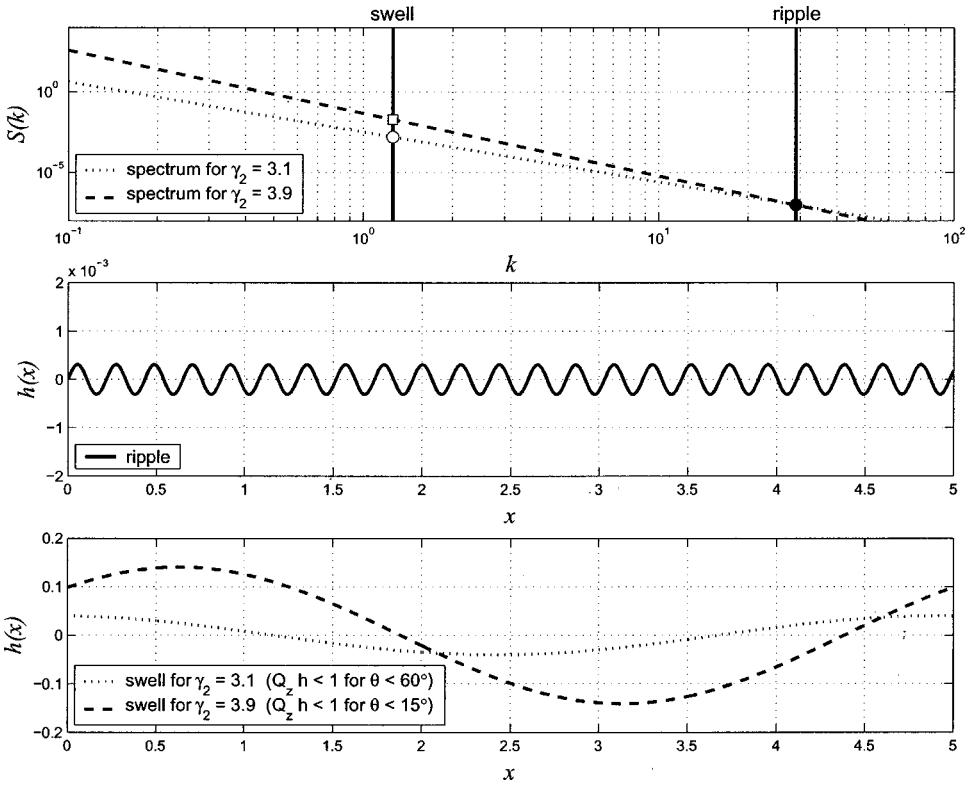

FIG. 1. Illustration for comparing small-slope and perturbation theories, as described in the text. Note the different vertical scales on the two lower panels.

been tabulated for some types of rough ocean bottoms, no such taxonomy has even been attempted for the spectral peak.

B. Outline of the article

We develop a bistatic model for the interface component of bottom scattering based on local small-slope theory and incorporating shear. The physical quantity of interest is σ_n, the nonspecular component of the scattering strength. In the remainder of this Introduction we briefly motivate our adoption of a small-slope approach and introduce some preliminary material. In Sec. II we review the small-slope theory of the scattering amplitude for a rough interface on an elastic bottom. We then reduce this to the fundamental form $\sigma_n = P \times I$ in which P is an algebraic prefactor that depends on the geoacoustic properties of the bottom and I is a scattering integral that involves the roughness spectrum of the interface. Given Wurmser's recent determination of the form of P for elastic bottoms,[17] the only remaining task is the calculation of I. For this, we take the spectrum to have a power-law form "where it counts" (within a broad band of wave numbers containing the Bragg region) and invoke analytic techniques adapted from the sea-surface analysis of Dashen *et al.*[9] This yields a simplified expression for I that depends on only two quantities—the spectral exponent γ_2 and a composite parameter α. Unfortunately, even this simpler form remains analytically intractable. In Sec. III, we develop a novel method of evaluating it numerically for arbitrary α throughout a broad operational range of the spectral exponent, $2.4 \leqslant \gamma_2 \leqslant 3.9$. In Sec. IV we present the results of numerical trials that point up the differences between the small-slope and perturbative expressions for σ_n, and examine the dependence on frequency, scattering geometry, and environmental parameters. A summary and conclusions are provided in Sec. V.

C. Small-Slope versus perturbation theories

We are dealing with Bragg scattering from a random interface with a roughness, h, whose statistics we assume to be characterized by a power-law wave number spectrum $S(k) \propto k^{-\gamma_2}$. Figure 1 schematically illustrates why for small values of the spectral exponent γ_2, perturbation theory should work well, at least when the grazing angle θ is not large, whereas larger γ_2 values will require a small-slope approach. In the top panel, a particular pair of wave numbers is marked by vertical lines labeled "ripple" and "swell." These designations are borrowed from sea-surface terminology: the ripple is the Bragg component and the swell has a much longer wavelength. The broken lines are spectra with the same Bragg-scale value (●) but different exponents, the larger exponent corresponding to a larger swell component—(□) for $\gamma_2 = 3.9$ versus (○) for $\gamma_2 = 3.1$. The other two panels depict surface roughness on the two length scales. (Note that they use different scales on their h axes.) The middle panel contains a Bragg-scale ripple characteristic of both spectra, and the bottom panel has swell-component realizations for each of the γ_2 values. A rough criterion for the validity of perturbation theory is $Q_z h < 1$, where Q_z is the change in the acoustic wave number's vertical component due to scattering. For backscatter in water with sound speed c_w, the condition is $\sin\theta < c_w/(4\pi f h)$. We consider the situation at a moderately low frequency, $f = 3.5$ Hz, for which the ripple component clearly presents no problem. With *only* that component present, the surface is comparable to a planar

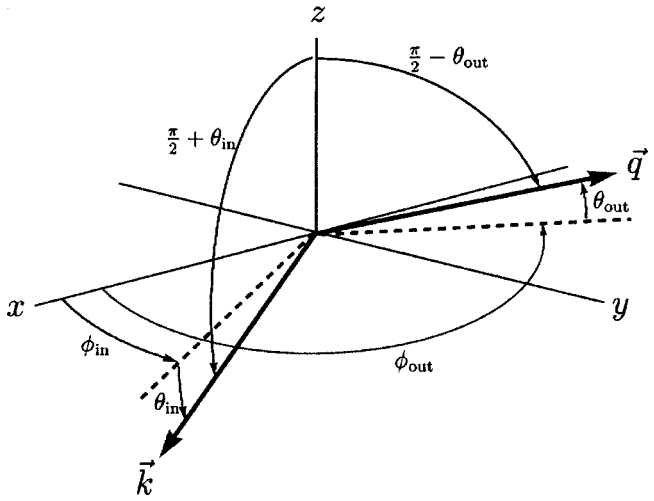

FIG. 2. Incident vector $\vec{k}=(K_w,\phi_{\rm in},\theta_{\rm in})$ and scattered vector $\vec{q}=(K_w,\phi_{\rm out},\theta_{\rm out})$.

diffraction grating and perturbation theory is perfectly adequate. For the swell component, however, a perturbation approach will be dependable below 60° in the $\gamma_2=3.1$ case and only below 15° for $\gamma_2=3.9$. For the smaller spectral exponent, the swell-plus-ripple surface is analogous to a diffraction grating whose ground plane merely has a slight undulation. For the larger one, it is more like a grating inscribed on a fun house mirror: the ground plane of the grating has long-wavelength undulations with significant amplitudes but only moderately small slopes and negligible curvature. The physical mechanism redirecting the incident field into nonspecular directions is still Bragg scattering from the ripple. The ripple has just been lifted and slightly tilted by the underlying swell. First-order small-slope theory, which is valid to all orders in h and to first order in its slope, and which neglects swell-scale curvature, is designed to handle just such cases.

Although the above discussion has been a qualitative one based on an oversimplified two-point spectrum, we will see that its central implications are borne out. At small γ_2, where the small-slope and perturbation theories should both be valid, they do, in fact, agree up to fairly high grazing angles (except in near-specular cases, where the latter diverges). For large γ_2, the two theories disagree, the difference being the greatest at higher grazing angles. In this regime only small slope remains valid. We should reemphasize here that we are expounding a *local* theory, which would not be able to handle the shadowing that would occur at very low angles if γ_2 became extremely large.

D. Preliminaries

We indicate 3-D vectors by arrows and their 2-D horizontal projections by boldface [e.g., $\vec{r}=(\mathbf{r},z)$, $\vec{k}=(\mathbf{k},k_z)$]. Plain symbols denote the magnitudes of 2-D components (e.g., $r=|\mathbf{r}|$, $k=|\mathbf{k}|$). The function $z=h(\mathbf{r})$ defines a rough but single-valued surface as measured from its average plane, $z=0$.

The incident and scattered wave vectors are specified in the customary modified spherical coordinates (Fig. 2):[21] $\vec{k}=(K_w,\phi_{\rm in},\theta_{\rm in})$ and $\vec{q}=(K_w,\phi_{\rm out},\theta_{\rm out})$ in which K_w is the wave number in the water, $0\leqslant\phi\leqslant 2\pi$ is an azimuth, and $0\leqslant\theta\leqslant\pi/2$ is a grazing angle. Their difference is $\vec{k}-\vec{q}=\vec{Q}$. Specular scattering corresponds to $(\phi_{\rm out},\theta_{\rm out})=(\phi_{\rm in},\theta_{\rm in})$, i.e., $\vec{Q}=(\mathbf{0},2k_z)$; backscatter is specified by $(\phi_{\rm out},\theta_{\rm out})=(\phi_{\rm in}+\pi,\theta_{\rm in})$, i.e., $\vec{Q}=2\vec{k}$.

We will repeatedly use the integral

$$\int_0^\infty J_0(\eta t)t^p\,{\rm d}t=\frac{2^p}{\eta^{1+p}}\frac{\Gamma(\frac{1}{2}+\frac{1}{2}p)}{\Gamma(\frac{1}{2}-\frac{1}{2}p)}. \tag{1}$$

The left-hand side is a Mellin transform[22] and the right-hand side is its analytic continuation[23] beyond the strip of analyticity $-1<{\rm Re}(p)<\frac{1}{2}$. As a function of p, this has its zeros at the odd positive integers and its poles at the odd negative integers.

II. ROUGH-INTERFACE SCATTERING

A. Scattering amplitude

The small-slope scattering amplitude $T(\vec{q},\vec{k})$ for a given rough interface $h(\mathbf{r})$ between two media is given by [Ref. 9, Eq. (13)]

$$T=i\frac{\beta}{Q_z}\int\left[e^{i\vec{Q}\cdot\vec{r}}\right]_{z=h(\mathbf{r})}{\rm d}^2\mathbf{r}+O(g^2,\zeta^2), \tag{2}$$

in which g and ζ are the slope and curvature of h (i.e., $g=|\partial h/\partial\mathbf{r}|$ and $\zeta=\lambda/R$, where λ is the wavelength of the incident field and R is the radius of curvature of the interface). β is determined by the acoustoelastic continuity that is physically inherent at the interface. In idealized cases where this continuity is replaced by imposed boundary values, β assumes simple forms (e.g., $\beta=4k_zq_z$ in the pressure-release limit[9]). Retaining the full physical continuity, however, produces surprisingly complicated expressions. Wurmser[17] gives a comprehensive treatment for two elastic media and deals with all the limiting forms.

For the fluid/elastic–solid case, the fully bistatic result for β is found as follows. With the z axis pointing upward, a general downgoing wave in the water will have a wave vector of the form $\vec{\kappa}=(\boldsymbol{\kappa},\kappa_z)$ with real $\boldsymbol{\kappa}$, negative κ_z, and $\vec{\kappa}\cdot\vec{\kappa}=K_w^2$, in which $K_w=\omega/c_w$ in terms of the water sound speed c_w. This wave will connect to bottom waves that have wave vectors $\vec{\kappa}_p=(\boldsymbol{\kappa},\kappa_{pz})$ and $\vec{\kappa}_s=(\boldsymbol{\kappa},\kappa_{sz})$, with $\vec{\kappa}_p\cdot\vec{\kappa}_p=K_p^2$ and $\vec{\kappa}_s\cdot\vec{\kappa}_s=K_s^2$, for which $K_p=\omega/c_p$ and $K_s=\omega/c_s$ in terms of the compressional and shear sound speeds c_p and c_s. Their vertical components are $\kappa_{pz}=-\sqrt{K_p^2-|\boldsymbol{\kappa}|^2}$ and $\kappa_{sz}=-\sqrt{K_s^2-|\boldsymbol{\kappa}|^2}$. In this context, we define the functions [Ref. 17, Eqs. (3.15), (3.22)]

$$a(\vec{\kappa})=\varrho\frac{\kappa_z}{\kappa_{pz}}\left(1-4\frac{|\boldsymbol{\kappa}|^2}{K_s^2}\frac{\kappa_{sz}}{K_s}\frac{\kappa_{sz}-\kappa_{pz}}{K_s}\right), \tag{3a}$$

$$b(\vec{\kappa})=\varrho\frac{\kappa_z}{\kappa_{pz}}\left(1-2\frac{|\boldsymbol{\kappa}|^2}{K_s^2}\right), \tag{3b}$$

$$\xi(\vec{\kappa})=\frac{\kappa_z}{\kappa_{pz}}\left(1-2\frac{\vec{\kappa}_p\cdot\vec{\kappa}_s}{K_s^2}\right), \tag{3c}$$

in which $\varrho=\rho_b/\rho_w$ is the bottom/water density ratio. Two downgoing waves in the water are of particular importance to the scattering problem, namely, the incident wave with $\vec{\kappa}=\vec{k}$ and the time-reversed scattered wave with $\vec{\kappa}=-\vec{q}$. With these indicated by the subscripts 1 and 2 [e.g., $a_1=a(\vec{k})$ and $a_2=a(-\vec{q})$], the bistatic result for a fully elastic bottom is

$$\begin{aligned}\beta=&[4(1-\varrho)(k_z q_z+\mathbf{k}\cdot\mathbf{q}\xi_1\xi_2)+8\varrho(\mathbf{k}\cdot\mathbf{q}/K_s)^2\xi_1\xi_2\\&-4\mathbf{k}\cdot\mathbf{q}(a_1-\xi_1)(a_2-\xi_2)+4K_w^2 a_1 a_2\\&+2K_s^2(a_1-b_1)(a_2-b_2)/\varrho-4K_p^2 b_1 b_2/\varrho]/\\&[(1+a_1)(1+a_2)].\end{aligned}\tag{4}$$

When the media are not homogeneous, as assumed here, this expression should still apply provided local parameter values (those prevailing within a few wavelengths of the interface) are used. Note that $T(-\vec{k},-\vec{q})=T(\vec{q},\vec{k})$, an indication of the reciprocity built into the theory.[17]

B. Scattering strength

We take $h(\mathbf{r})$ to be a stationary Gaussian random process. The scattering cross section in the limit of large ensonified area is Rayleigh distributed, and scattering is describable in terms of the ensemble-average cross section $\mathsf{s}=\langle|T/4\pi|^2\rangle$ (per unit solid angle in the $\vec{q}$ direction). With second-order terms neglected, Eq. (2) yields [Ref. 9, Eq. (31)]

$$\mathsf{s}=\left|\frac{\beta}{4\pi Q_z}\right|^2\int\int e^{i\mathbf{Q}\cdot(\mathbf{r}-\mathbf{r}')}\langle e^{iQ_z[h(\mathbf{r})-h(\mathbf{r}')]}\rangle \mathrm{d}^2\mathbf{r}'\,\mathrm{d}^2\mathbf{r}.\tag{5}$$

The average in the integrand can be expressed as[9] $\langle e^{iQ_z[h(\mathbf{u})-h(\mathbf{v})]}\rangle=e^{-Q_z^2[C(\mathbf{0})-C(\mathbf{u}-\mathbf{v})]}$, in which $C(\mathbf{r})=\langle h(\mathbf{r}),h(\mathbf{r}+\Delta\mathbf{r})\rangle$ is the correlation function of the surface roughness.[24] The average cross section for the rough surface is thus [Ref. 9, Eq. (37)]

$$\mathsf{s}=\left|\frac{\beta}{4\pi Q_z}\right|^2\int\int e^{i\mathbf{Q}\cdot(\mathbf{u}-\mathbf{v})-Q_z^2[C(\mathbf{0})-C(\mathbf{u}-\mathbf{v})]}\mathrm{d}^2\mathbf{u}\,\mathrm{d}^2\mathbf{v}.\tag{6}$$

An orthogonal coordinate transformation $(\mathbf{u},\mathbf{v})\mapsto[\frac{1}{2}(\mathbf{u}+\mathbf{v}),\ \mathbf{u}-\mathbf{v})\overset{\text{def}}{=}(\mathbf{w},\mathbf{r})$, together with the introduction of a beamwidth to ensure that $\int(\cdots)\mathrm{d}^2\mathbf{w}$ remains finite, yields the average scattering cross section *per unit area* (i.e., the scattering strength) [Ref. 9, Eq. (40)],

$$\sigma=\left|\frac{\beta}{4\pi Q_z}\right|^2\int e^{i\mathbf{Q}\cdot\mathbf{r}}e^{-Q_z^2[C(\mathbf{0})-C(\mathbf{r})]}\,\mathrm{d}^2\mathbf{r}.\tag{7}$$

The maximum correlation occurs at zero separation, $|C(\mathbf{r})|\leqslant C(\mathbf{0})=h_{\mathrm{rms}}^2$, and since $h(\mathbf{r})$ is a wide-band process, $C(\mathbf{r})$ ought to be concentrated within a correlation length of that point (within the disk $r<r_{\mathrm{cor}}$). Thus, for $r\gg r_{\mathrm{cor}}$, one should find $C(\mathbf{r})$ becoming negligible so that the $\exp\{-Q_z^2[C(\mathbf{0})-C(\mathbf{r})]\}$ factor in the integrand is well approximated by the constant $\exp\{-(Q_z h_{\mathrm{rms}})^2\}$. That indicates a delta-function divergence that may be separated out. Once this is done, Eq. (7) can be rewritten in terms of explicitly specular and nonspecular contributions [Ref. 9, Eq. (41)],

$$\begin{aligned}\sigma=&\left|\frac{\beta}{4\pi Q_z}\right|^2 e^{-(Q_z h_{\mathrm{rms}})^2}\Bigg\{(2\pi)^2\delta(\mathbf{Q})\\&+\int e^{i\mathbf{Q}\cdot\mathbf{r}}[e^{Q_z^2 C(\mathbf{r})}-1]\mathrm{d}^2\mathbf{r}\Bigg\}\overset{\text{def}}{=}\sigma_s+\sigma_n,\end{aligned}\tag{8}$$

an expression originally obtained by Voronovich[7,8] for the pressure-release case. The singularity is confined to the specular part, σ_s. In this article, we are interested in the *non*specular part, σ_n.

In both theoretical and applied work, the correlation is usually obtained from the spectrum, $C(\mathbf{r})=\int e^{i\mathbf{k}\cdot\mathbf{r}}S(\mathbf{k})\mathrm{d}^2\mathbf{k}$. The agenda is to start with $S(\mathbf{k})$, then determine $C(\mathbf{r})$, and finally obtain σ_n from Eq. (8). This means working out a sequence of two 2-D Fourier transforms. As will be seen below, even with the surface symmetry exploited to reduce these to 1-D Hankel transforms, some finesse is required to produce a useful result.

C. Isotropic roughness case

Since the roughness is *isotropic*, $C(\mathbf{r})$ and $S(\mathbf{k})$ really only depend on the *magnitudes* of their arguments, and thus may be written as simply $C(r)$ and $S(k)$. In this case we are left with the Hankel transforms,

$$C(r)=2\pi\int_0^\infty J_0(kr)kS(k)\mathrm{d}k,\tag{9}$$

$$\sigma_n=\left|\frac{\beta}{4\pi Q_z}\right|^2 2\pi\int_0^\infty J_0(Qr)r\underbrace{e^{-Q_z^2C(0)}[e^{Q_z^2C(r)}-1]}_{B}\mathrm{d}r.\tag{10}$$

For later convenience, we designate the indicated integrand factor as B.

Using the dimensionless range $y=Qr$, we may rewrite Eq. (10) as the product

$$\sigma_n=P\times I,\tag{11}$$

in which P is the algebraic factor,

$$P=\frac{1}{8\pi}\left|\frac{\beta}{Q_z Q}\right|^2,\tag{12}$$

and I is the spectral integral,

$$I=\int_0^\infty J_0(y)yB(y)\mathrm{d}y.\tag{13}$$

Jackson and co-workers have obtained expressions like Eq. (11), the difference being that they use a Kirchhoff approximation for P [Ref. 6, Eq. (38)], [Ref. 21, Eq. (11)]. Recent work, however, has turned to small-slope methods.[25–29] [In the backscatter geometry, Essen's T (an intensity transfer function, not a scattering amplitude) is related to P via $T=2\pi P\times(4\cot\theta)^2$ [Ref. 5, Eqs. (24) and (25)]. This factorization of σ_n is natural and convenient in two respects. First, except for their common dependence on the scattering geometry, the two factors depend on separate physical quantities (Table I). P is a function of the bottom's material properties but is independent of interface roughness and frequency; I depends on the roughness and frequency, but not the bottom

TABLE I. Dependence of the factors P and I on the physical variables of the problem. The (∗) indicates quantities that will later turn out to enter only as constituents of a single composite parameter, α.

	Interface roughness (w_2, γ_2, h_0)	Material properties (ρ_b, c_p, c_s)	Frequency (f)	Scattering geometry $(\theta_{\text{in}}, \theta_{\text{out}}, \phi)$
P	No	Yes	No	Yes
I	Yes	No	Yes∗	Yes∗

properties. Second, although P already has an easily implemented analytic form, I is still formulated as a double integral involving the roughness spectrum, and this will need more scrutiny before a numerical evaluation is attempted. The first step will be to adopt a suitable form for the spectrum, $S(k)$.

D. Roughness spectra

The simplest spectrum is a pure power law,[21]

$$S(k) = \frac{w_2}{(h_0 k)^{\gamma_2}}, \tag{14}$$

in which the spectral exponent is a dimensionless number in the range $2 < \gamma_2 < 4$ (Appendix A), h_0 is some reference length, and $w_2 = S(h_0^{-1})$ is the spectral strength whose physical dimension is $(\text{length})^4$. The h_0 is included mainly to make the denominator dimensionless. It does not represent a characteristic length for this spectrum. Indeed, since this $S(k)$ retains the same k dependence throughout all length scales, the $h(\mathbf{r})$ process that it characterizes is a random scaling fractal—a surface without any characteristic length. The fractal dimension of the surface is $D = 3 - \frac{1}{2}\gamma_2$, so the restriction $2 < \gamma_2 < 4$ corresponds to $1 < D < 2$ (Ref. 30, Sec. 2.2.1).

It is also worth noting that experimental measurement (e.g., fitting a straight line to a log–log plot of S vs k data points) can determine γ_2 and the combination $w_2/h_0^{\gamma_2}$, but *not* w_2 or h_0 separately. Any two sets of values, (γ_2, w_2, h_0) and (γ_2, w_2', h_0'), are equally valid descriptions of the data as long as $(h_0'/h_0)^{\gamma_2} = w_2'/w_2$. It is common practice is to refer w_2 to some standard h_0 reference value (we use one meter).

Although Eq. (14) describes many physical surfaces quite well over a wide span of length scales,[28,31] extrapolating it to vanishing k yields nonsensical results. For example, because the correlation corresponding to Eq. (14) is [Ref. 21, Eq. (14)]

$$C(r) = \frac{\pi w_2}{h_0^2} \frac{\Gamma(1 - \frac{1}{2}\gamma_2)}{\Gamma(\frac{1}{2}\gamma_2)} \left(\frac{r}{2h_0} \right)^{\gamma_2 - 2} \tag{15}$$

[from Eq. (1) with $p = 1 - \gamma_2$ and $\eta = r/h_0$], it follows that $C(r)$ vanishes at $r = 0$ and decreases steadily with increasing r. This unphysical behavior is a mathematical artifact produced by the divergence of $S(k)$ at the origin. It can be remedied by the simple expedient of introducing a cutoff at some small value $k = \epsilon$. Then, after $C(r)$ is obtained, one is free to "destroy the evidence" by proceeding under approximations in which ϵ does not appear or by actually letting $\epsilon \to 0$. (The procedure is similar in spirit to the use of an integrating factor to prevent a physically meaningful integral from diverging.) The spectral contributions of components in the surface ensemble certainly should *not* grow without bound as the wavelength increases, so it is reasonable to expect that removing the divergence from Eq. (14) might recover a physically reasonable result for $C(r)$. Furthermore, since the effects that concern us involve Bragg scattering, the details of the cutoff ought to be immaterial as long as it occurs well below the Bragg wave number region.

A straightforward way to implement the cutoff is simply to make the replacement $h_0 k \to \sqrt{1 + (h_0 k)^2}$ in Eq. (14), producing[9]

$$S(k) = \frac{w_2}{[1 + (h_0 k)^2]^{\gamma_2/2}}, \tag{16}$$

which closely approximates Eq. (14) for large k, with differences appearing only as k dwindles into the neighborhood of h_0^{-1}. Instead of $S(0) = \infty$, we now have $S(0) = w_2$. [Physically speaking, $S(0) = 0$ would be more realistic; however $S(0) < \infty$ is enough to do the job.] For *this* spectrum, h_0 *does* serve as a natural physical scale; h_0^{-1} is the spectral width. (As always, one might quibble about factors of 2 or so in defining this width, but h_0^{-1} will do as well as anything.) As long as this h_0^{-1} is well below the Bragg wave number k_{B}, the existence of the spectral cutoff should not influence any Bragg phenomena. The width of the corresponding cutoff correlation $C(r)$ is h_0. In other words, h_0 is simply the rough-surface correlation length, r_{cor}. Thus the condition $h_0^{-1} \ll k_{\text{B}}$ is equivalent to $\lambda_{\text{B}} \ll r_{\text{cor}}$, which is inherently necessary for significant Bragg scattering from the rough interface.

We can find the correlation for the cutoff spectrum by rescaling the k, r variables to the dimensionless forms $\kappa = h_0 k$, $\rho = r/2h_0$ (these are distinct from the κ and ϱ used in other contexts above) and introducing the Lipschitz[30] (*aka* Hurst[32]) exponent of the roughness (Appendix A),

$$\nu = \tfrac{1}{2}\gamma_2 - 1, \tag{17}$$

which falls within the range $0 \leqslant \nu \leqslant 1$. The correlation becomes

$$\begin{aligned} C(r) &= \frac{2\pi w_2}{h_0^2} \int_0^\infty \frac{\kappa J_0(2\kappa\rho)}{(1 + \kappa^2)^{1+\nu}} \, \mathrm{d}\kappa \\ &= C(0) \frac{2\nu}{\Gamma(1+\nu)} \rho^\nu K_\nu(2\rho), \end{aligned} \tag{18}$$

in which $J_0(\cdot)$ and $K_\nu(\cdot)$ are Bessel functions and

$$C(0) = h_{\text{rms}}^2 = \frac{\pi w_2}{h_0^2} \frac{1}{\nu} \tag{19}$$

is the mean-square roughness. Having exploited the cutoff to recover physical results, we can now "destroy the evidence." Instead of trying to force h_0^{-1} to vanish in some sense, we will simply resort to an approximation in which its precise value is immaterial.

III. SCATTERING STRENGTH ALGORITHM

The above cut-off spectrum has allowed the first of the two required Hankel transforms, Eq. (9), to be found in a physically meaningful closed form. Unfortunately, the second one, Eq. (10), remains intractable. When Eqs. (18) and (19) are used in Eq. (10), the remaining integral still is not susceptible to analytic evaluation and also remains remarkably resistant to common numerical techniques. (The widespread dissemination of results from a numerical calculation which, though carefully done, turned out to be wrong occasioned the publication of Ref. 9.) Further steps will be necessary to produce σ_n from Eqs. (11)–(13). We proceed by first obtaining an asymptotic form for the B factor in the integrand of Eq. (13) in terms of a new composite parameter α, and then merging a pair of approximations for overlapping ranges for α. For small α we use a power series. For larger α, we use a rational-function approximation that we then expand in a partial-fraction series. In each case, we are able to Hankel transform the terms of the series analytically. The result is a computational algorithm for the spectral integral, Eq. (13), that is reliable throughout the range of spectral exponents typically encountered in ocean environments, $2.4 \leqslant \gamma_2 \leqslant 3.9$.

A. Asymptotic form for *B*

Standard identities [Ref. 33, Eqs. (6.1.17) and (9.6.2)] allow Eq. (18), the analytic result for the cutoff correlation, to be rewritten in terms of the $I_{\pm\nu}(\cdot)$ Bessel functions as

$$C(r) = C(0)\Gamma(1-\nu)\times\rho^{\nu}[I_{-\nu}(2\rho) - I_{+\nu}(2\rho)]. \tag{20}$$

Another identity [Ref. 33, Eq. (9.6.10)] expresses the second factor as a pair of power series in the variable ρ^2:

$$\rho^{\nu}[I_{-\nu}(2\rho) - I_{+\nu}(2\rho)] = \sum_{m=0}^{\infty} u_m(-\nu)\rho^{2m} - \rho^{2\nu}\sum_{m=0}^{\infty} u_m(+\nu)\rho^{2m}, \tag{21}$$

in which the coefficients are

$$u_m(\nu) = [m!\,\Gamma(1+m+\nu)]^{-1}. \tag{22}$$

Using Eqs. (20)–(22) with the definition $d = Q_z^2 C(0)$, one can write

$$Q_z^2[C(0) - C(r)] = a(1+b) - c, \tag{23}$$

where $b = \Sigma_{m=1}^{\infty} b_m \rho^{2m}$ and $c = \Sigma_{m=1}^{\infty} c_m \rho^{2m}$, with

$$b_m = \frac{u_m(+\nu)}{u_0(+\nu)}, \quad c_m = d\times\frac{u_m(-\nu)}{u_0(-\nu)}, \quad a = d\times\frac{\Gamma(1-\nu)}{\Gamma(1+\nu)}\rho^{2\nu}. \tag{24}$$

Although b_m remains well behaved throughout the range $0 \leqslant \nu \leqslant 1$, both c_m and a diverge at the end points. [d diverges at $\nu = 0$ because of Eq. (19).] This can cause the same behavior in $C(0) - C(r)$. However, if the extremes of ν are contracted to $\nu_{\min} > 0$ and $\nu_{\max} < 1$, that cannot occur. Then one can reasonably hope to choose h_0 large enough to keep c and a small throughout the reduced range $\nu_{\min} \leqslant \nu \leqslant \nu_{\max}$, provided ρ remains of order unity or smaller. Then it would make sense to expand $\exp\{-Q_z^2[C(0) - C(r)]\}$ in a power series in a. Such an expansion results in[23]

$$B = e^{-a(1+b)+c} - e^{-d} = e^{-a} + \sum_{n=0}^{\infty} q_n(\rho^2)(-a)^n - e^{-d}, \tag{25}$$

in which each $q_n(\cdot)$ represents an infinite polynomial with positive coefficients. Furthermore, both the final term $\exp(-d)$ and the $n = 0$ term of the sum can be omitted entirely, since they actually contribute absolutely nothing to σ_n [because Eq. (1) vanishes when p is an odd positive integer]. A small-a asymptotic estimate $B \sim \exp(-a)$ then results from simply dropping the remaining $\Sigma_{n=1}^{\infty}(\cdots)$. (This is the step that "destroys the evidence" that a cutoff was installed in the spectrum. Keeping any of those $n > 0$ terms would lead to a cutoff-dependent result.)

Thus, with the frequency and geometry consolidated into the composite parameter,

$$\alpha \overset{\text{def}}{=} \frac{a}{(Qr)^{2\nu}} \propto f^{4-\gamma_2}, \tag{26}$$

and with the parametric dependence on α and ν made explicit, Eq. (13) becomes

$$I(\alpha,\nu) = \int_0^{\infty} J_0(y)\, y B(y;\alpha,\nu)\, \mathrm{d}_y, \tag{27a}$$

in which

$$B(y;\alpha,\nu) = e^{-\alpha y^{2\nu}}. \tag{27b}$$

Equation (27) is an asymptotic form that is valid within $\nu_{\min} \leqslant \nu \leqslant \nu_{\max}$ to the extent that

$$a = \frac{\Gamma(1-\nu)}{4^{\nu}\Gamma(1+\nu)} \times [(h_{\mathrm{rms}} Q_z)(r/r_{\mathrm{cor}})^{\nu}]^2 \tag{28}$$

is small. Note, however, that this does *not* imply that the parameter,

$$\alpha = \frac{\Gamma(1-\nu)}{4^{\nu}\Gamma(1+\nu)} \times \left[\frac{h_{\mathrm{rms}} Q_z}{(r_{\mathrm{cor}} Q)^{\nu}}\right]^2, \tag{29}$$

must also be small. This is essential. In backscatter situations, for instance, where $Q = 2K_w \cos\theta$, α will not be small when either θ or ν is large. Note also that the overall sizes of a and α are determined principally by their $[\cdots]$ factors rather than the common gamma-function ratio. (That ratio remains in the approximate range 3 ± 2 throughout $2.4 \leqslant \gamma_2 \leqslant 3.9$, so it is not the determining factor.)

B. Computational algorithm for *I*

Although Eq. (27) does simplify matters, a closed form for this Hankel transform exists in only a single case, $\gamma_2 = 3$ (Appendix B). A reliable algorithm is still needed to compute $I(\alpha,\nu)$ for α ranging from very small to very large values. To achieve this, we ultimately merge a pair of techniques based on contrasting approximations for $B(y;\alpha,\nu)$. One is a series for small α,[9,25] the other a rational-function approximation for large α,[34,35] and each of them allows Eq. (27a) to be integrated termwise in closed form. We develop these techniques below, and then address the operational meaning of "small" and "large" α when we merge the two.

1. Series formulation

For *small* α (i.e., small grazing angles), we have the Taylor series $B(y;\alpha,\nu)=\Sigma_{n=0}^{\infty}(-\alpha y^{2\nu})^n/n!$ so that, on reversal of the order of integration and summation, $I(\alpha,\nu)=\Sigma_{n=0}^{\infty}(-\alpha)^n/n!\times\int_0^{\infty}y^{2\nu n+1}J_0(y)\mathrm{d}y$. The remaining integral can be found in closed form [using Eq. (1) with $p=2\nu n+1$ and $\eta=1$]. The result is the approximation

$$I(\alpha,\nu)=\frac{2}{\pi}\sum_{n=1}^{\tilde{n}}(-)^{n+1}[2^{\nu n}\Gamma(\nu n+1)]^2\sin(\nu n\pi)\times\frac{\alpha^n}{n!}, \tag{30}$$

which is to be evaluated numerically for some finite $\tilde{n}$. [For $\nu=3/4$, this is Eq. (51a) of Ref. 9 with the typo 3/3 corrected to 3/4.] The remaining question of how large to make $\tilde{n}$ will be addressed later. It is clear, however, that when only the *first* term of this series is retained, so that $I\propto\alpha$, the result from Eq. (13) is

$$\sigma_n=\left|\frac{\beta}{2}\right|^2 S(Q)\propto f^{4-\gamma_2}, \tag{31}$$

where $S(k)$ is the pure power-law spectrum, Eq. (14). No evidence of the spectral cutoff remains, and σ_n, which diverges in the specular case $Q=0$, is simply the *first-order perturbation result*; i.e., the leading term from Eq. (8) for $Q_z h_{\mathrm{rms}}\ll 1$.

2. Rational-function formulation

When α is *large*, we use a rational-function approximation to $B(y;\hat{\alpha},\nu)$ for a fixed reference value $\hat{\alpha}$ of order unity. In the variable $x=y^2$, the approximation of order $[N,D]$ is

$$B(y;\hat{\alpha},\nu)\approx\underbrace{\frac{1+\Sigma_{j=1}^{N}n_j x^j}{1+\Sigma_{l=1}^{D}d_l x^l}}_{\text{rational polynomial form}}=\underbrace{\frac{\Pi_{j=1}^{N}(1-x/z_j)}{\Pi_{l=1}^{D}(1-x/p_l)}}_{\text{pole-zero form}}, \tag{32}$$

in terms of the polynomial coefficients n_j, d_l or the zeros and poles z_j, p_l. This approximation behaves correctly at the origin, where $B(0;\hat{\alpha},\nu)=1$, and the requirement $D-N>0$ makes it vanish properly for large y. Properly constructed, an approximation of this kind can be remarkably accurate.[36] In the present application, the only real difficulty occurs when poles or zeros happen to fall on the integration contour of Eq. (27a)—the $x>0$ axis. This, however, can be overcome by means of a ''stabilization'' procedure due to Drumheller.[37] The procedure first splits any pole $p>0$ [i.e., replaces p by a rotated complex pair $(pe^{+i\delta},pe^{-i\delta})$] and then introduces an additional zero $z=p/(2\cos\delta-1)$ to keep the value of $D-N$ unchanged. [The expression for z emerges from matching the first-order Maclaurin series for the two forms of Eq. (32).] We find that a rotation angle $\delta=90°$ serves very well, so that the replacement poles and the new zero are simply $(ip,-ip)$ and $-p$, respectively. Finally, positive zeros are dealt with in an analogous way: any zero $z>0$ is replaced by $(iz,-iz)$ and a new pole, $-z$, is introduced. At the conclusion of this procedure, we compute the residues r_m from the ''stabilized'' poles and zeros, and then convert Eq. (32) to partial-fraction form,

$$B(y;\hat{\alpha},\nu)=\sum_{m=1}^{D}\frac{r_m}{x-p_m}. \tag{33}$$

Given a reasonable choice for $[N,D]$, this produces an excellent approximation to the y dependence of $B(y;\hat{\alpha},\nu)$ throughout $0.2\leqslant\nu\leqslant 0.95$ (i.e., $2.4\leqslant\gamma_2\leqslant 3.9$).[34,35] It only remains to extend this to $\alpha\neq\hat{\alpha}$.

This extension is easily done because, for general α, Eq. (27b) scales according to $B(y;\alpha,\nu)=B(sy;\hat{\alpha},\nu)$ in terms of the scale factor $s=(\alpha/\hat{\alpha})^{1/2\nu}$. Thus, the partial-fraction decomposition of $B(y;\alpha,\nu)$ for general α is the right-hand side of Eq. (33) with $(r_m,p_m)\rightarrow(r_m/s^2,p_m/s^2)$, so that

$$I(\alpha,\nu)=\sum_{m=1}^{D}\frac{r_m}{s^2}\int_0^{\infty}\frac{J_0(y)y}{y^2-p_m/s^2}\mathrm{d}y. \tag{34}$$

The remaining integral is available in closed form under the condition $\mathrm{Re}(\sqrt{-p_m})>0$ (Ref. 38, No. 6.566.2), which is guaranteed by Drumheller's pole stabilization. The final result is

$$I(\alpha,\nu)=\sum_{m=1}^{D}\frac{r_m}{s^2}K_0\left(\frac{\sqrt{-p_m}}{s}\right), \tag{35}$$

in terms of the $K_0(\cdot)$ Bessel function.

In practice, we implement Eq. (32) by matching the rational-polynomial form to $B(y,\hat{\alpha},\nu)$ at $N+D$ points within an interval $0<x\leqslant x_{\max}$, with the points concentrated somewhat toward the lower end. We find it satisfactory in all practical cases to let $x_{\max}$ be the point where $B(y;\hat{\alpha},\nu)$ has fallen to 0.01 and to take $\hat{\alpha}=1$. Full details are to be found in Refs. 34 and 35. The rational-function orders $[N,D]$ are to be chosen empirically.

3. Unified formulation

Equations (30) and (35) apply to ''small'' and ''large'' α, respectively. We must now be specific about the practical meanings of those terms and about the how large $\tilde{n}$ and $[N,D]$ need to be. Figure 3 illustrates the situation for a particular ν. The solid line is the result of the series formulation, Eq. (30). It is an accurate representation of $I(\alpha,\nu)$ for the smallest α's and remains so until α has risen to the value indicated by $\triangle$, where it fails abruptly. The dashed line represents the rational-function formulation, Eq. (35). It remains good as α decreases from the largest values until a gradual oscillating degradation sets in at the point indicated by $\triangledown$. Clearly the ''small'' α region lies to the left of $\triangle$ and the ''large'' α region to the right of $\triangledown$. Within broad limits, increasing $\tilde{n}$ would shift $\triangle$ to the right, and increasing the $[N,D]$ values would shift $\triangledown$ to the left. (Decreasing these parameters would, of course, have the opposite effect.) The $\tilde{n}$ and $[N,D]$ values used in the figure are large enough to make the two α regions overlap substantially so that the two formulations for $I(\alpha,\nu)$ can be patched together into a unified version covering all α. This can be done by identifying the transition point $\bigcirc$ whose decibel α value lies halfway between those of $\triangledown$ and $\triangle$, and then simply using Eq. (30) to the left of $\bigcirc$ and Eq. (35) to the right of it. However, the $\bigcirc$ so obtained depends on the γ_2 used to produce the figure. To incorporate this dependence, we repeated the calculations

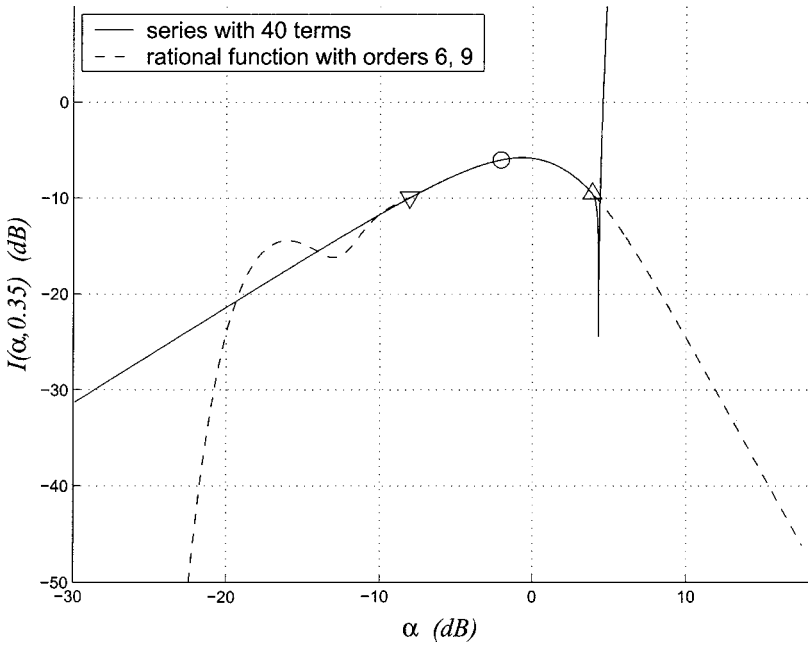

FIG. 3. $I(\alpha,\nu)$ vs α for $\nu=0.35$ (i.e., $\gamma_2=2.7$). The solid curve is the series formulation, Eq. (30), with $n=40$. The dashed curve is the rational-function formulation, Eq. (35), with $[N,D]=[6,9]$. $\triangle$ is the upper end of the "small" α region. ∇ is the lower end of the "large" α region. $\bigcirc$ is the transition point between the two regions.

throughout the operational range of γ_2, using the same $\tilde{n}$ and $[N,D]$ values, and then applied linear least-squares methods (Fig. 4). The final conclusion is that $\tilde{n}=40$ and $[N,D]=[6,9]$ can be used in all cases and that, as a function of γ_2, the transition point $\bigcirc$ occurs at

$$\log_{10}\alpha=-1.7567\gamma_2+4.4926. \tag{36}$$

This empirical rule is followed in all of the simulations below.

C. Performance of the algorithm

In summary, the nonspecular component of the bistatic small-slope scattering strength, σ_n, is given by Eq. (11) as the product of the bottom material factor P and the interface spectral integral I. We know P for the general fluid/elastic–solid case in terms of the β supplied by Eq. (4). We compute $I(\alpha,\nu)$ throughout the operational range of γ_2 by uniting a rational-function formulation for large α, Eq. (35),[34,35] with a series formulation for small α, Eq. (30)[9] (which also supplies the perturbation result for all α as a bonus).

In this section we conduct a set of monostatic tests to validate the performance of the model. (Bistatic cases are included in Sec. IV.) For a given bottom material, we compute backscatter values for σ_n vs θ, P vs θ, I vs α, and α vs θ—all parametrized by γ_2. The bottom material selected is limestone, with parameters inferred from measurements over a rocky bottom off the coast of Long Bay, South Carolina (as in Ref. 20, but with somewhat higher attenuations). Figures 5–9 illustrate the performance of our unified algorithm for monostatic scattering from this bottom. In these and subse-

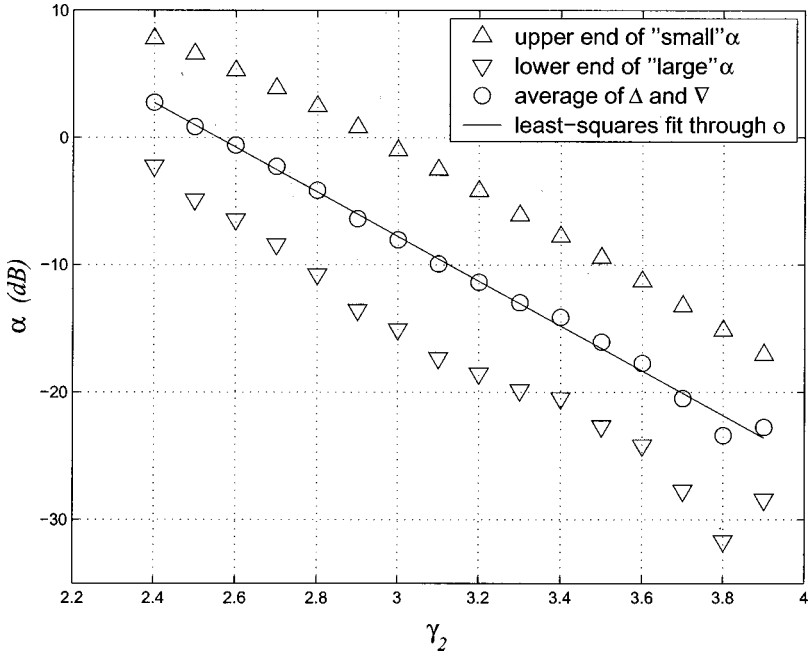

FIG. 4. The symbols retain the same meanings as in Fig. 3. γ_2 ranges through the values $2.4,2.5,\ldots,3.8,3.9 \overset{\text{def}}{=} 2.4{:}0.1{:}3.9$, and the straight line is the least-squares fit through the $\bigcirc$'s given by Eq. (36).

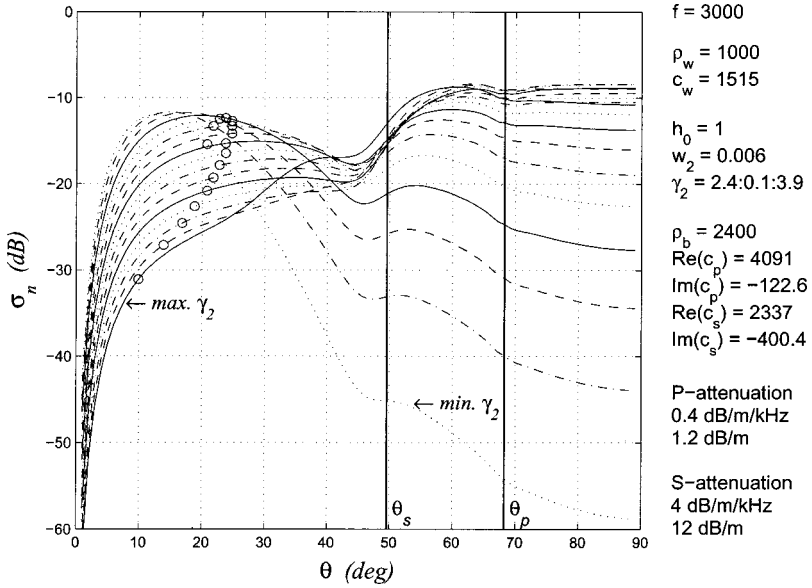

FIG. 5. The small-slope scattering strength versus grazing angle for the monostatic limestone cases specified in the sidebar on the right. Separate curves correspond to the different values of γ_2. The ○ symbol on each curve corresponds to the transition value of α for the unified formulation of $I(\alpha,\nu)$.

quent figures, the complete set of input variables for σ_n is displayed in a sidebar on the right (above the attenuations). Their values are always given in the mks system with the unit labels (Hz, kg/m^3, m/s, etc.) omitted. Ranges of values are represented in a Matlab-style "start:step:stop" notation; e.g., $u=1.8{:}0.2{:}2.2$ would mean that a variable u takes on the values (1.8,2.0,2.2) in whatever mks units are physically appropriate. The line style used to render the curves cycles through this sequence: dotted, dot–dashed, dashed, solid. Attenuations calculated from the complex sound speeds are displayed in the sidebar below the inputs, both in dB/m and in dB/m/kHz. In addition, the shear and compressional critical angles are indicated on the figures by vertical lines labeled θ_s and θ_p. These figures were all produced using $\theta=1°{:}1°{:}89°$.

Figure 5 contains 16 σ_n vs θ curves for a range of γ_2 values. These curves all exhibit a moderate dip about 5° below θ_s as well as a modest hump in the region between θ_s and θ_p, and those with smaller γ_2 values also have a sizable broad peak at small θ. Note that as θ increases, the entire family of curves eventually undergoes a near-total reversal of order. Attached to each curve is a symbol ○ that marks the transition value of α used in the unified formulation of $I(\alpha,\nu)$ for the prevailing γ_2. The α values associated with these ○'s come from Eq. (36) and thus decrease steadily as γ_2 grows. However, owing to the nonlinear relationship between θ and α (Fig. 8), their associated θ values are not monotonically related to γ_2.

Figure 6 illustrates the dependence of P and θ for the same environment. The figure actually contains separate curves for the same 16 γ_2 values, though these all coalesce into a single curve because P lacks any γ_2 dependence. Evidently, the dip just below θ_s and the hump between θ_s and θ_p in the previous figure are traceable to corresponding features here, and are thus associated with the scattering geometry and/or bottom properties rather than with the interface roughness. This is also true of the steep rise in σ_n at small θ.

Figure 7 shows the α dependence of $I(\alpha,\nu)$ as evaluated by the unified formulation (black curves). The gray lines in

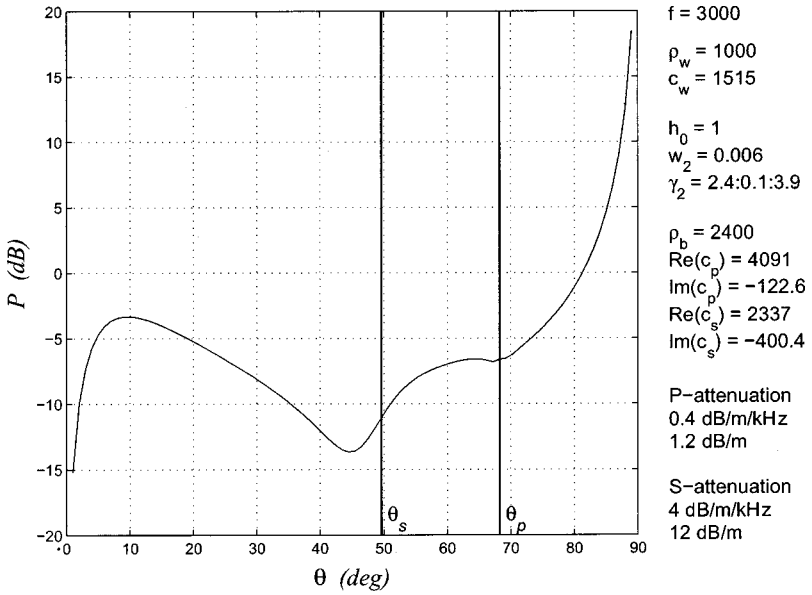

FIG. 6. The algebraic factor P versus the grazing angle.

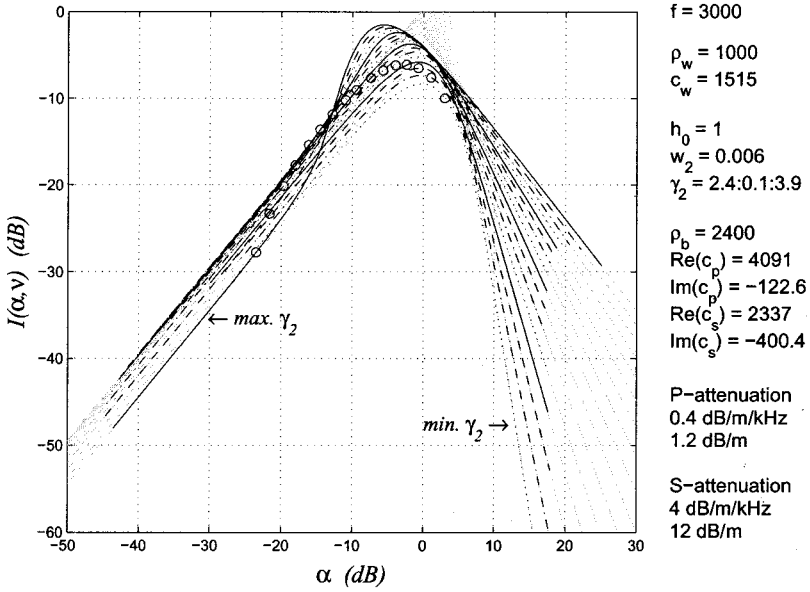

FIG. 7. Black curves: spectral integral $I(\alpha,\nu)$ versus the composite parameter α. The ○ symbol on each curve corresponds to the transition value of α for the unified formulation. Gray background lines: approximations to $I(\alpha,\nu)$ using the first terms of Eq. (30) and Eq. (C1) for α below and above 0 dB, respectively.

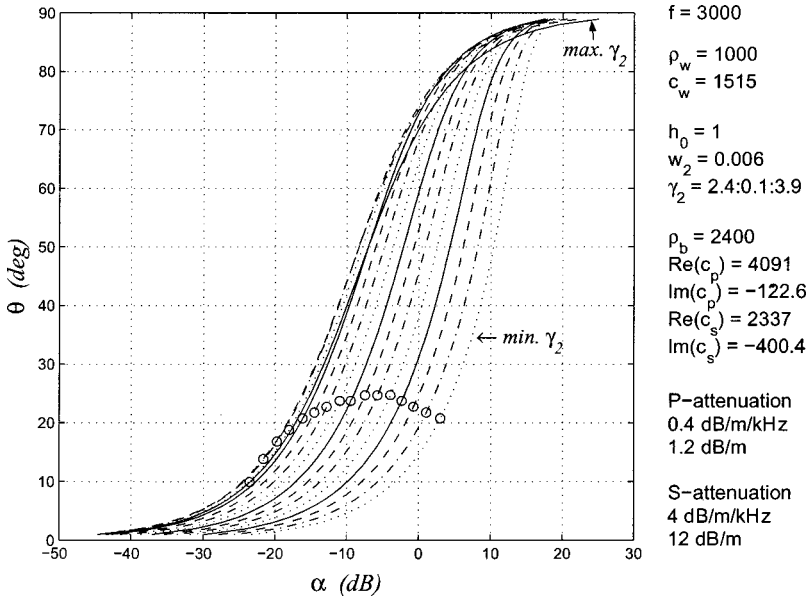

FIG. 8. The grazing angle θ versus the composite parameter α. The ○ symbol on each curve corresponds to the transition value of α for the unified formulation.

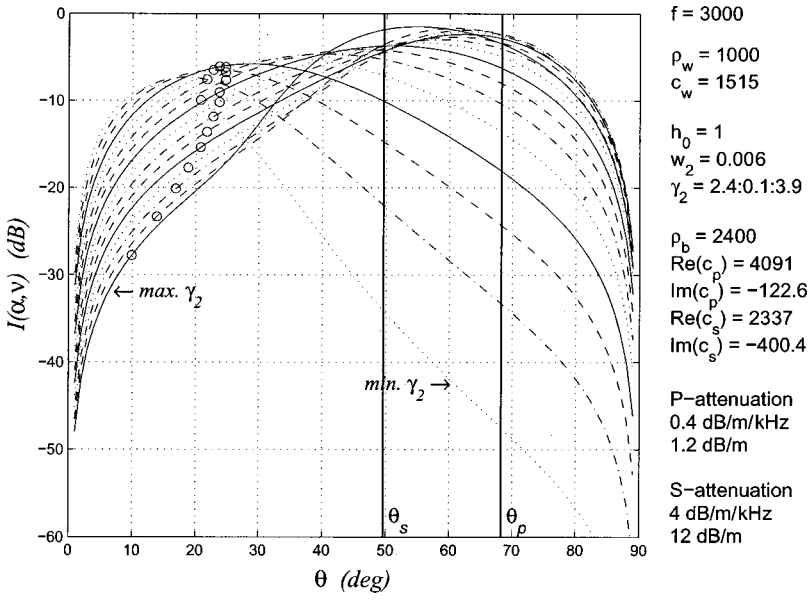

FIG. 9. Spectral integral $I(\alpha,\nu)$ versus grazing angle θ. The ○ symbol on each curve corresponds to the transition value of α for the unified formulation.

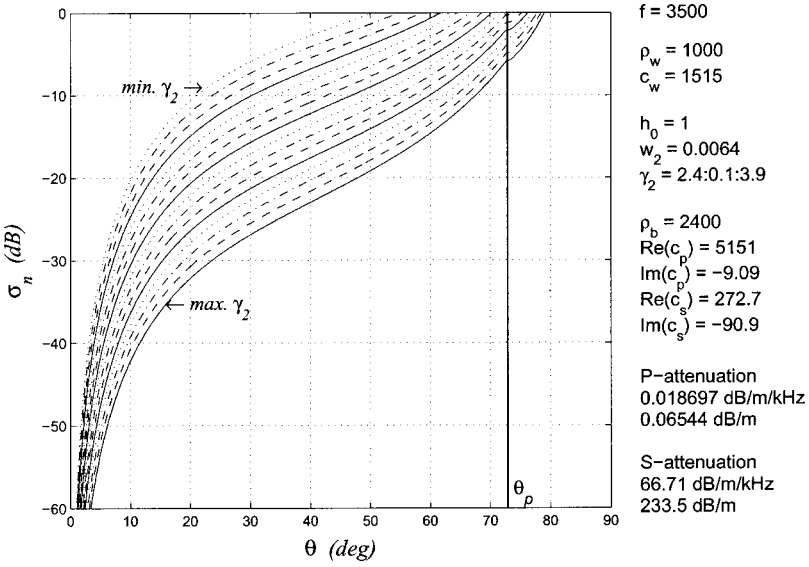

FIG. 10. The PT/F case: perturbation-theory scattering strength versus grazing angle for fluid basalt specified in the sidebar on the right. Separate curves correspond to the different values of γ_2.

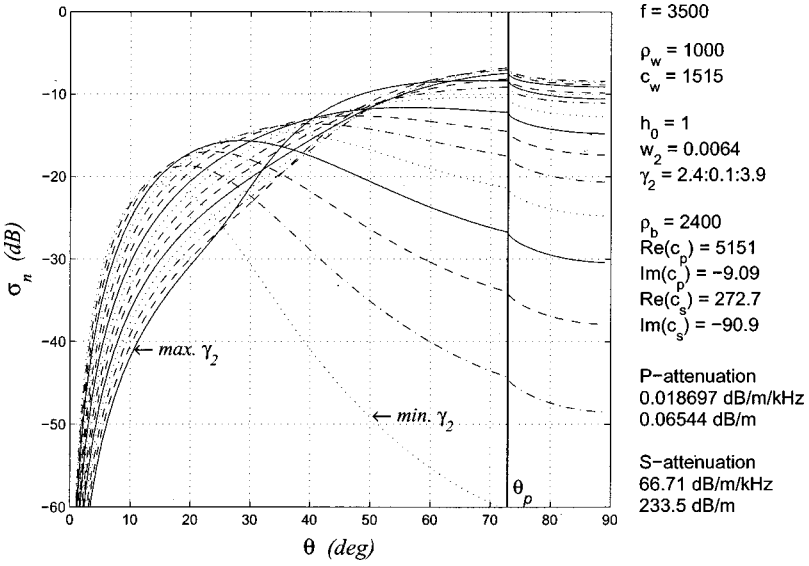

FIG. 11. The SS/F case: small-slope scattering strength versus grazing angle for the fluid basalt specified in the sidebar on the right. Separate curves correspond to the different values of γ_2.

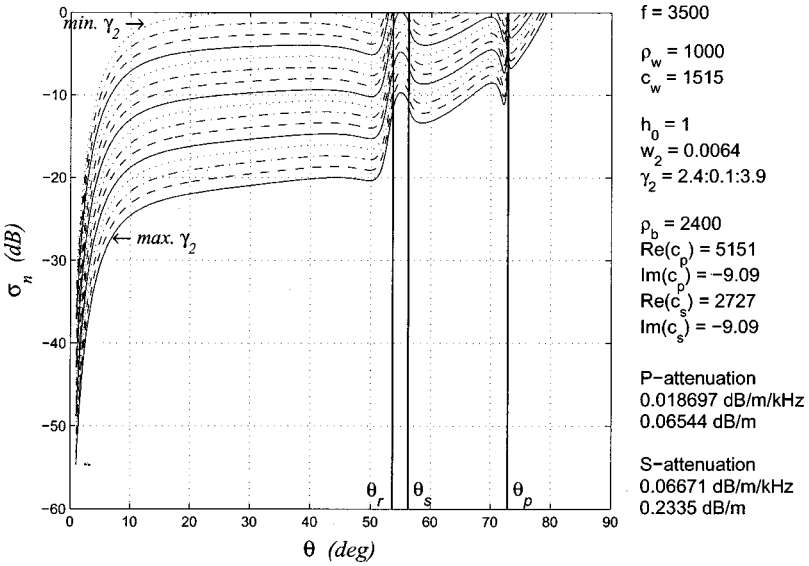

FIG. 12. The PT/E case: perturbation-theory scattering strength versus grazing angle for the realistic basalt specified in the sidebar on the right. Separate curves correspond to the different values of γ_2.

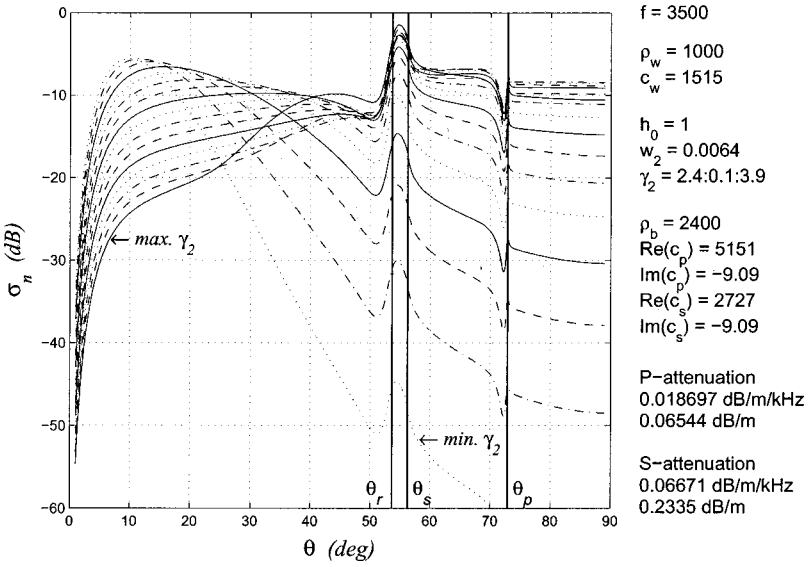

FIG. 13. The SS/E case: small-slope scattering strength versus grazing angle for the realistic basalt specified in the sidebar on the right. Separate curves correspond to the different values of γ_2.

the background represent the leading terms of two series approximations

(i) The parallel lines with slope $+1$ on the $\alpha<0$ dB side are produced by the first term of the series formulation, Eq. (30), i.e., $I(\alpha,\nu)\approx[2^{2\nu+1}\Gamma^2(\nu+1)\sin(\nu\pi)/\pi]\times\alpha$, and therefore embody the predictions of first-order perturbation theory. The black curves are asymptotic to these gray lines for small α. Their separation signals the breakdown of perturbation theory and hence the need for a small-slope treatment.

(ii) The gray lines on the $\alpha>0$ dB side with slopes $-1/\nu$ represent the first term of a large-α series (Appendix C), namely $I(\alpha,\nu)\approx[\Gamma(1/\nu)/2\nu]\times\alpha^{-1/\nu}$. Since this expression was not used in the unified formulation, the fact that the black curves are asymptotic to these gray lines for large α serves as a validation point for the unified formulation in that regime. As noted above, the curves were all generated from a common set of θ values. They occupy different α ranges because the $\theta\leftrightarrow\alpha$ mapping is parametrized by γ_2.

Figure 8 illustrates that mapping. It is clear that as γ_2 increases, the ○ symbols shift monotonically in α but not in θ. Figure 9 is the result of using the $\alpha\leftrightarrow\theta$ mapping to convert Fig. 7 to the independent variable to θ. The relation $\sigma_n=P\times I$ is reflected by the fact that Fig. 5 is the sum of Figs. 6 and 9. (The figures all use logarithmic scales.)

A few words are in order at this point about the interpretation of scattering strength results such as Fig. 5. As noted earlier, our formulation is not completely adequate when θ is very close to 0° because it does not incorporate shadowing. Though this effect can be modeled (e.g., as Thorsos has done for the air–sea interface by recourse to fourth-order perturbation theory[39]), we do not deal with it here. Also, in near-grazing applications, certain diffraction effects (including those associated with interface waves) can exist when curvature is present in either the incident phase front or the scattering interface. Our theory, since it assumes a planar incident wave and neglects interface curvature, does not include these. (We will return to this issue in Sec. IV B.) For the (monostatic) geometry used above, $\theta=90°$ is the specular direction. Although perturbation theory, Eq. (31), diverges there (an artifact of the noncutoff power-law spectrum, Sec. IV), our small-slope results remain well behaved because we are modeling only the *non*specular scattering strength.

IV. TRIALS

In this section we present a series of numerical trials for rough *basalt* bottoms. Basalt was chosen because (a) it is a material in which elasticity ought to be even more significant than limestone; (b) Essen's perturbative calculations for basalt are available as a benchmark;[5] and (c) experimental basalt data exist that should allow future data/model comparisons.[28] The principal results are plots of σ_n only, without separate displays for P and I. The labels SS and PT refer to small-slope and perturbation theory, while F and E distinguish between fluid and elastic sea floors.

A. Monostatic

The figures in this section were produced using a finer grazing angle increment, $\Delta\theta=0.1°$, in order to resolve any small details.

1. Spectral exponent and bottom material properties

Figures 10–13 (Table II) display the scattering strength $\sigma_n=P\times I$ as separate curves over the full operational range of spectral exponent values. I_{SS} is $I(\alpha,\nu)$ via the unified formulation and $I_{\mathrm{PT}}=2\pi|Q_zQ|^2S(Q)$ is the corresponding PT quantity. Those curves that have $\gamma_2=3.3$ are rendered heavier for later reference. Those with the largest value $\gamma_2=3.9$ (labeled "max γ_2") correspond to curves in Essen's work.[5] The spectral strength of the roughness is also obtained

TABLE II. The use of perturbation theory (PT) versus small-slope (SS) and fluid (F) versus elastic (E) bottoms in Figs. 10–13.

	I_{PT}	I_{SS}
P_{F}	Fig. 10	Fig. 11
P_{E}	Fig. 12	Fig. 13

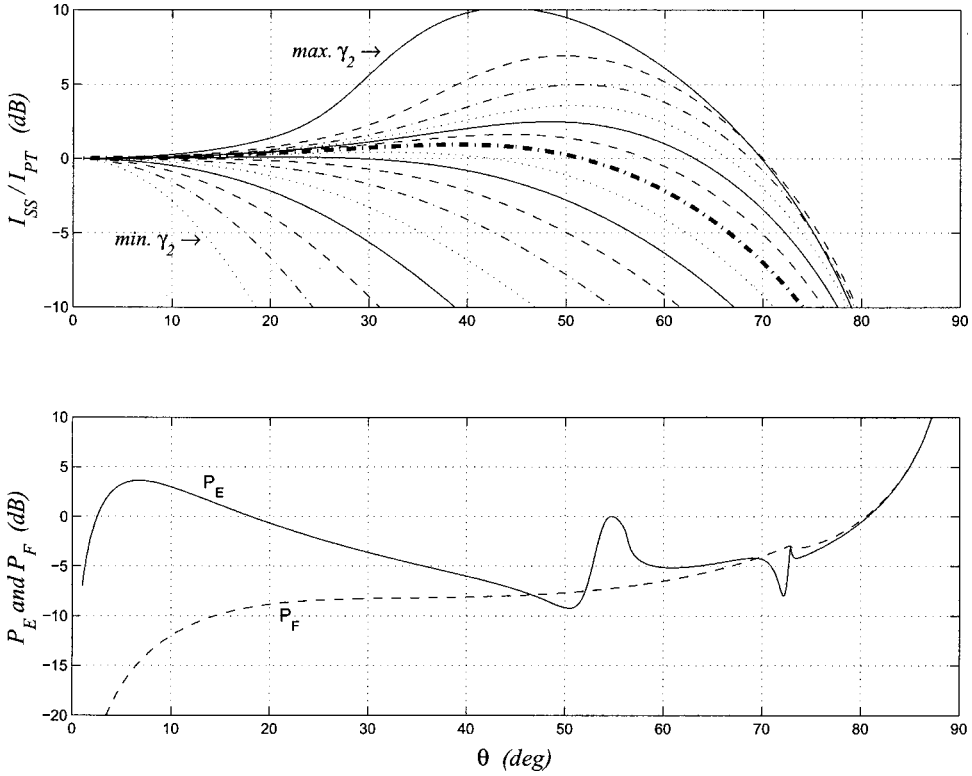

FIG. 14. A comparison among Figs. 10–13. Top: ratio of I_{PT} to I_{SS} in decibels. Bottom: P_{E} and P_{F} (the elastic and fluid forms of the factor P) in decibels.

from that source ($w_2 = 0.04/2\pi = 0.0064$) [Ref. 5, Eqs. (28) and (31)]. The first two cases, Figs. 10 and 11, deal with ''fluid'' basalt—a fictitious non-shear-supporting rock devised by Essen for model validation purposes. To simulate such material, we first assigned realistic basalt values to the bottom inputs, and then modified the complex shear speed via $(\mathrm{Re}\, c_s, \mathrm{Im}\, c_s) \mapsto (\frac{1}{10}\mathrm{Re}\, c_s, 10\,\mathrm{Im}\, c_s)$ to squelch the elasticity. Alternatively, we could have re-expressed β in terms of the Lamé parameters λ, μ, and then let $\mu \rightarrow 0$. [Equation (4) is well behaved in that limit and the numerical results are, in fact, the same.]

Figure 10 presents the fluid basalt results from first-order perturbation theory [Eq. (30) with $\tilde{n} = 1$]. Two features are notable in it.

(1) The effect of raising γ_2 is to lower σ_n by an amount that

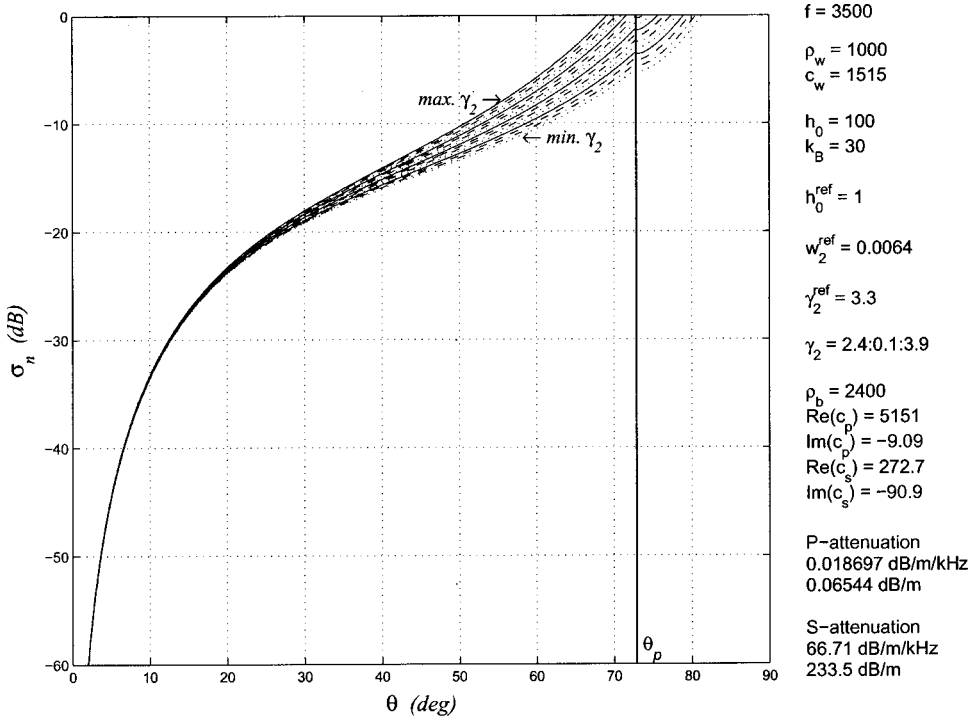

FIG. 15. PT/F case: perturbation-theory scattering strength versus grazing angle for fluid basalt specified in the sidebar on the right. Separate curves correspond to the different values of γ_2. This figure is the ''focused'' counterpart of Fig. 10.

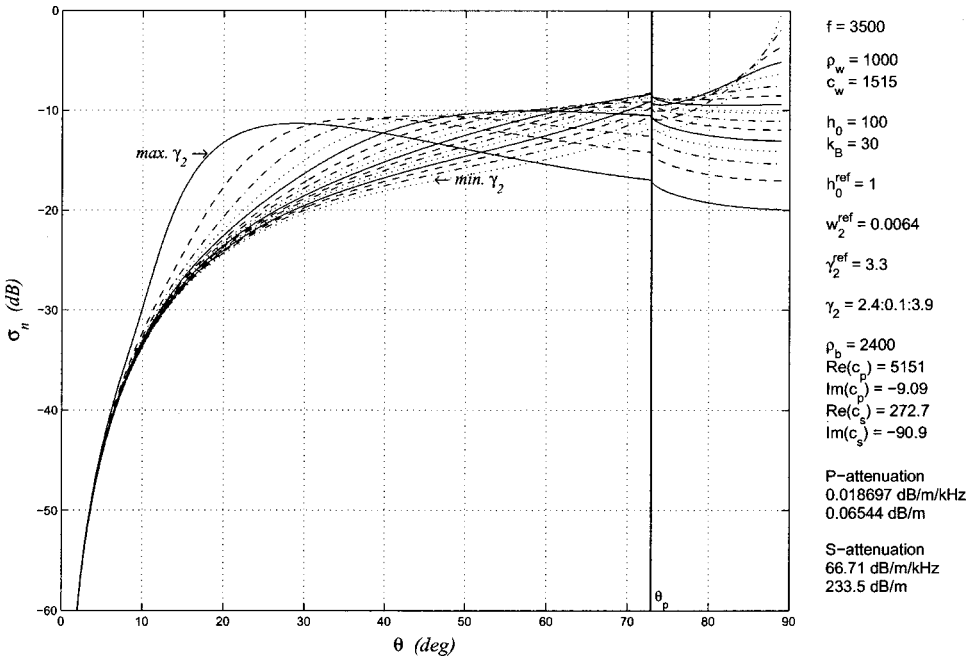

FIG. 16. The SS/F case: small-slope scattering strength versus grazing angle for the fluid basalt specified in the sidebar on the right. Separate curves correspond to the different values of γ_2. This figure is the "focused" counterpart of Fig. 11.

is independent of γ_2. This is to be expected since, in the PT approximation, $\sigma_n \propto Q^{-\gamma_2}$. Quantitatively, each increase of 0.1 in γ_2 ought to depress σ_n by $\log_{10} Q$ decibels. With $Q=2K_w \cos\theta$ for a monostatic geometry, this works out to a 1.4 dB drop at $\theta=30°$ (which agrees with the spread seen over the full γ_2 span of the figure: $1.4 \times 15 = 21$ decibels).

(2) The $\gamma_2=3.9$ curve is in good numerical agreement with Essen's corresponding curve [Ref. 5, Fig. 3(d), dashed curve], which was produced by a totally different algorithm. Our curve is 1–2 dB higher in the neighborhood of 30°, as it should because Essen's curve was computed for $\gamma_2=4$. [We avoid that value throughout this article because it produces $\alpha=\infty$, which our SS formulation does not handle properly (Appendix B).]

Figure 11 presents the corresponding results from small-slope theory. As in Fig. 5, these curves undergo a nearly complete reversal of order as the angle increases. There is agreement with Fig. 10 only for angles below a γ_2-dependent minimum. The best agreement seems to be the $\gamma_2=3.2$ curve, which remains very close to the corresponding perturbation theory curve out to $\theta \approx 40°$.

Figures 12 and 13 present the scattering results for realistic basalt for perturbation theory and small-slope theory, respectively. Here too, the "max. γ_2" curve in Fig. 12 agrees with Essen [Ref. 5, Fig. 3(d), solid curve]. The difference between perturbation and small-slope results is as great here as it was for the fluid basalt case. The results themselves are generally flatter for low angles and show additional features related to the presence of shear, notably a persistent narrow

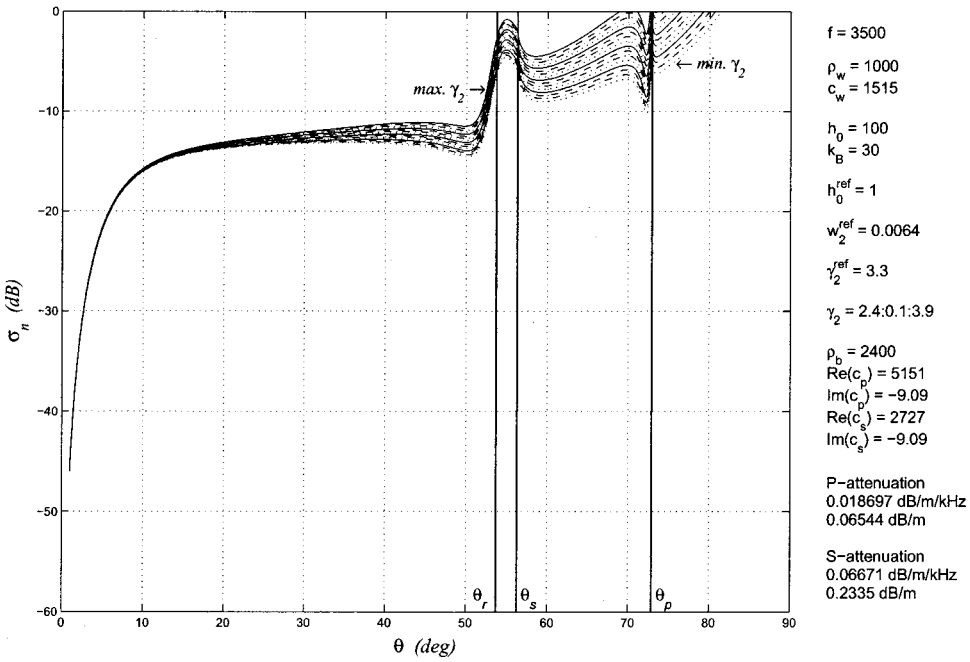

FIG. 17. The PT/E case: perturbation-theory scattering strength versus grazing angle for the realistic basalt specified in the sidebar on the right. Separate curves correspond to the different values of γ_2. This figure is the "focused" counterpart of Fig. 12.

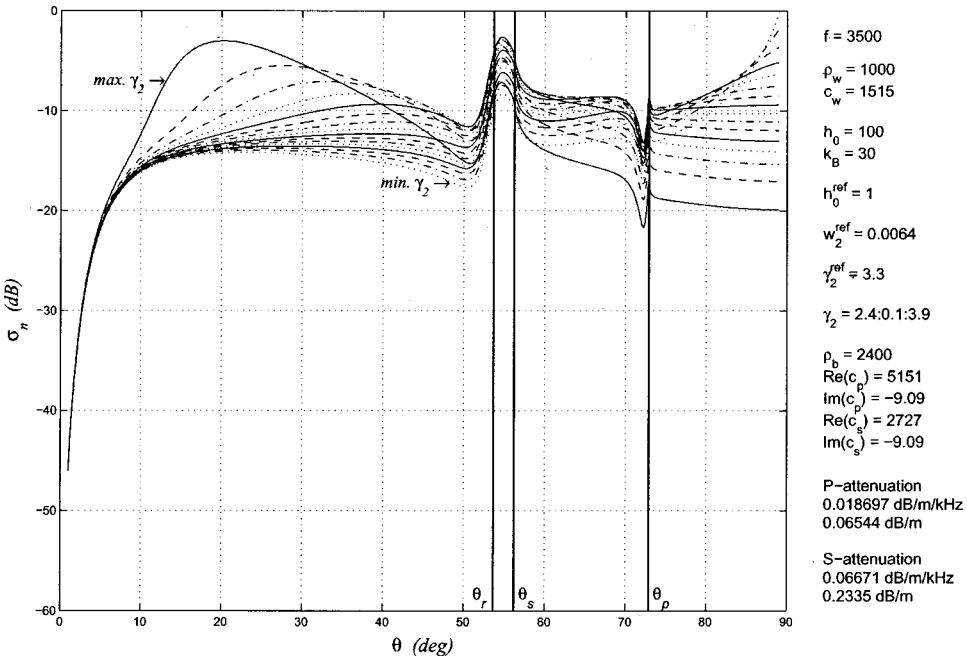

FIG. 18. The SS/E case: small-slope scattering strength versus grazing angle for the realistic basalt specified in the sidebar on the right. Separate curves correspond to the different values of γ_2. This figure is the "focused" counterpart of Fig. 13.

bump below θ_s. This occurs at the Rayleigh angle θ_r and thus appears to be related to the resonant excitation of a leaky Stoneley interface wave [Ref. 41, Sec. 5.4]. {θ_r is the location of a prominent maximum in $\partial\varphi/\partial\theta$, where φ is the phase of the reflection coefficient $R=|R|e^{i\varphi}$.[42] In terms of the function $a(\vec{k})$ in Eq. (3a), $R(\theta)=[a(\vec{k})-1)/(a(\vec{k})+1]$.}

Figure 14 summarizes the results of these SS vs PT and F vs E tests. In the top panel, one can see that SS differs from PT, where θ is not small. This is especially notable for large γ_2, as would be expected from the discussion of Fig. 1 in the Introduction. The agreement of SS and PT improves with decreasing γ_2, but only up to a point. Below $\gamma_2 \approx 3.3$ (heavy curve) it worsens again, which seems counterintuitive.

Evidently the discussion in the Introduction fails to fully explain Figs. 10–14 because these figures simply vary γ_2 while holding everything else fixed, and that is *not* the situation depicted in Fig. 1. In that figure, every γ_2 value "focuses" on the same surface ripple; i.e., there is a Bragg wave number k_B (the ripple) for which $S(k_B)$ remains the same regardless of γ_2. Figures 15–19 are "focused" in that spirit. For them, reference values for h_0^{ref}, γ_2^{ref}, w_2^{ref} and physical values of h_0, k_B are chosen first. Thereafter, whenever γ_2 is varied, the value of w_2 is readjusted to ensure that $w_2/(h_0 k_B)^{-\gamma_2}$ remains equal to $w_2^{\text{ref}}/(h_0^{\text{ref}} k_B)^{-\gamma_2^{\text{ref}}}$. We use $k_B=30$ (the approximate Bragg wave number for $f=3500$ and small θ) and $h_0=100$ (so that $h_0^{-1} \ll k_B$). The reference values are $h_0^{\text{ref}}=1$, $\gamma_2^{\text{ref}}=3.3$, and $w_2^{\text{ref}}=0.0064$ (corresponding to the heavy lines in Figs. 10–14). The results for these simulations are understandable in terms of the discussion accompanying Fig. 1. The curves in Figs. 15–18 all coalesce

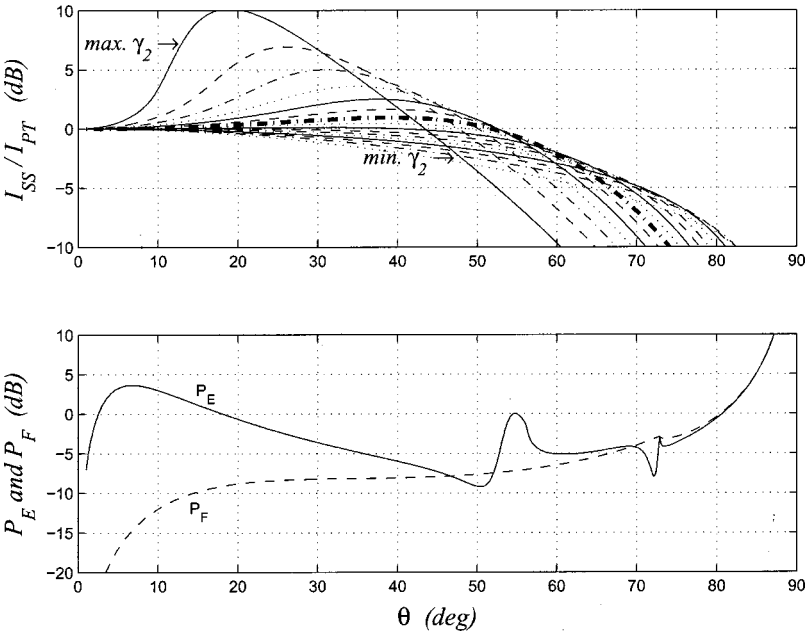

FIG. 19. A comparison among Figs. 15–18. Top: the ratio of I_{PT} to I_{SS} in decibels. Bottom: P_{E} and P_{F} in decibels. This figure is the "focused" counterpart of Fig. 14. The bottom panel is unchanged because "focusing" affects only the I factor.

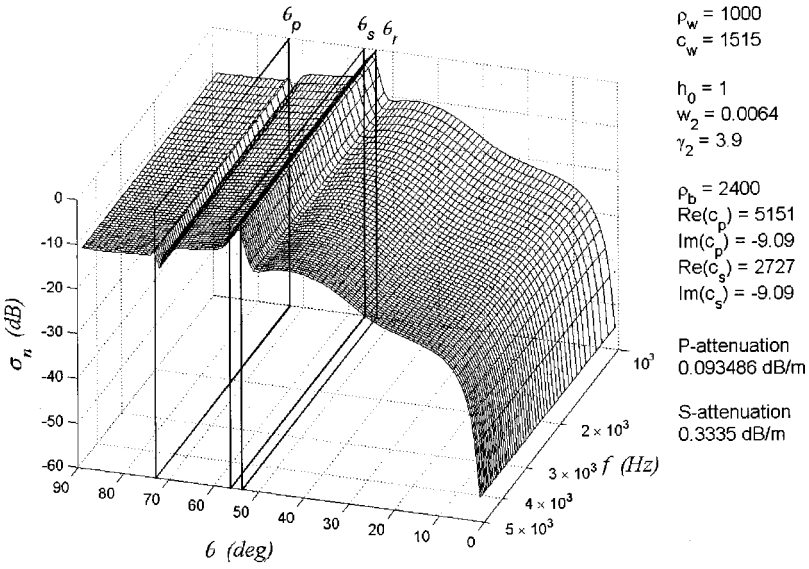

FIG. 20. Small-slope scattering strength versus grazing angle and frequency for the basalt specified in the sidebar on the right. Planes corresponding to $\theta_{\text{out}} = \theta_s, \theta_p, \theta_r$ are also indicated.

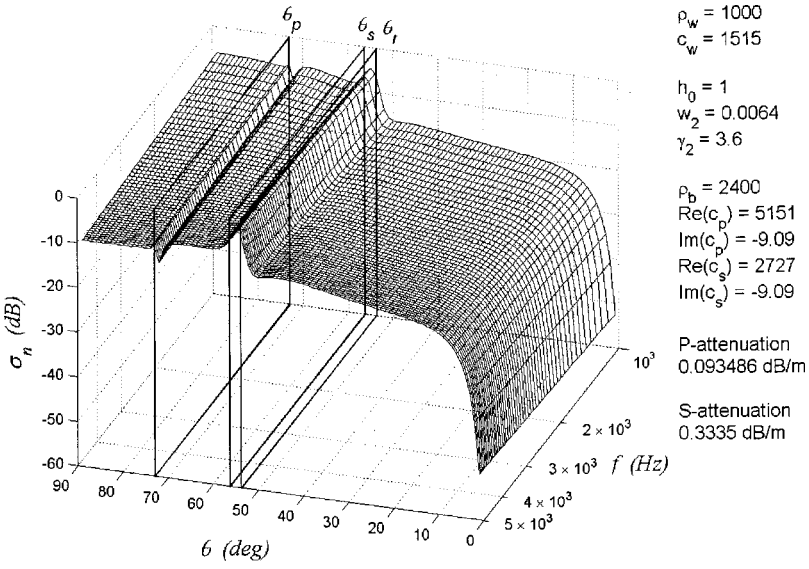

FIG. 21. Small-slope scattering strength versus grazing angle and frequency for the basalt specified in the sidebar on the right. Planes corresponding to $\theta_{\text{out}} = \theta_s, \theta_p, \theta_r$ are also indicated.

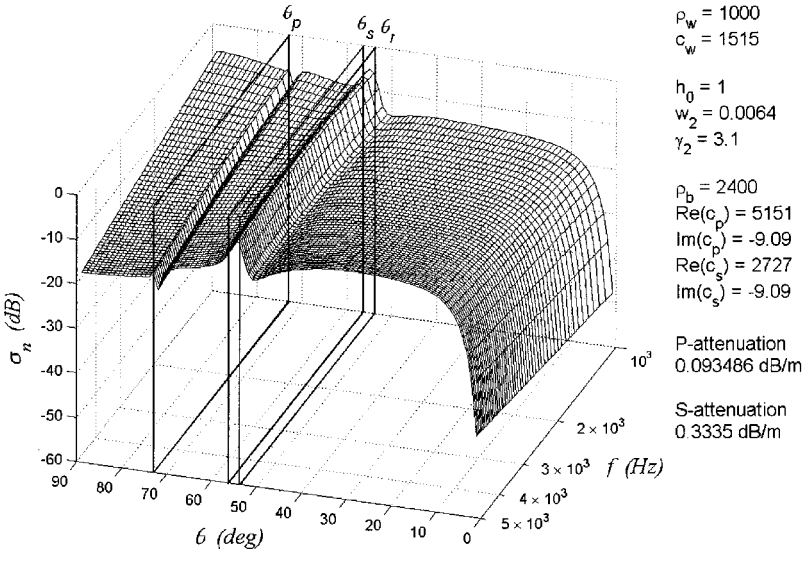

FIG. 22. Small-slope scattering strength versus grazing angle and frequency for the basalt specified in the sidebar on the right. Planes corresponding to $\theta_{\text{out}} = \theta_s, \theta_p, \theta_r$ are also indicated.

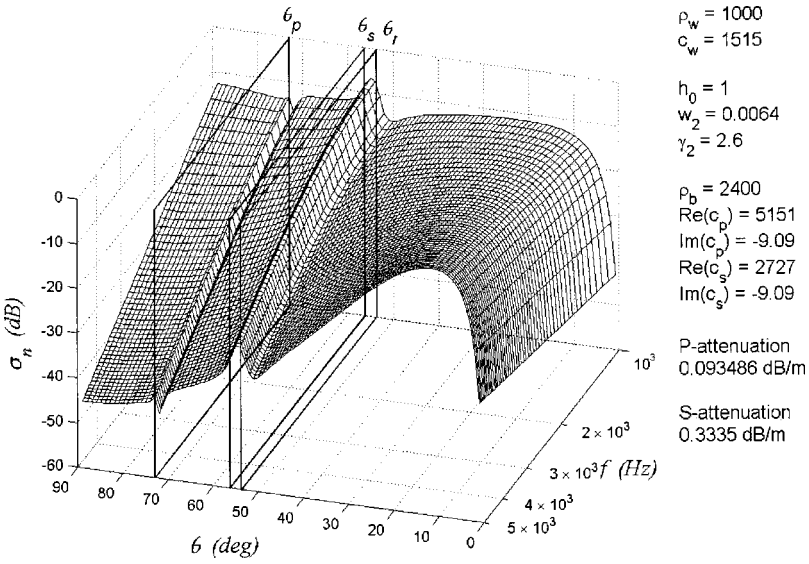

FIG. 23. Small-slope scattering strength versus grazing angle and frequency for the basalt specified in the sidebar on the right. Planes corresponding to $\theta_{\text{out}}=\theta_s,\theta_p,\theta_r$ are also indicated.

properly as $\theta\to 0$, which was not the case with Figs. 10–13. And the top panel of Fig. 19 indicates that, as γ_2 increases, PTs validity is uniformly restricted to smaller and smaller θ, which was not the case with Fig. 14. Note that at $\gamma_2=3.9$, PT is off by 3 dB, even at 10°, which is even worse than suggested by Fig. 14.

2. Frequency

We turn now to the frequency dependence of the scattering strength, restricting our attention to the SS case because the frequency dependence of PT is well known: $\sigma_n^{\text{PT}}\propto f^{4-\gamma_2}$. As with σ_n^{PT}, the frequency dependence of σ_n^{SS} disappears completely as γ_2 approaches 4 (because I depends on f only through $\alpha\propto f^{4-\gamma_2}$). For $\gamma_2<4$, however, I's frequency dependence is complicated *except* in the limits of near-grazing and near-normal incidence. For near-grazing incidence, $I\propto\alpha^1$ [the first term of Eq. (30)] while for near-normal incidence, $I\propto\alpha^{-1/\nu}$ [the first term of Eq. (C1)]. Thus, in these extremes, $\sigma_n\propto f^{\mu}$ with

$$\mu=\begin{cases}4-\gamma_2, & \text{for } \theta\approx 0°,\\ -2\dfrac{4-\gamma_2}{\gamma_2-2}, & \text{for } \theta\approx 90°,\end{cases}\tag{37}$$

and one expects the scattering strength to change by 3μ decibels per octave.

Figures 20, 21, 22, and 23 show SS scattering results from a basalt bottom with $\gamma_2=3.9$, 3.6, 3.1, and 2.6 throughout the frequency band 1 kHz$\leqslant f\leqslant$5 kHz. According to Eq. (37), the total change across this band should be $\Delta\sigma_n\approx 7\mu$ dB at the extreme grazing angles. (See Table III.) As expected, Fig. 20 with $\gamma_2=3.9$ is virtually independent of frequency: as f sweeps up through the band, σ_n rises (falls) by less than a decibel for small (large) grazing angles. In fact, γ_2 is so close to 4 that there is negligible frequency dependence at *any* angle. In Fig. 21, where $\gamma_2=3.6$, there is a shift of $\Delta\sigma_n\approx\pm 3$ dB at the extreme θ values. The overall frequency dependence brought on by this lowering of the spectral exponent is similar to what might be produced if the viewer were able to seize the left and right edges of the Fig. 20 surface in each hand and rotate them slightly in opposite senses. The twist imparted to the surface is only a small one, so the scattering strength acquires little frequency dependence overall. A stronger dependence begins to emerge with $\gamma_2=3.1$ in Fig. 22. There, $\Delta\sigma_n\approx -10$ dB for $\theta>\theta_p$. $\Delta\sigma_n\approx 6$ dB for $\theta\approx 0°$; however, for most subcritical angles $\theta<\theta_s$, the effect is substantially less. Finally, when the spectral exponent is reduced to $\gamma_2=2.6$ in Fig. 23, $\Delta\sigma_n$ rises by 10 dB at $\theta\approx 0°$ and falls by 30 dB at $\theta\approx 90°$. That much counter-rotation of the edges of the surface would seem likely to give a significant warp to most of its interior. And, indeed, that is the case. The scattering strength does, in fact, exhibit a significant frequency dependence for most grazing angles.

B. Bistatic

Here we examine bistatic simulations of the PT and SS formulations of σ_n, once again in the context of the basalt bottom. Owing to the vagaries of our plotting software, the PT plots all had to be truncated in the vicinity of the specular direction where they really ought to diverge. We fix θ_{in} and ϕ_{in} at representative values of 30° and 100° for all of the simulations. Figures 24 and 25 are the PT and SS results for $\gamma_2=3.9$. They both exhibit the same features, where θ_{out} is near θ_p, θ_s, or θ_r, and are qualitatively similar, except in near-specular geometries, $(\theta_{\text{out}},\phi_{\text{out}})\approx(\theta_{\text{in}},\phi_{\text{in}})$. Quantitatively, however, they are significantly different, as Fig. 26 illustrates. The quantity plotted in that figure is $\sigma_n^{\text{PT}}/\sigma_n^{\text{SS}}$. Since this is equal to $I_{\text{PT}}/I_{\text{SS}}$, the bottom material properties have no impact, so we have omitted the references to critical angles. It is clear here that even for nonspecular geometries, there is generally a significant difference (typically about 7

TABLE III. Exponent μ and the resulting $\Delta\sigma_n$.

	For $\theta\approx 0°$					For $\theta\approx 90°$			
γ_2	3.9	3.6	3.1	2.6	γ_2	3.9	3.6	3.1	2.6
μ	0.1	0.4	0.9	1.4	μ	−0.1	−0.5	−1.6	−4.7
$\Delta\sigma_n$	0.7	2.8	6.3	9.8	$\Delta\sigma_n$	−0.7	−3.5	−11.5	−32.7

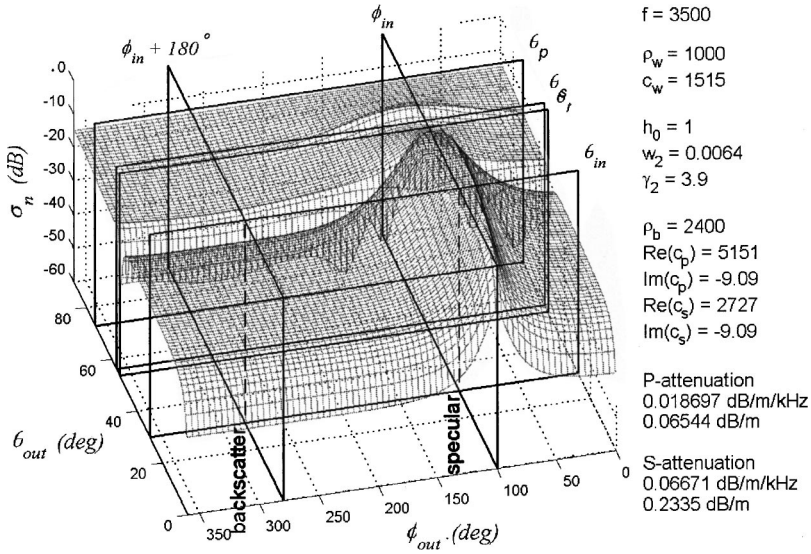

FIG. 24. Perturbation-theory scattering strength versus bistatic scattering angles for the basalt specified in the sidebar on the right. Planes corresponding to $\theta_{\text{out}} = \theta_s, \theta_p, \theta_r, \theta_{\text{in}}$ and $\phi_{\text{out}} = \phi_{\text{in}}, \phi_{\text{in}} + 180°$ are indicated. The specular divergence is artificially truncated at 0 dB.

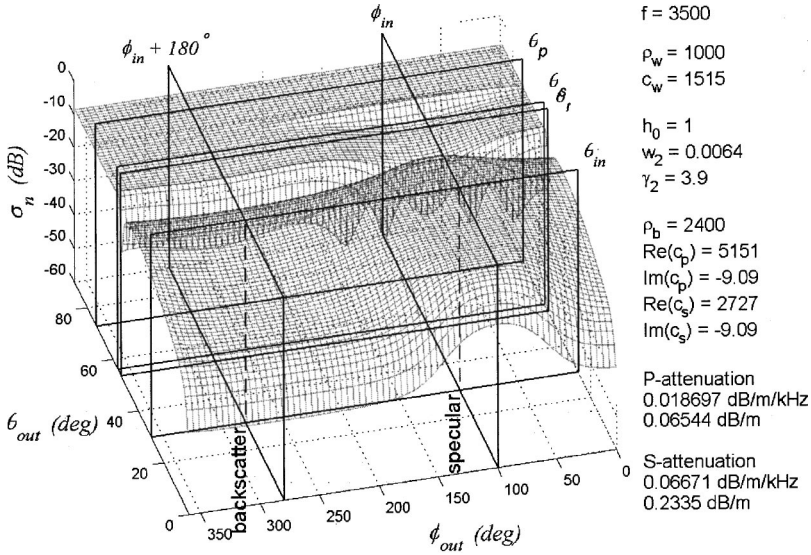

FIG. 25. Small-slope scattering strength versus bistatic scattering angles for the basalt specified in the sidebar on the right. Planes corresponding to $\theta_{\text{out}} = \theta_s, \theta_p, \theta_r, \theta_{\text{in}}$ and $\phi_{\text{out}} = \phi_{\text{in}}, \phi_{\text{in}} + 180°$ are indicated.

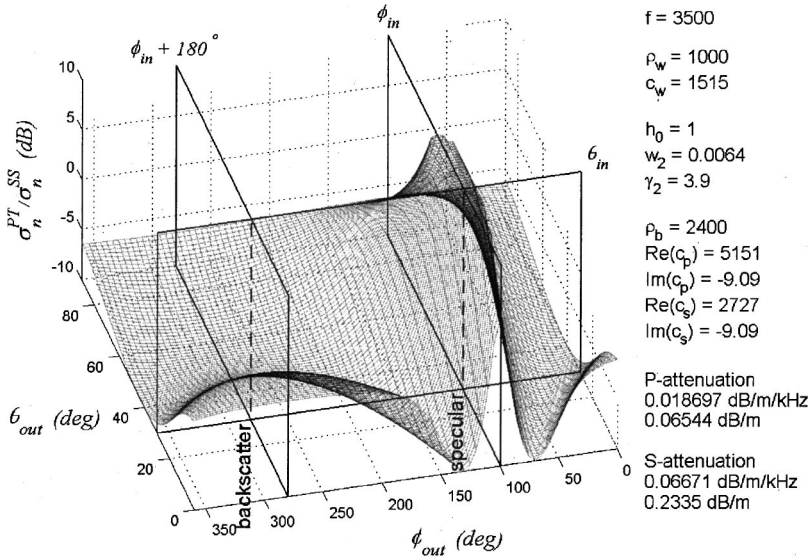

FIG. 26. $\sigma_n^{\text{PT}}/\sigma_n^{\text{SS}}$ versus bistatic scattering angles for the basalt specified in the sidebar on the right. Planes corresponding to $\theta_{\text{out}} = \theta_{\text{in}}$ and $\phi_{\text{out}} = \phi_{\text{in}}, \phi_{\text{in}} + 180°$ are indicated. The specular divergence is artificially truncated at 10 dB.

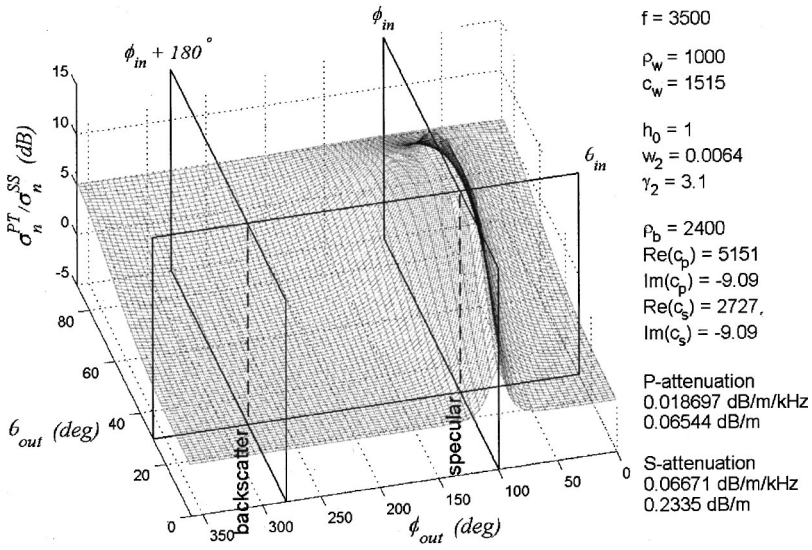

FIG. 27. $\sigma_n^{PT}/\sigma_n^{SS}$ versus bistatic scattering angles for the basalt specified in the sidebar on the right. Planes corresponding to $\theta_{out}=\theta_{in}$ and $\phi_{out}=\phi_{in},\phi_{in}+180°$ are indicated. The specular divergence is artificially truncated at 15 dB.

dB, and up to 10 dB in some directions). Figures 27 and 28 repeat this bistatic PT vs SS comparison for $\gamma_2=3.1$ and $\gamma_2=2.6$, respectively. For $\gamma_2=3.1$, there is very good agreement between PT and SS for nonspecular geometries with θ_{out} below about 50°. For $\gamma_2=2.6$, the comparison is rather poor even at low θ_{out} and much worse (more than 25 dB off) for high θ_{out}.

Figures 24–28 all use $\theta_{in}=30°$. Further investigation shows that, as this angle is varied, the small-slope scattering strength displays a marked sensitivity in the range $\theta_{in}\approx\theta_r\pm1°$. (The interval is narrow, but definitely excludes θ_s.) We attribute this behavior to the strong resonant excitation of a Stoneley interface wave. However, since Berman's numerical experiments have indicated possible problems with small-slope's accuracy in this case,[13] we have decided not to publish figures illustrating the effect until the matter is resolved.

V. SUMMARY AND CONCLUSIONS

We have presented a model for the nonspecular small-slope scattering strength of elastic sea floors as a function of frequency, bistatic geometry, geoacoustic descriptors, and interface roughness parameters. Our unified formulation for the scattering integral has allowed us to extend the capability for small-slope modeling over a wide range of spectral exponents, $2.4\leqslant\gamma_2\leqslant3.9$. We have examined the details of our model's performance through computations for a rough limestone bottom, and have validated its predictions through comparisons with existing perturbative results for both normal basalt and ''fluid basalt'' bottoms. Results indicate that the model should be able to correctly and accurately simulate the interface component of the scattering strength from essentially any ocean bottom of practical interest.

Our numerical simulations confirm that small-slope (SS) theory really does provide the kind of improvement over first-order perturbation theory (PT) that a back-of-the-envelope analysis suggests—for both fluid and elastic sea floors. For monostatic scattering geometries, we find that (a) at a given frequency, SS is superior to PT for large grazing angles and/or large spectral exponents, and (b) for smaller spectral exponents, the SS scattering strength develops a pronounced frequency dependence away from grazing inci-

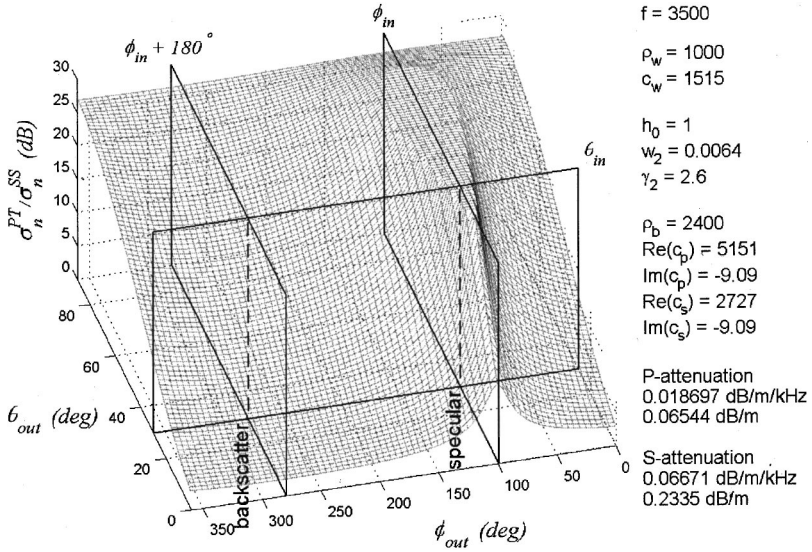

FIG. 28. $\sigma_n^{PT}/\sigma_n^{SS}$ versus bistatic scattering angles for the basalt specified in the sidebar on the right. Planes corresponding to $\theta_{out}=\theta_{in}$ and $\phi_{out}=\phi_{in},\phi_{in}+180°$ are indicated. The specular divergence is artificially truncated at 30 dB.

dence. Bistatic simulations indicate that PT is adequate for moderate values of γ_2 ($\sim$3, e.g., many sandy bottoms[31]), except for in-plane scattering cases and large grazing angles. However, SS should generally be used in other cases—especially with γ_2 values that are either large ($\sim$3.9, e.g., some basalt bottoms[5]) or small ($\sim$2.6, e.g., basalt on the slopes of the mid-Atlantic ridge[28]).

With one essential caveat, our investigation could have been be extended to cover scattering from the sea surface [γ_2 from 3.4 to 4.0 (Ref. 43)] by simply invoking the well-known limiting form of β for pressure-release boundary conditions. The caveat is that regimes in which the dominant-wave peak of the surface power spectrum is near the Bragg region must be avoided. Although small-slope theory still applies there, a different approach is required for calculating the scattering integral when the spectral peak is involved.[9,20]

We conclude that, in view of the results presented here, the modeling community would be justified in adopting SS techniques as a wholesale replacement for PT methods. For accurate scattering simulations for bottoms with known geoacoustic and roughness parameters, SS should certainly be used. Compared to PT, it is usually better and, at worst, equivalent. And with the developments reported here, it is no more trouble to use. For poorly known bottoms, using SS rather than PT could prevent attributing experimentally observed effects to the wrong physical causes (e.g., mistaking interface effects for sediment volume effects).

We note in closing that we have a program of model/data tests in progress using both laboratory and at-sea experimental data. Early results have already appeared,[28,29,40,4] and the remainder are planned for the near future.

ACKNOWLEDGMENTS

This work was supported by the Office of Naval Research. The authors are grateful for continuing technical discussions with Dr. David M. Drumheller (NRL) on the subject of rational-function approximations.

APPENDIX A: INTERFACE SPECTRA

In this appendix we review the various definitions of interface spectrum in popular use and examine the mean-square values of the roughness and slope of the interface—particularly the conditions for their convergence or divergence. The notation differs somewhat from that in the body of the article.

We suppose that the interface roughness $h(\mathbf{r})$ is not only single valued but also differentiable and Fourier transformable over the reference plane [i.e., that $\mathbf{g}(\mathbf{r})=\partial h(\mathbf{r})/\partial \mathbf{r}$ and $\xi(\mathbf{k})=(2\pi)^{-2}\int h(\mathbf{r})e^{+i\mathbf{k}\cdot\mathbf{r}}\mathrm{d}^2\mathbf{r}$ make sense]. Since the two-point correlation is

$$C(\mathbf{x}-\mathbf{y})=\langle h(\mathbf{x})h(\mathbf{y})\rangle=\int e^{-i\mathbf{k}\cdot(\mathbf{x}-\mathbf{y})}S(\mathbf{k})\mathrm{d}^2\mathbf{k}, \tag{A1}$$

its second derivative is

$$\frac{\partial}{\partial \mathbf{x}}\cdot\frac{\partial}{\partial \mathbf{y}}C(\mathbf{x}-\mathbf{y})=\langle \mathbf{g}(\mathbf{x})\cdot\mathbf{g}(\mathbf{y})\rangle = \int e^{-i\mathbf{k}\cdot(\mathbf{x}-\mathbf{y})}S(\mathbf{k})\mathbf{k}\cdot\mathbf{k}\,\mathrm{d}^2\mathbf{k}. \tag{A2}$$

Thus, the mean-square values of the roughness and its gradient are

$$h_{\mathrm{rms}}^2=\lim_{\mathbf{y}\to\mathbf{x}}\langle h(\mathbf{x})h(\mathbf{y})\rangle=\int S(\mathbf{k})\mathrm{d}^2\mathbf{k}, \tag{A3}$$

$$g_{\mathrm{rms}}^2=\lim_{\mathbf{y}\to\mathbf{x}}\langle \mathbf{g}(\mathbf{x})\cdot\mathbf{g}(\mathbf{y})\rangle=\int S(\mathbf{k})|\mathbf{k}|^2\,\mathrm{d}^2\mathbf{k}. \tag{A4}$$

Roughness spectra are defined in a variety of ways with a considerable overlap of notation and nomenclature. We do the following. In rectangular coordinates $\mathbf{k}=(k_x,k_y)$, we write $S(\mathbf{k})=R(k_x,k_y)$, so that

$$h_{\mathrm{rms}}^2=\int\int_{-\infty}^{+\infty}R(k_x,k_y)\mathrm{d}k_x\mathrm{d}k_y=\int_{-\infty}^{+\infty}\varrho(k_x)\mathrm{d}k_x, \tag{A5}$$

where

$$\varrho(k_x)=\int_{-\infty}^{+\infty}R(k_x,k_y)\mathrm{d}k_y \tag{A6}$$

is the reduced 1-D spectrum. Similarly, in polar coordinates $\mathbf{k}=(k,\theta)$ we write $S(\mathbf{k})=P(k,\theta)$, so that

$$h_{\mathrm{rms}}^2=\int_0^{\infty}\int_0^{2\pi}P(k,\theta)\mathrm{d}k\,\mathrm{d}\theta=\int_0^{\infty}\varpi(k)\mathrm{d}k, \tag{A7}$$

in terms of the reduced 1-D spectrum,

$$\varpi(k)=\int_0^{2\pi}P(k,\theta)\mathrm{d}\theta. \tag{A8}$$

The essential symmetry $S^*(\mathbf{k})=S(-\mathbf{k})$ manifests itself as $P^*(k,\theta)=P(k,\theta+\pi)$, $\varpi^*(k)=\varpi(k)$, $R^*(k_x,k_y)=R(-k_x,-k_y)$, and $\varrho^*(k_x)=\varrho(-k_x)$. [Sometimes, in a practice carried over from time-series analysis, the symmetry of $\varrho(k_x)$ is exploited to ''fold it over'' into a spectrum that vanishes for negative k_x and has a doubled value for positive k_x. We refrain from doing this with spatial spectra, basically because left and right do not differ in the same fundamental way that past and future do.] The 1-D polar form $\varpi(k)$ is sometimes known as a ''scalar wave number spectrum.'' The 1-D rectangular form $\varrho(k_x)$ is often useful in analyzing experimental data (e.g., bottom relief data, which are usually taken along 1-D tracks[28,31]).

We indicate the physical dimensions of quantities using ''$\doteqdot$'' and powers of the basic mass, length, and time symbols M, L, and T (mainly as a way of keeping the lengths straight). Taking energy as an example, $E\doteqdot ML^2T^{-2}$. For the variables of principal interest here, $\mathbf{k}\doteqdot L^{-1}$; $\mathbf{r}$, $h\doteqdot L$; $C\doteqdot L^2$; $\xi\doteqdot L^3$; and $S\doteqdot L^4$. The physical dimensions of the four distributions above are $R\doteqdot L^4$ and ϱ, P, $\varpi\doteqdot L^3$.

In the *isotropic* case, $S(\mathbf{k})$ depends on $\mathbf{k}$'s magnitude k but not its direction θ. This is often a good approximation and, as a simplifying step in theoretical developments, it is almost universal. As a result,

$$\varpi(k)=2\pi kP(k,\cdot),\quad \text{for } 0<k<\infty, \tag{A9}$$

which is what Essen[5] calls $G(k)$. In the body of this article, $P(k,\cdot)$ is denoted $S(k)$. Because of the isotropic symmetry, the full 2-D description is recoverable from a reduced 1-D description,

$$\varrho(k_x)=\frac{1}{\pi}\int_{|k_x|}^{\infty}\frac{1}{\sqrt{k^2-k_x^2}}P(k,\cdot)\,\mathrm{d}k,\quad \text{for } -\infty<k_x<+\infty, \tag{A10}$$

$$P(k,\cdot)=-2\int_{k}^{\infty}\frac{k}{\sqrt{k_x^2-k^2}}\frac{\mathrm{d}\varrho(k_x)}{\mathrm{d}k_x}\mathrm{d}k_x,\quad \text{for } 0<k<\infty. \tag{A11}$$

Those two equations constitute a one-to-one mapping between $\varrho(k_x)$ and $P(k,\cdot)$ (an Abel transform pair, in fact[45]). More general results can be found for the nonisotropic case,[45] though they are of very limited utility.

When the roughness spectrum has the *power-law* form,

$$S(\mathbf{k})=\frac{w_2}{(h_0|\mathbf{k}|)^{\gamma_2}},\quad \text{for } 0<|\mathbf{k}|<\infty, \tag{A12}$$

with h_0, w_2, and γ_2 as described in the body, the mean-square roughness and slope are $h_{\mathrm{rms}}^2=2\pi w_2 h_0^{-2}\int_0^{\infty}\kappa^{1-\gamma_2}\,\mathrm{d}\kappa$, and $g_{\mathrm{rms}}^2=2\pi w_2 h_0^{-4}\int_0^{\infty}\kappa^{3-\gamma_2}\,\mathrm{d}\kappa$, in which the integration variable is the dimensionless wave number $\kappa=h_0k$. Regardless of the value of γ_2, both integrals diverge. This is not really surprising for a fractal surface, though it is instructive to consider why it occurs. With $b>a$,

$$\int_a^b\kappa^p\,\mathrm{d}\kappa=\left\{\begin{array}{l}\dfrac{b^{|p+1|}-a^{|p+1|}}{|p+1|},\quad \text{for } p>-1\\ \log b/a,\quad \text{for } p=-1\\ \dfrac{a^{-|p+1|}-b^{-|p+1|}}{|p+1|},\quad \text{for } p<-1\end{array}\right\}>0. \tag{A13}$$

Thus $\int_0^{\infty}\kappa^p\,\mathrm{d}\kappa$ always diverges, but one can now see how that comes about. For $p\geqslant -1$, the divergence is due to the behavior of the integrand at $\kappa=\infty$; for $p\leqslant -1$, it is due to the behavior at $\kappa=0$.

For the pure power-law spectrum, h_{rms}^2 is always infinite. When $\gamma_2\leqslant 2$, this is because the spectrum obeys a power law for $h_0k\gg 1$ (i.e., $\lambda\ll h_0$); when $\gamma_2\geqslant 2$, it is due to the spectrum's power-law form for $h_0k\ll 1$ (i.e., $\lambda\gg h_0$). g_{rms}^2 is always infinite too. For $\gamma_2<4$ this is attributable to the power-law form of the spectrum where $h_0k\gg 1$ (i.e., $\lambda\ll h_0$); for $\gamma_2>4$ it comes from the power-law form, where $h_0k\ll 1$ (i.e., $\lambda\gg h_0$). The basic reason for adopting the range $2<\gamma_2<4$ is to guarantee that the divergence of h_{rms}^2 comes from the small-k end of the spectrum, while g_{rms}^2 diverges due to the large-k end. Then, when a small-k cutoff is installed to give the surface a physically satisfying, finite, mean-square roughness, it still retains the fractal-like characteristic of having a divergent mean-square slope.

The infinite values of these moments have no operational significance because they are a result of taking Eq. (A.12) at face value at $k=0$ and $k=\infty$ (i.e., at $\lambda=\infty$ and $\lambda=0$), despite the fact that spectrum is only meant to be taken seriously in a *finite* interval, $0<k_{\min}\leqslant k\leqslant k_{\max}<\infty$. As Jackson put it,[46,47] "Using a fractal model with a power-law relief spectrum is one way of acknowledging that the bottom relief possesses scales (namely, $0<k<k_{\min}$ and $k_{\max}<k<\infty$) that are outside the range of interest of the acoustic model." Specifically, for $\gamma_2>2$, the $|\mathbf{k}|^{-\gamma_2}$ dependence could not possibly persist indefinitely as $|\mathbf{k}|\to 0$. If it did, then roughness components with progressively longer wavelengths would make progressively larger contributions to h_{rms}, ultimately producing $h_{\mathrm{rms}}=\infty$, which is the opposite of what actually occurs. Any real-world spectrum will have a cutoff, $k_{\min}$, below which the power-law form $S(\mathbf{k})\propto|\mathbf{k}|^{-\gamma_2}$ ceases to apply. Since we are only concerned with *Bragg scattering* here, our essential assumption is that $k_{\min}$ is well below the Bragg wave number k_{B}.

For the idealized spectrum, Eq. (A12), the polar 1-D distribution is

$$\varpi(k)=\frac{2\pi}{h_0}\frac{w_2}{(h_0k)^{\gamma_2-1}},\quad \text{for } 0<k<\infty. \tag{A14}$$

The rectangular 1-D distribution Eq. (A10) is

$$\varrho(k_x)=\frac{w_2}{h_0^{\gamma_2}}\frac{\sqrt{\pi}}{|k_x|^{\gamma_2-1}}\times\frac{\Gamma[\frac{1}{2}(\gamma_2-1)]}{\Gamma(\frac{1}{2}\gamma_2)},\quad \text{for } -\infty<k_x<+\infty. \tag{A15}$$

This has the same functional form as the full 2-D spectrum, Eq. (A12),[46,47] namely

$$\varrho(k_x)=\frac{w_1}{(h_0|k_x|)^{\gamma_1}},\quad \text{for } -\infty<k_x<+\infty, \tag{A16}$$

where

$$\gamma_1=\gamma_2-1, \tag{A17}$$

$$w_1=\frac{\sqrt{\pi}}{h_0}\frac{\Gamma(\frac{1}{2}\gamma_1)}{\Gamma(\frac{1}{2}\gamma_2)}w_2\doteqdot L^3. \tag{A18}$$

This $\varrho(k_x)$ spectrum indicates a surface with a Lipschitz exponent $\nu=(\gamma_1-1)/2$ [meaning that $|h(x+\Delta)-h(x)|\sim\Delta^{\nu}$ for small Δ], which corresponds to the fractal dimension $D=2-\nu$.[30] Thus, the range $2<\gamma_2<4$ corresponds to $1<D<2$.

APPENDIX B: ANALYTIC $I(\alpha,\nu)$

In this appendix we deal with a closed-form analytic evaluation of the scattering integral $I(\alpha,\nu)$.

There is a closed form in only one case, $\nu=\frac{1}{2}$ (i.e., $\gamma_2=3$). In this instance, Eqs. (26) and (27a), respectively, become

$$\alpha=\frac{a}{Qr}=Q_z^2\frac{w_2}{h_0^2}\times\frac{2\pi}{h_0Q}, \tag{B1a}$$

$$I\left(\alpha,\frac{1}{2}\right)=\int_0^{\infty}J_0(y)ye^{-\alpha y}\,\mathrm{d}y=\frac{\alpha}{(1+\alpha^2)^{3/2}}. \tag{B1b}$$

When the backscatter form of $\vec{Q}$ is invoked, Eq. (26) becomes

$$\alpha = \frac{w_2}{h_0^4} \times \frac{\pi \Gamma(1-\nu)}{\nu \Gamma(1+\nu)} \times \frac{(2h_0 K_w \sin\theta)^2}{(4h_0 K_w \cos\theta)^{2\nu}}. \tag{B2}$$

For $\nu = \frac{1}{2}$, this becomes

$$\alpha = \underbrace{4\pi \frac{w_2 K_w}{h_0^3}}_{\alpha_0} \sin\theta \tan\theta, \tag{B3}$$

so that Eq. (B1b) reduces to

$$I = \frac{\alpha_0 \sin^2\theta \cos^2\theta}{(\cos^2\theta + \alpha_0^2 \sin^4\theta)^{3/2}}. \tag{B4}$$

The maximum I value, $2\sqrt{2}/9 \approx 0.385$, occurs where $\alpha_0 = \cos\theta/\sqrt{2}\sin^2\theta$.

The $\nu = 1$ (i.e., $\gamma_2 = 4$) case *appears* to have a closed-form solution too:

$$I(\alpha,1) = \int_0^\infty J_0(y) y e^{-\alpha y^2} \, dy = \frac{e^{-1/4\alpha}}{2\alpha}. \tag{B5}$$

But $\alpha \propto \Gamma(1-\nu)$, so that in the $\nu \to 1$ limit, we have $\alpha \to \infty$ and $I(\alpha,\nu) \to 0$.

APPENDIX C: LARGE $-\alpha$ SERIES

In this appendix we develop a large-α series representation for Eq. (27a).

The Bessel series, $J_0(y) = \Sigma_{n=0}^\infty (-1)^n (2^n n!)^{-2} y^{2n}$ readily yields $I = \Sigma_{n=1}^\infty (-1)^{n+1} M_n$; where $M_n = (2/\nu) \times [2^n \Gamma(n)]^{-2} \Gamma(n/\nu)/\alpha^{n/\nu} > 0$. (The α, ν arguments of I and M_n are left implicit.) This alternating series is convergent for $\nu > \frac{1}{2}$, and thus, for n large enough that M_n decreases monotonically with increasing n, the error incurred in truncating it after $n = \hat{n}$ is bounded in magnitude by $M_{\hat{n}}$. This provides a way to determine, for given α and ν, how many terms are required to achieve a predetermined accuracy. We find that for $\nu > \frac{1}{2}$,

$$I(\alpha,\nu) = \frac{2}{\nu} \sum_{n=1}^{\hat{n}} (-1)^{n+1} [2^n \Gamma(n)]^{-2} \frac{\Gamma(n/\nu)}{\alpha^{n/\nu}}, \quad \text{for } \hat{\alpha} < \alpha, \tag{C1}$$

with $\hat{n}$ and $\hat{\alpha}$ taken from Table IV, achieves three-figure accuracy. For backscattering geometries, α increases with θ, so Eq. (C1) applies at larger grazing angles. In earlier efforts[28] this series was exploited to provide the large-α part of the unified formulation. It has been supplanted in that role by the rational-function technique, which never requires summing large numbers of terms.

TABLE IV. $\hat{\alpha}$ and $\hat{n}$ for $3 < \gamma_2 < 4$.

γ_2	3.1	3.2	3.3	3.4	3.5	3.6	3.7	3.8	3.9
$\hat{\alpha}$	0.39	0.25	0.20	0.15	0.12	0.08	0.05	0.03	0.025
$\hat{n}$	6545	610	155	93	62	60	62	67	54

[1] D. R. Jackson and I. Ivakin, "Scattering from elastic sea-beds: First-order theory," J. Acoust. Soc. Am. **103**, 336–345 (1998).
[2] I. Ivakin and D. R. Jackson, "Effects of shear elasticity on sea bed scattering: Numerical examples," J. Acoust. Soc. Am. **103**, 336–345 (1998).
[3] P. D. Mourad and D. R. Jackson, "A model/data comparison for low-frequency bottom backscatter," J. Acoust. Soc. Am. **94**, 344–358 (1993).
[4] M. D. Max, "Gas hydrates and acoustically laminated sediments: Potential environmental cause of anomalously low acoustic bottom loss in deep-ocean sediments," Naval Research Laboratory Report 9235, February 1990.
[5] H.-H. Essen, "Scattering from a rough sedimental seafloor containing shear and layering," J. Acoust. Soc. Am. **95**, 1299–1310 (1994).
[6] D. R. Jackson, D. P. Winebrenner, and A. Ishimaru, "Application of the composite roughness model to high-frequency bottom backscattering," J. Acoust. Soc. Am. **79**, 1410–1422 (1986).
[7] A. G. Voronovich, "Theory of sound scattering by a free corrugated surface," Sov. Phys. Acoust. **30**, 444–448 (1984).
[8] A. G. Voronovich, "A unified description of wave scattering at boundaries with large and small roughness," in *Progress in Underwater Acoustics*, edited by H. M. Merklinger (Plenum, New York, 1986), pp. 25–34.
[9] R. Dashen, F. S. Henyey, and D. Wurmser, "Calculations of acoustic scattering from the ocean surface," J. Acoust. Soc. Am. **88**, 310–323 (1990).
[10] R. Dashen and D. Wurmser, "Approximate representations of the scattering amplitude," J. Math. Phys. **32**, 986–996 (1991).
[11] R. Dashen and D. Wurmser, "Applications of the new scattering formalism: The Dirichlet boundary condition," J. Math. Phys. **32**, 997–1002 (1991).
[12] D. H. Berman and D. K. Dacol, "Manifestly reciprocal scattering amplitudes for rough interface scattering," J. Acoust. Soc. Am. **87**, 2024–2032 (1990).
[13] D. H. Berman, "Simulations of rough interface scattering," J. Acoust. Soc. Am. **89**, 623–636 (1991).
[14] D. K. Dacol and D. H. Berman, "Sound scattering from a randomly rough fluid–solid interface," J. Acoust. Soc. Am. **84**, 292–304 (1988).
[15] T. Yang and S. L. Broschat, "Acoustic scattering from a fluid–elastic–solid interface using the small slope approximation," J. Acoust. Soc. Am. **96**, 1796–1804 (1994).
[16] R. Dashen and D. Wurmser, "A new theory for scattering from a surface," J. Math. Phys. **32**, 971–985 (1991).
[17] D. Wurmser, "A manifestly reciprocal theory of scattering in the presence of elastic media," J. Math. Phys. **37**, 4434–4447 (1996).
[18] E. I. Thorsos and S. L. Broschat, "An investigation of the small slope approximation for scattering from rough surface: Part I. Theory," J. Acoust. Soc. Am. **97**, 2082–2093 (1995).
[19] S. L. Broschat and E. I. Thorsos, "An investigation of the small slope approximation for scattering from rough surfaces: Part II. Numerical studies," J. Acoust. Soc. Am. **101**, 2615–2625 (1997).
[20] R. C. Gauss, R. F. Gragg, R. W. Nero, D. Wurmser, and J. M. Fialkowski, "Broadband models for predicting bistatic bottom, surface, and volume scattering strengths," J. Underwater Acoust. (accepted for publication).
[21] K. L. Williams and D. R. Jackson, "Bistatic bottom scattering: Model, experiments, and model/data comparison," J. Acoust. Soc. Am. **103**, 169–181 (1998).
[22] N. Bleistein and R. A. Handelsman, *Asymptotic Expansions of Integrals* (Holt, Reinhart and Winston, New York, 1975).
[23] Maple 7, Waterloo Maple, Inc., Waterloo, Ontario, Canada.
[24] N. G. van Kampen, *Stochastic Processes in Chemistry and Physics* (North-Holland, Amsterdam, 1992).
[25] D. Wurmser, R. F. Gragg, and R. C. Gauss, "Calculations of acoustic scattering from an elastic ocean bottom," J. Acoust. Soc. Am. **104**, 1809 (1998).
[26] R. C. Gauss, D. Wurmser, R. W. Nero, and J. M. Fialkowski, "New bistatic models for predicting bottom, surface, and volume scattering strengths," *Proceedings of the 28th Meeting of The Technical Cooperation Program Maritime, Systems Group, Technical Panel Nine (TTCP MAR TP-9)*, 18–22 October 1999 (Naval Research Laboratory, Washington, DC) (also available via e-mail from the authors).
[27] D. R. Jackson, "High-frequency bistatic scattering model for elastic sea-floors," Applied Physics Laboratory, University of Washington, Technical Memorandum 2-00, February 2000.
[28] R. F. Gragg and D. Wurmser, "Scattering from rough elastic ocean floors: Small-slope theory and experimental data," in *Proceedings of the Environmentally Adaptive Sonar Technologies (EAST) Peer Review*, 8–11 Feb-

ruary 2000, Austin, TX, Office of Naval Research, Code 321, Arlington, VA, 2000, CD-ROM. (Also available via e-mail from the authors.)
[29] R. F. Gragg and D. Wurmser, ''Scattering from rough elastic ocean floors,'' in *Proceedings of the 5th European Conference on Underwater Acoustics*, ECUA 2000, edited by M. E. Zakharia *et al.*, 10–13 July 2000, Lyon, France.
[30] J. A. Oglivy, *Theory of Wave Scattering from Random Rough Surfaces* (Adam Hilger, New York, 1991).
[31] K. B. Briggs, ''Microtopographical roughness of shallow-water continental shelves,'' IEEE J. Ocean. Eng. **14**, 360–367 (1989).
[32] I. Simonsen, D. Vandembroucq, and S. Roux, ''Electromagnetic wave scattering from conducting self-affine surfaces: an analytic and numerical study,'' J. Opt. Soc. Am. **18**, 1101–1111 (2001).
[33] M. Abramowitz and I. A. Stegun, *Handbook of Mathematical Functions* (Dover, New York, 1965).
[34] D. M. Drumheller and R. F. Gragg, ''Numerical evaluation of an integral found in the theory of scattering from rough interfaces,'' Naval Research Laboratory Memorandum Report 7140-00-8436, 17 March 2000, CD-ROM.
[35] D. M. Drumheller and R. F. Gragg, ''Evaluation of a fundamental integral in rough-surface scattering theory,'' J. Acoust. Soc. Am. **110**, 2270–2275 (2001).
[36] W. H. Press, B. P. Flannery, S. A. Teukolsky, and W. T. Vetterling, *Numerical Recipes* (Cambridge University Press, Cambridge, 1986).
[37] D. M. Drumheller, ''Padé approximations to matched filter amplitude probability functions,'' IEEE Trans. Aerosp. Electron. Syst. **35**, 1033–1044 (1999).
[38] I. S. Gradshteyn and I. M. Ryzhik, *Table of Integrals, Series, and Products* (Academic, Press, New York, 1963).
[39] E. I. Thorsos, ''Acoustic scattering from a 'Pierson–Moskowitz' sea surface,'' J. Acoust. Soc. Am. **88**, 335–349 (1990).
[40] R. J. Soukup, ''Scattering measurements and interface model validations for a rocky bottom at 2–4 kHz,'' J. Acoust. Soc. Am. **109**, 2300 (2001).
[41] G. Caviglia and A. Morro, *Inhomogeneous Waves in Solids and Fluids* (World Scientific, Singapore, 1992).
[42] H. L. Bertoni and T. Tamir, ''Unified theory of Rayleigh-angle phenomena for acoustic beams at liquid–solid interfaces,'' Appl. Phys. **2**, 157–172 (1973).
[43] R. C. Gauss and J. M. Fialkowski, ''A broadband model for predicting bistatic surface scattering,'' in Ref. 29.
[44] R. J. Soukup and R. F. Gragg, ''Backscatter measurements and model validation for a limestone bottom at 2–4 kHz,'' J. Acoust. Soc. Am. (in preparation).
[45] J. M. Bergin, ''Analytical and physical aspects of two-dimensional spectra associated with stationary random processes,'' Naval Research Laboratory Report 8995, August 1986.
[46] D. R. Jackson, ''Third report on TTCP bottom scattering measurements: Model development,'' for The Technical Cooperation Program, Subgroup G, Panel 11, Applied Physics Laboratory, University of Washington, Report 8708, September 1987.
[47] D. R. Jackson, ''APL-UW high-frequency ocean environmental acoustic models handbook,'' Applied Physics Laboratory, University of Washington, Technical Report 9407, October 1994.

Effect of circumferential edge constraint on the acoustical properties of glass fiber materials

Bryan H. Song and J. Stuart Bolton[a)]
1077 Ray W. Herrick Laboratories, School of Mechanical Engineering, Purdue University, West Lafayette, Indiana 47907-1077

Yeon June Kang[b)]
School of Mechanical and Aerospace Engineering, Seoul National University, San 56-1 Shinlim-Dong, Kwanak-Ku, Seoul 151-742, Korea

(Received 1 June 1999; revised 17 August 2001; accepted 27 August 2001)

It has been noted that the absorption coefficient of a porous material sample placed in a standing wave tube is affected at low frequencies by the nature of the sample's edge constraint. The edge constraint has the effect of inhibiting the motion of the solid phase of the material. The latter can be strongly coupled to the material's fluid phase, and hence the incident sound field, by viscous means at low frequencies. Here the absorption effect noted earlier was demonstrated experimentally. The main focus of the work, however, was on a corresponding transmission loss effect. The material considered was aviation grade glass fiber in two densities. It was found that the edge constraint results in a shearing resonance of the sample at which frequency the transmission loss is a minimum: below that frequency the transmission loss increases with decreasing frequency to a finite low frequency limit proportional to the sample's flow resistance. It was found that the constraint effect could be modeled by using a poroelastic finite element model. It was also found that the transmission loss of the edge-constrained samples approximated that of unconstrained samples at frequencies above approximately 100 Hz when measured in a 10-cm-diam tube. [DOI: 10.1121/1.1413752]

PACS numbers: 43.20.Gp, 43.20.Mv, 43.58.Bh [DEC]

I. INTRODUCTION AND BACKGROUND

While developing a transfer matrix method for estimating the wave number and characteristic impedance of porous materials,[1] the transmission losses of two glass fiber materials were measured in a modified standing wave tube. Those measurements revealed that the constraint of the samples around their edges had a significant effect on their transmission loss and other acoustical properties at low frequencies. The materials considered were aviation-grade glass fibers, and the samples were 2.9 cm in diameter and 7.5 cm in depth. The transmission losses of these materials exhibited minima in the 400–500 Hz range. Below that frequency, the transmission loss appeared to increase with decreasing frequency to a finite low frequency limit while at higher frequencies the transmission loss was largely similar to that of a laterally infinite sheet of the same material. A similar effect had been noted earlier when measuring the transmission loss of expandable sealant materials placed in the same apparatus.[2] It was suggested in the latter case that the binding, or constraint, of the samples around their circumference by the standing wave tube caused the measured results to differ from those of laterally infinite, plane sheets, particularly at low frequencies in which region there can be strong viscous coupling between the fluid and solid phases of a porous material.

The effect of edge constraint on the surface normal impedance of fibrous samples placed in a standing wave tube had been noted earlier by Beranek,[3] and the effects of low frequency coupling between the fluid and solid phases of a porous material on the absorption and impedance of layers of porous material have been considered by Bolton[4] and Allard *et al.*[5] However, the effect of edge constraint on the transmission loss of fibrous materials has not been examined previously. Since the effect of the sample edge constraint is to substantially increase the low frequency transmission loss of porous materials, in the present instance to levels well above those predicted by the mass law, an examination of this effect may have some significance with respect to the design of low frequency noise barriers.

The main purpose of the work reported here was therefore to investigate the effect of edge constraint on the normal incidence acoustical properties (i.e., transmission loss, absorption, and surface normal impedance) of glass fiber materials placed in a standing wave tube. First, the background to this problem is considered, and then the measurement procedures and materials used here are described briefly. Next, the finite element model that was used to represent the effect of circumferential edge constraint is described. The dependence of the predicted transmission loss and absorption on a number of material parameters is then discussed. The latter information was used to identify a set of material parameters that resulted in good agreement between the finite element model predictions and the measurements. Next, measured and predicted results related to normal incidence transmission loss, absorption coefficient, and surface impedance are presented and compared to the corresponding results when the edge constraint was removed. An example is then presented to illustrate the effect of the strength of the edge-

a)Electronic mail: bolton@ecn.purdue.edu
b)Electronic mail: yeonjune@plaza.snu.ac.kr

constraint condition on the low frequency transmission loss and absorption coefficient of edge-constrained samples. Finally, conclusions are drawn regarding the ability to infer the properties of laterally infinite samples of fibrous materials from measurements made in standing wave tubes.

A. Effects of edge conditions on acoustical properties of materials placed in standing wave tubes

The earliest reference to the effect of sample edge conditions on standing wave tube measurements appears to be by Beranek, who compared the calculated surface impedance of samples of a lightweight, porous absorbing blanket with measured results.[3] He found that calculated and measured results were difficult to match below 500 Hz, which he attributed to ''binding'' of the sample around its circumference. He speculated that the edge constraint caused the sample to behave like a resistive diaphragm at low frequencies and to exhibit resonances and antiresonances absent from the response of an infinitely extended, finite-depth layer. It was inferred that the impedance of porous materials should be measured by using as large a diameter tube as possible if measured results were to approach the values expected for large, unconstrained samples in the low frequency range. Kosten and Janssen made similar observations with respect to elastic porous materials such as foams.[6] They also pointed out the conflict between the requirements that the sample must fit into the standing wave tube tightly enough that there are no air spaces around the sample while at the same time it should fit loosely enough that the solid phase of the sample can vibrate freely. In practice it may not be possible to satisfy both requirements simultaneously. Allard and Delage have also shown that the low frequency absorption coefficient of high flow resistivity foams can be very sensitive to the existence of small air gaps around the circumference of the sample (e.g., when the sample diameter was 0.4 mm smaller than the tube diameter).[7] They noted that this effect is particularly evident when there is strong coupling between the fluid and solid phases of the material, i.e., when the parameter $\sigma/\rho_1\omega \gg 1$ (where σ is the flow resistivity, ρ_1 is the bulk density of the expanded solid phase, and ω is the circular frequency).

A further demonstration of the effect of edge constraint on the normal incidence absorption coefficient of polyurethane foam samples 0.0254 m deep and 0.029 m in diameter was presented by Ingard *et al.*[8] They found significant differences between results for the cases in which the foam was held tightly by the walls of the sample holder or was cut so that the sample fit loosely in the tube (but presumably without there being air gaps around the sample circumference). In particular, the first major absorption peak was reduced in magnitude and was shifted to a higher frequency by the edge constraint. They noted that ''intimate'' contact between the sample and the tube wall could alter the acoustically induced motion of the material's solid phase, thus altering the frequency dependence of the absorption coefficient.

Later, Cummings performed a study complementary to Beranek's and that of Allard and Delage in which he examined theoretically and experimentally the effect of air gaps between a sound-absorbing material and the standing wave tube wall.[9] For both isotropic polyurethane foam and anisotropic glass fiber samples it was found that air gaps had a less noticeable effect on the measured impedance at low frequencies than at high frequencies and that the resistance was generally decreased by the presence of air gaps while the reactance was largely unaffected (at least by relatively small air gaps). It was also noted that air gaps tended to have a greater significance in the case of media having relatively high flow resistivities. Cummings also noted that some part of the effect of an air gap may be to release the sample edge constraint, thus minimizing the effect of the frame waves and transverse waves induced by viscous and inertial coupling between the fluid and solid phase of the porous material acting in conjunction with the edge constraint.

Kang and Bolton used a finite element model based on the Biot theory[10,11] to predict the effects of edge constraints on the sound absorption and transmission loss of relatively stiff, partially reticulated foams.[12,13] They noted that at low frequencies the edge constraint had the effect of increasing the magnitude of the imaginary part of the foam's surface normal impedance, i.e., the edge constraint apparently stiffened the material. The latter behavior contrasts with the effect of an air gap around the sample. Also in contrast to the effect of air gaps, the edge constraint was found to affect the resistance and reactance in approximately equal measure. The edge-constraint effect was found to be particularly marked in the case of foams having a membrane bonded to their incident surface, in which case the foam's solid phase is directly excited by the action of the membrane, hence causing the frame wave to be well excited directly and the transverse wave contribution to be significant owing to the edge constraint. The net effect of the edge constraint on finite-depth layers of membrane-surfaced foams was to increase the frequency of the first absorption peak and to reduce the latter's magnitude: This finding was similar to that reported earlier by Ingard in the case of unfaced foams.[8] Numerical predictions also showed that the low frequency transmission loss of a finite-depth, constrained foam plug should be increased compared with that of an unconstrained plug. In particular, it was predicted that the low frequency transmission loss of an edge-constrained plug was limited to a finite value appropriate for a rigid porous material; the limiting value presumably being related to the total flow resistance of the finite-depth layer. This behavior contrasts with that of an unconstrained porous plug, in which case the low frequency limit of the transmission loss is 0 dB. It was also noted that the edge-constraint effect became small at frequencies above the cut-on of the first shearing cross mode within the porous material, and that frequency was proportional to the square root of the *in vacuo* Young's modulus (all other material parameters being held constant).

Johansen *et al.* have used a two-dimensional, axisymmetric finite element implementation of the second formulation of the Biot theory[14] to predict the effect of air gaps around a standing wave tube sample,[15] i.e., the case considered by Cummings analytically; but in this case the effect of the frame and transverse waves was modeled. They found qualitative agreement between Cumming's data and the predicted surface normal impedance, i.e., the air gap caused a

significant reduction of the real impedance without having a noticeable effect on the reactance. However, edge-constraint effects were not considered: that is, the contact between the elastic porous material and the tube wall was assumed to be frictionless. Vigran *et al.* compared two-microphone, free-field measurements of the surface normal impedance and absorption coefficient of a large foam sample with measurements of the same material made within a 4-cm-diam standing wave tube (when the samples were either glued to the tube walls or were sized so that they were tightly constrained) and with axisymmetric finite element predictions with and without constrained edge conditions imposed.[16] They showed both experimentally and numerically that the polyurethane foam samples were stiffened by the edge constraint with the result that resonance features associated with frame motion were shifted to higher frequencies when compared to the free-field results. This conclusion was the same regardless of whether the samples were glued to the walls of the sample holder or were tightly held by friction. They also found, at least for the relatively stiff, partially reticulated, high flow resistivity foam that they considered, that a tube diameter of at least 10 cm was required to approximate free-field absorption results. They therefore noted that the edge-constraint effect could have a significant effect on standing wave tube measurements, particularly for relatively stiff, partially reticulated, high flow resistivity foams (or more generally, for materials and frequency ranges in which there is strong coupling between the motion of the solid and fluid phases).

Thus, to date, it has been found in both experimental and numerical work that the major effect of sample edge constraint is both to stiffen the sample and increase its resistance at low frequencies when compared with the impedance of large, unconstrained samples of the same material. This effect combined with the presence of frame and shear waves which are coupled to each other and to the airborne wave by the effect of the edge constraint make it possible for additional low frequency resonances to occur, as had been noted previously for laterally infinite plane materials.[4,5] Finally, both finite element simulations[13] and measurements on expanded foams[2] have suggested that the second major effect of edge constraint is to increase the low frequency transmission loss of porous layers to a finite limit controlled by the flow resistance of the layer. The latter conclusion is pursued here with respect to light, fibrous materials.

B. Measurements of mechanical properties of glass fiber

As part of the present work, the elastic properties of glass fiber samples as installed in a standing wave tube were estimated by fitting finite element predictions to measurements of transmission loss and absorption coefficient. Thus it is appropriate to review briefly prior work related to the estimation of these properties.

The complex Young's and shear moduli can have an important effect on the acoustical characteristics of noise control materials. Pritz developed a measurement procedure in which a cylindrical specimen was excited longitudinally at one end and was loaded by a mass at its other end; the acceleration transfer function measured between the shaker and the loading mass was then used to estimate the frequency-dependent complex Young's modulus of the material.[17,18] He found that both the *in vacuo* Young's modulus and the loss factor for a variety of fibrous materials were essentially independent of frequency in the 100 Hz–3 kHz range. The *in vacuo* loss factors for these materials were found to lie between 0.006 and 0.026. Note that all of the materials Pritz tested were denser by approximately an order of magnitude or more than the materials considered in the present work. Wilson and Cummings subsequently used a two-thickness implementation of Pritz's technique to determine the *in vacuo* dynamic structural properties of glass fiber materials, e.g., complex wave number, characteristic impedance, and Young's modulus.[19] For glass fiber compressed to a density of 24 kg/m^3 they found the Young's modulus to be approximately 3.3×10^3 Pa: they were unable to obtain accurate estimates of the loss factor, however.

Ingard *et al.* performed *in vacuo* measurements using an apparatus similar to that of Pritz.[8,20] They also considered relatively dense glass fiber material (approximately 96 kg/m^3) and found that it was stiffer than air and had a loss factor of approximately 0.04.

Note finally that a number of authors have commented on the nonlinear dynamic response of fibrous materials, i.e., their apparent stiffness depends on the strain level at which the sample is tested.[5,8,17,18] It has also been suggested that fibrous materials are stiffer by possibly large factors at small strains than at large strains;[5] it is reasonable to expect that this behavior is dependent on the detailed microstructure of the material. These observations are significant in the present context since the strain imposed on a fibrous material by an acoustic excitation (as in a typical standing wave tube) is likely to be smaller than that imposed by a mechanical shaker of the type used previously to make measurements of the dynamic mechanical properties of fibrous media.

II. MEASUREMENT PROCEDURES AND MATERIALS TESTED

A. Experimental apparatus and procedures

The experimental procedures used to obtain estimates of the absorption coefficient, surface normal impedance, and the transmission loss of cylindrical glass fiber samples were based on earlier work by Bolton *et al.*[2] and Song and Bolton.[1]

The measurements were made using a modified standing wave tube (the Brüel and Kjær Two-Microphone Impedance Measurement Tube Type 4206): see Fig. 1. Note that the Brüel and Kjær standing wave tube is nominally suitable for both low frequency (100–1600 Hz) and high frequency (500–6400 Hz) measurements. In the work presented here the high and low frequency tubes (2.9 and 10-cm-i.d., respectively) were modified by the addition of custom-made sections as shown in Fig. 1. The downstream section of each tube was separated from the upstream section by a sample holder of the same internal diameter as the up- and downstream sections. The two microphone locations in both the up-and downstream tube sections were separated by 2 cm in

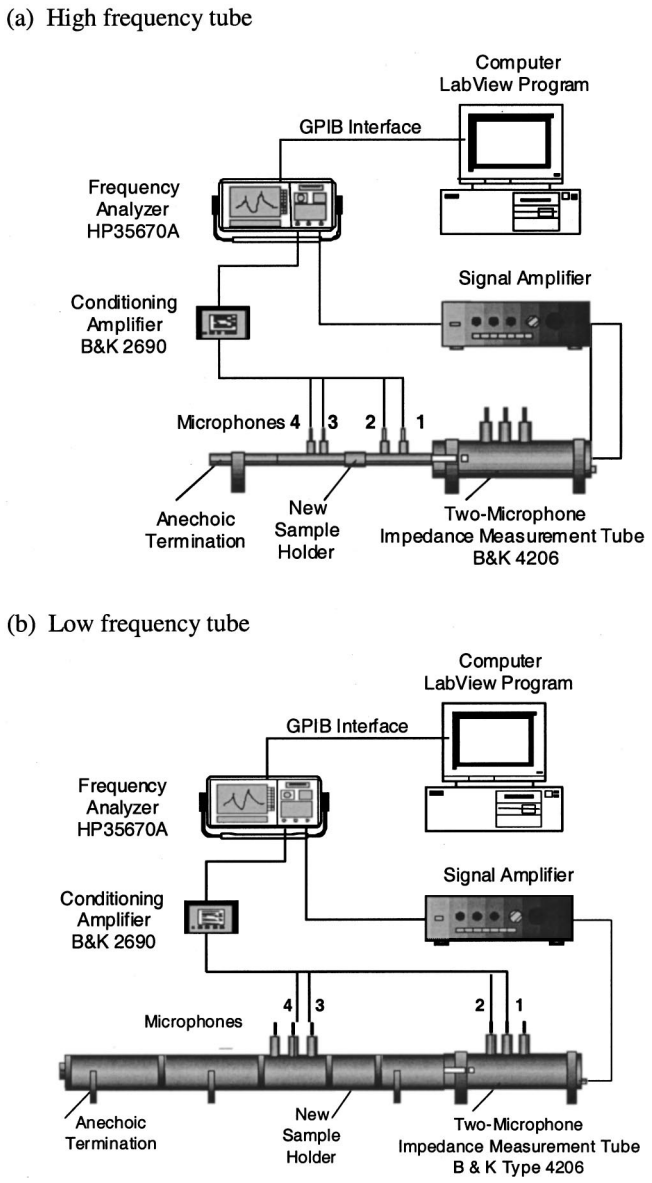

FIG. 1. Schematic of four-microphone measurement setup: (a) high frequency tube, (b) low frequency tube.

the high frequency case and 5 cm in low frequency case. In the high frequency tube, measurement position 2 was located 21.2 cm from the front surface of the sample, and measurement position 3 was located 13.6 cm from the rear surface of the sample. In the low frequency case, measurement position 2 was located 35 cm from the front surface of the sample, and measurement position 3 was located 17.4 cm from the rear surface of the sample. Note that the sample holders used here were sufficiently stiff that the frequency of their first ovalling modes were well above the frequency range of interest. Note also that the high frequency results presented here are nominally accurate only in the frequency range 500–6400 Hz. Nonetheless, it is believed that the current results are reasonably accurate to lower frequencies (e.g., 100 Hz) owing to careful phase calibration of the microphones and to the fact that the reactivity of the sound fields in the up- and downstream sections was low owing both to the presence of an anechoic termination and the absorptive properties of the materials under test. Similarly, it is believed that the low frequency tube results are accurate to a lower frequency of approximately 50 Hz.

The approximately anechoic terminations that terminated the downstream section of both tubes were created by packing a standard sample holder with a depth of polyurethane foam. The foam was cut into small pieces that were packed progressively more densely toward the downstream end of the termination. The absorption coefficient of the high frequency termination was greater than 0.96 in the frequency range 500–6400 Hz while the absorption coefficient of the low frequency termination was greater than 0.92 in the frequency range 100–1600 Hz. Note that an anechoic termination is not required by the measurement procedure used here, but its use improves the accuracy of the transfer function estimates on which the procedure is based by causing the reactivity of the sound field in the downstream section to be low.[1]

The loudspeaker at the upstream end of the apparatus was used to generate a broadband random signal over the frequency range 100–6400 Hz in the high frequency case and 50–1600 Hz in the low frequency case. A four-microphone approach was adopted here in contrast with the measurement procedure described earlier in which a single roving microphone was used.[1,2] The transfer functions between the output of microphone 1 (treated as an input) and the outputs of microphones 2 and 3, H_{21} and H_{31}, respectively, and the transfer function between the output of microphone 3 (treated as the input) and the output of microphone 4, H_{43}, were estimated over the prescribed frequency band by using a HP 35670A frequency analyzer. A microphone switching calibration procedure based on that suggested in the ASTM E 1050-90, two-microphone standing wave tube standard[21] was used to minimize the effects of microphone phase mismatch. The measurement was controlled and the transfer function data was analyzed using LabView software running on a personal computer.

B. Calculation of transmission loss, absorption coefficient, and surface normal impedance

In the implementation of the four-microphone method employed here, three transfer functions were measured; i.e., $H_{21}=P_2/P_1$, $H_{31}=P_3/P_1$, and $H_{43}=P_4/P_3$, where P_1-P_4 may be considered the complex sound pressures at microphone locations 1–4. The complex sound pressures may themselves be represented as a superposition of plane wave components: See Fig. 2. The coefficients A to D represent the complex magnitudes of the plane wave components in the up- and downstream tube sections, and the latter may easily be expressed in terms of the complex pressures P_1-P_4, or alternatively, in terms of P_1 and H_{21}, H_{31} and H_{43}, i.e.,

$$A=\frac{jP_1(e^{jkx_2}-H_{21}e^{jkx_1})}{2\sin k(x_1-x_2)}, \tag{1a}$$

$$B=\frac{jP_1(H_{21}e^{-jkx_1}-e^{-jkx_2})}{2\sin k(x_1-x_2)}, \tag{1b}$$

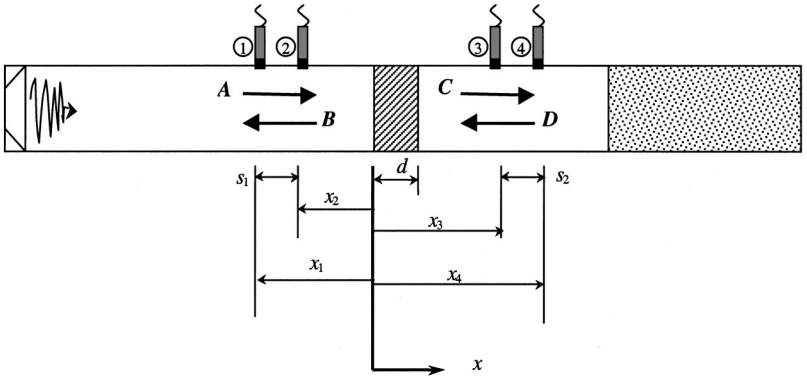

FIG. 2. Geometry for plane wave decomposition procedure.

$$C=\frac{jP_1H_{31}(e^{jkx_4}-H_{43}e^{jkx_3})}{2\sin k(x_3-x_4)}, \tag{1c}$$

$$D=\frac{jP_1H_{31}(H_{43}e^{-jkx_3}-e^{-jkx_4})}{2\sin k(x_3-x_4)}. \tag{1d}$$

Here k denotes the wave number in the ambient fluid within the tube, x_1-x_4 represent the locations of measurement positions 1–4, and an $e^{+j\omega t}$ sign convention has been adopted. By following the procedures outlined in Ref. 1, the coefficients $A-D$ may be used to express the sound pressures and normal acoustic particle velocities on the up- and downstream faces of the sample (i.e., at $x=0$ and $x=d$, respectively) in terms of P_1 and the three transfer functions. The latter information may then be used to solve for the elements of the two-by-two transfer matrix that relates the pressures and particle velocities on the two faces of the sample.[1]

When the transfer matrix elements are known, the plane wave reflection coefficient, the plane wave transmission coefficient, and surface normal impedance of the sample may then be calculated based on a knowledge of H_{21}, H_{31}, and H_{43} for arbitrary tube termination conditions. Here it was of interest to calculate these quantities for the case of a perfectly anechoic termination, in which case the reflection coefficient, R_a, and transmission coefficient, T_a, are

$$R_a=\frac{H_{21}e^{-jkx_1}-e^{-jkx_2}}{e^{jkx_2}-H_{21}e^{jkx_1}}, \tag{2}$$

$$T_a=\frac{H_{31}\sin k(x_1-x_2)[e^{jkx_4}-H_{43}e^{jkx_3}]}{\sin k(x_3-x_4)[e^{jkx_2}-H_{21}e^{jkx_1}]}, \tag{3}$$

when expressed in terms of the measured transfer functions. The anechoic surface normal impedance, Z_{na}, can similarly be expressed as

$$Z_{\mathrm{na}}=j\rho_0c\,\frac{\sin kx_2-H_{21}\sin kx_1}{\cos kx_2-H_{21}\cos kx_1}, \tag{4}$$

where ρ_0c is the characteristic impedance of the ambient fluid. The normalized anechoic surface normal impedance is then $z_{\mathrm{na}}=Z_{\mathrm{na}}/\rho_0c$. Note that the use of Eqs. (2)–(4) to evaluate the acoustical properties of the sample serves to eliminate the effect of reflections from the tube termination, hence making knowledge of the tube termination impedance unnecessary. Reflections from the tube termination can result in errors when R_a is estimated as B/A and T_a is estimated from C/A.[1]

Finally, the absorption coefficient of the anechoically terminated sample is evaluated as $\alpha_a=1-|R_a|^2$ and the anechoic transmission loss as $\mathrm{TL}_a=10\log(1/|T_a|^2)$. Other tube termination conditions could be considered when evaluating the acoustical properties of the sample, e.g., a hard or partially reflecting termination could be assumed.[1] However, in the present instance it was convenient to compare the measured results with finite element calculations made under the assumption of a perfectly anechoic termination.

Finally, note that the wave number within the tube, k, was assumed to be complex and was calculated using a formula presented by Temkin [Eq. (6.6.9) in Chap. 6 of Ref. 22]. The latter formulation was found to represent the measured effects of wall losses more accurately than the wide duct formulas presented by Pierce,[23] which were used in early implementations of the present measurement procedure.

C. Materials tested

The materials tested in the present work were aviation-grade glass fibers: The measured densities and flow resistivities of the materials used, here identified by their colors (yellow and green), are listed in Table I. The sheets of glass fiber from which the samples were cut were nominally 1 in. thick, and cylindrical samples of the lining material were carefully cut to fit snugly inside the sample holder. Each

TABLE I. Poroelastic material properties used in calculations.

Material	Bulk density ($\mathrm{Kg/m^3}$)	Porosity	Tortuosity	Measured/ estimated flow resistivity (MKS Rayls/m)	Shear modulus (Pa)	Loss factor
Yellow	6.7	0.99	1.1	14 800/21 000	1200	0.35
Green	9.6	0.99	1.1	24 400/31 000	2800	0.275

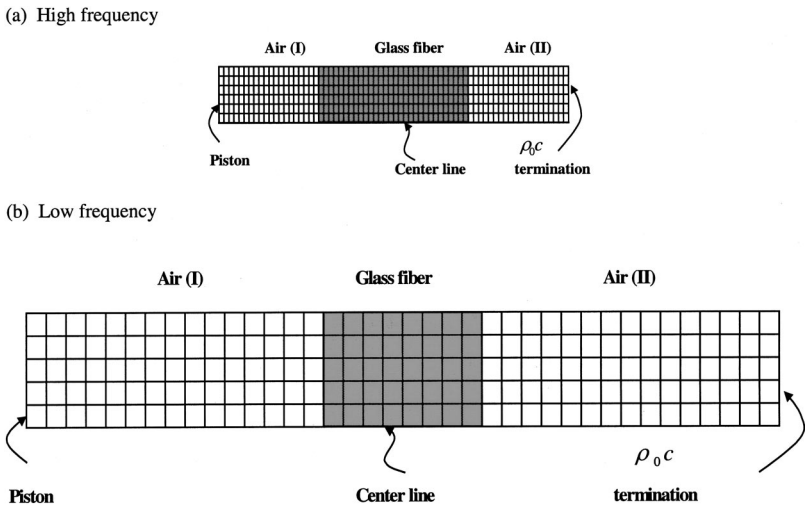

FIG. 3. Axisymmetric finite element model: (a) high frequency tube, (b) low frequency tube.

measurement reported here was made using three layers of lining material to give a total sample thickness of 3 in. The lining materials were carefully inserted into the sample holder so that the depth of the individual layers comprising the complete sample was preserved insofar as possible. Glass fiber materials of these relatively low densities are delicate so that it is difficult to insert the samples into the sample holder without distorting them slightly, thus introducing intersample variability. To reduce the effect of sample mounting differences and material variability, ten individual measurements were performed using a total of 30, 1-in.-deep samples; the results of the ten individual tests were then averaged to give the results presented here. Note that the parameter $\sigma/\rho_1\omega$ is unity at approximately 350 Hz for the yellow material and at approximately 400 Hz for the green material. Thus it should be expected that the motions of the fluid and solid phases of these materials are well coupled near and below these frequencies.

III. MODELING OF SOUND TRANSMISSION AND ABSORPTION

A. Finite element models

The acoustical performance of the cylindrical glass fiber samples was modeled using the code COMET/ACOUSTICS—SAFE (supplied by Automated Analysis Corporation of Ann Arbor, MI). This software is based on a finite element implementation of the Biot theory for wave propagation in elastic porous materials.[10] Specifically, it is based on the version of the Biot theory described previously by Bolton *et al.*[11] All of the results presented here were calculated using axisymmetric models, whose implementation has been described elsewhere.[24]

The axisymmetric finite element models used here are shown in Fig. 3. The gray elements represent a plug of glass fiber 0.075 m in length and 0.0145 m in radius for the high frequency tube case, and 0.05 m in radius for the low frequency tube case. The white elements represent the up- and downstream air spaces (i.e., air regions I and II) that were each 0.05 m in length and 0.0145 m in radius for the high frequency case, and 0.15 m in length and 0.05 m in radius for the low frequency case. The lower edge of the model represents the axis of symmetry while the upper edge represents the outer circumference of the duct. In the high frequency case, the model comprised 180 poroelastic elements and 240 air elements for a total of 420 elements having 497 nodes. Each of the elements had the same size, i.e., 0.0025 m in the axial direction and 0.002 417 m in the radial direction. In the low frequency case, the model comprised 40 poroelastic elements and 150 air elements for a total of 190 elements having 234 nodes. Each of the elements had the same size, i.e., 0.01 m in the axial direction and 0.01 m in the radial direction. All of the elements in the axisymmetric model were linear, four-node, quadrilateral elements. The parameters that were used to specify the properties of the poroelastic medium were flow resistivity, tortuosity, porosity, bulk density of the expanded material, bulk Young's modulus and corresponding loss factor, and Poisson's ratio.

A unit amplitude axial velocity was applied to the left-hand side of air region I to simulate a plane piston. The right-hand end of air space II was terminated by a $\rho_0 c$ impedance (i.e., a normalized impedance of unity), thus creating an anechoic termination.

B. Boundary conditions

The boundary conditions to be applied in the axisymmetric case have been considered in detail elsewhere,[24] and will only be described briefly here. Open surface boundary conditions were assumed to apply at both the front and rear surfaces of the glass fiber plug. In this case, normal volume velocity is conserved locally at the interface between the poroelastic medium and the exterior air space (i.e., neither the normal fluid or solid phase velocity is specified independently, only their area-weighted sum). In contrast, the exterior sound pressure is applied independently to the fluid and solid phases. The shear stress at an open interface is set equal to zero.

The duct circumference was itself assumed to be a rigid. Thus in the air regions, a zero normal velocity condition was applied in the radial direction at the duct wall. Within the poroelastic medium, the radial displacements of both the solid and fluid phases were set to zero at the duct circumference to model the hard wall boundary condition. To represent

the constraint of the glass fiber by contact with the duct wall, the axial component of the solid phase displacement was also set equal to zero at the duct wall, i.e., the material was considered to be ''bonded'' to the duct wall. Note, however, that the tangential displacement of the fluid component displacement within the porous material was not constrained at the duct wall, i.e., the fluid phase of the poroelastic medium was allowed to ''slip'' at the boundary.

To represent a case in which the glass fiber is not solidly attached to the duct wall but can slip axially even though it is constrained radially, it is only necessary to eliminate the requirement that the axial component of the solid phase displacement be zero at the duct wall. When a plane wave is incident at normal incidence on a plug of this sort, the acoustical behavior of the plug is the same as that of a laterally infinite, finite-depth sheet of material.[12] Thus the unconstrained case can be calculated using plane wave theory.[11] The latter theory was used to calculate the acoustical properties of the glass fiber plug when it was assumed to slip at the wall. The difference between the acoustical performance in the latter configuration and in the edge-constrained condition thus represents the acoustical impact of the edge constraint. In results presented in Sec. V, the effect of a partial edge constraint was simulated by reducing the stiffness of the row of poroelastic elements adjacent to the duct outer circumference.

C. Calculation of acoustical properties

For the purpose of generating numerical results to compare with the experimental results, the output of the finite element calculations was treated in a way similar to the experimental data. That is, after each run, the complex sound pressure was evaluated at two adjacent nodes on the axis of symmetry in both the up- and downstream tube sections. These data were then used in conjunction with Eq. (1) to evaluate the coefficients $A-D$ (D being negligible compared to the rest owing to the assumption of an anechoic termination). The plane wave reflection coefficient can then be evaluated as $R_a=B/A$ and the plane wave transmission coefficient as $T_a=C/A$ (these simple calculations being possible since the tube termination is truly anechoic in the numerical calculations). The absorption coefficient and transmission loss were then calculated as for the experimental data. Finally, the anechoic surface normal impedance was evaluated as $Z_{\mathrm{na}}=\rho_0 c(1+R_a)/(1-R_a)$.

IV. PROCEDURES FOR MATCHING MEASURED AND PREDICTED ACOUSTICAL PROPERTIES

It was of interest to find the set of material properties that resulted in good agreement between the measured and predicted results for the glass fiber plugs: These comparisons were based on an examination of the dependence of the behavior of the transmission loss and absorption coefficient on the various material properties.

In the finite element calculations, the bulk densities of the materials were set to their measured values. The porosity of both materials was set to 0.99, which is consistent with their low bulk densities. The tortuosity of both materials was set to a small value, 1.1, considered to be typical for low density fibrous materials.[25] The solid phase Young's modulus and Poisson's ratio were not chosen independently. Rather, the shear modulus was specified since it was found to control the location of the resonance features in the transmission loss and absorption coefficient results (see Sec. V A).

The flow resistivity, shear modulus, and loss factor listed in Table I were determined by first examining the dependence of the transmission loss and absorption coefficient on these parameters and then choosing a set of values that resulted in good agreement between measured and predicted values. The flow resistivities estimated in this way were found to be approximately 25% higher than the measured values (see Table I). This discrepancy is perhaps due to the neglect of pore shape factors[25] in the implementation of the Biot theory used here. Note also that it has been observed previously that the flow resistivity appearing in the Biot model must be increased beyond its measured value to achieve good agreement between measured and predicted acoustical properties for fine fiber materials of the type considered here.[26] It is also possible that the slight compression of the samples required to insert them into the standing wave tube results in an increase in flow resistivity. Nonetheless, the agreement between the measured and predicted values presented in Sec. V is sufficiently good to suggest that the set of material properties listed in Table I is reasonably accurate for the materials and configurations considered here.

V. DISCUSSION OF RESULTS

A. Parameter variation results

Here, the dependence of the predicted transmission losses and absorption coefficients on the material parameters discussed previously is considered. Note that for all the predicted results presented here, the material properties have been fixed at the values specified in Table I for the green material with the exception of the single parameter whose effect is being demonstrated. In addition, note that all of the predictions presented here are for 2.9-cm-diam, 7.5-cm-deep, edge-constrained cases.

1. Stiffness properties

First, consider the effect of Young's modulus, E_m, and Poisson's ratio, ν. In preliminary work, it was found that a wide range of Young's moduli and Poisson's ratios gave approximately the same results so long as the shear modulus ($G=E_m/2(1+\nu)$) remained constant. This effect is demonstrated in Fig. 4 (for a value of $G=2800$ Pa) where it can be seen that the Young's modulus and Poisson's ratio have essentially no independent impact on the absorption coefficient or transmission loss. Thus it appears that the single parameter, the shear modulus, controls the dynamics of the solid phase of the constrained fibrous plug (along with the material bulk density, of course).

The effect of shear modulus variation on the transmission loss and absorption coefficient is illustrated in Fig. 5. In these calculations the Poisson's ratio was fixed at 0.4 for the yellow material and 0.45 for the green material, and the Young's modulus was varied as necessary to achieve a speci-

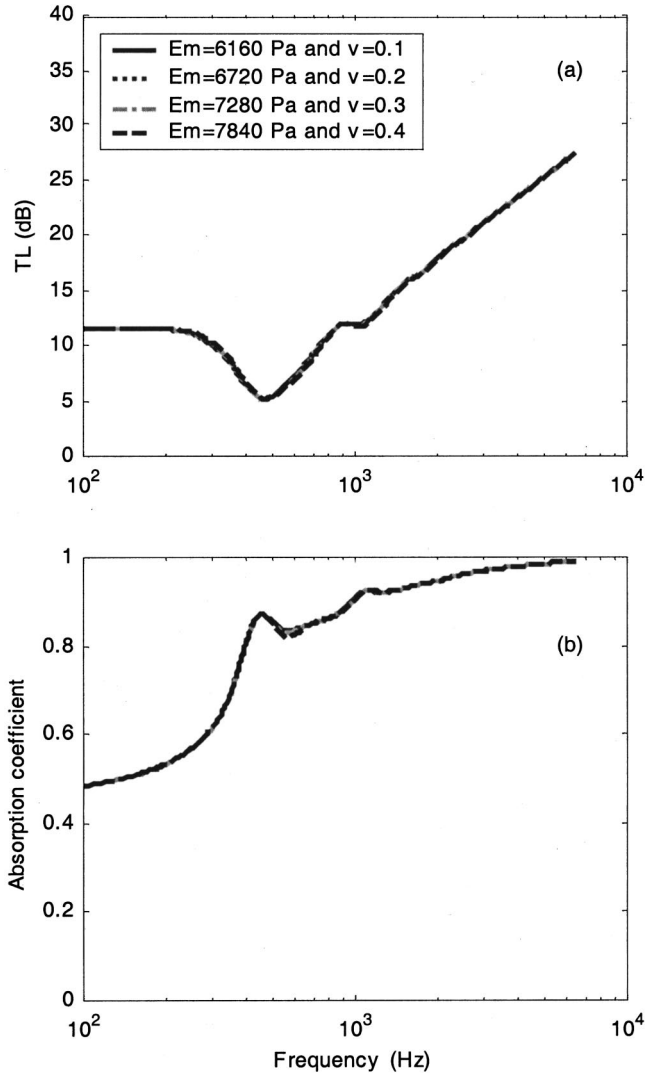

FIG. 4. Dependence of (a) transmission loss and (b) absorption coefficient on Young's modulus and Poisson's ratio at a fixed shear modulus ($G = 2800$ Pa).

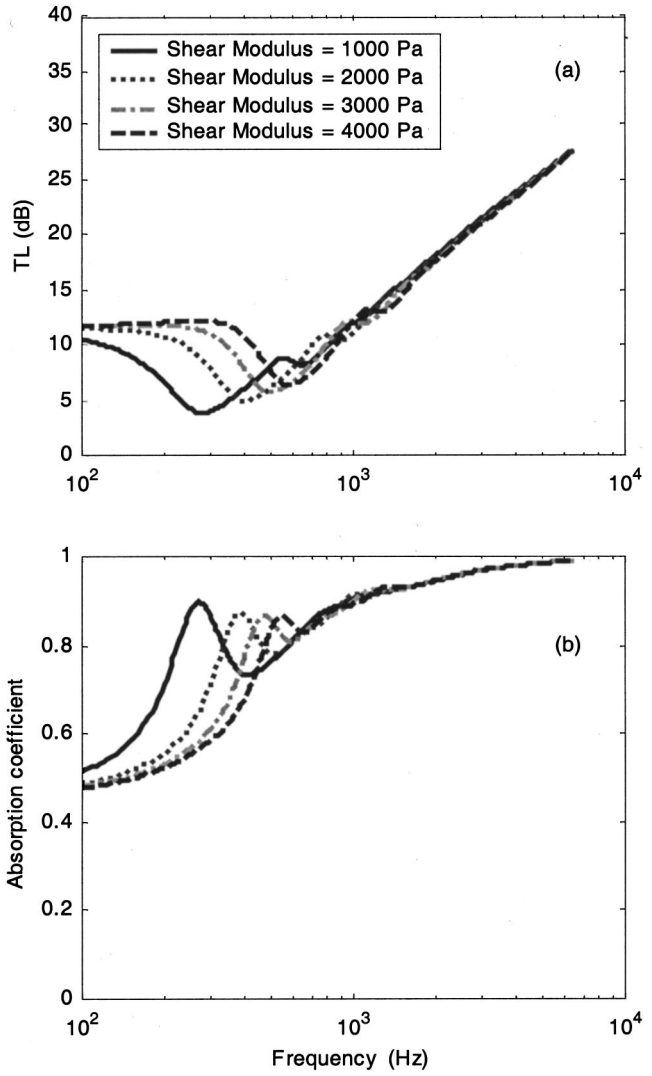

FIG. 5. Effect of shear modulus: (a) transmission loss and (b) absorption coefficient (parameters as for the green material listed in Table I except as noted).

fied shear modulus. It can be seen that the major effect of the shear modulus is to shift the minimum location in the transmission loss results [Fig. 5(a)], and the location of the corresponding peak in the absorption coefficient results [Fig. 5(b)]. It was found that the locations of the transmission loss minimum and the absorption coefficient peak shifted approximately in proportion to the square root of the shear modulus. These results suggest that the minimum of the transmission loss and the corresponding absorption peak are associated with a shearing resonance of the solid phase of the porous material, as suggested earlier elsewhere.[13] In such a motion, the material's solid phase moves axially: The axial motion is constrained to be zero at the outer circumference and is presumably a maximum at the center of the sample. Above the first resonance frequency, the effect of the shear modulus on both the transmission loss and absorption coefficient is modest, although some evidence of higher order shearing resonances is visible as the frequency is increased.

2. Loss factor

The effect of the *in vacuo* loss factor of the solid phase on the transmission loss and absorption coefficient is shown in Fig. 6. It can be seen in Fig. 6(a) that the loss factor controls the depth of the transmission loss minimum at the first shearing resonance frequency, and also at the progressively higher frequencies at which the higher order shearing modes are assumed to occur. A corresponding effect is visible in the absorption coefficient results [Fig. 6(b)].

3. Flow resistivity

Finally, the effect of flow resistivity on the transmission loss and absorption coefficient is shown in Fig. 7. In Fig. 7(a) it can be seen that the flow resistivity controls the low frequency limit of the transmission loss when the thickness of the material is fixed. In this frequency range, i.e., below the first shearing resonance, the material appears to behave essentially like a rigid porous material owing to the edge constraint, and so as the flow resistivity is increased, the transmission loss increases. It can also be seen that the flow resistivity has a large effect on the transmission loss above the first resonance frequency. Thus the flow resistivity has a significant impact on the transmission loss both below and above the frequency of the first shearing mode of the fibrous

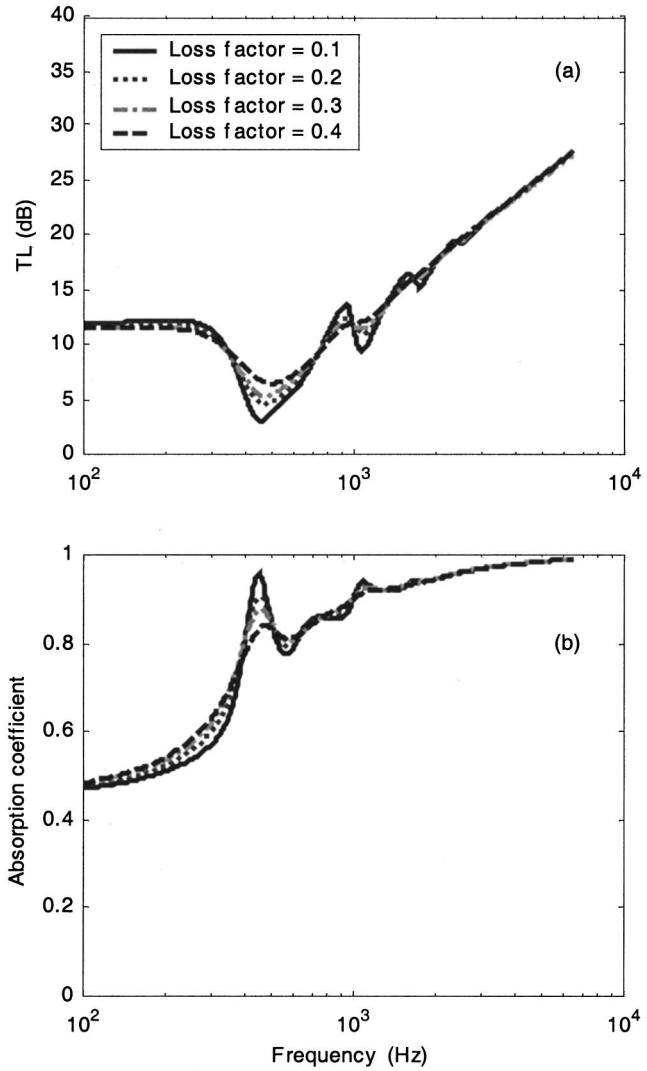

FIG. 6. Effect of loss factor: (a) transmission loss and (b) absorption coefficient (parameters as for the green material except as noted).

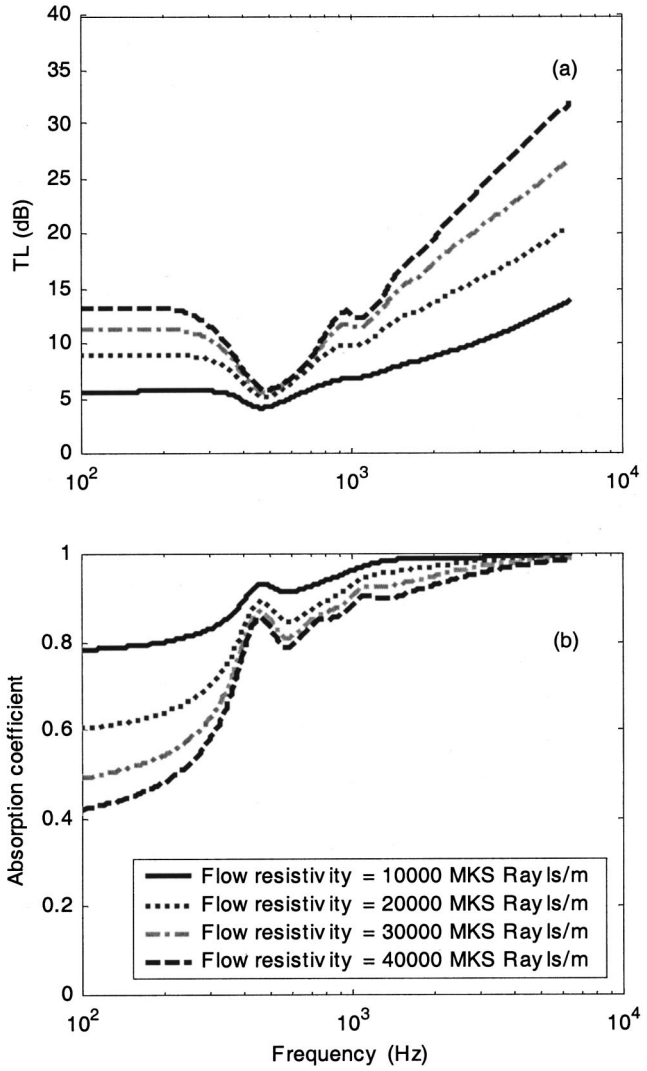

FIG. 7. Effect of flow resistivity: (a) transmission loss and (b) absorption coefficient (parameters as for the green material listed in Table I except as noted).

plug. The fact that the flow resistivity has a relatively small effect in the vicinity of the transmission loss minimum is consistent with the suggestion that the latter feature is associated with a shearing resonance of the solid phase, and that in this frequency range there is relatively small relative motion between the solid and fluid phases within the porous material. Similarly, it was found that the flow resistivity has a significant impact on the absorption coefficient over the complete frequency range considered [see Fig. 7(b)], although near the first shearing resonance frequency, its effect is decreased. Note that the absorption coefficient decreases monotonically as the flow resistivity of the material is increased as might be expected for an anechoically terminated fibrous layer.

4. Estimation of material parameters

From the above-presented illustrative results it may be concluded that the shear modulus controls the location of resonance features, that the loss factor controls the width and height or depth of those features, and that the flow resistivity controls both the low frequency limit and high frequency asymptote of the transmission loss.

Based on these observations, the flow resistivity, shear modulus, and loss factor were adjusted to produce good agreement between measurements and predictions for the green and yellow glass fiber in both small and large diameter configurations. The parameter search was further constrained by the requirement that a single set of parameters should yield reasonable agreement in both the small and large diameter configurations for both materials. The parameter values determined in this way are listed in Table I and the comparisons between the measured transmission losses, absorption coefficients and surface normal impedances and the corresponding predicted results are shown in Figs. 8, 9, and 10, respectively. These various results will be discussed in Sec. V B.

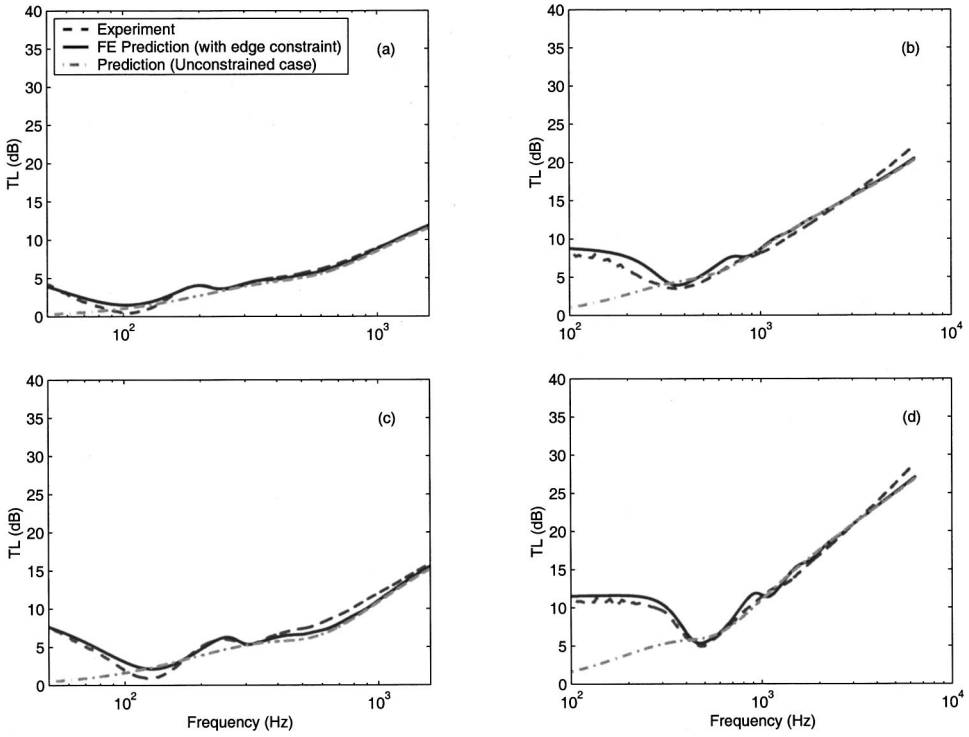

FIG. 8. Measured and predicted transmission losses: (a) yellow material in large tube, (b) yellow material in small tube, (c) green material in large tube, (d) green material in small tube. Line types are as indicated.

B. Comparison between measured and predicted results

1. Transmission loss

The measured and predicted transmission losses for the green and yellow materials in both large and small diameter configurations are shown in Fig. 8. It may be seen that there is good agreement between the edge-constrained finite element method (FEM) predictions and the measurements over the entire frequency range considered. Certainly, the location and depth of the resonance dip due to the first shearing mode of the sample are reproduced well. Note that the transmission loss minimum appears at a higher frequency for the green material than for the yellow material in both small and large diameter configurations: compare Figs. 8(a) and (c), and 8(b) and (d). This result is consistent with the shear moduli estimated for these two materials (see Table I). Note also that the first minimum in the transmission loss occurs at a lower frequency when the diameter of the material is increased. In the case of the green material, for example, the small diam-

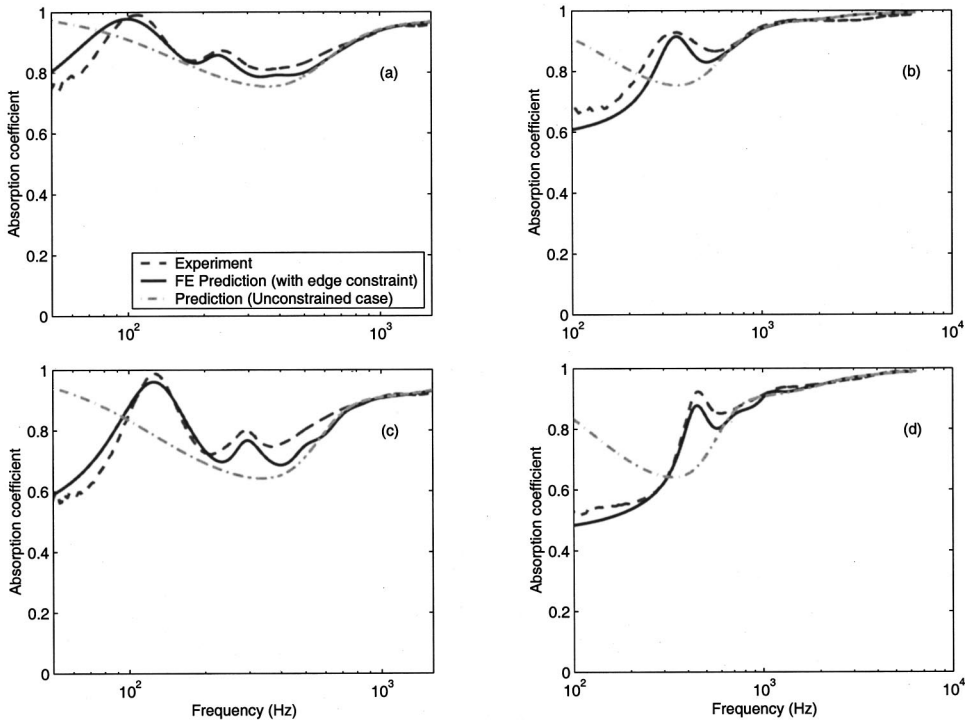

FIG. 9. Measured and predicted absorption coefficients: (a) yellow material in large tube, (b) yellow material in small tube, (c) green material in large tube, (d) green material in small tube. Line types are as indicated.

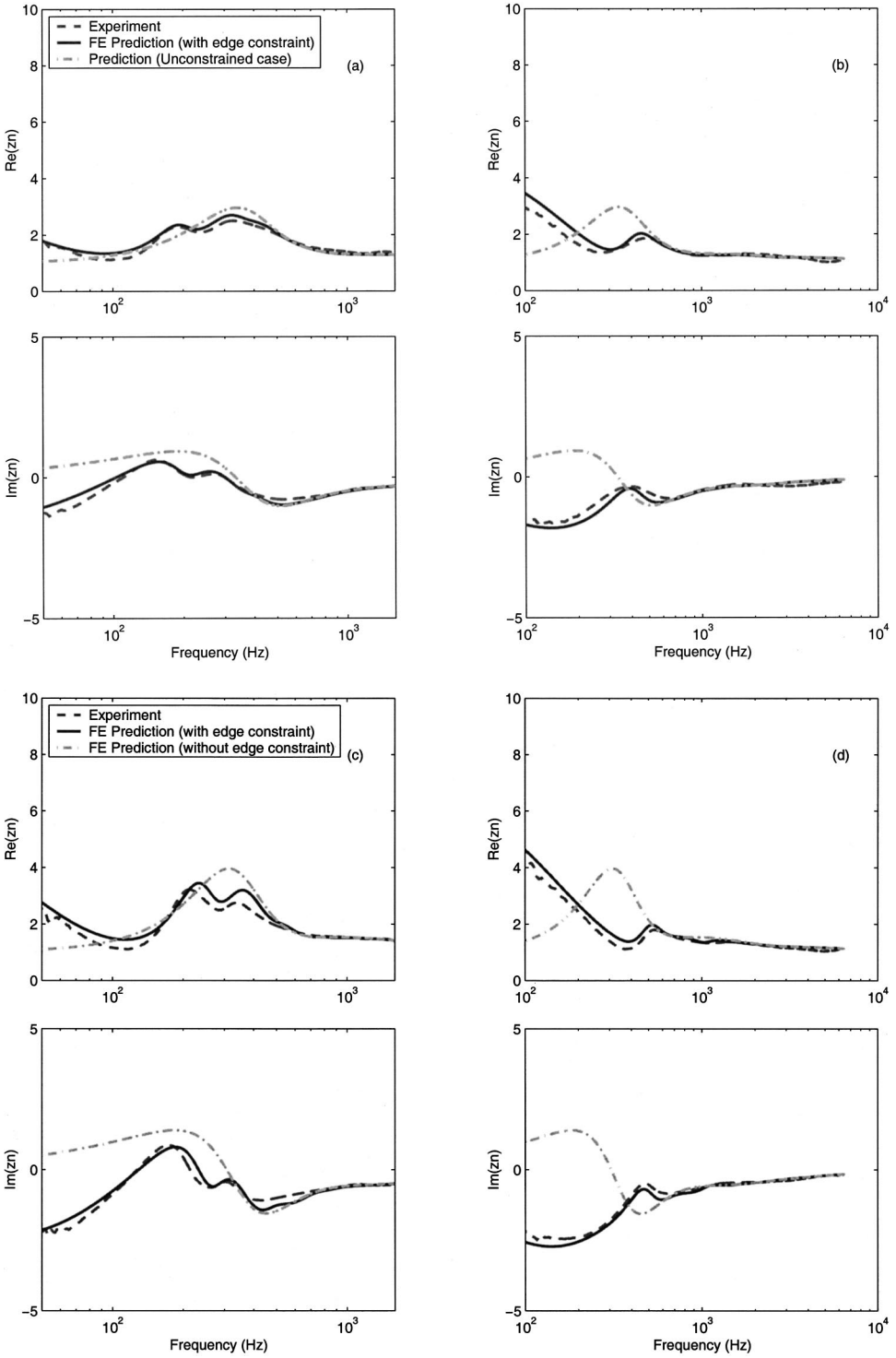

FIG. 10. Measured and predicted surface normal impedances: (a) yellow material in large tube, (b) yellow material in small tube, (c) green material in large tube, (d) green material in small tube. Line types are as indicated.

eter minimum occurs at approximately 450 Hz [Fig. 8(d)] while the corresponding minimum in the large diameter case occurs at approximately 150 Hz [Fig. 8(c)]. Thus the change in resonance location is approximately inversely proportional to the sample diameter as would be expected for a transverse resonance of the sample.

By comparing the measured and FEM-predicted results to predictions made without imposing an edge constraint, the effect of the latter is clear, i.e., the constraint causes the transmission loss to increase at low frequencies. As shown in Fig. 7(a), the low frequency limit of the transmission loss in the constrained configuration is controlled by the flow resistivity. The low frequency limiting behavior is particularly clear in the small diameter configuration for both materials [Figs. 8(b) and (d)]. It can be seen that the edge constraint causes the transmission loss of the small diameter samples to be increased by approximately 7 dB at 100 Hz in the case of the yellow materials, and by approximately 10 dB at 100 Hz for the green material. Thus, it may be concluded that the major effect of the edge constraint is to increase the transmission loss of the materials at low frequencies. Note that the transmission loss calculated according to the mass law

(i.e., assuming a limp barrier having the same mass per unit area as the glass fiber layer) is essentially the same as that of the unconstrained glass fiber layer in the region $(\sigma/\rho_1\omega) \gg 1$. For the yellow and green materials at 100 Hz, the mass law predictions for the transmission loss are 0.6 and 1.1 dB, respectively. Thus below the first shearing resonance the transmission loss of the edge-constrained glass fiber layers is well in excess of that of limp, impervious layers having equivalent masses per unit area.

It is believed that in the low frequency limit, the fibrous samples behave like rigid porous materials owing to the effect of the edge constraint. Thus the low frequency asymptotic behavior of rigid porous media was investigated by using a Biot–Allard-like relaxation model presented by Wilson.[27,28] As shown in the Appendix, the Biot–Allard-like relaxation model takes on a simple form in the low frequency limit and may easily be used to estimate the limiting values of the transmission and reflection coefficients and the surface normal impedance. By using this approach the low frequency limits of the transmission losses of the yellow and green samples (based on the estimated flow resistivities) were predicted to be 9.3 and 11.7 dB, respectively. These values are in good agreement with both the FE predictions and measurements for both materials in the case of the small diameter tube: See Figs. 8(b) and (d). In the large diameter configuration, the low frequency limit has not been reached for either material at the lowest frequency considered here [see Figs. 8(a) and (c)] owing to the relatively low frequency of the shearing resonance in the large diameter case.

2. Absorption coefficient

The predicted and measured absorption coefficients are shown in Fig. 9. There it may be seen that there is good agreement between the measured and predicted absorption for both yellow and green materials in both large and small diameter configurations. In particular, note that the character of the FEM predictions is much closer to that of the measurements than is that of the unconstrained predictions. Specifically, the latter predictions do not reproduce the local absorption peaks that occur for both materials in both configurations and that are associated with the corresponding transmission loss minima. In addition, the unconstrained predictions indicate that the absorption should increase monotonically toward unity at low frequencies when in fact the absorption decreases toward a low frequency limit significantly less than unity. The latter behavior is clear in the small diameter results for both materials: See Figs. 9(b) and (d). Note that the low frequency absorption is smaller in the constrained than in the unconstrained cases. But note that in the unconstrained case the ''absorption'' results primarily from sound transmission through the sample rather than from dissipation within the material as in the constrained case.

Based on the Biot–Allard-like relaxation model,[27,28] the low frequency limits of the absorption coefficients of the yellow and green samples are predicted to be 0.57 and 0.45, respectively. These predictions are in reasonable agreement with both the FE predictions and measurements in the small diameter case: See Figs. 9(b) and (d). However, the low frequency limit has not been reached in the large tube case at the lowest frequency considered here: See Figs. 9(a) and (c).

3. Surface normal impedance

The surface normal impedance results are shown in Fig. 10. Once again it may be seen that there is good agreement between the measurements and the FEM predictions for both the yellow and green materials. By comparison with the unconstrained predictions, it may be seen that the major qualitative effect of the edge constraint is to make the imaginary component of the impedance negative at low frequencies. i.e., to change the low frequency behavior of the sample from mass-like to stiffness-like. In the unconstrained case, it is presumed that at low frequencies the solid and fluid phases move together owing to the good coupling of the solid and fluid phases in this frequency range. Thus, in the low frequency limit, the most important property of the unconstrained sample is its inertia (note the mass-like linear increase of the reactance in the low frequency range in the unconstrained results). When constrained, the sample must shear at low frequencies to accommodate the acoustical motion, and so the most important property of the material in this case is its shear stiffness: hence the low frequency, stiffness-like impedance in the constrained case. In addition, the edge constraint causes the low frequency resistance to increase in both large and small configurations compared to the unconstrained prediction. Note that the low frequency limit of the resistance in the unconstrained case approaches zero since, in that case, the solid and fluid phases move together, there therefore being no relative motion between the two phases, and thus no resistance. In the constrained case, there must always be relative motion between the fluid and solid phases in the low frequency limit since the solid phase is constrained to have zero axial velocity at its circumference while there is no similar constraint imposed on the fluid phase. Thus, in the constrained case, it is believed that the resistance should increase with decreasing frequency to a limit of $\rho_0 c + \sigma d$ (see the Appendix) as for a rigid porous material. Here that limit has not yet been reached at the lowest frequencies considered in either the small or large diameter tube cases. Note finally that as suggested previously,[12,13] the edge constraint has a marked effect on both the real and imaginary parts of the impedance, as opposed to the case of circumferential air gaps which primarily affect the real part of the impedance.[9,15]

4. General comments

In summary, there is generally good agreement between the measured acoustical properties of the glass fiber samples and FEM predictions that take account of the sample edge constraint. The major effects of the edge constraint, i.e., the enhancement of the low frequency transmission loss and the low frequency stiffening of the material are accurately reproduced by the finite element predictions. The quality of the fit to the measured data could probably be improved by using an automatic optimization procedure, e.g., if it were possible to run COMET/ACOUSTICS inside a multidimensional optimization program so that the shear modulus, loss factor, and

flow resistivity could be optimized simultaneously. Nevertheless, the quality and consistency of the fits achieved here indicate that the major physical phenomena involved are represented accurately in the current model.

The values of the shear modulus and loss factor identified as part of the current work were somewhat larger than expected based on earlier work. But as suggested previously,[5] fibrous materials of the type considered here may exhibit relatively large stiffnesses at low strains, perhaps because of friction locking of the fibers or because of the slight compression of the material when it is constrained in the sample holder. Note that similarly large values for the *in vacuo* loss factors of aviation-grade glass fibers have also been measured recently in independent work not yet reported.[29]

C. Effect of edge constraint strength

When lightweight materials of the type considered here are placed in a standing wave tube, it is difficult to ensure uniform contact between the sample and the tube wall. Thus the strength of the edge constraint may vary along the length of the sample, and from sample to sample. Thus, it was of interest here to demonstrate the effect of varying the strength of the edge constraint. Here the degree of constraint was adjusted by varying the stiffness of the poroelastic elements immediately adjacent to the duct wall, i.e., the upper row of elements in Fig. 3(a). Here the green material, small diameter case was considered. For a Poisson's ratio of 0.45 and for Young's moduli ranging from 400 to 7000 Pa for the outer row of elements, the transmission loss and absorption coefficient were calculated: See Figs. 11(a) and (b), respectively. It may be seen that as the stiffness of the outer row of elements is reduced, thus reducing the degree of the constraint, both the transmission loss and absorption coefficient results approach those expected for the unconstrained case. It may thus be concluded that the edge constraint effect generally, and the enhancement of low frequency transmission loss in particular, depends on the quality of the contact between the porous material and the constraining surface. Note also that as the degree of edge constraint increases, the first peak in the absorption results shifts to higher frequencies and is reduced in magnitude as found earlier for foams.[8,12]

D. Effect of tube diameter on material property estimates

As a final note, the measured and predicted transmission losses and absorption coefficients measured using both small and large diameter tubes for the green material are plotted in Fig. 12 along with the corresponding constrained and unconstrained predictions.

It may be seen in Fig. 12(a) that the transmission loss measured in the large tube approximates the unconstrained case at frequencies above 100 Hz. The corresponding results measured using the small diameter tube approximate the unconstrained case at frequencies above 1 kHz. Thus, if it is wished to estimate the normal incidence sound transmission properties of large, unconstrained samples, the results from the large and small diameter tubes can be combined to span the frequency range 100 Hz–6.4 kHz, at least for the types of materials considered here.

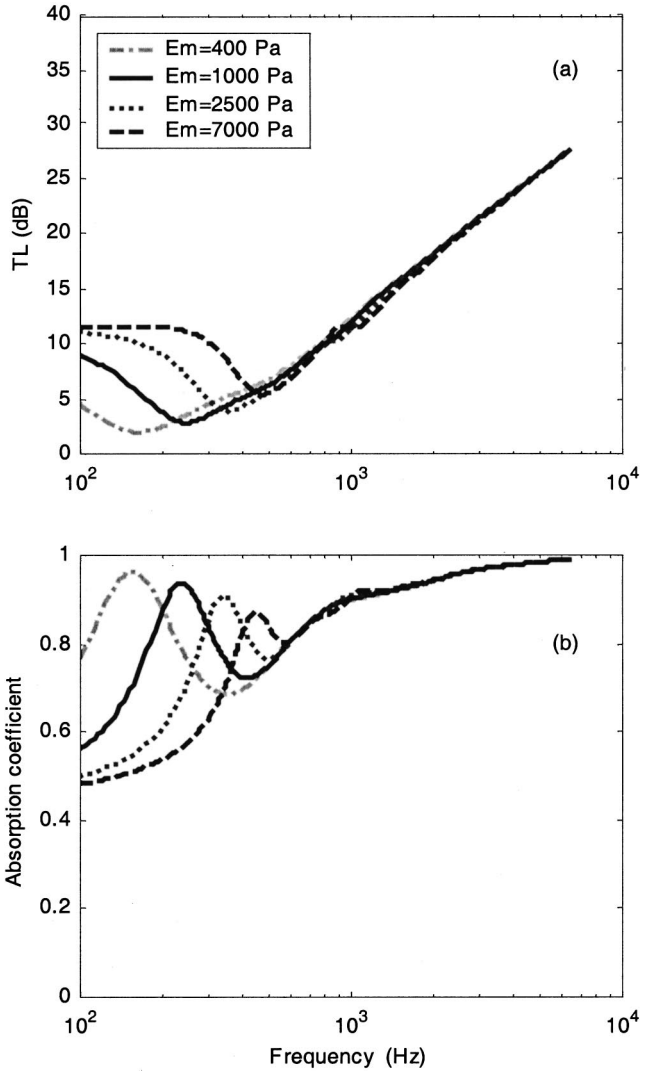

FIG. 11. The effect of varying the degree of edge constraint of the green material on: (a) transmission loss and (b) absorption coefficient.

The corresponding absorption coefficient results are shown in Fig. 12(b). There it may be seen that the large diameter results do not closely approach the unconstrained results until approximately 700 Hz. The small diameter results converge to the unconstrained case at approximately the same frequency. Thus absorption coefficient results for lightweight, relatively high flow resistivity materials of the type considered here should be treated with some caution at low frequencies, even when measured in a large diameter tube, if the intention of the measurements is to infer the properties of large, unconstrained pieces of material.

VI. CONCLUSIONS

The work reported here has confirmed that one effect of sample edge constraint in a standing wave tube is to stiffen the sample at low frequencies as suggested by earlier numerical results. This effect was found to have a significant impact on both the transmission loss and absorption coeffi-

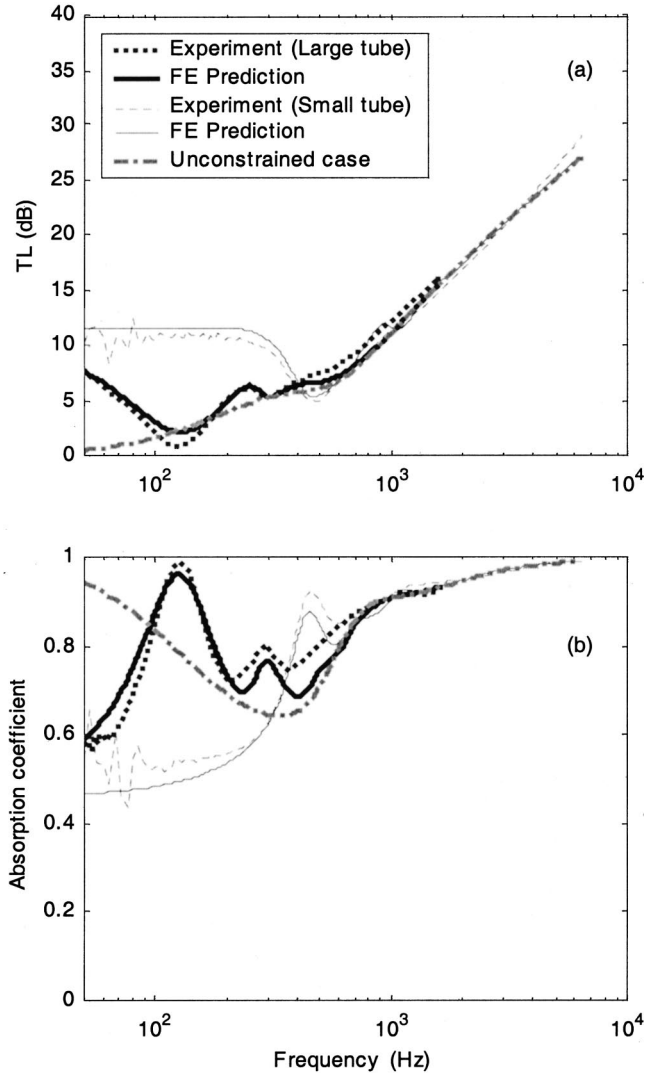

FIG. 12. Superimposed low and high frequency measurements and predictions for the green material: (a) transmission loss and (b) absorption coefficient.

cient. Thus the low frequency, normal incidence acoustical properties of porous materials measured in standing wave tubes should be treated with some caution if the intent of the measurements is to infer the properties of large area samples of the same materials. It was also shown here that the edge-constraint effect could be reproduced with reasonable fidelity by finite element predictions. However, the most striking experimental finding was that the transmission loss of edge-constrained porous materials is substantially enhanced beyond that expected for large area samples of the same material below the frequency of the first shearing mode of the sample (given that $\sigma/\rho_1\omega \gg 1$). It was found that for fibrous materials of the type considered here, the low frequency limit of the transmission loss of constrained samples is controlled by the material's flow resistivity. When the material has a relatively high flow resistivity, as in the present case, the transmission loss in this low frequency, flow resistivity-controlled region can be well in excess of that predicted on the basis of the material's mass per unit area. It is conceivable that this effect might be used to enhance the low frequency transmission loss of lined barriers if the lining were divided into segments that are held within a rigid frame. Thus the current findings may have practical implications for the design of noise control barriers.

ACKNOWLEDGMENTS

The experimental work reported here was performed while B.H.S. was a visiting student in the School of Mechanical and Aerospace Engineering at Seoul National University. He and J. S. B. are grateful to Y. J. K. both for his gracious hospitality and for providing the facilities required to perform the experimental work.

APPENDIX: LOW FREQUENCY LIMITS OF R_a, T_a, Z_{na}, AND α_a FOR RIGID POROUS MEDIA

In this Appendix, low frequency limiting expressions for the reflection coefficient, R_a, transmission coefficient, T_a, and surface normal impedance, Z_{na}, are derived for the case of an anechoically terminated, finite-depth, rigid porous layer. The derivation is based on the rigid porous material, Biot–Allard-like, relaxation model presented by Wilson.[27,28] In Wilson's model, the characteristic impedance and wave number are given by [Ref. 28, Eqs. (7) and (8)]

$$\frac{\rho_p c_p}{\rho_0 c} = \frac{q}{\Omega}\left[\left(1+\frac{\gamma-1}{\sqrt{1+j\omega\tau_{\text{ent}}}}\right)\left(1-\frac{1}{\sqrt{1+j\omega\tau_{\text{vor}}}}\right)\right]^{1/2}, \tag{A1}$$

$$\frac{k_p}{k} = q\left[\left(1+\frac{\gamma-1}{\sqrt{1+j\omega\tau_{\text{ent}}}}\right)\Big/\left(1-\frac{1}{\sqrt{1+j\omega\tau_{\text{vor}}}}\right)\right]^{1/2}, \tag{A2}$$

where $\rho_p c_p$ represents the characteristic impedance of the porous material, k_p is the wave number of the porous material, $\rho_0 c$ is the characteristic impedance of air, k is the wave number in air, q is the tortuosity (in Wilson's notation), Ω is the porosity, γ is the specific heat ratio, τ_{ent} is the characteristic time for the entropy mode, τ_{vor} is the characteristic time for the vorticity mode, and here an $e^{+j\omega t}$ sign convention has been assumed. In these expressions,

$$\tau_{\text{vor}} = \frac{2\rho_0 q^2}{\Omega\sigma}, \tag{A3}$$

$$\tau_{\text{ent}} = N_{\text{Pr}} s_B^2 \tau_{\text{vor}}, \tag{A4}$$

where σ represents the flow resistivity, N_{Pr} is the Prandtl number, and S_B is the pore shape factor. When it is assumed $\omega\tau_{\text{ent}} \ll 1$, $\omega\tau_{\text{vor}} \ll 1$, that products of small terms may be neglected, and that $1/\sqrt{1+j\omega\tau_{\text{vor}}}$, for example, can be expressed as $1-j\omega\tau_{\text{vor}}/2$, the characteristic impedance and wave number simplify to

$$\frac{\rho_p c_p}{\rho_0 c} = \sqrt{\frac{\sigma}{2\omega\rho_0\Omega\gamma}}(1-j), \tag{A5}$$

$$\frac{k_p}{k} = \sqrt{\frac{\sigma\Omega\gamma}{2\omega\rho_0}}(1-j). \tag{A6}$$

Next, note that the transfer matrix for a depth d of homogeneous, rigid porous material is[1]

$$\begin{bmatrix} T_{11} & T_{12} \\ T_{21} & T_{22} \end{bmatrix} = \begin{bmatrix} \cos k_p d & j\rho_p c_p \sin k_p d \\ j \sin k_p d/\rho_p c_p & \cos k_p d \end{bmatrix}. \quad \text{(A7)}$$

When it is assumed that $|k_p d| \ll 1$ (i.e., that the layer depth is small compared to a wavelength), Eq. (A7) becomes

$$\begin{bmatrix} T_{11} & T_{12} \\ T_{21} & T_{22} \end{bmatrix} = \begin{bmatrix} 1 & j\rho_p c_p k_p d \\ jk_p d/\rho_p c_p & 1 \end{bmatrix}. \quad \text{(A8)}$$

After substituting Eqs. (A5) and (A6) into Eq. (A8), the latter, in turn, becomes

$$\begin{bmatrix} T_{11} & T_{12} \\ T_{21} & T_{22} \end{bmatrix} = \begin{bmatrix} 1 & \sigma d \\ jkd\gamma\Omega/\rho_0 c & 1 \end{bmatrix}. \quad \text{(A9)}$$

The normal reflection and transmission coefficients and the surface normal impedance for the case of an anechoic termination can be written in terms of the transfer matrix elements as

$$R_a = \frac{T_{11} + T_{12}/\rho_0 c - \rho_0 c T_{21} - T_{22}}{T_{11} + T_{12}/\rho_0 c + \rho_0 c T_{21} + T_{22}}, \quad \text{(A10)}$$

$$T_a = \frac{2e^{jkd}}{T_{11} + T_{12}/\rho_0 c + \rho_0 c T_{21} + T_{22}}, \quad \text{(A11)}$$

$$Z_{\text{na}} = \frac{T_{11} + T_{12}/\rho_0 c}{T_{21} + T_{22}/\rho_0 c}. \quad \text{(A12)}$$

When the transfer matrix elements from Eq. (A9) are substituted into Eqs. (A10)–(A12), and ω is set to zero, the latter become, respectively,

$$R_a = \frac{\sigma d}{2\rho_0 c + \sigma d}, \quad \text{(A13)}$$

$$T_a = \frac{2\rho_0 c}{2\rho_0 c + \sigma d}, \quad \text{(A14)}$$

$$Z_{\text{na}} = \sigma d + \rho_0 c. \quad \text{(A15)}$$

Finally, the normal incidence, anechoic absorption coefficient becomes

$$\alpha_a = \frac{4\rho_0 c(\rho_0 c + \sigma d)}{(2\rho_0 c + \sigma d)^2}. \quad \text{(A16)}$$

[1] B. H. Song and J. S. Bolton, ''A transfer matrix approach for estimating the characteristic impedance and wave number of limp and rigid porous materials,'' J. Acoust. Soc. Am. **107**, 1131–1152 (2000).

[2] J. S. Bolton, R. J. Yun, J. Pope, and D. Apfel, ''Development of a new sound transmission test for automotive sealant materials,'' Society of Automotive Engineers 1997 Transactions 106, J. Passenger Cars (Section 6) 2651–2658 (1997).

[3] L. L. Beranek, ''Some notes on the measurement of acoustic impedance,'' J. Acoust. Soc. Am. **19**, 420–427 (1947).

[4] J. S. Bolton, ''Normal incidence absorption properties of single layers of elastic porous materials,'' J. Acoust. Soc. Am. Suppl. 1 **78**, S60 (1985).

[5] J.-F. Allard, C. Depollier, P. Guignouard, and P. Rebillard, ''Effect of a resonance of the frame on the surface impedance of glass wool of high density and stiffness,'' J. Acoust. Soc. Am. **89**, 999–1001 (1991).

[6] C. W. Kosten and J. H. Janssen, ''Acoustic properties of flexible and porous materials,'' Acustica **7**, 372–378 (1957).

[7] J.-F. Allard and P. Delage, ''Free field measurements of absorption coefficients on square panels of absorbing materials,'' J. Sound Vib. **101**, 161–170 (1985).

[8] U. Ingard, F. Kirschner, J. Koch, and M. Poldino, ''Sound absorption by porous, flexible materials,'' Proc. INTER-NOISE **89**, 1057–1062 (1989).

[9] A. Cummings, ''Impedance tube measurements on porous media: The effect of air-gaps around the sample,'' J. Sound Vib. **151**, 63–75 (1991).

[10] M. A. Biot, ''Theory of propagation of elastic waves in a fluid-saturated porous solid. I. Low frequency range. II. Higher frequency range,'' J. Acoust. Soc. Am. **28**, 168–191 (1956).

[11] J. S. Bolton, N.-M. Shiau, and Y. J. Kang, ''Sound transmission through multi-panel structures lined with elastic porous materials,'' J. Sound Vib. **191**, 317–347 (1996).

[12] Y. J. Kang and J. S. Bolton, ''Finite element modeling of isotropic elastic porous materials coupled with acoustical finite elements,'' J. Acoust. Soc. Am. **98**, 635–643 (1995).

[13] Y. J. Kang and J. S. Bolton, ''A finite element model for sound transmission through foam-lined double panel structures,'' J. Acoust. Soc. Am. **99**, 2755–2765 (1996).

[14] M. A. Biot, ''Mechanics of deformation and acoustic propagation in porous media,'' J. Appl. Phys. **33**, 1482–1498 (1962).

[15] T. F. Johansen, J.-F. Allard, and B. Brouard, ''Finite element method for predicting the acoustical properties of porous samples,'' Acta Acust. **3**, 487–491 (1995).

[16] T. E. Vigran, L. Kelders, W. Lauriks, P. Leclaire and T. F. Johansen, ''Prediction and measurements of the influence of boundary conditions in a standing wave tube,'' Acta Acust. **83**, 419–423 (1997).

[17] T. Pritz, ''Transfer function method for investigating the complex modulus of acoustic materials: Spring-like specimen,'' J. Sound Vib. **72**, 317–341 (1980).

[18] T. Pritz, ''Frequency dependence of frame dynamic characteristics of mineral and glass wool materials,'' J. Sound Vib. **106**, 161–169 (1986).

[19] R. Wilson and A. Cummings, ''An impedance technique for determining the dynamic structural properties of a porous material,'' Proc. INTER-NOISE **96**, 269–272 (1996).

[20] K. U. Ingard, *Notes on Sound Absorption Technology* (Noise Control Foundation, Poughkeepsie, NY, 1994).

[21] Anon., ''Standard test method for impedance and absorption of acoustical materials using a tube, two microphones, and a digital frequency analysis system,'' ASTM Stand. News 1050–90 (1990).

[22] S. Temkin, *Elements of Acoustics* (Wiley, New York, 1981).

[23] A. D. Pierce, *Acoustics: An Introduction to its Physical Principles and Applications* (Acoustical Society of America, New York, 1989).

[24] Y. J. Kang, B. K. Gardner, and J. S. Bolton, ''An axisymmetric poroelastic finite element formulation,'' J. Acoust. Soc. Am. **106**, 565–574 (1999).

[25] J.-F. Allard, *Propagation of Sound in Porous Media* (Elsevier, London, 1993).

[26] J.-F. Allard and Y. Champoux, ''New empirical equations for sound propagation in rigid frame fibrous materials,'' J. Acoust. Soc. Am. **91**, 3346–3353 (1992).

[27] D. K. Wilson, ''Relaxation-matched modeling of propagation through porous media, including fractal pore structure,'' J. Acoust. Soc. Am. **94**, 1136–1145 (1993).

[28] D. K. Wilson, ''Simple, relaxational models for the acoustical properties of porous media,'' Appl. Acoust. **50**, 171–188 (1997).

[29] A. Cummings (private communication).

Interpretation of the spectra of energy scattered by dispersed anchovies

Orest Diachok[a)]
Naval Research Laboratory, Washington, DC 20375

(Received 6 December 2000; revised 31 July 2001; accepted 27 August 2001)

The spectra of backscattered energy by dispersed anchovies, which were reported by Holliday (1972), reveal several peaks at frequencies that correspond to theoretically calculated resonance frequencies of year classes of anchovies. Theoretical calculations are based on concurrent measurements of distributions of swim bladder dimensions and a modified form of Minnaert's (1933) equation. Differences between calculated and measured values of the mean lengths of the second-, third-, and fourth-year classes are within experimental uncertainties ($\pm 8\%$). The calculated mean lengths of juvenile anchovies are in good agreement with historical measurements of the bounds on this parameter (Butler, 1989). Matching of theoretical calculations and measurements of backscattered energy level versus frequency yields estimates of the total Q of the spectral line, Q_T, and the relative number density per year class. The resultant estimate of Q_T of adult anchovies is approximately 4.4. This value of Q_T is consistent with laboratory measurements of the Q of individual anchovies, Q_0 (~ 7 at 15 m) and measurements of length distributions of year classes and depth distributions. Resultant estimates of relative number densities of year classes were consistent with historical measurements of the relative number densities of year classes of anchovies in the Southern California Bight. [DOI: 10.1121/1.1413996]

PACS numbers: 43.30.Ft, 43.30.Sf, 43.30.Vh [DLB]

I. INTRODUCTION

In 1972 Holliday published his pioneering paper on resonance scattering from fish with swim bladders. His acoustic measurements, which were made over the frequency range, 0.2–5.0 kHz, revealed that backscattered energy from anchovies exhibited peaks in the vicinity of calculated resonance frequencies of their swim bladders. Calculations were based on concurrent trawls, which showed that anchovies were the dominant species at his experimental sites at that time. These measurements were made at four widely separated sites in the Southern California Bight. Three of the measurements were made during the day (sites A, B, and C), and one at night (site D). The details of the experimental methods, data processing procedures, and the biological sampling strategy are described in Holliday (1972).

Anchovies form schools during the day. At night they typically reside in dispersed mode relatively close to the surface. The separation between anchovies, when they are in schools during the day, is normally one fish length (Graves, 1977), and the separation to wavelength ratio at the resonance frequency is much less than one (Diachok, 1999). Under this condition, schools act as ''bubble clouds,'' the resonance frequency of clouds is downshifted relative to the resonance frequency of a single fish, and the scattering and extinction cross sections (per fish) are reduced (Feuillade *et al.*, 1996; Diachok, 1999). Quantitative interpretation of Holliday's daytime measurements is complicated by limitations of existing theoretical models of bubble cloud effects. The model of Feuillade *et al.*, which provides the most accurate description of scattering by an ensemble of identical, closely spaced bubbles in the vicinity of the resonance frequency, is limited to schools which contain less than 100 fish; whereas actual schools contain 10^4–10^5 fish. At night these fish are dispersed (Aoki and Inagaki, 1988), and the separation to wavelength ratio at the resonance frequency is nominally equal to or greater than one. Under this condition, anchovies act as individual bubbles and the scattering and extinction cross sections may be computed from first principles (Feuillade and Werby, 1994; Foote, 1985).

Holliday (1972) assumed the following in his theoretical calculations of the spectra of backscattered energy. The spectrum may be calculated from the theory of scattering by a large number of identical, elongated air-filled bubbles. The effective radius of elongated bubbles was assumed to be equal to the radius of a sphere with the same volume. Q was assumed to be equal to the laboratory-based value of the Q of an individual fish, which at 6 m depth was equal to 5 (Baltzer and Pickwell, 1970). Effects of distributions of length and depth on spectral spreading (Q), and effects due to close proximity between fish in schools, were assumed to be negligible. These assumptions resulted in calculated spectra that were in fair agreement with both his daytime and nighttime measurements. In his later work, Holliday (1978a, b, c) provided analysis of broadband backscattering data, which were recorded during daytime in 1977, and showed that it is possible to isolate juvenile anchovies, adult anchovies, and adult mackerel in frequency space.

Subsequently, Feuillade *et al.* (1996) demonstrated that Holliday's (1972) daytime measurements (site A) were in better agreement with theoretical calculations, which incorporated the effects of close proximity between fish in schools. Their calculations, however, should be considered heuristic due to the limitations of their model, and their disregard of the effects of length and depth distributions on spectral spreading.

a)Electronic mail: orest@wave.nrl.navy.mil

Clay (1991) noted that Holliday's nighttime measurements (site D) were not consistent with Holliday's assumptions and Q equal to 5, and claimed that these data were in better agreement with calculations, which were based on his ''bent cylinder'' model of the swim bladder, and Q equal to 1.5. Clay, however also disregarded the effects of length and depth distributions on spectral spreading.

Anchovies, as well as other fish, may be characterized by their age and length. Juvenile anchovies, which are less than 1 year old, are generally smaller than about 10 cm. Juveniles occur in the largest numbers; and as they age their lengths increase, and their number densities per year class decline. There are, on average, progressively smaller numbers of 1, 2, and 3 year olds (Smith, 1999). In the Southern California Bight 1, 2, and 3 year olds are approximately 10, 12, and 14 cm long, respectively.

The objective of this paper is to review Holliday's nighttime measurements (site D), which are hypothetically not subject to bubble cloud effects, and to interpret these results in terms of scattering by dispersed anchovies that belong to specific year classes. This paper is organized as follows. Sections II, III, and IV provide summaries of the results of Holliday's measurements of length distributions, depth distributions, and backscattering, respectively. The classification of peaks observed in the spectrum of backscattered data is discussed in Sec. V. Section VI provides a description of the bioacoustic model, and a comparison of calculations with measurements. Sections VII and VIII provide comparisons of inferred values of Q (a measure of spectral width), and number density versus year classes from backscattering measurements, with concurrent and previously reported trawling data. Conclusions and recommendations for future research are summarized in Sec. IX.

II. MEASUREMENTS OF LENGTH DISTRIBUTIONS

The peak spawning time for anchovies in the Southern California Bight in the vicinity of site D is mid-March (Methot, 1981). The peak spawning month wanders by approximately ± 1 month from year to year. The standard deviation of spawning times within one year is approximately ± 1 month. The variation in spawning time is probably an important contributor to the spread in length distributions of all year classes. Multiple peaks in length distributions of juveniles have been observed (Holliday, 1978a, b, c), and hypothetically occur (Methot, 1983) as a result of several phenomena. Spawning is episodic (Hunter and Goldberg, 1980), and the growth and mortality of juveniles may be modulated by the temporal and spatial variability of prey and predators, and environmental conditions (Smith, private communication). The rate of growth is rapid during the first year and slower in subsequent years, as illustrated in Fig. 1 (Butler, 1989). Figure 1 illustrates the typical growth rate during the juvenile stage. The growth rates of juveniles spawned near the beginning (January) and end (May) of the spawning season are about 10% smaller. The growth rate of juveniles spawned during ''El Nino'' events is about 20% smaller. Both rate changes are probably due to lower densities of plankton concentrations during these periods.

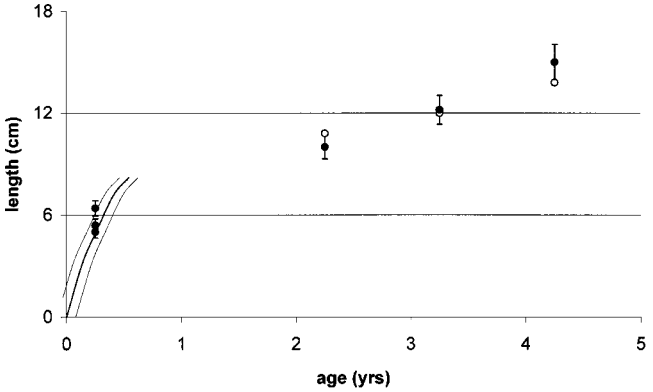

FIG. 1. Historical measurements of lengths of juvenile anchovies versus age starting from February 15 (—), March 15 (—), and April 15 (—) during a ''normal'' year (Butler, 1989), and the average lengths of adult anchovies derived from trawls (○) and backscattering data (●) versus age relative to March 15 derived from Holliday's (1972) data. Error bars indicate the uncertainty in backscattering based estimates of mean lengths: ±7%.

Holliday's trawling measurements were made in mid-June, three months (0.25 years) after the peak spawning time. Length distributions of juveniles could not be measured due to mesh size. His measurements indicate that site D was dominated by 2.25, 3.25, and 4.25 year old anchovies, which were on average 10.7, 12.2, and 13.6 cm long, respectively. It is noteworthy that mean lengths of year classes at sites D (25 samples) and C (90 samples), a nearby location, were approximately equal (within 0.2 cm). The mean lengths of 2.25 and 3.25 year old anchovies at sites A and B were larger, probably due to systematic geographical variations in this parameter (Parrish *et al.*, 1985). Since the data at sites C and D appear to be representative of the same population, they were combined to provide a larger database. The result is illustrated in Fig. 2. These data indicate that the average lengths of 2.25, 3.25, and 4.25 year olds were 10.8 ± 0.1, 12.1 ± 0.2, and 13.8 ± 0.3 cm, respectively. These measurements are consistent with previously reported measurements of these parameters in the Southern California Bight (Mallicoate and Parrish, 1981). There are insufficient data to determine if the distributions were non-Gaussian. The 3 dB down points of 2.25 year old anchovies were approximately ± 0.6 cm. The corresponding Q due to length distributions, Q_L, is 9. There are insufficient measurements of 3.25 and 4.25 year

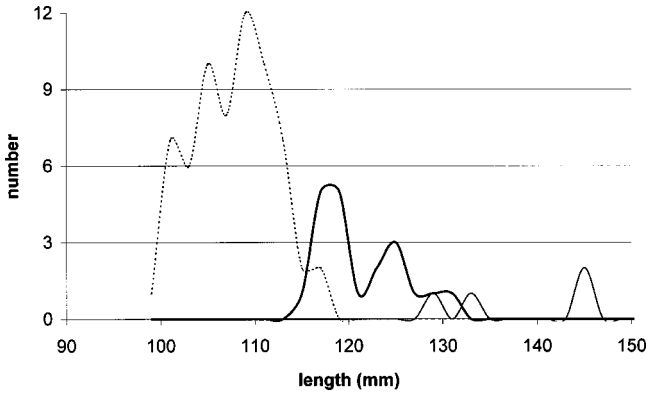

FIG. 2. The number versus length of 2.25 (···), 3.25 and 4.25 year old anchovies at sites C and D (Holliday, 1972).

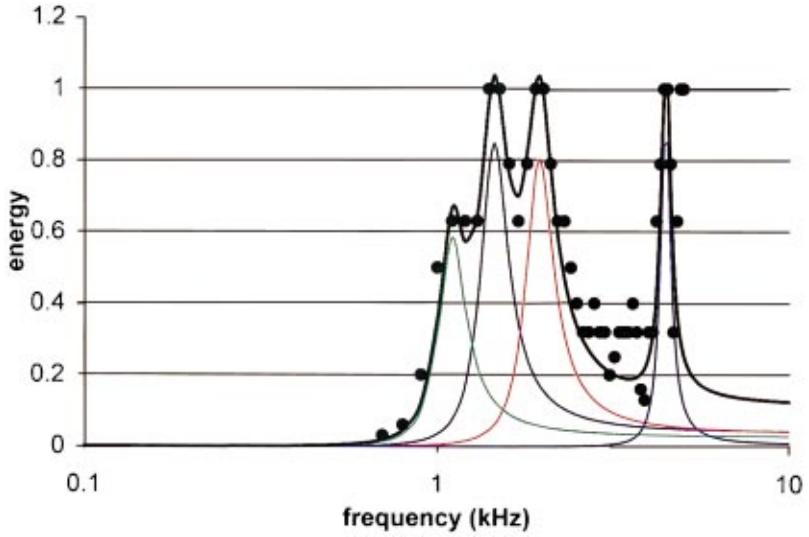

FIG. 3. Measurements (●) due to Holliday (1972) and calculations of backscattered energy versus frequency. Resonance frequencies of 4.45 (blue), 1.95 (red), 1.45 (blue), and 1.10 (green) kHz correspond to 0.25, 2.25, 3.25, and 4.25 year old dispersed anchovies. The heavy solid line represents the sum of contributions from year classes.

old anchovies to permit an accurate estimate of Q_L of these year classes. Mais' (1974) data indicate that Q_L is approximately independent of year class.

III. MEASUREMENTS OF DEPTH DISTRIBUTIONS

Holliday measured the depth distribution of anchovies with a hull mounted echo sounder. These measurements indicated that anchovies occupied depths between 10 and 20 m, and that the mean depth was approximately 15 m. The actual distribution of anchovies at this site was not reported. However, even if it had been reported, the measurement would have probably been biased by avoidance behavior. If anchovies were distributed uniformly over the interval, 10–20 m, then the standard deviation would be ± 2.9 m, which represents the upper bound. Previously reported echo sounder measurements at another site during spring suggest that the standard deviations of dispersed anchovies at night are equal to or less than ± 2 m (Barange *et al.*, 1996). The layer thickness of anchovies is hypothetically driven by the thickness of plankton layers, which may be as thin as 1 m during periods when there is a strong thermocline (Holligan and Harbour, 1977). These values correspond to Q's associated with depth distribution, Q_z, of 5.5 and 8, respectively. The actual thickness may have been less than 2 m, and the actual value of Q_z may have exceeded 8.

IV. MEASUREMENTS OF THE SPECTRUM OF BACKSCATTERED ENERGY

The spectrum of Holliday's measurements of backscattered energy at site D is shown in Fig. 3. This spectrum represents an ensemble average of several measurements. It should be noted that Fig. 3 provides relative energy levels, whereas Holliday's original data (his Fig. 7) is in decibels. Measurements were reported every 0.1 kHz. It should be noted that there are prominent peaks evident in this data at 1.45, 1.95, 4.45, and $\geqslant 5.0$ kHz. There also appear to be elevated energy levels at about 1.1 kHz, and slight peaks at 2.8 and 3.6 kHz.

V. CLASSIFICATION OF SPECTRAL PEAKS

The resonance frequency, f_0, of the swim bladders of anchovies is a function of the effective radius of the swim bladder at the surface, r_0, a correction for the eccentricity of the swim bladder, ϵ, and the depth of the fish, d, in accordance with a modified form of Minnaert's (1933) equation (Weston, 1967):

$$f_0 = 322\epsilon(1+0.1d)^{5/6}/r_0, \tag{1}$$

where f_0 is in hertz, d is in meters, r_0 is in centimeters, and ϵ is nondimensional. This equation is in good agreement with most near-surface ($\sim$6 m) laboratory measurements of the resonance frequencies of physostomes. Controlled measurements of f_0 of anchovies (Baltzer and Pickwell, 1970), char (Sundness and Sand, 1975), sprat and herring (Lovik and Hovem, 1979) were, respectively, 3%, 1%, 7%, and 22% higher than calculated values of f_0 based on Eq. (1), and measured values of r_0 and ϵ at the surface. Foote's (1985) observations suggest that the primary cause of differences between calculations and measurements is due to uncertainties associated with calculations of r_0 and ϵ from measurements of maximum lengths and widths. Equation (1) may be used to calculate the effective radii of swim bladders from measurements of f_0, provided that the magnitudes of d and ϵ are known, effects due to compression of swim bladders by gonads and full stomachs (Ona, 1990) are small, and the amount of gas in the swim bladder is independent of depth.

Holliday (1972) did not report on the number density of anchovies versus depth at site D, but it may be assumed that the distribution was nearly Gaussian (Barange *et al.*, 1996), and that the average depth was approximately 15 m. It will be assumed that the value of d was the same for all year classes. This assumption is consistent with the experimental observation that pelagic fish occupy depths at night where plankton concentrations are maximum (Culley, 1971); not at depths where they are neutrally buoyant.

Holliday's (1972) measurements were made in mid-June, after the peak of the spawning season, when the gonads of most anchovies were small. The stomachs of the majority of anchovies, which have been examined at sea, were essen-

tially empty (Loukashkin, 1970). In general, the compressive effects of gonads and full stomachs on physostomes' swim bladders may be expected to decrease with increasing depth.

The eccentricity of swim bladders of anchovy larvae changes ''abruptly'' from approximately 3 to 7 when they undergo metamorphosis, when they are about 3.5 cm long (Holliday, 1978a, b, c; Smith, 1999). The smallest anchovies, which will be considered in this paper, are larger than this critical length.

It will be assumed in this paper that transfer of gas between the swim bladder and the auditory ''bulla'' system, gas diffusion through the swim bladder membrane, and swallowing of air at the surface do not have a significant effect on swim bladder dimensions (Blaxter *et al.*, 1979). The amount of gas in adult physostomes' swim bladders is only approximately constant (Blaxter *et al.*, 1979). Their swim bladders are connected to the stomach by a narrow duct, and to the auditory ''bulla'' system by very fine ducts. The membrane, which surrounds the auditory system, is much less compliant than the swim bladder. As a result, as a physostome moves downward, a small amount of gas passes from the swim bladder to the auditory system, and in the reverse direction during ascents (Blaxter *et al.*, 1979). This phenomenon results in a small, depth-dependent reduction in the magnitude of r_0. In addition, physostomes lose gas very slowly (over periods of tens of days) by diffusion through the swim bladder membrane, and can replenish gas by occasionally swallowing air at the surface.

The depth dependence of the eccentricity, e, of swim bladders is not known. Investigators generally assume that it is independent of depth (Holliday, 1972; Love, 1993; Nero *et al.*, 1997; and Diachok, 1999). The good agreement between calculated and measured resonance frequencies of anchovies, viz., about 3% (Baltzer and Pickwell, 1970) indicates that this is a good approximation for this species. It will also be assumed that the magnitude of e is independent of year class. Based on these assumptions, frequencies of 1.45, 1.95, 4.45, and $\geqslant$5.0 kHz correspond to values of r_0 of 0.56, 0.42, 0.18, and $\leqslant$0.16 cm, respectively. The elevated levels at about 1.1 kHz correspond to r_0 equal to 0.74 cm, and the slight peak at 3.6 kHz corresponds to r_0 equal to 0.23 cm.

Holliday's (1978a, b, c) measurements of r_0 vs L permit estimation of L from these inferences. The relationship between r_0 and the length, L, of adult and juvenile anchovies taken off the coast of California is shown in Fig. 4. The empirical relationship between these parameters for larvae, which are shorter than 3 mm, is summarized by

$$L = 6.2 + 42.6 r_0, \tag{2}$$

where L is in centimeters and r_0 is in millimeters. This equation was derived from a combination of field and laboratory measurements (Holliday, 1978a, b, c). The empirical relationship between r_0 and L for anchovies, which are between 6 and 15 cm long, is summarized by

$$L = -14.51 + 81.31 \ln r_0, \tag{3}$$

where r_0 is in millimeters. This equation was derived from Holliday's field measurements, which were made in June 1971.

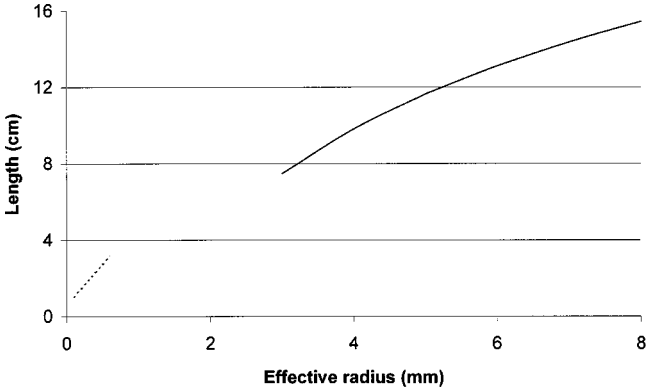

FIG. 4. Relationships between the lengths and effective radii of swim bladders of juvenile (···) and adult (—) swim bladders (Holliday, 1978a, b, c).

Holliday (1978a, b, c) fit another set of measurements of r_0 and L of anchovies, which were between 6 and 15 cm long, and were taken in September 1977 at another site, with another equation. The difference between Eq. (3) and his other equation is approximately $\pm$3%. The uncertainty in his measurements of r_0 is $\pm$5% (Holliday, 2001), the uncertainty in measuring resonance frequencies is approximately $\pm$3%, and the uncertainty in ϵ is approximately $\pm$3%. Consequently, the uncertainty in estimates of the average lengths of year classes, derived from backscattering data, is approximately $\pm$7%. For comparison, the uncertainty in the mean lengths of 2.25, 3.25, and 4.25 year old fish, which were derived from Holliday's trawls, are approximately $\pm$1%, $\pm$2%, and $\pm$3%, respectively.

Based on Eqs. (2) and (3), values of r_0 equal to 0.74, 0.56, 0.42, 0.23, 0.18, and $\leqslant$0.16 cm correspond to anchovy lengths of 15.0, 12.1, 10.0, 6.4, 5.4, and $\leqslant$5.0 cm, respectively. The estimated lengths of juveniles were based on extrapolations between Eqs. (2) and (3). A comparison between these estimates and trawling results is shown in Fig. 1. The difference between calculated and measured length estimates of 2.25, 3.25, and 4.25 year old fish are equal to $-$8%, 0%, and $+$8%, respectively, which are within the calculated experimental uncertainties associated with these year classes ($\pm$8%, $\pm$9%, and $\pm$10%, respectively).

It should be noted that backscattered energy at $\sim$1.1 kHz may have included contributions from several year classes including 4.25, 5.25, and 6.25 year olds, and that the calculated length may correspond to $\sim$5.25 year olds. This hypothesis is consistent with higher than expected number densities associated with this peak, which will be described in Sec. VIII. It should also be noted that trawling discriminates against small 2.25 year old anchovies due to mesh size (Mais, 1974); consequently the actual mean length of this year class may be significantly smaller than the trawling-based estimate.

The peaks at 3.6, 4.45, and $\geqslant$5.0 kHz are consistent with historical measurements of the lengths of juvenile (0.25 year old) anchovies, which were spawned within about 1.5 months of the peak spawning date (Butler, 1989), as shown in Fig. 1. In particular, anchovies which are $\leqslant$5.0, 5.4, and 6.4 cm long correspond to the following spawning times: later than or during mid-March, and approximately 1 March,

and approximately 1 February, respectively. This interpretation is qualitatively consistent with previous observations of multiple peaks in the lengths and birth dates of anchovies in the Southern California Bight (Holliday, 1978a, b, c; Methot, 1983). These lines may be part of a series of lines, some of which may be higher than 5 kHz and correspond to smaller anchovies, which were spawned at a later date.

Other possible causes of one or some of these high frequency peaks in the spectrum ($\geqslant$3.6 kHz): myctophids (nominally 5-cm-long fish with swim bladders), which were observed at some of Holliday's (1972) measurement sites, and siphonophores (zooplankters that are attached to nearly spherical gas ''balloons''). The latter are known to resonate at about 5 kHz (Stanton *et al.*, 1998).

VI. MODEL OF THE SPECTRUM

The level of backscattered energy from an ensemble of identical, widely separated bubbles is equal to the product of the number of bubbles per unit volume, n, and the scattering cross section, σ_S (Clay and Medwin, 1977), where

$$\sigma_S = 4\pi r^2[(1-f_0^2/f^2)^2 + 1/Q_0^2]^{-1} \tag{4}$$

and r is the radius, f is the frequency, f_0 is the resonance frequency, and Q_0 is defined as the Q of the individual fish and is equal to $f_0/\Delta f_0$, where Δf_0 is the width of the resonance measured at the 3 dB down points relative to the peak at f_0.

The measured spectrum will be modeled by assuming that all anchovies may be grouped into year classes in which all of the fish are identical. This assumption is reasonable in view of the apparently high Q_T (4.4) of year classes. An alternative procedure would be to calculate the spectrum based on measured length distributions. This approach, however does not seem warranted in this case, since Holliday's trawling measurements at site D were biased due to mesh size at small lengths and avoidance at large lengths (Holliday, 1972).

Furthermore, it will be assumed that all of the fish are at the same depth. This assumption also seems reasonable in view of the relatively narrow range of depths occupied by anchovies at night, and the high Q_Z (8) associated with their depth distributions.

Following Weston (1967), it was then assumed that Q_0 in Eq. (4) may be replaced by the effective Q of the backscattered energy, Q_T. This equation was then applied to each year class. The calculations shown in Fig. 3 were based on those values of Q_T and n that resulted in the best match to the data. The search assumed that Q_T was independent of year class for adults, but may be different for juveniles. The estimated values of Q_T of adults and juveniles were 4.4 and 12, respectively. The small peak at 3.6 kHz and the apparent peak at $f>5$ kHz, both of which may be due to juvenile anchovies, were disregarded in these calculations, in the interest of clarity.

New measurements, which cover a broader frequency range, are required to investigate the full spectrum of backscattering from juvenile anchovies. The observed lines of backscattered energy at 4.45, $\geqslant$5, and possibly 3.6 kHz may represent only a portion of a larger number of lines associated with juveniles.

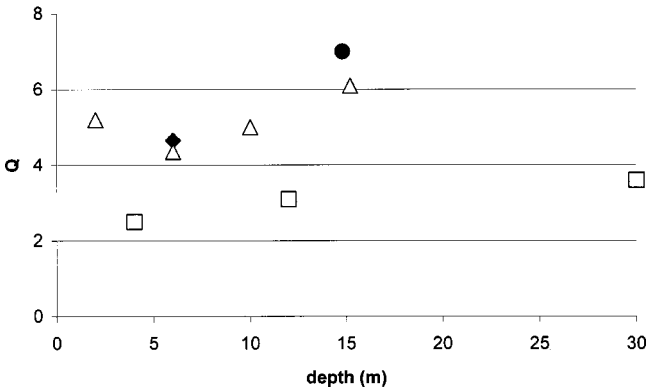

FIG. 5. Laboratory measurements of Q_0 of adult anchovies (♦) (Baltzer and Pickwell, 1970), char (△) (Sundness and Sand, 1975), and sprat (□) (Lovik and Hovem, 1979) versus depth, and the estimated value of Q_0 of adult anchovies derived from backscattering measurements (●).

VII. THE RELATIONSHIP BETWEEN Q_0 AND Q_T

The relationship between Q_T and Q_0, Q_Z and Q_L may be described by a modified form of an equation due to Weston (1967):

$$1/Q_T^2 = 1/Q_Z^2 + 1/Q_L^2 + 1/Q_0^2, \tag{5}$$

where Q_T is the total Q of the backscattered energy ''line,'' Q_Z is associated with the depth distribution, Q_L is associated with length distribution, and Q_0 is the inherent Q of a single swim bladder. Other possible causes of spectral spreading will be assumed to be small. An accurate measure of layer thickness is prerequisite to estimation of Q_0. Assuming that the layer thickness of anchovies was 2 m (Barange *et al.*, 1996), which corresponds to Q_Z equal to 8, and Q_T equals 4.4 and Q_L equals 8, results in Q_0 equal to approximately 7. Disregarding the effect of Q_Z provides an estimate of the lower bound on Q_0, 5.3. These estimates of Q_0 disregard the effects of the spread in values of r_0 (for a fixed value of L) on Q_T. According to Blaxter and Batty (1990), Q_r, which is associated with the spread in values of r_0 of herring, equals about 5. Consequently, the calculated best estimate of Q_0, and the lower bound on Q_0 may be significantly higher than 7 and 5.3, respectively. Assuming that Q_Z equals 5.5 (the lower bound) provides an estimate of the upper bound on the value of Q_0, viz., 18.

Figure 5 provides a comparison between laboratory measurements of the value of Q_0 of anchovies at 6 m (Baltzer and Pickwell, 1970), and two other physostomes, viz., sprat (Lovik and Hovem, 1979) and char at various depths (Sundness and Sand, 1975). These measurements indicate that Q_0 of physostomes increases with depth at depths greater than 6 m. The rate of change of the magnitude of Q_0 with depth between 6 and 15 m of anchovies and charr are comparable. It is noteworthy that the laboratory measurements of Q_0 were made in the near field of the fish, and as a result may not be accurate (Clay, 1991). The magnitude of the uncertainty has not been quantified.

Hypothetically, the apparent species dependence of Q_0

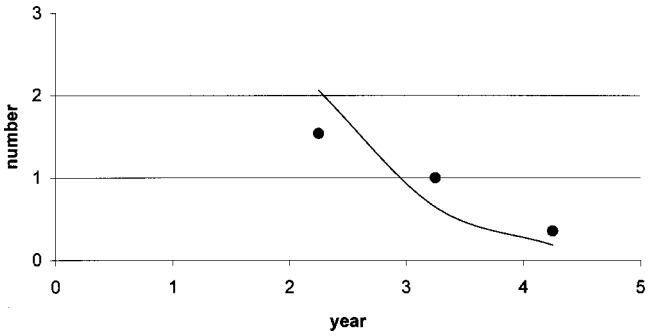

FIG. 6. The relative number of anchovies per year class derived from Holliday's (1972) backscattering measurements (●), and Mais' (1981) trawling data in the Southern California Bight in 1971 (—).

is due primarily to differences in the thickness and viscosity of the swim bladder membrane of these species (Feuillade *et al.*, 1996). The membrane of anchovy swim bladders is thin and ''delicate'' (Holliday, 2001). The ratio of the membrane thickness to effective radius of this species is approximately 0.01 (O'Connell, 1995). For most other species this ratio is larger. For example, the ratio of the membrane thickness to effective radius of cod swim bladders, which has a Q_0 of about 1.0 (at 10 m), is approximately equal to 0.1 (Feuillade and Nero, 1998).

Equation (5) suggests that Q_0 of juveniles is significantly greater than 12, provided that Q_L and Q_Z of juveniles are much higher than for adults. Such high values of Q_0 appear to be reasonable, in view of Artemov's (1991) measurements on 1-cm-long ''scad'' (*Trachurus mediterraneus ponticus*) larvae, which were between 7 and 12. Coincident measurements of the Q_T of adults and juveniles of sardines (Diachok *et al.*, 2000), and other species (Nero, 2000) also indicate that the Q's of adults are less than the Q's of juveniles and larvae. The relatively low Q of adults may be due to the increased amount of fish flesh that surrounds and dampens adult swim bladders. In contrast, larvae have virtually no fish flesh surrounding their swim bladders, and juveniles have a relatively small amount of fish flesh surrounding their swim bladders. The Q_0 of swim bladders, which have been removed from adult anchovies, are typically about 20 (Baltzer and Pickwell, 1970).

According to Holliday (2001), juveniles tend to occupy very thin plankton-rich layers, which are often less than 1 m thick; whereas adults tend to roam over greater depth ranges. This effect hypothetically results in higher values of Q_Z for juveniles. Spawning of anchovies is ''episodic'' (Hunter and Goldberg, 1980), which hypothetically results in narrow length distributions and high values of Q_L. Additional measurements are needed to confirm the validity of these hypotheses and interpretations.

VIII. NUMBER DENSITY

The estimated relative values of the number density decreased with age, qualitatively consistent with the data shown in Fig. 2, and with previously reported trawling measurements. Figure 6 provides a comparison between estimates of n derived from backscattering and historical measurements in 1971 due to Mais (1981). The reference point of these two sets of estimates is arbitrary, and was selected to provide good agreement ($\sim\pm30\%$) for age classes 2.25 and 3.25. Based on this criterion the number of 4.25 year old anchovies, which were derived from backscattering measurements, is approximately two times larger than the estimate derived from trawls. This may be due, in part, to incorrect classification of the backscattering data at 1.1 kHz. The latter may include contributions from several year classes including 4.25, 5.25, 6.25, and older fish.

It should be kept in mind that the backscattering experiments provide a sample over a circular area with a relatively small (<1 km) radius, whereas the historical data (Mais, 1981) represent an average over the entire Southern California Bight. In view of this, it would be unreasonable to expect exact agreement between these measurements. The results shown in this figure should not be interpreted as evidence that these methods yield comparable number densities, since the acoustic data are not calibrated. If the acoustic measurements had been calibrated, then estimation of absolute number densities would have been possible (Love, 1993).

The relative numbers of 1.25 year olds are not shown, because they were apparently not present at Holliday's trawling data. Furthermore, they were not evident in the backscattering data: there was no spectral peak that corresponded to 1.25 year old, $\sim$9 cm long anchovies.

The relative numbers of 0.25 year old anchovies are also not shown, since it may be necessary to take measurements over a broader frequency range than employed by Holliday (1972), to ensure measurement of contributions from the full distribution of juvenile lengths.

IX. SUMMARY, CONCLUSIONS, AND RECOMMENDATIONS FOR FUTURE RESEARCH

This paper provides evidence that juvenile through second- and, to some extent, third and fourth year classes of anchovies in the Southern California Bight may be resolved with broadband, backscattering measurements. Matching theoretical calculations, which account for scattering from an ensemble of identical, elongated, widely spaced bubbles (swim bladders), with measurements of the spectrum of energy backscattered by widely spaced anchovies resulted in estimates of the effective Q_T of these fish, and the relative number density per year class. The resultant estimates of Q_T were consistent with laboratory measurements of the Q of individual anchovies, Q_0, and measured distributions of lengths and depths. Resultant estimates of relative number densities were consistent with historical measurements of the relative number density of year classes of anchovies in the Southern California Bight.

Because of its relatively high Q_T associated with year classes (adults: $\sim$4.4 at 15 m) and rapid growth rate (>1.5 cm/year), anchovies appear to be a good target species for future scattering and absorption spectroscopy experiments. Other fish, such as herring and sardines, are characterized by an apparently smaller Q_0 (Lovik and Hovem, 1979; Diachok, 1999), and a slower growth rate (Lo *et al.*, 1997). As a result, spectral resolution of adult year classes of these species would be more challenging.

The good match between calculations and measurements of spectra supports the hypothesis that scattering by ancho-

vies is dominated by swim bladders, and that the contributions due to flesh and bones are small at frequencies below 5 kHz. It also supports the contention that essentially all of these fish are ''widely separated'' at night.

The validity of the unexpectedly high value of Q_T of juvenile anchovies ($\sim$12) needs to be confirmed. Backscattered energy and, in the case of absorption spectroscopy, transmitted energy needs to be measured at least every 0.2 kHz at frequencies above about 3 kHz to check these inferences. It is conceivable that some of the structure in the spectrum at high frequencies may have been caused by frequency dependent multipath interference.

The feasibility of monitoring the growth and mortality rates of juvenile anchovies, sardines, and other fish with scattering or absorption spectroscopy measurements should be investigated. Experiments could be conducted every few months at the same site, in concert with concurrent biological trawls that employ sufficiently fine mesh to capture 2-cm-long fish.

ACKNOWLEDGMENTS

This work was supported by the Office of Naval Research Biology and Acoustic Programs. I would like to thank Dr. Paul Smith of the Southwest Fisheries Science Center, National Marine Fisheries Service, for many helpful discussions and suggestions, and Dr. Clarence Clay and Dr. Van Holliday for reviewing this manuscript. I would also like to thank Dr. Steve Wolf, Head of the Shallow Water Acoustics Section, Dr. Steve Wales and Dr. Tom Hayward of the Naval Research Laboratory (NRL) for their reviews and comments, and Dr. Marshall Orr, Head of the Signal Processing Branch, NRL, and Dr. Ed Franchi, Superintendent of the Acoustics Division, NRL, for their support and encouragement.

Aoki, I., and Inagaki, T. (**1988**). ''Photographic observations on the behavior of Japanese anchovy, *Engraulis japonica*, at night in the sea,'' Mar. Ecol.: Prog. Ser. **43**, 213–221.

Artemov, Y. (**1991**). ''On the depth dependence of the sound scattering ability of fish larvae containing bladders,'' Oceanology **31**, 693–698.

Baltzer, W., and Pickwell, G. (**1970**). ''Resonant acoustic scattering from gas bladder fishes,'' in *Proceedings of an International Symposium on Biological Sound Scattering in the Ocean*, edited by B. Farquhar (USGPO, Washington, DC).

Barange, M. *et al.* (**1996**). ''Empirical determination of *in situ* target strengths of three loosely aggregated pelagic fish species,'' ICES J. Mar. Sci. **53**, 225–231.

Blaxter, J. *et al.* (**1979**). ''The herring swim- bladder as a gas reservoir for the acoustico-lateralis system,'' J. Mar. Biol. Assoc. U.K. **59**, 1–10.

Blaxter, J., and Batty, R. (**1990**). ''Swimbladder behavior and target strength,'' Rapp. P.-v. Reun. Cons. Int. Explor. Mer. **189**, 233–244.

Butler, J. (**1989**). ''Growth during the larval and juvenile stages of the northern anchovy, *Engraulis mordax*, in the California Current during 1980–84,'' Fish. Bull. **87**, 645–652.

Clay, C. (**1991**). ''Low-resolution acoustic scattering models: Fluid-filled cylinders and fish with swim bladders,'' J. Acoust. Soc. Am. **89**, 2168–2179.

Clay, C., and Medwin, H. (**1977**). *Acoustical Oceanography: Principles and Applications* (Wiley, New York).

Culley, M. (**1971**). *The Pilchard: Biology and Exploitation* (Pergamon, New York).

Diachok, O. (**1999**). ''Effects of absorptivity due to fish on transmission loss in shallow water,'' J. Acoust. Soc. Am. **105**, 2107–2128.

Diachok, O. *et al.* (**2000**). ''Estimation of the number density of fish from resonance absorptivity and echo sounder data,'' ICES J. Mar Sci. (in press).

Feuillade, C., and Werby, M. (**1994**). ''Resonances of deformed gas bubbles in liquids,'' J. Acoust. Soc. Am. **96**, 3684–3692.

Feuillade, C. *et al.* (**1996**). ''A low frequency acoustic scattering model for small schools of fish,'' J. Acoust. Soc. Am. **99**, 196–208.

Feuillade, C., and Nero, W. (**1998**). ''A viscous-elastic swim bladder model for describing enhanced frequency resonance scattering from fish,'' J. Acoust. Soc. Am. **103**, 3245–3255.

Foote, K. (**1985**). ''Rather high frequency scattering by swimbalddered fish,'' J. Acoust. Soc. Am. **78**, 688–700.

Graves, J. (**1977**). ''Photographic method for measuring the spacing and density within pelagic fish schools at sea,'' Fish. Bull. **75**, 230–234.

Holliday, D. (**1972**). ''Resonance structure in echoes from schooled pelagic fish,'' J. Acoust. Soc. Am. **51**, 1322–1332.

Holliday, V. (**1978a**). ''Data analysis and summary, MORDAX II March 1977,'' Tracor Document No. T-78-SD-002-U, Tracor, Inc.

Holliday, V. (**1978b**). ''Data analysis and summary. MORDAX III May 1977,'' Tracor Document No. T-78-SD-003-U, Tracor, Inc.

Holliday, V. (**1978c**). ''Data analysis and summary, MORDAX IV September 1977,'' Tracor Document No. T-78-SD-004-U, Tracor, Inc.

Holliday, V. (**2001**). Personal communication.

Holligan, P., and Harbour, D. (**1977**). ''The vertical distribution and succession of phytoplankton in the western English Channel in 1975 and 1976,'' J. Mar. Biol. Assoc. U.K. **57**, 1075–1093.

Hunter, J., and Goldberg, S. (**1980**). ''Spawning incidence and batch fecundity in northern anchovy, *Engraulis mordax*,'' Fish. Bull. **77**, 641–652.

Lo, N. *et al.* (**1997**). ''Population-growth of northern anchovy and Pacific sardine using stage-specific matrix models,'' Mar. Ecol.: Prog. Ser. **127**, 15–27.

Loukashkin, A. (**1970**). ''On the diet and feeding behavior of the northern anchovy, *Engraulis mordax*,'' Proc. Cal. Acad. Sci. **37**, 419–458.

Love, R. (**1993**). ''A comparison of volume scattering strength data with model calculations based on quasi-synoptically collected fishery data,'' J. Acoust. Soc. Am. **94**, 2255–2268.

Lovik, A., and Hovem, J. (**1979**). ''An experimental investigation of swim bladder resonances in fishes,'' J. Acoust. Soc. Am. **66**, 850–854.

Mais, K. (**1974**). ''Pelagic fish surveys in the California Current,'' Fisheries Bull. 162, Dept. Fish and Game, State of California.

Mais, K. (**1981**). ''Age composition changes in the anchovy, *Engraulis mordax*, central population,'' CalCOFI Report No. XXII.

Mallicoate, D., and Parrish, R. (**1981**). ''Seasonal growth patterns of California stocks of northern anchovy, *Engraulis mordax*, Pacific mackerel, *Scomber Japonicus*, and Jack Mackerel, *Trachurus symmetricus*,'' CalCOFI Report No. XXII.

Methot, R. (**1981**). ''Growth rates and age distributions of larval and juvenile northern anchovy, *Engraulis mordax*, with inferences on larval survival,'' Ph.D. thesis, University of California, San Diego.

Methot, R. (**1983**). ''Seasonal variation in survival of larval northern anchovy, *Engraulis mordax*, estimated from the age distribution of juveniles,'' Fish. Bull. **81**, 741–750.

Minnaert, F. (**1933**). ''On musical air bubbles and the sounds of running water,'' Philos. Mag. A **16**, 235–248.

Nero, R. *et al.* (**1997**). ''Low frequency acoustic measurements of Pacific hake, *Merluccius productus*, off the west coast of the United States,'' Fish. Bull. **96**, 329–343.

Nero, R. (**2000**). Personal communication.

O'Connell, C. (**1995**). ''The gas bladder and its relation to the inner ear in *sardinops caerulea* and *engraulis mordax*,'' Fish. Bull. 104, Fish. Bull. the Fish and Wildlife Service, **56**, 504–533.

Ona, E. (**1990**). ''Physiological factors causing natural variations in acoustic target strengths of fish,'' J. Mar. Biol. Assoc. U.K. **70**, 107–127.

Parrish, R. *et al.* (**1985**). ''Regional variations in the growth and age composition of northern anchovy, *Engraulis mordax*,'' Fish. Bull. **84**, 483–496.

Smith, P. (**1999**). Personal communication.

Stanton, T., Chu, D., and Weibe, P. (**1998**). ''Sound scattering by several zooplankton groups. II. Scattering models,'' J. Acoust. Soc. Am. **103**, 236–253.

Sundness, G., and Sand, O. (**1975**). ''Studies of a physostome swimbladder by resonance frequency analysis,'' J. Cons., Cons. Int. Explor. Mer. **36**, 176–182.

Weston, D. (**1967**). ''Sound propagation in the presence of bladder fish,'' in *Underwater Acoustics*, edited by V. Albers (Plenum, New York, 1967), Vol. 2, pp. 55–68.

Extinction theorem for object scattering in a stratified medium

Purnima Ratilal and Nicholas C. Makris
Massachusetts Institute of Technology, Cambridge, Massachusetts 02139

(Received 20 December 2000; revised 13 June 2001; accepted 10 July 2001)

A simple relation for the rate at which energy is extinguished from the incident wave of a far field *point source* by an obstacle of arbitrary size and shape in a *stratified medium* is derived from wave theory. This relation generalizes the classical extinction theorem, or optical theorem, that was originally derived for *plane wave* scattering in free space and greatly facilitates extinction calculations by eliminating the need to integrate energy flux about the obstacle. The total extinction is shown to be a linear sum of the extinction of each wave guide mode. Each modal extinction involves a sum over all incident modes that are scattered into the extinguished mode and is expressed in terms of the object's plane wave scatter function in the forward azimuth and equivalent plane wave amplitudes of the modes. The only assumptions are that multiple scattering between the object and wave guide boundaries is negligible, and the object lies within a constant sound speed layer. Modal extinction cross sections of an object for the extinction of the individual modes of a wave guide are then defined. Calculations for a shallow water wave guide show that, after correcting for absorption loss in the medium, the modal cross section of an object for mode 1 in a typical ocean wave guide is very nearly equal to its free space cross section. This new extinction theorem may be applied to estimate the cross section of an object submerged in a wave guide from a measurement of its forward scattered field. [DOI: 10.1121/1.1405522]

PACS numbers: 43.30.Ft, 43.30.Bp, 43.30.Gr [DLB]

I. INTRODUCTION

If an object is placed in the path of an incident wave, some of the intercepted power is scattered in all direction and the remainder is absorbed. The total power removed from the incident field as a result of scattering and absorption by the object is called extinction.[1] Van de Hulst has shown, in what has become known alternatively as the *extinction theorem*, *optical theorem*, and *forward scatter theorem*, that the extinction can be derived from the scattered far field in the forward direction. Specifically, the total extinction of a plane wave incident on an object in free space equals the imaginary part of the forward scatter amplitude multiplied by the incident intensity and $4\pi/k^2$ where k is the wave number.[2–4] This remarkably simple relationship reflects the fact that the extinction caused by the obstacle leads to shadow formation via destructive interference between the incident and forward scattered fields. The permanence of the extinction is maintained by the formation of a region of destructive interference that survives as an active *shadow remnant*[3] in perpetuity beyond the deep shadow.

The total power scattered by an object can be found by integrating the scattered intensity over a large control surface enclosing the object in the far field. This integration is usually difficult to perform and makes an alternative approach attractive. For nonabsorbing objects, the total power scattered by the object is the extinction.[5,6] One great advantage of the extinction theorem is that it eliminates the need to integrate the scattered energy flux around the object.

The extinction theorem is typically applied in acoustics to measure the *extinction* cross section of objects.[7] This equals twice the object's projected area in the high frequency limit, and so provides a useful method for estimating an object's size. The extinction theorem has many diverse applications in acoustics, such as those given in Refs. 8 and 9. It can also be used as a ''burglar alarm'' to detect and classify intruding objects that pass between a source and an acoustic receiver array.

In 1985 Guo[10] extended the extinction theorem to scattering by an object located next to an interface between two distinct acoustic half spaces. He found an expression for the extinction of an incident plane wave in terms of the far-field scattered pressures in the specular reflection and transmission directions, determined by Snell's law. In a wave guide, the effect of multimodal propagation ensures that the field incident on the object will arrive from many distinct directions. This, combined with the effect of absorption loss in the waveguide, will modify the extinction and scattering cross sections from their free space values. The free space extinction theorem and the half-space extension of Guo are therefore not applicable in a wave guide.

Here we use wave theory to derive a generalized extinction theorem by developing a relation for the rate at which energy is extinguished from the incident wave of a far field *point source* by an object of arbitrary size and shape in a *stratified medium*. Like its free space analogue, the relation is again remarkably simple. The total extinction is shown to be a linear sum of the extinction of each wave guide mode. Each modal extinction involves a sum over all incident modes that are scattered into the given mode and is expressed in terms of the object's plane wave scatter function in the forward azimuth and equivalent modal plane wave amplitudes. For the multiple incident plane waves in a wave guide, extinction is a function of not only the forward scatter amplitude for each of the incident plane waves but also depends on the scatter function amplitudes coupling each incident plane wave to all other plane waves with distinct direc-

tions that make up the incident field. The final relation greatly facilitates extinction calculations by eliminating the need to integrate energy flux about the object.

Our derivation begins with the time-harmonic scattered field from an object in a wave guide that is derived directly from Green's theorem.[11,12] The only simplifying assumptions are that multiple scattering between the object and wave guide boundaries is negligible and that the object lies within a constant sound speed layer. The simplicity of the resulting extinction relation in the wave guide follows from the fact that the full extinction is maintained in the region of active interference and that this region extends into the far field where separation of variables can be invoked. Energy fluxes necessary for the derivation can then be calculated in the far field in terms of wave guide modes and the object's plane wave scattering function.[12,13]

The extinction cross section of an object is defined as the ratio of its extinction to the rate at which energy is incident on unit cross sectional area of the object.[1] The extinction cross section reduces to the scattering cross section for nonabsorbing objects, and is useful in actively classifying targets since, as the ratio of the total extinction to the incident intensity, it depends only upon scattering properties of the target. This definition, however, is ambiguous in a wave guide because both the incident and scattered fields are comprised by superpositions of plane waves. Here scattering and propagation effects are not generally separable since they are convolved together in the extinction. Additionally, the incident intensity is not spatially constant. In spite of these difficulties, we find it convenient to interpret the extinction cross section *for an object in a wave guide* as the ratio of the extinction to the incident energy flux per unit area in the radial direction at the object's centroid. This definition is sensible when the object is in a constant sound speed layer and in the far field of the source.

Calculations for a shallow water wave guide, which have great relevance to active detection problems in ocean acoustics, show that an object's cross section for the combined extinction of all the modes of the wave guide is highly dependent on measurement geometry, medium stratification, as well as its scattering properties. In addition, the combined cross section fluctuates rapidly with range due to coherent interference between the modes. The presence of absorption in the medium can also significantly modify a measurement of the total scattering cross section. The practical implication of these findings is that experimental measurements of the total scattering cross section of an obstacle in a wave guide may differ greatly from those obtained for the same obstacle in free space and may lead to errors in target classification if the wave guide effects are not properly taken into account.

For an object submerged in a wave guide, we also define modal cross sections of the object for the extinction of the individual modes of the wave guide. The modal cross section of an object for the extinction of mode 1 in a typical ocean wave guide was found to be nearly equal to the free space cross section of the object. A potential application of the extinction theorem in a wave guide is then the estimation of the size of an object submerged in the wave guide from a measurement of the extinction it causes to mode 1. The generalized extinction theorem can also be used to determine the attenuation due to volume and surface scattering of guided waves propagating through stratified media such as the ocean or the earth's crust.

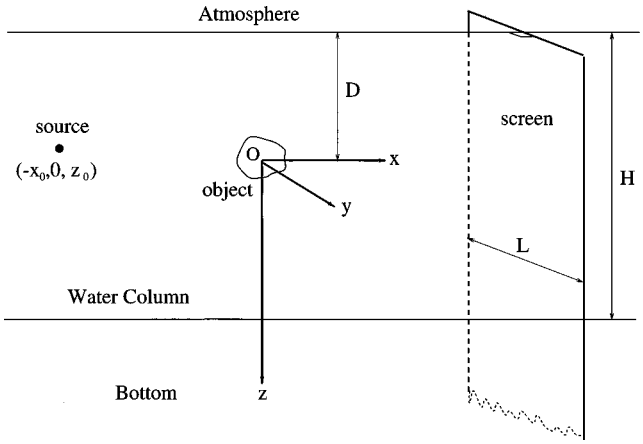

FIG. 1. The geometry of the problem showing an object in a stratified medium composed of a water column of thickness H overlying a bottom. The origin of the coordinate system is at the center of the object and the source is located at $(-x_0,0,z_0)$. The screen is normal to the x axis with width L and is semi-infinite in the z-direction penetrating into the bottom with an edge at the top of the water column.

II. THE GENERALIZED EXTINCTION THEOREM

In this section, we derive the extinction in the incident field of a far field point source due to an obstacle of arbitrary size and shape in a stratified medium. The general approaches for calculating extinction are discussed in Appendix A. Here, we adopt the intuitive approach of Van de Hulst[1,2,4] which involves integrating the energy flux, or intensity, over a screen placed a distance away from the object sufficiently large to register Fraunhofer diffraction, Eq. (A11). In the absence of the object, the total energy flux across the screen is maximal. In the presence of the object, the total energy flux across the screen is diminished by the shadow remnant. For a sufficiently large screen, the difference between these fluxes is the total extinction.

We focus on the Van de Hulst screen method for calculating extinction because it is of more practical use since it represents the type of measurement that can be made with a standard 2D planar or billboard array. This is discussed further in Sec. V. The other approach for calculating extinction using a control surface that encloses the object in a stratified wave guide is discussed in Appendix D. A control volume measurement would be very difficult to implement since it would require an array that completely encloses the object.

The origin of the coordinate system is placed at the object centroid with z axis vertically downward, and x axis parallel to the boundaries as shown in Fig. 1. The coordinates of the source are defined by $\mathbf{r}_0=(-x_0,0,z_0)$. The screen is positioned in forward azimuth on the $y-z$ plane at a horizontal range x from the object center. The width of the screen is L along the y direction and is semi-infinite in the z direction with an edge at the surface of the wave guide. Let $\mathbf{r}=(x,y,z)$ be the coordinates of a point on the screen. Spatial cylindrical (ρ,θ,z) and spherical systems (r,θ,ϕ) are de-

fined by $x=r\sin\theta\cos\phi$, $y=r\sin\theta\sin\phi$, $z=r\cos\theta$ and $\rho=x^2+y^2$. The horizontal and vertical wave number components for the nth mode are, respectively, $\xi_n=k\sin\alpha_n$ and $\gamma_n=k\cos\alpha_n$ where $k^2=\xi_n^2+\gamma_n^2$ and the wave number magnitude k equals the angular frequency ω divided by the sound speed c in the object layer. As discussed in Appendix A to measure the full extinction in the wave guide, we require $L>\sqrt{\lambda x}$, where x is the horizontal range of the screen from the object.

Assuming that the object is far from the source and the screen so that the range from the screen to the source is large, the incident field at location $\mathbf{r}$ on the screen for a source at $\mathbf{r}_0$, can be expressed as a sum of normal modes,

$$\Phi_i(\mathbf{r}|\mathbf{r}_0)=\frac{i}{d(z_0)\sqrt{8\pi}}e^{-i\pi/4}\sum_{l=1}^{\infty}u_l(z)u_l(z_0)\frac{e^{i\xi_l|\boldsymbol{\rho}-\boldsymbol{\rho}_0|}}{\sqrt{\xi_l|\boldsymbol{\rho}-\boldsymbol{\rho}_0|}}, \tag{1}$$

where $u_l(z)$ and ξ_l are the lth modal amplitude and horizontal wave number, respectively, and $d(z)$ is the density at depth z.

Using the formulation of Refs. 11 and 12 based on Green's theorem, the scattered field from the object at receiver $\mathbf{r}$ for a source at $\mathbf{r}_0$ is

$$\begin{aligned}\Phi_s(\mathbf{r}|\mathbf{r}_0)=&\sum_{m=1}^{\infty}\sum_{n=1}^{\infty}\frac{4\pi}{k}\\&\times[A_m(\mathbf{r})A_n(\mathbf{r}_0)S(\pi-\alpha_m,\phi;\alpha_n,\phi_0+\pi)\\&-B_m(\mathbf{r})A_n(\mathbf{r}_0)S(\alpha_m,\phi;\alpha_n,\phi_0+\pi)\\&-A_m(\mathbf{r})B_n(\mathbf{r}_0)S(\pi-\alpha_m,\phi;\pi-\alpha_n,\phi_0+\pi)\\&+B_m(\mathbf{r})B_n(\mathbf{r}_0)S(\alpha_m,\phi;\pi-\alpha_n,\phi_0+\pi)],\end{aligned} \tag{2}$$

where

$$\begin{aligned}A_m(\mathbf{r})&=\frac{i}{d(0)}(8\pi\xi_m\rho)^{-1/2}u_m(z)N_m^-e^{i(\xi_m\rho+\gamma_mD-\pi/4)},\\B_m(\mathbf{r})&=\frac{i}{d(0)}(8\pi\xi_m\rho)^{-1/2}u_m(z)N_m^+e^{i(\xi_m\rho-\gamma_mD-\pi/4)},\end{aligned} \tag{3}$$

$$A_n(\mathbf{r}_0)=\frac{i}{d(z_0)}(8\pi\xi_n\rho_0)^{-1/2}u_n(z_0)N_n^-e^{i(\xi_n\rho_0+\gamma_nD-\pi/4)},$$

$$B_n(\mathbf{r}_0)=\frac{i}{d(z_0)}(8\pi\xi_n\rho_0)^{-1/2}u_n(z_0)N_n^+e^{i(\xi_n\rho_0-\gamma_nD-\pi/4)}$$

are the down and up going plane waves in the layer of the object, D is the depth of the object center from the sea surface and $S(\theta,\phi;\theta_i,\phi_i)$ is the object's plane wave scatter function. The definition of the plane wave scatter function here follows that defined in Ref. 12 where the incident plane wave on the object is described in terms of the direction it goes to, so that for forward scatter in free space, $\theta=\theta_i$, $\phi=\phi_i$. The mode functions are normalized according to

$$\delta_{nm}=\int_{-D}^{\infty}\frac{u_m(z)u_n^*(z)}{d(z)}dz, \tag{4}$$

and are decomposable into up- and down-going plane waves in the layer of the object via

$$u_m(z)=N_n^-e^{i\gamma_n(z+D)}-N_n^+e^{-i\gamma_n(z+D)}. \tag{5}$$

N_n^- and N_n^+ are the amplitudes of the down- and up-going plane waves in this layer.

A number of assumptions have to be satisfied for the above formulation for the scattered field to be valid as noted in Ref. 12. In particular, multiple scattering between the object and wave guide boundaries is negligible, the object lies within a layer of constant sound speed, and the range from the object to source or receiver must be large enough that the scattered field can be approximated as a linear function of the object's plane wave scatter function. The last condition does not limit the generality of the final extinction expression since the full extinction can be registered on sufficiently large screens in the object's far field, but instead simplifies its derivation.

To calculate the extinction using the general formula of Eq. (A11), we first evaluate the integrand for the point $\mathbf{r}$ on the screen. The first term in the integrand of Eq. (A11) using Eqs. (A2), (1), (2), and (3) is

$$\begin{aligned}\mathbf{V}_i^*\Phi_s=&\frac{i}{d(z)d(z_0)d(0)2\omega k}\sum_{l=1}^{\infty}\sum_{m=1}^{\infty}\sum_{n=1}^{\infty}u_l^*(z_0)u_m(z)\left[\frac{\partial}{\partial z}u_l^*(z)\mathbf{i}_z-i\xi_l^*u_l^*(z)\mathbf{i}_x\right]\frac{e^{-i\Re\{\xi_l\}\sqrt{(x_0+x)^2+y^2}}}{\sqrt{\xi_l^*(x_0+x)}}\frac{e^{i\Re\{\xi_m\}\sqrt{x^2+y^2}}}{\sqrt{\xi_mx}}\\&\times[N_m^-e^{i\Re\{\gamma_m\}D}A_n(\mathbf{r}_0)S(\pi-\alpha_m,\phi;\alpha_n,0)-N_m^+e^{-i\Re\{\gamma_m\}D}A_n(\mathbf{r}_0)S(\alpha_m,\phi;\alpha_n,0)\\&-N_m^-e^{i\Re\{\gamma_m\}D}B_n(\mathbf{r}_0)S(\pi-\alpha_m,\phi;\pi-\alpha_n,0)+N_m^+e^{-i\Re\{\gamma_m\}D}B_n(\mathbf{r}_0)S(\alpha_m,\phi;\pi-\alpha_n,0)]\\&\times e^{-\Im\{\xi_l\}(x_0+x)}e^{-\Im\{\xi_m\}x}e^{-\Im\{\gamma_m\}D}.\end{aligned} \tag{6}$$

In the above expression, the terms representing absorption by the wave guide have been factored out explicitly to avoid confusion when conjugating the fields and also to keep track of absorption losses due to the wave guide. The exact expressions for $|\boldsymbol{\rho}-\boldsymbol{\rho}_0|=\sqrt{(x+x_0)^2+y^2}$ and $|\boldsymbol{\rho}|=\sqrt{x^2+y^2}$ were kept in the terms that determine the phase of the integrand while the approximations $|\boldsymbol{\rho}-\boldsymbol{\rho}_0|\approx(x+x_0)$ and $|\boldsymbol{\rho}|\approx x$ were used in the spreading and absorption loss factors, since x, $x_0\gg y$ can be satisfied for a screen that measures the full extinction.

Next we integrate Eq. (6) over the area of the screen. With the screen lying parallel to the $y-z$ plane, an area ele-

ment of the screen is $\mathbf{dS}=\mathbf{i}_x\,dy\,dz$. We use the orthorgonality relation in Eq. (4) between the modes $u_l^*(z)$ and $u_m(z)$ to integrate Eq. (6) over the semi-infinite depth of the screen in the wave guide. This reduces the triple sum over the modes to a double sum:

$$\begin{aligned}\int\int_{Sc}\mathbf{V}_i^*\Phi_s\cdot\mathbf{dS}&=\int_{-L/2}^{L/2}\int_{-D}^{\infty}\mathbf{V}_i^*\Phi_s\cdot\mathbf{i}_x\,dz\,dy\\&=\frac{1}{d(z_0)d(0)2\omega k}\sum_{m=1}^{\infty}\sum_{n=1}^{\infty}\frac{\xi_m^*}{|\xi_m|\sqrt{x(x_0+x)}}u_m^*(z_0)\\&\times\left\{\int_{-L/2}^{L/2}[N_m^-e^{i\Re\{\gamma_m\}D}A_n(\mathbf{r}_0)S(\pi-\alpha_m,\phi;\alpha_n,0)-N_m^+e^{-i\Re\{\gamma_m\}D}A_n(\mathbf{r}_0)S(\alpha_m,\phi;\alpha_n,0)\right.\\&-N_m^-e^{i\Re\{\gamma_m\}D}B_n(\mathbf{r}_0)S(\pi-\alpha_m,\phi;\pi-\alpha_n,0)+N_m^+e^{-i\Re\{\gamma_m\}D}B_n(\mathbf{r}_0)S(\alpha_m,\phi;\pi-\alpha_n,0)]\\&\left.\times e^{i\Re\{\xi_m\}(\sqrt{x^2+y^2}-\sqrt{(x_0+x)^2+y^2})}dy\right\}e^{-\Im\{\xi_m\}(x_0+2x)}e^{-\Im\{\gamma_m\}D}.\end{aligned}\tag{7}$$

In the above expression, the scatter function is dependent on y via the azimuth angle $\phi=\tan^{-1}(y/x)$. As discussed in Appendix A, the angular width of the active area on the screen in azimuth is of the order of $\sqrt{\lambda/x}$. We can therefore approximate the scatter function with its value at $\phi=0$ and factor it from the integral above since x is large. We also expand the exponent involving the variable y according to

$$\sqrt{(x_0+x)^2+y^2}\approx x_0+x+\frac{y^2}{2(x_0+x)},\tag{8}$$

$$\sqrt{x^2+y^2}\approx x+\frac{y^2}{2x}.\tag{9}$$

Applying the result of the following asymptotic integration over the width of the screen,

$$\int_{-L/2}^{L/2}S(\pi-\alpha_m,\phi;\alpha_n,0)e^{i\Re\{\xi_m\}(\sqrt{x^2+y^2}-\sqrt{(x_0+x)^2+y^2})}dy=e^{-i\Re\{\xi_m\}x_0}S(\pi-\alpha_m,0;\alpha_n,0)e^{i\pi/4}\sqrt{\frac{2\pi x(x_0+x)}{\Re\{\xi_m\}x_0}},\tag{10}$$

to Eq. (7), the integration of the first term in Eq. (A11) over the area of the screen in the wave guide becomes

$$\begin{aligned}\int\int_{Sc}\mathbf{V}_i^*\Phi_s\cdot\mathbf{dS}&=\frac{i}{d^2(z_0)d(0)4\omega k}\frac{1}{x_0}\sum_{m=1}^{\infty}\sum_{n=1}^{\infty}\frac{\xi_m^*}{|\xi_m|\sqrt{\Re\{\xi_m\}\xi_n}}u_m^*(z_0)u_n(z_0)e^{i\Re\{\xi_n-\xi_m\}x_0}\\&\times[N_m^-N_n^-e^{i\Re\{\gamma_m+\gamma_n\}D}S(\pi-\alpha_m,0;\alpha_n,0)-N_m^+N_n^-e^{i\Re\{-\gamma_m+\gamma_n\}D}S(\alpha_m,0;\alpha_n,0)\\&-N_m^-N_n^+e^{i\Re\{\gamma_m-\gamma_n\}D}S(\pi-\alpha_m,0;\pi-\alpha_n,0)+N_m^+N_n^+e^{i\Re\{-\gamma_m-\gamma_n\}D}S(\alpha_m,0;\pi-\alpha_n,0)]\\&\times e^{-\Im\{\xi_m+\xi_n\}x_0}e^{-\Im\{2\xi_m\}x}e^{-\Im\{\gamma_m+\gamma_n\}D}.\end{aligned}\tag{11}$$

Similarly, we can evaluate the second term in Eq. (A11) which gives

$$\begin{aligned}\int\int_{Sc}\mathbf{V}_s^*\Phi_i\cdot\mathbf{dS}&=-\frac{i}{d^2(z_0)d(0)4\omega k}\frac{1}{x_0}\sum_{m=1}^{\infty}\sum_{n=1}^{\infty}\frac{\xi_m^*}{|\xi_m|\sqrt{\Re\{\xi_m\}\xi_n^*}}u_m(z_0)u_n^*(z_0)e^{-i\Re\{\xi_n-\xi_m\}x_0}\\&\times[N_m^-{}^*N_n^-{}^*e^{-i\Re\{\gamma_m+\gamma_n\}D}S^*(\pi-\alpha_m,0;\alpha_n,0)-N_m^+{}^*N_n^-{}^*e^{-i\Re\{-\gamma_m+\gamma_n\}D}S^*(\alpha_m,0;\alpha_n,0)\\&-N_m^-{}^*N_n^+{}^*e^{-i\Re\{\gamma_m-\gamma_n\}D}S^*(\pi-\alpha_m,0;\pi-\alpha_n,0)+N_m^+{}^*N_n^+{}^*e^{-i\Re\{-\gamma_m-\gamma_n\}D}S^*(\alpha_m,0;\pi-\alpha_n,0)]\\&\times e^{-\Im\{\xi_m+\xi_n\}x_0}e^{-\Im\{2\xi_m\}x}e^{-\Im\{\gamma_m+\gamma_n\}D}.\end{aligned}\tag{12}$$

When we sum Eqs. (11) and (12), taking only the negative of the real part of the sum following Eq. (A11), we obtain the range dependent extinction $\mathcal{E}(x|\mathbf{r}_0)$ of the incident field in a wave guide due to an object at the origin measured by a screen at distance x from the object with source at $\mathbf{r}_0$,

$$\mathcal{E}(x|\mathbf{r}_0)=\frac{1}{d^2(z_0)d(0)2\omega k}\frac{1}{x_0}\sum_{m=1}^{\infty}\sum_{n=1}^{\infty}\frac{\sqrt{\Re\{\xi_m\}}}{|\xi_m|}\Im\Bigg\{\frac{1}{\sqrt{\xi_n}}u_m^*(z_0)u_n(z_0)e^{i\Re\{\xi_n-\xi_m\}x_0}$$
$$\times[N_m^-N_n^-e^{i\Re\{\gamma_m+\gamma_n\}D}S(\pi-\alpha_m,0;\alpha_n,0)-N_m^+N_n^-e^{i\Re\{-\gamma_m+\gamma_n\}D}S(\alpha_m,0;\alpha_n,0)$$
$$-N_m^-N_n^+e^{i\Re\{\gamma_m-\gamma_n\}D}S(\pi-\alpha_m,0;\pi-\alpha_n,0)+N_m^+N_n^+e^{i\Re\{-\gamma_m-\gamma_n\}D}S(\alpha_m,0;\pi-\alpha_n,0)]\Bigg\}$$
$$\times e^{-\Im\{\xi_m+\xi_n\}x_0}e^{-\Im\{2\xi_m\}x}e^{-\Im\{\gamma_m+\gamma_n\}D}. \tag{13}$$

From Eq. (13), we see that the total extinction is a linear sum of the extinction of each wave guide mode. The extinction of mode m involves a sum over all incident modes n that are scattered into that extinguished mode and is expressed in terms of the object's plane wave scatter function in the forward azimuth and equivalent plane wave amplitudes of the modes. The extinction decreases with source-object range x_0 in a wave guide due to geometrical spreading, and with source-object and object-receiver ranges, x_0 and x, due to absorption loss in the medium.

A. Effect of multiple incident plane waves

To understand the implications of Eq. (13), we consider several cases and examine the resulting expression for the extinction in each case.

1. Single mode excited by source

First we consider a source that excites only a single mode p. The incident field on the object and at the screen is determined by this single mode p. The triple sum in Eq. (6) reduces to a single sum over m in this case since both l and n can only take on the integer value p. The orthogonality relation between the modes $u_l^*(z)$ and $u_m(z)$ eliminates the sum over m leaving just a single term where $m=p$ in Eq. (7). Consequently, the expression for the extinction will have only one term corresponding to $m=n=p$, the mode excited by the source,

$$\mathcal{E}(x|\mathbf{r}_0)=\frac{1}{d^2(z_0)d(0)2\omega k}\frac{1}{x_0}\frac{\sqrt{\Re\{\xi_p\}}}{|\xi_p|}|u_p(z_0)|^2\Im\Bigg\{\frac{1}{\sqrt{\xi_p}}[(N_p^-)^2e^{i\Re\{2\gamma_p\}D}S(\pi-\alpha_p,0;\alpha_p,0)-N_p^+N_p^-S(\alpha_p,0;\alpha_p,0)$$
$$-N_p^-N_p^+S(\pi-\alpha_p,0;\pi-\alpha_p,0)+(N_p^+)^2e^{i\Re\{-2\gamma_p\}D}S(\alpha_p,0;\pi-\alpha_p,0)]\Bigg\}e^{-\Im\{2\xi_p\}(x_0+x)}e^{-\Im\{2\gamma_p\}D}. \tag{14}$$

Even though the scattered field from the object is composed of multiple modes m, only one of these can interfere destructively with the single incident mode p on the screen and it is precisely the scattered mode that has the same elevation angle as the incident mode.

Mode p is made up of an up-going and a down-going plane wave. Two of the four terms in Eq. (14) arise from the *forward* scatter of the up- and down-going plane waves of mode p, while the remaining two terms arise from the scatter of the incident down-going plane wave of mode p to an upgoing plane wave of the same mode and vice versa. This shows that when we have multiple plane waves incident on the object, the extinction will depend on not only the scatter function in the forward direction but also depend on the scatter function amplitudes coupling each incident plane wave to all other plane waves with distinct directions that make up the incident field.

2. Many modes excited by source

For a general harmonic source that excites many modes, the incident field on the screen is a sum of the contribution from various excited modes. Each of these incident modes on the screen will only interfere destructively in the forward azimuth with the corresponding scattered mode from the object with the same elevation angle. The scattering process causes the various incoming incident modes at the object to be coupled to each outgoing scattered mode through the scatter function and this leads to a *double sum* in the expression for the extinction in Eq. (13).

3. Large object-receiver range, x

Next we consider the scenario where the screen is placed at a sufficiently large distance from the object that only the first mode survives for both the incident field on the screen from the source and the scattered field from the object, i.e., $l=m=1$ in Eq. (6). The field incident on the object is still comprised by a sum over the modes n excited by the source since the range of the source from the object is not too large. The expression for the extinction in Eq. (13) then reduces to a single sum over the incident modes n on the object that are scattered into the outgoing mode $m=1$ that survives at the screen.

4. Large source to object range, x_0

If the source is placed at large distances away from the object, the field incident on the object and on the screen will be determined by the single mode $l=n=1$ that survives while the rest of the modes are stripped due to absorption in the wave guide. The extinction in this case has a single term

in Eq. (13) corresponding to $m=n=1$, the mode that survives at the screen. The expression for the extinction is given by Eq. (14) with $p=1$.

These examples illustrate the fact that it is really the interference between the incident field and the scattered field on the screen that determines the extinction. Only scattered field directions that have a fixed phase relationship with the incident field will contribute to the extinction. In the literature, extinction is often stated to be directly proportional to the forward scatter amplitude of a plane wave in free space. For multiple incident plane waves, however, the extinction is not simply a function of the forward scatter amplitude for each incident plane wave but also depends on the scatter function amplitudes coupling each incident plane wave to all other plane waves with distinct directions that make up the incident field. Guo's[10] result for the extinction of a plane wave by an object placed near an interface between two media can also be interpreted in this way.

B. Effect of absorption by the medium

The extinction of the incident field due to an object in the far field of a point source in free space with absorption in the medium is derived in Appendix C. Comparing the expression for extinction in a wave guide, Eq. (13), with that in free space, Eq. (C14) in Appendix C, we see that absorption in the medium lowers the extinction that we would otherwise measure in a lossless medium. In free space, the term due to absorption by the medium is separable from the properties of the object in the formula for the extinction. These terms, however, are in general, convolved in a wave guide with multimodal propagation. The convolution arises because the absorption loss suffered by each mode varies from mode to mode. Furthermore, the modes have varying elevation angles and they are thus scattered differently by the object depending on the elevation angle of the mode. In the wave guide, the absorption loss term can be separated from the term due to the object only if a single mode is incident on the object as seen from Eq. (14), which is the extinction caused by a single mode. One way this arises naturally in a wave guide is when the source to object separation is large enough that only mode 1 survives in the incident field on the object.

III. TOTAL SCATTERED POWER IN THE WAVE GUIDE

The total power scattered by an object in a wave guide can be obtained by integrating the scattered field intensity $\mathbf{V}_s^*\Phi_s$ around a closed control surface enclosing the object, as described in Eq. (A8). We let the control surface be a semi-infinite cylinder of radius R with a cap at the sea surface where $z=-D$. The axis of the cylinder is parallel to the z axis and passes through the object centroid.

The sea surface is a pressure-release surface where the total field vanishes. Since the incident field in the absence of the object is zero at the sea surface, the scattered field has to vanish as well. The scattered energy flux through the cap of the cylinder at $z=-D$ is zero. We need only integrate the scattered intensity over the curved surface of the cylinder to obtain the total scattered power.

From Eq. (2), we see that the scattered field is expressed as a sum of four terms. The scattered intensity at the surface of the cylinder can therefore be expressed as a sum of 16 terms, the first of which is

$$
\begin{aligned}
(\mathbf{V}_s^*\Phi_s)_1 = {} & \frac{i2\pi}{d(z)d^2(0)\omega k^2}\sum_{m=1}^{\infty}\sum_{n=1}^{\infty}\sum_{p=1}^{\infty}\sum_{q=1}^{\infty} u_p(z) \\
& \times\left[\frac{\partial}{\partial z}u_m^*(z)\mathbf{i}_z - i\xi_m^* u_m^*(z)\mathbf{i}_\rho\right]\frac{e^{i\Re\{\xi_p-\xi_m\}R}}{\sqrt{\xi_m^*\xi_p}R} \\
& \times N_m^{-*}N_p^- e^{i\Re\{\gamma_p-\gamma_m\}D}A_n^*(\mathbf{r}_0)A_q(\mathbf{r}_0) \\
& \times S^*(\pi-\alpha_m,\phi;\alpha_n,0)S(\pi-\alpha_p,\phi;\alpha_q,0) \\
& \times e^{-\Im\{\xi_m+\xi_p\}R}e^{-\Im\{\gamma_m+\gamma_p\}D}. \qquad (15)
\end{aligned}
$$

An area element on the curved surface of the cylinder is given by $\mathbf{dS}=\mathbf{i}_\rho R\,d\phi\,dz$. Making use of Eq. (4), the orthogonality relation between the modes, we integrate Eq. (15) over the semi-infinite depth of the cylinder and the resulting expression is

$$
\begin{aligned}
& \int\int (\mathbf{V}_s^*\Phi_s)_1\cdot\mathbf{dS} \\
& = \int_0^{2\pi}\int_{-D}^{\infty}(\mathbf{V}_s^*\Phi_s)_1\cdot\mathbf{i}_\rho\,dz\,d\phi \\
& = \frac{2\pi}{d^2(0)\omega k^2}\sum_{m=1}^{\infty}\sum_{n=1}^{\infty}\sum_{q=1}^{\infty}\frac{\xi_m^*}{|\xi_m|}|N_m^-|^2A_n^*(\mathbf{r}_0)A_q(\mathbf{r}_0) \\
& \quad\times\int_0^{2\pi}S^*(\pi-\alpha_m,\phi;\alpha_n,0)S(\pi-\alpha_m,\phi;\alpha_q,0)d\phi \\
& \quad\times e^{-2\Im\{\xi_m\}R}e^{-2\Im\{\gamma_m\}D}. \qquad (16)
\end{aligned}
$$

The above integral cannot be further evaluated without specifying the scatter function of the object. In general the total scattered power in the wave guide is a complex expression with a triple sum of 16 integrals. The real part of Eq. (16) gives the triple sum of just the first integral.

If there is no absorption by the object, the extinction caused by the object is due entirely to scattering. If the object is in a perfectly reflecting wave guide or a wave guide with small absorption loss, the total scattered power is the extinction. In that case, the complicated expression with triple sum of 16 integrals discussed above reduces to the simple expression of a double sum and no integral of Eq. (13). In a lossy wave guide, if we measure the extinction around a small control surface enclosing the object, the absorption loss inside the control volume is small and the above holds as well. Therefore, the extinction formula eliminates the need to integrate the scattered energy flux about the object in a wave guide when determining the scattered power.

IV. COMBINED AND MODAL EXTINCTION CROSS SECTIONS

The ratio σ_T between the rate of dissipation of energy and the rate at which energy is incident on unit cross sectional area of an obstacle is called the extinction cross sec-

tion of the obstacle.[1] In the wave guide, the intensity of the incident field on the object at the origin from a source at $\mathbf{r}_0$ is

$$\mathbf{I}_i(0|\mathbf{r}_0)=\Re\{\mathbf{V}_i^*(\mathbf{0}|\mathbf{r}_0)\Phi_i(\mathbf{0}|\mathbf{r}_0)\}$$
$$=\Re\left\{\frac{i}{d^2(z_0)d(0)8\pi\omega x_0}\sum_p^\infty\sum_q^\infty u_p^*(z_0)\right.$$
$$\left.\times\left[\frac{\partial}{\partial z}u_p^*(z)\bigg|_{z=0}\mathbf{i}_z-i\xi_p^*u_p^*(0)\mathbf{i}_x\right]u_q(z_0)u_q(0)\right.$$
$$\left.\times\frac{e^{i\Re\{\xi_q-\xi_p\}x_0}}{\sqrt{\xi_p^*\xi_q}}e^{-\Im\{\xi_p+\xi_q\}x_0}\right\}. \tag{17}$$

In our derivation, the screen is positioned normal to the x axis and it measures the extinction of the energy flux propagating in the x direction. We therefore normalize this extinction by the component of the incident intensity in the x direction to obtain the extinction cross section σ_T of the object in the wave guide,

$$\sigma_T(x|\mathbf{r}_0)=\frac{\mathcal{E}(x|\mathbf{r}_0)}{\mathbf{I}_i(\mathbf{0}|\mathbf{r}_0)\cdot\mathbf{i}_x}=\left(\frac{4\pi}{k}\sum_{m=1}^\infty\sum_{n=1}^\infty\frac{\sqrt{\Re\{\xi_m\}}}{|\xi_m|}\Im\left\{\frac{1}{\sqrt{\xi_n}}u_m^*(z_0)u_n(z_0)e^{i\Re\{\xi_n-\xi_m\}x_0}[N_m^-N_n^-e^{i\Re\{\gamma_m+\gamma_n\}D}S(\pi-\alpha_m,0;\alpha_n,0)\right.\right.$$
$$-N_m^+N_n^-e^{i\Re\{-\gamma_m+\gamma_n\}D}S(\alpha_m,0;\alpha_n,0)-N_m^-N_n^+e^{i\Re\{\gamma_m-\gamma_n\}D}S(\pi-\alpha_m,0;\pi-\alpha_n,0)$$
$$\left.\left.+N_m^+N_n^+e^{i\Re\{-\gamma_m-\gamma_n\}D}S(\alpha_m,0;\pi-\alpha_n,0)]\right\}e^{-\Im\{\xi_m+\xi_n\}x_0}e^{-\Im\{2\xi_m\}x}e^{-\Im\{\gamma_m+\gamma_n\}D}\right)$$
$$\times\left(\sum_p^\infty\sum_q^\infty\Re\{u_p^*(z_0)u_p^*(0)u_q(z_0)u_q(0)\sqrt{\xi_p^*/\xi_q}e^{i\Re\{\xi_q-\xi_p\}x_0}e^{-\Im\{\xi_p+\xi_q\}x_0}\}\right)^{-1}. \tag{18}$$

Equation (18) is due to the combined extinction of all the modes of the wave guide by the object and we define it to be the combined extinction cross section. This combined cross section of an object depends on the properties of the object which are convolved with the properties of the wave guide, as well as the source and object locations.

For a source that excites only a single mode p, the incident intensity on the object in the x direction is

$$\mathbf{I}_i(\mathbf{0}|\mathbf{r}_0)_p=\frac{i}{d^2(z_0)d(0)8\pi\omega x_0}|u_p(z_0)|^2|u_p(0)|^2\frac{\Re\{\xi_p^*\}}{|\xi_p|}e^{-\Im\{2\xi_p\}x_0}. \tag{19}$$

Dividing the extinction of mode p by the object in Eq. (14) with the intensity of the incident field composed solely of mode p in Eq. (19), we obtain the cross section of the object for the extinction of mode p,

$$\sigma_p(x)=\frac{4\pi}{k}\frac{1}{\sqrt{\Re\{\xi_p\}}}\frac{1}{|u_p(0)|^2}\Im\left\{\frac{1}{\sqrt{\xi_p}}[(N_p^-)^2e^{i\Re\{2\gamma_p\}D}S(\pi-\alpha_p,0;\alpha_p,0)-N_p^+N_p^-S(\alpha_p,0;\alpha_p,0)\right.$$
$$\left.-N_p^-N_p^+S(\pi-\alpha_p,0;\pi-\alpha_p,0)+(N_p^+)^2e^{i\Re\{-2\gamma_m\}D}S(\alpha_p,0;\pi-\alpha_p,0)]\right\}e^{-\Im\{2\xi_p\}x}e^{-\Im\{2\gamma_p\}D}. \tag{20}$$

We define Eq. (20) as the modal cross section of the object for the extinction of the individual modes of the wave guide. Analogous to plane waves in free space, the modes in a wave guide are the entity that propagate in the wave guide and determine the energy of the acoustic field in the wave guide. It therefore becomes meaningful to quantify the extinction caused by an object of the individual modes of the wave guide and subsequently the cross section of the object as perceived by the individual modes of the wave guide.

V. ESTIMATION OF OBJECT SIZE FROM EXTINCTION THEOREM IN AN OCEAN WAVE GUIDE

The extinction formula can be used to estimate the size of an object by measuring the extinction it causes in an incident beam. For instance, in astronomy, the size of a meteorite is estimated from the extinction it causes in the light reaching a telescope when the meteorite is in interstellar space between a star and the telescope, so long as the telescope is large enough to measure the entire shadow remnant.[4]

For an object that is large compared to the wavelength, its extinction cross section in free space, according to Babinet's principle, is equal to twice its geometrical projected area.[4] If we let T_p be the projected area of the object in the direction of an incident plane wave in free space, we obtain

$$\frac{4\pi}{k^2}\Im\{S_f\}=2T_p. \tag{21}$$

The size of the object is therefore directly related to the free space forward scatter function of the object for objects that are large compared to the wavelength. The forward scatter function can be determined from a measurement of the extinction caused by the object.

Extinction measurements usually involve integrating the intensity of the incident and total fields over a sufficiently large screen that registers the full extinction caused by the object. We measure the incident power on the screen in the absence of the object and the total power in the presence of the object. The difference between these two energy fluxes on the screen is the extinction.

An intensity measurement at a single point in space in the forward scatter direction is typically inadequate. This can be seen from Eq. (C3) for free space, and Eq. (6) in the wave guide, where the interference intensity $\mathbf{V}_i^* \Phi_s$ at a point depends very sensitively on the source and receiver positions which cause rapid fluctuation in the phase term. To determine the forward scatter function from a single receiver in the forward direction then requires extremely accurate knowledge of the source, object and receiver locations. In practical measurements, it may also be difficult to precisely locate the point sensor in the forward direction. This is especially true for large objects as they have very narrow forward scatter function peaks. Equation (C14) for the extinction in free space on the other hand has no phase dependence involving the source or screen position. Extinction measurement over a screen is therefore a more robust method for estimating the forward scatter amplitude and hence the size of an object. For measurements in a shallow water wave guide, the screen over which the intensity is integrated can be either a sufficiently large planar array, or a billboard array whose spacing between the sensor elements satisfies the Nyquist criterion for sampling the field in space.

In a wave guide, the extinction caused by an object, Eq. (13), depends not only upon the properties of the object through the scatter function, but also the properties of the wave guide and the measurement geometry. They are, in general, convolved in the expression for the extinction and are separable only when the incident field is composed of a single mode as evident in Eq. (14). This suggests a possible scenario for extinction measurements in a wave guide to extract the scatter function's forward amplitude and subsequently to estimate the size of an object.

For large source to object separation x_0, the mode that survives in the incident field is mode 1. Mode 1 of any wave guide propagates almost horizontally and we can approximate its elevation angle as $\alpha_1 \approx \pi/2$. In this case, the four scatter function amplitudes in Eq. (14) can be approximated as $S(\pi/2,0,\pi/2,0)$ and factored out of the equation for the extinction. Using the fact that for mode 1, $\Re\{\xi_1\} \gg \Im\{\xi_1\}$ we rewrite the extinction for mode 1 as

$$\begin{aligned}\mathcal{E}(x|\mathbf{r}_0) = & \frac{1}{d^2(z_0)d(0)2\omega k}\frac{1}{x_0}\frac{1}{\Re\{\xi_1\}}|u_1(z_0)|^2 \\ & \times \Im\{S(\pi/2,0;\pi/2,0)[(N_1^-)^2 e^{i\Re\{2\gamma_1\}D} \\ & - 2N_1^+ N_1^- + (N_1^+)^2 e^{i\Re\{-2\gamma_1\}D}]\} \\ & \times e^{-\Im\{2\xi_1\}(x_0+x)} e^{-\Im\{2\gamma_1\}D}. \end{aligned} \tag{22}$$

In a Pekeris wave guide,[14,15] with

$$N_1^+ = N_1^- \approx \frac{1}{i}\sqrt{\frac{d(0)}{2H}}, \tag{23}$$

using Eq. (5), we see that

$$\begin{aligned}|u_1(0)|^2 = & [(N_1^-)^2 e^{i\Re\{2\gamma_1\}D} - 2N_1^+ N_1^- \\ & + (N_1^+)^2 e^{i\Re\{-2\gamma_1\}D}] e^{-\Im\{2\gamma_1\}D}. \end{aligned} \tag{24}$$

The extinction formula for mode 1 therefore leads to

$$\begin{aligned}\mathcal{E}(x|\mathbf{r}_0) = & \frac{1}{d^2(z_0)d(0)2\omega k}\frac{1}{x_0}\frac{1}{\Re\{\xi_1\}}|u_1(z_0)|^2|u_1(0)|^2 \\ & \times \Im\{S(\pi/2,0;\pi/2,0)\} e^{-\Im\{2\xi_1\}(x_0+x)}. \end{aligned} \tag{25}$$

Equation (20) for the modal cross section of the object for mode 1 in the Pekeris wave guide, simplifies to

$$\sigma_1(x) = \frac{4\pi}{k}\frac{1}{\Re\{\xi_1\}}\Im\{S(\pi/2,0;\pi/2,0)\} e^{-2\Im\{\xi_1\}x}. \tag{26}$$

Since mode 1 propagates close to the horizontal, $\Re\{\xi_1\} \approx k$. The cross section of an object for the extinction of mode 1 in a Pekeris wave guide, Eq. (26), is almost identical to the cross section of the object for the extinction of plane waves in free space, Eq. (C16).

In Eqs. (25) and (26) the properties of the target are separated from the wave guide and geometric parameters. If we can measure the extinction of mode 1 caused by the object in the wave guide, we can estimate the free space forward scatter amplitude of the object and subsequently, the size of the object. A knowledge of the wave guide properties, and location of source, object and screen is necessary to correct for the spreading and absorption loss in the wave guide, as well as the amplitude of mode 1 at the source and object depths. Experimentally, we can estimate the source to object range x_0 from the arrival of the back scattered field from the object using a sensor that is co-located with the source.

As discussed in Eq. (21), the object size is related to the forward scatter function amplitude. The extinction of the higher order modes of the wave guide, apart from mode 1, depend on the scatter function amplitude in other directions in addition to the forward. It is therefore much more difficult to extract information about the size of the object from modes higher than mode 1 unless the object is compact as will be discussed in Sec. (VI E). For objects that are buried in sediments that are faster than water, mode 1 excited by a source in the water column does not penetrate into the bottom due to total internal reflection. The above method will therefore not be useful in estimating the size of objects buried in fast bottoms.

VI. ILLUSTRATIVE EXAMPLES

In all the illustrative examples, a water column of 100 m depth is used to simulate a typical continental shelf environment. The sound speed structure of the water column is isovelocity with constant sound speed of 1500 m/s, density of 1 g/cm^3 and attenuation of 6.0×10^{-5} dB/λ. The seabed is either perfectly reflecting or comprised of sand or silt half spaces. The density, sound speed and attenuation are taken to be 1.9 g/cm^3, 1700 m/s, and 0.8 dB/λ for sand, 1.4 g/cm^3, 1520 m/s, and 0.3 dB/λ for silt. Calculations are made of the combined and modal extinction, incident intensity on the ob-

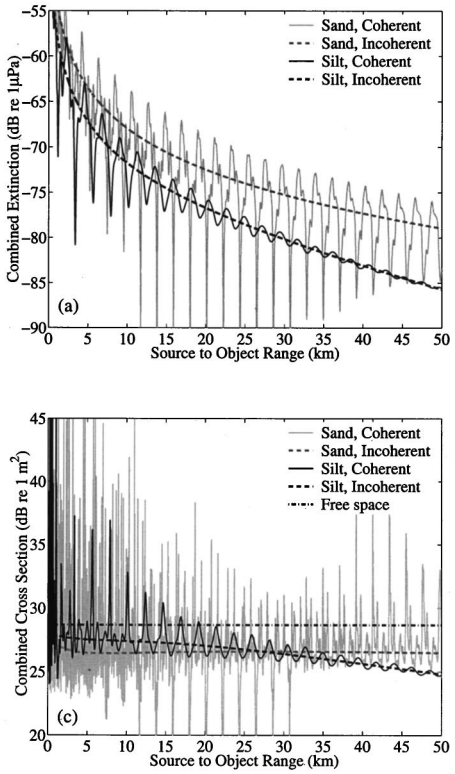

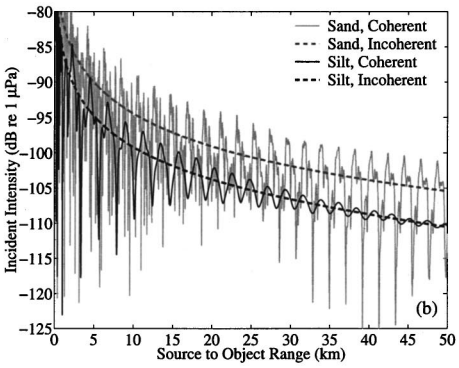

FIG. 2. (a) The combined extinction Eq. (13) of all the modes, caused by a pressure release sphere of radius 10 m centered at 50 m depth, in a Pekeris wave guide composed of 100 m water with either sand or silt half space is plotted as a function of x_0, its range from a point source of frequency 300 Hz also placed at the same depth in the wave guide. The separation of the screen from the object is the same as that of the source from the object at each source to object range, $x=x_0$. (b) The incident intensity on the sphere Eq. (17). (c) The combined cross section of the sphere Eq. (18). Both the coherent and incoherent approximation of the quantities are plotted in each subfigure.

ject, and, the combined and modal cross sections in various wave guides for different objects as a function of source, object and screen locations. The object size and frequency is also varied. Except for Sec. VI E, the frequency used in all other examples is 300 Hz.

A. Combined extinction cross section in different wave guides

First, we examine how the combined extinction of all the modes, caused by a pressure-release sphere of radius 10 m, in a Pekeris wave guide with either sand or silt bottom half space varies as a function of source to object range at a source frequency of 300 Hz. The source and sphere centers are located at $D=50$ m in the middle of the water column. The combined extinction measured by the screen Eq. (13), the incident intensity on per unit area of the sphere Eq. (17), and the combined cross section of the sphere Eq. (18) in the wave guides are plotted as a function of source to object separation x_0 in Figs. 2(a)–(c), respectively. At each x_0, the separation of the screen from the object is the same as that of the source from the object, i.e., $x=x_0$ The combined extinction is calculated using Eq. (13) with the scatter function for the sphere given by Eqs. (8) and (9) of Ref. 13 with $f(n)$ replaced by $(-1)^n f(n)$ to convert from Ingenito's definition to the standard one described in Ref. 12.

The combined extinction and incident intensity fluctuate with range due to the coherent interference between the modes. The resulting combined cross section of the sphere also fluctuates with range. The incident intensity and extinction are larger in the wave guide with sand bottom. The fluctuations in the fields are also greater in the sand bottom wave guide as compared to the silt bottom wave guide. The difference arise primarily because the number of trapped modes is larger for the sand half space due to the higher critical angle of 28.1° for the water to sand interface as compared with the 9.3° of water to silt leading to larger fields and fluctuations in the wave guide with sand bottom. For a screen placed at a fixed range from the object, it is the coherent extinction and cross section that we measure experimentally. From Fig. 2(c), we see that the coherent combined cross section of the object varies rapidly with range in the wave guide. Consequently, it is difficult to extract information about the size of the object from a measurement of its combined extinction of all the wave guide modes.

We find it useful to approximate the combined extinction measured by the screen and the incident intensity on the sphere as a single incoherent sum over the modes which provides an average trend to the curves as a function of range. Taking the ratio of the incoherent combined extinction and incident intensity, we obtain the incoherent combined cross section. The combined extinction, incident intensity and combined cross section of the sphere calculated incoherently, using Eqs (13), (17), and (18), respectively, by replacing the double sum with a single sum over the modes are plotted in Figs. 2(a)–(c). From the incoherent plots, we see that the extinction and the incident intensity decay with range due to geometrical spreading and absorption loss in a real wave guide.

In a perfectly reflecting wave guide, there is no absorption in the wave guide. Consequently, an incoherent approximation for σ_T is independent of range as can be seen from Eq. (18). The decay in the extinction due to spreading loss is compensated by spreading loss in the flux incident on the object which keeps the cross section a constant. In this case, the extinction measured by the screen is due entirely to the

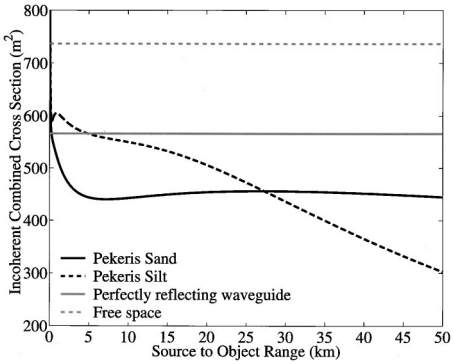

FIG. 3. Incoherent combined cross section of a 10 m radius pressure release sphere at 300 Hz source frequency in a Pekeris wave guide with sand bottom half space, Pekeris wave guide with silt bottom half space, perfectly reflecting wave guide, and free space as a function of source to object range x_0. For this plot, $x=x_0$. In the wave guides, the source and sphere center are located at 50 m water depth. The incoherent combined cross section is calculated using Eq. (18) by replacing the double sum over the modes with a single sum.

object. Figure 3 shows σ_T, calculated incoherently, plotted for a pressure-release sphere of radius 10 m in a perfectly reflecting wave guide as a function of x_0. In this figure $x=x_0$. The incoherent combined cross section of the object in free space with no absorption and in the Pekeris wave guide examples considered so far are also plotted for comparison. Figure 3 shows that this incoherent combined cross section for the extinction of all the wave guide modes differs significantly from the free space cross section of the object. So, it is difficult to obtain an estimate of the size of an object from an incoherent as well as a coherent measurement of its combined cross section.

B. Modal cross section in different wave guides

In this section, we will investigate how the modal extinction cross section of the 10 m pressure release sphere varies for the individual modes in various wave guides at 300 Hz. Figures 4(a) and (b) show the amplitudes of the modes at the source depth of 50 m in the Pekeris wave guide with sand and silt bottom, respectively. Only the propagating modes are plotted because these are the modes that compose the incident field on the object in the far field. These are the mode amplitudes at the object depth because the target is also at 50 m depth. The amplitude of the modes in the perfectly reflecting wave guide are plotted in Fig. 4(c). Only the even number modes are excited by the source at 50 m depth and they have the same amplitude.

The extinction of each individual mode in the Pekeris wave guide with sand bottom caused by the sphere and calculated using Eq. (14) are plotted in Figs. 5(a) and (b) at the source to object range of 1 km and 25 km, respectively. The screen is placed the same distance away from the object as the source in each case. The modal extinctions in the Pekeris wave guide with silt bottom at 1 km and 25 km are plotted in Figs. 5(c) and (d), respectively. Comparing Fig. 5 with Fig. 4, we see a dependence of the extinction of each mode on its amplitude at the object depth, with the more energetic modes being extinguished the most. The extinction of the modes vary with range due to spreading and absorption loss suffered by the modes. Absorption loss suffered by each mode as a result of absorption in a real wave guide is more severe for the high order modes due to their steeper elevation angles. The higher order modes are gradually stripped with increasing range and at sufficiently long ranges, the extinction caused by the object is very much limited to the extinc-

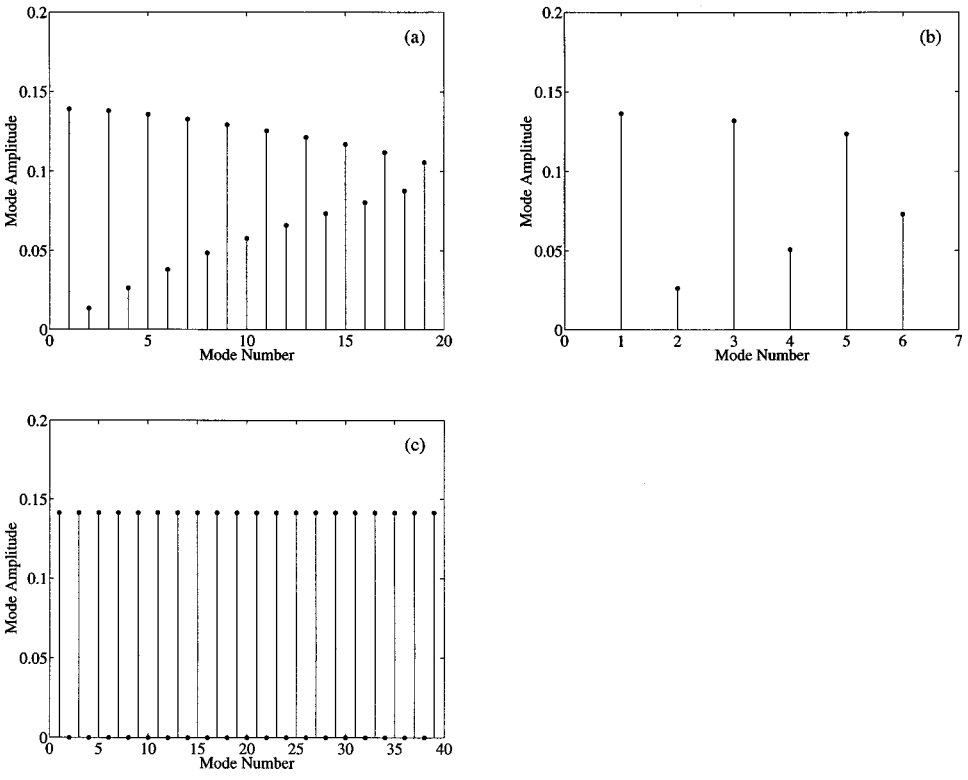

FIG. 4. Modal amplitude at the source and target depth of 50 m in (a) Pekeris wave guide with sand half space, (b) Pekeris wave guide with silt half space, and (c) perfectly reflecting wave guide for a frequency of 300 Hz.

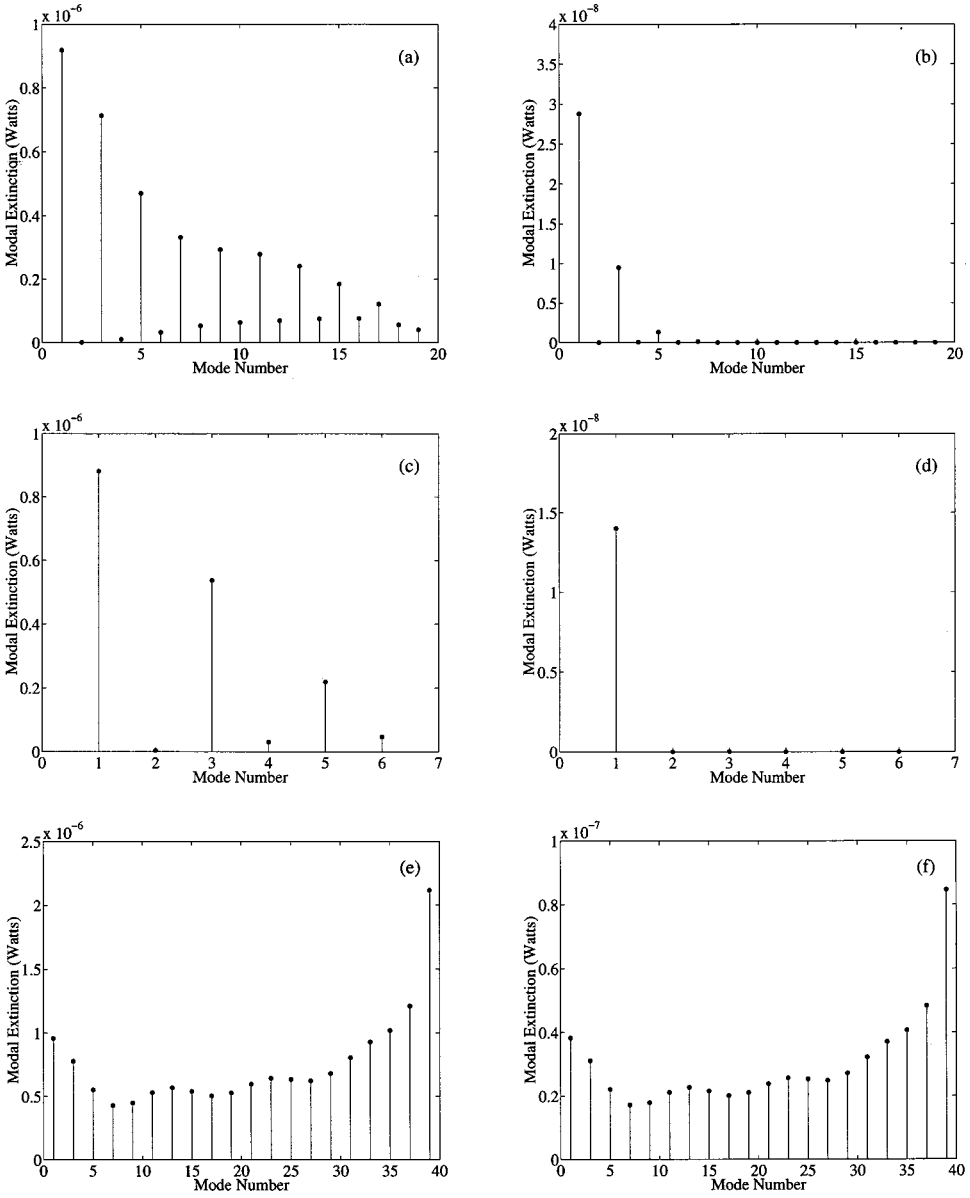

FIG. 5. Extinction of the individual modes Eq. (14) of the wave guide by the 10 m radius pressure release sphere at 50 m water depth with the source separated from the sphere by (a) 1 km range in a Pekeris sand half space wave guide, (b) 25 km range in a Pekeris sand half space wave guide, (c) 1 km range in a Pekeris silt half space wave guide, (d) 25 km range in a Pekeris silt half space wave guide, and (e) 1 km range in a perfectly reflecting wave guide, (f) 25 km range in a perfectly reflecting wave guide. The source depth is also 50 m and the source frequency is 300 Hz. The screen measuring the extinction is separated the same distance from the object as the source in each case.

tion of the first few propagating modes. For the perfectly reflecting wave guide in Figs. 5(e) and (f) at 1 km and 25 km, respectively, there is no absorption loss, so the extinction for each mode decays only with source to object range x_0. There is no mode stripping effect in a perfectly reflecting wave guide and the relative magnitude of the extinction across the modes remains the same, independent of range.

Figures 6(a)–(c) show the modal cross sections of the sphere, calculated using Eq. (20), for the extinction of the individual modes in the Pekeris sand, silt and perfectly reflecting wave guides, respectively. We set $x=0$ in Eq. (20) to obtain the modal cross section of the object corrected for absorption in the wave guide. In each of the wave guides illustrated in Fig. 6 we see that the modal cross section of the sphere for the extinction of mode 1 is very close to its cross section for the extinction of a plane wave in free space. For the higher order modes, the modal cross section of the object can be much larger or smaller than its free space value depending on the wave guide. We can calculate the forward scatter function amplitude of the object from a measurement of the extinction of mode 1 as discussed in Sec. V which allows us to estimate the size of the object.

C. Dependence of modal cross section on object depth

The modal cross section of an object depends on the depth of the object in the wave guide. We investigate how the modal cross section of the 10 m pressure release sphere varies when we lower its depth by half a wavelength distance to 52.5 m in the Pekeris silt, sand, and perfectly reflecting wave guides. We also lower the source depth to 52.5 m so that all the modes in the perfectly reflecting wave guide are excited by the source. The source frequency is 300 Hz.

Figure 7 shows the incoherent combined cross section of the sphere in the three wave guides. In the perfectly reflecting wave guide, the incoherent combined cross section of the sphere is now larger than its free space value. Figures 8(a)–(c) show the modal amplitudes in the three wave guides and

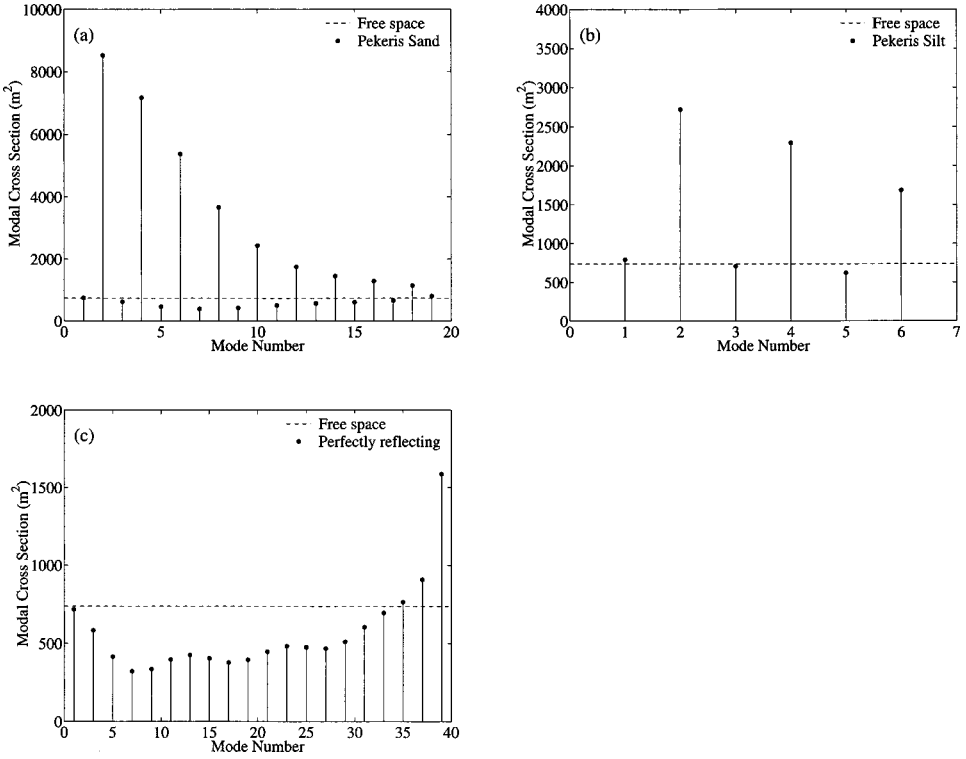

FIG. 6. Modal cross section Eq. (20) at 300 Hz of the 10 m radius pressure release sphere at 50 m water depth for the extinction of the individual modes in a (a) Pekeris sand half space wave guide, (b) Pekeris silt half space wave guide, and (c) perfectly reflecting wave guide. We set $x=0$ in Eq. (20) to remove the effect of absorption by the wave guide. The modal cross section of the sphere for mode 1 in each wave guide is almost equal to its free space cross section.

Figs. 9(a)–(c) show the modal cross sections, Eq. (20). In the perfectly reflecting wave guide Fig. 9(c), all modes that exist in the wave guide are scattered by the object to form the scattered field when it is at the shallower depth of 52.5 m, unlike in the previous example of Fig. 6 where it was at 50 m depth and only the excited odd number modes were scattered by the object. Comparing Fig. 9 with Fig. 6, we see that the modal cross section of most of the modes vary with object depth. For mode 1, however, in all the three wave guides, the modal cross section of the object remains close to its free space value.

D. Modal cross section for various object types

The cross section of the 10 m pressure release sphere is compared to that of a rigid or hard disk of radius 10 m in the wave guide. In free space, with the plane of the disk aligned normal to the direction of propagation of the incident waves, it is well known that its plane wave extinction cross section is equal to twice its projected area, which is 628.3 m^2 in this example. The cross section of a sphere in free space depends on the circumference of the sphere relative to the wavelength of the incident waves, i.e., $ka=2\pi a/\lambda$ where a is the radius of the sphere. The dependence of the extinction cross section of a pressure release or hard sphere on ka, in free space is plotted in Ref. 16. For a large pressure release sphere, high ka, the extinction cross section is roughly twice the projected area which is the same for both the sphere and the disk. For a compact pressure release sphere, small ka, the cross section of the sphere begins to exceed twice its projected area. For the present example, at 300 Hz source frequency, $ka=12.6$ and the extinction cross section of the sphere in free space is 736.7 m^2.

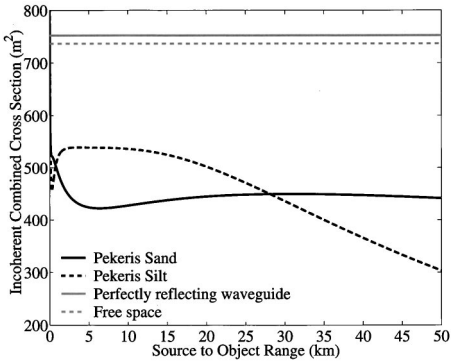

FIG. 7. Incoherent combined cross section of a 10 m radius pressure release sphere at 300 Hz source frequency in a Pekeris wave guide with sand bottom half space, Pekeris wave guide with silt bottom half space, perfectly reflecting wave guide, and free space as a function of source to object range x_0. For this plot, $x=x_0$. In the wave guides, the source and sphere center are located at 52.5 m water depth. The incoherent combined cross section is calculated using Eq. (18) by replacing the double sum over the modes with a single sum.

The incoherent combined cross section of the 10 m hard disk in the three different wave guides is plotted in Fig. 10. In free space, the cross section of the sphere at 300 Hz is only a little larger than that of the disk of the same radius. Comparing Figs. 3 and 10, we see that in the perfectly reflecting wave guide, the incoherent combined cross section of the sphere is much larger than that of the disk. The elevation angle of each mode of the wave guide increases with the mode number. Since the disk is aligned with it's plane parallel to the $y-z$ plane, the projected area of the disk perceived by each mode decreases as the elevation angle of the mode increases. For the sphere, however, each mode sees the same projected area, regardless of the elevation angle of the mode. Therefore the combined extinction of the modes by the sphere is much larger than by the disk. In the real wave guide, absorption by the wave guide alters the amplitude of each mode with the higher order modes

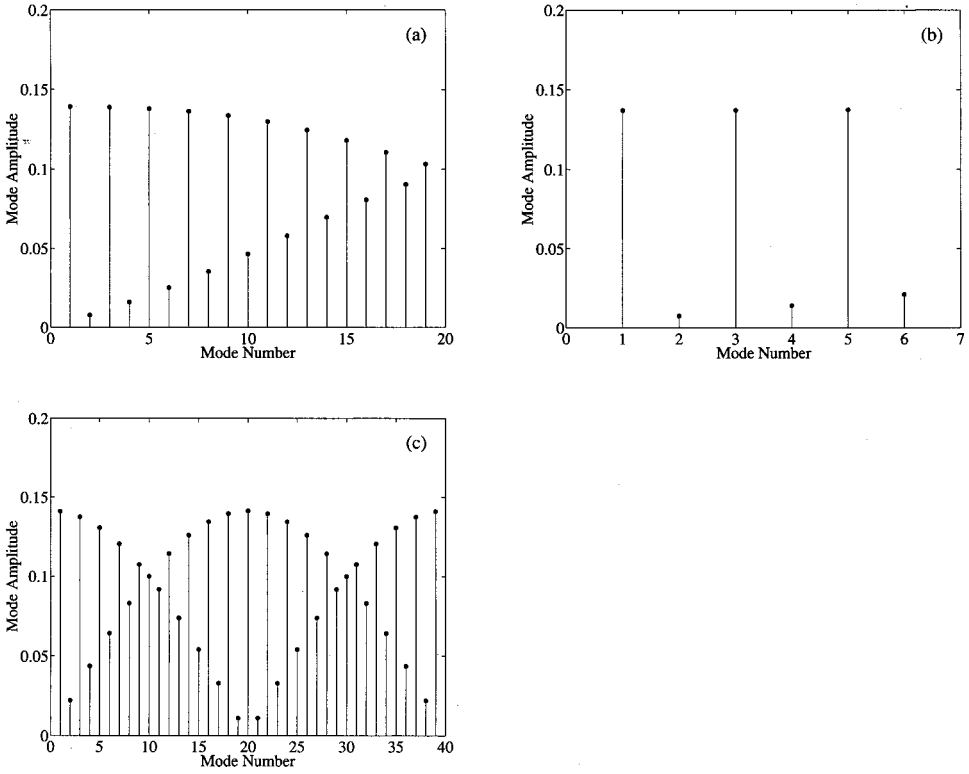

FIG. 8. Modal amplitude at the object depth of 52.5 m in (a) Pekeris wave guide with sand half space, (b) Pekeris wave guide with silt half space, and (c) perfectly reflecting wave guide for a frequency of 300 Hz.

suffering greater absorption losses than the lower order modes. The higher order modes are less important in determining the combined extinction in the real wave guide. Consequently, in a real wave guide, the incoherent combined cross section of the sphere is only slightly larger than that of the disk.

The modal cross section Eq. (20) of the disk for each mode of the Pekeris sand, silt, and the perfectly reflecting wave guide is plotted in Figs. 11(a)–(c), respectively. From Fig. 11, we see once again that the modal cross section of the object for the extinction of mode 1 is almost equal to its free space cross section. In the present example, the cross section of the disk is equal to twice its projected area. This example further illustrates that we can obtain a measure of the size of an object from the extinction of mode 1 in a wave guide.

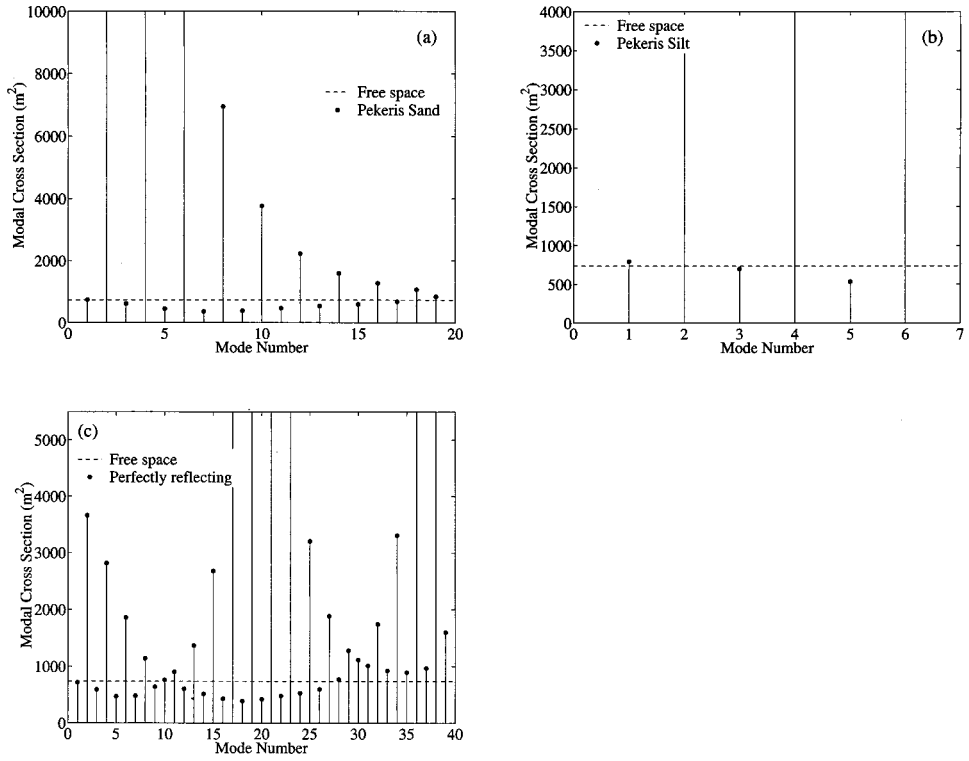

FIG. 9. Modal cross section Eq. (20) at 300 Hz of the 10 m radius pressure release sphere at 52.5 m water depth for the extinction of the individual modes in a (a) Pekeris sand half space wave guide, (b) Pekeris silt half space wave guide, and (c) perfectly reflecting wave guide. We set $x=0$ in Eq. (20) to remove the effect of absorption by the wave guide. The modal cross section of the sphere for mode 1 in each wave guide is almost equal to its free space cross section.

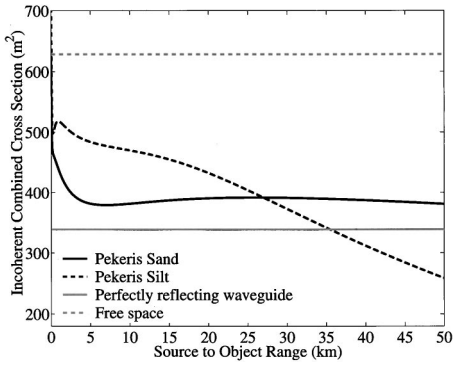

FIG. 10. Incoherent combined cross section of a hard disk of radius 10 m at 300 Hz source frequency in a Pekeris wave guide with sand bottom half space, Pekeris wave guide with silt bottom half space, perfectly reflecting wave guide, and free space as a function of source to object range x_0. For this plot, $x=x_0$. In the wave guides, the source and disk center are located at 50 m water depth with the disk aligned in the $y-z$ plane. The incoherent combined cross section is calculated using Eq. (18) by replacing the double sum over the modes with a single sum.

E. Dependence of modal cross section on object size and frequency

Here we investigate how the modal cross section Eq. (20) of a pressure release sphere at 50 m water depth compares with its free space cross section when we vary the size of the sphere and the frequency of the incoming waves. Figures 12(a)–(d) show the result in a Pekeris sand wave guide, plotted as a function of *ka*. The corresponding result in the Pekeris silt and perfectly reflecting wave guides are plotted in Figs. 13 and 14, respectively.

For a large sphere with the high *ka* of 62.8, we see from Figs. 12–14(d) that the modal cross section of the sphere for the high order modes fluctuates and departs drastically from the free space cross section for most of the modes. The modal cross section for mode 1, however, remains nearly equal to the free space cross section of the large sphere in each wave guide. For the compact sphere with the small *ka* of 0.1 on the other hand, Figs. 12–14(a), the modal cross section of most of the modes are fairly close to the free space cross section of the object.

Figures 15(a)–(d) show the scatter function amplitude plotted as a function of elevation angle of the modes at various *ka*. Compact objects scatter like point targets and they have an omnidirectional scatter function S_0. In Eq. (20), we see that the modal cross section depends on not only the forward scatter amplitude, but also the scatter function amplitude in nonforward directions. For a compact object, since the scatter function amplitude is a constant, independent of azimuth or elevation angles, we can factor it out in Eq. (20). Furthermore, in a perfectly reflecting wave guide, since[14,15]

$$N_p^+ = N_p^- = \frac{1}{i}\sqrt{\frac{d(0)}{2H}}, \tag{27}$$

N_p can be factored out of the equation as well. Consequently, for a compact object in the perfectly reflecting wave guide, Eq. (20) for the modal cross section reduces to

$$\sigma_p(x) = \frac{4\pi}{k}\frac{1}{\Re\{\xi_p\}}\Im\{S_0\}e^{-2\Im\{\xi_p\}x} \tag{28}$$

which resembles the expression for the free space cross section of the object in Eq. (C16). The modal cross section of the compact object in the wave guide will, however, be slightly larger than the free space cross section because of the dependence on the horizontal wave number of the mode ξ_p in the denominator of Eq. (28) instead of k as in Eq. (C16) for free space. The real part of the horizontal wave number decreases as the mode number increases. We see a gradual

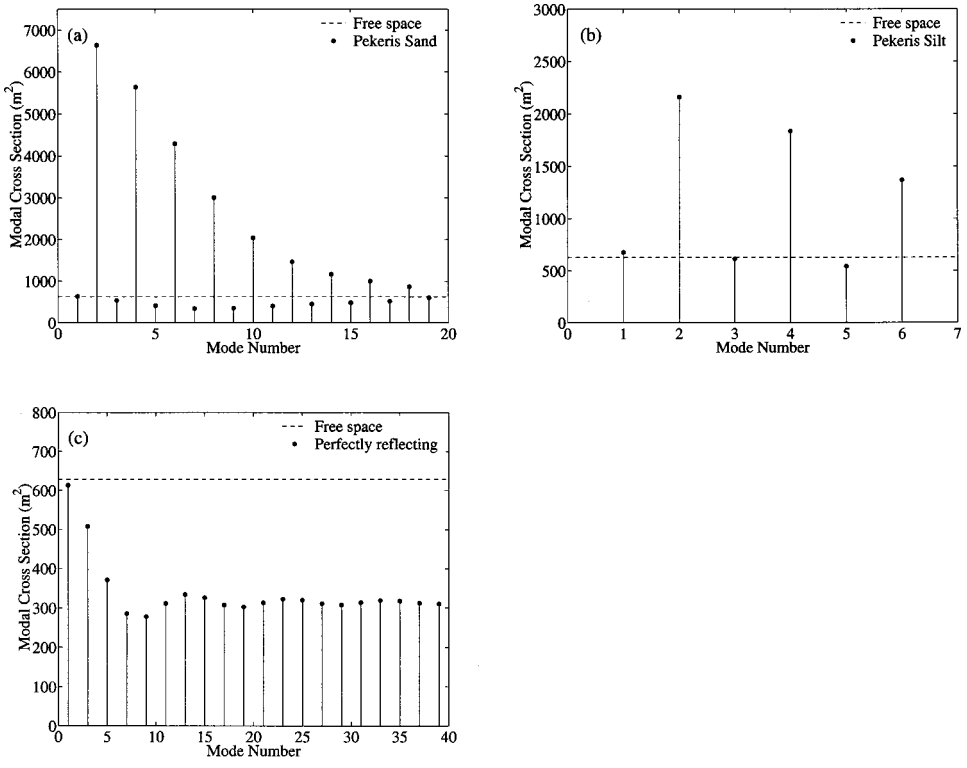

FIG. 11. Modal cross section Eq. (20) at 300 Hz of the 10 m radius hard disk at 50 m water depth for the extinction of the individual modes in a (a) Pekeris sand half space wave guide, (b) Pekeris silt half space wave guide, and (c) perfectly reflecting wave guide. We set $x=0$ in Eq. (20) to remove the effect of absorption by the wave guide. The modal cross section of the disk for mode 1 in each wave guide is almost equal to its free space cross section.

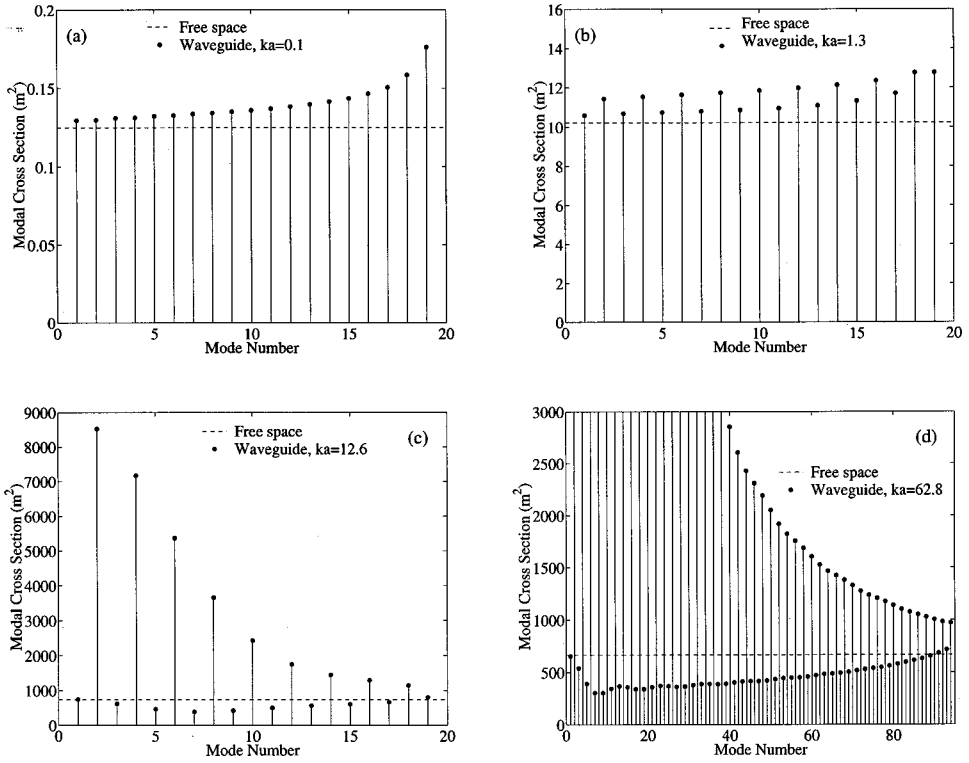

FIG. 12. Modal cross section Eq. (20) of a pressure release sphere at 50 m water depth for the extinction of the individual modes in a Pekeris sand half space wave guide with (a) sphere radius 0.1 m, 300 Hz source frequency, $ka=0.1$, (b) sphere radius 1 m, 300 Hz source frequency, $ka=1.3$, (c) sphere radius 10 m, 300 Hz source frequency, $ka=12.6$, and (d) sphere radius 10 m, 1500 Hz source frequency, $ka=62.8$. We set $x=0$ in Eq. (20) to remove the effect of absorption by the wave guide. Only the propagating modes are illustrated in each plot. The modal cross section of the sphere for mode 1 in each case is almost equal to its free space cross section.

increase in the modal cross section in Fig. 14(a) with increase in mode number for the compact sphere in the perfectly reflecting wave guide.

In a real wave guide, N_p is usually complex. For the lower order modes, N_p has a large imaginary component and we can still factor it out as we did for the perfectly reflecting wave guide. We also observe a trend of increase in modal cross section with mode number for the compact sphere in the examples of Figs. 12–13(a). This implies that for a compact object in a wave guide, as well as mode 1, we can also use the higher order modes to extract its omnidirectional scatter function amplitude from modal extinction measurements. Once the scatter function amplitude of a compact object is known, its size can be estimated.

VII. SUMMARY AND DISCUSSION

A generalized extinction theorem for the rate at which energy is extinguished from the incident wave of a far field

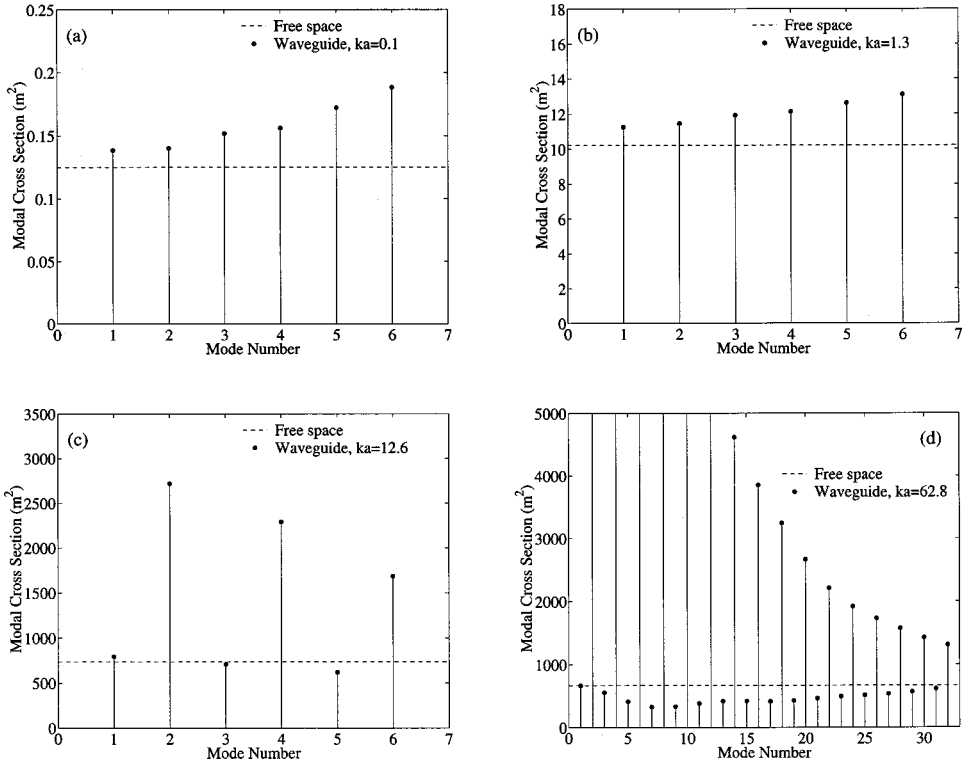

FIG. 13. Modal cross section Eq. (20) of a pressure release sphere at 50 m water depth for the extinction of the individual modes in a Pekeris silt half space wave guide with (a) sphere radius 0.1 m, 300 Hz source frequency, $ka=0.1$, (b) sphere radius 1 m, 300 Hz source frequency, $ka=1.3$, (c) sphere radius 10 m, 300 Hz source frequency, $ka=12.6$, and (d) sphere radius 10 m, 1500 Hz source frequency, $ka=62.8$. We set $x=0$ in Eq. (20) to remove the effect of absorption by the wave guide. Only the propagating modes are illustrated in each plot. The modal cross section of the sphere for mode 1 in each case is almost equal to its free space cross section.

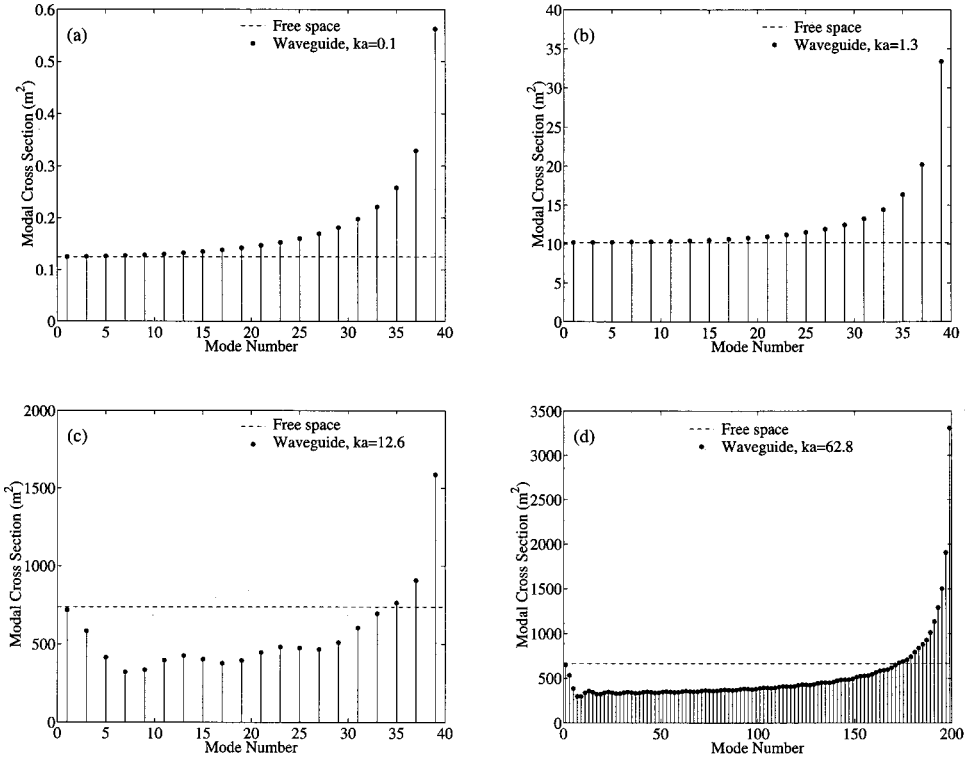

FIG. 14. Modal cross section Eq. (20) of a pressure release sphere at 50 m water depth for the extinction of the individual modes in a perfectly reflecting wave guide with (a) sphere radius 0.1 m, 300 Hz source frequency, $ka=0.1$, (b) sphere radius 1 m, 300 Hz source frequency, $ka=1.3$, (c) sphere radius 10 m, 300 Hz source frequency, $ka=12.6$, and (d) sphere radius 10 m, 1500 Hz source frequency, $ka=62.8$. The modal cross section of the sphere for mode 1 in each case is almost equal to its free space cross section.

point source by an object of arbitrary size and shape in a stratified medium has been developed from wave theory. In a wave guide, both the incident and scattered fields are composed of a superposition of plane waves or equivalently a superposition of modes. The total extinction is shown to be a linear sum of the extinction of each wave guide mode. Each modal extinction involves a sum over all incident modes scattered into the given mode and is expressed in terms of the objects's plane wave scatter function in the forward azimuth and equivalent modal plane wave amplitudes. In general, our results show that when we have multiple plane waves incident on an object, whether in a wave guide or in free space, extinction will be a function of not only the forward scatter amplitude for each incident plane wave but also the scatter function amplitudes coupling each incident plane wave to all other plane waves with distinct directions that comprise the incident field.

Our derivation greatly facilitates scattering calculations

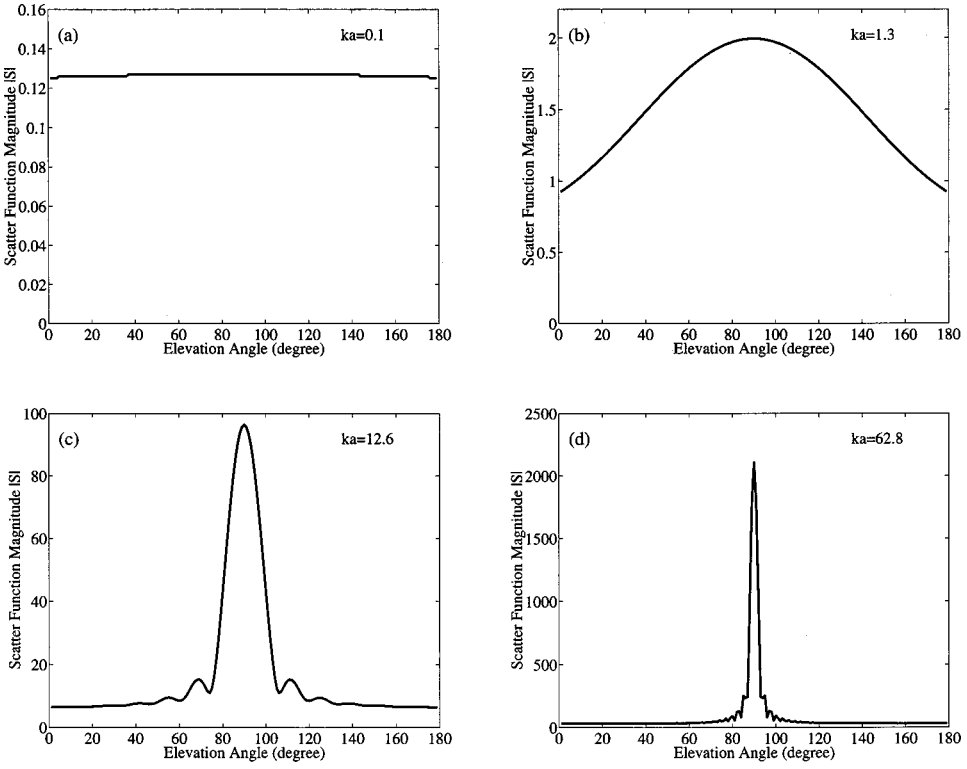

FIG. 15. The magnitude of the free space plane wave scatter function $S(\theta,\phi=0°,\theta_i=90°,\phi_i=0°)$ is plotted as a function of θ, the elevation angle for a pressure release sphere at (a) $ka=0.1$, (b) $ka=1.3$, (c) $ka=12.6$, and (d) $ka=62.8$. The forward scatter peak is at $\theta=90°$.

by eliminating the need to integrate energy flux about the object. The only assumptions are that multiple scattering between the object and wave guide boundaries is negligible, and the object lies within a constant sound speed layer.

Two extinction cross sections are defined for an object submerged in a wave guide. The first is the combined cross section which is the ratio of the combined extinction of all the modes of the wave guide to the total incident intensity in the radial direction at the object's centroid. Calculations for a shallow water wave guide show that both the combined extinction and the combined cross section of an object are highly dependent on measurement geometry, medium stratification, as well as the scattering properties of the object. They also fluctuate with range due to the coherent interference between the modes. Both are significantly modified by the presence of absorption in the medium. The presence of absorption typically means that the extinction and corresponding cross section of the obstacle in an ocean wave guide will be smaller than it's value in free space. The practical implications of these findings is that experimental measurements of the total scattering cross section of an obstacle in a wave guide may differ greatly from those obtained for the same obstacle in free space and may lead to errors in target classification if the wave guide effects are not properly taken into account.

We also define the modal cross section of an object for the extinction of an individual wave guide mode of a wave guide. We show that for an object submerged in a typical ocean wave guide, the modal cross section for the extinction of mode 1 is almost identical to the object's free space cross section, after correcting for absorption loss in the medium. This finding can be used to robustly estimate the size of objects submerged underwater from extinction measurements involving mode 1, which is often the dominant mode after long range propagation in a shallow water wave guide.

APPENDIX A: GENERAL APPROACH FOR CALCULATING EXTINCTION

There are two approaches to calculate the extinction of an incident field due to absorption and scattering by an object. In the first approach, we define a closed control surface C that encloses the object, but excludes the source. We let the origin of the coordinate system be at the object centroid. Let $\mathbf{r}_0$ be the position of the source and $\mathbf{r}$ be the position of a point on the control surface.

In the absence of the object, only the incident field Φ_i exists. The intensity of the incident field at location $\mathbf{r}$ on the control surface from a source at $\mathbf{r}_0$ is

$$\mathbf{I}_i(\mathbf{r}|\mathbf{r}_0)=\Re\{\mathbf{V}_i^*(\mathbf{r}|\mathbf{r}_0)\Phi_i(\mathbf{r}|\mathbf{r}_0)\}, \tag{A1}$$

where $\mathbf{V}_i(\mathbf{r}|\mathbf{r}_0)$ is the velocity vector of the incident field which, from Newton's law, can be expressed as

$$\mathbf{V}_i(\mathbf{r}|\mathbf{r}_0)=\frac{1}{i\omega d(\mathbf{r})}\nabla\Phi_i(\mathbf{r}|\mathbf{r}_0) \tag{A2}$$

for a harmonic field at frequency ω where $d(\mathbf{r})$ is the density at location $\mathbf{r}$. Integrating the incident intensity over the entire control surface C gives the net incident intensity flux $\mathcal{F}_i$ through the control surface,

$$\mathcal{F}_i=\Re\left\{\oint\oint_C \mathbf{V}_i^*\Phi_i\cdot\mathbf{dS}\right\}. \tag{A3}$$

In a lossless media, the incident energy flux entering the control surface has to equal that leaving the surface. Therefore in a lossless media,

$$\mathcal{F}_i=0. \tag{A4}$$

In the presence of the object, the total field at location $\mathbf{r}$ on the control surface for a source at $\mathbf{r}_0$ is the sum of the incident pressure field from the source and the scattered field from the object,

$$\Phi_T(\mathbf{r}|\mathbf{r}_0)=\Phi_i(\mathbf{r}|\mathbf{r}_0)+\Phi_s(\mathbf{r}|\mathbf{r}_0). \tag{A5}$$

The intensity of this total field at $\mathbf{r}$ on the control surface is

$$\mathbf{I}_T(\mathbf{r}|\mathbf{r}_0)=\Re\{\mathbf{V}_T^*(\mathbf{r}|\mathbf{r}_0)\Phi_T(\mathbf{r}|\mathbf{r}_0)\}. \tag{A6}$$

The total intensity integrated over the entire control surface C is the total energy flux $\mathcal{F}_T$ through C, or the total intercepted power,

$$\begin{aligned}\mathcal{F}_T&=\Re\left\{\oint\oint_C \mathbf{V}_T^*\Phi_T\cdot\mathbf{dS}\right\}\\&=\Re\left\{\oint\oint_C (\mathbf{V}_i^*\Phi_i+\mathbf{V}_i^*\Phi_s+\mathbf{V}_s^*\Phi_i+\mathbf{V}_s^*\Phi_s)\cdot\mathbf{dS}\right\}.\end{aligned} \tag{A7}$$

If the object absorbs some of the power incident on it, the net outward power flow through the control surface is equal in magnitude to the rate at which absorption takes place. Let W_a be the rate at which energy is absorbed by the obstacle, then $\mathcal{F}_T=-W_a$.

Let W_s be the total power scattered in all directions by the object,

$$W_s=\Re\left\{\oint\oint_C \mathbf{V}_s^*\Phi_s\cdot\mathbf{dS}\right\}. \tag{A8}$$

By definition, extinction is the sum of the total power absorbed and scattered by the object. Making use of Eqs. (A3), (A4), and (A8) in Eq. (A7), the extinction $\mathcal{E}$ due to the object in a lossless media is

$$\mathcal{E}=W_a+W_s=-\Re\left\{\oint\oint_C (\mathbf{V}_i^*\Phi_s+\mathbf{V}_s^*\Phi_i)\cdot\mathbf{dS}\right\}. \tag{A9}$$

From Eq. (A9) we see that extinction is a result of the interference between the incident and scattered fields over the control surface. For a plane wave in free space, the active region of the control surface over which the incident and scattered fields have a fixed phase relationship to interfere destructively lies within an angular width $\sqrt{\lambda/r}$ of the forward direction, where λ is the wavelength of the incident wave, and r is the distance of the control surface from the object centroid in the forward direction.[2,3,17] This region comprises the shadow remnant. Outside of this region, the

integrand in Eq. (A9) fluctuates too rapidly to contribute to the extinction.

Consequently, instead of integrating the interference flux over the entire control surface, we can replace the enclosed control surface by a screen *Sc* in the forward direction. From Eq. (A7), if we integrate the interference flux over the area of the screen, instead of the enclosed control volume, we obtain

$$-\Re\left\{\int\int_{Sc}(\mathbf{V}_i^*\Phi_s+\mathbf{V}_s^*\Phi_i)\cdot\mathbf{dS}\right\}$$
$$=\Re\left\{\int\int_{Sc}(\mathbf{V}_i^*\Phi_i-\mathbf{V}_T^*\Phi_T+\mathbf{V}_s^*\Phi_s)\cdot\mathbf{dS}\right\}. \quad \text{(A10)}$$

The first term on the right-hand side of Eq. (A10) is the incident flux $\mathcal{F}_i$ through the screen, which is the flux through the screen in the absence of the object. The second term is $\mathcal{F}_T$, the total flux through the screen in the presence of the object. The last term is the scattered flux through the screen. If we place the screen sufficiently far from the object so that $\mathbf{V}_s^*$ and Φ_s become small relative to $\mathbf{V}_i^*$ and Φ_i due to spreading loss, the scattered flux becomes negligible. For instance, for plane waves in free space, the spherical spreading of the scattered field causes the scattered field intensity to decrease with range with a $1/r^2$ dependence, while the incident intensity remains constant.

At any given range r of the screen from the object, to measure the full extinction caused by the object, the screen has to be much wider than $\sqrt{\lambda r}$. For a sufficiently large screen, the extinction $\mathcal{E}$ is, from Eq. (A10),

$$\mathcal{E}=\mathcal{F}_i-\mathcal{F}_T=-\Re\left\{\int\int_{Sc}(\mathbf{V}_i^*\Phi_s+\mathbf{V}_s^*\Phi_i)\cdot\mathbf{dS}\right\}, \quad \text{(A11)}$$

the difference between the incident flux measured by the screen in the absence of the object and the total flux in the presence of the object. This is the approach due to Van de Hulst for calculating the extinction by placing a sufficiently large screen in the forward direction to register the full extinction.

APPENDIX B: EXTINCTION, ABSORPTION, AND SCATTERING CROSS SECTIONS

The extinction, absorption, and scattering cross sections can be viewed as fictitious areas that intercept a portion of the incident power equal to the extinguished, absorbed or scattered power, respectively. The extinction cross section σ_T, by definition, is the ratio between the rate of dissipation of energy $\mathcal{E}$ and the rate at which energy is incident on unit cross-sectional area of the object I_i,

$$\sigma_T=\frac{\mathcal{E}}{I_i}. \quad \text{(B1)}$$

From Eq. (A9), we can also express the above as

$$\sigma_T=\frac{W_a+W_s}{I_i}=\sigma_a+\sigma_s, \quad \text{(B2)}$$

where σ_a and σ_s are the absorption and scattering cross sections, respectively. For a nonabsorbing object, $\sigma_a=0$, and the extinction cross section is then equal to the scattering cross section, $\sigma_T=\sigma_s$.

APPENDIX C: EXTINCTION FORMULA FOR SCATTERING IN AN INFINITE LOSSY UNBOUNDED MEDIA

We derive the formula for the extinction of an incident plane wave in the far field of a point source by an object in an infinite unbounded medium with absorption loss. We will derive the expression using both the control surface method and the Hulst screen method discussed in Appendix A and compare the resulting expressions. Let ν be the coefficient for absorption in the medium. We write the magnitude of the complex wave vector as $k=\kappa+i\nu$, where $\kappa=\omega/c$.

The object centroid coincides with the center of the coordinate system and we place the source at $\mathbf{r}_0=(0,0,-z_0)$. First we derive the formula using the control surface method, Eq. (A9). We let the control surface be a spherical surface of radius R centered at the object centroid. At any point $\mathbf{r}$ on the control surface, the incident field is given by the free space Green's function,

$$\Phi_i(\mathbf{r}|\mathbf{r}_0)=\frac{1}{4\pi}\frac{e^{ik|\mathbf{r}-\mathbf{r}_0|}}{|\mathbf{r}-\mathbf{r}_0|}. \quad \text{(C1)}$$

Since the object is in the far field of the point source, the incident field at the object can be approximated as composing of plane waves with amplitude $e^{ikz_0}/4\pi z_0$. The scattered field from the object at ranges far from the object can be expressed as

$$\Phi_s(\mathbf{r}|\mathbf{r}_0)=\frac{1}{4\pi}\frac{e^{ikz_0}}{z_0}\frac{e^{ikr}}{kr}S(\theta,\phi;0,0). \quad \text{(C2)}$$

The first term in the integrand of Eq. (A9) for this case is

$$\mathbf{V}_i^*\Phi_s=\frac{1}{16\pi^2}\frac{(\kappa-i\nu)}{\omega d}\frac{e^{-i\kappa\sqrt{x^2+y^2+(z+z_0)^2}}}{(x^2+y^2+(z+z_0)^2)}(r\mathbf{i}_\mathbf{r}+z_0\mathbf{i}_\mathbf{z})$$
$$\times\frac{e^{i\kappa z_0}}{z_0}\frac{e^{i\kappa\sqrt{x^2+y^2+z^2}}}{(\kappa+i\nu)\sqrt{x^2+y^2+z^2}}S(\theta,\phi;0,0)$$
$$\times e^{-\nu\sqrt{x^2+y^2+(z+z_0)^2}}e^{-\nu z_0}e^{-\nu\sqrt{x^2+y^2+z^2}}. \quad \text{(C3)}$$

In the above expression, we explicitly factor out the term representing absorption in the medium to avoid confusion when conjugating the fields and to keep track of absorption losses in the medium. On the control surface, $r=\sqrt{x^2+y^2+z^2}=R$. We will assume that $z_0\gg R$ since the object is in the far field of the point source. We use the approximation $\sqrt{x^2+y^2+(z+z_0)^2}\approx z+z_0$ in the term that determines the phase of the integrand, and the approximation $\sqrt{x^2+y^2+(z+z_0)^2}\approx z_0$ in the spreading loss factor. The resulting expression becomes,

$$\mathbf{V}_i^*\Phi_s=\frac{1}{16\pi^2}\frac{(\kappa-i\nu)}{\omega d(\kappa+i\nu)}\frac{e^{-i(\kappa+\nu)z}}{z_0^3}(z_0\mathbf{i}_\mathbf{z}+R\mathbf{i}_\mathbf{r})\frac{e^{i\kappa R}}{R}$$
$$\times S(\theta,\phi;0,0)e^{-2\nu z_0}e^{-\nu R}. \quad \text{(C4)}$$

Next, we integrate Eq. (C4) over the area of the enclosed spherical surface. An area element on the surface is

$\mathbf{dS}=\mathbf{i}_r R^2 \sin\theta\, d\theta\, d\phi$. Since $z_0 \gg R$ we need only consider the first term in Eq. (C4) and note that $\mathbf{i}_z \cdot \mathbf{i}_r = \cos\theta$. With $z = R\cos\theta$ on the spherical surface, we obtain

$$\oint \oint_C \mathbf{V}_i^* \Phi_s \cdot \mathbf{dS} = \frac{1}{16\pi^2} \frac{(\kappa - i\nu)}{\omega d(\kappa + i\nu) z_0^2 R} e^{i\kappa R} \times e^{-2\nu z_0} e^{-\nu R} \times \int_0^{\pi}\int_0^{2\pi} e^{-(i\kappa+\nu)R\cos(\theta)} S(\theta,\phi;0,0) \times \cos\theta \sin\theta\, d\theta\, d\phi. \tag{C5}$$

Making use of asymptotic integration,

$$\oint \oint_C \mathbf{V}_i^* \Phi_s \cdot \mathbf{dS} = \frac{i}{8\pi\omega d z_0^2} \frac{1}{\kappa + i\nu} e^{-2\nu z_0} (S(0,0;0,0) e^{-2\nu R} + S(0,\pi;0,0) e^{i2\kappa R}). \tag{C6}$$

Similarly, we integrate the second term of Eq. (A9) over the control surface and obtain

$$\oint \oint_C \mathbf{V}_s^* \Phi_i \cdot \mathbf{dS} = \frac{-i}{8\pi\omega d z_0^2} \frac{1}{\kappa + i\nu} e^{-2\nu z_0} (S^*(0,0;0,0) e^{-2\nu R} - S^*(0,\pi;0,0) e^{-i2\kappa R}). \tag{C7}$$

Summing Eqs. (C6) and (C7), taking only the negative of the real part of the sum, we obtain the extinction caused by an object in an infinite unbounded lossy medium using the control volume method,

$$\mathcal{E}_C(\mathbf{r}|\mathbf{r}_0) = \frac{1}{4\pi\omega d} \frac{e^{-2\nu(z_0+R)}}{z_0^2} \left(\frac{\kappa}{\kappa^2+\nu^2} \Im\{S(0,0;0,0)\} - \frac{\nu}{\kappa^2+\nu^2} \Re\{S(0,\pi;0,0) e^{i2\kappa R}\} e^{2\nu R} \right). \tag{C8}$$

Next, we derive the extinction using the Van de Hulst screen method, Eq. (A11). We start with the expression in Eq. (C3). We place a square screen of length L a sufficiently large distance from the object in the forward direction, parallel to the $x-y$ plane a distance z away from the object. As discussed in Appendix A, we require $L > \sqrt{\lambda z}$. Since z is large, we assume that for points on the active region of the screen, $z \gg \rho$ where $\rho = \sqrt{x^2+y^2}$. We use the approximations $\sqrt{x^2+y^2+(z+z_0)^2} \approx z + z_0 + [\rho^2/2(z+z_0)]$, and $\sqrt{x^2+y^2+z^2} \approx z + (\rho^2/2z)$ in the terms that determine the phase of the integrand, and the approximations $\sqrt{x^2+y^2+(z+z_0)^2} \approx z+z_0$ and $\sqrt{x^2+y^2+z^2} \approx z$ in the absorption and spreading loss factors. Equation (C3) simplifies to

$$\mathbf{V}_i^* \Phi_s = \frac{1}{16\pi^2} \frac{(\kappa - i\nu)}{(\kappa + i\nu)} \frac{1}{\omega\, dz_0\, z(z_0+z)} \times e^{i\kappa z_0 \rho^2/2z(z_0+z)} S(\theta,\phi;0,0) e^{-2\nu(z_0+z)}. \tag{C9}$$

We integrate Eq. (C9) using Eq. (A11) over the area of the screen. With the screen lying normal to the z axis, an area element of the screen is $\mathbf{dS} = \mathbf{i}_z\, dx\, dy$,

$$\int \int_{Sc} \mathbf{V}_i^* \Phi_s \cdot \mathbf{dS} = \frac{1}{16\pi^2} \frac{(\kappa - i\nu)}{(\kappa + i\nu)} \frac{1}{\omega d z_0 z(z_0+z)} e^{-2\nu(z_0+z)} \times \int_{-L/2}^{L/2}\int_{-L/2}^{L/2} e^{i\kappa z_0 \rho^2/2z(z_0+z)} S(\theta,\phi;0,0)\, dx\, dy. \tag{C10}$$

As discussed in Appendix A, the angular width of the active area on the screen is of the order of $\sqrt{\lambda/z}$ which is small for large z. We therefore approximate the scatter function with its value at $\theta=\phi=0$ and factor it out of the integral above. Integrating the resulting expression using asymptotic integration, we obtain

$$\int \int_{Sc} \mathbf{V}_i^* \Phi_s \cdot \mathbf{dS} = \frac{i}{8\pi\omega d z_0^2} \frac{1}{\kappa} S(0,0;0,0) \frac{(\kappa - i\nu)}{(\kappa + i\nu)} e^{-2\nu(z_0+z)}. \tag{C11}$$

Similarly, we integrate the second term in Eq. (A11) to obtain

$$\int \int_{Sc} \mathbf{V}_s^* \Phi_i \cdot \mathbf{dS} = \frac{-i}{8\pi\omega d z_0^2} \frac{1}{\kappa} S^*(0,0;0,0) e^{-2\nu(z_0+z)}. \tag{C12}$$

Adding the two expressions and taking only the negative of the real part of the sum, we obtain the extinction caused by an object in an infinite unbounded lossy medium using the screen method,

$$\mathcal{E}_{Sc}(\mathbf{r}|\mathbf{r}_0) = \frac{1}{4\pi\omega d} \frac{e^{-2\nu(z+z_0)}}{z_0^2} \frac{1}{\kappa} \times \left(\Im\{S(0,0;0,0)\} - \frac{\nu}{\kappa} \Re\{S(0,0;0,0)\} \right). \tag{C13}$$

The expression for the extinction using the control volume method Eq. (C8) and that obtained using Van de Hulst screen method Eq. (C13) are equal if $\nu = 0$. The second term in both equations arise due to absorption by the medium. The expressions for the absorption loss term differ because we integrate the energy flux over different surfaces. If ν is small compared to κ, $\nu/\kappa \ll 1$, we can ignore the second term in both equations, and letting $z = R$, the resulting expressions for the extinction are identical and become

$$\mathcal{E}(\mathbf{r}|\mathbf{r}_0) = \frac{1}{4\pi\omega d\kappa} \Im\{S(0,0;0,0)\} \frac{e^{-2\nu(z+z_0)}}{z_0^2}. \tag{C14}$$

This derivation shows that the screen method gives the true

extinction only if the absorption loss in the medium is small. From Eq. (C14), we see that absorption in the medium lowers the extinction that we would otherwise measure in a lossless medium. The $1/z_0^2$ factor is due to the spherical spreading of the incident field from the source to the object.

The incident intensity on the object in the z direction for $\nu/\kappa \ll 1$ is

$$\mathbf{V}_i^* \Phi_i = \frac{1}{16\pi^2} \frac{\kappa}{\omega d} \frac{e^{-2\nu z_0}}{z_0^2}. \tag{C15}$$

Dividing the extinction in Eq. (C14) with the incident intensity on the object Eq. (C15), we obtain the extinction cross section of the object in the infinite unbounded lossy media,

$$\sigma_T(z) = \frac{4\pi}{\kappa^2} \Im\{S(0,0;0,0)\} e^{-2\nu z}. \tag{C16}$$

Equation (C16) shows that a measurement of the cross section of an object in a lossy medium will be smaller than in a lossless medium. To obtain the true cross section of the object, independent of the medium, we have to correct for absorption in the lossy medium.

APPENDIX D: EXTINCTION FORMULA FOR SCATTERING IN A STRATIFIED WAVE GUIDE CALCULATED USING A CONTROL SURFACE THAT ENCLOSES THE OBJECT

Let the control surface be a semi-infinite cylinder of radius R with a cap at the sea surface where $z=-D$, similar to that defined in Sec. III. The axis of the cylinder is parallel to the z axis and passes through the object centroid. The source is located at $\mathbf{r}_0=(-x_0,0,z_0)$, and we assume that $R \ll x_0$.

As discussed in Sec. III, the sea has a pressure-release surface where both the incident and scattered fields vanish. The contribution of the interference flux through the cap at the sea surface $z=-D$ is zero. We need only integrate the interference flux in Eq. (A9) over the curved surface of the cylinder to obtain the extinction caused by the object.

Using Eqs. (1), (2), (3), and (A2), the first term in the integrand of Eq. (A9) on the curved surface of the cylinder, $\mathbf{R}=(x,y,z)$ is

$$\begin{aligned}
\mathbf{V}_i^* \Phi_s = {} & \frac{i}{d(z)d(z_0)d(0)2\omega k} \sum_{l=1}^{\infty} \sum_{m=1}^{\infty} \sum_{n=1}^{\infty} u_l^*(z_0) u_m(z) \left[\frac{\partial}{\partial z} u_l^*(z) \mathbf{i}_z - i\xi_l^* u_l^*(z) \mathbf{i}_x \right] \frac{e^{-i\Re\{\xi_l\}(x_0+x)}}{\sqrt{\xi_l^* x_0}} \frac{e^{i\Re\{\xi_m\}R}}{\sqrt{\xi_m R}} \\
& \times [N_m^- e^{i\Re\{\gamma_m\}D} A_n(\mathbf{r}_0) S(\pi-\alpha_m,\phi;\alpha_n,0) - N_m^+ e^{-i\Re\{\gamma_m\}D} A_n(\mathbf{r}_0) S(\alpha_m,\phi;\alpha_n,0) \\
& - N_m^- e^{i\Re\{\gamma_m\}D} B_n(\mathbf{r}_0) S(\pi-\alpha_m,\phi;\pi-\alpha_n,0) + N_m^+ e^{-i\Re\{\gamma_m\}D} B_n(\mathbf{r}_0) S(\alpha_m,\phi;\pi-\alpha_n,0)] e^{-\Im\{\xi_l\}x_0} e^{-\Im\{\gamma_m\}D}.
\end{aligned} \tag{D1}$$

In the above expression, the terms representing absorption by the wave guide have been factored out explicitly to avoid confusion when conjugating the fields and also to keep track of absorption losses due to the wave guide. Since $R \ll x_0$, the expansion $|\boldsymbol{\rho}-\boldsymbol{\rho}_0| = x_0 + x$ was used in the terms that determine the phase of the integrand while the approximation $|\boldsymbol{\rho}-\boldsymbol{\rho}_0| \approx x_0$ was used in the spreading and absorption loss factors. We ignore the absorption loss term $e^{-\Im\{\xi_l\}R}$ since it is small compared to $e^{-\Im\{\xi_l\}x_0}$.

Next we integrate Eq. (D1) over the curved surface of the cylinder. An area element on the surface of the cylinder is $\mathbf{dS} = \mathbf{i}_\rho R\, d\phi\, dz$. We use the orthorgonality relation in Eq. (4) between the modes $u_l^*(z)$ and $u_m(z)$ to integrate Eq. (D1) over the semi-infinite depth of the cylinder in the wave guide. This reduces the triple sum over the modes to a double sum,

$$\begin{aligned}
\oint \oint_C \mathbf{V}_i^* \Phi_s \cdot \mathbf{dS} &= \int_0^{2\pi} \int_{-D}^{\infty} \mathbf{V}_i^* \Phi_s \cdot \mathbf{i}_\rho R\, dz\, d\phi \\
&= \frac{1}{d(z_0)d(0)2\omega k} \sum_{m=1}^{\infty} \sum_{n=1}^{\infty} \frac{\xi_m^*}{|\xi_m| \sqrt{x_0 R}} u_m^*(z_0) e^{i\Re\{\xi_m\}R} e^{-i\Re\{\xi_m\}x_0} \\
&\quad \times \left\{ \int_0^{2\pi} [N_m^- e^{i\Re\{\gamma_m\}D} A_n(\mathbf{r}_0) S(\pi-\alpha_m,\phi;\alpha_n,0) - N_m^+ e^{-i\Re\{\gamma_m\}D} A_n(\mathbf{r}_0) S(\alpha_m,\phi;\alpha_n,0) \right. \\
&\quad - N_m^- e^{i\Re\{\gamma_m\}D} B_n(\mathbf{r}_0) S(\pi-\alpha_m\phi;\pi-\alpha_n,0) + N_m^+ e^{-i\Re\{\gamma_m\}D} B_n(\mathbf{r}_0) S(\alpha_m,\phi;\pi-\alpha_n,0)] \\
&\quad \left. \times e^{-i\Re\{\xi_m\}R\cos\phi} \cos\phi R\, d\phi \right\} e^{-\Im\{\xi_m\}x_0} e^{-\Im\{\gamma_m\}D}.
\end{aligned} \tag{D2}$$

The integral involving ϕ can be evaluated using the method of stationary phase. There are two stationary phase points corresponding to the forward azimuth $\phi=0$, and the back azimuth $\phi=\pi$. Applying the result of the following stationary phase integration over the azimuth angle ϕ,

$$\int_0^{2\pi} S(\pi-\alpha_m,\phi;\alpha_n,0)e^{-i\Re\{\xi_m\}R\cos\phi}\cos\phi\,d\phi=\sqrt{\frac{2\pi}{\Re\{\xi_m\}R}}e^{i\pi/4}[e^{-i\Re\{\xi_m\}R}S(\pi-\alpha_m,0;\alpha_n,0)$$
$$+ie^{i\Re\{\xi_m\}R}S(\pi-\alpha_m,\pi;\alpha_n,0)], \tag{D3}$$

to Eq. (D2), the integration of the first term in Eq. (A9) over the curved surface of the cylinder in the wave guide becomes

$$\oint\oint_C \mathbf{V}_i^*\Phi_s\cdot\mathbf{dS}=\frac{1}{d^2(z_0)d(0)4\omega k}\frac{1}{x_0}\sum_{m=1}^{\infty}\sum_{n=1}^{\infty}\frac{\xi_m^*}{|\xi_m|\sqrt{\Re\{\xi_m\}\xi_n}}u_m^*(z_0)u_n(z_0)e^{i\Re\{\xi_n-\xi_m\}x_0}$$
$$\times(i[N_m^-N_n^-e^{i\Re\{\gamma_m+\gamma_n\}D}S(\pi-\alpha_m,0;\alpha_n,0)-N_m^+N_n^-e^{i\Re\{-\gamma_m+\gamma_n\}D}S(\alpha_m,0;\alpha_n,0)$$
$$-N_m^-N_n^+e^{i\Re\{\gamma_m-\gamma_n\}D}S(\pi-\alpha_m,0;\pi-\alpha_n,0)+N_m^+N_n^+e^{i\Re\{-\gamma_m-\gamma_n\}D}S(\alpha_m,0;\pi-\alpha_n,0)]$$
$$-e^{i\Re\{2\xi_m\}R}[N_m^-N_n^-e^{i\Re\{\gamma_m+\gamma_n\}D}S(\pi-\alpha_m,\pi;\alpha_n,0)-N_m^+N_n^-e^{i\Re\{-\gamma_m+\gamma_n\}D}S(\alpha_m,\pi;\alpha_n,0)$$
$$-N_m^-N_n^+e^{i\Re\{\gamma_m-\gamma_n\}D}S(\pi-\alpha_m,\pi;\pi-\alpha_n,0)+N_m^+N_n^+e^{i\Re\{-\gamma_m-\gamma_n\}D}S(\alpha_m,\pi;\pi-\alpha_n,0)])$$
$$\times e^{-i\Im\{\xi_m+\xi_n\}x_0}e^{-\Im\{\gamma_m+\gamma_n\}D}. \tag{D4}$$

Similarly, we can evaluate the second term in Eq. (A9) which gives

$$\oint\oint_C \mathbf{V}_s^*\Phi_i\cdot\mathbf{dS}=-\frac{1}{d^2(z_0)d(0)4\omega k}\frac{1}{x_0}\sum_{m=1}^{\infty}\sum_{n=1}^{\infty}\frac{\xi_m^*}{|\xi_m|\sqrt{\Re\{\xi_m\}\xi_n^*}}u_m(z_0)u_n^*(z_0)e^{-i\Re\{\xi_n-\xi_m\}x_0}$$
$$\times(i[N_m^{-*}N_n^{-*}e^{-i\Re\{\gamma_m+\gamma_n\}D}S^*(\pi-\alpha_m,0;\alpha_n,0)-N_m^{+*}N_n^{-*}e^{-i\Re\{-\gamma_m+\gamma_n\}D}S^*(\alpha_m,0;\alpha_n,0)$$
$$-N_m^{-*}N_n^{+*}e^{-i\Re\{\gamma_m-\gamma_n\}D}S^*(\pi-\alpha_m,0;\pi-\alpha_n,0)+N_m^{+*}N_n^{+*}e^{-i\Re\{-\gamma_m-\gamma_n\}D}S^*(\alpha_m,0;\pi-\alpha_n,0)]$$
$$-e^{-i\Re\{2\xi_m\}R}[N_m^{-*}N_n^{-*}e^{-i\Re\{\gamma_m+\gamma_n\}D}S^*(\pi-\alpha_m,\pi;\alpha_n,0)-N_m^{+*}N_n^{-*}e^{-i\Re\{-\gamma_m+\gamma_n\}D}S^*(\alpha_m,\pi;\alpha_n,0)$$
$$-N_m^{-*}N_n^{+*}e^{-i\Re\{\gamma_m-\gamma_n\}D}S^*(\pi-\alpha_m,\pi;\pi-\alpha_n,0)+N_m^{+*}N_n^{+*}e^{-i\Re\{-\gamma_m-\gamma_n\}D}S^*(\alpha_m,\pi;\pi-\alpha_n,0)])$$
$$\times e^{-\Im\{\xi_m+\xi_n\}x_0}e^{-\Im\{\gamma_m+\gamma_n\}D}. \tag{D5}$$

We then sum Eqs. (D4) and (D5), taking only the negative of the real part of the sum following Eq. (A9). This leads to the range dependent extinction $\mathcal{E}(R|\mathbf{r}_0)$ of the incident field in a wave guide due to an object at the origin measured by a cylinder of radius R centered on the object with source at $\mathbf{r}_0$,

$$\mathcal{E}(R|\mathbf{r}_0)=\frac{1}{d^2(z_0)d(0)2\omega k}\frac{1}{x_0}\sum_{m=1}^{\infty}\sum_{n=1}^{\infty}\frac{\sqrt{\Re\{\xi_m\}}}{|\xi_m|}\Im\Bigg\{\frac{1}{\sqrt{\xi_n}}u_m^*(z_0)u_n(z_0)e^{i\Re\{\xi_n-\xi_m\}x_0}$$
$$\times[N_m^-N_n^-e^{i\Re\{\gamma_m+\gamma_n\}D}S(\pi-\alpha_m,0;\alpha_n,0)-N_m^+N_n^-e^{i\Re\{-\gamma_m+\gamma_n\}D}S(\alpha_m,0;\alpha_n,0)$$
$$-N_m^-N_n^+e^{i\Re\{\gamma_m-\gamma_n\}D}S(\pi-\alpha_m,0;\pi-\alpha_n,0)+N_m^+N_n^+e^{i\Re\{-\gamma_m-\gamma_n\}D}S(\alpha_m,0;\pi-\alpha_n,0)]\Bigg\}e^{-\Im\{\xi_m+\xi_n\}x_0}e^{-\Im\{\gamma_m+\gamma_n\}D}$$
$$+\frac{1}{d^2(z_0)d(0)2\omega k}\frac{1}{x_0}\sum_{m=1}^{\infty}\sum_{n=1}^{\infty}\frac{\Im\{\xi_m\}}{|\xi_m|\sqrt{\Re\{\xi_m\}}}\Im\Bigg\{\frac{1}{\sqrt{\xi_n}}u_m^*(z_0)u_n(z_0)e^{i\Re\{\xi_n-\xi_m\}x_0}e^{i\Re\{2\xi_m\}R}$$
$$\times[N_m^-N_n^-e^{i\Re\{\gamma_m+\gamma_n\}D}S(\pi-\alpha_m,\pi;\alpha_n,0)-N_m^+N_n^-e^{i\Re\{-\gamma_m+\gamma_n\}D}S(\alpha_m,\pi;\alpha_n,0)$$
$$-N_m^-N_n^+e^{i\Re\{\gamma_m-\gamma_n\}D}S(\pi-\alpha_m,\pi;\pi-\alpha_n,0)+N_m^+N_n^+e^{i\Re\{-\gamma_m-\gamma_n\}D}S(\alpha_m,\pi;\pi-\alpha_n,0)]\Bigg\}e^{-\Im\{\xi_m+\xi_n\}x_0}e^{-\Im\{\gamma_m+\gamma_n\}D}. \tag{D6}$$

After comparing the expression for the extinction calculated using the control surface method Eq. (D6), with that obtained using the Van de Hulst screen method Eq. (13), we see that they are identical only in the perfectly reflecting waveguide where $\Im\{\xi_m\}=0$. If the absorption loss in the waveguide is small, we can neglect the second term in Eq. (D6) and the resulting

expression will be similar to Eq. (13). The differences in Eqs. (13) and (D6) arise because of absorption loss in the medium and also because we integrate the energy fluxes over different surfaces in the two methods.

The Van de Hulst screen method is of more practical use because it represents the type of measurement that can be made with a standard 2D planar or billboard array. A control volume measurement, on the other hand, would be very difficult to implement since it would require an array that completely encloses the object.

[1] M. Born and E. Wolf, *Principles of Optics, Electromagnetic Theory of Propagation Interference and Diffraction of Light*, 6th ed. (Cambridge University Press, Cambridge, 1980).

[2] H. C. van de Hulst, ''On the attenuation of plane waves by obstacles of arbitrary size and form,'' Physica (Amsterdam) **15**, 740–746 (1949).

[3] L. I. Schiff, ''On an expression for the total cross-section,'' Prog. Theor. Phys. **11**, 288–290 (1954).

[4] H. C. van de Hulst, *Light Scattering by Small Particles* (Dover, New York, 1981).

[5] R. J. Urick, *Principles of Underwater Sound* (McGraw-Hill, New York, 1983).

[6] P. M. Morse, *Theoretical Acoustics* (Princeton University Press, Princeton, NJ, 1986).

[7] B. V. Smith and M. G. Ertugrul, ''A technique for the measurement of extinction cross-section,'' J. Sound Vib. **98**, 275–288 (1985).

[8] T. K. Stanton, ''Multiple scattering with applications to fish-echo processing,'' J. Acoust. Soc. Am. **73**, 1164–1169 (1983).

[9] F. P. Mechel, ''Iterative solutions for finite-size absorbers,'' J. Sound Vib. **134**, 489–506 (1989).

[10] Y. P. Guo, ''On sound energy scattered by a rigid body near a compliant surface,'' Proc. R. Soc. London **1943**, 543–552 (1995).

[11] F. Ingenito, ''Scattering from an object in a stratified medium,'' J. Acoust. Soc. Am. **82**, 2051–2059 (1987).

[12] N. C. Makris and P. Ratilal, ''A unified model for reverberation and submerged object scattering in a stratified ocean waveguide,'' J. Acoust. Soc. Am. **109**, 909–941 (2001).

[13] N. C. Makris, ''A spectral approach to 3-D object scattering in layered media applied to scattering from submerged spheres,'' J. Acoust. Soc. Am. **104**, 2105–2113 (1998); **106**, 518(E) (1999).

[14] F. B. Jensen, W. A. Kuperman, M. B. Porter, and H. Schmidt, *Computational Ocean Acoustics* (American Institute of Physics, New York, 1994).

[15] G. V. Frisk, *Ocean and Seabed Acoustics, A Theory of Wave Propagation* (Prentice Hall, New Jersey, 1994).

[16] *Electromagnetic and Acoustic Scattering by Simple Shapes*, edited by J. J. Bowman, T. B. A. Senior, and P. L. E. Uslenghi (North-Holland, Amsterdam, 1969).

[17] N. C. Makris, F. Ingenito, and W. A. Kuperman, ''Detection of a submerged object insonified by surface noise in an ocean waveguide,'' J. Acoust. Soc. Am. **96**, 1703–1724 (1994).

On the relative role of sea-surface roughness and bubble plumes in shallow-water propagation in the low-kilohertz region

Guy V. Norton
Naval Research Laboratory, Stennis Space Center, Mississippi 39529-5004

Jorge C. Novarini
Planning Systems, Inc., Long Beach, Mississippi 39560-9702

(Received 16 November 2000; revised 1 July 2001; accepted 31 August 2001)

In the low-kilohertz frequency range, acoustic transmission in shallow water deteriorates as wind speed increases. Although the losses can be attributed to two environmental factors, the rough sea surface and the bubbles produced when breaking- or spilling waves are present, the relative role of each is still uncertain. For simplicity, in terms of an average bubble population, the time- and space-varying assemblage of microbubbles is usually assumed to be uniform in range and referred to as ''the subsurface bubble layer.'' However the bubble population is range- and depth-dependent. In this article, results of an experiment [Weston *et al.*, Philos. Trans. R. Soc. London, Ser. A **265**, 507–606 (1969)] involving fixed source and receivers, and observations during an extended period of time under varying weather conditions are re-examined by exercising a numerical model that allows for the dissection of the problem. Calculations are made at 2- and 4-kHz. It is shown that at these frequencies and at wind speeds capable of generating breaking waves the main mechanism responsible for the excess loss in the shallow-water waveguide is the patchy nature of the subsurface bubble field. Refraction and attenuation within the pockets of high void fraction are minor contributors to the losses. © *2001 Acoustical Society of America.* [DOI: 10.1121/1.1414883]

PACS numbers: 43.30.Hw, 43.30.Dr, 43.30.Re [DLB]

I. INTRODUCTION

It is a well-known fact that acoustic propagation in shallow water deteriorates as the wind speed increases. However, it is not yet clear which is the dominant mechanism responsible for the increase in the transmission loss. In an earlier paper Weston and Ching (1989) addressed the problem in the low-kHz range (0.870 to 4.44 kHz) with reference to an experiment carried out in the shallow waters off the Bristol Channel (Weston *et al.*, 1969). The experiment is one of the few reported in the open literature involving fixed source and receivers and observations during an extended period of time under varying weather conditions. Weston and Ching reviewed the possible mechanisms involved in producing the high attenuation and fluctuations, namely surface waves, swell, wind-induced bubbles, hail, and fish shoals. Although they considered entrained air bubbles ''second in line to the throne,'' scattering at the sea surface being the first, they found the effect difficult to model and therefore their analysis was somewhat inconclusive. In a subsequent paper Weston (1989) went deeper into the analysis of the possible role of entrained bubbles. He attempted a study of the theoretical expectations and focused on the two main components, surface roughness and entrained bubbles. His analysis included bubble-induced refraction, attenuation, and surface decoupling (Lloyds' mirror effect). These latter effects were considered assuming a flat surface. The estimation of the losses due to surface roughness was based on previous theoretical treatments and treated separately from the bubble environment. Weston concluded for this particular experiment that surface roughness is the predominant mechanism responsible for the loss, whereas bubbles are probably significant but the junior partner, and fish shoaling were responsible for additional special effects.

Although full of physical insight, the theoretical treatment was carried out in a heuristic manner treating surface and bubbles separately. Weston made that limitation clear and pointed out (and emphasized) that both effects should be treated together. He also stated that the bubbles should eventually be considered with due regard to the patchy formation they present at sea (or bubble clouds as described by Thorpe, 1982) and not as a uniform layer as assumed in his analysis. Weston concluded that in his analysis there was sufficient uncertainty in the specification of the bubble population and in the applicability of the theory; bubbles could still in principle be the main cause of the wind-induced losses.

The uncertain findings on the role of bubbles in Weston's work is in stark contrast to the conclusions by Schneider (1987) for roughly the same low-kHz region. In an attempt to explain the enhancement in transmission loss induced by breaking waves observed in another shallow-water experiment (Wille *et al.*, 1987), Schneider carried out an analysis on results from a heuristic model. This model, based on stochastic ray tracing, assumes a uniform bubble layer and accounts for only resonant bubbles. Schneider concluded that transmission losses under breaking-wave conditions in shallow water could be successfully modeled if both attenuation due to resonant bubbles and scattering at the rough sea surface are taken into account. Therefore, the matter of the relative role of bubbles and surface roughness in shallow-water propagation begs for clarification.

Today, highly accurate numerical models are available that allow us to revisit the problem in which bubbles and

surface roughness are treated together and coherently within the propagation algorithm, including the patchy nature of the bubble field. The model adopted in this article handles refraction and scattering as well as the additional bubble-induced attenuation, with due regard to off-resonance bubbles. In addition, since it is a numerical solution to the wave equation the Lloyd's mirror effect or surface-decoupling effect (Weston, 1989) is implicitly included with due regard to surface roughness. Details of the specific environment of the experiment of reference are not available to reproduce it in detail. Therefore, in this work a shallow-water environment consisting of the same depth and range of wind speeds as in the experiment is considered. The water mass was close to isothermal during most of the experiment, so as a compromise an isovelocity profile has been adopted in this study. The geoacoustic model for the bottom is based on the basic information provided by Weston *et al.* (1969). The objective is to determine the relative influence of two main factors (bubbles and surface roughness) *on the trend* of the transmission loss and not to reproduce the absolute values for the losses of the particular experiment. Although results are presented for 2 and 4 kHz, the bulk of the analysis is carried out at 2 kHz. This frequency is representative of the band examined in Weston's data (0.3–4.44 kHz), since the threshold for resonances from individual bubbles is about 4 kHz (which corresponds to the largest bubbles found in bubble clouds in a significant number). Resonances from individual bubbles could bring in other mechanisms (such as multiple scattering among bubbles) not included in the current modeling effort. There are three main modeling aspects to the work presented in this paper. First, a model is adopted for the simulation of a spatially varying, temporally ''frozen'' bubbly environment [Novarini *et al.* (1998)]. It is largely based on Monahan's (1988) description for the stages of evolution of a type of bubble clouds, the bubble plumes. A brief description of the model is presented in Sec. II. Once the bubbly environment is simulated, another model based on standard approximate theory for propagation through bubbly media (Clay and Medwin, 1977) is used to replace the bubbly environment with an acoustically equivalent fluid medium with a perturbed sound speed and the associated attenuation (i.e., a complex index of refraction). Once the effective complex index of refraction of the bubbly medium is known, propagation in the presence of a rough surface is modeled with an algorithm developed by Norton *et al.* (1995) (EFEPE-CM). This hybrid model combines the split-step Padé solution for the finite-element parabolic equation (PE) method (Collins, 1993) with a conformal mapping algorithm (Dozier, 1984) which locally flattens each segment of the rough sea surface. Details of this model are presented in Sec. III. The combination of PE with conformal mapping has proven to produce results on surface scattering that match benchmark solutions. At this point it should be noted that the propagation model used is a two-dimensional model, with range and depth being the two coordinates. The environment, though, is four-dimensional (three spatial and one temporal). However, limiting ourselves to investigating the forward-propagated field, the PE method of solving the wave equation has been shown to give reliable and accurate results. Time evolution will not be considered. Consistent with the PE model, the surface roughness is assumed 1D, which implies long created surfaces. This is an appropriate approximation since in forward scattering the losses are mainly controlled by the rms surface height and not the spectral distribution. Along the same line, young bubble plumes are also three-dimensional. The footprint at the surface is the foam patch created by the breaking wave. It is usually described as a rectangular patch. In a way of averaging the relative orientation when taking the slice of the elongated plume for the modeling, we chose as its length the so-called ''characteristic length,'' defined as the square root of the area (Ding and Farmer, 1994).

Each component of the model has been tested separately, verifying the validity and robustness of the algorithm used. All inputs for the propagation model were well within the numerical limits.

While the modeling presented in this study is deterministic, i.e., for single realizations of a bubbly environment and a wind-driven sea surface, the statistical moments of the acoustic field are obtained through ensemble averages. The ability to introduce sea-surface roughness and bubble clouds together within a propagation model in a mathematically consistent manner provides a unique opportunity: it allows for the investigation of the magnitude of their individual contributions to forward propagation by including/removing the rough surface, bubble plumes, or both. Since the objective of this work is to determine the *relative influence* of bubbles and surface roughness *on the trend* of the total forward-propagated field and not to reproduce the absolute values for the losses of the particular experiment, the use of a two-dimensional modeling is sufficient.

II. THE RANGE-DEPENDENT BUBBLY ENVIRONMENT

In a paper revealing the patchy nature of the bubble layer, Thorpe (1982) observed that the aggregates of bubbles occur in the form of clouds. He identified the bubble clouds as one of two types: columnar clouds and billow clouds. The columnar type (also referred to as ''plumes'' because of their shape) appears to be roughly V-shaped, decreasing in width with depth (Crawford and Farmer, 1987). This is the type described by Monahan (1988, 1993) and modeled here. Monahan discretized the time evolution of a bubble plume into three stages, which he labeled $\boldsymbol{\alpha}$, $\boldsymbol{\beta}$, $\boldsymbol{\gamma}$, and associated two of them with two stages of whitecaps (type A: crest of the spilling breaker; type B: foam patch). Table I lists the main characteristics (void fraction and length at the surface, e-folding depth, and typical density at 100-μm bubble radius) of the bubble formations considered. The $\boldsymbol{\alpha}$ plumes are the subsurface extension of the spilling crest and therefore are associated with type A whitecaps.

These plumes have the highest void fractions (order of 10^{-1}–10^{-2}), but are very small in size and have a very short lifetime (less than 1 s). The whitecap type A evolves into a foam patch (whitecap type B) and associated with them are the $\boldsymbol{\beta}$ plumes (void fraction about 10^{-3} to 10^{-4}). The $\boldsymbol{\beta}$ plumes, which are attached to the foam patch, are bigger than the $\boldsymbol{\alpha}$ plumes and have a longer lifetime (about 4 s). The $\boldsymbol{\beta}$ plume then detaches from the foam patch and evolves into

TABLE I. Main characteristics of the bubble formations considered at a wind speed of 11 m/s.

	β plume	γ plume	Background layer
Horizontal length (m) ($@z=0$)	4	12	⋯
e-folding depth (m)	0.25	1.2	0.8
Spectral density ($m^{-3}\mu m^{-1}$) ($@a=100\ \mu m$)	10^5	10^3	10^0
Void fraction ($z=0$)	10^{-4}	10^{-6}	10^{-8}
$\Delta C(z=0,\ f=2$ kHz) (m/s)	980	15	1

a $\boldsymbol{\gamma}$ plume. The $\boldsymbol{\gamma}$ plume has a lower void fraction, larger dimension, and a longer lifetime than the $\boldsymbol{\beta}$ plume (see Table I for numerical specifications). The $\boldsymbol{\beta}$ plume drifts freely and may be affected by circulation processes (such as Langmuir cells). The $\boldsymbol{\gamma}$ plumes then decay into a weak, quasiuniform background layer. Both the $\boldsymbol{\beta}$ plumes and the $\boldsymbol{\gamma}$ plumes are modeled as conical intrusions with cross section decreasing exponentially with depth. At any given time, under conditions where breaking waves are occurring, there is always a collection of plumes in different stages of development. Based on Monahan's descriptions, previous parametrizations of bubble population and results from at-sea measurements, Novarini *et al.* (1998) set forth a model for the bubble distribution of the $\boldsymbol{\beta}$ plumes, $\boldsymbol{\gamma}$ plumes, and uniform (in range) background layer.

In the adopted model of the bubble plumes, the $\boldsymbol{\beta}$ plumes, $\boldsymbol{\gamma}$ plumes, and background layer share the same spectral form at small radii (smaller than about 50 μm). For larger radii the spectral slope for the $\boldsymbol{\beta}$ plumes is smaller than those for both the $\boldsymbol{\gamma}$ plume and background layer. Also, for both the $\boldsymbol{\gamma}$ plumes and background layer the slope for large radii becomes depth dependent. For each class the bubble concentration at a given radius and the overall void fraction of the plume are different (for a detailed description of the spectral forms see Novarini *et al.*, 1998). Because of the lack of sufficient information on bubbles in shallow water, we adopted this model for the bubbly environment in the region of interest, which under the oceanographic viewpoint can be classified as intermediate water (Kinsman, 1965).

As mentioned earlier, another mechanism believed to be responsible for bubble transport both down from the sea surface and back up to the sea surface in an organized manner is through an upper-ocean circulation mechanism known as Langmuir cells (Thorpe, 1984). There is strong evidence that, when present, the Langmuir circulation will affect the spatial distribution of bubble clouds (Zedel and Farmer, 1991). In the region of convergence of Langmuir cells the concentration of already existing bubbles created by breaking waves (like those in the $\boldsymbol{\gamma}$ plume and background layer) increases, creating vertical bands of bubbles, quasiperiodically spaced. However, Langmuir cells are not always present, while the downward transport induced by the orbital motion of the surface waves is always acting. In this work the effect of the Langmuir cells is not included.

To complete the picture it is necessary to specify the relative location of the plumes, their size, and geometrical aspect. Since the acoustic modeling will be carried out in two dimensions (range and depth), we will limit ourselves to the two-dimensional description of the plumes. Assuming the separation of the $\boldsymbol{\beta}$ plumes is equal to that of the whitecaps, it can therefore be obtained from the spacing between breaking waves. In this case we take the mean spacing between active breaking crests as determined by Ding and Farmer (1994). The regression line of their Fig. 13(d) for the mean spacing, Σ_β, is given by

$$\Sigma_\beta = 19.94 u_{10}^{0.27}, \tag{1}$$

where u_{10} is the wind speed in m/s at a height of 10 m above the sea surface.

In the case of the $\boldsymbol{\beta}$ plumes the footprint at the surface is the foam patch created by the breaking wave. It is usually described as a rectangular patch (Bondur and Sharkov, 1982). In a way of averaging the relative orientation when taking the slice of the elongated plume for the modeling, we chose as its length the so-called "characteristic length" defined as the square root of the area (Ding and Farmer, 1994). Therefore, the equivalent length (m) of the $\boldsymbol{\beta}$ plume at the surface is taken as $L_\beta(0)=(A_p)^{1/2}$, where A_p (the area, in m^2, of the foam patch) can be estimated from

$$\mathrm{A}_p = 17.0 + 0.0307(u_{10}-5.0)^2. \tag{2}$$

The area of the plume decays exponentially with depth and so too does the equivalent depth. The e-folding constant is given by $d_\beta = 0.0123\ u_{10}^2/5.9$ (Novarini *et al.*, 1998).

The $\boldsymbol{\gamma}$ plumes have a much longer lifetime than the originating breaking wave. They drift around and can be found almost everywhere. For practical purposes it can be assumed that close to the surface they are contiguous to each other. From Monahan's parametrization, the area of the $\boldsymbol{\gamma}$ plume at the surface can be estimated to be about 9 times that of the $\boldsymbol{\beta}$ plume; hence, its equivalent length at the surface is 3 times that of the 1D $\boldsymbol{\beta}$ plume. The area of the $\boldsymbol{\beta}$ plume is assumed to decay exponentially with depth.

Since we are interested in the ensemble average of the acoustic intensity, it is necessary to introduce statistical variations in the description of the plumes. These fluctuations in spacing, size, and concentration also eliminate spurious effects that may be introduced by a strict periodicity that should not occur in a natural environment. For example, within each bubble plume class ($\boldsymbol{\gamma}$ plume, $\boldsymbol{\beta}$ plume) the bubble concentration will change from plume to plume, the e-folding depth will fluctuate, the size of the foam patch will change, and the spacing between plumes will also be randomly distributed. This was accomplished by adopting Gaussian and uniform deviations with different variances.

Once the bubble distribution is known as a function of depth and range, the corresponding sound-velocity field in the effective medium (and thus the effective wave number) is calculated with due regard to both resonant and off-resonance bubbles (see the Appendix for details). Modeling bubble plumes results in a range- and depth-dependent complex sound velocity. This complex sound-velocity field is then used within the parabolic wave equation.

III. MODELING PROPAGATION IN AN OCEAN WAVEGUIDE WITH A ROUGH SEA SURFACE

A numerical algorithm that allows for range-dependent calculations in the presence of surface roughness has been implemented by Norton *et al.* (1995) (EFEPE-CM). The algorithm combines the split-step Padé solution for the finite-element parabolic equation method (Collins, 1993), (EFEPE) with a conformal mapping technique, originally set forth by Dozier (1984), that locally flattens a rough sea-surface segment. The resulting model, which shares the flexibility of PE to handle arbitrary environments, has been shown to produce benchmark-quality results for the sea-surface forward scattering problem (Norton and Novarini, 1996).

The method has been applied to study the effect of sea-surface roughness on low-frequency propagation in deep water (Norton and Novarini, 1998) and for the case of a point source in a realistic shallow-water waveguide (Norton and Novarini, 1996). In the latter study it was found that when using a point source where strong upward-refracting conditions exist (which will be the case when plumes are present), coherence effects and energy redistribution cannot be ignored. Additionally, it was confirmed that the results obtained from a simple procedure, which attempts to incorporate the effect of the surface roughness through a loss mechanism, are in error.

Although the current paper focuses on the combined effect of sea-surface roughness and bubble plumes, it should be made clear that in this simulation the bubble plumes are uncoupled from the rough surface. In reality, a young bubble plume ($\boldsymbol{\beta}$ plume in this paper) is originally attached to a breaking wave. However, as explained elsewhere, the numerical surfaces do not actually include breaking waves since they are created through a linear filtering technique. Therefore, in the present modeling effort the $\boldsymbol{\beta}$ plumes are positioned under arbitrary features of the surface relief, since the sharp breaking crests are not included. The lack of breaking waves should not affect the forward-scattered field that is mainly controlled by the rms surface height and by the long surface waves that are adequately included in the surface spectrum. However, it should be pointed out that in the current modeling the plumes ($\boldsymbol{\beta}$ or $\boldsymbol{\gamma}$) are attached to the surface profile and not to an imaginary average flat plane.

The rough surfaces were generated by a linear filtering technique (Caruthers and Novarini, 1971). A set of random numbers (1D white surface) is passed through a filter whose transfer function (in the wave-number domain) is given by the square root of the desired power density spectrum of the output surface. In this case we chose the Pierson–Moskowitz (1964) spectrum for a fully developed wind-driven sea surface. It is a nondirectional spectrum suitable for the adopted 2D propagation model. Note that when converting a nondirectional frequency spectrum to a 1D wave-number spectrum, all the energy of the wave system goes in the wind direction. The spectral form for the power density spectrum is given by

$$S(K)=\frac{\alpha}{4|K|^3}\exp\left[-\frac{\beta g^2}{|K|^2u^4}\right]\ (\mathrm{m^2s^2}), \tag{3}$$

TABLE II. Environmental (bubble free) and model parameters used for simulations.

Depth (m)	Sound speed (m/s)	Density (g/cc)	Attenuation (dB/λ)
0.000	1500.0	1.0	0.0
39.00	1500.0	1.0	0.0
39.05	1836.0	2.0	0.5
80.00	1836.0	2.0	0.5
120.0	1836.0	2.0	10.0

Padè	Range step (m)	Depth step (m)
6	0.1 m	0.05 m

where K is the wave number in rad/m, u the wind speed in m/s, $g=9.81\,\mathrm{m\,s^{-2}}$, $\beta=0.74$, and $\alpha=0.0081$. Other choices could have been made to simulate the rough surface. For example, if the surfaces were assumed to be directional 2D surfaces with a Pierson–Moskowitz spectrum and slices are extracted from them, the spectral form will decay as K^{-4}. Although resonant scattering from the longer waves play a role near the specular direction, the rms height of the surface (which remains invariant) is still the predominant cause of scattering in the specular direction, which is associated with modal attenuation.

IV. NUMERICAL EXPERIMENTS

A. The environment

In order to re-examine Weston and Ching's analysis of the relative influence of bubbles and sea-surface roughness on shallow-water propagation, we need to simulate a set of shallow-water acoustic runs similar to those used in their analysis [see Weston and Ching (1989), and references therein for details]. To that end we have adopted a shallow-water waveguide of 39-m constant depth with a flat, fast bottom. Table II shows the environmental and model parameters used in the simulations. In the absence of bubbles the water mass is isovelocity. Two frequencies were considered, 2 and 4 kHz, and wind speeds (at a height of 10 m) of 5, 6, 7, 9, and 11 m/s.

The PE runs require adequate spatial sampling and an expanded numerical grid (in depth) to avoid spurious effects. The inclusion of the bubbles and the rough sea surface also imposes a requirement on the sampling intervals to properly resolve the 2D characteristics of the bubble clouds and the 1D structure of the deterministic rough sea surface. For the cases considered, the sampling increments are $\Delta r=0.1\,\mathrm{m}$ and $\Delta z=0.05\,\mathrm{m}$. A sediment half-space is assumed with a ramping attenuation increasing towards the end of the numerical grid to avoid reflections.

B. Results

For each frequency and wind speed, 20 surface realizations were used to obtain the ensemble average. This number was shown to be sufficient to produce a total field (PP^*) consisting of the incoherent part only. That is, the coherent part was sufficiently removed from the total. The data to be compared is loss versus wind speed. Following Weston and Ching (1989), the reference level used from which to mea-

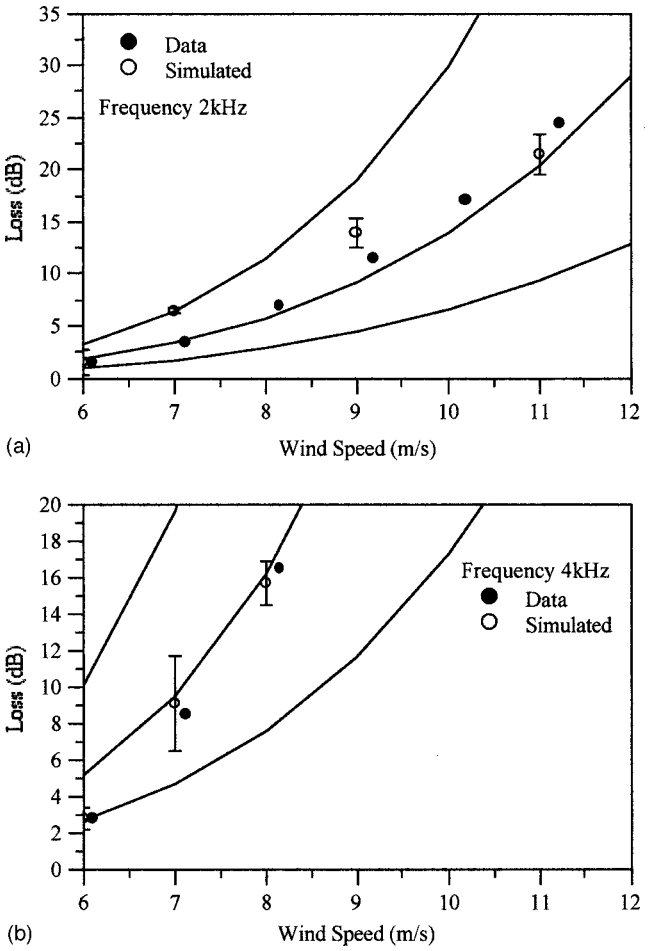

FIG. 1. Comparison of transmission loss versus wind speed at a range of 23 km. (● data, ○ simulated). Surface roughness and bubble plumes included in the modeling. Attenuation relative to that observed for a wind speed of 5 m/s. (a) 2 kHz; (b) 4 kHz.

sure the attenuation as the wind increases is the mean signal level at 5 m/s, for both the data and the simulated response. The data (average attenuation) were taken during May–June in 1969. This data set was selected because it contains data for the highest frequency (4 kHz) considered. The propagation path length was 23 km. Figure 1 depicts the comparison between data and simulation for the 2- and 4-kHz frequencies. The filled dots are data and the open dots are the simulated response. The three solid lines are based on the following numerical expression for the total dB attenuation presented by Weston and Ching:

$$\alpha_E = 4.94 \times 10^{-4} f^{1.5 \pm 0.1} W^{4 \pm 0.3}, \tag{4}$$

where f is frequency in kHz and W is wind speed in m/s. The extremes of the exponents result in the two extreme curves found in each figure. Good results were obtained for both 2- and 4 kHz.

Even though the simulation compares well to the data, understanding what physical mechanism(s) is (are) actually responsible for the loss is hidden in the result. Therefore, the question now becomes why do the simulated data agree as well as they do? Referring to the original paper by Weston and Ching (1989) and specifically to their Fig. 5, which depicts the dependence of averaged signal attenuation on wind speed for May–June 1969, it is apparent that the data below 1 kHz have a different shape than for frequencies above 1 kHz. This suggests that either different physical mechanisms are responsible for the attenuation at the different frequencies, or that the same mechanisms are responsible but their relative importance is different. With this in mind we turned our attention to the very good agreement between data and modeling results at 2 kHz, since there are more data to compare. An understanding of such an agreement can be achieved by dissecting the results of the modeling into its different components. We begin by ignoring the bubbles and include only the effects from a rough surface. These results, at wind speeds 7, 9, and 11 m/s, are compared to those obtained when a rough surface and the associated bubble plumes are both included (Fig. 2). As expected, when the wind speed decreases the bubble plumes have a smaller effect on the field. If bubbles are not included (only surface roughness considered), comparison with data deteriorates (Fig. 3). Note, however, that at low wind speeds the rough surface alone suffices to account for the losses. Note also that the trend of the simulated results does not follow the data. Obviously, the plumes have a deep impact on the modeled results, implying that the rough surface alone is not responsible for the observed loss in the measured data. The bubble plumes are working in conjunction with the rough surface to provide the observed losses.

The question now is to what extent is the patchiness of the bubble ''layer'' responsible for the extra loss? To answer this question, results that were obtained for the range-dependent bubble field will be compared with those obtained assuming a range-averaged (range-independent) but depth-dependent bubble layer. The latter bubble field was obtained by averaging the sound speed in range at each depth increment. Three wind speeds selected were 7, 9, and 11 m/s. Figure 4 portrays these results. As the wind speed increases so does the difference between the two cases. This indicates the importance of the range-dependent nature of the bubble field as compared to the range-independent case.

If indeed the range dependence of the bubble field is important, then the next question is, since the range-dependent field is composed of pockets of bubbles generating areas of high void fraction labeled as $\boldsymbol{\beta}$- and $\boldsymbol{\gamma}$ plumes, which one of these has the major impact on the acoustic field? To address this question we next look at the impact that a single class of plume ($\boldsymbol{\beta}$- and $\boldsymbol{\gamma}$ plume) alone has on the total propagated field. Figure 5 shows the total acoustic field expressed in dB for four different environments. First, the case when the full plume's representation and rough surface is used, second when $\boldsymbol{\beta}$ plumes only and a rough surface is used, third when $\boldsymbol{\gamma}$ plumes only and a rough surface is used, and finally when only a rough surface is used. It is obvious from Fig. 5 that the $\boldsymbol{\beta}$ plume provides the dominant mechanism that attenuates the field since it shows nearly as much loss as the full-plume case. The $\boldsymbol{\gamma}$ plume affects the field very little, as can be seen in the figure.

Knowing that the $\boldsymbol{\beta}$ plume is responsible for the loss, we investigate a dependence of the losses on the plume spacing. Plume spacing is related to the spacing between foam patches, since, as explained elsewhere, in Monahan classifi-

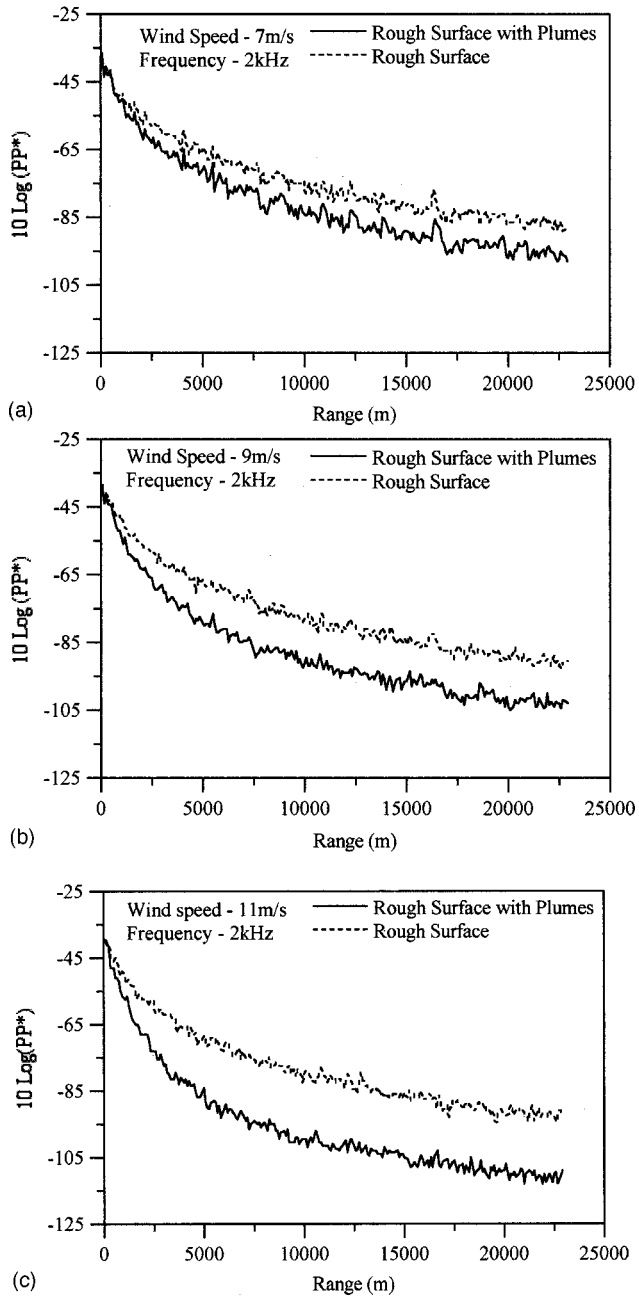

FIG. 2. Comparisons of results using rough surface with bubble plumes and rough surface alone. (a) 7-m/s wind speed; (b) 9-m/s wind speed; (c) 11-m/s wind speed.

cation of the plumes, the β plumes are attached to the foam patches from the active breaking waves. In the current method for determining the spacing (Ding and Farmer, 1994), the spacing of active breaking waves (and so of foam patches and corresponding β plumes) increases with increasing wind speed, resulting in fewer β plumes occupying a given propagation distance as the wind increases. An alternative description is that proposed by Wu (1992). Wu determined that the spacing between whitecaps decreased with increasing wind speed. This leads to a larger number of β plumes along the path. The new spacing is given by

$$\Sigma_{\beta} = 237.0 u_{10}^{-1.07}. \tag{5}$$

Adopting this new spacing between β plumes leads to approximately 40% more β plumes over the same propagation distance for a given wind speed.

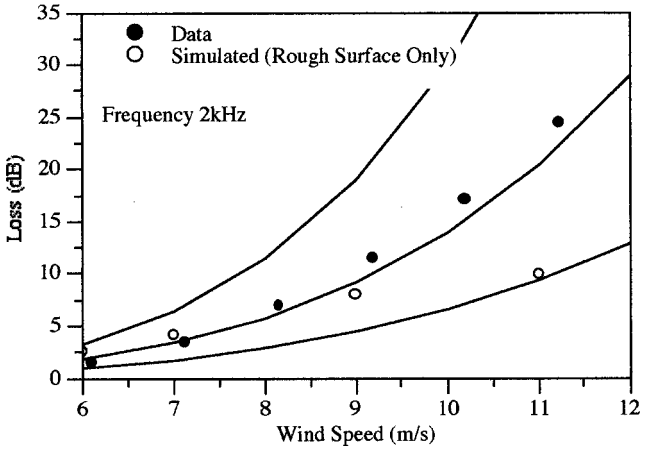

FIG. 3. Comparison of transmission loss versus wind speed at a range of 23 km at 2 kHz. (● data, ○ simulated). Only surface roughness is included in the modeling.

This radical difference in the two expressions for the spacing stems from the fact that Ding and Farmer (1994) assumed the spacing between foam patches is controlled by the dominant wavelength of the surface spectrum, with increases with wind speed.

On the other hand, Wu (1992) derived his equation from direct observations of whitecap coverage, which leads to a β-plume spacing inversely proportional to the wind speed. Direct observation of whitecap coverage may include both active whitecaps and foam patches not attached to active breaking waves. Those patches are not expected to contribute to bubble injection and therefore no plume will be attached to them. A clear discussion of the subject in connection with bubble clouds is still lacking in the literature.

A comparison of the resulting forward-propagating field based on the two different plume spacings is depicted in Fig. 6. Results for 5- and 7-m/s wind speed are nearly identical and thus are not shown. At 5 m/s the original spacing allowed for approximately 200 more β plumes than the new spacing, while at a wind speed of 7 m/s the original spacing allowed for approximately 90 fewer β plumes than the new spacing. At these low wind speeds the β plumes do not have a large effect on the forward field. There is a noticeable difference between the two results for a wind speed of 9 m/s. At this wind speed, the original β-plume spacing allowed for approximately 360 fewer β plumes than the new spacing, while for a wind speed of 11 m/s the original β-plume spacing allowed for approximately 600 fewer β plumes compare to the new spacing. For ranges in excess of 15 to 20 km, the results obtained are not as sensitive to plume spacing as they were at shorter ranges. This is due to the fact that the forward-propagated field has suffered many interactions with the surface and consequently with the underlying bubble field. This interaction removes energy propagating at these angles, resulting in an acoustic field that is composed of energy mainly propagating at angles closer to the horizontal, resulting in fewer surface interactions.

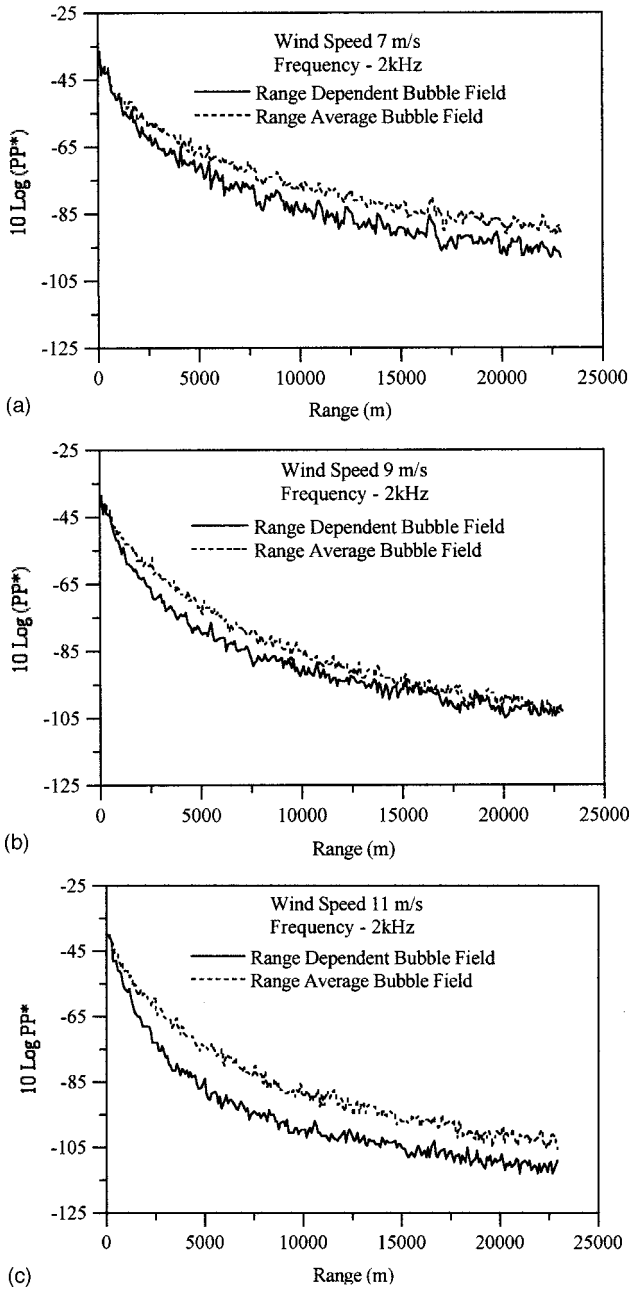

FIG. 4. Comparisons of the effect of a range-averaged and a range-dependent bubble field at 2 kHz. (a) 7-m/s wind speed; (b) 9-m/s wind speed; (c) 11-m/s wind speed.

V. ROLE OF INTERVENING MECHANISMS

Obviously, the $\boldsymbol{\beta}$ plume is the entity responsible for the loss observed in the data/simulation comparisons of Fig. 1. The question now becomes, which mechanism is responsible for the loss? That is, is the loss mechanism attenuation, scattering/diffraction, or refraction at the $\boldsymbol{\beta}$ plumes? The easiest loss mechanism to inspect is the attenuation. There is experimental evidence that depending on frequency and wind speed, young, short-lived bubble plumes may produce significant attenuation within the plume and the consequent screening of the overlying surface (Herwig and Nutzel, 1989). For the adopted model for the bubble environment, at 2 kHz and an 11-m/s wind speed, the attenuation at the surface within a $\boldsymbol{\beta}$ plume is 5.6 dB/m and decreases to 2.7 dB/m

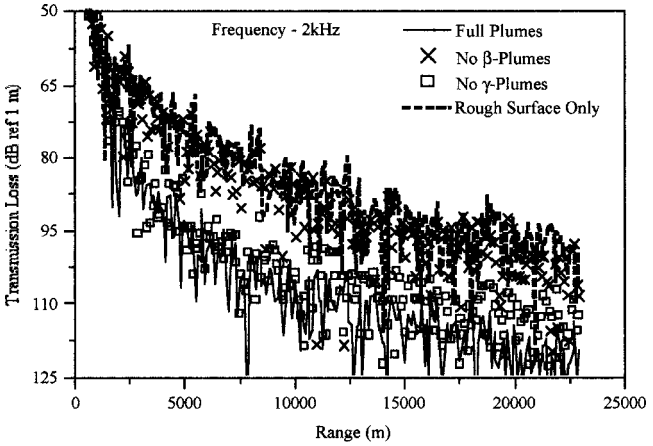

FIG. 5. Relative effect of the β plumes and γ plumes acting in conjunction with the surface roughness at $f=2$ kHz and $u=11$ m/s.

3 m below the surface (bottom of the plume). Since we perform a numerical calculation, the imaginary part of the index of refraction in the water column due to bubbles can be set to zero, resulting in a medium that imparts no attenuation. This result can be compared to the more accurate representation that includes the imaginary part. The results (not shown since they lie virtually on top of one another) indicate that attenuation at 2 kHz does not play an important role in forward propagation. This is understandable since the losses should

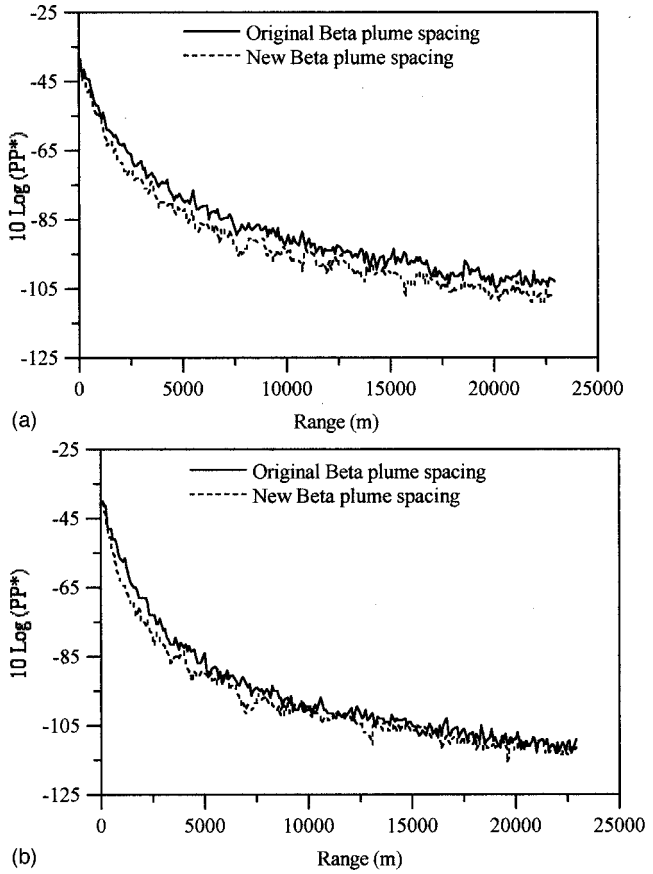

FIG. 6. Effect of β-plume spacing on the transmission loss at a frequency of 2 kHz. (a) 9-m/s wind speed; (b) 11-m/s wind speed.

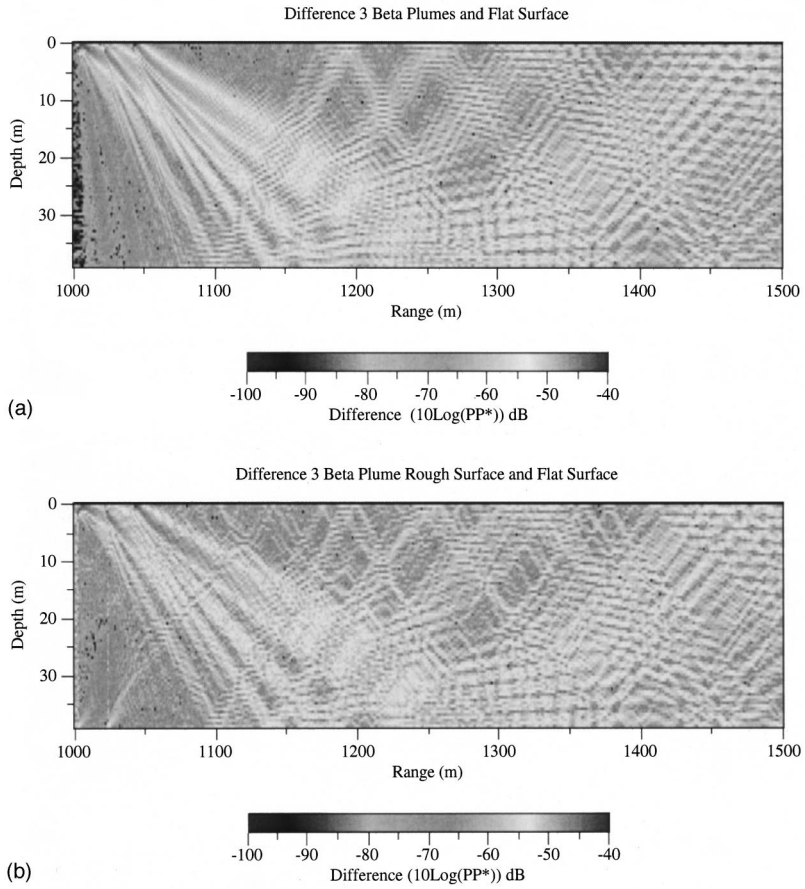

FIG. 7. Field plot showing effect of β plumes as scatterers. (a) Difference between the field due to three β plumes and that of a flat surface; (b) difference between the field due to a rough surface outline of three β-plumes and that of a flat surface.

be proportional to the overall distance traveled within the plumes and they are highly localized and sparsely distributed in range.

A rather simple numerical experiment is now presented that will help in determining whether the loss mechanism is scattering/diffraction or refraction. The experiment involves using only three $\boldsymbol{\beta}$ plumes attached to a flat surface. These three plumes are placed starting at approximately 1 km in range and spaced approximately every 20 meters. The total forward field is then calculated in range and depth. The plumes are then removed and the complex field once again determined. The two complex pressure fields are subtracted and the intensity of the difference is determined and expressed in dB. Figure 7(a) depicts this difference in the two fields. Notice that the plume locations are easily observed. The forward field of each plume shows an enhancement but it is not clear if this enhancement is due to refraction inside the plume or scattering at the plume. Utilizing the sound speeds associated with the $\boldsymbol{\beta}$ plumes, one can determine the maximum depth and range excursion for each plume. Once this is determined, a surface can be constructed that mimics the depth and range excursions of the $\boldsymbol{\beta}$ plumes, i.e., duplicates their outer contour. The surface is flat everywhere else. Utilizing this equivalent ''rough surface'' on the bubble-free medium, the total forward field can be determined and the resulting complex field is subtracted from the field without the rough surface. The resulting complex field is converted to intensity, expressed in dB and is depicted in Fig. 7(b). This resulting field is due totally to scattering/diffraction effects. Comparing this result to that of Fig. 7(a), marked similarities between the two fields can be observed. The forward field associated with each plume shows an enhancement similar to that of Fig. 7(a), thus indicating that scattering from the plumes is the major loss mechanism.

VI. CONCLUSIONS

The relative role of bubbles and surface roughness on the transmission loss associated with increasing wind speed in shallow-water propagation in the low-kHz regime has been examined. Even though model results were presented for 2- and 4 kHz, with a detailed analysis being made of the 2-kHz result, the observed trends should be applicable to frequencies from a few hundred Hz up to 4 kHz, since no new mechanisms come into play within that frequency band. Previously published results largely based on heuristic approaches with the bubble field represented as a range-independent layer show contradictory results on the influence of bubbles. Results from a 2D highly accurate numerical model, which incorporates bubble clouds and surface roughness in a coherent manner, indicate that the main mechanism responsible for the excess loss in the shallow-water waveguide seems to be the patchy nature of the subsurface bubble field. The refraction within the pockets of high void fraction (the $\boldsymbol{\beta}$ plumes in the adopted description of the bubble field) is a minor contributor to the losses. At the frequencies that are considered in this work (2 and 4 kHz), the attenuation inside the $\boldsymbol{\beta}$ plumes has essentially no effect on the transmission loss. The spacing of the $\boldsymbol{\beta}$ plumes has shown to have a big impact on the results. As more information becomes

available on the distribution and evolution of bubble plumes, further studies should dwell deeper into their role in shallow-water propagation. Also, when true 3D propagation models, capable of handling the full 3D nature of the environment, including the rough sea surface, become available, the possible contributions from out-of-plane scattering from plumes and surface should be evaluated.

ACKNOWLEDGMENTS

This work has been supported by the Office of Naval Research Program Element No. 61153N, Work Unit No. 71501200 and by a grant of HPC time from the DoD HPC Shared Resource Center (Stennis Space Center, MS). This document has been reviewed and is approved for public release. Both authors would like to thank R. Keiffer for the many helpful discussions concerning this work.

APPENDIX: SPECIFICATION OF AN EFFECTIVE FLUID MEDIUM

The sound speed in a bubbly media can be characterized by a complex number, the real part of which provides the phase velocity and the imaginary part leads to the attenuation. The effective complex sound speed in a bubbly mixture (c_{eff}) can be calculated as (Hall, 1989)

$$c_{\text{eff}}^{-2}=[(1-V)\boldsymbol{\rho}_W+V\boldsymbol{\rho}_{\text{gas}}][(1-V)K_W+\Delta K], \tag{A1}$$

where K_W is the compressibility of the water; r_w and r_g are the densities of water and air, respectively, V is the fractional volume occupied by bubbles, and ΔK is the complex compressibility introduced by the bubbles.

From Clay and Medwin (1977), ΔK is given by

$$\Delta K(f,z)=\frac{1}{f^2\boldsymbol{\rho}_w\boldsymbol{\pi}}\int_{a_{\min}}^{a_{\max}}\frac{n(a)a(Y^2-1-i\boldsymbol{\delta})}{(Y^2-1)^2+\boldsymbol{\delta}^2}da, \tag{A2}$$

with $Y=f_r/f$. The resonant frequency f_r of the bubbles and the damping constant δ are calculated with due regard to thermal and viscous effects. The reader is referred to Clay and Medwin (1977) for details and numerical values of the parameters involved.

We will refer to the phase velocity that occurs in the presence of the bubbles as the perturbed sound speed c_b which, is given by

$$c_b=\text{Re}\{c_{\text{eff}}\}, \tag{A3}$$

where Re denotes the real part, and the attenuation coefficient (in dB/m) is given by

$$\alpha_b=\left(\frac{20.0}{\ln(10.0)}\right)\text{Im}\left\{\frac{1.0}{c_{\text{eff}}}\right\}, \tag{A4}$$

where Im denotes the imaginary part.

For low void fractions ($V\ll\boldsymbol{\rho}_{\text{gas}}/\boldsymbol{\rho}_w$), say for void fractions smaller than 10^{-6}, Eq. (A1) can be simplified to

$$c_{\text{eff}}^{-2}=c_0^{-2}+\Delta K. \tag{A5}$$

This approximation has been widely used for the ''uniform background bubble layer.'' However, when dealing with void fractions typical of the $\boldsymbol{\beta}$ plume Eq. (A1) should be used instead of Eq. (A5).

In the calculation of c_{eff}, the maximum bubble radius at the surface is set to 1000 μm. We have assumed that the maximum bubble radius decreases with depth in the manner specified by Wu (1981)

$$a_{\max}(z)=a_{\max}(0)\exp\left(\frac{-z}{4.1}\right). \tag{A6}$$

The calculation of c_{eff} includes the contribution from bubbles of all radii (not just the resonant bubbles), with due regard to viscous and thermal effects. Multiple scattering between bubbles is ignored because, at the void fractions involved in the simulation (less than 10^{-4}), it has been shown they have no significant effect on the complex sound speed (Feuillade, 1995).

Bondur, V. G., and Sharkov, E. A. (**1982**). ''Statistical properties of whitecaps on a rough sea,'' Oceanology **22**, 274–279.

Caruthers, J. W., and Novarini, J. C. (**1971**). ''Numerical Modeling of Randomly rough surfaces with application to sea surfaces,'' Texas A&M Univ., Dept. Oceanography, Tech. Rep. Ref. 71-13-T.

Clay, C. S., and Medwin, H. (**1977**). *Acoustical Oceanography* (Wiley, New York).

Collins, M. D. (**1993**). ''A split-step Padé solution for the parabolic equation method,'' J. Acoust. Soc. Am. **93**, 1736–1742.

Crawford, G. B., and Farmer, D. M. (**1987**). ''On the spatial distribution of ocean bubbles,'' J. Geophys. Res. **92,** c8, 8231–8243.

Ding, L., and Farmer, D. (**1994**). ''Observations of breaking surface wave statistics,'' J. Phys. Oceanogr. **24**, 1368–1387.

Dozier, L. B. (**1984**). ''PERUSE: A numerical treatment of rough surface scattering for the parabolic wave equation,'' J. Acoust. Soc. Am. **75**, 1415–1432.

Feuillade, C. (**1995**). ''The collective acoustic properties of water containing resonating air bubbles, and its effect on the propagation of sound,'' J. Acoust. Soc. Am. **98**, 2937.

Hall, M. V. (**1989**). ''A comprehensive model of wind generated bubbles in the ocean and predictions of the effects on sound propagation at frequencies up to 40 kHz,'' J. Acoust. Soc. Am. **86**, 1103–1116.

Herwig, H., and Nutzel, B. (**1989**). ''The influence of bubbles on acoustic propagation and scattering,'' in *Underwater Acoustic Data Processing*, edited by Y. T. Chan, NATO ASI Series (Kluwer Academic, Dordrecht), pp. 105–111.

Kinsman, B. (**1965**). *Wind Waves: Their Generation and Propagation in the Ocean* (Prentice-Hall, Englewood Cliffs, NJ).

Monahan, E. C. (**1988**). ''Whitecap coverage as a fully monitor able indication of the rate of bubble injection into the oceanic mixed layer,'' in *Sea Surface Sound*, edited by B. R. Kerman (Academic, New York), pp. 85–96.

Monahan, E. C. (**1993**). ''Occurrence and evolution of acoustically relevant sub-surface bubble plumes and their associated, remote monitorable, surface whitecaps,'' in *Natural Physical Sources of Underwater Sound*, edited by B. V. R. Kerman (Kluwer Academic, Dordrecht), pp. 503–517.

Norton, G. V., Novarini, J. C., and Keiffer, R. S. (**1995**). ''Coupling scattering from the sea surface to a one-way marching propagation model via conformal mapping: Validation,'' J. Acoust. Soc. Am. **97**, 2173–2180.

Norton, G. V., and Novarini, J. C. (**1996**). ''The effect of sea surface roughness on waveguide propagation: A coherent approach,'' J. Acoust. Soc. Am. **99**, 2013–2021.

Norton, G. V., and Novarini, J. C. (**1998**). ''Enhancement of the total acoustic field due to the coupling effects from a rough sea surface and an underlying range-independent bubble layer,'' J. Acoust. Soc. Am. **103**, 1836–1844.

Novarini, J. C., Keiffer, R. S., and Norton, G. V. (**1998**). ''A model for variations in the range and depth dependence of the sound speed and attenuation induced by bubble clouds under wind-driven sea surfaces,'' IEEE J. Ocean. Eng. **23**, 423–438.

Pierson, W. J., and Moskowitz, L. (**1964**). ''A proposed spectral form for fully developed wind seas based on the similarity theory of S. Kitaigorodskii,'' J. Geophys. Res. **69**, 5181–5190.

Schneider, H. G. (**1987**). ''Modelling wind dependent acoustic transmission loss due to bubbles in shallow water,'' in *Progress in Underwater Acoustics*, edited by H. M. Merklinger (Plenum, New York), pp. 509–516.
Thorpe, S. A. (**1982**). ''On the clouds of bubbles formed by breaking waves in deep water and their role in the air–sea gas transfer,'' Philos. Trans. R. Soc. London, Ser. A **304**, 155–210.
Thorpe, S. A. (**1984**). ''The effect of Langmuir circulation on the distribution of submerged bubbles caused by breaking waves,'' J. Fluid Mech. **142**, 151–170.
Weston, D. E., and Ching, P. A. (**1989**). ''Wind effects in shallow water acoustic transmission,'' J. Acoust. Soc. Am. **86**, 1530–1545.
Weston, D. E. (**1989**). ''On the losses due to storm bubbles in oceanic sound transmission,'' J. Acoust. Soc. Am. **86**, 1546–1552.
Weston, D. E., Horrigan, A. A., Thomas, S. J. L., and Revie, J. (**1969**). ''Studies of sound transmission fluctuations in shallow coastal areas,'' Philos. Trans. R. Soc. London, Ser. A **265**, 507–606.
Wille, P., Gayer, D., Ginzkey, L., and Schunk, E. (**1987**). ''Measurements of wind dependent acoustic transmission loss in shallow water under breaking wave conditions,'' in *Progress in Underwater Acoustics*, edited by H. M. Merklinger (Plenum, New York), pp. 501–508.
Wu, J. (**1981**). ''Bubble population and spectra in near-surface ocean: Summary and review of field measurements,'' J. Geophys. Res. **86**, 457–464.
Wu, J. (**1992**). ''Individual characteristics of white caps and volumetric description of bubbles,'' IEEE J. Ocean. Eng. **17**, 150–158.
Zedel, L., and Farmer, D. (**1991**). ''Organized Structures in subsurface bubble clouds: Langmuir circulation in the upper ocean,'' J. Geophys. Res. **96**, 8889–8900.

Interface scattering by poroelastic seafloors: First-order theory

Kevin L. Williams
Applied Physics Laboratory, College of Ocean and Fishery Sciences, 1013 N.E. 40th Street, Seattle, Washington 98105-6698

James M. Grochocinski
Corning, Incorporated, SP-AR-128N, Corning, New York 14831

Darrell R. Jackson
Applied Physics Laboratory, College of Ocean and Fishery Sciences, 1013 N.E. 40th Street, Seattle, Washington 98105-6698

(Received 6 April 2001; revised 6 August 2001; accepted 30 August 2001)

A perturbation model is developed for sound scattering by a poroelastic seafloor having roughness small compared to the acoustic wavelength. The sediment is assumed to be homogeneous and isotropic with wave propagation described by Biot's equations. When applied to sandy sediments, the model predicts backscattering levels that are substantially lower than those of a fluid model having the same roughness, density, sound speed, and attenuation. © *2001 Acoustical Society of America.* [DOI: 10.1121/1.1414704]

PACS numbers: 43.30.Gv, 43.30.Hw, 43.20.Fn, 43.30.Ma [DLB]

I. INTRODUCTION

The Born approximation (first-order perturbation theory) has been widely applied to sound scattering by rough seafloors with the sediment modeled either as a fluid[1–5] or as an elastic medium.[6–14] The purpose of this paper is to extend previous work to the more general poroelastic (Biot) case. Poroelastic effects can substantially reduce the reflection coefficient of sandy sediments compared to the equivalent fluid or elastic cases.[15,16] Consequently, it is of interest to determine whether a similar reduction occurs in scattering due to interface roughness.

For efficiency in presentation, the derivation will employ Ivakin's method[14] originally used for the elastic case, and the treatment of Biot's equations and parameters will be patterned after Stoll and Kan.[15] This article is organized as follows. Section II defines the seafloor model, defining material parameters, roughness statistics, Biot's equations of motion, and the boundary conditions that must be imposed at the water–sediment interface. Section III summarizes the zeroth-and first-order solutions of Biot's equations, and gives the main result, an expression for the bistatic scattering cross section. Section IV compares the predictions of the Biot and fluid models for reflection and scattering in sand; conclusions and recommendations for future work are given in Sect. V, and the details of the derivation are contained in the Appendix.

II. SEAFLOOR MODEL

A. Scattering geometry

Figure 1 depicts the general physical situation to be considered. A rough interface described by the random function

$$x_3 = \zeta(\mathbf{R}), \tag{1}$$

separates a lossless, homogeneous fluid from a homogeneous, isotropic poroelastic sediment. In Eq. (1) and following equations, the upper-case bold letters **R** and **K**, with or without subscripts, will denote two-dimensional transverse position and wave vectors, respectively. All other bold letters will denote three-dimensional vectors. Thus, the three-dimensional position vector, **r**, is decomposed into its transverse and vertical components as

$$\mathbf{r} = (\mathbf{R}, x_3), \tag{2}$$

where

$$\mathbf{R} = (x_1, x_2). \tag{3}$$

In the final expression for scattering cross section, interface roughness will be described by the spectral density function, $W(\mathbf{K})$, where **K** is the two-dimensional spectral argument. This spectrum is normalized such that the double integral over the horizontal wave vector components (over both positive and negative values of the two components) yields the mean-square relief relative to the mean seafloor x_3 coordinate.

B. Biot theory

Following Stoll and Kan,[15] potentials Φ_s, Φ_f, $\boldsymbol{\Psi}_s$, $\boldsymbol{\Psi}_f$ will be defined giving the displacement vectors of the skeletal frame **u** and the pore water **U** as

$$\mathbf{u} = \nabla\Phi_s + \nabla\times\boldsymbol{\Psi}_s, \tag{4}$$

$$\beta(\mathbf{u}-\mathbf{U}) = \nabla\Phi_f + \nabla\times\boldsymbol{\Psi}_f, \tag{5}$$

where β is the sediment porosity. In terms of these potentials, and assuming $\exp(-i\omega t)$ time dependence, Biot's equations are

$$H\nabla^2\Phi_s - C\nabla^2\Phi_f = -\omega^2\rho\Phi_s + \omega^2\rho_f\Phi_f, \tag{6}$$

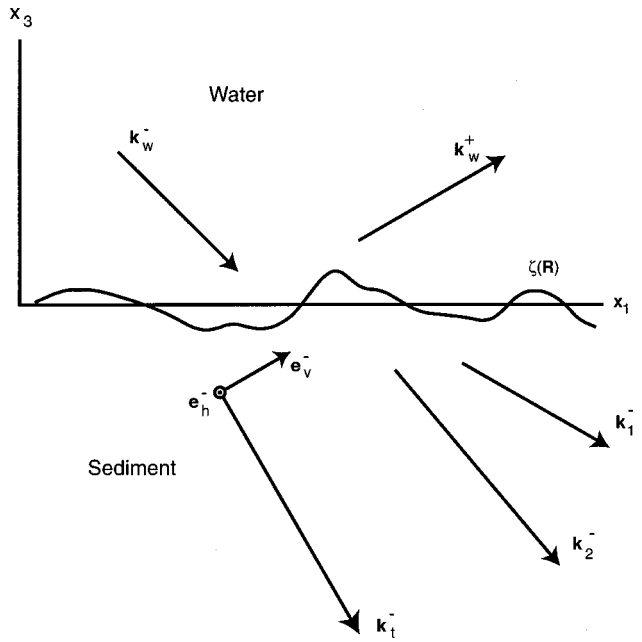

FIG. 1. Geometry relevant to bistatic scattering from a random poroelastic seafloor. This is a two-dimensional view, but the analysis is three-dimensional. The wave vectors for the incident and scattered fields in water are denoted $\mathbf{k}_w^-$ and $\mathbf{k}_w^+$, respectively, the wave vectors for the fast and slow waves in the sediment are denoted $\mathbf{k}_1^-$ and $\mathbf{k}_2^-$, respectively, and the shear wave vector is denoted $\mathbf{k}_t^-$. The two shear polarization unit vectors are $\mathbf{e}_h^-$ (horizontal polarization, directed out of page) and $\mathbf{e}_v^-$ (vertical polarization).

$$C\nabla^2\Phi_s - M\nabla^2\Phi_f = -\omega^2\rho_f\Phi_s + \frac{\omega^2\alpha\rho_f}{\beta}\Phi_f + \frac{i\omega F\eta}{\kappa}\Phi_f, \tag{7}$$

$$\mu\nabla^2\boldsymbol{\Psi}_s = -\omega^2\rho\boldsymbol{\Psi}_s + \omega^2\rho_f\boldsymbol{\Psi}_f, \tag{8}$$

and

$$\frac{-i\omega F\eta}{\kappa}\boldsymbol{\Psi}_f = -\omega^2\rho_f\boldsymbol{\Psi}_s + \frac{\omega^2\alpha\rho_f}{\beta}\boldsymbol{\Psi}_f. \tag{9}$$

In these equations, α is the structure constant or tortuosity, η and ρ_f are the viscosity and mass density of the pore fluid, κ is the permeability, and ρ_s is the sediment particle mass density. Other parameters appearing in these equations are

$$\rho = \beta\rho_f + (1-\beta)\rho_s, \tag{10}$$

$$H = (K_r - K_b)^2/(D - K_b) + K_b + 4\mu/3, \tag{11}$$

$$C = K_r(K_r - K_b)/(D - K_b), \tag{12}$$

$$M = K_r^2/(D - K_b), \tag{13}$$

and

$$D = K_r[1 + \beta(K_r/K_f - 1)], \tag{14}$$

where ρ is the total mass density, K_r is the bulk modulus of the individual sediment grains, K_f is the bulk modulus of the pore fluid, and K_b and μ are the bulk and shear moduli of the skeletal frame. Departure from Poiseuille flow as frequency increases is modeled by the function

$$F = \frac{\frac{\epsilon}{4}T(\epsilon)}{1 - \frac{2i}{\epsilon}T(\epsilon)}, \tag{15}$$

with

$$T = \frac{-\sqrt{i}J_1(\epsilon\sqrt{i})}{J_0(\epsilon\sqrt{i})}, \tag{16}$$

where $J_0(\epsilon\sqrt{i})$ and $J_1(\epsilon\sqrt{i})$ are cylindrical Bessel functions and

$$\epsilon = a\sqrt{\frac{\omega\rho_f}{\eta}}. \tag{17}$$

The parameter a is the "pore size."

C. Boundary conditions

The boundary conditions on the interface, $x_3 = \zeta(\mathbf{R})$, can be generalized from the flat interface case,[15] and are continuity of fluid movement (the "open pore" boundary condition[17])

$$\mathbf{N}\cdot(\nabla\Phi_s - \nabla\Phi_f + \nabla\times\boldsymbol{\Psi}_s - \nabla\times\boldsymbol{\Psi}_f) = \mathbf{N}\cdot\nabla\Phi_w, \tag{18}$$

equilibrium of tractions

$$[(H-2\mu)\nabla^2\Phi_s - C\nabla^2\Phi_f]\mathbf{N} + 2\mu(\mathbf{N}\cdot\nabla)(\nabla\Phi_s) + \mu(\mathbf{N}\cdot\nabla)\times(\nabla\times\boldsymbol{\Psi}_s) + \mu\nabla(\nabla\times\boldsymbol{\Psi}_s\cdot\mathbf{N}) = K_f\nabla^2\Phi_w\mathbf{N}, \tag{19}$$

and equilibrium of fluid pressure

$$M\nabla^2\Phi_f - C\nabla^2\Phi_s = -K_f\nabla^2\Phi_w. \tag{20}$$

The subscript, w, denotes the upper medium (water). The vector, $\mathbf{N}$, is the (unnormalized) interface normal

$$\mathbf{N} = -\nabla\zeta(\mathbf{R}) + \mathbf{e}_3, \tag{21}$$

where $\mathbf{e}_3$ is the unit vector in the vertical direction. In the last term on the left-hand side of Eq. (19) the gradient operator acts on the curl but not on the interface normal.

As the traction boundary condition, Eq. (19), is actually three equations, there are a total of five equations that must be satisfied. In the flat interface case[15] there are only four boundary conditions, as required to determine four unknowns: the compressional field in the water and three fields in the seafloor material (fast- and slow-wave fields and the shear field having vertical polarization). Scattering by the rough interface causes excitation of the other possible shear polarization (horizontal), so the additional boundary condition is needed to determine this additional unknown.

III. SOLUTIONS FOR WAVE FIELDS

The end result of the formulas to be presented is the scattering coefficient, σ, or scattering cross section per unit area per unit solid angle. The term "cross section" will be used for brevity, even though this quantity is dimensionless. The quantity $10\log\sigma$ is commonly called the scattering strength and is expressed in decibels. First-order perturbation theory will be used, in which the first step is to solve the plane-interface problem (the "zeroth-order" problem) and

then to obtain a correction that is a linear functional of the interface relief, $\zeta(\mathbf{R})$. This is the ''first-order'' problem. The first step in this process is to obtain plane-wave solutions for the infinite medium. Next, these are used to solve the reflection and transmission problem for the plane interface. Finally, a superposition of plane waves is used to obtain the first-order solution for the rough interface.

A. Plane waves

It is convenient to present a solution of the reflection (zeroth-order) and scattering (first-order) problems in terms of solutions of the unperturbed wave equations, in particular, plane waves propagating in the upward and downward directions (Fig. 1). The general form of these plane waves is

$$\exp(i\mathbf{k}_\alpha^{\pm}\cdot\mathbf{r}), \quad \alpha = w,1,2,t,$$

with the subscripts α denoting the wave vectors for compressional waves in the water (w), fast longitudinal waves in the seafloor (1), slow longitudinal waves in the seafloor (2), and shear waves in the seafloor (t), respectively. The superscripts $+$ and $-$ denote the direction of the wave propagation, upward and downward, respectively.

It is useful to write the general three-dimensional wave vectors in terms of the transverse components of the incoming and outgoing wave vectors

$$\mathbf{k}_\alpha^{\pm}(\mathbf{K}) = (\mathbf{K}, \pm k_w \nu_\alpha(\mathbf{K})). \tag{22}$$

The unperturbed wave equations obeyed by the potentials determine the relation between the transverse and vertical components of the wave vectors

$$\nu_\alpha(\mathbf{K}) = \sqrt{a_\alpha^{-2} - K^2/k_w^2}, \tag{23}$$

where

$$a_\alpha = c_\alpha / c_w \tag{24}$$

are the ratios of the various wave phase speeds to the water sound speed. Note that $a_w = 1$ and that the other ratios are complex, accounting for attenuation in the sediment.

The following unit vectors specify the directions of propagation:

$$\mathbf{e}_\alpha^{\pm}(\mathbf{K}) = \mathbf{k}_\alpha^{\pm}(\mathbf{K})/k_\alpha, \tag{25}$$

where

$$k_\alpha = \frac{\omega}{c_\alpha}, \quad \alpha = w,1,2,t, \tag{26}$$

are the wave numbers, respectively, of compressional waves in water, fast and slow waves in the seafloor, and shear waves in the seafloor. The latter three wave numbers are complex and are found by inserting plane-wave solutions into Biot's equations for the infinite medium. Consider longitudinal waves of the form

$$\Phi_s = \exp(i\mathbf{k}_\beta\cdot\mathbf{r}), \tag{27}$$

$$\Phi_f = \gamma_\beta \exp(i\mathbf{k}_\beta\cdot\mathbf{r}), \tag{28}$$

where $\beta = 1,2$ corresponds to the fast and slow waves. Biot's equations give the relation

$$(Hk_\beta^2 - \rho\omega^2)\left(m\omega^2 - Mk_\beta^2 + i\frac{F\eta\omega}{\kappa}\right) + (Ck_\beta^2 - \rho_f\omega^2)^2 = 0, \tag{29}$$

with $m = \alpha\rho_f/\beta$, to be solved for the fast- and slow wave numbers. At the same time, the ratio of the two potentials, Φ_f/Φ_s, is found to be

$$\gamma_\beta = \frac{\rho c_\beta^2 - H}{\rho_f c_\beta^2 - C}. \tag{30}$$

The analogous relations for shear waves are

$$\mathbf{\Psi}_s = \mathbf{e}_h(\mathbf{K})\exp(i\mathbf{k}_t\cdot\mathbf{r}), \tag{31}$$

$$\mathbf{\Psi}_f = \gamma_t \mathbf{e}_h(\mathbf{K})\exp(i\mathbf{k}_t\cdot\mathbf{r}), \tag{32}$$

$$(\mu k_t^2 - \rho\omega^2)\left(m\omega^2 + i\frac{F\eta\omega}{\kappa}\right) + \rho_f^2\omega^4 = 0, \tag{33}$$

$$\gamma_t = \frac{\rho}{\rho_f} - \frac{\mu}{\rho_f c_t^2}. \tag{34}$$

There are two plane-wave shear polarizations to consider, both having particle displacement normal to the direction of propagation. The shear wave having particle displacement in the direction

$$\mathbf{e}_h^{\pm}(\mathbf{K}) = \mathbf{k}_t^{\pm}\times\mathbf{e}_3/K = (K_2/K, -K_1/K, 0), \tag{35}$$

is ''horizontally polarized'' as the particle displacement is in a horizontal plane. Although the polarization vector does not depend upon whether propagation is upward or downward, the superscripts $\pm$ are used for consistency with the vertical polarization case. A plane shear wave having transverse wave vector, $\mathbf{K}$, and particle displacement in the direction of the unit vector

$$\mathbf{e}_v^{\pm}(\mathbf{K}) = \mathbf{e}_h^{\pm}\times\mathbf{k}_t^{\pm}(\mathbf{K})/k_t = \mp\mathbf{K}a_t\nu_t(\mathbf{K})/K + \mathbf{e}_3 K/k_t, \tag{36}$$

is ''vertically polarized,'' as the displacement is in a vertical plane. In this case, the polarization vector depends upon whether the wave is propagating upward or downward. Although incidence of a plane pressure wave in water upon a poroelastic medium with plane interface only gives rise to vertically polarized shear waves (as well as to fast and slow longitudinal waves), scattering by interface roughness causes conversion into both vertical and horizontal polarizations, as will be seen.

The expressions above for wave vectors and polarization vectors are written in terms of a general transverse wave vector, $\mathbf{K}$, for later use in the theoretical development. In computing the scattering cross section, however, one must take $\mathbf{K} = \mathbf{K}_{i,s}$. In this case, it is convenient to define the transverse components in terms of the angular coordinates of interest

$$\mathbf{K}(\theta,\phi) = (k_w\cos\theta\cos\phi, k_w\cos\theta\sin\phi), \tag{37}$$

and

$$\mathbf{K}_{i,s} = \mathbf{K}(\theta_{i,s}, \phi_{i,s}), \tag{38}$$

where θ_i and θ_s are the grazing angles of the incident and scattered acoustic waves, respectively, and ϕ_s and ϕ_i are the azimuthal angles of the incident and scattered waves, respec-

tively. The unit vectors can then be expressed as follows:

$$\mathbf{e}_{\alpha}^{\pm}(\mathbf{K}) = a_{\alpha}[\cos\theta\cos\phi, \cos\theta\sin\phi, \pm\nu_{\alpha}(\mathbf{K})], \tag{39}$$

$$\mathbf{e}_{h}^{\pm}(\mathbf{K}) = [\sin\phi, -\cos\phi, 0], \tag{40}$$

$$\mathbf{e}_{v}^{\pm}(\mathbf{K}) = a_{t}[\mp\nu_{t}(\mathbf{K})\cos\phi, \mp\nu_{t}(\mathbf{K})\sin\phi, \cos\theta], \tag{41}$$

with

$$\nu_{\alpha}(\mathbf{K}) = \sqrt{a_{\alpha}^{-2} - \cos^2\theta}. \tag{42}$$

In Eqs. (39)–(42), subscripts *i* and *s* must be added to **K** and to the angles θ and ϕ as appropriate.

B. Reflection and scattering

The derivation of the first-order perturbation theory results presented here is given in the Appendix. The scattering cross section is of the form

$$\sigma(\mathbf{K}_s, \mathbf{K}_i) = |H_w(\mathbf{K}_s, \mathbf{K}_i)|^2 W(\mathbf{K}_s - \mathbf{K}_i), \tag{43}$$

where W is the roughness spectrum defined in Eq. (71), and $H_w(\mathbf{K}_s, \mathbf{K}_i)$ is the first element of the column matrix

$$H(\mathbf{K}_s, \mathbf{K}_i) = \begin{pmatrix} H_w(\mathbf{K}_s, \mathbf{K}_i) \\ H_1(\mathbf{K}_s, \mathbf{K}_i) \\ H_2(\mathbf{K}_s, \mathbf{K}_i) \\ H_v(\mathbf{K}_s, \mathbf{K}_i) \\ H_h(\mathbf{K}_s, \mathbf{K}_i) \end{pmatrix}. \tag{44}$$

As noted in the Appendix, the elements of $H(\mathbf{K}_s, \mathbf{K}_i)$ determine, to first order in roughness amplitude, the plane-wave spectra (scattering amplitudes) of energy scattered into the water, into compressional waves in the seafloor, and into vertically and horizontally polarized shear waves in the seafloor (Appendix). This matrix is computed as follows:

$$H(\mathbf{K}_s, \mathbf{K}_i) = k_w^2 Y_1(\mathbf{K}_s)[P^{(3)}(\mathbf{K}_s)]^{-1} B(\mathbf{K}_s, \mathbf{K}_i) D_0(\mathbf{K}_i). \tag{45}$$

In this equation, $D_0(\mathbf{K}_i)$ is a six-row column vector comprised of the five reflection and transmission coefficients contained in the column vector, $S_0(\mathbf{K}_i)$, and supplemented with unity in the last row

$$D_0(\mathbf{K}_i) = \begin{pmatrix} S_0(\mathbf{K}_i) \\ - - - \\ 1 \end{pmatrix}. \tag{46}$$

An expression for computation of $S_0(\mathbf{K}_i)$ will be given later. The subscript $_0$ denotes zeroth order, that is, the flat-interface solution equivalent to that given by Stoll and Kan.[15] The matrix $B(\mathbf{K}_s, \mathbf{K}_i)$ is

$$B(\mathbf{K}_s, \mathbf{K}_i) = k_w^{-1}[(K_{s1} - K_{i1})E^{(1)}(\mathbf{K}_i) + (K_{s2} - K_{i2}) \times E^{(2)}(\mathbf{K}_i)] - E^{(3)}(\mathbf{K}_i) Y_2(\mathbf{K}_i). \tag{47}$$

The matrices Y_1 and Y_2 are

$$Y_1(\mathbf{K}) = \begin{pmatrix} \nu_w(\mathbf{K}) & 0 & 0 & 0 & 0 \\ 0 & \nu_1(\mathbf{K}) & 0 & 0 & 0 \\ 0 & 0 & \nu_2(\mathbf{K}) & 0 & 0 \\ 0 & 0 & 0 & \nu_t(\mathbf{K}) & 0 \\ 0 & 0 & 0 & 0 & \nu_t(\mathbf{K}) \end{pmatrix}, \tag{48}$$

$$Y_2(\mathbf{K}) = \begin{pmatrix} \nu_w(\mathbf{K}) & 0 & 0 & 0 & 0 & 0 \\ 0 & -\nu_1(\mathbf{K}) & 0 & 0 & 0 & 0 \\ 0 & 0 & -\nu_2(\mathbf{K}) & 0 & 0 & 0 \\ 0 & 0 & 0 & -\nu_t(\mathbf{K}) & 0 & 0 \\ 0 & 0 & 0 & 0 & -\nu_t(\mathbf{K}) & 0 \\ 0 & 0 & 0 & 0 & 0 & -\nu_w(\mathbf{K}) \end{pmatrix}, \tag{49}$$

The subscripts 1 and 2 on Y_1 and Y_2 do not relate to orders of pertubation; they merely serve to distinguish between the two matrices. There are three matrices, $E^{(n)}(\mathbf{K})$, defined for each of the coordinate indices, $n = 1,2,3$

$$E^{(n)}(\mathbf{K}) = \left(\begin{array}{ccccc:c} P_{w1}^{(n)}(\mathbf{K}) & P_{11}^{(n)}(\mathbf{K}) & P_{21}^{(n)}(\mathbf{K}) & P_{v1}^{(n)}(\mathbf{K}) & P_{h1}^{(n)}(\mathbf{K}) & Q_1^{(n)}(\mathbf{K}) \\ P_{w2}^{(n)}(\mathbf{K}) & P_{12}^{(n)}(\mathbf{K}) & P_{22}^{(n)}(\mathbf{K}) & P_{v2}^{(n)}(\mathbf{K}) & P_{h2}^{(n)}(\mathbf{K}) & Q_2^{(n)}(\mathbf{K}) \\ P_{w3}^{(n)}(\mathbf{K}) & P_{13}^{(n)}(\mathbf{K}) & P_{23}^{(n)}(\mathbf{K}) & P_{v3}^{(n)}(\mathbf{K}) & P_{h3}^{(n)}(\mathbf{K}) & Q_3^{(n)}(\mathbf{K}) \\ P_{w4}^{(n)}(\mathbf{K}) & P_{14}^{(n)}(\mathbf{K}) & P_{24}^{(n)}(\mathbf{K}) & P_{v4}^{(n)}(\mathbf{K}) & P_{h4}^{(n)}(\mathbf{K}) & Q_4^{(n)}(\mathbf{K}) \\ P_{w5}^{(n)}(\mathbf{K}) & P_{15}^{(n)}(\mathbf{K}) & P_{25}^{(n)}(\mathbf{K}) & P_{v5}^{(n)}(\mathbf{K}) & P_{h5}^{(n)}(\mathbf{K}) & Q_5^{(n)}(\mathbf{K}) \end{array}\right), \tag{50}$$

where the dashed vertical line in Eq. (50) separates it into the 5×5 matrices, $P^{(n)}(\mathbf{K})$, and the column matrices, $Q^{(n)}(\mathbf{K})$. The five rows of $E^{(n)}(\mathbf{K})$ correspond to the five boundary conditions; the first five columns correspond to the five wave types: reflected and scattered pressure waves in water, fast and slow waves in sediment, and vertically and horizontally polarized shear waves in sediment. The sixth column corresponds to the incident wave in water.

The elements of $P^{(n)}(\mathbf{K})$ and $Q^{(n)}(\mathbf{K})$ are

$$P_{wm}^{(n)}(\mathbf{K}) = K_w k_w \delta_{mn}, \quad m = 1,2,3, \tag{51}$$

$$P_{w4}^{(n)}(\mathbf{K}) = -K_w k_w \delta_{3n}, \tag{52}$$

$$P_{w5}^{(n)}(\mathbf{K}) = -e_{wn}^{+}(\mathbf{K}), \tag{53}$$

$$P_{1m}^{(n)}(\mathbf{K}) = -k_1^2 k_w^{-1}[(H-2\mu-\gamma_1 C)\delta_{mn} + 2\mu e_{1m}^{-}(\mathbf{K}) e_{1n}^{-}(\mathbf{K})], \quad m=1,2,3, \tag{54}$$

$$P_{14}^{(n)}(\mathbf{K}) = -k_1^2 k_w^{-1}(M\gamma_1 - C)\delta_{n3}, \tag{55}$$

$$P_{15}^{(n)}(\mathbf{K}) = k_1 k_w^{-1}(1-\gamma_1) e_{1n}^{-}(\mathbf{K}), \tag{56}$$

$$P_{2m}^{(n)}(\mathbf{K}) = -k_2^2 k_w^{-1}[(H-2\mu-\gamma_2 C)\delta_{mn} + 2\mu e_{2m}^{-}(\mathbf{K}) e_{2n}^{-}(\mathbf{K})], \quad m=1,2,3, \tag{57}$$

$$P_{24}^{(n)}(\mathbf{K}) = -k_2^2 k_w^{-1}(M\gamma_2 - C)\delta_{n3}, \tag{58}$$

$$P_{25}^{(n)}(\mathbf{K}) = k_2 k_w^{-1}(1-\gamma_2) e_{2n}^{-}(\mathbf{K}), \tag{59}$$

$$P_{vm}^{(n)}(\mathbf{K}) = \mu k_t^2 k_w^{-1}[e_{tm}^{-}(\mathbf{K}) e_{vn}^{-}(\mathbf{K}) + e_{tn}^{-}(\mathbf{K}) e_{vm}^{-}(\mathbf{K})], \quad m=1,2,3, \tag{60}$$

$$P_{v4}^{(n)}(\mathbf{K}) = 0, \tag{61}$$

$$P_{v5}^{(n)}(\mathbf{K}) = -k_t k_w^{-1}(1-\gamma_t) e_{vn}^{-}(\mathbf{K}), \tag{62}$$

$$P_{hm}^{(n)}(\mathbf{K}) = -\mu k_t^2 k_w^{-1}[e_{tm}^{-}(\mathbf{K}) e_{hn}^{-}(\mathbf{K}) + e_{tn}^{-}(\mathbf{K}) e_{hm}^{-}(\mathbf{K})], \quad m=1,2,3, \tag{63}$$

$$P_{h4}^{(n)}(\mathbf{K}) = 0, \tag{64}$$

$$P_{h5}^{(n)}(\mathbf{K}) = k_t k_w^{-1}(1-\gamma_t) e_{hn}^{-}(\mathbf{K}), \tag{65}$$

$$Q_{m}^{(n)}(\mathbf{K}) = K_w k_w \delta_{mn}, \quad m=1,2,3, \tag{66}$$

$$Q_{4}^{(n)}(\mathbf{K}) = -K_w k_w \delta_{n3}, \tag{67}$$

$$Q_{5}^{(n)}(\mathbf{K}) = -e_{wn}^{-}(\mathbf{K}), \tag{68}$$

where K_w is the bulk modulus of the upper fluid (water) taken equal to K_f in all numerical examples.

The matrix of reflection and transmission coefficients, $S_0(\mathbf{K}_i)$, is computed as follows:

$$S_0(\mathbf{K}_i) = -[P^{(3)}(\mathbf{K}_i)]^{-1} Q^{(3)}(\mathbf{K}_i). \tag{69}$$

The five elements of this matrix are denoted

$$S_0(\mathbf{K}_i) = \begin{pmatrix} W_w(\mathbf{K}_i) \\ W_1(\mathbf{K}_i) \\ W_2(\mathbf{K}_i) \\ W_v(\mathbf{K}_i) \\ W_h(\mathbf{K}_i) \end{pmatrix}, \tag{70}$$

and are the in-water reflection coefficient for compressional waves and the transmission coefficients for the fast and slow longitudinal waves and the two shear waves in the seafloor (see the Appendix). Note that $W_h(\mathbf{K}_i) = 0$.

IV. MODEL RESULTS

To compare the Biot model with the fluid model for backscattering, the following Biot parameters will be used as typical of sandy seafloors. Porosity, $\beta = 0.40$, grain density, $\rho_s = 2650\,\mathrm{kg/m^3}$, mass density of water and pore fluid, $\rho_f = 1000\,\mathrm{kg/m^3}$, bulk modulus of grains, $K_r = 3.6\times10^{10}\,\mathrm{Pa}$, bulk modulus of frame, $K_b = 4.4\times10^{7} - i2.0\times10^{6}\,\mathrm{Pa}$, shear modulus of frame, $\mu = 2.6\times10^{7} - i1.25\times10^{6}\,\mathrm{Pa}$, bulk modulus of water and pore fluid, $K_f = 2.25\times10^{9}\,\mathrm{Pa}$, viscosity, $\eta = 0.001\,\mathrm{kg/m/s}$, permeability, $\kappa = 1.0\times10^{-10}\,\mathrm{m^2}$, tortuosity, $\alpha = 1.25$, and pore size, $a = 5\times10^{-5}\,\mathrm{m}$.

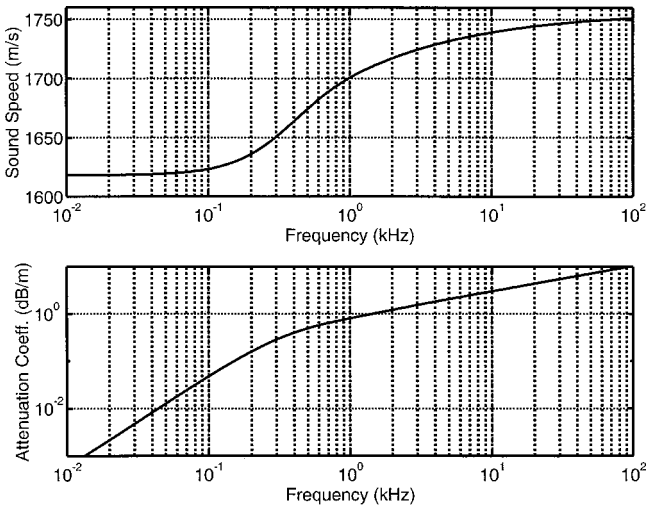

FIG. 2. Fast wave speed and attenuation as functions of frequency for Biot parameters typical of sand.

With these Biot parameters, there is considerable dispersion in the fast wave as evident in Fig. 2, which shows the frequency dependence of the speed and attenuation. This dispersion will be incorporated in the fluid model in order that the comparison of the Biot and fluid models exhibits only effects due to differing boundary conditions. In an actual application of either model, the fast wave speed and attenuation would most likely be measured or at least assigned values consistent with historical data, approximately taking account of dispersion. Thus, the fluid model will be taken to have compressional wave speed and attenuation equal to the corresponding fast-wave parameters. The fluid model is then fully specified by assigning the mass density the value ρ, the true net density of the Biot medium.

Figure 3 compares the reflection coefficient magnitude (in dB) for the two models at four frequencies. As expected,[15] the Biot model has a significantly lower reflection coefficient at steep grazing angles for frequencies of order 1 kHz and above, and measurements of the reflection coefficient offer a means of discriminating between the two models.[16]

In treating interface scattering, the roughness spectrum is taken to be

$$W(\mathbf{K}) = \frac{w_2}{(h_0 K)^{3.05}}, \tag{71}$$

with $w_2 = 0.00005\,\mathrm{m^4}$, and where h_0 is a scaling factor equal to one unit of length, introduced so that the dimensions of w_2 do not depend upon the value of the power-law exponent. Equation (71) assumes that roughness is a stationary and isotropic random process, with a spectrum that obeys a simple power law.

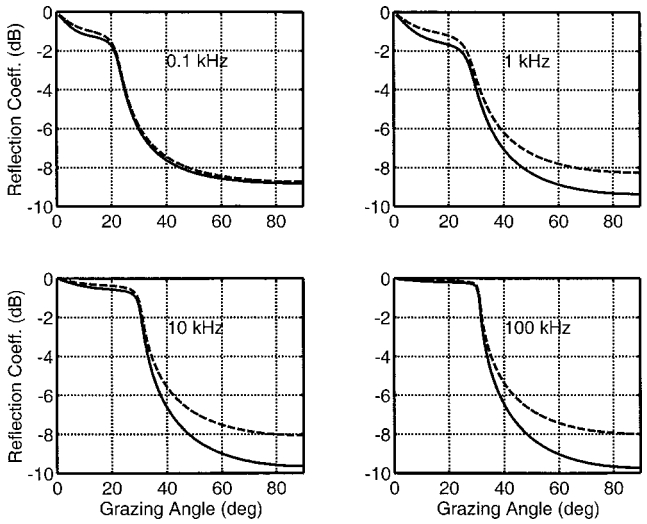

FIG. 3. Comparison of the reflection coefficient for the fluid (dashed line) and Biot (solid line) models for sand at selected frequencies.

Figure 4 shows that the Biot model predicts significantly lower backscattering strengths at frequencies of order 1 kHz and above. The maximum difference between the two models occurs for grazing angles smaller than 20° at the higher frequencies, and is about 3 dB. A difference of this magnitude is larger than the errors of a carefully conducted backscatter measurement, so such measurements should be capable of discriminating between the Biot and fluid models.

V. CONCLUSIONS AND RECOMMENDATIONS

First-order perturbation theory has been used to develop expressions for the bistatic scattering strength of poroelastic seafloors. Applied to the backscattering problem in sand, the Biot model predicts backscattering strengths as much as 3 dB lower than the fluid model, indicating that it should be possible to discriminate experimentally between the two models. The formulation developed here is readily extended to higher perturbation orders and to the small-slope approximation.[12] One concern in the use of perturbation theory for unconsolidated sediments is the low phase speed of the slow and shear waves. At higher frequencies, the roughness relief may not be small compared to the slow- and shear wavelengths, but, given the weak coupling into these waves, it is not obvious that the resulting errors are significant. Further work is needed to assess this situation.

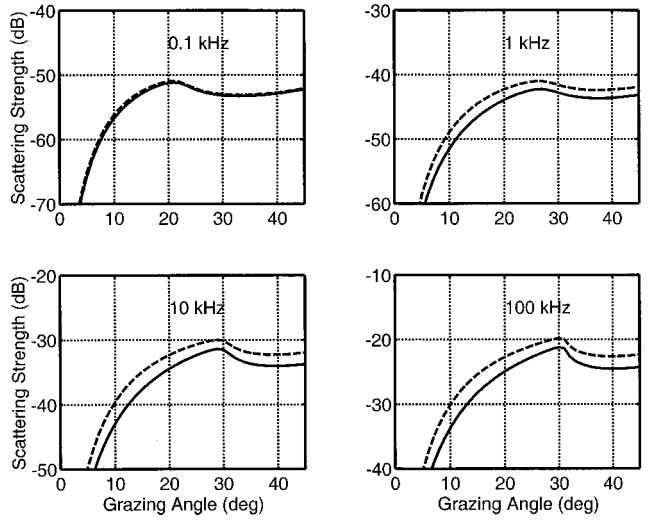

FIG. 4. Comparison of the backscattering strength for the fluid (dashed line) and Biot (solid line) models for sand at selected frequencies.

ACKNOWLEDGMENTS

This work was supported by the Office of Naval Research. The authors benefited from discussions with Dr. Steven Kargl, Dr. Miguel Nathwani, Dr. Eric Thorsos, and Dr. Dajun Tang.

APPENDIX: INTERFACE SCATTERING

The scattered field in the water above the highest point on the interface can be expressed as a superposition of plane waves. Plane-wave superpositions will also be used to describe the fields in the sediment. If the incident field is a plane wave of unit amplitude having wave vector with transverse component, $\mathbf{K}_i$, then the scattered potential for particle displacement in the water is represented in terms of a spectrum of plane waves

$$\Phi_w(\mathbf{r}) = \int \frac{d^2K}{k_w \nu_w(\mathbf{K})} A_w(\mathbf{K},\mathbf{K}_i) \exp(i\mathbf{k}_f^+(\mathbf{K})\cdot\mathbf{r}), \quad \text{(A1)}$$

where $A_w(\mathbf{K},\mathbf{K}_i)$ is the scattering amplitude, taken in the form of Ivakin[18] and related to the transition matrix (“T matrix”)[19,20] as follows:

$$A_w(\mathbf{K},\mathbf{K}_i) = k_w \nu_w(\mathbf{K}) T(\mathbf{K},\mathbf{K}_i). \quad \text{(A2)}$$

The potential, $\Phi_w(\mathbf{r})$, does not include the incident field but does include all other portions of the field (coherent and incoherent). The scattering amplitude will be used to obtain the scattering cross section through the equation[19–22]

$$\langle A'_w(\mathbf{K}_s,\mathbf{K}_i) A'^*_w(\mathbf{K}_s,\mathbf{K}'_i)\rangle = \delta(\mathbf{K}_i - \mathbf{K}'_i)\sigma(\mathbf{K}_s,\mathbf{K}_i), \quad \text{(A3)}$$

where $A'_w(\mathbf{K}_s,\mathbf{K}_i) = A_w(\mathbf{K}_s,\mathbf{K}_i) - \langle A_w(\mathbf{K}_s,\mathbf{K}_i)\rangle$ is the incoherent component of the scattering amplitude, and it is assumed that the interface roughness is a stationary random process in the two transverse (horizontal) coordinates. The water column is assumed to be homogeneous, supporting plane waves.

In matching the boundary conditions, the plane-wave expansion for the field in water, Eq. (A1), is used, along with analogous expansions for the fast, slow, and shear fields. Thus,

$$\Phi_\beta(\mathbf{r}) = \int \frac{d^2K}{k_w \nu_\beta(\mathbf{K})} A_\beta(\mathbf{K},\mathbf{K}_i) \exp(i\mathbf{k}_\beta^-(\mathbf{K})\cdot\mathbf{r}), \quad \beta = 1,2, \quad \text{(A4)}$$

describes the fast- and slow-wave fields and

$$\boldsymbol{\Psi}(\mathbf{r}) = \int \frac{d^2K}{k_w \nu_t(\mathbf{K})} \mathbf{A}_t(\mathbf{K},\mathbf{K}_i) \exp(i\mathbf{k}_t^-(\mathbf{K})\cdot\mathbf{r}), \quad \text{(A5)}$$

where

$$\mathbf{A}_t(\mathbf{K},\mathbf{K}_i) = \mathbf{e}_h^-(\mathbf{K}) A_v(\mathbf{K},\mathbf{K}_i) + \mathbf{e}_v^-(\mathbf{K}) A_h(\mathbf{K},\mathbf{K}_i) \quad \text{(A6)}$$

describes the shear wave field. As before, the expansions include both the coherent and incoherent parts of the fields. The incoherent roughness scattering amplitudes in the Born approximation have the general form

$$A'_\alpha(\mathbf{K}_s,\mathbf{K}_i)=iH_\alpha(\mathbf{K}_s,\mathbf{K}_i)Z(\mathbf{K}_s-\mathbf{K}_i),\quad \alpha=w,1,2,v,h, \tag{A7}$$

where $Z(\mathbf{K})$ is the Fourier transform of the interface relief function, Eq. (1). Using Eq. (A7), Eq. (A3) leads directly to the equation for the roughness scattering cross section, Eq. (43).

The scattering amplitudes are determined by imposing the boundary conditions, Eqs. (18)–(20), on the fields. To organize this derivation, it is convenient to use Ivakin's method,[14] combining all of the boundary conditions and plane-wave expansions in matrix expressions.

First, the boundary conditions can be written in the form

$$X^{(1)}\partial_1\zeta(\mathbf{R})+X^{(2)}\partial_2\zeta(\mathbf{R})-X^{(3)}=0, \tag{A8}$$

with $x_3=\zeta(\mathbf{K})$. Here, $\mathbf{X}$ is a five-element column matrix and a three-dimensional spatial vector, with each element corresponding to one of the boundary conditions, in the order of Eqs. (18)–(20). The 1-component of $\mathbf{X}$ is the sum of all terms multiplying $\partial_1\zeta(\mathbf{R})$, the 2-component is the sum of all terms multiplying $\partial_2\zeta(\mathbf{R})$, and the 3-component is the sum of all terms that do not contain a derivative of $\zeta(\mathbf{R})$. Note that the left side of Eq. (A8) is the dot product of $\mathbf{X}$ with the interface normal vector, $\mathbf{N}$.

In the next step, the plane-wave expansions for the potentials are substituted into Eq. (A8). The spatial derivatives in the boundary conditions are readily implemented in the plane-wave expansions, where the operator $\nabla=i\mathbf{k}_\alpha^{\pm}$. At this stage, the column matrix $\mathbf{X}$ is in the form

$$X^{(n)}=\int d^2K E^{(n)}(\mathbf{K})U, \tag{A9}$$

where

$$U=\begin{pmatrix} \nu_w^{-1}(\mathbf{K})A_w(\mathbf{K},\mathbf{K}_i)\exp(i\mathbf{k}_w^+(\mathbf{K})\cdot\mathbf{r}) \\ \nu_1^{-1}(\mathbf{K})A_1(\mathbf{K},\mathbf{K}_i)\exp(i\mathbf{k}_1^-(\mathbf{K})\cdot\mathbf{r}) \\ \nu_2^{-1}(\mathbf{K})A_2(\mathbf{K},\mathbf{K}_i)\exp(i\mathbf{k}_2^-(\mathbf{K})\cdot\mathbf{r}) \\ \nu_t^{-1}(\mathbf{K})A_v(\mathbf{K},\mathbf{K}_i)\exp(i\mathbf{k}_t^-(\mathbf{K})\cdot\mathbf{r}) \\ \nu_t^{-1}(\mathbf{K})A_h(\mathbf{K},\mathbf{K}_i)\exp(i\mathbf{k}_t^-(\mathbf{K})\cdot\mathbf{r}) \\ k_w\delta(\mathbf{K}-\mathbf{K}_i)\exp(i\mathbf{k}_w^-(\mathbf{K})\cdot\mathbf{r}) \end{pmatrix}. \tag{A10}$$

Note that the last row of U represents the incident plane-wave field in the water. The elements of the matrix $\mathbf{E}$ are given in the main text, and embody the essentials of the reflection and scattering problems. Once the problem is cast in this form, the remainder of the solution is formally identical to the elastic case.[14] For completeness, these final steps will be repeated here.

To obtain the zeroth- and first-order solutions, the scattering amplitudes are expressed as sums of zeroth- and first-order terms, the former being the flat-surface solution and the latter being linear functionals of $\zeta(\mathbf{R})$

$$A_\alpha(\mathbf{K},\mathbf{K}_i)=A_\alpha^{(0)}(\mathbf{K},\mathbf{K}_i)+A'_\alpha(\mathbf{K},\mathbf{K}_i). \tag{A11}$$

Also, the exponentials are expanded to first order in $\zeta(\mathbf{R})$ with $x_3=\zeta(\mathbf{R})$

$$\exp(i\mathbf{k}_\alpha^{\pm}(\mathbf{K})\cdot\mathbf{r})=\exp(i\mathbf{K}\cdot\mathbf{R})[1\pm ik_w\nu_\alpha(\mathbf{K})\zeta(\mathbf{R})+\cdots]. \tag{A12}$$

Finally, a Fourier transform of Eq. (A8) with respect to $\mathbf{R}$ is taken; the definition

$$Z(\mathbf{K})=\frac{1}{(2\pi)^2}\int d^2R\exp(-i\mathbf{K}\cdot\mathbf{R})\zeta(\mathbf{R}) \tag{A13}$$

is used, and the derivatives of $\zeta(\mathbf{R})$ in Eq. (A8) are treated using

$$i\mathbf{K}Z(\mathbf{K})=\frac{1}{(2\pi)^2}\int d^2R\exp(-i\mathbf{K}\cdot\mathbf{R})\nabla\zeta(\mathbf{R}). \tag{A14}$$

The zeroth-order terms yield

$$P^{(3)}(\mathbf{K}_i)Y_1^{-1}(\mathbf{K}_i)\mathbf{A}^{(0)}(\mathbf{K}_s,\mathbf{K}_i)+k_w\mathbf{Q}^{(3)}(\mathbf{K}_i)\,\delta(\mathbf{K}_s-\mathbf{K}_i)=0, \tag{A15}$$

where

$$A^{(0)}(\mathbf{K}_s,\mathbf{K}_i)=k_wY_1(\mathbf{K}_i)S_0(\mathbf{K}_i)\,\delta(\mathbf{K}_s-\mathbf{K}_i), \tag{A16}$$

is a column matrix comprised of the zeroth-order scattering amplitudes. If the first element of this matrix is inserted in Eq. (A1), one sees that the first element of $S_0(\mathbf{K}_i)$ is the plane-wave reflection coefficient. Similarly, the other elements can be inserted in Eqs. (A4) and (A5) to show that the remaining elements of $S_0(\mathbf{K}_i)$ are transmission coefficients. The zeroth-order results can be summarized by noting that Eqs. (A15) and (A16) are equivalent to Eq. (69).

The equation for first-order terms is

$$ik_w^2B(\mathbf{K}_s,\mathbf{K}_i)D_0(\mathbf{K}_i)Z(\mathbf{K}_s-\mathbf{K}_i)$$
$$-P^{(3)}(\mathbf{K}_s)Y_1^{-1}(\mathbf{K}_s)A'(\mathbf{K}_s,\mathbf{K}_i)=0, \tag{A17}$$

where $B(\mathbf{K}_s,\mathbf{K}_i)$ is given by Eq. (47) and $A'(\mathbf{K}_s,\mathbf{K}_i)$ is a column matrix comprised of the first-order approximation to the incoherent scattering amplitudes. Equation (A17) is equivalent to Eqs. (45) and (A7).

[1] E. Y. Kuo, "Wave scattering and transmission at irregular surfaces," J. Acoust. Soc. Am. **36**, 2135–2142 (1964).
[2] D. R. Jackson, D. P. Winebrenner, and A. Ishimaru, "Application of the composite roughness model to high-frequency bottom backscattering," J. Acoust. Soc. Am. **79**, 1410–1422 (1986).
[3] D. R. Jackson and K. B. Briggs, "High-frequency bottom backscattering: roughness versus sediment volume scattering," J. Acoust. Soc. Am. **92**, 962–977 (1992).
[4] D. R. Jackson, K. B. Briggs, K. L. Williams, and M. D. Richardson, "Tests of models for high-frequency seafloor backscatter," IEEE J. Ocean. Eng. **21**, 458–470 (1996).
[5] K. L. Williams and D. R. Jackson, "Bistatic bottom scattering: Model, experiments, and model/data comparison," J. Acoust. Soc. Am. **103**, 169–181 (1998).
[6] A. D. Lapin, "Sound scattering at a rough solid surface," Sov. Phys. Acoust. **10**(1), 58–64 (1964).
[7] A. D. Lapin, "Scattering of sound by a solid layer with rough boundaries," Sov. Phys. Acoust. **12**(1), 46–51 (1966).
[8] D. K. Dacol and D. H. Berman, "Sound scattering from a randomly rough fluid–solid interface," J. Acoust. Soc. Am. **84**, 292–302 (1988).
[9] W. A. Kuperman and H. Schmidt, "Rough surface elastic wave scattering in a horizontally stratified ocean," J. Acoust. Soc. Am. **79**, 1767–1777 (1986).
[10] E. Y. T. Kuo, "Acoustic wave scattering from two solid boundaries at the

ocean bottom,'' IEEE J. Ocean. Eng. **17**, 159–170 (1992).
[11] H. H. Essen, ''Scattering from a rough sedimental seafloor containing shear and layering,'' J. Acoust. Soc. Am. **95**, 1299–1310 (1994).
[12] T. Yang and S. L. Broschat, ''Acoustic scattering from a fluid–elastic–solid interface using the small slope approximation,'' J. Acoust. Soc. Am. **96**, 1796–1803 (1994).
[13] D. Wurmser, ''A manifestly reciprocal theory of scattering in the presence of elastic media,'' J. Math. Phys. **37**, 4434–4479 (1996).
[14] D. R. Jackson and A. N. Ivakin, ''Scattering from elastic sea beds: First-order theory,'' J. Acoust. Soc. Am. **103**, 336–345 (1998).
[15] R. D. Stoll and T. K. Kan, ''Reflection of acoustic waves at a water–sediment interface,'' J. Acoust. Soc. Am. **70**, 149–156 (1981).
[16] N. P. Chotiros, ''Inversion of sandy ocean sediments,'' in *Full Field Inversion Methods in Ocean and Seismo-Acoustics*, edited by O. Diachok, A. Caiti, P. Gerstoft, and H. Schmidt (Kluwer, Dordrecht, 1995), pp. 353–358.
[17] H. Deresiewicz and R. Skalak, ''On uniqueness in dynamic poroelasticity,'' Bull. Seismol. Soc. Am. **53**, 783–788 (1963).
[18] A. N. Ivakin, ''Sound scattering by inhomogeneities of an elastic half-space,'' Sov. Phys. Acoust. **36**(4), 377–380 (1990).
[19] G. G. Zipfel, Jr. and J. A. DeSanto, ''Scattering of a scalar wave from a random rough surface: A diagrammatic approach,'' J. Math. Phys. **13**, 1903–1911 (1972).
[20] E. I. Thorsos and D. R. Jackson, ''The validity of the perturbation approximation for rough surface scattering using a Gaussian roughness spectrum,'' J. Acoust. Soc. Am. **86**, 261–277 (1989).
[21] A. G. Voronovich, *Wave Scattering from Rough Surfaces* (Springer, Berlin, 1994).
[22] D. H. Berman, ''Renormalization of propagation in a waveguide with rough boundaries,'' J. Acoust. Soc. Am. **92**, 309–314 (1992).

The propagation of ultrasound within a gas jet

D. A. Hutchins,[a] C. S. McIntyre, D. W. Choi, D. R. Billson, and T. J. Robertson
School of Engineering, University of Warwick, Coventry CV4 7AL, United Kingdom

(Received 1 March 2000; revised 10 July 2001; accepted 24 August 2001)

A study is presented in which the directional characteristics of an ultrasonic signal have been modified due to propagation within an axial jet. The radiated ultrasonic field from a transducer positioned within the air jet has been studied at frequencies above 100 kHz for the first time. The effects of nozzle shape, nozzle diameter, and variations in air jet velocity and temperature have been investigated. At high air flow velocities, divergence of the ultrasonic beam was observed. This was attributed to the increased acoustic velocities in the direction of the flow. An effective waveguide was also demonstrated by cooling the air jet to below-ambient temperatures, so that the acoustic velocity in the air jet was lower than that in the surrounding ambient atmosphere. The result is likely to be of use in air-coupled ultrasonic materials inspection. © *2001 Acoustical Society of America.*
[DOI: 10.1121/1.1413998]

PACS numbers: 43.35.Ae, 43.28.Py [SGK]

I. INTRODUCTION

Air-coupled ultrasound is being used increasingly as a method for materials inspection without contact.[1] Despite the fact that the difference in acoustic impedance between air and solid materials such as metals and polymers is large, recent developments in transducer technology have made it possible for signals to be transmitted through the solid material under test, using air as the coupling medium. The present article investigates the possibility of transmitting ultrasonic signals along a gas jet, which would act as a form of waveguide. Within this waveguide, the propagation characteristics can be controlled, so that improved conditions for transmission can be obtained (e.g., increased directivity and lower attenuation). Such changes would be induced by differences in the gas flow velocity and temperature between the gas jet and its surroundings, which in turn lead to a difference in the acoustic velocity. Note that materials inspection using air-coupled ultrasound is usually conducted at frequencies below 3 MHz, because of excessive attenuation at higher frequencies.[2,3] Hickling and Marin[4] developed a term for the practical range of an ultrasonic transducer in air, called the extinction distance, over which the received signal decays by a factor of $1/e$. For example, the extinction distance is 50 mm at 1 MHz, at standard temperature and pressure (STP), and the present work is thus restricted mainly to signals below 1 MHz in frequency.

A schematic diagram of how propagation in a gas jet might be achieved is shown in Fig. 1. An ultrasonic transducer is situated within a pipe containing flowing gas, to which an exit nozzle is fitted. The nozzle shape is chosen so as to produce a gas jet with the required properties, in most cases one with a reasonably constant flow velocity region at the exit region. The design of such a transducer system has some features in common to the use of water jets as a means of coupling ultrasound into materials.[5] Air jets would be the gaseous equivalent, aiming to provide a stable environment for propagation to the sample, so that imaging for defects, etc., could be achieved with air coupling alone.

The interaction of acoustic waves with nonstationary gas has been studied extensively, both in free space[6–14] and in ducts.[15–17] Most of this research was performed at audible frequencies, and in some cases at very high gas flow rates. Some of this work[11] showed that a radial gradient in gas flow velocity leads to acoustic refraction, as depicted in Fig. 2. This shows a wavefront at AB which, at a time t later, has moved to $A'B'$. This assumes that the component at point B travels at a faster velocity than at A, so that the wave will refract or bend outwards. This results in a region of low sound intensity or ''cone of silence'' along the axis of the flow, which accompanies divergence of the sound field.[11,13] Note that the effects of refraction are important in noise reduction from aircraft engines, and the above effects are well-documented. In the present application, the aim is to use the gas jet as a propagation medium for an ultrasonic signal. Any refraction would lead to ultrasonic beam spreading, and subsequent detrimental effects on signal amplitude and spatial resolution, and hence should be minimized. Conversely, confinement of the beam would be an advantage. One way in which this might be achieved is to change the sound speed in the gas jet itself, so that it is lower than the surrounding air into which it travels (e.g., by changing the gas or lowering the temperature in the gas jet). The latter effect has been observed at audible frequencies within a cold nitrogen gas jet,[18] where convergence towards the jet axis was seen. This

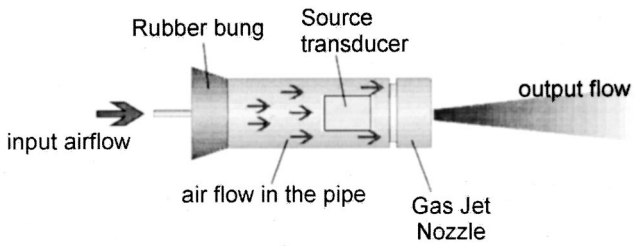

FIG. 1. Concept of a gas jet containing an ultrasonic field, generated by an air-coupled ultrasonic transducer.

[a]Electronic mail: dah@eng.warwick.ac.uk

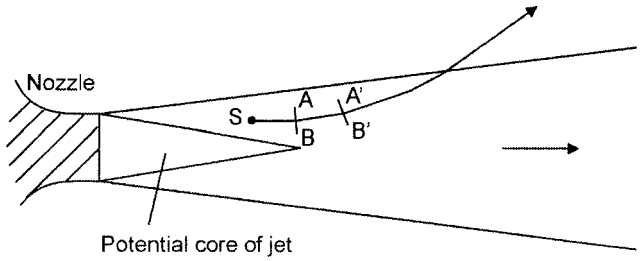

FIG. 2. The possible refraction effect on an acoustic wave in a flow from a jet (after Ref. 21).

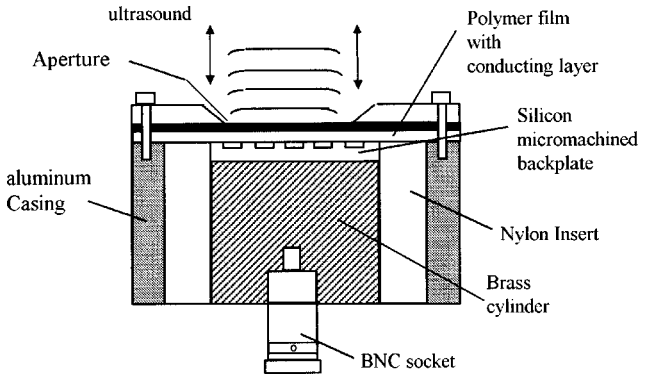

FIG. 4. Schematic diagram of the capacitive ultrasonic transducer used for these measurements to generate an ultrasonic signal within the air jet.

demonstrated that waveguide effects should be observable using a low temperature jet.

This article extends the above research by studying the radiated ultrasonic field from a transducer, generating ultrasound within the air flow of a gas jet. This has been achieved at various gas jet velocities and temperatures. The aim is to investigate the interaction of high frequency (>100 kHz) sound waves with gas jets, and to study divergence of beams due to refraction. Work using cold air jets will then be used to determine whether an effective waveguide in free space can be obtained. It should be noted that the intended application of this technique is air-coupled NDE, where interaction with a sample would be required. This will inevitably modify both the gas jet profile and the ultrasonic beam. The present work should thus be considered an initial study of the waveguide characteristics only.

II. EXPERIMENTAL METHOD

The experiments were designed to study the ultrasonic field emitted from a transducer, placed within a gas jet. The presence of gas flow was expected to modify the directional characteristics of the beam, and it was thus important that these effects be studied. It was also necessary to investigate the choice of exit nozzle, so that a stable environment for acoustic propagation was produced. As will be described, an ogive nozzle was chosen for study, as the internal shape is designed to produce an increased region of laminar flow within the gas jet.

Spatial variations in both the ultrasonic field and the gas flow velocity across two-dimensional sections throughout the gas flow were required, so that the interaction between the two could be studied. This was achieved by scanning miniature ultrasonic receivers and flow velocity sensors through the same sections of flow. This is shown in Fig. 3. Scanning was performed in a horizontal plane using an $X-Y$ linear stage, driven by standard stepper motors. These were controlled using a Labview program, running on an IBM PC, and a two-axis programmable stepper motor driver unit. The data was then displayed on a Tektronix TDS540 digital oscilloscope, and subsequently transferred to the PC for storage and later analysis. The transducer within the pipe, and the scanning plane, were carefully aligned with each other using a HeNe laser. Each scan commenced at the center of the nozzle aperture as a reference point for all scans, over typical distances of 80 mm axial (z) and 80 mm radial (r). Typical scans were performed by recording data at 1-mm spatial intervals, well within the specifications of the linear stages. A regulated compressed air supply was used to provide a constant gas pressure at one end of the 50-mm-diam pipe con-

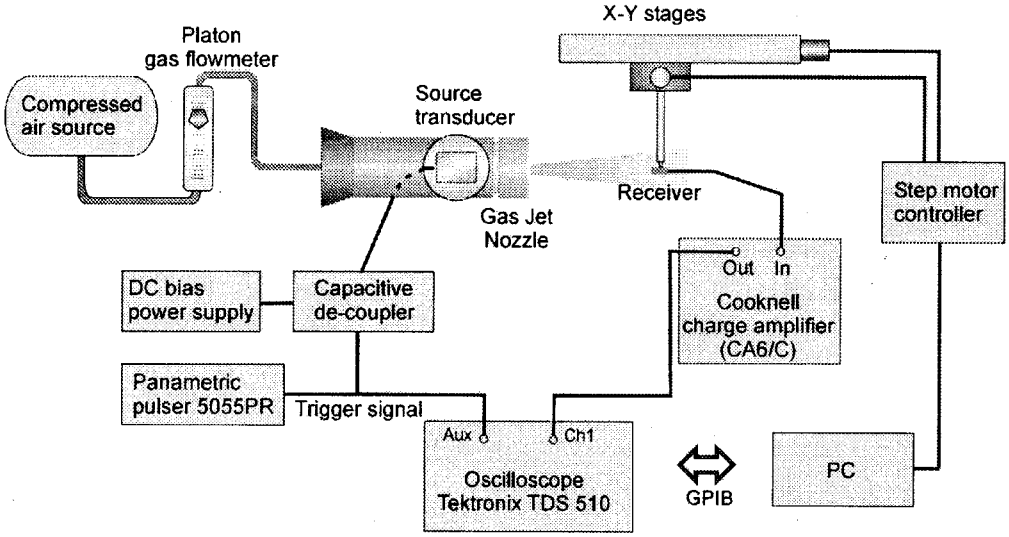

FIG. 3. Experimental arrangement for the measurement of acoustic and gas flow velocity fields.

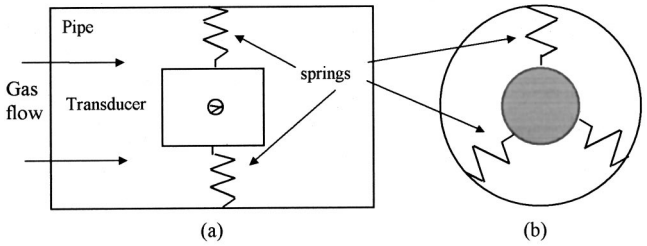

FIG. 5. Method of locating the capacitive transducer within the pipe container showing (a) side view and (b) end view.

taining the transducer. The total volumetric flow rate of air was controlled at the input using a Platon Flowbits gas flow measuring tube, and could be preset to a value in litres/minute.

A schematic diagram of the capacitive transducer held within the pipe containing air flow is shown in Fig. 4. These transducers use a thin polymer membrane attracted against a machined metal or silicon backplate, which causes a layer of air to be trapped behind the membrane.[19] It is important in these devices that the backplate surface features are well-controlled, so that the mechanical behavior of the device can be predicted. The present device contained a micromachined silicon backplate, the characteristics of which were predictable in terms of bandwidth and radiated field.[20] The 5-μm-thick Mylar polymer membrane had a grounded metal coating on the outer surface. This, together with the metallized silicon backplate, formed the two electrodes of the capacitor. The aluminum case was grounded, and fitted with a front aperture of 10-mm diameter, which defined the active area of the device. A dc bias was used to attract the membrane to the backplate, to increase the rigidity of the membrane and hence extend the upper frequency limits of operation. Mechanical springs were used to locate the transducer within the 50-mm-diam polyethylene pipe containing the gas flow, to which various nozzle profiles with exit orifice diameters in the 4–20-mm range were attached (Fig. 5). The springs allowed small adjustments in position to be made, so that the transducer could be aligned centrally within the container. They also minimized disruption to the air flow within the pipe due their small flow cross-section (although this was not crucial, due to the use of the ogive nozzle design described later in this work).

Variations in air flow velocity within the gas jet were measured using a hot-wire aneomometer[21] (Airflow TA5), with a 1-mm-diam active area. A voltage output corresponding to the velocity of the air flowing over the wire was produced, which was measured using a digital voltmeter before being transferred to the PC. Note that the hot-wire anemometer displayed the magnitude of the gas velocity in ms^{-1}, but not the direction of the flow. The acoustic field was measured by using a miniature capacitive detector similar in design to that used as the source. This detector was 3 mm in diameter. Although a smaller detector would have been desirable to minimize directionality and to reduce disruption to the air jet, a 1-mm detector was found to give very similar results but at a reduced sensitivity and signal to noise ratio. Hence,

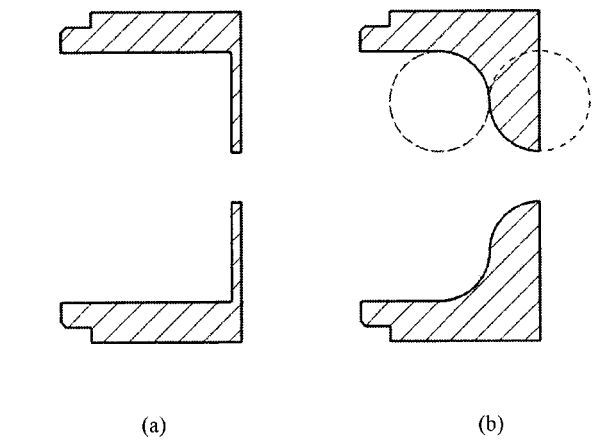

FIG. 6. The two exit orifice configurations used to generate gas jets. (a) A circular aperture of 10-mm diameter in a flat plate, (b) a nozzle based on an "ogive" curve.

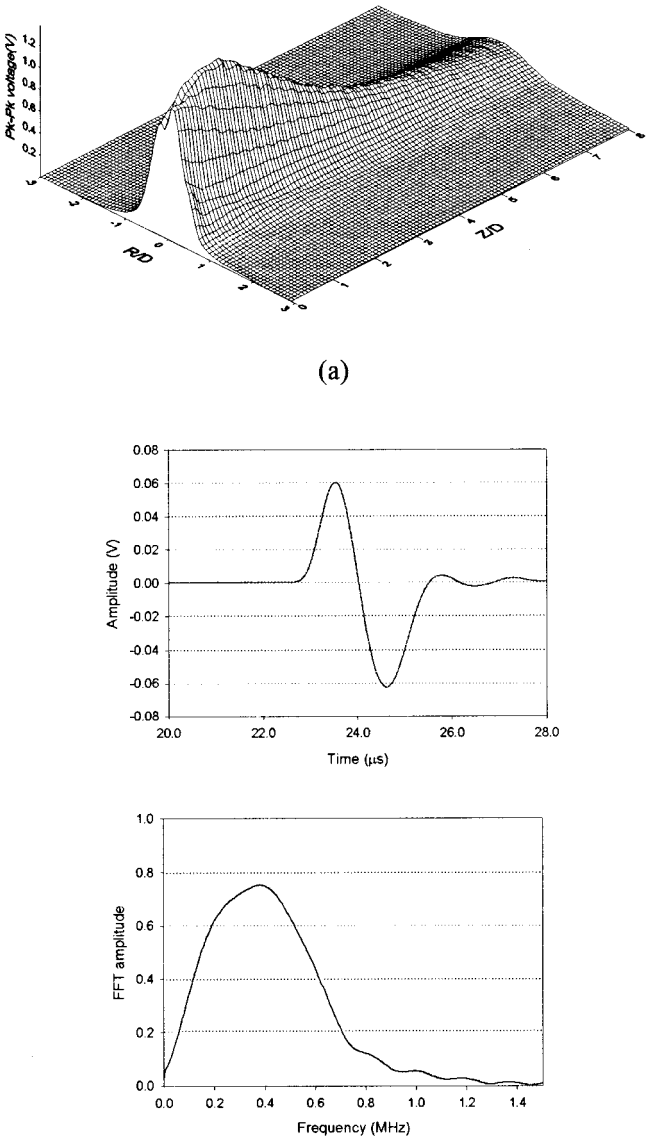

FIG. 7. (a) Typical free-field radiated sound field from the capacitive ultrasonic transducer. (b) A typical waveform detected on-axis, together with the corresponding frequency spectrum obtained via a FFT.

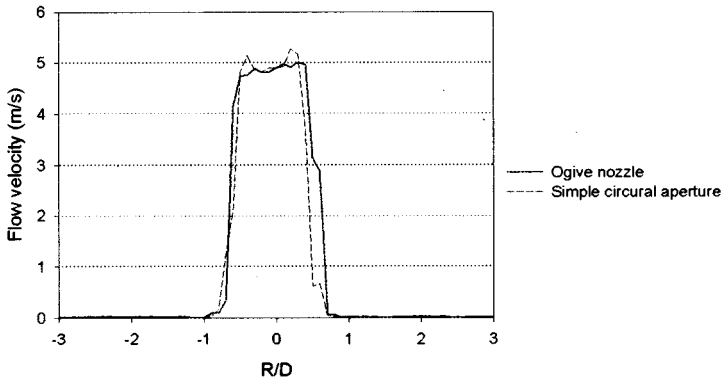

(a)

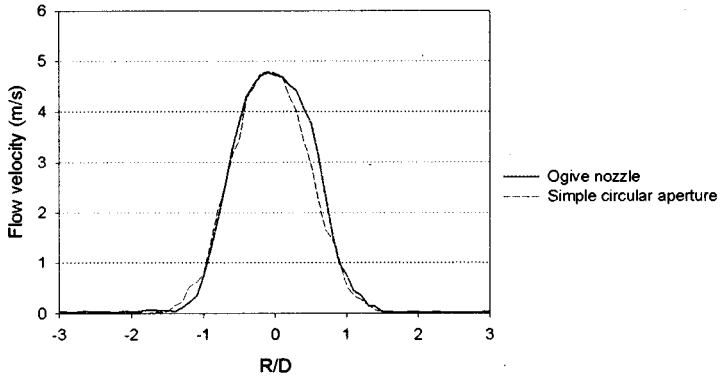

(b)

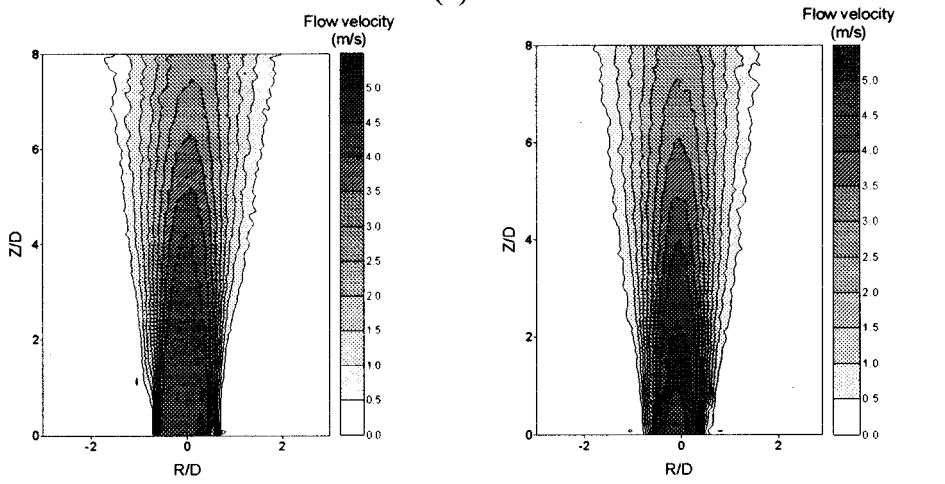

(c)

FIG. 8. (a) Gas flow velocity variations across the exit of each aperture shown in Fig. 7, as measured with the hot wire anemometer, for an axial exit velocity of 4.8 ms^{-1}. (b) Velocity variations at a distance of 30 mm from the orifice. (c) Two-dimensional sections of air flow velocity for the two nozzles.

the 3-mm detector was used throughout. The oscilloscope was used to record the ultrasonic waveform at 1-mm intervals throughout the scan. These were then postprocessed to obtain spatial variations in an acoustic parameter, using automated PC-based software with a moving time window to remove multiple reflections. In the plots presented here, the peak-to-peak amplitude of the received transient was recorded, although spectral and travel time data were available if required.

Two nozzle configurations were investigated, as shown in Fig. 6. Note that Reynolds numbers within the approximate range of 1600–7200 were present, due to the range of flow velocities and nozzle diameters used. Hence, turbulent jets would be produced, confirmed in the present experiments by observation of jet properties. The first design [Fig. 6(a)] was a circular aperture of 10 mm diameter, cut through a flat plate (i.e., with square-cut lips), whereas the second [Fig. 6(b)] was based on an ''ogive'' curve,[22] which is used

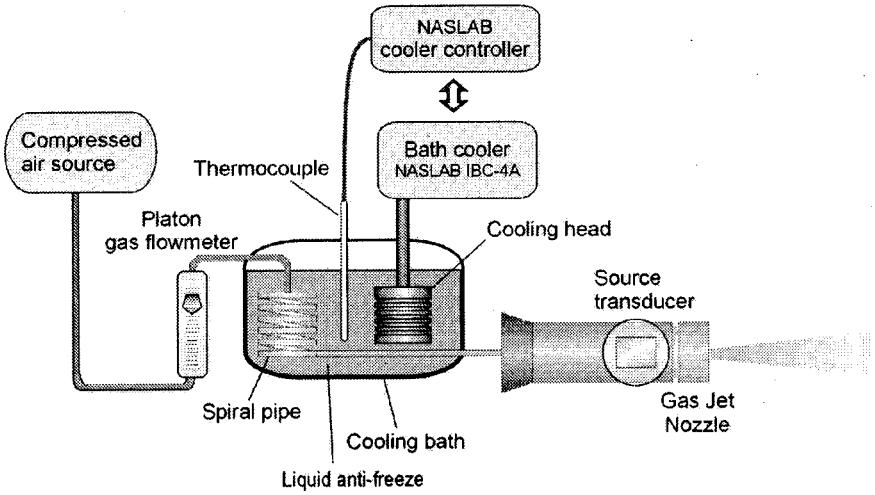

FIG. 9. Apparatus used to cool air jets to temperatures below ambient.

to optimize laminar flow. It can be seen that the ogive curve is formed from partially following the outline of two circles. The curve is designed to minimize drag, and hence energy loss, in the gas itself. It also accelerates the gas flow smoothly, reducing the disturbance caused by the transducer and spring mounting. Compared to the circular aperture, the ogive nozzle results in thinner shear layers at the interface between the jet and the ambient medium, and an extended potential core (where the flow is laminar). Outside the potential core, within the shear layer, the flow is turbulent. A greater region of laminar flow was considered to be of advantage, hence the reason for studying the ogive nozzle.

Figure 7(a) shows the radiated sound field from the transducer mounted in the pipe, before a nozzle or any gas flow was introduced. It can be seen from this figure that the sound field is similar to those already reported for a device of this nature[20] in that the maximum amplitude at the expected nearfield/farfield boundary is present, with a lack of side lobes. This arises primarily from the well-damped response of the device. This is illustrated in Fig. 7(b), which shows a

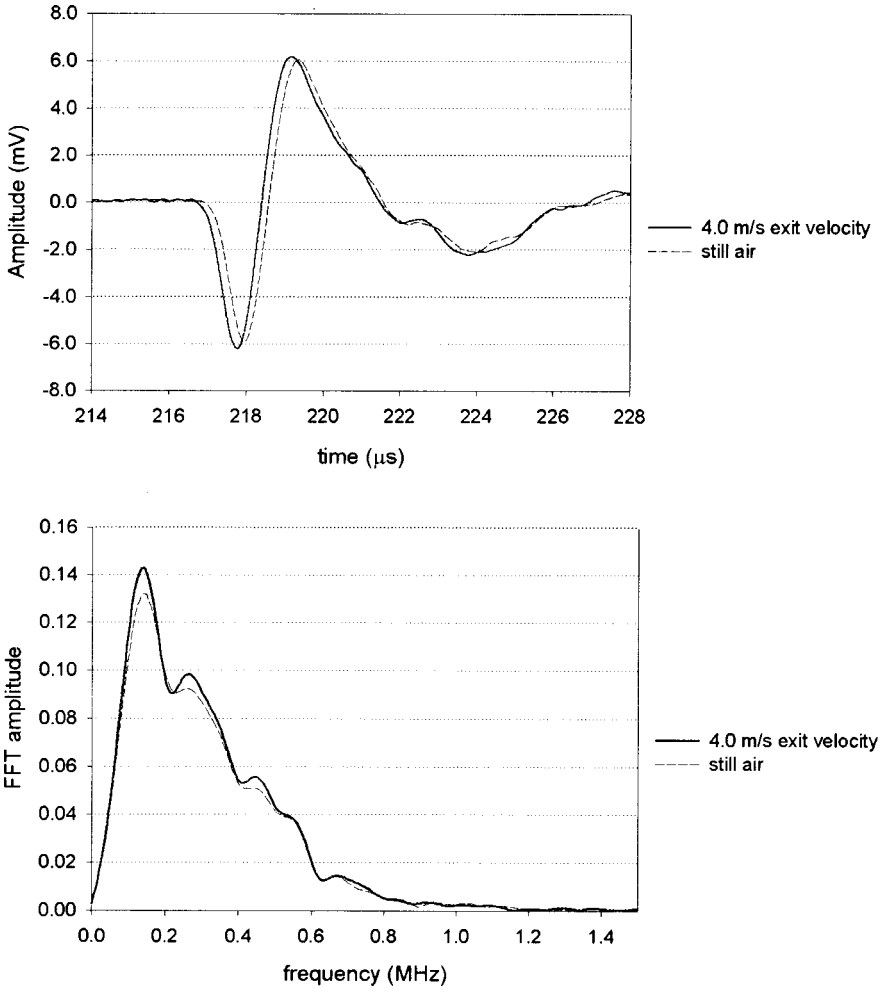

FIG. 10. The ultrasonic waveform and corresponding spectrum obtained on-axis at the exit of the ogive nozzle, in both still air (dotted) and when the axial exit flow velocity was 4.0 ms^{-1} (solid line).

typical waveform detected on-axis, together with the corresponding frequency spectrum obtained via a fast Fourier transform (FFT). It is evident that the capacitive transducer emitted an ultrasonic transient with a center frequency of approximately 400 kHz, with useful energy up to approximately 1 MHz.

The gas flow velocity variations across the exit of each nozzle are shown in Fig. 8(a), as measured with the hot wire anemometer, for the same axial exit velocity of 4.8 ms^{-1}. It can be seen that a more uniform velocity profile existed from the ogive nozzle [Fig. 6(b)] than from the simple circular aperture [Fig. 6(a)]. These differences were less marked at distances further away from the nozzle exit, as shown at 30-mm distances in Fig. 8(b). Figure 8(c) demonstrates that the flow fields from the two nozzles exhibit some differences over the 60×80-mm^2 area studied, in particular the greater extent of uniform flow velocity in the case of the ogive nozzle. If the air jet is to be used as a stable medium within which to propagate ultrasonic signals, minimal refraction would be preferred, such that most of the ultrasonic energy is contained within the flow. This would be minimized in a region of constant flow (and hence ultrasonic) velocity. Because of the above-mentioned advantages, the ogive nozzle was chosen for further study in terms of the emitted ultrasonic field and the creation of ultrasonic waveguides. Note also that the smooth acceleration of gas caused by the internal shape of this nozzle [Fig. 6(b)] would also reduce any flow disturbance due to the transducer and its mounting. A second such nozzle was thus fabricated, with a diameter of 5 mm, to allow a greater range of exit velocities to be studied.

Experiments were also conducted with the temperature of the air jet cooled below ambient. The additional apparatus used to obtain this cooling is shown in Fig. 9, and was placed between the regulated compressed air source and the pipe containing the ultrasonic transducer. The air was passed through a coil of brass tubing, which was immersed in a cylindrical bath of methanol. This was cooled to temperatures down to $-30\,°C$ using a Naslab bath cooler and temperature controller. All tubing and pipe-work had to be insulated to minimize heat transfer into the cool gas. The bath was set at a predetermined temperature, and gas flow introduced. The system was then left for some hours to reach equilibrium, and gas temperatures checked at various locations. It was found that exit gas temperatures varied with flow rate, as would be expected. Typically, gas jet exit temperatures could be produced which were 20 °C or more below ambient laboratory temperatures, for exit gas velocities of up to 20 ms^{-1}.

III. RESULTS AND DISCUSSION

A. Gas jet at room temperature

The characteristics of the radiated ultrasonic field from the ogive nozzle were first measured with the air jet being at the same temperature as that in the surrounding laboratory. Figure 10 shows the ultrasonic waveform and corresponding spectrum obtained on-axis at the exit of the ogive nozzle, in both still air (dotted) and when the exit flow velocity was 4 ms^{-1} (solid line). The nozzle has caused some distortion to the time waveform [cf. Fig. 7(a) in free space], presumably due to increased scattering of higher frequencies by the nozzle itself. This has limited the upper frequency response to approximately 600–800 kHz, with a peak response now at 200 kHz. It can also be seen that the flow of air caused a slight shift in the waveform arrival time, due to the flow-induced increase in axial acoustic velocity. Note, however, that both the waveform shape and the frequency response were relatively unaffected by gas flow. Figure 11 shows the radiated ultrasonic field, measured as peak to peak amplitude variations, in both still air, and in the presence of an exit air flow velocity of 4 ms^{-1}. The field without gas flow is evidently less divergent, and decays less rapidly in the axial (z) direction. This implies that the air jet has influenced the radiated sound field by increasing divergence. Note, however, that the results in still air show that the smooth curves within the nozzle have succeeded in producing a well-behaved secondary acoustic source.

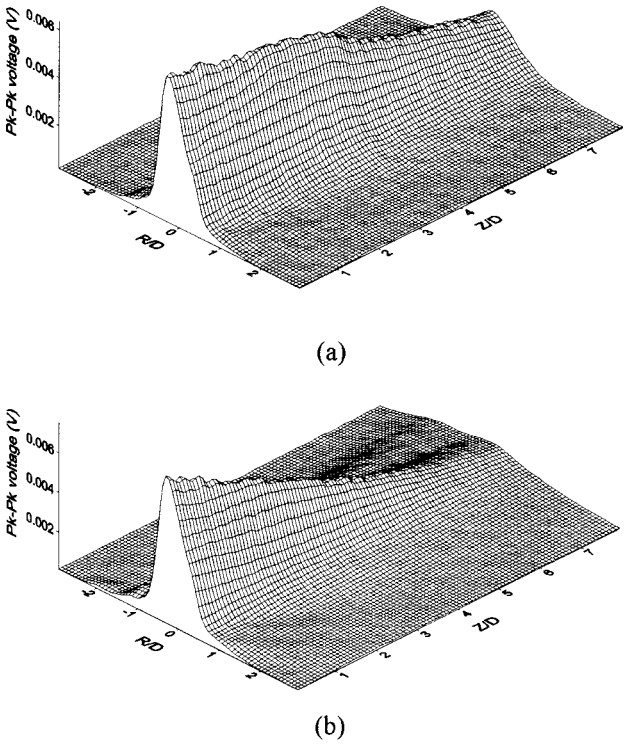

(a)

(b)

FIG. 11. The radiated ultrasonic field from the ogive nozzle of 10-mm diameter, measured as peak to peak amplitude variations, in (a) still air and (b) in the presence of an exit axial air flow velocity of 4.0 ms^{-1}.

Experiments were also performed on a range of ogive nozzle aperture diameters of 10 to 20 mm and exit flow velocities in the range 2–4 ms^{-1} (10 mm being the size of the active element of the source transducer). These diameters resulted in reduced air flow velocities, and the introduction of gas flow was found to have little effect on the ultrasonic beam emanating from each nozzle. However, the use of a smaller ogive diameter of 5 mm allowed increased jet velocities of up to 20 ms^{-1} to be studied.

Figure 12 shows both (a) the air jet flow velocity profile at an exit velocity of 4 ms^{-1} and (b) the radiated sound field in the absence of flow for the 5-mm nozzle. The smaller nozzle has led to a change in the gas jet properties, compared

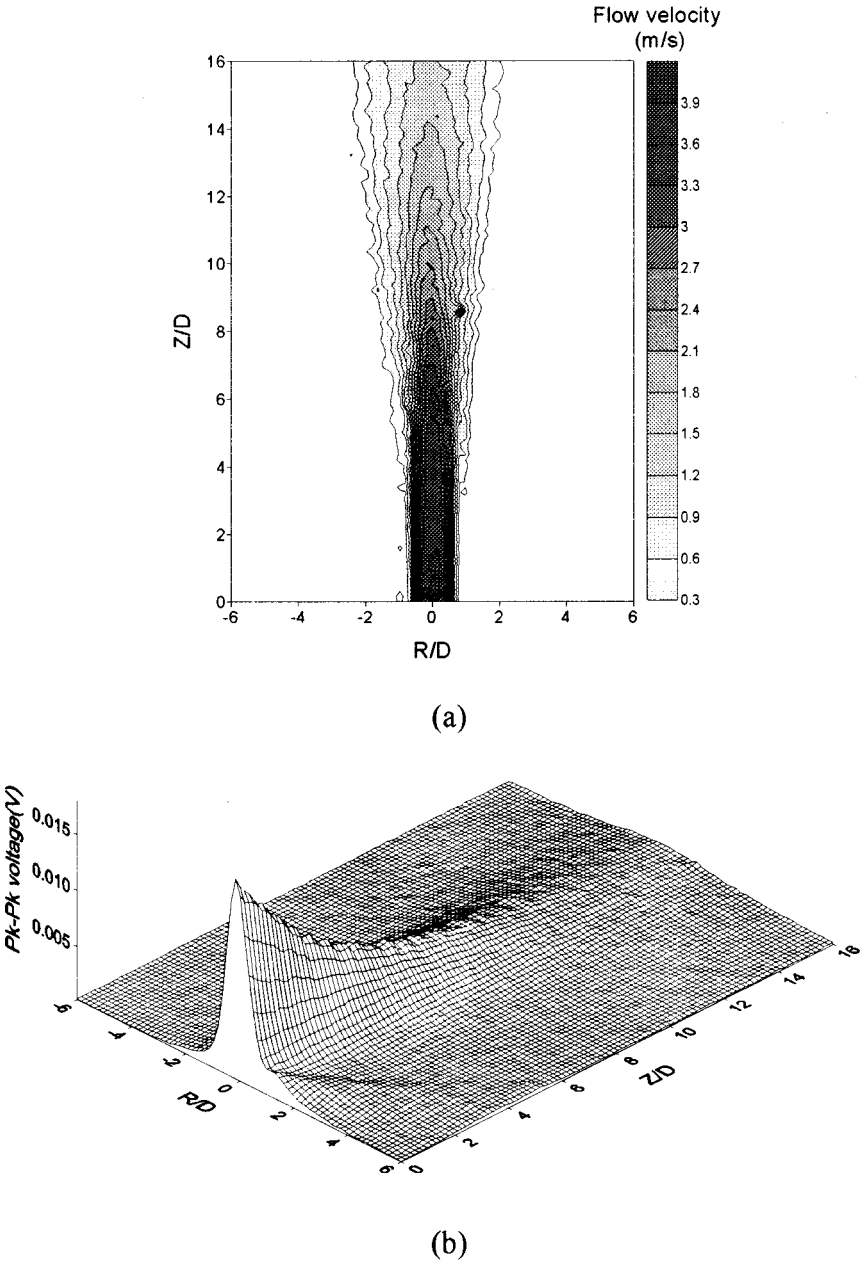

FIG. 12. Measured properties of the 5-mm-diam ogive nozzle. (a) The air jet flow variations for exit velocity of 4.0 ms^{-1} and (b) the radiated ultrasonic field in the absence of flow.

to those of the 10-mm ogive nozzle [shown earlier in Fig. 8(c)]. The sound field in the absence of air flow has also been affected by the narrower nozzle diameter, with a greater axial decay as expected from a smaller aperture. Introducing gas flow caused a marked effect on the radiated ultrasonic beam for the 5-mm-diam ogive nozzle. This is shown in Fig. 13 for three jet velocities of 4.5, 9 and 19.8 ms^{-1}. Comparison of Figs. 11 and 13 indicates that the introduction of gas flow caused significant side lobes in the ultrasonic field to appear, along with an increased axial decay in ultrasonic amplitude. These effects became more severe as the gas jet velocity increased. In particular, the angle at which the main side lobe appeared increased with the jet velocity.

The features observed in Fig. 13 could partially be explained by reference to Fig. 2, and consideration of refraction phenomena. Divergence would arise because of the higher propagation velocity of acoustic energy along the jet than in the still air outside. Let us assume a constant gas flow velocity, U, and an acoustic wavelength λ in air which is much smaller than the gas jet diameter d. This is approximately true at 500 kHz, assuming $\lambda = 0.66$ mm and $d = 5$ mm. Consider a plane wavefront traveling at some angle θ_1 to the normal to the gas jet axis. Analysis of the standard equations for group or energy velocity leads to a prediction of the refracted angle θ_2 within the still air as

$$\sin\theta_2 = (c_2/(c_2 + U\cos\theta_1))\sin\theta_1, \tag{1}$$

where c_1 and c_2 are the speed of the sound wave in regions of gas jet flow and still air, respectively. Consider Fig. 13(c), where a typical flow speed in the central region of the jet close to the nozzle exit was $U = 18\,ms^{-1}$. Assuming a value of the speed of sound in still air of 331.4 ms^{-1} at room temperature and standard pressure,[4] and propagation within the gas jet close to the axial direction (i.e., θ_1 is close to 90° and $\sin\theta_1$ is thus close to unity) gives $\theta_2 \sim 71.5°$ (or a divergence angle from the axis of 18.5°). The ultrasonic field

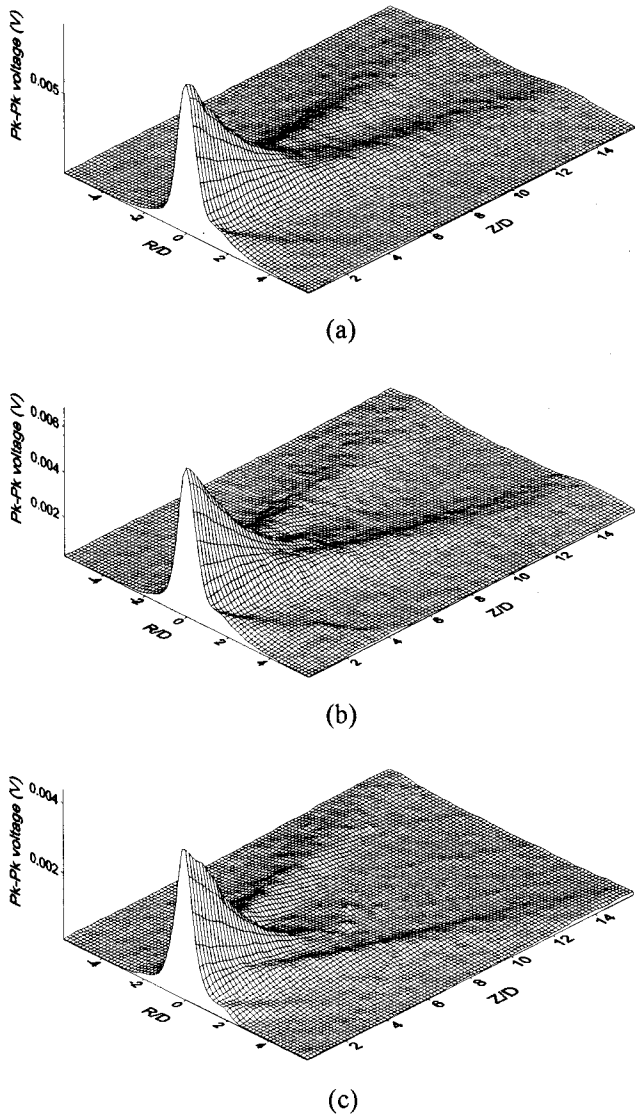

FIG. 13. Radiated ultrasonic fields from the 5-mm-diam ogive nozzle, for exit jet velocities of 4.5, 9.0 and 19.8 ms^{-1}.

of Fig. 13(c) indicates a divergence angle for the main side lobes of $20°\pm2°$, and hence the two values are in reasonable agreement. The above assumes a single velocity within the gas jet, and a sharp boundary to still air, neither of which would be actually present, and hence the above is at best an approximation.

A better explanation arises from the presence of the interface (a shear layer) between the jet and the ambient medium. Sound waves incident on this interface are partly reflected back into the jet and partly transmitted outside. For such a jet, the transverse wavenumber (K) in the jet can be written as

$$K=(\omega/c)[(1-\mathrm{M}\cos\theta)^2-\cos^2\theta]^{1/2}, \tag{2}$$

where $\mathrm{M}=U/c_2=0.0543$ is the Mach number of the jet and θ is the angle of propagation from the jet axis. The sound waves become evanescent when $K=0$, or when

$$\cos\theta=1/(1+\mathrm{M}). \tag{3}$$

This leads to a value for θ of 18.5°. Thus, $\theta=18.5°$ is the evanescence angle of sound waves in the jet, and the observed phenomena appear as side lobes, because propagation is possible only for $\theta<18.5°$, and not for $\theta>18.5$.

B. Cooled air jets

It is evident from the above that the air jets have caused divergence of the ultrasonic field emitted from the ogive nozzle. As explained earlier, one of the aims of this research was to investigate whether the ultrasonic beam could be contained within the gas jet itself, which would act as a waveguide. From the results above, it would appear that one way to achieve this is to reduce the sound velocity within the gas jet to below ambient values. This would lead to possible containment of the ultrasonic beam within the jet, instead of divergence, as there would now be less transmission of sound outside the jet. This was investigated using the apparatus of Fig. 9, to cool the air jet exiting the nozzle to below room temperature.

Figure 14 presents the results of experiments using an ogive exit diameter of 5 mm and a gas jet exit velocity of 10 ms^{-1}. The air within the jet was cooled in turn from room temperature (23 °C) to a minimum of −0.5 °C. It will be evident that the behavior seen at room temperature [Fig. 14(a)] was as observed earlier, with divergence of the ultrasonic beam. However, this was gradually modified as the gas jet was cooled. The rapid axial decay with distance was reduced, and the side lobes decreased in angle and intensity. At the lowest temperature, no side lobes were present, and a single central beam existed with a gradual decay in amplitude [Fig. 14(d)]. These features are all consistent with a waveguide effect. As noted earlier, gas flow increases the ultrasonic propagation velocity within the gas jet, and the result was a divergence of ultrasonic energy. Conversely, the introduction of cooler air reverses this effect, by reducing the angle θ in Eq. (2). The properties of this beam will be dictated primarily by the properties of the gas jet, in terms of the flow and temperature profiles. It has been demonstrated, however, that an effective waveguide has been produced. This is consistent with earlier observations, where acoustic refraction and focusing were observed in a much colder liquid nitrogen gas jet.[15] The interesting observation here is that cooling by a factor of just over 20 °C caused a marked change in behavior.

IV. CONCLUSIONS

A study has been presented in which an ultrasonic signal has been generated within an air jet. The interaction of the radiated ultrasonic field from an ultrasonic transducer within the gas flow has been studied for the first time. The aim of this work was to obtain a transduction system using air jets to form an ultrasonic waveguide; the present work represents an initial study of the complicated phenomena that would result.

A capacitive transducer was chosen as the source, because of its wide bandwidth and well-damped response. This was then inserted into a pipe, and the radiated field measured as a function of exit nozzle design and gas flow rate. The

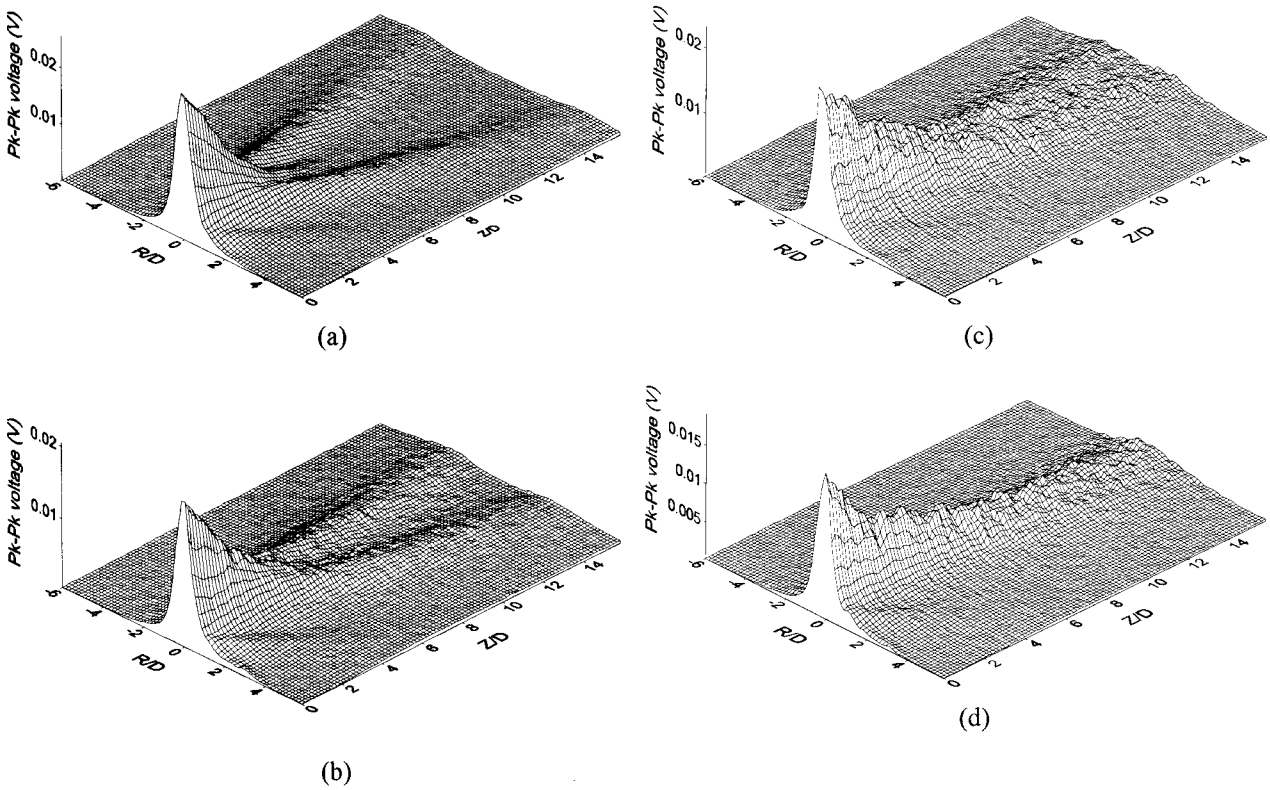

FIG. 14. Radiated ultrasonic fields for cooled air jets from the 5-mm-diam ogive nozzle, for an exit velocity of 10 ms^{-1}. Exit temperatures of the gas jet are (a) room temperature (23 °C), (b) 10.5 °C, (c) 5 °C and (d) −0.5 °C.

ogive nozzle, designed to produce an effective gas jet with low energy loss, was selected, and tested at various flow rates. It was found that, with the gas jet at ambient temperatures, the effect of increased flow rate was to induce divergence of the radiated ultrasonic beam. This agrees with earlier studies of acoustic signals in gas jets, at lower (audible) frequencies, and arose from the increased acoustic velocity in the direction of gas flow. Experiments were thus performed in which the air jet was cooled to temperatures below ambient. It was demonstrated that, for the same exit velocities, the directional characteristics of the ultrasonic beam could be influenced. At lower temperatures, the acoustic velocity within the air jet decreased. This was seen to result in a more directional ultrasonic field, with the gas jet acting as a waveguide.

Further experiments are under way to investigate this phenomenon further. Of particular interest will be to determine whether the technique can be used to propagate ultrasound over larger distances then previously, with a reduced attenuation, but with a good directivity. This will use lower temperatures, and mixtures of gases other than air. This work will be reported in due course.

ACKNOWLEDGMENTS

The authors would like to thank the Engineering and Physical Sciences Research Council for sponsoring this work, and for providing studentships for Craig McIntyre and Toby Robertson. Thanks are also due to Dr C. T. Shaw for useful advice on nozzle design, and to an anonymous reviewer for providing helpful comments on the properties of gas jets.

[1] W. A. Grandia and C. M. Fortunko, "NDE applications of air-coupled ultrasonic transducers," in *Proceedings, 1995 IEEE Ultrasonics Symposium* (1995), Vol. 1, pp. 697–709.
[2] H. E. Bass, L. C. Sutherland, J. Piercy, and L. Evans, "Absorption of Sound by the Atmosphere," in *Physical Acoustics Vol. XVII*, edited by W. P. Mason and R. N. Thurston (Academic, New York, 1984), pp. 145–232.
[3] L. J. Bond, C.-H. Chiang, and C. M. Fortunko, "Absorption of ultrasonic waves in air at high frequencies (10-20 MHz)," J. Acoust. Soc. Am. **92**, 2006–2015 (1992).
[4] R. Hickling and S. P. Marin, "The use of ultrasonics for gauging and proximity sensing in air," J. Acoust. Soc. Am. **79**, 1151–1160 (1986).
[5] G. V. Blessing and D. G. Eitzen, "Ultrasonic sensor for measuring surface roughness," in SPIE Vol. 1009, "Surface measurement and characterisation" (1988), pp. 281–289.
[6] E. Dokumachi, "Sound transmission in narrow pipes with superimposed mean flow and acoustic modelling of automobile catalytic converters," J. Sound Vib. **182**, 799–808 (1995).
[7] N. Duverlie and P. Gatignol, "Sound propagation in a turbulent sheared flow," Acustica **82**, S170 (1996).
[8] R. Vedantham and J. Hunter, "Sound wave propagation through incompressible flows," Wave Motion **26**, 319–328 (1997).
[9] P. Joseph, C. L. Morfey, and P. A. Nelson, "Active control of source sound power radiation in uniform flow," J. Sound Vib. **212**, 357–364 (1998).
[10] L. M. B. C. Campos, "On waves in gases. 1. Acoustics of jets, turbulence and ducts," Rev. Mod. Phys. **58**, 117–182 (1986).
[11] C. K. W. Tam and L. Auriault, "Mean flow refraction effects on sound radiated from localised sources in a jet," J. Fluid Mech. **370**, 149–174 (1998).
[12] L. M. B. C. Campos, "On longitudinal acoustic propagation in convergent and divergent nozzle flows," J. Sound Vib. **117**, 131–151 (1987).
[13] J. Atvars, L. K. Schubert, and H. S. Ribner, "Refraction of sound from a point source placed in an air jet," J. Acoust. Soc. Am. **37**, 168–170 (1965).

[14] G. W. Ford and W. C. Meecham, ''Scattering of sound by isotropic turbulence of large Reynolds number,'' J. Acoust. Soc. Am. **32**, 1668–1672 (1960).
[15] E. Grande, ''Refraction of injected sound by a very cold nitrogen jet,'' J. Acoust. Soc. Am. **38**, 1063–1064 (1965).
[16] U. Ingard and V. K. Singhal, ''Sound attenuation in turbulent pipe flow,'' J. Acoust. Soc. Am. **55**, 535–538 (1974).
[17] A. Michalke, F. Arnold, and F. Holste, ''On the coherence of the sound field in a circular duct with uniform mean flow,'' J. Sound Vib. **190**(2), 261–271 (1996).
[18] P. O. A. L. Davies, ''Realistic models for predicting sound propagation in flow duct systems,'' Noise Control Eng. J. **40**(1), 135–141 (1993).
[19] D. W. Schindel, D. A. Hutchins, L. Zou, and M. Sayer, ''The design and characterisation of micromachined air-coupled capacitive transducers,'' IEEE Trans. Ultrason. Ferroelectr. Freq. Control **42**, 42–50 (1995).
[20] A. G. Bashford, D. Hutchins, and D. W. Schindel, ''Radiated fields of an air-coupled capacitance transducer,'' Ultrasonics **34**(2-5), 169–172 (1996).
[21] R. W. Perry, *Hot-Wire Aenomometry* (Clarendon, Oxford, 1982).
[22] P. J. Lamont, ''Pressures around an inclined ogive cylinder with laminar, transitional or turbulent separation,'' AIAA J. **20**, 1492–1499 (1982).

Acoustic attenuation in a three-gas mixture: Results

Yefim Dain and Richard M. Lueptow[a)]
Department of Mechanical Engineering, Northwestern University, Evanston, Illinois 60208

(Received 19 January 2001; revised 13 July 2001; accepted 24 August 2001)

Acoustic attenuation in a mixture of gases results from the combined effects of molecular relaxation and the classical mechanisms of viscosity and heat conduction. Consequently, the attenuation depends on the composition of the gas mixture, acoustic frequency, temperature, and pressure. A model of the relaxational attenuation that permits the calculation of acoustic attenuation is used to predict the effect of composition, frequency, temperature, and pressure on the acoustic attenuation in a three-component gas mixture of nitrogen, methane, and water vapor. The attenuation spectrum is dependent upon the composition through the appearance of peaks in the spectrum related to the relaxation frequencies of the particular components and their relaxing complexes. The relaxation peak related to methane dominates except at low methane concentrations, where the nitrogen peak, which is dependent upon the water vapor and methane concentration, is evident. Temperature and pressure significantly alter the relaxation frequency and the degree of attenuation, but water vapor plays little role in the attenuation. © *2001 Acoustical Society of America.*
[DOI: 10.1121/1.1413999]

PACS numbers: 43.35.Ae, 43.35.Fj [SGK]

I. INTRODUCTION

Molecular relaxation and the classical mechanisms of viscosity and heat conduction determine the acoustic attenuation in a mixture of gases, depending on the composition of the gas mixture, the acoustic frequency, the temperature, and the pressure. The absorption and dispersion of sound waves in polyatomic gases due to molecular relaxation has been studied for nearly seven decades.[1–6] The molecular relaxation processes can lead to a complicated mechanism of vibrational–translational and vibrational–vibrational energy transfer between different molecular energy levels resulting in several effective relaxation frequencies, depending on the vibrational modes of the species involved in the relaxation processes. The relaxational attenuation has been modeled for pure gases, binary mixtures of gases, and air with carbon dioxide in several ways.[5–9] We have recently extended the Schwartz, Slawsky, and Herzfeld model[5] for the relaxational component of attenuation to a mixture of three or more polyatomic gases at room temperatures based on molecular constants.[10] Although experimental data against which to compare the model are sparse, our theoretical prediction of attenuation for a binary mixture of nitrogen and water vapor and for pure methane match experimental results quite well.[10]

In this paper, we continue our earlier work by using our model to predict the effect of composition, frequency, temperature, and pressure on the acoustic attenuation in a three-component gas mixture of nitrogen, methane, and water vapor. We investigate this particular combination of gases for two reasons. First, the values of the molecular constants necessary to calculate the transition probabilities are available in the literature. Second, the nitrogen–methane–water mixture is representative of gas mixtures that are industrially important. For low concentrations of methane, the mixture is representative of a combustible air–fuel mixture, with the nitrogen and water vapor representing moist air. (Obviously, the neglect of oxygen in this simplified model is significant.) For high concentrations of methane, the mixture is representative of natural gas, which consists of 75%–99% methane with smaller quantities of higher hydrocarbons and inert components including nitrogen and water vapor.[11]

The focus in this paper is to investigate the effect of composition, frequency, temperature, and pressure on acoustic attenuation using the model from our earlier work.[10] While all of these factors are expected to play a role in the degree of attenuation, the dependence of attenuation on each of them is not readily apparent. The model from our earlier paper permits the independent variation of each of the factors to determine their impact on the attenuation. This allows the prediction of the acoustic attenuation under a variety of conditions in multicomponent gas environments.

II. THE MODEL FOR ACOUSTIC ATTENUATION

A complete description of the theoretical model that we used to calculated the results presented here is given in Dain and Lueptow.[10] Here we only describe the highlights of the model. The theory is based on the Euler gas equations to model a continuous medium consisting of a polyatomic gas mixture accompanied by nonlinear semimacroscopic population equations for the number of molecules in a given energy state.[12] We assume no diffusion of gas components and ignore the effect of rotational relaxation on the acoustic attenuation, since the rotational relaxation contribution is quite similar to the classical contribution at the frequencies that we are considering[9,13] and is negligible in the range of frequencies where the vibrational relaxation is significant.

The Euler equations are in the standard form except that the total energy of the gas mixture depends not only on the gas temperature, but also on the internal temperatures of the excited molecular mode. Molecules gain and lose vibrational

a)Electronic mail: r-lueptow@northwestern.edu

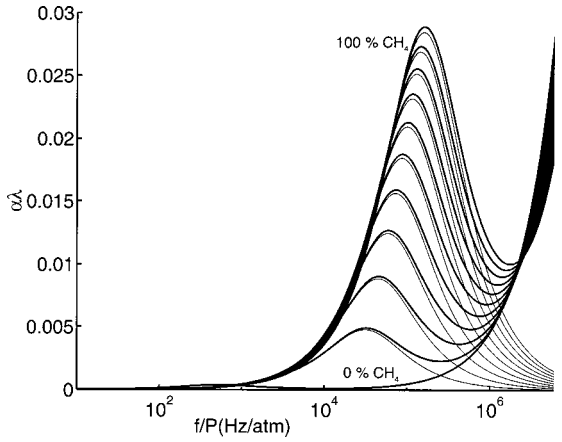

FIG. 1. Nondimensional acoustic attenuation spectrum for 0%,10%,20%, . . . ,100% methane concentrations (from lowest to highest at the relaxational peak) with 3% water vapor (except for 100% methane) and the remainder nitrogen at 297 K. Bold curves are the total attenuation (relaxational plus classical) and fine curves are the relaxational component only.

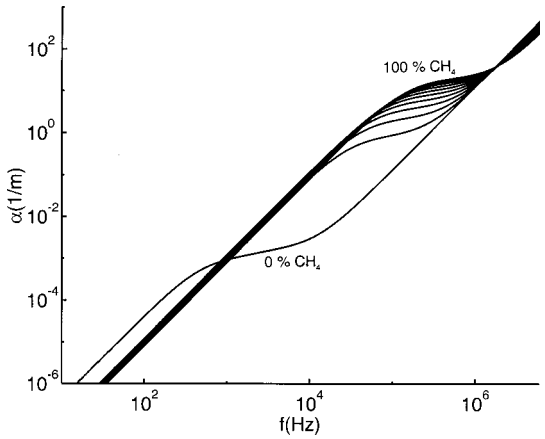

FIG. 2. Dimensional total acoustic attenuation spectrum for 0%,10%,20%, . . . ,100% methane concentrations (from lowest to highest at 10^5 Hz) with 3% water vapor (except for 100% methane) and the remainder nitrogen at 1 atm and 297 K.

and translational energy in collisions by vibrational–translational and vibrational–vibrational energy exchange. We assume that at room temperature only the lowest vibrational modes are significant and only one-quantum collisional reactions are possible. The relaxation equations are dependent on the collision rates of molecules based on kinetic theory for a gas of rigid spheres and the transitional probabilities of energy exchange per collision between different vibrational modes based on a solution of the Schrödinger equation.[6] The resulting system of first-order differential equations can be solved numerically for the internal temperatures related to the excited modes and substituted into the Euler energy equation, which is solved assuming a plane acoustic wave. The attenuation due to viscous dissipation and irreversible heat conduction are based on the classical formulation by Stokes and Kirchhoff[14] using the coefficient of shear viscosity, the thermal conductivity, and the specific heats of the gas mixtures calculated according to commercial software.[15]

In this paper we use the relaxation model along with the classical mechanisms to analyze the acoustic attenuation under a variety of conditions. We present the results of computational experiments to determine the effects of composition, frequency, temperature, and pressure. The goal of these computational experiments is to determine the nature of the effect of these variables on the acoustic attenuation.

III. RESULTS

A. Effects of composition

We first consider the effect of composition on the acoustic attenuation spectrum for a temperature of 297 K and a water vapor concentration of 3%, near its maximum value at this temperature and a pressure of 1 atm. Figure 1 shows the acoustic attenuation spectrum for 100% methane and for 0%, 10%,20%, . . . ,90% methane concentrations with 3% water vapor and the remainder nitrogen. Bold curves represent the total attenuation (relaxational plus classical) while the fine curves represent the relaxational component of attenuation plotted against f/P, where f is the frequency and P is the pressure. This horizontal scale reflects the dependence of the relaxation time on energy exchange between molecules. The time between molecular collisions is inversely proportional to the pressure. Consequently, the relaxation frequency, which is the inverse of the relaxation time, is proportional to pressure. This proportionality is expressed by the dependence of attenuation on the quotient f/P. The acoustic attenuation α is nondimensionalized by the wavelength of the sound λ, which in turn is dependent on the frequency and speed of sound for that gas composition.

It is immediately evident from Fig. 1 that the relaxational component of attenuation dominates at low frequencies. The classical component of relaxation dominates at high frequencies. The peak in the curves at $f/P \sim 10^5$ Hz/atm is the relaxation frequency related to the relaxation of methane modified slightly by the presence of nitrogen and water. The attenuation at the relaxational frequency of methane is so large that it dominates classical attenuation and the relaxational frequency of nitrogen, which occurs at much lower frequencies and is not evident on the scale of Fig. 1. The relaxational frequency occurs at higher frequencies as the fraction of methane in the mixture increases. For pure methane, this relaxational frequency is at $f/P \sim 1.5 \times 10^5$ Hz/atm based on our model. The dominance of classical attenuation at high frequencies comes about because of the dependence of both shear viscosity and heat conductivity contributions to the attenuation on the square of the frequency.[14,16]

The results in Fig. 1 also show a strong dependence of the attenuation on composition in the frequency range 10^5 Hz/atm$< f/P < 10^6$ Hz/atm. At low frequencies ($f/P < 10^4$ Hz/atm) and in the range of frequencies where classical attenuation begins to dominate ($f/P > 10^6$ Hz/atm), the dependence of the attenuation on composition is minimal.

It is helpful to plot the attenuation spectra at 1 atm using a dimensional scale for the attenuation, as shown in Fig. 2, to clearly show the wide range of attenuation. Again we show the attenuation for gas compositions ranging from 0% to 90% methane with 3% water and the remainder nitrogen as

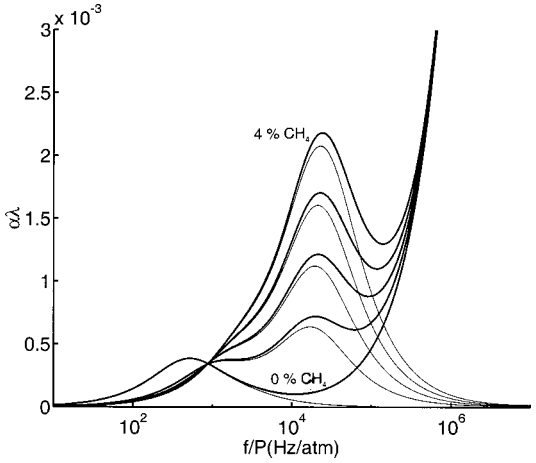

FIG. 3. Nondimensional acoustic attenuation spectrum for 0%, 1%, 2%, 3%, and 4% methane concentrations (from lowest to highest at 10^4 Hz/atm) with 3% water vapor and the remainder nitrogen at 297 K. Bold curves are the total attenuation and fine curves are the relaxational component only.

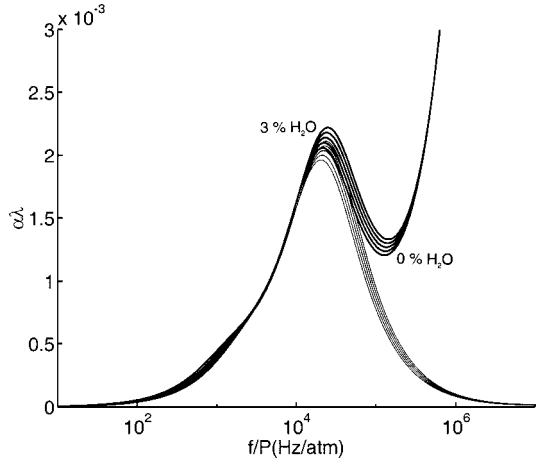

FIG. 4. Nondimensional acoustic attenuation spectrum for 0%, 1%, 2%, and 3% water vapor concentrations (from lowest to highest at 10^4 Hz/atm) with 4% methane and the remainder nitrogen at 297 K. Bold curves are the total attenuation and fine curves are the relaxational component only.

well as 100% methane. The knee at the lower frequency for 0% methane is related to the relaxation frequency of nitrogen. The knee at nonzero methane concentrations is associated with the relaxation frequency of methane. The attenuation is greatest at the highest frequencies. The dependence of the attenuation on the methane concentration is greatest for 10^5 Hz$<f<10^6$ Hz. In this frequency range, the attenuation can vary be more than an order of magnitude with methane concentration.

We now return briefly to the issue of including the rotational relaxation contribution. Although we cannot calculate this contribution because the appropriate values for methane are not available, we can assume that the rotational relaxation contribution is less than the classical contribution. If a contribution this large were added to the classical contribution, the only effect in Fig. 1 would be a negligible leftward shift of the attenuation spectrum at the highest frequencies ($f/P>10^6$ Hz/atm), where classical contributions dominate. Likewise, there would be a very slight upward shift in the dimensional curves in Fig. 2 for $f>10^6$ Hz. Thus, qualitative results including rotational relaxation are identical to those shown and the quantitative results only change by an inconsequential amount.

As mentioned earlier, the relaxation frequency of nitrogen is not evident in Fig. 1 and is only visible for zero methane concentrations in Fig. 2. This is a consequence of the large relaxational effect of methane. The relaxational frequency of nitrogen becomes evident only at low concentrations of methane as shown in Fig. 3. Note that the vertical scale in Fig. 3 is greatly expanded compared to Fig. 1 to make visible the relaxation frequency of nitrogen at $f/P \sim 10^3$ Hz/atm. When no methane is present, only the relaxation frequency of nitrogen as modified by water is evident. The presence of water vapor increases the relaxational frequency above the relaxational frequency for pure nitrogen of about 9 Hz/atm.[17] The relaxation peak related to water vapor is too small to appear as a separate relaxational peak in the spectrum. The presence of even small quantities of methane (as small as 1%) results in the appearance of a strong relaxational peak for methane. As the fraction of methane increases, the relaxation frequency for the nitrogen shifts to higher frequencies and the attenuation due to the methane increases so that the methane peak dominates. The effect of nitrogen is evident only as a slight kink in the curve at 10^3 Hz/atm for 2% methane and higher concentrations.

Varying the water vapor concentration over nearly the full range of compositions thermodynamically possible at this temperature and pressure has little effect on the relaxational attenuation, as indicated in Fig. 4. The small effect of water vapor on the relaxational attenuation near 10^3 Hz/atm occurs because the relaxational peak for nitrogen is shifted to the right in the presence of water. The more obvious effect of water vapor is to increase the amplitude of the relaxational peak for methane near 10^4 Hz/atm and shift the peak to a slightly higher frequency due to the methane–water relaxational complex. Nevertheless, the influence of water vapor on the attenuation spectrum is much smaller than the influence of similar concentrations of methane.

Given the strong dependence of acoustic attenuation on the fraction of methane in the mixture, one might consider the relationship between the attenuation and the methane concentration by plotting the total dimensionless attenuation (relaxational plus classical) as a function of composition for several frequencies, as shown in Fig. 5. Three curves are plotted for each frequency corresponding to water vapor concentrations of 0%, 1.5%, and 3% with nitrogen making up the remainder of the mixture. (The concentration of water vapor is evident at the right end of the curves. The curve ending furthest to the left is 3% water vapor, and the curve ending furthest to the right is 0% water vapor.) The near overlap of the curves for different water vapor concentration confirms that the presence of water vapor is nearly inconsequential compared to the effect of methane concentration. At the lowest frequencies, the nondimensional attenuation is not a monotonic function of the methane fraction. The attenuation at the higher frequencies increases monotonically with methane fraction.

The dimensional attenuation at ten frequencies ranging

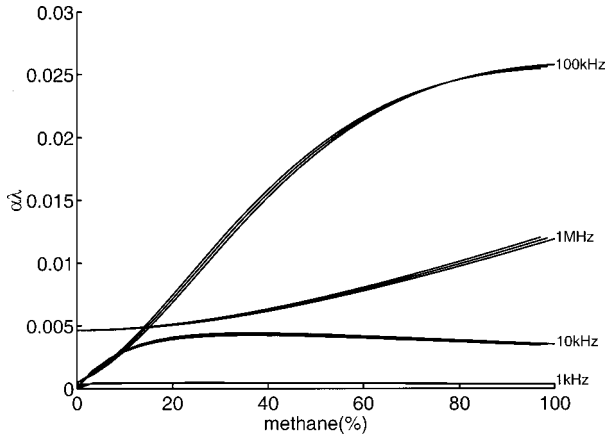

FIG. 5. Dependence of nondimensional total attenuation on methane concentration for 0%, 1.5%, and 3% water vapor with the remainder of the mixture nitrogen at 297 K. (The curve ending furthest to the left at the right end is 3% water vapor, and the curve ending furthest to the right is 0% water vapor.)

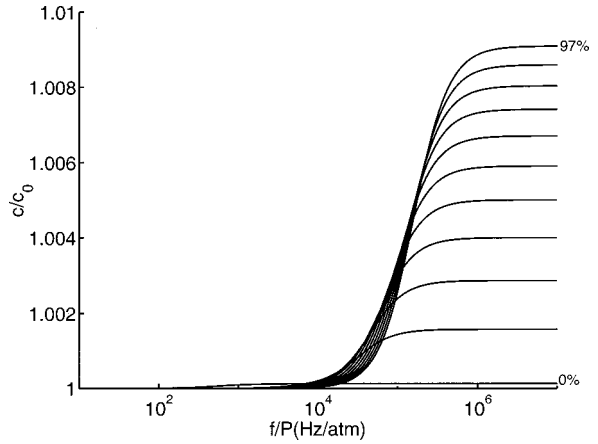

FIG. 7. Dependence of the sound speed normalized by the equilibrium sound speed on frequency for 0%,10%,20%, . . . ,90%,97% methane concentrations (from lowest to highest at the highest frequency) with 3% water vapor and the remainder nitrogen at 297 K.

from 100 kHz to 1 MHz is shown in Fig. 6. The dimensional attenuation is much larger at higher frequencies than at lower frequencies. However, the dimensional attenuation is not a monotonic function of methane concentration for high frequencies (800 kHz–1 MHz) at low methane concentrations or the lowest frequency (100 kHz) at high methane concentrations. At frequencies from 200 to 700 kHz the dimensional acoustic attenuation is monotonic, varies substantially over the range of methane concentrations, and is significant in magnitude. For instance, the attenuation at 500 kHz monotonically varies by nearly a factor of 6 from $\alpha = 3.3\ \mathrm{m}^{-1}$ at 0% methane to $\alpha = 19.0\ \mathrm{m}^{-1}$ at 100% methane.

The molecular relaxation not only affects attenuation, but also alters the sound speed. The sound speed c normalized by the equilibrium sound speed c_0 is plotted in Fig. 7 as a function of frequency. The equilibrium sound speed is that at low frequencies (much less than the relaxation frequency) calculated based on the classical equation using the translational temperature.[18,19] As shown in Fig. 7, the normalized sound speed increases slightly at the relaxation frequency of methane, but the increase is quite small, even for very large methane concentrations. This increase comes about when the frequency of the sound wave is sufficiently high so that its period is less than the relaxation time of methane. Under these conditions, the specific heat at constant volume, which is based on the internal energy of the gas, is decreased because of the reduced contribution of the vibrational energy transfer resulting in a higher sound speed.[20] Of course, the increase in the equilibrium sound speed c_0 with methane concentration because of the decreased molecular weight of the mixture, which is not evident in Fig. 7 because of the normalization scheme, is much greater than the increase due to molecular relaxation at high frequencies.

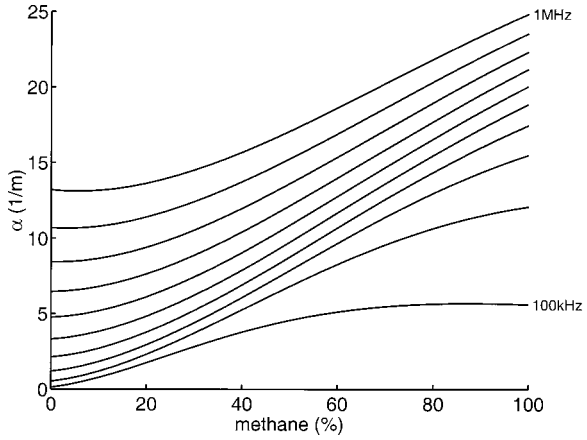

FIG. 6. Dependence of dimensional total attenuation on methane concentration for 0% water vapor with the remainder of the mixture nitrogen at 1 atm and 297 K. The curves correspond to 100 kHz increments in frequency.

B. Effect of temperature

The effect of temperature on the attenuation is shown in Fig. 8. In these figures, two curves are plotted at 297 and 323 K, one for 0% water vapor and the other for 3% water vapor. At the lowest temperature, 243 K, only 0% water vapor is considered because of the low partial pressure of water. At the low methane concentration, the effect of variation in temperature on the nondimensional attenuation is small, as shown in Fig. 8(a). However, at higher methane concentrations the effect of temperature is quite significant [Figs. 8(b) and (c)], particularly near the relaxational frequency of methane. In these cases, an increase in temperature results in a slight increase in the relaxational frequency and a substantial increase in the relaxational attenuation. The curves merge at low frequencies. At high frequencies, the classical attenuation increases substantially but the curves do not merge. In all cases, the water vapor plays little role in the effect of temperature on attenuation, as is evident from the curves for 0% and 3% water vapor concentrations overlaying each other. [In Fig. 8(a), the separate curves are only evident at the relaxational frequency of methane. In Figs. 8(b) and (c), the curves are so close that they appear only as thickened curves.]

C. Effect of pressure

All of the spectra to this point (except Fig. 2) have used the frequency divided by pressure as the independent vari-

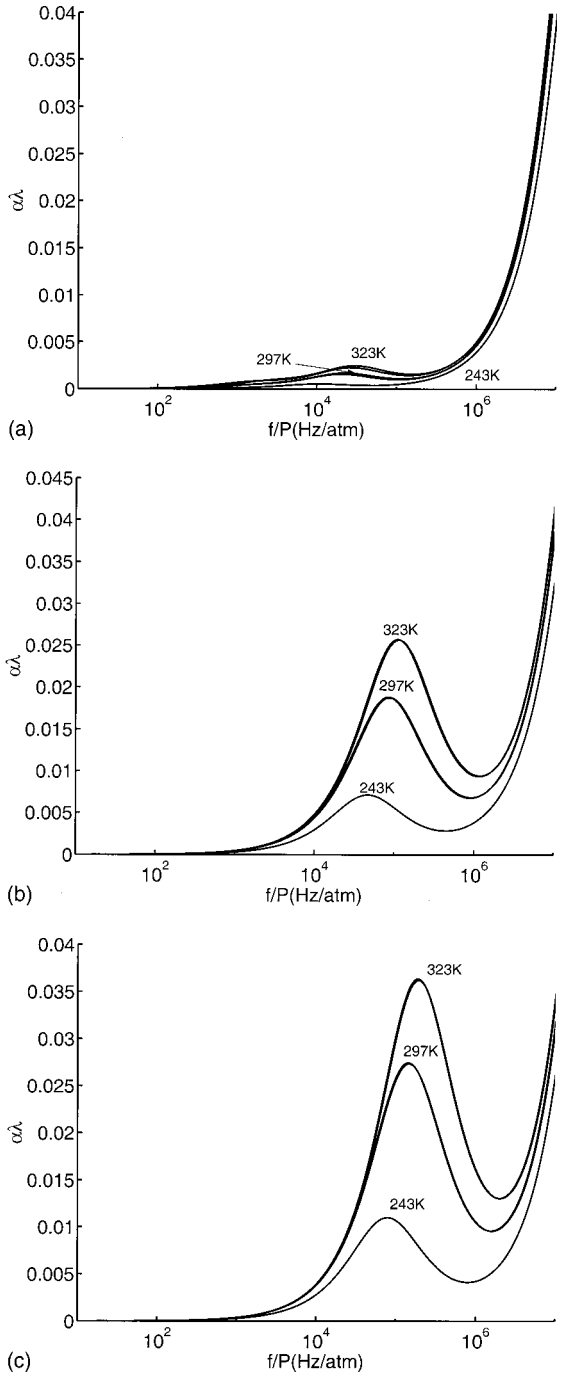

FIG. 8. Effect of temperature on the nondimensional total attenuation spectrum. For 297 and 323 K, the curves for 0% and 3% water vapor concentrations are shown, although they overlap in most cases. For 243 K, the water vapor concentration is zero: (a) 3% methane, 0% and 3% water vapor, and remainder nitrogen; (b) 50% methane, 0% and 3% water vapor, and remainder nitrogen; (c) 90% methane, 0% and 3% water vapor, and remainder nitrogen.

able reflecting the natural dependence of the nondimensional relaxational attenuation on pressure. It is, however, instructive to directly consider the effect of pressure on the spectrum of the attenuation, α, as shown in Fig. 9. The variation in pressure noticeably shifts the attenuation spectrum. However, the shape of the spectrum is essentially unchanged. Nevertheless, at any one frequency, the shift in the spectrum due to pressure has a significant effect on the attenuation at that frequency.

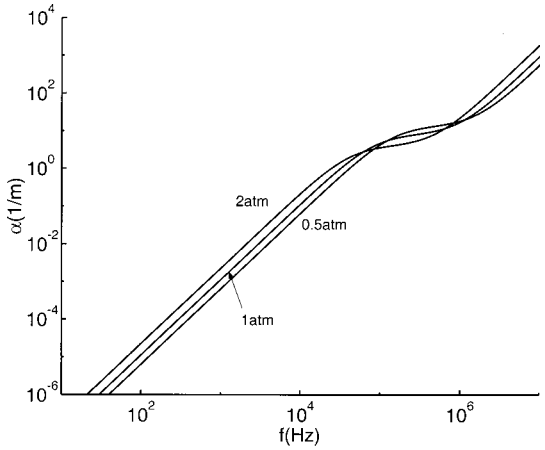

FIG. 9. Effect of pressure on the dimensional total attenuation spectrum for 50% methane, 3% water vapor, 47% nitrogen.

IV. SUMMARY

Our interest in a predictive model for acoustic attenuation came about because of the relation of the acoustic attenuation spectrum to gas composition. The key issue that arises is the dependence of acoustic attenuation on composition given the variability in temperature, pressure, and contaminants such as water vapor. Consider the acoustic attenuation at a frequency of 500 kHz for which the dependence of the attenuation on the fraction of methane was shown in Fig. 6. The attenuation is monotonic, relatively large, and varies by nearly an order of magnitude over the range of methane concentrations. But consider the extremes of the conditions for outdoor ambient temperatures from 243 to 323 K and water vapor concentrations from 0 to 3%. Except at the lowest methane concentration shown in Fig. 8, the attenuation varies substantially over this temperature range at 500 kHz. However, the variation of the attenuation with humidity at any particular temperature is negligible. We might also consider situations where the pressure changes. From Fig. 9, it is evident that the attenuation varies by a factor of 2 at 500 kHz for pressures from 0.5 to 2.0 atm.

To summarize, we have used a model of relaxational attenuation along with the model for classical attenuation to predict the total acoustic attenuation in a three-component mixture of nitrogen, methane, and water vapor. The attenuation spectrum is dependent upon the composition through the appearance of peaks in the spectrum related to the relaxation frequency of the particular components and their relaxing complexes. The relaxation peak related to methane dominates the spectrum except at very low methane concentrations, where the nitrogen peak is evident. Classical attenuation plays a significant role at high frequencies. Temperature and pressure significantly alter the relaxation frequency and the degree of attenuation. But the presence of water vapor plays little role.

ACKNOWLEDGMENTS

Support from the Department of Energy under subcontract from Commercial Electronics, Inc. (Broken Arrow, OK) and from the Ford Motor Company are gratefully acknowledged.

[1] C. Zener, ''Interchange of translational, rotational and vibrational energy in molecular collisions,'' Phys. Rev. **37**, 556–569 (1931).
[2] L. Landau, ''Zur theorie der energieubertragung bei stoessen,'' Phys. Z. Sowjetunion **1**, 88–98 (1932a).
[3] L. Landau, ''Zur theorie der energieubertragung II,'' Phys. Z. Sowjetunion **2**, 46–51 (1932b).
[4] L. Landau and E. Teller, ''Zur theorie der Schalldispersion,'' Phys. Z. Sowjetunion **10**, 34–43 (1936).
[5] R. N. Schwartz, Z. I. Slawsky, and K. F. Herzfeld, ''Calculation of vibrational relaxation times in gases,'' J. Chem. Phys. **20**, 1591–1599 (1952).
[6] F. Tanzcos, ''Calculation of vibrational relaxation times of the chloromethanes,'' J. Chem. Phys. **25**, 439–447 (1956).
[7] L. B. Evans, H. E. Bass, and L. C. Sutherland, ''Atmospheric absorption of sound: Theoretical predictions,'' J. Acoust. Soc. Am. **51**, 1565–1575 (1972).
[8] H. E. Bass, H.-J. Bauer, and L. B. Evans, ''Atmospheric absorption of sound: Analytical expressions,'' J. Acoust. Soc. Am. **52**, 821–825 (1972).
[9] H. Bass, L. Sutherland, J. Piercy, and L. Evans, ''Absorption of sound by the atmosphere,'' in *Physical Acoustics*, edited by W. P. Mason and R. N. Thurston (Academic, Orlando, 1984), Vol. XVII, pp. 145–232.
[10] Y. Dain and R. M. Lueptow, ''Acoustic attenuation in three-component gas mixtures,'' J. Acoust. Soc. Am. **109**, 1955–1964 (2001).
[11] W. E. Liss, W. H. Thrasher, G. F. Steinmetz, P. Chowdiah, and A. Attari, ''Variability of natural gas composition in select major metropolitan areas of the United States,'' Report No. GRI-92/0123, 1992.
[12] M. N. Kogan, *Rarefied Gas Dynamics* (Plenum, New York, 1969).
[13] G. L. Gooberman, *Ultrasonics: Theory and Application* (Hurt, New York, 1968), pp. 113–138.
[14] A. B. Bhatia, *Ultrasonic Absorption* (Dover, New York, 1967), pp. 51–88.
[15] PPDS2 for Windows (National Engineering Laboratory, Glasgow, 1998).
[16] K. F. Herzfeld and T. A. Litovitz, *Absorption and Dispersion of Ultrasonic Waves* (Academic, New York, 1959), pp. 185–257.
[17] H. E. Bass, L. C. Sutherland, A. J. Zuckerwar, D. T. Blackstock, and D. M. Hester, ''Atmospheric absorption of sound: Further developments,'' J. Acoust. Soc. Am. **97**, 680–683 (1995).
[18] W. Vincenti and C. Kruger, *Introduction to Physical Gas Dynamics* (Wiley, New York, 1965).
[19] A. J. Matheson, *Molecular Acoustics* (Wiley-Interscience, New York, 1971), pp. 8–46.
[20] R. W. B. Stephens and A. E. Bate, *Acoustics and Vibrational Physics* (Arnold, London, 1966), pp. 760–768.

Measurement of electrostrictive coefficients of polymer films

François M. Guillot[a] and Jacek Jarzynski
School of Mechanical Engineering, Georgia Institute of Technology, Atlanta, Georgia 30332-0405

Edward Balizer
Naval Surface Warfare Center, Carderock Division, Code 645, West Bethesda, Maryland 20817

(Received 11 June 2001; accepted for publication 15 September 2001)

A new technique to experimentally determine the electrostrictive coefficients of thin polymer films is presented. This technique is a second-order extension of the first-order quasistatic method for the measurement of piezoelectric coefficients previously introduced by Guillot and Jarzynski [J. Acoust. Soc. Am. **108**, 600–607 (2000)]. In the present method, electrically induced strains are measured optically on a rubber-encapsulated sample. These strains are used in a Rayleigh–Ritz procedure that minimizes the total energy of the sample and whose output is a set of three tensile electrostrictive coefficients. The total energy of the sample includes elastic contributions from the polymer and the encapsulating rubber as well as two quadratic electromechanical terms corresponding to Maxwell stress and to electrostriction. Therefore, the external electrostatic effects can be separated from the intrinsic electrostrictive behavior, and the measured coefficients are true material properties. Data obtained on two types of polyurethanes submitted to a bias field of approximately 4 MV/m at 2 kHz and at room temperature are presented. It was found that these materials possess very large electrostrictive coefficients and that the Maxwell stress effect is responsible for less than 13% of their total electromechanical behavior.
[DOI: 10.1121/1.1416905]

PACS numbers: 43.38.Ar, 43.38.Fx, 43.35.Sx, 43.28.Tc [SLE]

I. INTRODUCTION

Polymer materials with electromechanical properties such as piezoelectricity are of interest in many fields of acoustics, where they are used in a large number of applications including sonars, loudspeakers, ultrasonic transducers, and actuators. Renewed interest in polymers for electromechanical applications has sprung from the discovery of a very large electrostrictive effect in some polyurethane elastomers,[1] which makes these materials exciting new transduction materials. The substantial magnitude of the observed strains combined with the polyurethanes' high compliance has lead some researchers to investigate the possibility of using electrostrictive polymer films as advantageous alternatives to piezoelectric materials (such as polyvinylidene fluoride, or PVDF) in sonar[2] and loudspeaker[3] designs. Their unique properties can also be exploited in special actuator applications,[4] where requirements combine large displacements and compact size, as is the case for microactuators used in the construction of microelectromechanical systems (MEMS).[5] Other potential applications include interactive tactile Braille readers for the blind[6] and artificial muscles.[7]

However, the poor fundamental understanding of electrostriction in polyurethanes and the lack of reliable and complete electrostrictive coefficient data has hindered the development of polyurethane-based electromechanical applications. The extremely soft nature of these materials renders the determination of their electromechanical coupling constants quite delicate, because the measurement results are extremely sensitive to the experimental conditions (especially the mechanical boundary conditions). For this reason, established methods that have been successfully used to measure electrostrictive coefficients on harder materials such as ceramics and glass[8–10] cannot be readily applied to polyurethanes. Most of the available polyurethane data have been obtained on constrained samples,[11–15] and therefore represent apparent coefficients rather than true coefficients. Furthermore, most studies have concentrated on measuring only one constant, the thickness coefficient.[1,16]

Therefore, it appeared that both the fundamental understanding of polyurethane electrostriction as well as its practical use would benefit from accurate measurements of a *complete* set of *true* electrostrictive coefficients. The present article introduces a technique capable of performing such measurements. The technique is an extension of a method recently introduced to measure piezoelectric coefficients on polymer films,[17] where unelectroded samples are sandwiched between an aluminum plate (acting as a rigid backing) and an aluminum foil using two layers of a soft silicone rubber. Electric field-induced strains are optically measured in all three directions by a laser Doppler vibrometer and used as input parameters in a Rayleigh–Ritz energy minimization procedure implemented symbolically in Mathcad. The exact mechanical boundary conditions are automatically taken into account in the procedure by considering the appropriate energy functional for the sample, which results in the determination of the true tensile electrostrictive coefficients. Therefore, the measured coefficients are intrinsic material constants of the polyurethanes.

This article is divided into four sections. In Sec. II, basic definitions are presented in order to familiarize the reader with the phenomenon of electrostriction in polymers and to

[a]Electronic mail: francois.guillot@me.gatech.edu

introduce some concepts necessary for establishing the analytical framework of the method. Section III introduces the method itself, focusing on the sample preparation and measurements as well as on the energy minimization procedure. Section IV deals with experimental results obtained on two different types of polyurethanes. Finally, conclusions are drawn in Sec. V.

II. ELECTROSTRICTIVE CONSTITUTIVE EQUATIONS AND MAXWELL STRESS EFFECT

The purpose of this section is to introduce the equations governing the electromechanical behavior of electrostrictive materials and to introduce the coefficients that the method presented in this article aims at measuring.

A. Electrostrictive constitutive equations

Electrostriction is a second-order coupling between electrical and mechanical variables. Following the formalism introduced by Mason,[18] and choosing the strains S_{kl} and the electric fields E_m as independent variables, one can expand the stresses X_{ij} and the electric displacements D_n into a second-order Taylor series about their zero position:

$$X_{ij}=\frac{\partial X_{ij}}{\partial S_{kl}}S_{kl}+\frac{\partial X_{ij}}{\partial E_m}E_m+\frac{1}{2}S_{qr}\frac{\partial^2 X_{ij}}{\partial S_{qr}\partial S_{kl}}S_{kl}+S_{kl}\frac{\partial^2 X_{ij}}{\partial S_{kl}\partial E_m}E_m+\frac{1}{2}E_o\frac{\partial^2 X_{ij}}{\partial E_o\partial E_m}E_m, \tag{1}$$

$$D_n=\frac{\partial D_n}{\partial S_{kl}}S_{kl}+\frac{\partial D_n}{\partial E_m}E_m+\frac{1}{2}S_{qr}\frac{\partial^2 D_n}{\partial S_{qr}\partial S_{kl}}S_{kl}+S_{kl}\frac{\partial^2 D_n}{\partial S_{kl}\partial E_m}E_m+\frac{1}{2}E_o\frac{\partial^2 D_n}{\partial E_o\partial E_m}E_m. \tag{2}$$

The first-order partial derivatives define the following familiar constants:

elastic stiffness coefficients at constant electric field:

$$c^E_{ijkl}\equiv\frac{\partial X_{ij}}{\partial S_{kl}}, \tag{3}$$

dielectric permittivity coefficients at constant strain:

$$\varepsilon^S_{nm}\equiv\frac{\partial D_n}{\partial E_m}, \tag{4}$$

piezoelectric stress coefficients:

$$e_{mij}\equiv-\frac{\partial X_{ij}}{\partial E_m}=\frac{\partial D_m}{\partial S_{ij}}, \tag{5}$$

which relate to the second-order partial derivatives as follows:

$$\frac{\partial^2 X_{ij}}{\partial S_{qr}\partial S_{kl}}=\frac{\partial}{\partial S_{qr}}\left(\frac{\partial X_{ij}}{\partial S_{kl}}\right)=\frac{\partial c^E_{ijkl}}{\partial S_{qr}}, \tag{6}$$

$$\frac{\partial^2 X_{ij}}{\partial S_{kl}\partial E_m}=\begin{cases}\dfrac{\partial}{\partial E_m}\left(\dfrac{\partial X_{ij}}{\partial S_{kl}}\right)=\dfrac{\partial c^E_{ijkl}}{\partial E_m},\\ \dfrac{\partial}{\partial S_{kl}}\left(\dfrac{\partial X_{ij}}{\partial E_m}\right)=\dfrac{\partial}{\partial S_{kl}}\left(-\dfrac{\partial D_m}{\partial S_{ij}}\right)\\ \qquad=-\dfrac{\partial^2 D_m}{\partial S_{kl}\partial S_{ij}}=-\dfrac{\partial e_{mij}}{\partial S_{kl}},\end{cases} \tag{7}$$

$$\frac{\partial^2 X_{ij}}{\partial E_o\partial E_m}=\begin{cases}\dfrac{\partial}{\partial E_o}\left(\dfrac{\partial X_{ij}}{\partial E_m}\right)=-\dfrac{\partial e_{mij}}{\partial E_o},\\ \dfrac{\partial}{\partial E_o}\left(-\dfrac{\partial D_m}{\partial S_{ij}}\right)=-\dfrac{\partial^2 D_m}{\partial E_o\partial S_{ij}}\\ \qquad=\dfrac{\partial}{\partial S_{ij}}\left(-\dfrac{\partial D_m}{\partial E_o}\right)=-\dfrac{\partial \varepsilon^S_{mo}}{\partial S_{ij}},\end{cases} \tag{8}$$

$$\frac{\partial^2 D_n}{\partial E_o E_m}=\frac{\partial}{\partial E_o}\left(\frac{\partial D_n}{\partial E_m}\right)=\frac{\partial \varepsilon^S_{nm}}{\partial E_o}. \tag{9}$$

The coefficients defined in Eqs. (6) and (9) are the quadratic stiffnesses and quadratic dielectric coefficients at constant strain, respectively. The other quantities appearing in Eqs. (7) and (8) represent second-order coupling between mechanical and electrical variables. For polyurethane materials, however, a number of simplifying assumptions apply: (1) They do not exhibit any piezoelectric behavior and their e_{mij} coefficients are therefore zero. (2) Their quadratic stiffness coefficients defined by Eq. (6) are negligible. (3) The variations of their stiffness coefficients with respect to the electric fields are negligible, and the coefficients defined by Eq. (7) are therefore ignored. The only two relevant second-order quantities left are, therefore,

electrostrictive stress coefficients:

$$Q_{moij}\equiv\frac{1}{2}\frac{\partial \varepsilon^S_{mo}}{\partial S_{ij}}=\frac{1}{2}\frac{\partial e_{mij}}{\partial E_o}, \tag{10}$$

quadratic dielectric permittivity coefficients at constant strain:

$$O^S_{nmo}\equiv\frac{1}{2}\frac{\partial \varepsilon^S_{nm}}{\partial E_o}. \tag{11}$$

Therefore, in the case of electrostrictive polyurethanes, Eqs. (1) and (2) reduce to

$$X_{ij}=c^E_{ijkl}S_{kl}-Q_{moij}E_mE_o, \tag{12}$$

$$D_n=\varepsilon^S_{nm}E_m+2Q_{nmkl}E_mS_{kl}+O^S_{nmo}E_mE_o. \tag{13}$$

These are the constitutive equations describing the electromechanical behavior of the material. Note that Eq. (10) provides the most fundamental definition of electrostriction, which is a phenomenon that stems from the variations of the dielectric properties of a material with respect to mechanical variables. By analogy with piezoelectricity, one can also define electrostrictive *strain* coefficients M_{moij}, which relate the strains to the square of the electric field

$$S_{ij}=M_{moij}E_mE_o. \tag{14}$$

It can be easily shown that they satisfy the following relationship,

$$Q_{moij} = M_{mokl} c^E_{klij},$$

and that they are analogous to the d_{mij} piezoelectric coefficients. The M_{moij} coefficients are the quantities that are to be experimentally obtained in order to characterize the electrostrictive behavior of the polyurethanes.

B. Maxwell stress effect

Maxwell stress is a well-known quantity that results from the electrostatic interaction between two surfaces charged with opposite charges.[19] In the case of a thin film of polymer material, if a voltage is applied in order to create an electric field in the thickness direction of the film, this voltage will generate charges of opposite signs on the two surfaces of the film perpendicular to the thickness direction. This creates an attraction between the two surfaces which results in the deformation of the film. The corresponding stress (Maxwell stress) is related to the square of the electric field, and is therefore a quadratic effect analogous to electrostriction, but one should realize that Maxwell stress is an *external* effect, independent of intrinsic electromechanical properties of the material such as the ones represented by the M_{mokl} coefficients. Nonetheless, this external effect needs to be taken into account in the analysis, because it will contribute to the deformation of the film in exactly the same manner as the electrostrictive effect. In the case of a homogeneous dielectric, Maxwell stress is given by[20]

$$X^{\mathrm{Max}}_{ij} = \varepsilon^S_{ik} E_k E_j - \tfrac{1}{2} \varepsilon^S_{ij} E_k E_k. \tag{15}$$

This expression needs to be incorporated into Eq. (12) in order to fully characterize the quadratic electromechanical behavior of the material. Although Eq. (15) clearly indicates that Maxwell stress is proportional to the square of the electric field, it is not exactly in the same tensor form as Eq. (12). To combine these two equations in a significant manner using the same notation, one should consider the particular case of the electrical excitation that is used in our measurements. As will be explained in Sec. III, the only nonzero component of the electric field vector is E_3,

$$(E)_t = (0 \quad 0 \quad E_3). \tag{16}$$

The quadratic electric field tensor $E_m E_o$ appearing in Eq. (12) can be written as a vector with the following structure:

$$E_m E_o = (E^2)_t = (E_1^2 \quad E_2^2 \quad E_3^2 \quad E_2 E_3 \quad E_1 E_3 \quad E_1 E_2), \tag{17}$$

which, for our measurements, will therefore reduce to

$$E_m E_o = (E^2)_t = (0 \quad 0 \quad E_3^2 \quad 0 \quad 0 \quad 0). \tag{18}$$

In this case, the only nonzero components of the Maxwell stress tensor [Eq. (15)] are

$$\begin{aligned} X^{\mathrm{Max}}_{11} &= -\tfrac{1}{2} \varepsilon^S_{11} E_3^2, \\ X^{\mathrm{Max}}_{22} &= -\tfrac{1}{2} \varepsilon^S_{22} E_3^2, \\ X^{\mathrm{Max}}_{33} &= \tfrac{1}{2} \varepsilon^S_{33} E_3^2, \end{aligned} \tag{19}$$

which can be expressed in tensor form as

$$X^{\mathrm{Max}}_{ij} = \mathrm{Max}_{moij} E_m E_o, \tag{20}$$

where Max_{ijmo} is the Maxwell tensor defined as

$$[\mathrm{Max}] = \mathrm{Max}_{ijmo} = \frac{1}{2} \begin{bmatrix} 0 & 0 & 0 & 0 & 0 & 0 \\ 0 & 0 & 0 & 0 & 0 & 0 \\ -\varepsilon^S_{11} & -\varepsilon^S_{22} & \varepsilon^S_{33} & 0 & 0 & 0 \\ 0 & 0 & 0 & 0 & 0 & 0 \\ 0 & 0 & 0 & 0 & 0 & 0 \\ 0 & 0 & 0 & 0 & 0 & 0 \end{bmatrix}. \tag{21}$$

Therefore, *for the particular case of the electrical excitation used in our measurements*, Eqs. (12) and (15) can be combined to yield

$$X_{ij} = c^E_{ijkl} S_{kl} + (\mathrm{Max}_{moij} - Q_{moij}) E_m E_o. \tag{22}$$

Equation (22), along with Eq. (13), completely describes the electromechanical behavior of the polyurethane films in the configuration used for our measurements. It should be emphasized once more that, strictly speaking, the Maxwell tensor does not belong to the electrostrictive equations, but that it should be taken into account in the measurements. Since the Maxwell tensor is completely determined by the knowledge of the dielectric permittivity coefficients of the material, it is possible to factor out its contribution to the total response of the film and therefore to identify the isolated contribution due to the Q_{moij} (or M_{moij}) tensor only. The next section presents the principles of the method to perform these measurements.

III. PRINCIPLE OF THE METHOD

A. Sample preparation and measurements

The sample preparation and the measurements are essentially the same as the ones used in the piezoelectric case, and the reader is therefore referred to our previous publication[17] for a complete description of the experimental procedure. The main features of these procedures are briefly summarized below. Figure 1 depicts the sample configuration for the experimental measurements. The polyurethane film (whose Young's modulus varies from 7 to 30 MPa for the materials studied here) is attached to the aluminum plate and to the aluminum foil using two layers of soft silicone rubber (whose Young's modulus is 5.3 MPa). The plate acts as a rigid backing and forces the film to deform only in a thickness mode (suppressing spurious bending modes) whereas the foil is free to move in the 3-direction. The voltage is applied between the plate and the foil, thereby eliminating the need for deposited metal electrodes, which would greatly constrain the film. The plate and the foil are essentially electrodes, but they are mechanically decoupled from the polymer by the silicone layers, whose effect on the film deformation can be completely taken into account in the energy minimization procedure. The electrical excitation consists of an ac voltage at frequency f combined with a large dc bias voltage, and it is given by $V = V_{\mathrm{ac}} \cos(\omega t) + V_{\mathrm{dc}}$. Furthermore, the electric field inside the polymer is given by $E_p = V/(2t + 2h\varepsilon_p/\varepsilon_r)$, where ε_p and ε_r are the dielectric con-

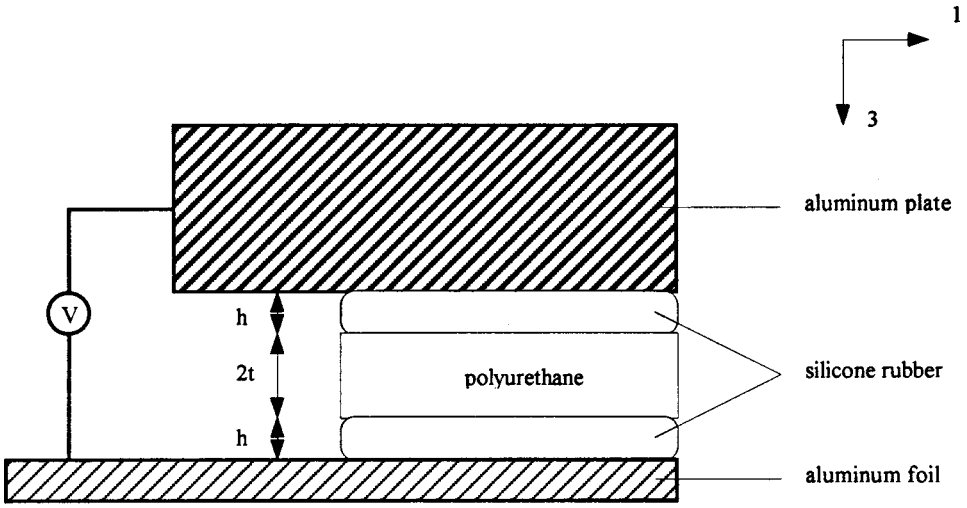

FIG. 1. Polyurethane film encapsulated in silicone rubber. Typical sample dimensions are 4 mm by 6 mm; $2t$ varies between 50 and 100 μm from sample to sample; h is on the order of 10 μm, and the aluminum foil thickness is 17 μm.

stants of the polyurethane and the silicone rubber, respectively. The induced strains are proportional to the square of the electric field

$$E_p^2 = \left[\frac{1}{2t + 2h\varepsilon_p/\varepsilon_r}\right]^2 \left[\frac{1}{2}V_{\mathrm{ac}}^2 + V_{\mathrm{dc}}^2 + 2V_{\mathrm{ac}}V_{\mathrm{dc}}\cos(\omega t) + \frac{1}{2}V_{\mathrm{ac}}^2\cos(2\omega t)\right],$$

which possesses three components: a dc term, a first-order term (at frequency f), and a second-order term (at frequency $2f$). The laser vibrometer performs dynamic measurements, and the dc term is therefore not taken into account. Furthermore, since the amplitude of the first-order term is proportional to the large dc bias voltage, this term is the dominant one in the above equation, and it is therefore the easiest one to obtain experimentally. The vibrometer (configured for out-of plane displacement measurements) is then used to measure the electrostrictive strains at frequency f in all three directions, as illustrated in Fig. 2. It provides three experimental displacement values: $u_1(L)$, $u_2(w)$, and $u_3(t)$. The next section will explain how these values are used in the Rayleigh–Ritz procedure to obtain the electrostrictive coefficients of the materials.

B. Rayleigh–Ritz minimization procedure

1. Admissible displacement fields

Implementing the Rayleigh–Ritz procedure first requires the choice of a set of trial functions for the displacement fields inside the polyurethane film. Finite-element simulations were performed in order to determine what kind of admissible displacement fields had to be considered to model the deformation of the sample depicted in Fig. 1. The results of these simulations indicated that the sides of the sample exhibited a curved displacement profile across the film thick-

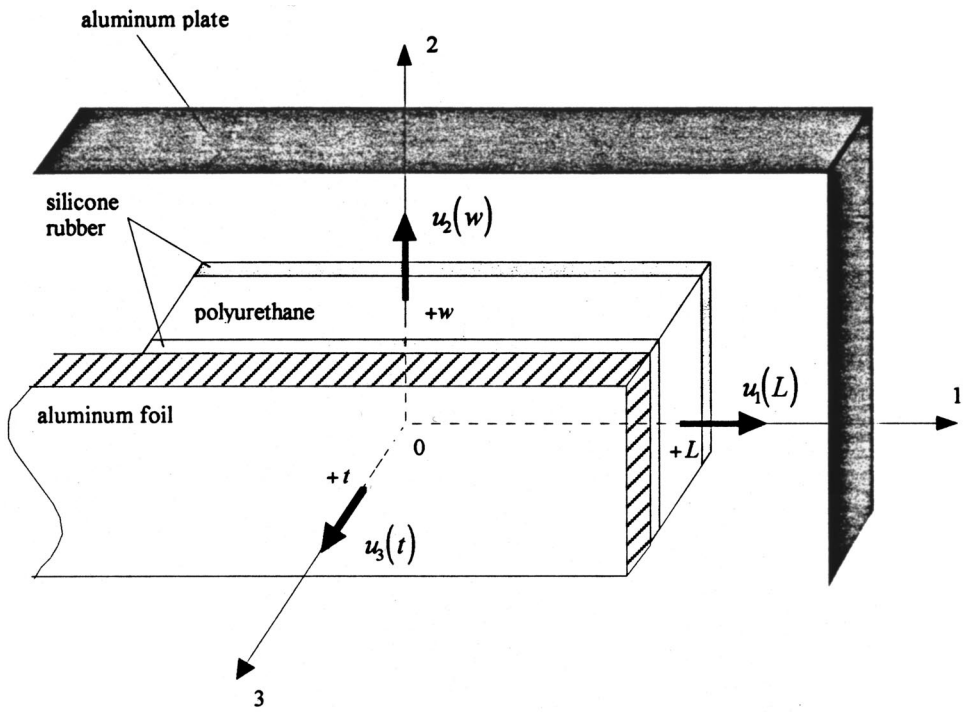

FIG. 2. Vibrometer measurement locations. $u_1(L)$, $u_2(w)$ and $u_3(t)$ are the experimental values of the electric field-induced displacements in the three directions ($2L$, $2w$, and $2t$ are the film dimensions).

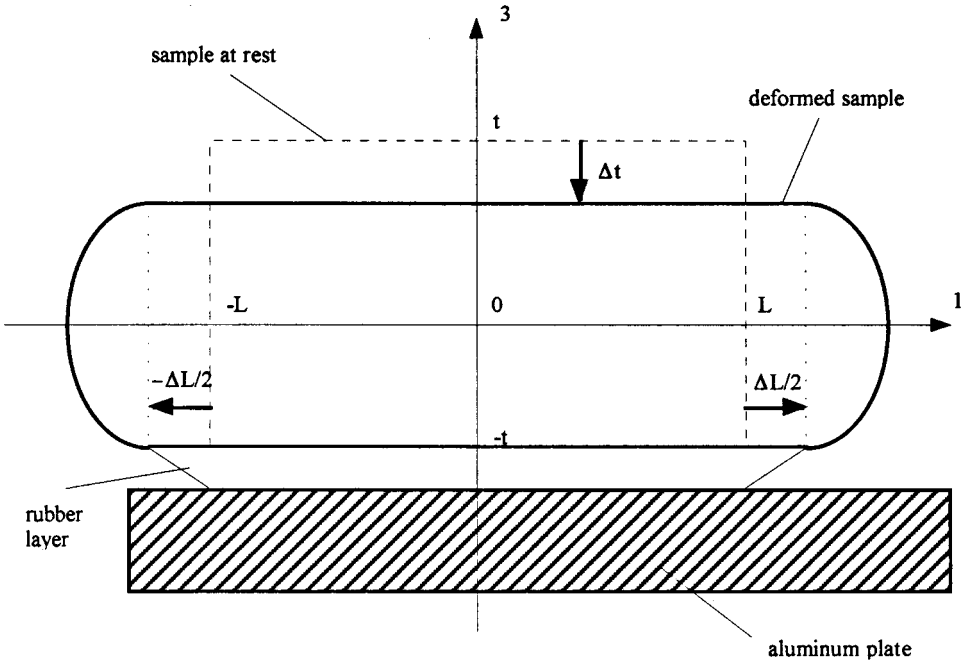

FIG. 3. Polyurethane sample displacements in the 1–3 plane. The aluminum foil and the upper rubber layer are not shown.

ness. The simplest $u_1(x_1,x_2,x_3)$ and $u_2(x_1,x_2,x_3)$ displacement fields of this type that can be assumed possess a quadratic dependence with respect to the x_3 coordinate:

$$u_1(x_1,x_3)=x_1\left[\frac{\Delta L}{2L}+A(t^2-x_3^2)\right], \tag{23}$$

$$u_2(x_2,x_3)=x_2\left[\frac{\Delta w}{2w}+B(t^2-x_3^2)\right]. \tag{24}$$

In Eqs. (23) and (24), $2L$, $2w$, and $2t$ are the length, the width, and the thickness of the sample, respectively, ΔL and Δw are the total sample elongations in the 1- and 2-directions *along the polymer–rubber interface*, and A and B are constants. The corresponding $u_3(x_1,x_2,x_3)$ displacement field is given by

$$u_3(x_3)=x_3\left[\frac{\Delta t}{2t}+C(t^2-x_3^2)\right]+\frac{\Delta t}{2}, \tag{25}$$

where Δt is the total thickness change and C is another constant. When compared to the results of the finite element analysis, it was found that the above displacement field accurately described the polyurethane deformations and they were therefore chosen for the energy minimization procedure. The polyurethane displacement fields in the 1–3 plane are illustrated in Fig. 3.

Given the above displacement fields, the next step is to determine what the output of the optical system is, i.e., how $u_1(L)$, $u_2(w)$, and $u_3(t)$ relate to the quantities appearing in Eqs. (23)–(25). The simplest case is addressed first, that of the thickness measurement. To measure $u_3(t)$, the incident light of the optical probe is focused on the aluminum foil, whose motion is uniform in the 1–2 plane. Therefore,

$$u_3(t)=u_3(x_3)_{|x_3=t}=\Delta t. \tag{26}$$

The other two measurements of $u_1(L)$ and $u_2(w)$ are rendered more complicated by the fact that the incident light beam diameter (80 μm) is on the same order as the sample thickness ($2t$ varies between 50 and 100 μm for the films used in this work). This situation is illustrated in Fig. 4, in the case of measurements along the 1-direction. One can see that the optical probe output is an average of the displacement profile over the light beam area. For the case illustrated by Fig. 4, where the beam axis is collinear with the mid-section axis of the sample side, the modulation of the light scattered from the side of the sample is proportional to

$$u_1(L)=\frac{1}{2r}\int_{-r}^{r}u_1(L,x_3)\,dx_3, \tag{27}$$

where r is the light beam radius. In cases where the sample thickness $2t$ is less than the beam diameter $2r$, then r needs to be replaced by t in the above integration. Equation (27) can be easily evaluated and yields

$$u_1(L)=\frac{\Delta L}{2}+AL\left(t^2-\frac{r^2}{3}\right). \tag{28}$$

Similarly, measurements along the 2-direction yield

$$u_2(w)=\frac{\Delta w}{2}+Bw\left(t^2-\frac{r^2}{3}\right). \tag{29}$$

The validity of the above two equations was verified experimentally by measuring $u_1(L)$ and $u_2(w)$ at different locations across the sample thickness and by using these experimental values to successfully reconstitute the displacement profiles of the sides given by Eqs. (23) and (24). Equations (28) and (29), along with Eq. (26), define the experimentally measured values provided by the laser vibrometer. The next section examines how these values are used in the Rayleigh–Ritz minimization procedure in order to obtain the electrostrictive coefficients.

2. Energy functional

In this section, the energy functional of the sample (including the polyurethane film and both rubber layers) is de-

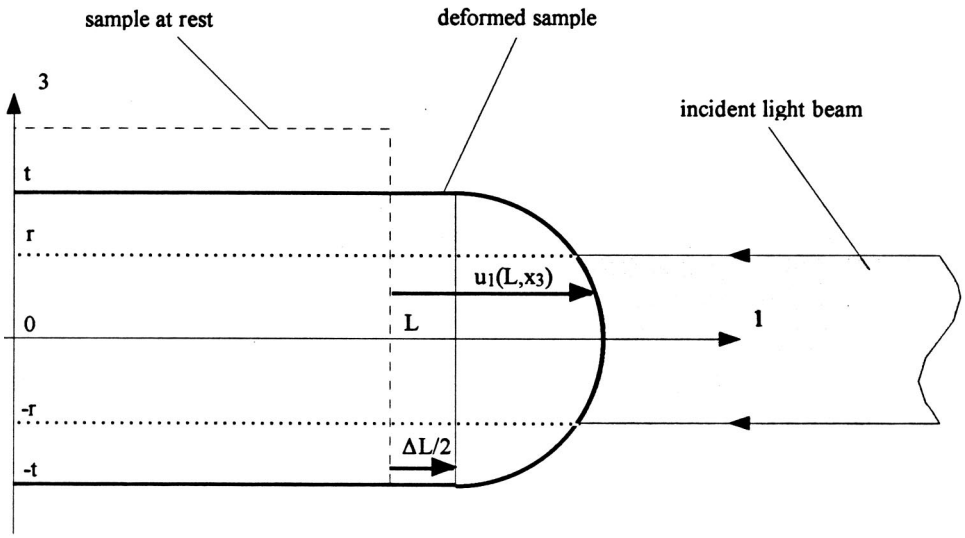

FIG. 4. In-plane displacement measurement along the 1-direction.

rived. Quasistatic conditions are assumed and the kinetic energy is therefore neglected, since the driving frequency is well below the fundamental thickness resonance frequency. Assuming that the sample is subjected to a quasistatic electric field at a constant temperature, the electric Gibbs free energy G_2 is a minimum for the sample. G_2 is defined as[21]

$$G_2 = U - E_n D_n - TS, \tag{30}$$

where U is the internal energy density, the E_n are the electric fields, the D_n are the electric displacements, T is the temperature, and S is the entropy. It is this function that is used to compute the total energy of the polymer/rubber composite and that is minimized in the Rayleigh–Ritz procedure. One can show that the thermal effects have a negligible impact on the sample deformation (as detailed in the Appendix), and G_2 is therefore a function of the strains S_{ij} and of the electric fields E_n only. Since the polyurethanes are electrostrictive, second-order energy terms must be considered. For this purpose, following the approach presented by Mitsui *et al.*,[22] G_2 is expanded in a Taylor series including up to cubic terms,

$$\begin{aligned} G_2 = G_2^0 &+ \frac{\partial G_2}{\partial S_{ij}} S_{ij} + \frac{\partial G_2}{\partial E_m} E_m + \frac{1}{2} S_{ij} \frac{\partial^2 G_2}{\partial S_{ij} \partial S_{kl}} S_{kl} \\ &+ S_{ij} \frac{\partial^2 G_2}{\partial S_{ij} \partial E_m} E_m + \frac{1}{2} E_m \frac{\partial^2 G_2}{\partial E_m \partial E_n} E_n \\ &+ \frac{1}{6} \frac{\partial^3 G_2}{\partial S_{ij} \partial S_{kl} \partial S_{qr}} S_{ij} S_{kl} S_{qr} + \frac{1}{2} \frac{\partial^3 G_2}{\partial S_{ij} \partial S_{kl} \partial E_m} S_{ij} S_{kl} E_m \\ &+ \frac{1}{2} \frac{\partial^3 G_2}{\partial S_{ij} \partial E_m \partial E_n} S_{ij} E_m E_n + \frac{1}{6} \frac{\partial^3 G_2}{\partial E_m \partial E_n \partial E_o} E_m E_n E_o , \end{aligned} \tag{31}$$

where the equilibrium state has been defined by $G_2^0 = 0$, and where, at equilibrium, the stresses and the electric displacements are zero. By definition, G_2 satisfies the following relationships:

$$X_{ij} = \frac{\partial G_2}{\partial S_{ij}}, \tag{32a}$$

$$D_m = - \frac{\partial G_2}{\partial E_m}, \tag{32b}$$

which allow Eq. (31) to be rewritten as

$$\begin{aligned} G_2 = G_2^0 &+ X_{ij}^0 S_{ij} - D_m^0 E_m + \frac{1}{2} S_{ij} \frac{\partial X_{ij}}{\partial S_{kl}} S_{kl} - S_{ij} \frac{\partial D_m}{\partial S_{ij}} E_m \\ &- \frac{1}{2} E_m \frac{\partial D_m}{\partial E_n} E_n + \frac{1}{6} \frac{\partial^2 X_{ij}}{\partial S_{kl} \partial S_{qr}} S_{ij} S_{kl} S_{qr} \\ &+ \frac{1}{2} \frac{\partial^2 X_{ij}}{\partial S_{kl} \partial E_m} S_{ij} S_{kl} E_m + \frac{1}{2} \frac{\partial^2 X_{ij}}{\partial E_m \partial E_n} S_{ij} E_m E_n \\ &- \frac{1}{6} \frac{\partial^2 D_m}{\partial E_n \partial E_o} E_m E_n E_o . \end{aligned} \tag{33}$$

All the coefficients appearing in Eq. (33) have been previously defined in Eqs. (3)–(9). Recognizing that the first three terms in Eq. (33) are zero, and recalling that, for polyurethanes, the coefficients in the fifth, seventh, and eighth terms are also zero, Eq. (33) reduces to

$$\begin{aligned} G_2 = &\tfrac{1}{2} S_{ij} c_{ijkl}^E S_{kl} - \tfrac{1}{2} E_m \varepsilon_{nm}^S E_n - S_{ij} Q_{mnij} E_m E_n \\ &- \tfrac{1}{3} O_{nmo}^S E_m E_n E_o , \end{aligned} \tag{34}$$

where use has been made of definitions (10) and (11). The first two terms of Eq. (34) represent the first-order elastic and dielectric energy densities, respectively. The third term is the second-order mutual energy density (representing second-order electromechanical coupling) and the fourth term is the second-order dielectric density. Expression (34) is the basis for the computation of the total energy in the polymer and in the rubber and it is the quantity that needs to be minimized with respect to displacements in the Rayleigh–Ritz procedure. However, because both the first- and second-order dielectric energy densities do not depend on strain explicitly, their derivatives with respect to displacements are zero, and they do not need to be taken into account when computing the total energy for the minimization procedure. Strictly

speaking, the first-order dielectric energy does depend on strain through the permittivity coefficients: $\partial \varepsilon^S_{mn}/\partial S_{ij} = 2Q_{mnij}$ (this is the very definition of electrostriction). In the minimization procedure, however, only the energy terms that depend *explicitly* on strain need to be considered, and it is assumed that the permittivity coefficients are constant. Not doing so would lead to taking *twice* into account the *same* electrostrictive effect when performing the Rayleigh–Ritz minimization: once through the electrostrictive energy $[\partial G_{2,\mathrm{elec}}/\partial S_{ij} = (\partial/\partial S_{ij})(-S_{ij}Q_{mnij}E_mE_n) = -Q_{mnij}E_mE_n]$ and once through the dielectric energy $[\partial G_{2,\mathrm{diel}}/\partial S_{ij} = (\partial/\partial S_{ij})(-\frac{1}{2}E_m\varepsilon^S_{nm}E_n) = -\frac{1}{2}(\partial \varepsilon^S_{nm}/\partial S_{ij})E_mE_n = -Q_{mnij} \times E_mE_n]$. This leaves the elastic and the second-order electromechanical energy densities as the only two relevant contributions to the total energy of the sample.

The energy of the polyurethane film is considered first; its two contributions are therefore given by

$$G^{\mathrm{poly}}_{2,\mathrm{elas}} = \frac{1}{2}\int_{-t}^{t}\int_{-w}^{w}\int_{-L}^{L}(S)_t[c^E](S)\,dx_1\,dx_2\,dx_3, \quad (35)$$

$$G^{\mathrm{poly}}_{2,\mathrm{elec}} = -\int_{-t}^{t}\int_{-w}^{w}\int_{-L}^{L}(E^2)_t[Q](S)\,dx_1\,dx_2\,dx_3. \quad (36)$$

However, implicitly "buried" within the generic second-order electromechanical energy density is the term corresponding to Maxwell stress, which needs to be taken into account separately. Referring to Eq. (22), which is the constitutive equation relating the stress to the other variables, it is obvious that, by analogy with Eq. (36), the energy term corresponding to Maxwell stress is

$$G^{\mathrm{poly}}_{2,\mathrm{Max}} = \int_{-t}^{t}\int_{-w}^{w}\int_{-L}^{L}(E^2)_t[\mathrm{Max}](S)\,dx_1\,dx_2\,dx_3. \quad (37)$$

Since we are interested in measuring the M_{moij} coefficients, it is convenient to use relation (15), $Q_{moij} = M_{mokl}c^E_{klij}$, expressed in matrix form, to rewrite Eq. (36) as

$$G^{\mathrm{poly}}_{2,\mathrm{elec}} = -\int_{-t}^{t}\int_{-w}^{w}\int_{-L}^{L}(E^2)_t[M][c^E](S)\,dx_1\,dx_2\,dx_3. \quad (38)$$

The energy contribution from the rubber layers is now addressed. Examining Eq. (34) (without the dielectric energy densities) and recalling that silicone rubber is not a piezoelectric or an electrostrictive material reveals that the only contributions from the layers are the elastic and the Maxwell stress energies. It is assumed that the latter is negligible because of the very small thickness of the layers (typically less than 10 μm) and of the small dielectric constant of silicone ($\varepsilon_r = 2.7$). This assumption was validated both numerically (by finite elements) and experimentally. This leaves the elastic energy as the sole contribution from the silicone rubber. Both rubber layers are subjected to a shear strain due to the lateral motions of the polymer film (cf. Fig. 3). The polyurethane displacement fields show that these lateral motions *along the rubber–polymer interface* correspond to the elongations ΔL and Δw. It can be shown[17] that in this case, the total elastic energy inside both rubber layers is given by

$$G^{\mathrm{rubber}}_{2,\mathrm{elas}} = \frac{\mu_r}{3}\frac{Lw}{h}[(\Delta L)^2 + (\Delta w)^2], \quad (39)$$

where μ_r is the silicone rubber shear modulus. Therefore, the total energy of the sample that is to be minimized with respect to the displacements is given by the sum of the quantities defined in Eqs. (35) and (37)–(39):

$$\begin{aligned} G_2 &= G^{\mathrm{poly}}_{2,\mathrm{elas}} + G^{\mathrm{poly}}_{2,\mathrm{elec}} + G^{\mathrm{poly}}_{2,\mathrm{Max}} + G^{\mathrm{rubber}}_{2,\mathrm{elas}} \\ &= \frac{1}{2}\int_{-t}^{t}\int_{-w}^{w}\int_{-L}^{L}(S)_t[c^E](S)\,dx_1\,dx_2\,dx_3 \\ &\quad - \int_{-t}^{t}\int_{-w}^{w}\int_{-L}^{L}(E^2)_t[M][c^E](S)\,dx_1\,dx_2\,dx_3 \\ &\quad + \int_{-t}^{t}\int_{-w}^{w}\int_{-L}^{L}(E^2)_t[\mathrm{Max}](S)\,dx_1\,dx_2\,dx_3 \\ &\quad + \frac{\mu_r}{3}\frac{Lw}{h}[(\Delta L)^2 + (\Delta w)^2]. \end{aligned} \quad (40)$$

3. Procedure results

We now examine the different terms appearing in Eq. (40) in order to find out what kind of information the Rayleigh–Ritz procedure is able to provide. The stiffness tensor $[c^E]$ is completely defined through the knowledge of the elastic properties of the polyurethanes. The Maxwell tensor [Max] is completely defined by the dielectric properties of the material, which, in the polyurethane case, reduce to one dielectric constant, ε_p:

$$[\mathrm{Max}] = \frac{1}{2}\varepsilon_p\varepsilon_0\begin{bmatrix} 0 & 0 & 0 & 0 & 0 & 0 \\ 0 & 0 & 0 & 0 & 0 & 0 \\ -1 & -1 & 1 & 0 & 0 & 0 \\ 0 & 0 & 0 & 0 & 0 & 0 \\ 0 & 0 & 0 & 0 & 0 & 0 \\ 0 & 0 & 0 & 0 & 0 & 0 \end{bmatrix}. \quad (41)$$

The strain vector (S) inside the polymer is defined in terms of the displacement constants ΔL, Δw, Δt, A, B, and C appearing in the expressions for the displacement field. The quadratic electric field vector is given by $(E^2)_t = (0\ 0\ E_p^2\ 0\ 0\ 0)$, where E_p is the electric field inside the polymer resulting from the application of a voltage across the thickness of the sample. For our measurements, the first-order term of the quadratic electric field is considered; as mentioned earlier, the amplitude of this term is proportional to the ac excitation voltage and to the large dc bias voltage. Because only $E_3E_3 \neq 0$, the electrostrictive coefficients that are responsible for the deformation of the film are the M_{33ij} $(i,j = 1,2,3)$. However, among them, the shear electrostrictive coefficients (i.e., those coefficients such that $i \neq j$) are zero. Therefore, only the tensile coefficients M_{3311}, M_{3322}, and M_{3333} play a role in the deformation. It follows that G_2 is a function of ΔL, Δw, Δt, A, B, C, M_{3311}, M_{3322}, and M_{3333}. These are the unknown quantities in the procedure, as all the other parameters are numerically defined.

The procedure is implemented in Mathcad as follows. The M_{33ii} coefficients are defined symbolically and the displacement constants ΔL, Δw, Δt, A, B, and C are defined as

unknown parameters in the displacements fields. The energy functional G_2 is minimized with respect to the unknown constants:

$$\frac{\partial G_2}{\partial \Delta L}=0, \quad \frac{\partial G_2}{\partial A}=0,$$
$$\frac{\partial G_2}{\partial \Delta w}=0, \quad \frac{\partial G_2}{\partial B}=0, \tag{42}$$
$$\frac{\partial G_2}{\partial \Delta t}=0, \quad \frac{\partial G_2}{\partial C}=0.$$

The above system of equations is solved symbolically for the six displacement constants, yielding expressions for these constants as a function of the M_{33ii} coefficients:

$$\begin{aligned}
\Delta L &= a_1 M_{3311}+a_2 M_{3322}+a_3 M_{3333}+a_4,\\
\Delta w &= b_1 M_{3311}+b_2 M_{3322}+b_3 M_{3333}+b_4,\\
\Delta t &= c_1 M_{3311}+c_2 M_{3322}+c_3 M_{3333}+c_4,\\
A &= d_1 M_{3311}+d_2 M_{3322}+d_3 M_{3333}+d_4,\\
B &= e_1 M_{3311}+e_2 M_{3322}+e_3 M_{3333}+e_4,\\
C &= f_1 M_{3311}+f_2 M_{3322}+f_3 M_{3333}+f_4,
\end{aligned} \tag{43}$$

where the a's, b's, c's, d's, e's, and f's are numerical constants that depend on the experimental parameters (sample geometry, material properties, and electrical excitation). Among these, the ones with the subscript 4 correspond to the Maxwell tensor contribution and therefore do not multiply one of the electrostrictive coefficients. Expressions (43) are then used to compute the quantities $u_1(L)$, $u_2(w)$, and $u_3(t)$, defined by Eqs. (26), (28), and (29), which represent experimental values of the displacements. This leads to another system of equations

$$\begin{aligned}
u_1(L) &= g_1 M_{3311}+g_2 M_{3322}+g_3 M_{3333}+g_4,\\
u_2(w) &= h_1 M_{3311}+h_2 M_{3322}+h_3 M_{3333}+h_4,\\
u_3(t) &= l_1 M_{3311}+l_2 M_{3322}+l_3 M_{3333}+l_4,
\end{aligned} \tag{44}$$

where the g's, h's, and l's are another set of constants. This last system is solved for the M_{33ii} coefficients using the experimentally measured values of $u_1(L)$, $u_2(w)$, and $u_3(t)$. One should note that this method provides the true electrostrictive material properties of the polyurethanes, because the mechanical boundary conditions and Maxwell stress have been taken into account by the procedure (mathematically, they are contained in the g's, h's, and l's constants). This allows for the direct evaluation of the intrinsic electromechanical behavior of the materials. In other words, the measured M_{33ii} coefficients are true coefficients, independent of the experimental conditions and clearly distinguished from the analogous Maxwell effect.

IV. EXPERIMENTAL RESULTS

A. Experimental procedure and measurement results

This section presents experimental results obtained on two different types of materials. The first one is a commercially available polyurethane manufactured by the DOW Company; this material, DOW 2103-80 AE, is biaxially stretched. The second one is a polyurethane that was synthesized especially for this work at the Naval Surface Warfare Center, Carderock Division; this material is unstretched and is referred to as PM 2000. The thicknesses of the DOW and the PM 2000 films were 56×10^{-6} m and 76×10^{-6} m, respectively. Because these materials absorb moisture, they were dried for 48 h at 50 °C under vacuum prior to measurements. Both were cut with a razor blade in 4 mm by 6 mm samples. The films were then attached to the aluminum plate and to the aluminum foil using the silicone rubber. The rubber was let to cure for 24 h under vacuum, with a uniform pressure exerted on the sample by a soft elastic ball. For the measurements, the samples were driven at 2 kHz with a 200-V amplitude ac voltage combined with a dc bias voltage that produced an electric field on the order of 4 MV/m inside the polyurethane. While in the measuring apparatus, the samples were constantly subjected to a dry nitrogen flow, to maintain them in a low-moisture environment at constant temperature (22 °C). The thickness response was measured first, at several locations (40, typically) on the surface of the sample, to ensure that the motion was uniform and that the sample was undergoing pure thickness vibrations. The measured thickness response was computed from the average of the displacements obtained at the various locations. Next, in-plane displacements were measured by focusing the laser beam on the sample sides. Observing the samples under a microscope, the beam was positioned approximately at the center of the side to be measured. Precise centering was achieved by varying the vertical position of the probe until the maximum measured displacement was detected.

Table I presents some material properties for both types of polyurethanes, summarizes the electrostrictive coefficient measurement results, and compares the polyurethane electromechanical activity with that of PVDF. For each material, the polyurethane electrostrictive coefficient values are averaged over the results from three different samples. The d_{333} piezoelectric coefficient of PVDF was measured using our method applied to piezoelectric materials. The percentage quantity refers to the contribution of the electrostrictive response to the total strains experienced by the samples in all three directions. It therefore represents the contribution of intrinsic electrostriction relative to that of the Maxwell stress effect. The equivalent piezoelectric coefficient is provided to facilitate the comparison of the electromechanical activity of the polyurethanes and of PVDF. It is related to the electrostrictive coefficient according to $d_{333}=2M_{3333}E_3$. Finally, the last column of Table I contains values of the coupling factor k_{333}, which gives an indication of how much electrical energy is converted into mechanical energy by the transduction mechanism. It is given by $k_{333}=d_{333}/\sqrt{S^E_{3333}\varepsilon^X_{33}}$, and it is, strictly speaking, an equivalent coupling factor, since use is made of the equivalent piezoelectric coefficient to compute its value. A more rigorous way to evaluate the coupling factor would be to use its most general definition, which is the ratio of the mutual energy density (the electrostrictive energy density, in this case) to the geometric mean of the elastic energy density and the dielectric energy density. However,

TABLE I. Properties of two electrostrictive polyurethanes and comparison with piezoelectric PVDF polymer.

Material	Density (kg/m^3)	Young's modulus (MPa)	Dielectric constant	Electrostrictive coefficients ($10^{-18}\,m^2/V^2$)	Standard deviations (three samples)	% electrostriction to total strains	Equivalent piezoelectric coefficient d_{333} at 4 MV/m (10^{-12} m/V)	Coupling factor k_{333} at 4 MV/m
DOW	1130.0	30.1	7.1	$M_{3311}=14.0$	1.2	94		
		30.1		$M_{3322}=11.4$	0.4	93		
		27.9		$M_{3333}=-16.3$	0.6	90	−128	0.088
PM 2000	1080.0	7.2	7.8	$M_{3311}=41.5$	4.1	90		
				$M_{3322}=34.1$	4.5	87		
				$M_{3333}=-74.6$	7.2	88	−587	0.190
PVDF	1760	2300	12	N/A	N/A	N/A	−37	0.165

for our purpose of comparing the performance of the various materials, the above-mentioned definition is sufficient.

One can see that both polyurethanes exhibit substantial electrostrictive coefficients resulting in equivalent piezoelectric coefficients about 3.5 (DOW) and 16 (PM 2000) times larger than that of PVDF. The coupling factors, however, are not substantially higher than in the PVDF case, because the polyurethanes are much more compliant than this material. Although this could be considered a disappointing result, one should keep in mind that, in the electrostrictive case, the coupling factor is directly proportional to the bias field, and that it is evaluated in Table I for a relatively low bias value. Therefore, the coupling factor of PM 2000 could be made significantly larger than that of PVDF by using a larger bias voltage. Even though this reasoning does not take into account the likely variations of the electrostrictive coefficients with the bias field (which should be measured in a subsequent study), it clearly indicates that polyurethanes such as PM 2000 have better performances than PVDF.

Another interesting fact is that the deformations due to the Maxwell stress effect account for no more than 13% of the total strains in any direction. This is an important finding that proves that most of the electromechanical activity in these polyurethanes stems from intrinsic electrostriction. This is in contrast with the findings of other studies that claim that Maxwell stress is responsible for approximately 50% of the polyurethane strain response.[11,12] For example, we measured an M_{3333} coefficient of $-16.3\times10^{-18}\,m^2/V^2$ on the DOW material. The corresponding "Maxwell-stress strain coefficient" for this material, R_m, can be calculated from the dielectric and elastic constant data, and is approximately $-10^{-18}\,m^2/V^2$. In Ref. 12, Zhang *et al.* measured an *overall* electrostriction strain coefficient R_{3333} (including both intrinsic electrostriction and maxwell stress contributions: $R_{3333}=M_{3333}+R_m$) on the order of $-2\times10^{-18}\,m^2/V^2$. This discrepancy between our results and theirs is most likely due to the fact that they used electroded samples and therefore measured a constrained response (the Maxwell stress contribution is calculated and is independent of the measuring technique). Based on the values that we obtained, it is our conclusion that, from a phenomenological standpoint, the electrostatic attraction, compared to intrinsic electrostriction, is a minor factor in the mechanical response of polyurethane films subjected to an electric field. From a practical standpoint, when the material is used with stiff metal electrodes (typically gold) deposited on its surface (and is therefore highly constrained), the *calculated* Maxwell stress contribution to the total response is of course likely to be substantial. However, in applications where compliant electrodes are used[5] (such as graphite powder in a conductive gelatin-glycerol-salt binder[3]), the contribution from intrinsic electrostriction will dominate the overall response, and is therefore an important quantity to know.

B. Result discussion

DOW 2103-80 AE is the only material among the two electrostrictive polyurethanes studied in this work for which some data has been published in the literature. Table II compares our results to previously available values from other researchers. Barger used an accelerometer to measure the response of a stack of 100 electroded samples. The material was therefore loaded by the accelerometer and constrained by the electrodes. These problems were partially compensated by the large number of samples in the stack, but this experimental configuration was most likely responsible for his small measured coefficients. Wang used a laser interferometer on 178-μm-thick single-layer electroded samples epoxied on a sample holder. Although in this case the samples were not loaded, the electrodes and the epoxy constrained the films and were to blame for the very small measured response shown in Table II. The only experimental technique previously available that can directly measure electrostrictive coefficients approaching their true values is the one used by Zhenyi *et al.*,[1] where the sample is sandwiched between two glass plates forming a parallel plate capacitor whose change in capacitance due to the film deformation can be monitored. Because the samples do not need to be electroded, this experimental method provides minimal loads and constraints on the samples. The drawback is that it can only be used for thickness coefficient measurements. Zhenyi *et al.* reported an

TABLE II. Comparison of experimentally measured electrostrictive coefficients on DOW 2103-80 AE with published data.

	M_{3311} ($10^{-18}\,m^2/V^2$)	M_{3322} ($10^{-18}\,m^2/V^2$)	M_{3333} ($10^{-18}\,m^2/V^2$)
Experimental	14.0	11.4	−16.3
Barger (Ref. 2)	1.0	⋯	−4.6
Wang (Ref. 11)	0.5	⋯	−2.3

TABLE III. Sensitivity of results to measured displacements for DOW 2103-80 AE.

5% increase in measured displacement	% change in M_{3311}	% change in M_{3322}	% change in $\lvert M_{3333}\rvert$
$u_1(L)$	+11	−6	+3
$u_2(w)$	−5	+10	+3
$\lvert u_3(t)\rvert$	0	0	0

M_{3333} coefficient value of $-33\times10^{-18}\,\mathrm{m^2/V^2}$ obtained with the capacitor technique, but on a different type of DOW polyurethane (PT6100S). The following remarks can therefore be made regarding the validity of the new method introduced in this article. As expected, it provides larger electrostrictive coefficients than any other method, because of its unique capability to take precisely into account the constraints imposed on the sample and to compute material properties that are independent from the boundary conditions. Furthermore, the measured thickness coefficients are on the same order as those provided by a method applied to a similar material where constraints are minimal. We therefore conclude that the experimental data obtained with our new method represent an accurate assessment of the electrostrictive activity in polyurethane materials.

To further establish the validity of the method, we studied the sensitivity of the results to several experimental parameters. These results are presented in Tables III and IV for the DOW material, where the variations in the computed electrostrictive coefficients are shown as a function of the change in values of the displacements and elastic constants input into the Mathcad program. Table III indicates that M_{3311} and M_{3322} are somewhat sensitive to variations in the values of the in-plane displacements and that M_{3333} is relatively insensitive to changes in any of the measured displacements. This is consistent with the fact that the samples experience the largest deformations in the in-plane directions. As for the dependence on elastic constants, Table IV reveals that a 10% uncertainty in the knowledge of these constants does not significantly affect the accuracy of the results. In this case as well, M_{3333} is the least affected of the three electrostrictive coefficients. One should note that because the material is biaxially stretched in the 1- and 2-directions, there is no quantitative difference in the variations of M_{3311} and M_{3322}. Similar results were found for the PM 2000 material, and it was therefore concluded that the accuracy of the method was not compromised by the uncertainties associated with the main experimental parameters.

Finally, more consolidating remarks can be drawn from examining Table I. Repeatability of the measurements was established by computing the standard deviations for each coefficient, on both samples (DOW and PM 2000). These values are small for the DOW material, but they are larger for the PM 2000 one. This is attributed to the fact that the latter material is extremely soft, which makes it the most difficult one to measure accurately. Nevertheless, the PM 2000 standard deviations are about 10%, which is reasonable. Also, since PM 2000 is isotropic, and since DOW is biaxially stretched by the same amount in the 1- and 2-directions, the M_{3311} and M_{3322} coefficients for both of these materials should theoretically be identical. Although this is not exactly the case, the values of the two coefficients are close. Furthermore, since the DOW material is stretched, one would expect that the ratio of its M_{3311} and M_{3322} to its M_{3333} be different than that of the unstretched PM 2000. Table I indicates that this is the case, since the ratio of the in-plane to the out-of-plane coefficients is approximately 50% for PM 2000, while it is on the order of 75% for DOW. These remarks confirm that the experimental data are consistent with what is known of the material structure.

TABLE IV. Sensitivity of results to values of elastic constants of DOW 2103-80 AE.

10% increase in elastic constants	% change in M_{3311}	% change in M_{3322}	% change in $\lvert M_{3333}\rvert$
Y_1	−9	−9	0
Y_3	+2	+2	−7
ν_{12}	−10	−11	0
ν_{13}	0	0	+10

V. CONCLUSIONS

A new method for determining electrostrictive coefficients of polymer films was introduced. It is the first method capable of measuring a complete set of three tensile electromechanical coupling coefficients and of providing true material properties. It was successfully applied to the characterization of two different types of electrostrictive polyurethanes which were both found to exhibit a much larger electromechanical activity than PVDF. It was also established that intrinsic electrostriction accounts for at least 87% of the total strain response in these materials, which demonstrates that Maxwell stress is not the dominant mechanism governing the electromechanical properties of electrostrictive polyurethanes.

APPENDIX: COMPUTATION OF THE DIFFERENCE BETWEEN THE ISOTHERMAL AND THE ADIABATIC COMPRESSIBILITIES OF POLYURETHANES

To demonstrate that the thermal effects do not significantly impact the deformation of the sample, we computed the difference between the adiabatic and the isothermal compressibilities of the polyurethane materials; this difference is given by[23]

$$\Delta\beta = \frac{T\alpha^2}{C_p}, \tag{A1}$$

where T is the temperature, α is the thermal expansion coefficient, and C_p is the specific heat per unit volume at constant pressure. Using the following typical values for polyurethanes,[24,25] $\alpha = 10^{-4}\,\mathrm{K^{-1}}$ and $C_p = 1.386\times10^{6}\,\mathrm{J\cdot K^{-1}\cdot m^{-3}}$, $\Delta\beta$ was found to be equal to $2.16\times10^{-12}\,\mathrm{Pa^{-1}}$. On the other hand, the isothermal compressibility β of the polyurethanes is approximately $10^{-10}\,\mathrm{Pa^{-1}}$, which indicates that the difference between the adiabatic and the isothermal coefficients is on the order of 2%. This justifies ne-

glecting the thermal effects on the polyurethane sample deformations.

[1] M. Zhenyi, J. I. Scheinbeim, J. W. Lee, and B. A. Newman, ''High Field Electrostrictive Response of Polymers,'' J. Polym. Sci. Part B: Polym. Phys. **32**, 2721–2731 (1994).

[2] J. E. Barger, ''Electrostrictive polyurethane projector,'' J. Acoust. Soc. Am. **95**, 2857(A) (1994).

[3] R. Heydt, R. Pelrine, J. Joseph, J. Eckerle, and R. Kornbluh, ''Acoustical performance of an electrostrictive polymer film loudspeaker,'' J. Acoust. Soc. Am. **107**, 833–839 (2000).

[4] J. Kyokane, H. Ishimoto, H. Yugen, T. Hirai, T. Ueda, and K. Yoshino, ''Electrostriction Effect of Polyurethane Elastomer (PUE) and its Application to Actuators,'' Synth. Met. **103**(1–3), 2366–2367 (1999).

[5] R. E. Pelrine, R. D. Kornbluh, and J. P. Joseph, ''Electrostriction of Polymer Dielectrics with Compliant Electrodes as a Means of Actuation,'' Sens. Actuators A **64**, 77–85 (1998).

[6] E. Balizer, ''Polyurethane Electrostriction Morphology Dependence,'' Internal Funding Proposal, Naval Surface Warfare Center, Carderock Division (1995).

[7] J. E. Martin and R. A. Anderson, ''Electrostriction in field-structure composites: Basis for a fast artificial muscle?'' J. Chem. Phys. **111**(9), 4273–4280 (1999).

[8] Y. Sun, W. W. Cao, and L. E. Cross, ''Electrostriction Effect in Glass,'' Mater. Lett. **4**(8, 9), 329–336 (1986).

[9] Y. Sun, W. W. Cao, W. Y. Pan, Z. P. Chang, and L. E. Cross, ''Complete Determination of Electrostriction Tensor Components of KMnF3 Single Crystals at Room Temperature,'' J. Mater. Sci. Lett. **7**(4), 327–330 (1988).

[10] K. Rittenmyer, A. S. Bhalla, and L. E. Cross, ''Electrostriction in Fluoride Perovskites,'' Mater. Lett. **7**(11), 380–384 (1989).

[11] H. Wang, ''Electromechanical Effects in Polymeric Materials,'' Ph.D. dissertation, Pennsylvania State University, 1994, pp. 146–159.

[12] Q. M. Zhang, J. Su, C. H. Kim, R. Ting, and R. Capps, ''An experimental investigation of electromechanical responses in polyurethane elastomer,'' J. Appl. Phys. **81**(6), 2770–2776 (1997).

[13] Y. M. Shkel and D. J. Klingenberg, ''Electrostriction of polarizable materials: Comparison of models with experimental data,'' J. Appl. Phys. **83**(12), 7834–7843 (1998).

[14] S. Eury, R. Yimnirun, V. Sundar, P. J. Moses, S. J. Jang, and R. E. Newnham, ''Converse Electrostriction in Polymers and Composites,'' Mater. Chem. Phys. **61**, 18–23 (1999).

[15] J. Su, Q. M. Zhang, and R. Y. Ting, ''Space-charge-enhanced electromechanical response in thin-film polyurethane elastomers,'' Appl. Phys. Lett. **71**(3), 386–388 (1997).

[16] F. M. Guillot, J. Jarzynski, and E. Balizer, ''Electromechanical response of polymer films by laser Doppler vibrometry,'' J. Acoust. Soc. Am. **103**, 1421–1427 (1998).

[17] F. M. Guillot and J. Jarzynski, ''A new method for the absolute measurement of piezoelectric coefficients on thin polymer films,'' J. Acoust. Soc. Am. **108**, 600–607 (2000).

[18] W. P. Mason, *Piezoelectric Crystals and Their Application to Ultrasonics* (Van Nostrand, New York, 1950), pp. 296–304.

[19] L. D. Landau, E. M. Lifshitz, and L. P. Pitaevskii, *Electrodynamics of Continuous Media*, 2nd ed. (Pergamon, New York, 1984), pp. 64–66.

[20] W. K. H. Ponofsky and M. Phillips, *Classical Electricity and Magnetism*, 2nd ed. (Addison-Wesley, Reading, MA, 1962), p. 104.

[21] W. P. Mason, *Piezoelectric Crystals and Their Application to Ultrasonics* (Van Nostrand, New York, 1950), p. 34.

[22] T. Mitsui, I. Tatsuzaki, and E. Nakamura, *An Introduction to the Physics of Ferroelectrics* (Gordon and Breach Science, London, 1976), pp. 29–42.

[23] L. D. Landau and E. M. Lifshitz, *Theory of Elasticity*, 3rd ed. (Pergamon, New York, 1986), pp. 14–15.

[24] H. L. Anderson, *A Physicist's Desk Reference*, 2nd ed. (Springer-Verlag, New York, 1989), p. 216.

[25] C. E. Harper, *Handbook of Plastics and Elastomers* (McGraw-Hill, New York, 1975), pp. 61–62.

Transient flexural waves in a disk and square plate from off-center impact

Michael El-Raheb
1000 Oak Forest Lane, Pasadena, California 91107

Paul Wagner
1020 Crestview Drive, Pasadena, California 91107

(Received 25 September 2000; accepted for publication 22 May 2001)

Flexural waves in a disk and square plate produced by off-center impact are analyzed. The effects on maximum transient stress $\sigma_{\max}$ of boundary shape, edge constraint, thickness, side of square plate or diameter of disk, and eccentricity of center of impact are studied. While prior analytical work has been confined to disks for simplicity, ballistic experiments were performed using square plates for practical reasons. The two geometries agree better for central impact or edges that are simply supported or clamped. Analytical results show some intensification as center of impact approaches the edge, but this is insufficient to explain the measured rise in residual projectile kinetic energy after penetrating a ceramic tile. This reveals the inadequacy of the crack initiation mechanism as the primary model of defeating the projectile by ceramic tiles. © *2001 Acoustical Society of America.*
[DOI: 10.1121/1.1390338]

PACS numbers: 43.40.At [PJR]

I. INTRODUCTION

Ceramic materials such as silicon carbide (SiC_2) and aluminum nitride (AlN) are presently used to harden structures against impact by high velocity projectiles. Replacing metal with these materials yields lower weight because of increased compressive strength in spite of reduced toughness. Compressive strength is paramount in breaking brittle projectiles, eroding soft projectiles, and dispersing momentum in the early stages of penetration. An important parameter in impacts against ceramic tiles with finite dimension is the eccentricity r_e defined as the distance between center of impact and tile center. Ballistic experiments on AlN tiles struck by tungsten cylindrical projectiles revealed that residual kinetic energy of the projectile, measured by depth of penetration ''DOP'' into an adjacent aluminum block, first diminishes with r_e, and then increases as the impact approaches the edge. This effect is caused by at least two mechanisms

(1) As the impact approaches the tile's edge, maximum transient stress $\sigma_{\max}$, which initiates microcracks in the brittle material, may intensify from constructive interference between waves radiating from the area of impact and earlier waves reflected from the edge. This is similar to the intensification of $\sigma_{\max}$ from central impact when tile size is reduced, also called ''tile size effect.'' This parametric study is the subject of this work.

(2) Even after crack initiation, resistance continues because the comminuted material persists due to inertia and reaction of nearby unbroken material, confining the residual projectile. This effect is also called ''self confinement'' and is not the subject of the present study.

Clearly, both mechanisms affect penetration although they act at different times, the first acts early before cracking starts, while the other acts later after cracking. A possible conclusion of this work which accounts for the first mechanism but neglects the second is the relative importance of each mechanism.

In the last two decades, general-purpose finite element, finite difference, and finite volume computer programs were developed for predicting penetration of projectiles in elastoplastic metals. Because of the large strains and strain rates involved during these events, nonlinear constitutive laws, energy balance, and shock discontinuities had to be addressed. These computer programs are successful in accurately predicting penetration depth and crater geometry in metals. This success relies on the fact that metals subjected to these intense transient loads behave almost like viscous fluids, which explains the widely used term ''hydro code.'' However, when applied to penetration in brittle materials, hydro codes are less successful especially in the later stage of the event when cracks form, breaking the material into small pieces with size depending on their vicinity to center of impact.

Since ceramic materials remain linear elastic before crack initiation, they can be analyzed using small amplitude linear flexural waves. Previous work treated transient waves from central impact in one-dimensional (1D) layered media,[1,2] plates,[3] thick disks,[4] two-dimensional (2D) axisymmetric layered media,[5] and stacks of layered plates adopting flexure theory.[6] No reference exits treating the asymmetric wave propagation in disks and square plates analytically.

The objective of this work is to study how $\sigma_{\max}$ changes with eccentricity while varying the following parameters:

(a) boundary shape, either disk or square plate,
(b) edge constraint, either simply supported or free,
(c) thickness and lateral dimension.

Relating how $\sigma_{\max}$ varies with these parameters to data from penetration experiments may clarify the relative importance of each mechanism on penetration. It is not the intent of this work to elaborate on the mechanics of penetration. Its intent

is to understand the transient stress state that initiates failure in a brittle material, and the sensitivity of this stress to the parameters above.

Section II treats flexural waves in a disk based on Mindlin's plate equations[7] for an asymmetric forcing pulse. Transient response uses an exact modal solution satisfying simply supported or free edges.

Section III A treats flexural waves in a square plate. Unlike the disk where circumferential and radial dependence separate yielding eigenfunctions which satisfy all natural boundary conditions exactly, the square plate does not allow separation of variables along the two axes x and y. Instead, a Galerkin solution is adopted. Trial functions of a 1D strip along x are determined that satisfy edge conditions at $x=(0,l)$ where l is side length. Since the plate is square, and constraints along the four edges are the same, trial functions along y are identical to those along x. Minimizing the error committed in the differential equations of motion by enforcing their orthogonality with the trial functions produces an eigenvalue problem. For simply supported and clamped edges, trial functions also satisfy the plate's edge constraints exactly. However, for free edges, the zero moment constraints are not satisfied identically yielding a stiffer constraint and a higher fundamental resonance than the free plate.

Section III B replaces the method in Sec. III A when applied to a plate with free edges by adopting a Chebychev collocation method. The plate is divided into identical rectangular elements and a lattice of points is superimposed into each element.

Section IV compares stress histories of disk and square plate with simply supported edges for different eccentricities r_e. This is followed by histories of the disk with free edges. A stress factor "α_σ" is defined as the ratio of $\sigma_{\max}$ for some r_e to $\sigma_{\max}$ for central impact. Plots of α_σ against r_e reveal regions of stress magnification ($\alpha_\sigma>1$), and regions of stress reduction ($\alpha_\sigma<1$), depending on plate thickness, lateral dimension, and edge constraint. The variation does not follow a simple trend since it depends on the interference between waves radiating from the area of impact and incoherent reflections from the edges.

II. DISK

Mindlin's plate equations[7] may be written in vector form as

$$\frac{D}{2}[(1-v)\nabla^2\Psi+(1+v)\nabla\Phi]-\kappa Gh(\Psi+\nabla w)=\frac{\rho h^3}{12}\frac{\partial^2\Psi}{\partial t^2}, \tag{1}$$

$$\kappa Gh(\nabla^2 w+\Phi)+p=\rho h\frac{\partial^2 w}{\partial t^2},$$
$$\Phi=\nabla\cdot\Psi,\quad D=\frac{Eh^3}{12(1-v^2)}, \tag{2}$$

where Ψ is the vector of rotations, w is transverse displacement, (ρ,v) are density and Poisson ratio, (E,G) are Young's and shear moduli, κ is shear constant, h is thickness, t is time, p is applied pressure, ∇^2 is the Laplacian and ∇ is the gradient operator. Taking the divergence of (1),

$$D\nabla^2\Phi-\kappa Gh(\Phi+\nabla^2 w)=\frac{\rho h^3}{12}\frac{\partial^2\Phi}{\partial t^2}. \tag{3}$$

Eliminating Φ from (2) and (3)

$$\left[\left(\nabla^2-\frac{1}{c_\epsilon^2}\frac{\partial^2}{\partial t^2}\right)\left(\nabla^2-\frac{1}{c_s^2}\frac{\partial^2}{\partial t^2}\right)+\frac{12}{c_\epsilon^2 h^2}\frac{\partial^2}{\partial t^2}\right]w=\left[\frac{1}{D}-\frac{1}{\kappa Gh}\left(\nabla^2-\frac{1}{c_s^2}\frac{\partial^2}{\partial t^2}\right)\right]p,$$
$$c_\epsilon^2=\frac{E}{\rho(1-v^2)},\quad c_s^2=\frac{\kappa G}{\rho}. \tag{4}$$

Eliminating $\nabla^2 w$ from (2) and (3) yields

$$\left[D\nabla^2-\frac{\rho h^3}{12}\frac{\partial^2}{\partial t^2}\right]\Phi=\rho h\frac{\partial^2 w}{\partial t^2}-p. \tag{5}$$

Taking the curl of (1)

$$\left[\frac{D}{2}(1-v)\nabla^2-\kappa Gh-\frac{\rho h^3}{12}\frac{\partial^2}{\partial t^2}\right](\nabla\times\Psi)=\mathbf{0} \tag{6}$$

from which it can be inferred that $(\nabla\times\Psi)$ is not a function of w while Ψ may actually be,

$$\Psi=\nabla[g(w)]+\nabla\times\Gamma, \tag{7}$$

where Γ is a vector potential for Ψ independent of w. Substituting (7) in (5) using the definition of Φ yields

$$\left[D\nabla^2-\frac{\rho h^3}{12}\frac{\partial^2}{\partial t^2}\right]\nabla^2 g=\rho h\frac{\partial^2 w}{\partial t^2}. \tag{8}$$

Substituting (7) in (6) using the identity

$$\nabla\times\nabla\times\mathbf{A}=\nabla(\nabla\cdot\mathbf{A})-\nabla^2\mathbf{A} \tag{9}$$

produces

$$\left[\frac{D}{2}(1-v)\nabla^2-\kappa Gh-\rho\frac{h^3}{12}\frac{\partial^2}{\partial t^2}\right]\nabla^2\Gamma=\mathbf{0}. \tag{10}$$

Defining $\tau=\nabla^2\Gamma$, reduces (10) to

$$\left[\nabla^2-\frac{12\kappa}{h^2}-\frac{2}{(1-v)c_\epsilon^2}\frac{\partial^2}{\partial t^2}\right]\tau=\mathbf{0}. \tag{11}$$

For a solid disk and periodic motions in time with frequency ω, the homogeneous solution of (4) takes the form

$$w(r,\theta,t)=w(r)\cos n\theta e^{i\omega t}, \tag{12a}$$

$$w(r)=C_1 J_n(\lambda_1 r)+C_2 J_n(\lambda_2 r), \tag{12b}$$

$$\overline{\lambda^4}-2\beta_1\lambda^2+\beta_2=0,$$
$$\beta_1=\frac{1}{2}\frac{c_\epsilon^2+c_s^2}{c_\epsilon^2 c_s^2}\omega^2,\quad \beta_2=\frac{\omega^2}{c_\epsilon^2}\left(\frac{\omega^2}{c_s^2}-\frac{12}{h^2}\right), \tag{12c}$$

where (r,θ) are radial and circumferential coordinates, n is circumferential wave number, $i=\sqrt{-1}$, and J_n is the Bessel function. Since $g(r)$ is a function of w, and from (8) linear with w, it can be expressed like (12a) and (12b) as

$$g_j(r)=C_g J_n(\lambda_j r), \quad \nabla^2 g_j=-\lambda_j^2 g_j, \quad j=1,2. \tag{13}$$

Substituting (13) in (8) yields

$$-\left[-\lambda_j^2+\frac{\omega^2}{c_\epsilon^2}\right]\lambda_j^2 C_{gj}=-\frac{12\omega^2}{h^2 c_\epsilon^2}C_j \tag{14}$$

then using (4), Eq. (14) simplifies to

$$C_{gj}=\frac{1}{\lambda_j^2}\left(-\lambda_j^2-\frac{\omega^2}{c_s^2}\right)C_j. \tag{15}$$

Taking the gradient of (14),

$$\nabla g_j=\left(\frac{\partial}{\partial r},-\frac{n}{r}\right)C_{gj}J_n(\lambda_j r). \tag{16}$$

Furthermore, since τ and Ψ are orthogonal and Ψ is in the plane of the disk then $\tau=(0,0,\tau_z)$ and

$$\tau_z=C_\tau J_n(\lambda_\tau r). \tag{17}$$

Substituting (17) in (11) produces the dispersion relation

$$\lambda_\tau^2=\frac{2\omega^2}{(1-v)c_\epsilon^2}-\frac{12\kappa}{h^2}. \tag{18}$$

Equation (18) exhibits a cutoff above

$$\omega_r=\sqrt{6\kappa(1-v)}\frac{c_\epsilon}{h}=\frac{\sqrt{12}c_s}{h} \tag{19}$$

which is the same as that in (12c). Finally, using λ_τ in (18) and since $\mathbf{\Gamma}$ and $\boldsymbol{\tau}$ are parallel then $\mathbf{\Gamma}=(0,0,\Gamma_z)$, and

$$\Gamma_z=C_\Gamma J_n(\lambda_\tau r). \tag{20}$$

Taking the curl of (20)

$$\nabla\times\mathbf{\Gamma}=\left(\frac{n}{r},-\frac{\partial}{\partial r}\right)C_\Gamma J_n(\lambda_\tau r). \tag{21}$$

Substituting (16) and (21) in (7) determines the solutions

$$\psi_r(r,\theta,t)=\cos n\theta e^{i\omega t}\times\left\{\sum_{j=1}^{2} C_{gj}\lambda_j J_n'(\lambda_j r)+\frac{n}{r}C_\Gamma J_n(\lambda_\tau r)\right\}, \tag{22a}$$

$$\psi_\theta(r,\theta,t)=\sin n\theta e^{i\omega t}\times\left\{\sum_{j=1}^{2} -\frac{n}{r}C_{gj}J_n(\lambda_j r)-\lambda_\tau C_\Gamma J_n'(\lambda_\tau r)\right\}, \tag{22b}$$

$$w(r,\theta,t)=\cos n\theta e^{i\omega t}\sum_{i=1}^{2} C_j J_n(\lambda_j r), \tag{22c}$$

where C_{gi} is related to C_i by (15).

Moments and shear resultants are expressed in terms of (ψ_r,ψ_θ,w) as

$$M_{rr}=D\left[\frac{\partial\psi_r}{\partial r}+v\left(\frac{\psi_r}{r}+\frac{1}{r}\frac{\partial\psi_\theta}{\partial\theta}\right)\right], \tag{23a}$$

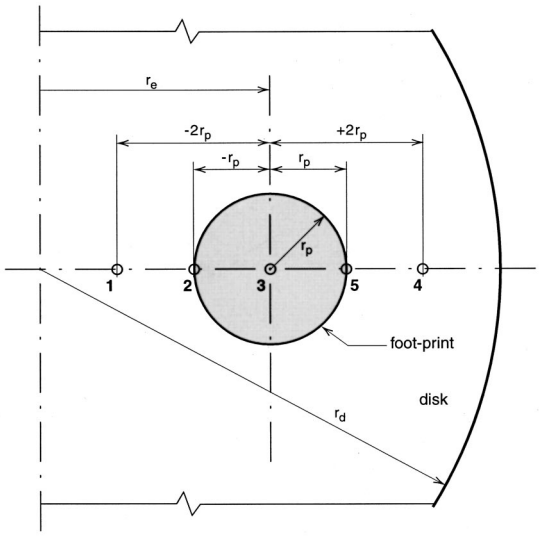

FIG. 1. Convention for sensor positions of eccentric footprint.

$$M_{\theta\theta}=D\left[v\frac{\partial\psi_r}{\partial r}+\frac{\psi_r}{r}+\frac{1}{r}\frac{\partial\psi_\theta}{\partial\theta}\right], \tag{23b}$$

$$M_{r\theta}=\frac{D(1-v)}{2}\left[\frac{1}{r}\frac{\partial\psi_r}{\partial\theta}+\frac{\partial\psi_\theta}{\partial r}-\frac{\psi_\theta}{r}\right], \tag{23c}$$

$$Q_r=\kappa Gh\left(\frac{\partial w}{\partial r}+\psi_r\right), \tag{23d}$$

$$Q_\theta=\kappa Gh\left(\frac{1}{r}\frac{\partial w}{\partial\theta}+\psi_\theta\right). \tag{23e}$$

For a solid disk with radius r_d, normal stresses on the disk surface are related to moment resultants by

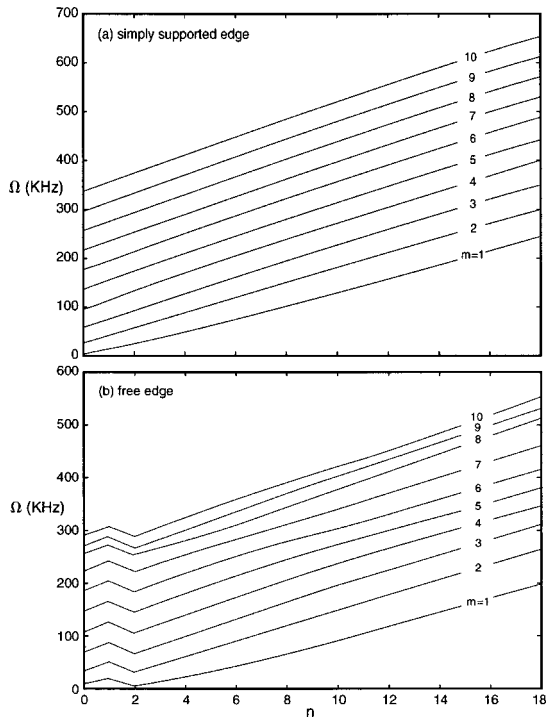

FIG. 2. Resonant frequency lines of disk as a function of "n" with "m" as parameter; $r_d=3''$, $h=0.5''$.

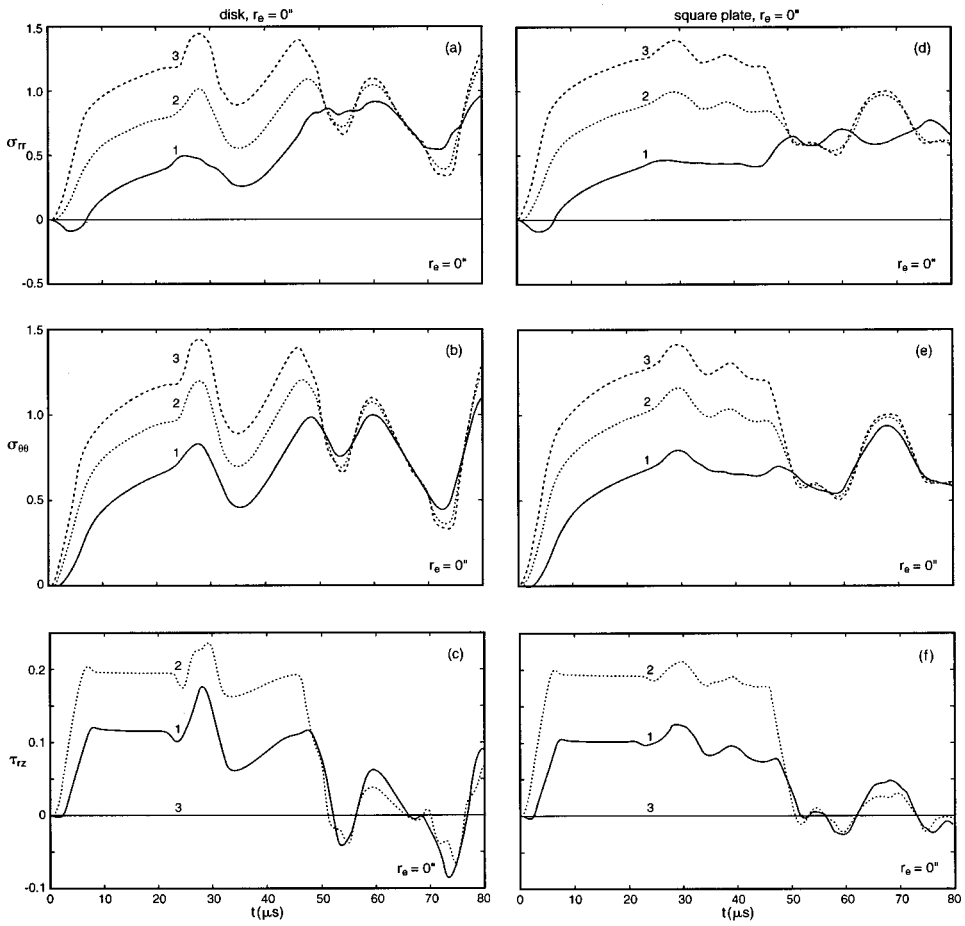

FIG. 3. Stress histories of disk and square plate with "simply supported edge:" $r_d=3''$, $h=0.5''$, $r_p=0.25''$, $r_e=0''$, $\Delta t_f=50\,\mu$s. (a), (b), (c)→disk; (d), (e), (f)→square plate.

$$\sigma_{rr}=\frac{6M_{rr}}{h^2},\quad \sigma_{\theta\theta}=\frac{6M_{\theta\theta}}{h^2},\quad \sigma_{r\theta}=\frac{6M_{r\theta}}{h^2} \tag{24a}$$

and shear stresses along the neutral plane are related to shear resultants by

$$\tau_{rz}=Q_r/h,\quad \tau_{\theta z}=Q_\theta/h. \tag{24b}$$

For a free edge

$$M_{rr}(r_d)\equiv M_{r\theta}(r_d)\equiv Q_r(r_d)=0 \tag{25a}$$

and for a simply supported edge

$$M_{rr}(r_d)\equiv \psi_\theta(r_d)\equiv w(r_d)=0. \tag{25b}$$

Substituting (22) in (23) then in either (25a) or (25b) produces the implicit eigenvalue problem

$$\mathbf{B}(a)\mathbf{C}=\mathbf{0}, \tag{26a}$$

where $\mathbf{B}$ is a 3×3 matrix of the fundamental solutions in (Ψ_r,Ψ_θ,w) and their first derivatives, and

$$\mathbf{C}=\{C_{g_1},C_{g_2},C_\Gamma\}^T. \tag{26b}$$

Expanding $\{\Psi_r,\Psi_\theta,w\}$ in terms of the eigenset $\{\omega_{nj};\eta_{rnj},\eta_{\theta nj},\varphi_{nj}\}$,

$$\psi_r(r,\theta,t)=\sum_{n=0}^{N}\sum_{j=1}^{M} a_{nj}\eta_{rnj}(r)\cos n\theta, \tag{27a}$$

$$\psi_\theta(r,\theta,t)=\sum_{n=0}^{N}\sum_{j=1}^{M} a_{nj}\eta_{\theta nj}(r)\sin n\theta, \tag{27b}$$

$$w(r,\theta,t)=\sum_{n=0}^{N}\sum_{j=1}^{M} a_{nj}\varphi_{nj}(r)\cos n\theta, \tag{27c}$$

where (M,N) is the number of radial and circumferential modes in the expansion. Substituting in (1) and (2) and enforcing the orthogonality of the eigenfunctions yields a set of uncoupled differential equations in the generalized coordinates a_{nj}:

$$\begin{aligned}&\ddot{a}_{nj}+\omega_{nj}^2 a_{nj}=-\frac{\pi(1+\delta_{n0})}{N_{nj}}p_{nj}f(t),\\ &N_{nj}=\rho h\langle\varphi_{nj}|r\varphi_{nj}\rangle\\ &\qquad+\frac{\rho h^3}{12}[\langle\eta_{rnj}|r\eta_{rnj}\rangle+\langle\eta_{\theta nj}|r\eta_{\theta nj}\rangle],\end{aligned} \tag{28}$$

where $(\dot{\cdot})$ is derivative w.r.t. time, δ_{n0} is the Knonecker delta, and $f(t)$ is time dependence of the forcing pulse. For a circular footprint of radius r_p and eccentricity r_e (see Fig. 1),

$$\begin{aligned}&p_{nj}=2p_0\int_0^{\theta_e}\int_{r_1}^{r_2}\varphi_{nj}(r)\cos n\theta r\,dr\,d\theta,\\ &\theta_e=\sin^{-1}(r_p/r_e),\\ &r_{1,2}=\tfrac{1}{2}[r_e\cos\theta\pm\sqrt{(r_e\cos\theta)^2-4(r_e^2-r_p^2)}].\end{aligned} \tag{29}$$

The solution of (28) can be expressed as a Duhamel integral

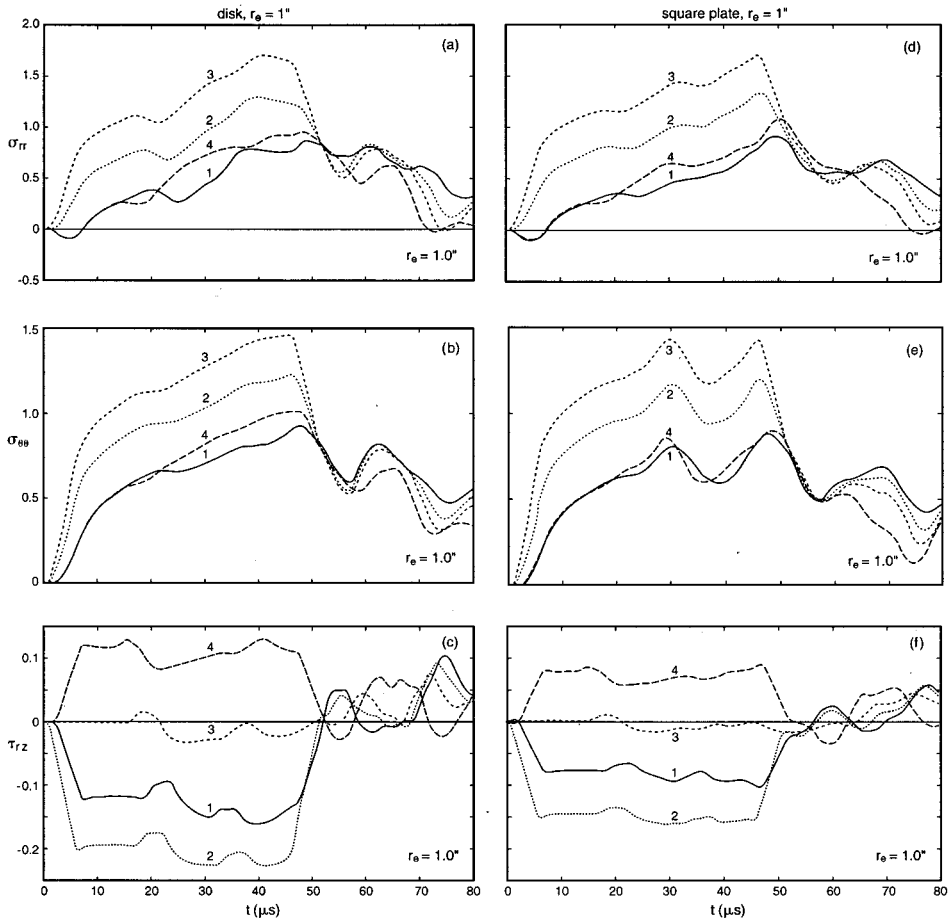

FIG. 4. Stress histories of disk and square plate with "simply supported edge:" $r_d=3''$, $h=0.5''$, $r_p=0.25''$, $r_e=1.0''$, $\Delta t_f=50\,\mu$s. (a), (b), (c)→disk; (d), (e), (f)→square plate.

$$a_{nj}(t)=-\frac{\pi(1+\delta_{n0})}{\omega_{nj}N_{nj}}p_{nj}\int_0^t f(\tau)\sin\omega_{nj}(t-\tau)d\tau. \quad (30)$$

A. Square plate with restrained edges

In Cartesian coordinates, Mindlin's equations are given by (1) and (2) with

$$\mathbf{\Psi}=\{\psi_x,\psi_y\}^T, \quad \Phi=\frac{\partial\psi_x}{\partial x}+\frac{\partial\psi_y}{\partial y}, \quad (31)$$

where (x,y) is a rectangular coordinate system with origin at the lower left corner of the square. Since solutions along x and y are not separable, a Galerkin approximation is adopted. Trial functions (φ_x,η_x) are defined on strips along x satisfying the edge constraints at $x=(0,l)$ and the 1D Mindlin's equations

$$D\frac{\partial^2\eta_x}{\partial x^2}-\kappa Gh\left(\eta_x+\frac{\partial\varphi_x}{\partial x}\right)=-\frac{\rho h^3}{12}\omega^2\eta_x, \quad (32a)$$

$$\kappa Gh\left(\frac{\partial^2\varphi_x}{\partial x^2}+\frac{\partial\eta_x}{\partial x}\right)=-\rho h\omega^2\varphi_x. \quad (32b)$$

For the square plate, trial functions (φ_y,η_y) along y are identical to (φ_x,η_x) since edge constraints are the same on all four edges. Expand (Ψ_x,Ψ_y,w) in terms of these trial functions:

$$\psi_x(x,y,t)=\sum_{i=1}^{N}\sum_{j=1}^{N}a_{ij}(t)\eta_{xi}(x)\varphi_{yi}(y), \quad (33a)$$

$$\psi_y(x,y,t)=\sum_{i=1}^{N}\sum_{j=1}^{N}a_{ij}(t)\varphi_{xi}(x)\eta_{yi}(y), \quad (33b)$$

$$w(x,y,t)=\sum_{i=1}^{N}\sum_{j=1}^{N}a_{ij}(t)\varphi_{xi}(x)\varphi_{yi}(y), \quad (33c)$$

where N is the number of trial functions in the expansion. Substituting (33) into Eqs. (1) and (2) gives

$$\mathcal{D}_1\equiv\sum_i\sum_j\left\{\frac{D}{2}[2\eta''_{xi}\varphi_{yi}+(1-v)\eta_{xi}\varphi''_{yi}+(1+v)\varphi'_{xi}\eta'_{yi}]a_{ij}-\kappa Gh\times(\eta_{xi}\varphi_{yi}+\varphi'_{xi}\varphi_{yi})a_{ij}-\frac{\rho h^3}{12}\eta_{xi}\varphi_{yi}\ddot{a}_{ij}\right\}=0, \quad (34a)$$

$$\mathcal{D}_2\equiv\sum_i\sum_j\left\{\frac{D}{2}[(1-v)\varphi''_{xi}\eta_{yi}+2\varphi_{xi}\eta''_{yi}+(1+v)\eta'_{xi}\varphi'_{yi}]a_{ij}-\kappa Gh\times(\varphi_{xi}\eta_{yi}+\varphi_{xi}\varphi'_{yi})a_{ij}-\frac{\rho h^3}{12}\varphi_{xi}\eta_{yi}\ddot{a}_{ij}\right\}=0, \quad (34b)$$

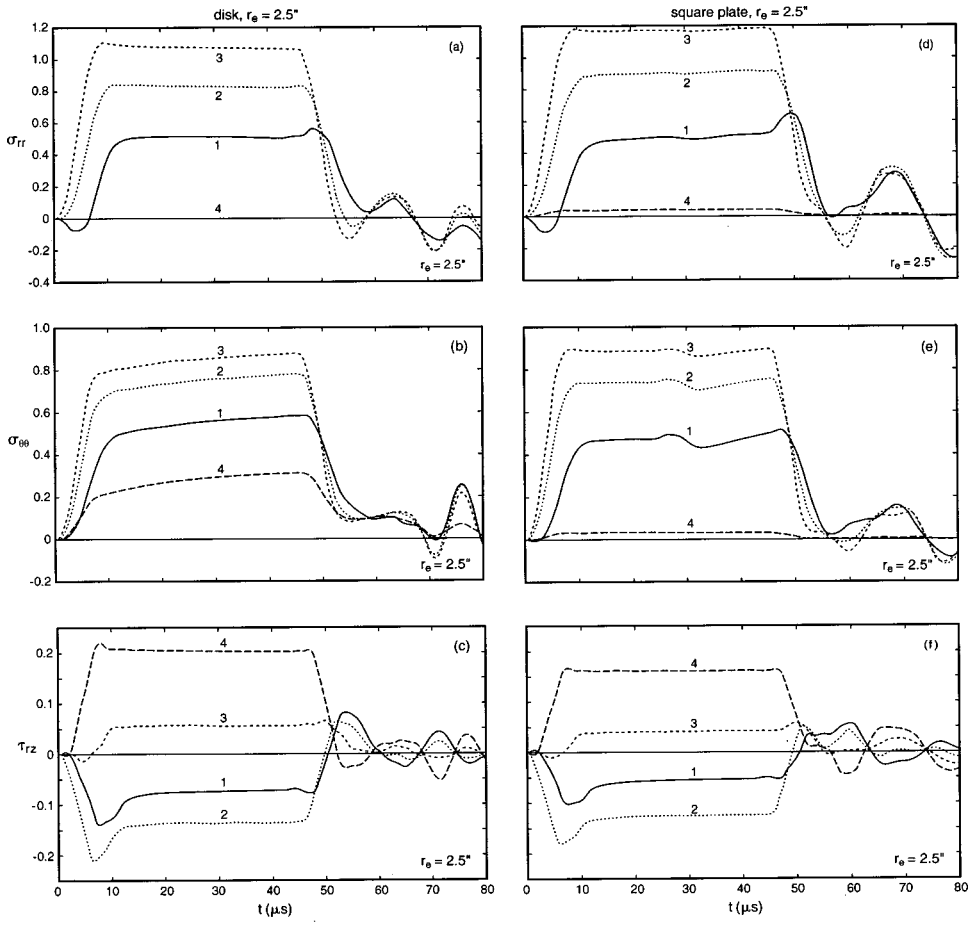

FIG. 5. Stress histories of disk and square plate with "simply supported edge:" $r_d = 3''$, $h = 0.5''$, $r_p = 0.25''$, $r_e = 2.5''$, $\Delta t_f = 50\,\mu$s. (a), (b), (c)→disk; (d), (e), (f)→square plate.

$$\mathcal{D}_3 \equiv \sum_i \sum_j \{\kappa G h(\varphi''_{xi}\varphi_{yi} + \varphi_{xi}\varphi''_{yi} + \eta'_{xi}\varphi_{yi} + \varphi_{xi}\eta'_{yi})a_{ij} - \rho h \varphi_{xi}\varphi_{yi}\ddot{a}_{ij}\} = -p, \tag{34c}$$

where $(\,)'$ is derivative w.r.t. the argument. Multiply $\mathcal{D}_1$ in (34a) by $(\eta_{xm}\varphi_{yn})$, $\mathcal{D}_2$ in (34b) by $(\varphi_{xm}\eta_{yn})$ and $\mathcal{D}_3$ in (34c) by $(\varphi_{xm}\eta_{yn})$, integrate over the square's surface, then add the three integrated equations to produce

$$\mathbf{A}_1\ddot{\mathbf{a}} + \mathbf{A}_2\mathbf{a} = \mathfrak{I}\mathbf{f}(t),$$
$$\mathfrak{I} = \left\{ 2\int_0^{\theta_e}\int_{r_1}^{r_2} \varphi_{xm}(r\cos\theta)\varphi_{yn}(r\sin\theta) r\, dr\, d\theta \right\}^T, \tag{35}$$

where the integral is over a circular footprint with eccentricity r_e as defined in (29), and $\mathbf{f}(t)$ is the time dependence of the forcing pulse.

Premultiplying (35) by $\mathbf{A}_1^{-1}$,

$$\ddot{\mathbf{a}} + \overline{\mathbf{A}}\mathbf{a} = \overline{\mathfrak{I}}\mathbf{f}(t), \quad \overline{\mathbf{A}} = \mathbf{A}_1^{-1}\mathbf{A}_2, \quad \overline{\mathfrak{I}} = \mathbf{A}_1^{-1}\mathfrak{I}. \tag{36}$$

To diagonalize $\overline{\mathbf{A}}$, apply the transformation

$$\mathbf{a} = \mathbf{V}\mathbf{a}^* \Leftrightarrow \mathbf{a}^* = \mathbf{V}^{-1}\mathbf{a} \tag{37}$$

$$\Rightarrow \ddot{\mathbf{a}}^* + \mathbf{V}^{-1}\overline{\mathbf{A}}\mathbf{V}\mathbf{a}^* = \mathbf{V}^{-1}\overline{\mathfrak{I}}\mathbf{f}(t) \tag{38}$$

and impose the condition

$$\mathbf{V}^{-1}\overline{\mathbf{A}}\mathbf{V} = \boldsymbol{\omega}^2. \tag{39}$$

This requires that $\mathbf{V}$ be the eigenvectors of $\overline{\mathbf{A}}$, i.e.,

$$[\overline{\mathbf{A}} - \boldsymbol{\omega}^2]\mathbf{V} = \mathbf{0} \tag{40}$$

and $\boldsymbol{\omega}$ the diagonal matrix of the corresponding eigenvalues.

Equations (36) then decouple in the generalized coordinate vector $\mathbf{a}^*$,

$$\ddot{\mathbf{a}}^* + \boldsymbol{\omega}^2\mathbf{a}^* = \mathbf{V}^{-1}\overline{\mathfrak{I}}\mathbf{f}(t) \tag{41}$$

with solution of each component in the form of Eq. (30). Moment and shear resultants and corresponding stresses are the Cartesian counterpart to (23) and (24):

$$M_{xx} = D\left(\frac{\partial\psi_x}{\partial x} + \upsilon\frac{\partial\psi_y}{\partial y}\right) \Rightarrow \sigma_{xx} = 6M_{xx}/h^2, \tag{42a}$$

$$M_{yy} = D\left(\frac{\partial\psi_y}{\partial y} + \upsilon\frac{\partial\psi_x}{\partial x}\right) \Rightarrow \sigma_{yy} = 6M_{yy}/h^2, \tag{42b}$$

$$M_{xy} = \frac{D(1-\upsilon)}{2}\left(\frac{\partial\psi_x}{\partial y} + \frac{\partial\psi_y}{\partial x}\right) \Rightarrow \sigma_{xy} = 6M_{xy}/h^2, \tag{42c}$$

$$Q_x = \kappa G h\left(\frac{\partial w}{\partial x} + \psi_x\right) \Rightarrow \tau_{xz} = Q_x/h, \tag{42d}$$

$$Q_y = \kappa G h\left(\frac{\partial w}{\partial y} + \psi_y\right) \Rightarrow \tau_{yz} = Q_y/h. \tag{42e}$$

They are expressed in terms of modal quantities by (33) noting that $\mathbf{a}$ is related to $\mathbf{a}^*$ by (37). For simply supported and

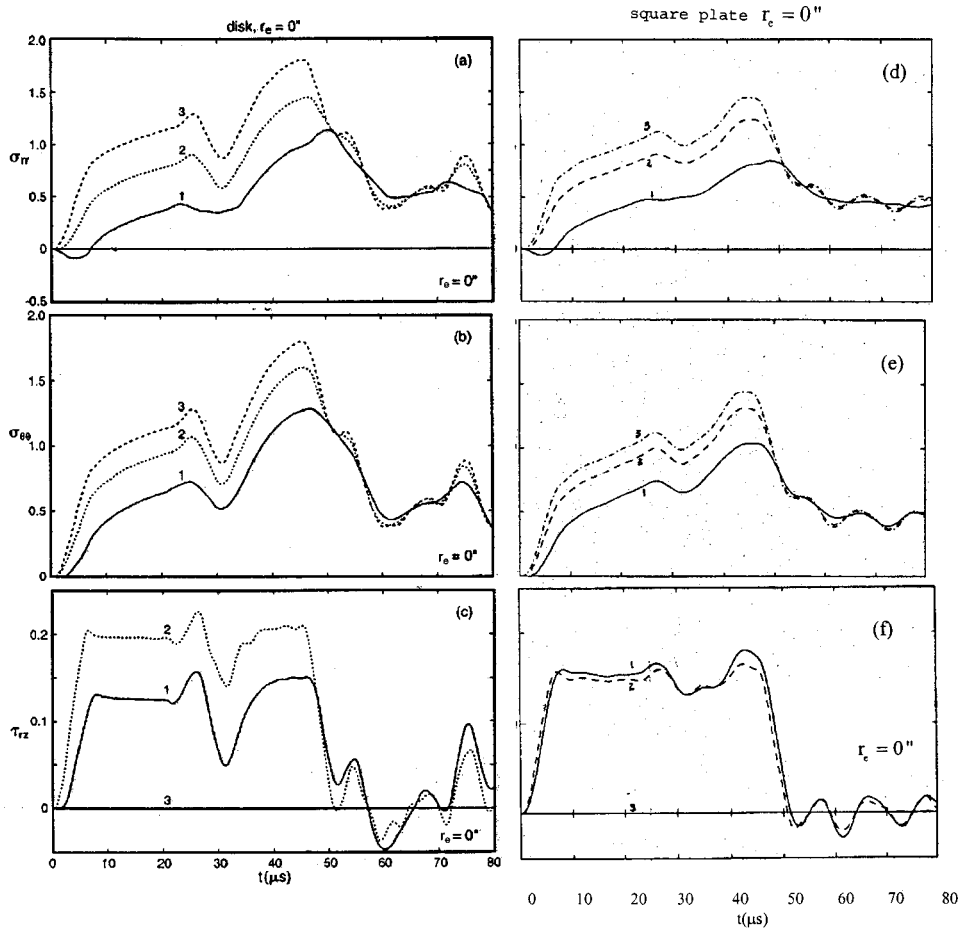

FIG. 6. Stress histories of disk and square plate with "free edge:" $r_d = 3''$, $h = 0.5''$, $r_p = 0.25''$, $r_e = 0''$, $\Delta t_f = 50\ \mu$s. (a), (b), (c)→disk; (d), (e), (f)→square plate.

clamped edges, expressions (33) satisfy the edge constraints identically. However, for free edges

$$M_{xx}(x_c, y) \equiv M_{yy}(x, y_c) = 0, \tag{43a}$$

$$M_{xy}(x_c, y) \equiv M_{xy}(x, y_c) = 0, \tag{43b}$$

$$Q_x(x_c, y) \equiv Q_y(x, y_c) = 0, \tag{43c}$$

where $x_c = (0, l)$ and $y_c = (0, l)$. Only (43c) is satisfied identically by these trial functions. For example,

$$M_{xx}(0,y) = D \sum_i \sum_j \left(\eta'_{xi}(0)\varphi_{yi}(y) + \upsilon \varphi_{xi}(0)\eta'_{yi}(y) \right) a_{ij}$$

$$= D \sum_i \sum_j \upsilon \varphi_{xi}(0)\eta'_{yi}(y) a_{ij} \tag{44}$$

which will not in general vanish. This error is equivalent to a spring loaded edge resisting rotation which stiffens the plate and raises its resonances.

B. Square plate with free edges

In Ref. 8 the problem of transient response of a rectangular plate was treated using a Chebychev collocation method dividing the plate into identical rectangular elements and superimposing into each element a lattice of points. The loci of these points satisfy

$$\left\{ (x_i, y_j) = \left(\cos\frac{\pi i}{2m}, \cos\frac{\pi j}{2n} \right), i = 0,...,2m; j = 0,...,2n \right\}. \tag{45a}$$

These pairs (x_i, y_j) are coordinates in a local scaled system at which the Mindlin plate equations in Cartesian coordinates are satisfied point by point. Continuity of the state vector is satisfied at the edges. Instead of a numerical integration in time as was done in Ref. 8, the results in this work were found by modal analysis and an exact integration in time similar to the steps taken for the disk in Sec. II, Eqs. (27)–(30). Because this solution method relies on calculating inner products among the modes and also the projection of the force distribution onto the set of modes, some distinctive highlights of the two steps will be given.

One characteristic of the Chebychev collocation method is that although the formulation is written in terms of the Chebychev polynomials, the actual solution directly yields the state vector

$$\{\mathbf{V}\} = \{(\Psi_x, \Psi_y, w)(x_i, y_j)\} \tag{45b}$$

at the collocation points (x_i, y_j) for each mode. Considering each element in turn, the Chebychev weights associated with each state vector first need to be found. In terms of the Chebychev polynomials $(T_p(x), T_q(x))$, $w(x,y)$ can be written also as

$$w(x_i, y_j) = \sum_p \sum_q a_{pq} T_p(x_i) T_q(y_j) \tag{46}$$

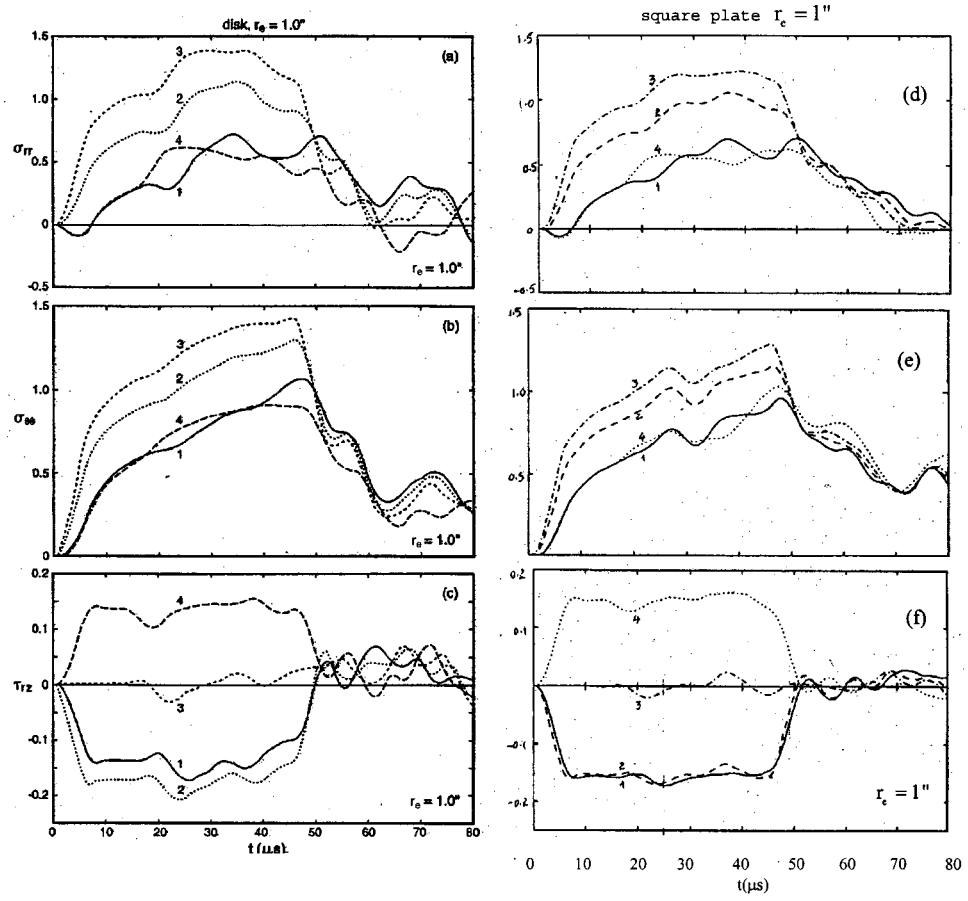

FIG. 7. Stress histories of disk and square plate with "free edge:" $r_d = 3''$, $h = 0.5''$, $r_p = 0.25''$, $r_e = 1.0''$, $\Delta t_f = 50\ \mu$s. (a), (b), (c)→disk; (d), (e), (f)→square plate.

which is easily solved for a_{pq}. Similarly, the Chebychev weights b_{pq} and c_{pq} corresponding to Ψ_x and Ψ_y are easily found.

Let the Chebychev weights associated with a different mode $\mathbf{V}'$ be $\{\alpha_{pq}, \beta_{pq}, \gamma_{pq}\}$. The inner product between the two modes over an element is then

$$\int_{\text{element}} \mathbf{V}\cdot\mathbf{V}'\, dA = \frac{1}{4}\sum_p \sum_q \sum_{p'} \sum_{q'} a_{pq}a_{p'q'} + \frac{h^2}{12}(b_{pq}\beta_{p'q'} + c_{pq}\gamma_{p'q'})n_{pp'}n_{qq'}, \tag{47}$$

$$n_{pq} = \frac{2}{1-(p+q)^2} + \frac{2}{1-(p-q)^2}.$$

The inner product over the entire plate is then found by summing over all the elements.

Finding the generalized force, which is the projection of the force distribution onto the set of modes, also utilizes the Chebychev weights. First, however, we need to classify the possible intersections between the circular footprint with uniform pressure and each of the rectangular elements. There are seven distinct ways a disk "*D*" and a rectangle "*R*" may intersect:

(1) the empty set "*O*"; in this case the element does not contribute to the generalized force,
(2) "*D*" is wholly within "*R*,"
(3) "*R*" is wholly within "*D*,"
(4) the intersection is partial and contains no corners of "*R*,"
(5) the intersection contains one corner of "*R*,"
(6) the intersection contains two corners of "*R*,"
(7) the intersection contains three corners of "*R*."

Cases (2) and (3) above may be computed in close form, while cases (4) and (7) require numerical quadrature.

Let the generalized force contributed by an element be

$$F_i = \int_{\text{element}} w(x,y)\, dA. \tag{48}$$

For case (2), transform coordinates to a disk-centered polar system (ρ,θ) in terms of which the element-centered rectangular coordinates (x,y) are

$$x = \rho\cos\theta + x_c, \quad y = \rho\sin\theta + y_c,$$

then

$$F_i = \sum_p \sum_q a_{pq} \sum_m^p \sum_n^q t_{pn}t_{qm}\left[\sum_i^n \binom{n}{i} x_c^i \sum_j^m \binom{m}{j} y_c^j \times \frac{r_d^{m+n-i-j+2}}{m+n-i-j+2} I(n-i, m-j)\right], \tag{49}$$

where r_d is disk radius, $\binom{n}{i} = n!/(n-i)!i!$ is the binomial coefficient, t_{pn} are values such that if $T_p(x)$ is the Chebychev polynomial

$$T_p(x) = \sum_n^p t_{pn}x^n \tag{50a}$$

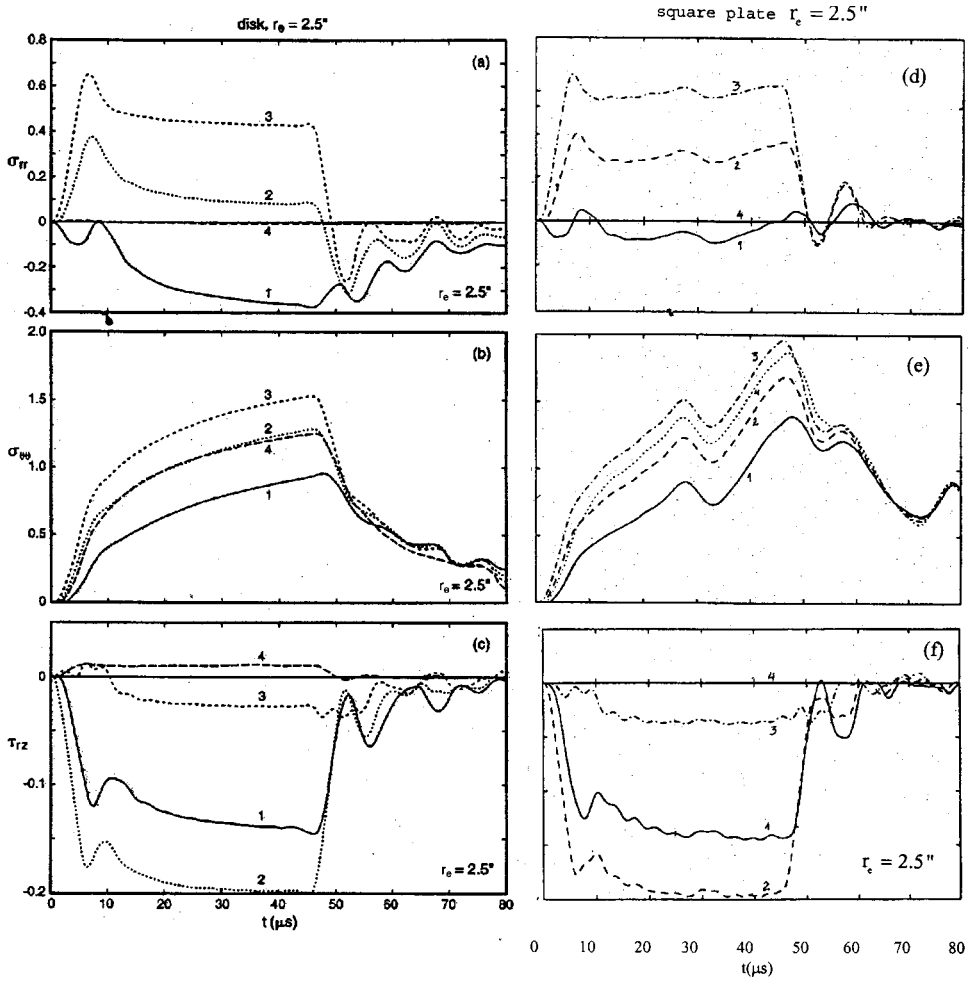

FIG. 8. Stress histories of disk and square plate with "free edge:" $r_d = 3''$, $h = 0.5''$, $r_p = 0.25''$, $r_e = 2.5''$, $\Delta t_f = 50\ \mu$s. (a), (b), (c)→disk; (d), (e), (f)→square plate.

and

$$I(n,m) = \int_0^{2\pi} \cos^n \theta \sin^m \theta \, d\theta \tag{50b}$$

which can be found recursively using

$$I(0,0) = 2\pi, \quad I(2,0) = I(0,2) = \pi, \quad I(2,2) = \frac{\pi}{4},$$

$$I(n,1) = I(1,n) = 0, \quad I(n+2,0) = \frac{(n+1)}{(n+2)} I(n,0),$$

$$I(n,2) = I(n,0) - I(n+2,0),$$

$$I(n,m+2) = I(n,m) - I(n+2,m),$$

$$I(n,m) = I(m,n).$$

For case (3),

$$F_i = \sum_p \sum_q a_{2p,2q} I_{2p} I_{2q}, \quad I_{2p} = \frac{2}{1-4p^2}. \tag{51}$$

The total generalized force results from summing the contributions of all the elements.

III. RESULTS

Results are divided into two parts. The first part compares disk and plate stress histories $(\sigma_{rr}, \sigma_{\theta\theta}, \tau_{rz})$ where plate side length equals disk diameter. The edges are simply supported. The purpose is to investigate in detail how response is affected by shape of boundary at different eccentricities of center of impact. Further comparisons are made with free edges to determine the effect of edge constraint. The second part studies the sensitivity of maximum transient stress $\sigma_{\max}$ to eccentricity at various lateral dimensions, thicknesses, pulse widths, and edge constraints. In all cases, the time dependence $f(t)$ of the forcing pulse is trapezoidal with 5 μs rise and fall times, and either 40 μs or 15 μs plateau of unit magnitude, yielding a total pulse width of 50 μs and 25 μs, respectively. The 50 μs is typical of a pressure pulse produced by a 50 caliber rifle projectile at 3000 ft/s. The forcing pressure is uniform over a circular footprint with radius $r_p = 0.25$ in and eccentricity r_e. Stress histories are computed at four radial positions or "sensors" as shown in Fig. 1. Sensors 1 and 4 are symmetric about center of impact and should yield identical histories prior to reflections from the edge. Sensor 2 is on the footprint perimeter and measures maximum shear stress τ_{rz} along the neutral plane. Sensor 3 is at the center of impact and measures maximum normal stresses σ_{rr} and $\sigma_{\theta\theta}$ on the plate's surface. Sensor 5 replaces sensor 4 only when the footprint touches the edge. Disks and square plates are made of AlN with properties

$$E = 40\times10^6 \ \text{lb/in}^2, \quad \rho = 3.04\times10^{-4} \ \text{lb s}^2/\text{in}^4, \quad \upsilon = 0.25.$$

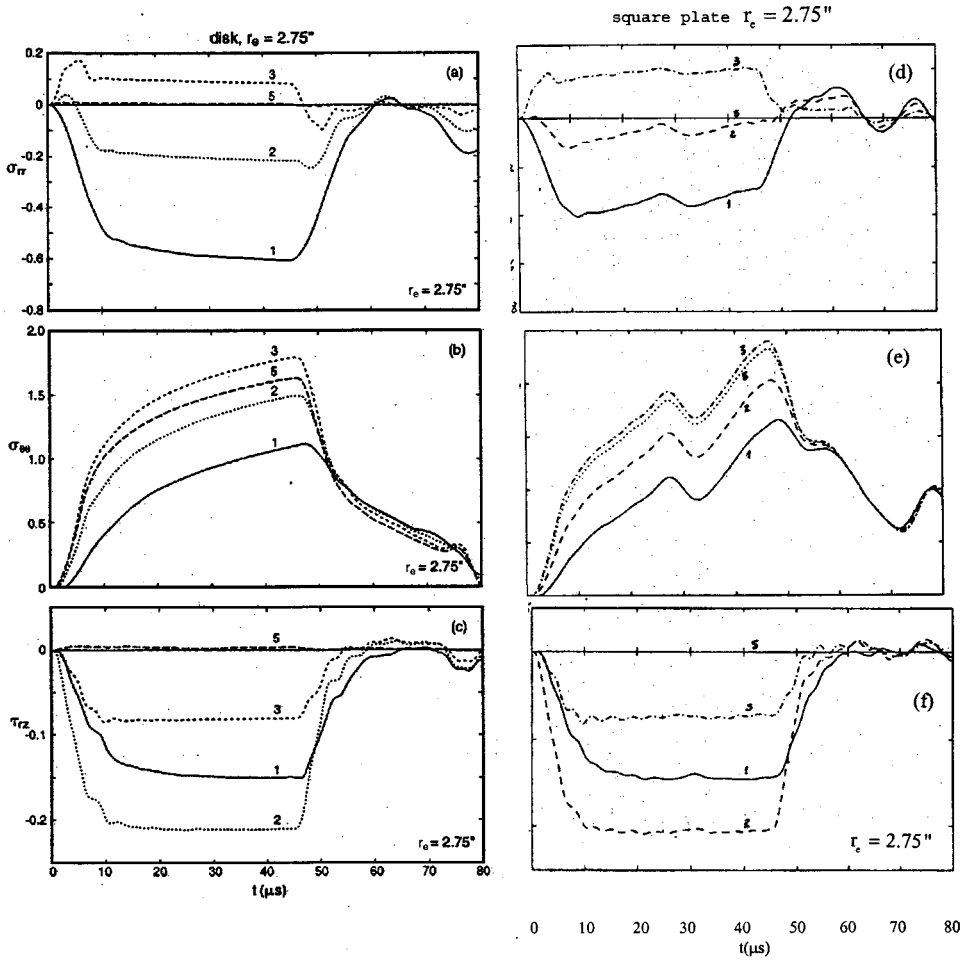

FIG. 9. Stress histories of disk and square plate with "free edge:" $r_d=3''$, $h=0.5''$, $r_p=0.25''$, $r_e=2.75''$, $\Delta t_f=50\,\mu$s. (a), (b), (c)→disk; (d), (e), (f)→square plate.

Both disk and plate have the same thickness and lateral dimensions, i.e., $h=0.5$ in and $l=2r_d=6$ in.

Figures 2(a) and (b) plot resonant frequency Ω in Hz against circumferential wave number n with radial wave number m as parameter for disks with simply supported and free edges. Shear modes are omitted since they do not contribute to response. For $n>2$, Ω varies almost linearly with n, and as expected, for fixed (m,n) Ω for simply supported edges is higher than Ω for free edges since the former yields a stiffer boundary for $n\geqslant 2$. For free edges Ω lines undergo a reversal in slope between $n=1$ and $n=2$ as shown in Fig. 2(b).

Figures 3, 4, and 5 compare disk and plate stress histories for $r_e=0$, 1 in and 2.5 in, respectively, for simply supported edges. For $r_e=0$ [see Figs. 3(a)–(f)], disk and plate reach the same maxima for all stress components. For the disk, reflections from the edge produce strong fluctuations in response because, in radiating from the center of impact, each wave front is reflected from the edge at the same time producing a condition of the reflected waves called coherence [see Figs. 3(a)–(c)]. For $r_e=1$ in [see Figs. 4(a)–(f)] maxima of both geometries are again the same. Histories at sensors 1 and 4 coincide in the first 15 μs from impact prior to reflections from the edge. For $r_e=2.5$ in [see Figs. 5(a)–(f)], the only change is that histories at sensors 1 and 4 never coincide because sensor 4 is at the edge. Stress histories resemble the trapezoidal shape of the forcing pulse because it is more important than the reflected waves in determining the shape of the response.

Figures 6–9 compare histories of the disk and square plate with free edges for $r_e=0$, 1, 2.5, and 2.75 in. Compar-

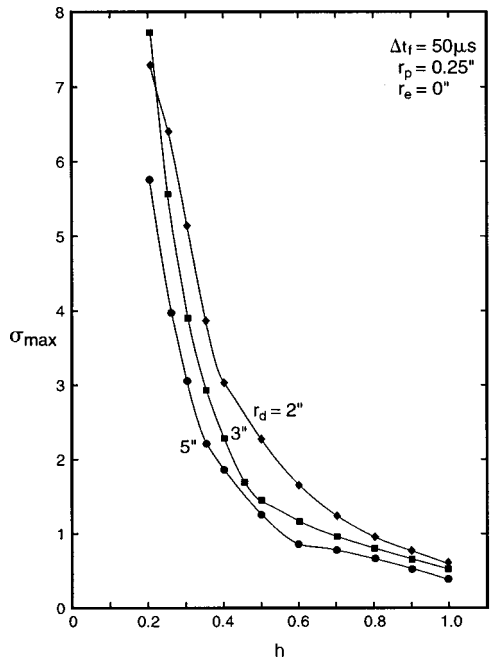

FIG. 10. Variation of $\sigma_{\max}$ with "h" for a disk with central impact, and "simply supported edge."

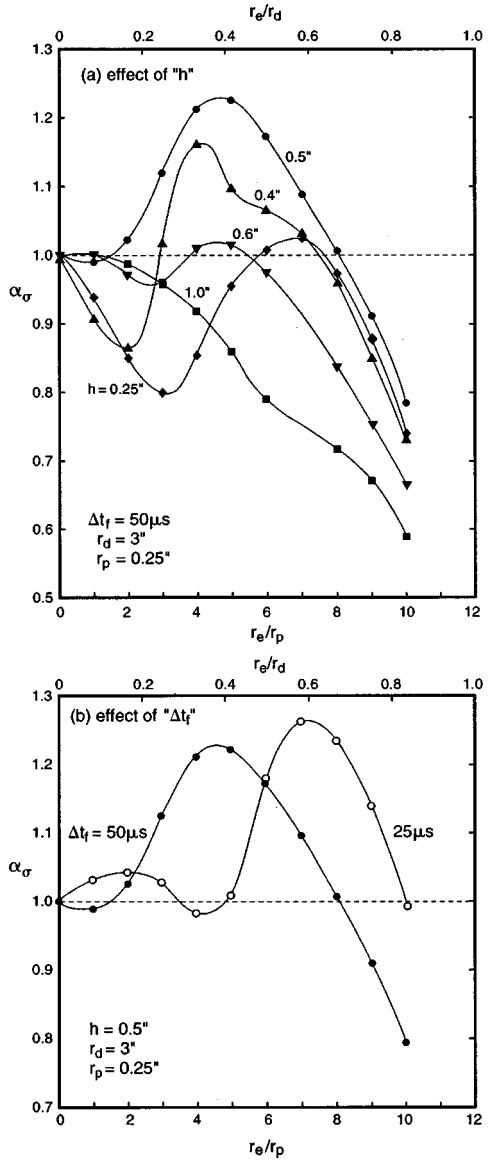

FIG. 11. Variation of "α_σ" with "r_e" for a disk with simply supported edge:" $r_d = 3''$.

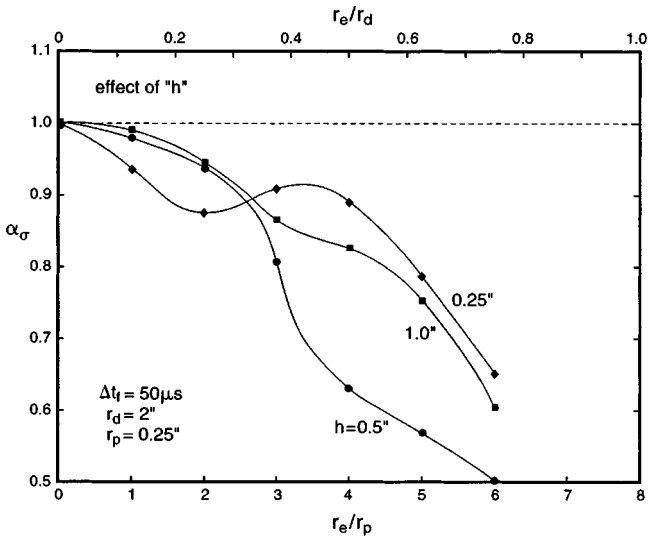

FIG. 12. Variation of "α_σ" with "r_e" for a disk with simply supported edge:" $r_d = 2''$.

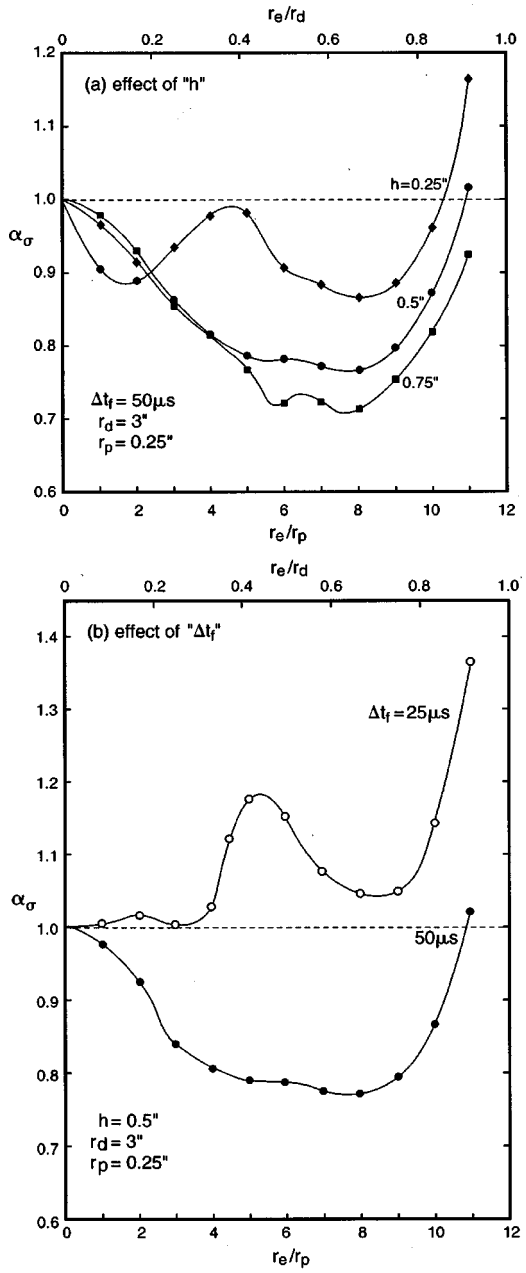

FIG. 13. Variation of "α_σ" with "r_e" for a disk with free edge:" $r_d = 3''$.

ing maximum stress for free and simply supported edges, the disk's is higher while the square plate's is comparable. For $r_e = 2.5$ in [see Figs. 8(a)–(c)], σ_{rr} is negative at sensor 1, and becomes positive at sensors 2 and 3. As center of impact approaches the free edge, it bends a sector of the disk like a cantilever producing negative flexural stress σ_{rr} at sensors remote from the edge [see Fig. 8(a)]. This is called the cantilever effect. For $r_e = 2.75$ in [see Figs. 9(a)–(c)], both sensors 1 and 2 record negative σ_{rr} as the cantilever sector of the disk is more flexible because its cord is shorter. This is also evidenced by the larger peak magnitude of σ_{rr} [compare Figs. 8(a) and 9(a)]. Although σ_{rr} diminishes with r_e, $\sigma_{\theta\theta}$ rises with r_e. Also as the sensor approaches the free edge, histories of disk and square plate differ qualitatively.

To study how the various parameters affect peak stress response $\sigma_{\max}$, let the stress factor α_σ be defined as

$$\alpha_\sigma(r_e)=\sigma_{\max}(r_e)/\sigma_{\max}(0). \tag{52}$$

An $\alpha_\sigma>1$ means a magnification from the situation of central impact, and an $\alpha_\sigma<1$ means a reduction. The feducial $\sigma_{\max}(0)$ for a disk with simply supported edges is plotted against h with r_d as parameter in Fig. 10. For fixed r_d, the $\sigma_{\max}$ line appears inversely proportional to h^2. This is consistent with the approximation derived in Ref. 3 for $\sigma_{\max}$ based on the approximate model of an expanding cone of influence:

$$\sigma_{rr}(0,t)=\sigma_{\theta\theta}(0,t)\approx\frac{3(1+\upsilon)}{2}p_0\frac{r_p^2}{h^2}\left[\ln\left(\frac{r_p}{\bar{l}}\right)-\frac{1}{4}\left(\frac{r_p}{\bar{l}}\right)^2\right], \tag{53}$$

$$\bar{l}=1.25\left(\frac{\pi c_\epsilon}{2\sqrt{3}}ht\right)^{1/2}+1.25r_p,$$

where c_ϵ is defined in (4) and p_0 in (29).

Figure 10 also shows that increasing r_d reduces $\sigma_{\max}$ for a fixed h because reflected waves contribute less to total stress. In fact, depending on pulse width Δt_f there is a threshold r_d above which $\sigma_{\max}$ does not change.[3] Figure 11(a) plots α_σ against r_e/r_p with h as parameter for a disk with simply supported edges, $r_d=3''$, and $0.25\,\text{in}\leqslant h\leqslant 1$ in. For $h=0.4$ in and 0.5 in, α_σ rises above unity, and well above the other h's. As r_e approaches the edge, α_σ diminishes smoothly for all h. Figure 11(b) plots α_σ for $h=0.5$ in and two Δt_f's. The shapes of the two curves are similar while the maximum α_σ's occur at different r_e's. Figure 12 plots α_σ for $r_d=2$ in. There, α_σ is always below unity. The plots of α_σ in Figs. 13(a) and (b) are for a disk with free edges. α_σ reaches a minimum near $r_e/r_p=8$, then rises smoothly with r_e for all h. This rise is consistent with the cantilever effect. In general, the shape of α_σ does not follow trends predictable by simplified models since it depends on the interference between waves radiating from the footprint and incoherent reflections from the edges. The interference is a function of disk geometry, eccentricity and pulse width.

IV. CONCLUSION

Transient waves in a thick disk and square plate forced by an eccentric pressure pulse were studied adopting a modal analysis to the Mindlin equations. Notable results are as follows.

(1) Stress histories at sensors symmetrically located from center of impact coincide until waves reflected from the boundary interfere with the outgoing waves from the footprint.

(2) For central impact, reflected waves in a disk produce strong fluctuations in stress history compared to the square plate because of coherence in the disk. These fluctuations intensify in the square plate as center of impact r_e moves toward the edge.

(3) Histories of the disk and square plate agree more in shape and magnitude for simply supported edges than for free edges.

(4) Stress factors $\alpha_\sigma(r_e)$ of peak stress response rises or falls from unity as r_e increases from zero to r_d, depending on h, r_d, and Δt_f. This change does not follow a trend predictable by simplified models because of the complicated interference between waves radiating from the footprint and incoherent reflections from the edges.

(5) For free edges, $\alpha_\sigma(r_e)$ always rises as r_e approaches the edge.

[1] M. El-Raheb, "Transient elastic waves in layered media: One-dimensional analysis," J. Acoust. Soc. Am. **94**, 172–184 (1993).
[2] M. El-Raheb, "Simplified models for transient uniaxial waves in a layered periodic stack," Int. J. Solids Struct. **34**, 2969–2990 (1997).
[3] M. El-Raheb, "Flexural waves in a disk soon after impact," J. Acoust. Soc. Am. **96**, 221–234 (1994).
[4] M. El-Raheb and P. Wagner, "Transient waves in a thick disk," J. Acoust. Soc. Am. **95**, 3287–3299 (1994).
[5] M. El-Raheb and P. Wagner, "Transient elastic waves in finite layered media: Two dimensional axisymmetric analysis," J. Acoust. Soc. Am. **99**, 3513–3527 (1996).
[6] M. El-Raheb, "Simplified models of transient elastic waves in finite axisymmetric layered media," J. Acoust. Soc. Am. **104**, 3369–3384 (1998).
[7] R. D. Mindlin, "Influence of rotary inertia and shear deformation on flexural motions of isotropic elastic disks," Trans. ASME, J. Appl. Mech. **73**, 31–38 (1951).
[8] B. Kjellmert, "A Chebyshev collocation multi-domain method to solve the Reissner-Mindlin equations for the transient response of an isotropic plate subjected to impact," Int. J. Numer. Methods Eng. **40**, 3689–3702 (1997).

Interpretation and identification of minimum phase reflection coefficients

J. Gregory McDaniel[a] and Cory L. Clarke
Department of Aerospace and Mechanical Engineering, Boston University, 110 Cummington Street, Boston, Massachusetts 02215

(Received 23 October 2000; revised 7 September 2001; accepted 10 September 2001)

If the acoustic reflection coefficient is minimum phase, then the causality condition can be used to reconstruct its phase from its magnitude. Such reconstructions are useful when environmental conditions obscure the phase, which is vital to understanding the dynamics of the reflecting object. However, the reconstructions are usually impossible because one cannot be sure that the reflection coefficient is minimum phase. The present work addresses this difficulty by formulating a time-domain description of the minimum phase condition and by identifying classes of submerged objects that always create minimum phase reflection coefficients. Numerical examples are used to confirm the analytical findings and to illustrate their applicability to objects that reflect sound with a wide range of magnitudes. © *2001 Acoustical Society of America.* [DOI: 10.1121/1.1416903]

PACS numbers: 43.40.Fz [CBB]

I. INTRODUCTION

It is often the case in experiments and sensing activities that the magnitude of a reflected or transmitted acoustic wave is more easily measured than its phase. While the magnitude can be accurately estimated from suitable time averages, ambient noise as well uncertainties in target and receiver locations conspire to contaminate the phase over broad frequency bands. These factors typically leave the experimentalist with nothing but an accurately measured reflection coefficient magnitude over the frequency range of interest. If the phase of the reflection coefficient was known, the complex valued reflection coefficient could be used to determine dynamics properties of the object that enhance its identification. For this reason, the present article is concerned with the finding of a reflection coefficient phase from its magnitude using causality.

Causality requires that the response of a system cannot precede its cause. Analysis of this condition in the frequency domain yields integral relationships between the real and imaginary parts of any transfer function. If the function is minimum phase, a property that shall be discussed in greater detail later, then its magnitude and phase are also related by causality. Derivations of these relations and their mathematical properties are given by Papoulis[1] and in *The Transform Handbook*.[2] The relations have been useful in physics and engineering, most notably in electromagnetic scattering theory,[3–6] and electrical network design.[7–10]

Recently, the problem of recovering nonminimum phase from the magnitude of a transfer function has received increased attention. Sarkar[11] presented a method that relies on a Fourier series expansion of the real and imaginary parts of the transfer function. The Fourier coefficients are initially chosen by recovering the minimum phase and are then iteratively adjusted so that the magnitude of the transfer function matches a measured value. While this technique has been useful in examples involving the antenna radiation-power patterns and microwave filters, it does not produce correct results for the problems considered here. The fundamental reason is that the reflection coefficient phase does not exhibit the same frequency characteristics as the phases in the electromagnetic examples considered by Sarkar.

The causality condition has been used to relate portions of transfer functions that arise in acoustic radiation problems. Such problems are often characterized by the frequency-dependent radiation impedance of a wetted surface, defined here as the ratio of surface pressure to velocity. Causality may be generally used to relate the real and imaginary parts of this transfer function, as was first suggested by Mangulis[12] and used by Radlinski and Meyers.[13] In these applications, the causality condition requires that an acoustic pressure on the surface cannot be produced until it acquires a nonzero velocity.

The one-dimensional acoustic reflection and transmission problems typically involve two transfer functions, which make the problems more complex than the radiation ones considered by Mangulis and Radlinski and Meyers. The first is the mechanical impedance of the object, defined here as the ratio of applied force to velocity. For this transfer function, the causality requirement is best described by considering the object *in vacuo* and applying a force to produce a specified velocity. The velocity is the input and the force is the output, so causality requires that no force may be measured until the velocity occurs. The second transfer function is the reflection coefficient, defined here as the ratio of the reflected wave amplitude to the incident wave amplitude. Here, causality requires that waves may not be reflected from an object before an incident wave arrives. Since the object impedance and the reflection coefficient are algebraically related, causal impedances produce causal reflection coefficients. These ideas were first explored by McDaniel[14] for one-dimensional acoustic reflections from mass-spring-dashpot systems.

The first goal of the present article is to interpret the

[a]Electronic mail: jgm@bu.edu

minimum phase condition for the reflection of a plane wave normally incident on a uniform impedance surface. This is achieved by reviewing existing descriptions of the minimum phase condition and describing a new time-domain interpretation. The second goal is to identify two classes of submerged objects that produce minimum phase reflection coefficients. The first class consists of objects that effectively transfer velocity and the second class consists of objects that effectively transfer force.

II. EXISTING DESCRIPTIONS OF THE MINIMUM PHASE CONDITION

In this section, existing descriptions of the minimum phase condition have been collected from a variety of disciplines and are presented first in the frequency domain and then in the time domain. The following Fourier transform convention is used:

$$H(\omega)=\mathcal{F}\{h(t)\}=\int_{-\infty}^{\infty}h(t)e^{i\omega t}dt, \tag{1}$$

$$h(t)=\mathcal{F}^{-1}\{H(\omega)\}=\frac{1}{2\pi}\int_{-\infty}^{\infty}H(\omega)e^{-i\omega t}d\omega. \tag{2}$$

Throughout this discussion, $h(t)$ is assumed to be the impulse response of a physical system and $H(\omega)$ is the transfer function for the system.

Before discussing the phase properties of $H(\omega)$, let us recall two conditions on passive linear physical systems. Since $h(t)$ is the response to a Dirac input at $t=0$, causality requires that $h(t)=0$ for $t<0$. The implication of this condition for $H(\omega)$ is more subtle. When time is negative, the inverse Fourier integral may be evaluated by closing a contour in the upper half of the complex frequency plane. The causal requirement of no response for negative times leads directly to the condition that $H(\omega)$ may not have poles in the upper half of the complex frequency plane. Further analysis[1,2] reveals that the real and imaginary parts of $H(\omega)$ are related by Hilbert transforms. Writing $H(\omega)=H_r(\omega)+H_i(\omega)$, causality requires that

$$H_i(\omega)=\mathcal{H}\{H_r(\omega)\}=\frac{1}{\pi}\int_{-\infty}^{\infty}\frac{H_r(y)}{\omega-y}dy, \tag{3}$$

$$H_r(\omega)=-\mathcal{H}\{H_i(\omega)\}=H_r(0)-\frac{1}{\pi}\int_{-\infty}^{\infty}\frac{H_i(y)}{\omega-y}dy. \tag{4}$$

The second condition is that the impulse response should be real-valued, or $\Im\{h(t)\}=0$. This condition is met by requiring

$$H(\omega)=H^*(-\omega), \tag{5}$$

where the superscripted * denotes the complex conjugate.

One description of the minimum phase condition, which is accepted by many as the definition, is that $H(\omega)$ may not have zeros in the upper half of the complex frequency plane.[1] This condition insures that the system's inverse transfer function is also causal because $H^{-1}(\omega)$ will have no poles in the upper plane if $H(\omega)$ has no zeros there.[9,15] The inverse impulse response, $\mathcal{F}^{-1}\{H^{-1}(\omega)\}$, is only causal when $H(\omega)$ is minimum phase. This concept often arises in the context of a causal inverse filter in noise control.[16] Zeros in the upper half of the complex frequency domain create phase shifts in the transfer function as frequency is varied along the real axis, which is the hallmark of a nonminimum phase function. In particular, passing beneath a zero in the upper half of the plane creates a phase shift of $(-\pi)$.[17] One can show that as frequency is varied from infinity to zero, a nonminimum phase function experiences a greater positive phase shift than a minimum phase function with the same magnitude.[18] This is the source of the *minimum phase* adjective.

Further insight into the minimum phase condition may be gained by expressing a nonminimum phase transfer function as a product of a minimum phase function, H_{mp}, and an all-pass function H_{ap},[16–19]

$$H_{\mathrm{nmp}}(\omega)=H_{\mathrm{ap}}(\omega)H_{\mathrm{mp}}(\omega). \tag{6}$$

Each of the two functions on the right is required to satisfy the causality and real-valued conditions in Eqs. (3)–(5). In addition, the all-pass function must have a unit magnitude at all frequencies,

$$|H_{\mathrm{ap}}(\omega)|=1. \tag{7}$$

In this way, each nonminimum phase function has an associated minimum phase function that has the same magnitude but a different phase.

One useful form of the all-pass function is given by Victor,[19]

$$H_{\mathrm{ap}}(\omega)=e^{i\omega D}\prod_j P(\omega,u_j). \tag{8}$$

The exponential term is recognized as a time shift D that creates a pure delay in response. For simplicity, we shall henceforth assumed that time has been referenced to the first occurrence of an output signal, so that $D=0$. The factors are defined as

$$P(\omega,u_j)=\frac{\omega-u_j}{\omega-u_j^*}. \tag{9}$$

These factors and their product are sometimes referred to as the Blaschke factors and product.[5] In order for H_{ap} to satisfy the causality and real-valued conditions, the Blaschke product must be carefully chosen. To satisfy the causality condition, the poles should be in the lower plane. This requires that $\Im\{u_j\}>0$. To satisfy the real-valued condition, the Blaschke product must have the property indicated in Eq. (5),

$$\prod_j P(\omega,u_j)=\prod_j P^*(-\omega,u_j). \tag{10}$$

This may be achieved by either choosing the Blaschke factors in pairs of the form $P(w,u_j)$ and $P(w,u_k)$, where $\Re\{u_j\}=-\Re\{u_k\}$, or by requiring a single factor to have a pure imaginary u_j.

Time-domain descriptions of the minimum phase condition have received far less attention in the literature but are interesting and useful. The present article shall use a descrip-

tion that was presented by Eisner[15] and involves the output energy of the system. Let the energy contained in an arbitrary response $g(t)$ up to time T be defined as

$$E_g = \int_{-\infty}^{T} |g(t)|^2 dt. \tag{11}$$

Let us further define $h(t)$ to be $g(t)$ convolved with an all-pass and causal function $p(t)$, so that $g(t) = h(t) * p(t)$. Then one can show that

$$E_h \geqslant E_g. \tag{12}$$

This implies that any multiplication by a causal all-pass function has the effect of decreasing the energy that has arrived up to a time T. The key implication of this result for the present work is that the response energy in a minimum phase system integrated up to time T is greater than that of a nonminimum phase system with the same frequency-domain magnitude.

For convenience of referral, we include the proof of Eq. (12) that was presented by Eisner. A truncated function $g_T(t)$ is defined according to

$$g_T(t) = \begin{cases} g(t), & t \leqslant T, \\ 0, & t > T. \end{cases} \tag{13}$$

This allows E_g to be expressed as an infinite integral instead of the semi-infinite integral given in Eq. (11),

$$E_g = \int_{-\infty}^{\infty} |g_T(t)|^2 dt. \tag{14}$$

Since we now have an infinite integral, Parseval's formula is applied to get

$$E_g = \int_{-\infty}^{\infty} |G_T(f)|^2 df. \tag{15}$$

If $p(t)$ is an all-pass function, then $|P(f)| = 1$. Inserting this unity factor in the integrand of Eq. (15) and again applying Paresval's formula results in

$$E_g = \int_{-\infty}^{\infty} |g_T(t) * p(t)|^2 dt. \tag{16}$$

As the integrand is always positive,

$$E_g \geqslant \int_{-\infty}^{T} |g_T(t) * p(t)|^2 dt. \tag{17}$$

Recalling that $p(t)$ is causal, one can show that $g_T * p = g * p = h$ for $t \leqslant T$. Inserting this relation into the above equation gives

$$E_g \geqslant \int_{-\infty}^{T} |h|^2 dt, \tag{18}$$

which is Eq. (12).

Finally, the minimum phase is often described as the phase obtained by taking the Hilbert transform of the logarithm of the magnitude.[13] If the minimum phase function is written as

$$H_{\mathrm{mp}}(\omega) = \exp(\alpha_{\mathrm{mp}} + i\theta_{\mathrm{mp}}), \tag{19}$$

then the minimum phase and log magnitude are related by

$$\theta_{\mathrm{mp}}(\omega) = \mathcal{H}\{\alpha_{\mathrm{mp}}(\omega)\}, \tag{20}$$

$$\alpha_{\mathrm{mp}}(\omega) = \alpha(0) + \mathcal{H}\{\theta_{\mathrm{mp}}(\omega)\}. \tag{21}$$

This description is of course related to the others. If $H_{\mathrm{mp}}(\omega)$ has no zeros in the upper plane, then one can create a new transfer function by taking the logarithm of Eq. (19). The real and imaginary parts of this new transfer function are related by the Hilbert transform relations in Eqs. (3) and (4), leading to the above equations.

III. A RESPONSE-BASED DESCRIPTION OF THE MINIMUM PHASE CONDITION

In this section, a time-domain description of the minimum phase condition is presented that complements the descriptions in the previous section by giving physical insight into the time-domain response of nonminimum phase functions. For clarity, the discussion begins with a simple form of the all-pass function in Eq. (8). Following discussion of this example, a generalization is presented.

Consider a single Blaschke factor,

$$H_{\mathrm{ap}}(\omega) = \frac{\omega - u}{\omega - u^*}. \tag{22}$$

The real-valued condition in Eq. (5) leads to the condition that u be pure imaginary. Writing $u = iu_i$, the function is expressed as

$$H_{\mathrm{ap}}(\omega) = 1 - u_i \frac{2u_i - i2\omega}{u_i^2 + \omega^2}. \tag{23}$$

When this function is taken into the time domain by Eq. (2), the following simple form results:[20]

$$h_{\mathrm{ap}}(t) = \begin{cases} 0, & t < 0, \\ \delta(t) - 2u_i e^{-u_i t}, & t \geqslant 0. \end{cases} \tag{24}$$

The frequency-domain multiplication of the all-pass and minimum phase functions in Eq. (6) amounts to a convolution in the time domain,

$$h_{\mathrm{nmp}}(t) = h_{\mathrm{ap}}(t) * h_{\mathrm{mp}}(t). \tag{25}$$

Using Eq. (24), the nonminimum phase impulse response is

$$h_{\mathrm{nmp}}(t) = h_{\mathrm{mp}}(t) - 2u_i[e^{-u_i t} * h_{\mathrm{mp}}(t)]. \tag{26}$$

Therefore, the nonminimum phase response is a sum of the minimum phase response and the response of the minimum phase system to an additional exponential forcing function.

Generalization of this result to the general case is conceptually straightforward. The all-pass function in Eq. (8) is cast in the form

$$H_{\mathrm{ap}}(\omega) = 1 - H_{\mathrm{rem}}(\omega). \tag{27}$$

Substituting Eq. (27) into Eq. (6) gives

$$H_{\mathrm{nmp}}(\omega) = H_{\mathrm{mp}}(\omega) - H_{\mathrm{mp}}(\omega) H_{\mathrm{rem}}(\omega), \tag{28}$$

or, in the time domain,

$$h_{\mathrm{nmp}}(t) = h_{\mathrm{mp}}(t) - h_{\mathrm{rem}}(t) * h_{\mathrm{mp}}(t). \tag{29}$$

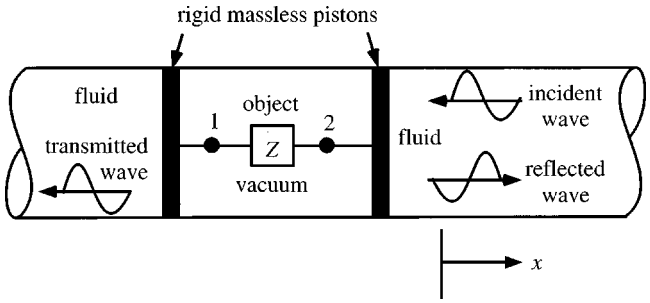

FIG. 1. A schematic of the one-dimensional reflection and transmission of acoustic waves by a passive linear object.

These results indicate that the nonminimum phase impulse response is the sum of the equivalent minimum phase impulse response and the response of the minimum phase system to a forcing function of $h_{\mathrm{rem}}(t)$.

It is interesting to note that this forcing function, $h_{\mathrm{rem}}(t)$, is causal and real-valued. One may observe the real-valued property by evaluating the real and imaginary parts of Eq. (27) at negative and positive frequencies. These evaluations lead to

$$H_{\mathrm{rem}}(\omega)=H^{*}_{\mathrm{rem}}(-\omega). \tag{30}$$

The remainder function is recognized as causal by taking the inverse Fourier transform of Eq. (27),

$$h_{\mathrm{rem}}(t)=\delta(t)-h_{\mathrm{ap}}(t). \tag{31}$$

Because $\delta(t)$ and $h_{\mathrm{ap}}(t)$ are both causal, $h_{\mathrm{rem}}(t)$ must be causal.

IV. A MINIMUM PHASE CONDITION FOR THE REFLECTION COEFFICIENT

In this and the following sections, the minimum phase condition is explored for the reflection coefficient of a passive object immersed in an infinite waveguide. For clarity, the one-dimensional problem shown in Fig. 1 will serve as the basis for discussion. In this figure, the object is positioned in an infinite waveguide of cross-sectional area A that contains a fluid with sound speed c and mass density ρ. Forces are transmitted between the object and the fluid via two rigid massless pistons. The object is ensonified by an incident wave, creating reflected and transmitted waves that propagate away from the object.

In the frequency domain, the dynamic properties of the object are completely described by an impedance matrix that relates forces and velocities at the ports labeled 1 and 2 in the figure according to

$$\begin{Bmatrix} F_1(\omega) \\ F_2(\omega) \end{Bmatrix} = \begin{bmatrix} Z_{11}(\omega) & Z_{12}(\omega) \\ Z_{21}(\omega) & Z_{22}(\omega) \end{bmatrix} \begin{Bmatrix} V_1(\omega) \\ V_2(\omega) \end{Bmatrix}, \tag{32}$$

where F_1 and F_2 are the forces applied to the object by the fluid in the directions of the velocities V_1 and V_2, all of which are defined as positive in the x direction. Reciprocity requires the impedance matrix to be symmetric, so that $Z_{12}(\omega)=Z_{21}(\omega)$. The effective impedance seen by the incident wave is simply $Z_{\mathrm{eff}}=F_2/V_2$.

This effective impedance is found by noting equal and opposite forces between the object and the fluid at port 1 and by noting that the fluid to the left of the object requires the ratio $F_1/V_1=-Z_{\mathrm{fl}}$, where $Z_{\mathrm{fl}}=\rho cA$. Algebraic combination of this result with Eq. (32) gives the effective impedance seen by the incident wave,

$$Z_{\mathrm{eff}}=Z_{22}-\frac{Z_{12}^2}{Z_{11}+Z_{\mathrm{fl}}}. \tag{33}$$

The effective impedance is the drive-point impedance presented by the object and the fluid to the left of the object if the fluid to the right of the object were removed. It has been shown that the drive-point impedance of any linear system, electrical or mechanical, belongs to a class of ''positive real'' functions.[1,21] These functions possess many interesting properties, but the most important to the present discussion is that the real part of a positive real function is positive in the upper half of the complex frequency plane and on the real frequency axis. This property, which is a direct consequence of causality and passivity, will be used in the following sections to identify minimum phase reflection coefficients for two special cases.

When an incident wave of unit amplitude strikes the object, a reflected wave is created that propagates away from the object. The acoustic pressure in the fluid due to this reflected wave is

$$P_r(\omega,x)=R(\omega)e^{ik(\omega)x}, \tag{34}$$

where R is the reflection coefficient and $k=\omega/c$ is the acoustic wavenumber. Continuity of force and displacement at the right-hand piston face yields an algebraic relationship between the reflection coefficient and the effective impedance,[22]

$$R(\omega)=\frac{z_{\mathrm{eff}}(\omega)-1}{z_{\mathrm{eff}}(\omega)+1}, \tag{35}$$

where the normalized effective impedance is

$$z_{\mathrm{eff}}(\omega)=Z_{\mathrm{eff}}(\omega)/(\rho cA). \tag{36}$$

The reflection coefficient is minimum phase when it has no zeros in the upper half of the complex frequency plane. One means of satisfying this condition is to require the real part of the numerator to be strictly positive or negative in this region, so that it cannot pass through a zero. If either

$$\Re\{z_{\mathrm{eff}}(\omega)\}>1 \quad \text{for } \Im\{\omega\}\geqslant 0 \tag{37}$$

or

$$\Re\{z_{\mathrm{eff}}(\omega)\}<1 \quad \text{for } \Im\{\omega\}\geqslant 0, \tag{38}$$

then R is minimum phase. Evaluation of these criteria requires a detailed knowledge of the generally complex-valued impedance matrix. In the envisioned applications, where only the magnitude of the reflection coefficient is measured, one usually knows very little about the impedance matrix and the above criterion are not helpful. This difficulty is overcome in the special cases described in the following two sections.

Before considering these special cases, let us develop some additional physical intuition of the minimum phase condition on the reflection coefficient by specializing the time-domain descriptions presented in the previous two sec-

tions. The reflection coefficient may be interpreted as the Fourier transform of the reflected pressure due to an incident wave that applies a Dirac pressure distribution to the object at time $t=0$. Since the magnitude of the acoustic intensity vector for a plane wave is $I=p^2/(\rho c)$, the energy quantity defined in Eq. (11) is proportional to the integrated acoustic energy that has left the object up to time T. Therefore, an object with a minimum phase reflection coefficient has the property of reflecting the acoustic energy faster than an object with the same magnitude of reflection coefficient but with a nonminimum phase.

The response-based description of the minimum phase property presented in the previous section also provides a physical basis for interpreting the reflection coefficient. In particular, Eq. (29) can be applied to the reflection problem by interpreting h_{nmp} as the pressure reflected by a nonminimum phase object. This pressure is a sum of two terms. The first is identified as the pressure reflected when a Dirac incident wave ensonifies a minimum phase object with the same reflection coefficient magnitude. The second term is the pressure radiated by the same minimum phase object when forced by a pressure distribution of $-h_{\mathrm{rem}}(t)$ applied to the object.

V. SYSTEMS WITH PERFECT VELOCITY TRANSFER

In this section, the reflection coefficient is shown to be minimum phase when the velocities at points 1 and 2 in Fig. 1 are equal. This situation is sometimes referred to as "perfect velocity transfer." While it is tempting to interpret this as a rigid body condition, one must bear in mind that the object may have internal degrees-of-freedom due to internal inertia and flexibility. The condition of perfect velocity transfer only requires that the boundary velocities at points 1 and 2 are equal. One example of such an object would be a very stiff container with an assemblage of masses, springs, and dashpots inside.

In order to understand the conditions that lead to perfect velocity transfer, Eq. (32) is inverted to the form

$$\begin{Bmatrix} V_1(\omega) \\ V_2(\omega) \end{Bmatrix} = \begin{bmatrix} Y_{11}(\omega) & Y_{12}(\omega) \\ Y_{21}(\omega) & Y_{22}(\omega) \end{bmatrix} \begin{Bmatrix} F_1(\omega) \\ F_2(\omega) \end{Bmatrix}, \tag{39}$$

where the admittance matrix is the inverse of the impedance matrix, $[Y]=[Z]^{-1}$. Equating the velocities leads to the condition

$$(Y_{11}-Y_{12})F_1=(Y_{22}-Y_{12})F_2. \tag{40}$$

For this equation to hold for arbitrary frequency-dependent forces, every element in the admittance matrix must be identical so that

$$[Y]=\begin{bmatrix} Y_{\mathrm{vt}} & Y_{\mathrm{vt}} \\ Y_{\mathrm{vt}} & Y_{\mathrm{vt}} \end{bmatrix}, \tag{41}$$

where the subscripted vt denotes the assumed "velocity transfer" property of the object. Substitution of this result into Eq. (39) yields the simple relation

$$F_{\mathrm{net}}=Z_{\mathrm{vt}}V, \tag{42}$$

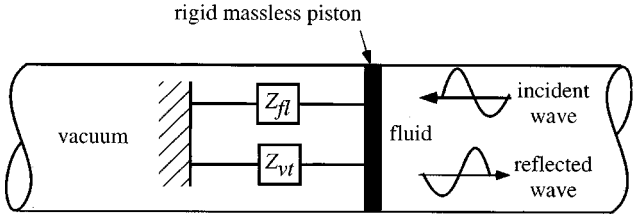

FIG. 2. A schematic of the system in Fig. 1 under the assumption that the object transmits velocity.

where the net force acting on the object is $F_{\mathrm{net}}=F_1+F_2$ and V is either V_1 or V_2. The velocity transfer impedance is simply $Z_{\mathrm{vt}}=1/Y_{\mathrm{vt}}$. This impedance acts in parallel to the acoustic impedance of the fluid to the left of the piston because the velocities of the fluid and the object are identical. Alternatively, the structural admittance acts in series with the fluid admittance.

A schematic of the reduced system is shown in Fig. 2. The normalized effective impedance defined by Eqs. (33) and (36) is simply

$$z_{\mathrm{eff}}=1+z_{\mathrm{vt}}. \tag{43}$$

Now, we use the previously quoted result that the drive-point impedance, z_{vt}, of a passive linear system is a positive real function. Its real part is always positive in the upper half of the complex frequency plane and the real part of z_{eff} is always greater than unity. Therefore, the condition in Eq. (37) is met and the reflection coefficient is always minimum phase.

To illustrate this result, let us consider objects that satisfy the velocity transfer assumption. For these examples, the impedance of the object is generated by the following Fourier series with real-valued Fourier coefficients:

$$z_{\mathrm{vt}}(\omega)=a_0+\sum_{n=1}^{N} a_n \exp\left(\frac{in\pi\omega}{\Omega}\right). \tag{44}$$

This function satisfies the causality condition in Eqs. (3) and (4), since the Hilbert transform of $\sin(n\pi\omega/\Omega)$ is $\cos(n\pi\omega/\Omega)$. For $n>0$, the coefficients are chosen by

$$a_n=\frac{a_0(1-2r_n)}{N}, \tag{45}$$

where r_n is a random number that is uniformly distributed over the interval $0\leqslant r_n\leqslant 1$. This selection insures that $\Re\{z_{\mathrm{vt}}\}>0$ and the system is therefore passive. In all of our simulations, we set $N=50$. The leading term, a_0, was used to control the magnitude of the impedance.

In the first example, we set $a_0=0.1$ to simulate an approximately pressure-release surface. The real and imaginary parts of the object impedance obtained by using this value in Eqs. (44) and (45) are shown in Fig. 3. The reflection coefficient was evaluated using Eq. (35). The magnitude and phase of the reflection coefficient are shown in Fig. 4. In the envisioned applications, the phase would not be known and causality would be used to predict it from the magnitude. To this end, a causally predicted phase is computed by inserting the magnitude of the reflection coefficient in Eq. (21). This

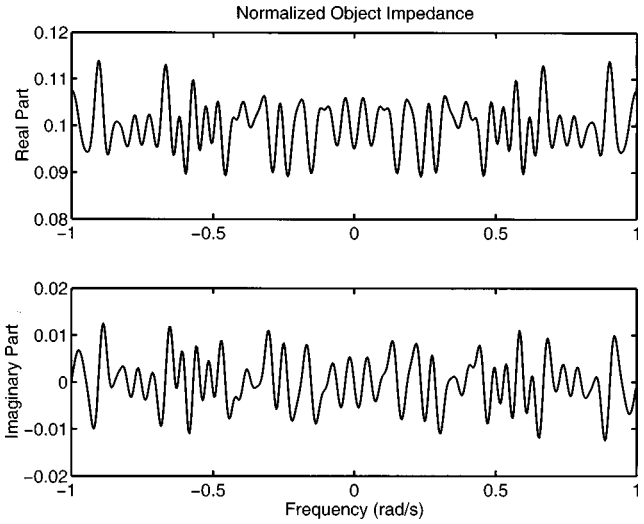

FIG. 3. Real and imaginary parts of normalized object impedance, z_{vt}, for an object that transfers velocity and has a low magnitude of impedance.

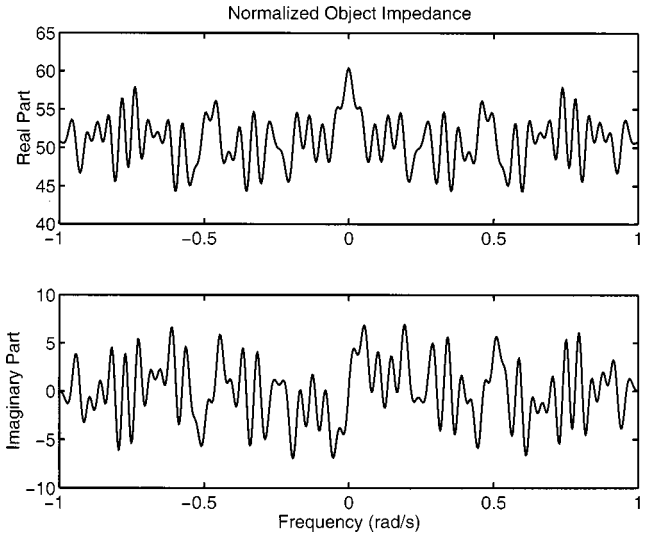

FIG. 5. Real and imaginary parts of normalized object impedance, z_{vt}, for an object that transfers velocity and has a high magnitude of impedance.

phase coincides with the actual phase in Fig. 4, indicating that the reflection coefficient is indeed minimum phase.

To further illustrate this result, an object with a large reflection coefficient magnitude was simulated by choosing $a_0=50$. The real and imaginary parts of the resulting impedance are shown in Fig. 5, where we see a magnitude that exceeds 0.95 everywhere. The magnitude and phase of the reflection coefficient are shown in Fig. 6. Again, the causally predicted phase coincides with the actual phase because the reflection coefficient is minimum phase.

VI. SYSTEMS WITH PERFECT FORCE TRANSFER

This section describes the minimum phase reflection coefficient that results when an object transmits force perfectly. To achieve this limit, the forces applied to the object by the fluid must be equal but opposite, $F_1=-F_2$. Physically, this condition results when the mass of the object is small. Newton's second law then requires the net force on the object to be zero. One example of such a system is a layer of air in water with a normally incident wave.

Applying this condition to Eq. (32) results in

$$(Z_{11}+Z_{12})V_1=-(Z_{12}+Z_{22})V_2. \tag{46}$$

For this equation to hold for arbitrary frequency-dependent velocities, the impedance matrix must have the form

$$[Z]=\begin{bmatrix} Z_{\mathrm{ft}} & -Z_{\mathrm{ft}} \\ -Z_{\mathrm{ft}} & Z_{\mathrm{ft}} \end{bmatrix}, \tag{47}$$

where the subscripted ft denotes the assumed ''force transfer'' property of the object.

Substitution of this result into Eq. (32) yields the simple relation

$$F_1=-F_2=Z_{\mathrm{ft}}(V_2-V_1). \tag{48}$$

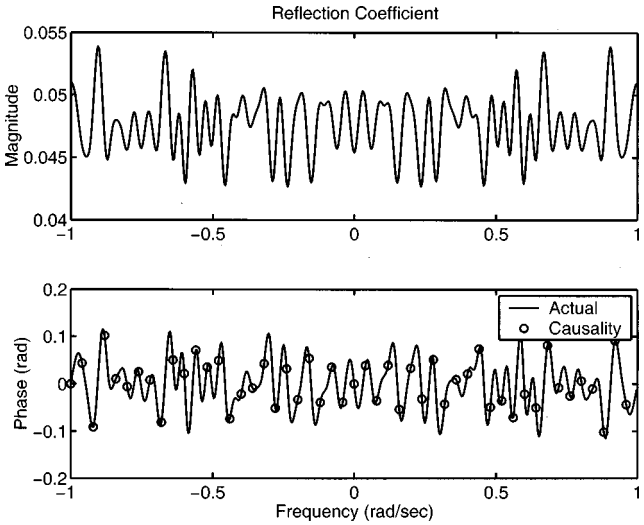

FIG. 4. Magnitude and phase of the reflection coefficient for an object that transfers velocity and has the impedance shown in Fig. 3. Causality is used to recover the phase from the magnitude.

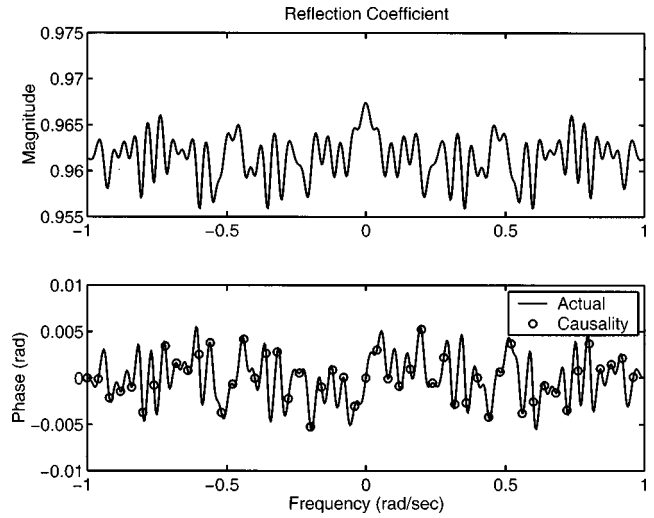

FIG. 6. Magnitude and phase of the reflection coefficient for an object that transfers velocity and has the impedance shown in Fig. 5. Causality is used to recover the phase from the magnitude.

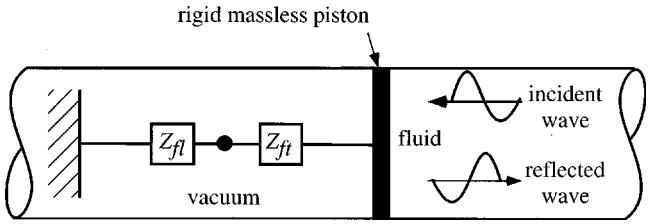

FIG. 7. A schematic of the system in Fig. 1 under the assumption that the object transmits force.

Recalling that $F_1 = -Z_{\mathrm{fl}} V_1$, one finds that this impedance acts in series with the acoustic impedance of the fluid to the left of the piston. Therefore, the normalized effective impedance is

$$z_{\mathrm{eff}} = \frac{z_{\mathrm{ft}}}{1 + z_{\mathrm{ft}}}. \tag{49}$$

A schematic of the reduced system is shown in Fig. 7. This reduced system can also be represented by parallel admittances, so that the effective normalized admittance is $y_{\mathrm{eff}} = 1 + y_{\mathrm{ft}}$. The reflection coefficient is found from Eq. (35),

$$R = \frac{1 - y_{\mathrm{eff}}}{1 + y_{\mathrm{eff}}}. \tag{50}$$

It has been shown[21] that the drive-point admittance is also a positive real function. Therefore, its real part is always positive in the upper half of the complex frequency plane and the real part of y_{eff} is always greater than unity. The condition in Eq. (38) is met and the reflection coefficient is always minimum phase.

This finding will be illustrated by generating random admittances in the same way that random impedances were generated in the previous section. The admittance of the object is generated by the following Fourier series with real-valued Fourier coefficients:

$$y_{\mathrm{ft}}(\omega) = a_0 + \sum_{n=1}^{N} a_n \exp\left(\frac{in\pi\omega}{\Omega}\right), \tag{51}$$

which is causal and real-valued in the time domain. The passivity condition is satisfied by the choice of a_n given in Eq. (45). Again, we set $N = 50$ in all of the examples.

Choosing $a_0 = 50$ creates a large object admittance that results in a small reflection. The real and imaginary parts of the object admittance obtained by using this value in Eqs. (51) and (45) are shown in Fig. 8. In order to show that the reflection coefficient for this object is minimum phase, it was evaluated using Eq. (35). The magnitude and phase of the reflection coefficient computed from Eq. (50) are shown in Fig. 9. As in the previous section, a causally predicted phase is computed by inserting the reflection coefficient magnitude in Eq. (21). This phase coincides with the actual phase in Fig. 9, indicating that the reflection coefficient is indeed minimum phase.

This finding persists even when the object admittance is very low. Choosing $a_0 = 0.1$ creates a low admittance whose real and imaginary parts are shown in Fig. 10. Figure 11 shows the magnitude and phase of the associated reflection

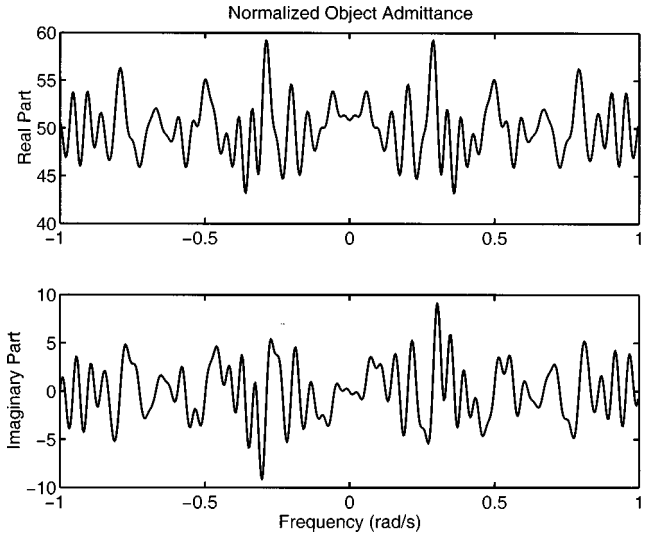

FIG. 8. Real and imaginary parts of normalized object admittance, y_{ft}, for an object that transfers force and has a high magnitude of admittance.

coefficient. Again, the agreement between the actual phase and the causally predicted phase confirms the analytical result that the reflection coefficient is minimum phase.

VII. CONCLUSIONS

A response-based description of the minimum phase condition in the time domain has been developed and applied to the one-dimensional interactions of acoustic waves with a submerged object. This description decomposes the nonminimum phase reflection into the reflection from an equivalent minimum phase structure and the radiation created by a forcing function applied to the object. An energy-based description of the minimum phase condition presented by Eisner has also been valuable. In particular, this description reveals that an object with a minimum phase reflection coefficient returns energy to the fluid sooner than an equivalent nonminimum phase object.

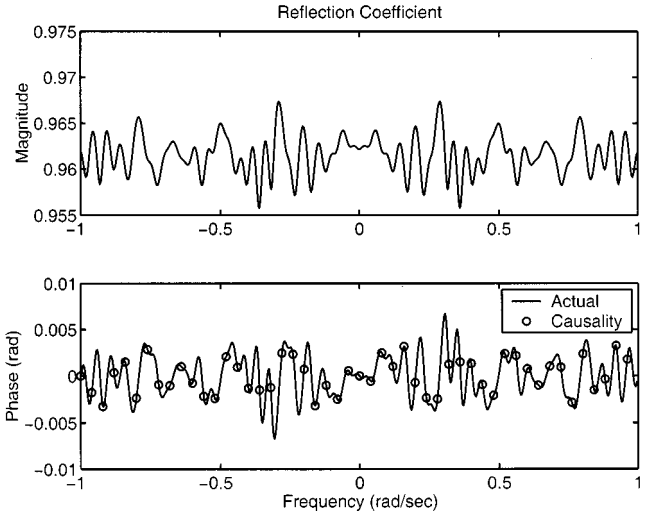

FIG. 9. Magnitude and phase of the reflection coefficient for an object that transfers force and has the admittance shown in Fig. 8. Causality is used to recover the phase from the magnitude.

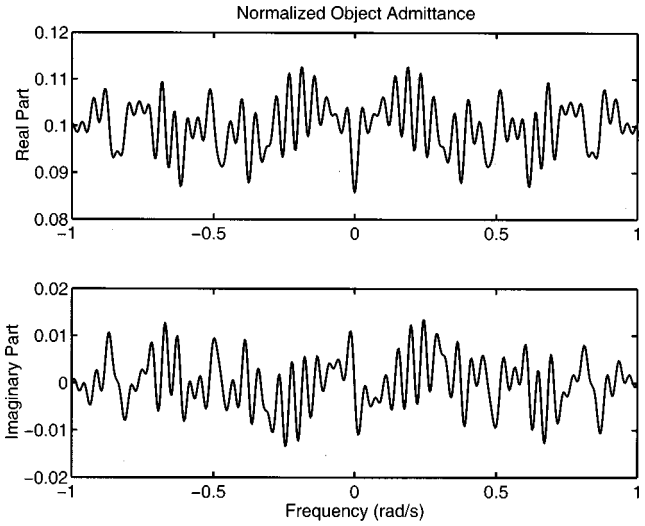

FIG. 10. Real and imaginary parts of normalized object admittance, y_{ft}, for an object that transfers force and has a low magnitude of admittance.

A condition on the impedance matrix was derived that guarantees a minimum phase reflection coefficient. While the condition is impossible to evaluate in cases where only the reflection coefficient magnitude is measured, it did lead to two special cases. In particular, it was shown that submerged objects that either transmit force or velocity from one body of fluid to another always create minimum phase reflection coefficients. The proofs were based on the positive real properties of drive-point impedance and admittance. The numerical examples confirmed these analytical results for structures with small and large reflection coefficients.

The results of this one-dimensional study are expected to be useful in two contexts. First, the results will be applicable to problems involving acoustic transmission through nonhomogeneous layers that satisfy either the force or velocity transfer condition. Here, the results allow one to characterize the frequency-dependent layer properties by only measuring the magnitude of reflected sound. Second, the results will provide a basis for analyzing more complex three-dimensional scattering problems. For example, monostatic scattering measurements for three-dimensional structures can be modeled by replacing the structure with an effective impedance screen that is perpendicular to the incident wave front. This will be the subject of a future paper.

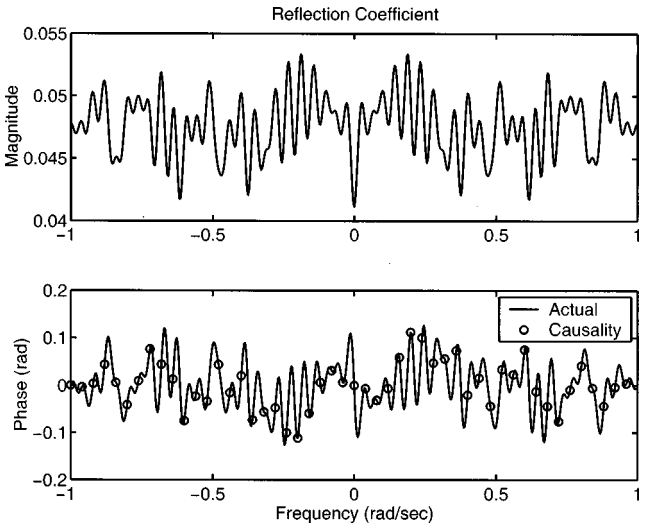

FIG. 11. Magnitude and phase of the reflection coefficient for an object that transfers force and has the admittance shown in Fig. 10. Causality is used to recover the phase from the magnitude.

ACKNOWLEDGMENTS

This work was supported by the Office of Naval Research under Grant No. N00014–99–1–1017. The authors are grateful for the encouragement and technical advice from Dr. Geoffrey Main and Dr. Luise Couchman during the course of the work. Portions of the work were inspired by conversations with Dr. Richard Weaver. Insights from Dr. Robert Burridge were useful in clarifying the mathematical properties of positive real functions.

[1] A. Papoulis, *The Fourier Integral and Its Applications*, Electronic Science Series (McGraw-Hill, New York, 1962).
[2] S. L. Hahn, ''Hilbert transforms,'' in *The Transforms and Applications Handbook*, edited by A. D. Poularikas, Studies in Applied Mechanics (CRC and IEEE, New York, 2000).
[3] H. A. Kramers, ''La difusion de la lumiere par les atomes,'' Estratto dagli Atti del Congresso Internazionale de Fisici Como **2**, 545–557 (1927).
[4] R. de L. Kronig, ''On the theory of the dispersion of x-rays,'' J. Opt. Soc. Am. **12**, 547–557 (1926).
[5] H. M. Nussenzveig, *Causality and Dispersion Relations* (Academic, New York, 1972).
[6] J. Hilgevoord, *Dispersion Relations and Causal Description* (North-Holland, Amsterdam, 1960).
[7] Y. W. Lee, ''Synthesis of electric networks by means of the Fourier transforms of Laguerre's functions,'' J. Math. Phys. (Cambridge, Mass.) **11**, 83–113 (1932).
[8] H. W. Bode, *Network Analysis and Feedback Amplifier Design* (Van Nostrand, Princeton, New Jersey, 1945).
[9] E. A. Guillemin, *Synthesis of Passive Networks* (Wiley, New York, 1957).
[10] T. T. Wu, ''Some properties of impedance as a causal operator,'' J. Math. Phys. **3**(2), 262–271 (1962).
[11] T. K. Sarkar, ''Generation of nonminimum phase from amplitude-only data,'' IEEE Trans. Microwave Theory Tech. **46**(8), 1079–1084 (1998).
[12] V. Mangulis, ''Kramers-Kronig or dispersion relations in acoustics,'' J. Acoust. Soc. Am. **36**, 211–212 (1964).
[13] R. P. Radlinski and T. J. Meyers, ''Radiation patterns and radiation impedances of a pulsating cylinder surrounded by a circular cage of parallel cylindrical rods,'' J. Acoust. Soc. Am. **56**, 842–848 (1974).
[14] J. G. McDaniel, ''Applications of the causality condition to one-dimensional acoustic reflection problems,'' J. Acoust. Soc. Am. **105**, 2710–2716 (1999).
[15] E. Eisner, ''Minimum phase for continuous time and discrete time functions,'' Geophys. Prospect. **32**, 533–541 (1984).
[16] M. Tohyama and T. Koike, *Fundamentals of Acoustic Signal Processing* (Academic, New York, 1998).
[17] R. H. Lyon, ''Statistics of phase and magnitude of structural transfer functions,'' in *Random Vibration—Status and Recent Developments, Studies in Applied Mechanics*, edited by I. Elishakoff and R. H. Lyon (Elsevier, Amsterdam, 1986), pp. 201–208.
[18] B. C. Kuo, *Automated Control Systems*, 6th ed. (Prentice Hall, Englewood Cliffs, NJ, 1991).
[19] J. D. Victor, ''Temporal impulse response from flicker sensitivities: causality, linearity, and amplitude data do not determine phase,'' J. Opt. Soc. Am. **6**, 1302–1303 (1989).
[20] K. B. Howell, ''Fourier transforms,'' in *The Transforms and Applications Handbook*, Studies in Applied Mechanics, edited by A. D. Poularikas (CRC Press and IEEE Press, 2000).
[21] E. A. Guillemin, *The Mathematics of Circuit Analysis* (Wiley, New York, 1949).
[22] A. D. Pierce, *Acoustics, An Introduction to Its Physical Principal and Applications* (Acoustical Society of America, Woodbury, NY, 1989).

On the emergence of the Green's function in the correlations of a diffuse field

Oleg I. Lobkis and Richard L. Weaver
Theoretical and Applied Mechanics, 104 South Wright Street, University of Illinois, Urbana, Illinois 61801

(Received 13 June 2001; revised 15 September 2001; accepted 17 September 2001)

A diffuse acoustic field is shown to have correlations equal to the Green's function of the body. Simple plausibility arguments for this assertion are followed by a more detailed proof. A careful version of the statement is found to include caveats in regard to how diffuse the field truly is, the spectrum of the diffuse field, and the phase of the receivers. Ultrasonic laboratory tests confirm the assertion. The main features of the direct signal between two transducers are indeed recovered by cross correlating their responses to a diffuse field generated by a third transducer. The quality of the recovery improves with increased averaging and the use of multiple sources. Applications are discussed. © *2001 Acoustical Society of America.* [DOI: 10.1121/1.1417528]

PACS numbers: 43.40.Qi, 43.40.Hb, 43.35.Yb [DEC]

I. INTRODUCTION

The literature of the last several years on diffuse ultrasonic fields in solids,[1–6] on diffuse vibrations in structural acoustics,[6–11] and on diffuse seismic fields in the earth's crust[12–14] has largely neglected the field's phase, and focused instead on the field's spectral energy density. This is for good reason; fields which have reflected or scattered many times from specimen surfaces or inclusions resist detailed analysis. The spectral energy density of such a field evolves slowly and in a manner that may be comprehended by theory, but the phase is not predicted. The amplitude of typical diffuse field signals is predictable; the details of the stochastic waveforms are not. More recently it has been pointed out that diffuse field phase, while not predictable, varies with specimen temperature in a simple fashion.[15,16]

While phase is not predictable, in many systems it is coherent. There are definite correlations that survive the multiple scattering. These correlations manifest in striking phenomena, acoustic time reversal (e.g., Refs. 17–20), and weak localization[21–23] being among them. Kramers–Kronig relations indicate that phase is related to features in spectral power densities, so a recent report that a diffuse field has fine spectral features related to local geometry[24] is implicitly also an indication that the field's phase has such information. There are also some indications in older work that local geometry information is implicit in diffuse field spectra.[3,4,25] Here it will be shown that one can be much more precise about the information in the fine features of the spectrum, and that the diffuse field, including its phase and amplitude variations in space and time, contains information exactly equivalent to local responses. More specifically, the temporal cross-correlation function between the signals received simultaneously in two distinct transducers is shown to be the signal which one transducer would receive when the other is given an impulsive excitation. The correlation displays all travel paths between the two points, including those with multiple reflections. A similar observation was recently made by Draeger and Fink.[20]

In the next section that assertion is given two rough proofs, each of which is intended to illuminate some of the basic physics behind the equivalence. Then the equivalence is derived more carefully, under certain approximations, for the case in which the field is generated by a third transducer and is not necessarily fully diffuse and/or may have spectral features of its own. Theoretical estimates are suggested for the amount of averaging necessary before convergence may be achieved. An ultrasonic laboratory demonstration, for the case of a reverberant solid body, is presented in Sec. IV. The article concludes with a discussion of some remaining discrepancies and of potential extensions and applications.

II. PLAUSIBILITY ARGUMENTS

That the correlations of a diffuse field are related to local transient responses is easy to establish. In this section two distinct arguments are presented. The first is based on the standard definition of a diffuse field, as one with uncorrelated random modal amplitudes with equal variances. The second is based on an assumption that an instantaneous diffuse field is spatially uncorrelated.

A. Plausibility argument no. 1

A diffuse field ϕ in a finite body may be expressed in modal form by

$$\phi(x,t)=\Re\sum_{n=1}^{\infty} a_n u_n(x)\exp\{i\omega_n t\}, \tag{1}$$

where the a_n are complex modal amplitudes and the u_n are the real orthogonal mode shapes. If the field is elastodynamic, u and ϕ are vector valued. The u_n are real and orthonormal:

$$\int \rho u_n\cdot u_m\, d^3\mathbf{x}=\delta_{nm}.$$

A statement that the field ϕ is diffuse with specified real spectral power density is equivalent to stating that the modal amplitudes are uncorrelated random variables

$$\langle a_n a_m^*\rangle=\delta_{nm}F(\omega_n), \tag{2}$$

where F is a smooth function related to spectral energy density, equal to $\frac{1}{2}F\langle u^2\rangle$ times the modal density.

It is a simple matter to construct the cross correlation of the fields at x and y:

$$\langle \phi(x,t)\phi(y,t+\tau)\rangle = \frac{1}{2}\Re\sum_{n=1}^{\infty} F(\omega_n)u_n(x)u_n(y) \times \exp\{-i\omega_n\tau\}. \quad (3)$$

If $F\sim$const and an antiderivative $\int_0^\tau(\,)d\tau$ is taken, this is readily recognized as similar to the Green's function G_{xy} governing propagation from x to y

$$G_{xy}(\tau) = \sum_{n=1}^{\infty} u_n(x)u_n(y)\frac{\sin\omega_n\tau}{\omega_n} \quad (\text{for } \tau>0, \quad 0, \text{ otherwise}). \quad (4)$$

The expression (3) differs from the time derivative of the actual Green's function by (a) the presence of the factor $F/2$ which modifies its spectrum, and (b) by (3)'s support at negative τ.

B. Plausibility argument no. 2

That local response would emerge from correlations of a diffuse field is also apparent from a propagator description. In the absence of external loads acting in the interval $[t,t+\tau]$, the field at time $t+\tau$ may be determined by propagation from initial conditions at time t by means of a matrix multiplication:

$$\begin{Bmatrix}\phi(y)\\ \dot\phi(y)\end{Bmatrix}_{t+\tau} = \int \frac{1}{\rho(x)}\begin{bmatrix}\dot G_{yx}(\tau) & G_{yx}(\tau)\\ \ddot G_{yx}(\tau) & \dot G_{yx}(\tau)\end{bmatrix}\begin{Bmatrix}\phi(x)\\ \dot\phi(x)\end{Bmatrix}_t d^3x. \quad (5)$$

This expression is not widely employed, but it is not difficult to prove. It follows readily from the usual definition of the Green's function as relating concentrated impulsive loads to subsequent responses, and a recognition that initial conditions $\{\phi(x),\dot\phi(x)\}$ may be established in a previously quiescent system by application of a distributed impulse $\phi(x)\,\delta(t)/\rho(x)$ and a distributed derivative-of-an-impulse $\dot\phi(x)\,\delta(t)/\rho(x)$.

A presumption that the fields at time t have no spatial correlations,

$$\langle \phi(x,t)\phi(y,t)\rangle = \delta^3(x-y)\Phi(x); \quad \langle \phi(x,t)\dot\phi(y,t)\rangle = 0, \quad (6)$$

then leads to a conclusion that the fields at different times *are* correlated:

$$\langle \phi(y,t+t) \quad \phi(x,t)\rangle = \Phi(x)/\rho(x) \quad \dot G_{yx}(\tau). \quad (7)$$

An actual field can be expected to have short-range correlations at fixed times, correlations with a range inversely proportional to the bandwidth of the diffuse field. Thus this argument is incompletely satisfactory.

Each of the above arguments establishes the plausibility of the assertion. Each also indicates that there may exist subtleties related to the spectrum of the diffuse field. Each has conveniently disregarded other subtleties as to what precisely is meant by the averaging $\langle\,\rangle$. In the next section we attempt a derivation of the central assertion, a derivation based on more precise statements about the spectrum of the diffuse field, and more precise statements as to what is meant by the averaging. It also treats practical complications that would attend the use of receivers with finite bandwidths.

III. DETAILED ARGUMENT

In practice, ultrasonic fields are diffuse only in a limited sense, even long after the source has acted. They do not precisely satisfy (2), if for no other reason then because it is far from clear what is meant by the averaging. The a_m are constants, independent of time and space. In practice there is no ensemble for laboratory averaging. Spatial averaging in the laboratory is avoided as tedious. Nevertheless, a particular transient source in a finite elastic body is expected to excite modes with no particular biases. There is a sense in which each mode receives a random amount of energy, proportional to its (random) participation at the site where the load is applied, and that short-range frequency averages ought to be equivalent to the theoretician's ensemble averages.

Here we consider an ultrasonic field to be created by a deterministic transient load applied at a source point "s" in an elastic body. This is the case in laboratory practice. Subsequent to the action of this source, and subsequent to the ring time of the receivers, the responses in two receivers at x and y, and at the source at s, are given by

$$V_x(t) = \sum_{n=1}^{\infty} u_n(x)u_n(s)\Im[\tilde X(\omega_n)\tilde S(\omega_n)\exp\{i\omega_n t\}/\omega_n],$$
$$V_y(t) = \sum_{n=1}^{\infty} u_n(y)u_n(s)\Im[\tilde Y(\omega_n)\tilde S(\omega_n)\exp\{i\omega_n t\}/\omega_n], \quad (8)$$
$$V_s(t) = \sum_{n=1}^{\infty} u_n(s)^2\Im[\tilde S(\omega_n)^2\exp\{i\omega_n t\}/\omega_n],$$

where $\tilde X$, $\tilde Y$, and $\tilde S$ are the transducer receiver functions at x and y and the source function at s. These expressions will be used only at late times, so the condition $t>$ ring time of transducers, need not be emphasized.

Our central assertion is that the direct signal from x to y is somehow present in the correlations of V_x and V_y. But it will be seen that it is not the actual direct response that is recovered, but rather an acausal waveform u_{xy} given by

$$u_{xy}(t) = \sum_{n=1}^{\infty} u_n(x)u_n(y)\Im[\tilde X(\omega_n)\tilde Y(\omega_n)\exp\{i\omega_n t\}/\omega_n] \quad \forall t. \quad (9a)$$

The acausal waveform u_{xy} (9a) is the signal that would be received if the Green's function (4) were extended (acausally) to negative τ:

$$u_{xy}(t) = Y(t)\otimes G_{xy}^{(\text{Extended})}(t)\otimes X(t), \quad (9b)$$

where we have assumed that the source function $X(t)$ of the transducer at x is identical to the receiver function of the same transducer. Equation (9b) differs from the actual signal v_{xy} received at x due to a source at y:

$$v_{xy}(t) = Y(t) \otimes G_{xy}(t) \otimes X(t), \tag{10}$$

which is the convolution of transducer functions Y and X with the causal Green's function (4). The two expressions are identical, however, at times after the ring time of the transducers X and Y.

A temporal cross-correlation function between V_x and V_y is constructed by means of a time integration over a finite time interval ΔT centered on time T with window function $W(t)$:

$$C_{xy}(\tau) = \int_{t=-\Delta T/2}^{t=\Delta T/2} W(t) V_x(T+t) V_y(T+t+\tau)\, dt. \tag{11}$$

Averaging over an ensemble and/or over a set of source positions is also a possibility. On substituting (8) into (9), one obtains (after dropping the terms $\sim \exp\{\pm i(\omega_n+\omega_m)t\}$ that vanish if the integration time ΔT is long enough compared to the period of a typical frequency)

$$C_{xy}(\tau) = \frac{1}{2} \sum_n \sum_m u_n(x) u_m(y)\ [u_n(s) u_m(s)]/ \\ \omega_m \omega_n \Re \tilde{X}(\omega_n) \tilde{S}(\omega_n) \tilde{Y}^*(\omega_m) \tilde{S}^*(\omega_m) \\ \times \exp\{-i\omega_m \tau\} \tilde{W}(\omega_n - \omega_m) \exp\{iT(\omega_n - \omega_m)\}. \tag{12}$$

The double sum now reduces to a single sum, the cross terms $n \neq m$ vanishing. This follows immediately if the window duration ΔT is long compared to the "break time," [26] equal to the inverse of the mean eigenfrequency spacing, $2\pi/\Delta\omega$. It also follows, even at moderate ΔT, if we perform a further average over a large number of window center times T. This is rather similar to the case ΔT large. It also follows in a statistical sense when it is recognized that the factor $u_n(s)$ $u_m(s)$ is stochastic, with zero mean unless $n=m$. An average over all source positions s cancels the cross terms, too, due to orthogonality of the modes. Similarly, an average over a small number of discrete sources s should accelerate the cancellations. Thus we approximate

$$C_{xy}(\tau) \approx \tilde{W}(0) \sum_n \frac{[u_n(s)]^2 |\tilde{S}(\omega_n)|^2}{2\omega_n^2} \Re \tilde{X}(\omega_n) \tilde{Y}^*(\omega_n) \\ \times u_n(x) u_n(y) \exp\{-i\omega_n \tau\}. \tag{13}$$

Alternatively,

$$\dot{C}_{xy}(\tau) \approx \tilde{W}(0) \sum_n \frac{[u_n(s)]^2 |\tilde{S}(\omega_n)|^2}{2} \Im \tilde{X}(\omega_n) \tilde{Y}^*(\omega_n) \\ \times u_n(x) u_n(y) \exp\{-i\omega_n \tau\}/\omega_n. \tag{14}$$

A similar relation was recently given by Draeger and Fink (Ref. 20, p. 613) in terms of convolutions between time-reversed and non-time-reversed signals, i.e., cross-correlation functions. They stated that the convolution of the backscattering impulse response at a source point s with the time-reversed version of u_{xy} is the same as the convolution of the time-reversed response at x to the source at s, with the response at y to the source at s. Their expression, as given, is impossible to evaluate, inasmuch as backscattering point source impulse responses are singular at all times while the source is acting. We do not doubt, however, that the expressions are closely related.

Except for the factor $|S|^2 u_n(s)^2/2$ and the factor Y^*, Eq. (14) rather resembles the acausal waveform (9). If the first factor could be eliminated, or deconvolved, and if the factor Y^* could be replaced with Y, it would be precisely u_{xy}. As it stands, (14) represents a distorted version of that response.

The first factor, $|S|^2 u_n(s)^2/2$, in the summation is a positive quantity that depends on the source. It is the work done by the source on mode number n. We recognize that it is stochastic, with uncorrelated rapid variations among neighboring modes. If τ is much less than the break time T_{break}, at which these variations may be resolved, and if $u_n(s)^2$ is uncorrelated with $u_n(x)$ and $u_n(y)$, then the factor may be replaced with its (short range) frequency average. We define a real positive quantity $f(\omega_n)$ that depends on source position and source time function, but varies only slowly with frequency:

$$f(\omega) = \tfrac{1}{2} \langle u_n(s)^2 \rangle |\tilde{S}(\omega)|^2. \tag{15}$$

That such modal factors are uncorrelated in this manner was also assumed in a recent derivation of SEA-like formulas for mean square responses in complex systems.[24] The brackets $\langle\ \rangle$ now represent an average over modes n with frequencies ω_n in the vicinity of ω. The quantity $f(\omega)$ is the spectral density of work done by the source, divided by the modal density in the structure. If $|S|$ is known, and the structure is reasonably simple in the vicinity of the source, then f may be estimated analytically.

Too commonly, in ultrasonics anyway, transducer functions are not known. Very commonly the source vicinity is too complicated to allow analytic estimation of $\langle u(s)^2 \rangle$. We therefore propose to determine f by measurements of the autocorrelation function of V_s, a quantity that is not difficult to obtain.

$$C_{ss}(\tau) = \int_{t=-\Delta t}^{t=\Delta T} W(t) V_s(T+t) V_s(T+t+\tau)\, dt, \tag{16}$$

$$C_{ss}(\tau) \approx \tilde{W}(0) \Sigma_n \frac{[u_n(s)]^4 |\tilde{S}(\omega_n)|^4}{2\omega_n^2} \cos\{\omega_n \tau\}. \tag{17}$$

The power spectral density of V_s is the Fourier transform of C_{ss} and is clearly

$$\tilde{C}_{ss}(\omega) = \pi \frac{dN(\omega)}{d\omega} \tilde{W}(0) \langle u(s)^4 \rangle |S(\omega)|^4/2\omega^2, \tag{18}$$

where $dN/d\omega$ is the structure's modal density. We take $\langle u^4 \rangle = E\langle u^2 \rangle^2$ and conclude

$$f(\omega) = \sqrt{\frac{\omega^2 \tilde{C}_{ss}(\omega)}{2E\tilde{W}(0)\pi[dN/d\omega]}}. \tag{19}$$

The identification $\langle u^4 \rangle = E\langle u^2 \rangle^2$, with $E=3$, is accepted for generic structures at late times T. It corrects C for the modal echo, an enhancement of the signal in the vicinity of the source. At earlier times T that enhancement is only two. E's transition from 2 to 3 takes place on a time scale of the

break time, $T_B = 2\pi\ dN/d\omega$. T_B is frequency dependent. Thus we take E to have a T- and ω-dependent value between 2 and 3, as described elsewhere.[21–23] In any case, variations in E are relatively unimportant compared to the more severe variations usually found in C_{ss}.

We now conclude with a statement that the cross-correlation function between V_x and V_y, after differentiation with respect to time, and deconvolving the known function f and Y^*/Y, is

$$\frac{i\omega\tilde{C}_{xy}(\omega)}{f(\omega)}\frac{\tilde{Y}(\omega)}{\tilde{Y}^*(\omega)} = \frac{i\omega\tilde{V}_x(\omega)\tilde{V}_y^*(\omega)}{f(\omega)}\frac{\tilde{Y}(\omega)}{\tilde{Y}^*(\omega)}$$
$$= \tilde{u}_{xy}(\omega) = \tilde{X}(\omega)\tilde{Y}(\omega)\tilde{G}_{xy}^{\text{Extended}}(\omega). \tag{20}$$

After inverse Fourier transforming this is the acausal signal $u_{xy}(t)$, Eq. (9).

Equation (20) has been derived using a modal expansion valid in finite systems for which the time and/or spatial averaging is finite. There is good reason [cf. the plausibility argument Eq. (5)] for thinking it valid for open infinite systems, but a proof thereof has not been given. This is an important avenue for future research.

IV. SPEED AND ACCURACY OF CONVERGENCE

A priori estimates of the degree of averaging necessary before the Green's function actually emerges from the correlation are possible. The derivation above [see discussion following Eq. (12)] suggests that time averaging of the correlation function over a period comparable to the break time, $T_{\text{break}} = 2\pi/\text{mean eigenfrequency spacing} = 2\pi/\Delta\omega$, should suffice. In fact, the result is exact if the time integration is taken over the break time and if an additional average over all source positions is taken. Break times usually exceed signal durations and therefore averaging over that much time is generally going to be impractical. In unbounded bodies, the break time is infinite. Averaging over all source positions is clearly impossible; averaging over a few may prove impractical. Nevertheless, there is reason to think that a more moderate amount of averaging should suffice if the intent is to construct waveforms over short times τ only.

In the propagator description (5) one sees that the signal at time $t+\tau$ and position y is composed of an incoherent superposition of contributions from a large number of distant (distance $c\tau$) positions x. The number of such positions x may be estimated by assigning a cubic (square in 2-D) half-wavelength to each independent position x, and calculating a volume (area) that contributes at time-difference τ of $4\pi c[c\tau]^2/3\Delta f$ (or $2\pi c[c\tau]/\Delta f$ in 2-D) where $\Delta f \approx f$ is the bandwidth of the Green's function that is to be recovered. The number of such positions is $N = 32\pi(f\tau)^2/3$ in 3-D and $8\pi\tau f$ in 2-D. Simple arguments assuming all such positions contribute equally, but that most contribute essentially noise and only one of them (the one at the position of the other transducer) is not noise, then allow one to estimate that the signal emerges from the noise after a number of averages greater than the number of positions N. As an independent term in the average is contributed at different times t separated by $1/\Delta f$, we conclude that the correlation function needs to be assembled from a signal of duration $\Delta T \gg N/\Delta f$. This corresponds to $\Delta T \gg 32\pi\ \tau(\tau f)/3$ in 3-D and $\Delta T \gg 8\pi\tau$ in 2-D. In a two-dimensional structure with a multi-branched dispersion relation, e.g., a thick plate, this estimate must be augmented by a factor equal to the number of branches that contribute at the frequency of interest.

V. PRACTICAL IMPLEMENTATION

We have attempted to reconstruct local responses from diffuse fields in the simple blocklike structure of approximate dimensions $80\times140\times200\,\text{mm}^3$ used in an earlier report.[23] It is illustrated in Fig. 1. The signals V_x, V_y, and V_s were obtained using broadband Valpey–Fisher pin-transducers for which the greatest sensitivity lies in a frequency range from 0.1 to nearly 2 MHz. The transducers were oil-coupled. Transient signals were generated by a Metrotek ultrasonic pulser, applied to transducer *s*. They were then amplified by 40 dB using battery-powered Panametrics preamplifiers, and digitized at 5 MSa/s. A 6.4-ms duration window of the transient signal (32 000 points) in each of the three receivers, *s*, *x*, and *y*, was captured, repetition averaged, and passed to a PC. The capture was then repeated for windows centered on successively later times T_D. A direct application of Eq. (20) is not appropriate. The latter part of the ~160-ms signal is significantly weaker than the initial part of it, as absorption has attenuated it. A direct implementation of (20) would effectively discard the great amount of information present in the latter parts of the signal.

To use all the information we therefore construct the following average:

$$\tilde{\chi}(\omega) = \sum_{D=1}^{N_D} \frac{i\omega\tilde{V}_x^D(\omega)\tilde{V}_y^{D*}(\omega)}{f(\omega)\exp\{-2\gamma(\omega)T_D\}}, \tag{21}$$

where the sum is over a series of $N_D(\approx 25)$ nonoverlapping successive "delays," each of width $\Delta T = 6.4$ ms, each centered on a different time T_D. It may be noted that we have not attempted to correct for the phase $\tilde{Y}(\omega)/\tilde{Y}^*(\omega)$. The exponential factor in the denominator is intended to compensate for absorption. In each term the factors $V(\omega)$ in the

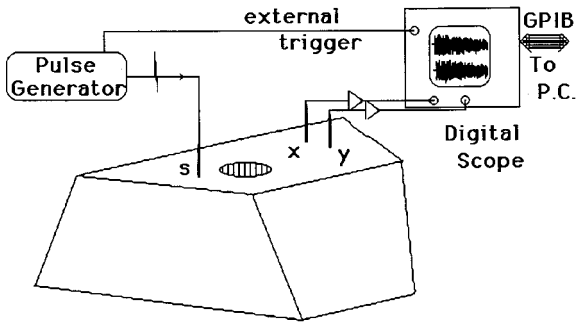

FIG. 1. Irregular block specimen (dimensions $\sim 80\times140\times200\,\text{mm}^3$ with 25-mm-diam cylindrical hole) and ultrasonic configuration. A transient pulse is created at **s** and the resulting diffuse field is detected simultaneously at **x** and **y** 20 mm apart.

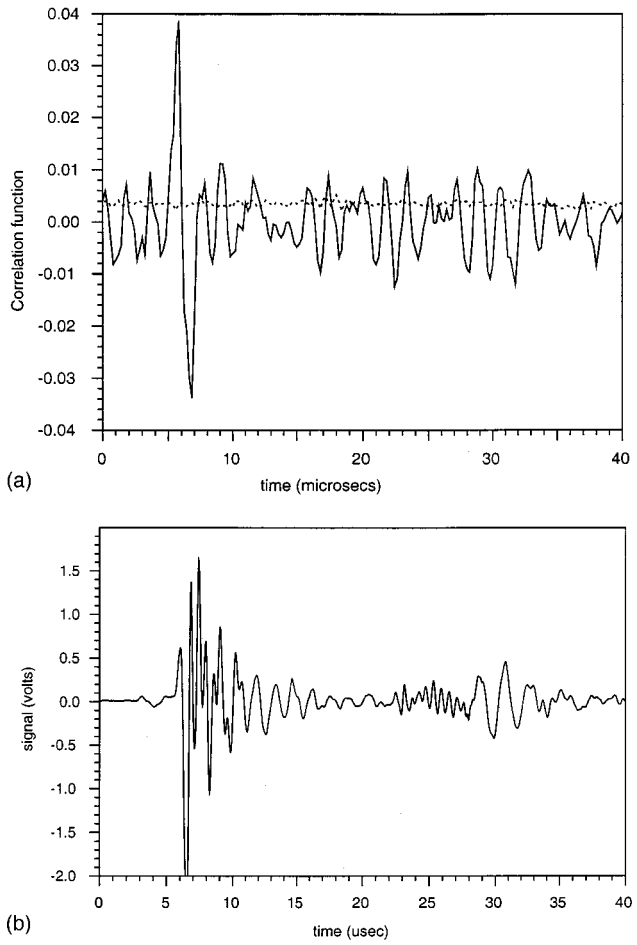

FIG. 2. (a) Correlation function $\chi(t)$ recovered from 161 ms of broadband diffuse data generated by an impulse at a single distant point *s*. The dotted line indicates the estimated rms statistical error. (b) Broadband direct "pitch-catch" signal from *x* to *y*.

denominator are constructed from the Fourier transforms of the signals $V(t)$ in the delayed time window centered on T_D.

V_x and V_y were captured simultaneously with a two-channel digitizer. If the capture were not simultaneous, small unavoidable fluctuations in temperature, it can be shown, will introduce uncontrolled time shifts between the contributions recovered at large delays *D*.

In (21) the factor *f*, and the decay rate γ, were constructed from the power spectral density observed in V_s by fitting $|\tilde{V}_s^D(\omega)|^2/E(\omega,T_D)$ to an exponential time dependence: $f(\omega)\exp\{-2\gamma(\omega)T_D\}$. The *f* and γ that are constructed from this show some random fluctuations that are at least partly a result of the finite sampling. They are therefore smoothed by application of cubic splines. Modal density $dN/d\omega$ is taken from theory. In three dimensions it is essentially proportional to ω^2.

The resulting χ is inverse Fourier transformed and compared with the direct pitch-catch signal v_{xy}. Figure 2 shows these two waveforms. Figure 2(a) shows the waveform recovered by this process; Fig. 2(b) shows the pitch-catch waveform obtained by pulsing the transducer at *x* and capturing the resulting transient at *y*. The main features of the direct pitch catch waveform [Fig. 2(b)] are clearly present in the correlation function [Fig. 2(a)]. One observes the direct

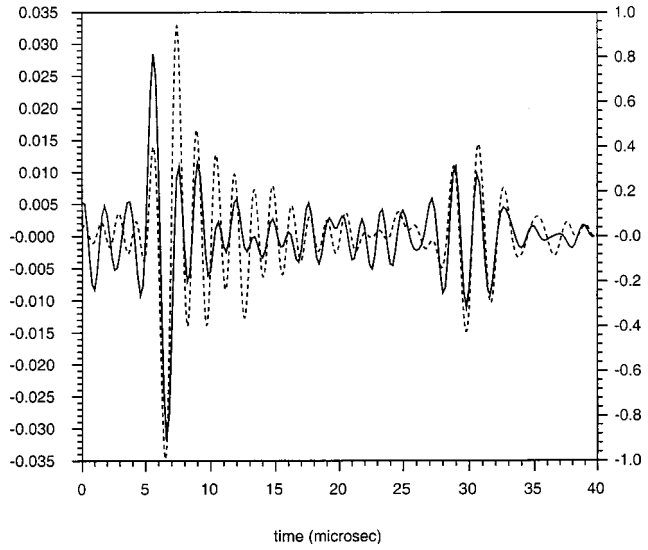

FIG. 3. Comparison of correlation function (solid line) and direct pitch catch signal (dashed line) after low-pass filtering, and including 350 ms of diffuse field data.

Rayleigh wave, which arrives at 7 μs, and the signal due to a reflection of a *P*-wave from the bottom at about 30 μs. The high-frequency feature at 25 μs is a Rayleigh wave that has reflected from a nearby edge. These plots confirm the present assertion; the Green's function *is* present in the correlations of a diffuse field. There are significant differences between the plots, however, and the question arises as to their cause.

Theory suggested that convergence is most thorough when an amount of time of the order of the break time is cross correlated. In this sample the break time is generally much greater than the 160 ms of data that was used to construct the correlation. (The break time is 120 ms at 200 kHz, and scales quadratically with frequency above there.) Therefore, the lack of perfect correspondence is not unexpected. Laboratory estimates may be composed for the degree of fluctuation that might be removed if one were to average over more time. The plot in Fig. 2(a) shows, in the horizontal dotted line, the root mean square deviation of $\chi(t)$ from its average among the 20 delays, divided by $\sqrt{20}$. This level is an estimate of the apparent error; its magnitude suggests that the differences between the correlation function and the direct pitch catch signal would be reduced with more averaging.

One way to do more averaging is to capture more than 160 ms. Unfortunately, the signal above 700 kHz and beyond 160 ms contains substantial noise and is not useful; high frequencies are too rapidly absorbed. To improve the convergence, we therefore eliminated the signal above 700 kHz by digital filtering, and captured a total of 50 delays, over 320 ms. The result is shown in Fig. 3, where it is compared with the digitally filtered direct pitch-catch signal. The agreement is much better.

Nevertheless, discrepancies remain. In an attempt to decrease these discrepancies, and in light of the theoretical indications that averaging over source positions *s* may be useful, the process is repeated for eight positions of the source *s*. The average of these (with a fixed new choice for positions *x* and *y*) is shown in Fig. 4. Figure 4(a) shows the comparison

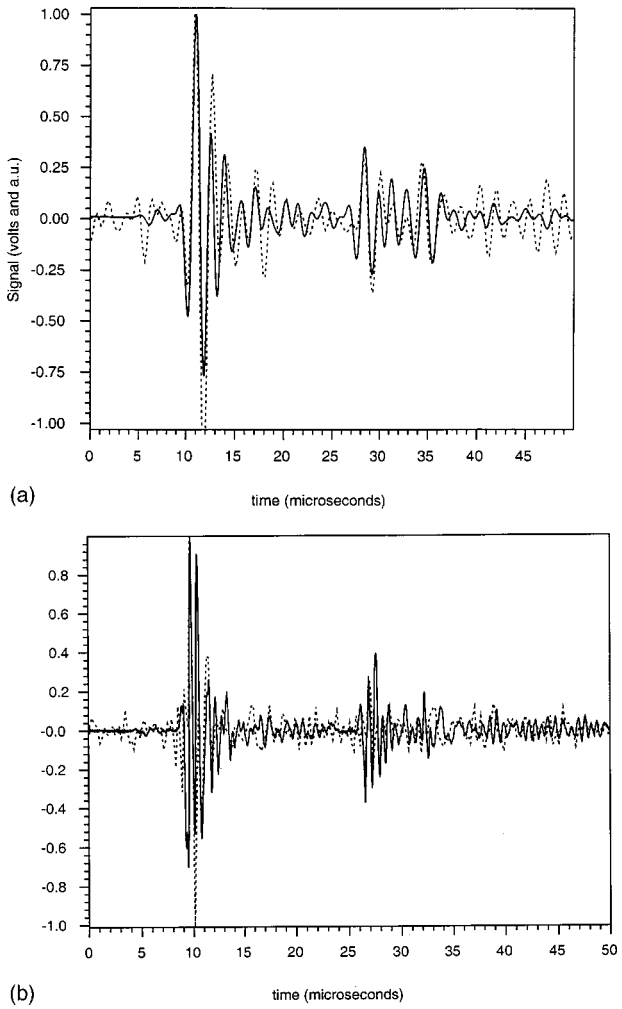

FIG. 4. (a) The average correlation function recovered from 190 ms of data generated by eight distinct positions of the source s (dashed line) is compared with the direct pitch-catch signal (solid line). Each waveform has been low-pass filtered at 900 kHz. The quality of the correspondence is much improved over that of Fig. 3. (b) The average correlation function without low-pass filtering, as recovered from 128 ms of data generated by eight distinct positions of the source s (dashed line) is compared with the direct pitch-catch signal (solid line).

between 900 kHz low-passed waveforms; Fig. 4(b) shows the case without low-pass filtering. For both plots, the discrepancies are reduced compared with those of Fig. 3. Remaining discrepancies are perhaps attributable to the phase of the receiver Y and/or to continued insufficiency in the amount of averaging.

VI. CONCLUSIONS

There may be some applications of these ideas in structural vibrations. The source of noise [or at least the source's power spectrum $f(\omega)$, with corresponding information about the source time function and local environment] might be inferable from Eq. (21) by comparing the noise correlations χ with directly obtained local responses v_{xy}. Arguments similar to those advanced here have recently been employed[24] to predict diffuse field energy spectra at x due to a source at s, i.e., $|V_x(\omega)|^2$, in terms of the spectrum at s due to the source at $s|V_s(\omega)|^2$, and the spectrum at x due to a source at x. It was argued there that such an ability may lend itself to efficient numerical predictions of mean power.

These observations may also have some applications to seismology. Increasing recent evidence[12–14] that seismic coda consist of multiply scattered, fully diffuse seismic waves suggests that correlations of seismic coda could reveal information on local stratigraphy. The very long ring times of lunar coda are especially intriguing. Cross correlation of years of seismic noise, on the earth or on the moon, might reveal features of local geologic structures.

Applications to ultrasonics are less clear. It would appear that the methods developed here, using a distant source to generate the diffuse field, might be useful whenever ultrasonic waveforms are desired from places at which it is difficult to insert an ultrasonic source, but where a receiver can be placed. A particularly intriguing possibility is using ambient thermal fluctuations to generate the diffuse ultrasonic field. Virtues of such a diffuse field include its broad spectrum (up to several TeraHertz at room temperature), the absence of any need to generate it, and its well understood statistics. It is, though, quite weak. That idea is pursued in other reports.[27]

Another intriguing idea is the possibility of applications to wave chaos theory.[26,28–30] In a ray-chaotic structure one expects rays to ergodically fill the entire available phase space. In practice, however, a ray that is absorbed, or reaches its ''break time,'' before filling phase space is effectively not chaotic, and the field not fully diffuse. Ray paths which are almost stable (''scars'' in the language of the community) can be expected to contribute to a correlation to an excessive degree if the source lies on that path. If the source does not lie on that path, but the two receivers do, one would expect the correlation to show excessively weak contributions from that path. Thus scars should distort the correlations predicted in this report. In particular one expects ray-chaotic structures (like the one used here) to generate better correspondence between correlations and direct pitch-catch signals than do highly symmetric and/or pseudo-integrable systems.

ACKNOWLEDGMENTS

We thank Bart van Tiggelen for encouragement and provocative conversations. This work was supported by the National Science Foundation through Grant No. 9988645.

[1] R. Weaver, ''On diffuse waves in solid media,'' J. Acoust. Soc. Am. **71**, 1608–1609 (1982).
[2] R. Weaver, ''Diffuse elastic waves at a free surface,'' J. Acoust. Soc. Am. **78**, 131–136 (1985).
[3] R. Weaver, ''Diffuse Waves in Finite Plates,'' J. Sound Vib. **94**, 319–335 (1984).
[4] R. Weaver, ''Laboratory studies of diffuse waves in plates,'' J. Acoust. Soc. Am. **79**, 919–923 (1986).
[5] J. A. Turner and R. L. Weaver, ''Radiative transfer of ultrasound,'' J. Acoust. Soc. Am. **96**, 3654–3674 (1994).
[6] M. J. Evans and P. Cawley, ''Measurement and prediction of diffuse fields in structures,'' J. Acoust. Soc. Am. **106**, 3348–3361 (1999).
[7] R. H. Lyon and R. G. DeJong, *Theory and Application of Statistical Energy Analysis* (Butterworths-Heimann, Boston, MA, 1995).
[8] E. H. Dowell and Y. Kubota, ''Asymptotic modal analysis and SEA of dynamical systems,'' J. Appl. Mech. **52**, 949–957 (1985).
[9] C. H. Hodges and J. Woodhouse, ''Theories of noise and vibration transmission in complex structures,'' Rep. Prog. Phys. **49**, 107–170 (1986).

[10] J. Woodhouse, ''An approach to the theoretical background of SEA applied to structural vibration,'' J. Acoust. Soc. Am. **69**, 1695–1709 (1981).
[11] B. R. Mace and P. J. Shorter, ''Energy flow models from Finite Element Analysis,'' J. Sound Vib. **233**, 369–389 (2000).
[12] G. C. Papanicolaou, L. V. Ryzhik, and J. B. Keller, ''Stability of the P to S energy ratio in the diffusive regime,'' Bull. Seismol. Soc. Am. **86**, 1107 (1996).
[13] J. A. Turner, ''Scattering and Diffusion of Seismic Waves,'' Bull. Seismol. Soc. Am. **88**, 276–283 (1998).
[14] R. Hennino, N. Trégourès, N. M. Shapiro, L. Margerin, M. Campillo, B. A. van Tiggelen, and R. L. Weaver, ''Observation of equipartition of seismic waves in Mexico,'' Phys. Rev. Lett. **86**, 3447–3450 (2001).
[15] R. L. Weaver and O. I. Lobkis, ''Temperature Dependence of Diffuse Field Phase,'' Ultrasonics **38**, 491–494 (2000).
[16] R. Weaver and O. Lobkis, ''Temperature dependence of ultrasonic diffuse fields, implications for the measurement of stress,'' in *Review of Progress in Quantitative Nondestructive Testing*, edited by D. O. Thompson and D. E. Chimenti (AIP Press, 2001), pp. 1480–1486.
[17] A. Derode, P. Roux, and M. Fink, ''Robust acoustic time-reversal with high-order multiple scattering,'' Phys. Rev. Lett. **75**, 4206–4209 (1995).
[18] A. Derode, A. Tourin, and M. Fink, ''Limits of time-reversal focusing through multiple-scattering: long range correlation,'' J. Acoust. Soc. Am. **107**, 2987–2998 (2000).
[19] C. Draeger, J-C. Aime, and M. Fink, ''One-channel time reversal in chaotic cavities: experimental results,'' J. Acoust. Soc. Am. **105**, 618–625 (1999).
[20] C. Draeger and M. Fink, ''One-channel time reversal in chaotic cavities: Theoretical limits,'' J. Acoust. Soc. Am. **105**, 611–617 (1995).
[21] V. N. Prigodin, B. L. Altshuler, K. B. Efetov, and S. Iida, ''Mesoscopic dynamical echo in quantum dots,'' Phys. Rev. Lett. **72**, 546–549 (1994).
[22] R. Weaver and J. Burkhardt, ''Weak Anderson localization and enhanced backscatter in reverberation rooms and quantum dots,'' J. Acoust. Soc. Am. **96**, 3186–3190 (1994).
[23] R. L. Weaver and O. I. Lobkis, ''Enhanced Backscattering and Modal Echo of Reverberant Elastic Waves,'' Phys. Rev. Lett. **84**, 4942–4945 (2000); J. de Rosny, A. Tourin, and M. Fink, ''Coherent backscattering of an elastic wave in a chaotic cavity,'' *ibid.* **84**, 1693–1696 (2000).
[24] R. L. Weaver, ''Equipartition and mean square responses in large undamped structures,'' J. Acoust. Soc. Am. **110**, 894–903 (2001).
[25] R. Weaver, ''On the time and geometry independence of elastodynamic spectral energy density,'' J. Acoust. Soc. Am. **80**, 1539–1541 (1986).
[26] E. J. Heller, ''Qualitative properties of eigenfunctions of classically chaotic Hamiltonian systems,'' in *Quantum Chaos and Statistical Nuclear Physics*, edited by T. H. Seligman and H. Nishioka (Springer Verlag, New York, 1986).
[27] R. L. Weaver and O. I. Lobkis, ''Ultrasonics without a source, Thermal fluctuation correlations at MHz frequencies,'' Phys. Rev. Lett. **87**, 134301 (2001); O. Lobkis and R. Weaver, ''Elastic wave thermal fluctuations, ultrasonic waveforms by correlation of thermal phonons,'' under review, J. Acoust. Soc. Am.
[28] O. Bohigas, ''Random matrix theories and chaotic dynamics,'' in Les Houches, session LII, 1989, in *Chaos and Quantum Physics* (Elsevier, Amsterdam, 1991).
[29] E. Bogomolny and E. Hugues, ''Semiclassical theory of flexural vibrations of plates,'' Phys. Rev. E **57**, 5404–5424 (1998).
[30] H-J. Stockmann, *Quantum Chaos: An Introduction* (Cambridge U.P., Cambridge, 1999).

An approximate analytic solution for the radiation from a line-driven fluid-loaded plate

Daniel T. DiPerna[a] and David Feit[b]
Naval Surface Warfare Center, Carderock Division, 9500 MacArthur Boulevard, West Bethesda, Maryland 20817

(Received 16 September 2000; revised 24 August 2001; accepted 3 September 2001)

In the analysis of a fluid loaded line-driven plate, the fields in the structure and the fluid are often expressed in terms of a Fourier transform. Once the boundary conditions are matched, the structural displacement can be expressed as an inverse transform, which can be evaluated using contour integration. The result is then a sum of propagating or decaying waves, each arising from poles in the complex plane, plus a branch cut integral. The branch cut is due to a square root in the transform of the acoustic impedance. The complex layer analysis (CLA) used here eliminates the branch cut singularity by approximating the square root with a rational function, causing the characteristic equation to become a polynomial in the transform variable. An approximate analytic solution to the characteristic equation is then found using a perturbation method. The result is four poles corresponding to the roots of the *in vacuo* plate, modified by the presence of the fluid, plus an infinity of poles located along the branch cut of the acoustic impedance. The solution is then found analytically using contour integration, with the integrand containing only simple poles.
[DOI: 10.1121/1.1414705]

PACS numbers: 43.40.Rj, 43.40.Jx [CBB]

I. INTRODUCTION

In this paper we propose a new approach to solve the fundamental problem of structural acoustics, which is that of a fluid-loaded elastic plate of infinite extent driven by a line or point force of harmonic time variation. This approach, which we refer to as complex layer analysis (CLA), replaces the semi-infinite acoustic domain by an acoustic fluid layer of thickness h, where h is a complex number. As a result the branch cut integral arising from the usual analysis is transformed into a sum of an infinite number of poles whose locations and residue contributions can be readily calculated. Complex layer analysis (CLA) is reminiscent of the work of Berenger,[1] who introduced the notion of perfectly matched layers (PML) for numerical grid truncation in time and frequency domain simulation of electromagnetic wave propagation.

This approach gives us new insight into the physical mechanisms governing the dynamic response and acoustic radiation processes in structural acoustic interaction problems. For such problems, in addition to the externally applied forces, the fluid medium in which the structure vibrates, generates unsteady pressures in response to the structural vibrations, which also act on the plate. The additional loading, being distributed over the entire extent of the plate, is highly nonlocal as differentiated from the more localized restoring forces due to the plate's elasticity. In one or more of its variant forms this problem, which can be mathematically formulated as an integrodifferential equation for the structural response field, has been extensively investigated by many authors[2–5] for more than 30 years, and is fundamental to our physical understanding of sound radiated and scattered by submerged structures. From these studies we have learned that the structural response can be interpreted as being made up of three disturbances. One, a propagating flexural wave whose phase speed is reduced by the presence of the fluid; two, an exponentially decaying standing wave disturbance reminiscent of the evanescent near field of a force excited plate *in vacuo*; and finally, a wave disturbance propagating with the acoustic wave speed of the ambient medium. In the case of a line-driven plate the fluid-modified flexural wave propagates as a straight crested wave with no spatial dependence of its amplitude, while the structure-modified acoustic wave has an amplitude that decreases with distance as $x^{-3/2}$.

Since the domain of the problem is of infinite extent in the directions parallel to the surface of the plate as well as normal to it, the problem is treated using Fourier transforms. Using such a formulation, the above-mentioned disturbances are associated with the singularities of the transform representation of the solutions. In the classical treatment of the problem the Fourier transform of the velocity field has both pole and branch point singularities. The pole contributions make up the discrete spectrum and these give rise to the fluid-modified flexural disturbances, both propagating and evanescent, while the structure-modified acoustic waves are associated with an integration along the branch cut (continuous spectrum.) The branch cut is introduced to define the appropriate Riemann sheet on which to evaluate the inverse transform, assuring that the acoustic field satisfies the Sommerfeld radiation condition.

While it is relatively straightforward to evaluate the farfield pressure using an asymptotic approximation,[6,7] the explicit evaluation of the velocity field on the plate is somewhat more problematic. As mentioned, the velocity field requires the knowledge of the pole locations, and this involves

[a]Electronic mail: dipernadt@nswccd.navy.mil
[b]Electronic mail: feitd@nswccd.navy.mil

the solution of a quintic algebraic equation that has no known closed-form solution. The poles to properly include in the evaluation depend on the particular branch cut chosen. The latter difficulty was the cause of some controversy in years past as to whether or not certain wave types existed or had any physical manifestation in the plate vibration field.[8,9] A number of previous studies of this problem avoided this issue since they primarily involved numerical evaluation[10–12] of the inverse transforms. The CLA presented here leads to explicit solutions for the wave types and an unequivocal determination of the physical mechanisms involved in the fluid-loaded plate vibration problem. Additionally, the fact that the branch cut can be accurately represented by a function with only poles implies that the original integrodifferential formulation for the structural response can be cast as a higher-order differential equation. The latter formulation, even for highly inhomogeneous structures, is then amenable to highly efficient numerical methods similar to transmission line theory. Presently, this type of analysis cannot be applied to structures in which there is a transmission path that is noncoincident with the structure (i.e., a fluid-borne path).

II. THEORY

The Fourier transform of the equation of motion for the fluid loaded plate can be written as

$$[\tilde{Z}_p(k_x)+\tilde{Z}_a(k_x)]\tilde{u}(k_x)=\tilde{f}(k_x), \tag{1}$$

where k_x is the axial wave number, $\tilde{u}(k_x)$ is the transform of the plate velocity, $\tilde{f}(k_x)$ is the transform of the applied force, and $\tilde{Z}_p(k_x)$ and $\tilde{Z}_a(k_x)$ are the spectral impedances of the plate and the fluid and are given by

$$\tilde{Z}_p(k_x)=-i\omega m\left(1-\frac{Dk_x^4}{m\omega^2}\right),$$
$$\tilde{Z}_a(k_x)=\frac{\rho\omega}{\sqrt{k^2-k_x^2}}, \tag{2}$$

where $k=\omega/c$ is the wave number in the fluid, c is the sound speed in the fluid medium, m is the mass per unit area of the plate, D is the flexural rigidity of the plate, ω is the angular frequency, and ρ is the density of the fluid. The Fourier transform pair is given by

$$\tilde{g}(k_x)=\int_{-\infty}^{\infty} g(x)e^{-ik_x x}\,dx,$$
$$g(x)=\frac{1}{2\pi}\int_{-\infty}^{\infty}\tilde{g}(k_x)e^{ik_x x}\,dk_x.$$

Solving Eq. (1) for the plate velocity and using the impedances given in Eq. (2) yields

$$\tilde{u}(k_x)=\frac{1}{D}\frac{-i\omega\tilde{f}(k_x)}{\left(k_x^4-k_f^4-\dfrac{i\rho\omega^2}{D\sqrt{k^2-k_x^2}}\right)}, \tag{3}$$

where $k_f=\sqrt[4]{m\omega^2/D}$ is the flexural wave number of the *in vacuo* plate. In the literature,[7,10,11] this equation has been inverse Fourier transformed using contour integration, with the result being a sum of residues evaluated at each of the poles, plus a branch cut contribution due to the square root in the fluid impedance. However, it is possible to make an approximation to the fluid impedance that no longer has a branch cut. To do this, we consider the case where the fluid has a pressure release surface at the location $z=h$. The transform of the pressure is thus

$$\tilde{P}(k_x,z)=Ae^{i\sqrt{k^2-k_x^2}z}+Be^{-i\sqrt{k^2-k_x^2}z}.$$

For a pressure release surface located at $z=h$, the boundary condition is $\tilde{P}(k_x,z=h)=0$, yielding

$$A=-Be^{-i2\sqrt{k^2-k_x^2}h}.$$

This gives us an expression for the pressure and velocity of the form

$$\tilde{P}(k_x,z)=2iBe^{-i\sqrt{k^2-k_x^2}h}\sin[\sqrt{k^2-k_x^2}(h-z)],$$
$$\tilde{V}(k_x,z)=-\frac{2iB\sqrt{k^2-k_x^2}e^{-i\sqrt{k^2-k_x^2}h}\cos[\sqrt{k^2-k_x^2}(h-z)]}{i\omega\rho}.$$

The impedance at the surface $z=0$ is then

$$\tilde{Z}_a(k_x)=\frac{\tilde{P}(k_x,z=0)}{\tilde{V}(k_x,z=0)}=-i\omega\rho h\frac{\mathrm{sinc}(\sqrt{k^2-k_x^2}h)}{\cos(\sqrt{k^2-k_x^2}h)},$$

where $\mathrm{sinc}(x)=\sin(x)/x$. This approximation to the acoustic impedance does not contain a branch cut because the sinc and cosine functions are both even functions, and it therefore does not matter which branch of the square root is taken. Comparing this expression with the second line of Eq. (2), we see that we can make the approximation

$$s(k_x)=\frac{1}{\sqrt{k^2-k_x^2}}\approx\frac{-ih\,\mathrm{sinc}(\sqrt{k^2-k_x^2}h)}{\cos(\sqrt{k^2-k_x^2}h)}. \tag{4}$$

Note that the right-hand side of this equation contains an infinite number of poles due to the cosine function in the denominator. These poles are located at

$$\sqrt{k^2-k_x^2}h=\frac{(2n+1)\pi}{2}=\alpha_n,\quad n=0,1,...,\infty,$$

or, equivalently,

$$k_x=\pm\sqrt{k^2-\frac{\alpha_n^2}{h^2}}=\pm k_n. \tag{5}$$

This means that the branch cut introduced due to the fluid loading can be approximated by a rational function with poles at the location described in Eq. (5). The actual location of these poles depend on how we choose *h*. If we choose *h* to be real and large, these poles become densely spaced along the real and imaginary k_x axes, which is precisely where the Ewing, Jardetzky, and Press (EJP) branch cut of $1/\sqrt{k^2-k_x^2}$ is located.[13] This is shown in Fig. 1(a). However, if we choose *h* to be complex, the location moves to the position shown in Fig. 1(b), which is closer to the Pekeris branch cut.[14]

The question that now arises is how to choose h so that the approximation in Eq. (4) is valid. The transform of the pressure in the layer and the infinite half-space are

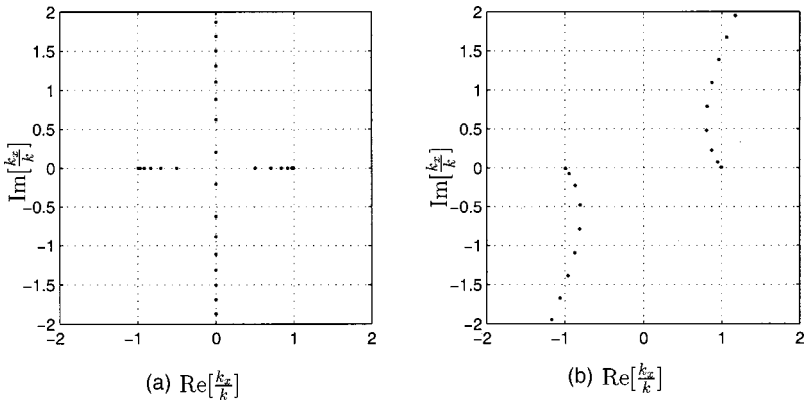

FIG. 1. Location of poles for approximate fluid loading term, along with integration path for the inverse Fourier transform. In (a), h was chosen to be real, placing the poles along the L-shaped branch cut. In (b), h is taken as complex, putting the branch cut closer to a Pekeris branch cut.

$$\tilde{P}^L(k_x,z)=A^L e^{i\sqrt{k^2-k_x^2}z}+B^L e^{-i\sqrt{k^2-k_x^2}z}, \tag{6}$$

$$\tilde{P}^H(k_x,z)=A^H e^{i\sqrt{k^2-k_x^2}z}, \tag{7}$$

where the superscripts L and H denote layer and infinite half-space, respectively. The expression for the pressure in the layer makes no assumptions on the definition of the square root operator, but the expression for the pressure in the infinite half-space requires the appropriate choice of the sign of the square root in order to remain on the same Riemann sheet. For these two expressions to be comparable, B^L must be small. In order to determine the values of h that make B^L small, we will let $h=h_0(1+i\sigma)$, where h_0 and σ are real positive constants. We now consider two distinct regimes of k_x: the subsonic case and the supersonic case. For the subsonic case, $k_x>k$, and energy is not being radiated into the fluid. We will let $\sqrt{k^2-k_x^2}=i\eta$, where η is a positive constant. If we evaluate the pressure in the layer at $z=h$, we get

$$\tilde{P}^L(k_x,z=h)=A^L e^{-\eta h_0}e^{-i\eta\sigma h_0}+B^L e^{\eta h_0}e^{i\eta\sigma h_0}. \tag{8}$$

For a soft boundary condition this expression equals zero. Solving for B^L gives

$$B^L=-A^L e^{-2\eta h_0}e^{-i2\eta\sigma h_0}. \tag{9}$$

The second exponential in this expression is oscillatory, and therefore has a magnitude of 1. The first exponential is decaying, since both η and h_0 are positive. B^L will therefore be much smaller than A^L as long as $e^{-2\eta h_0}\ll 1$. This is true for both real and complex values of h.

For the supersonic or radiating case, where $k_x<k$, we let $\sqrt{k^2-k_x^2}=\eta$, where η is again a positive constant. The pressure at $z=h$ is now

$$\tilde{P}^L(k_x,z=h)=A^L e^{i\eta h_0}e^{-\eta\sigma h_0}+B^L e^{-i\eta h_0}e^{\eta\sigma h_0}. \tag{10}$$

Solving for B^L for a soft boundary at $z=h$ gives

$$B^L=-A^L e^{i2\eta h_0}e^{-2\eta\sigma h_0}. \tag{11}$$

The first exponential is now oscillatory, and will have a magnitude of 1, but the second is now decaying. B^L will therefore be small, provided that $e^{-2\eta\sigma h_0}\ll 1$. This condition is now a function of σ. If $\sigma=0$, which corresponds to making the layer h real, this condition cannot be met. However, if σ is sufficiently large, the corresponding B^L will be small, and the pressure in the layer will approximate the pressure in the infinite half-space.

The approximation defined in Eq. (4) evaluated along the real k_x axis is shown in Fig. 2. for a real value of h. Both the real and imaginary parts are shown along with the exact function. This approximation is very poor for certain values of k_x/k. Notice that these points all occur when $k_x<k$, which corresponds to the supersonic case described above. In this case, energy is being radiated into the fluid, reflecting off the boundary at $z=h$ and returning to the plate surface. The result is a standing wave, or mode in the layer, which clearly

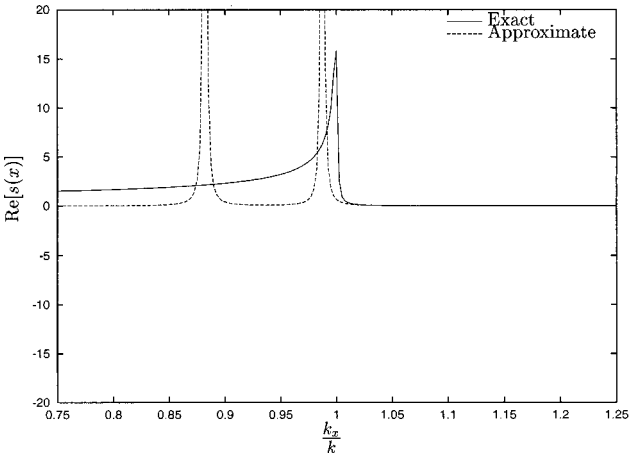

(a) Real part of $s(k_x)$ with real h

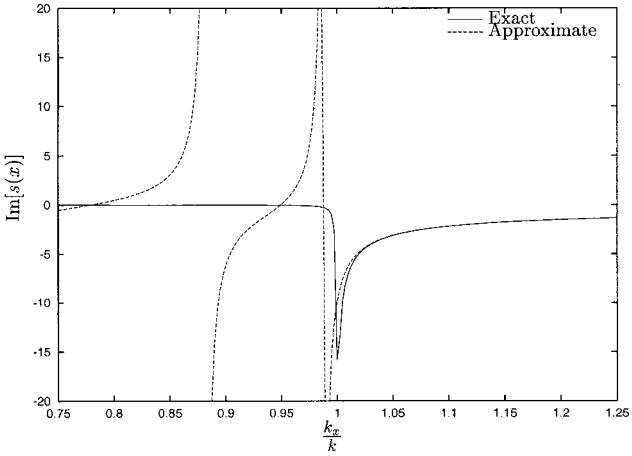

(b) Imaginary part of $s(k_x)$ with real h

FIG. 2. Approximation of Eq. (4) with real h. There is poor agreement whenever a pole of the approximation is near the real axis. Physically, this corresponds to a resonance or mode in the layer.

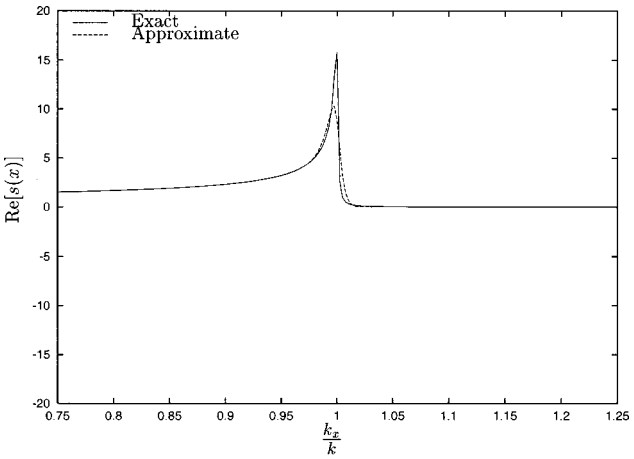

(a) Real part of $s(k_x)$ with complex h

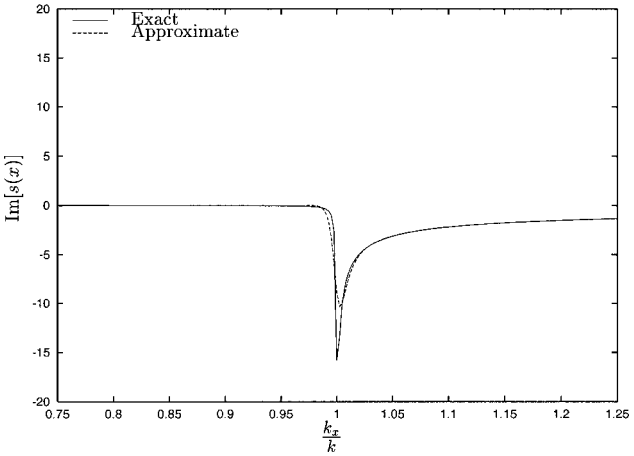

(b) Imaginary part of $s(k_x)$ with complex h

FIG. 3. Approximation of Eq. (4) for complex h. There is significantly improved agreement with the exact function because the poles of the approximation are now in the complex plane, and are far away from the real axis.

cannot exist in an infinite half-space. When $k_x > k$, there is no energy being radiated into the fluid, and the agreement between the approximation and the exact function is very good. Figure 3 shows the approximation using a complex value for h. As can be seen, using a complex value of h makes Eq. (4) a very good approximation. The poorest agreement is near $k_x = k$, but this is to be expected because if $\sqrt{k^2-k_x^2} = \eta \approx 0$, the condition that $e^{-2\eta\sigma h_0} \ll 1$ is violated.

We have thus shown that a rational function can be used to approximate the branch cut singularity in the transform of the fluid impedance. By using this rational function approximation in the fluid/structure interaction problem, we can obtain an approximate solution for the problem of the line-driven plate. Inserting the approximation given in Eq. (4) into Eq. (3), and clearing fractions we obtain

$$\tilde{u}(k_x) = \frac{1}{D} \frac{-i\omega \tilde{f}(k_x)\cos(\sqrt{k^2-k_x^2}h)}{\tilde{H}(k_x)}, \tag{12}$$

where the denominator is given by

$$\tilde{H}(k_x) = (k_x^4 - k_f^4)\cos(\sqrt{k^2-k_x^2}h) - k_f^4 \frac{\rho h}{m} \operatorname{sinc}(\sqrt{k^2-k_x^2}h). \tag{13}$$

In order to invert this Fourier transform using contour integration, we need to find the wave number roots, which occur when the denominator is equal to zero, or

$$\tilde{H}(k_x) = 0. \tag{14}$$

This is the characteristic equation of the system. This is a transcendental equation that must, in general, be solved numerically. Alternatively, an approximate analytic solution may be obtained using a perturbation method, which will be valid under conditions to be discussed later.

We proceed by introducing a parameter δ into Eq. (14), yielding

$$(k_x^4 - k_f^4)\cos(\sqrt{k^2-k_x^2}h) - \delta k_f^4 \frac{\rho h}{m} \operatorname{sinc}(\sqrt{k^2-k_x^2}h) = 0. \tag{15}$$

The original problem can then be recovered by letting $\delta \to 1$. We proceed by expanding this in a Taylor series about $k_x = \gamma_0$, letting $k_x = \gamma_0 + \delta\gamma_1$, and equating orders of δ equal to 0 to give a sequence of equations. The first of these is

$$(\gamma_0^4 - k_f^4)\cos(\sqrt{k^2-\gamma_0^2}h) = 0. \tag{16}$$

The solutions of this equation are as follows:

$$\gamma_0 = \pm k_f, \quad \pm ik_f, \quad \pm k_n, \tag{17}$$

which are the *in vacuo* plate flexural roots, and the roots located along the branch cut of the acoustic impedance, respectively. The roots along the branch cut are associated with fluid-borne waves in the layer. Corresponding to each of these roots there is a first-order term that satisfies the first-order equation in the perturbation solution:

$$\gamma_1[4\cos(\sqrt{k^2-\gamma_0^2}h)\gamma_0^3 - \operatorname{sinc}(\sqrt{k^2-\gamma_0^2}h)h^2\gamma_0(\gamma_0^4 - k_f^4)] - k_f^4 \frac{\rho h}{m} \operatorname{sinc}(\sqrt{k^2-\gamma_0^2}h) = 0.$$

The solutions of this equation are

$$\gamma_1 = \frac{k_f^4 \frac{\rho h}{m} \operatorname{sinc}(\sqrt{k^2-\gamma_0^2}h)}{[4\cos(\sqrt{k^2-\gamma_0^2}h)\gamma_0^3 - \operatorname{sinc}(\sqrt{k^2-\gamma_0^2}h)h^2\gamma_0(\gamma_0^4 - k_f^4)]}.$$

Combining the zeroth- and first-order terms and letting $\delta \to 1$, the fluid-loaded roots are located at

$$k_f^{\mathrm{fl}} = k_f\left[1 + \frac{\epsilon}{4M}\frac{1}{\sqrt{1-M^2}}\tanh\left(\sqrt{12}\frac{c}{c_p}\frac{h}{h_p}M\sqrt{1-M^2}\right)\right], \tag{18a}$$

$$k_e^{\mathrm{fl}} = ik_f\left[1 + \frac{\epsilon}{4M}\frac{1}{\sqrt{1+M^2}}\tan\left(\sqrt{12}\frac{c}{c_p}\frac{h}{h_p}M\sqrt{1+M^2}\right)\right], \tag{18b}$$

$$k_n^{\mathrm{fl}} = k_n - \frac{\rho}{m}\frac{1}{k_n h\left(1 - \frac{k_n^4}{k_f^4}\right)}, \tag{18c}$$

where k_f^{fl}, k_e^{fl}, and k_n^{fl} are the fluid-loaded flexural, evanescent, and fluid roots, respectively, and we have introduced

the intrinsic fluid loading parameter, $\epsilon=\rho c/\omega_c m$ and the phase Mach number $M=k_0/k_f$, which is the ratio of the *in vacuo* flexural wave speed to the acoustic wave speed. The coincidence frequency is given by $\omega_c=\sqrt{12}c^2/(h_p c_p)$, h_p is the plate thickness. These parameters were used extensively in the works of David Crighton on this subject. The results given in Eqs. (18a) and (18b) are useful only in the regime $M \gg \epsilon$, the regime referred to by Crighton[15] as "...the frequency range of light fluid loading ...". When $\epsilon \ll M$, the regime referred to by Crighton as "...heavy fluid loading...", a different perturbation scheme is more useful. Namely, this would be a perturbation about the zeroth-order solutions provided by the zeros of the second term of Eq. (15). When $\epsilon = O(M)$, in the frequency range of "...significant fluid loading...," neither type of perturbation can be rigorously justified, and the roots must be found numerically.

Assuming the forcing function is a line drive located at $x=x_0$, the plate velocity is given by

$$u(x)=\frac{1}{2\pi D}\int_{-\infty}^{\infty}\frac{-i\omega\cos(\sqrt{k^2-k_x^2}h)e^{ik_x(x-x_0)}}{\tilde{H}(k_x)}dk_x. \tag{19}$$

Since the approximation to the fluid impedance has eliminated the branch cut, this integral can be evaluated by closing the contour in the upper half-plane for $x>x_0$ to yield

$$u(x)=\frac{1}{2\pi D}\oint_C\frac{-i\omega\cos(\sqrt{k^2-k_x^2}h)e^{ik_x(x-x_0)}}{\tilde{H}(k_x)}dk_x. \tag{20}$$

Evaluating this integral yields

$$u(x)=R(k_f^{\mathrm{fl}})e^{ik_f^{\mathrm{fl}}(x-x_0)}+R(k_e^{\mathrm{fl}})e^{ik_e^{\mathrm{fl}}(x-x_0)}+\sum_{n=0}^{\infty}R(k_n^{\mathrm{fl}})e^{ik_n^{\mathrm{fl}}(x-x_0)}, \tag{21}$$

where $R(k_r^f)$ are the residues at each of the wave number roots k_r and are given by

$$R(k_f^{\mathrm{fl}})=\frac{\omega}{D\left(4(k_f^{\mathrm{fl}})^3+\frac{\rho h k_f^4 k_f^{\mathrm{fl}}}{m[k^2-(k_f^{\mathrm{fl}})^2]}\frac{[1-\mathrm{sinc}[\sqrt{k^2-(k_f^{\mathrm{fl}})^2}h]\cos[\sqrt{k^2-(k_f^{\mathrm{fl}})^2}h]]}{\cos^2[\sqrt{k^2-(k_f^{\mathrm{fl}})^2}h]}\right)},$$

$$R(k_e^{\mathrm{fl}})=\frac{\omega}{D\left(4(k_e^{\mathrm{fl}})^3+\frac{\rho h k_f^4 k_e^{\mathrm{fl}}}{m[k^2-(k_e^{\mathrm{fl}})^2]}\frac{\{1-\mathrm{sinc}[\sqrt{k^2-(k_e^{\mathrm{fl}})^2}h]\cos[\sqrt{k^2-(k_e^{\mathrm{fl}})^2}h]\}}{\cos^2[\sqrt{k^2-(k_e^{\mathrm{fl}})^2}h]}\right)}, \tag{22}$$

$$R(k_n^{\mathrm{fl}})=\frac{\omega}{D\left[4(k_n^{\mathrm{fl}})^3-\frac{\rho h k_f^4 k_n^{\mathrm{fl}}}{m(k^2-(k_n^{\mathrm{fl}})^2)}\left(\frac{\mathrm{sinc}(\sqrt{k^2-(k_n^{\mathrm{fl}})^2}h)}{\cos(\sqrt{k^2-(k_n^{\mathrm{fl}})^2}h)}-1\right)-(k_n^{\mathrm{fl}}h)[k_f^4-(k_n^{\mathrm{fl}})^4]h\frac{\mathrm{sinc}[\sqrt{k^2-(k_n^{\mathrm{fl}})^2}h]}{\cos[\sqrt{k^2-(k_n^{\mathrm{fl}})^2}h]}\right]}.$$

In practice, the infinite summation may be truncated after N terms, which seems reasonable since the contribution of the fluid terms are tending to n^{-4} as n becomes large.

One important issue that has not been addressed is that of how to choose the parameter h. The rule of thumb is that the complex layer must be larger than the largest wavelength at the plate–fluid interface. At low frequencies, the acoustic wavelength is larger than the flexural wavelength. At higher frequencies, the flexural wavelength is larger. Therefore, we chose h to be $h_0=20/\sqrt{|k^2-k_f^2|}$, which has the correct behavior at low and high frequencies. We also wish to keep $\sigma h/\lambda$ constant and large. However, the larger we make this constant, the more densely spaced the fluid poles and the more poles that will have significant residue contributions. For the examples in the following section, we have used the values $\sigma=1$, and $N=9$.

The fact that the number of poles that need to be included is relatively small is significant in that it suggests that the original coupled ordinary/partial differential equation system of the plate and fluid can be replaced by a higher-order system of ordinary differential equations, with the order of the new system of equations corresponding to the number of poles. Since the number of poles required is fairly small, this approach could lead to a highly efficient method of numerically solving more complicated problems. This approach will be described in further publications.

III. RESULTS

Figure 4 shows the nondimensional fluid-loaded flexural wave number variation [Eq. 18(a)] as a function of frequency. Below coincidence, the flexural root is purely real, indicating a propagating wave. It is located above the *in vacuo* plate flexural root, indicating that the fluid slows the flexural wave. Above coincidence, the flexural wave number lies below the acoustic wave number; the wave disturbance is supersonic, thereby radiating energy into the fluid, and the wave number has an imaginary component, giving rise to an exponential decay of the flexural wave component.

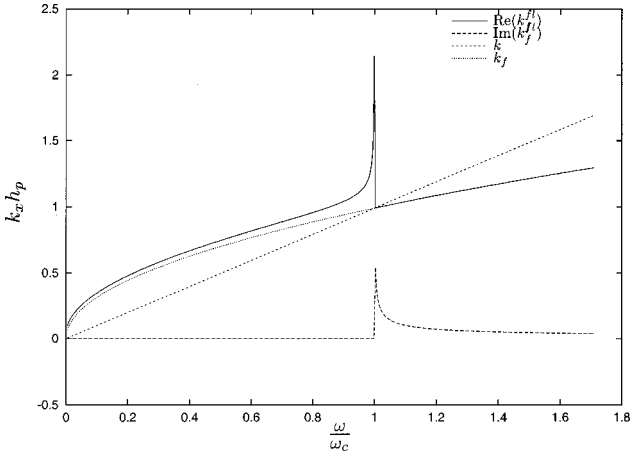

FIG. 4. Wavenumber roots for the fluid loaded plate obtained using Eq. (18). Real and imaginary parts are plotted along with the *in vacuo* flexural wavenumber and the acoustic wavenumber. When the *in vacuo* flexural wavenumber coincides with the acoustic wavenumber, there is a fundamental change in behavior of the fluid loaded root. Below coincidence, the flexural wavenumber is purely real, indicating that it propagates with no loss of energy. Above coincidence, however, it has an imaginary part, which indicates that it is radiating energy into the fluid and thus decays as it propagates.

In Fig. 5 we plot the magnitude of the residue contribution from each of the relevant poles, i.e., the propagating fluid-loaded flexural wave, evanescent flexural disturbances, and the first-order acoustic wave as a function of frequency. Since these magnitudes are related to the input power delivered to each type of disturbance, we note that there appears to be a sharing of energy between the propagating flexural wave and the acoustic waves, with the greatest interaction occurring in the vicinity of the coincidence frequency. Furthermore, it appears that the amount of power required to drive the flexural, evanescent, and propagating waves is approximately the same over the entire frequency range.

Figure 6 shows the normalized plate velocity magnitude as a function of the normalized distance for frequencies below and above coincidence. The solid lines are from the numerical inversion of the Fourier transform of the plate velocity using the exact expression for the acoustic impedance. The marked lines show the result of using the approximate expression for the acoustic impedance. As can be seen, the agreement is very good for all three frequencies. Figure 7 shows the normalized plate velocity as obtained by numerical integration of inverse Fourier transform using the exact acoustic impedance (solid lines), along with the result of using the perturbation solution. For $\omega/\omega_c \gtrsim 1$, the agreement is very good. However, as the frequency decreases below coincidence, the agreement becomes poorer. This is simply because the assumptions of a small perturbation have been violated, and is not an indication that the CLA approximation is poor.

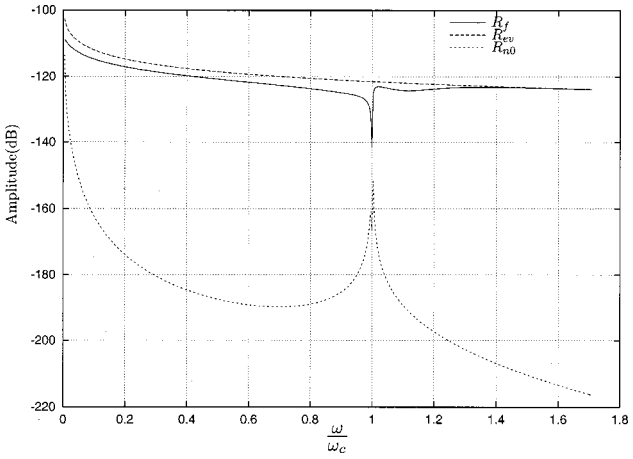

FIG. 5. Residues for different flexural, evanescent, and the lowest order fluid-borne waves. The peak and null in the fluid-borne and flexural wave amplitudes near coincidence indicate a strong sharing of energy between the fluid and structure near this frequency.

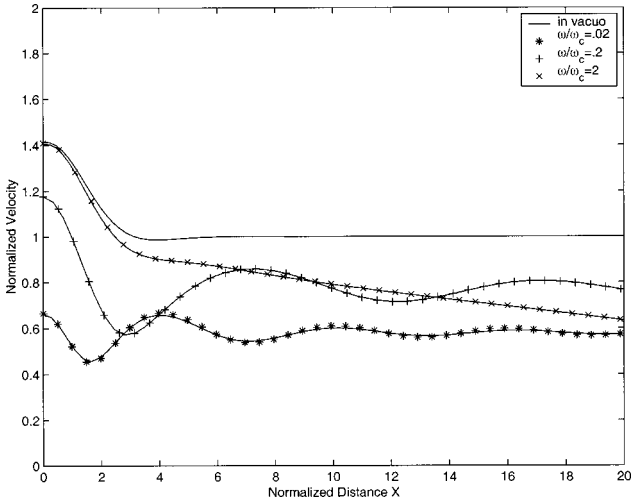

FIG. 6. Comparison of normalized plate velocity as a function of nondimensional distance $x = k_f x$ for frequencies $\omega/\omega_c = 0.02$, $\omega/\omega_c = 0.2$, and $\omega/\omega_c = 2.0$, along with the *in vacuo* response. Plotted are the results from numerically evaluating the inverse transform using the exact expression for the acoustic impedance(solid lines), and the approximate expression for the acoustic impedance(marked lines).

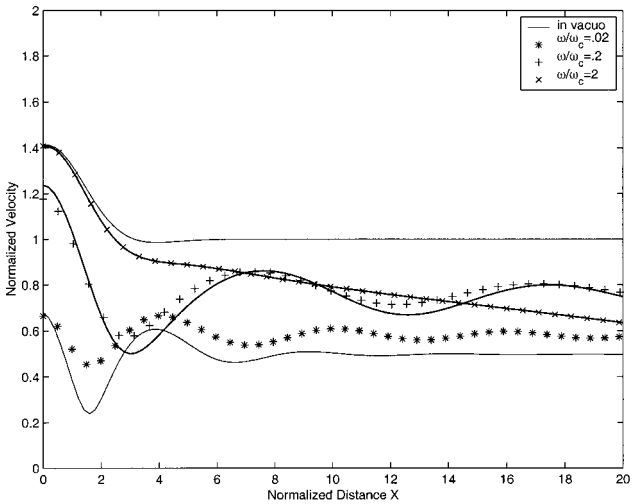

FIG. 7. Comparison of normalized plate velocity as a function of nondimensional distance $x = k_f x$ for frequencies $\omega/\omega_c = .02$, $\omega/\omega_c = 0.2$, and $\omega/\omega_c = 2.0$, along with the *in vacuo* response. Plotted are the results from numerically evaluating the inverse transform using the exact expression for the acoustic impedance (solid lines), and the perturbation solution (marked lines). The agreement above coincidence is excellent, with some error for $\omega/\omega_c = 0.2$, and significant error for $\omega/\omega_c = 0.02$.

IV. CONCLUSIONS

In this paper, we have introduced the concept of complex layer analysis (CLA). This was first shown to produce an excellent approximation of the branch cut in the Fourier transform of the acoustic impedance in terms of a rational function. This approximation was then used in conjunction with a perturbation technique to obtain an approximate analytic solution to the fundamental problem of structural acoustics, that of a line-driven fluid-loaded plate. This response obtained with the approximate approach compares very well with previous calculations which utilized numerical integration procedures.

ACKNOWLEDGMENTS

During the final preparations for submission of this paper we learned of the death of David G. Crighton, who contributed so much to the subject matter of this paper, and so we dedicate this paper to his memory. We also wish to acknowledge the Carderock Division of the Naval Surface Warfare Center ILIR program for supporting this work.

[1] J. P. Berenger, ''A perfectly matched layer for the absorption of electromagnetic waves,'' J. Comput. Phys. **114**, 185–200 (1994).
[2] L. Y. Gutin, ''Sound radiation from an infinite plate excited by a normal point force,'' Sov. Phys. Acoust. **10**, 369–371 (1965).
[3] G. Maidanik and J. Kerwin, ''Influence of fluid loading on the radiation from infinite plates below the critical frequency,'' J. Acoust. Soc. Am. **40**, 1036–1038 (1967).
[4] D. Feit, ''Pressure radiated by a point-excited elastic plate,'' J. Acoust. Soc. Am. **40**, 1489–1494 (1967).
[5] D. Crighton, ''Force and moment admittance of plates under arbitrary loading,'' J. Sound Vib. **20**, 209–218 (1972).
[6] L. B. Felsen and N. Marcuvitz, *Radiation and Scattering of Waves* (IEEE Press, New York, 1994).
[7] M. Junger and D. Feit, *Sound, Structures, and Their Interaction*, 2nd ed. (American Institute of Physics, Woodbury, 1993).
[8] W. A. Strawderman, S. H. Ko, and A. H. Nutall, ''The real roots of the fluid-loaded plate,'' J. Acoust. Soc. Am. **66**, 579–585 (1979).
[9] D. Crighton, ''The free and forced waves on a fluid loaded elastic plate,'' J. Sound Vib. **63**, 225–235 (1979).
[10] P. R. Nayak, ''Line admittance of infinite isotropic fluid-loaded plates,'' J. Acoust. Soc. Am. **47**, 191–201 (1970).
[11] D. Feit and Y. N. Liu, ''The nearfield response of a line-driven fluid-loaded plate,'' J. Acoust. Soc. Am. **78**, 763–766 (1985).
[12] J. M. Cuschieri and D. Feit, ''A hybrid numerical and analytical solution for the Green's function of a fluid-loaded elastic plate,'' J. Acoust. Soc. Am. **95**, 1998–2005 (1994).
[13] W. M. Ewing, W. S. Jardetzky, and F. Press, *Elastic Waves in Layered Media* (McGraw-Hill, New York, 1957).
[14] C. L. Pekeris, ''Theory of propagation of explosive sound in shallow water,'' in *Propagation of Sound in the Ocean* (Geol. Soc. Amer. Mem., 1948), p. 27.
[15] D. G. Crighton, A. P. Dowling, J. E. Pfowcs Williams, M. Heckl, and F. G. Leppington, *Modern Methods in Analytical Acoustics: Lecture Notes* (Springer-Verlag, Berlin, 1992).

Analysis and measurement of a matched volume velocity sensor and uniform force actuator for active structural acoustic control

P. Gardonio, Y.-S. Lee, and S. J. Elliott
Institute of Sound and Vibration Research, University of Southampton, Southampton SO17 1BJ, England

S. Debost
Thomson Marconi Sonar, 525, Route des Dolines, BP 157-06903, Sophia Antipolis, Cedex, France

(Received 8 December 2001; accepted for publication 23 August 2001)

This paper presents a theoretical and experimental study of the frequency response function of a matched volume velocity sensor and uniform force actuator for active structural acoustic control. The paper first reviews the design of a volume velocity sensor and uniform force actuator on a panel, using piezoelectric film with quadratic shaping of the electrodes. The frequency response function of a matched volume velocity sensor and uniform force actuator bonded on either sides of a panel is then studied in detail. This analysis shows that below 100 Hz the sensor–actuator response is controlled by the bending vibration of the panel and a good estimate of the volumetric component of the transverse vibration of the panel is achieved. At higher frequencies, however, the sensor–actuator response is controlled by the in-plane longitudinal and shear vibration of the panel, which causes the real part of the frequency response function to be not strictly positive and to be characterized by large amplitudes at higher frequencies. These two phenomena are important since they limit the possibility of implementing a stable direct velocity feedback control system using these transducers. © *2001 Acoustical Society of America.* [DOI: 10.1121/1.1412448]

PACS numbers: 43.40.Vn [PJR]

I. INTRODUCTION

In this paper an active structural acoustic control (ASAC) system is studied, in which only one structural actuator and one structural sensor are used to control the sound radiated by a panel.[1,2] It has been shown that in the low frequency region, where the dimensions of the panel are relatively small compared to an acoustic wavelength, the largest contribution to the sound radiation from the plate is due to the net volume velocity of the panel itself.[3,4] Volume velocity sensors have been developed[3] and are used as error sensors in ASAC systems for simple structures such as plates and beams. If such a transducer is used as an actuator, it will generate a uniform force over the panel to which it is attached. The novel feature investigated in this study is the matched configuration of such a distributed uniform force control actuator and a distributed volume velocity sensor.[3,5] Of particular interest is a system consisting of a distributed piezoelectric actuator bounded on one side of a panel, driven by a single input single output (SISO) feedback controller, to minimize the volume velocity vibration of the panel measured by a matched piezoelectric sensor which is bonded on the opposite side of the partition. With this type of system, reduction of sound transmission in the mid–low frequency range can, in principle, be achieved for both tonal or broadband random noise.[6]

The benefits expected from the use of a matched volume velocity distributed sensor and a distributed uniform force actuator are three: first, the spillover phenomenon[5] could be avoided; second, a simple SISO feedback controller is required by the control system[3,5] which allows the control system to be used in the case of random incident noise[6,7] and third, it should be possible to implement a stable direct velocity feedback (DVFB) control architecture[5,8] so that the control system is robust to all changes which can occur in the response of the structure.

In the following two sections, the principal features of a volume velocity sensor and uniform force actuator for a clamped panel are described. A third section discusses the possibility of using these two transducers together to implement direct velocity feedback ASAC control. The feasibility of such a smart panel is then assessed experimentally by analyzing the measured frequency response function of a test panel with two distributed piezoelectric transducers with shaped electrodes. Finally, the practical limitations are discussed for the implementation of DVFB control with this smart panel.

II. VOLUME VELOCITY SENSOR

The volume velocity sensor considered here can be regarded as a composite structure consisting of a film of piezoelectric material with electrodes on either side. The electrodes are usually very thin layers of metal which are deposited on the piezoelectric film surfaces. When such a sensor is bonded onto a panel, the vibration of the panel deforms the piezoelectric material so that it generates a distribution of charges on the surfaces of the two electrodes by means of the piezoelectric effect.[9,10] A charge output, $q(t)$, proportional to the plate vibration can therefore be measured by connecting a charge amplifier to the two electrodes. In this section a particular type of sensor is studied, whose charge output is proportional to the volume velocity component of the bending vibration of a clamped rectangular panel.

The charge on a piezoelectric element bonded on a plate can be derived from the induced strain across the surface. According to Lee's formulation,[11] the total charge output is given by two components: the charge generated by the bending vibration of the panel $q_b(t)$ and the charge due to the in-plane vibration of the panel $q_i(t)$ so that:

$$q(t)=q_b(t)+q_i(t), \tag{1}$$

where

$$q_b(t)=-\int_0^{L_y}\int_0^{L_x} h(x,y)S(x,y)\left[e_{31}\frac{\partial^2 w}{\partial x^2}+e_{32}\frac{\partial^2 w}{\partial y^2}+2e_{36}\frac{\partial^2 w}{\partial x\,\partial y}\right]dx\,dy \tag{2}$$

$$q_i(t)=\int_0^{L_y}\int_0^{L_x} S(x,y)\left[e_{31}\frac{\partial u}{\partial x}+e_{32}\frac{\partial v}{\partial y}+e_{36}\left(\frac{\partial u}{\partial y}+\frac{\partial v}{\partial x}\right)\right]dx\,dy, \tag{3}$$

where L_x and L_y are the width and length of the panel. In the above two formulas u, v and w are the displacements of the plate along the x, y and z directions, $h=h_s+h_{pe}/2$ represents the distance in z direction from the neutral plane of the plate to the middle plane of the piezoelectric film; h_s is half of the plate thickness and h_{pe} is the thickness of the sensor (piezoelectric material and electrodes). e_{31}, e_{32} and e_{36} are the piezoelectric stress constants and $S(x,y)$ is the spatial sensitivity function of the sensor.

Considering a rectangular panel supported along the four edges, Rex and Elliott[12] have shown that if the distributed piezoelectric transducer has a quadratic sensitivity along the x-direction and a constant sensitivity along the y- direction, so that

$$S(x,y)=-k(x^2-L_x x), \tag{4}$$

where k is a constant, then the charge output of Eq. (2) is proportional to the integrated transverse displacement of the whole surface of the panel.

Gardonio *et al.*[13] have derived analytical expressions for Eqs. (2) and (3) for the case in which the panel is clamped along the four edges and for the sensitivity of the piezoelectric transducer as in Eq. (4), such that:

$$q_b(t)=2e_{31}hk\int_0^{L_y}\int_0^{L_x} w(x,y)dx\,dy, \tag{5}$$

$$q_i=-2ke_{31}\int_0^{L_y}\int_0^{L_x}\left(\int u(x,y)dx\right)dx\,dy - 2ke_{32}\int_0^{L_y}\int_0^{L_x}\left(\int\int \frac{\partial v(x,y)}{\partial y}dx\,dx\right)dx\,dy. \tag{6}$$

Equation (5) shows that, this sensitivity distribution for a piezoelectric transducer bonded on a clamped panel generates a charge output proportional to the transverse displacement integrated over the panel surface. Thus, when the panel is excited in bending and the current is measured, $i(t)=dq(t)/dt$, then the sensor output is proportional to the volume velocity of the panel that is defined as follows:

$$Q(t)=\int_0^{L_y}\int_0^{L_x}\frac{dw(x,y)}{dt}dx\,dy. \tag{7}$$

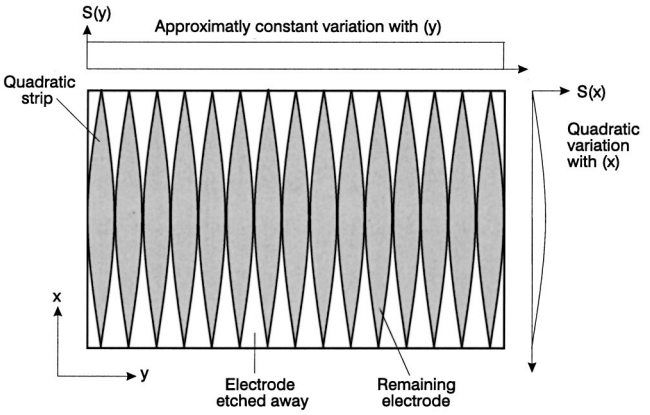

FIG. 1. A rectangular plate with a set of quadratically shaped electrodes for the measurement of the plate volume velocity vibration component.

There are various methods of achieving the required quadratic weighted sensitivity.[3] The easiest one is to implement a quadratically shaped electrode as shown in Fig. 1. The electrical impedance of the piezoelectric material is very high and therefore the electrical output is due purely to areas that are covered by the metal electrode. The electrode can be etched away to produce shaped strips which define the area over which the film is sensitive. The quadratic sensitivity in the x-direction has been obtained by etching the electrode surface to produce a discrete number of strips whose width varies quadratically along the x-axis, as shown in Fig. 1. The constant sensitivity is guaranteed if the strips have a sufficiently small width so that they are not affected by a large change in transverse displacement from one edge of the strip to the other. This assumption is generally valid if the wavelength of a structural bending mode is large compared to the width of the strip.[3] Therefore, for low bending wave number, the ''strip geometry'' of the electrodes shown in Fig. 1 approximates a quadratically weighted sensitivity in the x-direction and a constant sensitivity in the y-direction.

III. UNIFORM FORCE ACTUATOR

The design of a piezoelectric ''transverse uniform force actuator'' acting on a clamped rectangular panel is now considered. When a voltage is applied between the two electrodes, an electric field is generated across the piezoelectric material which then deforms because of the piezoelectric effect.[9,10] When such a piezoelectric actuator is bonded to the surface of a plate the piezoelectric effect produces a force field on the surface of the panel, which, in general, will cause it to bend, twist and stretch.[11]

Using the formulation presented by Lee,[11] the forced equations for the uncoupled transverse [Eq. (8) below] and in-plane [Eqs. (9) and (10) below] vibration of the panel generated by a layer of piezoelectric material bonded on to one surface of the panel can be written as:[13]

$$(D_s+D_{pe})\left(\frac{\partial^4 w}{\partial x^4}+2\frac{\partial^4 w}{\partial x^2\,\partial y^2}+\frac{\partial^4 w}{\partial y^4}\right)+m\frac{\partial^2 w(t)}{\partial t^2}$$
$$=-hV(t)\left(e_{31}\frac{\partial^2 S(x,y)}{\partial x^2}+2e_{36}\frac{\partial^2 S(x,y)}{\partial x\,\partial y}+e_{32}\frac{\partial^2 S(x,y)}{\partial y^2}\right), \tag{8}$$

$$\frac{2Y_s h_s}{1-\nu_s^2}\left(\frac{\partial^2 u}{\partial x^2}+\frac{1-\nu_s}{2}\frac{\partial^2 u}{\partial y^2}\right)+\frac{2Y_s h_s}{2(1-\nu_s)}\frac{\partial^2 v}{\partial x\,\partial y}-m\frac{\partial^2 u(t)}{\partial t^2}$$
$$=\left\{e_{31}\frac{\partial S(x,y)}{\partial x}+e_{36}\frac{\partial S(x,y)}{\partial y}\right\}V(t), \tag{9}$$

$$\frac{2Y_s h_s}{2(1-\nu_s)}\frac{\partial^2 u}{\partial y\,\partial x}+\frac{2Y_s h_s}{1-\nu_s^2}\left(\frac{1-\nu_s}{2}\frac{\partial^2 v}{\partial x^2}+\frac{\partial^2 v}{\partial y^2}\right)-m\frac{\partial^2 v(t)}{\partial t^2}$$
$$=\left\{e_{36}\frac{\partial S(x,y)}{\partial x}+e_{31}\frac{\partial S(x,y)}{\partial y}\right\}V(t), \tag{10}$$

where $V(t)$ is the voltage applied across the piezoelectric transducer and D_s and D_{pe} are given by the following expressions:

$$D_s=\frac{2Y_s h_s^3}{3(1-\nu_s^2)}, \tag{11}$$

$$D_{pe}=\frac{Y_{pe}(h_{pe}^3+3h_{pe}h_s^2+3h_{pe}^2h_s)}{3(1-\nu_{pe}^2)}, \tag{12}$$

where $m=2\rho_s h_s$ is the mass per unit area of the panel and ρ_s is the density of the material, Y_s, Y_{pe} and ν_s, ν_{pe} represent the Young's modulus and the Poisson's ratio of the panel and piezoelectric film, respectively. The condition necessary to generate a transverse uniform force actuator is to have a piezoelectric material with constant sensitivity function along the *y*-direction and quadratic sensitivity along the *x*-direction as given by Eq. (4). Such a piezoelectric transducer will thus give an output proportional to volume velocity when used as a sensor or generate a uniform forcing across the panel when used as actuator.

Substituting the sensitivity function in Eq. (4) into Eq. (8) and considering the boundary conditions due to the clamping of the panel, the transverse excitation term is found to be:[13]

$$f_n(x,y,t)=2\left(h_s+\frac{h_{pe}}{2}\right)e_{31}kV(t). \tag{13}$$

A piezoelectric actuator with constant sensitivity along the *y*-direction and quadratic sensitivity along the *x*-direction can be again obtained in practice by etching the electrode surface in such a way as to get a discrete number of strips whose width varies quadratically with *x* as shown in Fig. 1.

IV. PREDICTED TRANSFER RESPONSE

The volume velocity sensor and the uniform force actuator described in the previous two sections could be used together to form a matched sensor–actuator pair. A piezoelectric film with quadratically shaped electrodes, as shown in Fig. 1, could be bonded to each side of a clamped rectangular panel for example, so that one film is used to measure the net volume velocity due to the bending vibration of the panel and the other film is used to exert a transverse uniform force over the panel surface. The actuator and sensor are connected such that the phase response for bending vibration is between $\pm 90°$. The output of the volume velocity sensor could be fed back to the uniform force actuator to form a direct velocity feedback control system.[5] In this case, provided the control system is stable, the total error signal, $e(\omega)$, measured by the volume velocity sensor due to the primary disturbance, $d(\omega)$ (caused by air-borne or structure-borne excitations acting on the panel), is given by

$$\frac{e(\omega)}{d(\omega)}=\frac{1}{1+G(\omega)H(\omega)}, \tag{14}$$

where $G(\omega)=i(\omega)/V(\omega)$ is the sensor–actuator response (measured current per input voltage) and $H(\omega)$ is the response of the controller. If the controller is just a fixed gain, then by increasing this gain Eq. (14) can be made much smaller than unity and the volume velocity of the panel is reduced so that the sound transmission/radiation is attenuated. This control scheme is stable for any value of the gain provided that the real part of the sensor–actuator response, $G(\omega)$, is strictly positive.[5,8] Johnson and Elliott[5] have shown that in theory the transfer function of a matched volume velocity sensor and uniform force actuator pair bonded on a panel does have this property, although only bending vibration was considered in this analysis.

In this section the theoretical form of the sensor–actuator response $G(\omega)$ of the smart rectangular panel is discussed. The panel is taken to be clamped and the sensor and actuator distributed transducers are assumed to be made of PVDF (PVDF or PVF_2 stands for polyvinylidene fluoride polymer[14]) film with quadratically shaped electrodes, as shown in Fig. 1. This type of piezoelectric material has been widely used to construct distributed sensors of various shapes as discussed in Refs. 3 and 15–18. In contrast there are very few examples of actuation using PVDF distributed transducers.[19,20] This is probably because a relatively thick film of PVDF is needed for an actuator, since otherwise the high voltage required to generate realistic excitation levels could damage the piezoelectric properties of the material. A relatively thick electrode layer is also required on a PVDF film used as an actuator, since otherwise the current density will heat up and damage this layer.

The ratio $G(\omega)=i(\omega)/V(\omega)$, output current per input voltage, of the sensor–actuator transducer can be expressed as the sum of two frequency responses, one related to the bending vibration and the other related to in-plane longitudinal and shear vibration of the panel, so that:

$$G(\omega)=G_b(\omega)+G_i(\omega). \tag{15}$$

The frequency responses component due to bending vibration of the panel can be expressed from Eqs. (5) and (8) in terms of the bending modes of the panel:[13]

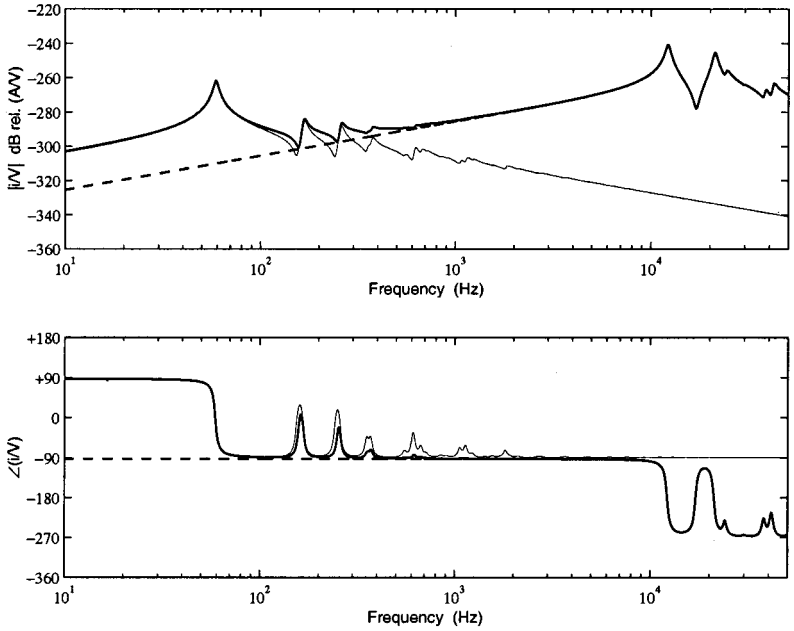

FIG. 2. Simulation of the output current from the volume velocity sensor per unit voltage input to the force actuator; solid line both bending and axial vibration effects; dashed line: only in-plane vibration effects; faint line: only bending vibration effects.

$$G_b(\omega)=\frac{i_b(\omega)}{V(\omega)}=4e_{31}^2k^2\left(h_s+\frac{h_{pe}}{2}\right)^2 \times \sum_{m=1,3,5,\cdots}^{\infty}\sum_{n=1,3,5,\cdots}^{\infty} A_{mn}C_{mn}, \quad (16)$$

where

$$A_{mn}=\frac{j\omega}{\Lambda_{b,mn}[\omega_{b,mn}^2(1+j\eta)-\omega^2]}, \quad (17)$$

$$C_{mn}=\left\{\frac{16L_xL_y}{\gamma_m\gamma_n}\sin\frac{\gamma_m}{2}\sin\frac{\gamma_n}{2}\right\}^2, \quad (18)$$

and $\omega_{b,mn}$ are the bending natural frequencies of the panel,[21] $\Lambda_{b,mn}$ is a modal normalization factor,[22] η is the loss factor and γ_m, γ_n are modal terms as from Ref. 21. The frequency response component due to in-plane vibration of the panel can be written, from Eqs. (6), (9), and (10), in terms of the panel's in-plane modes as:[13]

$$G_i(\omega)=\frac{i_i(\omega)}{V(\omega)}=-2e_{31}k^2\sum_{m=1,3,5,\cdots}^{\infty}\sum_{n=1,3,5,\cdots}^{\infty} B_{mn}(e_{31}D_{mn}^x + e_{32}D_{mn}^y), \quad (19)$$

where

$$B_{mn}=\frac{j\omega}{\Lambda_{i,mn}[\omega_{i,mn}^2(1+j\eta)-\omega^2]} \quad (20)$$

and

$$D_{mn}^x=2\left(\frac{L_x}{m\pi}\right)^4\left(\frac{L_y}{n\pi}\right)^2(1-\cos m\pi)(1-\cos n\pi), \quad (21)$$

$$D_{mn}^y=2\left(\frac{L_x}{m\pi}\right)^5\left(\frac{L_y}{n\pi}\right)(1-\cos m\pi)(1-\cos n\pi). \quad (22)$$

$\omega_{i,mn}$ are the in-plane natural frequencies of the panel,[23] $\Lambda_{i,mn}$ is a modal normalization factor[22] and η is the loss factor.

Since, the C_{mn}, D_{mn}^x and D_{mn}^y coefficients in Eqs. (18) and (21), (22) are real and positive for all modes then both of the sensor–actuator frequency response function components $G_b(\omega)$ and $G_i(\omega)$ are characterized by a sequence of alternating poles (resonance frequencies) and zeros (antiresonance frequencies) pairs.[24] Each of the two sensor–actuator response function components are thus minimum phase. The response of the $G_b(\omega)$ component is limited to between $\pm 90°$, and thus is positive real, but the response of the $G_i(\omega)$ component is limited to between $-90°$ and $-270°$ so that it is not positive real. In other words, the sensor–actuator transducers are arranged in such a way as that they can be assumed to be collocated with reference to bending vibration of the panel but not collocated with reference to in-plane vibration of the panel.

Figure 2 shows the simulated sensor–actuator total frequency response function $G(\omega)$ (solid line) and its two components $G_b(\omega)$ and $G_i(\omega)$ (faint and dashed lines, respectively) calculated assuming the geometry and physical constants of the panel and piezoelectric transducers to be those given in Tables I and II. The natural frequencies of the panel have been calculated assuming that the total stiffness is equal to $D=D_s+D_{pe}$ and the mass of the PVDF layers are $0.44kg$. This plot shows that below about 100 Hz the overall

TABLE I. Geometry and physical constants for the panel.

Parameter	Value
Dimensions	$L_{xs}\times L_{ys}=314\times 414$ mm
Thickness	$2h_s=1$ mm
Mass density	$\rho_s=2700$ Kg/m^3
Young's modulus	$Y_s=7.1\times 10^{10}$ N/m^2
Poisson ratio	$\nu_s=0.33$
Loss factor	$\eta_s=0.05$

TABLE II. Geometry and physical constants for the PVDF film.

Parameter	Value
Dimensions of the PVDF film	$L_{xpe}\times L_{ype}=306\times 406$ mm
Dimensions of the electrodes	$L_{xe}\times L_{ye}=300\times 400$ mm
Thickness of the PVDF film	$h_{pe}=0.5$ mm
Mass density	$\rho_{pe}=1780$ Kg/m^3
Young's modulus	$Y_{pe}=2\times 10^9$ N/m^2
Poisson ratio	$\nu_{pe}=0.29$
Piezoelectric stress constants	$e_{31}=0.052$ N/Vm
	$e_{32}=0.021$ N/Vm
	$e_{31}=0$

frequency response function is dominated by the component related to bending vibration of the panel and the (1,1) bending mode resonance frequency at 59 Hz is clearly seen. Above 100 Hz, however, the component related to in-plane vibration of the panel becomes more important and hides the resonances due to the higher order bending modes detected by the volume velocity sensor. The $G_i(\omega)$ frequency response function component shows a constant rising trend, typical of a low frequency stiffness control response, until the first two resonance frequencies for in-plane vibration occurs at about 12 kHz and 21 kHz. The response at these two resonance frequencies is about 20 dB higher than that at the first bending resonance frequency.

V. MEASURED TRANSFER RESPONSE

The response of the matched sensor–actuator pair is now assessed experimentally. A smart panel has been fabricated by bonding on either sides of an aluminum plate a film of PVDF piezoelectric material on which surfaces a thin layer of metal was deposited to form the electrode pair required either to detect or generate the electric field in the piezoelectric material. The quadratic sensitivity of the piezoelectric films, required to measure volume velocity motion or to generate a uniform force on the panel, has been obtained by etching away the outer electrodes to create a set of quadratically shaped strips, as shown in Fig. 1, which define the area over which the film is sensitive.

The panel has dimensions 440×340 mm and a thickness of 1 mm. These dimensions have been chosen to leave a portion of material of 13 mm on each side of the plate for the clamping. Therefore the surface of the plate free to vibrate has dimensions: 414×314 mm. The sensor and actuator elements have been made using PVDF films of dimensions 406×306 mm and thickness 0.5 mm. In order to avoid electrical breakdown, the metallization is only present over a surface of 400×300 mm. In this way along the four edges of the electrodes there is a margin of 3 mm of PVDF material that should avoid electric discharge. The outer electrodes have been etched away to give 40 quadratically shaped strips with maximum width $\delta=10$ mm and quadratic shaping which approximates the relation $y=-k(L_x x-x^2)$ with $k=2\delta/L_x^2$. Figure 3 shows the smart panel that has been built and used in the experimental study. The panel was clamped on a very rigid frame before its frequency response was measured to approximate the assumed boundary conditions.

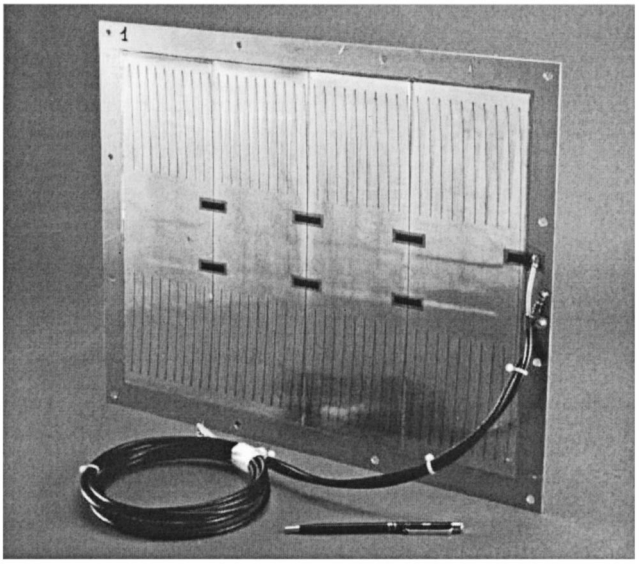

FIG. 3. The ASAC panel with the collocated and shaped PVDF uniform force actuator and volume velocity sensor.

The solid and faint lines of Fig. 4 compare the theoretical and measured transfer function $G(\omega)$ in a frequency range from 10 Hz to 50 kHz. This plot shows a relatively good agreement between the predicted and the experimental sensor–actuator frequency response functions. The importance of the in-plane coupling effects between the sensor and actuator transducer above about 100 Hz is therefore confirmed experimentally.

At about 200 Hz the frequency response function starts to linearly rise because of the ''low frequency'' in-plane stiffness effect. The plot in Fig. 4 shows some differences between the measured and predicted frequency response functions in the frequency range 200 Hz to 3 kHz. Lee[25] has found that because the PVDF piezoelectric transducers are much compliant than the plate on which they are bonded they tend to have in-plane resonant modes uncoupled from those of the plate, which occur at lower frequencies than those of the plate. The two bumps at about 1.3 kHz and 2 kHz are therefore due to rather heavily damped in-plane resonance frequencies associated with in-plane modes of the sensor and actuator piezoelectric films. Above the in-plane resonance frequency at 21 kHz the modulus of the sensor–actuator frequency response function start to fall again, so that at about 50 kHz the level of the response is about the same as that at the resonance frequency of the first bending mode.

The second key feature highlighted by Fig. 4 is the phase plot, which shows a phase shift of $-180°$ at the resonance frequency of the first bending mode of the panel at 59 Hz and a second phase shift of about $-180°$ at the resonance frequencies of the uncoupled in-plane modes of the piezoelectric transducers. The phase shift recovers to about $-90°$ between 5 and 10 kHz, but at the resonance frequencies of 12 kHz and 21 kHz, due to the in-plane longitudinal and shear natural modes of the panel, another phase shift of $-180°$ is introduced. The sensor–actuator frequency response function is not strictly positive real as confirmed by the Nyquist plot of the frequency response shown in Fig. 5, which highlights

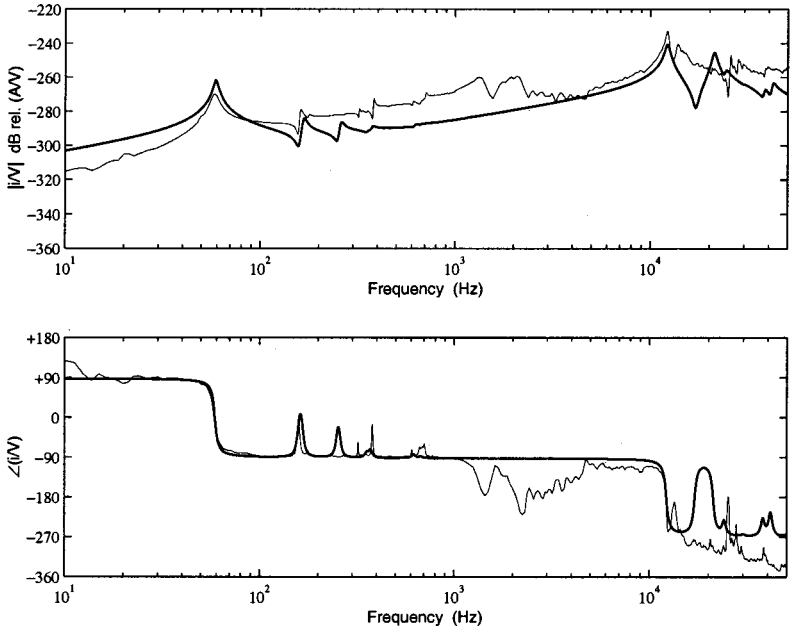

FIG. 4. Simulated (solid line) and measured (faint line) response of the output current from the volume velocity sensor per unit voltage input to the force actuator.

a clear problem of stability for the feedback control implementation. If a simple direct velocity feedback control scheme is used, then there is a clear stability problem caused by the extra $-180°$ phase shift at the resonance frequencies due to the uncoupled in-plane modes of the two piezoelectric films (circle number 1 in the Nyquist plot) and at the resonance frequencies due to the in-plane modes of the panel (circles number 2 and 5 in the Nyquist plot).

In conclusion, the measured frequency response function of the matched sensor–actuator pair studied in this paper is not strictly positive real above 1 kHz, because of in-plane coupling, and it is also characterized by a much larger amplitude than at the first resonance frequency. This leads to a stability problem for the implementation of direct velocity feedback. Although a compensator circuit could be considered to improve the stability of the control system, the increasing amplitude of the plant response due to in-plane coupling requires a relatively high order low pass characteristic to reduce its effects, which will inevitably lead to large phase shifts and potential stability problems at lower frequencies.

VI. CONCLUSIONS

In this paper the frequency response function of a matched volume velocity sensor and uniform force actuator bonded on to a panel has been studied both analytically and experimentally. The analysis has been carried out with a view to the possibility of direct velocity feedback control architecture for the implementation active structural acoustic control.

Below 100 Hz the sensor–actuator response is controlled by the bending vibration of the panel and a good estimate of the volumetric component of the transverse vibration of the panel is achieved. At higher frequencies, how-

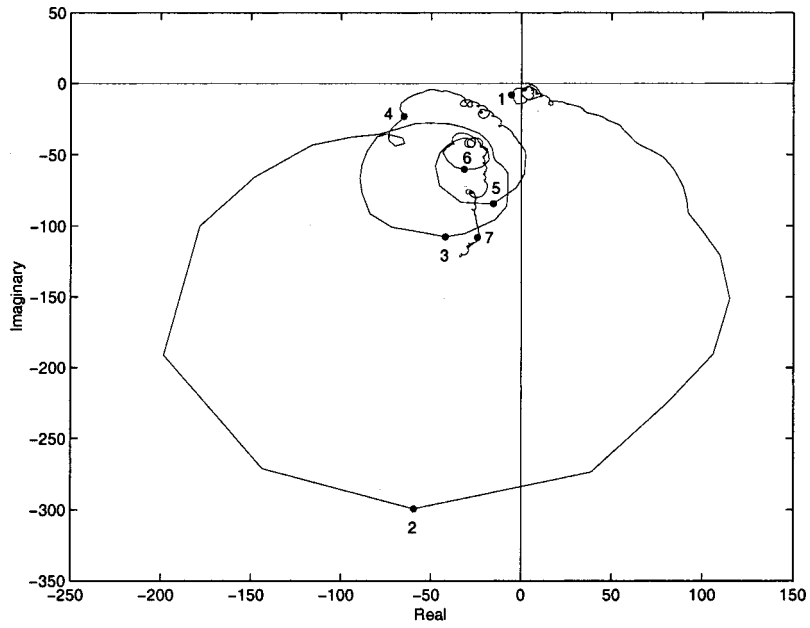

FIG. 5. Real and imaginary parts of the measured sensor–actuator transfer function. The marked points correspond to frequencies: 1⇒2187 Hz, 2⇒12 188 Hz, 3⇒13 688 Hz, 4⇒14 938 Hz, 5⇒25 563 Hz, 6⇒27 875 Hz, 7⇒46 813 Hz.

ever, the sensor–actuator response is instead controlled by the in-plane longitudinal and shear vibration of the panel. This phenomenon has two major effects on the frequency response function:

(a) the amplitude tends to rise with frequency and has peaks due to in-plane modes of the panel, which are about 20 dB higher than that due to the first bending mode of the panel;
(b) above 1 kHz the frequency response function is not strictly positive real because of the extra $-180°$ phase shifts generated by the uncoupled in-plane resonant modes of the actuator and sensor piezoelectric films and because of the in-plane resonant panel modes.

These two characteristics pose serious problems for the stability of a direct velocity feedback control system.

ACKNOWLEDGMENTS

The content of this paper is part of a Brite-Euram project supported by the EC under Contract No. BRPR-CT96-0154 DAFNOR, ''Distributed Active Foils for NOise Reduction.'' Also, the authors would like to thank G. Roux who built the smart panel with the volume velocity sensor and a uniform force actuator shown in Fig. 3.

[1] C. R. Fuller and R. J. Silcox, ''Active structural acoustic control,'' J. Acoust. Soc. Am. **91**, 519 (1992).
[2] C. R. Fuller, S. J. Elliott, and P. A. Nelson, *Active Control of Vibration* (Academic, London, 1996), Chaps. VIII and IX.
[3] M. E. Johnson, ''Active Control of Sound Transmission,'' Ph.D. thesis, University of Southampton (1996).
[4] S. J. Elliott and M. E. Johnson, ''Radiation modes and the active control of sound power,'' J. Acoust. Soc. Am. **94**, 2194–2204 (1993).
[5] M. E. Johnson and S. J. Elliott ''Active control of sound and vibration using volume velocity cancellation,'' J. Acoust. Soc. Am. **98**, 2174–2186 (1995).
[6] S. J. Elliott and T. J. Sutton, ''Performance of feed-forward and feedback methods for active control,'' IEEE Trans. Speech Audio Process. **4**, 214–223 (1996).
[7] M. E. Johnson, T. Sors, S. J. Elliott and B. Rafaely, ''Feedback control of broadband sound radiation using a volume velocity sensor,'' Proceedings of Active 97, Budapest, HU, 21–23 August (1997), pp. 1007–1020.
[8] M. J. Balas, ''Direct velocity feedback of large space structures,'' J. Guid. Control **2**, 252–253 (1979).
[9] P. Curie and J. Curie, Comptes Rendus **91**, 294 (1880).
[10] A. van der Ziel, Solid state physical electronics (1968).
[11] C. K. Lee, ''Theory of laminated piezoelectric plates for the design of distributed sensor/actuators. Part I: governing equations and reciprocal relationships,'' J. Acoust. Soc. Am. **87**, 1144–1158 (1990).
[12] J. Rex and S. J. Elliott, ''A new sensor for structural radiation control,'' Proceedings of the 1st International Conference on Motion and Vibration Control, 1992, pp. 339–343.
[13] P. Gardonio, Y.-S. Lee, S. J. Elliott, and S. Debost, ''A panel with matched PVDF volume velocity sensor and uniform force actuator pair for the active control of sound transmission,'' Proc. Inst. Mech. Eng. **215**(Part G), 187–206 (2001).
[14] H. Kawai, ''The piezoelectricity of polyvinylidene floride,'' Jpn. J. Appl. Phys. **8**, 975–976 (1969).
[15] D. M. Carey and F. B. Stulen, ''Experiments with a two-dimensional multi-modal sensor,'' Recent Advances in Active Control of Sound and Vibration, supplement, 41–52 (1993).
[16] F. Charette, C. Guigou and A. Berry, ''Development of volume velocity sensors for plates using PVDF film,'' Proceedings of ACTIVE 95 (1995), pp. 241–252.
[17] R. L. Clark, W. R. Saunders, and G. P. Gibbs, *Adaptive Structures* (Wiley, New York, 1998).
[18] A. Preumont, *Vibration Control of Active Structures* (Kluwer Academic, City, 1997).
[19] T. Bailey and J. E. Hubbard, ''Distributed piezoelectric-polymer active vibration control of a cantilever beam,'' J. Guid. Control **8**, 605–611 (1985).
[20] C. K. Lee and F. C. Moon, ''Modal sensors/actuators,'' ASME Trans. J. Appl. Mech. **57**, 434–441 (1990).
[21] P. Gardonio and S. J. Elliott, 1998 ISVR University of Southampton, Technical Report No. 277, ''Driving point and transfer mobility matrices for thin plates excited in flexure.''
[22] W. Soedel, *Vibrations of Shells and Plates* (Marcel Dekker, New York, 1993).
[23] J. N. Reddy, *Mechanics of Laminated Composite Plates* (CRC Press, New York, 1993).
[24] M. Tohyama and R. H. Lyon, ''Zeros of a transfer function in a multi-degree-of-freedom vibrating system,'' J. Acoust. Soc. Am. **86**, 1854–1863 (1997).
[25] Y.-S. Lee, ''Active Control of Smart Structures using Distributed Piezoelectric Transducers,'' Ph.D. thesis, University of Southampton (2000).

Polynomial relations for quasi-static mechanical characterization of isotropic poroelastic materials

Christian Langlois, Raymond Panneton,[a] and Noureddine Atalla
GAUS, Department of Mechanical Engineering, Université de Sherbrooke, Québec J1K 2R1, Canada

(Received 16 August 2001; accepted for publication 24 September 2001)

This paper proposes a quasi-static method for the characterization of the elastic properties of poroelastic materials. The method is based on the development of polynomial relations among compression stiffness, Young's modulus, Poisson's ratio, and shape factor derived from high order axisymmetrical finite element simulations on a disk-shaped poroelastic sample under static compression. The shape factor is defined as half the radius to thickness ratio of the sample. The polynomial relations account for the fact that the disk sample ''wants'' to bulge sideways when compressed between two rigid plates on which it is bonded. A compression test setup is used to measure the compression stiffness of two disk samples of different large shape factors. The measured stiffnesses together with the polynomial relations lead to a system of two equations and two unknowns. The solution of the system yields the Young's modulus and Poisson's ratio of the poroelastic material. Employing the proposed quasi-static method, Young's modulus, Poisson's ratio, and loss factor are measured for a poroelastic foam. The measured elastic properties are used in the Biot poroelasticity theory to predict the sound absorption coefficient of the foam. The prediction is finally compared with a standing wave tube measurement. A good correlation is obtained. [DOI: 10.1121/1.1419091]

PACS numbers: 43.40.Yq, 43.20.Ye, 43.40.At [JGM]

I. INTRODUCTION

Following the Biot theory,[1] the frame of an isotropic open-cell poroelastic material is defined by three macroscopic elastic properties: the loss factor and two of the following properties: shear modulus (G), Young's modulus (E), and Poisson's ratio (ν). These properties are usually complex and frequency dependent due to the viscosity of the frame,[2,3] mainly for polymeric foams. Therefore, a dynamic test should be performed to characterize these properties. Nevertheless, even if the dynamic modulus (G or E) can be higher than its static value, comparisons between simulations and measurements on multilayered panels showed that the use of constant elastic properties, measured at low frequencies, still yields good correlations.[4,5] Thus a quasi-static measurement of the elastic properties, such as proposed by Mariez *et al.*,[6] is sufficient for most acoustical and vibroacoustical problems. For open-cell poroelastic materials, this characterization should be performed in vacuum since the fluid motion in the porous network may affect the measurement.[7] Alternatively, a method consisting of removing numerically the fluid effects can also be used.[8] Another fact worth mentioning concerns the anisotropy of porous materials. A number of porous materials are of anisotropic nature. However, when the degree of anisotropy is low, it has been shown that an isotropic model gives better results than an anisotropic model.[9,10]

In the past, a number of methods have been proposed to measure the elastic properties of open-cell poroelastic materials. Some of the methods are based on uniaxial compression or transmissibility test applied on a disk-shaped sample assumed equivalent to a massless spring or a spring-mass system.[11–13] Other methods are based on a shear test[2] applied to a brick-shaped sample. In these aforementioned methods, the measured properties may be far from the true properties since the effects of the boundary conditions (here no-slip condition) are neglected. These effects are more important for small samples. To minimize the boundary conditions effects, Pritz[14] proposed a method based on long and slender rodlike porous samples. The Young's modulus is then determined from the longitudinal vibrations of the rod and the Poisson's ratio from the change in diameter when the rod is stretched. In practice, the use of a long and slender rod is the main limitation of the method since it is not easy to cut properly such a sample from commercially available porous materials. Contrary to the long and slender rod, a small disk- or brick-shaped sample can easily be cut from a plate of porous material. Therefore, to account for the finite size of the sample, i.e., the boundary conditions effects, Mariez *et al.*[6] and Sim and Kim[15] have investigated characterization methods, based on the finite element analysis. In the work by Mariez *et al.*, a cubic foam sample is compressed between two rigid plates—see Fig. 1. E and υ are adjusted in a static finite element model of the test setup to match the measured mechanical impedance (F/u) and the displacement ratio (v/u) at angular frequency ω. Angular frequency is sufficiently low so that the static model is a good approximation of the dynamic measurement. Consequently, the method applies for angular frequencies much lower than any resonances. The work by Sim and Kim is based on a transmissibility test performed on two disk-shaped samples of different shape factors. The shape factor is defined as half the radius to thickness ratio of the sample ($R/2L$). The first sample has a rather small shape factor so that a good initial estimate of the

[a]Electronic mail: raymond.panneton@gme.usherb.ca

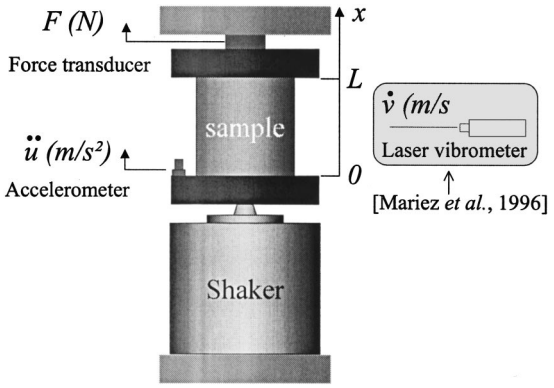

FIG. 1. Measurement setup for the compression test.

Young's modulus can be derived from the transmissibility measurement. Next, a finite element model is built to simulate the transmissibility on the second sample. The second sample has a large shape factor. Poisson's ratio is then adjusted so that the simulated transmissibility matches the measured one. The found Poisson's ratio is then used to identify a better estimate of the Young's modulus from the first sample and to carry on the iteration. The iteration stops when small changes are observed in E and υ. The main limitation of the two previous methods is that a finite element model needs to be built and solved during the characterization process—this may be time consuming.

In this paper, a straightforward method based on a quasi-static compression test is proposed to characterize the elastic properties of a disk-shaped poroelastic sample. A quasi-static test is preferred to a static test in view of circumventing the relaxation phenomenon in the statically compressed material. The originality of the method lies in the derivation of polynomial relations among compression stiffness, Young's modulus, Poisson's ratio, and shape factor from high order axisymetrical finite element simulations on a disk-shaped foam sample under static compression. The relations hold in the low frequency range—below any resonances—and account for the fact that the disk sample bulges sideways when compressed between rigid plates. A characterization procedure based only on the polynomial relations and a quasi-static compression test is proposed to identify simultaneously the static value of the Young's modulus and Poisson's ratio. The compression test is performed on two samples of different large shape factors. Here, the shape factor is defined as half the radius-to-thickness ratio $(R/2L)$. Such samples can be easily cut in commercially available porous materials. Contrary to previous works, only one type of measurement is needed—namely the mechanical impedance—and no iterations on a finite element model are carried out during the characterization process.

In the following, the experimental setup on which the method is based is discussed in Sec. II. In Sec. III, the theory behind the development of the polynomial relations is presented. In Sec. IV, an application of the characterization procedure on a poroelastic material is detailed. Finally, normal incidence absorption measurements in a standing wave tube are compared to predictions from the Biot–Allard model[4] using the elastic parameters measured with the proposed procedure.

II. MEASUREMENT SETUP

The measurement setup for which the characterization procedure is developed in the next sections is depicted in Fig. 1. It consists of a disk-shaped poroelastic sample sandwiched between two rigid plates. The side of the plates facing the sample is covered with sandpaper to prevent radial sliding at the sample-plate interfaces. An accelerometer is fixed on the bottom plate. A shaker using a pseudo-random noise in a frequency range well below any resonances; typically 0–100 Hz excites the bottom plate. The top plate is mounted on a force transducer fixed on a rigid wall. The accelerometer measures the acceleration $\ddot{u}(\omega)$ of the bottom plate, while the force transducer measures the reaction force $F(\omega)$ applied on the top plate. An FFT analyzer integrates twice the accelerometer signal, to obtain the displacement $u(\omega)$, and computes the transfer function or mechanical impedance, namely:

$$Z_m(\omega)=\frac{F(\omega)}{u(\omega)}. \tag{1}$$

To correct the transfer function from perturbations that are extraneous to the behavior of the tested sample, the calibration procedure proposed by Mariez *et al.*[6] can be used. In this case, a calibrated spring having a first resonance much higher than the frequency range of interest is tested on the setup. In this frequency range, the stiffness of the calibrated spring is assumed to be constant and equal to its static value k_0. The departure from this stiffness on the spring's transfer function is the error related to extraneous effects. The resulting correction function H_c for the experimental setup is then

$$H_c(\omega)=\frac{1}{k_0}\cdot\frac{F(\omega)}{u(\omega)}\bigg|_{\text{spring}}. \tag{2}$$

Consequently, the corrected reading for Eq. (1) is

$$Z_{mc}(\omega)=\frac{Z_m(\omega)}{H_c(\omega)}. \tag{3}$$

To ensure linearity in the porous material's behavior, strains applied to the sample should not exceed 5%.[2] Furthermore, since the skeleton of a porous material is usually not purely elastic, its elastic properties may vary with the initial strain. Consequently, the initial strain applied to the sample during the test should be as close as possible to its end application. Also, at low rates, where fluid flow and thermal processes are insignificant, and strains less than 5%, it is assumed that measurements in air are similar to measurements in vacuum. That simplifies the experimental setup and allows considering open-cell air-saturated poroelastic materials as elastic solids. Indeed, the proposed procedure has been done systematically in air and in vacuum, and no significant differences were found.

The corrected mechanical impedance given by Eq. (3) is complex valued. It can be rewritten by separating its real and imaginary parts as follows:

$$Z_{mc}(\omega)=K_m(\omega)+jX_m(\omega), \tag{4}$$

where $K_m(\omega)$ is the compression stiffness or mechanical resistance of the test sample at angular frequency ω, and $X_m(\omega)$ its reactance. At low frequencies, where inertial effects are insignificant, a good approximation of the reactance is the mechanical resistance times the loss factor of the material, that is,

$$Z_{mc}(\omega)\cong K_m(\omega)(1+j\,\eta(\omega)). \tag{5}$$

Consequently, in the quasi-static range of interest, the compression stiffness and loss factor are given by

$$K_m(\omega)=\mathrm{Re}(Z_{mc}(\omega)) \tag{6}$$

and

$$\eta(\omega)\cong\frac{\mathrm{Im}(Z_{mc}(\omega))}{\mathrm{Re}(Z_{mc}(\omega))}. \tag{7}$$

Finally, to measure macroscopically homogeneous elastic properties, the diameter of the test samples should contain at least seven cells,[16] i.e., the diameter and the thickness should be greater than 1 cm if the cells are 1 mm wide. Also, the test setup should allow the use of small columns of porous materials having a shape factor $(R/2L)$ greater or equal to 0.25, i.e., diameter $(2R)$ greater or equal to thickness (L). This is motivated by the following two reasons. (1) Typically, materials are commercially available in a thickness of 10 cm (4 in.) or less. (2) Acoustical tests in standing wave tube usually require disk-shaped samples of 3–10 cm in diameter.

III. POLYNOMIAL RELATIONS

A. Static finite element simulations

Let s be the shape factor defined previously, that is $R/2L$. For a long and slender column (typically $s<0.025$), the static compression stiffness is virtually not affected by either the Poisson's effect or the boundary conditions. In this case, the column can be characterized by the one-dimensional static compression stiffness given by

$$K_0=\frac{EA}{L}, \tag{8}$$

where A is the cross-section area of the column, and L its length. When the column is short (typically $s\geqslant 0.025$), the Poisson's effect and boundary conditions affect substantially the reading of the compression stiffness $K_m(0)$. In this case, substituting $K_m(0)$ for K_0 in Eq. (8) and solving for the Young's modulus lead to an apparent Young's modulus E' given by

$$E'=\frac{L}{A}K_m(0). \tag{9}$$

Dividing Eq. (9) by the true value of the Young's modulus yields the dimensionless ratio of the normalized static compression stiffness, namely:

$$\frac{E'}{E}=\frac{K_m(0)}{K_0}. \tag{10}$$

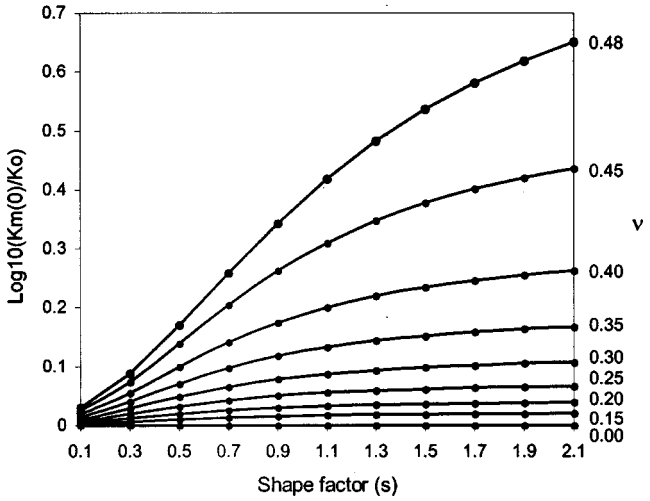

FIG. 2. Variations of the normalized static compression stiffness $[K_m(0)/K_0$ or $E'/E]$ as a function of the shape factor and Poisson's ratio. The dots are the results obtained from the axisymmetrical finite element model. Polynomial curves are plotted over these dots for each Poisson's ratio.

Since for large shape factors the Poisson's effect and the boundary conditions, together creating the sample to bulge sideways, heavily influence this ratio, it is worth exploring its variation in function of the Poisson's ratio and shape factor.

To do so, finite element (F.E.) simulations of the setup shown in Fig. 1 are performed. Since only static compression is simulated, the poroelastic sample is modeled as a solid material using the elasticity theory. Also, to account for the axisymmetry of the problem and to minimize the computation time and the size of the model, an axisymmetrical modeling is chosen. The mesh consists of four axisymmetrical elements. Lagrange's interpolation functions of the sixth order are used to obtain accurate results. The nodal variables are the radial (v) and axial (u) displacements. This leads to a finite element system of 169 nodes and 338 degrees of freedom (dofs). To represent the boundary conditions between the top rigid plate and the sample, radial and axial displacements are constrained at the upper nodes. For the rigid plate excited by the shaker, radial displacements are constrained at the lower nodes and an axial displacement u_0 is imposed.

In the F.E. simulations, for a given Young's modulus E, the static compression stiffness $K_m(0)$ as defined in Eq. (6) (at $\omega=0$) is computed for different combinations of Poisson's ratio and shape factor. The Poisson's ratio ranges from 0 to 0.48, and the shape factor from 0.1 to 2.1. The variation range for the Poisson's ratio is selected to represent typical range for sound absorbing porous materials such as fibrous and foams. Dividing the computed $K_m(0)$ by K_0 yields the normalized static compression stiffness which is independent of the Young's modulus. The results of the simulations are plotted in Fig. 2. It is noted that for small shape factors (long and slender columns), the normalized compression stiffness tends to 1 (0 in logarithm). Also, as the shape factor increases, the combined effects of the Poisson's ratio and boundary conditions, creating the bulge out deformation, become significant and the compression stiffness diverges from 1 (0 in logarithm). Similarly, when the Poisson's ratio in-

creases, the ratio $K_m(0)/K_0$ also diverges from 1. Consequently, one can note that for a combination of (E,s,ν) a unique value of $K_m(0)/K_0$ exists.

From this observation, one can conclude that following a measurement on a sample of a given large shape factor, if ratio $K_m(0)/K_0$ is known, then the material's properties can be determined from Fig. 2 used as an abacus. Unfortunately, in reality K_0 cannot be computed because the real Young's modulus is not known *a priori*. To circumvent this problem, Sim and Kim[15] used a first experiment on a column of small shape factor to obtain an estimate of the Young's modulus. However, as discussed in the Introduction, their method necessitates iterations and inversion on a finite element model. A better alternative is proposed in the following.

B. Polynomial relations in terms of the shape factor

Instead of using Fig. 2 as an abacus, each curve related to a specific Poisson's ratio can be written in the form of a polynomial in s of order M to facilitate its use, namely:

$$P_\nu(s)=\frac{K_m(0)}{K_0}=1+\sum_{i=1}^{M} C_i^\nu s^i, \tag{11}$$

where C_i^ν are the coefficients of the curve fit related to curve ν [recall that $K_m(0)$ simply means the compression stiffness measured at 0 Hz]. For the data provided in Fig. 2, where 11 curve fit points along s are available, order $M=10$ is chosen. For $s=0$, that is a column of infinite length, the polynomial is imposed to 1. This is consistent with the one-dimensional theory.

C. Polynomial relations in terms of the Poisson's ratio

For a given shape factor s, one can build from Eq. (11) a single polynomial in ν, namely:

$$P_s(\nu)=\frac{K_m(0)}{K_0}=1+\sum_{i=1}^{N} D_i^s \nu^i, \tag{12}$$

where the D_i^s are the curve fit coefficients of the new polynomial related to shape factor s. For the data provided in Fig. 2, where nine curve fit points along ν are available, order $N=8$ is chosen. It is worth noting that for a Poisson's ratio of zero, the polynomial falls to a value of 1. This is consistent with measurements on zero Poisson's ratio materials, such as glass wool,[17] for which a unit ratio $K_m(0)/K_0$ is found.

D. Quasi-static approximation

For the reasons stated in the introduction, only the frequency range well below any resonances is of interest here. In this frequency range, the inertia of the system is insignificant. Thus we can assume that the "static" polynomial relations still hold. Under this quasi-static approximation, the following substitution can be done in Eqs. (11) and (12):

$$K_m(\omega)\rightarrow K_m(0) \quad \text{for } \omega \ll \omega_1, \tag{13}$$

where ω_1 is the first resonance of the system.

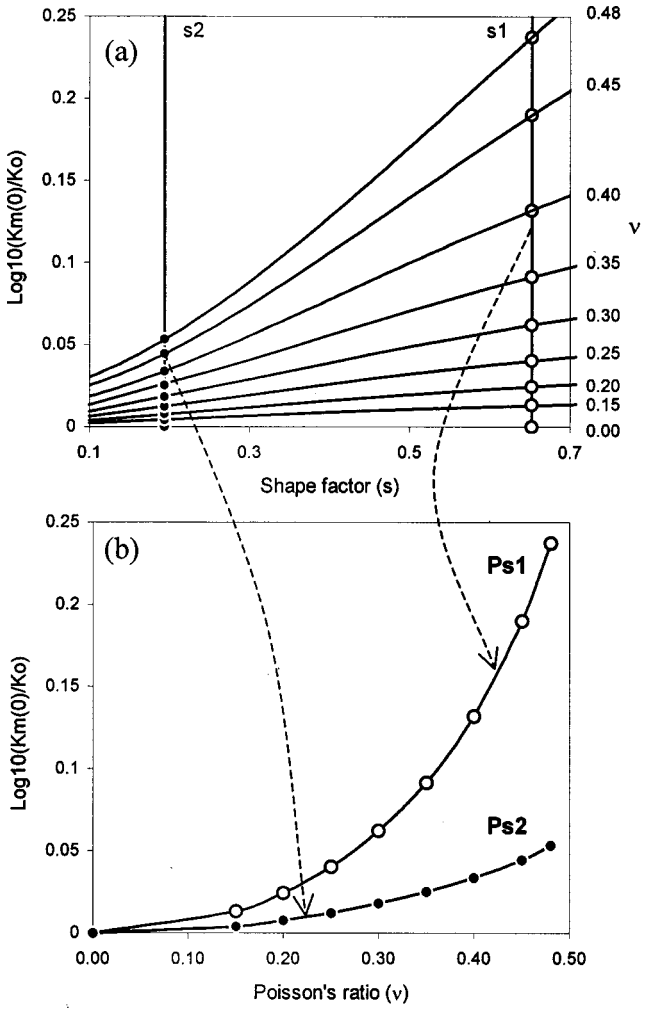

FIG. 3. Graphical representation of the procedure to build polynomials $P_{s_1}(\nu)$ and $P_{s_2}(\nu)$.

IV. CHARACTERIZATION EXAMPLE

This section presents an example of the characterization procedure using the previous polynomials [Eqs. (11) and (12)] with the experimental setup of Fig. 1. For this example, two disk-shaped samples of shape factors $s_1=0.6519$ and $s_2=0.1946$ are cut from an open-cell porous material, namely foam "*A*." Both samples have a thickness of 38.3 mm. Their respective diameter are 99.8 mm and 29.7 mm.

A. Building of the polynomials

Figure 3 gives a graphical representation on the building of the polynomials needed for the characterization. This is briefly a double interpolation procedure. First, the polynomial expression in Eq. (11) is evaluated at s_1 and s_2 for the different Poisson's ratios given in Fig. 2. The computed values—dots in Fig. 3(a)—are then used to form, with Eq. (12), the following polynomials in terms of the Poisson's ratio, namely:

$$P_{s_1}(\nu)=\frac{K_{m,s_1}(0)}{K_{0,s_1}}=3883\nu^8-7249\nu^7+5876\nu^6 -2630\nu^5+705\nu^4-111\nu^3+11\nu^2+1 \tag{14}$$

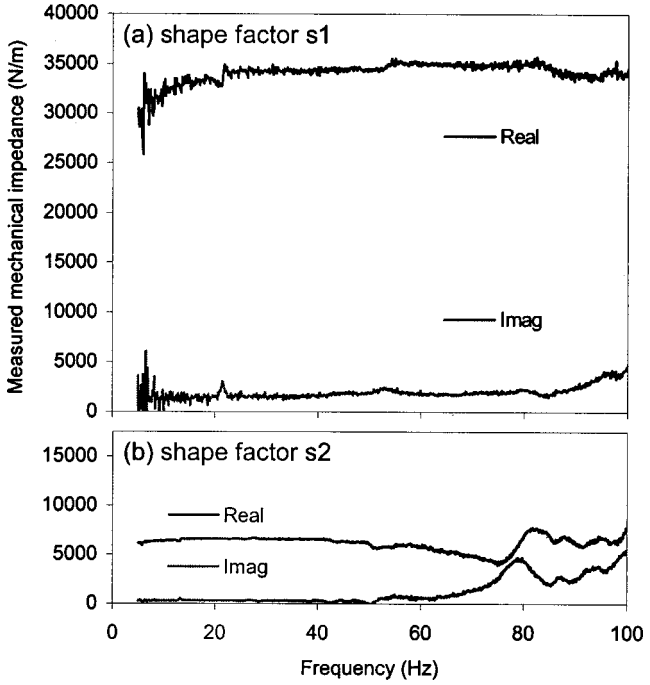

FIG. 4. Measured mechanical impedance $Z_m(\omega)$ for foam "*A*." The real part is the mechanical resistance or compression stiffness. The imaginary part is the mechanical reactance. (a) Shape factor of 0.6519. (b) Shape factor of 0.1946.

and

$$P_{s_2}(\nu)=\frac{K_{m,s_2}(0)}{K_{0,s_2}}=3235\nu^8-6308\nu^7+5153\nu^6 -2283\nu^5+592\nu^4-90\nu^3+8\nu^2+1, \tag{15}$$

where subscripts s_1 and s_2 indicate the sample associated to a variable. Both polynomials are plotted in Fig. 3(b). It is worth noting that the coefficients of the polynomials have been rounded for conciseness.

B. Measurement of the mechanical impedance

A measurement of the mechanical impedance is made on samples s_1 and s_2 following the experimental procedure described in Sec. II. The measured mechanical impedances are shown in Fig. 4. For frequencies below 20 Hz, the transducers give a noisy signal for the large shape factor. However, for frequencies between 20 and 80 Hz, the behavior of sample s_1 is quasi-static. For sample s_2, the behavior is quasi-static from the beginning of the curve up to 50 Hz. After the quasi-static range, the inertia of the system becomes significant and the behavior of the samples follows a complex evolution in function of the frequency.

C. Determination of the Poisson's ratio

Since the two samples are taken from the same material, they both share the same Young's modulus E, Poisson ratio ν, and damping loss factor η. Therefore, using the quasi-static approximation [Eq. (13)] and combining Eqs. (8), (9), (14), and (15) yields

$$E(\omega)=\frac{K_{m,s_1}(\omega)L_{s_1}}{P_{s_1}(\nu)A_{s_1}}=\frac{E'_{s_1}(\omega)}{P_{s_1}(\nu)} \tag{16}$$

and

$$E(\omega)=\frac{K_{m,s_2}(\omega)L_{s_2}}{P_{s_2}(\nu)A_{s_2}}=\frac{E'_{s_2}(\omega)}{P_{s_2}(\nu)}, \tag{17}$$

where $K_{m,s}(\omega)$ and $E'_s(\omega)$ are the measured compression stiffness and the apparent Young's modulus of sample s at angular frequency ω. L_s and A_s are the thickness and cross-section area of sample s. In these equations, polynomials P_{s_1} and P_{s_2} can be viewed as correction factors to apply on the apparent Young's moduli to obtain the true value of the Young's modulus.

Combining Eqs. (16) and (17) yields the following equation:

$$\frac{E'_{s_1}(\omega)}{P_{s_1}(\nu)}-\frac{E'_{s_2}(\omega)}{P_{s_2}(\nu)}=0. \tag{18}$$

Since the apparent Young's moduli are determined from the geometry of the samples and the measured compression stiffnesses [$K_{m,s_1}(\omega)$ and $K_{m,s_2}(\omega)$], the above equation has only one unknown: the Poisson's ratio. Consequently, the admissible root of the equation is the Poisson's ratio of the material. The admissible root shall be positive, real and in the variation range of ν; for this study, 0 to 0.48.

For the two samples of foam "*A*" under consideration ($s_1=0.6519$ and $s_2=0.1946$), using their respective polynomial expression given by Eqs. (14) and (15), their measured compression stiffness shown in Fig. 4, and their geometrical properties, the Poisson's ratio found from Eq. (18) is displayed in Fig. 5(a) for the 20–40 Hz frequency range. Over this range, the mean value and standard deviation of the Poisson's ratio are 0.450 and 0.003, respectively. This agrees with typical values found for foams.[18] The statistics are reported in Table I.

D. Determination of the Young's modulus

Once the Poisson's ratio is found over the frequency range of interest, the determination of the Young's modulus is straightforward. It is given by either Eq. (16) or Eq. (17) using the computed Poisson's ratio to evaluate the correction functions $P_{s_1}(\nu)$ and $P_{s_2}(\nu)$ to apply on the apparent Young's moduli. Figure 5(b) shows the Young's modulus computed over the 20–40 Hz frequency range from both equations (or samples). It is noted that the Young's modulus varies slightly around a mean value of 108 071 Pa with a standard deviation of 735 Pa. These statistics are reported in Table I.

E. Determination of the loss factor

The damping loss factor is computed directly from the real and imaginary parts of the measured mechanical impedance [Eq. (7)]. The loss factor computed over the 20–40 Hz frequency range is shown in Fig. 5(c). Once again, the loss

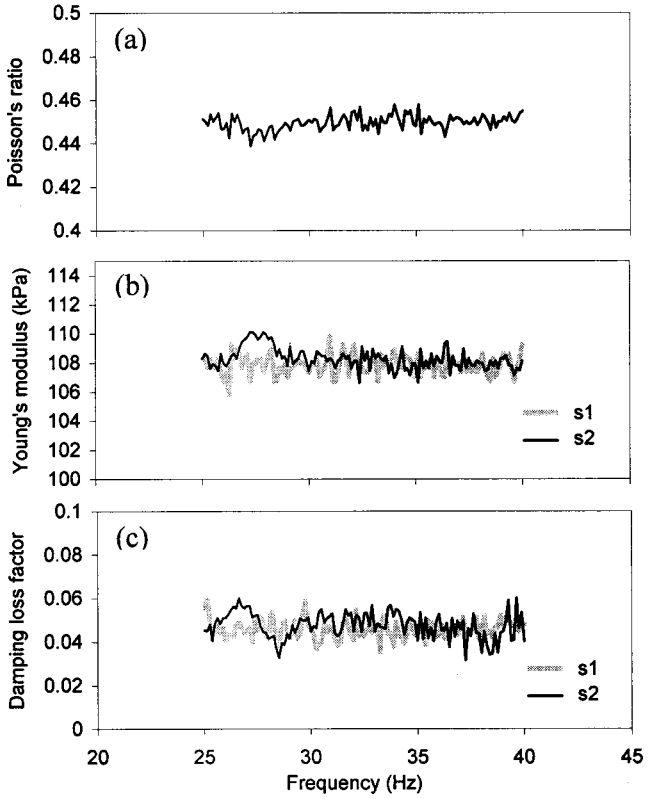

FIG. 5. Elastic properties determined from the proposed quasi-static method.

factor varies slightly around a mean value 0.045 with a standard deviation of 0.005. These statistics are reported in Table I.

F. Uniqueness of the solution

Here, an attempt to show the uniqueness of the solution given by the proposed procedure is illustrated. The demonstration is based on the graphical use of Eq. (18). In Fig. 6, both terms of Eq. (18) are plotted as a function of ν for an arbitrary frequency of 32.5 Hz. At this frequency, the apparent Young's moduli of samples s_1 and s_2 are 167.5 and 120.8 kPa, respectively. The intersection of the two curves occurs at the Poisson's ratio of foam "*A*" for which Eq. (18) falls to zero. Projecting the intersection point to the ordinate axis gives the true Young's modulus of the material. Theoretically, since both curves follow a monotonous evolution in function of ν and both apparent Young's moduli in Eq. (18) are independent of ν, the curves will intersect only once in the admissible variation range of ν. The same conclusion can also be drawn from Fig. 2, where the curves in ν never intersect, except at $s=0$.

TABLE I. Mechanical parameters of foam "*A*" from the data collected in the 20–40 Hz frequency range.

Properties	Mean	Standard deviation
Young's modulus (Pa)	108 071	±735
Poisson's ratio	0.450	±0.003
Loss factor	0.045	±0.005

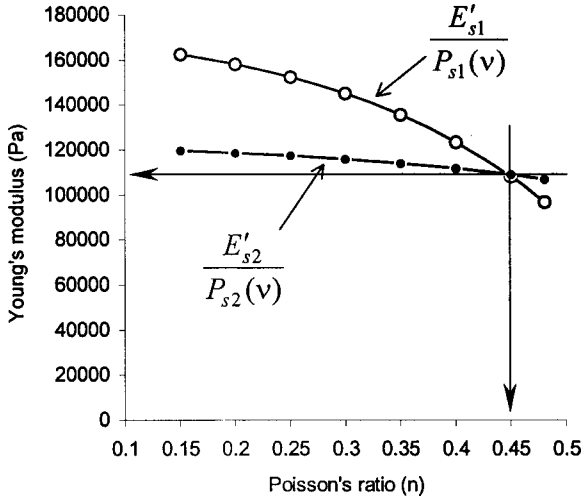

FIG. 6. Graphical representation of the identification of the Poisson's ratio and Young's modulus of foam "*A*" from Eq. (11) and samples s_1 and s_2. The curves are plotted for an arbitrary frequency of 32.5 Hz.

V. VALIDATION

In this section, the measured mechanical parameters listed in Table I are used to feed the Biot–Allard poroelastic model[4] to predict the normal incidence absorption coefficient of foam "*A*." The prediction will be compared to a standing wave tube measurement in a B&K 4206 tube following standard ASTM E 1050-86 (see Fig. 7). The 99 mm large tube is used. Two similar samples of foam "*A*" are measured. Both are 76.55 mm thick and their diameter is slightly larger than the tube diameter, which is 99.8 mm. The friction induced by the radial compression combined with adhesive prevent the samples from axial sliding on its contour. The rear side of the sample is bonded with adhesive to the rigid end of the tube. During the test, the temperature and atmospheric pressure are 20 °C and 980 mbar. The tube and the open foam are air-saturated.

In addition to the mechanical parameters of the foam, its bulk density and five acoustical parameters need to be fed into the Biot–Allard model. They are the open porosity, static airflow resistance, tortuosity, viscous characteristic length, and thermal characteristic length. While the bulk density and the two former acoustical parameters are measured directly using classical techniques,[7,19] the tortuosity is measured using an ultrasound technique,[19] and the two charac-

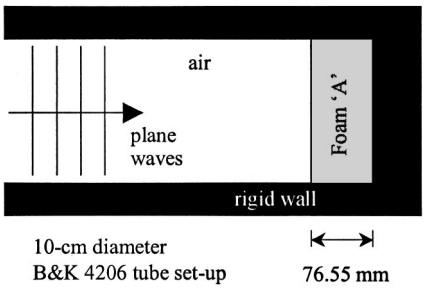

FIG. 7. Setup for the measurement of the normal incidence sound absorption coefficient. A B&K 4206 10 cm tube is used following standard ASTM E1050-86. The foam sample is bonded all around its contour and at the rear face with adhesive.

TABLE II. Acoustical parameters of foam "*A*."

Open porosity	0.995
Airflow resistivity (Ns/m^4)	12 569
Tortuosity	1.00
Viscous characteristic length (μm)	105
Thermal characteristic length (μm)	205
Bulk density (kg/m^3)	8.9

teristic lengths using an inverse identification algorithm.[20] The acoustical parameters of foam "*A*" are listed in Table II.

To take into account the effects of the boundary conditions on the sound absorption prediction, the Biot–Allard poroelastic model will be solved using the finite element method.[21] The boundary conditions applied on the discretized samples consist of constraining radial and axial displacements for nodes in contact with the tube wall. Since linear poroelastic finite elements offer a poor convergence under shear strain,[22] high order finite elements are used to ensure high accuracy in the results.

In Fig. 8, the FEM prediction of the sound absorption of a 76.55 mm thick layer of foam "*A*" is compared to the measurements on samples 1 and 2. It is first noted that the measurements on the two samples give similar results. Second, it is noted that the poroelastic simulation correlates well with the measurements, the dip in the absorption curve at 700 Hz being well predicted. To verify if the dip is really associated to the elasticity of the frame, a simulation using the rigid limit of the Biot–Allard model (i.e., equivalent fluid model[4]) is plotted. As shown in the figure, the rigid frame model does not predict the dip; therefore, one can conclude the dip is associated to the elasticity of the frame.

Also, Fig. 8 shows a prediction from the transfer matrix method of the Biot–Allard model.[4] This analytical approach assumes the sample to be of infinite lateral dimensions. It does not take the effects of the lateral boundary conditions (here no-slip) into account. This explains why its prediction is not good in the vicinity of the frame resonance.

To highlight the effects of an inaccurate measurement of the Young's modulus and Poisson's ratio, Fig. 9 and Fig. 10

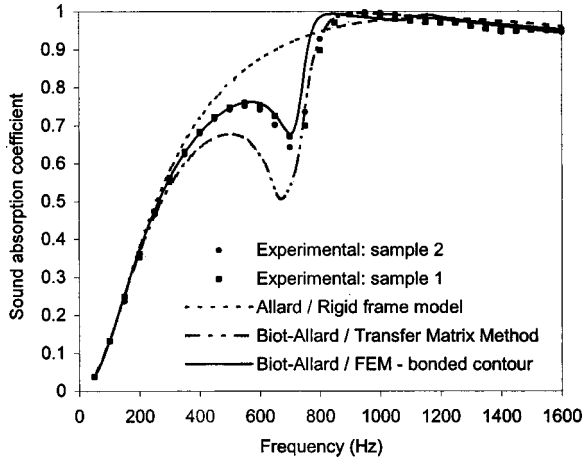

FIG. 8. Normal incidence sound absorption coefficient of a 76.55 mm thick layer of foam "*A*." Predictions versus standing wave tube measurements. Mechanical and acoustical parameters given in Table I and Table II are used in the prediction models.

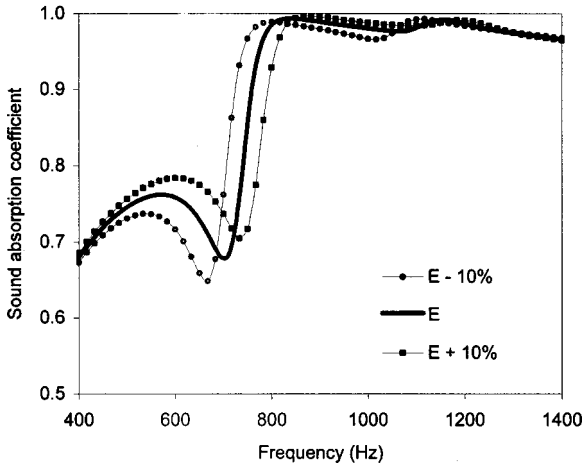

FIG. 9. Effects of a 10% variation of the Young's modulus on the normal incidence sound absorption of a 76.55 mm thick layer of foam "*A*."

compare the previous poroelastic prediction to a prediction with a $\pm 10\%$ variation in the Young's modulus and to a prediction with a $\pm 7\%$ variation of the Poisson's ratio, respectively; each variation being analyzed individually. It is observed that these small variations have a significant impact on the absorption curves, mostly for the Poisson's ratio. Therefore, the accuracy in the measurement of the elastic properties may be of paramount importance to obtain fine predictions.

A last comparison is now presented to warn those who may be tempted to inversely characterize the elastic properties from the absorption curve or to use the apparent Young's modulus directly measured from a compression or transmissibility test on a sample of a large shape factor. As an example, Fig. 11 presents a comparison of the sound absorption predicted using the true elastic parameters given in Table II to a prediction using the apparent Young's modulus measured on sample s_1 (see Sec. IV F). In this case, the apparent Young's modulus is 167.5 kPa and the Poisson's ratio is adjusted so the prediction curve best fits the measurement—here an optimal value of approximately 0.3 is found. This apparent couple ($E' = 167.5$ kPa, $\nu' = 0.3$) is valid only for

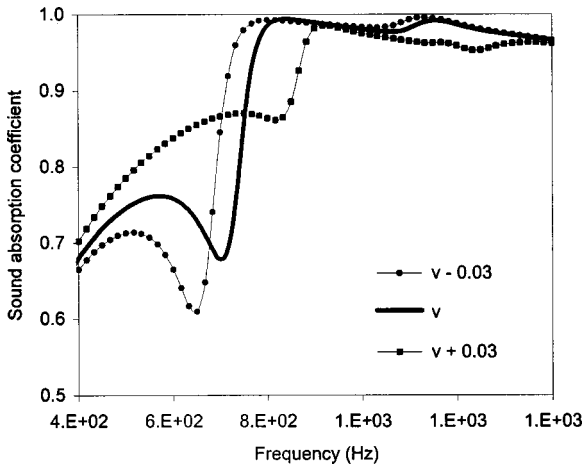

FIG. 10. Effects of a 7% variation (± 0.03) of the Poisson's ratio on the normal incidence sound absorption coefficient of a 76.55 mm thick layer of foam "*A*."

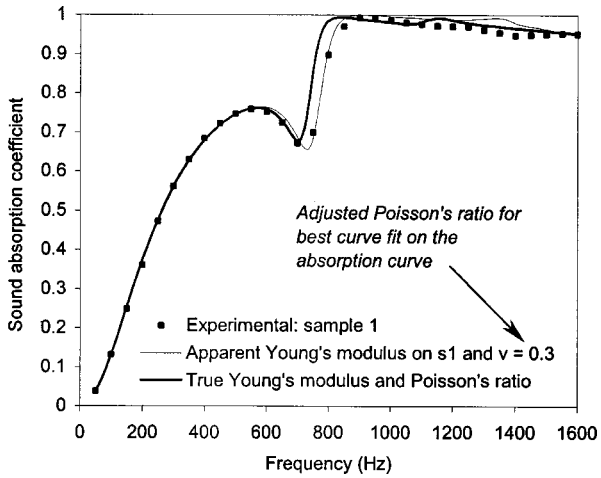

FIG. 11. Normal incidence sound absorption coefficient of a 76.55 mm thick layer of foam "*A*." Comparison between predictions using the true elastic properties ($E=108.1$ kPa, $\nu=0.45$) and the apparent Young's modulus measured on sample s_1 ($E'=167.5$ kPa) with an adjusted Poisson's ratio $\nu'=0.3$.

the configuration used for the inverse characterization of ν'. If another configuration is used, this apparent couple may lead to a bad prediction. This is highlighted in Fig. 12 for which the sound absorption is now predicted for a thickness of 50 mm. In this case, the prediction using the apparent values does not correlate anymore with the prediction using the true values. Finally, this last comparison highlights the fact that trying to inversely characterize the elastic properties from the absorption curve may be hazardous.

VI. CONCLUSION

In this paper, a quasi-static compression test method was proposed to determine the elastic properties of isotropic poroelastic materials. The method uses short columns of poroelastic materials easy to cut from commercially available materials. Its main originality lies in the development of polynomials linking together the compression stiffness, Young's modulus, Poisson's ratio, and shape factor. Contrary to previous methods accounting for the Poisson's effect and boundary conditions on small test samples, the developed method neither requires two axes of measurement (e.g., axial and radial) nor finite element inversion during the characterization process.

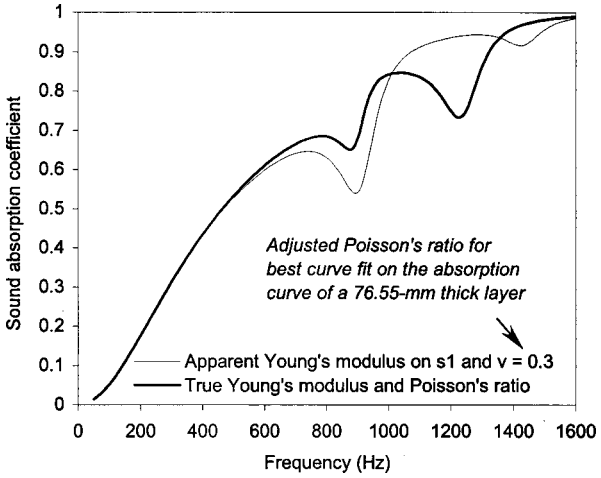

FIG. 12. Normal incidence sound absorption coefficient of a 50 mm thick layer of foam "*A*." Comparison between predictions using the true elastic properties ($E=108.1$ kPa, $\nu=0.45$) and the apparent elastic properties ($E'=167.5$ kPa, $\nu'=0.3$) adjusted to best fit the measurement on the 76.55 mm thick layer in Fig. 11.

The proposed characterization method was validated following the good correlation between the predicted and measured sound absorption coefficients of an elastic resonant foam sample. The prediction was obtained by a high order finite element Biot–Allard poroelastic model feeded with the elastic properties found by the proposed method. The measurement was obtained from a B&K 4206 standing wave tube. It was shown that the boundary conditions on the sample need to be taken into account to predict properly the standing wave tube measurement. Furthermore, it was highlighted that small errors on the measured elastic properties may lead to noticeable changes in the predicted absorption curve. A last study was presented to highlight the fact that trying to inversely characterize the elastic properties from the absorption curve may be hazardous.

Finally, the proposed method is general and Fig. 2 can be used as an abacus for the elastic characterization of, not only open-cell porous materials, but also solid materials and closed-cell porous materials. The limitations are that the materials need to have macroscopic homogeneous and isotropic elastic properties. Furthermore, the computed values in Fig. 2 are only valid in the quasi-static range, that is frequencies much lower than the first resonance of the system.

ACKNOWLEDGMENTS

N.S.E.R.C. Canada and F.C.A.R. Quebec supported this work.

[1] M. A. Biot, *Acoustic, Elasticity, and Thermodynamics of Porous Media—Twenty-One Papers by M. A. Biot*, edited by I. Tolstoy (American Institute of Physics, Woodbury, NY, 1992).
[2] N. C. Hilyard and A. Cunningham, *Low Density Cellular Plastics—Physical Basis of Behavior* (Chapman & Hall, London, 1994).
[3] T. Pritz, "Measurement methods of complex Poisson's ratio of viscoelastic materials," Appl. Acoust. **60**, 279–292 (2000).
[4] J. F. Allard, *Propagation of Sound in Porous Media: Modeling Sound Absorbing Materials* (Elsevier Applied Science, London, 1993).
[5] R. Panneton, "Modelisation numerique tridimensionnelle par elements finis des milieux poroelastiques" ("Finite element modeling of poroelastic media"), Ph.D. dissertation, Universite de Sherbrooke, Quebec, Canada, 1996.
[6] E. Mariez, S. Sahraoui, and J. F. Allard, "Elastic constants of polyurethane foam's skeleton for Biot model," Proceedings of Internoise 96, pp. 951–954 (1996).
[7] U. Ingard, *Notes on Sound Absorption Technology* (Noise Control Foundation, Poughkeepsie, NY, 1994).
[8] M. Melon, E. Mariez, C. Ayrault, and S. Sahraoui, "Acoustical and mechanical characterization of anisotropic open-cell foams," J. Acoust. Soc. Am. **104**, 2622–2627 (1998).
[9] N. Dauchez, "Etude vibroacoustique des materiaux poreux par elements finis" ("Finite element study of the vibroacoustics of porous materials"), Ph.D. dissertation, Universite de Sherbrooke, Quebec, Canada, 1999.
[10] N. Dauchez, S. Sahraoui, and N. Atalla, "Validation of 3-D poroelastic finite element from the impedance measurement of a vibrating foam sample," Can. Acoust. **4**, 94–95 (2000).
[11] Y. K. Kim and H. B. Kingsbury, "Dynamic characterization of poroelastic materials," Exp. Mech. **19**, 252–258 (1979).

[12] A. Wijesinghe and H. B. Kingsbury, ''Complex modulus of a poroelastic column,'' J. Acoust. Soc. Am. **65**, 90–95 (1979).
[13] A. Okuno, ''Dynamic response of structures containing poroelastic materials,'' Ph.D. dissertation, School of Mechanical Engineering, University of Delaware, 1986.
[14] T. Pritz, ''Transfer function method for investigating the complex modulus of acoustic materials: Rodlike specimen,'' J. Sound Vib. **81**, 359–376 (1982).
[15] S. Sim and K.-J. Kim, ''A method to determine the complex modulus and Poisson's ratio of viscoelastic materials from FEM applications,'' J. Sound Vib. **141**, 71–82 (1990).
[16] M. F. Ashby, A. G. Evans, N. A. Fleck, L. J. Gibson, J. W. Hutchinson, and H. N. G. Wadley, *Metal Foams: A Design Guide* (Butterworth-Heinemann, 2000).
[17] D. J. Sides, K. Attenborough, and K. A. Mulholland, ''Application of a generalized acoustic propagation theory to fibrous absorbents,'' J. Sound Vib. **19**, 49–64 (1971).
[18] L. J. Gibson and M. F. Ashby, *Cellular Solids* (Pergamon, Oxford, 1988).
[19] M. Henry, ''Mesure des parametres caractérisant un milieu poreux'' (''Measurement of porous materials parameters''), Ph.D. dissertation, Universite du Maine, Le Mans, France, 1997.
[20] Y. Atalla, R. Panneton, and Franck Sgard, ''Evolutionary strategy algorithm for a complete characterization of porous materials using a standing wave tube,'' J. Acoust. Soc. Am. **108**, 2519(A) (2000).
[21] N. Atalla, R. Panneton, and P. Debergue, ''A mixed pressure-displacement formulation for poroelastic materials,'' J. Acoust. Soc. Am. **104**, 1444–1452 (1998).
[22] N. Dauchez, S. Sahraoui, and N. Atalla, ''Convergence of poroelastic finite elements based on Biot displacement formulation,'' J. Acoust. Soc. Am. **109**, 33–40 (2001).

Active control of the volume acquisition noise in functional magnetic resonance imaging: Method and psychoacoustical evaluation

John Chambers,[a] Michael A. Akeroyd, A. Quentin Summerfield, and Alan R. Palmer
MRC Institute of Hearing Research, University Park, Nottingham NG7 2RD, United Kingdom

(Received 20 July 2000; revised 26 June 2001; accepted 9 August 2001)

Functional magnetic resonance imaging (fMRI) provides a noninvasive tool for observing correlates of neural activity in the brain while a subject listens to sound. However, intense acoustic noise is generated in the process of capturing MR images. This noise stimulates the auditory nervous system, limiting the dynamic range available for displaying stimulus-driven activity. The noise is potentially damaging to hearing and is distracting for the subject. In an active noise control (ANC) system, a reference sample of a noise is processed to form a sound which adds destructively with the noise at the listener's ear. We describe an implementation of ANC in the electromagnetically hostile and physically compact MRI scanning environment. First, a prototype system was evaluated psychoacoustically in the laboratory, using the electrical drive to a noise-generating loudspeaker as the reference. This system produced 10–20 dB of subjective noise-reduction between 250 Hz and 1 kHz, and smaller amounts at higher frequencies. The system was modified to operate in a real MR scanner where the reference was obtained by recording the acoustic scanner noise. Objective reduction by 30–40 dB of the most intense component in scanner noises was realized between 500 Hz and 3500 Hz, and subjective reduction of 12 dB and 5 dB in tests at frequencies of 600 Hz and at 1.9 kHz, respectively. Although the benefit of ANC is limited by transmission paths to the cochlea other than air-conduction routes from the auditory meatus, ANC achieves worthwhile attenuation even in the frequency range of maximum bone conduction (1.5–2 kHz). ANC should, therefore, be generally useful during auditory fMRI.
[DOI: 10.1121/1.1408948]

PACS numbers: 43.50.Ki, 43.50.Hg, 43.66.Vt, 43.66.Yw [MRS]

LIST OF SYMBOLS

$x(t)$	Noise time-domain wave form
$d(t)$	Noise time-domain wave form at point of noise control
$d'(t)$	Acoustic control wave form at point of noise control
$M(s)$	Transfer function from source to point of noise control
$H(s)$	Physical plant transfer function
$x(n)$	Reference signal to noise controller (sampled data stream)
$e(n)$	Error signal to the noise controller (sampled data stream)
$y(n)$	Output signal from the noise controller (sampled data stream)
$M(z)$	Digital filter model of $M(s)$
$H(z)$	Digital filter model of $H(s)$
$P(z)$	The best approximation of $H(z)$
$W(z)$	Adaptive filter coefficients
μ	Adaptation update coefficient
l	Leak coefficient
z	Unit delay operator

I. INTRODUCTION

Functional magnetic resonance imaging (fMRI) of the brain relies on the difference in blood oxygen level between stimulated and unstimulated epochs to determine areas of neural activity. For imaging the parts of the brain that respond to sound, the operation of the fMRI scanner itself poses some severe problems. First, the background noise caused by compressors and air conditioning is often clearly audible, and potentially produces activation in both stimulated and nominally unstimulated epochs. More importantly, acquisition induces a loud burst of sound that exceeds 110 dB SPL in 1.5 Tesla (T) scanners and can be as high as 130 dB SPL in 3 T scanners (Shellock *et al.*, 1998; Ravicz *et al.*, 2000; Miyati *et al.*, 1999; Foster *et al.*, 2000). This scanner noise is potentially damaging to the listener's hearing (Foster *et al.*, 2000), can be unpleasant, and leads to fatigue. The presence of the scanner noise may also affect the fMRI experiment, in that it stimulates the auditory regions of the brain, thus reducing the dynamic range available for activation by the stimulus of interest (Edmister *et al.*, 1999) and also raises the level at which stimuli must be presented to be heard clearly. Scanner noise also increases the complexity of the task, as the listener is required to separate the stimulus perceptually from the scanner noise.

Several techniques are routinely employed to reduce both the background noise and the scanner noise. These measures have mostly been passive. They include earplugs, ear

[a]Author to whom correspondence should be addressed; electronic mail: johnc@ihr.mrc.ac.uk

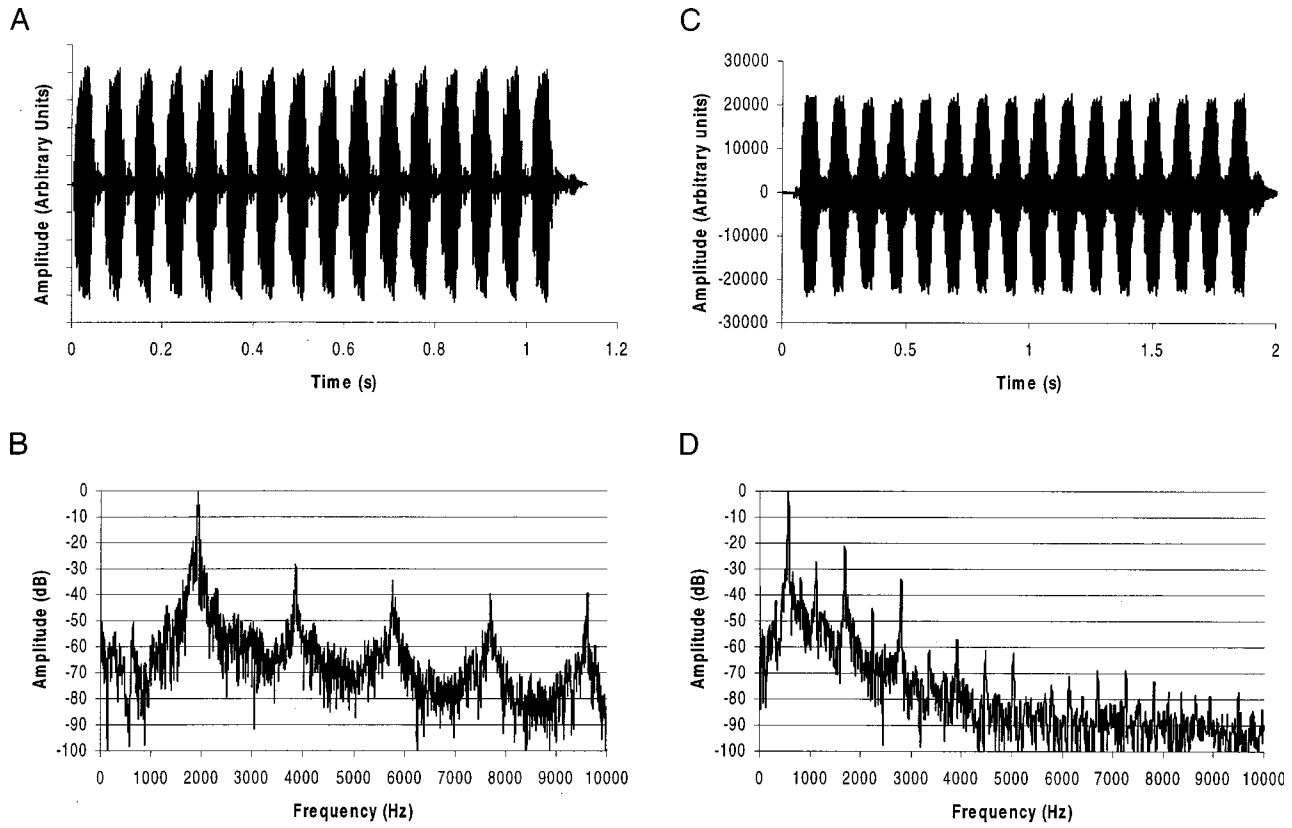

FIG. 1. Time wave forms (A) and (C) and amplitude spectra (B) and (D) of the volume acquisition noise of two 3T fMRI scanners operating in echo-planar mode. All 16 slices for a single volume acquisition are shown. No volume acquisition noise is present between the volume acquisitions.

defenders, and lining the scanner bore with sound-absorbing foam. However, since such methods provide only up to 40 dB of attenuation (Berger, 1983, 1986), the scanner noise still achieves levels of 70–90 dB SPL at the listener's ears.

The scanner noise in fMRI is created by the operation of the scanner while acquiring each slice of the complete volume of images (see Mansfield *et al.*, 1995). Echo planar imaging (EPI) sequences are commonly used for fMRI because they provide image acquisition of a volume using just a few slices, such as 16 or 32. The spectral characteristics and amplitude of the noise created in a particular scanner depend on the design of the scanner and on the switching sequence used to operate the scanner. The noise created by an EPI sequence differs from the noise generated by anatomical MRI sequences, in that most of the spectral energy is concentrated at one frequency in EPI but is dispersed in anatomical MRI. The amplitude of the noise is proportional to the strength of the magnetic field present in the scanner. Thus, as scanners with higher fields are introduced, problems of noise produced during scanning will increase.

In a typical application at 3 T the scanner noise consists of an initial impulse caused by the slice-select pulse and a tonal component lasting 70 ms or more at a frequency of between 500 and 2000 Hz determined by the gradient-readout switching frequency. Figure 1 shows the time wave form [panels (A) and (C)] and the spectrum [panels (B) and (D)] of this sound recorded in the bore of two 3 T scanners, one with a gradient-readout frequency of 1900 Hz and the other of 600 Hz. Both wave forms show 16 bursts of sound, each corresponding to one of the slices in the EPI volume. The spectra are essentially those of harmonic complex tones, with the majority of the acoustic energy concentrated at 1900 Hz and 600 Hz, although there is significant energy at higher frequencies.

The practical realization of an active sound-reduction apparatus is complicated by the special environment of the scanner. In particular, the apparatus must not affect the homogeneity of the magnetic field and thus cannot contain ferromagnetic components. One approach is to present the stimuli via long, nonmagnetic acoustic tubes. However, such tubes generally compromise the frequency and phase response of the sound delivery system. We have already addressed the problem of high fidelity sound delivery in MRI (Palmer *et al.*, 1998), which we achieved by placing electrostatic drivers from commercial headphones into commercial ear defenders. This system can present sounds at levels up to 120 dB in the ear canal, and also attenuates airborne sound by up to 30 dB below 1 kHz and by 40 dB above 1 kHz. Most important, the system has a smooth stable frequency and phase response to 20 kHz. These characteristics are necessary for wide-band active noise control. In this paper, we describe the use of this high-quality sound system, combined with a digital signal processor (DSP), to achieve active reduction of scanner noise in real time.

II. ACTIVE NOISE CONTROL AND FMRI

A. Previous studies

A small number of studies of active reduction of MRI noise have been reported. Ravicz *et al.* (1997) developed a

computer simulation of the method of recording the scanner sound, inverting it, and adding it to subsequent occurrences of the scanner sound. The method achieved 19 dB of attenuation at 1 kHz. McJury *et al.* (1997) described a feed-forward controller for anatomical MRI using the ''filtered-U'' LMS algorithm (Erikson, 1991) to produce a noise-reduction headset. The system was tested in the laboratory using pre-recorded scanner noise presented over a loudspeaker. A reduction of 10–15 dB in the level of the components of the scanning noise at frequencies below 350 Hz was reported. Chen *et al.* (1999) used a modified feed-back method with a second-order neural net to control the noise-reduction in a headset. This system was tested using loudspeaker-presented pre-recorded scanner noises. A reduction in the amplitude of the noise of 19 dB was reported.

Only two studies have evaluated the effects of active noise control in real scanners. Goldman *et al.* (1989) applied a Fourier transform to the signal received by an error microphone. A control signal was synthesized by inverting the phase of the major frequency components. This signal was played out synchronously with the scanner sound by utilizing the trigger pulse generated by the scanner control computer. By repeating this procedure, the canceling signal could be fine tuned for maximum noise reduction. It was reported that 14 dB of reduction was achieved. Pla *et al.* (1995) described a system that did not use a headset, but instead used a pair of piezoelectric speakers placed close to the listener's ears. The multichannel filtered-*x* algorithm (Burgess, 1981) was used to control the system. The derivation of the reference signal and the type and placement of the error microphones were not described, but the system was reported to achieve up to 25 dB of noise reduction at frequencies up to 1.2 kHz.

In summary, although it has been possible to achieve useful amounts of noise control in an MRI environment, no noise-control system has been described that works over the range of frequencies containing significant energy in fMRI EPI noise (i.e., 250 Hz to 4 kHz). Furthermore, no system has been evaluated to measure the benefit that is perceived by the subject. Our aim was to achieve active noise reduction over a wide frequency range and to evaluate the resulting system psychoacoustically.

B. Basic requirements

The sound pressure at a given spatial position is the linear sum of the pressures due to all sound waves arriving at that position. Active control is achieved by combining the incident sound with a pressure wave form created to be equal in amplitude and opposite in phase. The incident sound and the control sound then destructively interfere. The resultant sound pressure at the control point is equal to the difference between the pressures of the control and incident sound waves. Both the amplitude and the phase of the control sound are critical. The error amplitude for a mismatch of amplitude is given by Eq. (1) and for a mismatch of phase by Eq. (2):[1]

$$E = \mathrm{abs}(A_i - A_c), \tag{1}$$

$$E = 2\sin\left(\frac{\phi}{2}\right). \tag{2}$$

E is residual sound amplitude, A_i is the amplitude of the incident sound, A_c is the amplitude of the control sound, and ϕ is the phase error in radians between the incident and control sounds. For example, if a 40-dB reduction in amplitude is required, then, with the phases perfectly matched, the amplitude of the control sound must be matched to within 1%. Similarly, if the amplitudes are perfectly matched, the phase of the control sound must be matched to within 0.01 radians or 0.6°.

C. Alternative topologies

Noise-control systems for use in MRI could be based on either feed-back or feed-forward topologies. The feed-back topology uses a microphone placed close to the point where reduction is required to provide a reference signal that is inverted, processed, and then used to drive a control loudspeaker. The time required for the control signal to propagate from the loudspeaker to the microphone, and the necessity for maintaining stability at all frequencies, mean that the upper frequency of control for feed-back systems is commonly limited to a few hundred Hz. This limit is significantly below that required for fMRI, as significant acoustic energy generated by an EPI sequence is found at frequencies as high as 3–4 kHz (Fig. 1). Furthermore, there is only one input to a feed-back system: a microphone placed close to the ear. This microphone would pick up both the scanner sound and the stimuli of interest, and so the noise control system would attempt to cancel both.

The feed-forward topology uses a reference microphone placed close to the noise source to obtain an electrical version of the noise that is propagating towards the noise-control point. A processor takes this ''advanced'' noise and filters it so that when presented through the control loudspeaker, noise reduction is achieved. An ''error'' microphone, the placement of which defines the point of control (the ''monitoring point''), is placed close to the listener's ear and provides an electrical copy of the residual noise. This topology is more suitable than the feed-back topology for application in fMRI for two reasons. First, the availability of the advanced reference signal allows the system to compensate for the delays introduced by the distance between the control loudspeaker and the error microphone. Thus, potentially, the maximum frequency can be extended sufficiently to reduce high-frequency EPI gradient noise. Second, because the reference signal contains only the noise, the system can separate the scanner sound from the stimuli of interest. The effectiveness of this topology has been demonstrated in several applications, for example Kuo (1990, 1996). For these reasons, we implemented a feed-forward topology.

The environment of an MRI scanner presents both advantages and disadvantages for active noise control. One advantage is that the electrical wave form applied to the scanner coils is computer generated. Therefore, the onset of the gradient noise is precisely timed and a trigger pulse is avail-

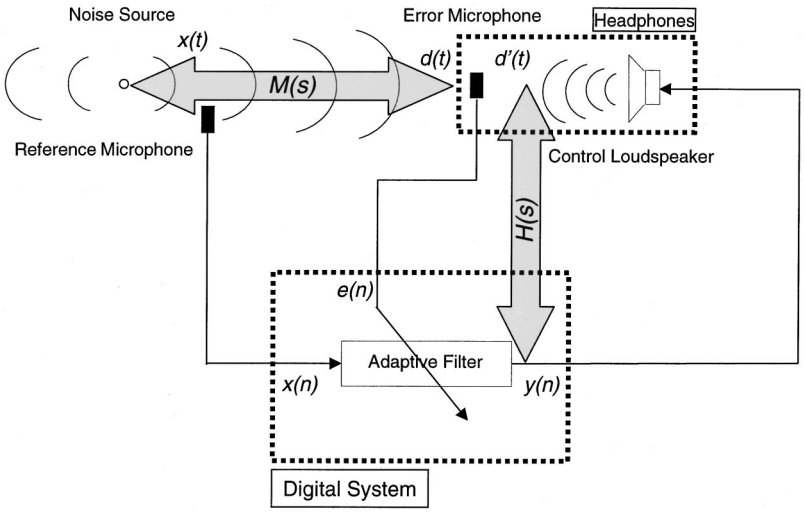

FIG. 2. Physical components of a single-channel feed-forward noise controller. See text for explanations of symbols.

able to indicate when the noise pulse will occur. Moreover, the same gradient-drive signal is repeated for each volume acquisition. Thus, the acoustic scanner noise is relatively stable in the time domain, although the amplitude of the wave form may change slowly over time, as discussed below. A disadvantage, however, is that the electrical signal applied to the gradient coils cannot be used directly as the advanced noise in the feed-forward topology, because the echoes of previous gradient-coil operations have significant energy, but are not present in the electrical signal. In addition, any ferromagnetic material in the vicinity of the listener's head distorts the magnetic field and hence the scanner images. Furthermore, kilowatts of radio-frequency (RF) energy are created during the scanning process and induce artifactual signals on any wiring inside the scanner bore.

In Sec. III we describe the design of a prototype noise controller which overcomes some of these problems. Section IV reports the results of a psychophysical experiment which evaluated the potential benefits of the prototype system. Section V describes modifications to this system that were made to allow it to be operated in a real scanner. Section VI describes a psychophysical evaluation of the modified system in a replica of 3 T scanner. Section VII describes the acoustic performance of the modified system in two real 3 T scanners. Finally, Sec. VIII discusses some limitations on any active noise-reduction system for fMRI.

III. PROTOTYPE NOISE-CONTROL SYSTEM

A. Design

The type of feed-forward noise-control system which we implemented is shown as a physical system in Fig. 2. A noise source generates a noise $x(t)$ whose wave form travels through a primary path with a transfer function $M(s)$, and generates a sound $d(t)$ at a particular point in space. This point is termed the ''monitoring point'' and is defined by the position of the error microphone. A reference microphone is placed close to the noise source and detects the acoustic signal that is propagating towards the monitoring point. Its sampled electrical signal $x(n)$ is fed into a DSP. The DSP filters $x(n)$ with an adaptive filter to provide the required frequency and phase shaping of the reference signal and produces an output signal $y(n)$. The output signal is converted to an electrical wave form which passes through an amplifier and a control loudspeaker to produce sound. This sound propagates to the monitoring point to become the control sound wave $d'(t)$ that destructively interferes with the incident wave $d(t)$. The transfer function of the output path from the DSP to the monitoring point, including the delays introduced by the propagation from the control loudspeaker to the monitoring point, is termed the ''plant'' and is represented by $H(s)$ in Fig. 2. The residual sound, detected by the error microphone, is sampled by the DSP to produce $e(n)$ which is used to update the characteristics of the adaptive filter.

B. Adaptive filters

It is beneficial to model the noise-control system in the z domain as the system is implemented as a discrete time sampled system. In Fig. 3, the continuous physical systems $M(s)$ and $H(s)$ are represented as sampled transfer functions $M(z)$ and $H(z)$, while the adaptive filter is split into its two components, the filter represented by $W(z)$ and the update algorithm, labeled LMS.

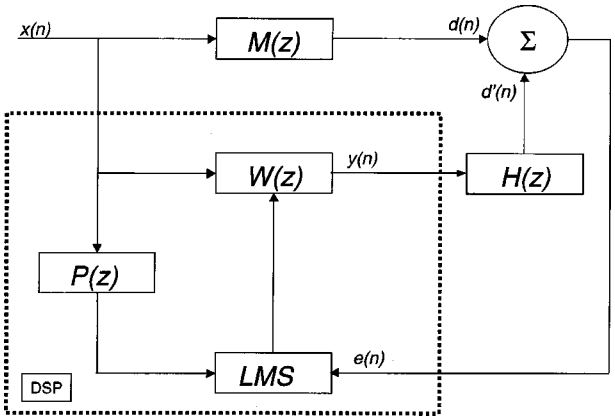

FIG. 3. Block diagram of the digital processing components of a single-channel noise controller with electrical reference, including models of the physical system $M(z)$ and $H(z)$. The system shown includes $P(z)$ to compensate for the effects of the plant.

The filter $W(z)$ is crucial to the operation of the noise-control system. When the filter is optimized for noise reduction, it adjusts the delay and amplitude of each frequency component of the reference signal $x(n)$ so that its output $y(n)$, after passing through the control amplifier and control loudspeaker, creates the maximum degree of destructive interference at the monitoring point. The characteristics of the filter need to be updated continuously to allow the system to adapt to changes in the primary path $M(z)$ resulting from listener movement or drift in the acoustic characteristics of the scanner.

The signal from the error microphone $e(n)$ indicates the characteristics of the residual sound present at the monitoring point. This error signal is used to create and adjust the filter $W(z)$. The basic least mean squares (LMS) method (Widrow, 1960), is an iterative method of adjusting the coefficients of an FIR filter using an error signal that is derived from the FIR filter output and desired signal $d'(n)$. The LMS algorithm adjusts the filter coefficients in such a way as to minimize the mean square value of this error signal $e(n)$. The error signal is multiplied by a small constant μ before being used to update the filter coefficients. The value of μ controls the overall system gain and hence the stability and rate of convergence of the adaptive filter.

This method is unsuitable without modification for use in a practical noise controller because the output of the filter $W(z)$ can act only through the plant. The plant transfer function $H(z)$ causes instabilities unless its effect on the update algorithm is compensated for. One method for compensation is to introduce an additional digital filter $P(z)$ whose transfer function is as close a match to the real plant as possible (a plant *model*) in the reference input to the LMS update algorithm. Nominally, there is then the same transfer function in both the reference $[P(z)]$ and error $[H(z)]$ inputs to the update algorithm and the system remains stable at all frequencies. This arrangement is called a single-channel feedforward filtered-*x* adaptive controller (Burgess, 1981; e.g., Elliott and Nelson, 1992).

Instability can also arise due to the accumulation of small errors in the coefficients of $W(z)$, for instance if the analogue-to-digital converter that digitizes the error signal has a DC offset. As the plant $H(z)$ is a vented acoustic system, it has no response at DC and so the DC output of the filter $W(z)$ increases in an attempt to compensate for the error, until the dynamic range of the system is exceeded. To avoid this problem, each coefficient is multiplied by a number just less than one, the ''leak'' coefficient l, on every sample, which makes the filter coefficients of $W(z)$ tend to zero over time. This leaky least means squared (LLMS) variant of the filtered-*x* algorithm prevents the filter coefficients from building up to large values due to small errors. The technique is a standard one in noise-control theory (see, for example, Elliot and Nelson, 1992). The model of the complete filtered-*x* system is shown in Fig. 3.

C. Plant model

In order to obtain $P(z)$, the estimate of the plant transfer function $H(z)$, we implemented a method based on the presentation of a maximum length sequence (Davies, 1966). An MLS is a pseudorandom sequence of ones (representing acoustic clicks) and zeros (representing silence). If a particular MLS is cross correlated with the same sequence, in which all the zeros have been replaced with minus ones, the value of the cross correlation is zero for all nonzero cross-correlation lags. Thus if the MLS is passed through a system with an impulse response $H(z)$, the output of the cross correlation is $nH(z)$, where n is the number of ones in the sequence. Therefore the impulse response of the acoustic system to a single click can be reconstructed mathematically from the response to several thousand closely spaced clicks, allowing a large number of averages to be performed quickly (Shi and Hecox, 1991).

In our application, the MLS sequence is presented over the control loudspeaker and received on the error microphone. The sequence has 2047 points of which 1024 are ones. It was presented at a rate of 800 points a second and so lasted for 2.559 s. The reconstruction is of the same length as the MLS and so also has a duration of 2.559 s. Of this, the first 30 ms are the linear impulse responses which we used as the plant model. In a perfectly linear system the remainder of the reconstruction contains only noise. Any practical system is not perfectly linear, and the nonlinearities produce wave forms in the reconstruction that correspond to second- and higher-order terms. The particular sequence which we used has the property that the higher-order nonlinear components appear in different parts of the reconstruction from the linear impulse response. By taking only the linear term, system nonlinearities in the plant are ignored (Thornton, 1997). This method gives a quick and very accurate way of obtaining the plant model. A more extensive description of these techniques can be found in Schetzin (1989).

IV. EXPERIMENT 1: EVALUATION OF THE PROTOTYPE NOISE-CONTROL SYSTEM

We measured the subjective benefit of the prototype noise-control system psychophysically by measuring detection thresholds for pure tones in a wide-band noise. The noise was presented through a loudspeaker, referred to as the ''noise-source'' loudspeaker. In the noise-reduction condition the noise-control system attenuated this noise. In a control condition the noise-control system was switched off. The difference in thresholds between the two conditions provides a measure of the subjective reduction in noise level achieved by the system. This value was compared with the amount of acoustic noise reduction measured objectively, which was defined as the difference in dB between the power spectra of the noise in the two conditions at the error microphone.

A. Methods

1. Implementation of active noise control

The laboratory implementation of the prototype noise-control system is illustrated in Fig. 4. The noise-control algorithm ran on a Texas Instruments C31 32-bit floating point DSP running at 40 MHz with a sampling rate of 12 ksamples/s and 16-bit amplitude quantization. This DSP control system received two inputs: the digitized electrical wave form $x(n)$ used to drive the noise-source loudspeaker and the digitized error signal $e(n)$ obtained from a Knowles hearing-

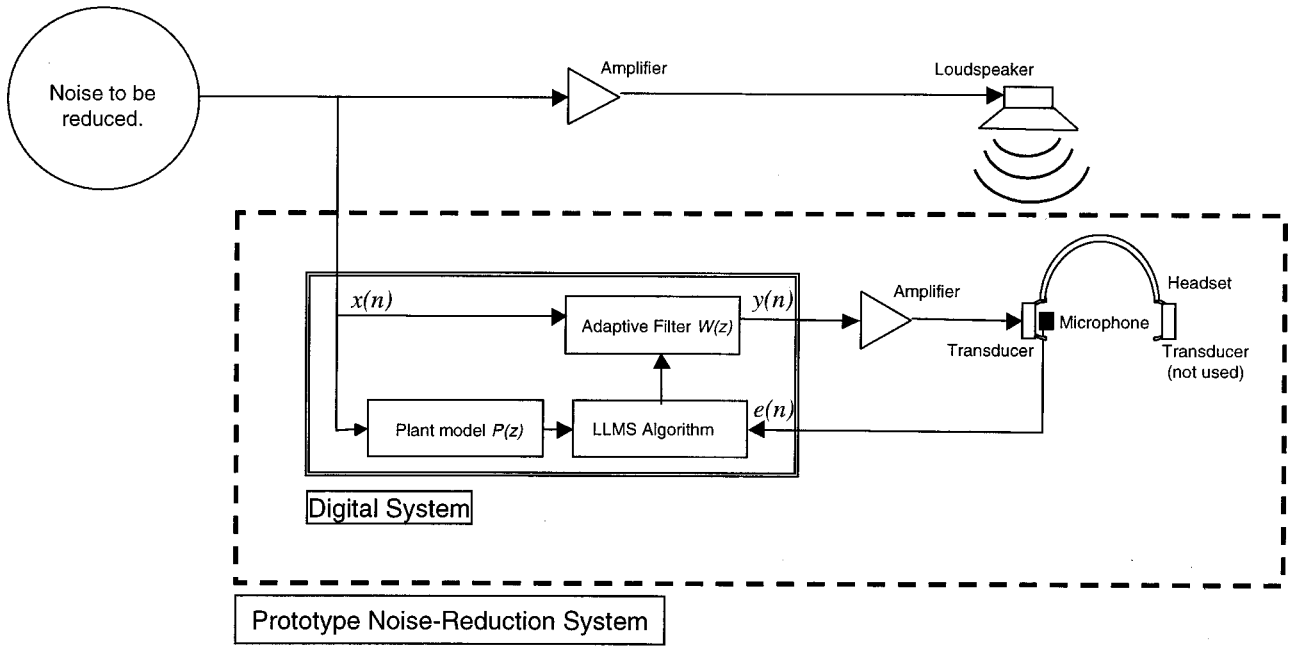

FIG. 4. Implementation of the prototype single-channel noise controller for Experiment 1.

aid microphone type EK-3024 mounted on the right-hand side of the stereo headphone set of the IHR fMRI sound system (Palmer *et al.*, 1998). This headset consists of a pair of Sennheiser electrostatic transducers built into a pair of Bilsom 2452 ear defenders. The error microphone was placed at the center of the right ear cup in front of the right transducer. Its output was amplified by a Brüel and Kjær measuring amplifier (Type 2636) and low-pass filtered at 4 kHz using a Kemo VBF8 filter. This signal was then digitized by a Burr Brown DSP 102 A/D converter to produce the error signal $e(n)$. The noise-control signal $y(n)$ was converted to analogue by a Burr Brown DSP202 D/A converter and low-pass filtered by a Kemo VBF8 filter at 4 kHz. It was then amplified and used to drive the right transducer of the headset which acted as the control loudspeaker.

The LLMS algorithm was implemented on the DSP with a length of 160 coefficients for both the adaptive filter $W(z)$ and the plant model $P(z)$. The plant model was obtained using the MLS method described in Sec. III C. Control software allowed the update and leak parameters to be modified. By setting the value of the update parameter μ to zero and the value of the leak parameter l to one, the controller could be frozen with the coefficients of $W(z)$ held constant to prevent the controller from attempting to remove the pure-tone signal which the listeners were trying to detect.

2. Apparatus

Listeners lay horizontal on their left-hand side in a double-walled sound-attenuating room, so that their right ear faced vertically upwards. They were supported by an air bed and their head was further supported by cushions. A loudspeaker (Audiomaster LS3/5A) was suspended directly above their right ear at a distance of 0.5 m. The listener wore the headset. Noise reduction was attempted only in the right ear. An EAR earplug (Arco Ltd.) was placed in the left ear.

3. Stimuli

The noise to be reduced was digitally generated white noise generated by a computer at a sampling rate of 22.05 ksamples/s. It was digitally low-pass filtered at 4 kHz and converted to analogue by a Crystal Semiconductors CS4328 D/A converter with integral Delta Sigma low-pass filter. It was presented through the suspended loudspeaker at a level of 100 dB SPL measured using a Brüel and Kær free-field response microphone (Type 4165, 12.7 mm diameter), placed at the position of the listener's head but with the listener absent, and a Brüel and Kjær measuring amplifier (Type 2636). The duration of the noise was 500 ms, including 20-ms raised-cosine ramps applied to the onset and offset.

The headset was used to present the pure-tone signals that were to be detected by the listeners. The signals were presented monaurally to the right ear. They were generated at a sampling rate of 20 ksamples/s with 16-bit amplitude quantization by the same computer that generated the filtered white noise. The pure tones were mixed as electrical signals with the output of the noise controller. The frequency of the tone was either 250, 500, 1000, 2000, or 3000 Hz. The tone had a duration of 250 ms, including 20-ms raised-cosine ramps applied to the onset and offset, and was presented in the temporal center of the masking noise.

4. Procedures

Once he was positioned, the subject was instructed to keep his head still. Then the plant model $P(z)$ was obtained. Next, the noise controller was switched on and used to reduce the 500-ms bursts of the noise. The filter coefficients

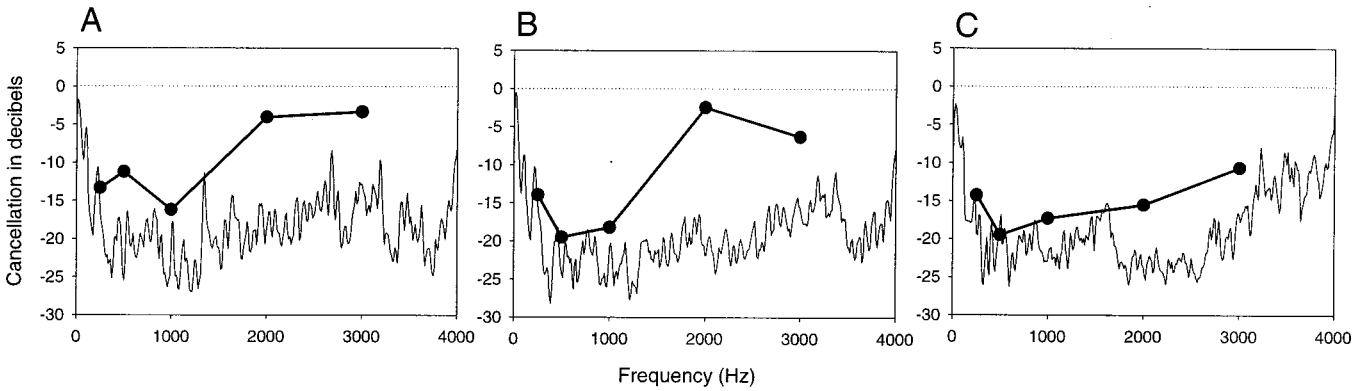

FIG. 5. Results of Experiment 1 for three subjects (A)–(C). Acoustic cancellation is plotted in thin lines and improvements in masked pure-tone thresholds by filled symbols connected by thick lines.

were updated automatically until the residual noise at the error microphone was no longer decreasing. At this point, the signal from the error microphones showed a reduction of at least 20 dB compared with the uncontrolled state for all subjects. Then the leak coefficient l was set to one and the update coefficient μ was set to zero in order to freeze the controller.

In the control condition, the noise-reduction system was turned off. Hence, the only reduction in the level of the noise at the right ear was provided by the passive attenuation of the ear defender. In the noise-reduction condition the noise-control system was used to further reduce the level of the noise at the right ear. Detection thresholds were measured in a two-interval, two-alternative forced-choice procedure employing a two-down, one-up adaptive rule in order to estimate the stimulus level at which detection was 70.7% correct (Levitt, 1971). Results were based on the average of five runs for each listener and for each combination of condition and signal frequency.

For each listener the power spectrum of the noise at the error microphone was measured in the control and noise-reduction conditions using an HP-3561A spectrum analyzer at a resolution of 12.5 Hz. Averages of the spectra from all control conditions, and separately for all the noise-reduction conditions, were obtained for each listener.

In half of the experimental sessions, thresholds and power spectra were first measured in the control condition at each frequency and then in the noise-reduction condition. In the other half of the experimental sessions the order was reversed.

5. Listeners

Three of the authors (J.C., M.A., and A.P.) participated as listeners. They all had hearing levels within normal limits at octave frequencies between 250 Hz and 4 kHz inclusive, and all had extensive experience in psychoacoustic tasks.

B. Results

The panels of Fig. 5 show results for the listeners individually. The symbols joined by thick lines mark the amount of subjective noise reduction; i.e., the difference in detection thresholds between the noise reduction and control conditions. The thin line plots the amount of objective noise reduction; i.e., the difference in power spectra between the noise reduction and control conditions.

Objectively, 10–25 dB of noise reduction were obtained at frequencies from 250 Hz to 3000 Hz. Subjectively, all three subjects showed 15–20 dB of reduction between 250 Hz and 1 kHz, with smaller amounts of reduction that varied among listeners between 1 kHz and 3 kHz.

The subjective noise reduction was almost as large as the objective noise reduction below 1 kHz, but was considerably less at higher frequencies. Specifically, for signal frequencies of 250 Hz, 500 Hz, and 1000 Hz the mean subjective noise reduction was 14, 17, and 17 dB, respectively. These values are similar to the objective noise reduction at the same frequencies, which was 18, 23, and 22 dB, respectively. In contrast, at 2000 Hz and 3000 Hz, the mean subjective noise reduction was only 7 dB, while the objective noise reduction was 22 dB and 15 dB, respectively. The deterioration in psychophysical noise reduction between 1000 and 2000 Hz was especially marked for listeners A and B. Possible bases for the deterioration are considered in the General Discussion.

In summary, a feed-forward noise-reduction system for fMRI, when implemented in an ideal arrangement where the reference signal was obtained directly from the electrical signal to a noise-source loudspeaker, achieved substantial subjective noise reduction. A broad-band noise was attenuated sufficiently to improve masked thresholds for pure tones by about 15 dB at frequencies up to 1 kHz and by 7 dB at 2 kHz and 3 kHz.

V. RECORDING NOISE-CONTROL SYSTEM

A. System topology

The prototype noise-control system cannot be used directly in a real scanner for two reasons. First, the intense bursts of radio-frequency (RF) energy generated by the scanner induce electrical artifacts in the microphone signals. Second, the computer-generated electrical drive to the gradient coils cannot be used successfully as the reference signal, because the intense echoes of the gradient-coil noise reflected from the walls of the scanner room and within the bore of the scanner are not reduced. Nor is it possible to

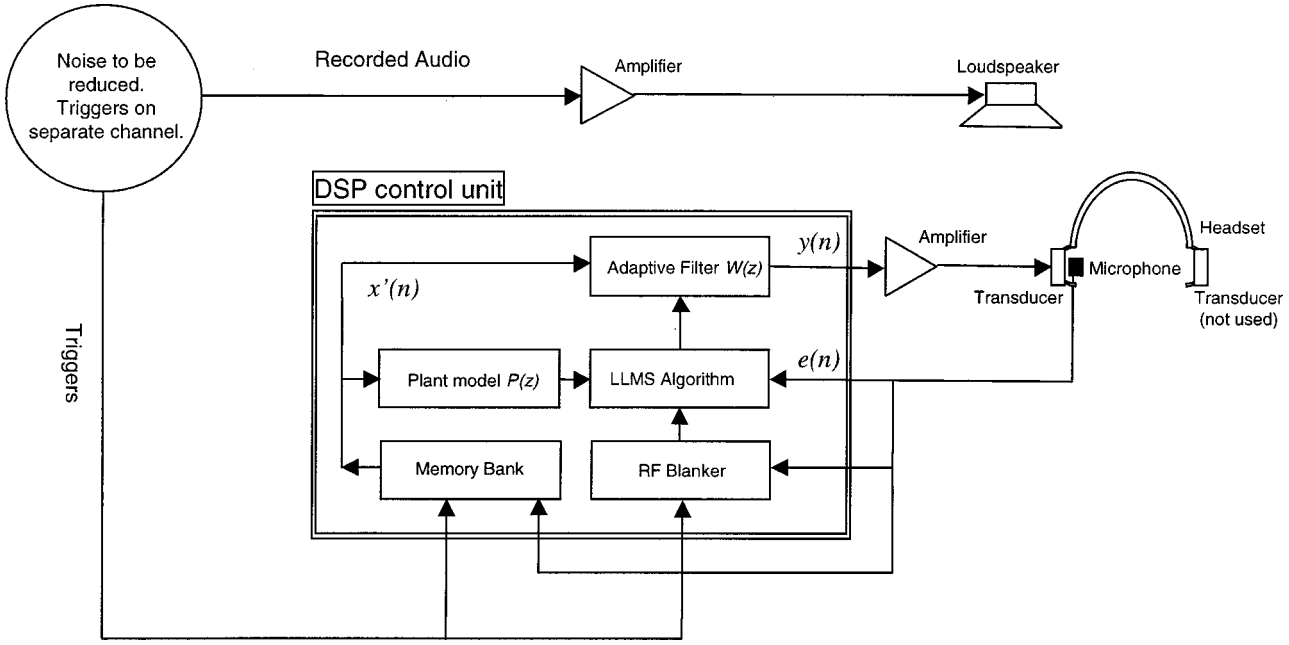

FIG. 6. Block diagram of the physical components of a single-channel noise controller using a recorded reference signal (see text for details).

place a microphone far enough away from the error microphone to obtain a reference that is sufficiently advanced for the DSP to have time to process the signal. The minimum time taken to process the reference signal is a function of the order of the anti-alias filters and of the sampling rate used in the DSP system (Elliot and Nelson, 1992). With the parameters of the prototype noise-reduction system, this time is of the order of 0.5 ms, so requiring a minimum separation of the reference microphone from the error microphone of 17 cm. This distance cannot be achieved in MR scanners because the listener's ears are less than this distance from the source of sound in the gradient coils.

In order to overcome these problems a new topology was developed and referred to as the ''recording noise-control system.'' The reference signal is not obtained in real time but from a recording made previously. The system has two modes: recording and controlling. The recording of the scanner noise is taken from the error microphone with the listener lying in the scanner. The recording is initiated by the trigger signal generated by the scanner-control computer. The RF energy is turned off while this recording is made. Hence the recording contains the direct acoustic noise of the gradient coils and its echoes after passing through the primary path, but is not contaminated by electrical artifacts. It has already been shown that the stability of scanner sounds is sufficient to allow this method of operation to work (Ravicz *et al.*, 1997). After obtaining a reference signal, the controller is placed in control mode. In this mode the adaptive filter does not run until the receipt of a trigger pulse from the scanner-control computer. On receipt of the trigger pulse, the controller starts real-time noise control, obtaining the reference signal from the memory bank and the error signal from the error microphone. The coefficients of the adaptive filter $W(z)$ are changed only during the noise-control operation. The duration of the recording is a free parameter that is limited only by the memory available to the DSP. Our current system is capable of recording up to 16 seconds of reference signal. One channel of the physical recording noise controller is illustrated as a physical system in Fig. 6.

This new topology has three advantages over the prototype arrangement. First, as the recording of the reference signal is made with the RF energy switched off there are no artifacts in the reference signal. Second, provided that the timing of the trigger pulse from the scanner control computer can be varied relative to the onset of the gradient-coil noise, the reference signal can be made to occur at any time before or after the gradient-coil noise begins. Thus the timing of the reference signal can be manipulated to optimize the operation of the adaptive filter. Third, the recording is made at the error microphone, so the reference has already passed through the primary path, which means the primary path does not need to be modeled by the adaptive filter $W(z)$.

The second and third advantages are illustrated by modeling the system in the z domain (Fig. 7). Since the recorded reference signal is taken from the error microphone, it has already passed through the primary path $M(z)$. We use a

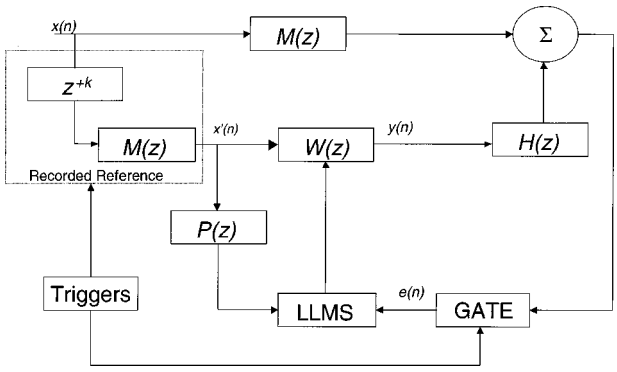

FIG. 7. Block diagram of the digital processing components of the single channel recording noise controller including models of the physical system $M(z)$ and $H(z)$.

negative time delay z^{+k} to model the ability to play out the recorded reference signal before the acoustic signal. If we let $x'(n)$ be the recorded reference, then

$$x'(n)=x(n)M(z)$$

and

$$e(n)=x(n)M(z)+x'(n)W(z)H(z)z^{+k}.$$

In the situation where the adaptive filter $W(z)$ has converged perfectly so that the error signal $e(n)$ is zero

$$x(n)M(z)=-x'(n)W(z)H(z)z^{+k},$$

but as

$$x'(n)=x(n)M(z),$$

then

$$H(z)W(z)z^{+k}=-1$$

and therefore

$$W(z)=-\frac{z^{-k}}{H(z)}.$$

Thus the adaptive filter $W(z)$ models the inverse of the plant, together with an overall delay. This delay is equal to the processing delay minus the advance added to the reference signal and should always be negative and hence causal. As the reference signal can be as far in advance as required (it is a user defined parameter in the cancellation software), the delay provided by $W(z)$ can be adjusted to provide optimum performance.

These advantages are accompanied by some inconvenient features. The first is the necessity to obtain a new reference recording when either the listener or the scanning protocol are changed. The second is the necessity to ensure that there is no variation in the time delay between the trigger pulse from the scanner control computer, the onset of the gradient-coil noise, and the start of the sampling by the DSP control unit. Any random jitter between the synchronization pulse and either of the latter two events results in a random time error between the noise from the gradient coils and the acoustic cancellation wave form. The adaptive algorithm adapts too slowly to compensate for a random timing difference on each volume acquisition. The result is a phase error that increases with frequency, and so a reduction of the degree of noise reduction at higher frequencies. The maximum jitter that will not degrade the performance of the system at 4 kHz to less than 25 dB of attenuation—the performance level that was obtained with the prototype system—is ± 2.2 μs. An A/D converter operating at 16 ksampls/s has an interval between samples of 62.5 μs. If the trigger pulse is presented asynchronously to the converter clock, there will be a maximum jitter of ± 31.25 μs and an average jitter of ± 15.6 μs. This amount of jitter would seriously compromise the performance of the system. To overcome this problem a new A/D and D/A converter system was built (Appendix A). It converts on a receipt of a trigger pulse from the DSP. As the clock rate of the DSP is 40 MHz, the new converter system exhibits less than ± 0.1 μs of jitter from the receipt of a trigger to the start of a recording or a noise control epoch.

It is also necessary to ensure that the error signal is not contaminated with RF-induced artifact, otherwise the adaptive filter does not converge properly. Initially we overcame this problem by training the adaptive filter with the RF switched off and then freezing the controller. However, although the electrical drive to the scanner coils is constant, the temperature of the scanner coils changes over time causing the amount of noise produced to change and the thus the amount of noise reduction to decrease. In a practical test it was found that noise reduction at 1.5 kHz declined from 30 dB to 20 dB over the course of a 10-minute run, indicating that the approach is not viable unless the controller is retrained at frequent intervals. Accordingly, a different approach was taken. The controller was left in its updating mode, but the output from the error microphone was gated to stop the artifactual impulse induced by the RF from being seen by the adaptive filter. This technique momentarily freezes the controller for the 5-ms duration of the RF pulse, while still allowing continuous updating for the remainder of the time. The gating device was termed the ''RF blanker'' as it blanked the error input for the duration of the RF artifact. The leak value is such that the filter coefficients do not change significantly over this time. Tests in a replica scanner (Appendix B) confirmed that the gating could not be detected by listeners.

VI. EXPERIMENT 2: SUBJECTIVE EVALUATION OF THE RECORDING NOISE-CONTROL SYSTEM

A. Methods

1. Procedures

Independent recording noise-control systems were implemented in each ear of an IHR fMRI headset. The subjective benefit of this two-channel system was assessed by listeners who adjusted the intensity of matching sounds until their loudness matched that of scanner sounds. The scanner sounds were obtained from digital recordings of the acoustic noise created by two 3 T scanners during EPI. The recordings were made within the bores of the scanners using the procedures described by Foster *et al.* (2000). The recorded noises were harmonic complex tones with fundamental frequencies of 600 Hz and 1900 Hz. The spectra and time histories of the recordings are shown in Fig. 1.

The matching stimuli were created by filtering the same scanner sounds to remove energy at frequencies remote from the fundamental. For the sound with a fundamental of 600 Hz, a low-pass filter at 1000 Hz was applied; for the sound with a fundamental of 1900 Hz, a band-pass filter of 1500–2500 Hz was applied. This step was taken for the following reason. Where most of the energy in a scanner sound falls in a restricted frequency range, the main effect of noise reduction is to attenuate components in that range. The levels of other components are not changed materially. Accordingly, by restricting the energy in the matching stimuli to the fundamental, which was the most intense component in the sounds that we used, subjects could match the loudness of the component that was most affected by noise reduction without interference from other components.

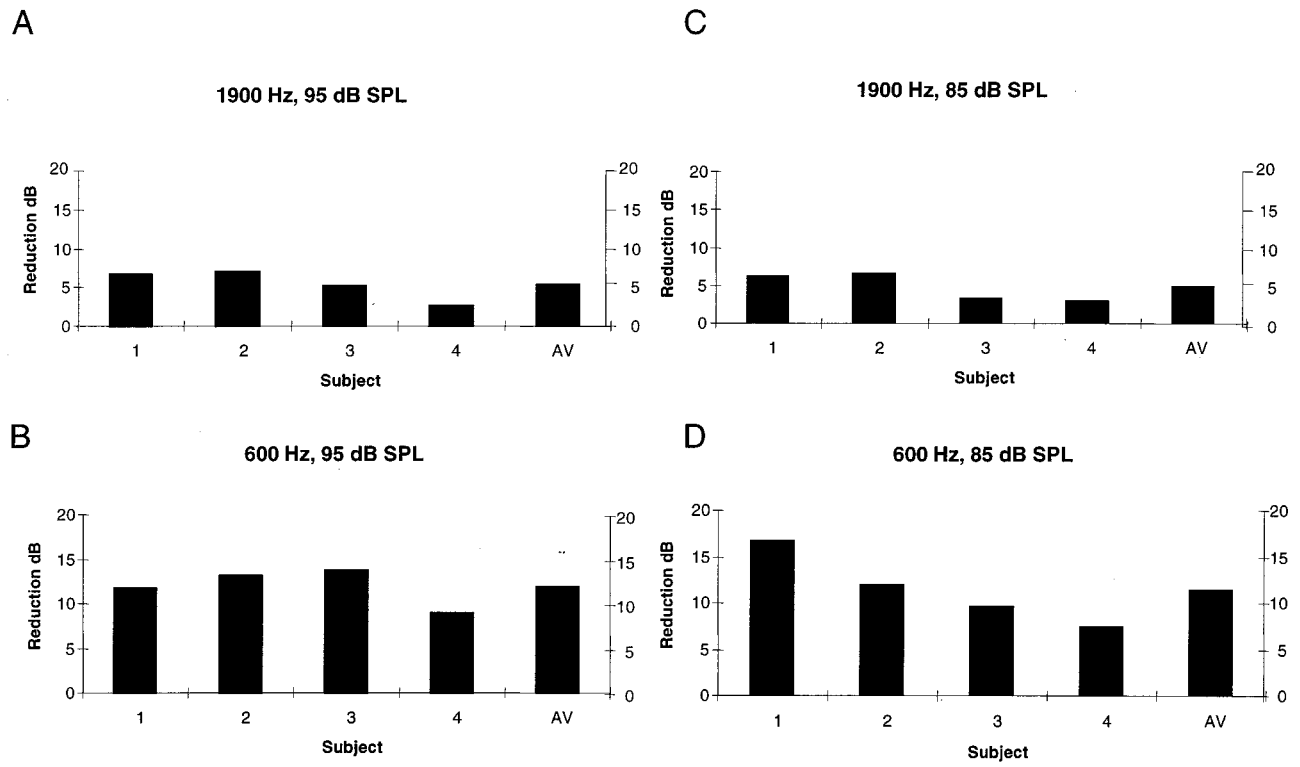

FIG. 8. Results of Experiment 2. Each numbered bar plots the subjective noise reduction experienced by a single subject at the specified intensity and frequency. The bar labeled AV indicates the group average.

Listeners lay supine within a plastic-and-wood replica of a 3 T scanner (Appendix B). The scanner sounds were presented through an array of in-built loudspeakers. Presentation levels of 85 dB SPL and 95 dB SPL were used. Levels were measured in the center of the ''head coil,'' with the listener absent, using a Brüel and Kjær free-field response microphone (Type 4165) and Brüel and Kjær measuring amplifier (Type 2636). Cancellation signals and matching stimuli were presented through an IHR fMRI headset. Cancellation signals were generated independently for each ear. Matching signals were presented binaurally.

Listeners matched the loudness of the scanner sounds in two conditions. In the control condition, the loudness of the scanner sound was measured without any noise control; i.e., the scanner sound was attenuated only by the ear defenders that are built into the headset. In the noise-reduction condition, the recording controller was used to reduce the level of the noise at both ears.

Loudness matching was performed using a one-up, one-down adaptive procedure. The scanner sound was presented and followed after an 800-ms silent interval by the corresponding matching stimulus. Listeners indicated whether the matching stimulus was louder or quieter than the scanner sound by pressing buttons on a response box. If the listener responded ''louder,'' the intensity of the matching sound was reduced; if the listener responded ''quieter,'' the intensity of the matching sound was increased. The size of the intensity change was controlled by the number of times the subject had changed from requesting a louder comparison sound to a quieter one, or *vice versa*. This change was termed a reversal. The size of the step in intensity was initially 5 dB. It changed to 3 dB after three reversals, and to 1 dB after a further three reversals. The run was concluded when the listener indicated by pressing a third button that the gradient-coil noise and the matching sound were of equal loudness. The difference between the intensities of the matching stimuli in the noise-reduction and control conditions was taken as a measure of subjective noise reduction.

Four listeners participated. They were three of the authors (J.C., Q.S., and A.P.) and one other, who all had extensive experience in psychoacoustic tasks. All had hearing levels within normal limits in both ears at frequencies between 250 Hz and 4 kHz, inclusive. Each of the eight conditions (two fundamental frequencies by two intensity levels, each with the controller on and off) was undertaken twice by each listener and the two measures of subjective noise reduction obtained in each condition were averaged. The ordering of the conditions was random and was different for each listener.

B. Results

The average match in the control conditions was 8.5 dB (95% confidence interval 6.8 to 10.3) higher when scanner sounds were presented at 95 dB SPL compared to 85 dB SPL, ranging over subjects and fundamental frequencies from 6.0 to 12.8 dB. The fact that the average matched difference does not differ significantly from the 10-dB difference in the stimuli encourages the belief that loudness matching was broadly accurate. The four panels of Fig. 8 show the difference in the intensity of the matching stimulus between the noise reduction and the control conditions for each combination of fundamental frequency (600 Hz or 1900 Hz) and level (85 dB SPL or 95 dB SPL). Results are plotted

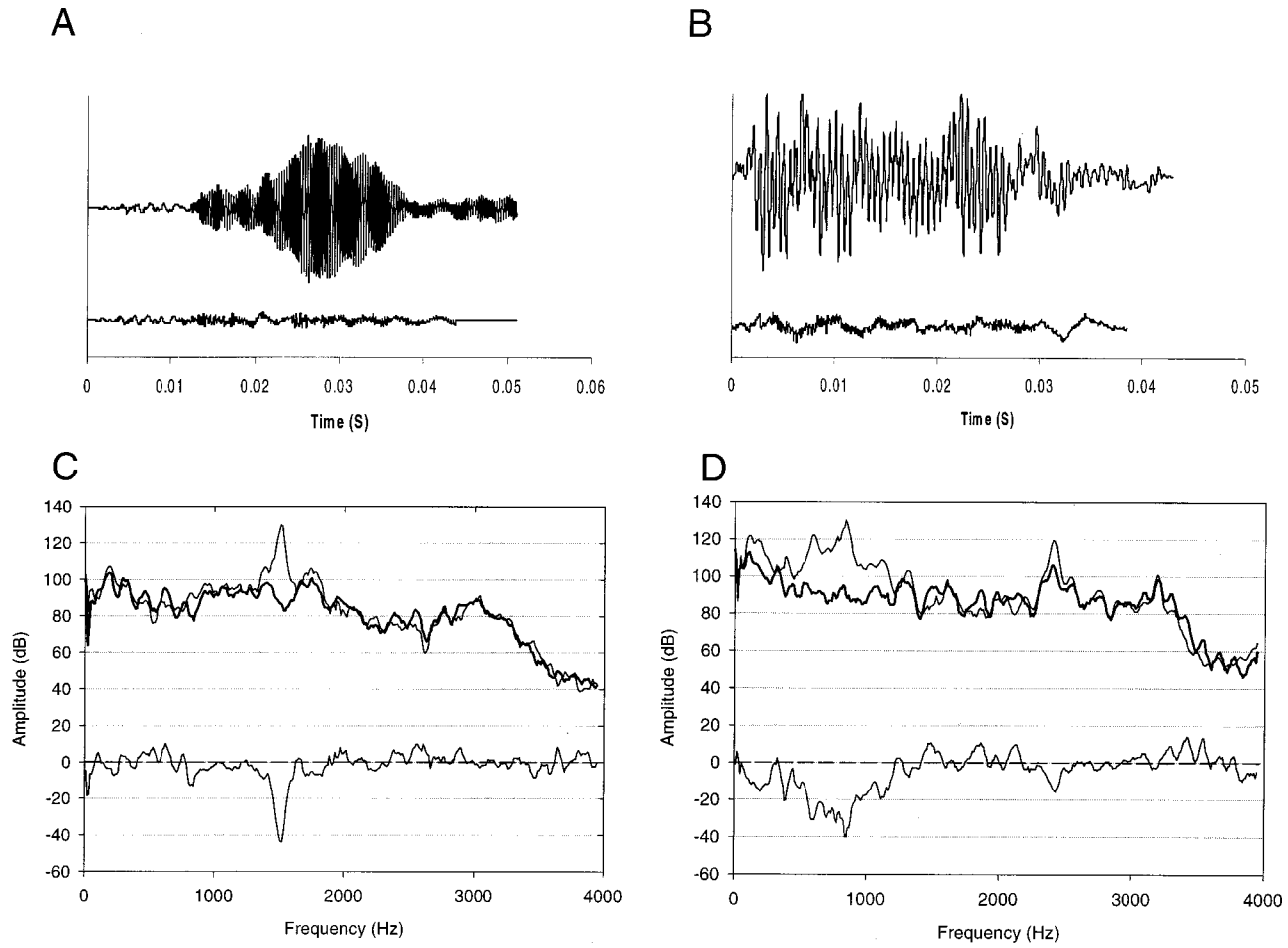

FIG. 9. Wave forms and their spectra recorded from the error microphone of the recording noise-control system during EPI in two real scanners. The upper traces in panels (A) and (B) show wave forms, and the thick lines in the upper parts of panels (C) and (D), show spectra of recordings made with the noise-control system off. The lower traces in panels (A) and (B) show wave forms, and the thin lines in the upper parts of panels (C) and (D) show spectra, of recordings made with the noise-control system on. The thin lines in the lower parts of panels (C) and (D) show the amount of attenuation achieved while operating with the radio frequency excitation off. The error microphone spectra are scaled in dB SPL.

for individual subjects and the mean. The intensity of the matching sound that was judged to have the same loudness as the scanner sound was always less in the noise-reduction condition than in the control condition. This subjective benefit averaged 12 dB at 600 Hz and 5 dB at 1900 Hz. The fact that more subjective reduction was measured at the lower frequency is consistent with the results of Experiment 1 (Fig. 5).

In summary, Experiment 2 demonstrates that the recording noise-control system can achieve a useful amount of subject noise reduction at both 600 Hz and 1900 Hz when tested with pre-recorded scanner sounds in a replica scanner.

VII. EXPERIMENT 3: OBJECTIVE EVALUATION OF THE RECORDING NOISE CONTROL SYSTEM

Although the acoustic environment of the replica scanner is similar to a real scanner, it could not be expected that the recording noise-control system would give similar amounts of noise reduction when used in a real scanner, because of the problems of RF interference. Accordingly, we measured the amount of objective noise reduction obtained in two 3 T scanners while they were performing EPI and compared those values with measures of objective noise reduction obtained in the replica scanner.

A. Measurements in real scanners

1. Methods

The same procedure was used in each scanner. A volunteer subject lay in the scanner wearing an IHR fMRI headset incorporating the two-channel recording noise-control system. The system obtained a plant model for each ear and then made a recording at each ear of a volume of EPI gradient noise with the RF excitation off. Next, the RF excitation was left turned off and the noise blanker disabled in order to obtain an ungated error microphone signal. Digital recordings were made of the scanner noise from the error microphone in the left ear with the noise-control system on and then off. The time domain signal of one volume in each condition of the recordings were Fourier transformed to obtain a spectra. Objective noise reduction was measured as the difference between spectra taken in the uncontrolled and in the noise-controlled conditions.

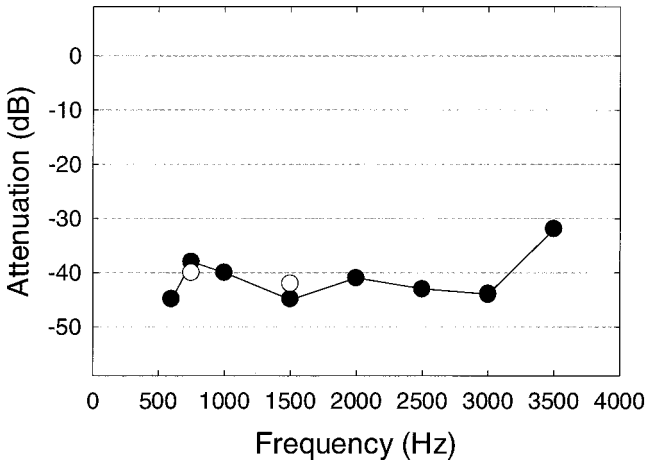

FIG. 10. Results of Experiment 3. (Filled circles) Objective attenuation of the fundamental component of simulated scanner sounds by the recording noise-control system in a replica scanner. (Open circles) Analogous measurements made in two real scanners.

2. Results

Panels (A) and (B) of Fig. 9 show the wave forms of the uncontrolled noise and the controlled noise from each scanner. Panels (C) and (D) show the spectrum of the uncontrolled noise (upper trace, thick line), the controlled noise (upper trace, thin line), and the difference between the spectra (lower trace, thin line). Comparison of the wave forms and of the spectra between the controlled and uncontrolled conditions illustrates that substantial attenuation of the scanner noise occurred. The largest effect was found at frequencies close to the fundamental [1500 Hz in panels (A) and (C); 750 Hz in panels (B) and (D)] where up to 40 dB of attenuation occurred. At frequencies remote from the fundamental, both attenuation and amplification occurred. Amplification was limited to 10–15 dB and occurred at frequencies where the uncontrolled spectrum level was low; e.g., between the fundamental and the second harmonic.

B. Measurements in the replica scanner

To evaluate the utility of the recording noise-control system for a range of possible scanner frequencies we simulated a range of scanner noises and measured the objective amount of noise control the system could produce on each fundamental component.

1. Methods

An accurate estimate was made of the long-term spectrum of the scanner sound with a fundamental frequency of 1.9 kHz (Fig. 1) by averaging a sequence of 1024-point FFTs. The 512 amplitude values were scaled arithmetically to define seven further spectra with fundamental frequencies of 500, 750, 1000, 1500, 2000, 2500, 3000, and 3500 Hz. Minimum phase FIR filters were programmed with the amplitude coefficients and used to filter a 7-ms burst of white noise. Sequences of 16 such bursts were concatenated and reverberated using a simulation of a moderately echoic room.[2] The resulting stimuli sounded like the noise within the bore of a scanner sampling a 16-slice volume during EPI.

Each stimulus was presented through the array of loudspeakers in the replica scanner. The procedure described in Sec. VII A 1 (with the difference that there was no RF to turn on and off) was employed to obtain recordings from one error microphone with the noise-reduction system turned off and turned on. Difference spectra were calculated. The attenuation at the frequency of the fundamental was measured and plotted as a function of fundamental frequency in Fig. 10.

2. Results

Approximately 40 dB of noise reduction were obtained at fundamentals from 600 Hz to 3000 Hz, inclusive, and approximately 30 dB at 3500 Hz, in the replica scanner. These values are similar to those measured at 750 Hz and 1500 Hz in real scanners (Fig. 9). The result confirms that the recording noise-control system achieves appreciable objective noise reduction across a wide frequency range. The system is limited in operation to 3800 Hz by the anti-alias filters used and this could explain the reduced noise reduction at 3500 Hz.

VIII. GENERAL DISCUSSION

A. Performance of the system

The recording noise-control system attenuates energy in the region of the most intense component of acoustic scanner noise by 30–40 dB in the frequency range from 500 Hz to 3500 Hz. This amount of noise reduction was measured across the frequency range in a replica scanner and at frequencies of 750 Hz and 1500 Hz in real scanners. In the majority of scanners performing EPI, the most intense component is the fundamental. The frequency range from 500 Hz to 3500 Hz embraces the fundamental frequencies of all EPI sequences used in current scanners. It is wider than the frequency range over which ANC has been demonstrated previously for fMRI.

We evaluated the subjective noise reduction experienced by listeners using psychophysical methods. We measured subjective reductions of between 8 and 17 dB at 600 Hz and between 3 and 8 dB at 1900 Hz. Our results are compatible with the conclusions of Ravicz *et al.* (1998) that, as the level of attenuation of sound at the auditory meatus exceeds that of the bone-conducted sound, the bone conduction becomes the primary path of sound to the cochlea and further attenuation of airborne sound has no perceptual effect. Berger (1993, 1986) describes the levels of bone conduction (through the head and torso) relative to the incident airborne sound pressure level. Bone-conducted sound at 500 Hz is 55 dB lower in level than the airborne sound, but gradually increases to a maximum that is only 40 dB below the airborne sound at about 1.5–2.0 kHz. At higher frequencies, the difference widens again; at 3 kHz the bone-conducted level about 50 dB below the air-conducted level. The Bilsom ear defenders that are incorporated in the sound system provide less than 30 dB of attenuation below 1 kHz and 30–40 dB between 1 kHz and 8 kHz. Therefore at low frequencies the ear defenders do not reduce the level of the airborne sound below the level due to bone conduction, and so the potential exists for active noise reduction to have a subjectively beneficial effect. However, at frequencies above 1 kHz the passive system alone reduces the airborne component to a level

close to the bone-conducted level and the amount of subjective benefit from active noise reduction is smaller. The variation in subjective benefit between subjects found in Experiment 1 (Fig. 5) at these higher frequencies may result from individual differences in the efficiency of the bone-conducted pathways.

At frequencies below 1 kHz, active noise control can materially attenuate the loudness of the sounds perceived by listeners in an fMRI experiment using EPI sequences. Above 1 kHz, the perceived reduction is smaller and depends upon the listener. Nonetheless, a subjective reduction of 5 dB was measured at 1.9 kHz where most listeners can detect the difference between the controlled and uncontrolled conditions and report that the EPI noise is more tolerable with active noise control. On the basis that a 5-dB reduction is worthwhile, we conclude that ANC would be beneficial under most circumstances.

In principle, it would be possible to use a conventional ear plug to increase the attenuation of airborne scanner noise over and above the attenuation achieved by ear defenders alone. However, the ear plug would need only to produce a small attenuation (12 dB at 600 Hz and 5 dB at 2000 Hz) to reach the limits of bone conduction, as we have demonstrated. At frequencies close to 2 kHz, in particular, ear plugs would produce little subjective benefit. However, communication with the subject through the head-phone system would be prejudiced, since it would be necessary to raise the sound level (perhaps by as much as 30 dB) to compensate for the ear plug attenuation. Thus high sound levels would need to be generated under the headphones, while the attenuation of the scanner noise at 2 kHz would not be large. Under such circumstances noise-control systems are to be preferred.

B. Limitations of the present experiments

The present experiments show subjective benefits of ANC in a replica scanner and objective benefits in both a replica scanner and in real scanners. The next step is to confirm that subjective benefits are realized in real scanners. Tests are required not only using psychophysical techniques like those in Experiment 2, but also to demonstrate that advantages accrue to the statistical reliability of the BOLD response.

C. Potential for further improvements

To maximize the benefit from ANC, it would be necessary to reduce the level of the bone-conducted sound reaching the cochlea. Ravicz *et al.* (1998) proposed two methods for reducing bone-conducted sound. Both methods exploit the principal of using sound-absorbing materials or a sound-shielding structure to reduce sound energy impinging on the body. A helmet to reduce the sound level incident on the subject's head was found to give subjective attenuation of the order of 55–65 dB, indicating that the bone-conduction levels had been significantly reduced. A coffin-like pod was then proposed to reduce sound transmission through the body, though not constructed. These ideas have potential. However, their realization would be bulky and implementing them safely in the confined space of an MR scanner could be problematic. They might add to the claustrophobia of the subject, and issues such as suffocation and speed of removal in an emergency would need to be addressed.

ACKNOWLEDGMENTS

We are grateful to the Department of Physics of the University of Nottingham and the Wolfson Brain Imaging Center, Addenbrookes Hospital Cambridge for allowing us to make the noise recordings in their scanners. We thank John Foster for advice and assistance in recordings of the fMRI noise, Dave Bullock for advice and assistance in electronic development, and Deborah Hall for advice on many aspects of fMRI. We also thank Michael Ravicz for detailed and helpful comments on a previous version of this paper.

APPENDIX A: PRACTICAL REALIZATION

The noise-control system described in this paper is an extension to the IHR fMRI sound system (Palmer *et al.*, 1998). It takes as its input the electrical signal from the error microphones in the headphones and a trigger pulse from the scanner for synchronization. One further digital input is used to distinguish between sound-recording and noise-control modes. The system outputs an audio signal which is input to a mixer in the IHR fMRI sound system.

A. Hardware

The controller is implemented as two monaural systems which share a power supply and trigger conditioning circuitry. Each controller consists of a ADSP-21061 processor (Analog Devices) running at 40 MHz, a serial communications unit for program loading and parameter setting via a PC RS232 port, a memory board implementing 128 K* 32 bit SRAM memory bank and a custom-built analogue converter board. This analogue board was designed for this project and uses a switched capacitor anti-alias filter for the A/D and D/A signal conditioning. The converters are 16 bit (Analog Devices) AD1866 and AD977 and are controlled directly by the processor. Conversions are phase locked to the processor clock thereby reducing sampling noise and greatly decreasing response times. This design has the added benefit that the sampling rate can be finely controlled by the processor.

B. Software

The software for the DSP board was written in assembler for maximum execution speed. The communication protocols and user interface were written in Microsoft Visual Basic 5.0. The software allows reading and writing of the memory areas of the DSPs for debugging and system analysis.

APPENDIX B: REPLICA SCANNER

In order to test the recording noise-control system we constructed a replica scanner from wood, plastic, and card. The replica is located in a sound-shielded room. An array of three loudspeakers driven from a power amplifier are mounted around the plastic ''head coil.'' This coil in turn is mounted inside a larger bore made of wood. These structures

are located on tables in such a way as to simulate the position of the bed in the 3 T scanner at the University of Nottingham Department of Physics. The amplifier is fed from the output of a custom designed computer sound system which is used to replay recorded scanner sounds. This control system can also provide a trigger pulse that is accurately locked in time to the sound generation. The replica can produce simulated gradient-coil noises at levels exceeding 110 dB SPL. We, and others to whom we have demonstrated the replica, report that the auditory (and visual) experience is satisfyingly similar to that of being in a real scanner.

[1]The calculation of the error in amplitude for a mismatch of phase is as follows. Assume that the incident signal is given by $i(t)=\sin(wt)$ and that the control signal, $c(t)$, is matched exactly in amplitude but is out of phase by π radians, apart from a small phase error ϕ, so that $c(t)=\sin(wt+\pi-\phi)$. Using the trigonometric identity $\sin A+\sin B=2\sin[(A+B)/2]\cos[(A-B)/2]$, the sum of the incident and control signals is $i(t)+c(t)=2\sin[wt+(\pi/2)-(\phi/2)]\cos[(\phi/2)-(\pi/2)]$. This sine term is the residual signal, whose amplitude is given by the cosine term. The cosine term can be simplified to $2\sin(\phi/2)$ using the trigonometric identity $\cos(A+B)=\cos A\cos B-\sin A\sin B$.

[2]Cool Edit 96 software by Syntrillium Software Corporation.

Berger, E. H. (**1983**). ''Laboratory attenuation of earmuffs and earplugs, both singly and in combination,'' Am. Ind. Hyg. Assoc. J. **44**, 321–329.

Berger, E. H. (**1986**). ''Method of measuring the attenuation of hearing protection devices,'' J. Acoust. Soc. Am. **79**, 1655–1687.

Burgess, J. C. (**1981**). ''Active adaptive sound control in a duct: a computer simulation,'' J. Acoust. Soc. Am. **70**, 715–726.

Chen, C. K., Chiueh, T.-D., and Chen, J.-H. (**1999**). ''Active cancellation system of acoustic noise in MR imaging,'' IEEE Trans. Biomed. Eng. **46**, 186–191.

Davies, W. D. T. (**1966**). ''Generation and properties of maximum length sequences,'' Control. Eng. 364–365.

Edmister, W. B., Talavage, T. M., Ledden, P. J., and Weisskoff, R. M. (**1999**). ''Improved auditory cortex imaging using clustered volume acquisitions,'' Hum. Brain Mapp **7**, 89–97.

Elliot, P. A., and Nelson, S. J. (**1992**). *Active Control of Sound* (Academic, San Diego, CA).

Eriksson, L. J. (**1991**). ''Development of the filtered-U algorithm for active noise control,'' J. Acoust. Soc. Am. **89**, 257–265.

Foster, J. R., Hall, D. H., Summerfield, A. Q., Palmer, A. R., and Bowtell, R. W. (**2000**). ''Sound level measurements and calculations of safe noise dosage during EPI at 3T,'' Magn. Reson. Imaging **12**, 157–163.

Goldman, A. M., Gossman, W. E., and Friedlander, P. C. (**1989**). ''Reduction of sound levels with antinoise in MR imaging,'' Radiology **173**, 519–550.

Kuo, S., and Chen, C. (**1990**). *Implementation of Adaptive Filters with the TMS320C25 and TMS320C30 Digital Signal Processing Application with the TMS320 Family* (Prentice Hall, Englewood Cliffs, NJ), Vol. 3.

Kuo, S. M., Panahi, I., Chung, K. M., Horner, T., Nadeski, M., and Chyan, J. (**1996**). Design of active noise control systems with the TMS320 family, Texas Instruments Application Report No. SPRA042.

Levitt, H. (**1971**). ''Transformed up-down methods in psychoaccoustics,'' J. Acoust. Soc. Am. **49**, 467–477.

Mansfield, P., Chapman, B. L. W., Bowtell, R., Glover, P., Coxon, R., and Harvey, P. R. (**1995**). ''Active acoustic screening: reduction of noise in gradient coils by Lorentz force balancing,'' Magn. Reson. Med. **33**, 276–281.

McJury, M., Stewart, R. W., Crawford, D., and Toma, E. (**1997**). ''The use of active noise control (ANC) to reduce acoustic noise generated during MRI scanning: Some initial results,'' Magn. Reson. Imaging **15**, 319–322.

Miyati, T., Tatsuo, B., Hiroshi, F., Mase, M., Narita, H., Imazawa, M., and Ohba, S. (**1999**). ''Acoustic noise analysis in echo planar imaging: Multicenter trial and comparison with other pulse sequences,'' IEEE Trans. Med. Imag. **18**, No. 8, 733–736.

Palmer, A., Bullock, D., and Chambers, J. (**1998**). ''A high output high quality sound system for use in auditory fMRI,'' Neuroimage **7**, S359.

Pla, F. G., Sommerfeldt, S. D., and Hedeen, R. A. (**1995**). ''Active control of noise in magnetic resonance imaging,'' Proceedings of Active 95, Noise Control Foundation: Poughkeepsie, New York, pp. 572–582.

Ravicz, M. E., and Melcher, J. R. (**1998**). ''Imager noise and noise-reduction during fMRI,'' Neuroimage **7**, S556.

Ravicz, M. E., Melcher, J. R., and Kiang, N. Y-S. (**2000**). ''Acoustic noise during functional magnetic resonance imaging,'' J. Acoust. Soc. Am. **108**, 1683–1696.

Ravicz, M. E., Melcher, J. R., Talavage, T. M., Benson, R. R., Rosen, B. R., and Kiang, N. Y.-S. (**1997**). ''Characterisation and reduction of imager-generated noise during functional resonance imaging (fMRI),'' Assoc. for Res. in Otolaryngol., Proceedings of the 20th midwinter meeting 205#819.

Schetzin, M. (**1989**). *Voltera and Wiener Series of Nonlinear Systems* (Krieger, Melbourne, FL).

Shellock, F. G., Ziarati, M., Atkinson, D., and Chen, D.-Y. (**1998**). ''Determination of gradient magnetic field-induced acoustic noise associated with the use of echo planar and three-dimensional, fast spin echo techniques,'' J. Magn. Reson Imaging **8**, 1154–1157.

Shi, Y., and Hecox, K. E. (**1991**). ''Nonlinear system identification by M-pulse sequences: application to brainstem auditory evoked responses,'' IEEE Trans. Biomed. Eng. **38**, 834–845.

Thornton, A. R. D. (**1997**). ''MLS and volterra series in the analysis of transient evoked otoacoustic emissions,'' Br. J. Audiol. **31**, 493–498.

Widrow, B., and Hoff, M. E. (**1960**). ''Adaptive switching circuits,'' IRE Western Electric Show and Convention Record, pp. 96–104.

A power conservation approach to predict the spatial variation of the cross-sectionally averaged mean-square pressure in reverberant enclosures

Linda P. Franzoni[a)]
Duke University, Mechanical Engineering and Materials Science, Box 90300, Durham, North Carolina 27708

(Received 18 August 2000; revised 7 August 2001; accepted 14 August 2001)

Although it is commonly assumed that broadband mean-square pressure levels are spatially uniform in reverberant enclosures, there is a gradual spatial variation, especially if the room is long in one direction, and/or the acoustic absorption is not applied uniformly to the enclosure boundaries. An equation for predicting the average cross-sectional sound pressure levels in a lightly damped enclosure with absorption is derived based on conservation of acoustic power. The derivation involves a one-dimensional boundary value problem, the solution of which is an estimate of the average sound pressure level at cross-sections in the interior. In its simplicity, the resulting formula is reminiscent of the classical Sabine formulation; however, this prediction contains a spatially varying function that depends upon the distribution of absorption (side-wall versus end-wall). The formula is demonstrated on a model problem consisting of a rectangular acoustic enclosure with a source on one end-wall, absorption on the opposing end-wall, and a combination of hard and absorbing side-walls. Comparisons with an exact numerical simulation show that the prediction works well for a wide range of absorption levels and provides an improvement over classical diffuse field theory, where the levels are assumed to be spatially uniform. A formula for the volume-averaged, broadband, mean-square pressure (a modified Sabine formula) is also derived and shown to give excellent agreement with the numerical simulations. [DOI: 10.1121/1.1409538]

PACS numbers: 43.55.Br, 43.55.Cs [JDQ]

I. INTRODUCTION

One component of noise in enclosures is the broadband high frequency acoustic field. Practical applications include vehicle interiors and architectural spaces with broadband sources when the wavelengths are short compared to the enclosure dimensions. In order to accurately predict the sound pressure level due to the broadband high frequency component at various spatial locations, extensive computations must be carried out. Numerical methods, such as finite element analysis (FEA)[1] or boundary element methods (BEM),[2] can be used, but are not very efficient for this type of sound field. These analyses must be performed on a frequency-by-frequency basis in the band, and since the wavelengths are small (high frequency), the number of elements required is large. Methods of this sort are more suited to low frequency sound fields.

Classical modal analysis (CMA)[3] is another method that is more suited to low frequency sound fields. It has the same limitations as FEA and BEM, in that calculations must be performed for each frequency in the band, and for high frequency sound fields there are a large number of participating modes at each frequency. In addition, if the enclosure is not ''lightly damped,'' then all the modes are coupled and the modal amplitudes cannot be obtained without inverting a full matrix.

Statistical energy analysis (SEA),[4] on the other hand, is particularly suited to high frequency broadband sound fields. However, since it is formulated in terms of averages of quantities that determine the sound pressure level, only an average sound pressure level is obtained for the interior. The space can be broken-up into substructures with coupling loss factors between them and averages for each substructure obtained, for a slightly more detailed description. The SEA method assumes ''light damping'' such that the sound field is diffuse and can reasonably be described by average properties.

Another method that resembles SEA, but is derived from CMA, is called asymptotic modal analysis (AMA).[5] AMA has the ability to predict spatial variation, but this involves summing over a large number of acoustic modes. In addition, AMA is currently limited to ''light damping,'' due to the inability to extract modal amplitudes directly, if the modes are fully coupled.

In addition to the aforementioned prediction techniques, various empirical relationships are sometimes used to obtain a rough estimate of sound fields within particular types of enclosures. Under certain conditions, these models relate physical quantities (such as source power, distance from source, room volume, wall surface characteristics, temperature, etc.) to the pressure field which would be expected in any similar environment. Models that fall into this category are not based on physical laws, but rather upon curve-fits to experimental data and algebraic functions of parameters known to affect the acoustic field. Hodgson gives a good summary of such models in an article that compares seven different empirical formulas for predicting noise levels in industrial workrooms.[6] The advantage of these methods is

a)Electronic mail: linda.franzoni@duke.edu

that good qualitative predictions can be easily achieved without the necessity of physical understanding.

In general, methods of predicting sound pressure levels in enclosures with broadband high frequency sound fields are either computationally intensive (resulting in detailed spatial information) or are fairly simple formulas that only predict overall level (no spatial detail). In this article, an approximate method for predicting slow spatial variation in reverberant enclosures will be presented. The fine scale rapid spatial variation that is captured by the more computationally intensive methods is missing, but it may be arguably unimportant. The new approximate method is based on energy conservation principles, assumes that the sound field is *locally* diffuse, and works remarkably well for cases with significant amounts of damping.

II. PREVIOUS WORK

Assuming that the sound field is diffuse (equal energy arrives at any point in the interior with equal probability from all incidence angles), the mean-square pressure is often assumed to be spatially uniform. By equating the power *into* the enclosure from acoustic sources to the power *out of* the enclosure via the absorptive surfaces of the enclosure, the mean-square pressure of the reverberant field is found to be approximately

$$\overline{p}^2_{\text{rev}}=\frac{4\rho c\Pi}{A}, \tag{1}$$

where Π is the total power into the enclosure from all acoustic sources, A is the total absorptivity of the enclosure (random incidence absorption coefficient times absorbing area covered for each surface), and ρc is the characteristic impedance of air. This simple formula based on the overall power balance in the enclosure is often attributed to Sabine, a complete derivation of which can be found in Ref. 7. Improvements to this approximation can be made by adjusting the absorptivity, as discussed in Ref. 7 for the Norris and Eyring or the Millington-Sette reverberation time formulas.

In Ref. 8, Franzoni and Labrozzi performed numerical simulations of the sound field in rectangular enclosures with different amounts and distributions of absorption on side- and end-walls. For that study, the sound source consisted of acoustic monopole sources on one of the end-walls. The mean-square pressure at points in the interior was computed from an exact (wave theory) solution. It was shown that the Sabine approximation for reverberant pressure [Eq. (1)] typically over-predicts the spatially-averaged *reverberant* level in the room, if the power is not adjusted to remove energy from the first reflection. Reference 8 also showed that the mean-square pressure levels are not necessarily spatially uniform, and that for long rectangular enclosures with damping distributions that are not uniformly applied, the spatial variation of mean-square pressure can be significant.

The results from numerous data sets collapsed with certain parameters, and Franzoni and Labrozzi were able to develop an empirical formula for the reverberant mean-square pressure as a function of one spatial variable for enclosures of the type shown in Fig. 1. The formula can be written as a

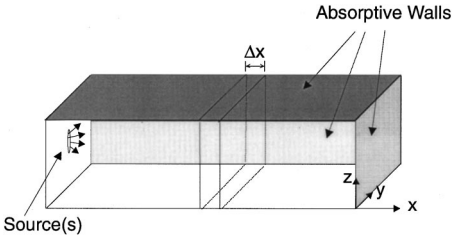

FIG. 1. Rectangular room, with source wall ($x=-L_x$), absorbing end-wall ($x=0$), and absorbing side-walls ($y=L_y$ and $z=L_z$).

modification of the Sabine formula, and is dependent upon the same variables (i.e., power, absorptivity, and acoustic impedance) as well as weighted absorption coefficients, a ratio of surface areas, and distance. The Franzoni–Labrozzi formula is given below:

$$\overline{p}^2_{\text{rev}}=\frac{4\rho c\Pi}{A}\left[\frac{(1-\overline{\alpha}_{\text{total}})(1-\overline{\alpha}_{\text{total}}/2)}{(1+\overline{\alpha}_w\overline{S}/2)}\right]e^{-(1/2)\overline{\alpha}_w\overline{S}\overline{x}}, \tag{2}$$

where $\overline{p}^2_{\text{rev}}$ is the cross-sectionally averaged mean-square pressure. The cross-section is perpendicular to the spatial variable in the argument of the exponential and it is normalized by the length in that direction ($\overline{x}=x/L_x$); the coordinate direction is defined in Fig. 1. The other variables in the expression are defined as follows: $\overline{\alpha}_{\text{total}}$ is the total absorptivity (random-incidence absorption coefficient times the area covered for each surface) divided by the total surface area of the enclosure $\overline{\alpha}_{\text{total}}=A/S_{\text{total}}$; $\overline{\alpha}_w$ is the absorptivity of the side walls divided by the total surface area of the side walls; and $\overline{S}$ is the ratio of side-wall surface area to cross-sectional surface area.

Note that the formula given above contains three components: the original Sabine formula, an absorptivity distribution correction factor, and a spatial term that varies exponentially. This formula was shown (Ref. 8) to agree remarkably well with the exact (computationally intensive) numerical simulations. Whereas Eq. (2) was derived empirically based on the results of numerous computer simulations, in the present article an analytical formula will be derived based on the principle of conservation of acoustic power.

III. THEORETICAL DEVELOPMENT

To facilitate this discussion, a rectangular room with sound sources on one wall and absorbing surfaces on three other walls is shown in Fig. 1. The acoustic sources produce broadband, high frequency sound. It is assumed that the interior sound field under consideration is *diffuse* in a *local* sense only. That is, around a given point in the enclosure, the energy from one side is equally probable from all directions on that side, but not necessarily equal to the energy from the other side. Also, the mean-square pressure is not assumed to be of equal magnitude at all spatial locations.

As derived in Ref. 7, the magnitude of the intensity vector, in a given direction, at a point in a diffuse field is given by

$$I=\frac{\overline{p}^2}{4\rho c}, \tag{3}$$

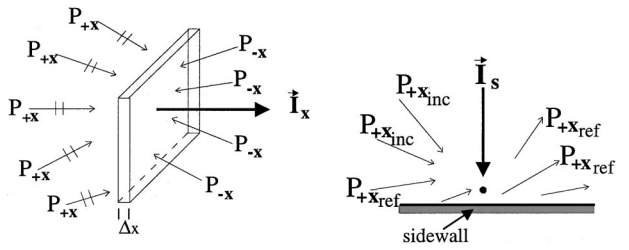

FIG. 2. Cross-section with left-traveling and right-traveling mean-square pressure components (left) and side wall section with incident (inc) and reflected (ref) right-traveling pressure waves.

where $\overline{p}^2$ is the mean-square pressure at the point and includes waves from all directions. If the sound field is a high frequency, broadband field, then the mean-square pressure can be assumed to consist of a right-traveling (increasing x) wave field superimposed on a left-traveling (decreasing x) wave field. In other words, the left- and right-traveling components of the sound field can be assumed to be uncorrelated from one another:

$$\overline{p}^2=\overline{p}^2_{+x}+\overline{p}^2_{-x}. \tag{4}$$

Formulas for intensity due only to the right- or left-traveling sound can be derived. For example, at an arbitrary point in the enclosure (not at a boundary), the magnitude of the intensity vector in the positive x direction, due to right-traveling waves, would be

$$I_{+x}=\frac{\overline{p}^2_{+x}}{2\rho c}, \tag{5}$$

where the subscript on mean-square pressure indicates that it is the component of mean-square pressure from the right-traveling $(+x)$ wave field only (see Fig. 2). An interpretation of this result is that it takes less mean-square pressure to produce the same intensity, if the waves are in the same direction as the intensity vector. Alternatively, comparing the standard formula Eq. (3) to Eq. (5), the mean-square pressure in Eq. (3) contains both components $(+x$ and $-x)$ but Eq. (5) only contains a single component, yet the intensity in both equations is a vector pointing in a single direction (say, $+x$).

In order to relate the intensity incident on a side-wall (in either the y or z direction) to the mean-square pressure of the right-travelling wave field, consider the right-traveling wave field as consisting of two components. One component includes waves that are incident on the side-wall, and the other consists of waves that have just been reflected from it, as shown in Fig. 2. The mean-square pressure due to right-traveling waves at the boundary is

$$\overline{p}^2_{+x}=\overline{p}^2_{+x_{\text{incident}}}+\overline{p}^2_{+x_{\text{reflected}}}. \tag{6}$$

However, the mean-square pressure that has been reflected is of less magnitude than the mean-square pressure that is incident. The reduction in magnitude is equal to $(1-\alpha_w)$, where α_w is the random-incidence absorption coefficient of the side-walls. Therefore,

$$\overline{p}^2_{+x}=\overline{p}^2_{+x_{\text{incident}}}+\overline{p}^2_{+x_{\text{incident}}}(1-\alpha_w)=(2-\alpha_w)\overline{p}^2_{+x_{\text{incident}}}. \tag{7}$$

The intensity vector in the direction of the boundary is only due to the incident mean-square pressure (the out-going pressure wave does not contribute). As a result, the intensity ''into'' the boundary is

$$I_{\text{sidewall}}=I_s=I_y=I_z=\frac{\overline{p}^2_{+x_{\text{incident}}}}{2\rho c}=\frac{\overline{p}^2_{+x}}{2\rho c}\left[\frac{1}{2-\alpha_w}\right], \tag{8}$$

where $\overline{p}^2_{+x}$ is the mean-square pressure associated with right-traveling waves, incident plus reflected.

In the above discussion, it is assumed that the mean-square pressure $\overline{p}^2_{+x}$ is relatively uniform over the cross-section. However, it is recognized that *very near* a side-wall, the components comprising $\overline{p}^2_{+x}$, namely $\overline{p}^2_{+x_{\text{incident}}}$ and $\overline{p}^2_{+x_{\text{reflected}}}$, will have different magnitudes due to the absorptivity at the side-wall. A detailed analysis of the spatial variation of $\overline{p}^2_{+x}$ across a given cross-section is provided in the Appendix. There, it is shown that, in general, the change in mean-square pressure across the cross-section is higher order (order α_w^2) and can therefore be neglected. Furthermore, the validity of Eqs. (7) and (8) is demonstrated in the Appendix.

Define β to be the fraction of surface area at a cross-section covered by absorbing material whose random incidence absorption coefficient is α_w. Further, define L_p and S as the length of the perimeter of the cross-section and its area, respectively. A power balance equation, equating the power into the cross-section of width Δx to the power out of the cross-section, can be written in terms of intensity.

$$I_xS=\left(I_x+\frac{dI_x}{dx}\Delta x\right)S+\alpha_w\beta L_p\Delta x I_s. \tag{9}$$

At x, the power into the cross-section from the previous adjacent cross-section is I_xS. The power out of the cross-section that goes into the next adjacent section is $(I_x+(dI_x/dx)\Delta x)S$. If there is absorption in the region over which Δx extends, then energy will be lost due to the absorbing walls or portion of the walls that is covered by the absorptive material. The left-hand side of Eq. (9) represents the power into the cross-section and the right-hand side represents the power leaving the cross-section. Note that if there were sources on the side-wall, such as transmission through the wall *into* the enclosure, the left hand side of Eq. (9) would contain an appropriate source term. Using Eqs. (5) and (8) and canceling common terms, Eq. (9) can be rewritten in terms of mean-square pressure:

$$\frac{d(\overline{p}^2_{+x})}{dx}+\frac{\alpha_w\beta L_p}{(2-\alpha_w)S}\overline{p}^2_{+x}=0. \tag{10}$$

The solution of this differential equation is

$$\overline{p}^2_{+x}=P_{+x}e^{-(\alpha_w\beta L_p)/((2-\alpha_w)S)x}. \tag{11}$$

Similar arguments can be made regarding the left-traveling $(-x)$ oblique wave field, with the result that

$$\overline{p}^2_{-x}=P_{-x}e^{+(\alpha_w\beta L_p)/((2-\alpha_w)S)x}, \tag{12}$$

where P_{+x} and P_{-x} are unknown coefficients of the mean-square pressure components, to be determined from application of the boundary conditions at the ends of the enclosure.

A. Boundary conditions

At the absorbing end-wall ($x=0$), the intensity of the left-traveling waves is equal to the reflection coefficient of the end-wall times the intensity of the right-traveling waves. In other words,

$$I_{-x}(0)=(1-\alpha_b)I_{+x}(0), \tag{13}$$

where α_b is the random incidence absorption coefficient of the absorbing end-wall. The mean-square pressure amplitudes are therefore related by

$$P_{-x}=(1-\alpha_b)P_{+x}. \tag{14}$$

At the other end-wall (the source wall), the power of the source (or sources) is equal to the area of the end-wall times the difference between the intensity in the $+x$ direction (due to right-traveling waves) and the intensity in the $-x$ direction (due to the left-traveling waves) times the cross-sectional area:

$$\Pi=S[I_{+x}(-L_x)-I_{-x}(-L_x)]. \tag{15}$$

B. Solution for cross-sectional average

As stated earlier, the left- and right-traveling fields can be assumed to be uncorrelated, such that the net mean-square pressure is a superposition of $\overline{p}^2_{+x}$ and $\overline{p}^2_{-x}$, as in Eq. (4). Writing Eq. (15) in terms of mean-square pressure components, using Eq. (14) to eliminate one of the mean-square pressure amplitudes, and superimposing $\overline{p}^2_{+x}$ and $\overline{p}^2_{-x}$ leads to the result

$$\overline{p}^2(x)=\frac{2\rho c\Pi}{S}\left[\frac{\cosh([\alpha_w\beta L_p/(2-\alpha_w)S]\,x)-\frac{1}{2}\alpha_b e^{+([\alpha_w\beta L_p/(2-\alpha_w)S]\,x)}}{\sinh([\alpha_w\beta L_p/(2-\alpha_w)S]\,L_x)+\frac{1}{2}\alpha_b e^{-([\alpha_w\beta L_p/(2-\alpha_w)S]\,L_x)}}\right]. \tag{16}$$

This is the expression for the cross-sectional average mean-square pressure as a function of distance. Due to the choice of coordinate system direction, x, the distance from the absorbing wall, is negative. Note that the parameters that appear in the above expression are the source power, absorption coefficients (which can be combined with the appropriate areas to produce absorptivities), the characteristic impedance, and the location of interest.

In the Franzoni–Labrozzi empirical formula [Eq. (2)] the spatial variation was simply an exponential function. Here, the spatial variation is slightly more involved, however, the formula is just as easy to use.

C. Modified Sabine formula for the spatial average

A spatial average can be calculated directly from Eq. (16) or, using some of the insights from the above derivation along with the simple energy conservation statement that the power into the enclosure equals the power out of the enclosure [as in the Sabine formula Eq. (1)], a modified Sabine equation for the spatial average can be formulated. In this derivation, it will be assumed that the mean-square pressure is the *average* mean-square pressure in the volume, but its components due to the incident and reflected waves will have different magnitudes as in the previous discussion.

The power out of the enclosure is that which is removed by the absorbing surfaces. Therefore,

$$\Pi_{\text{out}}=\sum_{\substack{\text{absorbing}\\ \text{surfaces},i}} I_{\substack{\text{into}\\ \text{surface}}}\alpha_i S_i, \tag{17}$$

where I is the intensity, α_i is the random incidence absorption coefficient of the ith absorbing surface (equivalent to the intensity transmission coefficient), and S_i is the surface area covered by the absorptive material. The intensity into the surface consists of two components: that of the reverberant field I_{rev}, and that directly from the source I_{direct}.

The reverberant component of intensity into an absorbing surface is related to the *average* (not at a boundary) mean-square pressure by Eq. (5); using the same arguments that led to Eq. (7):

$$I_{\text{rev}}=\frac{\overline{p}^2_{\text{incident}}}{2\rho c}=\frac{\overline{p}^2}{2\rho c}\frac{1}{(2-\alpha_i)}. \tag{18}$$

The average intensity from the source into the absorbing surface(s) is approximately related to the power into the enclosure by

$$I_{\text{direct}}\cong\frac{\Pi_{\text{in}}}{S_{\text{total}}}. \tag{19}$$

Therefore, the power removed by the absorbing surfaces is

$$\begin{aligned}\Pi_{\text{out}}&=\sum_{\substack{\text{absorbing}\\ \text{surfaces},i}} I_{\substack{\text{into}\\ \text{surface}}}\alpha_i S_i\\ &=\sum_i\frac{\overline{p}^2}{2\rho c(2-\alpha_i)}\alpha_i S_i+\sum_i\frac{\Pi_{\text{in}}}{S_{\text{total}}}\alpha_i S_i.\end{aligned} \tag{20}$$

Equating the power into the enclosure to the power out yields

$$\Pi_{\text{in}}=\sum_i\frac{\overline{p}^2}{2\rho c(2-\alpha_i)}\alpha_i S_i+\sum_i\frac{\Pi_{\text{in}}}{S_{\text{total}}}\alpha_i S_i. \tag{21}$$

Rearranging and solving for the average mean-square pressure

$$\overline{p}^2_{\substack{\text{spatial}\\ \text{average}}}=\frac{4\Pi_{\text{in}}\rho c}{\Sigma_i(\alpha_i S_i)/(1-\alpha_i/2)}\left(1-\sum_i\alpha_i S_i/S_{\text{total}}\right). \tag{22}$$

This result is a **modified Sabine formula** for the spatially-averaged reverberant mean-square pressure. If the same ab-

sorption coefficient applies to all covered surfaces, this simplifies to

$$\overline{p^2}_{\substack{\text{spatial}\\ \text{average}}} = \frac{4\Pi\rho c}{A}(1-\alpha/2)(1-A/S_{\text{total}}), \tag{23}$$

where A is the absorptivity and Π is the total power of sources in the room. The factors that modify the original Sabine formula can be interpreted as follows. The first term in parentheses is a correction due to the difference in mean-square pressure amplitude between in-coming and out-going waves, and the second term removes the power absorbed by the first reflection. The modified Sabine formula given by Eq. (22) will be shown in Sec. IV to be very accurate when compared to the exact numerical simulations of the sound field.

D. Spatial-average of cross-sectional values

Alternatively, a spatially-averaged mean-square pressure level could have been obtained by integrating Eq. (16) over $\overline{x}$ from -1 to 0. In the limit of small α_b and small α_w, a similar result is derived, as follows.

The spatial average of Eq. (16) is

$$\langle\overline{p^2}\rangle = \frac{2\rho c\Pi}{S}\int_{-1}^{0}\frac{\cosh(\gamma\overline{x})-(\alpha_b/2)e^{\gamma\overline{x}}}{\sinh(\gamma)+(\alpha_b/2)e^{-\gamma}}d\overline{x}, \tag{24}$$

where $\gamma = \alpha_w\beta L_p L_x/(2-\alpha_w)S$. Upon integrating, and evaluating the function at the limits of integration,

$$\langle\overline{p^2}\rangle = \frac{2\rho c\Pi}{S}\frac{1}{\gamma}\left(\sinh(\gamma)-\frac{1}{2}\alpha_b(1-e^{-\gamma})\right)\Big/ \left(\sinh(\gamma)+\tfrac{1}{2}\alpha_b e^{-\gamma}\right). \tag{25}$$

Assuming small γ (equivalent to small α_w) and small α_b, expanding the sinh and exponential in a Taylor series, and retaining terms of order γ and order α_b leads to

$$\langle\overline{p^2}\rangle = \frac{2\rho c\Pi}{S}\frac{1}{\gamma}\left(\gamma-\frac{1}{2}\alpha_b\gamma\right)\Big/\left(\gamma+\frac{1}{2}\alpha_b(1-\gamma)\right)$$
$$= \frac{2\rho c\Pi}{S}\left(1-\frac{1}{2}\alpha_b\right)\Big/\left(\gamma+\frac{1}{2}\alpha_b(1-\gamma)\right).$$

Substituting the expression for γ, and keeping the lowest order terms,

$$\langle\overline{p^2}\rangle = \frac{4\rho c\Pi}{[A_w/(1-\alpha_w/2)]+[A_b/(1-\alpha_b/2)]}, \tag{26}$$

where A_w is the absorptivity associated with the side wall absorptivity, α_w, and A_b is the end-wall absorptivity. The power has not been reduced to remove the first reflection. Once this is done, the formula for the spatially-averaged mean-square pressure in the enclosed volume becomes

$$\langle\overline{p^2}\rangle = \frac{4\rho c\Pi(1-A/S_{\text{total}})}{[A_w/(1-\alpha_w/2)]+[A_b(1-\alpha_b/2)]}, \tag{27}$$

where A is the total absorptivity. This formula is equivalent to the previously derived modified Sabine formula, given by Eq. (22).

IV. RESULTS: COMPARISON TO NUMERICAL SIMULATIONS

Having access to the numerical data of Ref. 8, comparisons were made between trajectory averages and the energy-based theoretical formula that includes spatial variation [Eq. (16)] for several cases. The numerical simulation data consisted of 11 trajectories from the source wall to the opposing end wall, along lines of constant (y,z) (see Fig. 1 for reference). These trajectories were then averaged to obtain the single curve that is presented. The simulations were performed in 1/3 octave bands, at a dimensionless center frequency wavenumber of $k_c L_x = 160$, which allowed for at least eight wavelengths along the smallest side of the enclosure. Only the reverberant field was included in the mean-

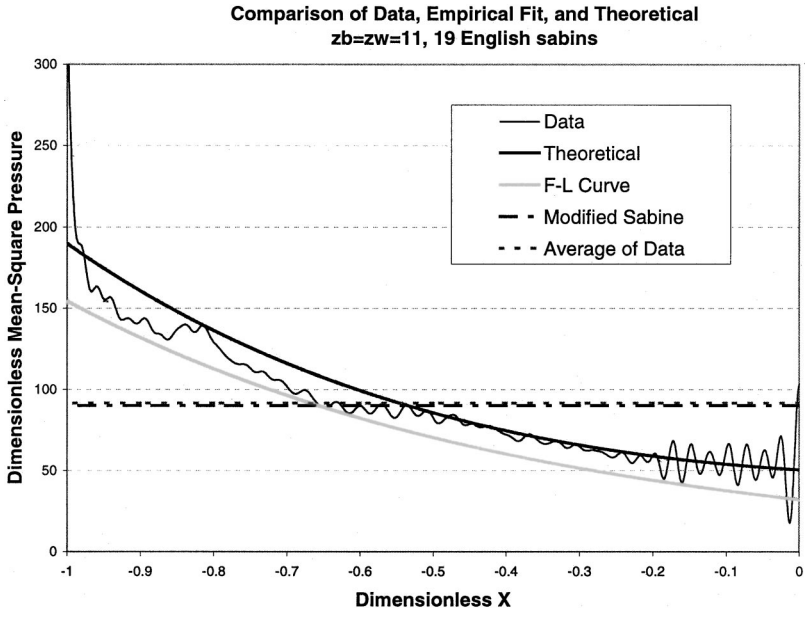

FIG. 3. Spatial variation of mean-square pressure (normalized) for a long rectangular room with absorptive side-walls and a hard end-wall. The random incidence absorption coefficient of the side-walls was $\alpha_w = 0.54$. The absorptivity of the room was 19 English sabins.

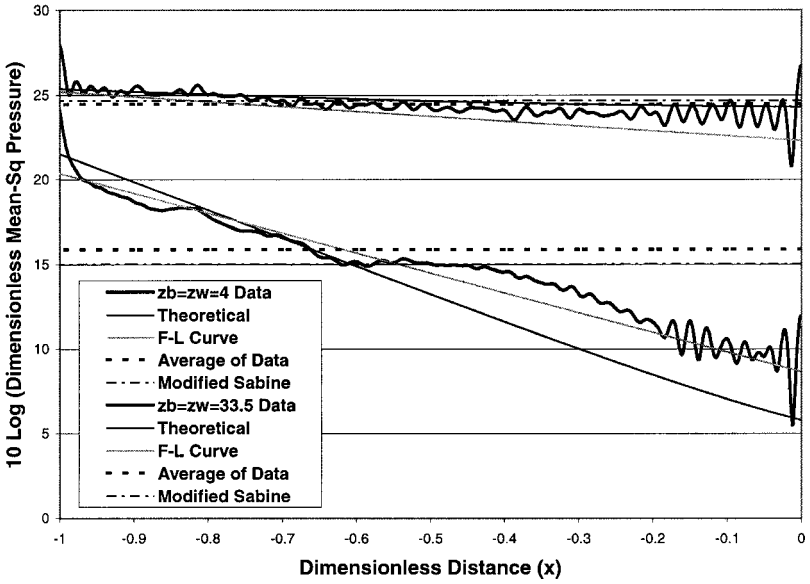

FIG. 4. Spatial variation shown in decibels for two cases with different absorptivity for the long rectangular enclosure. The upper set of curves corresponds to $\alpha_w = \alpha_b = 0.2$ (real normalized impedance of $z_b = z_w = 33.5$), for an absorptivity of 9 English sabins. The lower set of curves corresponds to a more absorptive case, $\alpha_w = \alpha_b = 0.8$ ($z_b = z_w = 4$), having an absorptivity of 32 English sabins.

square pressure calculation, that is, the mean-square pressure directly from the source (or sources) was removed from the total.

Figures 3–5 show example comparisons. The (exact) numerical simulation is capable of predicting both the gradual and *rapid* spatial variation, however the approximate formula derived in this article only predicts the overall *gradual* variation. For reference, the Franzoni–Labrozzi (F-L) empirical curve [Eq. (2)] and the uniform level of the reverberant mean-square pressure predicted by the modified Sabine equation [Eq. (22) or (27)] are also shown. It should be kept in mind that the F-L curve is a semi-empirical result that was developed based on this data set. Note that the direct field has been removed from the numerical data, leaving the reverberant field only. Similarly, the power absorbed by the first reflection has been removed from all of the approximate formulas, except Eq. (16). Therefore, the power Π in Eq. (16) should be replaced by $\Pi(1-A/S)$, where A is total absorptivity and S is total surface area. Thus, the predicted mean-square pressures in all formulas are consistent with the *reverberant* mean-square pressures that were computed in the numerical simulations (direct field removed). Figures 3 and 4 are for an elongated rectangular enclosure, and Fig. 5 is for a more evenly-shaped enclosure.

Figure 3 shows the results for a long rectangular enclosure ($L_z/L_x = 3/7$ and $L_y/L_x = 2/7$) with two ''hard'' end-walls. Two adjacent side-walls were covered by a real-valued impedance ($z_w/\rho c = 8.66$, $\alpha_w = 0.54$), such that the total English sabins for the enclosure was 19. The curves shown in Fig. 3 represent an average trajectory from the source wall to the opposite absorbing wall. The results are presented as a dimensionless mean-square pressure versus a dimensionless distance between source wall ($\overline{x} = -1$) and the opposite end-wall. The theoretical curve (new result) appears to show improvement over the Franzoni–Labrozzi (F-L) curve that was based upon collapsing numerical data from many cases similar to this one. In many instances, the new theoretical curve and the F-L curve actually cross each other, with both curves seeming to fit the data equally well.

Notice in the numerical simulation data that the mean-

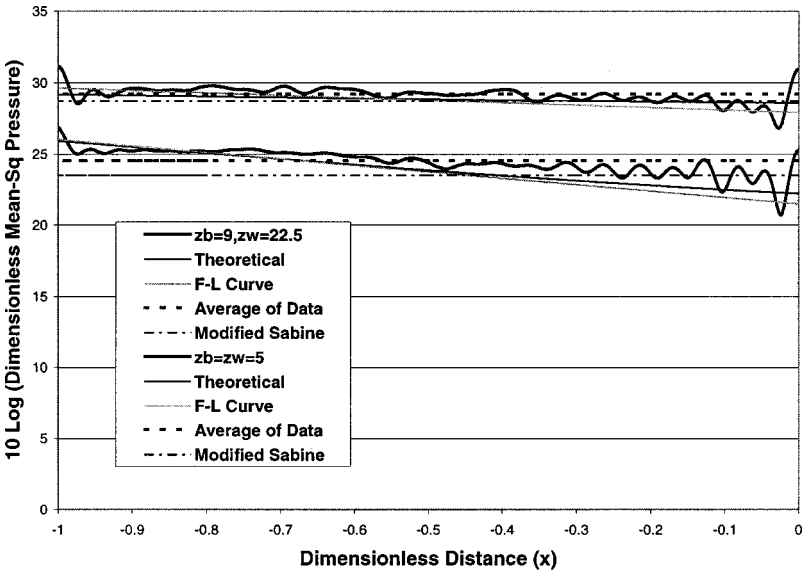

FIG. 5. Two absorptivity cases for the more evenly shaped enclosure. The upper set of curves corresponds to $\alpha_w = 0.3$, $\alpha_b = 0.5$ ($z_b = 9$, $z_w = 22.5$) for a total absorptivity of 18 English sabins. The lower set of curves corresponds to $\alpha_w = \alpha_b = 0.7$ ($z_b = z_w = 5$), 30 English sabins.

square pressure levels show a sharp increase right at the boundaries. This is due to the effect of intensification zones[9] (where all modes are spatially correlated), and is particularly pronounced at hard end-walls. The rapid spatial variation at the end-wall opposite the source may be due to the presence of one-dimensional waves that are not well absorbed. Most of the other waves (oblique incidence) will have experienced many reflections by the time they reach this end, and each reflection is diminished in strength. However, the one-dimensional waves are not strongly affected by the side-wall absorption, and therefore may be of relatively large amplitude at the absorbing end-wall.

Figure 4 shows a similar comparison on a decibel scale for the same elongated enclosure. Here, two different cases are shown. The upper set of curves corresponds to a case with relatively low absorption ($\alpha_w = \alpha_b = 0.2$), and the lower set of curves corresponds to a case that is highly absorptive. In fact, for the lower curves the random incidence absorption coefficient for the absorbing side-walls, as well as the absorbing end-wall, is $\alpha_w = \alpha_b = 0.8$ (absorptivity for the enclosure equaled 32 English sabins). Notice that the spatial variation from one end of the enclosure to the other is approximately 10 dB. For the more absorptive case, the F-L curve (from Ref. 8) is slightly more accurate at predicting the gradual spatial variation, however the new theoretical curve is still very good. In the less absorptive case shown here, the new theoretical curve shows improvement over the F-L curve at predicting the actual slow spatial variation. The less absorptive case corresponds to an overall absorptivity of 8 English sabins. For comparison, the previously shown plot (Fig. 3, corresponding to 19 English sabins) would lie in-between these two sets of curves, if it were plotted in dB.

A similar comparison is shown in Fig. 5, for a more evenly-shaped enclosure. Here, the enclosure dimensions are ratios of 4.7/3.5 and 3/3.5 with the 4.7 units by 3 units wall being on the end. Figure 5 shows a case with the same absorbing material on two side-walls and an end-wall, and a case with different amounts of absorption on the different surface areas. The upper set of curves corresponds to the case with unequal absorption on the various walls, two adjacent side-walls are covered, having a random incidence absorption coefficient of 0.3, and the end-wall material has a random incidence absorption coefficient of 0.5. The total absorptivity for this enclosure is 18 English sabins. In the more evenly-shaped room there is less spatial variation in mean-square level than in the more elongated room, for approximately the same absorptivity level. Recall that Fig. 3 showed a case with 19 English sabins for a more elongated enclosure. Had those results been plotted in decibels, the overall variation would have been about 5 dB, whereas in this room the variation is only a few decibels.

The lower set of curves in Fig. 5 corresponds to an equal distribution of absorption over exactly half of the enclosure. The random incidence absorption coefficient for each covered surface was 0.7, and the absorptivity of the enclosure was 30 English sabins. This was a very absorptive case, and even though the enclosure is more evenly-shaped, the level (from the numerical simulation) shows an overall spatial variation of at least 3 dB. The theoretical curve does a good job of estimating the gradual spatial variation, as does the F-L curve. It is surprising that the energy-based formula performs as well as it does for this particular enclosure, since the direction of interest is relatively short, and the absorption level is so high. With such large absorption levels, the assumption that the field is ''locally diffuse'' is starting to fail (here, and in the second case shown in Fig. 4).

Comparisons of other data sets showed similar (or better) agreement. Absorption coefficients up to 0.8 and down to 0.1 for side-wall absorption and lower for end-wall absorption were included in the comparisons. Enclosure absorptivities ranging from 6 to 32 English sabins for the elongated enclosure, and from 8 to 30 for the more cubic enclosure,

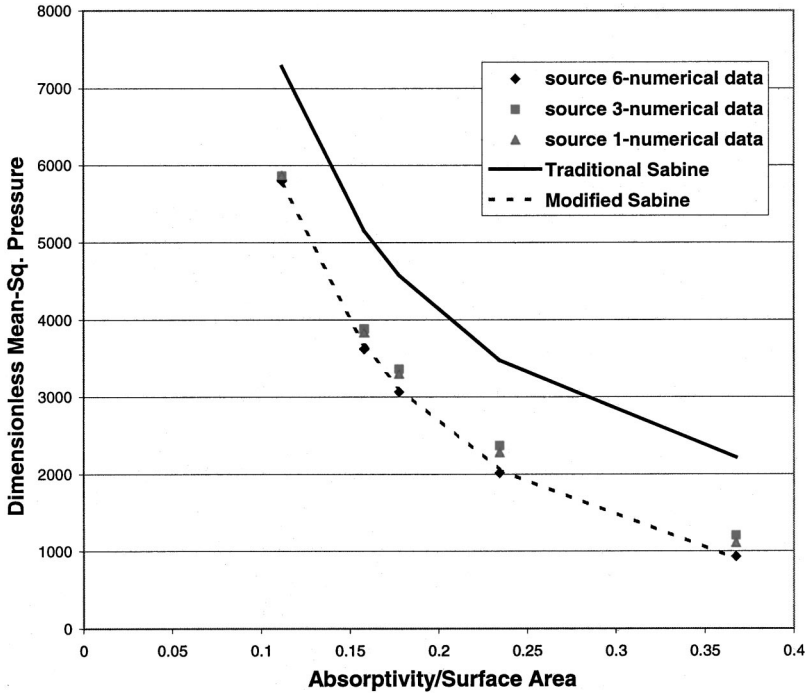

FIG. 6. Comparison between the traditional Sabine formula and modified Sabine formula for predicting numerical data. The numerical data was given for different source locations with different levels of absorption on the side-walls and the end-wall.

were investigated. (Random incidence absorption coefficients ranged from hundredths to 0.7 or 0.8, for individual wall coverings.) Some of the cases shown are for the most extreme examples, yet the comparisons are still fairly good. In fact, it was remarkable how well the approximate curve worked over the entire absorptivity range for both types of room shapes considering that the theory is based on an assumption that the sound fields are locally diffuse.

In Fig. 6, numerical simulation data is spatially averaged for different levels of absorption on the side- and end-walls. In these numerical simulations a single monopole source was placed on one of the end-walls. The data shown correspond to three different source locations on that wall (near the center, near a corner, and partway between the center and a corner). This data is compared to two approximate curves, the traditional Sabine formula for the spatial average (Ref. 7) and the modified Sabine formula derived in this article. While the traditional Sabine formula overpredicts the spatially-averaged reverberant level, the modified Sabine formula gives excellent agreement over a wide range of absorptivity levels.

V. CONCLUSIONS

For the case of an acoustic source (or sources) on an end-wall, and absorptive surfaces on side-walls and/or the opposite end-wall, the formula derived by energy conservation accurately predicts the slow spatial variation of mean-square pressure in the interior of a rectangular acoustic enclosure. In fact, it is surprising how well the approximate formula works, even for highly absorptive cases, since the derivation is based on assumptions that apply to quasi-diffuse sound fields. The process used to derive the formula can be used for cases other than a source on an end-wall; however, this case was chosen due to the availability of numerical data and the simplicity of analysis. For an interior source or sources, other boundary conditions (including continuity conditions between internal subregions) would have to be applied, but this should not present any problems.

In addition to a formula containing a spatially-varying term, a simple expression for the spatially-averaged mean-square pressure in the reverberant field was derived. This expression was seen as a modification of the classical Sabine formula (for steady-state levels). The modification contained a reduction of the power, equivalent to removing the power absorbed by the first reflection, and a term that accounts for the fact that the pressure waves into a surface are stronger than those reflected from the surface. This modified Sabine formula agrees very closely with the spatial average of the reverberant field for a variety of absorptivities.

ACKNOWLEDGMENTS

The work was supported by the National Science Foundation. The author is grateful for many valuable technical discussions with Dr. Donald Bliss at Duke University that led to the development of this theory. Plots of the type presented in this article (without comparison to the F-L curve) were originally made by Christopher Elliott, under the author's supervision, as a component of his Master's thesis at North Carolina State University.

APPENDIX: MEAN-SQUARE PRESSURE VARIATION ACROSS THE CROSS-SECTION

This appendix considers a model problem involving the reflection of two-dimensional oblique waves in a channel with one absorbing wall. The results show that the variations in mean-square pressure over the cross-section are small, being the order of absorption coefficient squared. Similar results are obtained for the three-dimensional case; the two-dimensional case is presented in the interest of convenience and simplicity. Therefore, the assumption used in the main text of the article that the mean-square pressure is approximately constant over an enclosure cross-section is justified. This analysis also justifies the assumptions made regarding incident and reflected mean-square pressures and intensities near absorbing surfaces.

The configuration to be analyzed is shown in Fig. 7. Parallel surfaces are separated by a distance L_y. The surface at $y=0$ is perfectly rigid whereas the surface at $y=L_y$ is characterized by a normal specific acoustic impedance $\overline{z_w}=z_w/\rho c$. The pressure field is governed by the two-dimensional wave equation and velocity components are derived from the momentum equation:

$$\frac{\partial^2 p}{\partial x^2}+\frac{\partial^2 p}{\partial y^2}-\frac{1}{c^2}\frac{\partial^2 p}{\partial t^2}=0, \tag{A1}$$

$$\vec{i}\frac{\partial u}{\partial t}+\vec{j}\frac{\partial v}{\partial t}=-\frac{1}{\rho}\vec{\nabla}p. \tag{A2}$$

The solution to the wave equation which satisfies the boundary condition at $y=0$ is readily shown to have the following form:

$$p=P\cos k_y y e^{i(\omega t-k_x x)}, \tag{A3}$$

where the wavenumber components are related by

$$k_x^2+k_y^2=k^2 \quad \text{and} \quad k=\frac{\omega}{c}. \tag{A4}$$

Applying the boundary condition at $y=L_y$ and using Eq. (A2), leads to an equation for the eigenvalues k_{y_n}:

$$(k_{y_n}L_y)\tan(k_{y_n}L_y)=i\frac{kL_y}{\overline{z_w}}. \tag{A5}$$

The infinite set of eigenvalues can be written in the form

$$k_{y_n}L_y=n\pi+\varepsilon_n. \tag{A6}$$

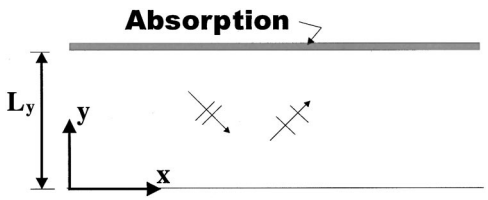

FIG. 7. Two-dimensional configuration to analyze the variation of mean-square pressure within the cross-section.

For convenience the wall impedance is now assumed to be entirely real, namely $\bar{z}_w=\bar{r}_w+i\bar{x}_w=\bar{r}_w+i0$. Substituting Eq. (A6) into Eq. (A5) and assuming that the magnitude of the right-hand-side of Eq. (A5) is small (essentially large impedance) leads to a solution of the following form,

$$\varepsilon_n \approx i\frac{kL_y}{n\pi\bar{r}_w}, \quad \text{for } n=1,2,3\ldots,$$
$$\varepsilon_0 \approx \sqrt{i\frac{kL_y}{\bar{r}_w}} \quad \text{for } n=0. \tag{A7}$$

In Eq. (A7) only the lowest order terms have been retained.

The absorption coefficient for oblique waves striking a wall with large real-valued normal impedance at angle θ_n is given by

$$\alpha_n=\frac{4\bar{r}_w\cos\theta_n}{(\bar{r}_w\cos\theta_n+1)^2}\approx\frac{4}{\bar{r}_w\cos\theta_n} \quad \text{if } \bar{r}_w\cos\theta_n\gg 1. \tag{A8}$$

The cosine of the incidence angle can be rewritten as

$$\cos\theta_n=\frac{k_{yn}L_y}{kL_y}=\frac{(n\pi+\varepsilon_n)}{kL_y}\approx\frac{n\pi}{kL_y}. \tag{A9}$$

Substituting Eqs. (A8) and (A9) into Eq. (A7) gives

$$\varepsilon_n\approx i\frac{kL_y}{n\pi\bar{r}_w}=i\frac{1}{\bar{r}_w\cos\theta_n}=i\frac{\alpha_n}{4}. \tag{A10}$$

Substituting Eqs. (A10) and (A6) into Eq. (A3) and expanding the trigonometric expression gives the following result for complex pressure of the nth oblique wave mode:

$$p_n=P_n\left[\cos n\pi\bar{y}\cosh\frac{\alpha_n}{4}\bar{y}-i\sin n\pi\bar{y}\sinh\frac{\alpha_n}{4}\bar{y}\right]e^{i(\omega t-k_x x)}, \tag{A11}$$

where $\bar{y}=y/L_y$. Calculating the mean-square pressure,

$$\bar{p}_n^2=\frac{|P_n|^2}{2}\left[\cos^2 n\pi\bar{y}\cosh^2\frac{\alpha_n}{4}\bar{y}+\sin^2 n\pi\bar{y}\sinh^2\frac{\alpha_n}{4}\bar{y}\right]. \tag{A12}$$

Using trigonometric identities and Taylor series expansions for the hyperbolic functions, assuming α_n is small, gives the following form for the mean-square pressure of the nth oblique wave mode:

$$\bar{p}_n^2=\frac{|P_n|^2}{4}\left(1+\frac{3}{2}\frac{\alpha_n^2}{4^2}\bar{y}^2\right)+\frac{|P_n|^2}{4}\cos 2n\pi\bar{y}\left(1-\frac{1}{2}\frac{\alpha_n^2}{4^2}\bar{y}^2\right). \tag{A13}$$

When a number of oblique waves are added together for different values of n and for different frequencies, the second term on the right will average to zero due to the rapid oscillation of $\cos 2n\pi\bar{y}$. The cross-sectional variation in mean-square pressure is then seen to be of the order α_n^2. This variation is assumed to be a higher-order effect $(3\alpha_n^2/32)$ and is neglected in the main body of the article. In practice, owing to the small size of the coefficient of α_n^2, this variation remains small even when the absorption coefficient is fairly large.

Returning to Eq. (A11), the pressure can be decomposed into a component propagating toward the absorbing surface and another propagating away from the surface. Evaluated at $y=L_y$, these components of pressure are given by

$$p_{n_{\text{incident}}}=\frac{P_n}{2}\left[\cosh\frac{\alpha_n}{4}+\sinh\frac{\alpha_n}{4}\right]e^{i(\omega t-k_{x_n}x-n\pi)}, \tag{A14}$$

$$p_{n_{\text{reflected}}}=\frac{P_n}{2}\left[\cosh\frac{\alpha_n}{4}-\sinh\frac{\alpha_n}{4}\right]e^{i(\omega t-k_{x_n}x+n\pi)}. \tag{A15}$$

Computing the mean-square pressure gives

$$\bar{p}^2_{n_{\text{incident}}}=\frac{|P_n|^2}{8}\left[\cosh\frac{\alpha_n}{4}+\sinh\frac{\alpha_n}{4}\right]^2$$
$$\approx\frac{|P_n|^2}{8}\left[1+\frac{\alpha_n}{2}+O[\alpha_n^2]\right], \tag{A16}$$

$$\bar{p}^2_{n_{\text{reflected}}}=\frac{|P_n|^2}{8}\left[\cosh\frac{\alpha_n}{4}-\sinh\frac{\alpha_n}{4}\right]^2$$
$$\approx\frac{|P_n|^2}{8}\left[1-\frac{\alpha_n}{2}+O[\alpha_n^2]\right]. \tag{A17}$$

Combining these expressions gives

$$\bar{p}^2_{n_{\text{reflected}}}=\bar{p}^2_{n_{\text{incident}}}\frac{[1-\alpha_n/2+O[\alpha_n^2]]}{[1+\alpha_n/2+O[\alpha_n^2]]}$$
$$\approx\bar{p}^2_{n_{\text{incident}}}\left[1-\frac{\alpha_n}{2}+O[\alpha_n^2]\right]. \tag{A18}$$

This result is consistent with Eq. (7) in the main text. Summing over n to encompass all modes at all incident angles would lead α_n to be replaced by α_{random} for a diffuse field. Similarly, referring to Eq. (A16) and the results of Eq. (A13), the incident intensity is

$$I_{n_{\text{incident}}}=\frac{|P_n|^2}{8\rho c}\left[1+\frac{\alpha_n}{2}+O[\alpha_n^2]\right]\approx\frac{|P_n|^2}{4\rho c}\frac{1}{2-\alpha_n}, \tag{A19}$$

which corresponds to Eq. (8) of the main text.

[1] V. Easwaran and A. Craggs, "On Further Validation and Use of the Finite Element Method to Room Acoustics," J. Vib. Acoust. **187**(4), 195–212 (1995).

[2] K. A. Hussain and K. S. Peat, "Boundary Element Analysis of Low Frequency Cavity Acoustical Problems," J. Sound Vib. **169**(2), 197–209 (1995).

[3] L. P. Franzoni and E. H. Dowell, "On the accuracy of modal analysis in reverberant acoustical systems with damping," J. Acoust. Soc. Am. **97**(1), 687–690 (1995).

[4] W. Ren and K. Attenborough, "Prediction of Sound Fields in Rooms Using Statistical Energy Analysis," Appl. Acoust. **34**(3), 207–220 (1991).

[5] L. F. Peretti and E. H. Dowell, "Asymptotic Modal Analysis of a Rectangular Acoustic Cavity Excited by Wall Vibration," AIAA J. **30**(5), 1191–1198 (1992).

[6] M. Hodgson "Experimental evaluation of simplified models for predicting noise levels in industrial workrooms," J. Acoust. Soc. Am. **103**(4), 1933–1939 (1998).

[7] L. E. Kinsler, A. R. Frey, A. B. Coopens, and J. V. Sanders, *Fundamentals of Acoustics*, 3rd ed. (Wiley, New York, 1982).

[8] L. P. Franzoni and D. S. Labrozzi, "A study of damping effects on spatial distribution and level of reverberant sound in a rectangular acoustic cavity," J. Acoust. Soc. Am. **106**(2), 802–815 (1999).

[9] L. F. Peretti and E. H. Dowell, "A Study of Intensification Zones in a Rectangular Acoustic Cavity," AIAA J. **30**(5), 1199–1206 (1992).

A profiled structure with improved low frequency absorption

Tao Wu, Trevor J. Cox,[a] and Y. W. Lam
School of Acoustics and Electronic Engineering, University of Salford, Salford M5 4WT, United Kingdom

(Received 26 June 2001; accepted for publication 17 August 2001)

It is possible to obtain good absorption from Schroeder diffusers if suitable alterations to the design are made. Interestingly, previous work has shown that good absorption appears possible below the design frequency when the diffusers are poorly constructed. This has inspired the design of a profiled absorber using perforated plates in some wells; the absorber has extended bass response. The paper presents a theory for the enhanced absorption and the important design parameters are discussed. Good agreement is shown between the prediction model and impedance tube measurements. The design of this absorber was first carried out using a numerical optimization, although a simplified design procedure is also outlined which is almost as good. The results clearly show that this type of profiled absorber extends the absorption at low frequencies while maintaining the good absorption at mid frequencies as well. © *2001 Acoustical Society of America.*
[DOI: 10.1121/1.1412443]

PACS numbers: 43.55.Ev, 43.55.Dt [JDQ]

I. INTRODUCTION

Schroeder diffusers have been widely used in concert halls, theatres, and studio control rooms.[1] There is evidence, however, of significant absorption when the diffusers are poorly designed.[2] Kuttruff,[3] Mechel,[4] Fujiwara *et al.*,[5] and Wu *et al.*[6] theoretically and practically investigated the absorption mechanism. Kuttruff presented the concept of additional air flow between the wells as the source of the excess absorption, although he could not obtain a prediction model which explained the high absorption measured by others. Mechel thoroughly discussed the absorption effect for the near field as well as the directivity for the far field, although his studies lacked direct experimental verification. Furthermore, Mechel indicated the possibility of a low-frequency band absorber by bending the wells, and using the primitive root rather than the quadratic residue sequence to gain better absorption. Wu *et al.* brought together measurement and prediction to provide proper evidence that the strong coupling between the wells is responsible for the high absorption. This was used to develop a new profiled absorber by arranging the depths of wells in one period properly using numerical optimization.

High absorption at low frequencies is the most difficult to achieve from these profiled devices, consequently, the challenge tackled in this paper is to get more absorption bandwidth from a given length. Interestingly, in the paper by Fujiwara,[5] it was reported that poorly constructed structures could provide high absorption below the lowest resonant frequency. It is speculated that this additional absorption came from cracks in the well bottoms forming Helmholtz resonators with air cavities behind. This inspired the idea that using perforated plates in some wells could significantly extend the absorption range towards the lower frequencies by adding mass to the system and so lowering the resonant frequency.

While the research presented here was in progress, Fujiwara[7] published a paper which contained measurement results on a structure with Helmholtz resonators in the wells, i.e., using a similar technique to add mass and to get better absorption in a low frequency range. Fujiwara presented no verified prediction model or design methodology for these structures; it appears the design was formed by trial and error. What is new in the paper below is a prediction model validated against measurement; a more complete understanding of the effects of the different elements in the absorber, and analytical design methodologies which will be used to get the best possible absorption from this structure.

First, the prediction model is presented including the effect of a perforated plate at different positions in the well. The simplest constant length structure with perforated plates in the wells has been optimized to obtain better absorption without any resistant layer on the top. However, as will be shown, this structure cannot provide wide frequency band absorption. It is essential to include different depth wells to get wide frequency range absorption. A numerical optimization is performed to obtain better absorption by adjusting the position of the perforated plates in the wells, and the depths of the wells. The theoretical results have been compared with experimental results, and good agreement achieved. The significant improvement at low frequency range is clearly shown when comparing this kind of absorber with profiled absorber without in-well perforations. The final part of the paper investigates a more straightforward design methodology than numerical optimization. It is shown that by following a couple of simple principles good absorption can be achieved without resorting to numerical optimization.

II. SINGLE WELL MODEL

A. The impedance of a perforated panel

Perforated panels have been used for some years in conjunction with acoustic compliance, and their ability to produce absorption at low frequencies, especially with resistive material, is well known. The perforated plates can be considered as a lattice of short tubes, where the pitch of adjacent tubes is small compared with wavelength of propagating

[a]Electronic mail: t.j.cox@salford.ac.uk

sound, but larger than the hole diameter. It is assumed that when sound flows through the holes, there is no motion in the plate itself, and the hole radius is larger than the boundary layer thickness. Then the specific acoustics impedance of the perforated plate is[8]

$$z_p = r_m + j\omega m \tag{1}$$

and

$$r_m = \frac{\rho}{\varepsilon}\sqrt{8\eta\omega}\left(1+\frac{t}{2a}\right), \tag{2}$$

$$m \approx \frac{\rho}{\varepsilon}\left[t + 2\delta a + \sqrt{\frac{8\eta}{\omega}}\left(1+\frac{t}{2a}\right)\right], \tag{3}$$

where ρ is the air density, ω is the angular frequency of propagating sound, ε is porosity of the plate, t is the thickness of the plate, a is the radius of the holes, δ is the end correction factor (≈ 0.85), and the last term is due to the boundary layer effect, in which η is the kinemetric viscosity of the air ($\approx 15\times 10^{-6}\ \mathrm{m^2/s}$).

B. The impedance at the entrance of a well

The impedance is needed at the entrance of a well containing a perforated plate and with resistive material at the well entrance. The well width of a profiled absorber is narrow compared with diffusers to provide more absorption, therefore the energy losses caused by viscous and thermal conduction in the wells cannot be neglected. In general, the well width $b \ll \lambda/2$, where λ is the wavelength of the sound, so that only fundamental modes are considered to propagate in each well. The propagation number in the wells is [9]

$$k_t \approx k + \frac{k}{2b}(1-j)[d_v + (\gamma-1)d_h], \tag{4}$$

where $k=\omega/c$, c is the speed of sound. d_v, d_h are the thickness of the viscous and thermal boundary layers, respectively, these can be found from Eq. (5) of Ref. 6. The wells should not be made too narrow, however, because then the resonance(s) would be destroyed. Considering a well length l_n, a perforated plate is fixed at l_{n1} from the opening of well. The impedance on the opening of the well can be derived by the multilayer transfer matrix as

$$z_w = \frac{\rho c z_1 \coth(jk_t l_{n1}) + (\rho c)^2}{z_1 + \rho c \coth(jk_t l_{n1})} + r, \tag{5}$$

where r is the resistivity of the material at the well entrance and z_1 is the total impedance at l_{n1} of a perforated plate and the cavity it covered. z_1 can be calculated by the following equation:

$$z_1 = r_m + j(\omega m - \rho c \cot(k_t(l_n - l_{n1}))). \tag{6}$$

When no perforated plate is used in the well, the entrance impedance simplifies to

$$z_w = r - j\rho c \cot(k_t l_n), \tag{7}$$

where l_n is the depth to the well bottom.

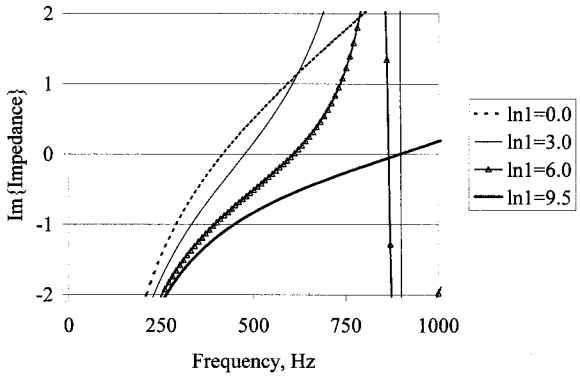

FIG. 1. Comparison of the imaginary part of impedance when moving a perforated plate form bottom to top of a 10 cm well. Distance from top of well to perforated plate, $ln1$, shown in legend.

C. Effect of perforated plate at different positions in the well

As can be seen from Eqs. (5) and (6), the position of the perforated plate in a well is important for the resonant frequency. Changing the position of perforated plate from bottom to opening in the well, the first resonant frequency of the well is gradually decreased, from the first resonant frequency of the well without perforated plate to the frequency with perforated plate on the top. This gives us a possibility to tune the well by adjusting the positions of the perforated plates. An example is given in Fig. 1, the width of well is 6 mm, length 10 cm, and the parameters of perforated plate are $\varepsilon = 5\%$, $a=1$ mm, $t=5$ mm, the plate's position in the well is $l_{n1}=9.5$ cm, 6.0 cm, 3.0 cm, and 0.0 cm, respectively. The first resonant frequency changes from 900 Hz to 415 Hz as expected. While this change of about an octave enables the wells to be differently tuned, it will be shown later that this is not a sufficient variation and so some wells without perforations are also needed.

III. ABSORPTION BY A PROFILED ABSORBER

A. Theoretical prediction

Profiled absorbers are periodic surface structures with rigid constructions, which consist of wells separated by thin walls. The wells have the same width, but different depths in one period.

The analysis method used in Ref. 6 is still valid for the structure employing perforated plates in wells. The structure is illustrated in Fig. 2. For the one-dimensional absorber, the sound field in front of the absorber is decomposed into the incident plane wave $p_e(x,z)$ and scattered field $p_s(x,z)$ as follows:

$$p(x,z) = p_e(x,z) + p_s(x,z) \tag{8}$$

and

$$p_e(x,z) = P_e e^{j(-xk_x + zk_z)},$$
$$p_s(x,z) = \sum A_n e^{j(-x\beta_n - z\gamma_n)}, \tag{9}$$

where $k_x = k\sin\theta_e$, $k_z = k\cos\theta_e$, and $\beta_n = k_x + n(2\pi/T)$, $\gamma_n = -jk\sqrt{[\sin\theta_e + n(\lambda/T)]^2 - 1}$, T is the width of one period.

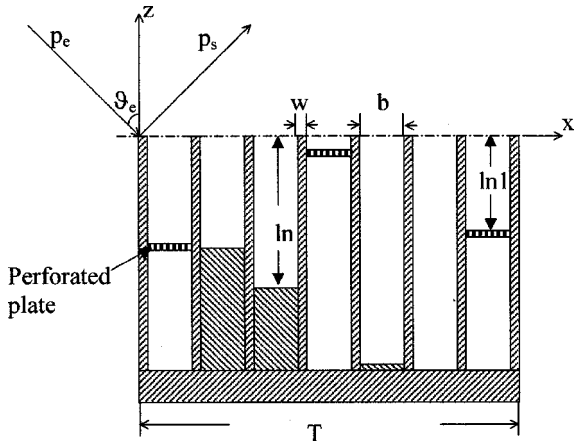

FIG. 2. One period of profiled sound absorber with perforated plates.

The coefficients, A_n, are solved by applying the boundary condition of the periodic impedance on the surface of the absorber.[6] The absorption coefficient of the absorber is then

$$\alpha(\theta_e)=1-\left|\frac{A_0}{P_e}\right|^2-\frac{1}{\cos\theta_e}\times\sum\left|\frac{A_{n_s}}{P_e}\right|^2\sqrt{1-(\sin\theta_e+n_s\lambda/T)^2}. \quad (10)$$

The summation runs over radiating spatial harmonics only.

For normal incident sound and narrow wells, when $\sin\theta_e+\lambda/T\leqslant 1$, there are only first order reflections, therefore the equivalent normalized impedance on the surface of the structure can be derived from

$$z_e=\frac{1+A_0/P_e}{1-A_0/P_e}. \quad (11)$$

B. Experimental result

In order to verify the above prediction model, a one-dimensional sample made from aluminum was built inside an impedance tube which had a cross-section size 54 $\times$54 mm. The parameters of perforated plate are porosity $\varepsilon=5.34\%$, $t=5$ mm, $a=1$ mm. Because of the impedance tube's size, the sample is limited to seven wells in one period, width of well 6 mm, well separator thickness 1 mm. As we will see later, this construction was optimized for a low frequency profiled absorber, which had a resistive layer on the top of the structure to enhance the losses due to coupling between the wells. Here, it was first measured without the resistive layer to validate the prediction model.

The measurement was carried out in an impedance tube. The procedure was the same as in previous paper,[6] which is similar to the two microphone standard technique. It is important to remember that in the theoretical predictions the mirror-image effect caused by impedance tube walls has to be included.

For conciseness, the following abbreviations in the normalized impedance graphs will be adopted throughout this paper. The real part of normalized impedance will be *R*, and the imaginary part *X*. The comparisons between predictions and measurements of absorption and impedance are shown in Fig. 3. Reasonably good agreement can be seen for the imaginary part of impedance and other parameters in the low frequency range. The slightly higher absorption at middle frequency are likely to be due to unavoidable gaps during the construction and installation of sample. The measurement results demonstrated the validation of prediction model for this kind of structure.

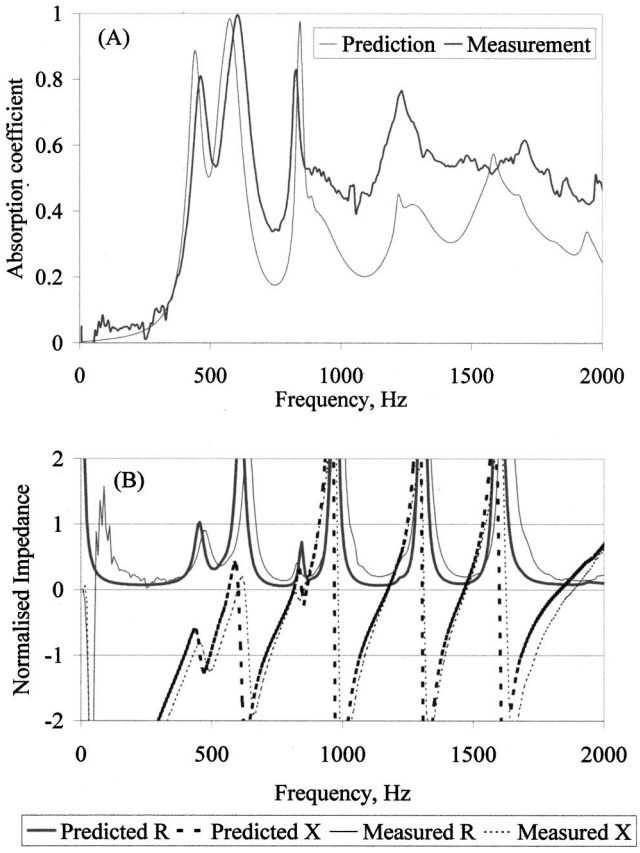

FIG. 3. Comparison of prediction model and experimental results of profiled absorber with perforated plates in some of the wells. (A) Absorption coefficient, (B) impedance.

IV. CONSTANT LENGTH ABSORBER WITH PERFORATED PLATES

With a validated prediction model, it is possible to use a trial and error search on a computer, a numerical optimization, to find the best design. The computer can change the absorption by moving the perforated plate in the wells and so tune the resonant frequency. The computer intelligently searches using a downhill simplex method;[10] the goal being to find the absorber with the highest average absorption. A similar technique was used in Ref. 6.

The absorption coefficient and impedance on the surface of structure combining constant length absorber and perforated plates are calculated for two cases: ''uniform'' construction with the perforated plate on the top of the structure, and ''optimized'' construction with the optimized structure with perforated plates at different positions in each well. The parameters are for constant length absorber, $N=7$ wells in one period, $b=6$ mm, $w=1$ mm, and well length $l_n=10$ cm; for the perforated plate, $\varepsilon=5\%$, $a=1.0$ mm, t

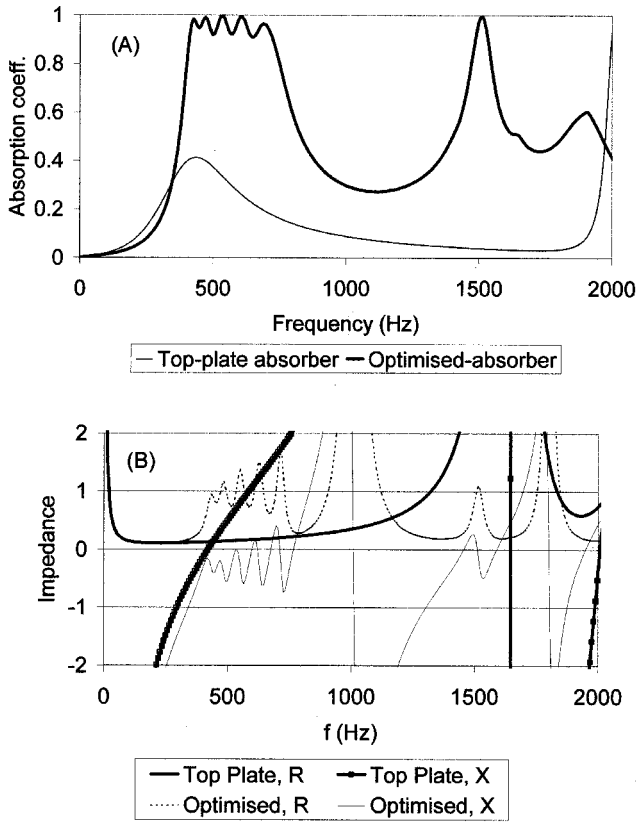

FIG. 4. Comparison between the optimized structure with variable plate position and absorber with plate fixed at the top, (a) absorption coefficient; (b) normalized impedance.

$=5$ mm. The results are shown in Fig. 4, and position sequence l_{n1} of perforated plates for optimized construction are 3.1, 0.1, 0.0, 7.2, 4.9, 6.2, 8.2 cm.

From Fig. 4(a), it is clearly seen that the absorption of the optimized construction is higher than the construction with the perforated plate on the top across the whole frequency range, and particularly at low frequencies, where the absorption coefficients are nearly 1. Even at the first resonant frequency of the uniform construction, where every well has contributed a resonance at that particular frequency, the absorption is still less than the optimized solution. Looking into the impedance graph Fig. 4(b), the optimized structure created a nonuniform surface impedance that scatters sound. The scattering enhances the coupling between the wells, which provides higher resistance when compared with the uniform construction. Although the absorption at low frequency is high in the optimized absorber, elsewhere is low. This is because the first resonant frequencies have been restricted within a small range, which is from the resonant frequency of structure with the perforated plate on the top to it on the bottom, the coupling in that frequency range is strong, elsewhere is poor. This is the problem alluded to before, where the frequency range of a perforated well could be tuned over what was shown to be only about an octave. This indicates that, in order to widen the frequency band, a variable depth sequence is necessary to provide better coupling over the whole frequency range of interest.

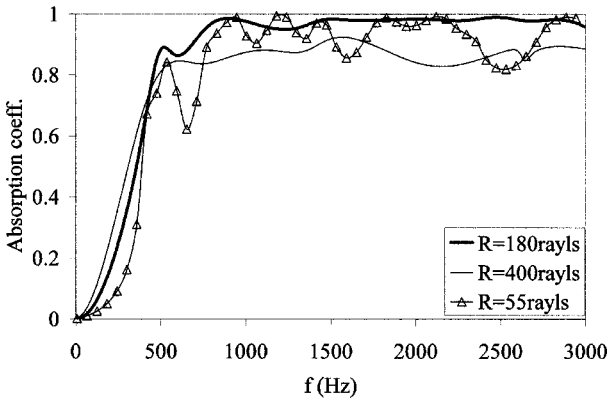

FIG. 5. The effect of the resistivity of the resistive layer on the absorption coefficient of optimized absorbers.

V. WIDEBAND ABSORBER

A. Theoretical discussions

From the investigations of Mechel[4] and the authors,[6] a better absorber can be obtained by properly placing the resonant frequencies across the whole frequency range of interest, and applying a proper resistant layer on the top of the structure. In Sec. IV, high absorption at low frequencies had been obtained, however, the frequency bandwidth was narrow. Changing some wells with constant depth to variable depth can solve this problem. At the higher frequency range, optimizing the depth sequence of variable wells is sufficient to obtain well-distributed resonant frequencies without perforated plates. Moreover, the use of perforated plates may cause strong coupling as is shown in Fig. 4(b), which makes it difficult to get uniform high absorption. Consequently, some variable depth wells with no perforated plates are used. The above discussion shows that, by optimizing the positions of perforated plates in the constant depth wells and the depth sequence of variable depth wells, the well-tuned and well-distributed resonant frequencies can be obtained. Great effort is needed to balance the number of constant wells and the number of variable wells in order to get better coupling at the low frequency range as well as high frequency range.

Again, a resistive layer is necessary to smooth the peaks and troughs seen in Fig. 4(a). The resistivity of the resistive layer must be chosen so that the well absorption is high over a reasonable bandwidth, so that the absorption troughs between resonances are removed. Too large a resistivity value, however, would lead to an overly damped system and the peaks of absorption would be significantly lowered. This is illustrated in Fig. 5, where three absorbers with different resistive layers are compared. Each of these absorbers was optimized numerically for best performance. It can be seen that too little resistance (55 Rayls) leads to an uneven performance, too much resistance (400 Rayls) leads to over damping. 180 Rays performs best, and so is used.

The perforated plate's parameters should be chosen carefully. As was seen in the previous paragraph, there is an optimum range of resistance that a well should offer. Consequently, overly small perforations should be avoided, otherwise additional resistive losses in the perforations is likely to detract from the performance.

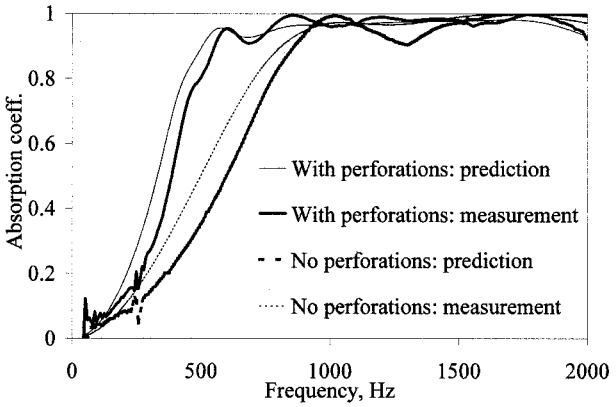

FIG. 6. Comparison of measurement and prediction for two types of absorber.

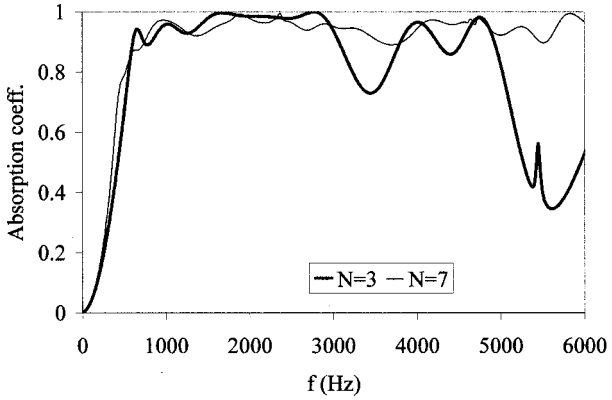

FIG. 7. Optimized absorbers for different number of wells per period *N*.

The other parameters under the control of the designer are the number of wells in a period, and the maximum depth of a well. The maximum depth controls the lowest frequency absorbed and was arbitrarily fixed at 10 cm for this study. For the work that follows, $N=7$ was chosen because it enables direct comparison, both theoretically and experimentally, with previous work. It will be shown later, however, that the number of wells per period can be reduced.

The absorber and perforated plates having the same parameters as the preceding section has been optimized. The number of constant wells with perforated plates is three, which were in wells 1, 4, 7; the number of variable wells without perforated plates is four; the resistant layer used has resistance 180 Rayls. In the range by the optimization process, the length of wells with perforated plates is fixed at 10 cm to guarantee a good performance at low frequencies; the variable depth's length is restricted to a maximum of 10 cm. The performance is optimized up to 3 kHz. The theoretical result is shown in Fig. 6 together with corresponding measurement results. The depth sequence is shown in Table I. Figure 6 also shows the comparison between the new structure and the optimized structure with the same parameters without perforated plates. It clearly shows the high absorption is now achieved at lower frequencies.

The results above also provide some circumstantial evidence as to why poorly constructed diffusers have high absorption,[5] with this high absorption occurring at low frequencies below the design frequency. There is a suggestion that this additional absorption must be due to coupling to air cavities. Hence, this emphasizes the need for well sealed constructions when trying to manufacture phase grating diffusers with low absorption.

B. Experimental verifications

The tests are carried out in the impedance tube, the optimization is repeated to take into account of mirror images, the resistance of the wire-mesh applied is 180 Rayls. The perforated plate is the same as tested in Sec. II B. The optimized structure is shown in Fig. 2.

Figure 6 also compares the prediction and the measurement of the sample and good agreement was found. In addition, the perforated design is compared to an optimized configuration without perforations, details of which are given in Ref. 6. The addition of perforations enables the absorber to start working at a frequency nearly an octave lower than before. This demonstrates the usefulness of this new design in gaining additional low frequency absorption.

C. Number of wells per period, *N*

A series of optimizations were carried to gain an understanding of the importance of the number of wells per period, *N*, to the quality of absorption obtained. Rather surprisingly, it was found that over the bandwidth being considered, up to 3 kHz, that an absorber based on $N=3$ works almost as well as one based on $N=7$. Figure 7 compares the performance for two optimized absorbers. Up to 3 kHz, the performance is comparable, but at a higher frequency, the higher *N* number performs better. This happens because the density of resonances is significantly less for $N=3$ above 3 kHz when compared to $N=7$. Reducing *N* could be useful as it simplifies the design and so may reduce manufacturing costs. Simi-

TABLE I. Some well sequence depths used (cm).

Sequence	l_{n1}	l_n	l_n	l_{n1}	l_n	l_n	l_{n1}
Optimized depth sequence	5.2	5.3	6.9	1	9.5	10	4.8
	l_n	l_n	l_n	l_n	l_n	l_n	l_n
Depths using new design technique, no perforations	10	4.9	3	6	4.2	7.6	3.7
	l_{n1}	l_n	l_{n1}	l_n	l_n	l_{n1}	l_{n1}
Depths using new design technique, with perforations	10	4.8	3.9	8	6.8	1	7

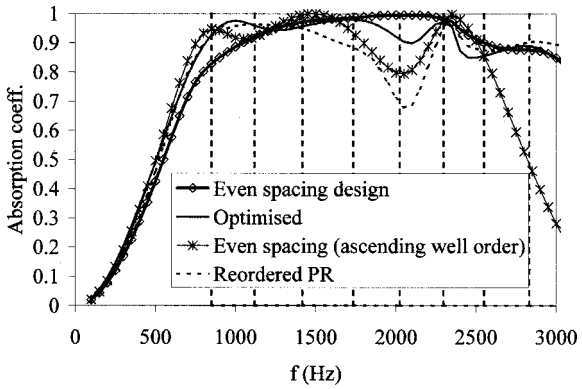

FIG. 8. Performance of four different absorbers without perforations. The vertical lines indicate the location of the well resonances for the even spacing design.

lar results were also found for absorbers without perforations. Incidentally, the choice of the correct value flow resistivity for the resistive layer is even more important for low N absorbers.

VI. SIMPLER DESIGN METHODOLOGY

In previous work, a numerical optimization procedure was used to obtain the depth sequence used. This is a slow and complex procedure. Consequently, a more straightforward design technique is desirable to practitioners. An analogy with Schroeder diffusers can be drawn. While it has been long established that the quadratic residue sequence can be bettered by optimization, for example, Ref. 11, the sequence remains popular because of the ease of using a small number of simple design equations.

A simple design procedure for the absorber will be outlined below, first the case of a profiled absorber with no perforated sheets will be considered as it is simpler, and then it will shown how this can be extended for the absorbers with perforated sheets.

A. Profiled absorber, no perforated sheet

At a first approximation, neglecting viscous boundary layer losses in the well, each well is a quarter wave resonator with resonant frequencies given by

$$f=\frac{(2m+1)c}{4l_n},\quad m=0,1,2,3,\ldots. \tag{12}$$

To maximize the absorption it is necessary to evenly space these resonant frequencies over the design bandwidth avoiding degenerate modes, i.e., modes with similar resonant frequencies. This can be simply achieved by a trial and error process using a calculation tool such as a spreadsheet. Once the depths are determined, it is necessary to order them to maximize the losses due to energy flow between the wells. To achieve this, wells causing adjacent frequency resonances, should not be physically next to each other. This can be done quickly by hand. Table I shows an example depth sequence formed using this procedure.

Figure 8 compares the performance of this design, to one produced using an optimizer.[6] The performance of the absorber using the simpler design procedure is good. As might be expected the optimization gives slightly better results, but that design involved considerably more computation and human effort. The resonance frequencies used during the design are also marked. The drop at high frequencies, >2.5 kHz, occurs due to lack of resonances in the region above 3 kHz. To illustrate that the ordering of the wells is important, the graph also shows the results when the wells are stacked in ascending order. There is considerably less absorption, demonstrating the importance of exploiting the well coupling.

This procedure has similarities to a design approach forwarded by Mechel.[4] He suggested placing adjacent-in-frequency resonant wells physically far apart to maximize coupling. He also suggested using a more even density of resonant modes by using a monotonically increasing well depth, like a ''reordered primitive root sequence.'' This system certainly improves on the quadratic residue sequence, but is not optimum. It is possible to get a more even mode density by a simple trial and error process than found with the reordered primitive root sequence (a linearly increasing depth sequence does not give even modal density). Furthermore ordering the wells in monotonically increasing depth does not maximize the spacing between adjacent resonant modes. Consequently, the new procedure can be seen as a better use and refinement of the principles laid down by Mechel. It also produces better absorbers. The ''reordered primitive root sequence,'' labeled ''reordered PR,'' is shown in Fig. 8. The new procedure produces a better absorber.

B. Profiled absorber with perforated sheets

The design is a little more involved when using perforated sheets. The problem is that the resonance frequencies of the compound wells cannot be predicted using a formula as simple as Eq. (12). Instead the resonances are located from the imaginary part of well entrance impedance, Eq. (5). It is not possible to analytically solve Eq. (5) to gain the resonant frequencies, but a simple numerical method quickly yields the values. (Again, during the design an assumption that the propagation number is not altered by viscous boundary losses is made to simplify the equation.) Then the two design principles are applied (i) the resonances are made as evenly spaced in frequency as possible, and (ii) the energy flow between wells maximized by dispersing wells with adjacent-in-frequency modes.

Figure 9 compares the new design methodology to the optimized depths previously presented. The depth sequence is given in Table I. As expected, the optimizer does slightly better, but the simplified design procedure produces high absorption from less effort.

VII. CONCLUSIONS

The above study has shown the usefulness of perforated sheets in the wells to achieve a more wide band absorption from a profiled construction. The optimized constant depth concept employing perforated plate can produce better absorption than the ordinary absorber with perforated plate fixed at the top of the cavity. However, the frequency band is still narrow. The new optimized structure combined variable

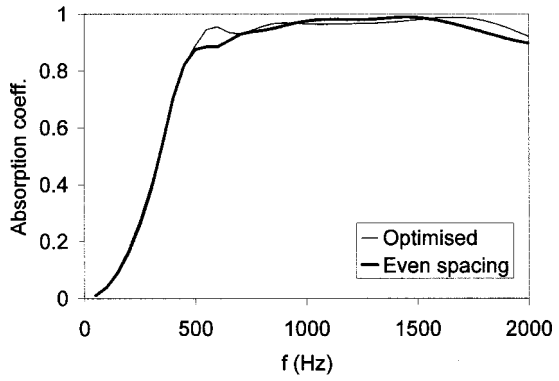

FIG. 9. Two absorbers using perforated plates in some of the wells. The first is designed using numerical optimization, the second by spacing resonances evenly in frequency.

depth sequence and perforated plates extends the absorption to lower frequencies as well maintaining good mid frequency absorption, and hence becomes a considerably better wide band absorber. In addition, a design procedure, which is more straightforward than numerical optimization, was outlined and shown to give high absorption designs.

Incidentally, this new design also does better than more traditional Helmholtz designs, where the perforated sheet and resistive material are at the well entrance. Optimizations were carried out on a series of different Helmholtz absorbers stacked next to each other, but the new design was better. The extra degrees of freedom offered by having a variably positioned perforated sheet in the well seems to be a key ingredient to the good broad band absorption, and the mass term in the traditional Helmholtz design causes problems in achieving broad band absorption as the mass term narrows the resonances. Consequently, an improved absorption structure has been produced and validated.

ACKNOWLEDGMENTS

This work was funded by the Engineering and Physical Sciences Research Council (EPSRC) of Britain, under Grant No. GR/L34396.

[1] P. D'Antonio and T. J. Cox, ''Diffusor application in rooms,'' Appl. Acoust. **60**, 113–143 (2000).
[2] K. Fujiwara and T. Miyajima, ''Absorption characteristics of a practically constructed Schroeder diffuser of quadratic-residue type,'' Appl. Acoust. **35**, 149–152 (1992).
[3] H. Kuttruff, ''Sound absorption by preudostochastic diffusers (Schroeder diffusers),'' Appl. Acoust. **42**, 215–231 (1994).
[4] F. P. Mechel, ''The wide-angle diffuser—A wide-angle absorber?,'' Acustica **81**, 379–401 (1995).
[5] K. Fujiwara and T. Miyajima, ''A study of the sound absorption of a quadratic-residue type diffuser,'' Acustica **81**, 370–378 (1995).
[6] T. Wu, T. J. Cox, and Y. W. Lam, ''From a profiled diffuser to an optimised absorber,'' J. Acoust. Soc. Am. **108**, 643–650 (2000).
[7] K. Fujiwara, K. Nakai, and H. Torihara, ''Visualisation of the sound field around a Schroerer diffuser,'' Appl. Acoust. **60**, 225–236 (2000).
[8] A. W. Guess, ''Result of impedance tube measurements on the acoustic resistance and reactance,'' J. Sound Vib. **40**, 119–137 (1975).
[9] P. M. Morse and K. Ingard, *Theoretical Acoustics* (McGraw-Hill, New York, 1968), Chap. 6, pp. 285–291.
[10] W. H. Press *et al.*, *Numerical Recipes* (Cambridge University Press, Cambridge, 1989), Chap. 10, pp. 289–293.
[11] T. J. Cox, ''Optimization of profiled diffusers,'' J. Acoust. Soc. Am. **97**, 2928–2941 (1995).

An acoustic boundary element method based on energy and intensity variables for prediction of high-frequency broadband sound fields

Linda P. Franzoni, Donald B. Bliss, and Jerry W. Rouse
Mechanical Engineering and Materials Science, Duke University, Durham, North Carolina 27708-0300

(Received 3 November 2000; revised 17 August 2001; accepted 11 September 2001)

A boundary element method is formulated in terms of time-averaged energy and intensity variables. The approach is applicable to high modal density fields but is not restricted to the usual low-absorption, diffuse, and quasiuniform assumptions. A broadband acoustic energy/intensity source is the basic building block for the method. A directivity pattern for the source is derived to account for local spatial correlation effects and to model specular reflections approximately. A distribution of infinitesimal, uncorrelated, directional sources is used to model the boundaries of an enclosure. These sources are discretized in terms of boundary elements. A system of equations results from applying boundary conditions in terms of incident, reflected, and absorbed intensity. The unknown source power for each element is determined from this system of equations. A two-dimensional model problem is used to demonstrate and verify the method. Exact numerical solutions were also obtained for this model problem. The results show that spatially varying mean-square pressure levels are accurately predicted at very low computational cost. © *2001 Acoustical Society of America.* [DOI: 10.1121/1.1416201]

PACS numbers: 43.55.Ka, 43.55.Br [JDQ]

I. INTRODUCTION

The analysis of high-frequency broadband sound fields is of interest in architectural acoustics and in the aircraft and automotive industries, where interior noise prediction and subsequent reduction are important. Numerical methods such as finite element analysis (FEA) or boundary element methods (BEM) are often used, since the geometries involved are not conducive to solution by purely analytical methods. Approximate high-frequency approaches include asymptotic modal analysis[1,2] and statistical energy analysis.[3] In the work to date, asymptotic modal analysis (AMA) has relied on simplifications, such as small damping and modal uncoupling. However, AMA could be modified to include the dominant effects of modal coupling, as described in Ref. 4. The statistical energy analysis method is only valid for lightly damped systems where diffuse field assumptions apply and requires the assignment of coupling loss factors between subsystems, which must be determined empirically. The presence of significant levels of surface absorption makes numerical methods such as FEA or BEM more applicable.

Both traditional finite element and traditional boundary element analyses must be performed on a frequency-by-frequency basis. Therefore, for a broadband calculation many successive FEA or BEM runs must be made at fixed frequency over closely spaced frequencies in a band, and the results combined. Another computationally expensive aspect of the traditional FEA and BEM methods is that the discretization of the sound field (in the case of FEA) or boundary (for BEM) must be done at a resolution of many elements per wavelength. For high-frequency analyses, this level of discretization leads to large systems of equations and large computational cost. The textbooks by Zienkiewicz[5] for FEA, and Brebbia[6] for BEM, are good references for these traditional numerical methods.

Alternative approaches for solving interior noise problems in the high-frequency domain have been developed. Recent work using energy finite elements for solving structural-acoustic problems has shown promising results,[7–9] although an artificial resistive effect must be introduced to relate intensity to energy gradient. In an earlier work, Miles[10] formulated integral equations for a rectangular enclosure with diffusely reflecting boundaries, using a model of Lambertian reflection at the boundaries.

In this paper, a novel boundary element method is described. The infinitesimal sound sources that make up an individual element are considered to be broadband, uncorrelated high-frequency sources. Because of this construct, the sound field can be determined by superposition of mean-square pressures, and the intensity vectors associated with incident and reflected energy from element to element can easily be determined. Unlike classical methods, the element size is large compared to the characteristic acoustic wavelength. The source power associated with each element is found by solving a system of equations that are the imposed boundary conditions on intensity at the control point (node) of each element.

The assumption that the individual infinitesimal sound sources are uncorrelated is valid as long as the wavelengths are short compared to the enclosure dimensions, the sound field contains a range of frequencies, and the damping is not too large. However, comparisons show that even when the damping is fairly large (i.e., the uncorrelated assumption is violated) the method still works quite well.

II. BACKGROUND THEORETICAL DEVELOPMENT

It is insightful to try to recast the governing equations in terms of energy and intensity variables. The linearized mass conservation law is stated as

$$\frac{\partial \rho}{\partial t} + \rho_o \vec{\nabla} \cdot \vec{\mathbf{u}} = 0, \tag{1}$$

where ρ is the acoustic density perturbation, ρ_o is the ambient density, and $\vec{\mathrm{u}}$ is the velocity vector. Conservation of momentum in linear form gives

$$\rho_o \frac{\partial \mathbf{u}}{\partial t} = -\nabla p, \tag{2}$$

where p is the acoustic pressure perturbation. The instantaneous energy density and intensity are defined as

$$\varepsilon = \frac{1}{2}\rho_o u^2 + \frac{1}{2}\frac{p^2}{\rho_o c^2}, \tag{3}$$

$$\mathbf{I} = p\mathbf{u}. \tag{4}$$

Multiplying Eq. (1) by p and Eq. (2) by $\rho_o \mathbf{u}$, assuming an isentropic gas for which $p = \rho c^2$, adding the equations, and regrouping the variables in terms of energy and intensity, results in the well-known governing equation

$$\frac{\partial \varepsilon}{\partial t} + \nabla \cdot \mathbf{I} = 0. \tag{5}$$

A second governing equation is obtained by multiplying Eq. (1) by $\mathbf{u}$ and Eq. (2) by $p/\rho_o c^2$, adding the equations, and regrouping the variables

$$\frac{1}{c^2}\frac{\partial \mathbf{I}}{\partial t} + \frac{1}{2}\rho_o[\mathbf{u}(\nabla \cdot \mathbf{u}) - (\mathbf{u} \cdot \nabla)\mathbf{u}] + \nabla \varepsilon = 0. \tag{6}$$

Time-averaging the above governing equations

$$\nabla \cdot \mathbf{I} = 0 \tag{7}$$

from Eq. (5), and from Eq. (6)

$$\tfrac{1}{2}\rho_o \langle \mathbf{u}(\nabla \cdot \mathbf{u}) - (\mathbf{u} \cdot \nabla)\mathbf{u} \rangle + \nabla E = 0, \tag{8}$$

where E is the time-averaged energy density, and $\mathbf{I}$ is the time-averaged intensity.

Referring to Eq. (8), it can be shown that the time-averaged quantity $\langle \mathbf{u}(\nabla \cdot \mathbf{u}) - (\mathbf{u} \cdot \nabla)\mathbf{u} \rangle$ is identically zero for a one-dimensional sound field, and is equal to zero for higher dimensions if the waves are assumed to be uncorrelated, broadband, random-incidence plane waves. Therefore, the implication of these assumptions is that the gradient of time-averaged energy density would equal zero. It follows that the mean-square pressure must be constant in this sound field. However, for actual enclosures with reflective and absorptive surfaces, this is physically unrealistic. Therefore, either the assumption that the waves are uncorrelated or that they are plane waves must be abandoned.

Consider an enclosure with absorptive and reflective boundaries that contains an acoustic source or sources. It is possible to replicate the interior sound field by replacing the enclosure boundaries with an equivalent continuous distribution of acoustic sources, as shown in Fig. 1. For a broadband

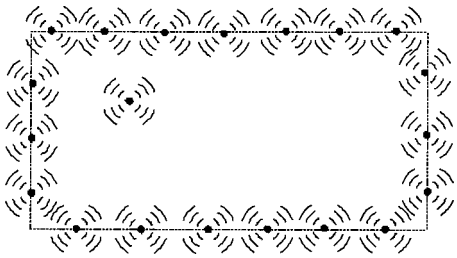

FIG. 1. An enclosure with an interior sound source whose boundaries have been replaced by acoustic sources.

sound field, the distributed sources modeling the enclosure boundary will be correlated only over a short spatial distance, typically less than a wavelength. These locally correlated source regions will radiate spreading waves into the enclosure. The spreading waves from different local regions will be uncorrelated. This reasoning suggests that the appropriate physical model in the high-frequency limit involves a distribution of uncorrelated *spreading waves* radiating from the boundary location. When uncorrelated spreading waves are used in Eq. (8), the time-averaged term involving velocities does not vanish. Then, the gradient of energy, and thus the spatial variation of mean-squre pressure, can be nonzero, which is physically correct. Note that modeling spreading waves with plane waves requires that the plane waves be correlated. Thus, in the physical model the plane-wave assumption is abandoned, and replaced by a distribution of *uncorrelated* sources for *spreading* waves emanating from the location of the enclosure boundary.

A. Uncorrelated mean-square pressure field

The preceding notion of using uncorrelated spreading waves will now be examined more closely by considering oblique waves striking a surface of infinite extent. At high frequencies, with very short wavelengths, this case can be considered to model reflections locally from an actual surface. In addition, a directivity function will be derived to account for the local (within a wavelength) spatial correlation.

Consider an oblique plane pressure wave of magnitude P_i, having frequency ω and wave number $k = \omega/c$, which is incident upon a surface at an angle θ. At any point in the wave field above the surface (see Fig. 2), the incident pressure p_i is described by

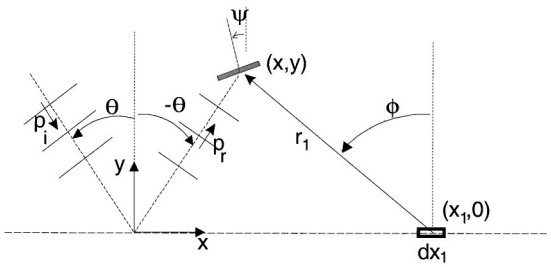

FIG. 2. Incident and reflected pressure waves, a surface in the field at point (x,y), and an infinitesimal segment of the boundary at point $(x_1,0)$ corresponding to a source.

$$p_i = P_i(k,\theta)e^{i(\omega t - kx\sin\theta - ky\cos\theta)}. \quad (9)$$

There is also a reflected wave of amplitude P_r, where

$$p_r = P_r(k,\theta)e^{i(\omega t - kx\sin\theta + ky\cos\theta)}. \quad (10)$$

The magnitudes of the two waves are related by

$$P_r(k,\theta) = R(k,\theta)P_i(k,\theta), \quad (11)$$

where $R(k,\theta)$ is a complex reflection coefficient. For an impedance boundary, the complex reflection coefficient is

$$R(k,\theta) = |R|e^{i\phi R}\frac{z_b(k)\cos\theta - \rho c}{z_b(k)\cos\theta + \rho c}. \quad (12)$$

The intensity reflection coefficient is given by

$$R_I(k,\theta) = R(k,\theta)R^*(k,\theta), \quad (13)$$

where R^* is the complex conjugate of R. The pressure is the sum of the incident and reflected pressures

$$p_c = p_i + p_r = P_i(k,\theta)(e^{iky\cos\theta} + R(k,\theta)e^{-iky\cos\theta}) \times e^{i(\omega t - kx\sin\theta)}, \quad (14)$$

where the subscript "c" is used to mean the complete or composite pressure. The mean-square pressure is

$$\overline{p_c^2} = p_c p_c^*/2 = \overline{p_i^2} + \overline{p_i^2}R_I + \overline{p_i^2}2|R|\cos(2ky\cos\theta - \varphi_R). \quad (15)$$

Now assume the oblique waves at each angle are broadband in a frequency band $\omega_l < \omega < \omega_u$; thus, $k_l < k < k_u$, where $k_l = k_c - \Delta k/2$ and $k_u = k_c + \Delta k/2$, for the arithmetic center frequency $k_c = (k_l + k_u)/2$. Further, assume waves at each angle are uncorrelated from waves at every other angle. Interpreting $\overline{p_i^2} = \overline{P_i^2}(k,\theta)dk\,d\theta$ (where $\overline{P_i^2}$ is a density of mean-square pressure per angle and frequency), the total mean-square pressure at a point above the surface is

$$\begin{aligned}\overline{p_{\text{tot}}^2} &= \int_{-\pi/2}^{+\pi/2}\int_{k_l}^{k_u}\overline{P_i^2}(k,\theta)[1 + R_I(k,\theta) \\ &\quad + 2\sqrt{R_I(k,\theta)}\cos(2ky\cos\theta - \varphi_R(k,\theta))]dk\,d\theta \\ &= \int_{-\pi/2}^{+\pi/2}[1 + R_I]\overline{P_i^2}|_{k_c}\Delta k(1 + O[\Delta k/2k_c]^2)d\theta \\ &\quad + \int_{-\pi/2}^{+\pi/2}\int_{k_l}^{k_u}\overline{P_i^2}(k,\theta)[2\sqrt{R_I(k,\theta)}\cos(2ky\cos\theta \\ &\quad - \varphi_R(k,\theta))]dk\,d\theta, \end{aligned} \quad (16)$$

where the slowly varying frequency-dependent terms have been expanded in a Taylor series about the center frequency.

With increasing distance above the surface, the last double integral of Eq. (16) vanishes rapidly and asymptotically, and is typically negligible for $y \geqslant \lambda$. For values of y beyond this region the mean-square pressure is uniform. For values of y nearer the surface, this term accounts for a mathematical boundary layer in which correlation between incident and reflected waves is important.[11,12] For instance, if the reflecting surface is rigid, the incident and reflected waves are in-phase at the wall, and the averaged mean-square pressure doubles within this "intensification zone." If the surface is absorbing, the levels in the correlation layer may be even lower than the uniform interior values. At high frequency, the thickness of the correlation boundary layer is very small.

The reflected pressure is given by

$$\overline{p_r^2} = \int_{-\pi/2}^{+\pi/2}R_I(k_c,\theta)\overline{P_i^2}(k_c,\theta)\Delta k\,d\theta. \quad (17)$$

Therefore, at locations beyond the correlation layer, the mean-square pressures are uniform, and the incident and reflected pressures are uncorrelated. The total mean-square pressure is the sum of the total incident and total reflected mean-square pressures.

$$\overline{p_{\text{total}}^2} = \overline{p_{\text{total}_{\text{incident}}}^2} + \overline{p_{\text{total}_{\text{reflected}}}^2}. \quad (18)$$

The reflected intensity components can be calculated in a similarly straightforward manner beyond the correlation boundary layer. For instance, the vertical component of time-averaged reflected intensity is given by

$$\mathbf{I}_{y_{\text{ref}}} = \mathbf{j}\int_{-\pi/2}^{+\pi/2}R_I(k_c,\theta)\cos\theta\frac{\overline{P_i^2}(k_c,\theta)}{\rho_o c}\Delta k\,d\theta. \quad (19)$$

B. Mean-square pressure sources with directivity

Reconsider the preceding problem formulation and replace the absorbing wall with a distribution of acoustic sources that produces the same reflected field. The normal velocity at the wall associated with the reflected wave field is given by

$$\begin{aligned} v_r(x,0)e^{i\omega t} &= \frac{p_r(x,0)}{\rho_o c}\cos\theta \\ &= \frac{R(k,\theta)P_i(k,\theta)}{\rho_o c}\cos\theta e^{i(\omega t - kx\sin\theta)}. \end{aligned} \quad (20)$$

Knowing the normal velocity at the wall, the reflected pressure field can be rewritten as an integral of the Green's function over the vibrating 2D surface. In the present case, this Green's function is the two-dimensional free-field acoustic monopole, namely

$$p_G = \frac{\rho_o ckQ}{4}H_0^{(2)}(kr)e^{i\omega t} \approx \frac{\rho_o ckQ}{2}\frac{e^{i(\omega t - kr - \pi/4)}}{\sqrt{2\pi kr}}, \quad (21)$$

where Q is the volumetric source strength. The asymptotic form for the Hankel function is appropriate when $r > \lambda$, typically beyond the correlation boundary layer. For a baffled point source on the surface, $dQ = 2v_r(x_1,0)dx_1$, where the factor of 2 accounts for the fact that the source distribution radiates both above and below the surface. The pressure contribution from a point on the surface is

$$dp = \rho_o c\frac{kv_r(x_1,0)dx_1}{\sqrt{2\pi kr_1}}e^{i(\omega t - kr_1 - \pi/4)}, \quad (22)$$

where $r_1 = \sqrt{(x - x_1)^2 + y^2}$ is the distance from the source to the point of evaluation (x,y); see Fig. 2.

The pressure due to contributions from the entire surface, for one frequency and one incidence angle, is given by

$$p_r = \int_{-\infty}^{+\infty} \frac{kR(k,\theta)P_i(k,\theta)\cos\theta}{\sqrt{2\pi kr_1}} e^{i(\omega t - kr_1 - kx_1 \sin\theta - \pi/4)} dx_1, \tag{23}$$

and the complex conjugate is

$$p_r^\star = \int_{-\infty}^{+\infty} \frac{kR\star(k,\theta)P_i^\star(k,\theta)\cos\theta}{\sqrt{2\pi kr_2}} \times e^{-i(\omega t - kr_2 - kx_2 \sin\theta - \pi/4)} dx_2, \tag{24}$$

where $r_2 = \sqrt{(x-x_2)^2 + y^2}$. The reflected mean-square pressure at a single frequency and incidence angle is

$$\overline{p_r^2}(k,\theta) = \frac{p_r p_r^\star}{2} = \int_{-\infty}^{+\infty}\int_{-\infty}^{+\infty} \frac{kR_I(k,\theta)|P_i(k,\theta)|^2 \cos^2\theta}{4\pi\sqrt{r_1 r_2}} \times e^{ik(r_2 - r_1 + (x_2 - x_1)\sin\theta)} dx_2\, dx_1. \tag{25}$$

To obtain the total reflected mean-square pressure, the above equation must be integrated over all incidence angles and over the frequency band. The resulting multiple integration can be expressed as

$$\overline{p_r^2} = \int_{-\infty}^{+\infty} \frac{1}{2\pi r_1} \left[\int_{-\infty}^{+\infty} \left(1 - 2\xi \frac{(x-x_1)}{r_1^2} + \frac{\xi^2}{r_1^2} \right)^{-1/4} \times \int_{-\pi/2}^{+\pi/2} \int_{k_l}^{k_u} kR_I \overline{P_i^2} \cos^2\theta e^{ik(r_2 - r_1 + \xi\sin\theta)} \times dk\, d\theta\, d\xi \right] dx_1, \tag{26}$$

where the variable $\xi = x_2 - x_1$ has been introduced. Outside the correlation boundary layer, namely for $y > \lambda$, the triple integral in square brackets can be shown to take on a relatively simple form dependent on $(x - x_1)$, y, and the properties of the product $R_I \overline{P_i^2}$. The triple integrand is evaluated in the following section by an indirect method. There is a fairly simple and interesting physical interpretation of this outcome, as explained below.

It will be demonstrated that the simplified integral based on Eq. (26) can be expressed in the following form:

$$\overline{p_r^2} = \int_{-\infty}^{+\infty} \frac{1}{2\pi r_1} \rho_o c w D(\phi_1) dx_1, \tag{27}$$

where w is twice the reflected power per unit length of surface (namely, twice the normal component of reflected intensity of the surface) and $D(\phi_1)$ is a directivity function, with angle ϕ_1 measured from the surface normal. The factor of 2 in power is due to the fact that half of the power radiates above the surface and half radiates below the surface.

Essentially, the integrand Eq. (27) is an energy/intensity source which can also be viewed as a type of Green's function. A single source of power output W would produce pressure and intensity

$$\overline{p_G^2} = \frac{\rho_o c W}{2\pi r} D(\phi), \tag{28}$$

$$\mathbf{I}_G = \frac{W}{2\pi r} D(\phi) \mathbf{e}_\phi, \tag{29}$$

where the directivity must satisfy the constraint

$$\int_{-\pi}^{+\pi} D(\phi) d\phi = 2\pi, \tag{30}$$

to conserve energy.

For an isolated 2D monopole of the form of Eq. (21), Eq. (28) and (29) would be the appropriate expressions for the far-field mean-square pressure and time-averaged intensity if $D(\phi) = 1$. However, when the sources are distributed along the surface, the directivity function is not unity for two reasons. First, there is a degree of local correlation (over distances $< \lambda$) between adjacent sources along the surface that introduces a directivity effect. Second, energy does not approach the surface uniformly from all directions, and the reflection coefficient depends on angle, so the resulting specularly reflected field has directional characteristics. The directivity function $D(\phi)$ must be derived to account for all these effects. This derivation is most easily done by the indirect approach of the next section, rather than by a direct evaluation of the multiple integral in square brackets in Eq. (26). In any event, the important conclusion is as follows: a reflecting surface in a high-frquency broadband sound field can be modeled by a distribution of uncorrelated directional energy/intensity sources on the surface.

C. Determination of the directivity function

The acoustic intensity into a surface oriented at an angle ψ from the vertical, as shown in Fig. 2, will be calculated two ways: (1) by adding the contribution of waves reflected from the boundary at all angles, and (2) by assuming the boundary is comprised of a continuous distribution of directional sources and summing the contributions from all sources. These two resulting intensity integrations are then compared, and the directivity function is deduced.

Following the development leading up to Eq. (19) and referring to Fig. 2, the intensity normal to the surface at ψ-orientation is given by

$$I_\psi = \int_{-\pi/2}^{+\pi/2} \frac{R_I(k_c,\theta)\overline{P_i^2}(k_c,\theta)\Delta k}{\rho_o c} \cos(\psi + \theta) d\theta, \tag{31}$$

where R_I is the intensity reflection coefficient of the surface, and the integration is over all incidence/reflection angles.

Referring to the development of Eqs. (27), (28), and (29), and again to Fig. 2, the incremental intensity component normal to the ψ-oriented surface from a source with directivity $D(\phi)$ is

$$dI_\psi = \frac{w dx_1}{2\pi r_1} D(\phi) \mathbf{e}_{r_1} \cdot \mathbf{e}_\psi. \tag{32}$$

Integrating over all sources

$$I_\psi = \int_{-\pi/2}^{+\pi/2} \frac{w}{2\pi} \frac{D(\phi)}{\cos\phi} \cos(\psi-\phi)\, d\phi, \tag{33}$$

where the geometrical relations: $(x_1 - x) = y \tan\phi$ and $r_1 \cos\phi = y$ have been used to change an integral over $-\infty < x_1 < \infty$ into an integral over $-\pi/2 < \phi < \pi/2$.

By comparison, substituting $-\theta$ for ϕ in Eq. (33), and eliminating the common terms between Eqs. (33) and (31)

$$\frac{R_I(k_c,\theta)\overline{P_i^2}(k_c,\theta)\Delta k}{\rho_o c} = \frac{w}{2\pi} \frac{D(-\theta)}{\cos\theta}. \tag{34}$$

Therefore, the undetermined portion of the integrand in Eq. (27) is found to be

$$\rho_o c w D(\phi_1) = 2\pi \cos\phi_1 R_I(k_c, -\phi_1)\overline{P_i^2}(k_c, -\phi_1)\Delta k. \tag{35}$$

In this expression the presence of $\cos(\phi_1)$ accounts for the local correlation between sources; this factor is present even when modeling reflections of a perfectly diffuse field from a rigid surface. The remaining functions of angle are due to specular reflection effects and due to the dependence of reflection coefficient on angle.

The function $R_I(k_c,\theta)\overline{P_i^2}(k_c,\theta)\Delta k$ can be expanded in a Fourier series, such that

$$R_I(k_c,\theta)\overline{P_i^2}(k_c,\theta)\Delta k = \sum_n \left[A_n \cos n\theta + B_n \sin n\theta\right]. \tag{36}$$

Substituting this result into Eq. (34), and letting $\theta = -\phi$

$$\frac{\rho_o c w}{2\pi} D(\phi) = \cos\phi \sum_n \left(A_n \cos n\phi - B_n \sin n\phi\right). \tag{37}$$

In the implementation of the boundary element method described later in the paper, only the first few terms of the Fourier series are retained. The Fourier coefficients are estimated from the normal and tangential components of intensity falling on a control point (boundary element node), as will be explained later.

III. INTEGRAL EQUATIONS

A. Steady state

Consider a two-dimensional acoustic enclosure whose boundary is described by the surface S. Physically, the boundary may consist of some rigid surfaces and surfaces that are flexible and/or absorptive. The sound field in the interior is assumed to be high frequency (small wavelengths relative to enclosure dimensions) and broadband.

To calculate the steady-state mean-square pressure levels in the interior using the energy boundary element method, the following formulation is employed. The enclosure boundary is replaced by a continuous distribution of uncorrelated, broadband, infinitesimal energy/intensity sources of strength dW/dS (power per length) and directivity $D(\theta_1)$ which may vary along the boundary contour. A single infinitesimal source, located by the vector $\mathbf{r}_1$ (see Fig. 3) produces an incremental intensity **dI** at a point on the boundary (located by $\mathbf{r}_s$), where **dI** is given by

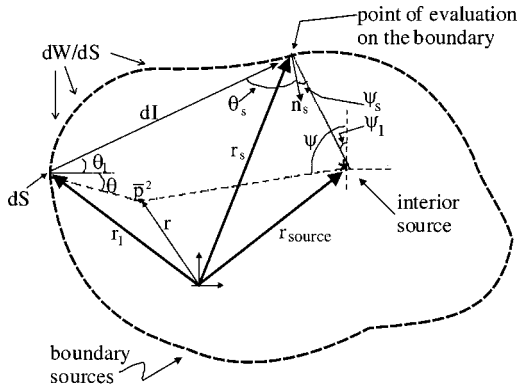

FIG. 3. An acoustic enclosure described by a continuous distribution of infinitesimal uncorrelated broadband sources of strength *dW/dS*.

$$\mathbf{dI}(\mathbf{r}_s) = \frac{(dW/dS)(\mathbf{r}_1) D(\theta_1)}{2\pi|\mathbf{r}_s - \mathbf{r}_1|} \cdot \frac{(\mathbf{r}_s - \mathbf{r}_1)}{|\mathbf{r}_s - \mathbf{r}_1|} dS, \tag{38}$$

where $D(\theta_1)$ is the directivity of the infinitesimal source in the direction of the point at which the intensity is calculated, and dS is an incremental surface area. The incident intensity at the point of evaluation on the boundary is given by the integral over all the incremental intensities that contribute at that point.

$$\mathbf{I}(\mathbf{r}_s) = \oint_S d\mathbf{I}(\mathbf{r}_s). \tag{39}$$

The intensity that is *reflected* from the point, $\mathbf{I}_R(\mathbf{r}_s)$, depends upon the absorptive properties of the boundary, and can be written in terms of the oblique incidence intensity reflection coefficient, $R_I(\theta_s)$ at that point, and the normal component of intensity. (The tangential component of intensity does not contribute to reflection back into the interior, although it does play a role in determining the directivity function.) The normal component of reflected intensity is then given by

$$\mathbf{n}_s \cdot \mathbf{I}_R(\mathbf{r}_s) = \oint_S R_I(\theta_s)\mathbf{n}_s \cdot d\mathbf{I}(\mathbf{r}_s), \tag{40}$$

where $\mathbf{n}_s(\mathbf{r}_s)$ is the unit normal into the enclosure from the boundary at the point $\mathbf{r}_s$. The incremental power that is emitted from a point on the surface is equal to $(dW/dS)(\mathbf{r}_s)dS$. In other words, the incremental intensity emitted from the point located at $\mathbf{r}_s$ is equal to $(dW/dS)(\mathbf{r}_s)$.

The intensity emitted from the point on the boundary must be equal to that reflected due to the incoming intensity vectors interacting with the boundary. In addition to the intensity contributed by the distribution of sources at the boundary, interior broadband high-frequency sources must also be taken into account. The intensity due to an internal source located at $\mathbf{r}_{\text{source}}$ is given by:

$$\mathbf{I}_{\text{source}}(\mathbf{r}_s) = \frac{W_{\text{source}} D_{\text{source}}(\psi_1)}{2\pi|\mathbf{r}_s - \mathbf{r}_{\text{source}}|} \cdot \frac{(\mathbf{r}_s - \mathbf{r}_{\text{source}})}{|\mathbf{r}_s - \mathbf{r}_{\text{source}}|}, \tag{41}$$

where $D_{\text{source}}(\psi_1)$ is the directivity associated with the source in the direction of ψ_1 (the angle made between the source and the point of evaluation).

Applying conservation of energy at the point $\mathbf{r}_s$ leads to the boundary condition integral equation

$$\frac{dW}{dS}(\mathbf{r}_s)=R_I(\psi_s)\mathbf{n}_s(\mathbf{r}_s)\cdot\mathbf{I}_{\text{source}}(\mathbf{r}_s)+\oint_S R_I(\theta_s)\mathbf{n}_s(\mathbf{r}_s)\cdot d\mathbf{I}(\mathbf{r}_s). \tag{42}$$

In the presence of multiple interior sources, the first term on the right-hand side would be a summation over all sources. The boundary is then discretized into boundary elements. In the present approach, each element is assumed to have constant strength, dW/dS. The discretized version of the above boundary condition equation is applied at the control point (midpoint) of each element, resulting in a system of equations for the unknown source strengths (dW/dS).

To calculate the mean-square presssure at a point in the interior (located by $\mathbf{r}$ in Fig. 3), the contribution of all boundary infinitesimal sources plus that of the interior sources must be added. Therefore, the mean-square pressure is given by

$$\overline{p^2}(\mathbf{r})=\oint_S \rho_o c\frac{dW}{dS}(\mathbf{r}_1)\frac{D(\theta)}{2\pi|\mathbf{r}-\mathbf{r}_1|}dS + \sum_{\substack{\text{interior}\\ \text{sources}}}\rho_o c W(\mathbf{r}_s)\frac{D_s(\psi)}{2\pi|\mathbf{r}-\mathbf{r}_{\text{source}}|}. \tag{43}$$

B. Unsteady case

For the time-dependent problem, the above formulation is modified. It is assumed that the time rate of change of source strength is slow compared to both the characteristic oscillation period and the characteristic transit time for waves across the enclosure. The intensity contribution from the time-dependent internal source $W_{\text{source}}(t)$ to the point of evaluation on the boundary is

$$\mathbf{I}_{\text{source}}(\mathbf{r}_s,t)=\frac{W_{\text{source}}\left(t-\frac{\tilde{r}}{c}\right)D_{\text{source}}(\psi_1)}{2\pi|\mathbf{r}_s-\mathbf{r}_{\text{source}}|}\cdot\frac{(\mathbf{r}_s-\mathbf{r}_{\text{source}})}{|\mathbf{r}_s-\mathbf{r}_{\text{source}}|}, \tag{44}$$

where $\tilde{r}$ is the distance from the source to the point of evaluation on the surface, namely

$$\tilde{r}=|\mathbf{r}_s-\mathbf{r}_{\text{source}}|. \tag{45}$$

Expanding the function that describes the source in a Taylor series about the point $\tilde{r}=0$

$$W_{\text{source}}\left(t-\frac{\tilde{r}}{c}\right)=W_{\text{source}}\left(t-\frac{\tilde{r}}{c}\right)\Big|_{\tilde{r}=0} + \frac{d}{d(t-\tilde{r}/c)}W_{\text{source}}\left(t-\frac{\tilde{r}}{c}\right)\Big|_{\tilde{r}=0}\times\frac{\partial(t-\tilde{r}/c)}{\partial\tilde{r}}(\tilde{r}-0)+\cdots. \tag{46}$$

Abbreviating W_{source} by W_s the above can be rewritten as

$$W_s(t-\tilde{r}/c)\approx W_s(t)+W_s'|_{\tilde{r}=0}(-\tilde{r}/c). \tag{47}$$

Then, noting that $W_s'|_{\tilde{r}=0}=\dot{W}_s(t)$, the time-dependent intensity contribution from the source is

$$\mathbf{I}_{\text{source}}(\mathbf{r}_s,t)\approx\frac{W_s(t)D_{\text{source}}(\psi_1)(\mathbf{r}_s-\mathbf{r}_{\text{source}})}{2\pi\tilde{r}^2} - \frac{1}{c}\frac{\dot{W}_s(t)D_{\text{source}}(\psi_1)(\mathbf{r}_s-\mathbf{r}_{\text{source}})}{2\pi\tilde{r}}. \tag{48}$$

Similarly, the time-dependent intensity from the boundary sources is

$$d\mathbf{I}(\mathbf{r}_s,t)\approx\frac{\left[\frac{dW}{dS}(\mathbf{r}_1,t)-\frac{|\mathbf{r}_s-\mathbf{r}_1|}{c}\frac{d\dot{W}}{dS}(\mathbf{r}_1,t)\right]D(\theta_1)}{2\pi|\mathbf{r}_s-\mathbf{r}_1|}\cdot\frac{(\mathbf{r}_s-\mathbf{r}_1)}{|\mathbf{r}_s-\mathbf{r}_1|}dS. \tag{49}$$

The normal component of the intensity contributes to the intensity reflected into the enclosure, and is calculated as before using Eq. (40). From conservation of energy at a point on the boundary, the time-dependent boundary condition becomes the following integral equation:

$$\frac{dW}{dS}(\mathbf{r}_s,t)=R_I(\psi_s)\frac{W_s(t)D_{\text{source}}(\psi_1)(\mathbf{r}_s-\mathbf{r}_{\text{source}})}{2\pi\tilde{r}^2}\cdot\mathbf{n}_s(\mathbf{r}_s) - R_I(\psi_s)\frac{\dot{W}_s(t)D_{\text{source}}(\psi_1)(\mathbf{r}_s-\mathbf{r}_{\text{source}})}{2\pi\tilde{r}c}\cdot\mathbf{n}_s(\mathbf{r}_s) + \oint_S R_I(\theta_s)\frac{\frac{dW}{dS}(\mathbf{r}_1,t)D(\theta_1)(\mathbf{r}_s-\mathbf{r}_1)}{2\pi|\mathbf{r}_s-\mathbf{r}_1|^2}\cdot\mathbf{n}_s(\mathbf{r}_s)dS - \oint_S R_I(\theta_s)\times\frac{\frac{d\dot{W}}{dS}(\mathbf{r}_1,t)D(\theta_1)(\mathbf{r}_s-\mathbf{r}_1)}{2\pi|\mathbf{r}_s-\mathbf{r}_1|c}\cdot\mathbf{n}_s(\mathbf{r}_s)dS. \tag{50}$$

This equation can be discretized over the boundary. The equation is applied at the control point of each boundary element, leading to a system of time-dependent equations, for the time-varying source strengths $dW(t)/dS$. Here, only one interior source is represented in the equation. For multiple sources, the first two terms would be inside a summation over all interior sources.

To calculate the mean-square pressures in the unsteady case, once the time-dependent source strengths are known, is straightforward. The contributions from the sources are integrated, as in the steady case, but a time shift must be included. The mean-square pressure at a point in the interior is given by

$$\overline{p^2}(\mathbf{r},t)=\rho_o c\frac{W_s(\mathbf{r}_{\text{source}},t)D_{\text{source}}(\psi)}{2\pi|\mathbf{r}-\mathbf{r}_{\text{source}}|}$$
$$-\rho_o c\frac{\dot{W}_s(\mathbf{r}_{\text{source}},t)D_{\text{source}}(\psi)}{2\pi|\mathbf{r}-\mathbf{r}_{\text{source}}|c}$$
$$+\oint_S \rho_o c\frac{dW}{dS}(\mathbf{r}_1,t)\frac{D(\mathbf{r}_1,\theta_1)}{2\pi|\mathbf{r}_s-\mathbf{r}_1|}dS$$
$$-\oint_S \rho_o c\frac{d\dot{W}}{dS}(\mathbf{r}_1,t)\frac{D(\mathbf{r}_1,\theta_1)}{2\pi|\mathbf{r}_s-\mathbf{r}_1|c}dS. \tag{51}$$

IV. DISCRETIZATION

A generic boundary element is shown in Fig. 4. A local coordinate system (subscript lc) is defined on the element, with its origin at the center of the element. The source power per unit length of the element is given by $w=W_E/l_E$, since constant strength elements have been used in the present study.

Using the differential forms of Eqs. (28) and (29), and integrating the contribution of the distributed sources, the mean-square pressure and acoustic intensity at a point of evaluation $(a_{\text{lc}},b_{\text{lc}})$ in the local coordinate system are given by

$$\overline{p^2}(a_{\text{lc}},b_{\text{lc}})=\int_{-l_E/2}^{+l_E/2}\frac{1}{2\pi r_1}\frac{\rho_0 c W_E}{l_E}D(\phi)dx_1$$
$$=\frac{\rho_0 c W_E}{2\pi l_E}\int_{\phi_{\text{lwr}}}^{\phi_{\text{upr}}}D(\phi)\sec(\phi)d\phi, \tag{52}$$

$$\mathbf{I}(a_{\text{lc}},b_{\text{lc}})=\int_{-l_E/2}^{+l_E/2}\frac{W_E}{2\pi r_1 l_E}D(\phi)\mathbf{e}_r(\phi)dx_1$$
$$=\frac{W_E}{2\pi l_E}\left(-\hat{\mathbf{i}}_{\text{lc}}\int_{\phi_{\text{lwr}}}^{\phi_{\text{upr}}}D(\phi)\tan\phi\,d\phi\right.$$
$$\left.+\hat{\mathbf{j}}_{\text{lc}}\int_{\phi_{\text{lwr}}}^{\phi_{\text{upr}}}D(\phi)d\phi\right), \tag{53}$$

where the lower and upper limits of integration corresponding to the endpoints of the element are:

$$\phi_{\text{lwr}}=\arctan\left(\left(\frac{-l_E}{2}-a_{\text{lc}}\right)\Big/\ b_{\text{lc}}\right),$$
$$\phi_{\text{upr}}=\arctan\left(\left(\frac{l_E}{2}-a_{\text{lc}}\right)\Big/\ b_{\text{lc}}\right). \tag{54}$$

The point of evaluation $(a_{\text{lc}},b_{\text{lc}})$ corresponds to a control point (node) of another boundary element or a point in the interior of the enclosure. Equation (53) is used to calculate intensity, from which the component normal to the receiving element is determined and the amount reflected due to this incoming intensity is calculated. This calculation is repeated to account for every element's intensity on every other element.

To calculate the intensity at the control point (center) of the element due to the distribution of sources along the element, Eq. (53) is applied in the limit as $(a_{\text{lc}},b_{\text{lc}})$ approaches the origin. The resulting normal intensity out of the element, designated $\mathbf{I}_{\text{cp}}$, is

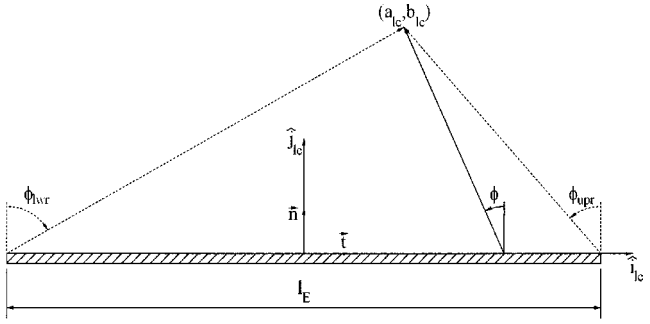

FIG. 4. A generic boundary element.

$$\mathbf{I}_{\text{cp}}=\frac{W_E}{2l_E}\hat{\mathbf{j}}_{\text{lc}}. \tag{55}$$

Equations (53) and (55) are used in the discretized boundary condition. In steady state, the discretized boundary condition resulting from Eq. (42) is

$$\mathbf{n}_i\cdot\mathbf{I}_{\text{cp}_{i_{\text{gc}}}}=-\sum_{j=1,j\neq i}^{m}(\mathbf{n}_i\cdot\mathbf{I}_{i,j\text{gc}})R_{i,j}(\overline{z_i},\theta_{i,j})$$
$$-\sum_{s=1}^{m_s}(\mathbf{n}_i\cdot\mathbf{I}_{i,s\text{gc}})R_{i,s}(\overline{z_i},\theta_{i,s}), \tag{56}$$

where $\overline{z_i}$ is the normalized acoustic inpedance and the negative signs account for the fact that the unit normals point *out* of the element where the boundary condition is applied, but the intensity vectors point *into* the element at the control point. The subscript gc is used to indicate that this condition is applied in the global coordinate system rather than the local (lc) coordinate system. Equation (56) applies to the ith element, and the summation over the index s represents the contribution of reflected intensity from the ith element due to multiple sources that may be in the interior.

V. SPECULAR REFLECTIONS

Applying Eq. (56), the discretized boundary condition equation at each control point yields a system of equations for the unknown source strengths of each element. The directivity function is not known, but is initially assumed to correspond to a single term in the Fourier series expansion [Eq. (37)], i.e., a simple cosine (which accounts for the local spatial correlation of neighboring sources). The resulting system of equations is solved at this order, and the elemental source powers are determined.

Next, a higher-order form of the directivity function is assumed [from Eq. (37)] and the results of the previous calculation are used to determine the unknown Fourier coefficients in terms of ratios of intensity components. Using this higher-order directivity function, the system of equations is redefined and elemental source powers are solved. This pro-

cedure is repeated iteratively until the resulting elemental source powers converge to within a percent (in practice, a few iterations are needed).

For the present numerical implementation, the higher-order directivity function is assumed to have the truncated form

$$D(\phi)=\cos\phi[f_0+f_1\cos\phi+f_2\sin\phi], \tag{57}$$

where the coefficients f_0, f_1, and f_2 are to be determined from properties of the previously computed sound field, and thereby include some effects of specular reflection. Two equations are determined from the ratios of normal to tangential components of intensity (two tangential components) and a third equation comes from applying conservation of energy.

Conservation of energy dictates that

$$\pi=\int_{-\pi/2}^{\pi/2} D(\phi)\,d\phi. \tag{58}$$

For the lowest-order directivity function, only one term in Eq. (55) is retained, $D(\phi)=f_0\cos\phi$, and from Eq. (58), the lowest-order solution for directivity is therefore

$$D(\phi)=\pi/2\cos\phi. \tag{59}$$

To compute the normal **j** component of intensity, Eq. (19) and Eq. (34) are used, such that

$$\mathbf{I}_n=\mathbf{j}\frac{w}{2\pi}\int_{-\pi/2}^{+\pi/2} D(\phi)\,d\phi. \tag{60}$$

Invoking conservation of energy [Eq. (58)]

$$I_n=\frac{w}{2}. \tag{61}$$

The **i** (tangential) component of intensity can be divided into two halves, that from the right $(-\phi)$ and that from the left $(+\phi)$. These two components of tangential intensity, in terms of the unknown directivity function, are

$$I_{tr}=-\frac{w}{2\pi}\int_{-\pi/2}^{0} D(\phi)\tan\phi\,d\phi, \tag{62}$$

$$I_{tl}=-\frac{w}{2\pi}\int_{0}^{+\pi/2} D(\phi)\tan\phi\,d\phi. \tag{63}$$

The ratios I_{tl}/I_n and I_{tr}/I_n can be written in terms of the unknown coefficients f_0, f_1, and f_2 by substituting Eq. (57) into Eqs. (62) and (63) and dividing by Eq. (61). From the previous-order solution of the boundary element equations, the source powers for each element are known and intensity components at every control point can be determined. The ratio of intensity components obtained from the previous-order boundary element solution is then equated to the ratios containing the unknown coefficients, resulting in two equations for the three unknowns. The third equation arises from energy conservation and is Eq. (58), written in terms of the unknowns f_0, f_1, and f_2. The resulting three-by-three system of equations is

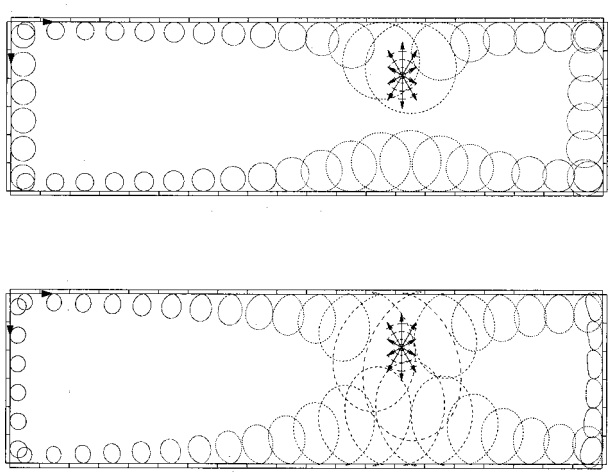

FIG. 5. Schematic showing source powers for each panel after the first iteration (top) versus the source powers after converging the solution, including specular reflection effects (bottom).

$$\begin{bmatrix} 2 & \pi/2 & 0 \\ -1 & -1/2 & -\pi/4 \\ 1 & 1/2 & -\pi/4 \end{bmatrix}\begin{Bmatrix} f_0 \\ f_1 \\ f_2 \end{Bmatrix}=\begin{Bmatrix} \pi \\ \pi(I_{tl}/I_n) \\ \pi(I_{tr}/I_n) \end{Bmatrix}, \tag{64}$$

where the ratios on the right-hand side are known from results of the previous iterative solution of the boundary element equations.

The new directivity function is different for each element and is based on the ratios of normal to tangential components of intensity at the control point of the element. Note that, if the right and left tangential components of intensity are equal magnitude (and opposite sign, due to sign convention), then the f_2 coefficient will be zero and there will be no sine term in the directivity function. Similarly, if the normal component of intensity is large compared to the tangential components, the term involving f_1 will be important.

Using the new directivity function for each element, the boundary condition equation is again applied. New source powers are obtained from the resulting system of equations, and the process of determining new directivity functions is repeated. This iterative scheme continues until the source powers converge. Figure 5 shows the initial and final directivity patterns associated with each element for a typical case. Initially, the sources have the same directivity pattern, $D(\phi)=f_o\cos\phi$, but are of different amplitude. After a few iterations, the directivity function changes shape to $D(\phi)=\cos\phi[f_0+f_1\cos\phi+f_2\sin\phi]$ to account for the specular reflections.

VI. MODEL PROBLEM

A two-dimensional model problem was used to demonstrate the method and to verify the results. The model problem consisted of a rectangular enclosure with two opposing absorptive walls and two opposing rigid walls, as shown in Fig. 6. The enclosure dimensions were in a ratio of 2 to 7, with the shorter walls being rigid. A dipole point source (broadband, high frequency) was placed in the interior, at a location approximately 1/3 of the vertical length (L_x), and 2/3 of the horizontal length (L_y) from the corner. The dipole was oriented such that the null line was normal to the rigid

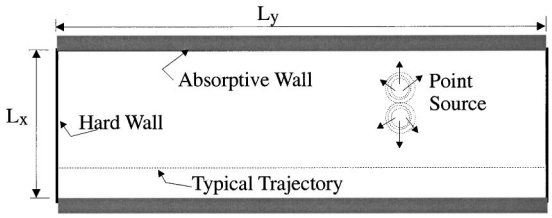

FIG. 6. A two-dimensional model problem with a dipole source in the interior.

walls. This orientation was chosen to eliminate the possibility of strong one-dimensional modes between parallel rigid walls in this idealized configuration.

For verification of the energy boundary element method, an exact solution of this problem was obtained. The exact solution was found by solving the wave equation in the enclosure in two unequal half-spaces that were divided along the line containing the source. Hard-wall and absorptive wall boundary conditions were applied, as well as matching conditions along the common line between the two half-spaces (accounting for a jump discontinuity in force at the dipole point source location). Accurate solutions involving the summation of thousands of modes were constructed at each frequency, and the results for a bandwidth were found by summing results for thousands of frequencies. Obtaining these ''exact'' solutions was a very computationally intensive process. In contrast, the boundary element results were obtained with negligible computational cost (fractions of a second versus many hours), a savings of many orders of magnitude. The boundary element results converged with 52 elements (20 in the L_y direction, and 6 in the L_x direction).

The comparison plots show trajectories that run parallel to the absorbing walls, for different amounts of absorption. In the exact solution frequency is a variable, and so the exact solution plots will be for different center frequencies using one-third-octave bands. The center frequencies are presented as dimensionless wave numbers, where the wave number has been multiplied by the shorter room dimension (L_x). For the white noise broadband power source used, the boundary element method is independent of frequency, but assumes that the waves are at high frequency and broadband. Therefore, for each trajectory (keeping absorption, point source location, and other geometric properties fixed) there will be only one boundary element curve. The exact solution results for different frequencies are expected to collapse to the boundary element result, if the frequencies are sufficiently high and broadband.

VII. RESULTS

In Fig. 7, results are shown for a single trajectory, $x/L_x=\overline{x}=0.2$, for different levels of absorption on the absorbing walls. As mentioned earlier, the point dipole interior source is located two-thirds of the way from a hard side wall (on the left) and approximately one-third of the way down from the upper (absorptive) wall. The trajectory is one-fifth of the way up from the bottom absorbing wall. Four curves are shown, corresponding to the different absorptivities (given as 2D random incidence absorption coefficients):

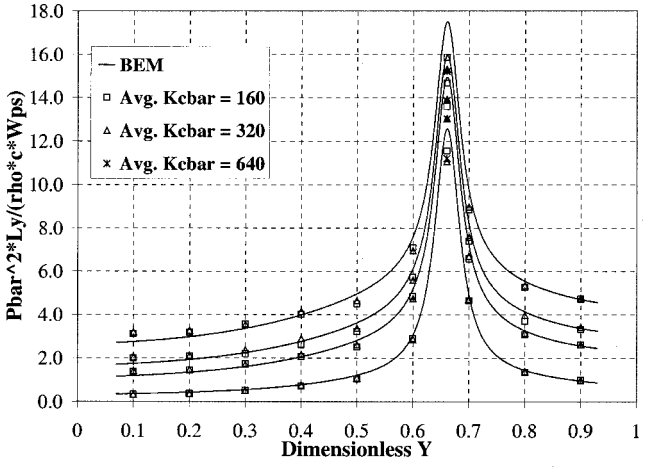

FIG. 7. Different $\overline{x}=0.2$ trajectories corresponding to different levels of absorption ($\alpha_{\text{rand}}=0.250$, $\alpha_{\text{rand}}=0.315$, $\alpha_{\text{rand}}=0.374$, $\alpha_{\text{rand}}=0.595$). The highest amplitude curve corresponds to the lowest amount of absorption. The solid curve represents boundary element results. Individual markers correspond to an exact solution.

$\alpha_{\text{rand}}=0.250$, $\alpha_{\text{rand}}=0.315$, $\alpha_{\text{rand}}=0.374$, $\alpha_{\text{rand}}=0.595$, where the least absorptive case corresponds to the highest curve, and vice-versa.

The exact solution is represented by markers for different center frequency wave numbers that have been normalized by L_x. All results are for one-third-octave bands. The exact solution markers correspond to spatial averages around a point where eleven closely spaced data points are taken. For example, the marker at $\overline{x}=0.5$ is a spatial average of eleven points between $\overline{x}=0.495$ and $\overline{x}=0.505$. The spatially averaged exact solution data points collapse independent of center frequency because the mean-square pressure is normalized with source power and the impedance is not frequency dependent (as a convenience). The agreement between this collapse and the boundary element prediction is excellent. Other simulations for different trajectories and source locations also show excellent agreement.

In Fig. 8, results are shown for the case where there are two point dipoles in the interior. The two dipoles are equally

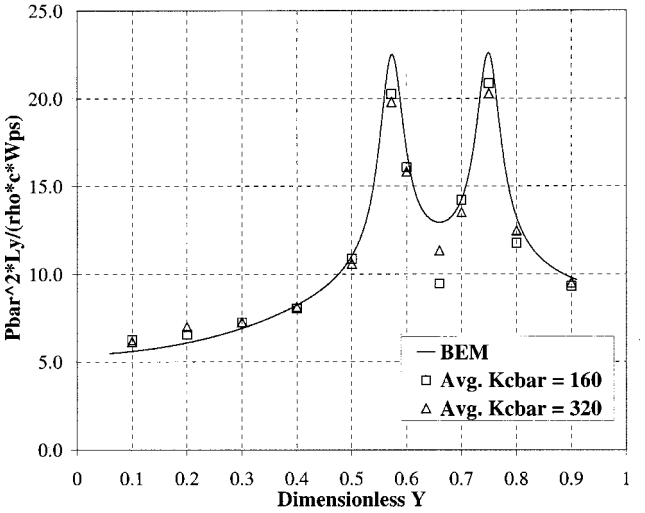

FIG. 8. The trajectory $\overline{x}=0.2$ for the case where two dipole sources are present.

spaced around the initial dipole location of two-thirds from the left-side hard wall. Again, the exact solution markers are showing collapse with frequency, as expected, and in general there is good agreement between the boundary element (solid curve) and the exact solution (markers). However, there is a noticeable failure at the centerline between the two dipoles, due to the presumption on the part of the current boundary element code that the interior sources are spatially uncorrelated. This is obviously not the case as the trajectory passes by the sources. The assumption of uncorrelated interior sources is not a fundamental limitation of the boundary element theory, but rather a correctable shortcoming in the code input description.

As a test of the frequency range applicability of the boundary element method, this model problem's results were compared at lower center frequencies than shown in the previous plots. Percent errors were calculated at various locations in the interior, and for each case having a given center frequency and absorptivity the average of these errors was computed for all available interior points. At high frequencies, average errors were less than 7% for all cases, including a wide range of absorptivities. This residual error probably arises from the following factors: the existence of some degree of spatial correlation, especially the strong first reflections near the source; the presence of 1D modes which are strongly correlated in one direction, and the fact that the directivity function was truncated after three terms, leading to an approximate treatment of specular reflection. Furthermore, average errors were less than 0.5 dB for $kL_x > 100$, and less than 1.0 dB for $kL_x > 40$. Note that L_x is the shorter enclosure dimension, so that the method was very accurate even when this enclosure dimension was only about 6 wavelengths long, corresponding to fairly low frequencies in realistic enclosures.

VIII. CONCLUSIONS

This work has shown that it is possible to replace the boundary of an enclosure with a distribution of uncorrelated, directional, energy/intensity sources and reproduce the high-frequency, broadband interior sound field. The boundary element method using these special sources to represent the surfaces of an enclosure has shown excellent agreement when compared to an exact solution for a two-dimensional rectangular enclosure. The boundary element results are obtained at a very small fraction of the computational cost required by the exact solution.

Boundary elements are often used in the analysis of structural vibration problems. For structural dynamics problems with properties similar to those presented in this paper for an acoustic enclosure, it is believed that an energy-based boundary element can be developed. Extension of the present work to structural systems is a subject of future research.

Future work is underway to develop the three-dimensional version of this method. Comparisons between experiments for irregular geometries and predictions of the boundary element method are also planned. An important future research topic will be the theoretical development of the method to include boundary sources associated with high-frequency wall vibration and sound transmission through enclosure boundaries.

ACKNOWLEDGMENT

This work was sponsored by the National Science Foundation.

[1] Y. Kubota and E. H. Dowell, "Asymptotic Modal Analysis for Sound Fields of a Reverberant Chamber," J. Acoust. Soc. Am. **92**, 1106–1112 (1992).
[2] L. F. Peretti and E. H. Dowell, "Asymptotic Modal Analysis of a Rectangular Acoustic Cavity Excited by Wall Vibration," AIAA J. **30**, 1191–1198 (1992).
[3] R. H. Lyon and R. G. DeJong, *Theory and Application of Statistical Energy Analysis*, 2nd ed. (Butterworth-Heinemann, Boston), 1995.
[4] L. P. Franzoni and D. B. Bliss, "A Discussion of Modal Uncoupling and an Approximate Closed-Form Solution for Weakly Coupled Systems with Application to Acoustics," J. Acoust. Soc. Am. **103**, 1923–1932 (1998).
[5] O. C. Zienkiewicz, *The Finite Element Method* (McGraw-Hill, New York, 1977).
[6] C. A. Brebbia, *The Boundary Element Method for Engineers* (Pentech, London, 1984).
[7] O. M. Bouthier and R. J. Bernhard, "Models of Space-Averaged Energetics of Plates," AIAA J. **30**, 616–623 (1992).
[8] F. Bitsie and R. J. Bernhard, "Sensitivity Calculations for Structural-Acoustic EFEM Predictions," Noise Control Eng. J. **46**, 91–96 (1998).
[9] R. J. Bernhard and J. E. Huff, "Structural-Acoustic Design at High Frequency Using the Energy Finite Element Method," J. Vac. Sci. Technol. A **121**, 295–301 (1999).
[10] R. N. Miles, "Sound Field in a Rectangular Enclosure with Diffusely Reflecting Boundaries," J. Sound Vib. **92**, 203–226 (1984).
[11] L. F. Peretti and E. H. Dowell, "Study of Intensification Zones in a Rectangular Acoustic Cavity," AIAA J. **30**, 1199–1206 (1992).
[12] R. V. Waterhouse and R. K. Cook, "Interference Patterns in Reverberant Sound Fields. II," J. Acoust. Soc. Am. **37**, 424–428 (1965).

The Monte Carlo method to determine the error in calculation of objective acoustic parameters within the ray-tracing technique

Javier Giner[a)]
Department of Financial Economy and Accounting, University of La Laguna, 38071-La Laguna, Tenerife, Spain

Carmelo Militello
Department of Fundamental and Experimental Physics, University of La Laguna, 38071-La Laguna, Tenerife, Spain

Amando García
Department of Applied Physics, University of Valencia, 46100-Burjassot, Valencia, Spain

(Received 21 September 2000; revised 10 August 2001; accepted 16 August 2001)

This article is an extension of the procedure to estimate errors in ray-tracing calculations of room response proposed by Giner *et al.* [J. Acoust. Soc. Am. **106**, 816–823 (1999)]. The previous article presented an expression to estimate the error in computing the energy reaching a receptor during a small time interval. This expression was obtained assuming that a pure ray-tracing program is used and a Monte Carlo Technique is applied. In the present work these ideas are extended in order to compute the objective acoustic parameters of a room. The corresponding equations are presented in closed form. Our results show that the number of rays involved in the analysis depends on the nature of the parameters to be evaluated. Some examples are shown in order to validate our conclusions.
 [DOI: 10.1121/1.1409373]

PACS numbers: 43.55.Ka, 43.55.Br [JDQ]

I. COMPUTATIONAL METHODS OF SIMULATION

This paper is mainly focused on the characterization of an estimator of the confidence on computing the objective acoustic parameters obtained with a pure ray-tracing technique.

The computational cost of the ray-tracing method is proportional to the number of rays and to the maximum simulation time. Because the number of rays are chosen so that the surface of a sphere, whose radius is proportional to the elapsed time, can be correctly sampled, we can establish that the computational cost grows with the third power of time. According to our experience, the analysis of a theater, with 364 active surfaces and 500 ms for the impulse response using 10^6 rays, can be carried out in about 2 h using a 400 MHz PC.

The principal disadvantage of the ray-tracing method is that the accuracy of the obtained results depends strongly on the number of rays used in the calculations. In a previous paper, Giner *et al.*,[1] we developed an expression, Eq. (1), to estimate the error in computing the sound energy reaching a receptor during a small time interval.

In Sec. II, we will show how to obtain an estimator of the confidence in the computed objective parameters.

II. THE CREDIBILITY OF THE OBJECTIVE ACOUSTIC PARAMETERS WITHIN A PURE RAY-TRACING PROGRAM

When we use the Monte Carlo Method we can guarantee that the standard deviation of our numerical experiments can be related with the error. Of course, we are not interested in running the same problem 1000 times but in obtaining an estimate of the standard deviation by running just one problem. The Monte Carlo Method establishes that it can be done if the number of rays is big enough. It must be noticed that when we run 1000 problems we can obtain 1000 different estimates. We can be confident that by using a big number of rays the standard deviation of the estimates will be lower.

We have established[1] that the error in computing the power reaching a receptor during a small time interval Δt can be estimated from the variance of P'_k, $\mathrm{Var}(P'_k)$:

$$\mathrm{Var}(P'_k)=\sum_{i=1}^{N_k} p_{i,k}^2-\frac{1}{N}\left(\sum_{i=1}^{N_k} p_{i,k}\right)^2, \tag{1}$$

where N is the number of rays in the simulation, N_k the number of rays that impacts the receptor during the kth time interval ($k=1,2,...,K$, where K is the total number of histogram intervals considered).

P'_k is the power value of a sound decay curve in the kth histogram interval:

$$P'_k=\sum_{i=1}^{N_k} p_{i,k} \tag{2}$$

and $p_{i,k}$ is the power of the ith ray ($i=1,2,...,N_k$) arriving during that interval. As $N\to\infty$, the error diminishes, $\mathrm{Var}(P'_k)\to 0$, and the mean value converges to its expectation value, $P'_k\to P_k$.

The relative error of P'_k can be computed as the square root of Eq. (1) times Eq. (2):

$$\mathrm{RelError}(P'_k)=\sqrt{\frac{\Sigma_{i=1}^{N_k} p_{i,k}^2}{(\Sigma_{i=1}^{N_k} p_{i,k})^2}-\frac{1}{N}}. \tag{3}$$

a)Electronic mail: jginer@ull.es

If we assume that a large number of rays is used, absorption over the walls is uniform, and rays have approximately the same mean path, Eq. (3) can be further simplified to

$$\text{RelError}(P'_k) = \sqrt{1/N_k - 1/N}. \tag{4}$$

In a given time interval, the fraction N_k/N must equal the relationship between the total area of the receptor images and the surface of the corresponding sphere of radius ct:

$$\frac{N_k}{N} = (4\pi c^3 t^2 \Delta t/V)\,(\pi r_d^2/4\pi(ct)^2). \tag{5}$$

The first parentheses in Eq. (5) represents the growth of the number of images in a time interval Δt (see Ref. 2). r_d is the receptor radius. Replacing Eq. (5) in Eq. (4) and assuming that $1/N$ is a small number, we can recover the general expression developed by Vorlander[3,4] [the expression at the right in Eq. (6)]:

$$\text{RelError}(P'_k) = \sqrt{\frac{V}{N\pi r_d^2 c\Delta t} - \frac{1}{N}} \cong \sqrt{\frac{V}{N\pi r_d^2 c\Delta t}}. \tag{6}$$

Then, under the assumptions of statistical acoustics, Eq. (6) can be used as an *a priori* error estimation. In other circumstances, our analysis is valid for any receptor within the room, and we can obtain the confidence of the results as a function of the receptor position after a computer run.

However, when extending the previous equation to cope with the confidence on computing the objective parameters like the SPL or the definition D we must face many problems.

First, the error in computing the objective acoustic parameters is not the same as computing the error of the power reaching a receptor during a small time interval. The calculation of the integral acoustic parameters, just as the level of sound pressure SPL or the definition parameter D, requires the determination of the incident energy within a time interval, normally bigger than the integration time. For example, to evaluate the SPL we need to know all the energy reaching a given receptor without distinguishing the arrival time. For the definition D we need to know the incidental energy during the first 50 ms, without any need to fraction this period in subintervals Δt.

Then, for computing time integrals there is no point in showing the dependence of the acoustic parameters with the time of integration Δt. Of course, their values can be obtained as a sum of the corresponding intensity values for each Δt, but then, the error sum is irrelevant.

It must be emphasized that our error measure, Eq. (1), produces lower errors for increasing values of Δt. The rationale behind this is that for a given experiment, during a small time interval, a ray can reach the receptor or not, resulting in a big uncertainty or error. For a big time interval the energy reaching the receptor will be almost independent of the particular numerical experiment, providing a low error estimate.

III. THE RAYS HITTING A RECEPTOR DURING A BIG TIME INTERVAL

In order to explain our ideas we will work with the source image space, Fig. 1. In this space, we have a lot of sources emitting rays to our receptor which is fixed in space. During a long period ΔT all the source images enclosed in a sphere of radius $c\Delta T$ will emit rays with a possibility to reach our receptor. Let us assume that from each source departs the same amount N of rays, being an exact image of the original ones. We must notice the following:

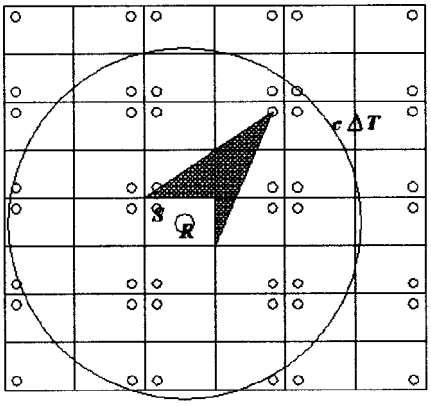

FIG. 1. Source image space. The gray zone shows the sector of the source image that can be considered to emit rays which are "independent events."

(1) If the room is ergodic we can say that from the receptor point of view each ray emitted from the image source is exploring a new direction.
(2) From all the rays departing from a given source image, only the ones reentering the source room through the corresponding image surface can hit or not hit our receptor. All other rays departing from the same source image cannot reenter into the room and, thus, they cannot be considered an independent event with the same hitting probabilities as the others. Consequently, only a fraction of the rays departing from the source images can be accounted for as independent events.
(3) If we consider an average room length l_m during the time $\delta T = l_m/c$ the average number of rays, emitted from all the source images, that can be counted as independent events is N.

Then, during a period ΔT the total number of independent events is, on average,

$$N_f = \frac{\Delta T}{\delta T} N, \tag{7}$$

a parameter which is well known in the literature as the *number of flights* and that can be easily computed with a suitable ray-tracing software.

Under these assumptions we can extend expression (1) to compute the variance of the power (Joules/s) reaching a given receptor during a time ΔT. For this "big" experiment we must consider that the total number of independent rays is not N but N_f. Calling $N_{\Delta T}$ the total number of rays that impact the receptor during ΔT, the sample variance $\text{Var}(P'_{\Delta T})$ of the function during ΔT is

$$\text{Var}(P'_{\Delta T}) = \sum_{i=1}^{N_{\Delta T}} p_i^2 - \frac{1}{N_f}\left(\sum_{i=1}^{N_{\Delta T}} p_i\right)^2. \tag{8}$$

This expression allows the evaluation of the error or indetermination of our estimations as a function of the number of rays used in the analysis.

IV. THE ERROR IN THE PARAMETERS *TOTAL ENERGY DENSITY*, SPL, AND *D*

When a pure ray-tracing program is used, the impulse source is discretized with an initial set of N rays. When $N \rightarrow \infty$, the theoretical total power, $P_{0-\infty}$, that reaches the receptor is

$$P_{0-\infty} = \lim_{N\rightarrow\infty} \sum_{i=1}^{N_{\Delta T}} p_i . \tag{9}$$

The ray-tracing estimation of $P_{0-\infty}$ is

$$P'_{0-\infty} = \sum_{i=1}^{N_{\Delta T}} p_i , \tag{10}$$

extending the sum to all the flights intercepted by the receptor. For ΔT we generally take the maximum value that can be reasonably handled by the usual computational facilities, typically 1 or 2 s.

The *total energy density* (J/m^3) at the receptor can be computed[5] as

$$E'_{0-\infty} = \frac{P'_{0-\infty}}{A_r c}, \tag{11}$$

where A_r is the receptor area and c is the sound velocity.

In the frame of the Monte Carlo method, we can establish a good estimation of the absolute error associated at the ray-tracing prediction of the total energy density:

$$\mathrm{AbsErr}(E'_{0-\infty}) = \sigma(E'_{0-\infty}) \equiv \sqrt{\mathrm{Var}(E'_{0-\infty})}, \tag{12}$$

as it has been defined in Eq. (8). Therefore, we have an estimation of the prediction:

$$E_{0-\infty} = E'_{0-\infty} \pm \mathrm{AbsErr}(E'_{0-\infty}). \tag{13}$$

The relative standard error of the total energy density will be

$$\mathrm{RelErr}(E'_{0-\infty}) \equiv \frac{\mathrm{AbsErr}(E'_{0-\infty})}{E'_{0-\infty}}. \tag{14}$$

The relative error in the ray-tracing estimation[6] of parameter SPL, denoted by RelErr(SPL′) and measured in dB, can be calculated following Kullowsky:[6]

$$\begin{aligned}\mathrm{RelErr}(\mathrm{SPL}') &= 10\log\frac{E'_{0-\infty}+\sigma(E'_{0-\infty})}{E_0} \\ &\quad - 10\log\frac{E'_{0-\infty}-\sigma(E'_{0-\infty})}{E_0} \\ &= 10\log\frac{E'_{-\infty}+\sigma(E'_{0-\infty})}{E'_{0-\infty}-\sigma(E'_{0-\infty})}.\end{aligned} \tag{15}$$

To evaluate the error in the estimation of the definition parameter, defined as D',

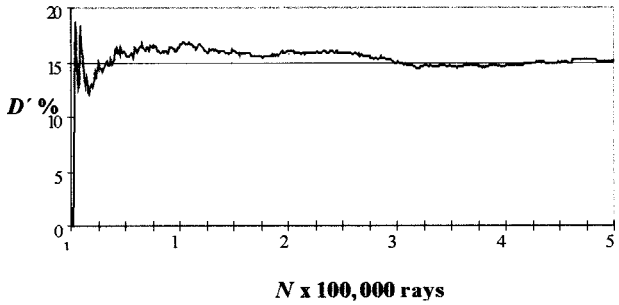

FIG. 2. Convergence of the definition parameter D'.

$$D' = \frac{E'_{0-50\ \mathrm{ms}}}{E'_{0-\infty}}, \tag{16}$$

we need to know the absolute error of the first 50 ms of impulsive response, $\mathrm{AbsErr}(E'_{0-50\ \mathrm{ms}})$:

$$\mathrm{AbsErr}(E'_{0-50\ \mathrm{ms}}) = \sqrt{\mathrm{Var}(E'_{0-50\ \mathrm{ms}})} \tag{17}$$

and the corresponding relative error:

$$\mathrm{RelErr}(E'_{0-50\ \mathrm{ms}}) = \frac{\mathrm{AbsErr}(E'_{0-50\ \mathrm{ms}})}{E'_{0-50\ \mathrm{ms}}}. \tag{18}$$

Being a quotient, the definition parameter will have a relative standard error given by the sum of the relative errors of numerator and denominator:

$$\mathrm{RelErr}(D') = \mathrm{RelErr}(E'_{0-50\ \mathrm{ms}}) + \mathrm{RelErr}(E'_{0-\infty}). \tag{19}$$

In Eq. (19), $\mathrm{RelErr}(E'_{0-\infty})$ is the relative standard error of all the energy measured. It is evident that the relative standard error in computing the quotient D' will always be bigger than the one to compute the total energy density.

The absolute standard error of D' will be

$$\mathrm{AbsErr}(D') = D'[\mathrm{RelErr}(E'_{0-50\ \mathrm{ms}}) + \mathrm{RelErr}(E'_{0-\infty})]. \tag{20}$$

V. EXPERIMENTAL VALIDATION

To prove the validity of the theoretical results presented in this paper, we have analyzed, for a particular case, the statistical distribution of the parameters D', $E'_{0-\infty}$, and SPL′.

The analysis has been carried out in a rectangular room of dimensions $27.5\times41.2\times34.4$ m. The source is placed at the point (10.3, 34.4, 13.7) m and the receiver at the point (17.2, 3.4, 20.6) m. The absorption coefficient for all the walls is equal to $\alpha = 0.19$. This specific room was studied, using deterministic methods (source image method), by Kristiansen *et al.*[7] The computed definition parameter obtained in the receiver is $D = 15.0\%$.

We have implemented here a simulation program based in a pure ray-tracing method. The source is isotropic and the emerging rays are selected using a uniform random procedure. For the reflections we have used the specular model, so that the results would be comparable with those obtained with the images method. The selected receptor was of spherical type with a radius of 0.75 m.

It can be seen in Fig. 2 that the ray-tracing model con-

TABLE I. Statistics of the parameters D', $E'_{0-\infty}$, and SPL′. 500 executions of $N=25\,000$ rays.

	Average (experimental)	Standard deviation (experimental)	Average of the predicted standard deviation [from Eqs. (20), (12) and (15)]
D' (%)	15.0	±3.1	±4.6
$E'_{0-\infty}$ (J/m^3)	6.5×10^{-6}	$\pm4.1\times10^{-7}$	$\pm4.1\times10^{-7}$
SPL′ (dB)	93.4	±0.6	±0.6

verges to the same result of the source image method when we increase the number of rays (N).

However, the most important feature of the theory exposed here is that with only one execution we can approximate the certainty of our computations. Let us show this through the following numerical experiment. We run 500 executions with $N=25\,000$ rays and a time limit $t_f=2$ seg. The sound source is random and isotropic and we take care that each run uses a different set of rays. The results are presented in Table I. For each run we evaluate D', $E'_{0-\infty}$, and SPL′ and its average over the 500 samples (first column). Then we computed the standard deviation of the 500 values (second column). In the third column, we present the average of the 500 predicted error values, calculated with Eqs. (20), (12), and (15).

The computed definition parameter D' takes the average value 15.0%, the same as the theoretical value. The 500 obtained values are distributed about the average value with an experimental standard deviation of ±3.1%. The theoretical deviations obtained with Eq. (20) were different for each execution, because it is only an estimator, but the corresponding values are distributed with a very low dispersion. The average of the 500 predicted standard deviations took the value 4.6%.

Figure 3 shows that the computed values of D' follow a normal distribution, as expected.

The results obtained for the total energy density $E'_{0-\infty}$ and SPL′ are similar. The 500 values are distributed about an average of 6.5×10^{-6} J/m^3 (corresponding to SPL′ $=93.4$ dB). The observed standard deviation of these values

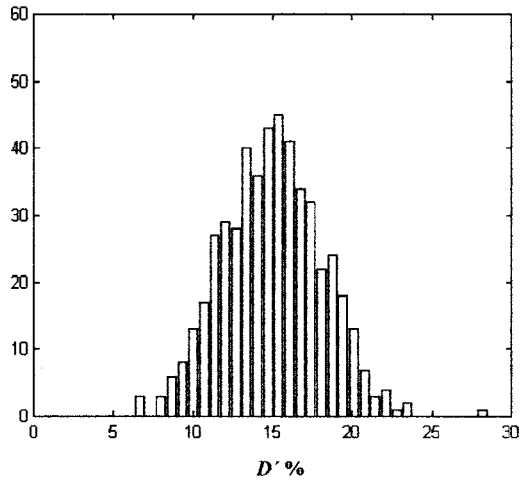

FIG. 3. Statistical distribution of the experimental definition parameter D' (%). 500 runs.

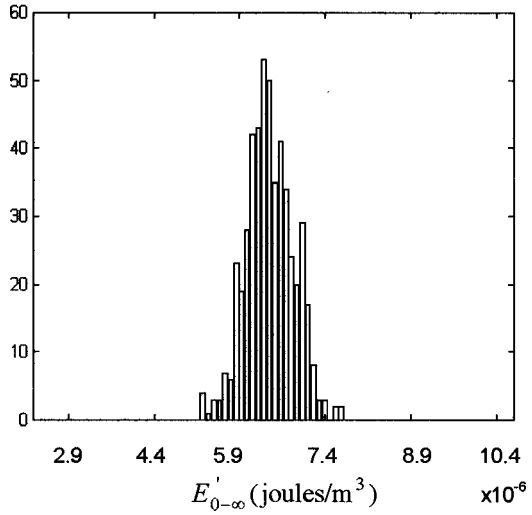

FIG. 4. Statistical distribution of the experimental total energy density $E'_{0-\infty}$(J/m^3). 500 runs.

is $\pm4.1\times10^{-7}$ J/m^3 [RelErr(SPL′)$=0.6$ dB], and the average of the 500 theoretical deviations predicted with Eqs. (12) and (15) are the same $\pm4.1\times10^{-7}$ J/m^3 [RelErr(SPL′) $=0.6$ dB].

In Fig. 4 we can see the distribution of the computed values for $E'_{0-\infty}$. These values follow a normal distribution and its standard deviation is low compared with that obtained for D', Fig. 3.

We must emphasize the difference of relative errors existing between both parameters. While the experimental relative error of the computed definition coefficient D' is RelErr(D')$=3.1/15.0\times100\approx20\%$, the experimental relative error of the total energy density $E'_{0-\infty}$ is only RelErr($E'_{0-\infty}$)$=6.5\times10^{-6}/4.1\times10^{-7}\times100\approx6\%$. The definition parameter is a quotient and, therefore, its relative error is the sum of relative errors of numerator and denominator. The denominator relative error coincides with the relative error of the total energy density. The remaining 14% come from the corresponding relative error in computing the energy of the early part of the impulse response. Therefore, in order to gain confidence in parameters like D, $C50$, $C80$, etc., we need to use a bigger number of rays than that needed for the total energy density or the SPL.

The above-mentioned numerical experiment has been repeated for $N=400\,000$ rays, but now limiting the number of executions to 30. For this number of rays, the error predicted by Eqs. (20), (12), and (15) are in accordance with the experimental error. The statistics are presented in Table II.

TABLE II. Statistics of the parameters D', $E'_{0-\infty}$, and SPL′. 30 executions of $N=400\,000$ rays.

	Average (experimental)	Standard deviation (experimental)	Average of the predicted standard deviation [from Eqs. (20), (12) and (15)]
D' (%)	15.1	±1.0	±1.1
$E'_{0-\infty}$ (J/m^3)	6.5×10^{-6}	$\pm1.2\times10^{-7}$	$\pm1.2\times10^{-7}$
SPL′ (dB)	93.4	±0.2	±0.2

TABLE III. Variation with the absorption coefficient of the parameters SPL′ and D'. Their relative errors appear in brackets.

Average absorption coefficient	SPL′ [RelErr(SPL′)]	D' [RelErr(D')]
$\alpha=0.25$	93.9 dB [±0.3 dB]	49.2% [±7%]
$\alpha=0.50$	90.3 dB [±0.4 dB]	78.4% [±9%]
$\alpha=0.90$	87.6 dB [±0.6 dB]	99.1% [±14%]

The estimated definition parameter D' takes the average value 15.1%, with a standard deviation ±1.0%. In fact, 20 of the 30 obtained values (approximately 68%) are found within the standard deviation interval. The average of the 30 theoretical deviations obtained with Eq. (20) is practically equal to the experimental value, ±1.1%. The same can be said about $E'_{0-\infty}$ or SPL′.

The difference between using 25 000 rays or a quantity 16 times greater, 400 000 rays, is that the expected error should decrease in an approximate factor 4, as we expected by statistical Eq. (6). If the relative error of the definition parameter was 20%, now it is approximately 4 times smaller, i.e., 6%. If the relative error of $E'_{0-\infty}$ was 6%, with 400 000 rays this error is less than 2%. Then, after a run we can have an approximate idea of how many rays we need to improve the quality of our results up to a given level. We can stop our program after a big number of rays have been launched and decide on whether to stop the run or continue.

VI. THE INFLUENCE OF THE AVERAGE ABSORPTION COEFFICIENT ON THE ESTIMATION ERROR OF THE INTEGRAL ACOUSTIC PARAMETERS

Finally, the effect of the average absorption coefficient on the calculation of these integral expressions has been analyzed.

As a rule, increasing the average absorption coefficient of the room will increase the spatial and time variance of the energy distribution. To cope with this, we need more rays in order to decrease the error in computing the objective acoustic parameters. In order to confirm the assertion we have run the same rectangular room described in Sec. V, but now using $N=100\,000$ rays. The source and the receptor remained in the same position. The parameters SPL′ and D' were evaluated for three different absorption coefficients $\alpha=0.25$, $\alpha=0.50$, and $\alpha=0.90$. The results are presented in Table III. The relative errors appear in brackets.

To increase the average absorption coefficient of the room means to increase the relative error of our estimations. This result is of great importance. It means that impulsive answers with a fast decay need to be computed using a big number of rays.

VII. CONCLUSIONS

With the use of Eqs. (12), (15), and (20) an estimation of the principal objective parameters and their precision can be computed. Within the pure ray-tracing technique, it has been demonstrated that it is possible to determine the confidence and credibility of the results. Moreover, we can have an estimation on how many rays are needed to reach a given confidence level.

For instance, for 25 000 rays, the values of the computed parameter $E'_{0-\infty}$ present a relative deviation of 7%, and those of D' a relative deviation of the 20%. These relative deviations descend to 2% and 6%, respectively, when 400 000 rays are used. This is not surprising because it is a common property of the Monte Carlo method. What is actually important is that we can predict quite well the experimental values of the deviation. This allows us to conclude that the starting hypotheses are not in disagreement with the observed facts.

ACKNOWLEDGMENTS

We thank Professor M. Vorländer for his encouragement to continue our work on error estimation of the ray-tracing technique. His comments on our previous paper are also greatly appreciated.

[1] J. Giner, C. Militello, and A. Garcia, "Ascertaining confidence within the ray-tracing method," J. Acoust. Soc. Am. **106**, 816–823 (1999).
[2] H. Kuttruff, *Room Acoustics*, 2nd ed. (Applied Science, 1979).
[3] M. Vorländer, "Die genauigkeit von berechnungen mit dem raumakustichen Schallteilchenmodell und ihre Abhängigkeit von der Rechenzeit," Acustica **66**, 90–96 (1988).
[4] M. Vorländer (private communication).
[5] L. Cremer and H. A. Müller, *Principles and Applications of Room Acoustics* (Applied Science, 1982).
[6] A. Kullowsky, "Error investigation for the ray tracing technique," Appl. Acoust. **15**, 263–274 (1982).
[7] U. R. Kristiansen, A. Krokstad, and T. Follestad, "Extending the image method to higher-order reflections," Appl. Acoust. **38**, 195–206 (1993).

On the sound insulation of wood stud exterior walls

J. S. Bradley[a] and J. A. Birta
Institute for Research in Construction, National Research Council, Montreal Road, Ottawa K1A 0R6, Canada

(Received 6 April 2001; revised 15 August 2001; accepted 6 September 2001)

This article reports the results of a series of measurements of the sound transmission loss of exterior wood stud walls. The measurements were made using standard laboratory procedures in which the walls were built between two reverberation chambers. The outdoor–indoor transmission class is used to rate the relative effectiveness of the various constructions. The measurement results are used to illustrate the influence of key parameters of the constructions on measured sound transmission loss values and to give guidance for future designs. The overall sound insulation of these wood stud walls, to typical outdoor noises, is shown to be limited by two types of low-frequency resonances. An understanding of these low-frequency limitations can most effectively lead to superior sound insulation in similar wood stud walls. © *2001 Acoustical Society of America.*
[DOI: 10.1121/1.1416200]

PACS numbers: 43.55.Rg, 43.55.Nd [JDQ]

I. INTRODUCTION

In North America, homes are commonly built with wood stud exterior walls, which are often required to be effective barriers to outdoor noises such as those from aircraft and road traffic. Improved sound insulation of homes is frequently the only practical means of reducing the impact of aircraft and other outdoor noises. However, the scarcity of published measurements concerning the sound transmission loss of modern exterior wall constructions has made it difficult to design cost-effective solutions to sound insulation problems. Modern energy conservation requirements have led to more air tight and thicker walls with more thermal insulation than in older constructions. Existing data could only be found for older styles of construction and almost always exclude the important lower frequency bands.[1]

This article presents analyses of the measurements of the sound transmission loss of a series of exterior wood stud walls. The walls are representative of contemporary constructions used in climates where significant thermal insulation is required. The measurements included important low-frequency bands to make it possible to correctly characterize the overall effectiveness of the walls when exposed to typical outdoor sounds.

This work is part of a larger project to measure the sound transmission loss of various exterior building facade components and to develop a computer-based procedure for the design of the sound insulation of buildings exposed to aircraft noise. The sound transmission loss of over 100 constructions has been measured in standard laboratory tests.[2] These have included various roof constructions and windows as well as 41 wood stud walls. A report with the complete data has been published.[3] The current article focuses on the influence of key construction parameters, of the 41 wood stud walls, on the resulting sound transmission loss values.

The laboratory measurements were obtained for ideal conditions in which sound is incident on the test walls more or less equally from all directions. When an aircraft flies by a building, the sound is incident from a more limited range of angles. Because of the directional properties of aircraft noise radiation and the varying position of the aircraft, the incident sound energy also varies with angle of incidence to the exposed building facade.[4] As a result it is expected that sound insulation measured in the field with aircraft as the noise source will differ from measurements of the same constructions in the laboratory. However, it was felt that the sound insulation of building facade elements could be most accurately characterized in standard laboratory tests and that corrections could later be derived to better approximate the differences that occur in the field. These corrections will later be obtained from work that includes measurements of the sound insulation of a simple test structure and actual houses exposed to real aircraft flyovers. The current article considers only the laboratory measurements.

The new laboratory data are used in this article to illustrate the effects of varied: surface mass, stud size, stud spacing, structural breaks, and cavity thermal insulation on the sound transmission loss of exterior walls. The influence of these parameters is shown directly for a number of constructions and the trends from these results provide more general guidance for achieving improved sound insulation in other wood stud walls. The new results also add to our understanding of the importance of low-frequency resonances that typically limit the overall sound insulation of exterior wood stud walls.

In addition to the sound transmission loss values measured as a function of $\frac{1}{3}$ octave band frequency, the overall sound insulation of each wall was rated in terms of the outdoor–indoor transmission class (OITC).[5] The OITC rating provides a simple means of rank ordering the effectiveness of the various walls and is a measure of the overall A-weighted level reduction for the wall using a standard source spectrum said to be representative of typical outdoor noises. It is not appropriate to use the STC (sound transmis-

[a]Electronic mail: john.bradley@nrc.ca

sion class[6]) for exterior walls exposed to sounds with significant low-frequency sound energy.

II. MEASUREMENT AND CONSTRUCTION DETAILS

The sound transmission loss tests were carried out following the ASTM E90 procedure[2] according to which the walls are constructed between two reverberation chambers. For the current tests the two reverberation chambers had volumes of 250 and 138 m^3. Walls were constructed in a massive test frame that was positioned between the two chambers and in which walls were constructed measuring 2.44 m high (8 ft.) by 3.66 m long (12 ft.) The test frame rolls into place on heavy steel tracks and is sealed into place between the two chambers with pneumatic seals as well as with foam seals and metal adhesive tape. Both chambers contain diffusing panels to increase the randomization of sound reflections.

The actual test procedure exceeded the requirements of the ASTM E90 standard in several ways. Until recently the standard has required measurements to be made only in the $\frac{1}{3}$ octave bands from 125 to 4000 Hz, but in this work measurements were reported for the $\frac{1}{3}$ octave bands from 50 to 5000 Hz. The additional lower frequency measurements are particularly important because typical outdoor sound sources such as aircraft noise contain significant low-frequency sound energy. Although there are larger uncertainties associated with the lower frequency measurements, including these lower frequency measurements led to an improved understanding of the important low-frequency transmission loss of wood stud walls. In the laboratory measurements, sound levels were measured at nine independent locations in the source and the receiving reverberation chambers. Similarly, reverberation times were measured from the ensemble average of ten decays at the same nine independent microphone positions in the receiving chamber. The tests were repeated for both directions of propagation through the test partitions and the results presented here are the averages of the two tests.

Most walls were constructed as variations of a base wall. The base wall consisted of 38-mm by 140-mm wood studs with a 406-mm stud spacing. These have traditionally been referred to as 2 by 6 studs but here are described as 140-mm studs. The base wall included vinyl siding directly attached to 11-mm oriented strand board (OSB) sheathing as the outer surface and 13-mm gypsum board as the internal surface. Both the OSB and the gypsum board were screwed to the wood studs. The details of the screw spacings were those recommended by the National Building Code of Canada. The stud cavity was filled with glass fiber thermal insulation. Except for specific additions and variations, all walls were constructed of these same materials.

Table I includes the surface densities of the various materials. Except where otherwise noted, all of the walls had vinyl siding on the exterior face and included a polyethylene vapor barrier immediately under the interior gypsum board. Only 13-mm-thick regular gypsum board and 11-mm-thick OSB sheathing were used.

To correctly interpret the significance of small differences between test results, it is important to known how accurately transmission loss measurements can be repeated on rebuilding the particular construction. Repeated measurements of the base wall construction give some indication of the expected repeatability of these measurements in terms of individual $\frac{1}{3}$-octave band results as well as in terms of OITC values. When the test frame was removed and repositioned with exactly the same construction, $\frac{1}{3}$-octave band transmission loss values repeated within less than ± 0.2 dB at all frequencies . Rebuilding the wall led to small differences that fluctuate with frequency. When rebuilding with the same materials, $\frac{1}{3}$-octave band transmission loss values changed by up to about 1 dB with a rms (root mean square) difference over all frequencies of 0.5 dB. When the wall was rebuilt with new materials the maximum change was about 2 dB and the rms difference 1 dB. In terms of OITC values, rebuilding with the same material led to a change of 0.3 and rebuilding with new materials led to a change of 0.7. Thus one cannot confidently identify the cause of small changes of less than about 0.7 in OITC values. In spite of this uncertainty, smaller changes are probably meaningful when only parts of the construction have been changed such as the addition of a second layer of gypsum board. Some changes are also more likely to be meaningful when they are observed to occur consistently over a range of frequencies.

TABLE I. Surface densities of the various materials used in these test walls.

Material and thickness	Surface density (kg/m^2)
Acrylic stucco (EIF), 6 mm	10.2
Aluminum siding, 0.6 mm	0.4
Brick, 89 mm	132.0
Cellulose (blown in), 140 mm	8.0
Cement stucco, 9.5 mm	15.6
Glass fiber batts, 152 mm[a]	1.4
Gypsum board, 13 mm (regular)	8.1
Mineral fiber, 140 mm	5.6
Oriented strand board (OSB), 11 mm	6.9
Polystyrene, 25 mm	0.6
Rigid glass fiber board, 25 mm	1.3
Vinyl siding, 1 mm	0.4
Wood fiber board, 13 mm	3.5

[a]Compressed to fit into 140-mm stud space.

III. BASIC PRINCIPLES

Many of the walls were variations from a base wall, described in Sec. II, and exhibit a number of common characteristics. Figure 1 illustrates the measured sound transmission loss measurements for the base wall and also for a second wall that includes a double layer of 13-mm gypsum board attached via resilient channels. That is, the single layer of gypsum board on the base wall was replaced with a double layer attached via screws to the resilient channels. These two walls illustrate the basic phenomena that influence the sound insulation of the various wood stud walls. The results quite obviously show the advantage of using resilient channels to create a structural break between the two outer surfaces. The wall with resilient channels has much superior sound transmission loss at higher frequencies. However, at very low frequencies, where the sound transmission loss is lowest, both walls have quite similar sound transmission loss values.

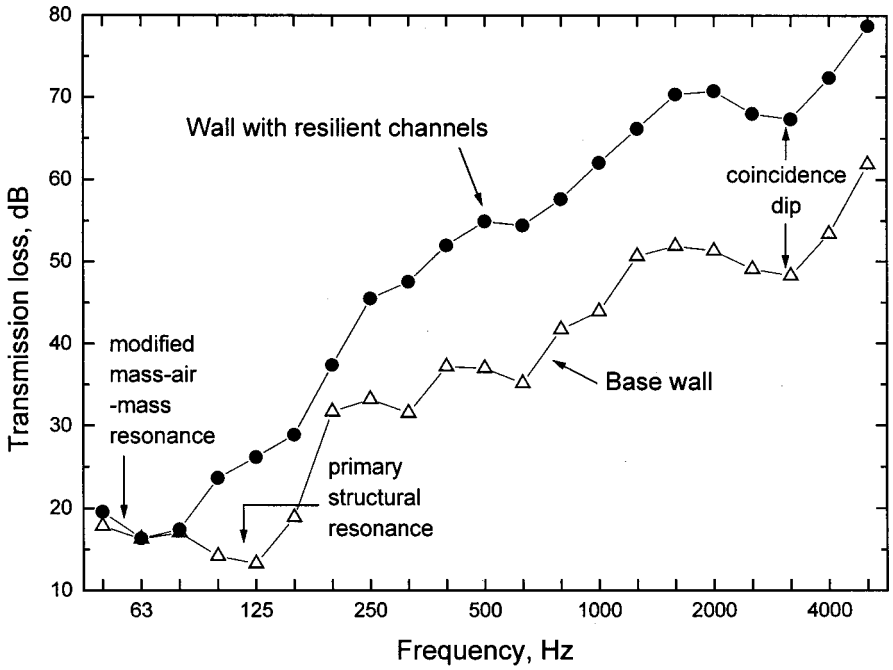

FIG. 1. Illustration of the basic phenomena influencing sound transmission loss for (a) the base wall, and (b) a wall with two layers of gypsum board on resilient channels.

The sound transmission loss curves in Fig. 1 include several dips that limit the overall sound insulation. Both curves include a dip at about 2.5 to 3.1 kHz. This is the well-known coincidence dip of the gypsum board and OSB panels that occurs when there is a coincidence between the velocity of bending waves in the panels and the incident sound.[7]

The lower frequency dips in the Fig. 1 results and later results will be explained mostly in terms of the results of work by Lin and Garrelick.[8] Their work does not seem to be widely known but does appear to explain the most important low-frequency features of sound transmission through these wood stud walls. At low frequencies the base wall includes a dip at about 125 Hz. This has not been clearly evident in many previous tests because the ASTM standard[2] did not previously require measurements below 125 Hz. The work of Lin and Garrelick would indicate that this is the primary structural resonance of the ribbed panel system formed by the stud wall and the rigidly attached surface layers. It is very important because it reduces the sound transmission loss of the wall to its lowest value for any frequency and hence limits the overall performance of the wall.

Lin and Garrelick also showed that when the two layers are not rigidly connected, the system is changed and no longer has a primary structural resonance. Thus, when one of the surface layers is mounted using resilient channels, this primary structural resonance no longer occurs. The ribbed panel system is effectively broken up and the two surface layers can vibrate more or less independently. However, for this case the two surface layers are still coupled by the stiffness of the air cavity and a mass–air–mass resonance occurs. The frequency of this resonance is determined by the combination of the masses of the surface layers and the stiffness of the contained air and for these walls is considerably lower in frequency than the primary structural resonance. A recent paper[9] has shown that the frequency of this resonance is modified by the addition of the stiffness of the resilient channels. This modified mass–air–mass resonance limits the low-frequency transmission loss of the wall with resilient channels. Again because the transmission loss of the wall is least in this frequency region, the resonance limits the overall performance of the wall.

Although the coincidence dip affects the sound transmission loss of the walls, it occurs at a frequency where the sound transmission loss is quite high. Thus, the coincidence dip is often of less practical importance because the transmitted sound energy is much greater at lower frequencies. However, the primary structural resonance seen in the base wall and the modified mass–air–mass resonance in the wall with resilient channels significantly limit the overall sound insulation of many walls and are therefore significant impediments to achieving improved sound insulation against typical outdoor noises.

The overall performance of the walls in this article are compared using the outdoor–indoor transmission class (OITC).[5] This is essentially the A-weighted level reduction with a standard source spectrum. Figure 2 compares this standard spectrum to an average spectrum for modern commercial jet aircraft from measurements made as part of this project. The OTIC source spectrum is seen to have relatively higher levels at very low and very high frequencies. Because the sound transmission loss of walls is most limited at lower frequencies, these increased source levels at lower frequencies would tend to exaggerate the expected indoor sound levels at lower frequencies relative to those expected for a typical aircraft noise spectrum.

Figure 3 illustrates the expected A-weighted indoor levels for the base wall and the two source spectra from Fig. 2. (Both calculations were made assuming a receiving room volume of 57 m^3, an exposed wall area of 10.7 m^2, and a receiving room reverberation time of 0.4 s, corresponding to an average living room.[10]) These results more clearly demonstrate the importance of the primary structural resonance at 125 Hz, which dominates the indoor A-weighted levels. The

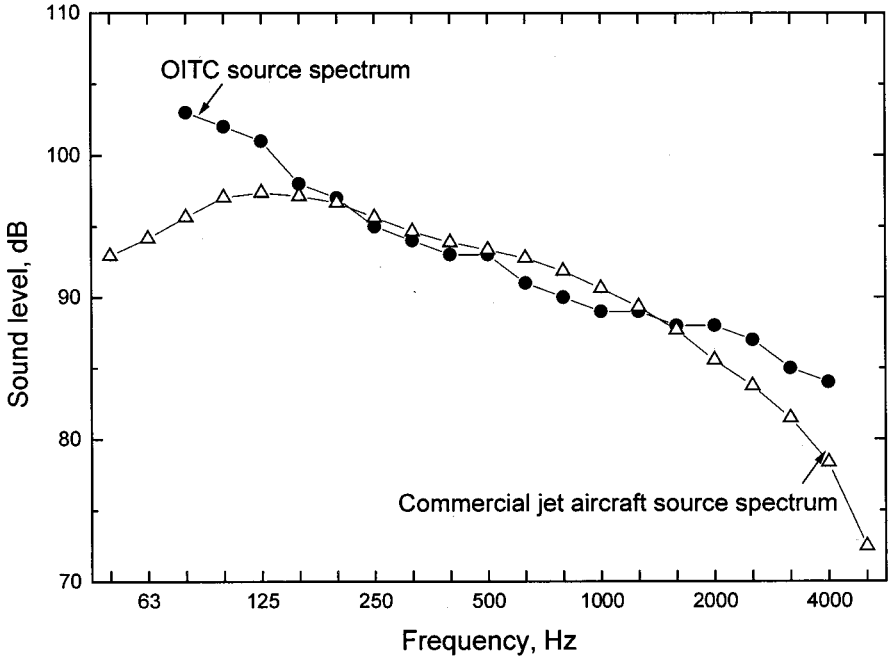

FIG. 2. Comparison of the standard OITC source spectrum with the source spectrum for modern commercial jet aircraft.

OITC source spectrum does exaggerate this effect a little. One could contemplate using different source spectra for different types of outdoor noise sources. Using an aircraft noise spectrum rather than the OITC source spectrum led to reduced overall level ratings of about 3 dB. However, the different source spectrum shape does not have much effect on the rank ordering of the constructions and using other nonstandard source spectra would detract from the beneficial generality of OITC rating.

Subsequent results will be presented as both conventional sound transmission loss versus frequency plots and also in terms of the expected indoor sound levels as illustrated in Fig. 3. Indoor levels were calculated using the same aircraft noise spectrum as in Fig. 2 and for the same average living room previously described. This form of plot directly shows the frequencies at which the highest levels occur and clearly indicates where the overall sound insulation is most critically limited.

IV. EFFECTS OF ADDING MASS

Figure 4 illustrates examples of adding more massive outer surface to a wood stud wall. The sound transmission loss is said to be mass controlled at frequencies above low-frequency resonances and below the coincidence dip region. In this region increased mass increases the measured sound

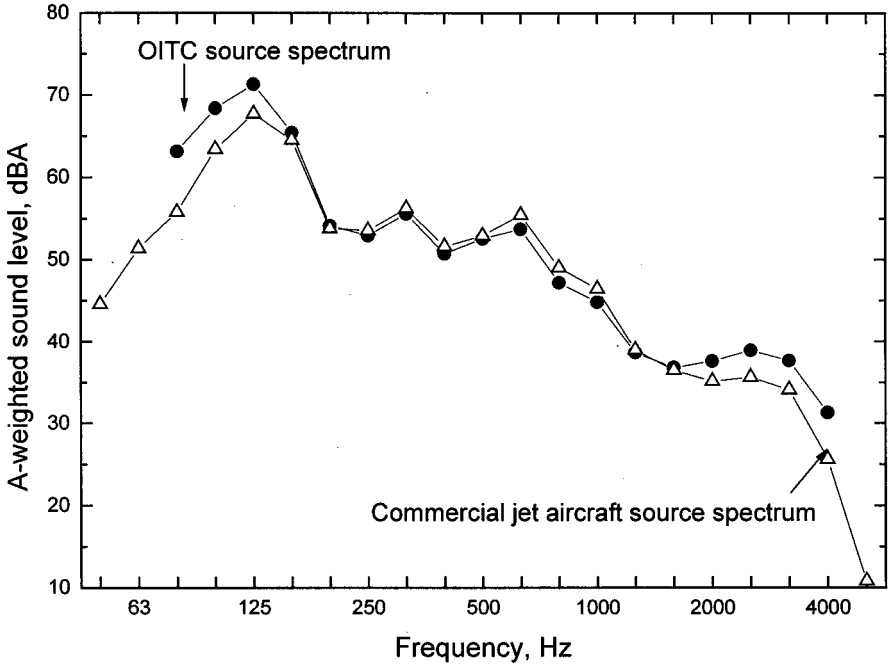

FIG. 3. Comparison of indoor A-weighted sound levels with the base wall and either the OITC source spectrum or the aircraft source spectrum from Fig. 2.

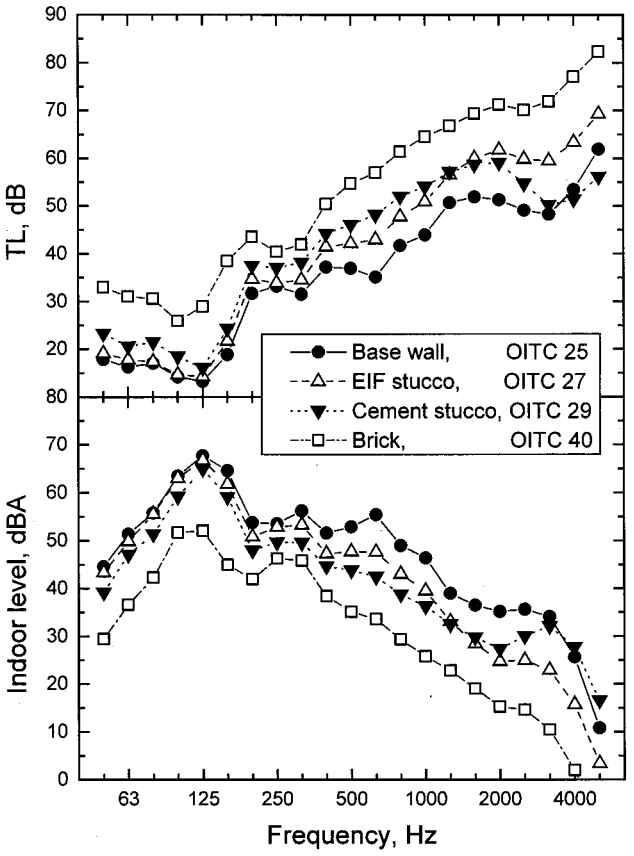

FIG. 4. Effects of adding mass to the base wall by adding heavier exterior surface layers. (See Table I for surface densities.)

transmission loss. The OITC value for the base wall is 25. This is increased to 27 when vinyl siding is replaced by acrylic (EIF) stucco and to 29 when a heavier cement stucco exterior is used. However, adding brick as the outer layer has a much greater effect on the OITC rating which is increased to 40.

The effect of the added mass on the resulting OITC ratings approximately follows a $10\log\{M/M_0\}$ relationship (where M is the total surface mass with additions and M_0 is the original total surface mass of the base wall). The expected increments in OITC ratings according to this relationship for various materials added to the base wall are given in Table II along with the measured OITC ratings.

The measured improvements in OITC ratings relative to the base wall case are generally very close to the $10\log\{M/M_0\}$ relationship. The improvement due to the brick is greater than might be expected because in addition to the much larger surface density (see Table I), there is effectively a structural break because the bricks are only connected to the rest of the wall via occasional metal ties.

TABLE II. Calculated expected increases due to increased mass and measured OITC ratings.

Added material	$10\log\{M/M_0\}$	Measured OITC
Base wall	···	25
Second layer gypsum board	1.9	27
Acrylic (EIF) stucco	2.2	27
Cement stucco	3.1	29
Alulminum siding	0	25
Brick	9.9	40

Adding the cement stucco, which adhered directly on the exterior sheathing, is seen to modify the shape of the transmission loss curve in Fig. 4 in the region of the coincidence dip. Although this may seem important on the transmission loss versus frequency plot, the indoor sound level plot indicates that these differences are of little practical importance because sound levels at these frequencies are more than 30 dB below the low-frequency maximum A-weighted levels. Replacing the exterior OSB sheathing with wood fiber board only had a small effect (not shown). Although the wood fiber board has a lower surface density (see Table I), the sound transmission loss increased by a few dB at higher frequencies when wood fiber board was used as the exterior sheathing. The overall OITC rating with wood fiber board was the same value of 25 as for the base case. When the vinyl siding was attached over external thermal insulation or over an air space, there were changes to the measured transmission loss at higher frequencies but the OITC rating did not change (not shown).

In all of the results in Fig. 4, the transmission loss is always least at the frequency of the primary structural resonance. That is, the overall indoor sound levels are always greatest at about 125 Hz and this limits the overall performance of the wall. This is also true even when brick is added to the wall except that this resonance frequency appears to shift to a slightly lower frequency. For these walls, further significant reductions of indoor sound levels would require modification of this resonance. There are other smaller peaks in the indoor sound levels of the base wall at 315 and 630 Hz. Their cause is not known but the peak in the 630-Hz band seems to vary with the surface treatment in Fig. 5. They are more than 10 dB below the 125-Hz peak in indoor levels and hence are of less practical importance.

V. EFFECTS OF STUD SIZE AND SPACING

Both stud size and stud spacing are found to influence the sound transmission loss of walls and the effects are not independent but interact such that the effect of stud size is more significant for larger stud spacings. Figure 5 illustrates results for four combinations of stud size and spacing. If the stud size of the base wall configuration (140-mm studs at 406-mm spacing) is decreased to 89-mm studs with the same spacing, the results in Fig. 5 indicate a reduction of the OITC rating from 25 to 24. However, increasing the stud spacing from 406 to 610 mm results in a 3-point improvement in OITC for the 89-mm studs and a 6-point improvement for the 140-mm studs. These improvements are largely the result of changes to the frequency of the primary structural resonance. Increasing the stud size (open symbols) lowers the frequency of this resonance and increasing the stud spacing (square symbols) leads to an even larger reduction in the resonance frequency. Because the maximum indoor sound levels occur at this resonance frequency, these modifications can significantly reduce indoor sound levels.

The important effects of stud spacing are further illustrated in Fig. 6 for 89-mm stud walls. Varying the stud spacing from 305 mm to 406 mm and to 610 mm systemati-

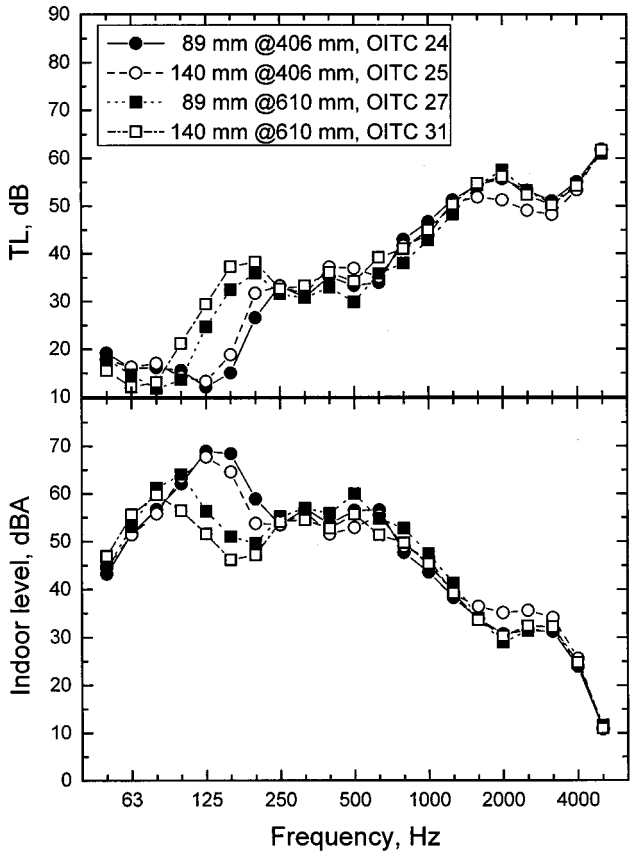

FIG. 5. The effects of varying stud size and stud spacing for wood stud exterior walls.

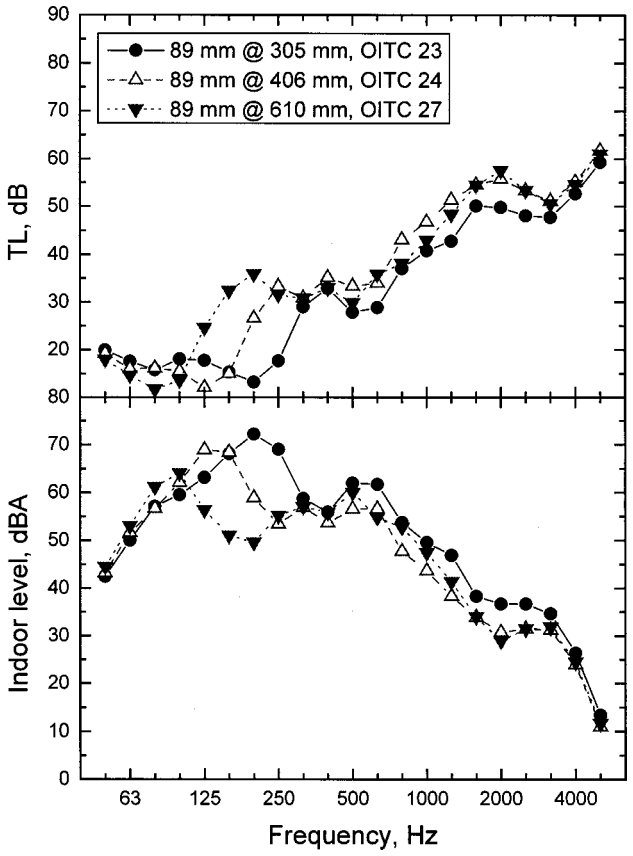

FIG. 6. Effects of varying stud spacing for 89-mm wood stud exterior walls.

cally reduces the resonance dip from 200 Hz to 125 Hz and to 80 Hz. These changes correspond to OITC ratings of 23, 24, and 27. The results of Figs. 5 and 6 clearly indicate the importance of the stud size and spacing on the overall performance of the wall. Variation of these parameters led to variations in OITC values from 23 to 31. It is thus possible to achieve substantial improvements in the sound transmission loss of wood stud walls by appropriate choice of stud size and spacing.

The measured shifts in the low-frequency resonance with varied stud spacings are particularly convincing evidence that this is the primary structural resonance that Lin and Garrelick predict. A simple mass–air–mass resonance would not be expected to shift in frequency with stud spacing.

VI. EFFECTS OF STRUCTURAL BREAKS

Including structural breaks in the construction of a wall improves the sound insulation by preventing the direct transmission of energy from one surface to the other. It also has the benefit of eliminating the primary structural resonance for the ribbed panel system formed by a stud wall without a structural break. Eliminating this resonance often removes the weakest component of the sound insulation and hence improves the overall performance of the wall. In these measurements, structural breaks were introduced either by mounting the gypsum board on resilient channels or by using staggered stud systems where two sets of 89-mm studs are built with a 140-mm plate and header so that that each surface of the wall is attached to a separate set of studs.

Figure 7 illustrates measured sound transmission loss values for three examples of walls that include resilient channels as well as results for the base wall configuration. As indicated previously in Fig. 1, adding resilient channels eliminates the primary structural resonance at about 125 Hz and introduces a modified mass–air–mass resonance in the 63-Hz $\frac{1}{3}$-octave band. At almost all frequencies above this, the addition of resilient channels leads to significant improvements in the measured sound transmission loss. For the case of a single layer of 13-mm gypsum board mounted on resilient channels, the OITC rating increased to 32 from the value of 25 for the base wall. For the wall with a double layer of gypsum board on resilient channels, the OITC rating increased to 34. When cement stucco was added to this last wall, the OITC was further increased to 41. This is slightly larger than the OTIC rating of 40 for the wall with a brick exterior and indicates that the combination of a structural break and adequate mass can provide superior sound insulation. A wall constructed with wood fiber board as the exterior sheathing and with a double layer of gypsum board on resilient channels on the interior surface had sound transmission loss characteristics very similar to the comparable wall constructed with OSB as the exterior sheathing.

The modified mass–air–mass resonances occur in or near the 63-Hz $\frac{1}{3}$-octave band as expected. The added stiffness of the resilient channel influences the frequency of this resonance,[9] but there is a small trend for the transmission

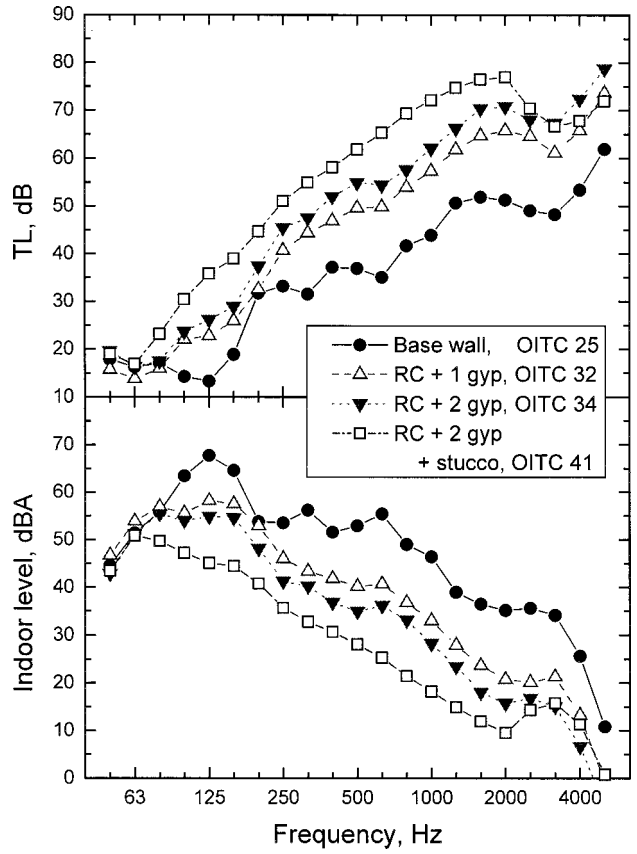

FIG. 7. Effects of various surface layers mounted on resilient channels (RC). (1 gyp=1 layer of 13-mm gypsum board; stucco is cement stucco attached to the exterior sheathing.)

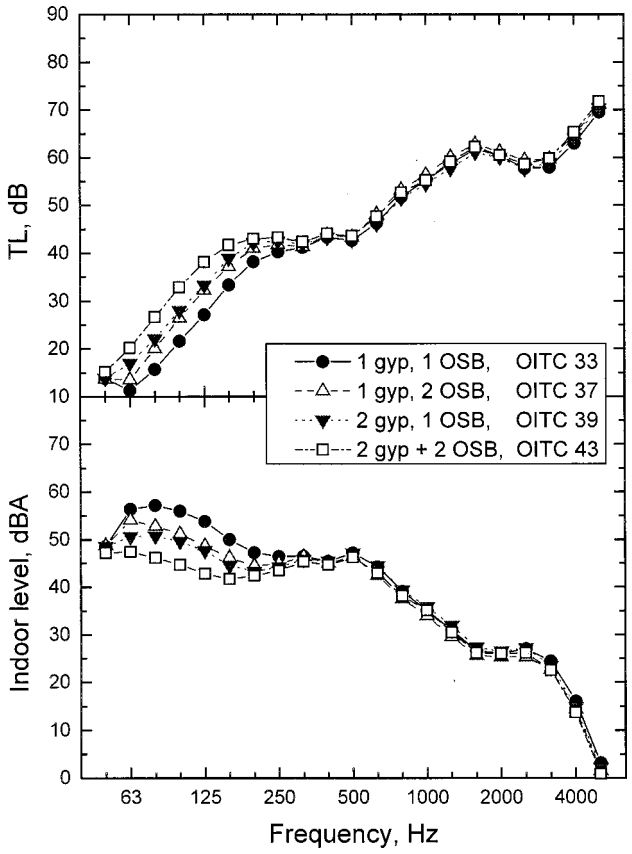

FIG. 8. Effects of various surface layers on a staggered wood stud wall. (1 gyp=1 layer of 13-mm gypsum board; 2 OSB=2 layers of 11-mm oriented strand board.)

loss versus frequency curve to indicate a small shift to lower frequencies with added surface mass.

Figure 8 shows the measured sound transmission loss values for four constructions based on staggered stud systems. In all cases the walls were constructed with two sets of 89-mm wood studs on a 140-mm plate and with a stud spacing of 610 mm. The four results in Fig. 8 show the effect of different surface treatments. The first set of results with a single layer of gypsum board on the inner surface and a single layer of OSB on the exterior surface had an OITC rating of 33 which is 8 points better than the base wall. The staggered stud construction effectively breaks the structural path between the two surface layers and eliminates the primary structural resonance found in the base wall. For the staggered stud walls the low-frequency sound transmission loss is limited by a mass–air–mass resonance which, as expected, seems to shift lower in frequency as more mass is added to the surface layers of the wall. Thus, doubling the OSB increases the OITC rating to 37 and doubling the gypsum board increases it to 39 because the gypsum board is heavier than the OSB. Doubling both external layers is seen to further increase the low-frequency sound insulation and leads to an OITC rating of 43.

The staggered stud constructions in Fig. 8 are more effective than the constructions with resilient channels in Fig. 7 because they have improved low-frequency performance. Although the surface masses are similar, the staggered stud walls have lower stiffness because they do not include the added stiffness of resilient channels. This leads to mass–air–mass resonances that are lower in frequency for the staggered stud walls and hence to improved low-frequency transmission loss.

These tests were repeated for similar staggered stud wall constructions but with a 406-mm stud spacing. The measured transmission loss values were very similar with only very small differences. This included the same unexpectedly small increase in transmission loss with increased surface mass at mid and higher frequencies that occurred for both stud spacings. The OITC ratings of the walls were identical to those of Fig. 8. When a wood stud wall includes a structural break, as in these staggered stud walls, the stud spacing is not important. The stud spacing is only important in walls without structural breaks because in these walls it influences the frequency of the primary structural resonance. Again, with the structural break and adequate mass, superior sound insulation can be achieved.

When resilient channels are added to a staggered stud wall system, further improvements are obtained in the measured sound transmission loss values indicating that the structural break created by the staggered studs in imperfect. Figure 9 compares measured sound transmission loss values for staggered stud walls including resilient channels (solid symbols) with similar walls without resilient channels (open symbols). For a staggered stud wall with a single layer of gypsum board and a double layer of OSB, adding resilient channels significantly increases the mid- and high-frequency

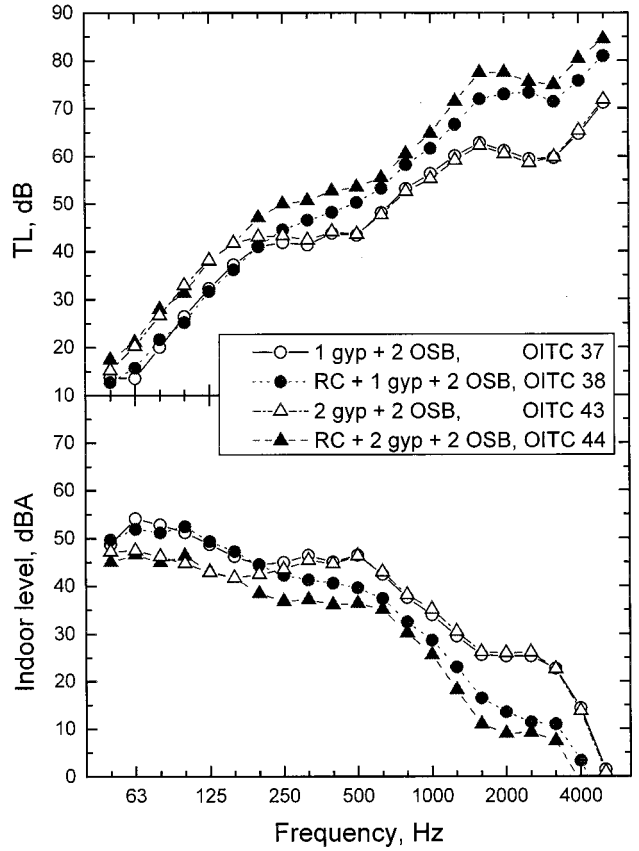

FIG. 9. Comparison of staggered wood stud walls with (solid symbols) and without (open symbols) added resilient channels (RC). (2 gyp=2 layers of 13-mm gypsum board; 2 OSB=2 layers of oriented strand board.)

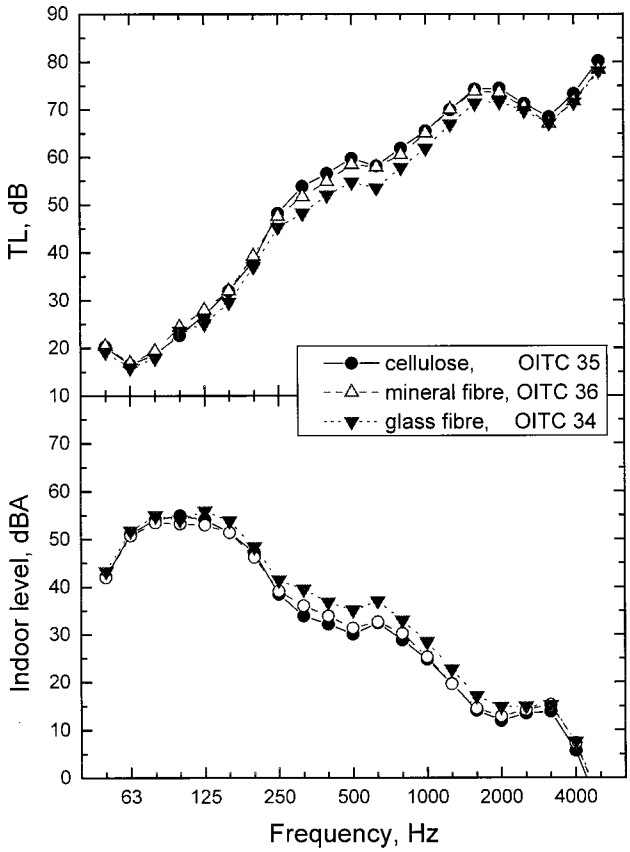

FIG. 10. Effects of different thermal insulations completely filling the stud cavity in walls with a double layer of gypsum board on resilient channels.

sound transmission loss. However, the OITC rating only increases from 37 to 38. Similarly, adding resilient channels to a staggered stud wall with double layers of both gypsum board and OSB only increased the OITC rating from 43 to 44.

In both examples in Fig. 9, adding resilient channels leads to large improvements in sound transmission loss above 250 Hz. It is likely that these results indicate an effective flanking path at higher frequencies via the plate and header that connect the two stud systems in the staggered stud walls without resilient channels. These results may give insight into the limitations of staggered stud wall systems but they are of less practical importance for typical outdoor noises because the overall sound insulation is most severely limited at the low frequencies. The staggered stud walls can provide OITC ratings of up to 44, which is 4 points greater than measured for the brick wall and hence can be an effective means of obtaining superior sound insulation.

VII. EFFECTS OF CAVITY INSULATION

The effects of different types of cavity insulation were measured for walls that included a double layer of 13-mm gypsum board mounted on resilient channels. The effects of different cavity insulations were expected to be more readily detectable (larger) for this wall construction. Three types of cavity insulation were evaluated. These were glass fiber batts, mineral fiber batts, and dry blown in cellulose fiber. Figure 10 compares the measured sound transmission loss values and shows that the different materials led to small changes in transmission loss and only at higher frequencies. Because the type of insulation did not greatly influence the important low-frequency sound transmission loss, the overall ratings of the walls did not change much. The OITC rating of 34 for the glass fiber insulation increased to 35 for the cellulose fiber and to 36 for the mineral fiber. These OITC increases were partially due to the rounding up to the nearest integer value that is part of the OITC calculation. (If the OITC values were calculated to one decimal place, the increases would be 0.7 and 1.7.)

These differences in OITC values are in one case the same as, and in the other case only a little larger than, the rebuild repeatability difference. One should therefore be cautious in attributing significance to these small differences and remember that other parameters have much larger effects on the overall sound insulation. It is also quite likely that the differences due to different cavity insulation material would be different for other wall constructions and much smaller for walls without a structural break.

VIII. DESIGN CHOICES

The various walls that were tested had OITC ratings varying from the OITC of 25 for the base wall to values in excess of the OITC of 40 obtained for a wall with a brick surface. All of the construction parameters that were considered influenced the overall sound insulation rating. The de-

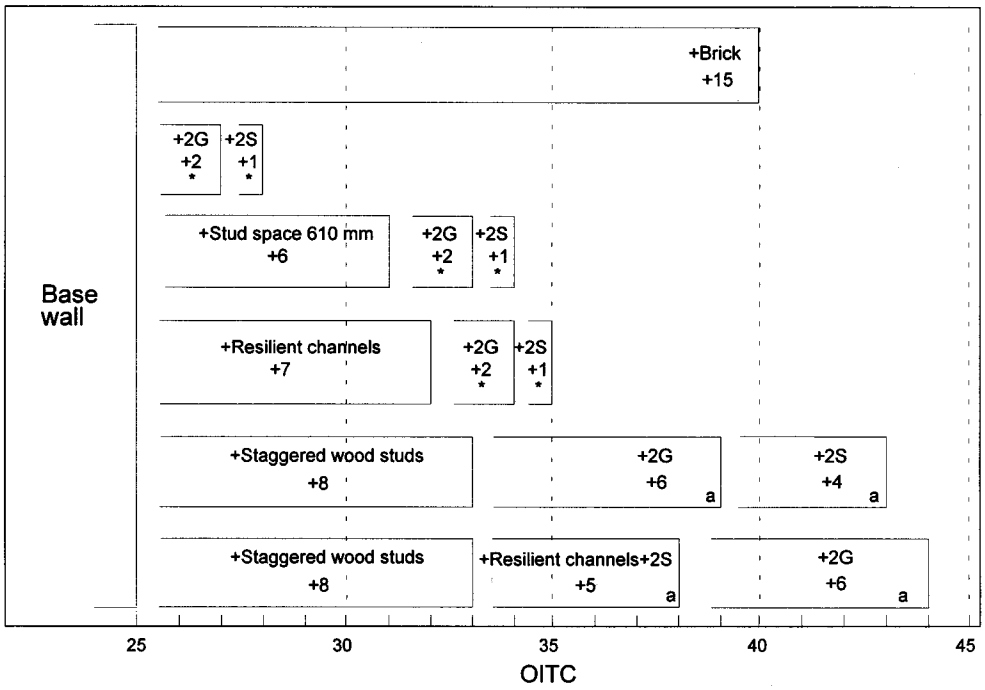

FIG. 11. Summary of OITC ratings for walls as increments relative to the OITC rating of the base wall. Base wall: vinyl siding on 11-mm OSB, 140-mm wood studs at 406-mm spacing and 13-mm gypsum board on the interior surface, with cavity filled with glass fiber batts. 2G=increment due to doubling the gypsum board. 2S=increment due to doubling the OSB sheathing. * indicates these increments are approximately equal to $10\log\{M/M_0\}$, where M is the total surface mass with the double layer and M_0 is the original total surface mass. "a" indicates cases where the added mass shifts the mass–air–mass resonance and substantially improves the OTIC rating.

signer needs an overview of the various results to help in selecting an appropriate construction with adequate sound insulation. The summary chart shown in Fig. 11 has been constructed to give an overview of the importance of each parameter. Although it is reasonably complete it does not include all combinations of parameters and relates only to 140-mm wood stud walls (traditionally referred to as 2 by 6 studs). Some comments concerning 89-mm wood stud walls (2 by 4 studs) are included below.

The chart in Fig. 11 shows increments in OITC ratings relative to that of the base wall. The total OITC rating for a given combination can be read off the lower horizontal axis or can be obtained by summing the various increments from the left of the chart. For example, the brick wall case has a total OITC rating of 40 which can be considered as the sum of 25 for the base wall and an increment of 15. The chart shows that substantial improvements can be obtained by (a) increasing the stud spacing, (b) adding resilient channels, or (c) using staggered stud walls. Of course, adding very large amounts of extra mass as in the case of brick or adding extra mass to staggered stud walls also produce large improvements to OITC ratings.

For single stud walls, adding extra mass by doubling layers usually only leads to modest improvements with increments that approximate $10\log\{M/M_0\}$. Thus doubling the gypsum board gives approximately a 2-dB increase in OITC and then adding a second layer of the OSB sheathing adds a further 1 point to the OITC rating (see also Table II). This is true for the basic wood stud walls and for the walls with resilient channels and this relationship approximately applies for other additions of surface mass.

Adding extra layers leads to larger increases in OITC ratings for staggered stud walls. The added mass of the extra layers is more effective for staggered stud walls because it greatly improves the low-frequency performance by lowering the mass–air–mass resonance of the walls. This does not occur when the added layers are mounted on resilient channels because the added stiffness of the resilient channels limits the shift of this resonance to lower frequencies.[9] The 15-dB increment when brick is added is probably composed approximately of a 10-dB increment for the added mass and a further 5-dB increment for the structural break that is also added.

Increasing the stud spacing or using resilient channels with an appropriate amount of added mass can produce significantly improved sound insulation ratings. These results suggest that with enough added mass and perhaps also optimizing the internal thermal insulation, OITC ratings of 35 or slightly more can be achieved for single stud walls. However, the staggered stud walls with double surface layers provided the highest OITC ratings that were a little superior to the measured brick wall. It is likely that the performance of the brick wall example could be improved if a larger stud spacing were used with the bricks because the results in Fig. 4 indicate its overall rating is limited by the dip at 100 Hz. A larger stud spacing would shift this dip to lower frequencies (see Figs. 5 and 6) and would be expected to improve the OITC rating.

Only a few 89-mm wood stud walls were tested and their sound insulation ratings were always a little lower than the corresponding 140-mm wood stud walls. For example, a wall similar to the base case wall but with 89-mm wood

studs had an OITC rating of 24, 1 point lower than the base case. When the stud spacing was increased to 610 mm, for an 89-mm wood stud wall, the OITC rating increased to 27 or 4 points lower than the corresponding 140-mm stud wall. For an 89-mm wood stud wall with two layers of gypsum board mounted on resilient channels, the OITC rating was 32. This is 2 points less than the corresponding 140-mm wood stud wall. In this latter comparison the 89-mm wood stud wall also included a 25-mm-thick layer of rigid glass fiber board under the vinyl siding which was not included in the 140-mm stud wall, but in other tests the external glass fiber board only influenced the higher frequency sound transmission loss and did not change the OITC rating. These limited examples indicate that results for 89-mm wood stud walls are 1 to 4 OITC points lower than those for the 140-mm wood stud walls summarized in Fig. 11.

IX. CONCLUSIONS

The overall effectiveness of the sound insulation of typical wood stud exterior walls is limited by poor performance at the low frequencies. Thus for typical outdoor noises, the loudest indoor sounds will be at low frequencies. It is therefore very important to concentrate on improving the low-frequency sound transmission loss to achieve better overall sound insulation.

It is also important that single number ratings used to rank order the sound insulation of exterior walls should correctly reflect the low-frequency performance of the walls. The ASTM OITC rating[5] is a simple method for obtaining an appropriate single number rating of the sound insulation of exterior walls. The STC rating used for interior walls is not suitable for exterior walls.

The low-frequency sound transmission loss is limited by two types of low-frequency resonances that increase the transmitted sound energy. The new results in this article support the work of Lin and Garrelick[8] that predict a low-frequency structural resonance for a wood stud wall with rigidly attached surface layers, but a fundamentally different mass–air–mass resonance when the surface layers are not rigidly connected. For walls without a structural break between the outer surface layers, the ribbed panel system of the studs and surface layers leads to a primary structural resonance that occurs at about 125 Hz for a 406-mm stud spacing. This limits the overall performance of walls without structural breaks. However, this resonance shifts with the stud spacing. Using a larger stud spacing lowers the frequency of this resonance and effectively improves the overall sound insulation rating for walls without structural breaks.

For walls with a structural break between the two outer surfaces, the low-frequency performance is limited by the mass–air–mass resonance due to the mass of the surface layers and the stiffness of the air in the stud cavity. Increasing the mass of the surface layers and the depth of the air space can lower the frequency of this resonance and also improve the overall sound insulation rating. However, where the structural break is achieved by using resilient channels, the possible shift of this resonance is limited by the presence of the stiffness of the resilient channels[9] and only modest improvements in the overall sound insulating rating occur when additional mass is added to the surface layers. If a staggered stud wall system is used to achieve a structural break between the surface layers, larger improvements in the overall sound insulation rating can be achieved. For staggered stud walls, increasing the mass of the surface layers systematically lowers the mass–air–mass resonance frequency and significantly improves the overall sound insulating rating.

Related effects have been reported previously for interior walls.[11,12] Low-frequency dips in transmission loss versus frequency curves shifted to lower frequencies when the stud spacing or the spacing of the screws holding the gypsum board into wood studs was increased. The effect of varied stud spacing is qualitatively similar to that reported in this article. The effect of screw spacing is presumably because reducing the number of screws gradually decreased the effectiveness of the rigid connection and the system gradually approached one with a structural break. In the same study, stud and screw spacing had very little effect for walls constructed on light weight steel studs. This, too, would be expected because the steel studs provide a structural break and so reducing the number of screws has little further effect.

Although only a small number of 89-mm wood stud walls were tested in this project, they provided inferior performance to the corresponding walls built with 140-mm wood studs. This is again due to problems at low frequencies. The low-frequency resonances that limit the overall performance of a wall tend to increase in frequency when the smaller studs are used and hence lead to inferior overall sound insulation ratings.

These results have quantified the effects on sound insulation ratings of the principal parameters defining wood stud wall constructions. They provide a practical understanding of the importance of each of these parameters and give guidance for the design of exterior wood stud walls with improved sound insulation. Appropriate combinations of structural breaks and added mass can increase the OITC rating from 25 for the base wall to over 40 dB.

ACKNOWLEDGMENTS

This work was jointly supported by Transport Canada, the Canadian Department of National Defense, and the National Research Council of Canada with additional support from Vancouver International Airport. The author would like to thank Dr. Ivan Bosmans for pointing out the significance of Ref. 8.

[1] H. J. Sabine and M. B. Lacher, ''Acoustical and Thermal Performance of Exterior Residential Walls, Doors and Windows,'' National Bureau of Standards (U.S.) Bldg. Sci. Ser. 77 (November 1975).
[2] ASTM E90-97, ''Standard Test Method for Laboratory Measurements of Airborne Sound Transmission Loss of Building Partitions and Elements'' (ASTM, Philadelphia, 1997).
[3] J. S. Bradley and J. A. Birta, ''Laboratory Measurements of the Sound Insulation of Building Façade Elements,'' Institute for Research in Construction Internal Report IR-818, October 2000.
[4] J. S. Bradley and J. A. Birta, ''Comparison of Laboratory and Field Measurements of Sound Insulation Against Aircraft Noise,'' Proceedings Inter Noise 2000, Nice, France.
[5] ASTM E1332, ''Standard Classification for Determination of Outdoor-

Indoor Transmission Class'' (ASTM, Philadelphia, 1990).
[6] ASTM E413, ''Classification for Rating Sound Insulation'' (ASTM, Philadelphia, 1999).
[7] L. L. Beranek, *Noise and Vibration Control* (McGraw–Hill, New York, 1971).
[8] G.-F. Lin and J. M. Garrelick, ''Sound transmission through periodically framed parallel plates,'' J. Acoust. Soc. Am. **61**, 1014–1018 (1977).
[9] J. S. Bradley and J. A. Birta, ''A Simple Model of the Sound Insulation of Gypsum Board on Resilient Supports,'' Noise Control Eng. J. **40**, Sept./Oct. (2001).
[10] J. S. Bradley, ''Acoustical Measurements in Some Canadian Homes,'' Can. Acoust. **14**(4), 19–21, 24–25 (1986).
[11] J. D. Quirt and A. C. C. Warnock, ''Influence of sound absorbing material, stud type, and spacing and screw spacing on the sound transmission through a double-panel wall specimen,'' Proceedings Inter Noise 93, Leuven, pp. 971–974.
[12] J. D. Quirt, A. C. C. Warnock, J. A. Birta, and R. E. Halliwell, ''Influence of stud type and spacing, screw spacing and sound absorbing material on sound transmission through a double panel wall system,'' J. Acoust. Soc. Am. **92**, 2470 (1992).

Origin of the bell-like dependence of the DPOAE amplitude on primary frequency ratio

Andrei N. Lukashkin[a] and Ian J. Russell
School of Biological Sciences, University of Sussex, Falmer, Brighton BN1 9QG, United Kingdom

(Received 23 March 2001; revised 11 September 2001; accepted 17 September 2001)

For low and medium sound pressure levels (SPLs), the amplitude of the distortion product otoacoustic emission (DPOAE) recorded from guinea pigs at the $2f_1$-f_2 frequency is maximal when $f_2/f_1 \approx 1.23$ and decreases for lower and higher f_2/f_1 ratios. The high-ratio slope of the DPOAE dependence on the ratio of the primary frequencies might be anticipated since the f_1 amplitude at the f_2 place is expected to decrease for higher f_2/f_1 ratios. The low-ratio slope of the dependence at low and medium SPLs of the primaries is actually one slope of a notch. The DPOAE amplitude recovers from the notch when the f_2/f_1 ratio is further reduced. In two-dimensional space formed by the f_2/f_1 ratio, and the levels of the primaries, the notch is continuous and has a level-dependent phase transition. The notch is identical to that seen in DPOAE growth functions. Similar notches and phase transitions were observed for high-order and high-frequency DPOAEs. Theoretical analysis reveals that a single saturating nonlinearity is capable of generating similar amplitude notch and phase transition when the f_2/f_1 ratio is decreased because of the increase in f_1 amplitude at the DPOAE generation place (f_2 place). The difference between the DPOAE recorded from guinea pigs and humans is discussed in terms of different position of the operating point of the DPOAE generating nonlinearity. [DOI: 10.1121/1.1417525]

PACS numbers: 43.64.Bt, 43.64.Jb, 43.64.Kc [BLM]

I. INTRODUCTION

A pure tone peaks at its characteristic place (CF) along the basilar membrane (BM) as a consequence of the frequency selectivity of the cochlear partition. Two primary tones f_1 and f_2 cause vibrations with amplitudes A_1 and A_2, respectively, at their CFs, however, vibrations due to these tones are spread over a wider BM region of some finite length (Fig. 1). If the frequency separation between the primaries f_1 and f_2 is small enough, then these tones will interact. This interaction is nonlinear and gives rise to the distortion products at frequencies nf_1+mf_2, where n and m are integers.

The amplitude, A_1, of the low-frequency primary at its CF place is a function of the SPL, L_1, at frequency f_1. However, the amplitude of the same primary at the site of DPOAE generation, which is thought to be close to the f_2 place (Brown and Kemp, 1984) (point **P**, Fig. 1), is reduced in amplitude by a value $\Delta A_1 = A_1 - A_1'$. Here A_1' is the effective amplitude of f_1 at the site of DPOAE generation. The amplitude reduction ΔA_1 will depend on the frequency separation between the primaries, i.e., on to the f_2/f_1 ratio. A lower f_2/f_1 ratio corresponds to a smaller reduction of the amplitude ΔA_1. Therefore, for the same amplitude, A_1, of the BM vibrations at the CF place, the closer the low-frequency primary, f_1^*, is to the place of DPOAE generation, **P**, the higher its effective amplitude, A_1^* (Fig. 1). Thus it is essential to take into account *the level-dependent behavior* of the DPOAEs when interpreting results of experiments where the f_2/f_1 ratio is varied. As an approximation of this kind of experiment one can consider the situation when the amplitude of f_1 varies with a fixed value of the f_2 amplitude. Detailed theoretical analysis of the inter-modulation distortion product (DP) amplitude and phase behavior at the output of a single saturating nonlinearity for this paradigm has been given previously (Lukashkin and Russell, 1999; Fahey *et al.*, 2000). It has been shown that a single saturating nonlinearity can generate a distinctive amplitude notch and corresponding phase transition for constant amplitude of either of the two primaries when the amplitude of the second primary is varied. A similar amplitude-phase pattern has been observed experimentally (Whitehead *et al.*, 1992a, b; Mills and Rubel, 1994; Mills, 1997; Parham, 1997). We also demonstrated (Lukashkin and Russell, 1999) that the difference between DPOAEs measured in human and rodents (Whitehead, 1998) could be explained in terms of different positions of the operating point of the DPOAE-producing nonlinearity.

In this paper we analyze the DPOAE amplitude and phase patterns, which occur due to changes in the amplitude of the primaries at the place of DPOAE generation when the ratio of the primaries varies. Theoretical predictions are compared with experimental data collected from guinea pigs and human subjects. We show that the bell-like shape of the DPOAE dependence on the ratio of the primaries can be due to level-dependent effects. First, the bell-like shape seems to be a consequence of the notch accompanied by a corresponding phase transition in the nonmonotonic DPOAE growth function. Second, the mutual suppression between the frequency components at the output of the saturating nonlinearity also shapes the DPOAE amplitude dependence on the ratio of the primaries.

II. THEORETICAL BACKGROUND

In this paper we identify the DPOAE-producing nonlinearity with the hair cell mechanoelectrical transducer. De-

[a]Electronic mail: a.lukashkin@sussex.ac.uk

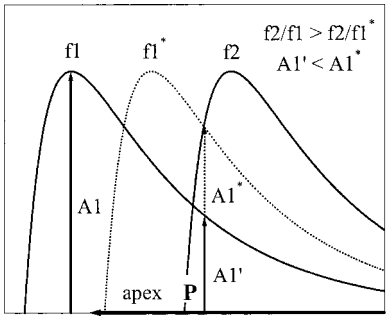

FIG. 1. Schematic pattern of excitation of high frequency, f_2, and low frequency, f_1 and f_1^*, primaries along the BM. Point **P** indicates the hypothetical place of the DPOAE generation. A_1 and A_2 are corresponding amplitudes of the primaries f_1 and f_2 in their CFs. A_1' and A_1^* are corresponding amplitudes of lower-frequency primaries f_1 and f_1^* in the DPOAE generation place. The amplitude of f_2 in the DPOAE generation place is assumed to be A_2 (see footnote 1).

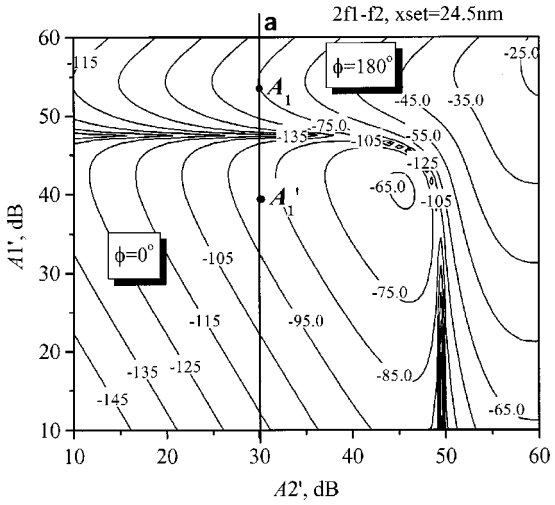

FIG. 2. Amplitude and phase angle of the DP at frequency $2f_1$-f_2 at the output of the nonlinearity $N(x)$ as a function of the amplitudes of the primary tones, A_1' and A_2'. Points $\mathbf{A_1}$ and $\mathbf{A_1'}$ represent the input signals to the nonlinearity $N(x)$ at the CF of f_1 and at the place of the DPOAE generation respectively. See main text for detailed explanation. Relative phase angle, ϕ, is indicated by labels inside each region of the plots limited by the notch. The shift of the operating point x_{set}=24.5 nm. The amplitude of the DPs is expressed in decibels *re*: $G_{tr\,max}$. 0 dB for the amplitudes of the primaries, A_1' and A_2', is equal to 0.1 nm.

tailed formulation of the model can be found elsewhere (Lukashkin and Russell, 1999). Briefly, we calculate the output of the nonlinearity $N(x)$ for the double sinusoidal input $x=A_1'\cos 2\pi f_1 t+A_2'\cos 2\pi f_2 t$, where A_1', A_2' and f_1, f_2 are the effective amplitudes and frequencies of the primaries, respectively. The nonlinearity $N(x)$ is considered in the form

$$N(x)=G_{tr}(x)-G_{tr}(0), \tag{1}$$

where x is the displacement of the hair bundle from its resting position, $G_{tr}(x)$ is the conductance of the hair cell mechanoelectrical transducer, and $G_{tr}(0)$ is the transducer conductance with zero displacement of the hair bundle. The conductance of the transducer $G_{tr}[x(t)]$ is given by (Crawford *et al.*, 1989; Kros *et al.*, 1995)

$$G_{tr}(x)=G_{tr\,max}\{1+\exp(a_2[x_2-x0-x_{set}-x]) \times[1+\exp(a_1[x_1-x0-x_{set}-x])]\}^{-1}, \tag{2}$$

where $G_{tr\,max}$ is the maximal transducer conductance, x_{set} is the steady state displacement of the hair bundle, and a_1, a_2, x_1, x_2 are constants. A constant $x0\approx 23.982$ nm is used to move the operating point into the point of inflection of the function Eq. (2) for a given set of constants a_1, a_2, x_1, x_2.

A. DP behavior in $A_1'\times A_2'$ space

Figure 2 shows the calculated amplitude and phase angles of the DP at the $2f_1$-f_2 frequency at the output of $N(x)$ as a function of the amplitudes, A_1' and A_2', of the primaries. A steady state displacement of the bundle (x_{set}=24.5 nm in this case) was chosen to obtain the amplitude notch with corresponding phase transition frequently observed for DPOAE recordings at the same frequency (Whitehead *et al.*, 1992a, b; Mills and Rubel, 1994; Mills, 1997; Parham, 1997). An analogous notch would be observed if the operating point of the nonlinearity were situated below the inflection point of the function $N(x)$ (see Fig. 3 in Lukashkin and Russell, 1999). Strong experimental evidence to support the chosen position of the operating point can be observed in the receptor potentials recorded from the outer hair cells. The receptor potential reveals a negative dc component in response to low SPL tones close to the characteristic frequency, in both low frequency (Dallos *et al.*, 1982; Dallos, 1986; Dallos and Cheatham, 1989) and high-frequency (Cody and Russell, 1987) regions of the cochlea. This negative dc component would be expected if the operating point were positioned above the point of inflection (Lukashkin and Russell, 1998). The response of DPOAEs to acoustical and electrical biasing of the cochlear partition (Frank and Kössl, 1996, 1997) also supports the location of the operating point above the point of inflection.

A cross-section along the straight line **a** in Fig. 2 corresponds to an experimental protocol when the amplitude A_2 is kept constant[1] (in this particular case at 30 dB *re*: 0.1 nm) and the amplitude A_1' varies. The frequency selectivity of the cochlea determines that the amplitude of the BM displacements at frequency f_1 in the DPOAE generation place decreases as the frequency separation between the primaries increases even when the sound pressure at frequency f_1 does not change. Equation (2) does not reflect the frequency selectivity of the real cochlea but this decrease in the BM displacement could be specified as the decrease, ΔA_1, in the amplitude of the input to the model. Let us remember that ΔA_1 is defined as the difference between the amplitude, A_1, of the BM displacement to the f_1 frequency at the f_1 CF place and the amplitude, A_1', at the site of DPOAE generation (Fig. 1). Then the thick points on line **a** correspond to different experimental conditions, when the sound pressure at frequency f_1 is the same but the ratio f_2/f_1 decreases from point $\mathbf{A_1}$ to $\mathbf{A_1'}$. Then in terms of the model, the input of the nonlinearity $N(x)$ at frequency f_1 is a function of two parameters, A_1 and ΔA_1, where A_1 *is analogous to* L_1, *i.e., to the SPL of the* f_1 *primary, and* ΔA_1 *is a model analogue of the ratio* f_2/f_1 *of the frequencies of the primaries*. Hence the double sinusoidal input signal to the nonlinearity can be expressed as

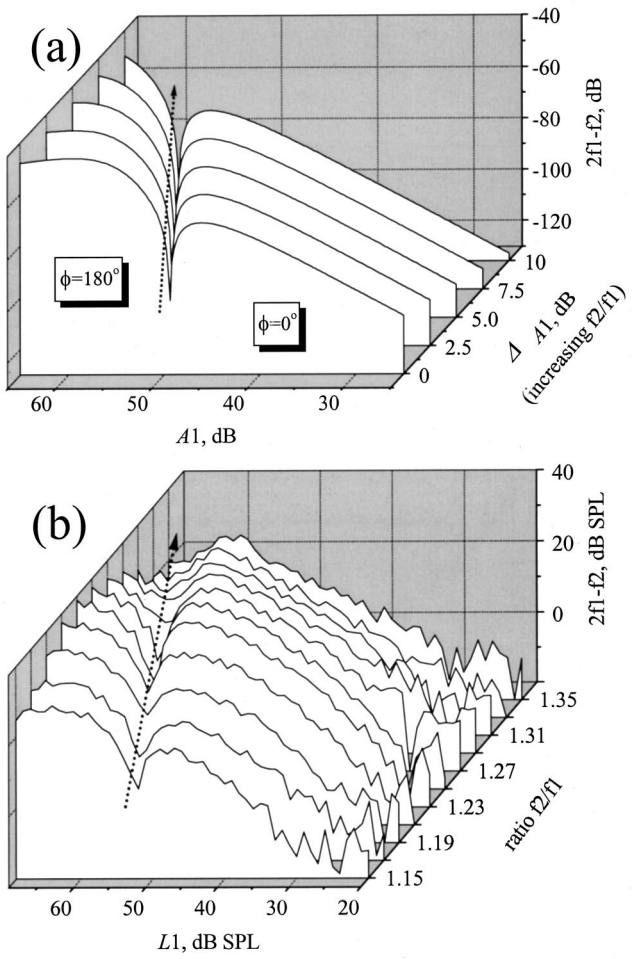

FIG. 3. (a) Amplitude and phase angle of the DP at frequency $2f_1$-f_2 at the output of the nonlinearity $N(x)$ as a function of the amplitude A_1. Curves were calculated for different levels of attenuation ΔA_1. Amplitude A_2 was constant and equal to 30 dB. Effective input amplitude A_1' to the nonlinearity was calculated as $A_1'=A_1+\Delta A_1$. Relative phase angle, ϕ, is indicated by labels inside each region of the plots limited by the notch. The shift of the operating point $x_{set}=24.5$ nm. Amplitude of the DPs is expressed in decibels *re*: $G_{tr\,max}$. 0 dB for the amplitudes of the primaries, A_1 and A_2, is equal to 0.1 nm. (b) Amplitude and phase angle of the DPOAE at frequency $2f_1$-f_2 as a function of L_1 recorded for different ratios f_2/f_1. High-frequency primary f_2 was 12 kHz and has a constant level of 48 dB SPL. Note the shift of the amplitude notch indicated by the dotted arrow.

$$x=A_1'2\pi f_1 t+A_2'\cos 2\pi f_2 t$$
$$=(A_1\text{-}\Delta A_1)\cos 2\pi f_1 t+A_2\cos 2\pi f_2 t.$$

Therefore, if the notch appears at a particular value of A_1', then the A_1 value leading to the appearance of the notch decreases when the f_1 frequency approaches f_2 (i.e., when the f_2/f_1 and ΔA_1 are small) [Fig. 3(a)]. Consequently the model predicts that the DPOAE amplitude notch has to appear for lower L_1 when the f_2/f_1 ratio is smaller and the L_2 level is kept constant.

B. DP behavior in $\Delta A_1 \times (A_1, A_2)$ space resembling rodent DPOAE

The description of the experimental paradigm above enables us to predict DPOAE behavior when f_1 is swept while f_2 and the SPLs of the both primaries are held constant. Thus the L_1 and its model analogue, i.e., A_1, remain constant. However, the amplitude reduction ΔA_1 undergoes changes to mimic the variation of the f_1 amplitude in the DPOAE generation place. Consequently, the effective input A_1' to the nonlinearity also changes. For example, the amplitude of the BM vibrations with frequency f_1 in place of the DPOAE generation increases when the f_1 primary comes closer to the f_2. In Fig. 2 it corresponds to the upward shift of the point $\mathbf{A_1'}$ along line **a**. The shift of point $\mathbf{A_1'}$ can be large enough to intersect the notch. Keeping in mind our model analogies: $\Delta A_1 - f_2/f_1$ and $A_1 - L_1$; we can conclude that the notch and corresponding phase transition could be observed at the DPOAE frequency for sufficiently large reductions in the $f2/f_1$ ratio [Fig. 4(a)]. Figure 4(a) illustrates this effect for different levels of primaries when both primaries grow in synchrony (the difference between the levels of primaries remains constant). Because the notch appears at a particular value of A_1', the value of ΔA_1, which is necessary to obtain the DP notch, depends on A_1 (the difference $A_1-\Delta A_1$ should be constant) (Fig. 2). If A_1 is set to a high level, then ΔA_1 must be set to larger values in order for the DP to be reduced and its phase to be reversed. Hence, if L_1 is high, larger f_2/f_1 ratios are required to obtain the notch and the corresponding phase transition observed in the DPOAEs. This shift of the notch gives rise to a distinctive diagonal canyon in the two-dimensional space of the ratio of the primaries and their amplitudes [Fig. 4(a)]. However, there is an obvious limitation on the range of A_2 values where the notch can be observe. For a chosen position of the operating point of the nonlinearity, a notch could not be observed at any values of A_1 and ΔA_1 above $A_2 > 49$ dB [Fig. 4(a)], i.e., when line **a** is shifted to the right of $A_2 = 49$ dB (Fig. 2).

From Fig. 4(a), it is clear that the amplitude of the DP decreases when ΔA_1 is reduced. In a real experiment this amplitude reduction appears when the frequency separation between the primaries is reduced. The effect is especially prominent for higher levels of the primaries and originates in mutual suppression between the primaries. The mechanism of the DP suppression is the same as that we described previously for suppression of the output at the frequencies of the primaries (Lukashkin and Russell, 1998). The energy of the input primaries is re-distributed between theoretically infinite number of DPs at the output of the saturating nonlinearity. Because the higher-order DPs at the output of the nonlinearity grow faster than the lower-order DPs, a decrease in the power output, i.e., suppression, can be observed at the frequencies of the lower-order DPs for high levels of the input primaries. Predictably the same outflow of energy from the low-order DPs takes place when only the input amplitude A_1' increases while the A_2' amplitude is kept constant, as we have considered in the current section.

A high-frequency DP $2f_2$-f_1 [Fig. 5(a)] demonstrates the same pattern of the amplitude and phase dependence in two-dimensional space of the ΔA_1 and the amplitudes of the primaries A_1 and A_2 for chosen position of the operating point. The essential difference between the $2f_1$-f_2 and $2f_2$-f_1 counterparts is a difference in slope of the amplitude dependence on ΔA_1 [Figs. 5(a), 6(a)]. Because only A_1' changes in this case while A_2' remains constant, the $2f_2$-f_1

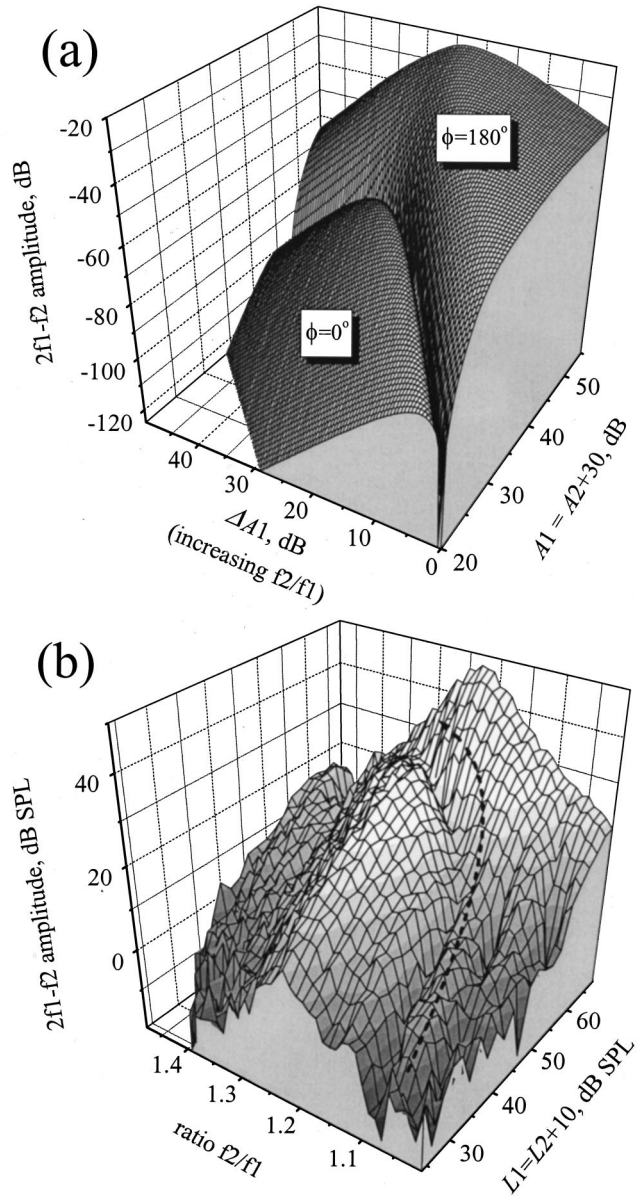

FIG. 4. (a) Amplitude and phase angle of the DP at frequency $2f_1$-f_2 at the output of the nonlinearity $N(x)$ as a function of the amplitudes of the primary signals, A_1 and A_2 and attenuation ΔA_1. Effective input amplitude A_1' at every point of two dimensions was calculated as $A_1'=A_2+\Delta A_1+30$ dB. Relative phase angle, ϕ, is indicated by labels inside each region of the plots limited by the notch. The shift of the operating point $x_{\text{set}}=24.5$ nm. The amplitude of the DPs is expressed in decibels *re*: $G_{\text{tr max}}$. 0 dB for the amplitudes of the primaries, A_1 and A_2, is equal to 0.1 nm. (b) Amplitude of the DPOAE at frequency $2f_1$-f_2 as a function of the amplitudes of the primary signals and ratio of their frequencies. f_2 was kept fixed at 12 kHz. L_2 was 10 dB SPL below L_1.

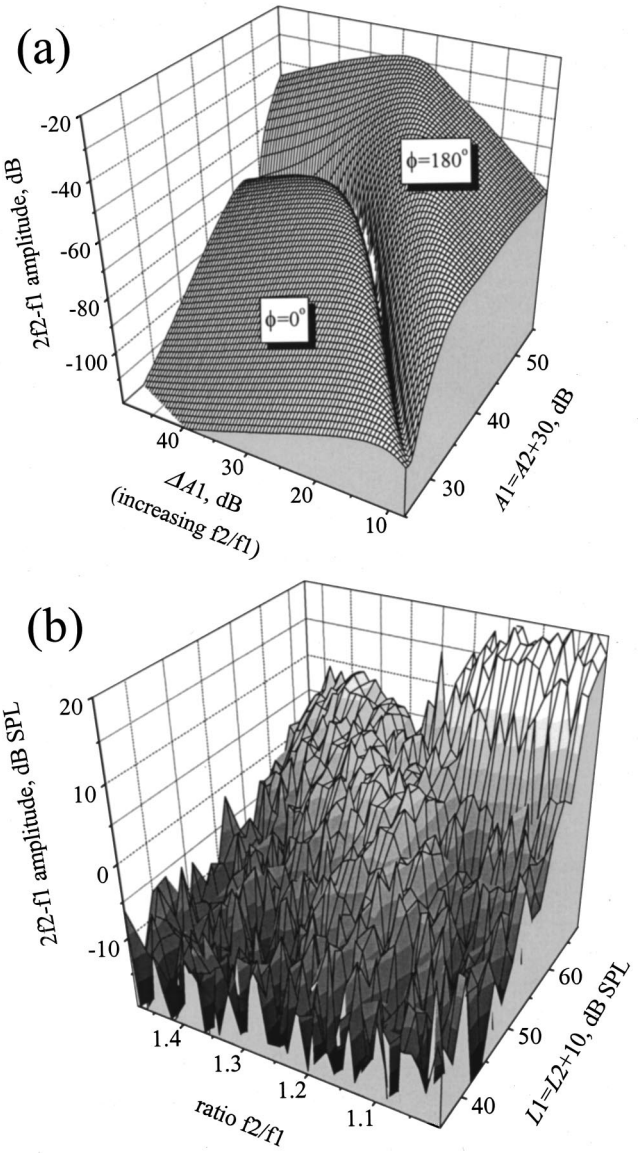

FIG. 5. As in Fig. 4 but for DP and DPOAE at frequency $2f_2$-f_1.

component grows with a slope of unity in the region that is far from saturation. However, under the same conditions $2f_1$-f_2 grows with a slope of two. Similar dependence (not shown) of the DP amplitude and phase on the ΔA_1 and amplitudes A_1 and A_2 is also observed for the higher-order DPs, e.g., $3f_1$-$2f_2$, $3f_2$-$2f_1$, $4f_1$-$3f_2$, etc., for the chosen position of the operating point. However, the notch occurs for progressively higher levels of the input signal A_1' or, when A_1 and A_2 are constant, for progressively lower ΔA_1 with increasing order of the DPs [Fig. 6(a)]. This effect leads to a shift in the peak of the DP amplitude, along the axis of ΔA_1. On the bases of this observation we can predict a shift of the higher-order DPOAE peaks toward smaller f_2/f_1 ratios for the same L_1 and L_2.

C. DP behavior in $\Delta A_1 \times (A_1, A_2)$ space resembling human DPOAE

We suggested (Lukashkin and Russell, 1998) that the amplitude notch and corresponding phase transition in DPOAE growth functions observed in some species of mammals could be due to the disappearance and sudden phase reversal of DPs seen at the output of a single saturating nonlinearity. However, the notch and phase transition cannot be observed for $2f_1$-f_2 DP when the operating point of the saturating nonlinearity is situated within a certain range near the point of inflection of the function $N(x)$ (Lukashkin and Russell, 1999). This kind of DP behavior resembles the monotonic growth of the DPOAE input–output functions frequently recorded from humans (Whitehead, 1998). When the

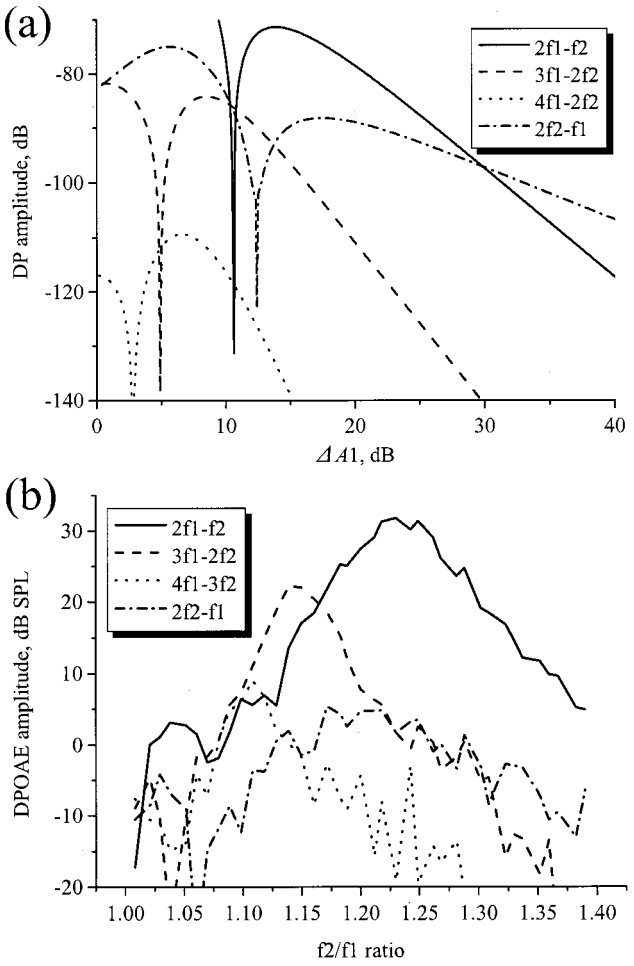

FIG. 6. (a) Amplitude of different order DPs at the output of the nonlinearity $N(x)$ as a function of attenuation ΔA_1. DP frequencies are indicated inside the panel for each curve. Amplitudes of the primaries were $A_2=A_1-30$ dB$=30$ dB. The shift of the operating point $x_{\text{set}}=24.5$ nm. Amplitude of the DPs is expressed in decibels *re*: $G_{\text{tr max}}$. 0 dB for the amplitudes of the primaries, A_1 and A_2, is equal to 0.1 nm. (b) Amplitude of the odd-order DPOAEs recorded from a guinea pig at four different frequencies as a function of the ratio f_2/f_1 of the primaries. f_2 was 12 kHz. DPOAE frequencies are indicated inside the panel for each curve. Amplitudes of the primaries were $L_1=L_2+10$ dB SPL$=52$ dB SPL for $2f_2$-f_1 and $L_1=L_2+10$ dB SPL$=46$ dB SPL for the other frequency components.

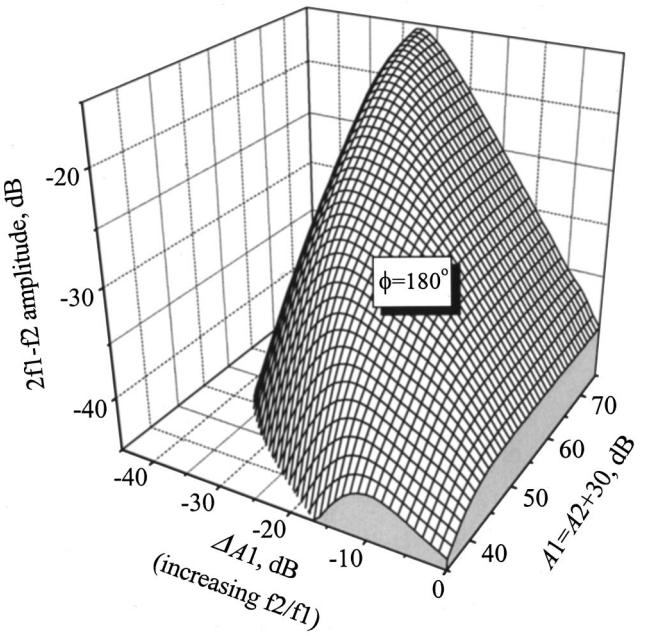

FIG. 7. Amplitude and phase angle of the DP at frequency $2f_1$-f_2 at the output of the nonlinearity $N(x)$ as a function of the amplitudes of the primary signals, A_1 and A_2 and attenuation ΔA_1. In this case the shift of the operating point $x_{\text{set}}=0$ nm. Effective input amplitude A_1' at every point of two dimensions was calculated as $A_1'=A_2+\Delta A_1+30$ dB. Relative phase angle, ϕ, is indicated by the label. Amplitude of the DPs is expressed in decibels *re*: $G_{\text{tr max}}$. 0 dB for the amplitudes of the primaries, A_1 and A_2, is equal to 0.1 nm.

operating point of the nonlinearity is situated near its point of inflection, modeling of the f_1 sweep, while f_2 is held constant using the same model analogues (ΔA_1-f_2/f_1,A_1-L_1), reveals the same bell-like shape of the DP amplitude dependence on the f_2/f_1 ratio (Fig. 7) as shown in Figs. 4(a), 5(a), and 6(a). However, *the amplitude notch does not appear in this case*. The decrease in the DP amplitude, when f_1 gets closer to the f_2 place (i.e., ΔA_1 is reduced), originates entirely from mutual suppression as a consequence of the redistributed energy of the primaries. The model also predicts a shift of the peak amplitude of the DPOAEs toward higher f_2/f_1 ratios for higher SPLs of the primaries (Fig. 7).

III. METHODS

Pigmented guinea pigs (250–350 g) were anaesthetized with the neurolept anaesthetic technique (0.06 mg/kg atropine sulphate s.c., 30 mg/kg pentobarbitone i.p., 250 μl/kg Hypnorm i.m.). Additional injections of Hypnorm were given every 40 min. Additional doses of pentobarbitone were used as needed to maintain an areflexive state. The heart rate was monitored with a pair of skin electrodes placed on both sides of the thorax. The animals were tracheotomized, artificially respired, and core temperature was maintained at 38 °C with a heating blanket and head holder. The middle ear cavity of the ear used for DPOAE measurements was open to equilibrate air pressure on both sides of the tympanic membrane (Zheng *et al.*, 1997).

Sound was delivered to the tympanic membrane by a closed acoustic system comprised of two Bruel & Kjaer 4133 1/2-in. microphones for delivering tones and a single Bruel & Kjaer 4133 1/2-in. microphone for monitoring sound pressure at the tympanum. The microphones were fed into a coupler that was positioned within the opening of the ear canal so that its tip was within 1 mm of the tympanic membrane. The sound system was calibrated *in situ* using a measuring amplifier (Hartley, Brighton, U.K.) for frequencies between 1 and 50 kHz, and known sound pressure levels were expressed in dB SPL *re*: 2×10^{-5} Pa. White noise for acoustical calibration and tone sequences for the ear stimulation were synthesised by a Data Translation 3010 board and delivered to the microphones at a sampling frequency of 200 kHz. Signal from the measuring amplifier was digitized at 200 kHz using the same board and averaged in the time domain. Amplitudes and phase angles of the spectral peaks were found from the resultant 4096 point time sequences. Phase data were corrected for the phase angles of the primaries (Mills and Rubel, 1997). Experimental control, data acquisition, and data analysis were performed using a PC with

programs written in Testpoint (CEC, MA, USA).

The following experimental procedures were used:

(i) DPOAE-grams (f_2 sweeps, f_2/f_1 ratio is constant, L_1 and L_2 are constant, L_2 is 10 dB SPL below L_1) for low level primaries were recorded on a regular basis during experiment (up to 5 h) to confirm that the animal remained in stable conditions. Data collected from an animal were discharged if the DPOAE level changed more than 5 dB at f_2 frequencies used for the other procedures.

(ii) DPOAE growth functions with increasing L_1 were measured while keeping L_2 and the frequencies of the primaries constant. The growth functions were measured at different L_2 so that we could use them to construct DPOAE behavior in two-dimensional space.

(iii) DPOAE ratio functions measured during f_1 sweeps with constant f_2. L_1 and L_2 were constant during each sweep with L_2 being 10 dB SPL below L_1. The ratio functions were measured at different L_1 so that we could use them to construct DPOAE behavior in two-dimensional space.

All procedures involving animals were performed in accordance with U.K. Home Office regulations.

IV. RESULTS

To simplify the model we assumed that, in the f_2 place, the growth of the f_1 amplitude expressed in decibels is inversely proportional to ΔA_1, i.e., to the f_2/f_1 ratio, for any level and ratio of the primaries. This is obviously a limitation. Tuning of the BM is very sharp for low SPLs (Russell and Nilsen, 1997) so that one can expect a fast increase of the f_1 amplitude as seen in the DPOAE generation place but only when f_1 is situated in the close vicinity of the f_2 place. Tuning becomes poorer for high SPLs and the vibration envelope extends further basally along the BM (Russell and Nilsen, 1997) so that one can expect a slow increase of the f_1 amplitude in the f_2 place when f_1 approaches the f_2 place. A slow increase of the f_1 amplitude should be observed for any level of primaries when the DPOAE generation place is located in the tail region of the f_1 envelope, i.e., for higher f_2/f_1 ratios. Because of the lack of any frequency selectivity in our model (two tones of equal amplitude produce equal input to the nonlinearity), the model does not show this type of dependence of the high-ratio slope on the amplitude of the primaries [Fig. 4(a)]. There is a second limitation that should be taken into account while comparing theoretical and experimental data. The model includes a ''perfect'' pointlike nonlinearity and the depth of the notches in this case is limited only by the resolution of the model, i.e., the number of calculations. The depth of the experimental notches cannot be infinitely improved by changing the experimental parameters with a smaller step because in this case the responses are generated by a distributed nonlinearity with time delay and damping. In this case the notches are smeared and phase transitions are less abrupt. Therefore, in taking into account the limitations of the model we did not try to fit the model parameters to the experimental data and confined our analysis confined to a qualitative comparison of the model and experimental observations.

A. DPOAE recorded from guinea pigs

Figure 3(b) shows DPOAE growth functions at frequency $2f_1$-f_2 recorded when L_1 was varied and L_2 was kept constant. Variations of the amplitude notch position for different ratios of primaries are similar to those expected if the notch occurs due to a single saturating nonlinearity [Fig. 3(a)]. The notch becomes broader and less pronounced for a larger f_2/f_1 ratios. The broadening of the notch might be anticipated because under these conditions the place of the DPOAE generation, i.e., the f_2 place, is situated in the far tail region of f_1 where the amplitude and phase gradients of the BM vibrations are much shallower (Russell and Nilsen, 1997). As a result of these shallow gradients, the DPOAE might be generated from an extended region of the BM and the vector summation of the DPOAE from different parts of this prolonged region might lead to a partial cancellation of the notch.

A prominent amplitude elevation and distinctive diagonal canyon appear in the two-dimensional space of the ratio of the primaries and their amplitudes for DPOAE recorded at frequencies $2f_1$-f_2 [Fig. 4(b)]. The pattern of the DPOAE amplitude in the two-dimensional space is remarkably similar to that produced by a single saturating nonlinearity [Fig. 4(a)]. The diagonal canyon in the theoretical figure [Fig. 4(a)] is identical to the amplitude notch of the DP growth functions. Essentially only the amplitude of the primaries was varied to reveal this canyon. The similarity between the theoretical and experimental data leads us to conclude that the diagonal canyon in the experimental data is also due to level-dependent effects and is produced by a single nonlinearity. It appears as a consequence of the increase of the f_1 amplitude in the DPOAE generation place with the reduction in frequency separation. Essentially the same amplitude pattern is observed for the high-frequency component $2f_2$-f_1 [Fig. 5(b)] when both the amplitude elevation and diagonal canyon can be seen. However, the amplitude elevation is not as prominent for $2f_2$-f_1 as it is for its low-frequency counterpart $2f_1$-f_2 [Fig. 4(b)] because of severe low-pass filtering in the relatively low-frequency place of the DPOAE generation. The best $2f_2$-f_1 ratio for the lowest SPLs, when $2f_2$-f_1 protrudes above the noise floor is around 1.2 and the $2f_2$-f_1 peak shifts in the direction of the higher f_2/f_1 ratios when the SPLs of the primaries are increased.

Cross-sections of the amplitude elevation by planes, which are perpendicular to the base of Figs. 4(b), 5(b), and parallel to the axis of the ratios, represent data collected during f_1 sweeps. The cross-sections have a bell-like shape that has been attributed to band-pass filtering of the DPOAE (Brown *et al.*, 1992; Allen and Fahey, 1993). It is obvious from our data [compare Figs. 4(a) and (b), 5(a) and (b), 6(a) and (b)] that the low-ratio slope of the bell-shape response to low and medium SPLs (up to $L_1 \cong 55$ SPL for $2f_1$-f_2 and $L_1 \cong 60$ dB SPL for $2f_2$-f_1) is actually one slope of the notch produced by a single saturating nonlinearity. The DPOAE amplitude recovers from the notch when the f_2/f_1 ratio is

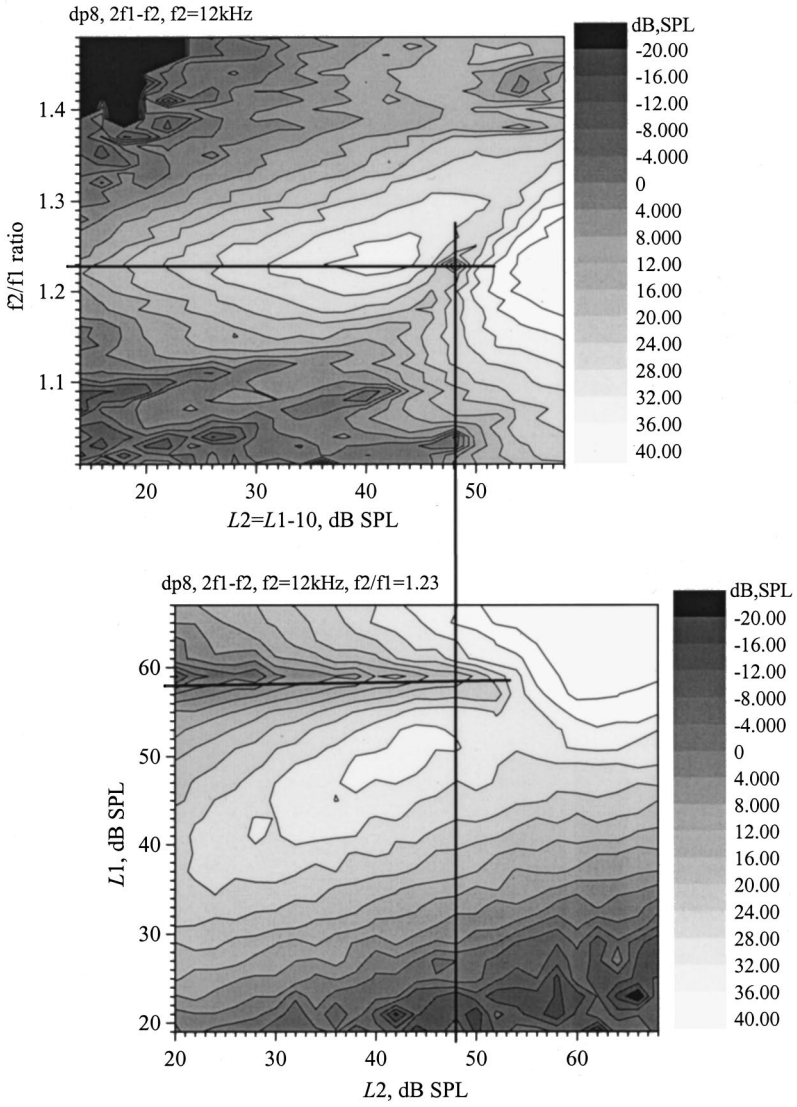

FIG. 8. Amplitude of the DPOAE at frequency $2f_1$-f_2 as a function of the amplitudes of the primary signals and ratio of their frequencies (top panel) and as a function of the amplitude of the primaries (bottom panel). f_2 was kept fixed at 12 kHz. L_2 was 10 dB SPL below L_1 for the top panel. Ratio f_2/f_1 was 1.23 for the bottom panel. The gray scale charts on the right of both panels show the corresponding amplitude of the $2f_1$-f_2 component in dB SPL.

further reduced. For higher SPLs, when the notch appears for relatively large f_2/f_1 ratios, the low-ratio slope of the bell-like dependence of the $2f_1$-f_2 amplitude could occur as a result of the suppression effect as demonstrated by our model calculations [Figs. 4(a), 5(a)]. Then the experimentally observed decrease of the slope for the smallest f_2/f_1 ratio might be expected because, under these conditions, the amplitude of f_1 at the DPOAE generation place reaches its maximum possible value that corresponds to the amplitude of the BM vibrations at the best frequency place. Furthermore, the high-ratio slope of the DPOAE dependence on the f_2/f_1 ratio might be anticipated since the f_1 amplitude at the DPOAE generation place will be expected to decrease for higher ratios of f_2/f_1. In connection with limitations of the model, we have shown that this decrease of the f_1 amplitude should be sharpest for low-ratio, low SPL primaries. Consequently one can expect the sharpest changes in the measured DPOAE amplitude for the same conditions in the experiment. Exactly these variations of the high-ratio slope are observed for the lower sideband components [Fig. 4(b)]. The concave shape of the high-ratio slopes of the low-frequency DPOAEs is best seen in Fig. 6(b). However, the slope of the high-frequency component $2f_2$-f_1 is formed by the low-pass BM filter and does not reveal a concave shape. Data presented in Fig. 6(b) also confirm the theoretically predicted shift [Fig. 6(a)] of the amplitude notch of the higher-order DPOAE in the direction of smaller f_2/f_1 ratios, when the effective amplitude of low-frequency primary f_1 is higher in the DPOAE generation place. When the amplitude of the lower sideband DPOAEs of different orders are plotted versus their frequencies (not shown) they confirm the well-established experimental fact that the DPOAEs peak at approximately the same frequency (Brown *et al.*, 1992; Allen and Fahey, 1993). However, our data reveal the same systematic variation of the peak frequency of the different order DPOAEs that has been recently reported by Schneider *et al.* (2001).

Theoretical data also explain the experimentally observed shift of the maximum DPOAE amplitude to a higher f_2/f_1 ratio with an increase in the amplitudes of the primaries. The shift of the maximum in this case is simply a consequence of the corresponding displacement of the amplitude notch. It is easier to recognize the shift of the DPOAE amplitude maximum using the contour plot shown in Fig. 8 (top panel). The contour plot also helps to show that the diagonal canyon observed in the two-dimensional space of the ampli-

tude of the primaries and their frequency ratio, $f_2/f_1 \times L_1, L_2$, and the notch in the two-dimensional space of the amplitude of the primaries, $L_1 \times L_2$, are identical. A straight line perpendicular to the ratio axis at the point $f_2/f_1 = 1.23$ intersects the diagonal canyon when $L_2 = 48$ dB SPL ($L_1 = L_2 + 10 = 58$ dB SPL) [Fig. 8 (top panel)]. Two straight lines corresponding to $L_2 = 48$ dB SPL and $L_1 = 58$ dB SPL intersect exactly at the bottom of the notch in $L_1 \times L_2$ space [Fig. 8 (bottom panel)]. Because the canyon spreads continuously in both directions from the point of intersection, which we considered in Fig. 8 (top panel), we conclude that the entire canyon is apparently due to an amplitude driven effect, i.e., because L_1 changes in the f_2 place during $f1$ sweeps.

The amplitude notch parallel to the L_2 axis in the $L_1 \times L_2$ space is distinctive and sharp [Fig. 8 (bottom panel)]. However, the same figure shows that the notch parallel to the L_1 axis is less pronounced. This partial elimination of the notch may occur because of broadening of the f_2 peak, i.e., the place of DPOAE generation, at high levels of L_2 (Russell and Nilsen, 1997) and subsequent phase cancellation between DPOAEs originating from different part of the broad peak.

B. DPOAE recorded from humans

Data collected for human subjects using the same experimental paradigms as in the current paper are widely available in the literature (see, for example, Harris *et al.*, 1989; Brown and Gaskill, 1990; Abdala, 1996; Stover *et al.*, 1999; Kummer *et al.*, 2000; Moulin, 2000). The pattern of the DPOAE behavior in this case is very much the same as the pattern of the calculated DP amplitude with the operating point of the nonlinearity situated near the point of inflection of the function (1). The notch and corresponding phase transitions are not observed for any amplitude of the primaries. Again, the similarity between the theoretically derived and measured curves provides full support for the model. Thus the model reproduces all of the major features of the experimental data (Fig. 7). The DPOAE amplitude grows due to an increase in L_1 in the f_2 place when separation between the primaries decreases. Suppression of the DPOAE amplitude is observed because of the re-distribution of the energy between the frequency spectral components with further reduction of the f_2/f_1 ratio. The maximum of the DPOAE shifts toward the larger f_2/f_1 ratio for higher SPLs of the primaries due to the more pronounced suppression which is caused by the high-level primaries. An amplitude notch is sometimes seen in human DPOAE responses recorded from low-frequency regions of the cochlea or from hearing-impaired subjects. This observation possibly indicates that under these circumstances the operating point of the DPOAE producing nonlinearity is situated further away from its point of inflection.

V. DISCUSSION

Data presented in this paper support the view that the dependence of the DPOAE amplitude on the ratio of primaries for DPOAEs recorded either from guinea pigs or from humans is a natural consequence of the nonlinearity and frequency selectivity of the system. Variations in the ratio of the primaries lead to changes in the effective amplitude of the low-frequency primary in the DPOAE generation place and consequent amplitude-dependent phenomena at the output of the nonlinearity, i.e., nonmonotonic growth of the distortion products and mutual suppression. We identified the DPOAE producing nonlinearity with the saturating input–output function of the mechanoelectical transducer. Exactly this type of nonlinearity shows suppression of the frequency spectral components at the output when the input signals reach the level of saturation of the transfer function (Lukashkin and Russell, 1998; Fahey *et al.*, 2000). We suggested that the decrease in the amplitude of the DPOAE observed for small f_2/f_1 ratios is due to the amplitude notch for low and intermediate values of SPLs of the primaries and to the mutual suppression for high level primaries. Allen and Fahey (1993) have considered the suppression mechanism to explain the DPOAE decrease at small ratios of the primaries. However, because the DPOAE spectral components of different orders peak at about the same frequency of half an octave below the f_2, a conclusion was made in favor of band-pass filtering of the DPOAE energy in the cochlea (Brown *et al.*, 1992; Allen and Fahey, 1993). This filter was associated with the tectorial membrane which, it has been proposed, is tuned to a frequency about a half of an octave below the CF of the BM in every location along the cochlear partition. However, the concept of a ''half an octave below'' filter could be an oversimplification of the experimental data (Stover *et al.*, 1999). Detailed investigation of the problem (Schneider *et al.*, 2001) reveals that there is a systematic variation of the DPOAE peak frequency depending on the order of the DPOAE. According to our data, the higher-order DPOAEs have maxima at lower f_2/f_1 ratios [Fig. 6(b)], i.e., at about the same frequency as the $2f_1$-f_2 component but the relative position of the DPOAE the maxima can vary depending on the conditions of the recording: the level of the primaries and the place of the DPOAE generation. Two factors also make it difficult to localize the DPOAE peaks exactly: the peaks become broader for high level primaries and the higher-order DPOAEs are contaminated by noise because of their small amplitude. Within the frame of the current model we are not able to compare the absolute position of the theoretical DP maxima along the DP frequency scale because experimental data on mapping ΔA_1 to the frequency ratio f_2/f_1 is lacking. Nevertheless, if we accept the less strict condition, that the higher-order DPOAEs peak at lower f_2/f_1 ratio, then the experimental data [Fig. 6(b)] are in full agreement with the prediction of the theory [Fig. 6(a)].

There are two experimental observations that cannot be explained by the ''filter'' theory but are in accordance with the level dependent effects of f_1 at the place of the DPOAE generation. First of all, the ''second filter'' cannot explain the bell-like shape of the high-frequency component $2f_2$-f_1 [Fig. 6(b)]. The $2f_2$-f_1 has a frequency higher than the f_2 primary and should be low-pass filtered by the ''second filter.'' However, its amplitude decreases with the reduction of the f_2/f_1 ratio as predicted by our model [Fig. 6(a)]. The second observation refers to the DPOAE amplitude dependence on the ratio of the primaries, which mimic the band-

pass filter responses, recorded from birds with a tectorial membrane of very different morphology and from the ears of lizards without tectorial membrane (Taschenberger *et al.*, 1995). Obviously, the ''second filter'' hypothesis cannot explain these last results. Neither can they explain the presence of the diagonal canyon in the two-dimensional space of the ratio of primaries and their amplitudes reported in this paper. The presence of the diagonal canyon cannot be explained if the bell-like shape of the DPOAE dependence on the ratio of the primaries is due to a single nonlinear resonance (van Dijk and Manley, 2001). In the last case the explanation of the DPOAE behavior involves a nonsaturating nonlinearity that does not show the amplitude notches with corresponding phase transitions in the output spectral components. An alternative explanation (Stover *et al.*, 1999) of the DPOAE dependence on the ratio of the primaries utilizes an idea about multiple sources for the DPOAE generation (Furst *et al.*, 1988; Whitehead *et al.*, 1992a, b; Brown *et al.*, 1996; Stover *et al.*, 1996). According to this hypothesis, the DPOAE is initially generated near the f_2 characteristic place and propagates in both basal and apical directions toward the DPOAE characteristic place, producing stimulus frequency emission at the DPOAE frequency. The stimulus frequency emission can also propagate basally and sum with the emission from the f_2 place. Therefore, the DPOAE emissions recorded in the ear canal would be the result of the vector summation of the emission from these two sources. Variation in the amplitude and phase of the DP from these two sources can give rise to a complex pattern of the vector sum, and, for example, originate its bell-like dependence on the f_2/f_1 ratio. We do not question the existence of the two sources of the DPOAE which is strongly supported by experimental evidence (Brown *et al.*, 1996; Moulin and Kemp, 1996a, b; Stover *et al.*, 1996; Wable *et al.*, 1996; Whitehead *et al.*, 1996; Fahey and Allen, 1997; He and Schmiedt, 1997; Heitmann *et al.*, 1998). It is possible that emission from the two sources may contribute into the decrease in the DPOAE amplitude when the separation between the primaries is reduced. On the basis of our data we cannot also totally exclude the possibility that the DPOAEs receive a ''second filtering.'' However, these models must include a saturating nonlinearity and frequency selectivity of the cochlea which, according to our data, can explain the experimental observation without the involvement of additional mechanisms.

ACKNOWLEDGMENTS

We thank Paul F. Fahey for valuable discussion of an early version of this work. This work was supported by a grant from the Wellcome Trust.

[1]Here and further we assume that the effective amplitude A_2' of the higher-frequency primary f_2 in the DPOAE generation place is A_2 and this does not change for different ratios of f_2/f_1, i.e., the place of generation is the same for different ratios of f_2/f_1. This assumption may be incorrect when f_2/f_1 is close to unity (Knight and Kemp, 2000).

Abdala, C. (**1996**). ''Distortion product otoacoustic emission ($2f_1$-f_2) amplitude as a function of f_2/f_1 frequency ratio and primary tone level separation in human adults and neonates,'' J. Acoust. Soc. Am. **100**, 3726–3740.

Allen, J. B., and Fahey, P. F. (**1993**). ''A second cochlear frequency map that correlates distortion product and neural tuning measurement,'' J. Acoust. Soc. Am. **94**, 809–817.

Brown, A. M., and Gaskill, S. A. (**1990**). ''Measurement of acoustic distortion reveals underlying similarities between human and rodent mechanical responses,'' J. Acoust. Soc. Am. **88**, 840–849.

Brown, A. M., and Kemp, D. T. (**1984**). ''Suppressibility of the $2f_1$-f_2 stimulated acoustic emissions in gerbil and man,'' Hear. Res. **13**, 29–37.

Brown, A. M., Gaskill, S. A., and Williams, D. M. (**1992**). ''Mechanical filtering of sound in the inner ear,'' Proc. R. Soc. London, Ser. B **250**, 29–34.

Brown, A. M., Harris, F. P., and Beveridge, H. A. (**1996**). ''Two sources of acoustic distortion products from the human cochlea,'' J. Acoust. Soc. Am. **100**, 3260–3267.

Cody, A. R., and Russell, I. J. (**1987**). ''The responses of hair cells in the basal turn of the guinea-pig cochlea to tones,'' J. Physiol. (London) **383**, 551–569.

Crawford, A. C., Evans, M. G., and Fettiplace, R. (**1989**). ''Activation and adaptation of transducer currents in turtle hair cells,'' J. Physiol. (London) **419**, 405–434.

Dallos, P. (**1986**). ''Neurobiology of cochlear inner and outer hair cells: intracellular recordings,'' Hear. Res. **22**, 185–198.

Dallos, P., and Cheatham, M. A. (**1989**). ''Nonlinearities in cochlear receptor potentials and their origins,'' J. Acoust. Soc. Am. **86**, 1790–1796.

Dallos, P., Santos-Sacchi, J., and Flock, A. (**1982**). ''Intracellular recordings from cochlear outer hair cells,'' Science **218**, 582–584.

van Dijk, P., and Manley, G. A. (**2001**). ''Distortion product otoacoustic emissions in the tree frog Hyla cinerea,'' Hear. Res. **153**, 14–22.

Fahey, P. F., and Allen, J. B. (**1997**). ''Measurement of distortion product phase in the ear canal of the cat,'' J. Acoust. Soc. Am. **102**, 2880–2891.

Fahey, P. F., Stagner, B. B., Lonsbury-Martin, B. L., and Martin, G. K. (**2000**). ''Nonlinear interactions that could explain distortion product interference response areas,'' J. Acoust. Soc. Am. **108**, 1786–1802.

Frank, G., and Kössl, M. (**1996**). ''The acoustic two tone distortions $2f_1$-f_2 and f_2-f_1 and their possible relation to changes in the gain and the operating point of the cochlear amplifier,'' Hear. Res. **98**, 104–115.

Frank, G., and Kössl, M. (**1997**). ''Acoustical and electrical biasing of the cochlear partition. Effects on the acoustic two tone distortions f_2-f_1 and $2f_1$-f_2,'' Hear. Res. **113**, 57–68.

Furst, M., Rabinowitz, W. M., and Zurek, P. M. (**1988**). ''Ear canal acoustic distortion at $2f_1$-f_2 from human ears: Relations to other emissions and perceived combination tones,'' J. Acoust. Soc. Am. **84**, 215–221.

Harris, F. P., Lonsbury-Martin, B. L., Stagner, B. B., Coats, A. C., and Martin, G. K. (**1989**). ''Acoustic distortion products in humans: Systematic changes in amplitude as a function of f_2/f_1 ratio,'' J. Acoust. Soc. Am. **85**, 220–229.

He, N., and Schmiedt, R. A. (**1997**). ''Fine structure of the $2f_1$-f_2 acoustic distortion product: Effects of primary level and frequency ratios,'' J. Acoust. Soc. Am. **101**, 3554–3565.

Heitmann, J., Waldmann, B., Schnitzler, H. U., Plinkert, P. K., and Zenner, H. P. (**1998**). ''Suppression of distortion product otoacoustic emissions (DPOAE) near $2f_1$-f_2 removes DP-gram fine structure-Evidence for a secondary generator,'' J. Acoust. Soc. Am. **103**, 1527–1531.

Knight, R. D., and Kemp, D. T. (**2000**). ''Indications of different distortion product otoacoustic emission mechanisms from a detailed f_1, f_2 area study,'' J. Acoust. Soc. Am. **107**, 457–473.

Kros, C. J., Lennan, G. W. T., and Richardson, G. P. (**1995**). ''Transducer currents and bundle movements in outer hair cells of neonatal mice,'' in *Active Hearing*, edited by A. Flock, D. Ottoson, and M. Ulfendahl (Elsevier Science, Amsterdam), pp. 113–125.

Kummer, P., Janssen, T., Hulin, P., and Arnold, W. (**2000**). ''Optimal L_1-L_2 primary tone level separation remains independent of test frequency in humans,'' Hear. Res. **146**, 47–56.

Lukashkin, A. N., and Russell, I. J. (**1998**). ''A descriptive model of the receptor potential nonlinearities generated by the hair cell mechanoelectrical transducer,'' J. Acoust. Soc. Am. **103**, 973–980.

Lukashkin, A. N., and Russell, I. J. (**1999**). ''Analysis of the f_2-f_1 and $2f_1$-f_2 distortion components generated by the hair cell mechanoelectrical transducer: Dependence on the amplitudes of the primaries and feedback gain,'' J. Acoust. Soc. Am. **106**, 2661–2668.

Mills, D. M. (**1997**). ''Interpretation of distortion product otoacoustic emission measurements. I. Two stimulus tones,'' J. Acoust. Soc. Am. **102**, 413–429.

Mills, D. M., and Rubel, E. W. (**1994**). ''Variation of distortion product otoacoustic emission with furosemide injection,'' Hear. Res. **77**, 183–199.
Mills, D. M., and Rubel, E. W. (**1997**). ''Development of distortion product emission in the gerbil: ''Filter'' response and signal delay,'' J. Acoust. Soc. Am. **101**, 395–411.
Moulin, A. (**2000**). ''Influence of primary frequencies ratio on distortion product otoacoustic emissions amplitude. I. Intersubject variability and consequences on the DPOAE-gram,'' J. Acoust. Soc. Am. **107**, 1460–1470.
Moulin, A., and Kemp, D. T. (**1996a**). ''Multicomponent acoustic distortion product otoacoustic phase in humans. I. General characteristics,'' J. Acoust. Soc. Am. **100**, 1617–1639.
Moulin, A., and Kemp, D. T. (**1996b**). ''Multicomponent acoustic distortion product otoacoustic phase in humans. II. Implications for distortion product otoacoustic emissions generation,'' J. Acoust. Soc. Am. **100**, 1640–1662.
Parham, K. (**1997**). ''Distortion product otoacoustic emissions in the C57BL/6J mouse model of age-related hearing loss,'' Hear. Res. **112**, 216–234.
Russell, I. J., and Nilsen, K. E. (**1997**). ''The location of the cochlear amplifier: Spatial representation of a single tone on the guinea pig basilar membrane,'' Proc. Natl. Acad. Sci. U.S.A. **94**, 2660–2664.
Schneider, S., Schoonhoven, R., and Prijs, V. F. (**2001**). ''Amplitude of distortion product otoacoustic emissions in the guinea pig in f_1- and f_2-sweep paradigms,'' Hear. Res. **155**, 21–31.
Stover, L. J., Neely, S. T., and Gorga, M. P. (**1996**). ''Latency and multiple sources of distortion product otoacoustic emissions,'' J. Acoust. Soc. Am. **99**, 1016–1024.
Stover, L. J., Neely, S. T., and Gorga, M. P. (**1999**). ''Cochlear generation of intermodulation distortion revealed by DPOAE frequency functions in normal and impaired ears,'' J. Acoust. Soc. Am. **106**, 2669–2678.
Taschenberger, G., Gallo, L., and Manley, G. A. (**1995**). ''Filtering of distortion-product otoacoustic emissions in the inner ear of birds and lizards,'' Hear. Res. **91**, 87–92.
Wable, J., Collet, L., and Chèry-Croze, S. (**1996**). ''Phase delay measurements of distortion product otoacoustic emissions at $2f_1$-f_2 and $2f_2$-f_1 in human ears,'' J. Acoust. Soc. Am. **100**, 2228–2235.
Whitehead, M. L. (**1998**). ''Species differences of distortion-product otoacoustic emissions: Comment on ''Interpretation of distortion product otoacoustic emission measurements. I. Two stimulus tones'' [J. Acoust. Soc. Am. **102**, 413–429 (1997)],'' J. Acoust. Soc. Am. **103**, 2740–2742.
Whitehead, M. L., Lonsbury-Martin, B. L., and Martin, G. K. (**1992a**). ''Evidence for two discrete sources of $2f_1$-f_2 distortion-product otoacoustic emission in rabbit: I: Differential dependence on stimulus parameters,'' J. Acoust. Soc. Am. **91**, 1587–1607.
Whitehead, M. L., Lonsbury-Martin, B. L., and Martin, G. K. (**1992b**). ''Evidence for two discrete sources of $2f_1$-f_2 distortion-product otoacoustic emission in rabbit: II: Differential physiological vulnerability,'' J. Acoust. Soc. Am. **92**, 2662–2682.
Whitehead, M. L., Stagner, B. B., Martin, G. K., and Lonsbury-Martin, B. L. (**1996**). ''Visualization of the onset of distortion-product otoacoustic emissions, and measurement of their latency,'' J. Acoust. Soc. Am. **100**, 1663–1679.
Zheng, Y. L., Ohyama, K., Hozawa, K., Wada, H., and Takasaka, T. (**1997**). ''Effect of anesthetic agents and middle ear pressure application on distortion product otoacoustic emissions in the gerbil,'' Hear. Res. **112**, 167–174.

A human nonlinear cochlear filterbank

Enrique A. Lopez-Poveda[a)]
Centro Regional de Investigación Biomédica, Facultad de Medicina, Universidad de Castilla-La Mancha, Campus Universitario, 02071 Albacete, Spain

Ray Meddis
Centre for the Neural Basis of Hearing, Department of Psychology, University of Essex, Colchester CO4 3SQ, United Kingdom

(Received 18 April 2001; revised 10 July 2001; accepted 10 September 2001)

Some published cochlear filterbanks are nonlinear but are fitted to *animal* basilar membrane (BM) responses. Others, like the gammatone, are based on *human* psychophysical data, but are linear. In this article, a human nonlinear filterbank is constructed by adapting a computational model of animal BM physiology to simulate human BM nonlinearity as measured by psychophysical pulsation-threshold experiments. The approach is based on a dual-resonance nonlinear type of filter whose basic structure was modeled using animal observations. In modeling the pulsation threshold data, the main assumption is that pulsation threshold occurs when the signal and the masker produce comparable excitation, that is the same filter output, at the place of the BM best tuned to the signal frequency. The filter is fitted at a discrete number of best frequencies (BFs) for which psychophysical data are available for a single listener and for an average response of six listeners. The filterbank is then created by linear regression of the resulting parameters to intermediate BFs. The strengths and limitations of the resulting filterbank are discussed. Its suitability for simulating hearing-impaired cochlear responses is also discussed.
[DOI: 10.1121/1.1416197]

PACS numbers: 43.64.Bt [LHC]

I. INTRODUCTION

Computational models of human peripheral frequency selectivity have a long history and a wide range of potential uses. They are a fast way to estimate excitation patterns along the cochlear partition in response to an arbitrary acoustic stimulus and have potential uses in, for example, signal compression algorithms, automatic speech recognition devices and simulations of individual patterns of hearing loss. Historically, the computations have used banks of linear gammatone filters (Patterson *et al.*, 1992) but more recently researchers have attempted to use nonlinear filters (Giguère and Woodland, 1994; Lyon, 1982; Carney, 1993; Goldstein, 1990, 1995; Lopez-Poveda *et al.*, 1998; Meddis *et al.*, 2001). Much of what we know about the nonlinear aspects of peripheral frequency selectivity is derived from animal studies, particularly from direct observation of the response of the cochlear partition to acoustic stimulation (Rhode, 1971; Rhode and Recio, 2000; Robles *et al.*, 1986, 1991; Sellick *et al.*, 1982; Yates *et al.*, 1990; Ruggero *et al.*, 1992). Nevertheless, this information is consistent with recent psychophysical observations showing changes with level of the filter's best frequency (BF) (McFadden and Yama, 1983) and bandwidth (BW) (Glasberg and Moore, 1990; Rosen *et al.*, 1998; for a review see Moore and Glasberg, 1987, and Moore, 1998). In this work we present a computational algorithm that was originally designed to accommodate animal observations and demonstrate how it can be adapted to simulate the hearing of a single human listener and the average hearing of a group of listeners.

The new filterbank aims to simulate the basilar membrane (BM) response using an array of point models (Lopez-Poveda *et al.*, 1998; Meddis *et al.*, 2001). It is similar in many respects to gammatone filterbanks that are in current use. The main difference is that each individual gammatone filter is replaced by a dual resonance nonlinear (DRNL) filter unit (to be described in detail later in this work). It has already been shown that the system can be used to model animal observations. The purpose of the present study is to show that, given suitable parameter changes, it can also be used to simulate human psychophysical data. The parameters of the DRNL units vary with respect to position along the cochlear partition but are fixed with respect to the intensity of the stimulus. Nevertheless, it is an emergent property of the system that the effective BW of each unit changes with signal level. The primary aim of the present study is to explore a new methodology for using human psychophysical data to identify parameters of the DRNL units. A second aim of the study is to identify mathematical functions that allow us to specify the parameters of DRNL units at any arbitrary BF.

Plack and Oxenham (2000) have recently published estimates of BM nonlinearity in normal listeners at BFs between 250 Hz and 8 kHz. These data will be used to help define the parameters of the DRNL units. They used a ''pulsation threshold'' paradigm (Houtgast, 1972), which is based on an auditory illusion whereby an interrupted sound is perceived as being continuous if there is sufficient energy from another sound during the interruptions. Plack and Oxenham presented a stimulus consisting of a signal tone at BF rapidly alternated on three occasions by a low-frequency (LF) tone

a)Electronic mail: ealopez@med-ab.uclm.es

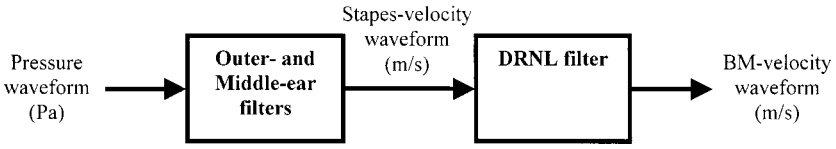

FIG. 1. Model diagram.

(where LF is defined as 0.6×BF). For every level of the BF tone, the level of the LF tone was adjusted to find the ''pulsation threshold,'' that is the level at which the perception of the signal changes from ''pulsed'' to ''continuous.'' They argue that this is the level at which the two tones are generating equal levels of BM activity in the auditory filter tuned to the BF tone (see also Houtgast, 1972). Their method assumes that the response to a signal as a function of intensity will be compressively nonlinear at the BF of a filter but linear in the low-frequency (LF) tail of the filter. This assumption has received support from both animal (e.g., Sellick *et al.*, 1982) and human (e.g., Oxenham and Plack, 1997; Nelson and Schroder, 1999) studies. As a result, a plot of the level of the LF tone at threshold versus the level of the BF tone provides an estimate of the BM response at BF. If the auditory system responds linearly to both tones, the pulsation threshold should increase linearly with increases in the level of the BF tone. In fact, the threshold rises only slowly as a function of the BF tone. This result is consistent with the idea that the system is nonlinear. Specifically, it shows that excitation rises more slowly as a function of the intensity of the BF tone when compared with the response to the LF tone. In addition, their results show that the amount of nonlinearity varies as a function of BF.

The aim of the modeling study is to find parameters that will allow a DRNL unit to simulate these results quantitatively as well as qualitatively. In what follows, we describe the model and the method used to choose appropriate parameters. Then, it is shown how well the model can be made to fit the data. By allowing the parameters to vary as a function of BF, it is shown that the data can be simulated quantitatively at six different BFs. It is shown that the parameters required to fit the data vary approximately linearly as a function of $\log_{10}$(BF). It is proposed that functions of this type could be used as a basis for defining complete DRNL filterbanks to represent the hearing of an individual listener as well as the average response of six listeners.

II. THE MODEL

The overall structure of the model is shown in Fig. 1. It consists of two main stages: (*i*) an outer/middle-ear filter function, which transforms a headphone-delivered sound pressure waveform into a stapes velocity waveform, and (*ii*) a DRNL filter that simulates the BM velocity of vibration in response to stapes velocity.

A. The outer/middle ear stage

A sound pressure waveform produces vibration of the tympanic membrane, which, in turn, induces the vibration of the stapes. Each of these two processes of the peripheral hearing is modeled by means of a linear-phase, 512-point, finite impulse response (FIR) filter. The coefficients of each FIR filter were obtained from empirical frequency responses by applying an inverse fast Fourier transform routine with MATLAB (The Mathworks, Inc., ver. 5.3).

The outer-ear (headphone pressure-to-eardrum pressure) frequency response is taken from Pralong and Carlile [1996, Fig. 1(e)] and is shown in Fig. 2(a). It corresponds to a typical human outer-ear pressure-gain function measured at a point close to the tympanic membrane when the stimulus is delivered through a pair of Sennheiser HD-250 Linear headphones. A response measured with a Sony MDR-V6 headset would have been preferred, as this is the model that Plack and Oxenham employed to collect their pulsation-threshold data. Unfortunately, such response is unavailable. However, both the MDR-V6 and HD-250 are circumaural headphones and have a fairly flat frequency response in the range of

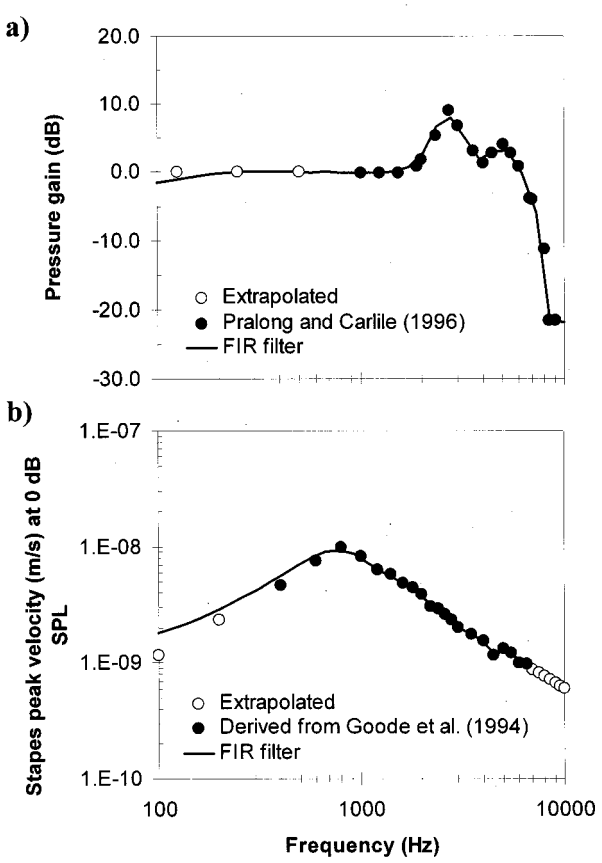

FIG. 2. Stage 1 of the model: human outer/middle ear filter functions. Filled symbols represent experimental data points. Open symbols represent extrapolation points used for evaluating the model over a wider frequency range. Lines represent the actual frequency response of the linear-phase, 512-point, FIR filters used in the model. (a) A typical human headphone-to-eardrum sound pressure gain (from Pralong and Carlile, 1996, Fig. 1E). (b) Stapes peak velocity (m/s) as a function of frequency for a sound pressure input of 0 dB SPL. The velocity values have been derived from the peak-to-peak stapes displacement data measured in cadavers by Goode *et al.* (1994, Fig. 1, set: 104 dB SPL). It is assumed that stapes velocity is linearly related to pressure.

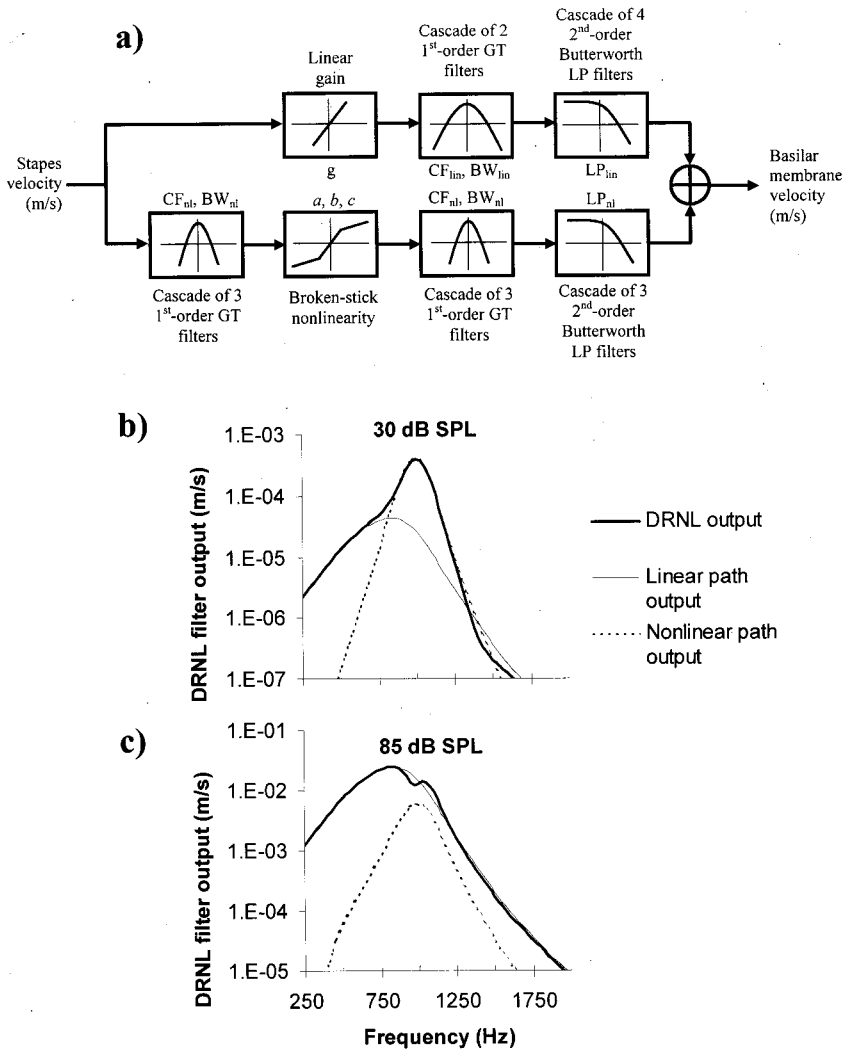

FIG. 3. (a) Stage 2 of the model: The DRNL filter (Meddis *et al.*, 2001). The parameters of each block are shown in the space between the linear (top) and the nonlinear (bottom) paths. The output signal from the DRNL filter is the sum of the signal coming out of each path. (b) Isointensity response of the linear (thin continuous line), and nonlinear (thin dotted line) filter-paths for an input level of 30 dB SPL. At this low intensity, the summed response of the DRNL filter (thick continuous line) is dominated by the response of the nonlinear path. (c) The same as (b) but for an input level of 85 dB SPL. In this case, the summed response is dominated by the response of the linear path. See text for details.

interest (100–8000 Hz). Hence, it is reasonable to assume that the outer-ear response of Fig. 2(a) is a good approximation to that measured with the MDR-V6 headset.

The middle-ear response (stapes velocity as a function of stimulus frequency) is shown in Fig. 2(b) for a stimulus level at the eardrum of 0 dB SPL. The data is derived from stapes displacement measurements in cadavers by Goode *et al.* (1994, Fig. 1) after sound pressure stimulation near the tympanic membrane. Consistent with the observations of Goode *et al.*, peak stapes velocity is assumed to increase linearly with stimulus pressure. The range of empirical data points has been extrapolated from 400–6500 Hz to 100–10 000 Hz [see Fig. 2(b)] in order to be able to evaluate the model over a wider frequency range. The extrapolation is consistent with the measurements of Kringlebotn and Gundersen (1985).

The same outer- and middle-ear filters have been used throughout the modeling work described next.

B. The DRNL filter

Stapes motion transmits energy to the intracochlear fluid, which induces, in turn, motion of the BM. This process is modeled by a DRNL filter (Meddis *et al.*, 2001) which simulates the velocity of vibration of a given site along the BM in response to a given stapes velocity waveform. Its structure and parameters are shown in Fig. 3(a). The input signal follows two independent paths, one linear and one nonlinear. In the linear path, a gain, g, is applied and then the signal is filtered through a cascade of (two or three, see later in this work) first-order gammatone (GT) filters (parameters: CF_{lin} and BW_{lin}) followed by a cascade of four second-order low-pass filters. In the nonlinear path, the input signal is filtered through a cascade of three first-order GT filters (parameters: CF_{nl} and BW_{nl}) followed by a nonlinear gain (see later in this work), followed by another cascade of three GT filters having the same parameters (CF_{nl} and BW_{nl}). During parameter estimation, the CF_{nl} is set to the frequency of the probe signal being studied and is not a free parameter. However, the CF of the linear path (CF_{lin}) is different and typically below CF_{nl} (see later in this work).

The nonlinear gain function is

$$y(t) = \mathrm{sign}[x(t)] \cdot \min[a|x(t)|, b|x(t)|^c], \tag{1}$$

where $x(t)$ and $y(t)$ are the input and the output signals of the nonlinearity, respectively, and a, b, and c are parameters of the model. The details of the time-domain digital implementation of the DRNL filter are given in the Appendix.

TABLE I. DRNL parameters at various signal frequencies used throughout to simulate the characteristics of subject YO's normal hearing. In principle, this set of parameters is ''subject specific.'' The bottom rows show the actual BF and BW_{3dB} of the DRNL filters.

Signal frequency (Hz)	250	500	1000	2000	4000	8000
			DRNL linear path			
No. cascaded GT filters	2	2	2	2	2	2
CF_{lin} (Hz)	235	460	945	1895	3900	7450
BW_{lin} (Hz)	115	150	240	390	620	1550
g	1400	800	520	400	270	250
LP_{lin} cutoff (Hz)	CF_{lin}	CF_{lin}	CF_{lin}	CF_{lin}	CF_{lin}	CF_{lin}
No. cascaded LP filters	4	4	4	4	4	4
			DRNL nonlinear path			
No. cascaded GT filters	3	3	3	3	3	3
CF_{nl} (Hz)	250	500	1000	2000	4000	8000
BW_{nl} (Hz)	84	103	175	300	560	1100
a	2124	4609	4598	9244	30274	76354
b $[(m/s)^{(1-c)}]$	0.45	0.280	0.130	0.078	0.060	0.035
c	0.25	0.25	0.25	0.25	0.25	0.25
LP_{nl} cutoff (Hz)	CF_{nl}	CF_{nl}	CF_{nl}	CF_{nl}	CF_{nl}	CF_{nl}
No. cascaded LP filters	3	3	3	3	3	3
DRNL filter BF (Hz)	260	508	1002	2006	3978	7720
DRNL filter BW_{3dB} (Hz)	47	70	118	210	415	755

The output from the DRNL filter is the sum of the output from the linear and the nonlinear paths. For consistency with its original description by Meddis *et al.*, it is assumed to represent BM velocity.

Although the DRNL unit is simple in construction, the effects of a change in signal level on its properties are not immediately apparent. To help visualize these, two extra figures are supplied. Figure 3(b) shows separately the filter output as a function of signal frequency for the linear and the nonlinear path for a 30 dB SPL input signal. These functions are generated using the parameters to be used later for the 1-kHz site (subject YO, Table I). The combined output of the DRNL unit is shown as the thick continuous line and is simply the sum of the two filter functions. Note that the nonlinear function dominates the output and is the main determinant of the shape of the summed output function. Figure 3(c) shows the same set of functions but this time for an 85 dB SPL signal. The linear filter function has grown considerably while the nonlinear filter function has grown very little. This is because the nonlinearity is compressive. As a consequence, the output from the linear function dominates the aggregate output. The thick line representing the summed output of the DRNL unit is now a much wider filter function than that shown in Fig. 3(b). In addition, we can see that the BF of the DRNL unit has shifted to a lower frequency.

At very low signal levels, the DRNL unit operates linearly. This is because the nonlinear path is linear for low signal inputs [see Eq. (1)]. At very high signal levels, the DRNL also operates essentially as a linear filter. This is because the linear filter comes to dominate the output. These properties of the DRNL filter are consistent with the data of Plack and Oxenham (2000) which often show a linear response at low signal levels, followed by a compressive nonlinearity and then followed by a return to linearity at 80 dB SPL. A similar return to linearity is also sometimes found in observations of animal BM response, although its significance is disputed (Ruggero *et al.*, 1996, Fig. 1; Johnstone *et al.*, 1986, Fig. 5; Rhode and Cooper, 1996, Fig. 7). Note that the effect of signal level on filter width, BF and nonlinearity are emergent properties of a level-independent set of model parameters.

III. MODELING HUMAN BM NONLINEARITY FOR NORMAL-HEARING SUBJECTS

A. Method

The model was tuned to simulate human BM nonlinearity as estimated by psychoacoustical experiments of pulsation threshold (Plack and Oxenham, 2000). Plack and Oxenham presented subjects with a stimulus consisting of a number of interleaved segments of a signal tone and masker tone. Each individual segment was ramped up and down (2-ms raised-cosine ramps) and the frequency of the masker was 0.6 times the frequency of the signal. They measured signal frequencies of 250, 500, 1000, 2000, 4000, and 8000 Hz. For any given signal level, the task was to measure the masker threshold level at which the subject reports the signal to sound ''pulsating'' as opposed to continuous. Background noise was used to prevent off-frequency listening. Figure 4 symbols show their experimental findings for one subject (YO, filled circles) together with the average response of the six subjects considered in their experiment (open circles).

Here, it is assumed that pulsation threshold occurs when the signal and the masker produce the same amount of excitation at the place of the BM of maximum excitation to the signal frequency. For this reason, the paradigm for evaluating the model was a simplified version of that used by Plack and Oxenham. Instead of using a pulsating stimulus, the signal tone and the masker tone were passed independently through the model. Signal and masker frequencies were the same as those used by Plack and Oxenham. Both tones had a duration

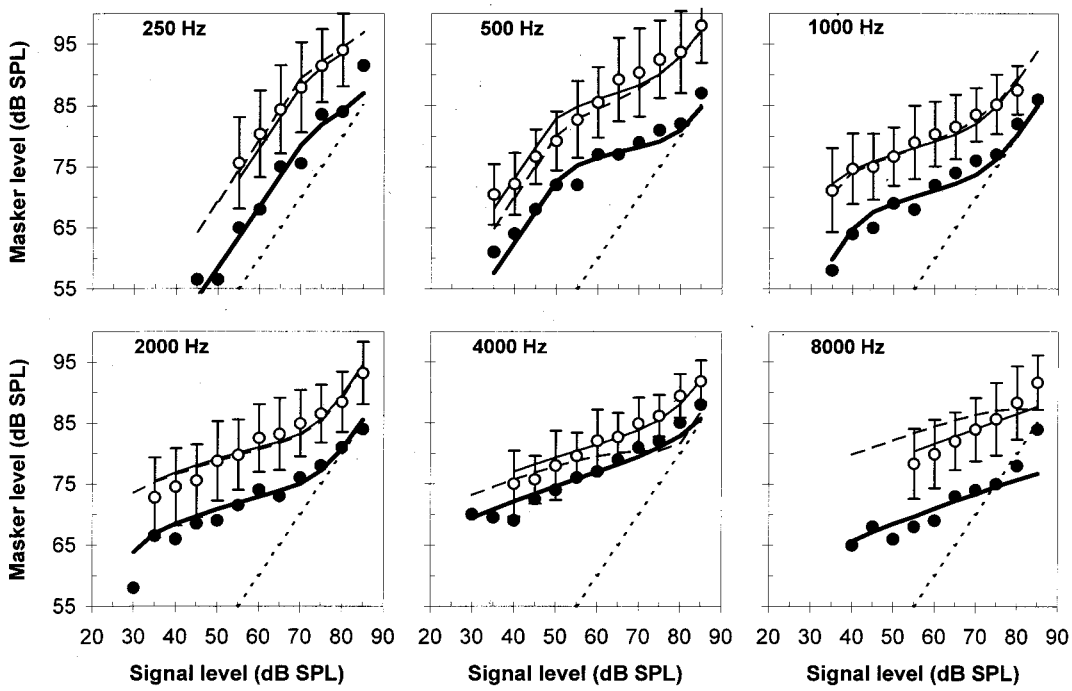

FIG. 4. Comparison between the experimental pulsation threshold data (Plack and Oxenham, 2000, Fig. 2) and the model. Filled symbols represent the data for subject YO. Open symbols represent the average data for the six listeners in the study. Error bars represent an interval of ±1 standard deviation. The thick continuous line represents the model behavior with the optimum set of parameters for subject YO (Table I). The thin continuous line shows the model behavior with the optimum set of parameters for the average data (Table II). The thin dashed line shows the response of the filterbank parameters calculated with the regression lines in Table III, average response. The dotted line illustrates a linear behavior. See text for details.

of 84 ms and were ramped up and down with 2-ms raised-cosine ramps. At each frequency, the signal level was varied within the ranges used by Plack and Oxenham. The sampling frequency (f_s) was 64 000 Hz.

At each BF, the model's peak response to the signal (O_S) and the masker (O_M) was measured during the last half of the stimulus duration in order to avoid any effects that may occur at the onset. For each signal level (L_S), the task was to find out a masker level (L_M) such that the ratio O_S/O_M was equal to (or just exceeded) a value of one.

B. Parameter optimization

Two sets of model parameters were chosen so as to optimize the match between the model results and the two sets of experimental data shown in Fig. 4. However, the model contains a large number of parameters. Not all of them were allowed to vary. Some parameters were fixed by introducing constraints to the search space. These constraints are based on our current understanding of the cochlear response as explained later in this work.

CF_{nl} was fixed at the probe signal frequency. Consistent with Meddis *et al.* (2001), the cut-off frequencies of the low-pass filters in the linear and the nonlinear paths (LP_{lin} and LP_{nl}) were fixed equal to the CF of the GT filters in their respective paths (CF_{lin} and CF_{nl}).

The compression exponent, *c*, was also fixed at 0.25 across BF. This may appear to be surprising in view of the fact that the slopes of the functions in Fig. 4 change with signal frequency. However, the slope of the psychophysical functions in Fig. 4 is only indirectly related to the compression function in Eq. (1). The psychophysical functions, in the model at least, are based on the summed activity of two components, only one of which is nonlinear. The linearity of one component dilutes the nonlinearity of the other in the output of the DRNL unit. We had previously found (Meddis *et al.*, 2001) that a fixed value of the compression exponent, *c*, was consistent with the variation observed in the slopes of the input/output functions in the animal data. By adopting the same strategy on this occasion, it was possible to produce a quantitative match to the data while benefiting from the need to estimate one parameter less.

Parameter *a* of the nonlinearity is responsible for the "sensitivity" at the tip of filter. It, therefore, determines the BM response at the absolute hearing threshold (AHT). There is evidence that AHT occurs at a BM velocity in the region of 5×10^{-5} m/s (Ruggero *et al.*, 1997). For this reason, *a* was fixed so that the DRNL filter output peak velocity is 5×10^{-5} m/s at the subject's hearing threshold.

Parameter CF_{lin} determines the BF of the DRNL filter at high levels, when the linear filter path dominates the DRNL output (see Fig. 3). There is physiological (e.g., Rhode and Recio, 2000) and psychophysical (McFadden and Yama, 1983) evidence of a shift in BF as a function of level. For this reason, an important initial constraint was set on CF_{lin} by requiring it to be lower than CF_{nl}. The shift found by McFadden and Yama from 65 to 95 dB SPL gives a ratio BF_{65}/BF_{95} of approximately 1.1 to 1.4. This does not imply directly that the ratio CF_{nl}/CF_{lin} must be set within that range in the model. Because the DRNL filter is the sum of two components, each of which consists of a number of cascaded gammatone filters, followed by low-pass filters, its BF is not equal to either CF_{lin} or CF_{nl}. However, by trial and error, we

TABLE II. DRNL parameters at various signal frequencies used throughout to simulate the average pulsation-threshold data. The bottom rows show the actual BF and BW_{3dB} of the DRNL filters. Note that, in this case, the number of cascaded GT filters in the linear path is 3, whereas it was 2 for subject YO (Table I; see text for details).

Signal frequency (Hz)	250	500	1000	2000	4000	8000
			DRNL linear path			
No. cascaded GT filters	3	3	3	3	3	3
CF_{lin} (Hz)	244	480	965	1925	3900	7750
BW_{lin} (Hz)	100	130	240	400	660	1450
g	1150	850	520	410	320	220
LP_{lin} cutoff (Hz)	CF_{lin}	CF_{lin}	CF_{lin}	CF_{lin}	CF_{lin}	CF_{lin}
No. cascaded LP filters	4	4	4	4	4	4
			DRNL nonlinear path			
No. cascaded GT filters	3	3	3	3	3	3
CF_{nl} (Hz)	250	500	1000	2000	4000	8000
BW_{nl} (Hz)	84	103	175	300	560	1100
a	2194	5184	7558	9627	22288	43584
b $[(m/s)^{(1-c)}]$	0.450	0.280	0.130	0.078	0.045	0.030
c	0.25	0.25	0.25	0.25	0.25	0.25
LP_{nl} cutoff (Hz)	CF_{nl}	CF_{nl}	CF_{nl}	CF_{nl}	CF_{nl}	CF_{nl}
No. cascaded LP filters	3	3	3	3	3	3
DRNL filter BF (Hz)	258	508	998	2006	3978	7720
DRNL filter BW_{3dB} (Hz)	50	68	118	210	415	755

have been able to conclude that the observed BF_{65}/BF_{95} ratio can be modeled by setting the ratio $CF_{nl}/CF_{lin} \geqslant 1.025$ approximately (see Tables I and II).

Another important constraint was set by requiring the DRNL filter functions near threshold to have 3-dB-down bandwidths (BW_{3dB}) that are consistent with the human psychophysical observations specified in the formula given by Glasberg and Moore (1990) (see later in this work). This criterion constrains BW_{nl} as the nonlinear filter path dominates the DRNL filter function at threshold. It does not mean, however, that BW_{nl} is set equal to the value given by Glasberg and Moore. Since the DRNL filter function at threshold is the result of a number of cascaded GT filters, the effective DRNL filter BW is somewhat lower than BW_{nl}, the BW of the individual GT filters. As a result, BW_{nl} must be greater than the human psychophysical bandwidths (see Tables I and II).

A weaker constraint was introduced on BW_{lin} so that the effective DRNL filter BW at high levels (when the linear filter dominates the DRNL filter output) is larger than at threshold, in agreement with psychophysical human filter functions. It was decided not to set any stronger numerical constraints on BW_{lin} as it deeply influences DRNL filter output to the masker and hence the psychophysical data functions in Fig. 4. These functions can be characterized (from left to right) as an initial linear, a compressed, and a final linear section. When concentrating on these separate features, the modeler was able to use the following rules when varying the remaining parameters (b, g, and BW_{lin}) to optimize the fit. The gain b was varied to set the height of the compressed section in the functions of Fig. 4. Finally, once parameter a has been fixed (see earlier in this work), the gain g together with BW_{lin} were set so that the height of the initial linearity could be reproduced and so that O_M (the response to the masker) is approximately equal to O_S (the response to the signal) at 85 dB SPL, in agreement with the psychophysical data of Fig. 4.

With the above mentioned constraints, the variable parameters were varied manually to optimize the fit by minimizing the Euclidean distance between the psychophysical data and the model results. Parameters to fit the data of subject YO (Table I) were found in the first place. These were then adjusted to find optimum parameters to fit the average pulsation thresholds in the Plack and Oxenham study (Table II). It is important to notice that across BFs the experimental average pulsation thresholds are 8 to 9 dB higher than those of subject YO (in Fig. 4, compare open and closed symbols). Based on our main assumption that pulsation threshold occurs when the masker and the signal produce equal levels of BM excitation (see also Houtgast, 1972, and Plack and Oxenham, 2000), this result implies that the auditory filters corresponding to the average response are necessarily steeper in their low-frequency tail (at $0.6\times$BF) than those of subject YO. In the model, this effect can be achieved in two ways: either by reducing BW_{lin} or by increasing the number of cascaded gammatone filters in the linear path. The necessary adjustments to BW_{lin} would require its value to be lower than BW_{nl}, hence violating one of the constraints set previously. It was, therefore, decided to allow the number of cascaded gammatone filters in the linear path to vary from two (for subject YO) to three (for the average response) in order to account for the ''vertical'' variability in pulsation thresholds. The issue is further discussed in Sec. IV.

C. Creating a human filterbank

A computational model like the one presented here is expected to be used as part of larger models of the auditory periphery. This sort of application usually requires a filterbank rather than a discrete number of filters.

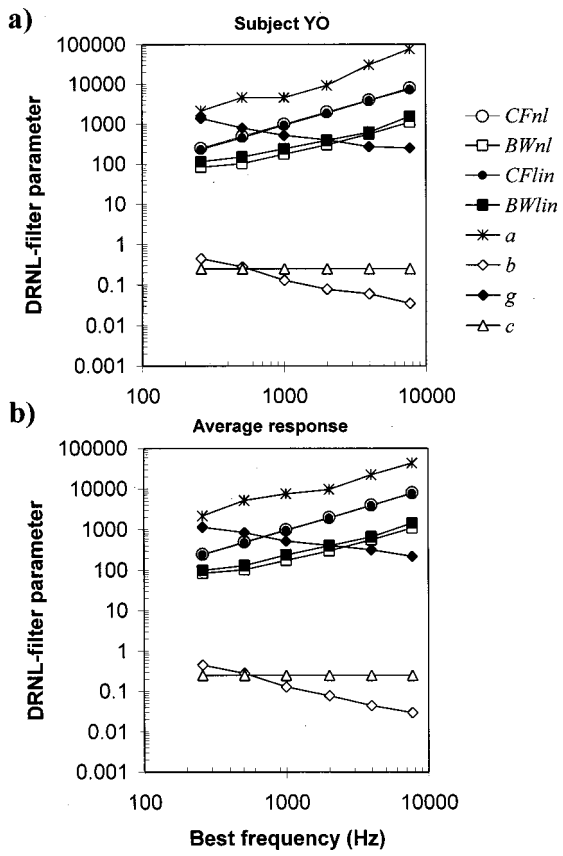

FIG. 5. Optimum model parameters as a function of BF. (a) Parameters for subject YO, Table I. (b) Parameters to fit the average data of six listeners, Table II. Note that the relationship between $\log_{10}$(parameter) and $\log_{10}$(BF) can be approximated as linear in both cases. Note also that the most variable parameter from a linear regression is *a*, which is adjusted to fit the subjects' threshold.

Figure 5 shows the variation of the two sets of model parameters as a function of BF. In both cases, it shows that the logarithm of each parameter as a function of the logarithm of BF can be approximated by a linear relationship as follows:

$$\log_{10}(\text{parameter}) = p_0 + m \log_{10}(\text{BF}), \tag{2}$$

where p_0 and m are the regression coefficients. This result suggests a possible way of creating a filterbank by linear regression of each parameter at intermediate BFs. The regression coefficients, p_0, and m, have been estimated for each parameter using least squares regression and are reported in Table III. With these regression equations, it is possible to specify the values of the free parameters for a DRNL representation of YO's or the average-listener's hearing at BFs between 250 Hz and 8 kHz. In what follows, only the results of the average-response filterbank are shown as those for subject YO's filterbank are similar.

D. Results

1. Input/output curves

Figure 4 compares the experimental data (Plack and Oxenham, 2000, Fig. 2) and the model results for both data sets (subject YO and average responses). For the most part, the fit is quantitatively very good in both cases. At BF=250 Hz, the model masking function is mainly linear, while at 1000 Hz, the model shows a three stage function (linear, compressed, then linear again). At 8000 Hz, the model replicates the almost wholly compressed nature of the function except for the return to linearity at high signal levels. The only significant failures occur at BF=2000 Hz, where the model fails to simulate the linearity at 30 dB SPL for subject YO, and at BF=8000 Hz, where the model fails to simulate the linearity at 80–85 dB SPL. The failure at 2000 Hz is linked to one of the parameter constraints that fixes the tip sensitivity parameter, *a*, to agree with the YO's or the average hearing threshold. It may also be a consequence of the fact that the outer-ear or the cadaver-based, middle-ear function do not correspond to subject YO's. The failure at 8000 Hz is linked to the deep notch in the outer-ear response [see Fig. 2(a)]. Pralong and Carlile (1996) pointed out that the greatest variability in outer-ear responses from trial to trial occurs precisely at around 8000 Hz. Their result is consistent with the findings of Kulkarni and Colburn (2000) and Møller *et al.* (1995). This suggests that at this particular frequency the outer-ear function shown in Fig. 2(a) is inappropriate to model the response of the subjects with the headphones used by Plack and Oxenham. Although not shown here, we did find an almost perfect match to the 8-kHz data assuming a flat outer-ear response at this frequency.

TABLE III. Regression-line coefficients p_0 and m for creating the filterbank assuming a relationship of the form: $\log_{10}(\text{parameter}) = p_0 + m \log_{10}(\text{BF})$, with BF expressed in Hz.

	Subject YO		Average response	
DRNL filter parameter	p_0	m	p_0	m
CF_{lin}	−0.102 05	1.023 85	−0.067 62	1.016 79
BW_{lin}	0.184 58	0.744 70	0.037 28	0.785 63
CF_{nl}	−0.059 12	1.018 32	−0.052 52	1.016 50
BW_{nl}	−0.037 39	0.775 79	−0.031 93	0.774 26
a	0.788 80	1.017 92	1.402 98	0.819 16
b	1.439 70	−0.751 38	1.619 12	−0.818 67
c	−0.602 06	0.000 00	−0.602 06	0.000 00
g	4.305 06	−0.509 42	4.204 05	−0.479 09
$\text{LP}_{\text{lin cutoff}}$	−0.102 05	1.023 85	−0.067 62	1.016 79
$\text{LP}_{\text{nl cutoff}}$	−0.059 12	1.018 32	−0.052 52	1.016 50

The dashed thin line in Fig. 4 shows the fit to the average data using the filterbank parameters calculated by linear regression. The overall behavior is maintained. The filterbank response is within one standard deviation of the average response for the most cases. The fit, however, gets worse, as would be expected from using a set of parameters that is not optimum for the specific data set.

2. Thresholds and filter bandwidths

Figure 6(a) shows a good match between the experimental and the model thresholds (assumed to occur at an output velocity of 5×10^{-5} m/s) both for subject YO and the average data. This justifies the values selected for parameter *a*.

The figure also shows the thresholds estimated with the average-filterbank parameters. The larger deviations between experimental and filterbank values are less than 5 dB. They

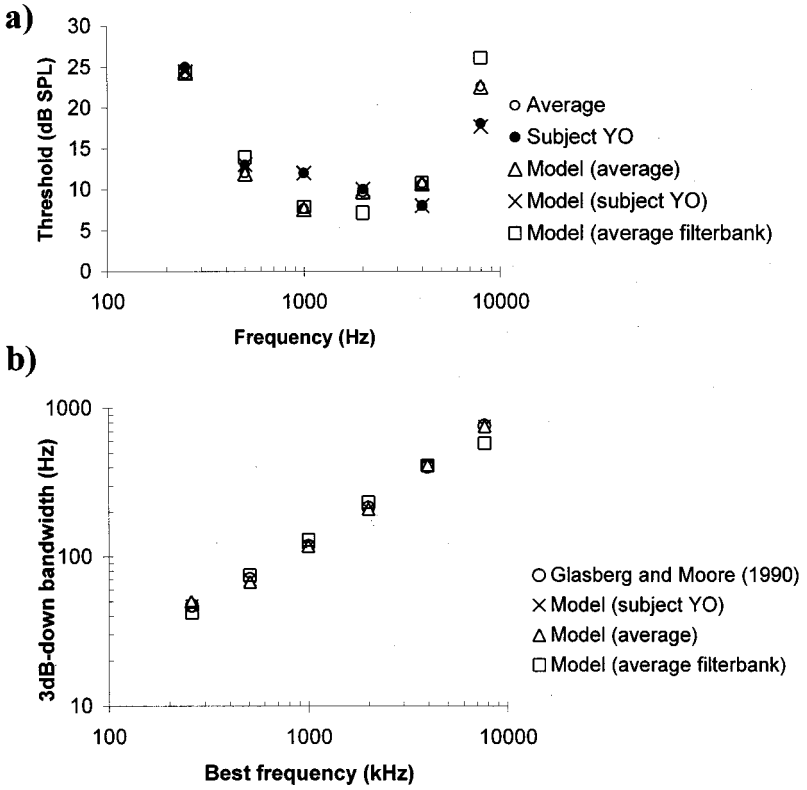

FIG. 6. (a) Experimental and model thresholds. Absolute threshold is assumed to occur at a BM velocity 5×10^{-5} m/s. Subject YO's thresholds (filled circles) match the corresponding model thresholds (crosses) estimated with the parameters in Table I. Likewise, the average threshold of the six listeners (open circles) match the model response (open triangles) calculated with the parameters in Table II. The thresholds estimated using the average-filterbank interpolated parameters (squares) are a reasonable match to the experimental average thresholds. The larger discrepancies at 0.5, 2, and 4 kHz are less than 5 dB and are the result of the deviation between the optimum (Table II) and the regression values for parameter *a*. (b) A 3-dB-down bandwidth of the modeled filters compared with the human data as predicted by the Glasberg and Moore (1990) formula. Note the good match between them. The largest discrepancy occurs for the filterbank at 8 kHz. See text for details.

occur at 0.5, 2.0, and 8.0 kHz and correspond to the largest deviations of the optimum values of parameter *a* over its regression line [Fig. 5(b)].

Figure 6(b) shows the approximate BW_{3dB} of the modeled filters compared with the human as calculated by the Glasberg and Moore (1990) formula:

$$BW_{3dB}\cong 0.89\times ERB\cong 0.89\times[24.7\times(4.37BF+1)], \quad (3)$$

where BF is expressed in kHz. The modeled BW_{3dB} were calculated directly from the isoresponse curves and not by applying the *critical band* paradigm used by Glasberg and Moore. For this purpose, the isoresponse curves were evaluated at a number of stimulus frequencies around the filter's BF enough to determine the 3-dB-down cutoff frequencies with reasonable accuracy (±2 Hz). It can be seen that the DRNL filter BWs are a good match to the psychophysical data. The average filterbank BW_{3dB} match the human bandwidths except for 8 kHz, where the filterbank BW_{3dB} is around 150 Hz lower.

3. Isointensity response

Figure 7(a) shows the isointensity response of the model with the set of parameters given in Table II, optimized to fit the average pulsation threshold data (the response with the subject YO parameters of Table I is similar). The curves correspond to stimulus levels from 30 to 70 dB SPL in steps of 10 dB and have been normalized to give a gain of 0 dB at their peak value. The psychophysical filtershapes derived by Baker *et al.* (1998) are shown in Fig. 7(b) for comparison. Finally, Fig. 7(c) shows the filter shapes of the average filterbank (Table III).

The model curves show distinct notches below BF that are not reported in the psychophysical literature. In the model, the notches are the result of phase cancellation between the outputs of the linear and nonlinear paths. Similar notches have been consistently observed in physiological measurements of the cochlear partition in chinchilla (e.g., Rhode and Recio, 2000) and may be the explanation for ''Nelson's notches'' (Kiang *et al.*, 1986, Fig. 5) occasionally reported in auditory nerve rate/intensity functions. If human listeners monitor a number of adjacent filters simultaneously and pay attention to the filter with the best signal/noise ratio, it is unlikely that these notches will be observed psychophysically as they offer a relatively poor signal to noise ratio.

The model filter function gets wider as the level of the stimulus increases. This is an important property of the DRNL filter consistent with the physiological (e.g., Rhode and Recio, 2000) and psychophysical behavior (e.g., Baker *et al.*, 1998; Rosen *et al.*, 1998; Glasberg and Moore, 2000).

Although not seen in Fig. 7, from 65 to 95 dB SPL there is a shift in the model BF towards lower BFs such that the ratio BF_{65}/BF_{95} ranges from about 1.10 (at BF=4 kHz) to 1.24 (at BF=8 kHz). The shifts are even larger (1.15 to 1.52) with YO's optimum parameters. Such shifts are consistent with the physiology (e.g., Rhode and Recio, 2000) and have also been observed psychophysically when adequate nonsimultaneous masking paradigms are employed (e.g., McFadden and Yama, 1983).

IV. DISCUSSION

The modeling exercise had two main aims. The first aim was to show that DRNL filters could be used to simulate psychophysical estimates of filter width and compression. The second aim was to show that the DRNL parameter changes are orderly with respect to BF. The close qualitative

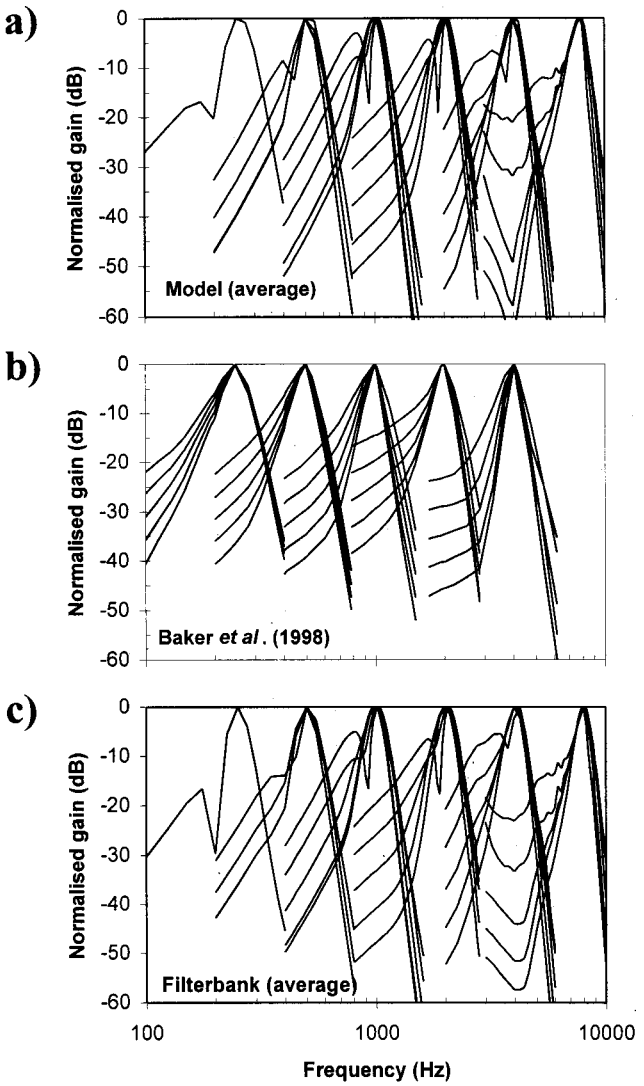

FIG. 7. (a) Isointensity curves modeled with the optimum parameters to match the average data (Table II). The response has been normalized to give a gain of 0 dB at its peak value. (b) Psychophysical filter shapes by Baker *et al.* (1998, Fig. 1). In both sets of curves, the stimulus level ranged from 30 to 70 dB SPL. (c) Isointensity curves modeled with the average-filterbank parameters (Table III).

and quantitative fits of the modeling results to the psychophysical data in Fig. 4 indicate that the first aim has been met with respect to both a single listener, YO, and the average response of six listeners. Similarly, the good fit of the regression functions in Table III suggests that the relationship between the parameters and BF is orderly enough to allow a filterbank to be generated for any point along the basilar membrane. This appears to be the case at least for the region representing a range of BFs between 250 Hz and 8 kHz.

The fitting process depends critically on three important assumptions. First, it assumes that the DRNL architecture gives an adequate account of the response of the cochlear partition to acoustic stimulation. Arguments in favor of this assumption are presented in Meddis *et al.* (2001). Second, it assumes that the pulsation threshold really does represent a condition in which the excitation of the masker, O_M, is equal to that generated by the probe signal, O_S. Arguments in favor of this assumption are presented by Houtgast (1972) and Plack and Oxenham (2000). However, the data of Plack and Oxenham also show that subjects with similar absolute hearing thresholds have pulsation thresholds that differ by as much as 20 dB (cf. subjects AO and YO in the original study). If the assumption was strictly correct, it would imply that their filters would be as much as 20 dB different at the masker frequency. Such intersubject variability seems rather large. Moore (1998, Fig. 3.19) gives an example of intersubject variability at BF=1 kHz, where the filter shapes of four subjects at 600 Hz (=0.6×BF) differ by no more than 10 dB. Therefore, it is possible that the pulsation threshold occurs at ratios O_S/O_M less than one for some subjects. The topic needs further investigation.

The third assumption is that listeners are able to attend selectively to the output of a single filter. This assumption is made in many psychophysical experiments and has proved to be of pragmatic value. To reduce the risk associated with this assumption, Plack and Oxenham (2000) took steps to minimize off-frequency listening.

The study does have some technical weaknesses that will need to be addressed in future studies. The outer ear function used in the model was based on measurements made on different subjects wearing different headphones from those in the Plack and Oxenham study. Furthermore, the middle-ear function used in the model was based on measurements made in cadavers. Ideally, we should have used measurements of the stapes response to headphone-delivered acoustic stimulation for the same subjects, with the same headphones as used in the psychophysical study. This is, of course, not practical and it is not immediately clear how this function is to be best estimated. Although the subjects' audiograms were available, they could not be used as a substitute for an outer/middle ear function because this would imply that no processes subsequent to the outer/middle ear contributes to the audiogram.

A second weakness of the model is that it does not address the issue how the filter BF changes with signal level. Animal studies show that BF does shift in this way. If this is also the case with human listeners, then it follows that listeners must redirect their attention to a different site when the probe signal level changes. We have made no attempt here to model this effect. In effect, the procedure previously described assumes that adjacent filters have very similar characteristics. This is despite that fact that the study as a whole shows that the characteristics of the filters are changing along the cochlear partition. Future studies will need to use a fine grain filterbank with facilities for taking the output from the filter whose *current* BF corresponds to the probe signal frequency.

The DRNL model is a point model in that there are no connections between the individual filter units. As a consequence, distortion products generated in one DRNL unit do not propagate to other units. This is unlikely to give rise to fatal difficulties when modeling the response to two tones at well-spaced frequencies, as is the case the Plack and Oxenham data. However, one of the attractions of a nonlinear filterbank is its potential for modeling such phenomena as two-tone suppression and combination tones. In this respect, while the DRNL units of the filterbank proposed earlier are

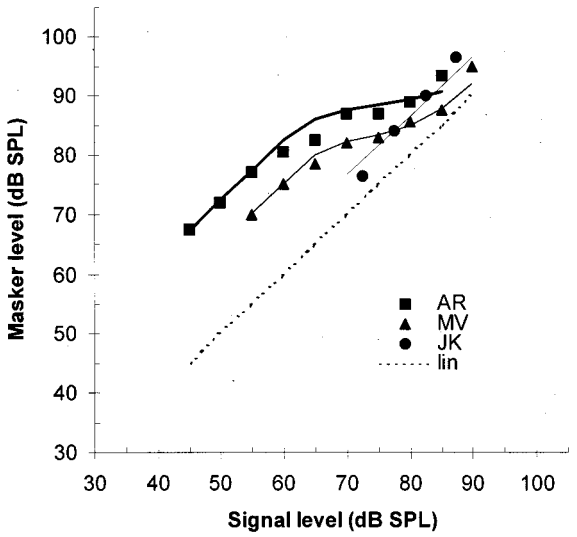

FIG. 8. Model fits (continuous lines) to hearing-impaired responses of the three different subjects (symbols). Experimental data from Oxenham and Plack (1997, Fig. 5). The dotted line illustrates a linear behavior. The frequency of the signal and the masker are 2 and 1 kHz, respectively. Note that subjects MV and AR show mild hearing loss (thresholds of 44 and 37 dB SPL, respectively). Subject JK, however, suffers from severe hearing loss (threshold=67 dB SPL) and hence shows no compression. The parameters in Table I (2 kHz) where used, except for the gains (*a*, *b*, and *g*), which were reduced to model impaired hearing, and BW_{lin} which, in the case of subject JK, was also reduced to model severe impaired hearing. The parameter modifications with respect to those in Table I are as follows: for subject AR, $a=480$, $b=0.06$, and $g=95$; for subject MV, $a=220$, $b=0.035$, and $g=95$; for subject JK, $a=0$, b=irrelevant given that a equals zero, $g=30$, and $BW_{lin}=320$.

able to generate ''local'' suppression and distortion products (Meddis *et al.*, 2001), a more complete model is needed to simulate effects that are not local to the probe tone. For instance, suppression has been shown to occur for suppressor tones with frequencies well below the probe (Abbas and Sachs, 1976; Duifhuis, 1980). Models alternative to the DRNL filter exist that claim to be able to account for this phenomenon (Goldstein, 1990, 1995). Future work is required to address this issue as far as the DRNL is concerned, as well as to make a detailed comparison concerning the relative merits of the various nonlinear filters that have been published recently.

The modeling study above was careful to use the data of a single subject (at least for the compression data). This is because DRNL units may prove useful for modeling the impaired hearing of individuals. If this proves to be feasible on a routine basis, it could be used to optimize the characteristics of hearing aids before supplying them to patients. Figure 8 shows an example of how the model can be tuned to fit hearing-impaired data for three different subjects (Oxenham and Plack, 1997, Fig. 5). In this case, the signal frequency was 2 kHz and the masker frequency 1 kHz. The model was evaluated using the same paradigm as described earlier. The parameters were identical to those in Table I (2 kHz) for normal-hearing subject YO, except for the gains (*a*, *b*, and *g*), which were reduced to model impaired hearing. For subject JK, with severe hearing loss, it was also necessary to reduce BW_{lin} (see Fig. 8 caption). Further studies will be required to evaluate the potential of this methodology.

ACKNOWLEDGMENTS

The authors acknowledge the advice and support of Chris Plack. The authors also thank two anonymous reviewers for constructive comments on an earlier version of this article. The development of the DRNL filter has progressed over many years and has involved contributions from a number of collaborators. The authors would like to thank, in particular, Michael Hewitt, Trevor Shackleton, and Mike Stone for substantial assistance at various times. Author EALP's work was supported by the Junta de Comunidades de Castilla La Mancha (Consejería de Sanidad, Ref. 2001-01044) and by the Universidad de Castilla–La Mancha.

APPENDIX: DIGITAL IMPLEMENTATION OF THE DRNL FILTER

The DRNL filter was implemented digitally in the time domain by implementing each of its filters and gains as a digital component. The implementation of each building component was done as follows.

1. The gammatone filters

The GT filter has an impulse response of the form (Patterson *et al.*, 1992)

$$h(t)=kt^{(n-1)}\exp(-2\pi Bt)\cos(2\pi f_c t+\varphi) \quad (t\geqslant 0), \tag{A1a}$$

$$h(t)=0 \quad (t<0), \tag{A1b}$$

where n is the order of the filter, B is its bandwidth, f_c is its center frequency, φ is its phase, and k is a gain.

The DRNL filter uses several cascades of first-order ($n=1$) GT filters only (see Fig. 3 and main text). They were implemented digitally as an infinite impulse response filter as follows (M. Stone, Exp. Psychology Lab., Cambridge, UK, personal communication, see also Slaney, 1993):

$$y[i]=a_0\cdot x[i]+a_1\cdot x[i-1]-b_1\cdot y[i-1] - b_2\cdot y[i-2], \tag{A2}$$

where $[i]$ refers to the ith sample of the digital signal, x and y are the input and output signals to/from the filter, respectively, and the coefficients are calculated as follows:

$$a_0=\left|\frac{1+b_1\cos\theta-jb_1\sin\theta+b_2\cos(2\theta)-jb_2\sin(2\theta)}{1+\alpha\cos\theta-j\alpha\sin\theta}\right|, \tag{A3a}$$

$$a_1=\alpha\cdot a_0, \tag{A3b}$$

$$b_1=2\alpha, \tag{A3c}$$

$$b_2=\exp(-2\phi), \tag{A3d}$$

where

$$\theta=2\pi f_c dt, \tag{A3e}$$

$$\phi=2\pi B dt, \tag{A3f}$$

$$\alpha=-\exp(-\phi)\cos\theta, \tag{A3g}$$

and $j=\sqrt{(-1)}$, and dt is the sampling period of the digital signal.

2. The low-pass filters

The DRNL filter implementation includes several cascades of second-order Butterworth lowpass filters (see Fig. 3 and main text). These were implemented digitally as follows:

$$y[i]=C\cdot x[i]+2\cdot C\cdot x[i-1]+C\cdot x[i-2]-D\cdot y[i-1]-E\cdot y[i-2], \tag{A4}$$

where the coefficients are

$$C=\frac{1}{1+\sqrt{2}\cot\theta+\cot^2\theta}, \tag{A5a}$$

$$D=2C(1-\cot^2\theta), \tag{A5b}$$

$$E=C(1-\sqrt{2}\cot\theta+\cot^2\theta), \tag{A5c}$$

and

$$\theta=\pi f_c dt, \tag{A5d}$$

where f_c is the 3-dB-down cut-off frequency of the low-pass filter, and dt is the sampling period of the digital signal.

3. The linear gain

The gain in the linear path of the DRNL filter was implemented digitally in the time domain as follows:

$$y[i]=g\cdot x[i], \tag{A6}$$

where $[i]$ refers to the ith sample of the digital signal, and x and y are the input and output signals to/from the linear gain stage, respectively.

4. The nonlinearity

The time domain digital implementation of the ''broken-stick'' nonlinearity was as follows:

$$y[i]=\text{sign}(x[i])\cdot\min(a|x[i]|,\ b|x[i]|^c), \tag{A7}$$

where $[i]$ refers to the ith sample of the digital signal, x and y are the input and output signals to/from the nonlinearity, and a, b, and c are parameters.

Abbas, P. J., and Sachs, M. B. (**1976**). ''Two-tone suppression in auditory-nerve fibers: Extension of stimulus response relationship,'' J. Acoust. Soc. Am. **59**, 112–122.

Baker, R. J., Rosen, S., and Darling, A. M. (**1998**). ''An efficient characterisation of human auditory filtering across level and frequency that is also physiologically reasonable,'' in *Psychophysical and Physiological Advances in Hearing*, edited by A. R. Palmer, A. Rees, A. Q. Summerfield, and R. Meddis (Whurr, London), pp. 81–88.

Carney, L. H. (**1993**). ''A model for the responses of low-frequency auditory-nerve fibers in cat,'' J. Acoust. Soc. Am. **93**, 401–417.

Duifhuis, H. (**1980**). ''Level effects is psychophysical two-tone suppression,'' J. Acoust. Soc. Am. **67**, 914–927.

Giguère, C., and Woodland, P. C. (**1994**). ''A computational model of the auditory periphery for speech and hearing research. I. Ascending path,'' J. Acoust. Soc. Am. **95**, 331–342.

Glasberg, B. R., and Moore, B. C. J. (**1990**). ''Derivation of auditory filter shapes from notched-noise data,'' Hear. Res. **47**, 103–138.

Glasberg, B. R., and Moore, B. C. J. (**2000**). ''Frequency selectivity as a function of level and frequency measured with uniformly exciting notched noise,'' J. Acoust. Soc. Am. **108**, 2318–2328.

Goldstein, J. L. (**1990**). ''Modeling rapid wave form compression on the basilar membrane as multiple-band-pass-nonlinearity filtering,'' Hear. Res. **49**, 39–60.

Goldstein, J. L. (**1995**). ''Relations among compression, suppression, and combination tones in mechanical responses of the basilar membrane: data and MBPNL model,'' Hear. Res. **89**, 52–68.

Goode, R. L., Killion, M., Nakamura, K., and Nishihara, S. (**1994**). ''New knowledge about the function of the human middle ear: development of an improved analog model,'' Am. J. Otol. **15**, 145–154.

Houtgast, T. (**1972**). ''Psychophysical evidence for lateral inhibition in hearing,'' J. Acoust. Soc. Am. **51**, 1885–1894.

Johnstone, B. M., Patuzzi, R., and Yates, G. K. (**1986**). ''Basilar membrane measurements and the travelling wave,'' Hear. Res. **22**, 147–153.

Kiang, N. Y. S., Liberman, M., Charles, S. W. F., and Guinan, J. J. (**1986**). ''Single unit clues to cochlear mechanisms,'' Hear. Res. **22**, 171–182.

Kringlebotn, M., and Gundersen, T. (**1985**). ''Frequency characteristics of the middle ear,'' J. Acoust. Soc. Am. **77**, 159–164.

Kulkarni, A., and Colburn, H. S. (**2000**). ''Variability in the characterization of the headphone transfer function,'' J. Acoust. Soc. Am. **107**, 1071–1074.

Lopez-Poveda, E. A., O'Mard, L. P., and Meddis, R. (**1998**). ''A revised computational inner-hair cell model,'' in *Psychophysical and Physiological Advances in Hearing*, edited by A. R. Palmer, A. Rees, A. Q. Summerfield, and R. Meddis (Whurr, London), pp. 112–119.

Lyon, R. F. (**1982**). ''A computational model of filtering, detection, and compression in the cochlea,'' IEEE Proceedings, pp. 1282–1285.

McFadden, D., and Yama, M. F. (**1983**). ''Upward shifts in the masking pattern with increasing masker intensity,'' J. Acoust. Soc. Am. **74**, 1185–1189.

Meddis, R., O'Mard, L. P., and Lopez-Poveda, E. A. (**2001**). ''A computational algorithm for computing nonlinear auditory frequency selectivity,'' J. Acoust. Soc. Am. **109**, 2852–2861.

Møller, H., Hammershøl, D., Jensen, C. B., and Sørensen, M. F. (**1995**). ''Transfer characteristics of headphones measured on human ears,'' J. Audio Eng. Soc. **43**, 203–217.

Moore, B. C. J. (**1998**). *Cochlear Hearing Loss* (Whurr, London).

Moore, B. C. J., and Glasberg, B. R. (**1987**). ''Formulae describing frequency selectivity in the perception of loudness, pitch and time,'' in *Frequency Selectivity in Hearing*, edited by B. C. J. Moore (Academic, London).

Nelson, D. A., and Schroder, A. C. (**1999**). ''Forward masking recovery and peripheral compression in normal-hearing and cochlear-impaired ears,'' J. Acoust. Soc. Am. **106**, 2176–2177(A).

Oxenham, A. J., and Plack, J. C. (**1997**). ''A behavioral measure of basilar-membrane nonlinearity in listeners with normal and impaired hearing,'' J. Acoust. Soc. Am. **101**, 3666–3675.

Patterson, R, Robinson, K., Holdsworth, J., McKeown, Zhang, C., and Allerhand, M. (**1992**). ''Complex sounds and auditory imaging,'' in *Auditory Physiology and Perception*, edited by Y. Cazals, K. Horner, and L. Demany (Pergamon, Oxford, England), pp. 429–443.

Plack, C. J., and Oxenham, A. J. (**2000**). ''Basilar-membrane nonlinearity estimated by pulsation threshold,'' J. Acoust. Soc. Am. **107**, 501–507.

Pralong, D., and Carlile, S. (**1996**). ''The role of individualized headphone calibration for the generation of high fidelity virtual auditory space,'' J. Acoust. Soc. Am. **100**, 3785–3793.

Rhode, W. S. (**1971**). ''Observations of the vibration of the basilar membrane in squirrel monkey using the Mössbauer technique,'' J. Acoust. Soc. Am. **49**, 1218–1231.

Rhode, W. S., and Cooper, N. P. (**1996**). ''Nonlinear mechanics in the apical turn of the chinchilla cochlea *in vivo*,'' Aud. Neurosci. **3**, 102–121.

Rhode, W. S., and Recio, A. (**2000**). ''Study of the mechanical motions in the basal region of the chinchilla cochlea,'' J. Acoust. Soc. Am. **107**, 3317–3332.

Robles, L., Ruggero, M. A., and Rich, N. C. (**1986**). ''Basilar membrane mechanics at the base of the chinchilla cochlea. I. Input-output functions, tuning curves, and response phases,'' J. Acoust. Soc. Am. **80**, 1364–1374.

Robles, L., Ruggero, M. A., and Rich, N. C. (**1991**). ''Two-tone distortion in the basilar membrane of the cochlea,'' Nature (London) **349**, 413–414.

Rosen, S., Baker, R. J., and Darling, A. (**1998**). ''Auditory filter nonlinearity at 2KHz in normal hearing listeners,'' J. Acoust. Soc. Am. **103**, 2539–2550.

Ruggero, M. A., Rich, N. C., and Recio, A. (**1996**). ''The effect of intense acoustic stimulation on basilar membrane vibrations,'' Aud. Neurosci. **2**, 329–345.

Ruggero, M. A., Robles, L., and Rich, N. C. (**1992**). ''Two-tone suppression in the basilar membrane of the cochlea: Mechanical basis of auditory-nerve rate suppression,'' J. Neurophysiol. **68**, 1087–1099.

Ruggero, M. A., Rich, N. C., Recio, A. Shyamla Narayan, S., and Robles, L. (**1997**). ''Basilar-membrane responses to tones at the base of the chinchilla cochlea,'' J. Acoust. Soc. Am. **101**, 2151–2163.

Sellick, P. M., Patuzzi, R., and Johnstone, B. M. (**1982**). ''Measurements of basilar membrane motion in the guinea pig using the Mössbauer technique,'' J. Acoust. Soc. Am. **72**, 131–141.

Slaney, M. (**1993**). ''An efficient implementation of the Patterson-Holdsworth auditory filter bank,'' Apple Computer Technical Report #35, Apple Computer, Inc.

Yates, G. K., Winter, I. M., and Robertson, D. (**1990**). ''Basilar membrane nonlinearity determines auditory nerve rate-intensity functions and cochlear dynamic range,'' Hear. Res. **45**, 203–220.

Distortion product otoacoustic emission input/output functions in normal-hearing and hearing-impaired human ears

Patricia A. Dorn,[a] Dawn Konrad-Martin, Stephen T. Neely, Douglas H. Keefe, Emily Cyr, and Michael P. Gorga
Boys Town National Research Hospital, Omaha, Nebraska 68131

(Received 2 May 2001; revised 8 September 2001; accepted 17 September 2001)

DPOAE input/output (I/O) functions were measured at 7 f_2 frequencies (1 to 8 kHz; $f_2/f_1=1.22$) over a range of levels (−5 to 95 dB SPL) in normal-hearing and hearing-impaired human ears. L_1-L_2 was level dependent in order to produce the largest 2 f_1-f_2 responses in normal ears. System distortion was determined by collecting DP data in six different acoustic cavities. These data were used to derive a multiple linear regression model to predict system distortion levels. The model was tested on cochlear-implant users and used to estimate system distortion in all other ears. At most but not all f_2's, measurements in cochlear implant ears were consistent with model predictions. At all f_2 frequencies, the ears with normal auditory thresholds produced I/O functions characterized by compressive nonlinear regions at moderate levels, with more rapid growth at low and high stimulus levels. As auditory threshold increased, DPOAE threshold increased, accompanied by DPOAE amplitude reductions, notably over the range of levels where normal ears showed compression. The slope of the I/O function was steeper in impaired ears. The data from normal-hearing ears resembled direct measurements of basilar membrane displacement in lower animals. Data from ears with hearing loss showed that the compressive region was affected by cochlear damage; however, responses at high levels of stimulation resembled those observed in normal ears. © *2001 Acoustical Society of America.* [DOI: 10.1121/1.1417524]

PACS numbers: 43.64.Ha, 43.64.Jb [BLM]

I. INTRODUCTION

Distortion product otoacoustic emissions (DPOAEs) are produced by nonlinear mechanisms within the cochlea that are tied to outer hair cell (OHC) function. Normal OHC function is necessary for the auditory sensitivity, sharp frequency resolution, and wide dynamic range that are hallmarks of normal auditory function. A literature exists describing normal patterns of DPOAEs [see Probst *et al.* (1991) or Lonsbury-Martin *et al.* (2001) for reviews]. It is well known that damage to the OHCs results in reduced auditory sensitivity (e.g., Dallos *et al.*, 1978; Liberman and Dodds, 1984). As a consequence, one would expect that some relation would exist between DPOAEs and auditory threshold. Indeed, many studies have shown that DPOAEs are reduced or absent in ears with hearing loss (e.g., Martin *et al.*, 1990; Bonfils and Avan, 1992; Avan and Bonfils, 1993; Gorga *et al.*, 1993, 1996, 1997, 2000; Stover *et al.*, 1996; Kim *et al.*, 1996). DPOAEs are now in common use for the purposes of identifying normal or impaired auditory function, as defined by threshold sensitivity. In these applications, eliciting stimuli are typically presented at a single moderate level, DPOAE level (or signal-to-noise ratio, SNR) is measured, and a determination is made as to whether the response would be expected from an ear with normal hearing or an ear with hearing loss. The clinical utility of these measurements is based on the theory that OHC function is important in determining both DPOAE level and auditory sensitivity.

Furthermore, damage to the OHCs might be expected to affect the way cochlear responses grow with level. For example, normal input/output (I/O) functions derived from direct basilar membrane (BM) measurements (Ruggero and Rich, 1991; Ruggero *et al.*, 1997) and from ear-canal recordings (Norton and Rubel, 1990; Whitehead *et al.*, 1992a, b; Mills *et al.*, 1993; Mills and Rubel, 1994) in lower animals show a similar pattern of response. When a place on the BM is driven at its best or characteristic frequency (CF), there is linear growth in response to low stimulus levels, nonlinear growth at moderate levels, and a linear response to stimuli presented at high levels (e.g., Ruggero and Rich, 1991). However, when this same place is driven by a tone whose frequency is well below CF, the level at which motion is first detected is elevated, there is little or no evidence of compression, and the slope is steeper, compared to the slope for CF tones. Following administration of furosemide, an agent known to affect the stria vascularis (which maintains the endocochlear potential that serves as the power supply for OHC motility), the lowest level at which BM motion was detected was elevated, compression was reduced, and the slope of the I/O function was steepened when the stimulus was at CF. Thus, disabling the OHCs resulted in a response to a tone at CF that was reminiscent of the response to a tone lower in frequency relative to CF. Interestingly, the administration of furosemide had no influence on the response to the tone below CF.

Similar patterns have been observed in indirect measurements of response growth to tonal stimuli from lower animals with normal and abnormal cochlear function. Specifically, DPOAE I/O functions were nearly linear at levels close

[a]Electronic mail: dornp@boystown.org

to threshold, demonstrated compression for moderate-level stimuli, and showed a more linear pattern at high levels. (Whitehead *et al.*, 1992b; Norton and Rubel, 1990; Mills and Rubel, 1994; Ruggero and Rich, 1991). Systematic changes in these DPOAE I/O functions were observed following the administration of ototoxic drugs or soon after the animal was sacrificed. DPOAE threshold was elevated, the region of compression was reduced, and the slope steepened. Just as the normal DPOAE I/O function resembled direct BM measurements from lower animals, so did the DPOAE I/O function following cochlear insult.

DPOAE I/O data have been described in terms of two distinct sources (Norton and Rubel, 1990; Whitehead *et al.*, 1992a, b; Mills and Rubel, 1994). One is a low-level source that is active, sharply tuned, and governed by interactions between the OHCs and mechanical motion of the BM. This source is physiologically vulnerable, as evidenced by large response changes at low and moderate levels when the cochlea is damaged. In the two-source model, there also is a high-level source that is thought to be passive, underlies the active components at low-levels, and reflects BM vibration without acting upon it. This source is more resistant to cochlear trauma, shows little reduction in amplitude between pre-and post-trauma conditions, and exhibits response growth that is more linear, compared to the low- and moderate-level portion of the I/O function. Whitehead *et al.* (1992a, b) further note that the low-level and high-level portions of the function are differentially altered with explorations into the frequency (regions from 1 to 10 kHz) and level (45 to 75 dB SPL) space. In addition to the two-source model to describe DPOAE I/O functions, a single-source model has also been presented (Lukashkin and Russell, 1999) to account for observed DPOAE I/O function patterns. They suggest that any system having a saturating input–output function, such as the mechanoelectrical transduction of the OHCs, can produce these patterns.

In summary, data from lower animals reveal that direct measures of BM motion and indirect DPOAE measures of cochlear-response properties are similar, at least in form, for a wide range of levels in ears with normal hearing, and undergo similar changes in ears with induced cochlear lesions. While direct measurements of BM motion are impossible in humans, DPOAE measurements are feasible. Currently, DPOAEs are used mainly to detect threshold hearing loss. Given the similarities between direct and indirect measures of cochlear responses for a wide range of conditions in lower animals, however, it is possible that DPOAE measurements will provide information regarding suprathreshold processing in humans. Indeed, our own preliminary findings in three subjects with normal hearing and one subject with mild hearing loss suggested that DPOAEs can provide indirect measures that are at least qualitatively similar to what has been observed in lower animals (Neely *et al.*, 2000). It is useful to consider responses from normal and impaired human ears in light of direct and indirect measurements in healthy and traumatized ears of lower animals, thus affording an opportunity to compare outcomes from human and lower animal research. This may help determine the extent to which indirect DPOAE measurements in humans can be used to provide insights into cochlear function over a wide range of levels that are similar to estimates based on direct measurements in lower animals.

The present study was designed to measure DPOAE I/O functions in humans over a wide range of input levels, with a goal of determining the extent to which these data can be used as indirect measures of cochlear-response properties for both normal and impaired ears. The responses obtained in humans with normal hearing are compared to the responses seen in humans with hearing loss. To the extent that DPOAE I/O functions are measures of cochlear-response growth, these comparisons help to describe the changes in response growth that occur as a consequence of hearing loss in humans.

II. METHODS

A. System distortion

The level of distortion produced by the measurement system was estimated by measuring distortion products in six different cavities: (1) an IEC711 coupler with the ER-10C microphone at the standard distance from the coupler's microphone, (2) an IEC711 coupler with the ER-10C within 1 mm of the microphone, (3) a standard 2-cm^3 coupler, (4) a small brass cavity (0.1 cm^3), (5) a 10-m PVC tube (internal diameter = 8 mm), and (6) a 65-cm^3 syringe. The distance between the tip of the ER-10C probe and the end of the cavity ranged from less than 1 mm (the close position in the IEC711 coupler and in the 0.1-cm^3 brass tube) up to 10 m (the 10-m tube). This set of cavity measurements was used in efforts to determine the source of system distortion. The cavities with small volumes (the IEC711 coupler with the probe unit close to the microphone and the small brass cavity) were chosen because targeted levels could be achieved with less voltage delivered to the loudspeakers. Thus, these conditions should isolate distortion due mainly to the ER-10C probe's microphone and amplifier. Measurements in the large cavity (65-cm^3 syringe) were included because this represented a condition in which larger voltages were needed to achieve targeted SPLs. These measurements were included to help determine if system distortion was generated by the loudspeakers. Measurements in standard cavities (IEC711 coupler with the probe in the standard position, the 2-cm^3 cavity) were included to represent the standard conditions for the ''average'' human ear. The measurements in the long tube were chosen because the tube presents an impedance similar to that seen in an anechoic termination roughly corresponding to a normal average ear canal, without standing waves. Such standing waves are present in standard cavities and in human ear canals. The distortion in each of these cavities was similar, and did not allow us (on the basis of these measurements) to isolate the source exclusively to the stimulation or recording side of the measurement system. However, the availability of measurements in all six cavities allowed us to derive a predictive model of system distortion.

Signal levels were calibrated in each cavity, so that all measurements were made for equivalent SPLs at the probe microphone. Cavity measurements were made with primary levels of 75 to 85 dB SPL (f_2 frequencies at 6 and 8 kHz) or

75 to 95 dB SPL (f_2 frequencies at 1, 1.5, 2, 3, and 4 kHz), determined by the output limitations of the loudspeakers in the ER-10C. The ER-10C probe system was modified in order to bypass the 20-dB attenuator in the probe driver-amp and, thus, enabled us to achieve these output levels. In addition to the developed SPLs, the voltages (dBV) needed to drive the two loudspeakers to achieve these SPLs and the primary frequencies were noted. These values were used as input variables into a multiple linear regression to provide an estimate of system distortion. For each cavity, data were input to the linear model if the measured stimulus levels (L_1 and L_2) were within 1 dB of the target value. Because L_2 had linear growth, the predictive linear model for system distortion could be extended down to lower L_2 levels ($<$75 dB SPL). The following predictive linear model for system distortion (D), in dB SPL, was derived:

$$D = 1.57L_2 + 1.89V_1 + -2.51V_2 + 1.48f_2 - 106.90, \qquad (1)$$

where L_2 represents levels from 75 to 85 or 95 dB SPL in 5-dB steps. V_1 and V_2 are the voltages (in dBV) needed to drive the loudspeakers that produced f_1 and f_2, respectively. The f_2 frequencies were 1, 1.5, 2, 3, 4, 6, and 8 kHz.

To obtain an overall estimate of the level below which reliable data could not be obtained, the energies derived from these system-distortion estimates were added to the measured noise-floor estimates in each ear to determine a distortion-plus-noise level (D+N). The D+N estimates were dominated by noise at levels below 70 dB SPL and by distortion at levels of 70 dB SPL and above. It should be noted that in the development of the predictive linear model previously presented, more complicated models involving more input variables were evaluated, such as interaction and squared value terms. However, the derived estimates of system distortion from these more complex models were similar to those obtained with the simpler model. The distortion estimate (D) was first applied to cochlear-implant users to test the model. Cochlear-implant users were selected because it was assumed that any distortion measured from their implanted ears (device turned off) would not be of cochlear origin, due to the magnitude of their hearing losses and the implant surgical procedure.

B. Subjects

DPOAE I/O functions were measured in 27 ears from 27 subjects (aged 14 to 40 years) having thresholds of 20 dB HL or better (*re*: ANSI, 1996) at octave and half-octave frequencies from 0.250 to 8 kHz. These measures were also made in 84 ears from 50 subjects (aged 13 to 83 years) with hearing loss ranging from 25 to $>$70 dB HL. In addition, four subjects with cochlear implants were used (implanted ear with device turned off) in efforts to describe the levels at which system distortion occurred (as described in Sec. II A). All subjects had normal middle-ear function, based on 226-Hz tympanometry, at the time of the DPOAE test.

C. Stimuli

DPOAE I/O functions were measured in response to pairs of primary tones, labeled f_1 and f_2, at a fixed $f_2/f_1 = 1.22$, with f_2 ranging from 1 to 8 kHz in half-octave steps. The DPOAE I/O functions were measured at L_2 levels ranging from -5 to 85 dB SPL (6 and 8 kHz) or from -5 to 95 dB SPL (1, 1.5, 2, 3, and 4 kHz). The levels of the stimuli were determined in the ear canal at the plane of the probe. Primary tones were presented such that as L_2 decreased below 65 dB SPL, the separation between L_1 and L_2 increased. This level difference paradigm has been shown to maximize the measured level of the $2f_1 - f_2$ DPOAE in normal-hearing ears (Whitehead *et al.*, 1995; Kummer *et al.*, 1998; Janssen *et al.*, 1998).

In some subjects, due to equipment limitations, it was difficult to attain the target stimulus level in the ear canal at higher levels. As a consequence, the only data points retained for further analyses were those for which the average ear-canal level $(L_1+L_2)/2$, was within ± 3 dB of the target level. This resulted in the removal of 213 data points, with the majority (141) occurring at 95 dB SPL and mainly at f_2 frequencies from 1.5 to 4 kHz. In contrast, the number of data points meeting this inclusion criterion were 4967, meaning that, for the majority of ears and stimulus conditions, targeted SPLs were achieved.

D. Procedures

DPOAE measures were obtained with the subject comfortably seated in a sound-treated booth. The primary tones were generated using a Pinnacle (Turtle Beach) sound card and delivered to the ear canal by means of an ER-10C (Etymotic Research) probe-microphone system, in which the probe driver-preamp was modified in order to recover 20 dB of attenuation. The ER-10C houses two loudspeakers (receivers) and a microphone that were coupled to the ear canal by means of a foam probe tip. The two primary tones were generated by separate channels of the sound card, delivered individually to each loudspeaker, and mixed acoustically in the ear canal. Testing was performed using a PC running custom-designed software (EMAV, Neely and Liu, 1993) that enables the use of measurement-based stopping rules. Data collection at each point on the I/O function continued until the noise floor during individual measurements was equivalent to the estimated level of system distortion based on coupler measurements, or after 32 s of artifact-free averaging, whichever occurred first. A stopping rule based on coupler measures of system distortion was used because these estimates were level dependent, increasing as primary level increased above 70 dB SPL (see Fig. 2). For L_2 levels $\leqslant$70 dB SPL, this rule resulted in a stopping criterion (D+N) of between -20 and -30 dB SPL, because the criterion was dominated by noise at these moderate and low primary levels. Thus, a stopping rule based on noise level could have been used. However, there would have been little point in stopping at a fixed noise level (for example, -20 or -30 dB SPL) for primary levels $\geqslant$75 dB SPL because ''response'' levels at $2f_1 - f_2$ equivalent to system distortion levels would not have been interpretable as biological responses, regardless of the noise level measured at adjacent frequencies. A stopping criterion based on the sum of system distortion and noise took this into account.

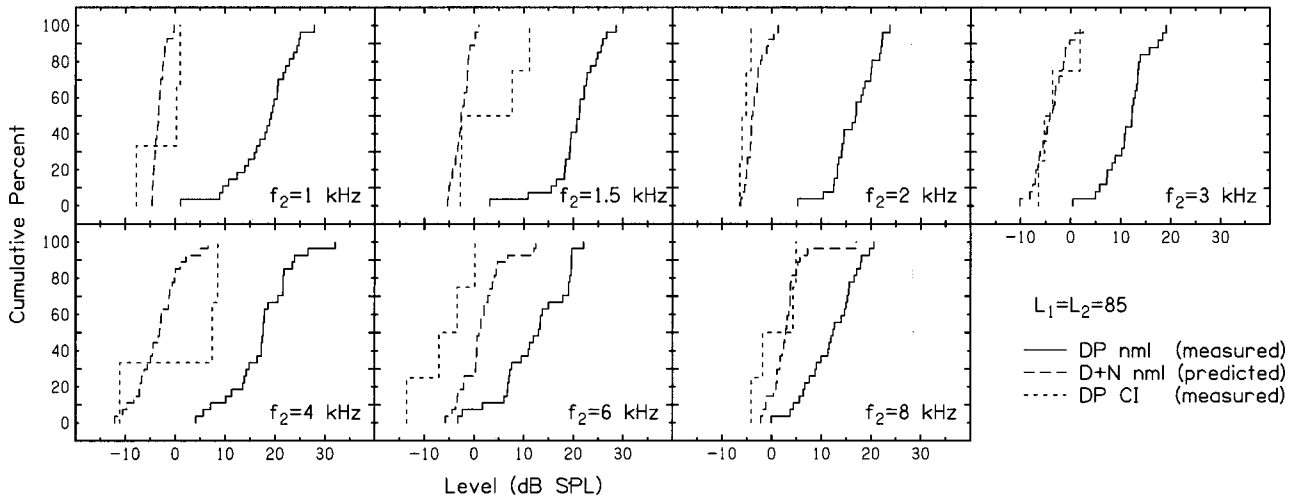

FIG. 1. Cumulative distributions (in percent) of DPOAE response levels at seven f_2 frequencies in normal-hearing subjects (solid line) and in cochlear-implant subjects (short dashed line) when $L_1=L_2=85$ dB SPL. An overall estimate of system distortion and noise (D+N, long dashed line) is displayed for the normal-hearing group.

III. RESULTS

A. Estimates of system distortion

Estimates of system distortion, as determined through the cavity measurements and analyses described earlier, were used to help ascertain if measures obtained at high stimulus levels were of biological origin or due to system distortion generated by the hardware. The estimate of D+N in normal ears was viewed in relation to DPOAE levels from normal ears ($N=27$). The same measurements were made in ears with cochlear implants ($N=3$ at 1 and 4 kHz or $N=4$ at 1.5, 2, 3, 6, and 8 kHz) to determine whether distortion products (DPs) measured under these circumstances were similar to estimates of D+N. If so, these apparent DPs may be interpreted as arising from system distortion. Recall that cochlear-implant subjects were included to provide a model of a biological system in which cochlear-generated distortion should not occur. Although data will be presented for a single high-level condition, similar data were acquired for all high-level primaries ($\geqslant$75 dB SPL).

Figure 1 displays estimates of D+N and DPOAEs in subjects with normal hearing at each f_2 in the form of cumulative distributions (in percent). Cumulative distributions of the DP also are shown for the group of subjects with cochlear implants. The results shown in this figure are for the stimulus condition in which $L_1=L_2=85$ dB SPL. This primary level was chosen because it was the highest targeted SPL that could be achieved at all seven test frequencies.

DPOAEs in normal-hearing subjects were separated from estimates of D+N at all seven frequencies. In addition, the DPs from subjects with cochlear implants were similar to or less than D+N estimates at five of seven frequencies (1, 2, 3, 6, and 8 kHz), consistent with model predictions, but were higher than D+N at 1.5 and 4 kHz. Even for these two frequencies, however, DPOAEs from ears with normal hearing were separated from DPs in ears with cochlear implants. Thus, we would conclude that at this L_2, measured DPOAE levels were biological in origin, at least in ears with normal hearing. Unfortunately, the differences between D+N and cochlear-implant cumulative distributions increased (with higher distortion in cochlear-implant ears) at the higher L_2 levels of 90 and 95 dB SPL, even though distributions of DPs in ears with cochlear implants remained separated from distributions of DPOAEs in ears with normal hearing. The distributions of D+N and DPOAEs from normal-hearing subjects also remained separated at these higher L_2 levels.

Given that the DPOAEs in normal ears were highest in level, that estimates of D+N were the lowest in level, and that DPs from ears with cochlear implants were greater than D+N, but less than those observed in ears with normal hearing, several hypotheses may be suggested. The responses from normal ears included all possible sources of distortion, including distortion generated by biological sources as well as distortion generated by the hardware used to elicit and record these responses. However, it was observed that in normal-hearing ears, DPOAEs exceeded the level produced by cochlear-implant subjects and estimates of system distortion (assuming that the D+N measured in the couplers estimates the D+N levels occurring when testing in ears). This observation suggests that the distortion measured in normal ears was of biological origin.

The more complicated interpretation is associated with the data from subjects with cochlear implants. These are ears in which cochlear-generated distortion was not expected. The combination of pre-implant hearing loss (which would be consistent with at least severe loss of both OHCs and inner hair cells) and the changes to any residual nonlinear cochlear mechanical response as a result of implantation would likely eliminate all cochlear sources of distortion. Yet, the distortion measured in the ear canals of these implant subjects sometimes exceeded estimates of D+N (see, for example, Fig. 1, $f_2=4$ kHz). If we accurately estimated D+N, then it may not be entirely appropriate to associate the distortion measured in their ear canals with system distortion, meaning that an alternative, as yet undetermined, biological source might exist.

In summary, the above observations led us to conclude

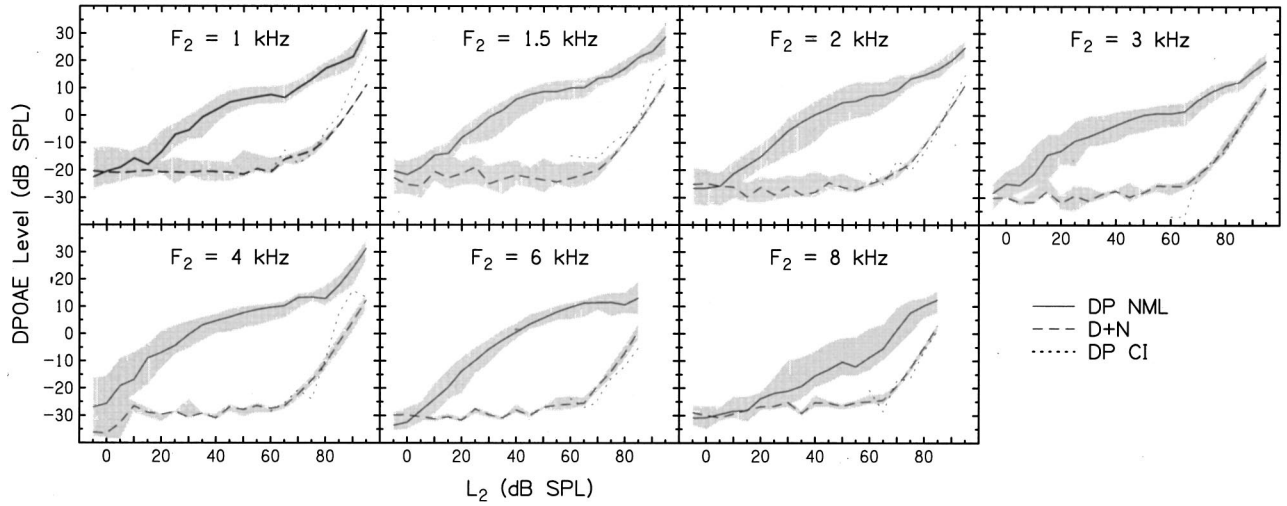

FIG. 2. DPOAE I/O functions for normal-hearing subjects at seven f_2 frequencies. Median DPOAE levels (solid line) and median D+N levels (dashed line) are shown, along with their associated interquartile ranges (25th and 75th percentiles, shaded regions). Median data from cochlear-implant subjects are shown as dotted lines.

that our measurements of DPOAEs were biological (cochlear) in origin, at least for subjects with normal hearing. As will be shown subsequently (Fig. 3), similar conclusions may apply for some subjects with hearing loss, but we are less confident of the source of the DPOAE as the magnitude of hearing loss increases into the moderate-to-severe range. As a consequence, caution must be exercised when considering data points at those higher levels in ears with hearing loss, due to the fact that, for some of these subjects, their responses were not well separated from those observed in cochlear-implant ears.

B. DPOAE I/O functions in subjects with normal hearing

Figure 2 displays DPOAE I/O functions for normal-hearing subjects. The median DPOAE levels and median D+N levels are shown, along with their associated interquartile ranges (25th to 75th percentile, shaded regions). The median DPs from subjects with cochlear implants are also shown in each panel. Medians were chosen to be consistent with other representations in this figure. At all f_2 frequencies except 8 kHz, DPOAEs from ears with normal hearing increased above the overall noise estimate (D+N) with a relatively steep slope, followed by a compressive region for moderate input levels. Starting at between 60 and 75 dB SPL, the slope of the I/O function steepened. The steeper high-level segment was not obvious at 6 and 8 kHz, compared to lower frequencies, which may be partially due to stimulus output limitations at these two frequencies. The overall pattern was reminiscent of what has been reported from direct measurements of basilar-membrane motion in lower animals (Ruggero *et al.*, 1997; Ruggero and Rich, 1991). This finding was not surprising, given that DPOAEs are tied to BM mechanics. At 8 kHz, the D+N function was similar to that of other f_2 frequencies; however, DPOAE level at low stimulus levels had a slope that was less than was observed at other frequencies. In addition, the range of levels over which compression was obvious was reduced at 8 kHz, in comparison to all other f_2 frequencies. Finally, greater variability was observed at 8 kHz, although it was unclear how this would contribute to the differences in the shape of I/O functions. Even with these differences across f_2, separation between DPOAE and D+N functions was observed for the entire range of stimulus levels, including high L_2 levels (all f_2 frequencies) once DPOAE threshold was exceeded. Furthermore, DPOAE levels in ears with normal hearing exceeded the levels observed in subjects with cochlear implants. At three f_2 frequencies (1, 1.5, and 4 kHz), the median DPs from implanted ears exceeded D+N at the highest L_2 levels. At the other four f_2 frequencies, the median levels in subjects with cochlear implants were at or below system distortion. All of these findings support the view that high-level responses were of biological origin in normal human ears. In spite of these observations, we remain cautious in our interpretation of results for levels >85 dB SPL.

C. DPOAE I/O functions in subjects with hearing loss

Data from subjects with hearing loss were grouped according to degree of loss and are presented in Fig. 3. Within this figure, median data from the normal-hearing and hearing-loss groups are represented by a series of thinning solid lines; the thinner the line, the greater the hearing loss. In addition, median data from subjects with cochlear implants are included as dotted lines. There are several observations to be made from these data. DPOAE I/O functions from ears with hearing loss differ from those observed in ears with normal hearing. This was true regardless of the amount of hearing loss. I/O functions from ears with hearing loss were characterized by elevations in threshold (defined as the lowest level at which the DPOAE exceeds D+N), reduced range of stimulus levels over which compression was apparent, and, as a consequence, steeper slopes through the moderate-level range, compared to I/O functions in the normal-hearing group. At 2 and 4 kHz, this increase in DPOAE threshold and steepening of the slope through the

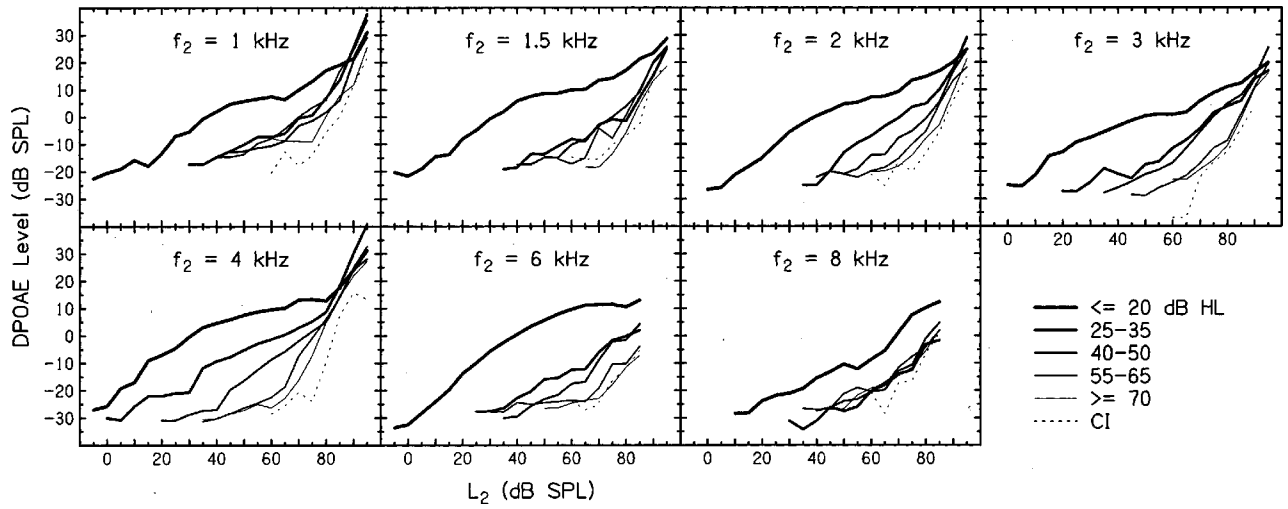

FIG. 3. DPOAE I/O functions at seven f_2 frequencies in subjects with normal-hearing and in subjects with hearing loss. Data are grouped according to audiometric threshold. Median data are represented by a series of thinning solid lines; the thinner the line, the greater the hearing loss. Data from the normal-hearing subjects (thickest solid line) are reproduced from Fig. 2 for comparison purposes. Dotted lines represent median data from cochlear-implant subjects.

compressive region systematically changed as hearing loss increased. At the other frequencies, changes in the I/O function were observed, but the pattern of change was less orderly with regard to magnitude of hearing loss. At 8 kHz, the median DPOAE I/O functions from all impaired ears (regardless of the magnitude of hearing loss) were clustered together and differed less from the values seen in patients with cochlear implants. With few exceptions ($f_2=8$ kHz), those cases in which the estimated DPOAE level was indistinguishable from the data produced by ears with cochlear implants were restricted to hearing losses of 55 dB HL or more. At high levels, the grouped data from most of the hearing-loss categories approximated the pattern observed in normal ears and exceeded the median level from cochlear-implant users, the exception to this being the data for an f_2 of 8 kHz. These observations should be considered with the knowledge that system distortion increases as stimulus level increases, thus making it more difficult to separate it from high-level responses in impaired ears.

Regardless of the source of distortion, the combination of DPOAE threshold elevation and near-normal response levels at high stimulus levels resulted in DPOAE I/O functions that were steeper in impaired ears, compared to I/O functions in ears with normal hearing. In turn, these data suggest that response growth, as estimated by DPOAE I/O functions, is more rapid in impaired ears.

D. DPOAE I/O slope estimates in normal and impaired ears

In an effort to quantify the DPOAE I/O functions to help in comparisons between normal-hearing and hearing-impaired ears, the following equation was used to fit the DPOAE data:

$$d(s)=n+\frac{g_0 s}{1+(g_1 s)^{1-p}}+(g_2 s)^2. \tag{2}$$

The term d refers to the distortion magnitude represented as a power. (To convert to level in dB, one would need to multiply the log of d by 10.) The signal power is represented by $s=10^{L2/10}$. The values of the parameters n, g_0, g_1, p, and g_2, were selected to fit the data. These parameters were estimated separately for each measurement. Parameter g_0 can be interpreted to represent the product of the forward and reverse transfer functions for the middle ear (Kemp, 1980). Parameter g_1 can be interpreted to represent the forward transfer function for the middle ear (Keefe, 2001). Parameter p determines the maximum amount of compression. These three parameters relate to the low-level and compressive portion of the I/O function. The parameter g_2 determines the high-level portion of the function and n is noise (independent of signal level). This equation was fitted separately to the median data for each group, including the data from subjects with normal hearing, subjects with hearing loss, and cochlear-implant subjects. The fits to the DPOAE I/O functions accounted for 98.6% of the variance across all f_2 frequencies and all groups.

The derivative of Eq. (2) was used to provide an estimate of the slope of the DPOAE I/O functions with respect to L_2. This approach provided a much smoother slope estimate than taking the difference between adjacent points on the fitted I/O function. Figure 4 presents slope estimates as a function of L_2, following the convention used in Fig. 3 for representing data from different groups by using different line weights.

The slope estimates for data derived from ears with normal hearing at frequencies below 8 kHz were the most straightforward and will be described first. The slope estimates were characterized initially by a steep rise to a local maximum asymptotic value near 1 dB/dB for L_2 levels of 10–20 dB SPL, going from threshold to the level at which the slope began to decrease as level was increased. The upper L_2 limit for the initially steep slope seldom exceeded 30 dB SPL. Beyond this level, the slope decreased to minimum slopes of between 0.1 to 0.3 dB/dB. This range of reduced slopes corresponded to the compressive region of the DPOAE I/O function and extended up to an L_2 of about 80

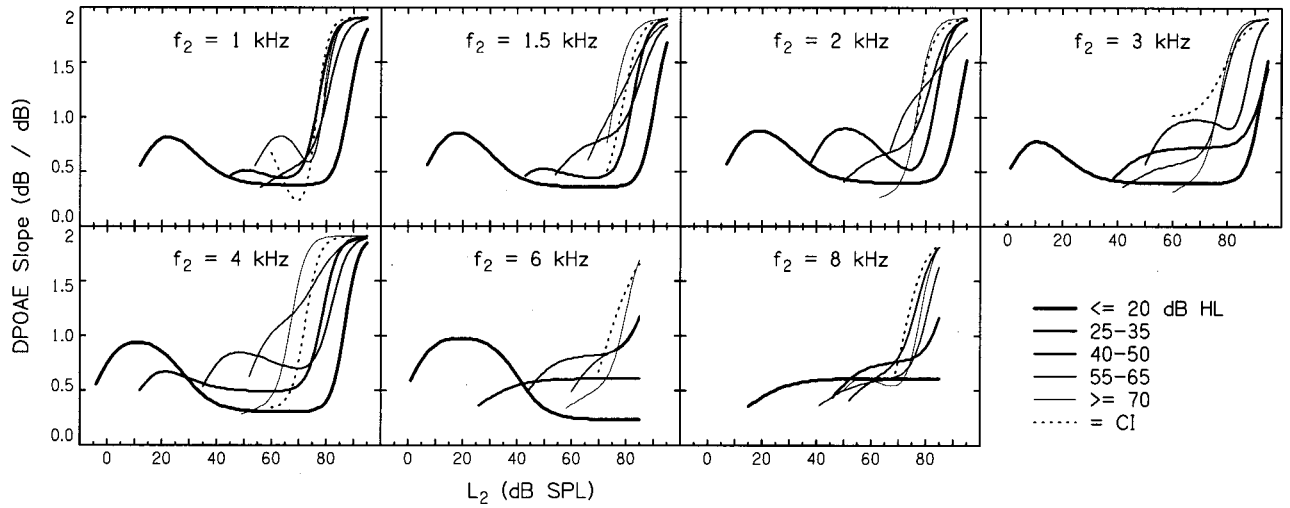

FIG. 4. Slope estimates from DPOAE I/O functions at seven f_2 frequencies. Data are grouped according to audiometric threshold, following the convention used in Fig. 3.

dB SPL. This region was followed by a rapid increase in slope as level increased above 80 dB SPL. The range (in dB) between the early peak at low levels and the steep rise at high levels was used as an estimate of the range of levels over which compression occurred (see Table I).

Among ears with hearing loss, the clearest slope pattern was observed at 4 kHz. For the two mildest hearing-loss groups, the slope initially rose to a local maximum, but achieved this slope at a higher L_2 compared to data from normal ears. Furthermore, the reduction in slope following the initial peak was less than that observed in ears with normal hearing. The steeply rising, high-level portion of the I/O functions actually shifted towards lower L_2 levels, compared to normal. It follows, therefore, that with hearing loss, the slope estimates indicated that both the amount of compression (the extent to which slope decreased for moderate level primaries) and the range of levels over which compression was observed were reduced.

The pattern in ears with greater hearing loss and for some of the other f_2 frequencies was more complex. The initial peak in the slope function, evident in normal ears, was frequently not present in the slope functions of ears with hearing loss, especially among ears with greater degrees of hearing loss. In addition, it was not always possible to identify a range of L_2 levels over which reduced slopes (i.e., compression) were evident. Rather, many of these slope functions were characterized only by a steeply sloping, high-level portion.

Table I presents the range of compression (in dB) for the six f_2 frequencies at which it could be estimated from the slope functions of Fig. 4. The range of compression was defined from the level of the initial low-level "peak" to the high level at which the slope attained the same value as it did for the initial peak. For all conditions, in order to identify a compressive range, the (fitted) SNR had to be at least 3 dB at the level of the initial peak. At 6 kHz, the high-level steep slope was not observed; therefore, the highest level tested ($L_2 = 85$ dB SPL) was taken as the upper limit of the compressive range. Empty cells in the table (25–35 dB HL group at $f_2 = 3$ and 6 kHz; 40–50 dB HL group at $f_2 = 1$, 1.5, 2, 3, and 6 kHz) as well as the absence of certain hearing-loss groups (55–65 and $\geqslant$70 dB HL groups at all f_2 frequencies) indicated that a compressive region (as defined from the slope functions) could not be identified for these conditions. Subjects with normal hearing produced the largest range of compression, varying from 65 to 79 dB. In the mild (25–35 dB HL) and moderate (40–50 dB HL) hearing-loss groups, the range of compression was always reduced compared to that found in the normal-hearing group.

Table II provides estimates of maximum compression, defined as the minimum slope within the compressive range. The smaller the values in the table, the greater the amount of compression. Lower minimum slopes were found for the normal-hearing group. Thus, greater reduction in output (i.e., compression) relative to linear growth with increases in level was observed in ears with normal hearing, compared to subjects with hearing loss. For all conditions in which it was possible to estimate a compressive range, compression was less in ears with hearing loss, as evidenced by the fact that minimum slopes were larger in these ears. Another way of stating this observation is that response grew more rapidly

TABLE I. Range of compression (dB).

Hearing group (dB HL)	f_2 frequency (kHz)					
	1	1.5	2	3	4	6
$\leqslant$20	65	71	72	79	75	76
25–35	21	27	32		53	
40–50					30	

TABLE II. Maximum compression (minimum DP I/O slope in dB/dB).

Hearing group (dB HL)	f_2 frequency (kHz)					
	1	1.5	2	3	4	6
$\leqslant$20	0.31	0.29	0.34	0.34	0.24	0.16
25–35	0.39	0.39	0.47		0.44	
40–50					0.67	

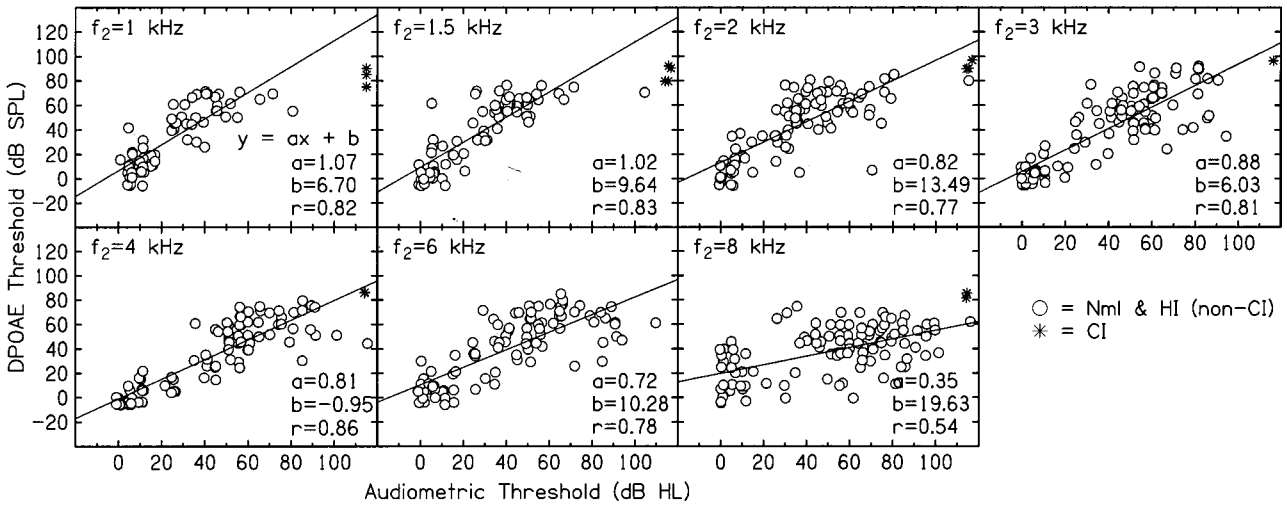

FIG. 5. Scatter plots of DPOAE threshold as a function of audiometric threshold for all subjects at each f_2. Circles represent individual data from normal-hearing and hearing-impaired (non-cochlear-implant) subjects, while asterisks represent individual data from cochlear-implant subjects. DPOAE threshold was defined as a response that was 3 dB above the estimate of D+N for each subject. Within each panel, the line was derived from a linear regression that was fit to the data, excluding cochlear implant data and data in which DPOAE thresholds in any ear were equivalent to the lowest "DPOAE thresholds" from among the implanted ears (see text for more detail). The correlation coefficient (r), slope (a), and intercept (b) are provided within each panel for each linear regression.

above DPOAE threshold in ears with hearing loss than it did in ears with normal hearing.

It may be important to recognize some of the limitations in the present data, the most important of which relates to system distortion, which would present greater problems for the high-level portions of the I/O functions. We are confident that the measured DPOAEs in ears with normal hearing were biological in origin because they exceeded estimates of system distortion. We are less certain regarding the DPOAEs that were measured in ears with hearing loss, especially as the hearing loss increased above 50–60 dB HL. It is possible that other sources of distortion may have contributed to these measurements. Still, there were many conditions in which the results suggested that the measured DPOAE level in ears with milder hearing losses were biological in origin (i.e., not due to system distortion), and there is little doubt that the slopes of these functions differ in ears with normal hearing from those observed in ears with any degree of hearing loss.

In summary, the data presented in Figs. 3 and 4 and in Tables I and II indicated that the range of stimulus levels over which compression was evident and the amount of compression was reduced in ears with hearing loss compared to subjects with normal hearing. In addition, only the steep, high-level portion of the DPOAE I/O function remained as the hearing loss worsened.

E. DPOAE threshold as a function of audiometric threshold

DPOAE I/O functions can also be used to estimate DPOAE thresholds. The expectation is that as audiometric thresholds become poorer, DPOAE thresholds should worsen since both are indirect measures of peripheral auditory-system function and are associated with OHC function. Behavioral thresholds were measured using standard clinical audiometric procedures with a step size of 5 dB. DPOAE threshold was defined as the lowest level at which the DPOAE was $\geqslant$3 dB above the estimate of D+N for each subject. If the DPOAE was never 3 dB above D+N, then no measurable threshold could be identified. In the interest of simplicity, DPOAE and audiometric thresholds were compared for the case when f_2 was equal to audiometric frequency, even though we know that correlations exist across frequency, both for DPOAEs and for audiometric threshold (Dorn *et al.*, 1999). Figure 5 shows scatterplots of DPOAE threshold as a function of audiometric threshold for all subjects at each f_2. Cochlear-implant subjects' threshold data (plotted at the upper audiometric limit of 115 dB HL) are shown with asterisks and are included to serve as an upper bound on DPOAE threshold. The best cochlear-implant DPOAE threshold for a given f_2 occurred at a level that was equivalent to the poorest DPOAE threshold included for all other subjects. It could be argued that comparisons between DPOAE and audiometric thresholds should be made only for those conditions in which OHCs might be contributing to both responses. Since it is unlikely that there are any surviving OHCs in the cochlear-implant ears, their "thresholds" were not included in subsequent analyses. In addition, the threshold data from any other subject whose DPOAE threshold was equivalent to the best "threshold" among implanted ears was excluded from analyses. This approach resulted in the exclusion of data points only for hearing-impaired ears mainly at 1 and 1.5 kHz. The remaining threshold data were fit with a linear regression (solid lines, Fig. 5), from which the correlation coefficient (r), slope (a), and intercept (b) were determined and are provided in each panel. As expected, DPOAE thresholds increased as audiometric thresholds increased, with slopes of 0.35 (8 kHz) to 1.07 (1 kHz), although the relationship was variable. With the exception of 8 kHz [a frequency for which the correlation coefficient (0.54) was also the lowest], the slopes ranged from 0.72 to 1.07. Correlations of 0.77 to 0.86 were observed at other f_2 frequencies, including lower frequencies, such as 1 kHz,

where the inherently poor SNR makes DPOAE measurements less reliable, especially near DPOAE threshold. Even after applying the above exclusion criteria (related to thresholds in implanted ears), some caution is necessary in the interpretation of data points for audiometric thresholds exceeding about 60 dB HL. Assuming that DPOAEs are generated by the OHC system, and assuming that OHC damage can account for hearing losses up to about 60 dB HL and that greater losses must involve other parts of the auditory system (such as the inner hair cells), it is not expected that a relationship should exist between DPOAE and audiometric thresholds for losses exceeding 60 dB HL. This issue relates to other concerns regarding the correct interpretation of high-level DPOAEs, expressed as part of the description of DPOAE I/O functions in ears with moderate-to-severe hearing loss.

IV. DISCUSSION

A. DPOAE I/O functions in normal ears

This study demonstrates that it is possible to measure DPOAE I/O functions across a wide range of stimulus levels in humans. In normal ears, the response growth exhibits a three-part function, being linear at low levels, compressive at moderate levels, and linear to expansive at high levels (see Fig. 2). These functions resemble direct measurements of BM I/O functions (Ruggero and Rich, 1991; Ruggero *et al.*, 1997), as well as indirect measurements, such as DPOAE recordings made in healthy lower animals (Whitehead *et al.*, 1992a; Norton and Rubel, 1990). In the present study and others (Whitehead *et al.*, 1992a; Ruggero *et al.*, 1997), where the lower end of the I/O function ($<$20 dB SPL) is measured, linear or near-linear response growth is seen. Consistent with the observations made from other studies in lower animals (Ruggero and Rich, 1991; Ruggero *et al.*, 1997; Norton and Rubel, 1990; Whitehead *et al.*, 1992a, b), compressive nonlinear growth occurs at moderate stimulus levels. In the present study, the amount of normal compression, defined by the slope of the DPOAE I/O function at moderate levels, ranges from 0.16 to 0.34 dB/dB across f_2 frequencies (1 to 6 kHz). These values are similar to slope estimates derived from chinchilla BM velocity-intensity functions (Ruggero *et al.*, 1997), where the measured slopes were in the range of 0.2 to 0.5 dB/dB.

At high stimulus levels, previous work has shown that response growth is steeper, compared to the slope at moderate levels, with slopes that approach linearity (Ruggero *et al.*, 1997; Whitehead *et al.*, 1992a). In the present study, DPOAE level grew expansively with slopes exceeding 1 dB/dB, at least for the five f_2 frequencies at which it was possible to make measurements (1–4 kHz). The reasons for this expansion are not entirely clear. The high-level portion of the I/O function has few data points associated with it, due to limitations in system output and distortion. Thus, the slope of this portion of the function might be less reliably estimated. One could also speculate that the expansive growth might reflect intermodulation distortion produced by the recording system. However, normal DPOAE levels at maximum stimulus levels were between 9 dB (8 kHz) and 20 dB (1 kHz) greater than estimates of system distortion (mean difference of 14.4 dB). Thus, the estimated DPOAE amplitude was between 2.5 and 10 times larger than the estimated amplitude of system distortion. Assuming that our estimate of system distortion is reliable, it would be likely that these high-level estimates of DPOAE level are dominated by sources other than the system hardware. While we do not have a good explanation of the source of the high-level, expansive portion of the DPOAE I/O function, it would appear to be biological in origin, at least in ears with normal hearing.

At 6 and 8 kHz, measurements were possible only up to 85 dB SPL, because higher levels could not be achieved by the sound card output and the probe loudspeakers. Given the observation that compressive nonlinear regions were observed up to approximately 80 dB SPL for lower f_2 frequencies, it is possible that our inability to produce higher levels was the reason why the expansive, high-level region was not observed in the present DPOAE I/O functions at these two frequencies. Further, the slope remained relatively constant at approximately 0.6 dB/dB in ears with normal hearing when $f_2 = 8$ kHz, once L_2 exceeded 20 dB SPL. Thus, we did not observe a range of moderate levels over which compression was observed, which was unlike all other f_2 frequencies, including 6 kHz. It is possible that the L_1,L_2 level paradigm (in which the differences between L_1 and L_2 increased as primary levels decreased) did not maximize responses from normal ears at 8 kHz. Perhaps a different separation between primary levels was needed to maximize distortion in the cochlea at this frequency. In addition, it may be important that middle-ear transmission at 8 kHz is reduced compared to middle-ear transmission for the other f_2 frequencies (Voss *et al.*, 2000; Keefe, 2001). This may have reduced L_2 and/or L_1, and altered the effective relationship between L_1 and L_2, as represented in the cochlea.

B. Changes in DPOAE I/O functions due to hearing impairment

In comparison to normal-hearing subjects, the DPOAE I/O functions for the subjects with hearing loss were characterized by (1) threshold elevation, (2) a reduction in response levels, (3) a linearization of response growth at moderate levels, and (4) steeper response growth at high levels. This steepening occurred at levels that were similar to, or lower than, the levels at which this steepening occurred in ears with normal hearing. Thus, the range of input levels over which compression occurred was reduced in ears with hearing loss. In many respects, these observations are similar to those made in lower animals whose ears have undergone trauma (Ruggero and Rich, 1991; Whitehead *et al.*, 1992b; Norton and Rubel, 1990). In general, these changes were most clearly observed in ears with mild and moderate degrees of hearing loss. With greater degrees of hearing loss at essentially all f_2 frequencies, and for all hearing-loss groups at some f_2 frequencies (1.5 and 8 kHz), the compressive region was abolished, and all that remained was linear (or expansive) response growth (see Figs. 3 and 4). The outcome at 8 kHz, where any degree of hearing loss drives most of the data points into the overall noise estimate (D+N), could be due to the measurement issues raised in the section above.

The data reported by Ruggero and Rich (1991) suggest that the OHCs are responsible for the compressive nonlinear behavior of the cochlea for CF tones, showing that reversible damage to the OHC system (through the administration of furosemide) compromises the cochlea's ability to respond nonlinearly. Interestingly, furosemide treatment had little or no effect on the I/O function when the driver frequency was significantly lower than CF. This means that nonlinear response behaviors at a specific place along the cochlea are observed only when that place is driven by frequencies at or near its CF. Direct BM measurements to moderate-level stimuli made in post-furosemide-treated chinchillas resulted in a linearization of the I/O function at CF, which returned to a normal nonlinear pattern when the animal was allowed to recover from the treatment. As always, direct assessments of cochlear response properties in humans are impossible to obtain. However, given the present results in humans with normal hearing and in some subjects with hearing loss, it would appear that DPOAE measurements in humans could be used to describe cochlear mechanical response properties over a wide range of levels. Furthermore, the similarity between direct measurements in lower animals and indirect measurements in humans suggests that the indirect data can be used to estimate both the range of levels over which compression is observed and the amount of compression that exists.

C. Generation of the I/O function

The existence of two sources, one dominant at low levels of stimulation and the other dominant at high levels, has been hypothesized by others (Whitehead *et al.*, 1992a, b; Norton and Rubel, 1990; Mills and Rubel, 1994). The low-level source is considered to be an active process powered by the micromechanical feedback loop between the motile OHCs and BM vibration. This process is responsible for compressive nonlinearities and is physiologically vulnerable, reflecting the vulnerability of the OHCs to cochlear insult. This view appears to be consistent with the present data from humans, in which DPOAE threshold is elevated and the range and amount of compression is reduced in the presence of hearing loss. The high-level source has been viewed as a passive process, whereby BM activity occurs due to macromechanical properties of the system. It dominates at high levels and/or when the active low-level source has been abolished. Having described the hypotheses about the high-level portion of the I/O function, it is important to note that the mechanisms responsible for the low- and moderate-level portions of the I/O function (whether directly or indirectly measured) are known, while the mechanisms responsible for (and perhaps even the existence of) the high-level portion of the function are not well understood. In the context of the single-source model (Lukashkin and Russell, 1999), the mechano-electrical transduction of the outer hair cells could be the source for the high-level portion of the DPOAE I/O functions observed in human ears. Regardless of whether a one- or two-source model provides the most parsimonious explanation for the slope of DPOAE I/O functions, there clearly are differences between the DPOAE I/O functions observed in normal and impaired ears at low and moderate levels of stimulation.

The nonlinear compressive region, evident at low-to-moderate stimulus levels in the human data presented here, presumably corresponds to a low-level active source. In the presence of hearing loss, the active process diminishes and the passive process dominates. In the present study, it was assumed that the site of lesion for the hearing-impaired subjects was the OHC system, a reasonable assumption given what is known about the effects of cochlear insults in lower animals. Therefore, their hearing losses would represent dysfunction of the active-energy source. The range of levels over which the OHC and BM feedback loop operates and the amount of compression were calculated from the slopes of the DPOAE I/O functions in normal and impaired ears (Fig. 4), and presented in Tables I and II. The active range (in dB) is largest and the amount of compression greatest for normal-hearing subjects. Similar estimates of range and amount of compression were possible for only a subset of the present data from subjects with hearing loss, restricted to the milder hearing-loss groups for f_2 frequencies of 1, 1.5, 2, and 4 kHz. A comparison of the data from these groups with similar measurements from subjects with normal hearing indicated that the range of levels over which the active process operates is diminished and responses are less compressed as hearing loss increases. The fact that this pattern was observed only for groups of subjects with milder hearing losses is consistent with the view that DPOAEs are generated by the OHC system, and that the OHC system contributes to response properties only for levels up to about 60 dB HL. For greater hearing losses, the loss cannot be attributed solely to the OHCs. Thus, it may not be surprising that changes to the compressive nonlinearity associated with OHC function cannot be quantified with the present analysis approach once the loss exceeds the dynamic range of the OHCs.

The reason why similar patterns were not observed among the milder hearing-loss groups at other f_2 frequencies is not obvious. This partly results from the fact that the slopes of DPOAE I/O functions frequently did not show the initial peak that was characteristic of responses from ears with normal hearing, even though the responses were reliably measured, exceeding the estimate of D+N. At 8 kHz in the normal-hearing ears, the shape of the I/O function at low and moderate levels was different from that observed at the other f_2 frequencies. Further, at 8 kHz, much of the hearing-impaired data were indistinguishable from DPs measured in ears with cochlear implants. This observation is surprising, in that it would suggest that DPOAEs are present in normal ears but absent for any degree of hearing loss at this frequency. We would expect that a range of levels exists over which there is a relationship between DPOAE level and audiometric threshold (e.g., Martin *et al.*, 1990; Gorga *et al.*, 2002). Taking the present observations to their logical conclusion, the data at 8 kHz indicate that OHCs either are present and functional (ears with normal hearing) or absent or completely dysfunctional (ears with any degree of hearing loss). We do not believe that this is, in fact, the case; as a consequence, the mechanisms responsible for the observations at 8 kHz remain unclear. There are other possible causes for the outcome at 8 kHz. Perhaps a non-optimal

L_1/L_2 ratio is, in part, responsible for the measurements obtained at this frequency, thus leading to a situation in which f_1 had a greater suppressing effect on f_2 compared to other primary pairs. Other considerations are middle-ear transmission and standing waves in the ear canal, both potentially altering the signal level that is actually delivered to the cochlea, thereby altering the effective primary levels.

D. System distortion estimates and high-level DPOAEs

The cochlear-implant subjects served as a biological system that was not expected to produce distortion. At higher levels (above 85 dB SPL) and for some f_2 frequencies, the measured responses in their ear canals were not as low as the D+N estimates for normal ears; however, the responses seen in ears with cochlear implants were always less than the DPOAE levels from normal ears. In normal ears at these higher levels, estimates of noise and DPOAE levels were distinct from each other at all f_2 frequencies, suggesting that these responses were biological in origin. While the response levels in ears with cochlear implants were less than those seen in normal ears, they sometimes exceeded the estimates of D+N. One interpretation of the data in cochlear-implant ears is that some part of the biological system (excluding the OHC system) is responsible for the measured DPs, assuming that our estimate of D+N accurately describes system distortion. Given this constellation of outcomes, several possible explanations exist for the source of high-level distortion. These DPOAEs could be thought of as emanating from three possible sources : (1) a biological source dominated by normal cochlear activity, primarily the OHC system, (2) a biological source, but excluding the OHC system (e.g., the BM or middle ear), or (3) a nonbiological source, related to system distortion. We consider the second possible source to be the most speculative, representing the least likely scenario. Effort was expended to control for and understand the limits of system distortion. We recognize the possibility that our estimate of system distortion may underestimate the actual level at which distortion is produced by the hardware. At this point, we can only speculate as to the source of the measured distortion and provide the above three possible explanations. The present data do not allow us to more definitively identify the source in cochlear-implant ears and ears with moderate-to-severe hearing losses.

E. Relationship between DPOAE and audiometric thresholds

The range of slope and correlation values found when DPOAE and audiometric thresholds were compared are similar to the results reported by Martin *et al.* (1990), Nelson and Kimberley (1992), and Sukfüll *et al.* (1996), indicating that a positive relationship exists between the two threshold measures. Gorga *et al.* (1996) also found a similar relationship with the further observation that DPOAE thresholds in the mild HL group often overlapped those observed in ears with normal hearing, indicating that the most ambiguity in separating normal from impaired ears occurred with mild hearing losses. Harris (1990) noted that the correspondence between the amount of reduction in DPOAE level and degree of loss when behavioral thresholds were between 20 and 50 dB HL was not clear. In contrast, relationships between DPOAE level and audiometric threshold have been described within the range of normal hearing (Dorn *et al.*, 1998) and within the range from normal hearing up to moderate hearing loss (Gorga *et al.*, 2002). While the correlation is not sufficient to permit precise predictions of auditory threshold from DPOAE measurements, both DPOAE threshold and DPOAE level are related to audiometric threshold. Such a relationship should not be surprising, since DPOAE measures and auditory sensitivity are related to the same underlying system (the OHCs) for thresholds up to about 50–60 dB HL.

F. DPOAE I/O functions in clinical applications

The observation of steeper DPOAE I/O functions in ears with hearing loss as compared to normal ears may correlate with other measures of abnormally rapid response growth, such as loudness recruitment. Schlauch *et al.* (1998) described a relationship between BM I/O functions and psychophysical measures of loudness. They measured loudness in humans and, from those data, derived I/O functions. The derived I/O functions were compared to the BM data of Ruggero *et al.* (1997). The results were promising in that a relationship between the psychophysical and physiological measures was found in individuals with loudness recruitment. Zhang and Zwislocki (1995) provided evidence to support the notion that loudness recruitment is present at the hair-cell level by making pre- and post-noise-exposure I/O measurements in the gerbil cochlea. They concluded that abnormal growth in loudness was locally determined and not a consequence of abnormal spread of excitation.

A connection between behavioral, basilar membrane, and hair-cell measures with respect to loudness is important when considering possible clinical applications of DPOAE I/O functions. Behavioral measures of loudness may not be possible in many populations (e.g., infants, children, patients with developmental delays). If DPOAE I/O measures can be associated with growth of loudness, then the development of a clinical DPOAE I/O measure would make it possible to identify those impaired ears that exhibit loudness recruitment. That information could then be applied to the selection of appropriate amplification characteristics, such as compression threshold and compression ratio.

V. SUMMARY

The main observations from the present study include the following:

(1) It was possible to measure DPOAE I/O functions over a wider range of levels in both normal and impaired ears than in previous studies.
(2) Predicted estimates of system distortion, based upon a linear model derived from several cavity measurements and tested on a group of cochlear-implant subjects, provides evidence that the measured DPOAEs in normal ears are biological in origin, even at high levels. In spite of these efforts, responses obtained at stimulus levels above 85 dB SPL must be viewed with caution.

(3) The DPOAE I/O functions from normal ears are reminiscent of basilar membrane I/O functions derived from direct measurements and from DPOAE measurements in lower animals. These functions are steep at low and high stimulus levels, with a compressive region at moderate levels.
(4) I/O functions obtained in subjects with hearing loss may be characterized as having steeper slopes, and the amount of compression and the range of levels over which compression occurs is reduced, as compared to subjects with normal hearing.
(5) The normal compressive growth of DPOAEs may be interpreted as an indication of reduced cochlear-amplifier gain with increases in stimulus level. The transition from a compressive region to a region of steep slope may mark the upper limit of cochlear-amplifier function, assuming that high-level distortion is due to the OHCs.
(6) The observation of steeper DPOAE I/O functions in ears with hearing loss compared to normal ears might relate to other measures of abnormally rapid response growth, such as loudness recruitment.

ACKNOWLEDGMENTS

This work was supported by NIH Grant No. DC02251. Portions of this work were presented at the 24th Midwinter Meeting of the Association for Research in Otolaryngology. We thank two anonymous reviewers for their helpful comments and suggestions.

ANSI S3.6-1996 (**1996**). ''Specifications for Audiometers'' (American Institute of Physics, New York).
Avan, P., and Bonfils, P. (**1993**). ''Frequency specificity of human distortion product otoacoustic emissions,'' Audiology **32**, 12–26.
Bonfils, P., and Avan, P. (**1992**). ''Distortion-product otoacoustic emissions. Values for clinical use,'' Arch. Otolaryngol. Head Neck Surg. **118**, 1069–1076.
Dallos, P., Harris, D., Ozdamar, O., and Ryan, A. (**1978**). ''Behavioral, compound action potential, and single unit thresholds: relationship in normal and abnormal ears,'' J. Acoust. Soc. Am. **64**, 151–157.
Dorn, P. A., Piskorski, P., Gorga, M. P., Neely, S. T., and Keefe, D. H. (**1999**). ''Predicting audiometric status from distortion product otoacoustic emissions using multivariate analyses,'' Ear Hear. **20**, 149–163.
Dorn, P. A., Piskorski, P., Keefe, D. H., Neely, S. T., and Gorga, M. P. (**1998**). ''On the existence of an age/threshold/frequency interaction in distortion product otoacoustic emissions,'' J. Acoust. Soc. Am. **104**, 964–971.
Gorga, M. P., Nelson, K., Davis, T., Dorn, P. A., and Neely, S. T. (**2000**). ''Distortion product otoacoustic emission test performance when both $2f1-f2$ and $2f2-f1$ are used to predict auditory status,'' J. Acoust. Soc. Am. **107**, 2128–2135.
Gorga, M. P., Neely, S. T., and Dorn, P. A. (**2002**). ''Distortion product otoacoustic emission in relation to hearing loss, in *Octoacoustic Emissions: Clinical Applications*, 2nd Edition, edited by M. S. Robinette and T. J. Glattke (Thieme Medical Publishers, Inc., New York), pp. 243–272.
Gorga, M. P., Neely, S. T., Ohlrich, B., Hoover, B., Redner, J., and Peters, J. (**1997**). ''From laboratory to clinic: a large scale study of distortion product otoacoustic emissions in ears with normal hearing and ears with hearing loss,'' Ear Hear. **18**, 440–455.
Gorga, M. P., Stover, L., Neely, S. T., and Montoya, D. (**1996**). ''The use of cumulative distributions to determine critical values and levels of confidence for clinical distortion product otoacoustic emission measurements,'' J. Acoust. Soc. Am. **100**, 968–977.
Gorga, M. P., Neely, S. T., Bergman, B., Beauchaine, K. L., Kaminski, J. R., Peters, J., and Jesteadt, W. (**1993**). ''Otoacoustic emissions from normal-hearing and hearing-impaired subjects: distortion product responses,'' J. Acoust. Soc. Am. **93**, 2050–2060.
Harris, F. P. (**1990**). ''Distortion-product otoacoustic emissions in humans with high frequency sensorineural hearing loss,'' J. Speech Hear. Res. **33**, 594–600.
Janssen, T., Kummer, P., and Arnold, W. (**1998**). ''Growth behaviour of the $2f_1-f_2$ distortion product otoacoustic emission in tinnitus,'' J. Acoust. Soc. Am. **103**, 3418–3430.
Keefe, D. H. (**2001**). ''Spectral shapes of forward and reverse transfer functions between ear canal cochlea estimated using DPOAE input/output functions,'' J. Acoust. Soc. Am. (in press).
Kemp, D. T. (**1980**). ''Towards a model for the origin of cochlear echoes,'' Hear. Res. **2**, 533–548.
Kim, D. O., Paparello, J., Jung, M. D., Smurzynski, J., and Sun, X. (**1996**). ''Distortion product otoacoustic emission test of sensorineural hearing loss: performance regarding sensitivity, specificity and receiver operating characteristics,'' Acta Oto-Laryngol. **116**, 3–11.
Kummer, P., Janssen, Y., and Arnold, W. (**1998**). ''The level and growth behavior of the $2f_1-f_2$ distortion product otoacoustic emission and its relationship to auditory sensitivity in normal hearing and cochlear hearing loss,'' J. Acoust. Soc. Am. **103**, 3431–3444.
Liberman, M. C., and Dodds, L. W. (**1984**). ''Single-neuron labeling and chronic cochlear pathology. III. Stereocilia damage and alterations of threshold tuning curves,'' Hear. Res. **16**, 55–74.
Lonsbury-Martin, B. L., Martin, G. K., and Whitehead, M. L. (**2001**). ''Distortion product otoacoustic emissions,'' in *Otoacoustic Emissions Clinical Applications*, edited by M. S. Robinette and T. J. Glattke (Thieme, New York), pp. 83–109.
Lukashkin, A. N., and Russell, I. J. (**1999**). ''Analysis of the f_2-f_1 and $2f_1-f_2$ distortion components generated by the hair cell mechanoelectrical transducer: Dependence on the amplitudes of the primaries and feedback gain,'' J. Acoust. Soc. Am. **106**, 2661–2668.
Martin, G. K., Ohlms, L. A., Franklin, D. J., Harris, F. P., and Lonsbury-Martin, B. L. (**1990**). ''Distortion product emissions in humans: III. Influence of sensorineural hearing loss,'' Ann. Otol. Rhinol. Laryngol. **99**, 30–42.
Mills, D. M., Norton, S. J., and Rubel, E. W. (**1993**). ''Vulnerability and adaptation of distortion product otoacoustic emissions to endocochlear potential variation,'' J. Acoust. Soc. Am. **94**, 2108–2122.
Mills, D. M., and Rubel, E. W. (**1994**). ''Variation of distortion product otoacoustic emissions with furosemide injection,'' Hear. Res. **77**, 183–199.
Neely, S. T., Gorga, M. P., and Dorn, P. A. (**2000**). ''Distortion product and loudness growth in an active, nonlinear model of cochlear mechanics,'' in *Proceedings of the International Symposium on Recent Development in Auditory Mechanics*, edited by H. Wada, T. Takasaka, K. Ikeda, K. Ohyama, and T. Koike (World Scientific, Singapore), pp. 237–243.
Neely, S. T., and Liu, Z. (**1993**). ''EMAV: Otoacoustic emission averager,'' Tech. Memo No. 17 (Boys Town National Research Hospital, Omaha).
Nelson, D. A., and Kimberley, B. P. (**1992**). ''Distortion-product emissions and auditory sensitivity in human ears with normal hearing and cochlear hearing loss,'' J. Speech Hear. Res. **35**, 1142–1159.
Norton, S. J., and Rubel, E. W. (**1990**). ''Active and passive ADP components in mammalian and avian ears,'' in *Mechanics and Biophysics of Hearing*, edited by P. Dallas, C. D. Geisler, J. W. Matthews, M. A. Ruggero, and C. R. Steele (Springer-Verlag, New York), pp. 219–226.
Probst, R., Lonsbury-Martin, B. L., and Martin, G. K. (**1991**). ''A review of otoacoustic emissions,'' J. Acoust. Soc. Am. **89**, 2027–2067.
Ruggero, M. A., and Rich, N. C. (**1991**). ''Furosemide alters organ of corti mechanics: evidence for feedback of outer hair cells upon the basilar membrane,'' J. Neuro. **11**, 1057–1067.
Ruggero, M. A., Rich, N. C., Recio, A., Narayan, S. S., and Robles, L. (**1997**). ''Basilar-membrane responses to tones at the base of the chinchilla cochlea,'' J. Acoust. Soc. Am. **101**, 2151–2163.
Schlauch, R. S., DiGiovanni, J. J., and Ries, D. T. (**1998**). ''Basilar membrane nonlinearity and loudness,'' J. Acoust. Soc. Am. **103**, 2010–2020.
Stover, L., Gorga, M. P., Neely, S. T., and Montoya, D. (**1996**). ''Toward optimizing the clinical utility of distortion product otoacoustic emission measurements,'' J. Acoust. Soc. Am. **100**, 956–967.
Sukfüll, M., Schneeweib, S., Dreher, A., and Schorn, K. (**1996**). ''Evaluation of TEOAE and DPOAE measurements for the assessment of auditory thresholds in sensorineural hearing loss,'' Acta Oto-Laryngol. **116**, 528–533.

Voss, S. E., Rosowski, J. J., Merchant, S. N., and Peake, W. T. (**2000**). ''Acoustic responses of the human middle ear,'' Hear. Res. **150**, 43–69.

Whitehead, M. L., Lonsbury-Martin, B. L., and Martin, G. L. (**1992a**). ''Evidence for two discrete sources of $2f_1-f_2$ distortion-product otoacoustic emission in rabbit: I. differential dependence on stimulus parameters,'' J. Acoust. Soc. Am. **91**, 1587–1607.

Whitehead, M. L., Lonsbury-Martin, B. L., and Martin, G. L. (**1992b**). ''Evidence for two discrete sources of $2f_1-f_2$ distortion-product otoacoustic emission in rabbit: II. Differential physiological vulnerability,'' J. Acoust. Soc. Am. **92**, 2662–2682.

Whitehead, M. L., McCoy, M. J., Lonsbury-Martin, B. L., and Martin, G. K. (**1995**). ''Dependence of distortion product otoacoustic emissions on primary levels in normal hearing and impaired ears. I. Effects of decreasing L_2 below L_1,'' J. Acoust. Soc. Am. **97**, 2346–2358.

Zhang, M., and Zwislocki, J. J. (**1995**). ''OHC response recruitment and its correlation with loudness recruitment,'' Hear. Res. **85**, 1–10.

Effects of draining cochlear fluids on stapes displacement in human middle-ear models[a)]

Richard M. Lord, Eric W. Abel, and Zhigang Wang
Department of Mechanical Engineering, University of Dundee, Dundee, Scotland

Robert P. Mills
Otolaryngology Unit, Department of Surgery, University of Edinburgh, Edinburgh, Scotland

(Received 16 April 2001; accepted for publication 25 September 2001)

Displacement-frequency characteristics of the stapes footplate were measured in five human temporal bones before and after draining the vestibule. Measurements were made in the 0.125–8 kHz range at 80 dB input sound pressure level, using a laser Doppler vibrometer. A circuit model was also used to predict stapes displacement. The temporal bone studies show a slight decrease in stapes footplate displacement at low frequency, and little change above 1 kHz. The displacement change is not as great as that found by other investigators or predicted by the model. There is little difference in stapes motion in temporal bones when the inner ear is intact or drained. © *2001 Acoustical Society of America.* [DOI: 10.1121/1.1419095]

PACS numbers: 43.64.Ha, 43.64.Bt [BLM]

I. INTRODUCTION

The middle-ear transmits acoustic signals from the ear canal to the inner ear. The acoustic input impedance of the inner ear represents the mechanical load driven by the middle ear. This input impedance $\mathbf{Z}_{IE}$ is composed of the linear combination of the impedance associated with the stapes $\mathbf{Z}_S$, the annular ligament $\mathbf{Z}_{AL}$, and the cochlea/round window $\mathbf{Z}_C$, such that $\mathbf{Z}_{IE}=\mathbf{Z}_S+\mathbf{Z}_{AL}+\mathbf{Z}_C$ (Zwislocki, 1962). The acoustical input to the inner ear is the stapes volume velocity $\mathbf{U}_S$,[1] defined as the product of stapes-footplate area and linear velocity (Lynch *et al.*, 1982). Since $\mathbf{Z}_{IE}$ is the ratio of the effective sound pressure at the cochlea oval window $\mathbf{P}_V$, to the stapes volume velocity $\mathbf{U}_S$, any change of $\mathbf{Z}_{IE}$ may result in a change of $\mathbf{U}_S$ and $\mathbf{P}_V$. Draining the cochlear fluids decreases $\mathbf{P}_V$ (Puria, 1997) but the effect on $\mathbf{U}_S$ and therefore stapes displacement is not well known. Measurements of stapes-footplate displacement before and after draining the cochlear fluids allow conclusions to be drawn about the nature of $\mathbf{Z}_{AL}$, $\mathbf{Z}_S$, and $\mathbf{Z}_C$. This study directly examines the effect of draining the cochlear fluids on stapes displacement in human temporal bones and an electrical analog model.

Some measurements of the effects of draining the cochlea on stapes displacement, inner-ear impedance, and umbo displacement have been reported. Gundersen and Høgmoen (1976) found that the vibratory pattern of the ossicles was unaltered but vibration amplitude was larger after the fluid was drained from the cochlea. Sound pressure levels[2] (SPL) from 100 to 125 dB were used due to the sensitivity of their holographic method. Gyo *et al.* (1987) reported stapes-head displacements, before and after draining the cochlea, for one temporal bone sample also under high stimulation levels (124 dB SPL). Draining the cochlea increased stapes displacement by about 8 dB at 1 kHz, with largest displacement increases at high frequency and small changes at low frequency. Destruction of the cochlear partition or draining of the inner-ear fluids has been shown to cause changes in middle-ear motion and impedance (Møller, 1965). Lynch *et al.* (1982) measured $\mathbf{Z}_{IE}$ in cats and found the magnitude of the impedance to decrease for all frequencies when fluid was removed from the cochlea, with largest reductions above 1 kHz. With the fluid removed, $|\mathbf{Z}_{IE}|$ at high frequencies tended toward that which would result from the mass of the stapes. Merchant *et al.* (1996) measured a similar result in one human temporal bone. The impedance was found to reduce by a factor of 1.4 at low frequency, being dominated by the stiffness and resistance of the annular ligament. A damped resonance at 3.5 kHz marked the point of interaction of the annular ligament stiffness and the mass of the stapes, and above 4 kHz the impedance was that due to the stapes mass. The fluid filled cochlea and the round window dominate the impedance of the intact inner ear above 2 kHz (Merchant *et al.*, 1996). Shinohara *et al.* (1997) reported that destruction of the cochlea in guinea pigs ''slightly decreased'' umbo and incus long-process displacements at low frequency (less than 1 kHz) but they were increased at higher frequencies. Murakami *et al.* (1998) investigated the effect of increasing the inner-ear pressure. They found that stapes velocity decreased at all frequencies as inner-ear pressure was increased.

The stapes-footplate displacements reported here were measured with both the cochlea intact and the cochlear fluids drained in five human temporal bones, at a sound pressure level of 80 dB. These displacements are compared with the predictions of an electrical analog model, the direct measurements of Gyo *et al.* (1987), and the measurements reported by others who have either left the cochlea intact or drained its fluids, depending on their measurement method.

Human studies of this nature can only be performed *in vitro* in cadaver temporal bone specimens, as the experiment requires destruction of the inner ear. The degree to which

[a)]Results of one *in vitro* study were presented in R. M. Lord, R. P. Mills, and E. W. Abel, ''An anatomically shaped incus prosthesis for reconstruction of the ossicular chain,'' Hear. Res. **145**, 141–148 (2000).

human cadaver middle ears model the mechanical function of the living ear was assessed by Rosowski *et al.* (1990) using the input impedance to the middle ear. They found the *in vitro* impedance of cadaver middle ears to be indistinguishable from *in vivo* measurements provided that the temporal bones were kept moist and the middle-ear pressure controlled. Other studies have shown that temporal bone measurements are repeatable for up to 6 h (Vlaming, 1986; Stasche *et al.*, 1994). After this time deterioration of the ossicular chain or dehydration of the ligaments, tendons, or tympanic membrane reduces the reliability of the results.

The temporal bones used in this study were stored by freezing, and thawed for use. Rosowski *et al.* (1990) reported that freezing and thawing have little effect on *in vitro* middle-ear impedance and Schön (1999) found that specimens which were repeatedly defrosted and refrozen showed no changes. However, the work of Merchant *et al.* (1996) suggests that some changes may occur in temporal bone preparations that have been frozen and thawed and that leaks in the cochlea may allow air to enter the inner ear thereby making the cochlea compressible. Ravicz *et al.* (2000) found that freezing and thawing caused a reduction in the magnitude of the input impedance to the inner ear $|\mathbf{Z}_{IE}|$, although not all bones measured showed this reduction. There is therefore, some variation in opinion on this matter.

Temporal bone preparations vary according to the method used to measure stapes displacement. It may be advantageous to gain access to the stapes footplate by removing or draining the cochlea. This allows *in vitro* measurements of the footplate displacement to be made in the direction of the assumed velocity vector of the motion,[3] by approaching the footplate from the vestibular side. In order to measure stapes displacement with the cochlea intact, measurements must be made from the lateral side of the footplate (the surface exposed to the tympanic cavity) at an angle to the assumed direction of motion and therefore a cosine correction should be applied.

By directly examining the effect of draining the cochlear fluids on stapes displacement at a physiological sound pressure level, this paper addresses the validity of temporal bone preparations that have had the cochlea drained. From a practical standpoint, there is some merit in being able to measure stapes displacement from a medial approach, namely that preparation and alignment time can be significantly reduced, and that no cosine correction need be applied to the measurement. Draining the cochlear fluids allows this measurement approach to be used. A larger sample of temporal bone preparations than previously reported is used and these results are compared with the predictions of an electrical model.

II. METHODS

A. Laser Doppler measurement

A Polytec laser Doppler vibrometer (CLV-700, 800 with 1000-velocity decoder) was used to measure the velocity of the stapes footplate in temporal bone samples. Three approaches to the footplate were taken: from the middle-ear cavity with the cochlea intact, from the middle-ear cavity with the cochlea drained of fluid, and from a medial approach viewing the footplate from the internal auditory meatus.

B. Temporal bone preparation

Harvested temporal bones were obtained from refrigerated human cadavers. These contained the bony external meatus, middle ear, inner ear and the internal auditory meatus. Temporal bone samples were kept frozen at $-20\,^{\circ}\mathrm{C}$ in the state in which they were removed from the cadaver. Specimens were allowed to thaw for 60–90 min, during which time they were prepared for testing. Preparations involved opening the middle-ear cavity by a cortical mastoidectomy with a posterior tympanotomy so that the laser beam could be focused on the stapes footplate. Care was taken to ensure that the ossicular chain and tympanic membrane were intact and otologically normal.

A spot of retro-reflective paint (3M Scotchlite reflective liquid 7210, containing glass microbeads) was painted as centrally as possible on the footplate in order to provide a target for the laser. A useful signal could not be achieved without this reflective coating (Abel *et al.*, 2000). The mass of the paint used was insignificant being not more than 0.5% that of the stapes (Lord *et al.*, 2000).

A 4 mm diameter plastic tube (length 40 mm) was adhered to the ear canal using a rapid-set epoxy resin. This was connected to a closed-backed 50 mm diameter transducer via a conical flare. A path was drilled obliquely into the ear canal to allow a probe microphone to monitor the SPL within 2 mm of the tympanic membrane. A 2.2 mm diameter probe tube (length 20 mm) was inserted in this path and a microphone attached to this tube.

During the experiment the temporal bones were not moistened except during preparation when irrigation was required. Gentle suction was used to remove excess fluid. After the initial measurement with the intact cochlea, subsequent preparation was necessary to drain the vestibule. The internal auditory meatus was drilled until the posterior of the stapes footplate was exposed. A spot of retro-reflective paint was applied centrally on the medial side of the footplate so that a further set of results could be obtained of displacement in the direction of assumed maximal displacement. All measurements were made with the middle-ear cavities open.

C. Measurement setup

The measurement setup was the same as that described in a previous paper (Lord *et al.*, 2000). The temporal bone was clamped and mounted on micro-positioning stages allowing three-dimensional manipulation of the bone specimen into the optical path of the laser.

The temporal bone clamp together with the optical head of the laser was mounted on a platform providing vibration isolation from possible external sources. A signal generator and an audio amplifier controlled the sound stimuli presented to the tympanic membrane. A probe microphone was constructed using a Knowles EK-3103 transducer calibrated for the 20 mm long tube exposed to a perpendicular sound field. The microphone and probe tube were calibrated in a B&K

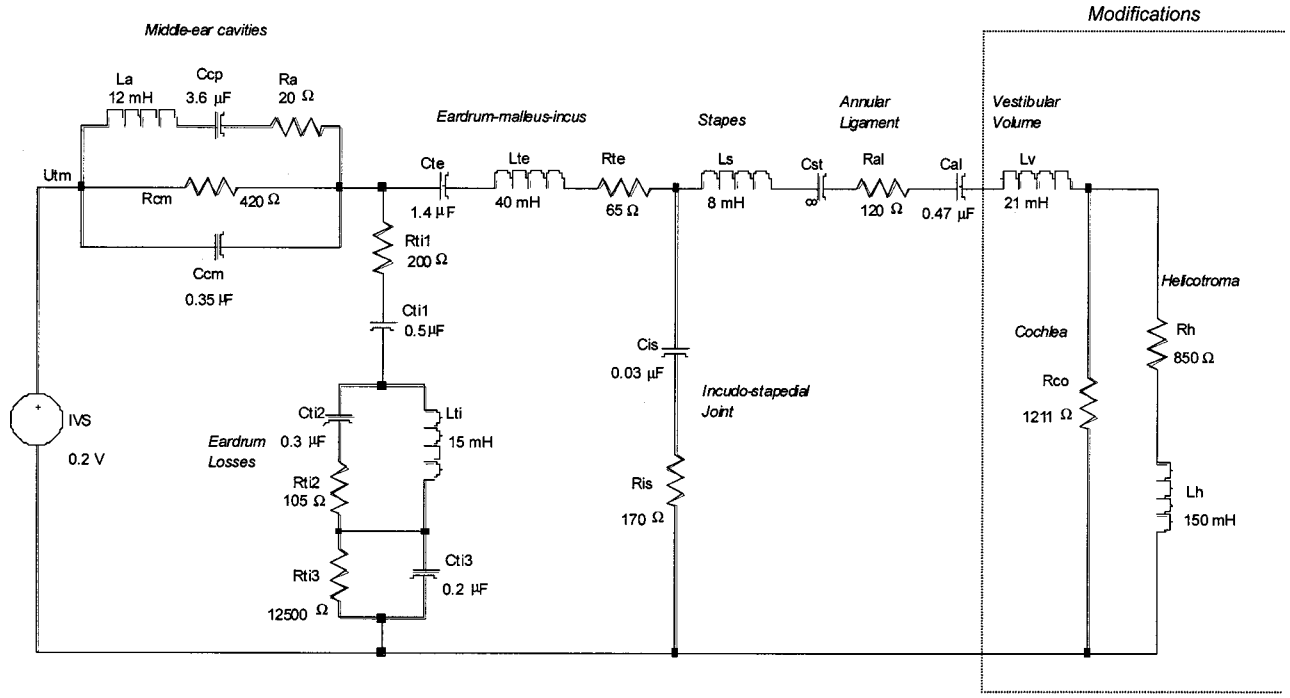

FIG. 1. Modified Pascal electrical analog circuit model of the middle ear (from Pascal *et al.*, 1998).

Anechoic Test Chamber using a substitution method. The calibrating standard was a flat response 1/2-inch microphone. Sound pressure level was kept constant at 2 mm from the tympanic membrane and the source amplification adjusted to ensure the microphone response corresponded to 80 dB SPL at each measurement frequency. The laser spot was focused on the applied reflective paint with the aid of a microscope.

D. Experimental protocol

Fourteen pure tones in the frequency range 0.125–8 kHz and at 80 dB SPL were applied to the tympanic membrane. The measurement signals of the vibrometer and microphone were sampled at 30 kHz to a desktop PC for subsequent analysis. The laser signal was pre-filtered using a band-pass filter of 0.08–10 kHz. Measurement time for a complete characteristic was 20–25 min.

Measurements were made with the cochlea and vestibule intact. The vestibule was drained of fluid and the measurements repeated. A cosine correction was required for both these measurements as they were made at an angle to the assumed motion of the stapes. The cosine correction was estimated using the rotation stage of the experimental rig. The angle of rotation between the lateral and medial measurements was about 40 deg. The bone was realigned so that the stapes motion could be measured using a vestibular approach and further data recorded. No cosine correction to the latter measurement was required.

E. Electrical analog

The effect of changing the inner-ear load on stapes displacement was also investigated using a circuit model. The electrical analog of the normal middle ear described by Zwislocki (1962) was used with the modifications proposed by Pascal *et al.* (1998). Zwislocki considered the middle-ear mechanism to consist of five functional units: the middle-ear cavities; the tympanic membrane; the tympanic membrane/malleus/incus; the incudo-stapedial joint; and the stapes/cochlea/round-window, with the associated muscles or ligaments (Zwislocki, 1962). Pascal's model modifies the last part of the circuit analogous to the action of the stapes and cochlear impedance. Nonlinear components are proposed for the annular ligament, and the acoustic reflex, however, only the linear model of Pascal is used in this study since its valid range extends to 80 dB SPL. The advantage of Pascal's model for use in this study is that the inner-ear components are already isolated and appropriate values have been determined, which makes the task of inner-ear modification simpler. The transformer ratio between the tympanic membrane and stapes footplate is approximately 17 and must be considered in computation, although it is not shown in the model. The model and corresponding values are given in Fig. 1.

The basic modification to the model made in this study was to reflect the removal of the cochlear fluid by reducing the impedance of the cochlea, $\mathbf{Z}_C$. A cochlear resistance R_{co}, the vestibular volume L_v and components relating to the helicotrema, R_h and L_h (Fig. 1) represent $\mathbf{Z}_C$. With no fluid in the cochlea, the vestibular volume mass L_v was reduced to 0.03 mH and R_{co} was modified to 10 Ω, due to the small volume of air behind the footplate in the vestibule. No further impedance was offered by the helicotrema so R_h and L_h were set to zero.

The volume velocity of the stapes is analogous to the current through L_s in the circuit model. This current was converted to a displacement, assuming a footplate area of 3.2 mm^2 (Békésy, 1960).

III. RESULTS

Five temporal bone samples were used in this study. The mean peak to peak displacements were calculated by integra-

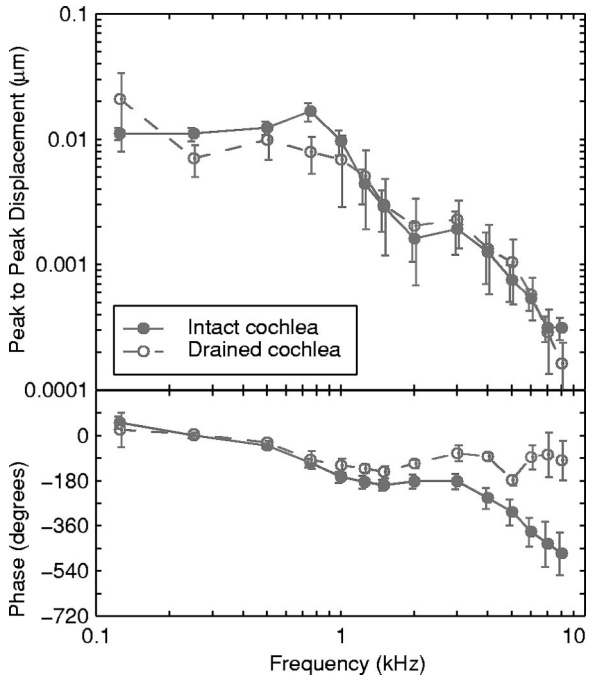

FIG. 2. Mean ($n=5$) stapes-footplate displacement, before and after draining the cochlear fluids in human temporal bone. Input was 80 dB SPL at the tympanic membrane. The standard error of the mean is also shown. The lower plot shows the phase difference between the stimulus and the stapes response.

tion of the velocity signal with respect to time. The phase angle was calculated from the delay between the tympanic membrane stimulus and the measured velocity signal. The signal from the probe microphone was acquired through the same interface as the vibrometer signal such that any phase shift due to the equipment is identical for both signals, and the phase difference between the two is independent of the apparatus. The mean footplate displacements are shown in Fig. 2 for an input stimulus of 80 dB SPL. The standard-error-of-the-mean is also shown. A cosine correction equivalent to an angle of approximately 40 deg was applied to the lateral approach measurements of stapes displacement.

With the cochlea intact the stapes response is flat for frequencies up to 700 Hz with a mean peak to peak displacement of 11.5 nm and individual values ranging from 5.7 to 14.2 nm. At 750 Hz the average response rises to a peak of 16.6 nm although one temporal bone sample peaked at a frequency closer to 1 kHz. Above this peak the average amplitude decreases at a rate of about −15 dB/octave, to a local minimum at 2 kHz, of 1.6 nm. A second peak is observed at 3 kHz above which the response rolls off at about −12 dB/octave. The average roll-off above 750 Hz is just less than −9.5 dB/octave. The gradients were determined using a linear regression.

The mean phase lag increases with frequency. At low frequency the stimulus and response are in phase. At 700 Hz the signals are 90 deg out of phase, the displacement lags behind the pressure stimulus. At 1000 Hz, the delay corresponds to 180 deg phase shift, and the displacement continues to lag behind stimulus as frequency increases. The standard error bars indicate that all five temporal bones closely followed this characteristic phase response.

When the fluid of the cochlea is drained the low frequency stapes response is no longer flat, but in general is 4 dB less than the response of the stapes and intact cochlea. At very low frequency, 125 Hz, the response is 6 dB greater after draining and the peak previously observed at 750 Hz is not present; instead the displacement response is 6 dB less. Above 1.25 kHz the response is similar to the intact situation and about 2 dB greater. The phase data indicate changes at high frequency. At 2 kHz the pre- and post-draining situations differ by 90 deg, above 5 kHz by more than 180 deg. The phase lag between the stimulus and response is less in drained preparations.

The drained preparations allowed a further set of measurements to be taken from a medial approach with a target centrally on the underside of the stapes footplate. The average movement of the measurement point normal to the plane of the stapes footplate (medial approach measurements) shows some differences compared with measurements taken from the lateral side of the footplate (Fig. 3).

The displacements measured from the two approaches are of approximately the same magnitude from 250 to 1500 Hz. The stapes displacement at 150 Hz has a smaller component normal to the footplate plane than might be interpreted from the lateral approach data. The local minimum at 2 kHz is not observed from the medial approach and the higher frequency measurements are about 6 dB greater. The normal component of the displacement response decreases at about 11 dB/octave.

The electrical analog model predicts stapes displacement of a similar magnitude to that measured in the temporal bone experiments (Fig. 4). Stapes displacement rolls off at about 11 dB/octave. With the drained cochlea, stapes displacement increases at all frequencies. The largest increase is at 1 kHz, which exhibits a resonant peak.

IV. DISCUSSION

A. Stapes-footplate displacement with intact cochlea

The intact cochlea results are similar to those reported in the literature (Fig. 5). The studies shown were all undertaken in human temporal bone preparations with intact cochleae and are normalized to an input stimulus of 80 dB SPL. The mean of Vlaming's four samples is converted from rms displacements reported in their Fig. 5 (Vlaming, 1986). Their measurements are in response to 80 dB SPL stimulus at the eardrum. The line marked "Gyo *et al.*" is taken from the measurement at the stapes head of one temporal bone stimulated at 124 dB SPL (Gyo, 1987, their Fig. 5a). In converting the reported data to 80 dB SPL, linearity is assumed. The recent data of Aibara *et al.* (2001) are calculated from the mean stapes velocity per unit input pressure measured in a sample of 11 temporal bones. All studies exhibit a decrease in stapes displacement above 1 kHz, rolling off at about −14 dB/octave. The data of Vlaming and Aibara show a peak at around 1 kHz with flat responses at lower frequency. Gyo's data do not show this peak and have a larger low frequency displacement than shown in other studies. The data from this

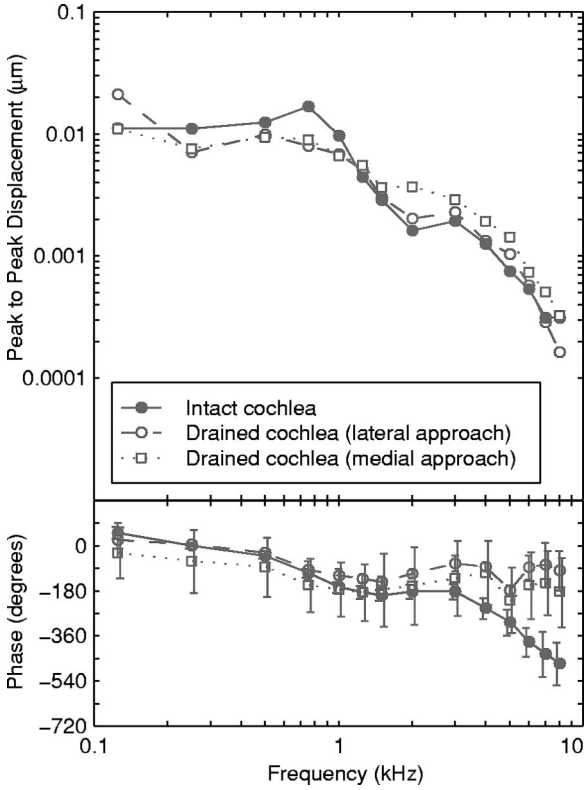

FIG. 3. Mean ($n=5$) stapes-footplate displacement, before and after draining the cochlear fluids in human temporal bone. Input was 80 dB SPL at the tympanic membrane. The footplate response before and after draining the cochlea was measured with a lateral approach from within the middle ear cavity. A cosine correction has been applied to these measurements. The footplate response after the cochlea was drained was also measured with a medial approach, from the drained vestibule. No cosine correction was applied as measurement was in-line with assumed direction of movement. The lower plot shows the phase difference between the stimulus and stapes response.

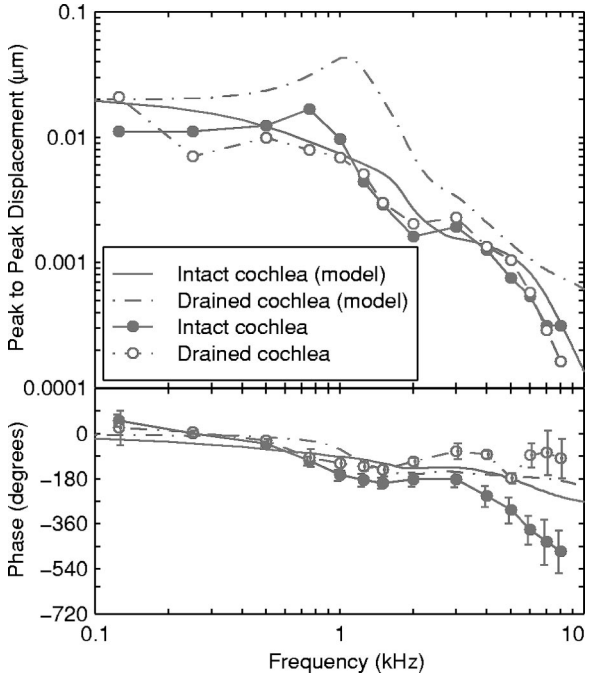

FIG. 4. Electrical analog predictions of stapes-footplate displacement for a stimulus of 80 dB SPL at the tympanic membrane, compared with the lateral approach data. The lower plot shows the phase difference between the stimulus and stapes response.

study (marked Lord *et al.*, Fig. 5) compares favorably with other studies but also exhibits a secondary peak. The resonance at 750 Hz is below the 1 kHz peak reported by Vlaming and Aibara but agrees well with the measurement of Gyo. Below 750 Hz stapes displacements are similar to Aibara's findings, being relatively independent of frequency. Between 750 Hz and 2 kHz the results of this study are similar to those of Gyo. At higher frequencies the displacements are found to be in agreement with those of Aibara and Vlaming. The major difference between the findings in this study and those of previous researchers is the dip in the mid–high frequencies.

B. Opening the middle-ear cavity

Measurements in cat middle ears suggest that this dip is a result of opening the middle-ear cavities (Guinan and Peake, 1967). Rosowski *et al.* (1990) argue that opening the middle-ear air spaces has little effect on the human middle-ear input impedance. They suggest that opening the middle-ear cavities causes less than a 10% decrease in input impedance to the middle ear, at low frequencies. McElveen *et al.* (1982) found that a wide opening made in the mastoid cavity of a human temporal bone produced a notch at about 1.5 kHz in umbo displacement. Goode *et al.* (1989) suggest that it is the mastoid air cells that cause a notch in the displacement from 2 to 3 kHz. Hudde and Engel (1998) found that removing the mastoid air cells results in a dip between 1 and 3 kHz, corresponding to the antrum resonance. The 2 kHz notch observed in this study therefore accords with previous work.

C. Draining the cochlear fluids

At 80 dB SPL draining the cochlea *in vitro* appears to have a small effect on the magnitude of stapes vibration (Fig. 3). At low frequencies, draining the cochlea reduces vibration amplitude whereas above 1 kHz stapes displacement increases by about 3 dB. This result is similar to that reported by Shinohara (1997) in guinea pigs.

Gyo *et al.* (1987) took direct measurements of stapes displacement before and after draining the cochlea. Their result has been normalized to an 80 dB SPL stimulus at the tympanic membrane and shown with the results from this study (Fig. 6). Gyo measured an increase of up to 8 dB in stapes-head displacement above 500 Hz when the cochlear fluids were drained. A resonant peak at 700 Hz was introduced by draining the fluids. No resonant peak was present in Gyo's intact cochlea measurement, although this may be masked by an increased low frequency amplitude response. The intact measurement of Gyo *et al.* is greater than the intact measurement in this study for frequencies less than 700 Hz. Both studies measure similar displacements above 700 Hz.

The circuit model was used to predict displacement increase after draining the inner-ear fluids (Fig. 4). A resonance

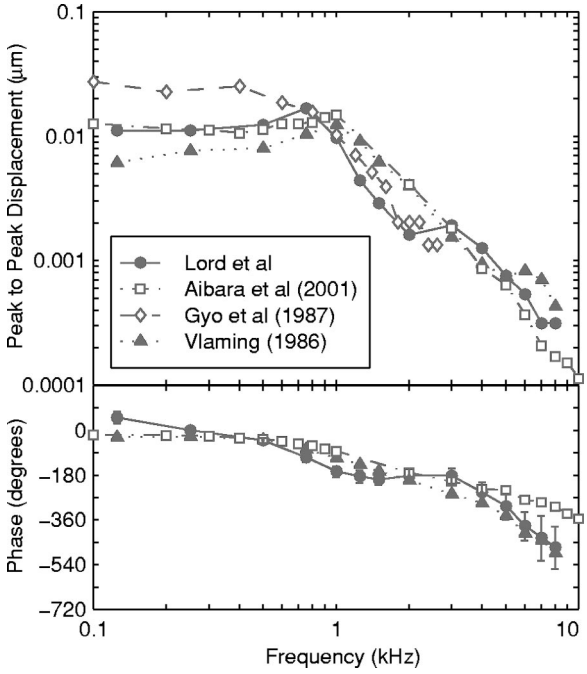

FIG. 5. Stapes-displacement responses in human temporal bone reported in the literature, normalized to 80 dB SPL at the tympanic membrane. Means are reported for Lord *et al.* (this study) $n=5$, Aibara *et al.* (2000) $n=11$, and Vlaming (1986) $n=4$. Gyo measured peak to peak stapes head displacement in one temporal bone. Aibara *et al.* measured footplate volume-velocity which has been converted to displacement assuming a footplate area of 3.2 mm^2. Vlamings rms displacement results have been converted to peak-to-peak values. The lower plot shows the phase difference between the stimulus and stapes response.

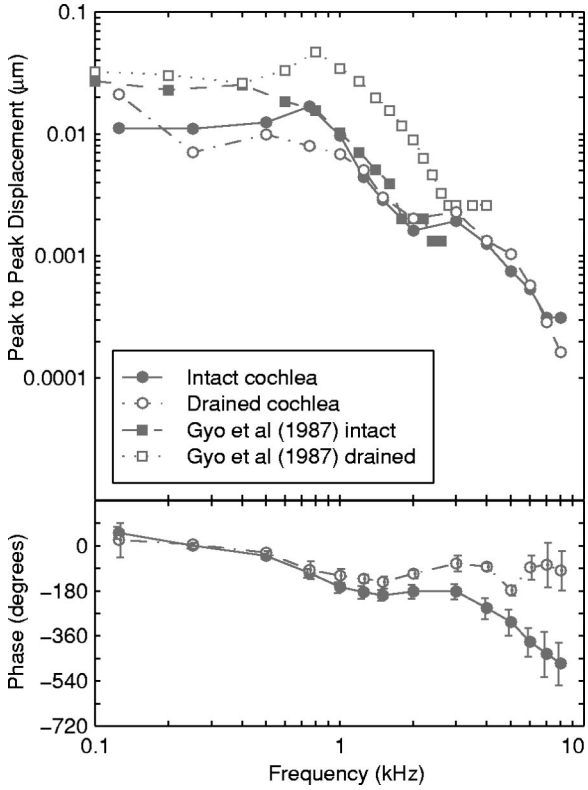

FIG. 6. Stapes-displacement, before and after draining the cochlear fluids. Gyo *et al.* stapes head response has been normalized to 80 dB SPL at the tympanic membrane. The lower plot shows the phase difference between the stimulus and stapes response.

peak at 1 kHz is also present in the drained cochlea circuit model that is not previously present. The results of Gyo *et al.* for intact and drained displacements fit well with the analog model prediction. However, Gyo's results were recorded with a much higher input stimulus level, which is out of the reported validity range of the model. Linearity of the ossicular chain in response to sound pressure at the tympanic membrane has been reported over a wide range of input levels. Guinan and Peake's (1967) measurements in cats indicate that for frequencies below 1.5 kHz the intact feline middle ear is linear up to 130 dB SPL. Andersen *et al.* (1963) demonstrate that the human middle ear[4] exhibits a linear response to stimulation level up to an input stimulus of 110 dB SPL and Gundersen (1972) finds linearity for sound pressures up to 115 dB. At higher levels a pronounced lack of proportionality was demonstrated in their recordings. Rubinstein *et al.* (1966) found in human cadavers that the linear limit is around 104 dB SPL. Goode *et al.* (1994) show that stapes motion is linear at 124 dB SPL. Normalizing Gyo's results from 124 dB SPL to an input stimulus of 80 dB SPL is probably valid.

Gyo's results were measured from the stapes head whereas the other measurements in this study were measured from the stapes footplate. There is a possibility that the stapes is not acting as a rigid body, especially at the high sound pressure levels used to stimulate the ossicles in their study. However, this point should not be overemphasized since the data presented by Gyo *et al.* represent only one temporal bone sample. In general Gyo's data match the expected result predicted by circuit models and from impedance measurements.

D. Dehydration of the annular ligament

One factor that may affect the temporal bone study and cause the drained cochlea stapes displacement to be of lower magnitude than theory predicts, is a drying and stiffening of the annular ligament. There is an implicit order bias in the experimental protocol, as stapes displacement with an intact cochlea must be measured prior to draining the cochlea. If the measurement and preparation time is significant then some drying of the annular ligament will undoubtedly occur between measurements. The frequency response of the stapes, to 14 pure tones, took 20–25 min to measure. The subsequent draining of the cochlea and realignment of the bone sample took up to an hour. Although the annular ligament was not purposefully moistened, irrigation was used during preparation. It is possible that there was some stiffening of the annular ligament in this study, however, data from our research group show no change in response 4.5 h after having opened the inner ear (Fig. 7).

E. Use of thawed temporal bones

The work of Ravicz *et al.* (2000) suggests that freezing and thawing can have a significant effect on the inner-ear input impedance. The artificial introduction of air into the cochlea resulted in a decrease of $|\mathbf{Z}_{IE}|$ in all cases. While this was not the case with each freeze and thaw cycle of temporal

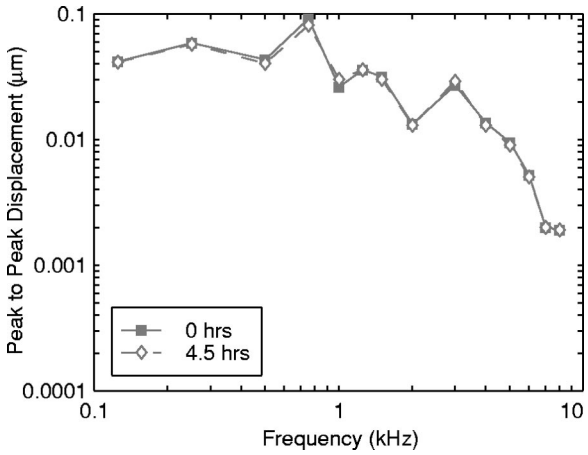

FIG. 7. Stapes-displacement, stimulated at 90 dB SPL immediately after draining the inner ear and after a period of 4.5 h.

bones in their study, it is thought to be the mechanism by which thawed samples are affected. It may have been the case that the temporal bones used in this study were partially drained at the start of the experiment, in which case subsequent ''draining'' would have had no further effect on inner-ear impedance. However, when compared with the experimental work of Aibara (2001) and Vlaming (1986) the data presented here are consistent whether initially drained by freezing or deliberately drained by removal of the inner ear. It should be noted that Vlaming (1986) used frozen and thawed temporal bones, and Aibara (2001) and Gyo (1987) used fresh samples.

F. Stapes motion

If stapes motion were purely pistonlike the magnitude of the displacement should be the same at all points on the footplate. Reported differences between the lateral and medial approach measurements may be due to the location of the targets, although these were both located as centrally as possible on the footplate. Using two approaches to the footplate, one from an oblique angle and the other in-line with the assumed maximal displacement (i.e., the pistonlike component), shows that stapes motion, in preparations with drained cochlea, is not purely one dimensional but exhibits some other motion components at mid-high frequency. This is in agreement with the findings of Gyo *et al.* (1987), Heiland *et al.* (1999), and others.

The fact that Gyo's intact data differs from the experimental results of other workers at low frequency may result from the choice of measurement position on the stapes. Evidence for this is given by Gyo (1987), ''the displacement amplitudes of the spheres differed greatly according to their location on the stapes.'' There is therefore the possibility that the stapes footplate is not moving in the same manner as the stapes head. The circuit model does not account for this fact and would predict the ''bulk'' stapes motion, as though it were the stapes head. Perhaps this is the reason that the circuit model and Gyo's data are similar, and may explain differences between circuit models and experimental data. More work is needed regarding stapes motion.

V. CONCLUSIONS

Stapes-footplate displacements measured in temporal bones with intact cochlea are similar to those reported by other investigators. Despite the use of thawed temporal bones, the footplate response was similar to a previous study using fresh temporal bones. There was no evidence of dehydration of the annular ligament. Differences were consistent with other data reporting the 2 kHz notch to be the probable result of opening the middle-ear cavity. The subsequent draining of the cochlea resulted in no change of stapes displacement at frequencies above 1 kHz. Below this frequency stapes displacement was found to have slightly decreased. Results from an electrical analog model show that stapes displacement is expected to increase at all frequencies. A previous study of stapes-head displacement showed that vibration amplitude increased by as much as 8 dB at frequencies above 700 Hz, with little change in amplitude below 500 Hz. The results presented here suggest that draining the cochlea in human temporal bones has little effect on stapes footplate motion.

It is clear that the discrepancy between these results and those of Gyo *et al.* (1987) and the circuit model needs to be explained. Some explanations for the differences between the two studies include the level of stimulation, and the measurement position on the stapes (head or footplate). One approach to this would be to measure the effect of draining the cochlear fluids on stapes motion over a wide range of sound pressure levels. Multipoint measurements of the stapes motion and the rigidity of the stapes could also be investigated.

ACKNOWLEDGMENT

This work was supported in part by the Scottish Hospitals Endowment Research Trust, Edinburgh, EH3 9EE, and Remedi, Bath, BA2 9HT.

[1]Assuming one-dimensional motion of the stapes footplate, and a linear response of the system to frequency and pressure.
[2]Sound pressure levels in dB SPL are referenced to 20 μPa.
[3]Assuming a pistonlike motion of the stapes, the velocity vector is the line along which the stapes moves. This common assumption may oversimplify the actual motion of the footplate, but is a limitation of a single point measurement system.
[4]Andersen *et al.* (1963) measure round window displacement. The cochlea has been shown to be incompressible (Kringlebotn, 1995), and therefore round window volume displacement is equal to oval window volume displacement.

Abel, E. W., Lord, R. M., Mills, R. P., and Wang Z. (**2000**). ''Methodology for laser vibrometer studies of stapes footplate displacement,'' in *The Function and Mechanics of Normal, Diseased and Reconstructed Middle Ears*, edited by J. J. Rosowski and S. N. Merchant (Kugler, The Hague), pp. 89–97.

Aibara, R., Welsh, J. T., Puria, S., and Goode, R. L. (**2001**). ''Human middle-ear sound transfer function and cochlea input impedance,'' Hear. Res. **152**, 100–109.

Andersen, H. C., Hansen, C. C., and Neergard, E. B. (**1963**). ''Experimental studies on sound transmission in the human ear II,'' Acta Oto-Laryngol. **56**, 307–317.

Gyo, K., Aritomo, H., and Goode, R. L. (**1987**). ''Measurement of the ossicular vibration ratio in human temporal bones by use of a video measuring system,'' Acta Oto-Laryngol. **103**, 87–95.

Goode, R. L., Nakamura, K., Gyo, K., and Aritomo, H. (**1989**). ''Comments on 'Acoustic transfer characteristics in human middle ears studied by a SQUID magnetometer method' [J. Acoust. Soc. Am. **82**, 1646–1654 (1987)],'' J. Acoust. Soc. Am. **86**, 2446–2449.
Goode, R. L., Killion, M., Nakamura, K., and Nishihara, S. (**1994**). ''New knowledge about the function of the human middle ear: development of an improved analog model,'' Am. J. Otol. **15**, 145–154.
Guinan, J. J., and Peake, W. T. (**1967**). ''Middle-ear characteristics of anesthetized cats,'' J. Acoust. Soc. Am. **41**, 1237–1261.
Gundersen, T. (**1972**). ''Prostheses in the ossicular chain II. Construction of prosthesis for the incus: Postoperative study of the data,'' Arch. Otolaryngol. **96**, 423–425.
Gundersen, T., and Høgmoen, K. (**1976**). ''Holographic vibration analysis of the ossicular chain,'' Acta Oto-Laryngol. **82**, 16–25.
Heiland, K. E., Goode, R. L., Asai, M., and Huber, A. M. (**1999**). ''A human temporal bone study of stapes footplate movement,'' Am. J. Otol. **20**, 81–86.
Hudde, H., and Engel, A. (**1998**). ''Measuring and modeling basic properties of the human middle ear and ear canal. Part II: Ear canal, middle ear cavities, eardrum, and ossicles,'' Acust. Acta Acust. **84**, 894–913.
Kringlebotn, M. (**1995**). ''The equality of volume displacements in the inner ear windows,'' J. Acoust. Soc. Am. **98**, 192–196.
Lord, R. M., Mills, R. P., and Abel, E. W. (**2000**). ''An anatomically shaped incus prosthesis for reconstruction of the ossicular chain,'' Hear. Res. **145**, 141–148.
Lynch, T. J., Nedzelnitsky, V., and Peake, W. T. , (**1982**). ''Input impedance of the cochlea in cat,'' J. Acoust. Soc Am. **72**, 108–130.
McElveen, J. T., Goode, R. L., Miller, C., and Falk, S. A. (**1982**). ''Effect of mastoid cavity modification on middle ear sound transmission,'' Ann. Otol. Rhinol. Laryngol. **91**, 526–532.
Merchant, S. N., Ravicz, M. E., and Rosowski, J. J. (**1996**). ''Acoustic input impedance of the stapes and cochlea in human temporal bones,'' Hear. Res. **97**, 30–45.
Møller, A. R. (**1965**). ''An experimental study of the acoustic impedance of the middle ear and its transmission properties,'' Acta Oto-Laryngol. **60**, 129–149.
Murakami, S., Gyo, K., and Goode, R. L. (**1998**). ''Effect of increased inner ear pressure on middle ear mechanics,'' Otolaryngol.-Head Neck Surg. **118**, 703–708.
Pascal, J., Bourgeade, A., Lagier, M., and Legros, C. (**1998**). ''Linear and nonlinear model of the human middle ear,'' J. Acoust. Soc. Am. **104**, 1509–1516.
Puria, S., Peake, W. T., and Rosowski, J. J. (**1997**). ''Sound-pressure measurements in the cochlea vestibule of human-cadaver ears,'' J. Acoust. Soc. Am. **101**, 2754–2770.
Ravicz, M. E., Merchant, S. N., and Rosowski, J. J. (**2000**). ''Effect of freezing and thawing on stapes-cochlear input impedance in human temporal bones,'' Hear. Res. **150**, 215–224.
Rosowski, J. J., Davis, P. J., Merchant, S. N., Donahue, K. M., and Coltrera, M. D. (**1990**). ''Cadaver middle ears as models for living ears: Comparisons of middle ear input immittance,'' Ann. Otol. Rhinol. Laryngol. **99**, 403–412.
Rubinstein, M., Feldman, B., Fischler, H., Frei, E. H., and Spira, D. (**1966**). ''Measurement of stapedial-footplate displacements during transmission of sound through the middle ear,'' J. Acoust. Soc. Am. **40**, 1420–1426.
Schön, F., and Müller, J. (**1999**). ''Measurements of ossicular vibrations in the middle ear,'' Audiol. Neuro-Otol. **4**, 142–149.
Shinohara, T., Nishihara, S., Murakami, S., Gyo, K., and Yanagihara, N. (**1997**). ''Effects of inner ear modifications on the middle ear,'' in *Proceedings of the International workshop on middle ear mechanics in research and otosurgery*, edited by K.-B. Hüttenbrink (Bibliothek der HNO-Universitätsklinik, Fetscherstraße 74, D-01307, Dresden, Gemany), pp. 107–110.
Stasche, N., Foth, H.-J., Hörmann, K., Baker, A., and Huthoff, C. (**1994**). ''Middle ear transmission disorders–Tympanic membrane vibration analysis by Laser-Doped-Vibrometry,'' Acta Oto-Laryngol. **114**, 59–63.
Vlaming, M. S. M. G., and Feenstra, L. (**1986**). ''Studies on the mechanics of the normal human middle ear,'' Clin. Otolaryngol. **11**, 353–363.
von Békésy, G. (**1960**). *Experiments in Hearing* (McGraw-Hill, New York).
Zwislocki, J. (**1962**). ''Analysis of the Middle-Ear Function. Part I: Input impedance,'' J. Acoust. Soc. Am. **34**, 1514–1523.

Multicomponent stimulus interactions observed in basilar-membrane vibration in the basal region of the chinchilla cochlea

William S. Rhode[a] and Alberto Recio
Department of Physiology, University of Wisconsin, Madison, Wisconsin 53706

(Received 8 May 2001; revised 23 August 2001; accepted 7 September 2001)

Multicomponent stimuli consisting of two to seven tones were used to study suppression of basilar-membrane vibration at the 3–4-mm region of the chinchilla cochlea with a characteristic frequency between 6.5 and 8.5 kHz. Three-component stimuli were amplitude-modulated sinusoids (AM) with modulation depth varied between 0.25 and 2 and modulation frequency varied between 100 and 2000 Hz. For five-component stimuli of equal amplitude, frequency separation between adjacent components was the same as that used for AM stimuli. An additional manipulation was to position either the first, third, or fifth component at the characteristic frequency (CF). This allowed the study of the basilar-membrane response to off-CF stimuli. CF suppression was as high as 35 dB for two-tone combinations, while for equal-amplitude stimulus components CF suppression never exceeded 20 dB. This latter case occurred for both two-tone stimuli where the suppressor was below CF and for multitone stimuli with the third component=CF. Suppression was least for the AM stimuli, including when the three AM components were equal. Maximum suppression was both level- and frequency dependent, and occurred for component frequency separations of 500 to 600 Hz. Suppression decreased for multicomponent stimuli with component frequency spacing greater than 600 Hz. Mutual suppression occurred whenever stimulus components were within the compressive region of the basilar membrane.
[DOI: 10.1121/1.1416198]

PACS numbers: 43.64.Kc [LHC]

I. INTRODUCTION

The operation of the cochlea has principally been studied using simple stimuli such as tones and/or clicks. This has provided an enormous amount of information about this complicated nonlinear system. However, because the cochlea is nonlinear, one cannot predict the response to a novel stimulus in a straightforward manner (e.g., Rhode, 1971; Sellick *et al.*, 1982; Robles *et al.*, 1986). If one wishes to understand processing of complex sounds more representative of the acoustic ecology, it is necessary to present stimuli whose spectra are more realistic than those of clicks and single tones. In particular, two-tone and multitone suppression effects are studied here.

Although the response of the auditory nerve (AN) to various stimuli largely reflects basilar-membrane response to the same stimuli, it would be beneficial to employ the same stimulus set for basilar-membrane studies that has been used to study AN behavior, as a way to understand the nature of AN responses. Some commonly used stimuli for the study of AN function are amplitude-modulated (AM) signals and harmonic complexes (Javel, 1980; Joris and Yin, 1992). The responses of auditory-nerve fibers (ANFs) to AM signals indicate an enhancement of modulation depths over a range of frequencies and intensities.

Horst *et al.* (1986, 1990) studied the representation of multicomponent ($N=4$ to 64) octave band stimuli centered at the characteristic frequency (CF) of AN fibers in the cat. They observed that edges of the stimulus spectrum were dominant in the response with increasing N, and response to the center component was reduced under these conditions. Similar behavior is observed at the level of basilar-membrane mechanics for N as low as 3, and it appears that frequency spacing of stimulus components is the most important factor (Rhode and Recio, 2001).

Two-tone suppression has been studied at the level of the auditory nerve (e.g., Sachs, 1969; Javel, 1981; Javel *et al.*, 1978; Javel *et al.*, 1983; Delgutte, 1990), in cochlear mechanics (e.g., Rhode, 1977; Ruggero *et al.*, 1992; Cooper and Rhode, 1996b; Nuttall and Dolan, 1993), and via hair-cell recording (Sellick and Russell, 1979; Cheatham and Dallos, 1990; Nuttall and Dolan, 1993). Results indicate that much of the behavior seen in the auditory nerve arises as a result of cochlear mechanics. However, there have been limited cochlear mechanical studies using more complex stimuli (cf. Recio and Rhode, 2000). To help reduce that limitation, single-, two-, three (AM)-, five-, and seven-tone stimuli were used in the present study to further explore nonlinear effects at the level of basilar-membrane vibration.

II. METHODS

Methods are essentially those detailed in Cooper and Rhode (1992). Seven chinchilla cochleas were studied at approximately the 3–4-mm location [characteristic frequency (CF)=6.5–8.5 kHz]. All procedures were approved by the Animal Care and Use Committee of the University of Wisconsin.

[a]Electronic mail: rhode@physiology.wisc.edu

Each animal was anesthetized with sodium pentobarbital using a dose rate of 75 mg/kg. Additional smaller doses were administered to maintain the animal in a deeply areflexive state. All anesthetics were administered intraperitoneally. A tracheotomy was performed to ensure an open airway. After the ear was surgically removed, four screws were implanted in the skull and fixed with dental cement, forming a rigid base. A bolt was then cemented at the base to provide a stable fixation of the skull to a head holder that has six degrees of freedom for positioning the cochlea under the microscope.

The bulla was opened widely and a silver ball electrode was positioned so as to touch the round window for the purpose of recording the compound action potential (CAP) of the auditory nerve in response to short-duration tones (16 ms) for each animal. Because we recorded only in the high-frequency region of the cochlea, the stimulus was stepped in 2-kHz increments from 2 to 20 kHz. At each frequency, a visual detection threshold for N_1 was determined by viewing an average of 20 repetitions as the stimulus level was varied in 1-dB steps. If thresholds were above our best threshold curve by more than 20 dB, no data were collected. High CAP thresholds equated to little or no compression in the hook region (Sellick *et al.*, 1982). CAPs were not typically recorded after mechanical measurements were initiated except to verify that they increased whenever mechanical sensitivity decreased. Any change in mechanical sensitivity was taken as a sign of a deteriorating cochlea.

The overlying cochlear bone was shaved down using a microchisel until the remaining tissue and/or bone debris could be removed with the microelectrode pick. Gold-coated polystyrene beads 25 μm in diameter served as retroreflectors. They were placed in the perilymph and allowed to sink to the basilar membrane. They have a specific gravity of 1.05 that should minimize any loading of the basilar membrane. A glass cover slip was placed over the opening with no hydromechanical seal. Perilymph wicked up to the glass, and beads could then be imaged without detrimental effects on the measurements that occur through an unstable interface between the perilymph and air.

An opening in the bony ear canal, immediately over the tympanic membrane, was made so that the probe tube of a $\frac{1}{2}$ -in. Bruel & Kjaer condenser microphone could be visualized as it was positioned parallel to the tympanic membrane within 1 millimeter of the tip of the malleus, the probe was fixed in place with dental cement, forming a closed-field acoustic system. The opening was sealed with a glass cover after a 45-μm bead was placed on the tympanic membrane at the tip of the malleus (or umbo). The bead was used as a retroreflector for the interferometer and allowed measurement of the transfer function of the malleus. The sound source was a RadioShack supertweeter dynamic phone for all stimuli except two-tone stimuli. In the latter case, reverse-biased $\frac{1}{2}$-in. condenser microphones that were compensated for frequency flatness were used.

A. AM stimuli

AM signals were synthesized and presented using a TDT system (Tucker-Davis Technologies®) system [Eq. (1)]

$$S(t) = (1 + m \cdot \mathbf{sin}(2\pi f_{\mathrm{mod}} t))\mathbf{sin}(2\pi f_{\mathrm{carr}} t). \quad (1)$$

The carrier frequency, f_{carr}, was set equal to the characteristic frequency of the basilar membrane. The modulation frequency was varied in 100-Hz steps from 100 to 1000 Hz, and above 1 kHz was set to 1250, 1500, and 2000 Hz. The modulation coefficient (m) was set to 0.5, 1.0, or 2.0 where $m = 2$ results in three equal-amplitude sine tones. Stimulus level was varied from 0 to 90 dB SPL in 5-dB steps. Stimuli were 30 ms in duration, 8 times at a rate of 10/s. A cosine envelope with 1-ms rise/fall time was used for all stimuli. Amplitude and phase were determined using a phase-locked loop technique that computes dc and the Fourier component (sine wave fit, abbreviated as sinfit).

B. Multicomponent stimuli

A subset of these stimuli consisted of five equal-amplitude sinewaves with the first, third, or fifth component frequency set equal to the CF of the basilar-membrane location under study. The frequency separation of stimulus components was varied in steps of 100 Hz up to 1 kHz and set to 1250, 1500, and 2000 Hz above 1 kHz. $f_{\mathrm{mod}} > 2000$ Hz was not explored because ANFs do not show any AM temporal coding for this condition. Stimulus level was varied from 0 to 90 dB SPL in 5-dB steps. The stimulus level for multicomponent stimuli always refers to the level of the center (CF) component. Stimuli were 30 ms in duration, repeated 8 times at a rate of 10/s. Analysis consisted of determining the amplitude of nine response components around CF using the sinfit procedure described above. The amplitude at the difference frequency was also determined but was insignificant or buried in the noise except for high levels and large frequency separations.

Another stimulus consisted of seven equal-amplitude sine waves with the middle component always set equal to CF. These stimuli had the same difference frequencies as the five-component stimuli and were analyzed in the same manner except that 11 components were analyzed using the sinfit technique. The level of the center component is specified throughout the paper.

The component amplitudes of each stimulus used (three, five, and seven-component stimuli) were compensated by the acoustic calibration.

C. Two-tone stimuli

Two-tone suppression (2TS) data were collected in order to provide a comparison for suppression effects due to multiple components. These data were also important for determining whether suppression effects are compatible with the large body of literature on 2TS in cochlear mechanics. The two-tone paradigm consisted of a 30-ms probe stimulus at CF and a 30-ms suppressor tone delayed 10 ms relative to the probe onset. Generally, eight repetitions of the combination were presented at a rate of 10/s. The probe tone was held constant while input–output (I/O) functions were collected as the suppressor tone was varied in 5-dB SPL steps from a maximum to a minimum (usually 90 to 0 dB SPL). The suppressor frequency was then changed and the process re-

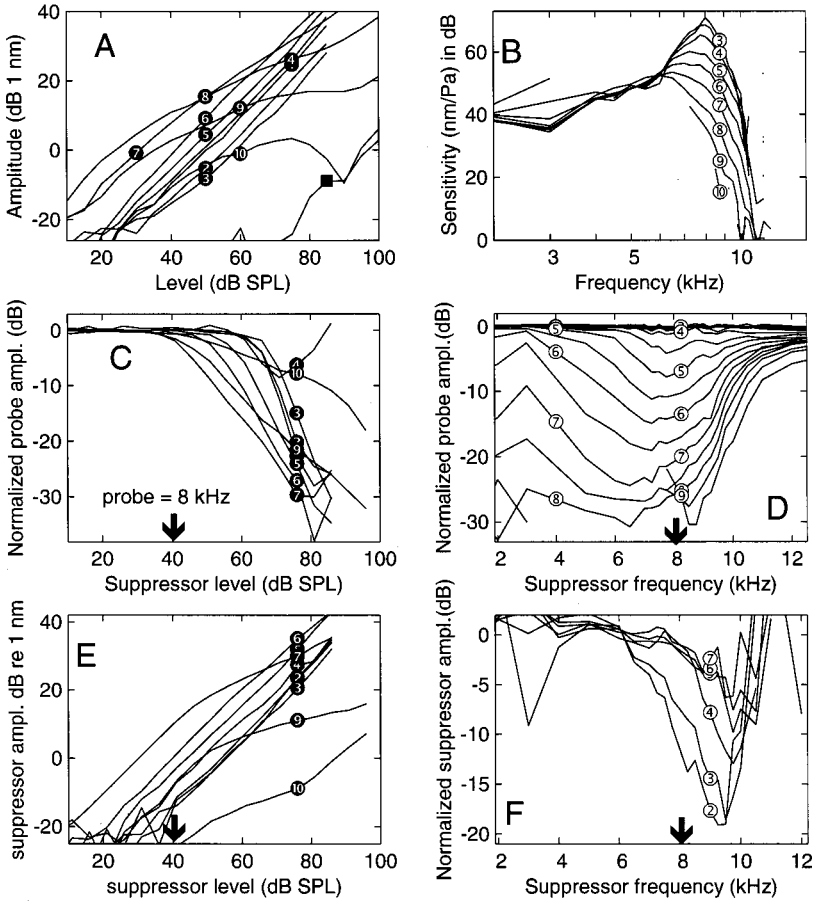

FIG. 1. Single- and two-tone responses for a basal cochlear region with CF=8000 Hz. Symbol key: solid symbol=x kHz, e.g., ❷=2 kHz; open symbol=x dB SPL, e.g., ②=2 times 10=20 dB SPL. (A) Single-tone amplitude I/O functions at the indicated frequencies with only a subset of the data shown for clarity. Symbol exception: ■=11 kHz. (B) Normalized isolevel curves (sensitivity=amplitude at 1 Pascal frequency transfer functions) derived from the I/O curves shown in panel (A). A two-tone suppression study is shown in panels (C) through (F). (C) Probe amplitude I/O curves that have been normalized to 0 dB for a 20-dB SPL suppressor to emphasize probe suppression as a function of suppressor level; probe level=40 dB SPL and only a third of the I/O curves are shown. (D) Isolevel normalized probe amplitude curves derived from the I/O curves in panel (C). This is the normalized probe amplitude versus frequency function representation of the data in panel (C) for the full data set. (E) Suppressor amplitude I/O curves taken at the same time as the data in panel (C). (F) Normalized isolevel suppressor amplitude curves derived by subtracting the single-tone data in panel (B) from the isolevel suppression amplitudes obtained from the I/O functions in panel (D) for the condition when the level of the probe is 40 dB SPL. The arrow indicates the frequency of the probe tone. Chinchilla Ct17.

peated. The probe level was varied in 10-dB steps. I/O functions for 20–40 suppressor frequencies were presented at each probe level with closer frequency spacing near CF than away from it. A Hamming window (Rabiner and Gold, 1975) was applied to the response before analysis occurred.

D. Single-tone basilar-membrane and middle-ear vibration measurements

Basilar-membrane input–output (I/O) functions were determined using 30-ms tone bursts with 1-ms raised-cosine rise and fall times and presented every 100 ms. The stimulus level covered a 100-dB SPL range in 5-dB SPL steps. A minimum of eight basilar-membrane and four middle-ear responses were averaged for each stimulus condition. Analysis consisted of Fourier decomposition of the steady-state portion of the averaged response at the stimulus frequency. Measurements of the basilar-membrane I/O function at CF were made throughout the experiment to monitor preparation stability. Vibration of the ossicles was measured at the tip of the manubrium (umbo) or at the incudo–stapedial joint or both locations before and/or after basilar-membrane measurements.

E. Displacement measurements

Mechanical responses were measured using a custom-built displacement-sensitive heterodyne laser interferometer (Cooper and Rhode, 1992). The laser was coupled to the preparation using a long working distance lens (Nikon SLWD 5X, NA 0.1). The laser was focused to a spot $\sim 5\ \mu$m in diameter on the reflective beads. The interferometer was not sufficiently sensitive to measure basilar-membrane vibration without the gold-coated beads. Instantaneous phase was measured using two single-cycle phase meters that worked in quadrature. Phase meter outputs were sampled at 250 kHz and the phase was unwrapped using custom software. Response amplitudes were corrected for the frequency response of the recording system. The noise floor was <5 pm/$\sqrt{\text{Hz}}$.

III. RESULTS

A. Two-tone interactions

Two-tone studies were conducted along with three-, five-, and seven-tone studies. They provide data needed to determine whether or not suppression or distortion effects of multitone stimuli are predictable from two-tone results. Two-tone studies involved the collection of displacement-level (I/O) functions during simultaneous presentation of a probe and suppressor tone. The probe tone was always set to the best frequency of the basilar-membrane location under study.

Prior to presentation of any complex stimulus, the single-tone response was collected in order to determine the CF of the region under study. A portion of the I/O functions for one study is shown in Fig. 1(A), where the symbol attached to each I/O function indicates the stimulus frequency in kHz. I/O functions are linear for frequencies <6 kHz. Nonlinear growth in amplitude of basilar-membrane vibration occurs for frequencies >6 kHz. The slope of the I/O

function, or growth rate, equals 1 for a linear system. Growth rates <1 dB/dB are characteristic of a nonlinear compressive system, and greater than 1 for an expansive nonlinearity. An expansive nonlinearity is seen at 10 kHz for levels >90 dB SPL, just beyond the notch in the I/O function, which is accompanied by a rapid change in the response phase ($\sim 180°$, not shown). Compression at CF ($=8$ kHz) begins around 20 dB SPL with a growth rate of 0.36 (dB/dB) between 40 and 70 dB SPL.

The complete set of I/O functions can be recast as a set of transfer functions normalized by stimulus level [Fig. 1(B)] where deviation from linearity is seen by a lack of superposition of the individual isolevel functions for frequencies above 6 kHz. At CF, a reduction in sensitivity of ~ 45 dB occurs as sound pressure is increased from 30 to 100 dB SPL. Response amplitude to a CF tone was 1.5 nm at 20 dB SPL and was among the best of this experiment series (0.25, 0.3, 0.4, 1.0, 1.4, 1.5, 1.6 nm at 20 dB SPL). A significant portion of differences in amplitude is likely due to the variability in the radial location of the basilar-membrane measurement, as there is limited control on where the reflective bead falls. The maximum displacement is a function of the radial location of the bead on the basilar membrane.

In a two-tone suppression (2TS) paradigm, the motion in response to the probe tone (40 dB SPL at CF=8 kHz) is reduced as the suppressor level is increased beyond a certain threshold [a subset of I/O functions is shown in Fig. 1(C)]. Suppressor frequencies near the probe frequency exhibit the lowest suppression thresholds, <40 dB SPL or slightly below the level of the probe. As suppressor frequency increases, suppression threshold increases and the amount of suppression decreases. As the suppressor frequency decreases below CF ($=$probe frequency) the rate of suppression, measured as the slope of the curves in Fig. 1(C), approaches 1 dB/dB. The rate of suppression decreases as suppressor frequency increases above CF. These latter relations are seen best in Fig. 1(D), where probe suppression is shown as a reduction of probe amplitude versus suppressor frequency with suppressor level the parameter (probe level=40 dB SPL). When the suppressor level is near 40 dB SPL the first signs of suppression are seen in the vicinity of CF. As the suppressor level is increased, the range of frequencies that suppresses the probe widens, and the amount of suppression increases to ~ 30 dB for suppressor levels >80 dB SPL. Because probe amplitude is monotonically decreasing with increasing suppressor level, it is hypothesized that probe suppression would continue to increase with higher suppressor levels than were used here. Similar maximum amounts of suppression (25–35 dB) were obtained in the other six preparations.

An alternate method of expressing the interaction of two tones is to plot the amplitude I/O functions of the suppressor tones [Fig. 1(E)] corresponding to the probe I/O functions [Fig. 1(C)]. Compared to the single-tone I/O functions [Fig. 1(A)] these are more linear and the notch in the 10-kHz function is not present. Mutual suppression of the probe and the suppressor response components can be seen by subtracting the single-tone isolevel curves shown in Fig. 1(A) from the suppressor isolevel curves obtained from the data in Fig. 1(E) with the result shown in Fig. 1(F). The 40-dB SPL probe tone at CF is shown to have a suppressive effect on the second tone that extends from 6 to 11 kHz, nearly an octave, and can be seen to suppress the second tone by more than 18 dB at 9.5 kHz. As suppressor level is increased, suppression due to the probe tone is reduced in both amplitude and frequency extent. The probe tone at CF has its strongest suppressive effect for the cochlear region basal to its location with the location of the maximum effect increasing with suppressor level. At this point it should be obvious that the terms, probe/suppressor, are merely a convenience since both the probe and the suppressor produce suppression of the other component with the caveat that both must reside in the compressive region of the basilar membrane for mutual suppression to occur.

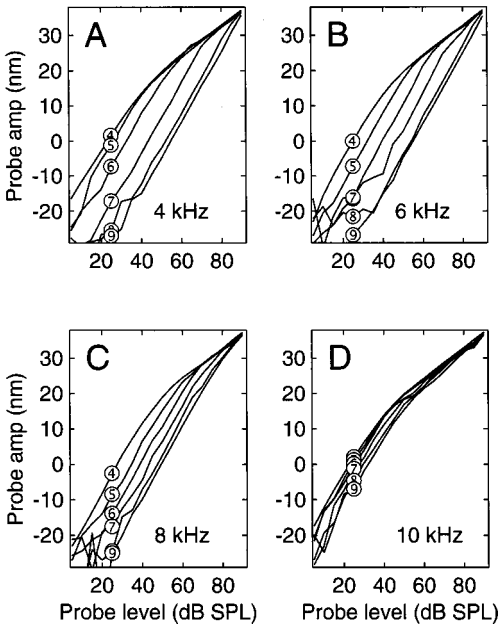

FIG. 2. I/O curves that are similar to those collected from the auditory nerve in a two-tone suppression paradigm. Probe amplitude versus probe level with suppressor level varied (CF=6500 Hz). The suppressor frequency is indicated as a parameter in each panel. Probe level was varied in 5-dB SPL steps. Responses with amplitudes less than -28 dB *re* 1 nm are removed from the display since they were below the system noise level. Cb057.

Two-tone neural suppression in the auditory nerve has been extensively studied (e.g., Sachs, 1969; Javel *et al.*, 1983; Delgutte, 1990). One typical display method for auditory-nerve 2TS I/O functions is to examine the effect of a suppressor tone at several levels on the I/O function at CF for a nerve fiber. This AN paradigm was used in one study of the mechanical correlate of neural 2TS when the suppressor tone was held constant while the I/O function at CF ($=6.5$ kHz) was measured (Fig. 2). The typical rightward shift observed in the rate-level AN I/O functions with increasing suppressor level is also seen in the mechanical I/O functions for all suppressor frequencies. Larger shifts with each level increment occur for suppressor frequencies lower than CF [4 and 6 kHz in Figs. 2(A) and (B), respectively]. As the I/O response function shifts to the right with increasing suppressor level, the probe amplitude response stays linear to proportionally higher levels. In all other studies, the suppres-

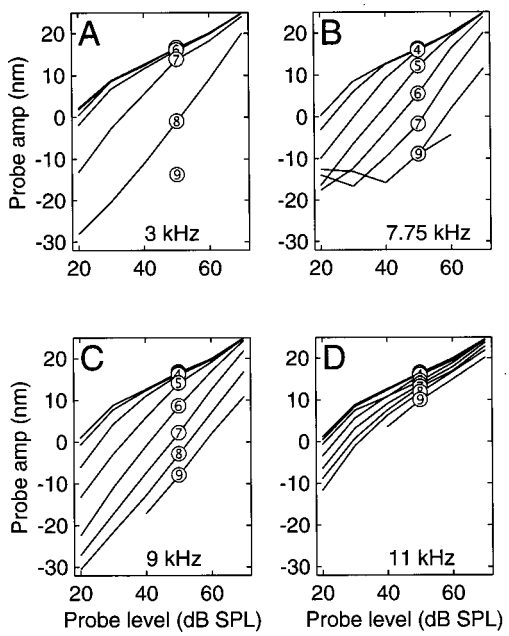

FIG. 3. I/O curves that are similar to those collected from the auditory nerve in a two-tone suppression paradigm. Data were collected in the manner described in the Methods section: Probe I/O functions were collected while the suppressor level was stepped in 5-dB SPL increments. The suppressor level is indicated on each curve and the suppressor frequency is given in each panel. Data are from the same experiment as the data shown in Fig. 1 where CF=8 kHz (Ct17).

sor level was decremented in 5-dB steps from 90 to 0 dB SPL to produce the I/O functions while the probe level was held constant. Results for one of these studies shown in Fig. 3 are presented in the same format as in Fig. 2, although the probe levels are fewer (six versus 19) and also the range of levels is smaller than that in Fig. 2 (20 to 70 vs 0 to 90 dB SPL). The rightward shift of the probe amplitude function for a 10-dB suppressor level increase is as much as 18 dB at 3000 Hz or a rate of suppression of 1.8 dB/dB (Fig. 3, CF=8 kHz). The magnitude of the shift to the right of the probe response curves increases with decreasing suppressor frequencies. The shift is relatively constant, usually $\sim$1 dB/dB, once the suppressor frequency is in the linear region of the basilar-membrane response. Probe amplitude I/O functions are linear to higher levels as the suppressor level is raised. In general, this mechanical 2TS behavior closely parallels comparable neural 2TS data.

Three views of two-tone suppression are presented in Fig. 4 for three probe levels (30-, 50-, and 70 dB SPL in rows 1, 2, and 3, respectively). Suppression thresholds of an 8-kHz, 30-dB SPL probe by a near-CF suppressor are of equal or even lower ($\sim$20 dB SPL) levels than probe levels [Fig. 4(A)]. With increasing suppressor level, the frequency extent of suppression increases until all lower frequencies suppress the probe. On the high-frequency side of the probe, suppression occurred at least up to 15 kHz, the highest frequency suppressor that was employed. It appears that suppression continues with further increases in suppressor frequency, though there is a relatively small reduction of the probe. Near CF there is a ''break'' in the isolevel curves for levels $>$60 dB SPL (indicated by the solid line below the abscissa) that is a result of leakage in the frequency analysis routines due to the width of the Fourier filters (see the discussion below).

As the probe level is increased to 50 and 70 dB SPL [Figs. 4(B) and (C), respectively], the suppressor level that just begins to suppress the probe remains roughly 10 dB less than the probe level. The ''break'' in the 30-dB SPL isolevel curves near CF doesn't occur when the probe is at higher levels ($>$40 dB SPL). To avoid possible damage of the cochlea by stimulus levels $>$95 dB SPL, the suppressor level never reached 40–50 dB above the probe level, which is necessary to see the break. For probe levels between 20 and 30 dB SPL the suppressor level can be as much as 60 dB greater than the probe level. Another effect of increasing probe level is that the suppressor frequency that produces maximum suppression moves to lower values.

Iso-suppression curves for 1, 10, and 20 dB of suppression are compared to the single-tone 1-nm iso-amplitude curve [Figs. 4(D), (E), and (F): dashed line=1-nm iso-amplitude curve]. Iso-suppression curves lose their ''tip'' as probe level increases and become nearly constant up to a cutoff frequency. It is also apparent that the high-frequency side of the suppressive region extends beyond the 1-nm iso-amplitude region. The single-tone 1-nm iso-amplitude region can be viewed as the excitatory region for an AN fiber with the same CF, essentially a frequency threshold curve.

Slopes of the probe I/O functions [cf. Fig. 1(C)] versus suppressor frequency are shown with suppressor level as a parameter [Figs. 4(G), (H), and (I)]. These slopes define the rate of suppression and (for the convenience of using the same ordinate scale) are compared to the negative of the single-tone I/O growth rates where rates $<$1 dB/dB define the nonlinear or compressive region [column 3, Figs. 4(G), (H), and (I), single-tone data at 70 dB SPL indicated by the dashed line]. Suppression rates approach $-$1 dB/dB for sufficiently high suppressor levels in the frequency region where single-tone growth rates are 1 dB/dB, i.e., the linear region of basilar-membrane single-tone response. In the compressive region around CF, the suppression rate is 0.3 dB/dB and decreases to 0.2 dB/dB at 11.5 kHz. Suppression rate decreases as growth rate decreases and is not equal to zero even at 15 kHz, a frequency that is beyond the single-tone response region. It is noteworthy that suppression occurs for frequencies $>$11 kHz, even though the single-tone displacement is less than 0.1 nm for levels $<$70 dB SPL. Above 70 dB SPL the single-tone vibration is complicated by the fact that there is a notch in the 10-kHz I/O function, and the compression slope is negative, zero, or greater than 1 dB/dB depending on the stimulus level. The fact that there is suppression in what has traditionally been labeled the plateau region of the basilar-membrane transfer function (e.g., Rhode, 1971; Cooper and Rhode, 1996a) suggests that the vibration of the basilar membrane is influenced by tones nearly an octave above CF and possibly more.

Perhaps a more telling relationship is the relative suppressor-to-probe amplitude that results in a fixed reduction of the probe across both frequency and probe level (Fig. 5). This relation shows that the suppressor amplitude required to produce 1 dB of suppression is near that of the probe amplitude for frequencies up to CF and is nearly inde-

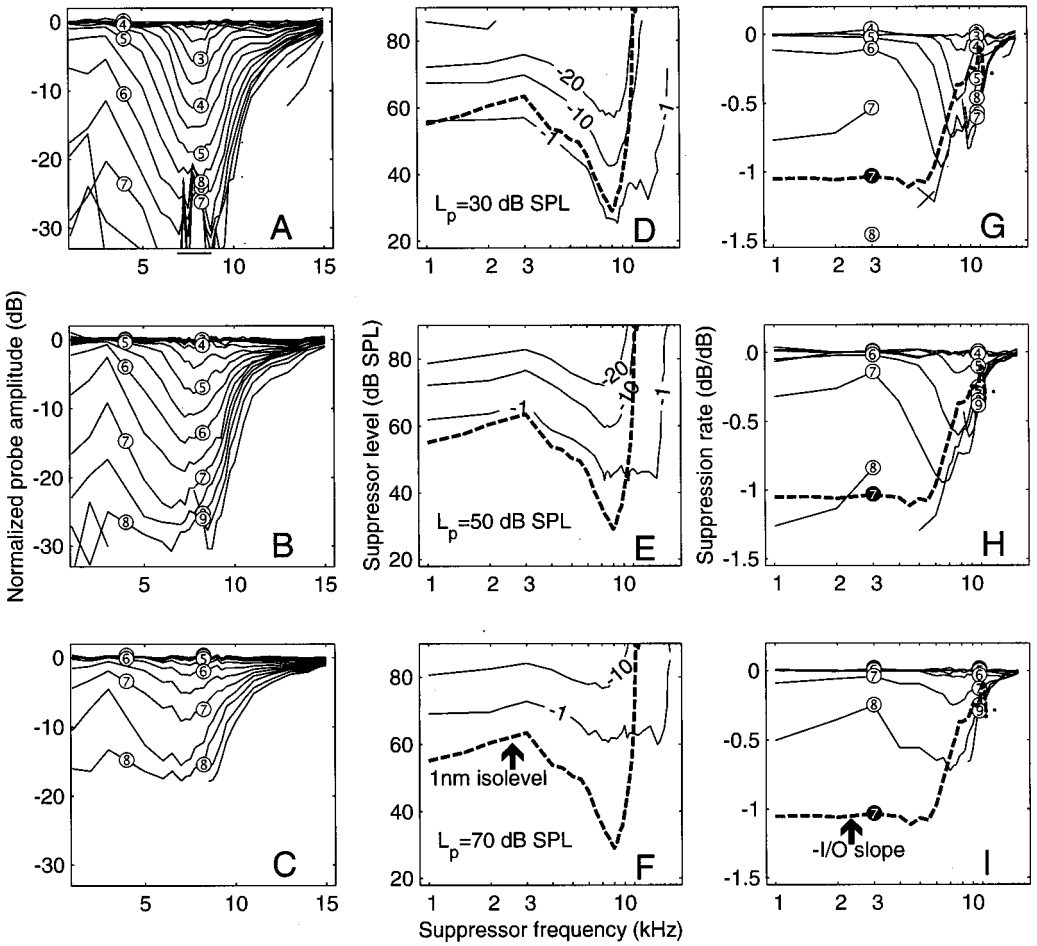

FIG. 4. Suppression from several perspectives. Column 1: Isolevel suppression curves for 5-dB increments in level (10-dB levels are indicated with a numbered symbol: e.g., 30 dB SPL=10 times ③ while the probe is at 30, 50, and 70 dB SPL in rows 1, 2, and 3, respectively. Column 2: Suppressor levels necessary to reduce the probe amplitude −1, −10, or −20 dB (labeled solid lines). The 1-nm iso-amplitude curve for a single tone is repeated in each panel (dashed line). Column 3: The suppression rates for the three probe levels at 10-dB SPL increments (solid lines and numbered symbols). The negative of the slope of single-tone I/O curves (defined as compression) at 70 dB SPL is superimposed in each panel (dashed line, ❼) where −1 dB/dB is linear and 0 dB/dB is complete compression (Ct17).

pendent of the probe amplitude for frequencies <CF/2. Beyond CF, the required suppressor amplitude decreases rapidly and can be as small as 1% of the probe amplitude. This latter number is intriguing and suggests that the probe is affected by what is happening in the region basal to 8 kHz. This is consistent with the fact that there is suppression even when the suppressor frequency is beyond the single-tone upper cutoff frequency for a particular place. In order to reduce the probe amplitude by 12 dB, the suppressor amplitude has to be increased over 20 dB. The suppressor-to-probe relation as a function of frequency is seen to be similar for all probe levels employed.

B. Multitone suppression

Suppression effects in BM responses to AM stimuli were studied by analyzing the amplitude of the CF component of the basilar-membrane response to an AM signal relative to the single-tone response. From results shown in Fig. 6, it is clear that there is a systematic increase in probe suppression with increasing modulation depth. There is only a modest amount of suppression (1–2 dB) at 50% modulation, for which the amplitudes of sideband components are 12 dB less than the carrier amplitude [Fig. 6(A)]. However, suppression increases for 100% modulation, in which case the sideband components amplitudes are 6 dB less than carrier amplitude [Fig. 6(B)]. While suppression is dependent on both the stimulus level and the modulation frequency, the

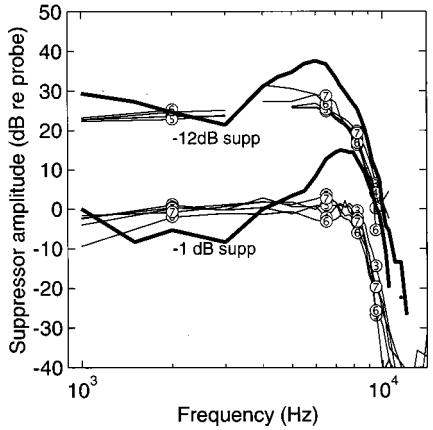

FIG. 5. Suppression amplitude is given in dB relative to probe amplitude for 1- and 12-dB suppression of the probe. Probe level was varied from 30 to 70 dB SPL (thin lines and indicated by symbols). The 30- and 70-dB SPL single-tone isolevel curves are superimposed (thick lines) for comparison. CF=8 kHz, Ct17.

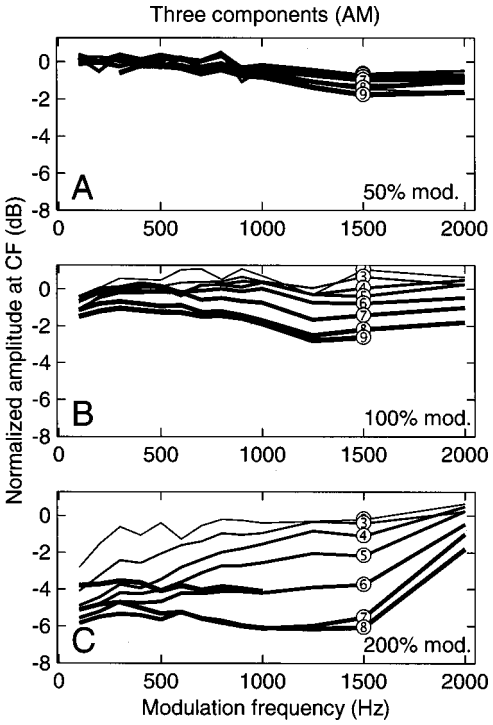

FIG. 6. Suppression of the CF component versus modulation frequency when the stimulus is an amplitude-modulated signal with modulation depths of 50%, 100%, and 200% for panels (A), (B), and (C), respectively. Ct17.

relation is not straightforward across stimulus level. This is clearest when the AM carrier and sidebands are equal in amplitude (200% modulation) where a nonmonotonic relation between suppression and level exists for modulation frequencies <1 kHz [Fig. 6(C)]. While suppression increases with level from 20 to 70 dB SPL, suppression decreases regardless of modulation frequency for stimulus levels above 70 dB SPL (Fig. 7). This inflection in I/O curves at CF may result from a linearization of the I/O functions with level >75 dB SPL.

Suppression of the CF component during presentation of five-component stimuli behaves somewhat similarly to that for AM stimuli. In this instance, there is a strong dependency on which of the five components is positioned at CF (Fig. 8).

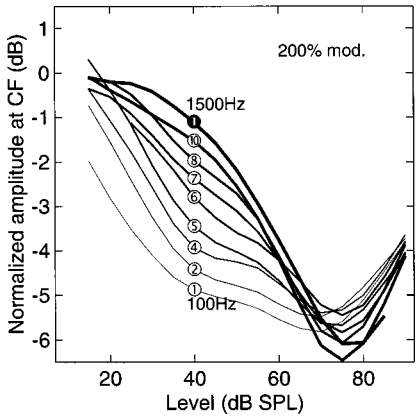

FIG. 7. Probe suppression I/O curves when the modulation depth is 200% as a function of the level of the center (carrier) component. F_{mod} is indicated by the symbols, e.g., ③ = 300 Hz; ❶ = 1500 Hz. Line thickness increases with increasing f_{mod}.

With the first component placed at CF and the remaining four components higher in frequency than CF, suppression is relatively small, <4 dB for small frequency separation of the components at 60-dB SPL stimulus level. Maximum suppression occurs when the third (center) component=CF [Fig. 8(B)]. In this case, suppression can reach 10 dB for modulation frequencies as high as 800 Hz with the maximum occurring at 70 dB SPL. Suppression decreases for frequency separations >800 Hz. Finally, when the fifth component=CF and the remaining four components are lower in frequency than CF, suppression reaches 7.5 dB at a frequency separation of 400 Hz and decreases rapidly for larger frequency separations [Fig. 8(C)]. Suppression is increased somewhat over the case when the first component is set to CF but less than when the third component frequency=CF. Suppression as a function of level when the stimulus is centered on CF is similar to that of the AM stimulus (Fig. 9). Suppression increases with stimulus levels up to 70 dB SPL and decreases for higher levels. Suppression is inversely proportional to frequency separation of the components. These results replicate those from previous studies of suppression in that energy on the low side of CF is more effective in suppressing CF tones than energy of higher frequency.

Mutual suppression effects are present whenever there is more than one stimulus component. Such effects are presented in Fig. 10 for the case when component frequency separation is 500 Hz for two, three, five, and seven-component equal-amplitude stimuli. The amplitude of each component is shown in relation to the single-tone amplitude (dot-dash line). At the 30-dB SPL level (③), stimuli are in the linear response region and track the single-tone curve.

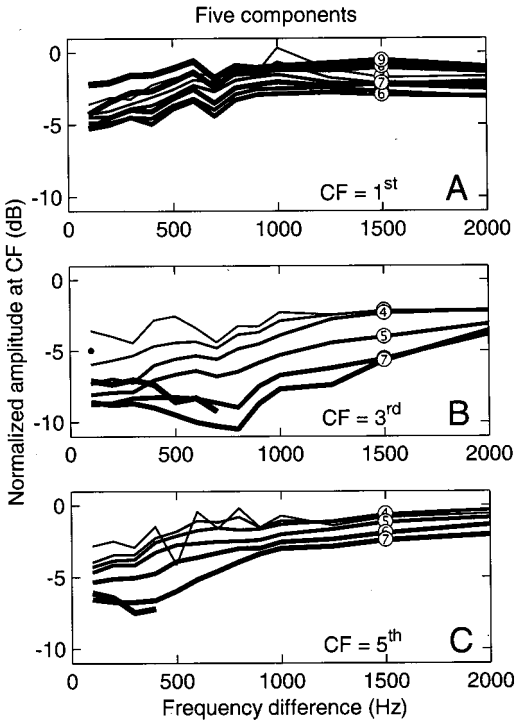

FIG. 8. Suppression of the CF component is shown when the stimulus consisted of five-equal amplitude sinewaves. The first, third, or fifth component is set equal to the CF in (A), (B), and (C), respectively. Ct17.

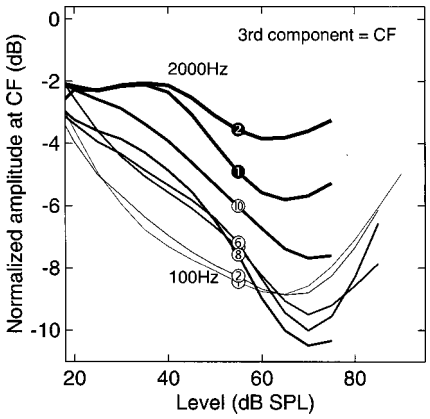

FIG. 9. Probe suppression I/O curves as a function of the level of the third component when the third component of the five-component stimulus is positioned at CF. Frequency spacing of the components indicated by the symbols, e.g., ③=300 Hz. Line thickness increases with increasing spacing frequency.

For two tones at 30 dB SPL there is nearly no suppression of either component regardless of whether the suppressor frequency is above (solid line) or below (dashed line) the probe tone (at CF=8000 Hz). When the level of the tones is increased to 60 dB SPL (⑥), there is a mutual suppression of ~2 dB. The low-frequency component is least reduced, as expected, based on having the more linear I/O function for the individual components. That is, the rate of growth or slope of the I/O function decreases as the frequency increases in the compressive region. When three equal-amplitude stimuli are presented [200% modulation, Fig. 10(B)], a similar result occurs with the amount of mutual suppression increasing relative to the two-tone case. The results for the five- and seven-component cases [Figs. 10(C) and (D)] establish a trend of increasing mutual suppression with an increase in the number of components.

While there will always be some AN fibers for which CFs are located at the center of a complex stimulus, the majority will have CFs displaced relative to the frequency center of the stimulus. This latter condition was explored by positioning the first, third, or fifth component of the five-component signal at CF in order to examine the differential response to these conditions (Fig. 11). Even at 30 dB SPL there is some suppression of individual components when either the third (dashed line) or first (thin solid line) component is at CF where suppression is measured by the deviation from the single-tone response (dot-dash lines). Lower-frequency (<CF) components are least suppressed in each case. When stimulus level is increased to 60 dB SPL, there is as much as 30-dB suppression of the higher-frequency components (first=CF, thin solid line) with the CF component suppressed the least. With the third-component frequency equal to CF (dashed line) there is still 5–6-dB suppression of individual components with the lowest-frequency component nearly equal to the single-tone result. Finally, when the fifth-component frequency equals CF (thick solid line), mutual suppression is the smallest of the three conditions, and the lowest-frequency component is even slightly higher in amplitude than the tone-alone condition.

C. Unequal-amplitude components

Most natural stimuli are not composed of equal-amplitude components. Mutual suppression effects when stimulus components were not equal were studied for AM stimuli with modulation <200%. Such stimuli are analogous to a three-formant stimulus in speech signals. When f_{mod} is

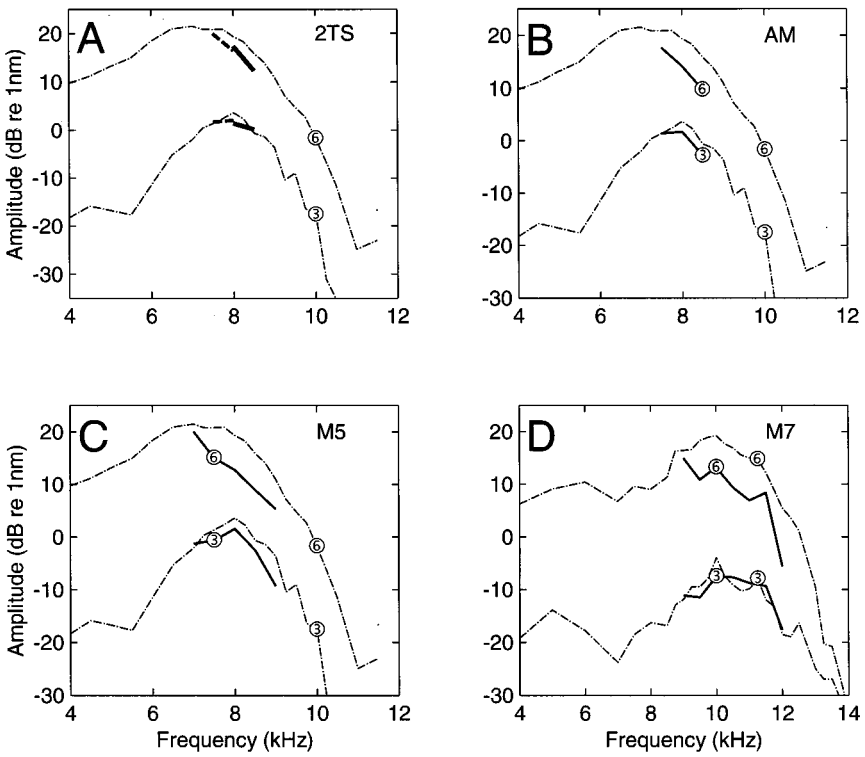

FIG. 10. Component response amplitudes for four multicomponent stimuli at probe levels of 30 and 60 dB SPL when the difference frequency is 500 Hz and CF=8000 Hz. Single-tone isolevel functions (dash-dotted lines) also at 30 and 60 dB SPL are superimposed. Number of stimulus components is varied: two, three, five, and seven in panels (A) through (D), respectively. (A) Response amplitudes for the two components when the second frequency is CF+500 Hz (solid line) and CF−500 Hz (dashed line). (B) Response amplitude for the three components of an AM stimulus for 200% modulation (three equal-amplitude components). (C) Response amplitudes for the five components of the five equal-amplitude stimulus when the third component=CF. (D) Response amplitudes of the seven components when the fourth component frequency=CF. (A), (B), and (C) data from Ct17. (D) data from Ct23.

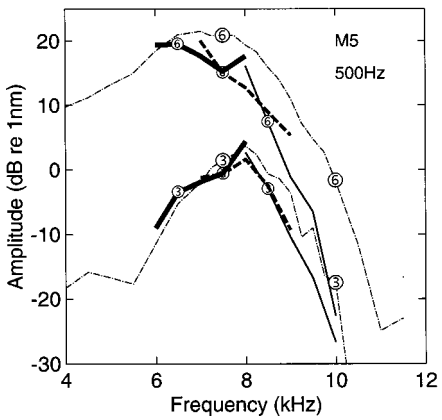

FIG. 11. Response amplitudes when the stimulus consists of five equal-amplitude components at levels of 30 and 60 dB SPL. The component whose frequency is set to CF (8000 Hz) is component one (solid thin line), component three (dashed line), or component five (thick solid line). Component frequency difference is 500 Hz. Single-tone data (dashed-dotted lines) at the indicated levels are also shown. (Ct17).

<200 Hz [e.g., Figs. 12(A), (E), (I)] the response to each sideband is about equal. There is an increase in suppression of both sidebands with increasing AM level up to 70 dB SPL and a decrease with further level increases. Maximum suppression of sidebands by the carrier is ~ 8 dB [Fig. 12(A)]. Suppression is reduced as modulation depth increases [Figs. 12(E), (I)].

As f_{mod} increases beyond 200 Hz there is a divergence of the fate of the upper and lower sideband responses. Less suppression of the lower sidebands occurred while at the same time the upper sideband response was attenuated by cochlear filtering [Fig. 12(B)]. Again, there is less sideband suppression at higher modulation depths [Figs. 12(F), (J)]. At a modulation depth of 200% [Fig. 12(J)] the lower sideband amplitude is greater than the carrier amplitude due to its suppression of the carrier. With higher f_{mod} the amplitude of the lower sideband grows faster than the other AM components, while the upper sideband amplitude is often 20–30 dB less than the lower sideband. These responses essentially consist of two components: the lower sideband and the carrier response.

Mutual suppression of stimulus response components is dependent on the relative amplitudes, frequency content, and position of the acoustic spectra relative to the characteristic frequency of each cochlear location. A near-CF component has the largest effect when it is larger than the surrounding components. When the AM modulation frequency is 100 Hz and carrier frequency set at CF, response amplitudes are all in the linear range of basilar-membrane I/O curves for low stimulus levels. Therefore, no suppression is observed (Fig. 13, 20 dB SPL). When the stimulus level is at 70 dB SPL, the sidebands are reduced relative to their expected amplitudes given the input spectra. The largest reduction occurs for a modulation depth of 25%, where there is a substantial deviation from the expected amplitudes. The magnitude of the deviation is reduced as modulation depth is increased from 50% to 100% [Figs. 13(B) and (C)]. Nevertheless, in each instance the carrier had a suppressive effect on the sideband components. In effect, the response spectra were ''sharpened'' up. For stimulus levels greater than 80 dB SPL the I/O curves begin to approach linearity and the response spectrum is no longer sharpened. When the input spectrum consists of equal-amplitude components ($m=2$), the carrier no longer suppresses the sideband response components; in fact, for small modulation frequencies the carrier is suppressed by the sidebands [Fig. 13(D)]. This spectral edge enhancement effect similar to Mach bands in vision was

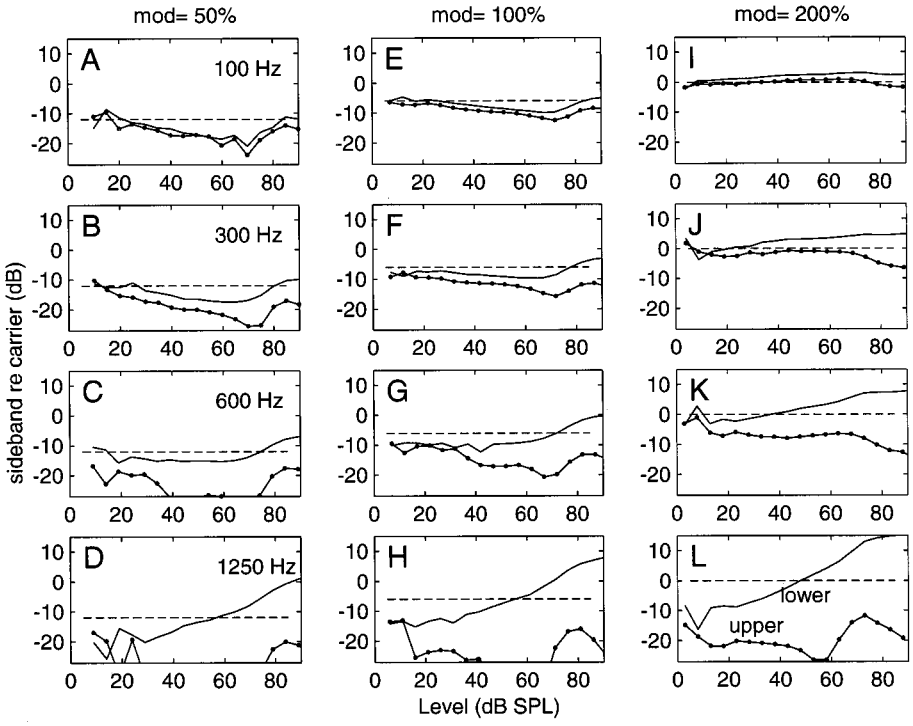

FIG. 12. Sideband suppression by the carrier for an AM basilar-membrane response is shown when the modulation depth was 50%, 100%, and 200% in columns 1, 2 and 3, respectively. f_{mod} is indicated in the left-hand panel for each row. The dashed lines mark the amplitudes of the sidebands relative to the carrier in the stimulus. The amplitude difference in basilar-membrane response between the lower/upper sideband amplitudes and the carrier amplitude is indicated by the solid/dotted lines.

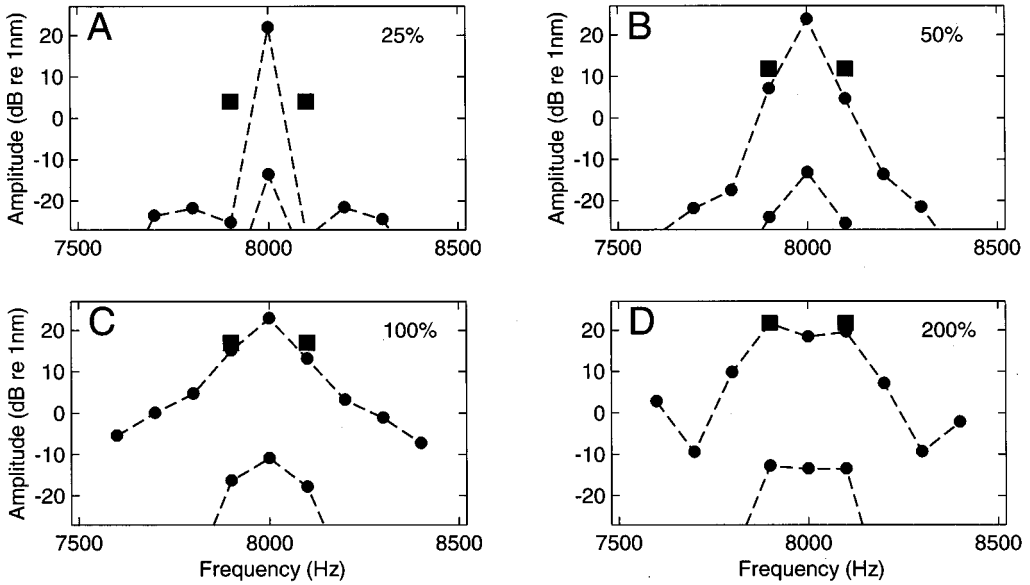

FIG. 13. The response spectrum for AM signals with $f_{mod}=100$ Hz, and modulation depths of 0.25, 0.5, 1.0, and in panels (A) through (D), respectively. The carrier is set to CF=8000 Hz. In each panel the response spectra are shown for nine harmonics of 100 Hz at two levels: 20 dB SPL in the linear portion of the I/O curve and 70 dB SPL in the compressive or nonlinear region of the response. ● symbols indicate the data points and ■ indicate the expected sideband amplitudes based on the input spectrum. The additional three values on each side of the AM response spectrum are a result of nonlinear distortion. The cochlear filter is essentially flat over this 200-Hz range of input frequencies and its equivalent linear system should not alter the input spectrum. Ct07.

shown previously for stimuli with 5 and 7 components (Rhode and Recio, 2001).

D. Phase functions

AN discharge phase has been shown to exhibit a lag/lead relative phase relation for stimulus frequencies below/above CF with increasing stimulus level (Anderson *et al.*, 1971). Basilar-membrane phase relations are largely compatible with the neural observations. In the chinchilla midfrequency range, phase relations appear to be somewhat more complex. At low stimulus levels the results are compatible; phase lags with increasing level for stimulus frequencies below CF, and phase leads above CF [Fig. 14(A)]. However, for stimulus frequencies above CF, increasing the level above 70 dB SPL results in increasing phase lags, as there are phase lags at all stimulus frequencies at the highest stimulus levels. Phase data can also be seen for all stimulus frequencies in Fig. 14(B). For stimulus levels below 70 dB SPL there is little phase change at CF (8000 Hz), but increasing phase lags occurred at higher levels. As much as a 130° phase lag occurred below CF and ~90° phase lead above CF.

In the presence of a second tone, phase behavior is somewhat similar but is a function of the relative levels and frequencies. A common stimulus paradigm in a 2TS experiment is to place the probe tone at CF and to vary the suppressor level and frequency while holding the probe frequency and level constant. The probe phase for a low-level probe exhibits a small lead with level for most suppressor frequencies [Fig. 15(A)]. At higher probe levels, there are mostly phase lags with increasing suppressor level regardless of suppressor frequency [Figs. 15(B), (C)]. The phase of the suppressor behaves similarly to the single-tone phase as a function of level and frequency [Figs. 15(D), (E), (F)]. One difference is that as the probe level increases (>45 dB SPL) only phase lags are seen, regardless of level or frequency. In general, there is not much difference between probe and suppressor phases.

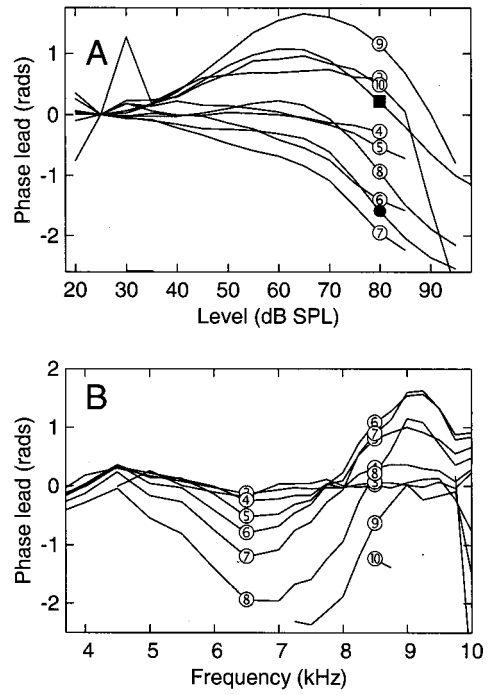

FIG. 14. Phase portion of the basilar-membrane mechanical transfer function where CF=8000 Hz. (A) Phase I/O functions for selected frequencies: frequency=1000 times the symbol number; ●=7500 Hz and ■=8500 Hz. The phase at 25 dB SPL was used to normalize each I/O curve. (B) Phase versus frequency functions at the levels indicated by the symbols: level=10 times symbol number. Phase at 20 dB SPL was subtracted from each curve to normalize them. Ct17.

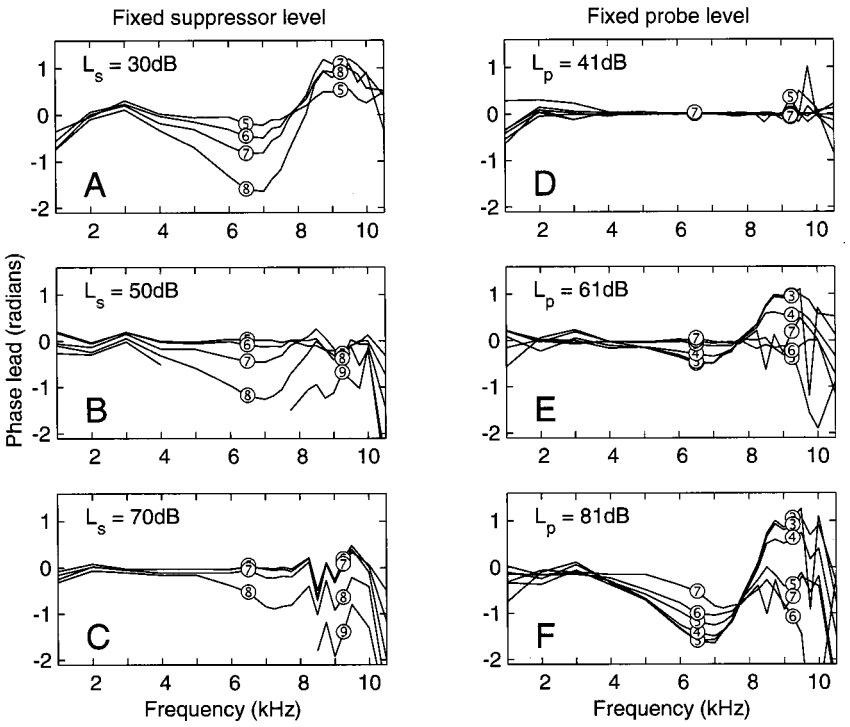

FIG. 15. Phase I/O functions for both the probe and the suppressor tone as the level of the probe or suppressor is varied for a select set of suppressor frequencies. Symbol assignment for suppressor frequency as in Fig. 11. (A), (B), and (C). Probe phase as a function of frequency is shown when the probe level (L_p) is at 30, 50, and 70 dB SPL, respectively. (D), (E), and (F). Suppressor phase I/O function when the probe levels are 30, 50, and 70 dB SPL, respectively.

Phase-versus-frequency transfer functions illustrate the phase lag/lead relation when the suppressor is the 8-kHz tone at several levels [Figs. 16(A), (B), (C)]. Increasing suppressor level reduces the phase variation with probe level [Fig. 16(C)]. There is little variation for probe levels <70 dB SPL [Figs. 16(B) and (C)]. In the right column, the probe level is held constant at the level indicated in each panel and the suppressor level is varied. There is little phase change for low levels of the probe [Fig. 16(D)] while for high levels the lag/lead relation is present. In the latter case [Fig. 16(F)], increasing the suppressor level reduces the phase variation (cf. the ④ and ⑦ curves).

IV. DISCUSSION

A. Principal achievements of this study

(1) New two-tone suppression data are provided with greater detail than previously available.
(2) These data support the view that neural 2TS phenomena largely reflect cochlear mechanics as observed in the vibration of the basilar membrane.
(3) Information is provided about mutual suppression: suppression of a CF tone by a roaming suppressor and suppression of a roaming probe by a fixed tone at CF.
(4) Spectral edge enhancement of multicomponent responses was observed in the vibration of the basilar membrane (cf. Horst *et al.*, 1986). That is, suppression of the middle component(s) of a multicomponent stimulus by surrounding components for three, five, and seven equal-amplitude component stimuli is described.
(5) Suppression of individual components is described for an amplitude-modulated signal when the sideband components are 0, -6, -12, and -18 dB smaller than the carrier.
(6) Phase relations are described that are not entirely congruent with earlier observations.

This study was undertaken to determine the representation of a subset of multicomponent stimuli in the motion of the basilar membrane (cf. Rhode and Recio, 2001). How several stimulus components interact and mutually suppress each other has implications for understanding the processing of complex stimuli, such as speech and music, within the cochlea. Any cochlear nonlinearity, such as the I/O function for hair cells or the half-wave rectifier at the hair cell synapse, will result in suppression. However, the principal basis for suppression is the frequency-dependent compressive nonlinearity in the cochlea that results in differential growth rates of vibration in response to tones. The compressive region resulting from a tone at CF extends over an octave (Rhode and Recio, 2000; Russell and Nilsen, 1997). Response to tones above CF is increasingly compressed as frequency is increased until the stimulus exits the compressive region and enters what has been labeled the plateau region of the transfer function for the basilar membrane (Rhode, 1971; Cooper and Rhode, 1996a). This above-CF linear region has been associated with a second mode of vibration that corresponds to the fast wave (e.g., Olson, 1998; Rhode and Recio, 2001; Cooper and Rhode, 1996a).

B. Two-tone suppression: Slopes and magnitude

Ruggero *et al.* (1992) state that neural two-tone rate suppression appears to originate in mechanical phenomena at the level of the basilar membrane. However, there remains some difficulty in explaining two-tone rate suppression when the suppressor is lower in frequency than the CF of the AN fiber because the sum of the individual amplitudes of basilar-membrane vibration in response to the two tones is always at

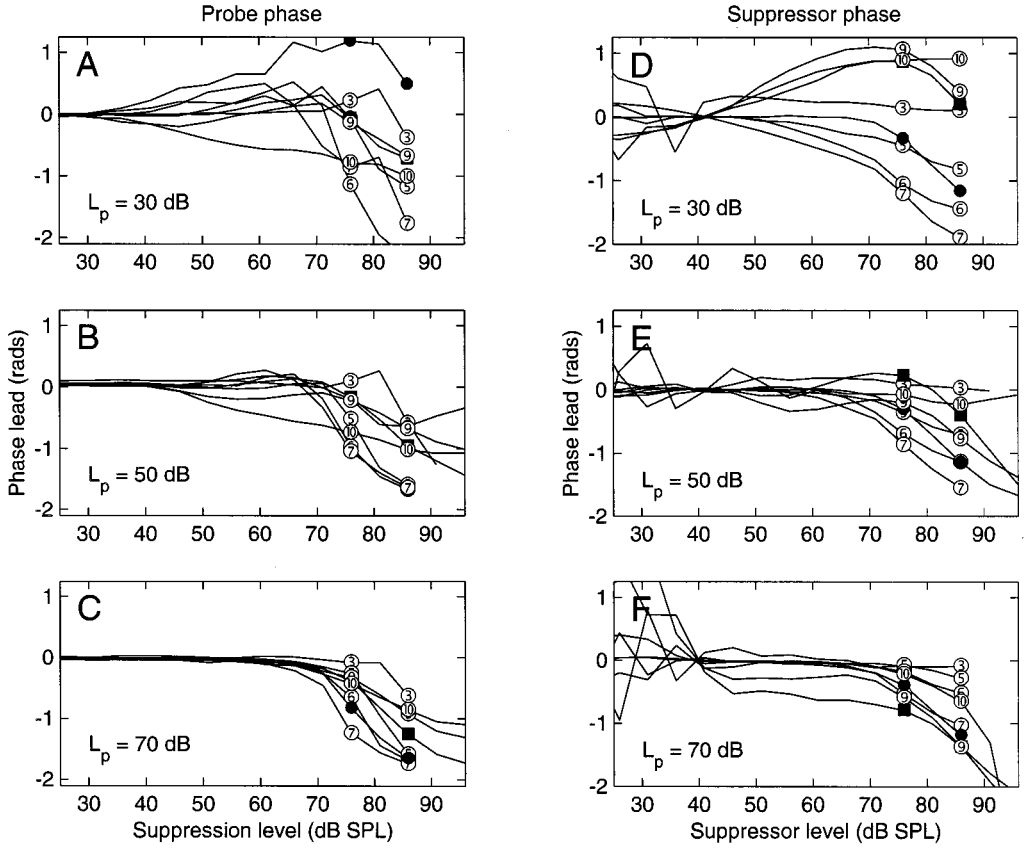

FIG. 16. Probe phase versus frequency transfer functions for a suppressor tone at 8000 Hz and the levels indicated in each panel. L_p = probe level and L_s = suppressor level in dB SPL. (A) 30-dB SPL suppressor at 8000 Hz. Probe level = 10 times the symbol number. (B) 50-dB SPL suppressor. (C) 70-dB SPL suppressor. Right column. (D), (E), and (F). Probe phase at probe levels of 41, 61, and 81 dB SPL, respectively. 8-kHz suppressor at 10 times the number of the symbol in dB SPL and ●=7500 Hz, ■=8500 Hz. Ct17.

least as large as that of the CF tone alone (Cooper, 1996; Geisler and Nuttall, 1997; also data reported here such as for frequencies below CF in Fig. 5). The complete mechanism of two-tone rate suppression in the AN under these conditions remains unexplained and likely requires an additional mechanism that provides another stage of filtering at the level of the hair cell or auditory nerve (Cai and Geisler, 1996; Temchin *et al.*, 1997). A proposal has also been made for direct influence of cochlear potentials on excitation of afferent dendrites as a cause for suppression (Hill *et al.*, 1989).

For high side suppressors (i.e., suppression of a probe stimulus by a tone whose frequency is higher than CF), displacement of the basilar membrane in the presence of a suppressor tone can be less than that to the probe tone alone (Ruggero *et al.*, 1992; Cooper and Rhode, 1996b). Also, it was shown here that suppression can occur when suppressor amplitude is only 1% of that of the probe tone (Fig. 5). This result suggests that at least high-side suppression is a spatially distributed phenomenon, because the suppressor can have an effect even when the suppressor tone excitation does not or barely overlaps with the region for the probe tone. This result agrees with others who have noted that for suppressors above CF, a region of the cochlea is likely involved (Yates *et al.*, 1989; Geisler *et al.*, 1990; Geisler, 1992). This result also implies that cochlear models have to incorporate more than independent point representations of the cochlear partition. The spatial extent and variation of the nonlinearity as a function of suppressor frequency has not typically been adequately addressed in these models (cf. Baker, 2000).

Present results are largely compatible with previous results (Cooper, 1996; Nuttall and Dolan, 1993; Geisler and Nuttall, 1997; Ruggero *et al.*, 1992). Suppression magnitudes of up to 35 dB were found over the range of suppressor/probe levels that were employed. There were several limitations imposed by the stimulating and measurement apparatus: (1) maximum stimulus levels were limited to <100 dB SPL either by the desire to avoid either temporary or permanent threshold shifts; (2) limitations in maximum stimulus levels that could be produced; and (3) the limited range of the interferometer. Finally, the use of relatively short (20-ms overlap of the 30-ms probe and suppressor tones) tones limited the accuracy of analysis because the width of the Fourier filter results in leakage between components. Leakage of a large component into another analysis component was seen whenever: (1) the amplitude of the suppressor was 25 to 30 dB greater than that of the probe; (2) the suppressor frequency was near to that of the probe; and (3) at low levels of the probe. It is likely that larger suppression magnitudes than those measured (~ 35 dB) occur in the cochlea, as there is no reason to believe that the monotonic decreasing probe I/O functions do not continue as the sup-

pressor level increases. For example, the probe amplitude I/O functions in Fig. 3(B) exhibit a 40-dB rightward shift for a 40-dB suppressor level shift. Such shifts are in line with those recorded in AN fibers (Javel *et al.*, 1983; Delgutte, 1990).

A number of auditory-nerve studies have shown suppression slope to vary with suppressor frequency relative to probe located at CF (Javel *et al.*, 1983; Ruggero *et al.*, 1992; Delgutte, 1990). Above CF, the neural suppression slope varies from -0.2 dB/dB and increases as the suppressor frequency decreases so that when it is an octave lower than CF the average slope ranges between -1 and -2 dB/dB. In an extensive study of the suppression growth, Delgutte showed that it varied from 0.5 to over -3 dB/dB. The larger values occur for suppressors one to several octaves below CF. We found up to -1.8 dB/dB for a suppressor frequency $<$CF/2 [Fig. 3(A)]. Mechanical suppression slopes appear to be closely correlated with growth rate of basilar-membrane motion. Mechanical suppression growth rates appear to be sufficient to explain those observed in AN for two-tone suppression. Because a second stimulus component in the mechanical linear region produces a suppression rate of -1 dB/dB, the shift in the CF neural curve should be proportional to the reciprocal of the growth rate at the probe frequency. For example, if the growth rate at CF was 0.33 dB/dB, then the neural curve should shift 3 dB/dB. This value is at the upper end of the neural shifts found by anyone. It is likely that there are several factors that enter into producing the scatter in the neural data, but the most prominent is the way the mechanical growth rate varies with CF. For CFs <1 kHz the mechanics exhibits much less compression than in the frequency region >5 kHz. Also, varying neural thresholds and gain functions of the hair cells lead to further spread in the neural growth rates.

C. Suppression thresholds

There is some controversy about the level at which a low-side suppressor takes effect. Cooper (1996) noted that relatively constant suppressor amplitudes are necessary to establish the suppression threshold in guinea pig. This conclusion draws support from the studies of Schmiedt (1982) in gerbil AN, where the lower threshold boundary of a 2TS area below CF is nearly absolute in level over a large range of fiber CFs. Temchin *et al.* (1997) found AN modulation and rate thresholds to be very similar at $\sim$70 dB SPL in chinchilla. In the present study, for a 30-dB SPL probe level, the -1-dB iso-suppression curve is nearly identical to the 1-nm isolevel curve for frequencies $<$CF and a suppressor level of 56 dB SPL. This compares to the 1.5–3 nm found for a 1-dB iso-suppression in the guinea pig at suppressor levels of 80–90 dB SPL (Cooper, 1996). It was also found that the suppressor level necessary to produce a 1-dB reduction in the probe amplitude increases as the probe level increases at a less than proportional rate ($\sim$12-dB increase for a 40-dB increase in probe level). This latter response is expected because the growth rate of the CF response is $\sim$0.3 dB/dB of input; therefore, a 40-dB change in the input results in a 12-dB change in the output. At low-stimulus levels, the suppression amplitude to produce a 1-dB suppression is approximately the same as the probe amplitude (1 nm). It is worth noting that suppression thresholds vary 10–20 dB even within an animal (Schmiedt, 1982).

Neural rate thresholds do not appear to be explicitly related to a fixed displacement of BM because they can vary as much as 80 dB at a given CF in individual cats (Liberman, 1978; Cooper, 1996). However, in young cats Liberman found that the spread of thresholds at a given CF was fairly narrow, 10–20 dB. The spread in thresholds could be largely due to hair-cell and AN synapse morphological differences that are correlated with spontaneous rate in ANFs (Liberman, 1978). This suggests that the underlying reason for the increase in spread with age is alterations in postprocessing of basilar-membrane motion such as changes in the physiological condition of hair cells. Such a hypothesis is difficult to prove given the difference between the experimental conditions for mechanics, hair-cell recording, and auditory-nerve recording. It is entirely possible that there would be closer agreement if all procedures were conducted under a single regimen.

D. Mutual suppression

Mutual suppression was shown to occur with two-tone stimulation [Figs. 1(D) and (F)]. With a tone at CF, suppression occurs with a second tone varying in frequency from an arbitrary low value to as much as an octave above CF. Suppression slope decreases rapidly for frequencies above CF and the maximum suppression) also decreases. When the tone at CF is considered the suppressor, suppression is limited to a smaller frequency region, e.g., 6–11 kHz or roughly ± 0.5 octave. Mutual suppression observed in inner hair-cell recordings has been suggested as a mechanism that results in sharpening the cochlear filter (Cheatham and Dallos, 1990).

E. Phase effects

Suppression by a high- or low-side suppressor results in a phase change in the BM response to a CF probe. There is some controversy in the literature as to behavior of phase of the probe tone as a function of suppressor tone level (Cooper, 1996). There are studies showing phase leads with increasing suppressor level (Rhode and Cooper, 1993; Cooper, 1996); however, others show phase lags (Ruggero *et al.*, 1992). Figure 14 showed that the relative phase change seen in the probe phase is nearly always an increasing phase lag of up to 90° as the suppressor level increases regardless of suppressor frequency. However, for relatively low probe levels and suppressor frequencies just below the probe frequency ($=$CF), there is initially a phase lead, never $>$90°, that turns into a phase lag as high suppressor levels are attained. Concomitant with the changes in probe phase are changes in the phase of the suppressor that are also a function of probe level and suppressor frequency (Fig. 15, column 2). The increase in phase for probe level at 30 db SPL occurs for suppressor frequencies above CF, while all tones with frequencies below CF show phase lags with increasing suppressor level. For probe levels >40 dB SPL, there is only an increasing phase lag with increasing suppressor level regardless of frequency (Fig. 14).

Cooper (1996) reported phase leads with increasing suppressor level in the vicinity of CF (~26-kHz cochlear region in the guinea pig) of similar magnitude to those presented here, although at higher suppressor levels (>80 dB SPL). He also found that 2TS phase changes were similar to those that occurred when single-tone levels were increased by an amount that caused an appropriate decrease in BM response sensitivity. This difference could be due to species difference and/or cochlear location.

AN studies of 2TS have demonstrated that rate/level functions shift to the right with increasing suppressor level (e.g., Javel *et al.*, 1983). Based on cochlear mechanical studies, the underlying explanation is likely that the cochlear partition exhibits the same behavior (Figs. 3 and 4 in Nuttall and Dolan, 1993). These observations address the hypothesis that suppression is equivalent to a simple attenuation of the motion of the basilar membrane; however, one has to consider phase behavior of the two tones. For high-side suppressors Nuttall and Dolan found that the hypothesis is valid, but they noted that this conclusion differs from that obtained in hair-cell recording in the apex of the guinea pig, where Cheatham and Dallos (1989, 1990) found a phase lead during suppression, opposite to observations in the base. It was suggested that there could be different suppression mechanisms in apex and base. The mechanics in these two regions have considerable similarity (Cooper and Rhode, 1992; Rhode and Cooper, 1996) as there is a compressive nonlinearity in each region and isolevel vibration curves are very similar to auditory-nerve frequency threshold curves. In the apex, however, there is a smaller amount of cochlear amplification that exists over the entire frequency response of the apical region.

F. Multiple tones and suppression

Suppression has been demonstrated psychophysically using the pulsation threshold method with vowel-like sounds (Houtgast, 1974), for multiple-component stimuli (4–64) in an octave centered at the characteristic frequency of an auditory-nerve fiber (Horst *et al.*, 1990), and for multicomponent stimuli such as speech in the auditory nerve (Sachs and Young, 1980). It has been suggested that suppression could be a way for the formants in speech signals to be enhanced relative to the neighboring components. Here, suppression in BM responses to AM stimuli is shown to be dependent on modulation frequency, modulation depth, and stimulus level. The amount of suppression of CF responses increased with level and modulation depth. At any of the modulation depths studied, the largest amount of suppression occurred for stimuli with modulation frequencies around 1500 Hz, and was smallest at either the lowest (100 Hz) or largest (2000 Hz) modulation frequencies. However, the magnitude of carrier suppression does not vary greatly as a function of modulation frequency.

There are prominent mutual suppression effects that occur for small modulation frequencies (see Fig. 13). The greatest suppression of the sideband response occurred when $f_{\mathrm{mod}}=100$ Hz and for small modulation depths ($m<0.5$). This had the effect of sharpening the response spectrum when the response components were in the nonlinear portion of the basilar-membrane I/O curve. It was also shown when AM components were all equal ($m=2$) that sideband response amplitudes were greater than the carrier. This spectral edge enhancement also occurs when the number of components is either five or seven and the component frequency separation is small (<300 Hz; see Rhode and Recio, 2001). The effect is analogous to the Mach band in vision (Carterette *et al.*, 1969).

The fact that the response amplitudes are a complex function of frequency separation, modulation depth, and stimulus level was demonstrated in Fig. 12. With f_{mod} and/or level increases the lower sideband suppresses the carrier and in effect results in an overmodulated response (Rhode and Recio, 2001). This is due to the fact that the lower sideband is located in the linear portion of the cochlear response where the growth rate is 1 dB/dB and the carrier is at CF and is in the compressive region where growth rate is ~0.3 dB/dB. Therefore, the lower sideband grows faster than the carrier and must drive the outer hair cell into its saturated region (Geisler, 1992). The result is that the CF response component is reduced. The upper sideband of the AM stimulus is largely eliminated by the cochlear filter and hence does not play a significant role.

As the number of components increases [Fig. 8(B)], the amount of suppression measured in responses to five-component stimuli with a frequency separation of 1500 Hz is approximately the same as the one measured using 200% AM stimuli [Fig. 6(C)]. However, five-component stimuli produced greater suppression at lower frequency separations (700 Hz) than measured in AM responses with similar component frequency separation. Greatest suppression occurs when more stimulus components are located relatively close to CF (but not too close).

Multitone suppression can result in larger suppression effects than those produced by two tones when components are symmetrically placed around CF. Results suggest that mutual suppression between signal components is not as large as might be expected based on summing two-tone suppression amplitudes. In fact, the net result of multiple tones on suppression of the probe tone can be less than for two tones in some circumstances. Suppression is dependent on the number, level, and frequency composition of the stimulus. Low-frequency (<CF) suppressors at high levels produce the greatest suppression. At low stimulus levels, the CF component has the strongest suppressive effect possibly because all the other components are in the linear region of basilar-membrane vibration.

V. SUMMARY

There is overall agreement that suppression largely originates in cochlear mechanics. The present results reinforce this conclusion and further show the basilar-membrane role in the processing of multitone stimuli. The effect is pervasive and a complex function of stimulus features: component amplitudes, number of components, frequency separation, and distribution of the components relative to characteristic frequency. This effect has implications for how complex signals such as speech are processed even before they enter the central auditory system.

ACKNOWLEDGMENTS

This work was supported by the National Institute of Deafness and Communications Disorders, Grant No. R01 DC 01910. Special thanks are given to C. Dan Geisler, Mario Ruggero, and Keith Kluender for reviewing an earlier version of this manuscript. We also thank Wiebe Horst and an anonymous reviewer for their comments.

Anderson, D.J., Rose, J.E., Hind, J.E., and Brugge, J.F. (**1971**). ''Temporal position of discharges in single auditory nerve fibers within the cycle of a sin-wave stimulus: Frequency and intensity effects,'' J. Acoust. Soc. Am. **49**, 1131–1139.

Baker, G. (**2000**). ''Pressure-feedforward and piezoelectric amplification models for the cochlea,'' Ph.D. thesis, Stanford University.

Cai, Y., and Geisler, C.D. (**1996**). ''Suppression in auditory-nerve fibers of cats using low-side suppressors. I. Temporal aspects,'' Hear. Res. **96**, 94–112.

Carterette, E., Friedman, M.P., and Lovell, J.D. (**1969**). ''Mach bands in hearing,'' J. Acoust. Soc. Am. **45**, 986–998.

Cheatham, M.A., and Dallos, P. (**1989**). ''Two-tone interactions in inner hair cell receptor potentials: ac versus dc effects,'' Hear. Res. **43**, 135–140.

Cheatham, M.A., and Dallos, P. (**1990**). ''Two-tone suppression in inner hair cell responses,'' Hear. Res. **40**, 187–196.

Cooper, N.P., and Rhode, W.S. (**1992**). ''Basilar membrane mechanics in the hook region of cat and guinea-pig cochlea,'' Hear. Res. **63**, 163–190.

Cooper, N.P. (**1996**). ''Two-tone suppression in cochlear mechanics,'' J. Acoust. Soc. Am. **99**, 3087–3098.

Cooper, N.P., and Rhode, W.S. (**1996a**). ''Fast travelling waves, slow travelling waves and their interactions in experimental studies of apical cochlear mechanics,'' Aud. Neurosci. **2**, 289–299.

Cooper, N.P., and Rhode, W.S. (**1996b**). ''Two-tone suppression in apical cochlear mechanics,'' Aud. Neurosci. **3**, 123–134.

Delgutte, B. (**1990**). ''Physiological mechanisms of psychophysical masking: Observations from auditory-nerve fibers,'' J. Acoust. Soc. Am. **87**, 791–809.

Geisler, C.D. (**1992**). ''Two-tone suppression by a saturating feedback model of the cochlear partition,'' Hear. Res. **63**, 203–211.

Geisler, C.D., and Nuttall, A.L. (**1997**). ''Two-tone suppression of basilar membrane vibrations in the base of the guinea pig cochlea using 'low-side' suppressors,'' J. Acoust. Soc. Am. **102**, 430–440.

Geisler, C.D., Yates, G.K., Patuzzi, R.B., and Johnstone, B.M. (**1990**). ''Saturation of outer hair cell receptor currents causes two-tone suppression,'' Hear. Res. **44**, 241–256.

Hill, K.G., Strange, G., Gummer, A.W., and Mo, J. (**1989**). ''A model proposing synaptic and extra-synaptic influences on the responses of cochlear nerve fibers,'' Hear. Res. **39**, 75–90.

Horst, J.W., Javel, E., and Farley, G.R. (**1986**). ''Coding of spectral fine structure in the auditory nerve. I. Fourier analysis of period and interspike interval histograms,'' J. Acoust. Soc. Am. **79**, 398–416.

Horst, J.W., Javel, E., and Farley, G.R. (**1990**). ''Coding of spectral fine structure in the auditory nerve. II. Level-dependent nonlinear responses,'' J. Acoust. Soc. Am. **88**, 2656–2681.

Houtgast, T. (**1974**). *Lateral Suppression in Hearing* (Academische Pers B. V., Amsterdam).

Javel, E. (**1980**). ''Coding of AM tones in chinchilla auditory nerve: Implications for the pitch of complex tones,'' J. Acoust. Soc. Am. **68**, 133–146.

Javel, E. (**1981**). ''Suppression of auditory nerve responses I. Temporal analysis, intensity effects and suppression contours,'' J. Acoust. Soc. Am. **69**, 1735–1745.

Javel, E., Geisler, C.D., and Ravindran, A. (**1978**). '' Two-tone suppression in auditory nerve of the cat: Rate-intensity and temporal analyses,'' J. Acoust. Soc. Am. **63**, 1093–1104.

Javel, E., McGee, J., Walsh, E.J., Farley, G.R., and Gorga, M.P. (**1983**). ''Suppression of auditory nerve responses. II. Suppression threshold and growth, iso-suppression contours,'' J. Acoust. Soc. Am. **74**, 801–813.

Joris, P.X., and Yin, T.C.T. (**1992**). ''Responses to amplitude-modulated tones in the auditory nerve,'' J. Acoust. Soc. Am. **91**, 215–232.

Liberman, M.C. (**1978**). ''Auditory-nerve response from cats raised in a low-noise chamber,'' J. Acoust. Soc. Am. **63**, 442–455.

Nuttall, A.L., and Dolan, D.F. (**1993**). ''Two-tone suppression of inner hair cell and basilar membrane responses in the guinea pig,'' J. Acoust. Soc. Am. **93**, 390–400.

Olson, E.S. (**1998**). ''Observing middle and inner ear mechanics with novel intracochlear pressure sensors,'' J. Acoust. Soc. Am. **103**, 3445–3463.

Rabiner, L.R., and Gold, B. (**1975**). *Theory and Applications of Digital Signal Processing* (Prentice Hall, Englewood Cliffs, NJ).

Recio, A., and Rhode, W.S. (**2000**). ''Basilar membrane responses to broadband stimuli,'' J. Acoust. Soc. Am. **108**, 2281–2298.

Rhode, W.S. (**1971**). ''Observations of the vibration of the basilar membrane in squirrel monkey using the Mössbauer technique,'' J. Acoust. Soc. Am. **49**, 1218–1231.

Rhode, W.S. (**1977**). ''Some observations of two-tone interactions measured using the Mössbauer effect,'' in. *Psychophysics and Physiology of Hearing*, edited by E.F. Evans and J.P. Wilson (Academic, London), pp. 27–41.

Rhode, W.S., and Cooper, N.P. (**1993**). ''Two-tone suppression and distortion production on the basilar membrane in the hook region of cat and guinea pig cochleae,'' Hear. Res. **66**, 31–45.

Rhode, W.S., and Cooper, N.P. (**1996**). ''Nonlinear mechanics in the apical turn of the chinchilla cochlea *in vivo*,'' Aud. Neurosci. **3**, 101–121.

Rhode, W.S., and Recio, A. (**2000**). ''Study of mechanical motions in the basal region of the chinchilla cochlea,'' J. Acoust. Soc. Am. **107**, 3317–3332.

Rhode, W.S., and Recio, A. (**2001**). ''Basilar membrane response to multicomponent stimuli in chinchilla.'' J. Acoust. Soc. Am. **110**, 981–994.

Robles, L., Ruggero, M.A., and Rich, N.C. (**1986**). ''Basilar membrane mechanics at the base of the chinchilla cochlea. I. Input–output functions, tuning curves, and response phases,'' J. Acoust. Soc. Am. **80**, 1364–1367.

Ruggero, M.A., Robles, L., and Rich, N.C. (**1992**). ''Two-tone suppression in the basilar membrane of the cochlea: Mechanical basis of auditory-nerve rate suppression,'' J. Neurophysiol. **68**, 1087–1099.

Russell, I.J., and Nilsen, K.E. (**1997**). ''The location of the cochlear amplifier: Spatial representation of a single tone on the guinea pig basilar membrane,'' Proc. Natl. Acad. Sci. U.S.A. **94**, 2660–2664.

Sachs, M.B. (**1969**). ''Stimulus-response relation for auditory-noise fibers: Two-tone stimuli,'' J. Acoust. Soc. Am. **45**, 1025–1036.

Sachs, M.B., and Young, E.D. (**1980**). ''Effects of nonlinearities on speech encoding in the auditory nerve,'' J. Acoust. Soc. Am. **68**, 858–875.

Schmiedt, R.A. (**1982**). ''Boundaries of two-tone rate suppression of cochlear-nerve activity,'' Hear. Res. **7**, 335–351.

Sellick, P.M., and Russell, I. (**1979**). ''Two-tone suppression in cochlear hair cells,'' Hear. Res. **1**, 227–236.

Sellick, P.M., Patuzzi, R., and Johnstone, B.M. (**1982**). ''Measurement of basilar membrane motion in the guinea pig using the Mössbauer technique,'' J. Acoust. Soc. Am. **72**, 131–141.

Temchin, A.N., Rich, N.C., and Ruggero, M.A. (**1997**). ''Low-frequency suppression of auditory-nerve responses to characteristic-frequency tones,'' Hear. Res. **113**, 29–56.

Yates, G.K., Geisler, C.D., Patuzzi, R.B., and Johnstone, B.M. (**1989**). ''Saturation of receptor currents accounts for two-tone suppression,'' in *Cochlear Mechanisms*, edited by J.P. Wilson and D.T. Kemp (Plenum, New York), pp. 177–188.

DPOAE suppression tuning: Cochlear immaturity in premature neonates or auditory aging in normal-hearing adults?

Carolina Abdala[a)]
House Ear Institute, Children's Auditory Research and Evaluation Center, 2100 West Third Street, Los Angeles, California 90057

(Received 6 June 2001; revised 10 September 2001; accepted 17 September 2001)

Previous work has shown that distortion product otoacoustic emission (DPOAE) suppression tuning curves (STCs) recorded from premature neonates are narrower than adult STCs at both low and high frequencies. This has been interpreted to indicate an immaturity in cochlear function prior to term birth. However, an alternative explanation for this finding is that adult DPOAE STCs are broadened and reflect cochlear hair cell loss in normal-hearing adults due to aging, and natural exposure to noise and ototoxins. This alternative hypothesis can be tested by studying suppression tuning in normal-hearing school-aged children. If normal-hearing children, who have not aged significantly or been exposed to noise/ototoxins, have DPOAE suppression tuning similar to adults, the auditory aging hypothesis can be ruled out. However, if children have tuning similar to premature neonates and dissimilar from adults, it implicates aging or other factors intrinsic to the adult cochlea. DPOAE STCs were recorded at 1500, 3000, and 6000 Hz using optimal parameters in normal-hearing children and adults. DPOAE STCs collected previously from premature neonates were used for age comparisons. In general, results indicate that tuning curves from children are comparable to adult STCs and significantly different from neonatal STCS at 1500 and 6000 Hz. Only the growth of suppression was not adultlike in children and only at 6000 Hz. These findings do not strongly support the auditory aging hypothesis as a primary explanation for previously observed neonatal–adult differences in DPOAE suppression tuning. It suggests that these age differences are most likely due to immaturities in the neonatal cochlea. However, nonadultlike suppression growth observed in children at 6000 Hz warrants further attention and may be indicative of subtle alternations in the adult cochlea at high frequencies.
[DOI: 10.1121/1.1417523]

PACS numbers: 43.64.Kc [BLM]

I. INTRODUCTION

Previous work has shown that premature neonates have narrower DPOAE suppression tuning than adults at low (1500 Hz) and high (6000 Hz) $f2$ frequencies (Abdala *et al.*, 1996; Abdala, 1998, 2001). The most common interpretation of this finding is that the cochlea of premature neonates has a subtle immaturity in function and, therefore, is producing nonadultlike frequency tuning as measured by DPOAE suppression. However, the results can also be interpreted to indicate that normal-hearing adults have lost some of their cochlear frequency resolution due to natural hair cell loss associated with aging and exposure to ototoxins and noise.

The auditory *aging* hypothesis (*aging* defined here as hair cell loss from cumulative effect of lifelong noise exposure, exposure to ototoxins, and aging processes) interprets the DPOAE suppression data to suggest that the adult cochlea is responsible for producing broadened suppression tuning curves (STC). The *immaturity* hypothesis interprets the data to suggest that premature neonates have a subtle cochlear immaturity producing excessively sharp tuning curves and this factor accounts for the neonatal–adult age differences in DPOAE suppression tuning. It is not possible to determine which interpretation is more accurate based only on the studies that have been conducted thus far, nor on existing evidence in the literature.

It is a tenable hypothesis that the cochlea of these very premature neonates is coding frequency in an immature fashion. The last documented events to occur in the sequence of cochlear maturation take place during the last trimester of fetal life and involve innervation of the outer hair cells (Lavigne-Rebillard and Pvjol, 1987, 1988). The observed adult–neonatal age difference in DPOAE suppression tuning may reflect immaturity in outer hair cell function or efferent regulation of outer hair cell function. Anatomical and physiological studies of the human cochlea generally support this interpretation (Abdala *et al.*, 1999; Lavigne-Rebillard and Pujol, 1988). The role of the immature middle ear has also been considered as an explanation for these age differences. This possibility has been reviewed in detail in previous reports from our laboratory. [See Abdala (1998, 2001) for detailed discussion of this topic.]

It is also a tenable hypothesis that normal-hearing adults show broadened tuning because of aging-related, subclinical hair cell loss and subtle cochlear alterations. Cochlear hair cell loss begins early in life and proceeds with age (Bredberg, 1968). It is not known what percentage of outer hair cell loss can be tolerated before perceptual difficulties are noted and the audiogram shows elevated thresholds. There can be a significant reduction in DPOAE amplitude with age,

a)Electronic mail: cabdala@hei.org

even in adults that have stable audiograms with hearing thresholds in the normal range (Lonsbury-Martin *et al.*, 1990, 1991; Stover and Norton, 1993). Lonsbury-Martin and colleagues observed that high-frequency DPOAE amplitude decreased and detection threshold generally increased with age in a group of normal-hearing adults. A subsequent study from this group found that DPOAE amplitude and threshold measures for frequencies above 2000 Hz were effective in detecting changes in cochlear function (Lonsbury-Martin *et al.*, 1991). These investigators conclude that subtle changes in the micromechanical properties of hearing take place with aging, even in patients with hearing that falls into a normal range as defined by clinical standards.

There is also some indication that elevated behavioral thresholds in the ultra-high-frequency range (8–16 kHz) are correlated with reduced OAE amplitude recorded at lower frequencies (Avan *et al.*, 1997). In this study, age and ultra-high-frequency audiometric thresholds were also correlated, making it somewhat difficult to parse out the effect of threshold elevation and aging. A more recent report, however, found that the factor of age alone (not age combined with audiometric threshold) correlates with decreased DPOAE amplitude in normal-hearing adults (Dorn *et al.*, 1998). This finding suggests that processes related to aging may impact cochlear output and DPOAE generation even in the absence of audiometric threshold elevation.

Consequently, either the immaturity or aging hypotheses, or a combination of the two, provides plausible explanations for why premature neonates have nonadultlike DPOAE suppression tuning at 1500 and 6000 Hz. The present study sought to address this issue by recording DPOAE suppression tuning in a group of individuals with mature cochleae, but lacking exposure to ototoxins and noise and having undergone minimal aging. Normal-hearing school-aged children met these criteria and served as subjects in the present study. If age-related hair cell loss is causing broadened DPOAE suppression tuning in normal-hearing adults, children should have narrower and sharper tuning curves than adults. Conversely, if some subtle immaturity in cochlear function is causing excessive tuning sharpness in premature neonates, then normal-hearing school-aged children should have DPOAE STCs that are broader than STCs recorded in premature neonates and more like adult curves. If both immaturity and adult hair cell loss are factors, then children may show some intermediate value of suppression tuning.

II. METHODS

A. Subjects

Twenty-six normal-hearing children, 13 males and 13 females, ranging in age from 8 to 12 years (mean=10 years) participated in this study. Eleven left ears and 15 right ears were used for testing. The subjects lived in the suburban regions surrounding Los Angeles and were recruited by written announcements distributed at elementary schools or by association with employees of the House Ear Institute. All pediatric subjects had negative histories of otologic disease and audiometric thresholds $<$15 dB HL from 250 to 8000 Hz at the time of test. Additionally, all children had a normal screening tympanogram (-75 to $+50$ dapa) at test to ensure normal middle ear function.

Twenty-three normal-hearing adults ranging in age from 17 to 35 years (mean=26 years) participated as subjects (7 male, 16 female). Eight right ears and 15 left ears were tested. Adult subjects had audiometric air-conduction threshold of $<$15 dB HL from 250 to 8000 Hz and a negative history of otologic disease. They were recruited from the House Ear Institute employee pool. Adults and children were tested in a sound-treated booth in the Children's Auditory Research and Evaluation Center while sitting quietly in a comfortable arm chair. Data from a group of 202 previously tested premature neonates aged 31–37 weeks conceptional age at test were also included for comparison with children's data (Abdala, 2001).

B. Instrumentation and signal analysis

An Ariel DSP16+ signal processing and acquisition board housed within a personal computer with Pentium processor was used to generate stimuli and acquire data. The Ariel board was connected to an Etymotic Research ER-10C probe system and to an analog high-pass filter (12 dB/oct; 710 Hz high-pass cutoff). The ER-10C probe contains two output transducers and a low-noise microphone. The two primary tones and the suppressor tone were generated by the DSP processor. The primary tone at $f1$ was generated by one D/A-converter and delivered via one transducer. The primary tone at $f2$ and the suppressor tone (fs) were produced by the second D/A-converter and output through the second transducer.

The signal at the probe microphone was high-pass filtered and sampled at a rate of 50 kHz with a sweep length of 4096 samples, giving a frequency resolution of 12.2 Hz. Twenty-five sweeps of the microphone signal were added and comprised one block for $f2=3000$ and 6000 Hz. Due to elevated noise in the low frequencies, 50 sweeps were added to make up one block at 1500 Hz.

C. Data acceptance criteria

Acceptance criteria were as follows: (1) Noise measurements for three frequency bins (12.2 Hz wide) on either side of the $2f1$-$f2$ frequency had to be $<$0 dB SPL to assure appropriate subject state and (2) the measured DPOAE level had to be at least 5 dB above the average noise measured in the same six bins around the distortion product frequency to be accepted into the grand average.

The program attempted up to six blocks of either 25 or 50 sweeps to achieve the absolute noise criteria of 0 dB SPL and the S/N ratio of 5 dB. If both of these criteria were not met after six attempted blocks, no data were collected and the next condition was initiated. In addition, sweeps were accepted into a block of data only when the estimated rms level in that sweep did not exceed a user-controlled artifact rejection threshold. This level was set for each subject based on observations of baseline activity level determined early in the test session, and modified if necessary during the test.

D. Calibration

An *in situ* calibration procedure was conducted on both output transducers before each subject was tested. Tones of fixed voltage were presented to the transducers at 250 Hz intervals from 500 to 15 000 Hz and the resulting SPL of these tones recorded in each ear canal. Based on this information, an equalization of output levels was performed for each subject to achieve target stimulus levels across test frequencies.

Intermodulation distortion produced by the recording system at $2f1-f2$ was measured with the probe in a Zwislocki coupler for all test conditions. The mean level of distortion was -21 dB SPL. In no case did the level exceed -17 dB SPL. The recording system noise floor was determined using a similar method with no tones present. The level of system noise floor ranged between -22 and -27 dB SPL depending on frequency.

The existence of standing waves at 6000 Hz may have underestimated SPL at the tympanic membrane by 4 or 5 dB (based on quarter wave length estimates; Dirks and Kincaid, 1987). Prior to conducting this experiment, the difference between levels recorded at the entrance of the ear canal with the ER-10C probe microphone and levels recorded at the tympanic membrane with an ER-7 tube microphone was measured in a small group of adult subjects. Consistent with the data of Siegel *et al.* (1994), the variable manner in which standing waves impact acoustic energy in each individual ear canal makes attempted correction of this interference ineffective. However, both subject groups (adults and school-aged children) were affected by this factor and, therefore, any age effects observed between these two groups cannot easily be attributed to standing waves.

E. Procedure

For the collection of DPOAE suppression tuning curves, the ratio between primary tone $f1$ and $f2$ was kept constant at 1.21 and the level separation at 10 dB (L1>L2). Three $f2$ frequencies were presented: 1500, 3000, and 6000 Hz. Primary tones were presented at two levels: low-level $=55-45$ dB SPL and high-level$=75-65$ dB SPL. DPOAEs evoked by 55–45 dB primary tones at 1500 were not easily recorded above the noise floor when suppressed by 6 dB or more; for this reason, the low-level category for 1500 Hz was adjusted to 65–55 dB SPL.

Custom-designed software for the collection of DPOAE suppression tuning curves was developed at the Children's Auditory Research and Evaluation Center, House Ear Institute. An unsuppressed DPOAE was initially measured for a given $f2$ frequency. A suppressor tone (*Fs*) was then presented simultaneously with the primary tones and its level increased in 5-dB steps over a range of intensities. Twelve to 15 suppressor tones with frequency ranging from 1 oct below to $\frac{1}{4}$ oct above $f2$ were presented at intervals between 25 and 150 cents (1 oct$=$1200 cents). To generate isosuppression tuning curves, the *Fs* level that reduced DPOAE amplitude by 6 dB was determined from the suppression growth function (DPOAE amplitude$\times$suppressor level) using linear interpolation and plotted as a function of *fs*.

F. Data analysis

The data analysis was conducted in the same manner as previously described in various publications (Abdala, 2001). Briefly, the following variables were quantified and analyzed: (1) Q10 value; (2) Q10 difference score was calculated by subtracting the Q value in the high-level condition from Q in the low-level. Q difference score (Q_{DS}) is thought to estimate the enhancement of tuning effect provided by the cochlear amplifier; (3) slope (dB/oct) of the low- and high-frequency sides of the tuning curve; (4) tuning curve tip frequency/level; and (5) slope of suppression growth was measured from the record of DPOAE amplitude as a function of suppressor level for six to eight suppressor tones in each $f2$ condition.

III. RESULTS

A. DPOAE suppression tuning curves

The tuning curves generated in this study for children and adult subjects are presented in Fig. 1, along with tuning curves generated from premature neonates in a previous study. Children have STC morphology and level effects similar to adults. DPOAE STCs recorded with high-level primary tones from adult subjects and children show a flattened low-frequency flank for 1500 Hz and, more obviously, for 6000 Hz. This is in contrast to the relatively steep low-frequency slope observed when STCs are recorded with low-level primary tones. Premature neonates do not appear to show a broadening effect or flattened low-frequency slope when tuning curves are recorded with high-level primary tones.

B. STC width (Q10)

1. Level effects

Level by frequency (2×3) factorial ANOVAs for Q10 were conducted separately for each age group to assess whether tuning curve width was significantly influenced by primary tone level. Consistent with anecdotal observations, both adults and children showed a level effect ($F=18.99$, $p=<0.0001$, and $F=8.27$, $p=0.0057$, respectively) indicating that STCs were broader and more bowl-shaped when recorded with high- versus low-level primary tones. A frequency effect was also present but not relevant since different primary tone levels were used at different $f2$ frequencies (see Sec. II). Premature neonates did not show a level effect, indicating that STC width was not significantly different whether recorded with primary tones that were low or high level. There were no interactions between level and frequency for any age group.

Figure 2 shows mean Q10 value for children, adults, and premature neonates at the three $f2$ frequencies; primary tone level (low- versus high) is designated by line (solid/dashed). The separation between solid and dashed lines clearly demonstrates the consistent trend for high-level primary tones to produce broader tuning (i.e., smaller Q values) only in adults and children.

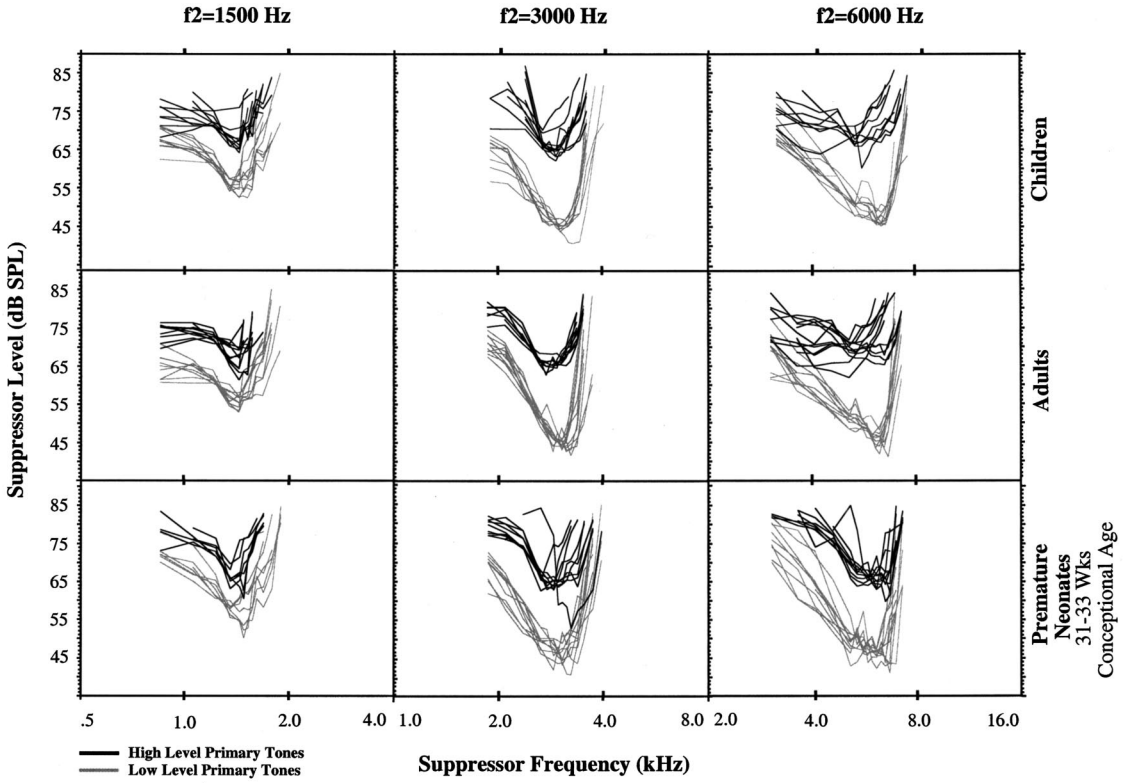

FIG. 1. 175 DPOAE suppression tuning curves recorded with high-level (black) and low-level primary tones (gray) in 23 normal-hearing adults, 26 normal-hearing children, and 47 premature neonates with conceptional ages of 31–33 weeks. Tuning curves were recorded at three $f2$ frequencies.

2. Age effects

Figure 3 displays the mean Q10 values for each age group. Adults and children showed similar mean Q10 values and a characteristic configuration across $f2$ frequency; that is, Q values slightly increased from 1500 to 3000 Hz and then decreased or remained stable from 3000 to 6000 Hz. Age by frequency (3×3) factorial ANOVAs for Q10 value were conducted separately for low- and high-level data to evaluate the impact of age on STC width. The question of primary interest was whether STC width in children was comparable to STC width in adults. Again, the frequency effect was not of importance to the particular research question in this experiment and has been examined in previous published work from our laboratory (Abdala *et al.*, 1996).

There was an age effect on Q10 for both low- and high-level primary tone conditions ($F=4.04$, $p=0.0083$ and $F=15.33$, $p=0.0001$, respectively), as well as interactions between age and frequency. The interactions suggest that age effects were only present at some $f2$ frequency conditions; therefore, subsequent one-way ANOVAs were conducted at each frequency separately. Only STCs recorded at 1500 and 6000 Hz were significantly impacted by age. *Post hoc t*-tests were used to make age group comparisons at 1500 and 6000 Hz (adults versus children; children versus neonate). Q values from children were not significantly different than adult values at either low or high primary tone levels. The children's STCs, however, were significantly broader than premature neonatal STCs in all conditions except 1500 Hz STCs measured at low-levels.

C. Q difference score

The Q difference score (Q_{DS}) was calculated by subtracting the mean tuning curve Q10 value recorded with high-level primary tones from the mean Q10 value recorded with low-level primary tones. It is considered a simple estimate of the *tuning enhancement* effect provided by the cochlear amplifier. Figure 4 is a plot of Q_{DS} as a function of age group for $f2$ frequencies of 1500 and 6000 Hz. Data collected from term neonates in a previous study (Abdala, 2001) has been added to better define the age continuum for Q_{DS}. This figure shows that the Q_{DS} generally increases with age and is largest in adults and children. Adults and children show generally comparable Q difference scores at both 1500 and 6000 Hz. When these same data are plotted as a function of $f2$ frequency (Fig. 4 inset), the similarity of adult and children's Q_{DS} is even more apparent. This similarity suggests that the cochlear amplifier is enhancing tuning in a comparable manner for adults and children; in both groups, mean Q values derived with low primary tone levels are approximately 0.75 units greater (narrower) than Q derived with high-level stimuli for 1500 Hz. For 6000 Hz, low-level STCs produce mean Q values of 1.6 units greater than high-level STCs.

In contrast to adults and children, premature neonates have a 0 Q_{DS} at 1500 Hz, indicating that stimulus level did not impact tuning at this frequency, and a mean difference score of just over 0.5 units at 6000 Hz, indicating minimal impact of primary tone level on STC width at this frequency.

Figure 5 shows the level effect on STC width and shape

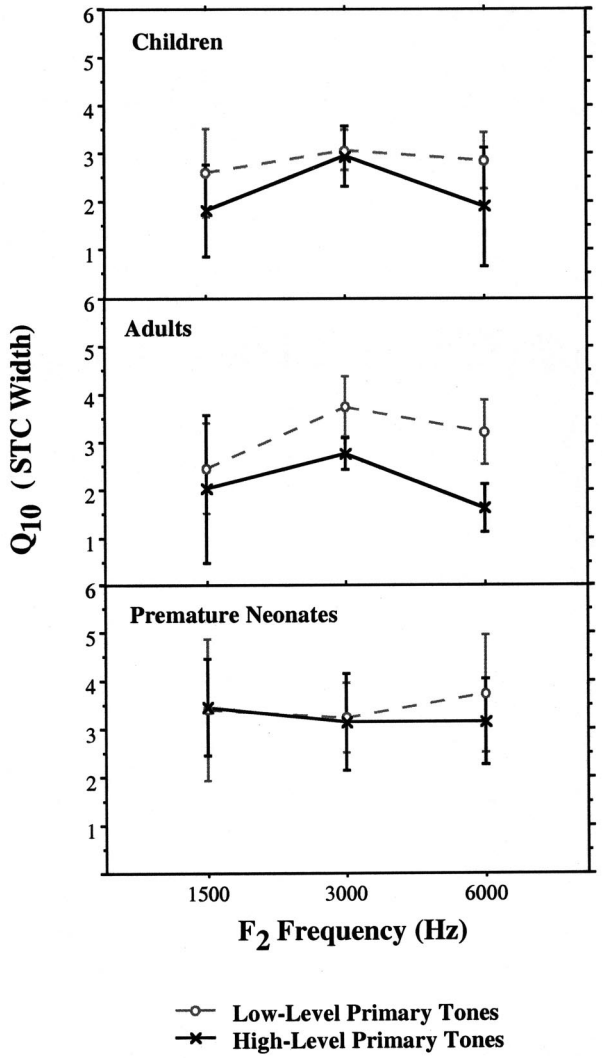

FIG. 2. Mean Q10 values for DPOAE STCs as a function of $f2$ frequency for children, adults, and premature neonates. Q values for STCs recorded with low- (dashed line) and high-level (solid line) primary tones are shown. Error bars represent ± 1 standard deviation.

in four individual subjects. These four subjects had DPOAE STCs generated with both low- and high-level primary tones at 6000 Hz. The low- and high-level STCs are superimposed in Fig. 5. The lowest frequency point on each STC was normalized to 0 dB and all other points reflect a shift from this value. As is evident, the children shown here as examples have a sharp, narrow curve for low-level recordings and a broad, flattened curve in the high-level condition, with a peak shift toward lower frequencies. The primary difference between the low- and high-level patterns is slope of the low-frequency flank. This slope becomes considerably more shallow when going from low- to high-level primary tones, thus producing a less-tuned curve. Adults show this same level effect [see Fig. 5(c)]. An example of low- and high-level tuning for one representative premature neonate is also presented for comparison purposes [Fig. 5(d)]. In contrast to adults and children, premature subjects generally retained both shape and narrow tip of the tuning curve at high levels of stimulus presentation.

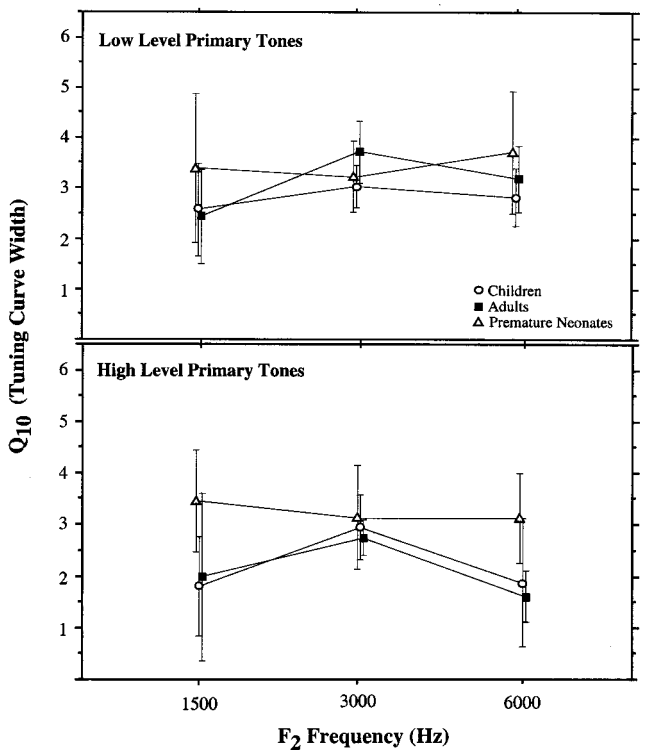

FIG. 3. Mean Q10 values for DPOAE STCs recorded with low-and high-level primary tones at three $f2$ frequencies. Error bars represent ± 1 standard deviation.

D. Slope

Separate age by level ANOVAs were conducted for slope on the low- and high-frequency flank of the STC. On the low-frequency flank, age effects were present at 1500 and 6000 Hz only (age effects: $F=12.4$, $p=0.0001$ and $F=10.06$, $p=0.0001$, respectively); interactions between age and level were also present at these two frequencies. *Post hoc* age group comparisons (unpaired *t*-tests) were conducted on low-frequency slope at 1500 and 6000 Hz; these compari-

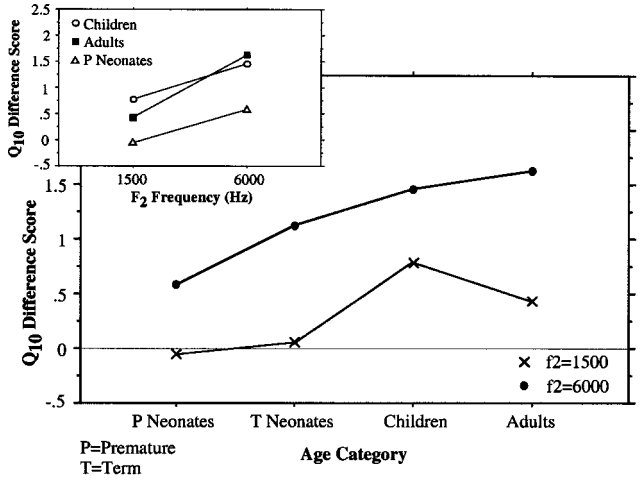

FIG. 4. Mean Q10 difference score (low-level Q minus high-level Q) for all age groups at 1500 and 6000 Hz. Data from a group of term neonates tested in a previous experiment were added to establish a more complete age continuum. Q difference score generally increases with age. The inset graph plots Q10 difference score as a function of $f2$ frequency.

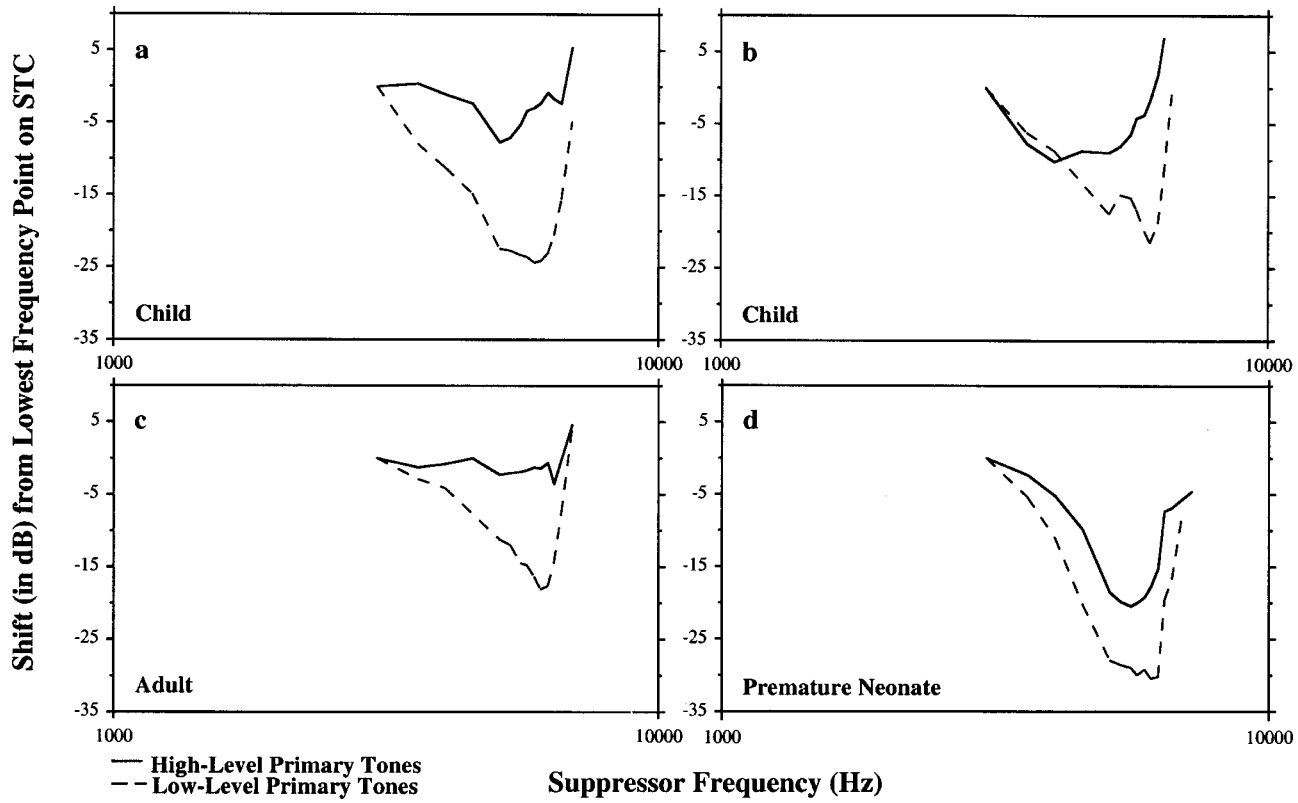

FIG. 5. Suppression tuning curves from four individual subjects that had both low- and high-level data (two children, one adult, and one premature neonate). The lowest frequency point on both curves was normalized to 0 dB and all other points reflect a shift from this value.

sons indicate that slope measured from children and adults did not differ for either $f2$ frequency. However, premature neonates had steeper mean slope than children at both $f2$ frequencies (1500 Hz: $p=0.0058$; 6000 Hz: $p=0.0051$). There were no age effects or interactions between age and level at 3000 Hz.

On the high-frequency flank, there was no effect of age or interaction between age and level at 1500 Hz and 6000 Hz. At 3000 Hz, there was an age effect ($p=0.0001$) and an interaction between age and level ($p=0.01$). In general, at 3000 Hz adults had steeper slope than either neonates or children for STCs generated with low-level primary tones.

E. Tip characteristics

Level by age ANOVAs for *tip frequency* were conducted for the three $f2$ frequencies separately. There was no age effect or level by age interaction at 1500 or 3000 Hz. There was an age effect on tip frequency at 6000 Hz only ($F=6.81$, $p=0.0003$), as well as an interaction between age and level. Subsequent *posthoc* age group comparisons at 6000 Hz showed that adults and children had comparable tip frequency values at 6000 Hz while premature neonates had a higher tip frequency than children for STCs measured in the high-level condition [$p=0.0001$; see Fig. 6(a)].

Age by level ANOVAs for *tip level* were done separately at each $f2$ frequency. There was an age effect on tip level at 1500 and 6000 Hz only and no interactions. *Post hoc* age group contrasts (one-way ANOVAs) further defined the age

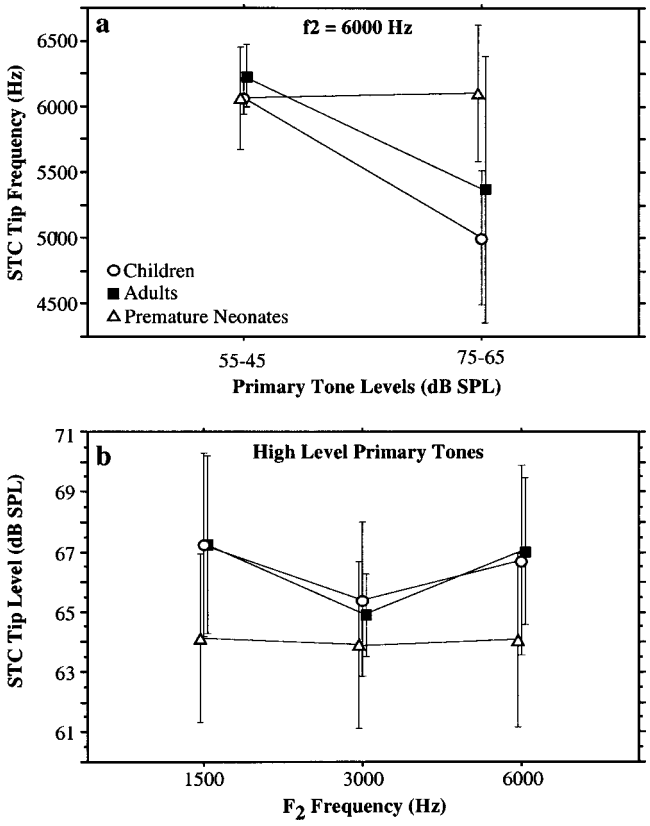

FIG. 6. (a) DPOAE STC tip frequency at 6000 Hz at low and high levels for the three age groups. (b) Tip level at three $f2$ frequencies for high-level primary tones. Error bars represent ± 1 standard deviation.

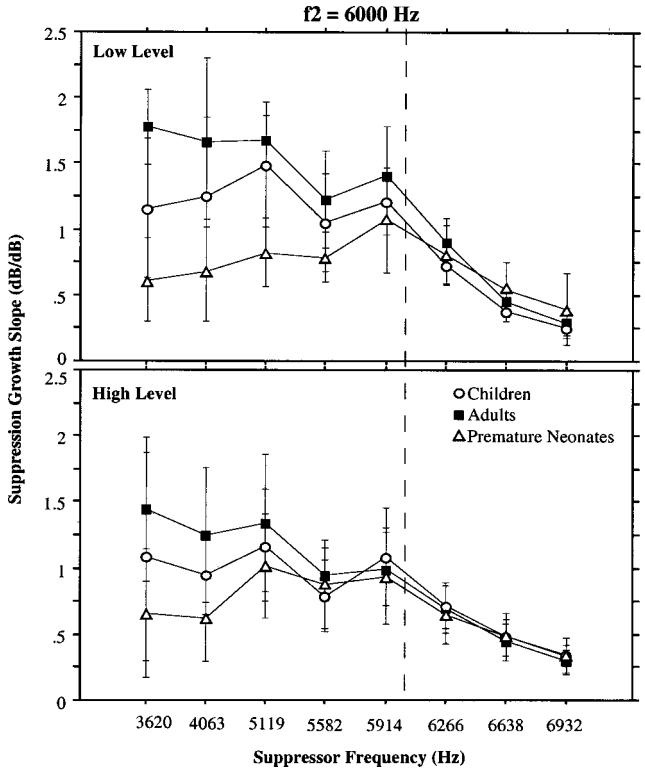

FIG. 7. Suppression growth (slope value in dB/dB) as a function of suppressor frequency for $f2$ frequency of 6000 Hz. Both low- and high-level primary tone conditions are shown. Error bars represent ± 1 standard deviation.

effects at 1500 and 6000 Hz; STC tip level was comparable for children and adults at both frequencies. However, tip levels were lower in premature neonates than children at both 1500 and 6000 Hz [$F=6.55$, $p=0.012$; $F=18.35$, $p=0.0001$; see Fig. 6(b)].

F. Suppression growth

The rate at which the DPOAE amplitude decreases as suppressor level increases was measured by deriving a slope value from this function. It has been shown previously that neonates generally have more shallow suppression growth than adults (Abdala, 1998, 2001), especially for suppressor tones lower in frequency than $f2$. With few exceptions, this seemed to be the case in the present study as well, particularly in the low-level primary tone condition. This trend is most evident at $f2=6000$ Hz as can be seen from Fig. 7. Neonates have the shallowest growth of suppression for suppressor tones lower in frequency than $f2$ while adults have the steepest growth. Children's data either fell between the adult and neonatal values or closely approximated adult values as can be seen from this figure.

IV. DISCUSSION

The purpose of this investigation was to determine whether normal-hearing children who have not been exposed to ototoxins or traumatic noise and who we presume have not had significant loss of cochlear sensory cells, have adultlike DPOAE suppression tuning. The answer to this question is important because it addresses the hypothesis that auditory aging and hair cell loss in normal-hearing adults can produce broadened DPOAE suppression tuning. School-aged children should show narrower and sharper suppression tuning than adults if normal-hearing adults truly have significantly compromised cochlear function due to hair cell loss.

The findings of the present study indicate that children have DPOAE STC width, slope, and tip features like adults and significantly different from premature neonates at $f2$ frequencies of 1500 and 6000 Hz. Children were also adultlike with respect to the influence of primary tone level on tuning curve width; high levels produced broader tuning than low levels. Premature neonates showed no such level effect. The general absence of age effects at $f2$ frequency of 3000 Hz is a consistent finding in DPOAE suppression studies and has been discussed in detail in previous publications (Abdala *et al.*, 1996; Abdala, 1998). It may indicate very early maturation of the basilar membrane regions coding input of this frequency.

The findings do not support the hypothesis that adult DPOAE suppression tuning is adversely affected (broadened) by hair cell loss associated with aging and general exposure to noise and ototoxins. The significant difference between DPOAE suppression tuning recorded from premature neonates and children suggests that the cochlea of neonates is still showing subtle immaturities in function.

A. Q difference score

The Q difference score (Q_{DS}) is thought to reflect the strength of the cochlear amplifier effect on tuning. Although the Q_{DS} was larger in adults and children than in neonates, it cannot be concluded that the tuning enhancement effect is more developed and robust in adults and children than in neonates. When one scrutinizes the data, it is clear that both the adult and children's Q difference scores are large because the high-level tuning curve becomes broad and detuned at high primary tone levels, *not* because the cochlear amplifier-mediated tuning (i.e., low-level tuning) is sharper or better in adults and children than in neonates. We have concluded in previous work that the relatively small Q_{DS} in neonates occurs because it was not possible to reach the level of cochlear amplifier saturation in this age group (Abdala, 2001); therefore, it was not possible to produce primarily passive basilar membrane motion when high-level primary tones at 75–65 dB SPL were presented. This indicates that the range of levels over which the cochlear amplifier functions may not be adultlike in premature neonates but appears to be comparable in adults and children, again suggesting a neonatal immaturity and not adult hair cell loss.

B. Suppression rate

Rapid growth of DPOAE suppression may suggest extensive spread of energy on the basilar membrane. That is, if a suppressor tone is able to efficiently suppress the probe ($f2$ is considered to be the probe in this example), then it must be concluded that the excitation pattern evoked by the suppressor has spread from its nominal frequency region to the region of DPOAE generation (i.e., $f2$). The more effective the suppressor, measured by how steep the suppression growth, the more spread of energy occurred on the basilar membrane

as the suppressor tone was increased in level. Following this logic, it appears that adults and children have a more extensive spread of masking toward the base of the cochlea. This can be seen in the steep suppression growth observed in adults and children for suppressor tones lower in frequency than $f2$. Neonates, in contrast, show a more shallow growth of suppression as the suppressor tone is increased, suggesting more restricted basalward spread of excitation on the basilar membrane.

In past reports, we have hypothesized that the marked spread of excitation in the adult cochlea might reflect poor frequency resolution in an aging auditory system, rather than an immaturity on the part of premature neonates. The present study could not entirely rule out this possibility at the highest frequency tested. Although children showed a pattern of suppression growth similar to adults, they were not quite adultlike in slope values at 6000 Hz. Children's mean values often fell between neonatal and adult values or came close to approximating adult values (see Fig. 7). This ''mixed'' result would be expected if neonatal cochlear immaturity *and* subtle auditory aging/hair cell loss effects were both influencing the suppression results. It is interesting that only the suppression growth data elucidated an effect that could be interpreted to indicate adult aging/hair cell loss, and only at 6000 Hz. In all other metrics of DPOAE suppression tuning, children were found to be adultlike.

V. SUMMARY

The findings of this study suggest that adult aging and hair cell loss cannot solely or predominantly account for the neonatal–adult differences previously observed in DPOAE suppression tuning (Abdala, 2001). The DPOAE suppression tuning of children is generally like that of adults. Suppression tuning of premature neonates, however, is unlike that of either adults or children. Premature neonates have sharper tuning at both 1500 and 6000 Hz with a steeper low-frequency slope and with lower tip levels and shallower suppression growth than either adults or children. Additionally, stimulus level does not affect neonatal DPOAE suppression in an adultlike fashion. These results cannot reflect aging of the adult cochlea since school-aged children have the same STC characteristics as adults. The only exception to this is seen for the growth of suppression at the highest $f2$ frequencies; here, children were not adultlike, nor were they like neonates. This leaves open the possibility that factors related to aging and hair cell loss may contribute at high frequencies. Further study is needed to examine this question.

The primary interpretation of DPOAE STC data, that there is a subtle immaturity in cochlear function during the last trimester, appears to offer the most parsimonious explanation for why suppression tuning is nonadultlike in premature neonates. We hypothesize that the most likely source of adult–neonatal differences in DPOAE suppression tuning is an immaturity in cochlear physiology and/or efferent regulation of outer hair cell function prior to term birth.

ACKNOWLEDGMENTS

This work was supported by Research Grant No. 1 R29 DC03552 from the National Institutes of Deafness and Other Communication Disorders, National Institutes of Health, and by the House Ear Institute. The author would like to thank Leslie Visser-Dumont and Ellen Ma for extensive data collection and management.

Abdala, C. (**1998**). ''A developmental study of DPOAE (2 f1-f2) suppression in human premature neonates,'' Hear. Res. **121**, 123–138.

Abdala, C. (**2001**). ''Maturation of the human cochlear amplifier: DPOAE suppression tuning curves at low and high primary tones levels,'' J. Acoust. Soc. Am. **110**, 1465–1476.

Abdala, C., Ma, E., and Sininger, Y. (**1999**). ''Maturation of medial efferent system function in humans,'' J. Acoust. Soc. Am. **105**, 2392–2402.

Abdala, C., Sininger, Y., Ekelid, M., and Zeng, F.-G. (**1996**). ''Distortion product otoacoustic emission suppression tuning curves in human adults and neonates,'' Hear. Res. **98**, 38–53.

Avan, P., Elbez, M., and Bonfils, P. (**1997**). ''Click-evoked otoacoustic emissions and the influence of high-frequency hearing losses in humans,'' J. Acoust. Soc. Am. **101**, 2771–2777.

Bredberg, G. (**1968**). ''Cellular pattern and nerve supply of the human organ of Corti,'' Acta Oto-Laryngol., Suppl. **236**, 1–135.

Dirks, D., and Kincaid, G. (**1987**). ''Basic acoustic considerations of ear canal probe measurements,'' Ear Hear. **8** (Suppl 5), 60–67.

Dorn, P., Piskorski, P., Keefe, D., Neely, S., and Gorga, M. (**1998**). ''On the existence of an age/threshold/frequency interaction in distortion product otoacoustic emissions,'' J. Acoust. Soc. Am. **104**, 964–971.

Lavigne-Rebillard, M., and Pujol, R. (**1986**). ''Development of the auditory hair cell surface in human fetuses,'' Anat. Embryol. **174**, 369–377.

Lavigne-Rebillard, M., and Pujol, R. (**1987**). ''Surface aspects of the developing human organ of Corti,'' Acta Oto-Laryngol., Suppl. **436**, 43–50.

Lavigne-Rebillard, M., and Pujol, R. (**1988**). ''Hair cell innervation in the fetal human cochlea,'' Acta Oto-Laryngol. **105**, 398–402.

Lonsbury-Martin, B., Cutler, W., and Martin, G. (**1991**). ''Evidence for the influence of aging on distortion-product otoacoustic emissions in humans,'' J. Acoust. Soc. Am. **89**, 1749–1759.

Lonsbury-Martin, B., Harris, F., Hawkins, M., Stagner, B., and Martin, G. (**1990**). ''Distortion product otoacoustic emissions in humans: I. Basic properties in normal-hearing subjects,'' Ann. Otol. Rhinol. Laryngol. **99**, Suppl 147, 29–44.

Siegel, J. (**1994**). ''Ear-canal standing waves and high-frequency sound calibration using otoacoustic emission probes,'' J. Acoust. Soc. Am. **95**, 2589–2597.

Stover, L., and Norton, S. (**1993**). ''The effects of aging on otoacoustic emissions,'' J. Acoust. Soc. Am. **94**, 2670–2681.

Energy-independent factors influencing noise-induced hearing loss in the chinchilla model

Roger P. Hamernik[a] and Wei Qiu
Auditory Research Laboratory, State University of New York, 107 Beaumont Hall, Plattsburgh, New York 12901

(Received 21 February 2001; revised 17 August 2001; accepted 20 August 2001)

The effects on hearing and the sensory cell population of four continuous, non-Gaussian noise exposures each having an A-weighted $L_{eq}=100$ dB SPL were compared to the effects of an energy-equivalent Gaussian noise. The non-Gaussian noise conditions were characterized by the statistical metric, kurtosis (β), computed on the unfiltered, $\beta(t)$, and the filtered, $\beta(f)$, time-domain signals. The chinchilla ($n=58$) was used as the animal model. Hearing thresholds were estimated using auditory-evoked potentials (AEP) recorded from the inferior colliculus and sensory cell populations were obtained from surface preparation histology. Despite equivalent exposure energies, the four non-Gaussian conditions produced considerably greater hearing and sensory cell loss than did the Gaussian condition. The magnitude of this excess trauma produced by the non-Gaussian noise was dependent on the frequency content, but not on the average energy content of the impacts which gave the noise its non-Gaussian character. These results indicate that $\beta(t)$ is an appropriate index of the increased hazard of exposure to non-Gaussian noises and that $\beta(f)$ may be useful in the prediction of the place-specific additional outer hair cell loss produced by non-Gaussian exposures. The results also suggest that energy-based metrics, while necessary for the prediction of noise-induced hearing loss, are not sufficient. [DOI: 10.1121/1.1414707]

PACS numbers: 43.64.Wn, 43.66.Ed [MRL]

I. INTRODUCTION

Contemporary noise standards (e.g., ISO-1999, 1990; ANSI S3.44, 1996) are based on the assumption that an energy metric such as the equivalent noise level (L_{eq}) is sufficient for estimating the potential of a noise stimulus to cause noise-induced hearing loss (NIHL). While the L_{eq} may be an adequate index for estimating the hazard associated with exposure to Gaussian, steady-state noise exposures, such exposures are more typical of controlled laboratory experiments rather than industrial noise environments. The latter are often non-Gaussian, with a sound-pressure level (SPL) that varies over the course of the workday and is punctuated by high-level impulsive components or other type of noise transients. Available data, from laboratory-based experiments (Lei *et al.*, 1994; Dunn *et al.*, 1991), as well as epidemiological studies (Passchier-Vermeer, 1983; Sulkowski *et al.*, 1983; Thiery and Meyer-Bisch, 1988) indicate that while an energy metric may be necessary, it is not sufficient for the prediction of NIHL. Other variables of the noise exposure must be considered. Unfortunately there are a large number of stimulus variables that can be used to characterize a complex noise environment.

Experimental studies such as those of Clark *et al.* (1987) and others have shown the importance of the temporal structure of an exposure on the threshold shift (TS) dynamics following exposures to various interrupted noises. Since temporal variables do not affect an energy metric and since there are an infinite number of very different noise exposures characterized by the same L_{eq}, it seems reasonable that a metric that would incorporate both temporal and level variables might be a useful adjunct to the L_{eq} metric. One such metric is the kurtosis, β, of a sample distribution which is defined as the ratio of the fourth-order central moment to the squared second-order central moment of the distribution. Erdreich (1986) was perhaps the first to suggest the use of kurtosis to identify/characterize impulsive noise environments for application to hearing conservation strategies. This statistic, used to estimate the deviation of a distribution from the Gaussian, can be computed on the unfiltered, $\beta(t)$, and the filtered, $\beta(f)$, time-domain signal. With non-Gaussian signals, $\beta(f)$ can serve as a useful adjunct to conventional spectral analysis (Dwyer, 1984).

The potential of the β metrics for identifying hazardous noise environments was demonstrated by Lei *et al.* (1994). They hypothesized that for the same total energy and spectrum a high-kurtosis noise exposure is more hazardous to hearing than a Gaussian exposure, and that this effect is frequency dependent. Using a very limited set of exposure parameters, $\beta(t)$ and $\beta(f)$ were shown: (i) to rank order the degree of hearing trauma and (ii) to reflect the frequency specificity of trauma.

The data presented in this paper extend the results of Lei *et al.* (1994) by considering more generalized non-Gaussian signals as well as spectral influences.

II. METHODS

Fifty-eight chinchillas were used as subjects. Each animal was made monaural by surgical destruction, under anes-

[a]Author to whom correspondence should be addressed. Electronic mail: roger.hamernik@plattsburgh.edu

thesia, of the left cochlea. During this procedure a bipolar electrode was implanted, under stereotaxic control, into the left inferior colliculus and the electrode plug cemented to the skull for the recording of auditory-evoked potentials (AEP). The AEP was used to estimate pure-tone thresholds, and surface preparations of the organ of Corti were used to estimate the inner- and outer hair cell (IHC, OHC) populations. Additional details of the experimental methods, beyond those presented below, may be found in Ahroon *et al.* (1993).

A. Experimental protocol

The animals were randomly assigned to one of five experimental groups with 11 or 12 animals/group. Following a 2-week postsurgical recovery, three AEP preexposure audiograms were obtained (on different days) on each animal at octave intervals between 0.5 and 16.0 kHz. If the mean of the three audiograms, at two or more frequencies, fell beyond one standard deviation of laboratory norms (Hamernik and Qiu, 2000), in the direction of poorer thresholds, the animal was rejected from the group. Two animals out of 60 were rejected because preexposure thresholds did not meet the criterion.

The animals were exposed to one of the noise conditions described below, five or six at a time, 24 h/day, for 5 consecutive days. Animals were given free access to food and water and rotated through the bank of six cages daily. The SPLs, across cages, in the middle of each cage, varied within ± 1 dB. During the exposure, animals were removed daily for less than 0.5 h for AEP testing. The mean of the five audiograms thus obtained defined asymptotic threshold shift (ATS). Thirty days following the last exposure day, three more audiograms were collected on different days and the mean used to define permanent threshold shift (PTS). Following audiometric testing the animals were killed under anesthesia. Their right cochlea was removed and prepared for surface preparation histology from which sensory cell populations along the length of the basilar membrane were determined.

B. Noise measurement and analyses

During the 5-day exposures the noise field was monitored with a Larson Davis 814 sound-level meter equipped with a 1/2-in. microphone. The noise was maintained at an L_{eq} of 100 dB(A) SPL. The acoustic signal produced by the Electro-Voice Xi-1152/94 speaker system was transduced by a Brüel and Kjær 1/2-in. microphone (model 4134), amplified by a Brüel & Kjær (model 2610) measuring amplifier and fed to a Windows PC-based analysis system. The design and digital generation of the acoustic signal is detailed in Hsueh and Hamernik (1990, 1991). The signal was sampled at 48 kHz with a recording duration of 5.5 min. $\beta(t)$ was computed over 40 s of the digitized temporal waveform. Similarly, $\beta(f)$ was computed over a 40-s interval on octave bands of the digitally filtered temporal samples. Center frequencies of the octave bands were the same as the audiometric test frequencies. The samples of every window were convolved with the impulse response of the octave bandwidth filter. The filter was designed as an infinite impulse response digital filter in which the coefficients of the impulse response

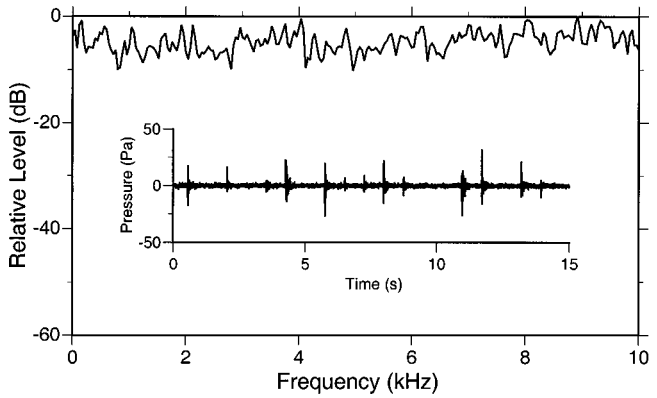

FIG. 1. The average spectrum obtained from a 40-s sample of the digitized waveform. The spectrum was the same for each of the five noise exposures. The inset shows a 15-s sample of the pressure–time waveform of a non-Gaussian exposure. Impact peak SPLs and interimpact intervals were randomly varied.

were obtained from the Signal Processing toolbox of MATLAB 5.3 (The Math Works Inc.). The filtering process was performed repeatedly to obtain $\beta(f)$ over successive octave bands.

C. Noise exposures

The animals were exposed for 5 consecutive days (24 h/day) to one of the following five exposure conditions, identified by group number.

G-43 Gaussian noise, $\beta(t)=3$. Reference condition.

G-44 Non-Gaussian noise, $\beta(t)=25$. The impact peak SPLs varied randomly between 115 and 128 dB. The impact was created from three 400-Hz bands of energy centered on 1.0, 2.0, and 4.0 kHz. The level of the background Gaussian noise was kept at 95 dB(A) SPL.

G-49 Non-Gaussian noise, $\beta(t)=33$. The impact peak SPLs varied randomly between 115 and 129 dB. The impact was created from the band of energy between 0.710 and 5.680 kHz. The level of the background Gaussian noise was kept at 92 dB(A) SPL.

G-50 Non-Gaussian noise, $\beta(t)=21$. The impact peak SPLs varied randomly between 114 and 128 dB. The impact was created from a single 400-Hz band of energy centered at 2.0 kHz. The level of the background Gaussian noise was kept at 95 dB(A) SPL.

G-55 Non-Gaussian noise, $\beta(t)=25$. The impact peak SPLs varied randomly between 117 and 129 dB. The impact was created from a broad band of energy between 0.125 and 10.0 kHz. The level of the background Gaussian noise was kept at 95 dB(A) SPL.

Each exposure had in common the same flat spectrum between 0.125 and 10.0 kHz shown in Fig. 1 and was presented at an $L_{eq}=100$ dB(A). The five exposures differed only in their temporal structure, which was designed to produce one Gaussian and four different non-Gaussian exposure

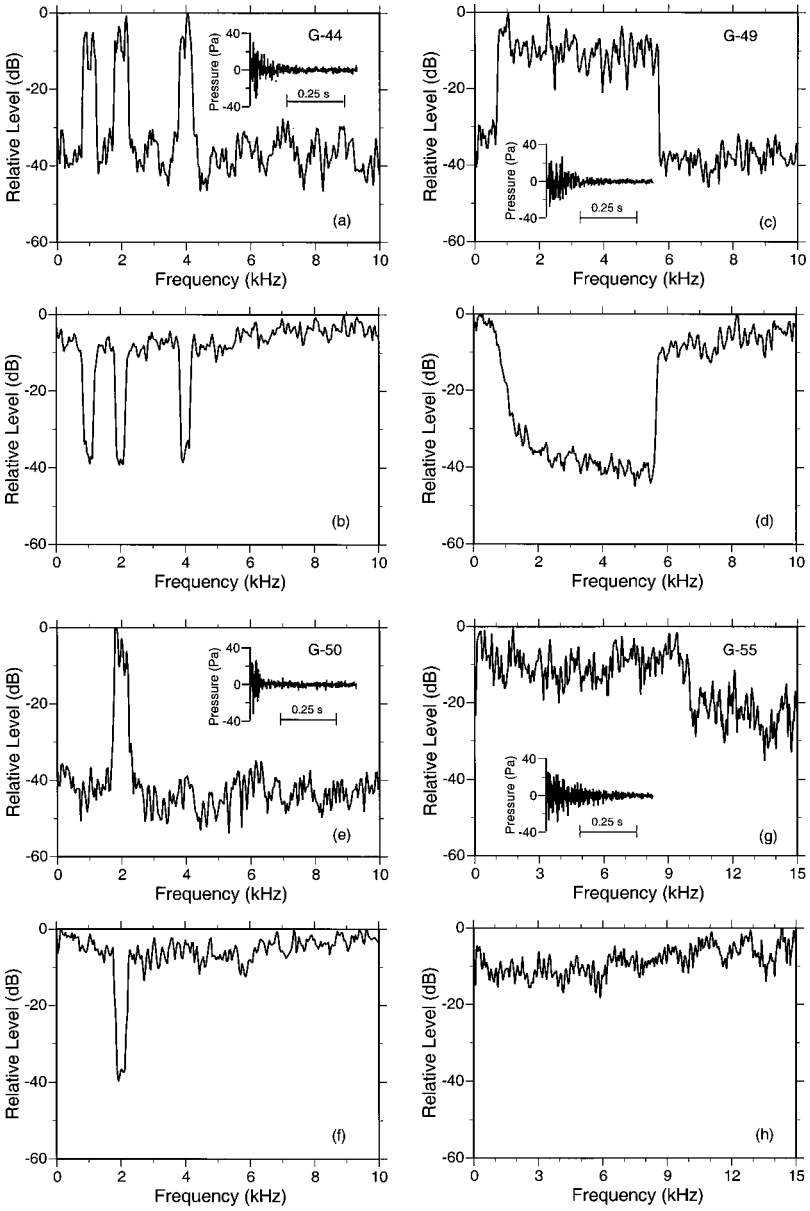

FIG. 2. The upper panels (a), (c), (e), and (g) show the spectrum of the impact that was used to create the character of each of the indicated non-Gaussian noise exposures. The inset shows a typical impact waveform. The lower panels (b), (d), (f), and (h) show the respective spectra of the Gaussian noises that were mixed with the impact stimuli.

conditions, three of which (G-44, G-50, and G-55) had similar values of $\beta(t)$. The non-Gaussian conditions were designed in the frequency domain as described by Hsueh and Hamernik (1990, 1991) and were the result of inserting impacts, whose spectra were complementary to the background Gaussian noise, into the otherwise Gaussian signal. The impact peak levels were randomly varied between the limits indicated above and the probability of an impact occurring in a 750-ms window was set at 0.6. The inset in Fig. 1 shows a 15-s sample of the non-Gaussian waveform. Variation in $\beta(f)$ was achieved by varying the spectrum of the impacts.

Figures 2(a)–(h) illustrate the waveform and spectrum of each of the non-Gaussian noises. Each of the top panels in Fig. 2 shows the spectrum of the impacts along with a pressure–time waveform of one of the impacts. The lower panels in Fig. 2 show the spectrum of the continuous background Gaussian noise that was combined with the impacts to produce the non-Gaussian signals. The Gaussian component of the non-Gaussian exposure had a spectrum that was complementary to that of the impact and a level (L_b) that was dependent on the value of $\beta(t)$. Generally, if the impact peak and interval histograms were kept approximately the same, $\beta(t)$ could be increased by decreasing L_b.

For exposure conditions G-44, -50, and -55, not only was the overall L_{eq} the same but the L_{eq} of the impact component (i.e., the L_{eq} of the exposure with the Gaussian noise component filtered out) of these exposures was also the same [i.e., $L_{eq}=98$ dB(A)]. Table I gives the 1/3-octave band levels of each noise exposure. Values shown are the mean values obtained from eight 40-s samples of the digitized waveform.

III. RESULTS

In the following figures data points are given with standard error (se) bars. When no error bar is present the se is less than the size of the datum symbol. The mean preexposure AEP audiogram for all 58 animals along with individual group means are shown in Fig. 3, where they are compared

TABLE I. Mean total and third-octave-band sound-pressure levels (dB SPL) over 5-day exposure period for all experimental groups.

Third-octave band cf (kHz)	G-43	G-44	G-49	G-50	G-55
0.25	84	74	78	81	87
0.32	84	76	79	81	89
0.40	84	76	78	81	88
0.50	84	76	79	81	89
0.63	85	76	81	82	89
0.80	84	86	90	80	88
1.00	85	91	91	82	89
1.25	84	85	89	79	86
1.60	83	82	89	87	85
2.00	83	94	89	97	84
2.50	82	84	90	85	83
3.15	85	84	91	82	87
4.00	86	94	91	83	86
5.00	88	84	92	85	88
6.30	91	88	85	89	90
8.00	94	90	88	92	92
10.00	96	92	89	93	93
12.50	95	92	90	91	90
16.00	94	91	89	91	90
Mean L_{eq}	103	101	102	101	102
Mean L_{eqA}	100	100	101	100	100
s.d.	0.04	0.26	0.65	0.23	0.77

to laboratory norms. The overall se was very small and the five group means at all test frequencies were within ±4 dB of each other. Figures 4(a)–(d) show the PTS and the percent OHC loss for the four non-Gaussian exposure conditions

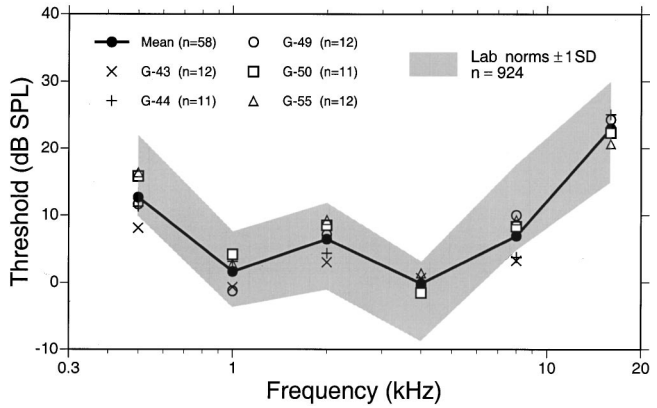

FIG. 3. The mean AEP audiograms for the entire group of animals and for the five individual groups compared to the laboratory norms based on a population of 924 animals.

compared to the Gaussian G-43 noise exposure. It is clear from this figure that for the two indices of trauma, PTS and OHC loss, the four non-Gaussian exposure conditions (G-44, G-49, G-50, and G-55) produced more severe permanent changes in the auditory system than did the Gaussian exposure. In the most extreme cases (G-49 and G-55) there is as much as 40 to 50 dB more PTS and 8 to 9 times the mean OHC loss at the most affected frequencies than in the Gaussian exposure, despite the same L_{eq} and spectrum in each of the exposures. For clarity, IHC losses are not shown. IHC losses were, as is usually the case in NIHL, much less than

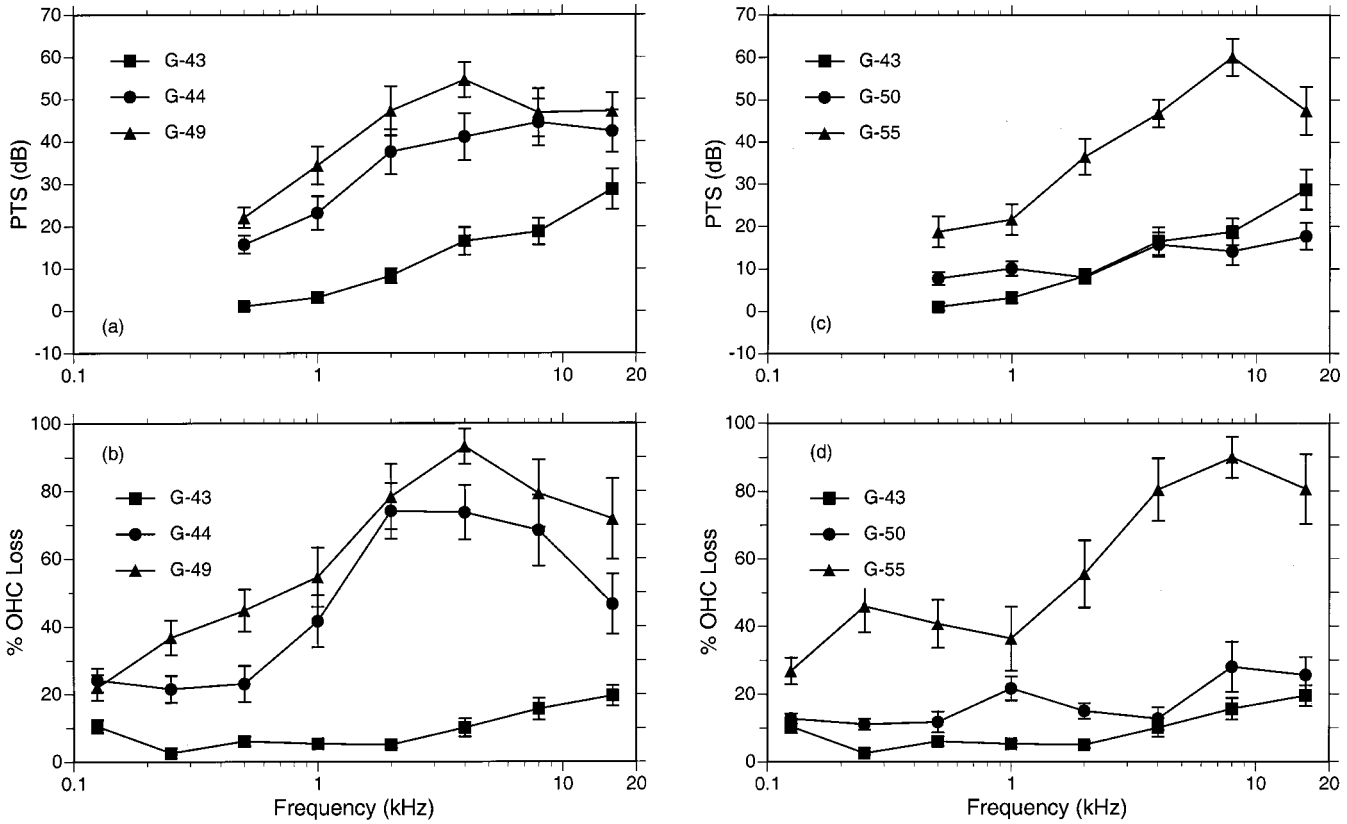

FIG. 4. Each of the upper panels (a) and (c) compares the mean PTS measured in the four groups exposed to the indicated non-Gaussian noise with the group exposed to the energy-equivalent Gaussian noise. The lower panels (b) and (d) show the corresponding mean percent OHC loss computed over adjacent octave band lengths of the basilar membrane in these groups.

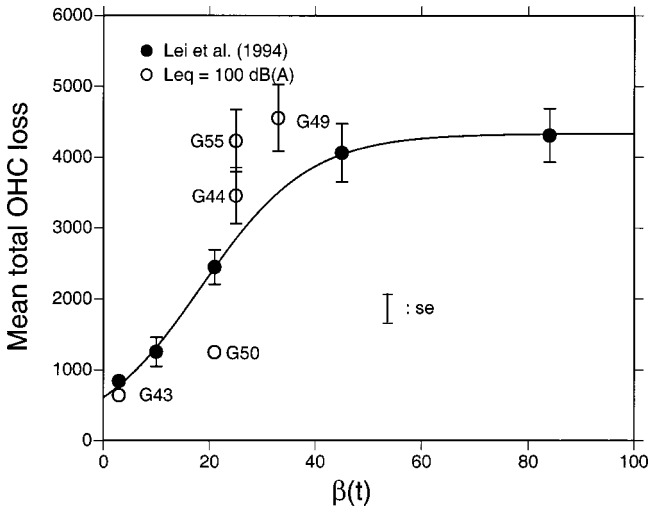

FIG. 5. The group mean total OHC loss in each of the five experimental groups as a function of $\beta(t)$ compared to similar data taken from Lei *et al.* (1994).

OHC losses for each group, but were greater in each of the non-Gaussian exposures than in the Gaussian.

A slightly different perspective on these data is shown in Fig. 5, where the total group mean OHC loss is plotted as a function of $\beta(t)$ and compared to the results of Lei *et al.* (1994). Seen in this figure, for similar values of $\beta(t)$, is the steady increase in sensory cell loss in groups G-50, G-44, and G-55 as the spectrum of the impact transient in the non-Gaussian noise is widened. The OHC loss for the G-50 exposure, having only 400-Hz bandwidth transients, approaches the loss seen in the $\beta(t)=3$, Gaussian condition, but is significantly larger (*t*-test, $\alpha=0.05$). Despite the different bandwidths of the impacts the total energy of only the transients in the G-44, G-50, and G-55 non-Gaussian conditions was approximately the same $[L_{eq}=98\,\text{dB(A)}]$ but the cell loss increased nevertheless.

In order to increase $\beta(t)$ for exposure group G-49, L_b was reduced to 92 dB(A). The other exposure variables were similar to those of group G-55. Although the increase in $\beta(t)$ was modest $[\beta(t)=33$ vs $\beta(t)=25]$, there was a small increase in the mean OHC loss consistent with the trends in the Lei *et al.* (1994) data. This difference was, however, not statistically significant.

The relation between the OHC loss in consecutive octave bands along the basilar membrane and the variable $\beta(f)$ computed on the filtered octave band noise signal is shown in Fig. 6. In this figure the percent OHC loss data represents the difference in the percent loss, in consecutive octave band lengths of the basilar membrane, between the indicated non-Gaussian group and the Gaussian group. There is a clear suggestion that, for those exposures that did produce substantial sensory cell loss, the profile of OHC loss difference and $\beta(f)$ are somewhat congruent, with the cell loss profile shifted about an octave to the high frequencies relative to the $\beta(f)$ profile. This is in agreement with the results of Lei *et al.* (1994). For group G-50 there is comparatively little difference in octave band percent OHC loss and it is scattered along the length of the basilar membrane. This profile of cell loss difference bears no resemblance to $\beta(f)$.

IV. DISCUSSION

The equal energy hypothesis (EEH) had its origins in the retrospective studies of populations exposed to industrial noise (Burns and Robinson, 1970; Robinson, 1976). Originally applied to steady-state noise exposures, the EEH was extended to encompass industrial impact noise by Martin (1976). The EEH now forms the foundation of the current international noise exposure standard (ISO-1999, 1990). A number of studies both experimental and demographic (see, e.g., Lei *et al.*, 1994) indicate that the EEH is not an adequate predictor of NIHL. The results of Lei *et al.* showed that in addition to an energy metric, the kurtosis of an exposure stimulus which is a statistical metric incorporating both the temporal and amplitude characteristics of the noise needs to be considered in the prediction of the hazards of an exposure. The data presented in this paper are an extension of the results of Lei *et al.* (1994) and are in agreement with their results. These data show that for non-Gaussian noises the kurtosis of the amplitude distribution computed on the filtered and unfiltered temporal signal provides information on

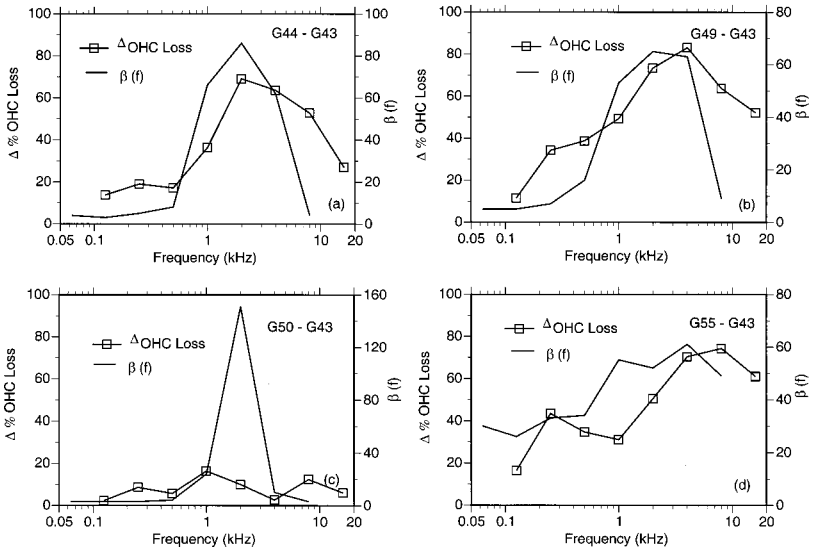

FIG. 6. The difference between the percent OHC loss produced by the indicated non-Gaussian and Gaussian exposure conditions computed over octave band lengths of the basilar membrane is shown and compared with the frequency specific kurtosis, $\beta(f)$, profile.

hazardous noise exposures that cannot be obtained from the L_{eq} metric. The exposures used by Lei *et al.* had an overall $L_{eq}=100$ dB; those in the present study had an $L_{eq}=100$ dB(A), a relatively minor difference which is emphasized by the same OHC loss following exposure to the two reference $\beta(t)=3$ conditions shown in Fig. 5. The other eight data points in this figure represent the results of exposures that all had approximately the same L_{eq}. Each of these exposures produced more severe OHC loss than the Gaussian noise conditions. Clearly L_{eq} is not sufficient for the estimation of the hazard of exposure to this limited set of non-Gaussian noise exposures.

These data also address the proposition of Martin (1976) and others who advocate the application of an L_{eq} metric for the evaluation of impact noise. Consider in Fig. 5 the four data points associated with the $20<\beta(t)<25$ exposures. The L_{eq} of just the transients in each of these exposures is roughly the same [97–98 dB(A)]. The transients in three of the exposures (G-50, G-44, and G-55) are impacts, while in the Lei *et al.* (1994) data point they are broadband Gaussian noise bursts. The three impact-containing exposures differ appreciably only in the frequency content of the impacts; nevertheless, each of these exposures produces a different level of OHC loss which systematically increases as the bandwidth of the impacts increase. Similarly, the exposure G-55 and the Lei *et al.* (1994), $\beta(t)=21$ exposure differ only in the nature of the transient, i.e., impulses in the former and noise bursts in the latter. In both cases, while the OHC loss is greater than in the Gaussian reference condition, there is a significant difference between the two non-Gaussian data points with the impact containing stimulus causing much greater OHC loss.

ACKNOWLEDGMENTS

This work was supported by Grant No. 1-R01-OH02317 from the National Institute for Occupational Safety and Health. The able technical assistance of George A. Turrentine, Ann Johnson, and Diane Fresch is greatly appreciated. In conducting the research described in this study, the investigators adhered to the ''Guide for the Care and Use of Laboratory Animals,'' prepared by the Committee on Care and Use of Laboratory Animals of the Institute of Laboratory Animal Resources, National Research Council [DHHS Publication No. (NIH) 86-23, revised 1985].

Ahroon, W. A., Hamernik, R. P., and Davis, R. I., (**1993**). ''Complex noise exposures: An energy analysis,'' J. Acoust. Soc. Am. **93**, 997–1006.

ANSI (**1996**). ANSI S3.44-1996, ''American National Standard Determination of Occupational Noise Exposure and Estimation of Noise-induced Hearing Impairment'' (American National Standards Institute, New York).

Burns, W., and Robinson, D. W. (**1970**). *Hearing and Noise in Industry* (Her Majesty's Stationery Office, London).

Clark, W. W., Bohne, B. A., and Boettcher, F. A. (**1987**). ''Effects of periodic rest on hearing loss and cochlear damage following exposure to noise,'' J. Acoust. Soc. Am. **82**, 1253–1264.

Dunn, D. E., Davis, R. R., Merry, C. J., and Franks, J. R. (**1991**). ''Hearing loss in the chinchilla from impact and continuous noise exposure,'' J. Acoust. Soc. Am. **90**, 1979–1985.

Dwyer, R. F. (**1984**). ''Use of the kurtosis statistic in the frequency domain as an aid in detecting random signals,'' IEEE J. Ocean. Eng. **OE-9**(2), 85–92.

Erdreich, J. (**1986**). ''A distribution based definition of impulse noise,'' J. Acoust. Soc. Am. **79**, 990–998.

Hamernik, R. P., and Qiu, W. (**2000**). ''Correlations among evoked potential thresholds, distortion product otoacoustic emissions, and hair cell loss following various noise exposures in the chinchilla,'' Hear. Res. **150**, 245–257.

Hsueh, K. D., and Hamernik, R. P. (**1990**). ''A generalized approach to random noise synthesis: Theory and computer simulation,'' J. Acoust. Soc. Am. **87**, 1207–1217.

Hsueh, K. D., and Hamernik, R. P. (**1991**). ''Performance characteristics of a phase domain approach to random noise synthesis,'' Noise Control Eng. J. **36**, 18–32.

ISO-1999 (**1990**). International Organization for Standardization. ''Acoustics: Determination of occupational noise exposure and estimation of noise-induced hearing impairment,'' ISO-1999, Geneva.

Lei, S-F., Ahroon, W. A., and Hamernik, R. P. (**1994**). ''The application of frequency and time domain kurtosis to the assessment of hazardous noise exposures,'' J. Acoust. Soc. Am. **96**, 1435–1444.

Martin, A. (**1976**). ''The equal energy concept applied to impulse noise,'' in *Effects of Noise on Hearing*, edited by D. Henderson, R. P. Hamernik, D. S. Dosanjh, and J. Mills (Raven, New York), pp. 421–453.

Passchier-Vermeer, W. (**1983**). ''Measurement and rating of impulse noise in relation to noise-induced hearing loss,'' in *Proceedings of the 4th International Congress—Noise as a Public Health Hazard*, edited by G. Rossi (Torino, Italy), pp. 143–157.

Robinson, D. W. (**1976**). ''Characteristics of occupational noise-induced hearing loss,'' in *Effects of Noise on Hearing*, edited by D. Henderson, R. P. Hamernik, D. S. Dosanjh, and J. H. Mills (Raven, New York), pp. 383–405.

Sulkowski, W. J., Kowalska, S., and Lipowczan, A. (**1983**). ''Hearing Loss in Weavers and Drop-Forge Hammermen: Comparative Study on the Effects of Steady-State and Impulse Noise,'' in *Proceedings of the 4th International Congress—Noise as a Public Health Hazard*, edited by G. Rossi (Edizioni Tecniche a cura del Centro Ricerche E Studi Amplifon, Milano Italy), pp. 171–184.

Thiery, L., and Meyer-Bisch, C. (**1988**). ''Hearing loss due to partly impulsive industrial noise exposure at levels between 87 and 90 dB(A),'' J. Acoust. Soc. Am. **84**, 651–659.

Towards a measure of auditory-filter phase response

Andrew J. Oxenham[a)]
Research Laboratory of Electronics, Massachusetts Institute of Technology, Cambridge, Massachusetts 02139

Torsten Dau[b)]
Hearing Research Center, Department of Biomedical Engineering, Boston University, 44 Cummington Street, Boston, Massachusetts 02215

(Received 19 February 2001; revised 22 June 2001; accepted 4 September 2001)

This study investigates how the phase curvature of the auditory filters varies with center frequency (CF) and level. Harmonic tone complex maskers were used, with component phases adjusted using a variant of an equation proposed by Schroeder [IEEE Trans. Inf. Theory **16**, 85–89 (1970)]. In experiment 1, the phase curvature of the masker was varied systematically and sinusoidal signal thresholds were measured at frequencies from 125 to 8000 Hz. At all signal frequencies, threshold differences of 20 dB or more were observed between the most effective and least effective masker phase curvature. In experiment 2, the effect of overall masker level on masker phase effects was studied using signal frequencies of 250, 1000, and 4000 Hz. The results were used to estimate the phase curvature of the auditory filters. The estimated relative phase curvature decreases dramatically with decreasing CF below 1000 Hz. At frequencies above 1000 Hz, relative auditory-filter phase curvature increases only slowly with increasing CF, or may remain constant. The phase curvature of the auditory filters seems to be broadly independent of overall level. Most aspects of the data are in qualitative agreement with peripheral physiological findings from other mammals, which suggests that the phase responses observed here are of peripheral origin. However, in contrast to the data reported in a cat auditory-nerve study [Carney *et al.*, J. Acoust. Soc. Am. **105**, 2384–2391 (1999)], no reversal in the sign of the phase curvature was observed at very low frequencies. Overall, the results provide a framework for mapping out the phase curvature of the auditory filters and provide constraints on future models of peripheral filtering in the human auditory system. [DOI: 10.1121/1.1414706]

PACS numbers: 43.66.Dc, 43.66.Nm [SPB]

I. INTRODUCTION

One of the earliest and most fundamental stages of auditory processing is the frequency analysis that takes place in the cochlea. This stage has often been likened to a bank of overlapping bandpass filters, and much effort has gone into characterizing the magnitude response of these ''auditory filters'' (e.g., Fletcher, 1940; Zwicker *et al.*, 1957; Plomp, 1964; Patterson, 1976; Houtgast, 1977; Glasberg and Moore, 1990). In contrast, the phase response of the auditory filters has received much less attention. This may be due in part to the longstanding belief that the ear is essentially ''phase deaf'' (Helmholtz, 1954), and that in many situations auditory perception can be understood in terms of the power spectrum of a stimulus (i.e., by discarding the phase information). Although a number of studies have since shown that the ear is sensitive to changes in stimulus phase both within an auditory filter (Mathes and Miller, 1947; Zwicker, 1952; Goldstein, 1967) and, to a lesser extent, across filters (Patterson, 1987), they have mostly assumed either implicitly or explicitly that any effect of the auditory filters themselves on the stimulus phase can be ignored. In many circumstances, the phase response of the auditory system is indeed irrelevant. Also, there are only certain aspects of the phase response that have any psychophysically measurable influence. For instance, both the absolute phase, θ, and the group delay, $d\theta/df$, are generally only meaningful in the context of a fixed time reference and cannot be estimated psychophysically (Goldstein, 1967; Kohlrausch and Sander, 1995). When defining individual auditory filters, the first term that has any psychophysical relevance is the phase curvature, $d^2\theta/df^2$, which is the rate of change of group delay as a function of frequency.

Following from the work of Smith *et al.* (1986), Kohlrausch and Sander (1995) provided instances in which it is clear that the phase response of the auditory filters cannot be ignored. They used equal-amplitude harmonic tone complexes with the phases set according to an equation proposed by Schroeder (1970), which have come to be known as Schroeder-phase stimuli. These stimuli are characterized by very flat temporal envelopes and can be thought of as repeating rising (Schroeder negative, or m_-) or falling (Schroeder positive, or m_+) linear frequency sweeps. It has been found that when these stimuli are used as maskers they can produce pure-tone masked thresholds that differ by more than 20 dB, with the m_+ stimulus generally producing the lower threshold. Schroeder-phase stimuli have constant phase curvature, implying that the frequency sweep rate is constant (see Kohlrausch and Sander, 1995, Fig. 2). It has been proposed that the positive phase curvature of the m_+ stimulus interacts

a)Electronic mail: oxenham@mit.edu
b)Present address: Medizinische Physik, Universität Oldenburg, 26111 Oldenburg, Germany. Electronic mail: torsten.dau@medi.physik.uni-oldenburg.de

with the phase curvature of the auditory filter to produce a highly modulated filtered waveform with a phase curvature close to zero, such as a sine-phase complex. This implies that the curvature of the auditory filter must be negative, so that it compensates in some degree for the positive curvature of the m_+ masker. In the case of the m_- stimulus, the negative curvature of the stimulus is simply increased by the auditory filter, resulting in a filtered waveform that still has a relatively flat temporal envelope. The argument that signal thresholds are related to the degree of modulation of the masker waveform after auditory filtering was supported by the finding that m_+ maskers generally produce much more modulated masking period patterns than do m_- maskers, suggesting that the m_+ maskers produce highly modulated, or ''peaky'', waveforms after cochlear filtering, while the response to m_- stimuli is characterized by much flatter filtered waveforms (Kohlrausch and Sander, 1995).

Psychophysical results from studies using Schroeder-phase stimuli in normal-hearing listeners have suggested that the phase curvature of the auditory filters is negative at all frequencies tested so far (Smith *et al.*, 1986; Kohlrausch and Sander, 1995; Carlyon and Datta, 1997a, b). This conclusion can be compared qualitatively with measures of cochlear phase response in the physiological literature. Evidence for negative phase curvature in the chinchilla peripheral auditory system has been found at the level of the basilar membrane (BM) (Ruggero *et al.*, 1997; Rhode and Recio, 2000). Similarly, in the guinea pig, negative curvature in the form of an upward frequency glide in the BM impulse response has been reported by de Boer and Nuttall (1997). While the sign of the curvature from these studies is consistent with that found psychophysically, a quantitative comparison is made difficult by the fact that all these BM data were recorded from the basal, or high-frequency, end of the cochlea, at characteristic frequencies (CFs) well above the signal frequencies studied in psychophysical experiments so far. Carney *et al.* (1999) analyzed the responses of auditory-nerve fibers in the cat, which allowed the examination of a wide range of CFs. They also found evidence of a frequency glide in the impulse response, indicating a nonzero phase curvature. However, an upward frequency glide, consistent with negative phase curvature, was found only for auditory-nerve fibers with CFs above about 1.5 kHz. Around 1 kHz, no glide was apparent, and below about 750 Hz a downward frequency glide was observed, indicating positive phase curvature at low CFs. A similar, albeit less clear, trend can be observed in the phase response curves from the cat auditory-nerve data of Pfeiffer and Molnar (1970). In contrast, auditory-nerve data from the squirrel monkey seem to indicate no reversal of phase curvature at low CFs; instead, data from CFs of 200 and 1000 Hz both show essentially zero phase curvature (Anderson *et al.*, 1970). In some of the few BM data available from the apical turn of the cochlea (Cooper and Rhode, 1996), there appears to be no significant curvature in the phase response of the guinea pig at a place along the BM with a CF of around 400 Hz. Due to the sparsity of data, however, it is not clear whether these differences represent true species differences or simply measurement uncertainty.

The data from Carney *et al.*, together with other phase data from the BM or auditory nerve, have recently been analyzed by Shera (2001a). He concluded that, once normalized for CF, the frequency glides in the impulse responses were relatively constant across different species and across CF, at least above about 1.5 kHz. He referred to the regions above and below 1.5 kHz (in the cat) as the ''scaling'' and ''non-scaling'' regions, respectively. The cat's hearing extends to approximately 50–60 kHz. If we assume that the mechanics of the cat and human cochlea are similar to within a scale factor (Greenwood, 1990), the transition frequency of between 1 and 1.5 kHz found by Carney *et al.* in the cat may correspond to a frequency of around 300 to 500 Hz in humans. No behavioral estimates of phase curvature have been made below 500 Hz in humans so far. Furthermore, behavioral estimates of phase curvature at higher frequencies have not been sufficiently extensive for any general conclusions to be drawn on whether the phase response in humans scales with CF at higher frequencies.

The present study had two main aims. The first aim was to estimate the phase curvature of the auditory filters over a wide range of center frequencies. If the mechanics of the human cochlea are similar to those of the cat, a reversal in the sign of the phase curvature might be expected at very low signal frequencies. More generally, a knowledge of the phase properties of the auditory filters will be important in modeling the human auditory periphery. As pointed out by others (e.g., de Boer and Nuttall, 1997), the temporal properties of the BM responses in various animals provide very strong constraints for models of cochlear mechanics. The second aim of the study was to investigate whether, and how, phase curvature changes as a function of level. One consistent feature of physiological measures of phase curvature is their level invariance (for a recent review and theoretical implications, see Shera, 2001b). This feature has not yet been tested behaviorally in humans.

II. EXPERIMENT 1. EFFECTS OF SIGNAL FREQUENCY ON ESTIMATED PHASE CURVATURE

A. Methods

1. Stimuli

Thresholds were measured for a sinusoidal signal in the presence of a harmonic tone complex masker. The masker had a total duration of 320 ms and was gated on and off with 30-ms raised-cosine ramps. The signal was temporally centered within the masker and had a total duration of 260 ms, gated with 50-ms raised-cosine ramps. The signal frequency (f_s) was selected from octave frequencies between 125 and 4000 Hz. The signal was added to the masker with a starting phase that was selected randomly from trial to trial. The masker always comprised components between $0.4f_s$ and $1.6f_s$. This bandwidth was chosen because Oxenham and Dau (2001) found that only components within this range contributed to the threshold of a 2-kHz signal in an m_+ masker. The phases of the components were selected according to a modification of Schroeder's (1970) equation, as suggested by Lentz and Leek (2001):

$$\theta_n = C\pi n(n-1)/N, \quad -1 \leqslant C \leqslant 1. \tag{1}$$

A Schroeder positive (m_+) or Schroeder negative (m_-) complex is generated when $C=1$ or $C=-1$, respectively. When $C=0$, a sine-phase complex is generated. The phase curvature of the complex was

$$\frac{d^2\theta}{df^2} = C\frac{2\pi}{Nf_0^2}. \tag{2}$$

By varying the C value from -1 to 1, a range of masker phase curvatures, or frequency sweep rates, can be generated (see also Schreiner *et al.*, 1983, and Mehrgardt and Schroeder, 1983). In one set of conditions, signal frequencies of 125, 250, 500, and 1000 Hz were tested and the masker fundamental frequency (f_0) was set to $0.1f_s$. At signal frequencies of 250 and 1000 Hz, two other masker f_0's were also tested: 12.5 and 50 Hz at 250 Hz, and 25 and 50 Hz at 1000 Hz. At signal frequencies of 2000 and 4000 Hz, the masker f_0 was set to 50 Hz. Signal thresholds were measured for values of C between -1 and 1 in steps of 0.25. The overall level of the masker was 75 dB SPL. For the most common case of 13 components (when $f_0=0.1f_s$) this corresponded to a level of about 64 dB SPL per component.

The stimuli were generated digitally and played out using a LynxOne (LynxStudio) sound card with 16-bit resolution at a sampling rate of 32 kHz. The stimuli were passed through a programmable attenuator (TDT PA4) and headphone buffer (TDT HB6) before being presented to the listener's left ear via Sennheiser HD 580 headphones. Listeners were seated in a double-walled sound-attenuating booth.

2. Procedure

An adaptive three-interval, three-alternative, forced-choice procedure was used in conjunction with a 2-down, 1-up tracking rule to estimate the 70.7%-correct point on the psychometric function (Levitt, 1971). Each interval in a trial was separated by an interstimulus interval (ISI) of 500 ms. The intervals were marked on a computer monitor and feedback was provided after each trial. Listeners responded via the computer keyboard or mouse. The initial step size was 5 dB, which was reduced to 2 dB after the first four reversals. Threshold was defined as the mean of the remaining six reversals. Three threshold estimates were initially made for each condition. If the standard deviation across the three runs was greater than 4 dB, another three estimates were made and the mean of all six was recorded. The conditions were run using a randomized blocked design, with all conditions within one repetition being presented before embarking on the next repetition. The order of presentation of the conditions was selected randomly for each listener and each repetition. Once a signal frequency and masker f_0 had been selected, all the C values for that condition were tested in random order before the next condition was run. Measurements were made in 2-h sessions, including many short breaks. No more than one session per listener was completed in any one day.

3. Listeners

The four listeners (one male—PG) were all paid for their participation. Their ages ranged from 20 to 29 years (mean 23 years). All had absolute thresholds of less than 15 dB HL at octave frequencies between 250 and 8000 Hz and had previously taken part in a similar experiment. All were given between 1 and 2 h further practice before data were collected.

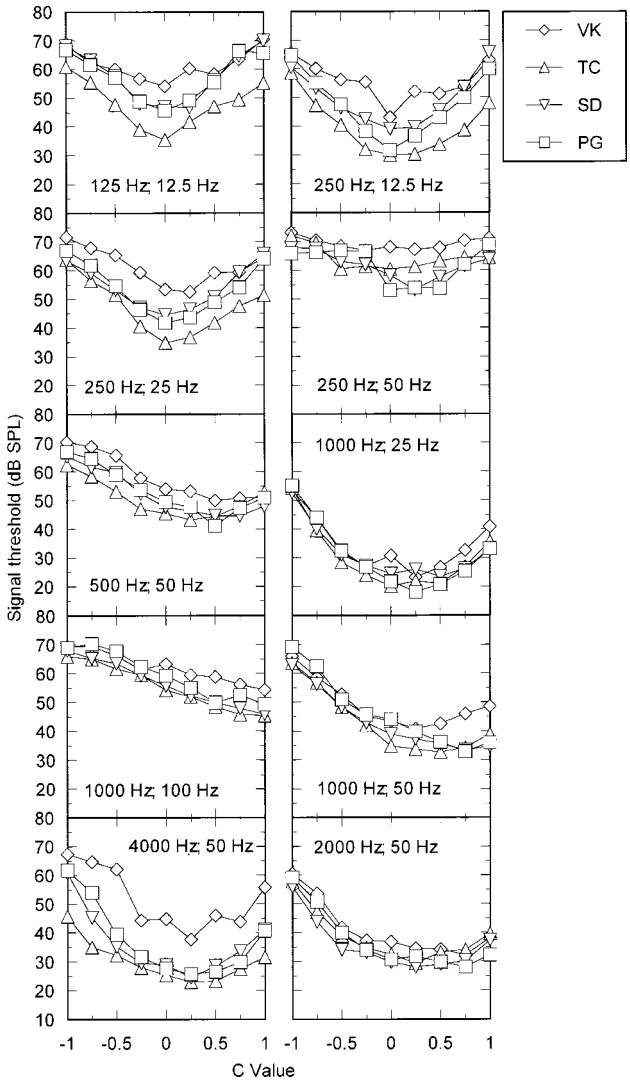

FIG. 1. Individual data from all the conditions tested in experiment 1. The first and second number in each panel denote the signal frequency and the fundamental frequency of the masker, respectively.

B. Results

The individual data from all conditions are shown in Fig. 1, with signal threshold plotted as a function of masker C value. The first and second numbers in the panel captions denote the signal frequency and the masker f_0, respectively. There are some considerable individual differences in masked threshold values. However, the trends in the data are very similar across listeners. For this reason, the discussion of the data will refer solely to the mean values.

In interpreting these data, it is assumed that the minimum in masking is achieved when the phase curvature of the stimulus is equal in magnitude but opposite in sign to the phase curvature of the auditory filter centered at the signal frequency. In this way, the minimum threshold is achieved

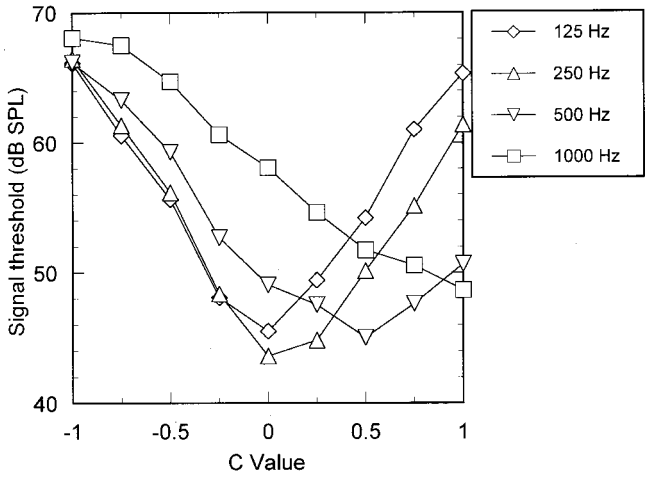

FIG. 2. Mean data showing masked thresholds as a function of masker phase curvature at four signal frequencies. The masker bandwidth and fundamental frequency were always proportional to the signal frequency.

when the filtered waveform most closely resembles a sine-phase complex and is maximally peaky. In support of this assumption, Kohlrausch and Sander (1995) have shown a strong correlation between the peakiness of a filtered waveform (as estimated using masking period patterns) and the threshold for a long-duration sinusoidal signal in a given masker. The second assumption is that the phase curvature of the auditory filters can be approximated as constant within the filter passband. This assumption seems to be valid for all mammalian species studied so far. For instance, Carney *et al.* (1999) found that the instantaneous frequency glides from their cat auditory-nerve impulse responses were well fitted with straight lines, thereby implying a constant phase curvature. This conclusion is also supported by de Boer and Nuttall's (1997, 2000a, b) guinea pig BM data, as analyzed by Shera (2001a). A plot of group delay as a function of frequency at any given CF (Shera's Fig. 4) shows that the group delay can be reasonably well approximated by a straight line for frequencies above about half an octave below CF. A straight line on these coordinates implies constant curvature. Finally, it is important to note that, in contrast to stimuli with maximally ''flat'' envelopes (Schroeder, 1970; Hartmann and Pumplin, 1988), the phase relationships producing the maximally peaky envelope do not depend on the magnitudes of the components. In other words, for a given masker, the magnitude spectrum of the auditory filter, the headphones, and the outer/middle-ear transform, should not affect the value of C at which the minimum threshold occurs.

The data are discussed in the following three sections. The first examines conditions in which the f_0 and masker bandwidth were proportional to the signal frequency; the second examines the effects of changing f_s while f_0 is held constant at 50 Hz; the third examines the effects of changing f_0 while keeping f_s fixed at 250 or 1000 Hz.

1. Effects of signal frequency with a variable f_0: A test of scaling symmetry at low CFs

Figure 2 shows the mean data for signal frequencies of 125, 250, 500, and 1000 Hz. The masker f_0 was always $0.1f_s$. Thresholds are plotted as a function of C value, and the different symbols represent different signal frequencies, as shown in the legend. There are large variations in threshold as a function of masker phase at all signal frequencies; all curves have maximum masking differences of at least 20 dB. As the total number of masker components is constant in these four conditions ($N=13$), the phase curvature of the masker is inversely proportional to the square of the signal frequency [see Eq. (2)]. This inverse-square relationship is also what would be expected of filters with scaling symmetry (Kohlrausch and Sander, 1995; Shera, 2001a). In other words, if the auditory filters were of constant shape and bandwidth when plotted on a logarithmic frequency axis (e.g., constant-Q filters), their phase curvature would be expected to vary inversely with the square of the filter CF. Therefore, if scaling symmetry applied to auditory filters with CFs between 125 and 1000 Hz, all four curves shown in Fig. 2 should have the same value of C at the point of minimum masking. This is clearly not the case. Instead, the masking minimum at 1 kHz occurs at (or above) $C=1$, and there is a rapid trend for the C value to decrease with decreasing signal frequency, such that at 125 and 250 Hz, the minimum appears to lie at or close to $C=0$. Interestingly, at 125 and 250 Hz, the functions are very similar for $C<0$, but diverge somewhat for $C>0$. This point is discussed further in Sec. IV.

In some respects the results are consistent with physiological estimates of cochlear phase response. Shera has pointed out that approximate scaling symmetry appears to hold at frequencies above about 1.5 kHz in the cat, but not below. As the signal frequencies in Fig. 2 were all below 1.5 kHz, one might not expect to find scaling symmetry in the phase curvature. In other respects, however, our data are not consistent with physiological findings, at least in the cat. As mentioned in the Introduction, Carney *et al.* (1999) found that the sign of the phase curvature reversed at frequencies below about 1000 Hz. Such a reversal would be manifest by negative C values at the point of minimum masking. Our data, down to 125 Hz, show no evidence for such a reversal. Instead, the phase curvature tends to zero at the lowest signal frequencies. It is not clear whether this difference is due to the different techniques (physiological vs behavioral) or whether it reflects true species differences. As mentioned in the Introduction, the fact that the available data from squirrel monkey (Anderson *et al.*, 1970) also seem to show zero curvature at low CFs leaves open the possibility of species differences.

2. Effects of signal frequency with a fixed masker f_0: A test of scaling symmetry at higher CFs

Figure 3 shows the mean data for the five signal frequencies, including 2000 and 4000 Hz, tested with a fixed masker f_0 of 50 Hz. A general trend is that the maximum masking difference increases with increasing signal frequency. This is expected, as the bandwidth of the auditory filters increases with increasing CF while, in this case, the f_0 or component density remains constant. For these conditions, a doubling of f_s leads to a doubling of N, as the absolute

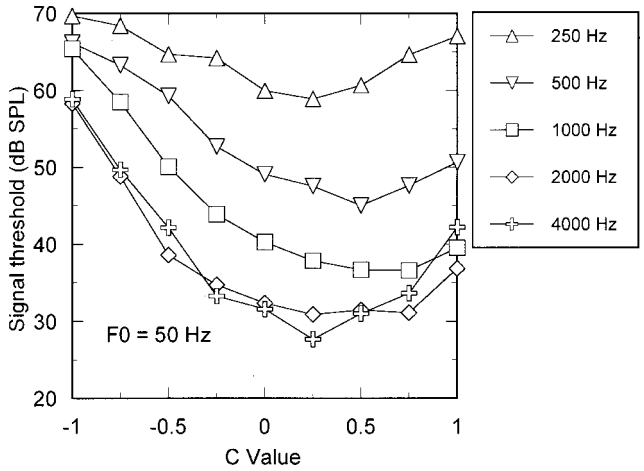

FIG. 3. Mean data showing masked thresholds as a function of masker phase curvature at five signal frequencies, from 250 to 4000 Hz. The masker bandwidth was proportional to the signal frequency, but the masker fundamental frequency was held constant at 50 Hz.

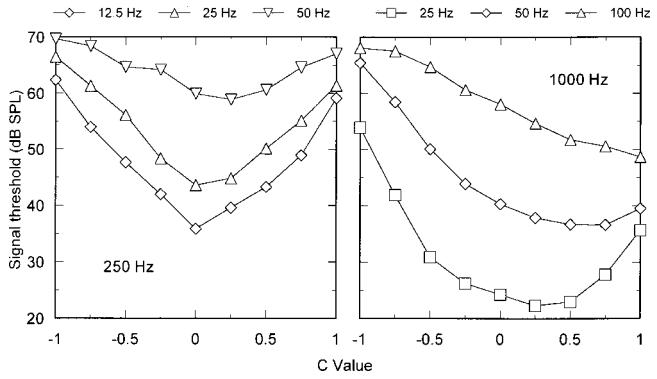

FIG. 4. Mean thresholds as a function of masker curvature at signal frequencies of 250 Hz (left panel) and 1000 Hz (right panel). Values given in the legend represent the masker fundamental frequencies tested.

bandwidth of the masker doubles. Therefore, if the auditory filters exhibited scaling symmetry, then the C value at the point of minimum masking should double with every halving of f_s. There is some indication of this type of relationship between 1000 and 4000 Hz, in that the C value of the minimum decreases with increasing f_s. However, as in Fig. 2, this relationship breaks down for f_s lower than 1000 Hz, with the C value at the minimum actually moving in the opposite direction. The results from the two highest signal frequencies provide some indication that auditory filters with CFs above about 1000 Hz may exhibit some form of scaling symmetry, as has also been found in the cat above about 1.5 kHz. However, as this conclusion is based on only two signal frequencies it must be treated with some caution. A further condition at a signal frequency of 8 kHz was tested on a new group of listeners after the original data had been collected. These data are described in Sec. II C.

3. Effects of masker f_0: A test of consistency

If the point of minimum masking is determined by the interaction between the phase curvature of the masker and the auditory filter then, for a given signal frequency, the masker C value at the threshold minimum should vary with masker f_0 in a predictable manner. Specifically, a doubling of f_0 should lead to a doubling of the C value at the minimum. (As the masker bandwidth is fixed, N is approximately inversely proportional to f_0, leading to the phase curvature being inversely proportional to f_0, rather than f_0^2.) In this way the data provide a consistency test of the hypothesis underlying this work, as well as providing multiple estimates of phase curvature at a given signal frequency.

Figure 4 shows the mean data for signal frequencies of 250 Hz (left panel) and 1000 Hz (right panel) as a function of masker C value. The different symbols denote different masker f_0's. Data in the right panel ($f_s = 1000$ Hz) are in broad agreement with expectations: a doubling of f_0 from 25 to 50 Hz leads to an increase in the C value at the minimum from about 0.25 to between 0.5 and 0.75. Another doubling from 50 to 100 Hz leads to the minimum point being found at $C = 1$ (or above). Data in the left panel (250 Hz) show C values of 0 at the minimum for f_0's of 12.5 and 25 Hz, but a minimum of around 0.25 for an f_0 of 50 Hz. This is also consistent with the above prediction, and suggests that the "true" minima at the two lower f_0's lie somewhere between $C = 0$ and $C = 0.25$. Finally, the data in Fig. 4 replicate the earlier finding (Kohlrausch and Sander, 1995) that increases in masker f_0 lead to decreases in the maximum masking differences observed.

Supplemental experiments were carried out with signal frequencies of 125 and 250 Hz, using a number of masker C values between -0.25 and 0.25, in an effort to more closely define the point of minimum masker. However, the resulting masking functions were too flat to specify the minimum with any degree of accuracy.

C. Masking with a signal frequency of 8 kHz

The data in Fig. 3 indicate that the phase curvature of the auditory filters may scale with CF for signal frequencies above about 1 kHz. However, this conclusion is based only on data from 2 and 4 kHz. To extend these findings, data were collected from four new listeners, aged between 23 and 32 years, who all had normal hearing as defined in experiment 1 and were given at least 2 h training. Each threshold reported is the mean of four estimates. The maskers had the same relative bandwidth as in the original experiment, extending from 0.4 to $1.6 f_s$. The new listeners were tested on a condition with $f_s = 8000$ Hz and $f_0 = 200$ Hz. This is similar to the earlier 2-kHz condition, but scaled upwards by a factor of 4. If scaling symmetry holds for the phase response of the auditory filters between 2000 and 8000 Hz, then the C value producing the minimum threshold should be similar for these two conditions.

The individual (symbols) and mean (solid curve) results from this experiment at 8 kHz are shown in Fig. 5, together with the mean results at 2 kHz, replotted from Fig. 3 (dashed curve). As in previous experiments, there are some considerable individual differences. The individual masking minima tend to lie between C values of 0.25 and 0.75, which is similar to the range found at 2 kHz. Thus, the data do not rule out the possibility that the auditory filter's phase curvature scales with CF above about 1 kHz, although the vari-

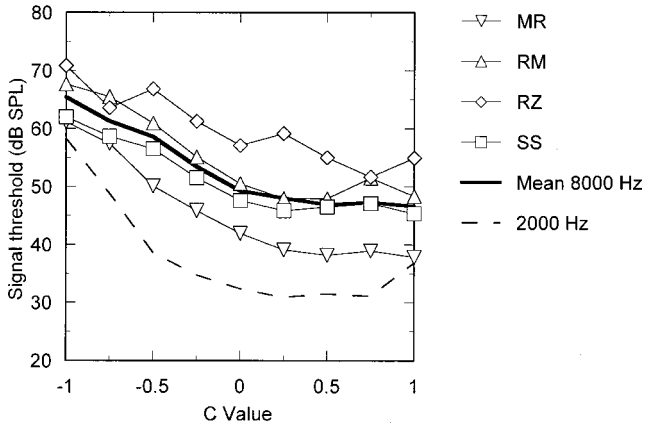

FIG. 5. Individual (symbols) and mean (solid curve) data for a signal frequency of 8000 Hz. The dashed curve denotes mean data with a 2-kHz signal, replotted from Fig. 3.

ability in the data tempers any strong conclusions. Nevertheless, there are certainly no gross deviations from the assumption of scaling symmetry, such as those observed at the lower signal frequencies.

D. Discussion: Role of peripheral compression

Experiment 1 shows that the interaction between the auditory-filter phase curvature and that of the stimulus plays a large role across a very wide range of signal frequencies. The finding of large masking differences even at the lowest frequencies is noteworthy. Physiological and psychophysical data have suggested that compression in the input–output function of the basilar membrane may be reduced or even absent at low CFs (Cooper and Yates, 1994; Hicks and Bacon, 1999; Plack and Oxenham, 2000). It has been shown using the temporal-window model that when some temporal smoothing occurs, peripheral compression is essential in producing large m_-/m_+ masking differences (Oxenham and Dau, 2001). Because of this, the fact that hearing-impaired listeners seem to show little or no phase effects in masking (Summers and Leek, 1998; Summers, 2000) has been interpreted as evidence for the importance of peripheral compression. The present data therefore lead to the conclusion either that compression is still present at low frequencies, or that compression is not necessary to account for the data at low frequencies.

A review of the literature on compression at low frequencies suggests that it may be premature to rule out the possibility that peripheral compression is present at very low frequencies. There are very few reliable data of BM motion in the apical, or low-frequency, end of the cochlea, due to the technical difficulties of measuring there without causing structural damage (Cooper and Rhode, 1996). All the other measures, physiological (Cooper and Yates, 1994) and psychological (Hicks and Bacon, 1999; Plack and Oxenham, 2000), rely on indirect measures. These measures assume that the compression is frequency selective, and that frequencies well below CF are processed linearly. As pointed out by Plack and Oxenham (2000), if the compression at low frequencies were not frequency selective, i.e., if all frequencies were compressed equally, then none of the measures used so far would reveal this compression. There are some physiological indications that this may be the case. For instance, Rhode and Cooper (1996) reported some nonlinear gain in the apical turn of the chinchilla cochlea but showed that, unlike in the basal turn, the gain did not appear to be frequency selective.

On the other hand, the f_0's used in conjunction with the lowest signal frequencies are so low that the period of the stimulus may be large compared with the duration of the temporal window, or smoothing function used to characterize auditory temporal resolution. For instance, at 125 Hz, the f_0 of 12.5 Hz corresponds to a period of 80 ms. This is considerably greater than the hypothesized duration of the temporal window, which is generally assumed to be around 10 ms (e.g., Oxenham and Moore, 1994). As shown by Oxenham and Dau (2001), when the temporal window is small compared with the period of the masker, large masking differences can be predicted without compression, and compression ceases to make much difference in the predictions.

In summary, the large differences in threshold at the lowest signal frequencies do not necessarily imply the presence of peripheral compression. However, they do suggest that hearing-impaired listeners should exhibit large masking differences due to phase changes if sufficiently low f_0's are employed. Preliminary data indicate that hearing-impaired listeners in fact continue to show reduced effects of masker phase even at very low f_0's (Dau and Oxenham, 2001). If confirmed, this finding may provide indirect evidence for peripheral compression at low CFs in normal hearing.

III. EXPERIMENT 2. EFFECTS OF MASKER LEVEL ON ESTIMATED PHASE CURVATURE

The results from experiment 1 showed large effects of masker phase at all signal frequencies tested. Note, however, that the results would have looked rather different if only m_+ and m_- waveforms had been used, corresponding to $C=1$ and $C=-1$, respectively. For instance, no phase effects at a signal frequency of 125 Hz would have been observed at all (see Fig. 2). Earlier studies have shown that masking differences between m_- and m_+ maskers decrease at low levels (Carlyon and Datta, 1997a, b) and are also somewhat reduced at very high levels (Summers and Leek, 1998). It has been hypothesized that this may be due to a reduction in peripheral compression, a narrowing of the auditory-filter bandwidth (at low levels), or a combination of these (Carlyon and Datta, 1997a). While quantitative simulations support both of these hypotheses (Oxenham and Dau, 2001), it remains possible that the phase response of the auditory filters changes with level in such a way that the differences between the filtered m_- and m_+ waveforms are reduced at low and high levels. In other words, the lack of an m_-/m_+ difference at low levels may be due to the two particular phase relationships chosen by past experimenters, rather than to a lack of any phase effects at low levels *per se*.

A second rationale for examining the effects of level stems from physiological results, which suggest that phase curvature in the mammalian cochlea is level invariant (de Boer and Nuttall, 1997; Recio *et al.*, 1998; Carney *et al.*, 1999; de Boer and Nuttall, 2000b). This finding is somewhat

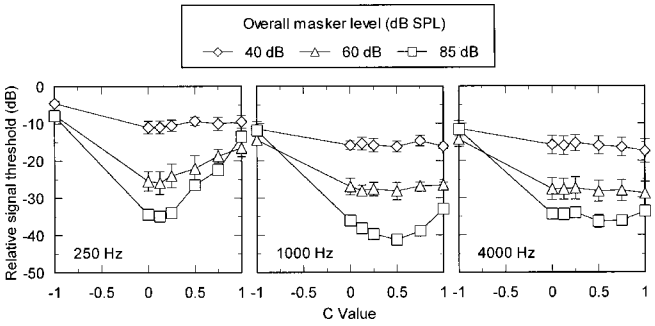

FIG. 6. Mean masked thresholds, relative to the masker component level, as a function of masker curvature at three signal frequencies (250, 1000, and 4000 Hz). Error bars denote ±1 se of the mean across the four listeners. The different symbols denote different overall masker levels.

counterintuitive. In most physical filters, bandwidth and phase response covary. The fact that this seems not to be the case for the mammalian cochlea provides strong constraints for models of peripheral auditory processing (Shera, 2001b). The present experiment was designed to examine whether the same level invariance could be found for the phase curvature in human auditory filters.

A. Methods

The stimuli and procedures were the same as in experiment 1 unless otherwise stated. The masker bandwidth again extended from 0.4 to $1.6f_s$. The masker f_0 was 25, 50, and 100 for signal frequencies of 250, 1000, and 4000, respectively. Each masker was presented at overall levels of 40, 60, and 85 dB SPL. At 250 Hz, this corresponded to a masker component level 11.1 dB lower than the overall level; at 4000 Hz, this difference was 16.7 dB. Equation (1) was used to generate the phases of the masker components, with C values of -1, 0, 0.125, 0.25, 0.5, 0.75, and 1 tested. In pilot tests, it was noticed that distortion products became audible for the highest masker level at 4000 Hz. For this reason, a low-pass Gaussian white noise with a cutoff frequency of 1200 Hz was added to all the 4000-Hz maskers at a spectrum level 15 dB below the average spectrum level of the masker. This was sufficient to mask any audible distortion products. Four female listeners aged between 20 and 43 were paid for their participation in this experiment. One (TC) had taken part in experiment 1. The other three were given at least 2 h practice before data were collected. Their hearing was normal as defined in experiment 1. Each threshold reported is the mean of at least three threshold estimates. If after three estimates the standard deviation was greater than 4 dB, a further three measurements were made and the mean of all six estimates was recorded.

B. Results and discussion

The mean results are shown in Fig. 6. The error bars represent ±1 standard error of the mean. As the signal levels used in this experiment cover a very wide range in terms of dB SPL, Fig. 6 plots signal thresholds relative to masker component level for ease of comparison. The results were similar across listeners, both in terms of general trends and absolute values. It can be seen that relative thresholds are generally lower and vary more with phase at the highest masker level than in the other two conditions. The signal-to-masker ratio at threshold is roughly constant with overall masker level only for the conditions producing the most masking (generally $C=-1$). For other C values, the threshold signal-to-masker ratio varies with masker level by as much as 25 dB. These very large changes in signal-to-masker ratio imply a very gradual growth of masking, more in line with that normally found in forward masking than in simultaneous masking. This is consistent with the idea that thresholds in highly modulated maskers are governed by forward masking of the portions of the signal in the masker's temporal valleys, produced by the masker's temporal peaks (Bacon and Lee, 1997; Oxenham and Plack, 1998).

At the lowest masker level, the fact that thresholds vary so little with masker phase makes it difficult to draw strong conclusions about whether the phase curvature varies with level. However, it is clear that the failure of others (e.g., Carlyon and Datta, 1997b) to find large phase effects at low levels was not due to simply the wrong choice of phases. Instead, it appears that the reduction in phase effects at low levels may indeed be a consequence of reduced peripheral compression and/or narrow filter bandwidth. Where masking minima are apparent in the lower masker-level conditions, they appear to occur at the same C values as at the highest masker level. This suggests that phase curvature does not vary greatly with stimulus level. This is consistent with the findings from impulse responses of auditory-nerve fibers (Carney *et al.*, 1999) and from direct measurements of BM response (de Boer and Nuttall, 1997; Recio *et al.*, 1998).

One caveat should be borne in mind when comparing these data to those from physiological studies. As with studies of auditory-filter shape, we assume for simplicity that the use of a single frequency corresponds to estimating the response of a single CF region. However, due to the basal shift of the peak of the BM traveling wave at high levels, it is likely that the place maximally stimulated by a given frequency shifts somewhat with level. Consistent with all previous auditory-filter studies, however, we assume that the effects of this are of second-order importance. If the accuracy of our phase measurements warranted it, it would be a relatively trivial matter to take the assumed shifts of the traveling wave into account by altering the signal frequency accordingly.

IV. ESTIMATING THE PHASE CURVATURE OF THE AUDITORY FILTERS

Under the assumptions discussed in Sec. II B, the data from these experiments can be used to estimate the phase curvature of the auditory system at octave frequencies between 125 and 8000 Hz. Specifically, it is assumed that the phase curvature in the passband of the auditory filter is equal and opposite to that of the masker at the point of minimum masking. The same technique was used by Lentz and Leek (2001). However, they used only one masker bandwidth (200–5000 Hz) with one f_0 (100 Hz) and tested signal frequencies of 1, 2, 3, and 4 kHz.

The minimum C values (and hence the filter curvatures) were estimated across listeners and conditions from experi-

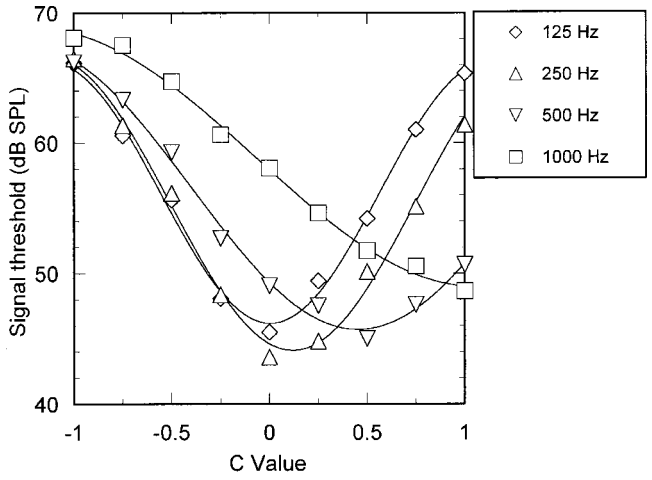

FIG. 7. Data replotted from Fig. 2 with curve fits using a sinusoidal function with four free parameters per condition [$y=A\sin(wx+p)+C$]. The minima of the fitted functions were used to estimate the auditory-filter curvature in method 2 (see the text for details).

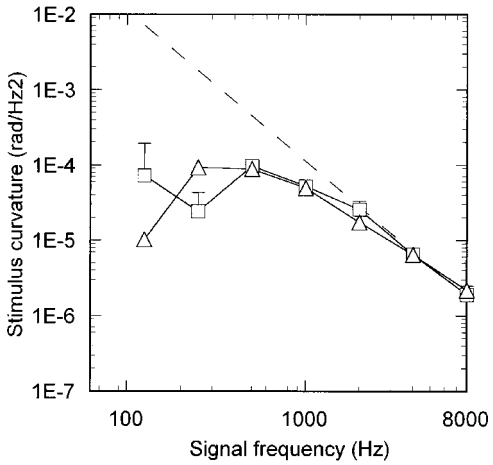

FIG. 8. Mean masker phase curvature producing masking minima, as a function of frequency. Squares and triangles represent estimates using methods 1 and 2, respectively (see the text for details). The slope of the dashed line shows the expected relationship if the auditory filters exhibited scaling symmetry. The error bars for method 1 represent +1 se of the mean and are shown where they exceed the size of the symbol. For method 2, error bars could be calculated only for signal frequencies of 250 and 1000 Hz, and in both cases did not exceed the size of the symbol.

ment 1 using two methods. Method 1 involved finding the C value that produced the lowest masked threshold for each listener individually in each condition. This value was then converted into a value of curvature using Eq. (2). The mean of these values for each signal frequency was then used to estimate the curvature of the auditory filter centered at that frequency. The number of estimates varied with signal frequency. Specifically, at 125, 500, 2000, 4000, and 8000 Hz, only one condition was tested with four listeners, meaning that only four estimates of the curvature were available at each CF. In contrast, at 250 and 1000 Hz, more estimates were available, as three f_0's were tested, giving 12 individual estimates. In the case of the 1000-Hz signal with the 100-Hz f_0, $C=1$ was chosen as the minimum for all listeners, even though it is possible that the ''true'' minimum may have occurred at a slightly higher C value. Eliminating this point did not markedly change the predictions. Overall, the advantage of this method is that it makes no assumptions regarding the form of the data. The disadvantage is that the estimates rely only on points around the minimum of the function and make no use of other data points.

Method 2 involved fitting a function to the mean data in every condition and calculating the C value at the minimum of the fitted function. A number of mathematical functions were tried. A sinusoidal function was found to provide a very good fit to all conditions. The percentage of variance accounted for by this function was always greater than 95% and in most cases was greater than 99%. Examples of the fits are shown in Fig. 7. The symbols are data replotted from Fig. 2; the curves are the best-fitting (in a least-squares sense) sinusoidal functions. The functions capture the main trends of the data. Other less obvious trends are also well described including, for instance, the divergence of thresholds between the 125- and 250-Hz conditions for C values greater than 0. In cases with more than one condition for a given signal frequency, the C values of the function minima were averaged. The main advantage of using a mathematical function is that all the data contribute to estimating the minimum point of the function. The disadvantage is that a function makes certain assumptions about the form of the data (e.g., that it is symmetric about the minimum point), which may not be justified. Because both methods have their strengths and weaknesses, the results from both are presented here.

Figure 8 shows the masker phase curvatures producing a masking minimum, estimated using method 1 (squares) and method 2 (triangles). The estimated phase curvature of the auditory filters has the same magnitude as the data shown in the figure, but with the opposite sign. The slope of the dashed line represents the pattern of results that would be expected if scaling symmetry prevailed throughout the frequency range tested. On first inspection, it seems that scaling symmetry may hold for frequencies above 1000 Hz, but clearly not below. In order to pursue the issue of scaling symmetry further, the estimated phase curvatures were transformed into dimensionless units by multiplying the curvature (originally in units of rad/Hz^2) by $f_s^2/2\pi$ (Shera, 2001a). When expressed in this way, for filters with scaling symmetry the resulting quantity should be constant and independent of CF. The transformed data from Fig. 8 are shown in Fig. 9. The other symbols denote estimates from earlier studies, discussed below. For frequencies above 250 Hz, the two methods are in reasonably good agreement. At the two lowest frequencies, however, the estimates differ considerably. It is interesting to note that the estimated standard errors for method 1 are also greatest at these two frequencies. At 125 Hz, zero phase curvature is less than 1 standard error below the mean from method 1, which is why it is not possible to plot the lower error bars on these logarithmic axes. The pattern of results is in broad agreement with our earlier conclusion that the phase curvature of the auditory filters may exhibit scaling symmetry at CFs from 2 to 8 kHz but departs severely from that pattern below about 1 kHz. However, at least using method 2, there is a trend towards an orderly

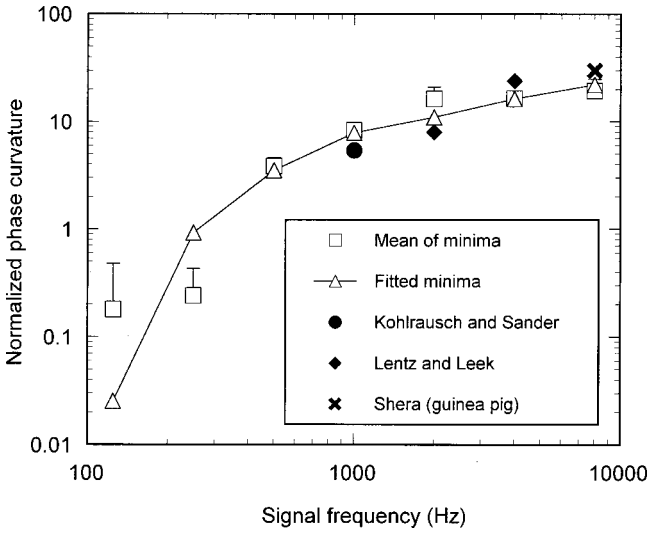

FIG. 9. Data from Fig. 8, transformed into dimensionless units by multiplying by $f_s^2/2\pi$. The filled symbols represent estimates from other studies, as indicated in the legend.

increase in relative curvature with increasing CF, as shown by the connecting lines, even at the higher signal frequencies.

It is possible to compare our estimates of phase curvature with those from two other studies in the literature. Converted into dimensionless units, Kohlrausch and Sander's (1995) estimate of auditory-filter phase curvature at 1100 Hz lies between -4.5 and -6.3 (the mean value is plotted as a filled circle in Fig. 9). Our estimates of -8.3 (method 1) and -7.8 (method 2) at 1000 Hz lie outside that range, but are within a factor of 2, corresponding to a change in C value from, for instance, 0.25 to 0.5. The range of masker phase curvatures used by Lentz and Leek (2001) did not extend sufficiently high to provide an accurate estimate of phase curvature at 1000 Hz. At 2000 and 4000 Hz, their estimated curvatures are around -8 and -24 (see the diamonds in Fig. 9), which are somewhat below and above our estimates, respectively. It is not clear what accounts for these discrepancies, although they may in part be due to individual differences. Also, as the measurement accuracy provided by this method is somewhat limited, a discrepancy by a factor of 2 can probably still be described as within the bounds of measurement uncertainty.

A recent analysis of BM and auditory-nerve phase-response data (Shera, 2001a) allows a cursory quantitative comparison of our results with BM data from the guinea pig. Shera's Fig. 4(b) plots group delay as a function of frequency in dimensionless units for a 17-kHz CF. The slope of the function can be reasonably approximated as constant for frequencies above about 0.7 CF. A linear regression of the function between 0.75 and 1.1 CF provides an estimate of 30 for the phase curvature in dimensionless units. In terms of place along the BM, a 17-kHz CF in the guinea pig corresponds roughly to an 8-kHz CF in human (Tsuji and Liberman, 1997). Thus, the physiological estimate from guinea pig BM data (cross in Fig. 9) and our behavioral estimate in human are in reasonable agreement. However, given the very limited data and their inherent uncertainty, more data are required to ascertain whether the patterns are indeed similar or whether systematic differences between species exist.

Because of the approximate nature of the measure, it is prudent not to place too much emphasis on the exact values reported here. In particular, for method 1 the mean phase curvature values at 125 and 250 Hz are not significantly different from zero. Nevertheless, the finding that the phase curvature does not scale with CF below about 1000 Hz is very robust. This departure from scaling at low CFs may be related to the relative broadening of the magnitude of the auditory filters at CFs below about 1000 Hz (e.g., Glasberg and Moore, 1990).

V. SUMMARY

The results provide a first indication of how the phase curvature of the auditory filters varies with level and characteristic frequency (CF) over a wide range. Experiment 1 showed that the phase responses of the auditory filters do not exhibit scaling symmetry at frequencies of 1000 Hz and below. This is consistent with physiological findings in other mammals (Shera, 2001a), as is the lack of an effect of overall level on estimated phase curvature (Shera, 2001b), found in experiment 2. In contrast to findings from auditory-nerve data in the cat (Carney *et al.*, 1999), however, our data show no evidence for a reversal of phase curvature at very low CFs in humans. It is not clear from our data whether scaling symmetry holds above 1000 Hz. Estimates using method 2 suggest a shallow but continuing increase in relative phase curvature at frequencies of 2 kHz and above, whereas the estimates from method 1 seem to be more constant. It has been argued that the frequency glides found in BM impulse responses provide strong constraints for models of cochlear mechanics (de Boer and Nuttall, 1997, 2000a, b; Shera, 2001a). The present data provide similarly strong constraints on models of human auditory filtering. Recent simulations (Oxenham and Dau, 2001) have shown that many of the filters currently used to simulate peripheral auditory processing, such as the gammatone (de Boer and Kruidenier, 1990), the gammachirp (Irino and Patterson, 1997, 2001), or transmission-line models (e.g., Strube, 1985), do not exhibit the phase curvature necessary to predict such data.

ACKNOWLEDGMENTS

This work was supported by the NIH/NIDCD Grant No. R01 DC 03909 (A.J.O.) and by the Max Kade Foundation and the Deutsche Forschungsgemeinschaft (DFG) (T.D.). The final version of this paper was prepared while the first author was a fellow at the Hanse Institute for Advanced Study in Delmenhorst, Germany. We are grateful to Chris Shera for fruitful discussions and suggestions, and for providing us with the results of his data analysis. Van Summers, Chris Plack, and Jennifer Lentz provided helpful comments on earlier versions of this manuscript. Stephan Ewert provided assistance with the programming.

Anderson, D. J., Rose, J. E., Hind, J. E., and Brugge, J. F. (**1970**). ''Temporal position of discharges in single auditory nerve fibers within the cycle of a sine-wave stimulus: Frequency and intensity effects,'' J. Acoust. Soc. Am. **49**, 1131–1139.

Bacon, S. P., and Lee, J. (**1997**). ''The modulated-unmodulated difference: Effects of signal frequency and masker modulation depth,'' J. Acoust. Soc. Am. **101**, 3617–3624.

Carlyon, R. P., and Datta, A. J. (**1997a**). ''Excitation produced by Schroeder-phase complexes: Evidence for fast-acting compression in the auditory system,'' J. Acoust. Soc. Am. **101**, 3636–3647.

Carlyon, R. P., and Datta, A. J. (**1997b**). ''Masking period patterns of Schroeder-phase complexes: Effects of level, number of components, and phase of flanking components,'' J. Acoust. Soc. Am. **101**, 3648–3657.

Carney, L. H., McDuffy, M. J., and Shekhter, I. (**1999**). ''Frequency glides in the impulse responses of auditory-nerve fibers,'' J. Acoust. Soc. Am. **105**, 2384–2391.

Cooper, N. P., and Rhode, W. S. (**1996**). ''Fast travelling waves, slow travelling waves and their interactions in experimental studies of apical cochlear mechanics,'' Aud. Neurosci. **2**, 289–299.

Cooper, N. P., and Yates, G. K. (**1994**). ''Nonlinear input–output functions derived from the responses of guinea-pig cochlear nerve fibres: Variations with characteristic frequency,'' Hear. Res. **78**, 221–234.

Dau, T., and Oxenham, A. J. (**2001**). ''Phase effects in masking in normal-hearing and hearing-impaired listeners,'' J. Acoust. Soc. Am. **109**, 2466.

de Boer, E., and Kruidenier, C. (**1990**). ''On ringing limits of the auditory periphery,'' Biol. Cybern. **63**, 433–442.

de Boer, E., and Nuttall, A. L. (**1997**). ''The mechanical waveform of the basilar membrane. I. Frequency modulations (glides) in impulse responses and cross-correlation functions,'' J. Acoust. Soc. Am. **101**, 3583–3592.

de Boer, E., and Nuttall, A. L. (**2000a**). ''The mechanical waveform of the basilar membrane. II. From data to models—and back,'' J. Acoust. Soc. Am. **107**, 1487–1496.

de Boer, E., and Nuttall, A. L. (**2000b**). ''The mechanical waveform of the basilar membrane. III. Intensity effects,'' J. Acoust. Soc. Am. **107**, 1497–1507.

Fletcher, H. (**1940**). ''Auditory patterns,'' Rev. Mod. Phys. **12**, 47–65.

Glasberg, B. R., and Moore, B. C. J. (**1990**). ''Derivation of auditory filter shapes from notched-noise data,'' Hear. Res. **47**, 103–138.

Goldstein, J. L. (**1967**). ''Auditory spectral filtering and monaural phase perception,'' J. Acoust. Soc. Am. **41**, 458–479.

Greenwood, D. D. (**1990**). ''A cochlear frequency-position function for several species—29 years later,'' J. Acoust. Soc. Am. **87**, 2592–2605.

Hartmann, W. M., and Pumplin, J. (**1988**). ''Noise power fluctuations and the masking sine signals,'' J. Acoust. Soc. Am. **83**, 2277–2289.

Helmholtz, H. L. F. (**1954**). *On the Sensations of Tone* (Dover, New York).

Hicks, M. L., and Bacon, S. P. (**1999**). ''Psychophysical measures of auditory nonlinearities as a function of frequency in individuals with normal hearing,'' J. Acoust. Soc. Am. **105**, 326–338.

Houtgast, T. (**1977**). ''Auditory-filter characteristics derived from direct-masking data and pulsation-threshold data with a rippled-noise masker,'' J. Acoust. Soc. Am. **62**, 409–415.

Irino, T., and Patterson, R. D. (**1997**). ''A time-domain, level-dependent auditory filter: The gammachirp,'' J. Acoust. Soc. Am. **101**, 412–419.

Irino, T., and Patterson, R. D. (**2001**). ''A compressive gammachirp auditory filter for both physiological and psychophysical data,'' J. Acoust. Soc. Am. **109**, 2008–2022.

Kohlrausch, A., and Sander, A. (**1995**). ''Phase effects in masking related to dispersion in the inner ear. II. Masking period patterns of short targets,'' J. Acoust. Soc. Am. **97**, 1817–1829.

Lentz, J. J., and Leek, M. R. (**2001**). ''Psychophysical estimates of cochlear phase response: Masking by harmonic complexes,'' J. Assoc. Res. Otolaryngol. (in press).

Levitt, H. (**1971**). ''Transformed up–down methods in psychoacoustics,'' J. Acoust. Soc. Am. **49**, 467–477.

Mathes, R. C., and Miller, R. L. (**1947**). ''Phase effects in monaural perception,'' J. Acoust. Soc. Am. **19**, 780–797.

Mehrgardt, S., and Schroeder, M. R. (**1983**). ''Monaural phase effects in masking with multicomponent signals,'' in *Hearing-Physiological Bases and Psychophysics*, edited by R. Klinke and R. Hartman (Springer, Berlin).

Oxenham, A. J., and Dau, T. (**2001**). ''Reconciling frequency selectivity and phase effects in masking,'' J. Acoust. Soc. Am. **110**, 1525–1538.

Oxenham, A. J., and Moore, B. C. J. (**1994**). ''Modeling the additivity of nonsimultaneous masking,'' Hear. Res. **80**, 105–118.

Oxenham, A. J., and Plack, C. J. (**1998**). ''Suppression and the upward spread of masking,'' J. Acoust. Soc. Am. **104**, 3500–3510.

Patterson, R. D. (**1976**). ''Auditory filter shapes derived with noise stimuli,'' J. Acoust. Soc. Am. **59**, 640–654.

Patterson, R. D. (**1987**). ''A pulse ribbon model of monaural phase perception,'' J. Acoust. Soc. Am. **82**, 1560–1586.

Pfeiffer, R. R., and Molnar, C. E. (**1970**). ''Cochlear nerve fiber discharge patterns: Relationship to the cochlear microphonic,'' Science **167**, 1614–1616.

Plack, C. J., and Oxenham, A. J. (**2000**). ''Basilar-membrane nonlinearity estimated by pulsation threshold,'' J. Acoust. Soc. Am. **107**, 501–507.

Plomp, R. (**1964**). ''The ear as a frequency analyzer,'' J. Acoust. Soc. Am. **36**, 1628–1636.

Recio, A., Narayan, S. S., and Ruggero, M. A. (**1998**). ''Basilar-membrane responses to clicks at the base of the chinchilla cochlea,'' J. Acoust. Soc. Am. **103**, 1972–1989.

Rhode, W. S., and Cooper, N. P. (**1996**). ''Nonlinear mechanics in the apical turn of the chinchilla cochlea *in vivo*,'' Aud. Neurosci. **3**, 101–121.

Rhode, W. S., and Recio, A. (**2000**). ''Study of mechanical motions in the basal region of the chinchilla cochlea,'' J. Acoust. Soc. Am. **107**, 3317–3332.

Ruggero, M. A., Rich, N. C., Recio, A., Narayan, S. S., and Robles, L. (**1997**). ''Basilar-membrane responses to tones at the base of the chinchilla cochlea,'' J. Acoust. Soc. Am. **101**, 2151–2163.

Schreiner, C., Urbas, J. V., and Mehrgardt, S. (**1983**). ''Temporal resolution of amplitude modulation and complex signals in the auditory cortex of the cat,'' in *Hearing—Physiological Bases and Psychophysics*, edited by R. Klinke and R. Hartmann (Springer, Berlin).

Schroeder, M. R. (**1970**). ''Synthesis of low peak-factor signals and binary sequences with low autocorrelation,'' IEEE Trans. Inf. Theory **16**, 85–89.

Shera, C. A. (**2001a**). ''Frequency glides in click responses of the basilar membrane and auditory nerve: Their scaling behavior and origin in traveling-wave dispersion,'' J. Acoust. Soc. Am. **109**, 2023–2034.

Shera, C. A. (**2001b**). ''Intensity invariance of fine time structure in basilar-membrane click response: Implications for cochlear mechanics,'' J. Acoust. Soc. Am. **110**, 332–348.

Smith, B. K., Sieben, U. K., Kohlrausch, A., and Schroeder, M. R. (**1986**). ''Phase effects in masking related to dispersion in the inner ear,'' J. Acoust. Soc. Am. **80**, 1631–1637.

Strube, H. W. (**1985**). ''A computationally efficient basilar-membrane model,'' Acustica **58**, 207–214.

Summers, V. (**2000**). ''Effects of hearing impairment and presentation level on masking period patterns for Schroeder-phase harmonic complexes,'' J. Acoust. Soc. Am. **108**, 2307–2317.

Summers, V., and Leek, M. R. (**1998**). ''Masking of tones and speech by Schroeder-phase harmonic complexes in normally hearing and hearing-impaired listeners,'' Hear. Res. **118**, 139–150.

Tsuji, J., and Liberman, M. C. (**1997**). ''Intracelluar labeling of auditory nerve fibers in guinea pig: Central and peripheral projections,'' J. Comp. Neurol. **381**, 188–202.

Zwicker, E. (**1952**). ''Die Grenzen der Hörbarkeit der Amplitudenmodulation und der Frequenzmodulation eines Tones,'' Acustica **2**, 125–133.

Zwicker, E., Flottorp, G., and Stevens, S. S. (**1957**). ''Critical bandwidth in loudness summation,'' J. Acoust. Soc. Am. **29**, 548–557.

Spatio-temporal analysis of irregular vocal fold oscillations: Biphonation due to desynchronization of spatial modes

Jürgen Neubauer[a)]
Institute for Theoretical Biology, Humboldt University Berlin, Invalidenstrasse 43, D-10115 Berlin, Germany

Patrick Mergell
Siemens Audiological Engineering Group, Gebberstrasse 125, D-91058 Erlangen, Germany

Ulrich Eysholdt
Department of Phoniatrics and Pediatric Audiology, Friedrich-Alexander-University Erlangen-Nuremberg, Bohlenplatz 21, D-91054 Erlangen, Germany

Hanspeter Herzel
Institute for Theoretical Biology, Humboldt University Berlin, Invalidenstrasse 43, D-10115 Berlin, Germany

(Received 23 February 2001; accepted for publication 7 August 2001)

This report is on direct observation and modal analysis of irregular spatio-temporal vibration patterns of vocal fold pathologies *in vivo*. The observed oscillation patterns are described quantitatively with multiline kymograms, spectral analysis, and spatio-temporal plots. The complex spatio-temporal vibration patterns are decomposed by empirical orthogonal functions into independent vibratory modes. It is shown quantitatively that biphonation can be induced either by left–right asymmetry or by desynchronized anterior–posterior vibratory modes, and the term ''AP (anterior–posterior) biphonation'' is introduced. The presented phonation examples show that for normal phonation the first two modes sufficiently explain the glottal dynamics. The spatio-temporal oscillation pattern associated with biphonation due to left–right asymmetry can be explained by the first three modes. Higher-order modes are required to describe the pattern for biphonation induced by anterior–posterior vibrations. Spatial irregularity is quantified by an entropy measure, which is significantly higher for irregular phonation than for normal phonation. Two asymmetry measures are introduced: the left–right asymmetry and the anterior–posterior asymmetry, as the ratios of the fundamental frequencies of left and right vocal fold and of anterior–posterior modes, respectively. These quantities clearly differentiate between left–right biphonation and anterior–posterior biphonation. This paper proposes methods to analyze quantitatively irregular vocal fold contour patterns *in vivo* and complements previous findings of desynchronization of vibration modes in computer modes and in *in vitro* experiments.
[DOI: 10.1121/1.1406498]

PACS numbers: 43.70.Aj, 05.45.Tp [AL]

I. INTRODUCTION

In the last years, several new promising concepts in the fields of voice and phonation diagnostics, modeling, signal classification, and analysis have been developed to shed light on mechanisms that cause irregular vocal fold oscillations. Laryngeal (video) stroboscopy is widely used in everyday clinical examinations as a tool for visualizing pathological vocal fold dynamics, but it is only appropriate for the investigation of periodically vibrating vocal folds (Wendler *et al.*, 1996). On the contrary, digital high-speed glottography allows the direct observation of the glottal dynamics and the separate analysis of the left and the right vocal fold vibrations (Eysholdt *et al.*, 1996; Hammarberg, 1995; Kiritani *et al.*, 1993). This examination method allows one to record data required for the analysis of transient, subharmonic, and temporally and spatially aperiodic vocal fold dynamics. Digital image processing algorithms can be applied to obtain time series of the oscillations of the vocal fold edges for further analysis (Wittenberg, 1998).

The theory of nonlinear dynamics provides the framework for classifying vocal instabilities (Herzel, 1993; Titze *et al.*, 1993). Stationary oscillations can be related to low dimensional attractors (limit cycle, torus, chaotic attractor) (Bergé *et al.*, 1984). Qualitative changes of the vocal fold dynamics due to variations of the myoelastic and aerodynamic properties can be classified as bifurcations. Examples are the phonation onset (Hopf bifurcation) and the appearance of subharmonics (period doubling bifurcation). In several studies, attractors and bifurcations have been analyzed in biomechanical models of the vocal folds (Berry *et al.*, 1994; Lucero and Gotoh, 1993; Mergell, 1998; Steinecke and Herzel, 1995). Recently, vocal irregularities have been describd by combining digital high-speed glottography and biomechanical modeling (Mergell *et al.*, 2000). The observed time series from a pathological voice could be reproduced with

[a)]Electronic mail: j.neubauer@biologie.hu-berlin.de

quantitative agreement in a simplified two-mass model by parameter adjustment. The underlying model assumptions neglect changes of the vocal fold properties along the anterior–posterior (AP) direction. Therefore, the model only captures left–right (LR) asymmetries.

However, there are several indications that anterior–posterior (AP) oscillation modes can contribute to irregular glottal oscillation patterns (Berry, 2000; Berry *et al.*, 1994; Farnsworth, 1940; Hess *et al.*, 1994; Švec *et al.*, 2000; Tigges *et al.*, 1999; Titze, 1973). Berry *et al.* (1994) used empirical orthogonal functions (EOFs) to determine the dominant spatial modes in a finite-element model of the vocal folds. They showed that even complicated vibration patterns can be explained by a few modes. Moreover, higher-order modes could be extracted from this biomechanical model for one case of irregular phonation. EOF studies of vocal fold tissue (e.g., excised larynx experiments) confirmed and extended the results obtained from theoretical models (Berry, 2001). Resonance studies of human vocal folds *in vivo* showed that the resonance frequencies correspond to distinct anterior–posterior modes (Švec *et al.*, 2000). Resonance frequencies of the modes of a finite-element model were found to be grouped around resonance frequencies that correspond to different anterior–posterior modes (Berry, 2001). From an endoscopic view, the modes within these groups cannot be distinguished, as they exhibit the same anterior–posterior vibration pattern. Generally, inferior–superior vibration modes cannot be resolved from the endoscopic view, because the upper vocal fold edge masks the lower parts of the folds.

Models more complex than simplified two-mass models are required to reproduce irregular spatio-temporal vibration patterns (Aliour-Haghighi *et al.*, 2000; Titze, 1973, 1976; Titze and Strong, 1975). Since there is always a trade-off between the spatial accuracy of measured myoelastic properties and the physiological completeness of the model, it is important to know how complex a low-order model must be to describe the vocal fold dynamics *in vivo* accurately. Modal analysis can answer this question and is an appropriate tool for the design of low-order models. The number of dominant empirical modes is related to the number of horizontal and vertical degrees of freedom that biomechanical models must provide to capture the effective glottal dynamics (Aubry *et al.*, 1991; Berry *et al.*, 1994; Breuer and Sirovich, 1991). To our knowledge, the concept of modal analysis has not yet been applied for spatio-temporal analysis of glottal vibration patterns *in vivo*.

This paper focuses on the quantitative study of anterior–posterior modes and of irregular phonation by desynchronization of anterior–posterior modes of vibration. Thus, in the following sections we present a quantitative analysis of complex and irregular spatio-temporal vibration patterns of the vocal folds based on three phonation examples. We analyze one example with normal healthy phonation that serves as a reference. In addition, we choose two high-speed sequences with irregular phonation to demonstrate two different kinds of mechanisms that lead to biphonation. The term ''biphonation'' characterizes phonation with two fundamental frequencies (Herzel and Reuter, 1997; Herzel and Wendler, 1991; Ishizaka and Isshiki, 1976; Kiritani *et al.*, 1995; Mergell and Herzel, 1997; Smith *et al.*, 1992; Wilden *et al.*, 1998). In general, biphonation can be induced by different glottal, pharyngeal, and aerodynamical oscillations with different oscillation frequencies. Possible mechanisms for biphonation are the natural or pathological asymmetry of vocal folds, the decoupling of vertical and horizontal vibratory modes within single vocal folds, the interaction with other mechanical or aerodynamical oscillators in the sub- and supraglottal airway, and the interaction with vortices produced by the glottal constriction of the airstream. (Herzel and Reuter, 1997; Mergell and Herzel, 1997; Tigges *et al.*, 1997).

As a first image processing step we introduce the technique of multiline kymography to extract time series of glottal edge points form digital high-speed recordings. We use spectral analysis and spatio-temporal plots of the multiline time series as conventional analysis tools both for simple data analysis and consistency check. Furthermore, we compute empirical orthogonal eigenfunctions (EOFs) from the time series of the vocal fold edge displacements about the estimated glottal midline. We argue that EOF analysis is the appropriate way to deal with spatio-temporal vibration patterns. Thus, the multiline time series are decomposed into empirical orthogonal functions. We use this method to measure the degree of desynchronization of anterior–posterior modes.

Furthermore, we suggest four different measures to quantify objectively spatio-temporal vibration patterns. We use the asymmetry coefficient according to Mergell *et al.* (2000) to measure left–right asymmetry. This coefficient is related to the asymmetry coefficient in simple two-mass models (Steinecke and Herzel, 1995). Similarly, we introduce an anterior–posterior asymmetry measure to describe anterior–posterior mode desynchronization. We use an entropy measure to quantify spatial irregularity, and we estimate the number of dynamically relevant glottal modes.

II. MATERIALS AND METHODS

Digital high-speed image sequences during phonation were recorded with the camera system CAMSYS+ 128 (described by Bloss *et al.*, 1993) at a sampling rate of 3704 frames per second with a spatial resolution of 128×64 pixels in combination with a rigid larynx endoscope [for further technical details and caveats cf. Wittenberg *et al.* (1995) and Wittenberg (1998)]. We examined the high-speed data of three subjects: Subject JN (male, 27 years) with a healthy voice, subject WS (female, 29 years) with a left recurrent nerve paralysis, and subject MM (female, 26 years) with a functional dysphonia. On basis of the Roughness–Breathiness–Hoarseness (RBH) scale subject WS was judged to be R1B1H2. Clinical stroboscopy revealed a prephonatory standstill of the left vocal fold, whereas the right vocal fold was found to be normal. During phonation stroboscopy was not applicable due to biphonic oscillation of the vocal folds. Clinical standard examination of subject MM gave no visible morphological peculiarities. The voice was judged on basis of the Roughness–Breathiness–Hoarseness (RBH) scale to the R2B1H2 with diplophonic episodes. In the following study, we label the high-speed sequences ''normal voice,'' ''recurrent nerve paralysis,'' and ''functional

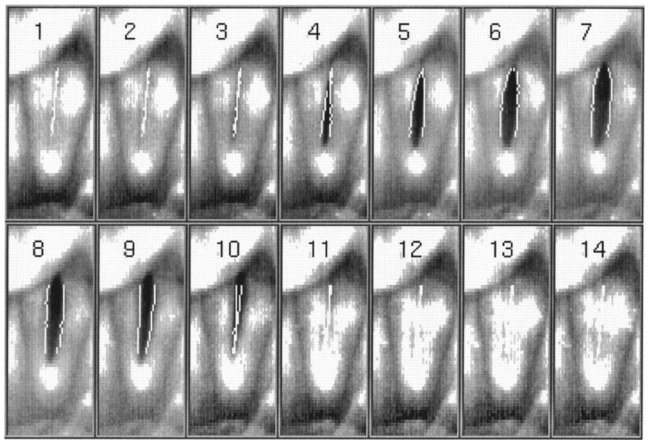

FIG. 1. Digital high-speed image sequence showing a glottal cycle with 21 tracked glottal contour points per vocal fold: subject JN with normal phonation. Every second frame is shown; the time interval between successively plotted frames is $\Delta t = 0.54$ ms. Note that the right arytenoid cartilage is visible in the left upper corner of the images. Thus, the upper and lower side of each frame correspond to the posterior and anterior side of the vocal folds, respectively. The left and right vocal folds are displayed on the right and left side of the digital images, respectively.

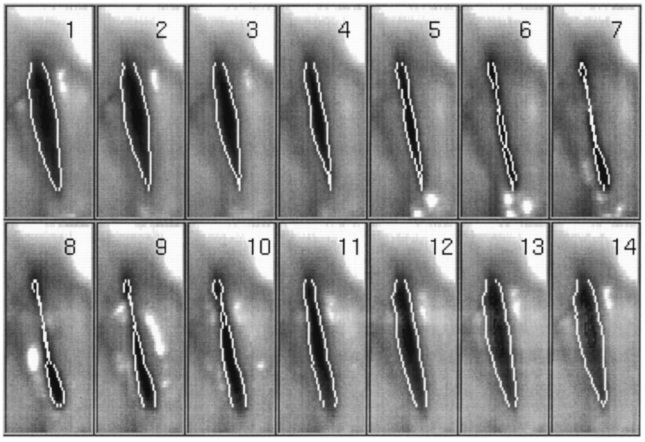

FIG. 3. Digital high-speed sequence with 39 tracked glottal contour points per vocal fold of subject MM (every frame shown, $\Delta t = 0.27$ ms). The upper and lower side of each frame correspond to the posterior and anterior side of the vocal folds, respectively.

dysphonia.'' We chose these particular pathological phonations because preliminary analysis of the corresponding sound data indicated biphonation. The pathological phonation examples were chosen out of about 100 recordings with indications for biphonation out of overall 4000 high-speed sequences. About ten of the biphonic phonations showed anterior–posterior vibration patterns. Figures 1–3 show one oscillation cycle taken from the digital image sequences of each subject. The highlighted glottal edge contours (i.e., the entirety of all glottal edge points of each vocal fold) are the results of our image processing algorithm that will be explained below. The algorithm for data reduction is a simplified and modified version of the kymographic image processing proposed by Wittenberg (1998).

A. Multiline kymography

As a first processing step, we extract all horizontal scan lines of each digital image over the visible vocal fold length, i.e., from the posterior side (arytenoid cartilage) to the anterior side (thyroid cartilage). The arytenoid side corresponds to the upper part of the digital images shown in Figs. 1–3, whereas the thyroid side corresponds to the lower part. The extracted scan lines are subsequently concatenated. In Figs. 4–6 we visualize the vocal fold dynamics by a few hundred subsequent scan lines. The resulting gray scale arrays (kymograms) show the change in distance between edge points on left and right vocal folds during phonation (Švec and Schutte, 1996; Tigges *et al.*, 1999). We mark the tracked glottal edge points of the left (upper line) and the right vocal fold (lower line) by white points.

We determine these edge points with a fixed gray value threshold for each kymogram. This threshold separates between image points from the glottal aperture and from the vocal fold tissue. As we use a rigid endoscope viewing the vocal folds from above (superior view), the tracked points correspond to points of the superior medial vocal fold edge or the inferior vocal fold edge. During the opening phase the tracked points are close to the superior medial edge, whereas during the closing phase the tracked points correspond to a point between superior and inferior edge. However, due to the limited spatial resolution of the camera system we cannot resolve vertical vibration modes of the vocal fold cover. The movement of the vocal fold edge points is related to the oscillations riding on the black–white interface of the binary segmented multiline kymograms (Mergell *et al.*, 2000; Wittenberg, 1997). We call the extracted time series ''high-speed glottograms'' (HGGs) following Wittenberg *et al.* (1995). Table I gives details on the data sets of the different phonation examples we use for spatio-temporal analysis of vocal fold vibration.

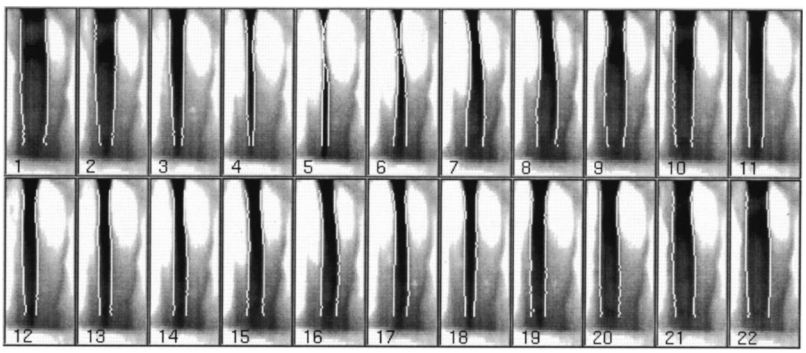

FIG. 2. Digital high-speed image sequence with 49 tracked glottal contour points per vocal fold of subject WS (every second frame shown, $\Delta t = 0.54$ ms for plotted frames). The upper and lower side of each frame correspond to the posterior and anterior side of the vocal folds, respectively.

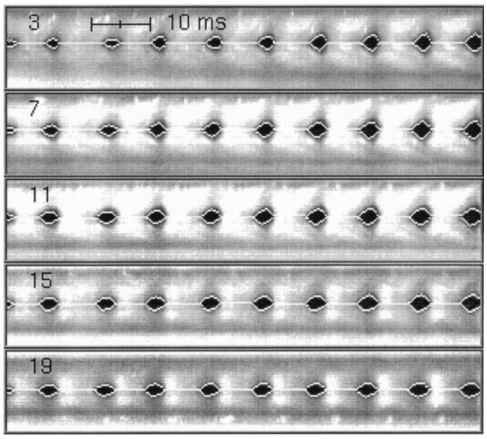

FIG. 4. Selected multiline kymograms (chosen from 21 kymograms) with highlighted extracted time series for subject JN (with normal phonation). The upper white line corresponds to the left vocal fold edge, the lower white line to the right vocal fold edge. Length of kymograms shown is $T=81$ ms. The numbers correspond to the scan line number along the posterior–anterior direction. The glottal aperture is black-coded, the surrounding is shown in different gray values. The vertical direction within each kymogram corresponds to the left–right direction of the digital high-speed image frames.

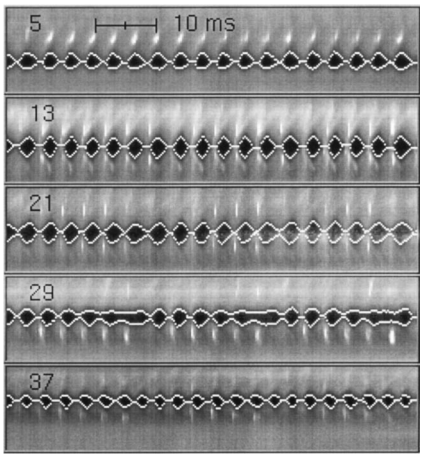

FIG. 6. Selected multiline kymograms for subject MM. Length of kymograms shown is $T=67$ ms. The upper white line indicates the left vocal fold edge; the lower white line indicates the right vocal fold edge. In each kymogram we observe nearly symmetrical oscillations of both vocal folds. However, we see an increasing modulation of both vocal fold oscillations comparing kymograms 13, 21, and 29 along the posterior–anterior direction. Thus, we observe desynchronization of vocal-fold oscillations along the anterior–posterior direction.

B. Time series preprocessing

The HGG data have to be preprocessed to avoid artifacts caused by relative horizontal movements and rotations of the observing endoscope about the glottis. Following previous work (Mergell *et al.*, 2000) we just correct for horizontal movements neglecting vertical movements that are assumed to be small within the short selected HGG sequences according to Wittenberg (1998). Therefore, we calculate the displacements of vocal fold edges about the glottal midline, which we estimate frame by frame (Fig. 7).

We first approximate the glottal midline by a regression line through the midpoints $(\overline{x_k}(t_i), y_k(t_i))$, of each scan line k, where the midpoints are

$$\overline{x_k}(t_i)=\tfrac{1}{2}(x_k^{(\mathrm{left})}(t_i)+x_k^{(\mathrm{right})}(t_i)). \tag{1}$$

Note that $y_k(t_i)=y_k^{(\mathrm{left})}(t_i)=y_k^{(\mathrm{right})}(t_i)$. Here, $k=1,...,N$ indcates the kymogram number and $i=1,...,M$ is the time index (see Fig. 7). We describe the estimated glottal midline of frame t_i by the slope $m(t_i)$ and the intercept $b(t_i)$. The slope and the intercept both contain parts of the glottal dynamics and slow modulations caused by relative movements between the high-speed camera and the glottis. As we correct the HGG data only for slow modulations, we apply a moving average procedure to the time series $m(t_i)$ and $b(t_i)$ (length of averaging window: 50 ms, corresponding cutoff frequency: 20 Hz). We choose the cutoff frequency of this low-pass filtering process close to the maximum tremor frequency of about 16 Hz (Riviere *et al.*, 1998). Thus, the filtered values $\overline{m}(t_i)$ and $\overline{b}(t_i)$ are slowly modulated. We calculate the vocal fold displacements $d_k^{(\alpha)}(t_i)$ as the distance of the extracted contour points from the estimated glottal midline

$$d_k^{(\alpha)}(t_i)=\left[x_k^{(\alpha)}(t_i)-\frac{y_k(t_i)-\overline{b}(t_i)}{\overline{m}(t_i)}\right]\sin\varphi(t_i). \tag{2}$$

Here, $\varphi(t_i)=\arctan(\overline{m}(t_i))$ is the inclination angle of the glottal midline, $\alpha\in\{\text{left,right}\}$ specifies the side, and

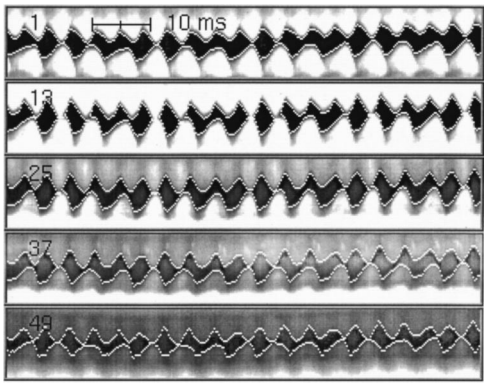

FIG. 5. Selected multiline kymograms for subject WS. Length of kymograms shown is $T=81$ ms. The upper white line follows the left vocal fold edge; the lower white line follows the right vocal fold edge. In each kymogram we observe desynchronization of the left and right vocal fold oscillation: Five oscillation maxima of the left vocal fold (upper line) correspond to four oscillation maxima of the right vocal fold (lower line).

TABLE I. Details on time series from different subjects with normal and irregular phonation. The sampling rate was 3704 frames per second for all time series. The difference in length is due to the different length of high-speed sequences obtained from the clinical investigation and due to the selection of stationary segments. With respect to the typical oscillation frequencies the number of measured cycles is sufficient for a statistical analysis such as our EOF estimation calculations.

Subject	Phonation	Number of glottal contour points	Length of time series [ms]	Typical frequency [Hz]
JN (healthy)	normal	21	1215	120
WS (recurrent nerve paralysis)	irregular	49	618	197
MM (functional dysphonia)	irregular	39	354	270

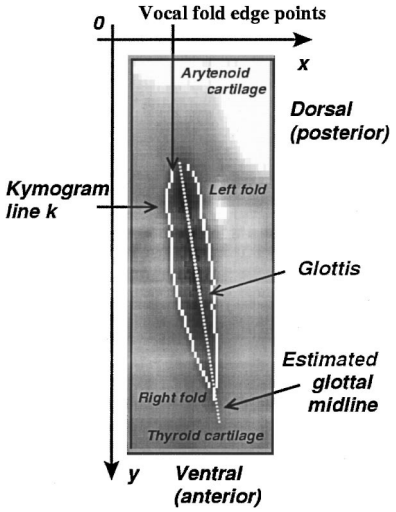

FIG. 7. Coordinate system for analysis of digital high-speed images: Vocal fold edge points of left and right vocal fold are highlighted. The distances of the estimated glottal midline to the vocal fold edge points are used as vocal fold displacements for further analysis.

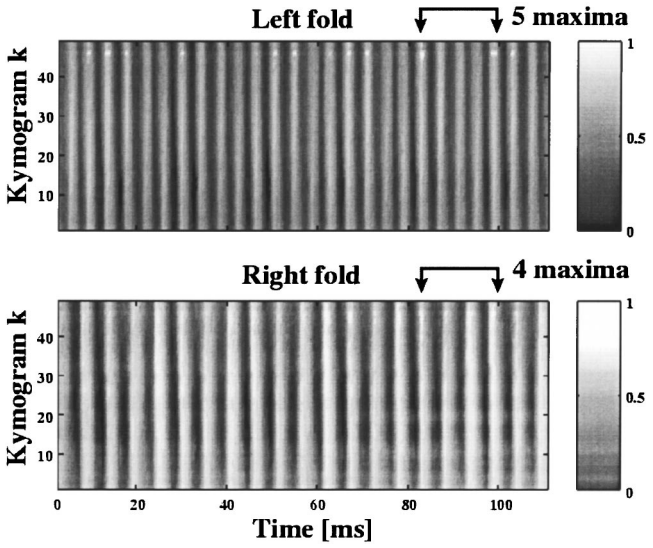

FIG. 8. Spatio-temporal plots of the scaled oscillatory component $\delta_k^{(\alpha)}(t_i)$ of vocal fold edge points for subject WS (with left recurrent nerve paralysis). Left and right vocal folds are desynchronized, which suggests left–right asymmetry of vocal fold properties. Bright regions display glottal opening; dark regions code for vocal fold edge points with glottal closure. The maximum positive excursions are rescaled to unity; the minimum negative excursions are rescaled to zero. The lower part/upper part of each plot corresponds to the temporal evolution of posterior/anterior vocal fold edge points. During four oscillation maxima on the right vocal fold, five oscillation maxima appear on the left side. Vertical homogeneity of the vertical bright stripes during glottal opening indicates no relevant anterior–posterior asymmetry.

$x_k^{(\alpha)}(t_i)$ and $y_k(t_i)$ are the image coordinates of the vocal fold contour points (see Fig. 7). In this way, slow horizontal and rotational modulations contained in $\overline{m}(t_i)$ and $\overline{b}(t_i)$ are removed from the HGG data $(x_k(t_i), y_k(t_i))$.

C. Calculation of the empirical orthogonal functions

The technique of empirical orthogonal functions is an appropriate method for analyzing complex and irregular spatio-temporal glottal motion patterns. It can be used to decompose glottal contour dynamics into principal modes of vibration (Berry *et al.*, 1994).

As we are only interested in the oscillation of the vocal folds about their dynamic rest position, we subtract the temporal averages (average over whole length of time series) from the vocal fold displacements of left and right vocal folds

$$\delta_k^{(\alpha)}(t_i) = d_k^{(\alpha)}(t_i) - \overline{d_k^{(\alpha)}}. \tag{3}$$

We calculate the EOFs $\Phi_k^{(\alpha)}$, $k=1,...,N$, from the oscillatory components $\delta_k^{(a)}(t_i)$. EOFs represent a decomposition of the contour dynamics $\delta_k^{(\alpha)}(t_i)$ into different spatial oscillating modes.

Furthermore, we compute the corresponding eigenvalues $\lambda_k^{2(\alpha)}$ which are the weights or the contributions of the EOFs on average to the complete spatial dynamics.

To analyze the dynamics of the EOFs, we calculate the time-varying contribution of different modes (EOFs) $\Phi_k^{(\alpha)}$. These contributions are called temporal coefficients $\Psi_l^{(\alpha)}(t_i)$. For a more detailed description of the empirical orthogonal functions, we refer to the Appendix.

According to Mergell *et al.* (2000), the ratio $Q_{\mathrm{lr}}^{(\mathrm{exp})}$ of the lower and higher fundamental frequency of left and right vocal folds parametrizes the laryngeal left–right asymmetry. Similarly, we measure anterior–posterior asymmetry with the ratio $Q_{\mathrm{ap}}^{(\mathrm{exp})}$ of the lower and higher fundamental frequency of the first two temporal coefficients. This quantity measures the average temporal irregularity of the spatio-temporal oscillation pattern of a single vocal fold over the chosen time interval.

To parameterize the spatial irregularity, we calculate Shannon's entropy $S_{\mathrm{tot}}^{(\alpha)}$ from the EOF weights of each vocal fold. This entropy quantifies the degree of disorder of the mode decomposition. For a further discussion of the entropy measure, we refer to the Appendix.

For the sake of comparability and robustness, we introduce a simple threshold criterion for the estimation of dynamically relevant modes. We reconstruct the observed time series of the glottal contour points with a subset of the calculated EOFs. To find the required subset size we start with the first EOF with the largest weight, add subsequent EOFs with smaller and smaller value, until the difference between the reconstructed and the observed time series $\delta_k^{(\alpha)}(t_i)$ is smaller than a certain threshold.

III. ANALYSIS OF SPATIO-TEMPORAL GLOTTAL PATTERNS

A. Spectral analysis of spatio-temporal plots

We use spatio-temporal plots of the oscillatory component $\delta_k^{(\alpha)}(t_i)$ to discuss qualitatively the vibration patterns of different phonation examples. Therefore, we encode the time series $\delta_k^{(\alpha)}(t_i)$ in gray scale values in a space-time coordinate system. Bright regions correspond to positive values, whereas dark areas indicate negative values. For the sake of visualization, the values of $\delta_k^{(\alpha)}(t_i)$ are normalized.

In Fig. 8 we illustrate the desynchronization of left and

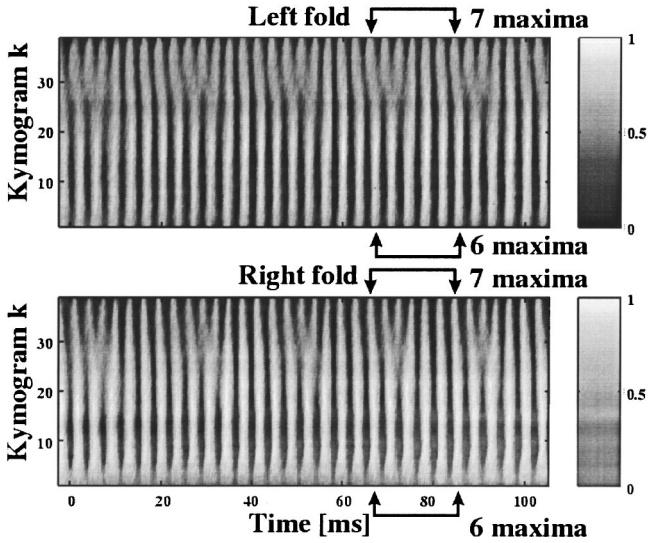

FIG. 9. Spatio-temporal plots of the scaled elongations $\delta_k^{(\alpha)}(t_i)$ for subject MM (with functional dysphonia). During seven oscillation maxima in the upper part of the spatio-temporal plots, six maxima appear in the lower part. The symmetry between left and right spatio-temporal plot is roughly preserved.

right vocal fold vibrations for subject WS. During four oscillation maxima on the right vocal fold we observe five oscillation maxima on the left vocal fold. Left–right asymmetry is $Q_{\mathrm{lr}}^{(\mathrm{exp})} \approx 4/5$. Note that there is no significant difference between the lower (posterior side) and the upper (anterior side) part of each spatio-temporal plot. Therefore, anterior–posterior asymmetry is estimated as $Q_{\mathrm{ap}}^{(\mathrm{exp})}=1$. Here, we use the anterior–posterior asymmetry as the ratio of lower and higher oscillation frequencies of vibrations close to the anterior or posterior end of the vocal folds.

The spatio-temporal plots for time series of subject MM (Fig. 9) show nearly seven oscillation maxima in the upper part (anterior side) in contrast to nearly six maxima in the lower part (posterior side) of the vocal folds. We observe left–right symmetrical oscillations of the vocal folds, $Q_{\mathrm{lr}}^{(\mathrm{exp})}=1$.

On the level of time series from single kymograms, we examine spectra of selected time series of vocal fold edge points (HGGs). The spectra from subject WS show a pronounced left-right asymmetry. In Fig. 10 we exemplify two spectra for two different locations on each vocal fold. One location is close to the anterior side (kymogram line number $k=40$), the other is close to the posterior side of the vocal folds (kymogram line number $k=10$). All apparent peak frequencies $f_{m,n}$ can be explained by linear combinations of just two independent frequencies f_l and f_r: $f_{(m,n)}=mf_r+nf_l$, $m,n \in \mathbb{Z}=\{0,\pm 1,\pm 2,\ldots\}$. The fundamental frequencies are $f_r \approx 197$ Hz and $f_l \approx 265$ Hz. Thus left–right asymmetry is $Q_{\mathrm{lr}}^{(\mathrm{exp})}=f_r/f_l \approx 0.74$. For both anterior and posterior postions on the vocal folds, the corresponding spectra of left and right vocal folds reveal a significant left–right asymmetry. The peak frequency at f_r is dominant in the spectra of the right vocal fold, whereas for the left vocal fold the dominant frequency can be found at f_l. On the basis of these two chosen time series, anterior–posterior asymmetry is $Q_{\mathrm{ap}}^{(\mathrm{exp})}=1$, indicating no anterior–posterior asymmetry.

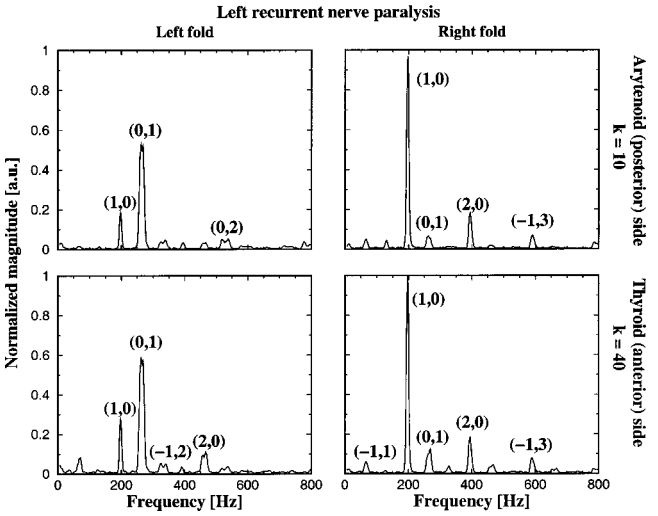

FIG. 10. Comparison of normalized spectra of $\delta_k^{(\alpha)}(t_i)$ of left and right vocal fold at anterior (kymogram line number $k=40$) and posterior side (kymogram line number $k=10$) of each vocal fold (normalization to amplitude maximum of all spectra shown). All amplitude maxima can be explained by linear superposition of two independent frequencies $f_r \approx 197$ Hz and $f_l \approx 265$ Hz: $f_{(m,n)}=mf_r+nf_l$. Left–right asymmetry is $Q_{\mathrm{lr}}^{(\mathrm{exp})} \approx 0.74$. The dominant peak frequency for both spectra of the right vocal fold is at f_r, whereas for the left vocal fold both spectra have dominant peak frequencies at f_l. The spectral peaks are marked by their corresponding numbers (m,n).

In Fig. 11 we show two spectra from subject MM. With these two chosen time series, we find left–right symmetry to be preserved, $Q_{\mathrm{lr}}^{(\mathrm{exp})}=1$. But, spectra for anterior (kymogram line number $k=30$) and posterior positions (kymogram line number $k=10$) differ significantly. Spectra for the posterior positions from the left and right side are dominated by the peak frequency $f_p \approx 271$ Hz. At the anterior side, the spectra of both left and right side show dominant peak frequencies at f_p and $f_a \approx 338$ Hz. Anterior–posterior asymmetry is $Q_{\mathrm{ap}}^{(\mathrm{exp})}=f_p/f_a \approx 0.80$. Thus, we observe the desynchronized oscilla-

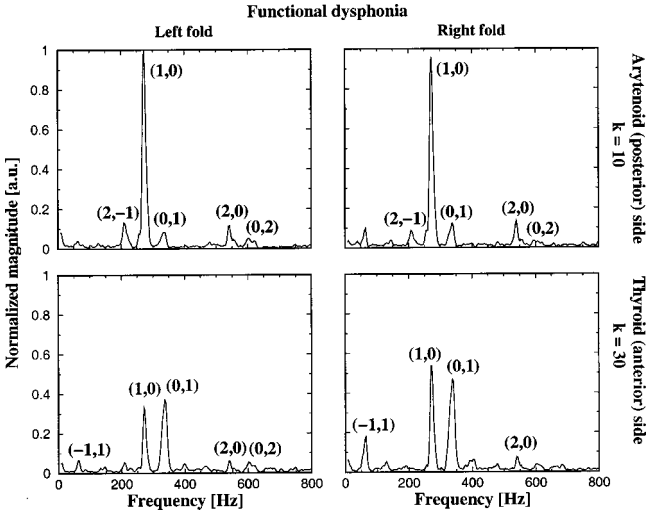

FIG. 11. Comparison of normalized spectra of displacements $\delta_k^{(\alpha)}(t_i)$ of left and right vocal folds at anterior (kymogram line number $k=30$) and posterior side (kymogram line number $k=10$) of each vocal fold (normalization as above): Maxima can be interpreted by linear superposition (m,n) of independent frequencies $f_p \approx 271$ Hz and $f_\alpha \approx 338$ Hz. Anterior–posterior asymmetry is $Q_{\mathrm{ap}}^{(\mathrm{exp})} \approx 0.80$.

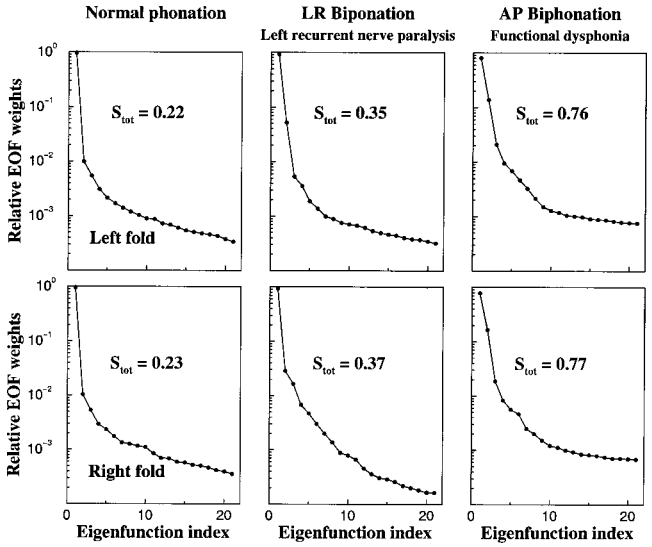

FIG. 12. First 21 values of the relative EOF weights for three phonation examples for left (upper row) and right (lower row) vocal folds. The information entropy $S_{\mathrm{tot}}^{(\alpha)}$ measures the overall spatial irregularity. As explained in the text, we introduce the term LR biphonation for the LR asymmetrical phonation of subject WS and AP biphonation for AP asymmetrical phonation of subject MM.

tion of vocal fold edge points within each single vocal fold. Here, the two independent frequencies f_p and f_a are enough to deduce all present peak frequencies.

For the sake of visualization and explanation we counted the number of maxima of the spatio-temporal plots (see Figs. 8 and Fig. 9) for equal time intervals. The ratio of the number of maxima is different from the ratio of the fundamental frequencies observed by spectral analysis of selected time series of vocal fold edge points. This illustrates the limitation of visual inspection. For example, a superposition of trigonometric functions with a frequency ratio of 4:5 can lead to 6 or 8 distinct maxima.

B. EOF analysis of spatio-temporal vibration patterns

In Fig. 12 we show the relative weights $p_k^{(\alpha)} = \lambda_k^{2(\alpha)} / \Sigma_l \lambda_l^{2(\alpha)}$ (cf. the Appendix) of the EOF decomposition for the three phonation examples. The relative weights express the relative contribution of different EOFs to the measured spatio-temporal oscillation pattern. We plot the first 21 relative weights on a logarithmic scale, as they cover about four orders of magnitude. In all three cases the sequence of weights decays rapidly, whereas higher-order weights decrease rather slowly. However, by comparison we see that the decay of the first few weights strongly depends on the phonation example. The cumulative sum of the first five values of the relative EOF weights, given in Table II, supports this statement. Thus, we can use the shape of the weight distribution to distinguish the spatial irregularity of different phonation examples. We use Shannon's entropy $S_{\mathrm{tot}}^{(\alpha)}$ (cf. the Appendix) as an overall measure for the shape, i.e., the broadness of the different distributions.

We find that $S_{\mathrm{tot}}^{(\alpha)}$ becomes significantly larger for the three phonation examples. Correspondingly, the weight distributions become broader. $S_{\mathrm{tot}}^{(\alpha)}$ increases from LR and AP symmetrical oscillation (normal phonation) via LR asymmetrical, but AP symmetrical oscillation to AP asymmetrical but LR symmetrical oscillation (Fig. 12). We observe no significant left–right difference of the spatial irregularities $S_{\mathrm{tot}}^{(\mathrm{left})}$ and $S_{\mathrm{tot}}^{(\mathrm{right})}$.

We estimate the number of dynamically relevant modes choosing a threshold of 97% for reconstruction quality. Table II shows that 97% of the observed time series can be explained by two modes for both vocal folds for subject JN exhibiting LR and AP symmetrical phonation (normal phonation). For subject WS showing LR asymmetrical vibration, we find that two modes on the left side and three modes on the right side, respectively, are sufficient. For subject MM exhibiting AP asymmetrical phonation, we have to include four modes on both sides.

Figures 13–15 display the empirical orthogonal functions associated with the first five weights. For all three phonation examples, the first EOF reveals the uniform outward and inward movement of the vocal folds resulting in a general increase and decrease of glottal opening area. The second EOF illustrates vocal fold displacements with a phase shift of 180 deg between the anterior and the posterior side of the vocal folds. In most cases we find that their wavelength is roughly twice the wavelength of the first EOFs. The

TABLE II. Cumulative sum $\Sigma \lambda_m^{2(l/r)}$ for the first five values of the relative EOF weights for three phonation types. For subject JN (with normal phonation) and for subject WS (with LR asymmetrical phonation), the first mode already covers more than 90% of the glottal contour dynamics. However, for the subject MM (with AP asymmetrical phonation) the first mode just carries about 80% of the observed time series. Weights of higher modes become rapidly smaller, but are still specific for the type of phonation. To explain more than 97% of the observed glottal dynamics, two modes have to be taken into account for subject JN, two or three modes, respectively, for subject WS, and four modes for subject MM (indicated numbers in bold face).

	Cumulative sum $\Sigma_m \lambda_m^{2(\alpha)}$, $\alpha \in \{\mathrm{left,right}\}$ for					
	LR and AP symmetry		LR asymmetry		AP asymmetry	
Eigenfunction index	(normal phonation) left [%]	right [%]	(recurrent nerve paralysis) left [%]	right [%]	(functional dysphonia) left [%]	right [%]
1	96.7	96.6	92.8	93.2	80.1	78.2
2	**97.7**	**97.7**	**97.9**	96.1	94.0	94.7
3	98.3	98.2	98.5	**97.7**	96.1	96.5
4	98.6	98.5	98.8	98.4	**97.0**	**97.3**
5	98.8	98.7	99.0	98.9	97.7	97.9

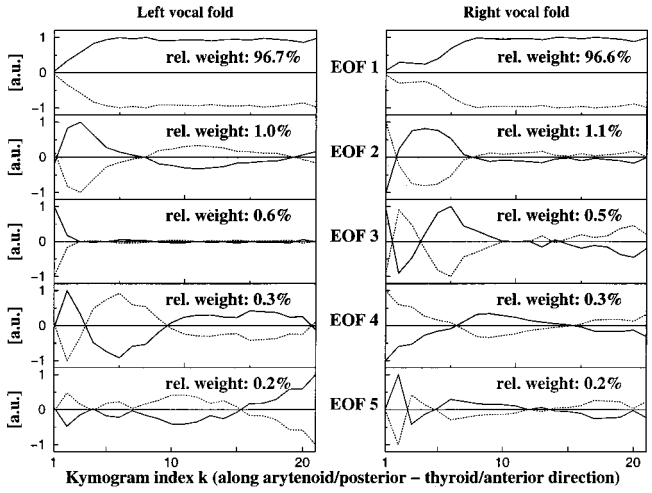

FIG. 13. First five normalized empirical orthogonal functions for centered time series from subject JN (with normal healthy phonation): Maximum and minimum excursion of the EOFs are shown (normalization to amplitude maxima). The relative weights, indicated in the plots, reflect the contribution of the EOFs to the reconstruction of the observed glottal dynamics. Thus, over 90% of the observed time series is explained by the first EOFs.

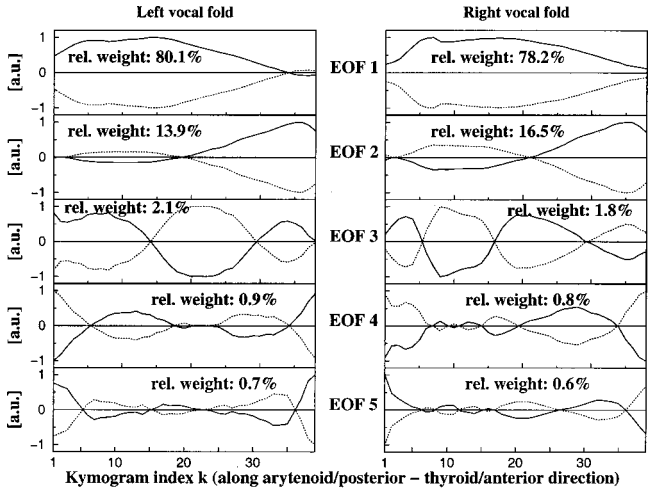

FIG. 15. First five normalized empirical modes for centered time series from subject MM: Maximum and minimum excursion of the EOFs are shown (normalization as above). The first two EOFs are required to capture more than 90% of the time series.

structure of all higher EOFs is more difficult to generalize due to increasing fluctuations resulting from the finite spatial and temporal resolution of the high-speed camera and the noise of the recordings. We call all modes higher than the first "anterior–posterior (AP) modes."

In Figs. 16–18 we plot the spectra of the corresponding temporal coefficients, that express the temporal evolution of the EOFs. For subject JN (regular phonation) we find that all peak frequencies of both left and right vocal folds are harmonically related to the fundamental frequency of about $f_0 \approx 127$ Hz. Here, left–right asymmetry $Q_{\mathrm{lr}}^{(\mathrm{exp})}$ and anterior–posterior asymmetry $Q_{\mathrm{ap}}^{(\mathrm{exp})}$ both are unity. Additionally, we see that temporal coefficients for higher EOFs contain more and more noise.

For subject WS (irregular phonation), the spectra of the first temporal eigenfunction reveal a pronounced left–right asymmetry. The spectrum of the first left temporal coefficient is dominated by the peak frequency $f_l \approx 265$ Hz; the spectrum of the first right temporal eigenfunction has the dominant peak frequency $f_r \approx 197$ Hz. The left–right asymmetry is $Q_{\mathrm{lr}}^{(\mathrm{exp})} = f_r / f_l \approx 0.74$. Linear superposition $f_{(m,n)} = m f_r + n f_l, m, n \in \mathbb{Z}$ of the two independent left and right frequencies explains the peak frequencies of all remaining spectra, apart from noisy contributions.

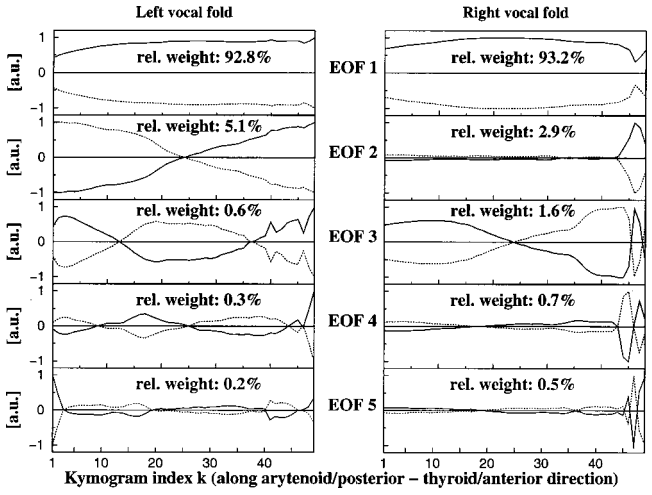

FIG. 14. First five normalized EOFs for centered time series from subject WS: maximum and minimum excursion of the EOFs are shown (normalization as above). The first EOFs are enough to explain more than 90% of the time series. Due to scaling, the phase shift between anterior and posterior side of the second EOF of the right fold cannot be seen as clearly as on the left fold.

For subject MM (irregular phonation), the first two spectra of the temporal eigenfunctions are roughly symmetric about the left and right side. On each vocal fold side, however, we observe a significant difference in peak frequency for the first two temporal coefficients: For both first temporal coefficients, the peak frequency is $f_p \approx 271$ Hz. Both spectra of the second temporal coefficients have a peak frequency $f_a \approx 338$ Hz. We use the indices "p" and "a" for f_p and f_a, because we observe the main spatial contribution of the first (and second) EOF in the posterior (and anterior) part of the vocal folds (see Fig. 15). The anterior–posterior asymmetry is $Q_{\mathrm{ap}}^{(\mathrm{exp})} = f_p / f_a \approx 0.80$. Linear combinations $f_{(m',n')} = m' f_p + n' f_a$, $m', n' \in \mathbb{Z}$ of these independent frequencies explain all remaining peak frequencies in the shown spectra.

IV. DISCUSSION

The aim of this paper was to analyze spatially complex and temporally irregular glottal contour patterns of pathological phonation. Mode analysis of spatio-temporal patterns of vocal-fold displacements *in vivo* with empirical orthogonal functions appeared to be an appropriate tool to extract principal glottal vibration modes from high-speed recordings. EOF analysis can extract excited modes from measured time series. Although we applied this method to analyze only three examples of normal and pathological phonation, the presented method and the shown effect of left–right desynchronization and anterior–posterior desynchronization are of

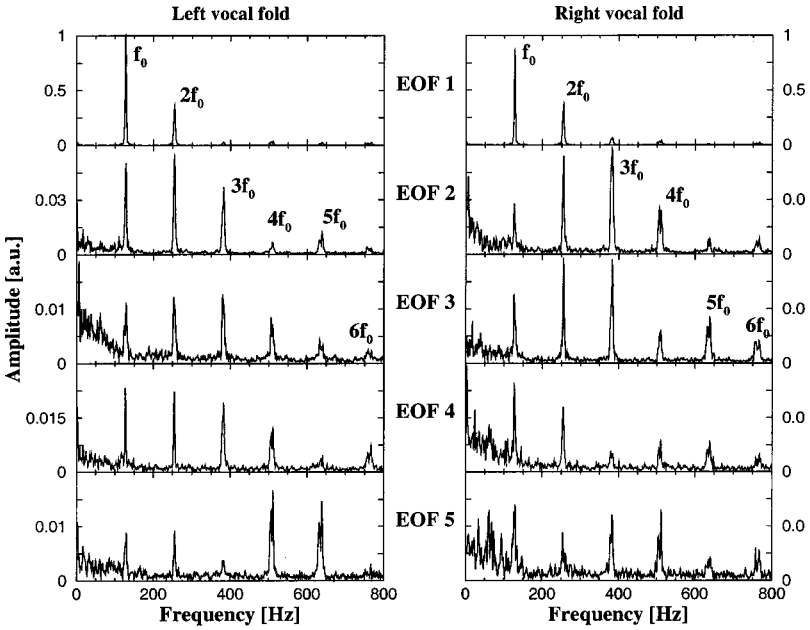

FIG. 16. Normalized magnitude spectra (linear scale) of first five temporal eigenfunctions for subject JN (with normal healthy phonation) (normalization to amplitude maximum of all spectra shown): All spectra consist of harmonically related peak frequencies together with noise contributions increasing with EOF number.

general validity. Previous theoretical studies of biomechanical models (Herzel, 1993; Titze *et al.*, 1993) support this point of view.

This paper presents the analysis of two different types of biphonation generated by different glottal mechanisms. Biphonation is already known to be induced by left–right asymmetry of the vocal folds, and strong interaction with the supraglottal vocal tract is assumed to ease biphonation (Mergell and Herzel, 1997; Titze and Story, 1997). We presented data from a patient with left recurrent nerve paralysis, where we observed the desynchronization of left- and right vocal fold oscillations. We found, that biphonation, i.e., the existence of two fundamental frequencies, can be explained in this case by only the first mode of the EOF decomposition of left and right oscillations. This result strongly supports the notion that biphonation was induced by a left–right asymmetry of the vocal folds due to the paralyzed left vocal fold. We presented this example to contrast it with our finding of another mechanism for biphonation.

Therefore, we presented data on a patient with functional dysphonia, where we observed dsynchronized oscillations of vocal fold edge points on each vocal fold. In addition to the uniform inward and outward movement of the vocal folds, we observed oscillation patterns with a prominent phase shift between anterior and posterior side of the vocal folds. We found that these higher modes vibrate independently form the basic spatially uniform mode, as we see two independent oscillation frequencies in the spectra of the temporal coefficients of the EOFs. Thus, we provide experimental evidence that desynchronization of modes can be observed in voice disorders, as previously suggested by theoretical considerations (Herzel *et al.*, 1994; Titze *et al.*, 1993). Theoretically, the vocal folds can be considered as complex, visco-elastic, three-dimensional structures, that can generate

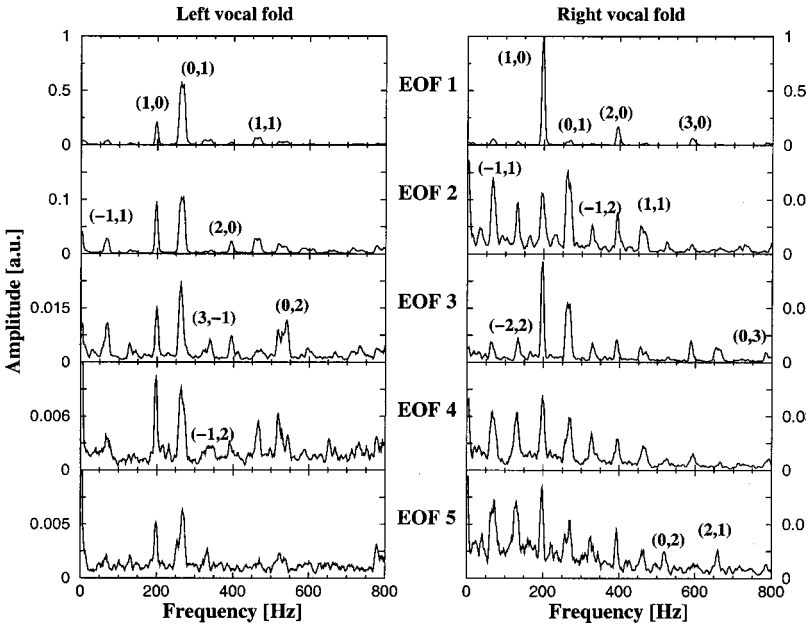

FIG. 17. Normalized magnitude spectra of first five temporal eigenfunctions for subject WS (normalization as above): The left–right asymmetry ratio $Q = f_r / f_l = 0.74 \approx 4/5$ observed in the first temporal eigenfunctions associated with the first EOF reflects the laryngeal asymmetry. The main spectral information is already contained in the first temporal eigenfunctions.

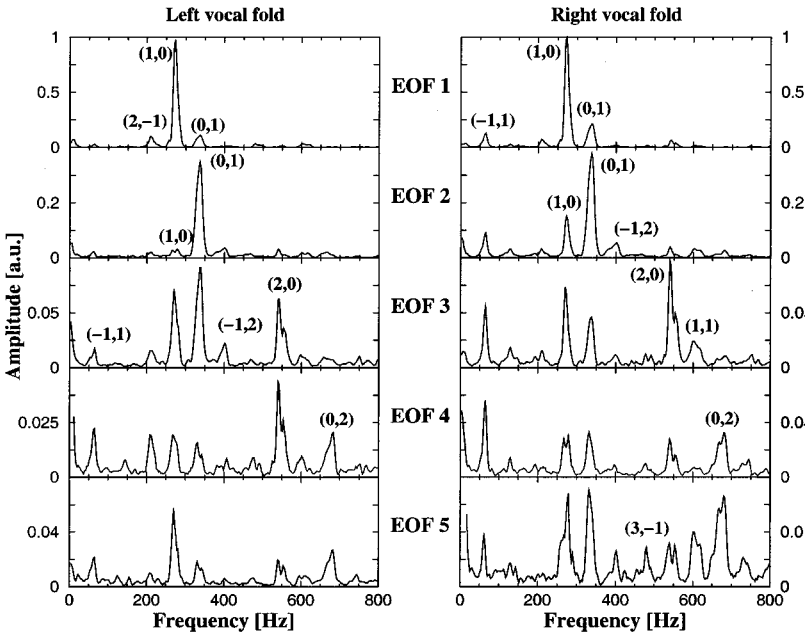

FIG. 18. Normalized magnitude spectra of first five temporal eigenfunctions for subject MM (normalization as above): The left–right asymmetry ratio $Q=1$ of the first two temporal eigenfunctions indicates laryngeal left–right symmetry. AP asymmetry is indicated by the qualitative difference in the spectral content of the first and the second temporal eigenfunctions. Therefore, the main spectral information is contained in the first two EOFs.

complex spatio-temporal vibration patterns by many different oscillating structures. We extend biphonation, so far experimentally known to result from the desysnchronized oscillation of the entire left and right vocal folds (Mergell *et al.*, 2000), to toroidal behavior of two oscillating structures on single vocal folds. For a clearer distinction, we introduce the term ''LR biphonation'' for the first case, and the term ''AP biphonation'' for the second case to express the interaction of the first EOF with different AP modes (i.e., higher EOFs) that generates biphonation.

We have provided four measures that characterize spatio-temporal oscillation patterns observed in digital high-speed recordings: the left–right asymmetry Q_{lr}, the anterior–posterior asymmetry Q_{ap}, the information entropy S_{tot} as spatial irregularity, and the number of relevant modes. Table III summarizes the results for the phonation examples shown. For normal phonation, both Q_{lr} and Q_{ap} are equal to unity, and the entropy and the number of modes are small. For LR asymmetrical vibration, Q_{lr} is significantly smaller than unity (due to the higher fundamental frequency of the paralyzed vocal fold). Within measuring accuracy Q_{ap} is unity. The spatial irregularity, described by S_{tot}, and the number of modes are significantly larger than for normal phonation. We conclude, that due to the spatial irregularity higher modes are excited, which are synchronized within single vocal folds, but desynchronized between either vocal fold (due to the paralysis of the left vocal fold). For the AP asymmetrical oscillation, Q_{ap} is significantly smaller than unity, and Q_{lr} is unity. The increased entropy S_{tot} and the larger number or relevant mods, compared to recurrent nerve paralysis, indicate a further increase in spatial irregularity. We conclude that on either vocal fold higher modes are excited. These modes can vibrate independently, presumably due to invisible anterior–posterior inhomogeneities. We suggest that modes on both vocal folds could be synchronized due to short moments of vocal fold contact and the airstream. This conclusion deserves further investigation analyzing more pathological phonation examples showing anterior–posterior biphonation.

TABLE III. Summary of measures quantifying spatio-temporal vocal-fold vibration patterns for three phonation examples: Phonation patterns are described by the left–right asymmetry, anterior–posterior asymmetry, the overall spatial irregularity, and the number of dynamically relevant EOF modes. The number of relevant modes is related to the spatial irregularity. Thus, it could be connected to the minimum number of degrees of freedom that a prospective biomechanical model for the individual pathology should provide.

Subject	Left–right asymmetry $Q_{\mathrm{lr}}^{(\mathrm{exp})}$	Anterior–posterior asymmetry $Q_{\mathrm{ap}}^{(\mathrm{exp})}$	Spatial irregularity		Number of relevant modes	
			$S_{\mathrm{tot}}^{(l)}$	$S_{\mathrm{tot}}^{(r)}$	Left	Right
JN	1.0	1.0	0.22	0.23	2	2
WS	0.74	1.0	0.35	0.37	2	3
MM	1.0	0.80	0.76	0.77	4	4

In this paper we describe methods to analyze irregular spatio-temporal vocal fold oscillations quantitatively. First, we applied spectral analysis to time series of selected vocal-fold edge points along the anterior–posterior direction. In general this method is not appropriate to decompose spatio-temporal oscillation patterns, as the choice of the time series is quite arbitrary and the interdependence between different time series associated with different edge points along the anterior–posterior direction is lost. However, this approach can provide first hints to the underlying mechanism of irregular vocal fold oscillations. Nevertheless, for a quantitative and consistent spatio-temporal analysis we used empirical orthogonal functions to decompose the HGG data into different modes. This concept incorporates correlations of different time series and resolves the dynamics of different spatial modes. The results for the left–right asymmetry and the anterior–posterior asymmetry with both methods were consistent. Nevertheless, we could quantify the spatial irregularity by only using empirical orthogonal functions to decompose the observed spatio-temporal patterns into a hi-

erarchy of different spatial modes. Of course, this method works similar to a rough and just qualitative analysis of subsequent high-speed frames done by a observer with less sophisticated methods.

We showed data on three subjects with normal phonation, LR biphonation, and AP biphonation. We used the terms ''healthy phonation,'' ''left recurrent nerve paralysis,'' and ''functional dysphonia'' just as labels to discriminate between the time series. It is beyond the scope of this paper to discuss the connection of the pathophysiology of the subjects with the observed phonation patterns. Nevertheless, the presented analysis method may help to replace the ill-defined term ''functional'' by a more detailed diagnosis. In contrast to cases with clearly visible morphological changes of the vocal folds, the term functional dysphonia is used for pathological phonation with no apparent structural change in the larynx (Kotby *et al.*, 1993; Wittenberg *et al.*, 1997). So until now ''functional'' just states the absence of diagnostic methods to describe the pathology on basis of direct observations. With this paper we suggest to use the EOF analysis to quantify the dynamics of hoarseness related to dysfunctions of the laryngeal configuration hidden in the complex vibratory patterns.

As a possible mechanism for the desynchronization of the first two modes, we suggest that inhomogeneities of the vocal fold tissue properties like local, hidden morphological changes in deeper tissue layers could induce and support the independent vibration of modes. These endoscopically invisible changes in vocal fold tissue properties might decrease the coupling between anterior and posterior parts of the vocal folds facilitating biphonation. Here, we use the term inhomogeneities to express the deviance (like local morphological changes) from the normal inhomogeneity occurring along the anterior–posterior direction together with the different layer structure.

To a certain extent, the recorded HGG time series are contaminated with noise originating from different sources. Examples are finite temporal and spatial sampling accuracy, and thermal noise of the CCD chip used in the digital camera. Uncertainties of the vocal fold edge detection process due to blurred recordings and due to mucus or light tissue structure on the surface of the vocal folds are further noise sources. We find noisy contributions in the EOF modes, in their weights, and in their temporal coefficients. Due to noise, the sequence of weights of higher modes of the EOF decomposition decrease rather slowly (Landa and Rosenblum, 1991; North *et al.*, 1982), As we do not model the generation of noise, we use a simple and robust threshold criterion to estimate the dynamically relevant modes. Thus, we can compare the number of relevant modes of different phonation examples and of previous theoretical work. For a more sophisticated criterion, more information about mechanisms generating noise in the digital high-speed observations has to be considered (see Landa and Rosenblum, 1991). As the weights of higher modes have negligible values due to noise, we used only the first 21 weights to calculate Shannon's entropy S_{tot} and to plot the weight distribution (Fig. 12) for the sake of comparability.

Using endoscopy and a high-speed setup, several systematic errors of the recording procedure and the extraction of time series of vocal fold points have to be taken into account. For a detailed discussion of blurring due to finite temporal and spatial resolution, technical problems with rotation, vertical and horizontal relative movement between glottis and endoscope, and the ambiguity of vocal fold edge detection due to inferior–superior vibratory mode we refer to previous work (Wittenberg, 1998; Wittenberg *et al.*, 1997). Regarding the finite temporal and spatial resolution we must restrict our analysis to a range given by Shannon's sampling theorem. Furthermore, we neglect the influence of higher-frequency components because they cannot be resolved by the finite spatial and temporal resolution of the high-speed camera system. However, since EOF analysis is based on averaging, random fluctuations are suppressed.

EOF analysis of time series obtained from three-dimensional biomechanical simulations of normal and chaotic vocal-fold oscillations (Berry *et al.*, 1994) show that two modes are enough to capture the vibration pattern of normal phonation. In these extensive computer simulations of a model with 414 degrees of freedom, four dominant EOFs could still explain even more complex dynamics. We found similar results analyzing *in vivo* data. As we analyze HGG data for the upper vocal fold edge only, the first two modes found in the biomechanical model (Berry *et al.*, 1994) nearly correspond to the first EOF of the *in vivo* data. The major limitation of *in vivo* data obtained with our high-speed setup is, that the time series from the endoscopic view show the dynamics of mainly the upper vocal fold edge. Therefore, all modes related to the vertical vocal fold direction cannot be distinguished.

This work proposes a method for a systematic development of appropriate low-dimensional biomechanical models. These models could incorporate left–right asymmetries and anterior–posterior inhomogeneities to simulate irregular spatio-temporal vibration patterns. We could reduce multiple trajectories of vocal fold edge points to a few principal vibrating modes, which could then be used in model simulations. The number of degrees of freedom of appropriate low-dimensional models should correspond to the number of principal vibrating modes observed *in vivo*. Here, for subject JN the measured dynamics from 21 vocal fold edge points on each vocal fold can be reduced to the dynamics of two modes. Similarly, we could compress the observed dynamics of 49 glottal edge points of subject WS into two or three modes, respectively. For subject MM, a reduction of the dynamics of 39 observed edge points to four principal modes could be obtained. Thus, models simulating AP mode dynamics might be derived in a systematic way from high-speed observations, where inhomogeneities of the viscoelastic properties of the vocal folds, e.g., localized morphological changes, could be incorporated. This hypothesis deserves further investigation.

Our clinical motivation for using EOF analysis was to measure ''AP modes'' known from literature and frequently observed qualitatively in clinical everyday work (Hess *et al.*, 1994; Tigges *et al.*, 1999). The main impact of EOF analysis is the measurement of the dynamics of spatial modes crucial for the description of AP modes. Thus, empirical orthogonal

analysis could reveal endoscopically invisible morphological and, moreover, functional changes of myoelastic properties of the vocal folds. Moreover, we could expect that in other cases also visible modifications such as cicatrices from operations, small polyps, nodules, cysts, or tumors may affect nodes and antinodes of surface waves in the surface tissue of the vocal folds. Local stiffening of visible superficial vocal-fold tissue or local stiffening or atrophy of invisible deeper mucosal and muscular tissue may also constrain certain modes of vocal fold vibration. With EOF analysis, aerodynamical and visco-elastical excitation mechanisms for AP modes may be examined. The coupling of AP modes and the sub- and supraglottal tract can be studied as well. Thus, with EOF analysis a more detailed diagnosis for pathological phonation may be provided using the measures proposed in this paper. Moreover, EOF analysis may give hints for surgery and speech therapy. From the viewpoint of nonlinear dynamics, these suggestions merit a closer analysis of models that exhibit AP modes. Excitation mechanisms and the bifurcation structure of vocal-fold models revealing spatio-temporal vibration patterns are of clinical importance for the diagnosis of irregular phonation.

V. CONCLUSION

This paper shows that spatio-temporal glottal contour patterns obtained from high-speed observation of pathological phonation can be decomposed into modes using EOF analysis. Therefore, laryngeal asymmetries can be quantified. We have extended previous methods that analyze time series of single vocal fold edge points (Mergell *et al.*, 2000) to analyze the complete vocal fold contour, i.e., the entirety of the upper vocal fold edge points. We also have extended the technique of multiline kymography, described by Tigges *et al.* (1999).

We have found a new generation mechanism for the known phenomenon of biphonation. We have also shown experimentally that so-called AP modes are excited during vocal fold oscillations, and we quantify the weights of AP modes. We have observed that AP modes oscillate independently from the basic glottal mode. This behavior leads to biphonation. Thus, we provide experimental evidence for the desynchronization of modes previously observed in theoretical models (Alipour-Haghighi *et al.*, 2000; Berry *et al.*, 1994; Titze *et al.*, 1993) and in *in vivo* experiments, e.g., with excised larynges (Berry, 2000). Thus, our method of examining high-speed observations of vocal fold vibrations *in vivo* compliments previous findings in computer models and *in vitro* high-speed studied in the laboratory. We suggest the use of EOF analysis to systematically develop simple low-dimensional biomechanical models of vocal folds using direct, endoscopic high-speed observations of vocal fold oscillations *in vivo*.

ACKNOWLEDGMENTS

This work has been supported by the Deutsche Forschungsgemeinschaft. We thank M. Tigges and T. Wittenberg at the Dept. of Phoniatrics and Pediatric Audiology (University Erlangen-Nuremberg) for many fruitful discussions. We thank D. Berry for valuable suggestions.

APPENDIX: EMPIRICAL ORTHOGONAL FUNCTION ANALYSIS

The method of empirical orthogonal (eigen)functions is used to extract independent spatio-temporal structures from complex spatio-temporal vibration patterns. It uses correlations between the time series of the vocal fold edge points to decompose the complex spatio-temporal vibration pattern into principal modes of vibration (Berry *et al.*, 1994). In the literature, the terms ''coherent structures,'' ''spatio-temporal structures,'' ''principal modes,'' or just ''modes'' have been used interchangeably (Aubry *et al.*, 1991; Berry *et al.*, 1994). The EOF method is also called principal components analysis, biorthogonal decomposition. Karhunen–Loéve expansion, proper orthogonal decomposition, principal factor analysis, singular-value analysis, and the singular spectrum analysis (see Berry *et al.*, 1994). In principle, the idea of empirical orthogonal function analysis is to find an orthogonal coordinate system in state space for which all data points are decorrelated.

Here, we are interested in independent spatio-temporal structures about the rest position of the vocal folds. Therefore, the excursion $d_k^{(\alpha)}(t_i)$ from the glottal midline is divided into a mean and a oscillatory component

$$\delta_k^{(\alpha)}(t_i) = d_k^{(\alpha)}(t_i) - \overline{d_k^{(\alpha)}}. \tag{A1}$$

Here, $k=1,...,N$ indicates the kymogram number, $i=1,...,M$ is the time index, and $\alpha \in \{\text{left,right}\}$ specifies the side of the vocal folds. The mean $\overline{d_k^{(\alpha)}} = \langle d_k^{(\alpha)}(t_i) \rangle_{t_i}$ represents the dynamic equilibrium of each vocal fold, where $\langle \cdot \rangle_{t_i}$ denotes a time average. The covariance matrix $\mathbf{C}^{(\alpha)}$ measures linear interdependencies of the fluctuations $\delta_k^{(\alpha)}(t_i)$ about the dynamic equilibrium at different locations k,l of each vocal fold

$$C_{kl}^{(\alpha)} = \frac{1}{M} \sum_{i=1}^{M} \delta_k^{(\alpha)}(t_i)\, \delta_l^{(\alpha)}(t_i) = \langle \delta_k^{(\alpha)}(t_i)\, \delta_l^{(\alpha)}(t_i) \rangle_{t_i}, \tag{A2}$$

with $k,l=1,...,N$. The covariance matrix is a real, symmetric, and positive semidefinite matrix, which can be diagonalized and has real and nonnegative eigenvalues

$$\mathbf{C}^{(\alpha)} \Phi_l^{(\alpha)} = \lambda_l^{2(\alpha)} \Phi_l^{(\alpha)}. \tag{A3}$$

The normalized eigenvectors $\Phi_l^{(\alpha)}$, $l=1,...,N$, correspond to the empirical orthogonal functions (EOF). Sometimes, they are called ''topos'' to indicate their topological meaning (Aubry *et al.*, 1991). The corresponding eigenvalues $\lambda_l^{2(\alpha)}$ carry the weights of the normalized EOFs. They express the variance of the associated EOF about the dynamic equilibrium. The eigenfunctions define a set of orthogonal directions in the N-dimensional state space $\{\delta_k^{(\alpha)}\}$, and the eigenvalues measure the variance of the observed set of states projected onto their corresponding EOF axis. The first eigenfunction is the direction in state space, for which the variance is maximal.

The total variance E_{tot} of the centered set of states $\{\delta_k^{(\alpha)}(t_i)\}$ is given by the sum of the eigenvalues $\lambda_l^{2(\alpha)}$ of the EOFs

$$E_{\text{tot}}^{(\alpha)} = \sum_{l=1}^{N} \lambda_l^{2(\alpha)} = \langle \delta_k^{(\alpha)}(t_i)\, \delta_k^{(\alpha)}(t_i) \rangle_{k,t_i}. \tag{A4}$$

$\lambda_l^{2(\alpha)}$ is the variance of one single spatio-temporal structure about the dynamic equilibrium of the vocal fold α, with $\alpha \in \{\text{left,right}\}$. As the EOFs $\Phi_l^{(\alpha)}$ establish an orthonormal system, the oscillatory components $\delta_k^{(\alpha)}(t_i)$ can be written as a linear superposition

$$\delta_k^{(\alpha)}(t_i) = \sum_{l=1}^{N} a_l^{(\alpha)}(t_i) \Phi_l^{(\alpha)}(k). \tag{A5}$$

The temporal expansion coefficients $a_l^{(\alpha)}(t_i)$ are determined by the projection of the oscillatory components onto the eigenfunctions

$$a_l^{(\alpha)}(t_i) = \sum_{k=1}^{N} \delta_k^{(\alpha)}(t_i) \Phi_l^{(\alpha)}(k). \tag{A6}$$

Sometimes, the temporal coefficiens are called ''chronos,'' as they express the chronological importance of the associated topos (Aubry *et al.*, 1991). They can also be regarded as temporal eigenfunctions corresponding to their associated EOFs, that can be thougth of as spatial eigenfunctions. Finally, the oscillations of the vocal fold edges about their dynamical equilibrium can be decomposed as

$$\delta_k^{(\alpha)}(t_i) = \sum_{l=1}^{N} \lambda_l^{(\alpha)} \Psi_l^{(\alpha)}(t_i) \Phi_l^{(\alpha)}(k), \tag{A7}$$

with $\Psi_l^{(\alpha)}(t_i)$ defined by

$$a_l^{(\alpha)}(t_i) = \lambda_l^{(\alpha)} \Psi_l^{(\alpha)}(t_i). \tag{A8}$$

To characterize different kinds of complex spatio-temporal patterns for different laryngeal pathologies, we propose measures that provide overall information about the distribution of spatio-temporal vibration modes.

The eigenvalues $\lambda_l^{2(\alpha)}$ contain information about the distribution of variance in the state space $\{\delta_l^{(\alpha)}\}$ in the direction of the modes. The information entropy (Shannon's entropy) measures the degree of disorder of irregular spatio-temporal glottal contour patterns. It quantifies the shape of the eigenvalue distribution. The relative weights of each EOF

$$p_l^{(\alpha)} = \lambda_l^{2(\alpha)} / E_{\text{tot}}^{(\alpha)}, \tag{A9}$$

can be regarded as a probability distribution for the projection of an observation onto the directions of the EOFs $\Phi_l^{(\alpha)}$ in state space $\{\delta_k^{(\alpha)}\}$. Thus, the information entropy $S_{\text{tot}}^{(\alpha)}$ is an overall quantity for the degree of disorder of this distribution

$$S_{\text{tot}}^{(\alpha)} = -\sum_{l=1}^{N} p_l^{(\alpha)} \log p_l^{(\alpha)}. \tag{A10}$$

If only a single eigenvalue is nonzero, the information entropy is zero. Then, a single empirical function is present. Furthermore, $S_{\text{tot}}^{(\alpha)}$ will be small for a sharply peaked distribution $p_l^{(\alpha)}$, whereas for a broad distribution, $S_{\text{tot}}^{(\alpha)}$ will become large. In the limit of equidistributed EOFs, where all eigenvalues become equal, the information entropy reaches it global maximum $S_{\max} = \log N$.

Alipour-Haghighi, F., Berry, D. A., and Titze, I. R. (**2000**). ''A finite element model of vocal fold vibration,'' J. Acoust. Soc. Am. **108**, 3003–3012.

Aubry, N., Guyonnet, R., and Lima, R. (**1991**). ''Spatiotemporal analysis of complex signals: Theory and application,'' J. Stat. Phys. **64**, 683–739.

Bergé, P., Pomeau, Y., and Vidal, C. (**1984**). *Order Within Chaos* (Herman, Paris).

Berry, D. A. (**2001**). ''Mechanism of modal and nonmodal phonation,'' J. Phonetics (in press).

Berry, D. A., Herzel, H., Titze, I. R., and Krischer, K. (**1994**). ''Interpretation of biomechanical simulations of normal and chaotic vocal fold oscillations with empirical eigenfunctions,'' J. Acoust. Soc. Am. **95**, 3595–3604.

Bloss, H., Backert, C., and Raguse, A. (**1993**). ''CAMSYS high-speed camera system,'' Fraunhofer Gesellschaft IIS, Erlangen, Germany.

Breuer, K. S., and Sirovich, L. (**1991**). ''The use of the Karhunen-Loève procedure for the calculation of linear eigenfunctions,'' J. Comput. Phys. **96**, 277–296.

Eysholdt, U., Tigges, M., Wittenberg, T., and Pröschel, U. (**1996**). ''Direct evaluation of high-speed recordings of vocal fold vibrations,'' Folia Phoniatr. Logop. **48**, 163–170.

Farnsworth, D. W. (**1940**). ''High-speed motion picture of the human vocal folds,'' Bell Lab. Rec. **18**, 203–208.

Hammarberg, B. (**1995**). ''High-Speed Observations of Diplophonic Phonation,'' in *Vocal Fold Physiology*, edited by O. Fujimura and M. Hirano (Singular, San Diego), Chap. 21, pp. 343–345.

Herzel, H. (**1993**). ''Bifurcations and chaos in voice signals,'' Appl. Mech. Rev. **46**, 399–413.

Herzel, H., Berry, D. A., Titze, I. R., and Saleh, M. (**1994**). ''Analysis of vocal disorders with methods from nonlinear dynamics,'' J. Speech Hear. Res. **37**, 1008–1019.

Herzel, H., and Reuter, R. (**1997**). ''Whistle register and biphonation in a child's voice,'' Folia Phoniatr. Logop. **49**, 216–224.

Herzel, H., and Wendler, J. (**1991**), ''Evidence of chaos in phonatory samples,'' in Proc. EUROSPEECH (Genova), edited by ESCA, pp. 263–266.

Hess, M., Gross, M., and Herzel, H. (**1994**). ''Hochgeschwindigkeitsaufnahmen von Schwingungsmoden der Stimmlippen,'' Otorhinolaryngol. Nova **4**, 307–312.

Ishizaka, K., and Isshiki, N. (**1976**). ''Computer simulation of pathological vocal-cord vibration,'' J. Acoust. Soc. Am. **60**, 1193–1198.

Kiritani, S., Hirose, H., and Imagawa, H. (**1993**). ''High-speed digital image analysis of vocal fold vibration in diplophonia,'' Speech Commun. **13**, 23–32.

Kiritani, S., Imagawa, H., and Hirose, H. (**1995**). ''Vocal fold vibrations associated with involuntary voice changes in certain pathological cases,'' in *Vocal Fold Physiology*, edited by O. Fujimura and M. Hirano (Singular, San Diego), pp. 269–281.

Kotby, M., Titze, I., Saleh, M., and Berry, D. (**1993**). ''Fundamental frequency stability in functional dysphonia,'' Acta Oto-Laryngol. **113**, 439–444.

Landa, P. S., and Rosenblum, M. G. (**1991**). ''Time series analysis for system identification and diagnostics,'' Physica D **48**, 232–254.

Lucero, J. C., and Gotoh, T. (**1993**). ''On the threshold pressure and the minimum sustaining pressure in the vocal fold oscillation,'' J. Acoust. Soc. Jpn. **14**, 213–214.

Mergell, P. (**1998**). ''Nonlinear Dynamics of Phonation—Highspeed Glottography and Biomechanical Modeling of Vocal Fold Oscillations,'' Ph.D. thesis, Shaker, Aachen.

Mergell, P., and Herzel, H. (**1997**). ''Modelling biphonation—the role of the vocal tract,'' Speech Commun. **22**, 141–154.

Mergell, P., Herzel, H., and Titze, I. (**2000**). ''Irregular vocal fold vibration—High-speed observation and modeling,'' J. Acoust. Soc. Am. **108**, 2996–3002.

North, G. R., Bell, T. L., and Cahalan, R. F. (**1982**). ''Sampling errors in the estimation of empirical orthogonal functions,'' Mon. Weather Rev. **110**, 699–706.

Riviere, C. N., Rader, R. S., and Thakor, T. V. (**1998**). ''Adaptive canceling of physiological tremor for improved precision in microsurgery,'' IEEE Trans. Biomed. Eng. **45**, 839–846.

Smith, M. E., Berke, G. S., Gerrat, B. R., and Kreiman, J. (**1992**). ''Laryngeal paralyses: Theoretical considerations and effects on laryngeal vibration,'' J. Speech Hear. Res. **35**, 545–554.
Steinecke, I., and Herzel, H. (**1995**). ''Bifurcations in an asymmetric vocal-fold model,'' J. Acoust. Soc. Am. **97**, 1874–1884.
Švec, J. G., Horáček, J., Šram, F., and Veselý, J. (**2000**). ''Resonance properties of the vocal folds: *In vivo* laryngoscopic investigation of the externally excited laryngeal vibrations,'' J. Acoust. Soc. Am. **108**, 1397–1407.
Švec, J. G., and Schutte, H. K. (**1996**). ''Videokymography: High-speed line scanning of vocal fold vibration,'' J. Voice **10**, 201–205.
Tigges, M., Mergell, P., Herzel, H., Wittenberg, T., and Eysholdt, U. (**1997**). ''Observation and modeling glottal biphonation,'' Acust. Acta Acust. **83**, 707–714.
Tigges, M., Wittenberg, T., Mergell, P., and Eysholdt, U. (**1999**). ''Imaging of vocal fold vibration by digital multi-plane kymography,'' Comput. Med. Imaging Graphics **23**, 323–330.
Titze, I. R. (**1973**). ''The human vocal cords: A mathematical model I,'' Phonetica **28**, 129–170.
Titze, I. R. (**1976**). ''On the mechanics of vocal-fold vibration,'' J. Acoust. Soc. Am. **60**, 1366–1380.
Titze, I. R., Baken, R., and Herzel, H. (**1993**). ''Evidence of chaos in vocal fold vibration,'' in *Vocal Fold Physiology: Frontiers in Basic Science*, edited by I. Titze (Singular, San Diego), pp. 143–188.
Titze, I. R., and Story, B. (**1997**). ''Acoustic interactions of the voice source and the lower vocal tract,'' J. Acoust. Soc. Am. **101**, 2234–2243.
Titze, I. R., and Strong, W. J. (**1975**). ''Normal modes in vocal cord tissues,'' J. Acoust. Soc. Am. **57**, 736–744.
Wendler, J., Seidner, W., Kittel, G., and Eysholdt, U. (**1996**). *Lehrbuch der Phoniatrie und Pädaudiologie* (Thieme, Stuttgart, New York).
Wilden, I., Herzel, H., Peters, G., and Tembrock, G. (**1998**). ''Subharmonics, biphonation, and deterministic chaos in mammal vocalization,'' Bioacoustics **9**, 171–196.
Wittenberg, T. (**1997**). ''Automatic motion extraction from laryngeal kymograms,'' in *Advances in Quantitative Laryngoscopy*, edited by T. Wittenberg, P. Mergell, M. Tigges, and U. Eysholdt (Abteilung Phoniatrie, Göttingen), pp. 21–28.
Wittenberg, T. (**1998**). ''Wissesnsbasierte Bewegungsanalyse von Stimmlippenschwingungen anhand digitaler Hochgeschwindigkeitsaufnahmen,'' Ph.D. thesis, Shaker, Aachen.
Wittenberg, T., Mergell, P., Tigges, M., and Eysholdt, U.(**1997**). ''Quantitative characterization of functional voice disorders using analysis of high-speed video and modeling,'' in Proc. ICASSP-97, 21–24 April, Munich, Germany, Vol. 3.
Wittenberg, T., Moser, M., Tigges, M., and Eysholdt, U. (**1995**). ''Recording, processing and analysis of digital highspeed sequences in glottography,'' Mach. Vision Appl. **8**, 399–404.

A method of applying Fourier analysis to high-speed laryngoscopy

Svante Granqvist[a)]
Department of Speech, Music and Hearing, Royal Institute of Technology, Stockholm, Sweden

Per-Åke Lindestad[b)]
Department of Logopedics and Phoniatrics, Karolinska Institute, Huddinge University Hospital, Stockholm, Sweden

(Received 25 May 2000; accepted for publication 18 June 2001)

A new method for analysis of digital high-speed recordings of vocal-fold vibrations is presented. The method is based on the extraction of light-intensity time sequences from consecutive images, which in turn are Fourier transformed. The spectra thus acquired can be displayed in four different modes, each having its own benefits. When applied to the larynx, the method visualizes oscillations in the entire laryngeal area, not merely the glottal region. The method was applied to two laryngoscopic high-speed image sequences. Among these examples, covibrations in the ventricular folds and in the mucosa covering the arytenoid cartilages were found. In some cases the covibrations occurred at other frequencies than those of the glottis. © *2001 Acoustical Society of America.*
[DOI: 10.1121/1.1397321]

PACS numbers: 43.70.Jt [AL]

I. INTRODUCTION

The periodicity of the vocal-fold vibrations is a highly relevant aspect of voice production, both in normal and in pathological voices. The periodicity, or lack of periodicity, is typically described in terms of jitter and/or shimmer, period-to-period correlation, or by spectral characteristics (see, e.g., Titze and Liang, 1993; Hess, 1983). Analysis of such characteristics is generally applied to acoustic signals recorded from microphones, but can also be used on signals derived from physiological events such as EGG or airflow recorded from flow masks.

Another method for acquisition of physiological data is direct visual inspection of the vocal folds by means of laryngoscopy. This method is often combined with stroboscopy (see, e.g., Švec, 2000) to visualize the vibrations of the vocal folds. However, aperiodicities associated with some voice qualities make stroboscopy inappropriate, since it requires periodic vibration and a single, measurable fundamental frequency. One way to circumvent this problem is to use high-speed imaging, a technique that has been used for many decades (see, e.g., Moore *et al.*, 1962; Dunker *et al.*, 1964). High-speed imaging therefore also offers an informative description of aperiodic vocal-fold oscillations, since each vibratory cycle is documented in terms of a sequence of several images. Recently, digital high-speed imaging of the larynx has become more commonly used, mainly because of reduced costs and improved light sensitivity of high-speed cameras with digital storage (see, e.g., Kiritani *et al.*, 1988; Hammarberg, 1995; Kiritani, 1995; Köster *et al.*, 1999; Eyshold *et al.*, 1996). Moreover, modern cameras can now produce images of acceptable quality when combined with standard clinical optical instruments.

A problem associated with video recordings in general, however, is visual interpretation. In particular, it is sometimes hard to observe which parts of the larynx are vibrating, at what frequencies, and in what phase relation to other vibrations. One solution is to use kymography, which can be acquired directly from a single-line camera (Švec and Schutte, 1996) or by extraction from high-speed image sequences (Tigges *et al.*, 1999; Larsson *et al.*, 2000). Such kymographic images give a good view of the movements of the vocal folds, periodic or nonperiodic, but only for part of the image, i.e., the single line. Another method for data extraction from high-speed images is detection of the edges of the glottis (e.g., Larsson *et al.*, 2000), which can be used for glottal area and flow calculations. Such methods are mostly applicable, however, only to the glottis, as they generally cannot reveal oscillations in other parts of the larynx.

This paper presents a new method to visualize periodic or quasiperiodic oscillations in the entire laryngeal area. The basic idea is to extract time signals from consecutive images. The resulting signals are Fourier transformed and can be displayed in different ways, for example in terms of a coloring of the laryngeal image. The method can be seen as a way of condensing data from all of the images within an image sequence and for all locations within those images into one or a few more informative images, displaying relevant oscillatory frequencies.

II. MATERIAL

Digital high-speed recordings were made at the department of Logopedics and Phoniatrics at Huddinge University Hospital. The subject was a male with a healthy voice (co-author P-Å L). Laryngoscopy was performed using either a flexible (Olympus ENF, P3) or a rigid (70° Hopkins 8706 CJ, Karl Storz) endoscope. The light source was a Storz 600 with a halogen lamp. The endoscopes were connected to the cam-

[a)]Electronic mail: svante.granqvist@speech.kth.se
[b)]Electronic mail: Per-Ake.Lindestad@logphon.hs.sll.se

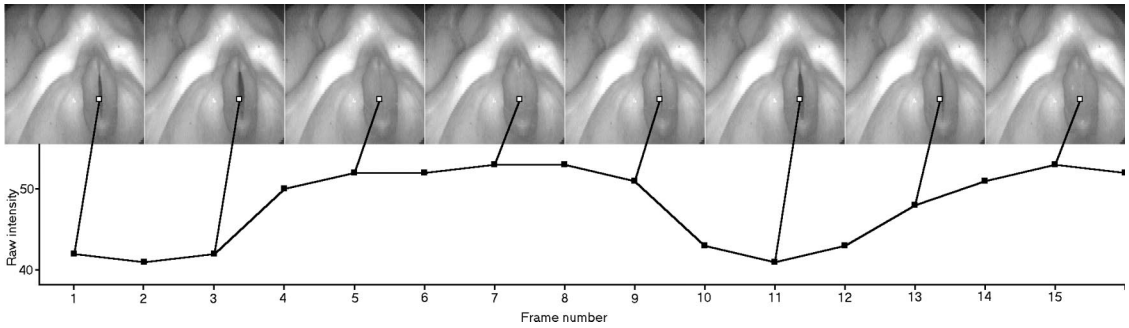

FIG. 1. Derivation of a single time sequence from an image sequence. The lower graph displays the time-varying intensity at the indicated pixel in the upper series of images. Alternatively, a similar intensity curve can be derived from the average intensity over an entire line, rather than from a single pixel. For clarity, every second image in the sequence has been excluded in the figure.

era system via an Olympus AR-L2 C-adapter. The camera system was a Weinberger Speedcam that was run at a frame rate of 1904 images per second, memory allowing recording of 2048 frames, or 1 s, approximately. The image resolution was 256×64 pixels. Images were stored and analyzed digitally. A Hamming window of 270 ms (512 points) was used for all Fourier transforms.

III. APPLICATIONS

The extraction of the time sequences can be applied either to a specific pixel or to a specific line in the image. This procedure involves three steps. First, the raw intensity data are extracted, i.e., the level of gray at the pixel in question, or the average level of gray of the line in question. This extraction is performed on each image with fixed line or point coordinates on a set of consecutive images, as illustrated in Fig. 1. The resulting data points are used to form consecutive samples in a time signal. Figure 2 (left) provides an example. Second, this time signal is scaled according to the average amplitude so as to eliminate the effect of different illumination in different parts of the image, Fig. 2 (middle). Third, the average of the signal is removed, Fig. 2 (right), since a large nonzero average component would obscure the lower part of the spectrum.

The time sequences thus obtained are then Fourier transformed. This results in a spectrum for each pixel or line. The output of these Fourier transforms contains amplitude and phase information as a function of frequency. Such Fourier analyses can be visualized in several ways simultaneously and preferably in conjunction with kymography and standard playback of the image sequence. Since there are four to five parameters involved (*x* position, *y* position, frequency, amplitude, and possibly phase), some of them have to be left out if a two- or three-dimensional graph is chosen. Four alternative modes seem particularly informative.

A. Single-pixel, all frequencies

In this mode of visualization, a single pixel is selected with a cursor. The Fourier transform of the light intensity at that pixel in the selected and consecutive images is displayed in a two-dimensional graph. The graph is an ordinary line spectrum display with frequency in Hz on the *x* axis and amplitude in dB on the *y* axis. For example, if the pixel or line is positioned at an oscillating glottis, a peak will appear in the amplitude spectrum at the glottal vibration frequency. This is illustrated in Fig. 3 pertaining to a high-pitched phonation. The figure shows a fundamental oscillation frequency of 210 Hz. $F0$ analysis of the corresponding sound, recorded simultaneously, yielded an $F0$ of 214 Hz.

B. Line average, all *y* positions, all frequencies

In this mode, the time curve is extracted by averaging the intensity for each line in the images. This yields a set of time sequences, one for each line. The sequences are Fourier transformed and the result is displayed in a three-dimensional graph with frequency on the *x* axis, vertical position on the *y* axis, and amplitude on the *z* axis, which is represented as level of gray. Figure 4 exemplifies such a three-dimensional graph, revealing major oscillation frequencies. At the level of the glottis in the image, shown to the left in figure, a dark line can be seen at 210 Hz. This line corresponds to the frequency of vocal-fold vibration; see above. The vertical line at 100 Hz is an artifact caused by

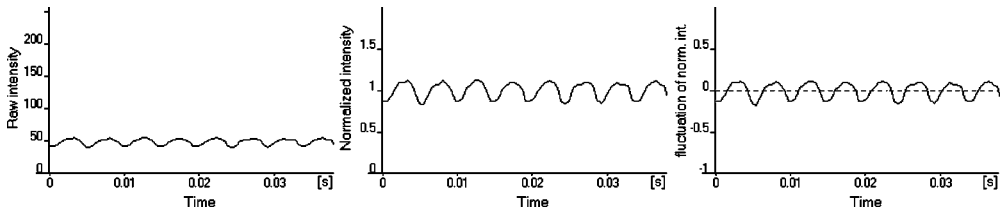

FIG. 2. Normalization of the time sequence, applied to compensate for differences in mean illumination strength and light absorption in different parts of an image. Left panel: raw signal taken from Fig. 1; middle panel: normalization of the same signal achieved by multiplying each value by a constant; right panel: resulting signal after removal of average. In this figure, the time window is longer than that used in Fig. 1.

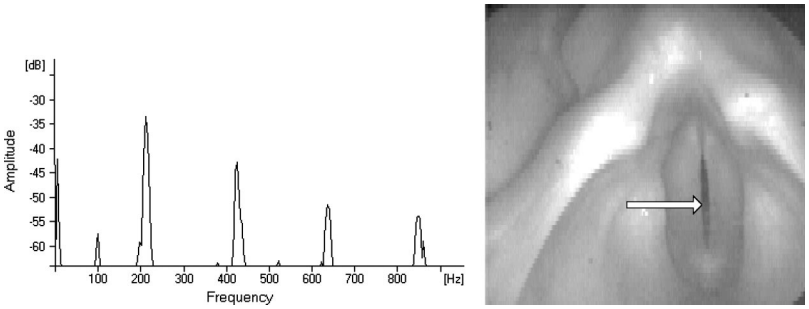

FIG. 3. Fourier transformation (512-point Hamming window) of the signal shown in the right panel of Fig. 2 yielding a spectrum for the selected point. The fundamental at 210 Hz corresponds to the vibration frequency.

light-source flickering. This was checked by analyzing the signal from a light sensor exposed to the light source; this signal contained a 100-Hz component. The flickering was probably due to the fact that the power supply of the lamp was not sufficiently stabilized. The averaging over lines as described above is preferable in cases where oscillatory similarities occur horizontally over the image. If, however, such similarities occur vertically, the averaging could be done over columns.

C. Full image, single frequency

In this mode, Fourier transforms are calculated for each pixel, and a single frequency from the Fourier transforms is selected. The magnitude of the oscillations at that frequency is displayed as color saturation on top of a single image selected from the original sequence. The image is then colored intensely in areas that oscillate at the selected frequency, e.g., in the glottal area. The image in Fig. 5 shows an example, illustrating the amplitude of the intensity variation at the frequency of 210 Hz. The oscillating vocal folds are intensely colored in red, since the light intensity variation in this area is great. The isolated red spots are artifacts caused by light reflections in the wet mucosa. The position of such a glare spot is highly sensitive to a tilting motion of the object, since this causes the light beam to move. At a given pixel this yields a great variation of light intensity and thus high amplitude and intense coloring, even though the motion is not large. Thus, such glare spots are of minor relevance.

D. Full image, single frequency, including phase information

A variant of the last method mentioned is to include the phase information from the Fourier transforms as the hue of the color. In this display mode, those areas of the image in which the intensities oscillate in different phase will be colored differently. The images in Fig. 6 illustrate this display mode for a hyperfunctional breathy phonation as produced by the same subject at a fundamental frequency of about 130 Hz. It must be noted, however, that this phonatory setting is not necessarily typical for a hyperfunctional breathy voice. It can be seen that the vocal folds and the ventricular folds are differently colored, due to an inverse phase relation in the intensity fluctuations between these areas. Careful examination of the high-speed recording confirmed that in this phonation the ventricular folds oscillated at the same frequency as the vocal folds, but in an opposite phase. Thus, the closed phase of the glottis was synchronous with the maximum separation of the ventricular folds. This is further illustrated by Fig. 7.

IV. DISCUSSION

When using the method presented here, certain aspects should be kept in mind. The approach in this paper is based on light-intensity fluctuation. This leads to some problems, since it introduces a nonlinear transfer function from motion to intensity. In particular, edges in the image will yield higher amplitude than flat surfaces, since a motion in a flat

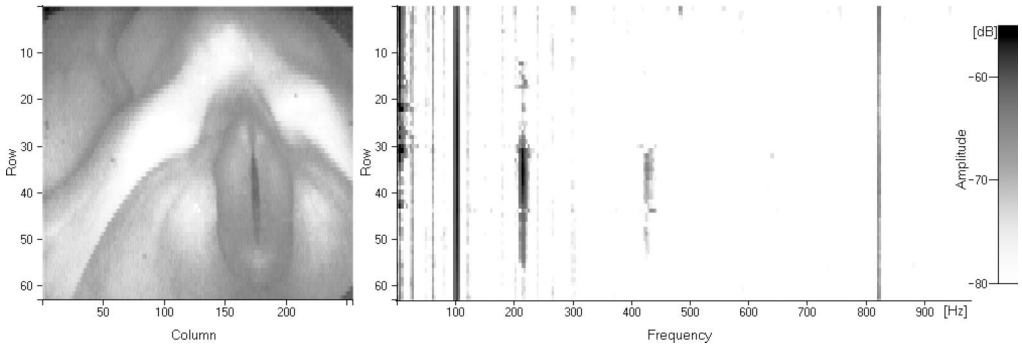

FIG. 4. Three-dimensional representation of spectra at lines rather than at single pixels of the image shown in Fig. 3. The *y* axis is identical with the one used in that image. The vertical bars refer to the oscillation frequencies of light intensity. The bar at 210 Hz corresponds to the vibration frequency of the vocal folds. The weak bar at 420 Hz reflects the second partial of the nonsinusoidal light oscillation at 210 Hz. The bar near 100 Hz is an artifact reflecting the flickering frequency of the light source used in this recording.

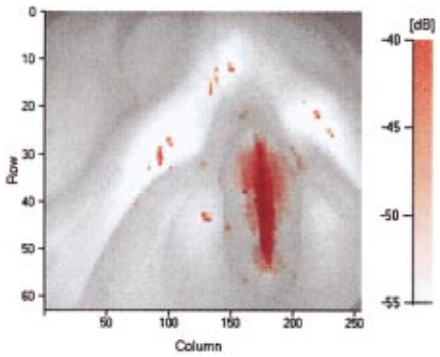

FIG. 5. Amplitude of oscillation, represented in terms of color saturation, at a selected frequency (210 Hz). The coloring has been superimposed on one of the frames from the image sequence.

surface leads to little intensity variation. On the other hand, glare spots will receive high amplitude, as they can move considerably even for a small tilt of the surface. The amplitudes of higher harmonics of the intensity oscillations seem relatively unimportant. To a large extent they are determined by the transfer function from motion to intensity, rather than by higher harmonics in the motion itself. Also, if the structures oscillate at several frequencies, combination tones can appear that are not necessarily present in the motion. However, if these limitations are kept in mind, the images seem quite useful for finding and displaying oscillatory movements in different parts of the larynx. Even though the method does not perform frequency analysis of the actual motion in the larynx, it can still be useful for detecting covibrations, e.g., in the ventricular folds or other structures close to the glottis. These vibrations might appear at the same frequency as that of the glottis, or at other frequencies.

Analysis of the movements of particular structures in an image would be advantageous. This, however, would require identification of such structures within the image. Automatic identification of components within an image is a complicated task, containing many sources of error. The Fourier analysis method can reveal oscillatory movements of the larynx, not obvious from direct inspection or kymography. Relevant information may emerge. For example, structures close to the larynx may oscillate at frequencies other than that of the vocal folds. Such oscillations may interfere with the folds' normal vibration but are not possible to visualize with standard stroboscopy. While high-speed imaging reveals such phenomena, analysis of the actual frequencies at which the structures oscillate is difficult. The case shown in Fig. 6 is an example of this, where vibrations at about a quarter of the fundamental frequency can be seen in the mucosa covering the arytenoid cartilages. The presence of this frequency is verified by the right kymogram in Fig. 7. Similar oscillations have been observed by Švec (2000) who used external excitation to study the resonance properties of the larynx. In this study, large oscillations in the arytenoid cartilages and ary-epiglottic folds were found in the range 50 to 75 Hz. The lower frequency in the present example is probably due to a different phonatory setting with more relaxed ary-epiglottic folds. It could be speculated that such an oscillation could disturb the glottal oscillation, especially near the phonation threshold. In models of vocal-fold vibration it is mostly assumed that the folds are attached to a rigid wall (see, e.g., Flanagan and Landgrat, 1968; Titze, 1973; Liljencrants, 1991; Wong *et al.*, 1991). If the structures to which the vocal folds are attached vibrate, such a model would fail to predict the behavior of the glottis. These types of oscillations are possible to visualize with kymography, but only at a single line of the image sequence. With the Fourier analysis method, the oscillations are visualized for one frequency at a time, but for the entire image.

The method also seems useful in printed representations of oscillations, where a moving playback of an image sequence is not available. Typically, entire sequences of images must be presented, image by image. Using the method presented here, the information contained in such sequences can be condensed to one or a few figures, particularly if a color scale is available.

The method presented here was applied to a limited material provided by one single subject with a healthy voice. The method, however, seems promising, as it offers information on relevant aspects of phonatory vibrations, which are difficult to detect by other means. It should be worthwhile to test the method on a larger material, including different types of phonation and clinical diagnoses.

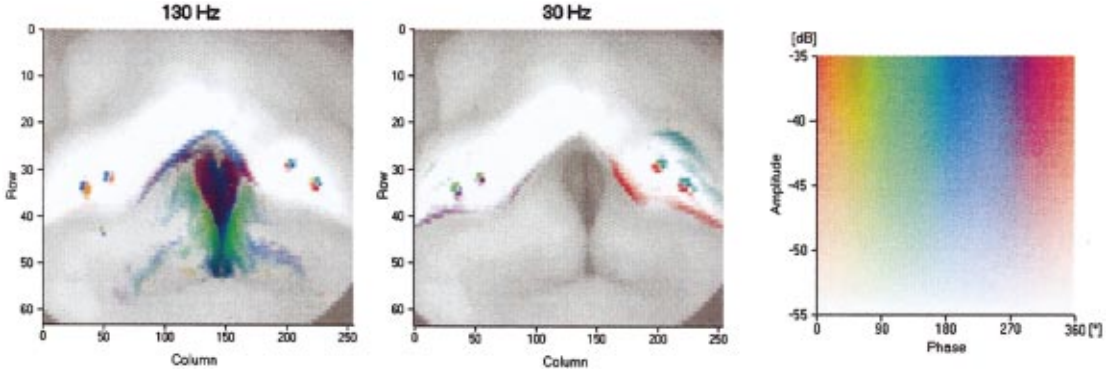

FIG. 6. Representations of intensity oscillations with different phases and covibrations. Phase relations are represented by color hue, and amplitude by color saturation. Left image: oscillations at 130 Hz. Oscillations in the vocal folds and in the ventricular folds are shown in different colors due to opposite phase in the intensity variations. Right image: oscillations at 30 Hz. The coloring reveals covibration in the mucosa covering the arytenoid cartilages.

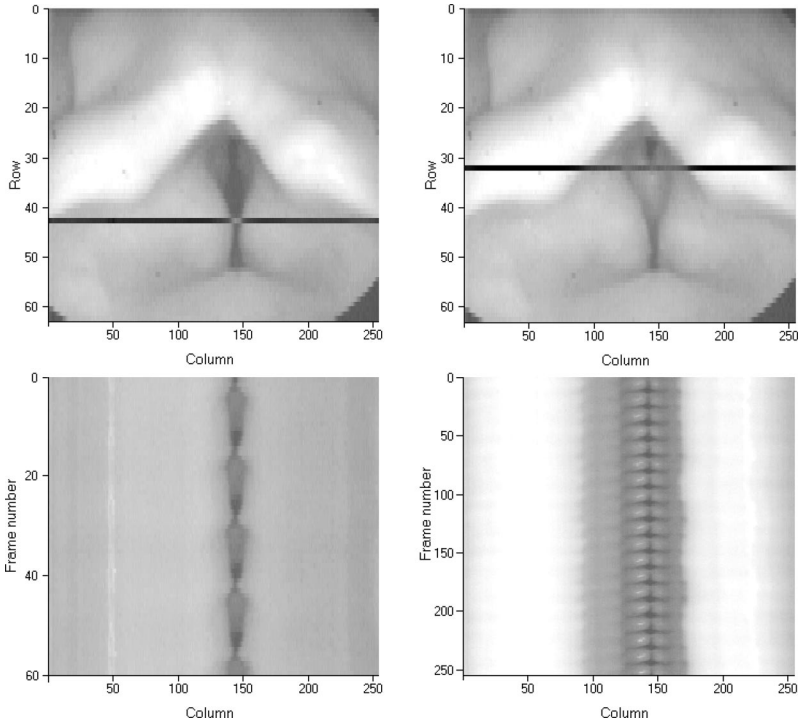

FIG. 7. Kymograms of the recording in Fig. 6. The left panel shows a kymogram at the ventricular folds. It can be seen that the closed phase of the glottis was synchronous with the maximum separation of the ventricular folds. The right panel shows a kymogram at the level of the arytenoid cartilages. On the right side of the kymogram, a low-frequency oscillation can be seen, which is consistent with the findings in the right laryngeal image in Fig. 6.

ACKNOWLEDGMENTS

We would like to thank Johan Sundberg and Britta Hammarberg for valuable input and editorial assistance. We would also like to thank Hans Larsson for valuable discussions and assistance with high-speed data handling. This work was supported by research grants from the Swedish Council for Work Life Research and the Swedish Research Council for Engineering Sciences.

Dunker, E., and Schlosshauer, B. (**1964**). ''Irregularities of the Laryngeal Vibratory Pattern in Healthy and Hoarse Persons,'' *Proceedings of Research Potentials in Voice Physiology*, edited by D. W. Brewer (State University of New York), pp. 151–184.

Eysholdt, U., Tigges, M., Wittenberg, T., and Proschel, U. (**1996**). ''Direct evaluation of high-speed recordings of vocal fold vibrations,'' Folia Phoniatr. Logop. **48**(4), 163–70.

Flanagan, J. L., and Landgraf, L. L. (**1968**). ''Self-oscillating source for vocal tract synthesizers,'' IEEE Trans **AU-16**, 57–64.

Hammarberg, B. (**1995**). ''High-Speed Observations of Diplophonic Phonation,'' in *Vocal Fold Physiology, Voice Quality Control*, edited by O. Fujimura and M. Hirano (Singular, San Diego), pp. 343–345.

Hess, W. (**1983**). *Pitch Determination of Speech Signals* (Springer, New York).

Kiritani, S., Imagawa, H., and Hirose, H. (**1988**). ''High-Speed Digital Image Recording for the Observation of Vocal Cord Vibration,'' in *Vocal Physiology: Voice Production, Mechanisms and Functions*, edited by O. Fujimura, pp. 261–269.

Kiritani, S. (**1995**). ''Recent Advances in High-Speed Digital Image Recording of Vocal Cord Vibration,'' Proceedings of International Congress of Phonetic Sciences **4**, 62–67.

Köster, O., Marx, B., Gemmar, P., Hess, M., and Künzel, H. J. (**1999**). ''Qualitative and quantitative analysis of voice onset by means of multidimensional voice analysis system (MVAS) using high-speed imaging,'' J. Voice **13**, 355–374.

Larsson, H., Hertegård, S., Lindestad, P.-Å., and Hammarberg, B. (**2000**). ''Vocal Fold Vibrations: High-Speed Imaging, Kymography and Acoustic Analysis,'' Laryngoscope **110**, 2117–2122.

Liljencrants, J. (**1991**). ''A translating and rotating mass model of the vocal folds,'' STL-QPSR, KTH, Stockholm 1/1991, 1–18.

Moore, P., White, F., and von Leden, H. (**1962**). ''Ultra-high speed photography in laryngeal physiology,'' J. Speech Hear Disord. **27**(2), 165–171.

Švec, J. G., and Schutte, H. K. (**1996**). ''Videokymography: High-speed line scanning of vocal fold vibration,'' J. Voice **10**, 201–205.

Švec, J. G. (**2000**). ''On Vibration Properties of Human Vocal Folds,'' Doctoral thesis, University of Groningen, The Netherlands.

Tigges, M., Wittenberg, T., Mergell, P., and Eysholdt, U. (**1999**). ''Imaging of vocal fold vibration by digital multiplane kymography,'' Comput. Med. Imaging Graph. **23**(6), 323–330.

Titze, I., and Liang, H. (**1993**). ''Comparison of *F*0 extraction methods for high-precision voice perturbation measurements,'' J. Speech Hear. Res. **36**, 1120–1133.

Titze, I. (**1973**). ''The human vocal cords: A mathematical model. I,'' Phonetica **28**, 129–170.

Titze, I. (**1974**). ''The human vocal cords: A mathematical model. II,'' Phonetica **29**, 1–21.

Wong, D., Ito, R. I., Cox, N. B., and Titze, I. R. (**1991**). ''Observation of perturbation in a lumped-element model of the vocal folds with application to some pathological cases,'' J. Acoust. Soc. Am. **89**, 383–394.

Effects of ethanol intoxication on speech suprasegmentals

Harry Hollien[a)]
Institute for Advanced Study of the Communication Processes, University of Florida, Gainesville, Florida 32611

Gea DeJong
CCS Department, City University of London, Hampton Square, London, United Kingdom

Camilo A. Martin
IASCP and Veteran's Administration Medical Center, Gainesville, Florida 32611

Reva Schwartz and Kristen Liljegren
Institute for Advanced Study of the Communication Processes, University of Florida, Gainesville, Florida 32611

(Received 18 April 2000; revised 20 August 2001; accepted 27 August 2001)

The effects of ingesting ethanol have been shown to be somewhat variable in humans. To date, there appear to be but few universals. Yet, the question often arises: is it possible to determine if a person is intoxicated by observing them in some manner? A closely related question is: can speech be used for this purpose and, if so, can the degree of intoxication be determined? One of the many issues associated with these questions involves the relationships between a person's paralinguistic characteristics and the presence and level of inebriation. To this end, young, healthy speakers of both sexes were carefully selected and sorted into roughly equal groups of light, moderate, and heavy drinkers. They were asked to produce four types of utterances during a learning phase, when sober and at four strictly controlled levels of intoxication (three ascending and one descending). The primary motor speech measures employed were speaking fundamental frequency, speech intensity, speaking rate and nonfluencies. Several statistically significant changes were found for increasing intoxication; the primary ones included rises in $F0$, in task duration and for nonfluencies. Minor gender differences were found but they lacked statistical significance. So did the small differences among the drinking category subgroups and the subject groupings related to levels of perceived intoxication. Finally, although it may be concluded that certain changes in speech suprasegmentals will occur as a function of increasing intoxication, these patterns cannot be viewed as universal since a few subjects (about 20%) exhibited no (or negative) changes. © *2001 Acoustical Society of America.* [DOI: 10.1121/1.1413751]

PACS numbers: 43.70.Gr [AL]

I. INTRODUCTION

Determining the presence, and especially the level, of intoxication can be a challenging task. Yet, decisions about this condition must be made frequently by clinicians, family members, law enforcement personnel, bartenders/servers, the courts, co-workers/supervisors, and others. As it turns out, many of them are based only on the observer's subjective assessment of the talker's speech. Yet, these judgments are made even though relatively little is known about the processes involved. For example, note the following questions: (1) is speech degradation *always* associated with intoxication, (2) does the severity and/or type of impairment vary from person to person, (3) do various types of drinking behaviors—and/or gender—have an influence on the process, (4) does severity of speech impairment correlate with increasing intoxication, (5) are the resultant speech patterns different for increasing and decreasing involvement, (6) can the presence of inebriation, and level of severity, always be detected? In any event, real life judgments about speech-intoxication relationships usually are made on the basis of incomplete or even inappropriate information. In turn, problems often are created and they can be substantial (see below and Hollien, 1993a, 1993b; NTSB, 1990a, 1990b).

An appropriate response, of course, would be to test the cited questions and this project is one of a series designed to do so (see also Hollien and Martin, 1996; Hollien *et al.*, 1998, 1999b, 2000, 2001b). In this instance, we have focused our efforts on a number of the suprasegmental patterns found in the speech of humans and how they may be changed as a function of serially increasing intoxication.

II. BACKGROUND

Although an extensive review of the relevant issues has been presented elsewhere (Hollien, 1993a, 1993b; Hollien and Martin, 1996), a brief reconsideration would appear useful. First, there is no question but the basic research on humans who have ingested ethanol is extensive. It is now clear that the consumption of even moderate amounts of alcohol can result in both impaired cognitive function (Arbuckle *et al.*, 1994; Hindmarch *et al.*, 1991; Sasaki *et al.*, 1995; Ste-

[a)]Author to whom correspondence should be addressed. Electronic mail: hollien@grove.ufl.edu

ingass *et al.*, 1994; Wallgren and Barry, 1970) and degraded sensory-motor performance (Bates, 1989; Connors and Maisto, 1980; Hill and Toffolon, 1990; Levine *et al.*, 1975). Since the speech act represents the output of several high-level, integrated systems (sensory, cognitive, motor), it also appears appropriate to assume that this process also could be susceptible to the effects of alcohol consumption. Indeed, it is known that interruptions or insults to any of these systems can result in speech/language impairment (Netsell, 1983). On the other hand, speech contains features which can provide information about a speaker's identity (see among others, Hollien, 1990, 2001a; Künzel, 1987; Nolan, 1983; Stevens, 1971) and/or the emotional states being experienced (Hicks and Hollien, 1981; Hollien *et al.*, 1987; Scherer, 1981, 1995). Thus, it would appear legitimate to suggest that intoxication might also be reflected in the voice/speech of the talker.

Speech–alcohol relationships: As will be seen, only a modest amount of research on possible intoxication-speech relationships has been reported and many confusions and controversies have resulted from these efforts (see below; also see Chin and Pisoni, 1997 for a reasonably complete review of the area).

One of the problem areas involves listeners' ability to (aural–perceptually) perceive the presence of intoxication in others. Most of the studies reported were based on some sort of ''intoxication–sober'' scale (examples, Hollien and Martin, 1996; Klingholz *et al.*, 1988; Pisoni and Martin, 1989; Sobelle *et al.*, 1972, 1982). The obtained results, while useful, have not been particularly definitive. Indeed, Klingholz *et al.* (1988) have suggested that sometimes intoxicated speakers sound sober and sober individuals sound drunk. Overall, subjects appear to vary substantially but, then, so did the approaches/methodologies used to study them. Among the more rigorous of these efforts was one reported by Pisoni and Martin (1989) who indicate that their listeners could correctly judge talkers as being intoxicated from 62% to 74% of the time (depending on the procedure used). Their data are quite stable and pretty much agree with ours (Hollien and Martin, 1996; Hollien *et al.*, 1998, 2001a, 2001b). Nonetheless, some confusion still exists as to just how accurate auditors can be when judging intoxication from speech.

Research focused on the physical and phonetic properties of motor speech can be even more confusing. Briefly, degradations in morphology and/or syntax have been reported or implied (Andrews *et al.*, 1977; Künzel, 1990; Natale *et al.*, 1980) but data are not always consistent across studies. Nor are those based on the assessment of misarticulations, phoneme substitutions, omissions, distortions, devoicing and so on (see also Lester and Skousen, 1974; Sobelle and Sobelle, 1972; Trojan and Kryspin-Exner, 1968). However, the pre-eminent focus in this area has been on paralinguistic and suprasegmental factors (see, for example, Behne *et al.*, 1991; Cooney *et al.*, 1998; Hollien and Martin, 1996; Hollien *et al.*, 1999b; Klingholz *et al.*, 1988; Künzel *et al.*, 1992; Pisoni and Martin, 1989; Sobelle *et al.*, 1982; Watanabe, 1994). Prominent among the speech behaviors studied are (a) speaking fundamental frequency (reportedly SFF level can be lowered, or raised or not changed; SFF variability usually is said to be increased), (b) speaking rate (most often said to be slowed), (c) the number and length of pauses (increases are observed sometimes but not always), (d) amplitude or intensity levels (sometimes reduced, sometimes not) and nonfluencies or misarticulations (most often said to be increased). Thus, the data here are substantial but the relationships and trends are not consistent.

It is only fair to point out that the investigators who have studied the motor speech and alcohol consumption relationships have faced rather severe difficulties when attempting to design and conduct their studies with acceptable precision. Some of the problems result from (1) employing varying (but traditional) dosage approaches, (2) using different groups of subjects in each of the procedures, (3) not rigorously controlling intoxication level, (4) not making precise speech measurements, (5) employing very small subject cohorts, and/or (6) not properly choosing and/or controling their subjects. It is of little wonder that the obtained data tend to be somewhat inconsistent across investigations. A reasonable response to these problems (plus those suggested by Chin and Pisoni, 1997; Hollien and Martin, 1996; and Klingholz *et al.*, 1988) would appear to be the application of highly controlled procedures plus some new techniques. The following investigation will attempt to provide more precise data about the effects of intoxication on certain suprasegmentals.

III. METHOD

A. Overview

A number of the procedures traditionally utilized in research on intoxication were modified or restructured in order to meet certain of the reservations cited above. They resulted in a highly structured study of (1) two relatively large groups of young adults (both male and female), (2) substantial amounts of controlled speech, and (3) an ethanol dosage procedure which permitted identification and control of predetermined levels of intoxication. The speech behaviors studied were (1) fundamental frequency, (2) speaking rate, (3) intensity level, and (4) nonfluencies.

B. Subjects

Speakers were 35 young adults—19 males and 16 females—who were selected on the basis of good health, nonuse of drugs and their drinking habits. They were sorted into roughly equal groups of light, moderate, and heavy drinkers (see below); all were between the ages of 21 and 32 years and exhibited no speech or hearing disorders. Further, only nonpregnant females were permitted to participate (urine test). A control group was originally included. However, it proved difficult to convince these individuals that they were being administered alcohol on a *continuing* basis, a factor which probably was due to the serial nature of ethanol administration. That is, in traditional studies, different subjects populate each group, they are provided a dose of ethanol and later assessed for intoxication level. In this case, subjects received repeated doses and assessments. In any event, the control group had to be abandoned. Moreover, since subjects' output was compared to his or her utterances when sober, each could serve as his/her own control.

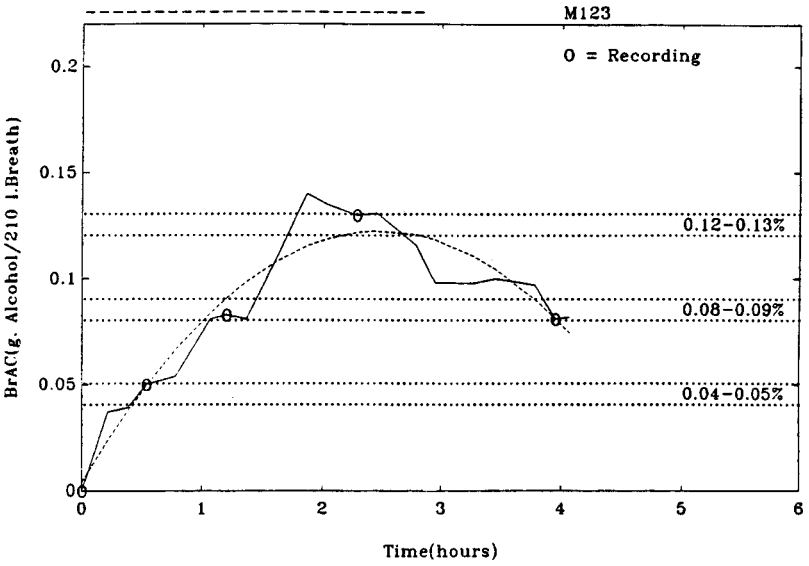

FIG. 1. Curve of subject Ml23's progress relative to level of intoxication from the beginning to the completion of the experimental portion of the run (BrAC readings were not recorded after the trial). Note that the speech samples were taken when he was in each of the windows. The smooth curve is a second-order polynomial.

Selection of subjects and classifying them with respect to their drinking patterns was based on standardized screening tests (Cahalan *et al.*, 1969; Pokorny *et al.*, 1972) plus a psychiatric interview. The interview was included in order to ensure that the data from the original tests were accurate and to eliminate those individuals who exhibited negative physical conditions, stress, fatigue and/or adverse psychological states. Subjects also were required to exhibit a General American dialect (agreement by three phoneticians), demonstrate the ability to perform the required tasks and not have eaten for 4–6 hours before the experiment was initiated (Jones and Jonsson, 1994; Millar *et al.*, 1992; Watkins and Adler, 1993). These procedures permitted the drinker category sort plus eliminated anyone who was a nondrinker, an alcoholic or problem drinker, or who had consumed any type of drugs (prescription medications included) which might interact with moderate doses of ethanol.

C. Speech samples

Four types of speech were produced by all subjects; trials were completed twice when they were sober (training first and, then, baseline) and once at each levels of intoxication. Research protocols required that they always were produced in the same sequence; they included (1) a standard phonemically balanced reading passage (the ''Rainbow Passage'' from Fairbanks, 1960), (2) sentences drawn from the Fisher-Logermann Test of Articulatory Competence (Fisher and Logermann, 1971), (3) diadochokinetic gestures (Fletcher, 1978; Westbury and Dembrovski, 1993) supplemented by two additional oral gestures: a) ''shapupie'' (Hollien *et al.*, 1999a, 1999b), ''buttercup'' (Kent *et al.*, 1987), and (4) extemporaneous speech in response to (neutral) requests such as ''Tell us about your favorite TV program.''

All utterances were produced in a quiet laboratory with two simultaneous recordings made of each speaker. This ''duplicate'' procedure was adopted in order to avoid losses due either to equipment failure or procedural disruption resulting from subject behavior. The primary microphone (EV 635A) was placed in a positioner and held a constant distance 6 in. from the subjects' mouth (and 4 in. from the midline); the backup unit was placed on a headband developed for such purposes by Hicks and Hollien (1981). Each was coupled to its own calibrated, grounded TEAC-300R analog tape recorder. All recordings used in this research were made with the primary system.

D. Dosage

While many acceptable procedures exist, most did not meet the criteria established for this research. Indeed, many investigators have struggled to resolve the problem but with varying degrees of success. For example, the ''traditional dosage procedure'' has varied substantially—from 0.66 gr/kg body weight (Nagoshi *et al.*, 1992) all the way up to 0.80 gr/kg body weight (Bauer *et al.*, 1992). Other variations occur also: double or single loading, targets of intoxication only, specified dosage with no blood alcohol level (BAL) determination and so on (Hill and Toffolon, 1990; Zacchia *et al.*, 1991). Because of these problems, subjects sometimes were ''lost'' due to ''negative reactions'' or nausea. Our response to the problem was a potassium enriched dosage which contained one-third each of (1) 40% rum or vodka, (2) Gatorade—the potassium it contains acts as an antagonist to the inhibiting effects of alcohol (Cantarou and Trumper, 1975), and (3) a soft drink of either orange juice or caffeine free cola (Zacchia *et al.*, 1991). As can be seen from Fig. 1, this approach provided a reasonable remedy to the problem of uneven absorption. Indeed, very few of the subjects experienced nausea or debilitating discomfort. Finally, the procedure mitigated the presumed male–female difference in ascending intoxication.

E. Control of intoxication level

The protocols employed involved serial growth and decay of intoxication (an approach which permitted a better control of its effects; it also paralleled the normal drinking process in humans) and the taking of data at specified points along the resulting ''curve.'' This sequencing procedure was not a radical departure from the traditional as others have recently employed somewhat similar approaches (Bates,

1989; Streufert *et al.*, 1992). The selected intoxication levels or windows included (1) sober (a breath-alcohol concentration—or BrAC—of 0.00), (2) BrAC 0.04–0.05 (mild intoxication), (3) BrAC 0.08–0.09 (legal intoxication level), and (4) BrAC 0.12–0.13 (severe intoxication). A fourth level, BrAC 0.09–0.08, permitted comparison of increasing and decreasing levels of intoxication; however, these data will not be reported here. All subjects were continually monitored. Great care was taken to record the actual and elapsed times (as a function of BrAC level), plus the intoxication level (or window) at which each of the speech samples was recorded. These levels were determined by use of one or more of four calibrated Alcopro, Inc., AlcoSensor IV breath analyzers. These units are chemically fueled (electrolytic) devices controlled by a microprocessor; their recovery time is about 2 minutes. To avoid measuring alcohol left in the oral tissues, subjects were required to rinse their mouth with tap water at least six times prior to each measurement. The recording sessions were initiated only after confirmation that the experimental BrAC window had been reached. It should be stressed that breath analyzers had to be employed because it was necessary to determine *immediately* when a subject had reached a specified level of intoxication and when he/she had left it. Thus, neither blood nor urine assessment could be used, primarily due to unacceptable analysis latencies and because BrAC is just as precise as are the others in assessing intoxication (Dubowski, 1985; Gullberg, 1992; Harding and Field, 1987; Jones, 1993; Lovell, 1972).

F. Measurement procedure

As stated, the analyzes performed were speaking fundamental frequency (SFF), speaking duration (DUR), vocal intensity (VI) and nonfluency assessment (NF). The procedure for assessing SFF was to isolate the standard reading passage plus 30 s of extemporaneous speech and process these segments by means of our computer-linked fundamental frequency indicator (FFI-12) system (Hollien, 1990). The resulting data were organized by sex and by drinking patterns. Reported data included mean SFF (in Hz and st) and standard deviation (SD).

The prosody measures (DUR) focused on the period of time subjects took to orally read the standard passage and also to complete 15 repetitions each of the three complex diadochokinetic gestures: pataka, buttercup, shapupie. The standard passage was digitized by means of the Kay Elemetrics CSL speech analysis system (Model 4300B) with the first and last inhalation removed. While the diadochokinetic gestures were digitized using the same system, all of the ''breaths'' were removed before measurement.

Third, reasonably valid measurements of vocal intensity could be made because each microphone was placed—and held—in constant relationship to subjects' lips. Thus, intensity artifacts were kept to a minimum. The Kay Elemetrics CSL also was used for assessing this parameter. The standard passage was digitized, all inhalations and pauses removed and the analysis module used to calculate average vocal intensity.

Fourth, the nonfluencies were systematically measured by a trained phonologist with extensive checks made by a phonetician (97% agreement). Eight different phonemic and word-choice errors were assessed (see Table I). Once the evaluation was complete, the errors were classified according to type and separated by sex and level of intoxication. Since no trends were found for the different types of nonfluencies or for gender, the data here were collapsed into a single value.

TABLE I. The nine criteria used to identify nonfluencies.

Criteria
(1) Additions (phoneme/word)
(2) Hesitations/pauses
(3) Repetitions
(4) Substitutions: A (phoneme/word)
(5) B (voicing)
(6) C (devoicing)
(7) Omissions (phoneme/word)
(8) Distortions
(9) Lengthening

IV. RESULTS

A. Speaking and fundamental frequency

The first of the four characteristics studied was speaking fundamental frequency (SFF or $F0$). Analyses were carried out for the three classes of drinkers for both the orally read passage and the extemporaneous speech. The data for the oral reading can be best understood by consideration of Table II where they are presented by gender and drinking level. As can be seen, SFF gradually rises with increasing intoxication level and it does so for both men and women. However, while this shift was about double for men (i.e., 1.0 st vs 0.5 st for women; see also Fig. 2), both proved to be statistically significant (fixed effects ANOVA) (men: $F=12.74$; df 3, 63; $F.05=2.68$, $p<0.01$ and women: $F=5.57$; df 3, 42; $F.05=2.76$, $P<0.01$). The procedure also permitted SFF contrasts to be made between all pairs of windows by means of two-tailed T tests. For the men, all were significant (0.05 level) except the BrAC 0.04 vs 0.08 contrast, whereas the women exhibited two nonsignificant relationships—i.e., the BrAC 0.00 to 0.04 and the BrAC 0.08 to 0.12 relationships. It appears that the source of these nonsignificant contrasts can be traced back to the BrAC 0.00–0.12 level reversals discussed later in this paper (men=5%; women=20%). Other SFF relationships are as follows.

Drinking groups: The trends for the three drinking habit groups (Table II) pretty much parallel each other; note that there is an overall increase in $F0$ for all six cohorts. However, only the shifts for the male light and moderate drinkers are significant and ''internal'' reversals (i.e., BrAC 0.00–0.04) can be seen for the male heavy drinkers and the female light drinkers. While these reversals are a little difficult to explain, there is the possibility that they may be related to the suggested upgrading of certain individuals' motor speech at mild intoxication levels (Hollien and Martin, 1996; Hollien *et al.*, 2000; Künzel, 1990). The two places where the present trends appear somewhat consistent with this notion are where the males are contrasted to the females (see again Fig. 2) and when the light and moderate drinkers of both

TABLE II. Summary table of speaking fundamental frequency levels (oral reading)[a] as a function of sobriety and increasing intoxication. Subjects were 19 men and 16 women, who were sorted into light, moderate, and heavy drinking cohorts. All means, except those for the overall data, are in Hertz only; shifts and standard deviations are in semitones. Intoxication is assessed by Breath Alcohol Concentration (BrAC).

Group	*N*	Level of intoxication (BrAC) 0.00	0.04	0.08	0.12	Overall shift
Men						
Light	6					
Mean (Hz)		113.0	113.5	114.6	119.0	0.9
S.D. (st)		2.6	2.5	2.6	2.9	
Moderate	8					
Mean (Hz)		108.9	115.7	116.9	118.0	1.4
S.D. (st)		2.5	2.9	2.9	2.9	
Heavy	5					
Mean (Hz)		115.3	114.8	117.0	119.2	0.6
S.D. (st)		2.6	2.6	3.0	2.8	
All males	19					
Mean (Hz)		112.1	114.5	116.2	118.6	
Mean (stl)		33.3	33.7	34.0	34.3	1.0
S.D. (st)		2.6	2.7	2.8	2.9	
Women						
Light	6					
Mean (Hz)		197.7	196.7	200.9	204.3	0.6
S.D. (st)		2.5	2.5	2.6	2.8	
Moderate	5					
Mean (Hz)		200.4	201.8	205.8	206.7	0.5
S.D. (st)		2.4	2.3	2.4	2.4	
Heavy	5					
Mean (Hz)		198.1	200.1	200.6	200.9	0.2
S.D. (st)		2.5	2.6	2.7	2.7	
All females	16					
Mean (Hz)		199.0	199.5	202.0	204.0	
Mean (stl)		43.2	43.3	43.6	43.7	0.5
S.D. (st)		2.5	2.5	2.6	2.7	

[a]The Rainbow Passage (Fairbanks, 1960).

sexes are compared to the heavy drinkers. Note also (Table II) that rise in $F0$ is only about half the extent for heavy drinkers than it is for the light/moderate ones. Thus, extended experience with high levels of intoxication *may* lead to reduction in the debilitating effects of this compound on motor speech behavior. Finally, the SFF patterns for the extemporaneous speaking conditions were very similar to those for oral reading (except that their mean levels were lower in all cases). Accordingly, these data are considered redundant and are not included.

SFF variability: One of the most consistently reported relationships is that $F0$ variability is raised as a function of increases in intoxication (Johnson *et al.*, 1990; Klingholz *et al.*, 1988; Künzel *et al.*, 1992; Pisoni *et al.*, 1985). As may be seen from reconsideration of Table II, this relationship was not supported by the present data. While there is a slight increase in this parameter, it is a rather weak one and it does not reach statistical significance.

To summarize, the most striking $F0$ relationship appears to be associated with SFF level and the present data may

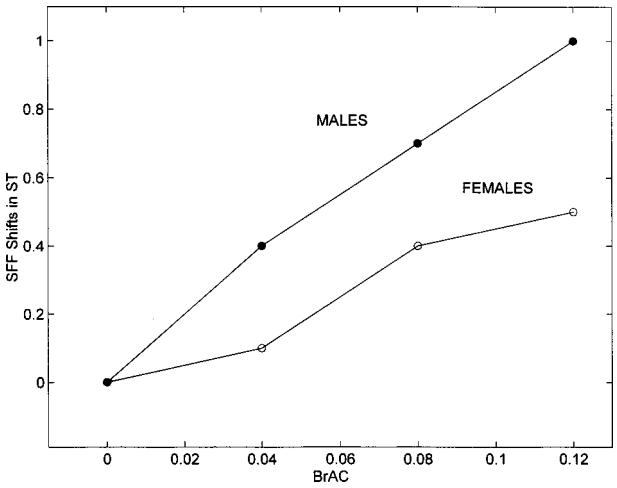

FIG. 2. Speaking fundamental frequency (SFF) shifts in semitones (st) relative to increasing levels of intoxication calculated with BrAC=0.00 as the common reference point. The measurements for the male subjects (top) are compared to the ones for the females (bottom).

serve to stabilize a relationship which so far has shown inconsistencies. That is, some researchers reported that $F0$ increased as a function of rise in intoxication (Behne and Rivera, 1990; Künzel *et al.*, 1992; reports by clinicians who treat alcoholics) whereas others have suggested that it decreases (Hollien and Martin, 1996; Johnson *et al.*, 1990; Klingholz *et al.*, 1988; Watanabe *et al.*, 1994) and yet others have found no change at all (Cooney *et al.*, 1998; Pisoni *et al.*, 1985; Sobelle *et al.*, 1982). The present data strongly support the position that SFF rises with increased intoxication, the validity here is underscored by the fact that the results were obtained under carefully controlled experimental conditions and in a manner that parallels ordinary human drinking patterns. Exceptions to this generally consistent trend will be considered in a later section.

B. Speaking duration and rate

Data on speaking rate/duration (DUR) were obtained on the 98-word orally read passage and the three (complex) oral gestures. The results for the passage are summarized in Table III. Note that, while the time taken to read the text increased with inebriation for both sexes, the greatest shift for the males occurs between the BrAC 0.04 and 0.08 windows

TABLE III. Summary table of the time (DUR) it took subjects to orally read the standard 98 word passage as a function of sobriety and three levels of intoxication. All values are in seconds; intoxication level is expressed by Breath Alcohol Concentration (BrAC).

Group	Level of intoxication (BrAC) 0.00	0.04	0.08	0.12	Shift (0.00–0.12)
Men					
Mean (s)	25.3	25.8	26.8	27.6	+2.3
S.D. (s)	2.9	2.5	2.1	2.5	
Women					
Mean (s)	25.1	25.5	25.7	27.5	+2.4
S.D. (s)	2.2	2.2	2.4	2.7	

TABLE IV. T-tests (2-tailed) evaluating the time taken to read the passage (DUR). All intoxication levels for both the male and female subject groups are included. Intoxication level is in Breath Alcohol Concentration (BrAC).

Contrasts (BrAC)	Males	Females
0.00–0.04	0.415	0.409
0.00–0.08	0.002[a]	0.220
0.00–0.12	0.001[a]	0.001[a]
0.04–0.08	0.022[a]	0.685
0.04–0.12	0.002[a]	0.001[a]
0.08–0.12	0.347	0.004[a]

[a]Significant at 0.05 level.

whereas the greatest for the females is found between BrAC 0.08 and 0.12. Overall, however, these between-gender differences were not statistically significant; nor were those for subjects when they were sorted on the basis of drinking habits. On the other hand, linear regressions calculated for the differences in intoxication levels were significant and an increasing overall trend was found (men: $F=6.74$, df 1,90; $F.05=3.84$; $P<0.01$; women: $F=6.85$, df 1,66; $F.05=3.92$; $P<0.01$). The next step was to investigate the differences among the individual windows. Here an ANOVA was calculated (significant for both sexes) as the basis for T-tests among all the BrAC levels. While significance was not usually found for adjacent categories, it was for nearly all of the contrasts involving two or more levels (see Table IV). However, this overall trend also was found to vary somewhat internally with a few individuals (both men and women) exhibiting at least one reversal. Nevertheless, it can be argued that, overall, speaking rate is slowed as intoxication level is increased and this finding is consist with data from virtually all other reports (see, for example, Behne *et al.*, 1991; Chin and Pisoni, 1997; Hollien *et al.*, 1998, 1999; Künzel *et al.*, 1992; Pisoni *et al.*, 1985).

The data for the combined diadochokinetic gestures was not as orderly as those for the reading passage. A summary of the time taken for the combined diadochokinetic gestures may be found in Table V. Unexpectedly, the female subjects took slightly longer to complete the required task than did the men (see again Table III) and the overall trend for the combined data is minimal. Indeed, none of the statistical tests were significant. Accordingly, the three gestures were analyzed separately, and it was found that most of the cited problems resulted from the unevenness in the patterns for ''pataka.'' Moreover, while a general trend for rise in task time (as a function of increasing intoxication) was found for both of the other two, a BrAC 0.00–0.04 reversal was observed for the ''shapupie'' gesture. While this relationship provides one of the very few bases for the notion that motor speech can be enhanced by mild dosages of ethanol (see also the $F0$ data in Table II), it is not possible to support the postulate by means of these data alone. In sum, diadochokinetic gestures do not appear to be as robust predictors of intoxication level as does connected speech.

TABLE V. Summary table of the mean time it took subjects to produce the three complex diadochokinetic gestures 15 times each. Stimuli were pataka, shapupie, and buttercup. All values are in seconds; intoxication levels are in Breath Alcohol Concentration (BrAC).

	Level of intoxication (BrAC)				
Group	0.00	0.04	0.08	0.12	Shift (0.00–0.12)
Men					
Mean (s)	6.3	6.2	6.4	6.6	0.3
S.D. (s)	0.6	0.6	0.8	0.7	
Women					
Mean (s)	6.5	6.5	6.7	6.8	0.3
S.D. (s)	0.5	0.5	0.6	0.6	

TABLE VI. Summary table of the nonfluencies exhibited by the 35 subjects as a function of increasing intoxication level. Values are the number of nonfluencies for each oral reading of the standard passage.

		Experimental condition (BrAC)			
Subjects	*N*	0.00	0.04	0.08	0.12
Males	19				
Mean		3.2	4.7	6.5	8.6
SD		2.0	2.6	3.1	3.4
Females	16				
Mean		2.2	3.5	4.7	6.1
SD		1.7	2.2	2.7	3.0
Mean	35	2.7	4.1	5.6	7.4

C. Vocal intensity

The third of the suprasegmental characteristics studied was vocal intensity (VI). Analyses were carried out only when the subjects orally read the Rainbow Passage. It was found that, while vocal intensity tended to shift slightly upward with increasing intoxication level, the changes were rather small, somewhat variable, and a number of reversals could be noted for both men and women. In short, while these data agree to some extent with those reported by Johnson *et al.* (1990), it must be said that systematically louder or softer speaking patterns do not appear to correlate very well at all with increasing intoxication (a finding not consistent with Sobelle *et al.*, 1982).

D. Nonfluencies

The fourth assessment involved a possible increase in observed nonfluencies as a function of serial intoxication; the summarized data may be found in Table VI. First, it can be noted that the increases in nonfluencies with rise in intoxication are orderly and quite robust; all were statistically significant (''overall'' data $F=33.11$, df 3,34; $F.05=2.92$). Also striking is the observation that the number of nonfluencies increased systematically for all 35 subjects; there were no ''overall'' reversals at all and only 14 of them (or ''no shifts'') occurred among the 105 adjacent windows contrasts. Most remarkable of all was the fact that the number of nonfluencies nearly tripled for the severely intoxicated condition and that this increase far exceeded those for any of the other parameters tested.

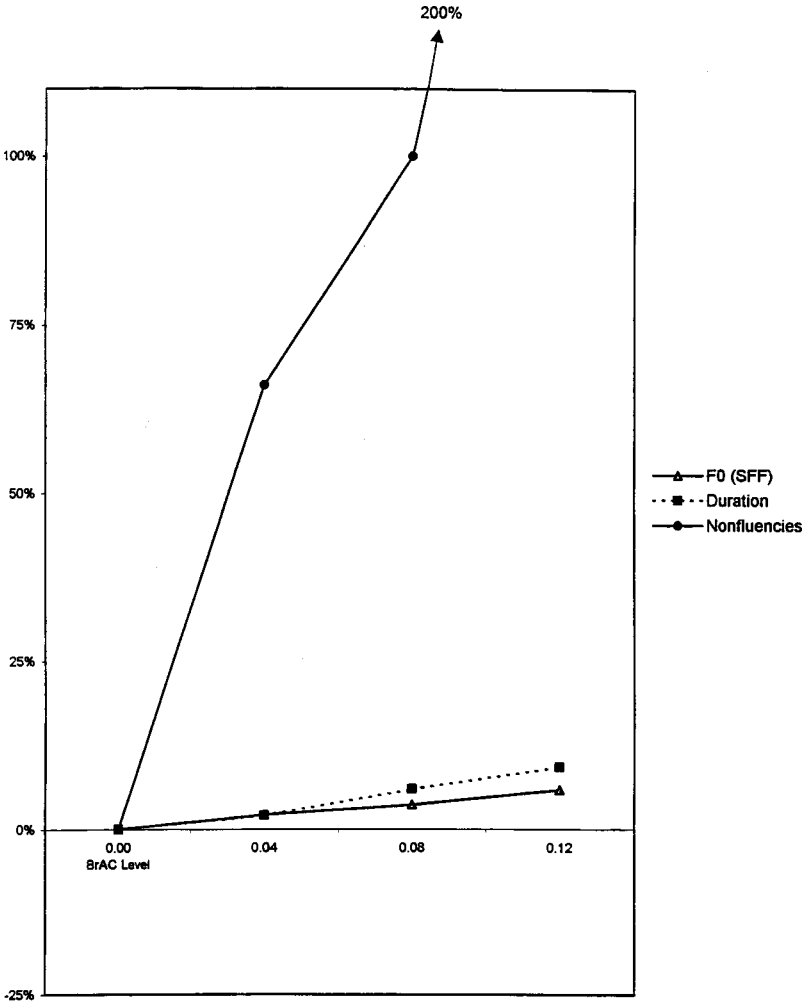

FIG. 3. Shift trends of the three most robust parameters when speech is assessed at levels of increasing intoxication.

The shifts for these three major factors (SFF, DUR, NF) are plotted in Fig. 3. Note that neither of the (upward) changes for SFF or rate (while significant) were as great as 10%. Finally, although somewhat more marked, this trend is in agreement with other reports where either nonfluencies or misarticulations were assessed in some manner (Künzel *et al.*, 1992; Lester and Skousen, 1974; Natale *et al.*, 1980; Pisoni *et al.*, 1985; Sobelle and Sobelle, 1972; Trojan and Kryspin-Exner, 1968).

V. DISCUSSION

One of the problems faced by virtually all of the researchers investigating speech–intoxication relationships is variability in subject behavior. This lack of uniformity has been explained as due to lack of precision on the part of the investigators (Klingholz *et al.*, 1988), because of markedly divergent research design (Hollien and Martin, 1996) and so on. Yet, some variability was found even in the present large-sample, highly controlled project. Of course, a few speakers (while normal) exhibited somewhat limited oral skills (perhaps intensifying the degradations), most appeared to show greater speech deficits than expected at low levels of intoxication but fewer at the higher (Fig. 4). This figure (Hollien *et al.*, 1998, 2000, 2001a, 2001b) is based on a number of perceptual studies which demonstrate the overestimation of intoxication involvement at low levels and the underestimation at the (higher) levels where inebriation is physiologically severe. However, these relationships can only partly explain our findings. Accordingly, the nature of the observed variability—and which of the subjects were responsible for it—was assessed directly. This procedure involved recording (and clustering) the number of the reversals for each subject and each parameter—both for the adjacent levels and overall (i.e., from BrAC 0.00 to 0.13). The results of this analysis can be found in Table VII. As may be seen, the reversals are

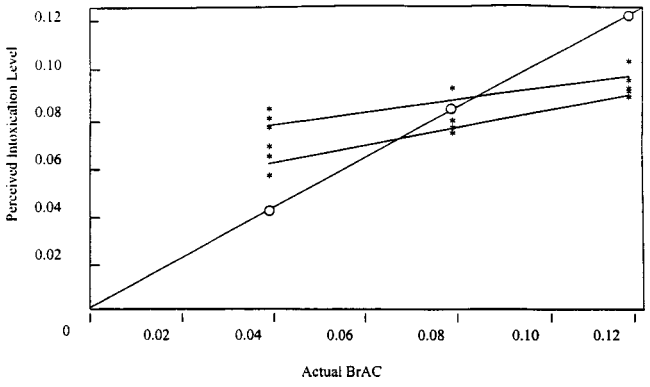

FIG. 4. Perceived intoxication level contrasted to physiologically measured levels from sober to severely intoxicated (BrAC 0.12–0.13). Data are summed for 35 talkers and 85 listeners (curve A) and 36 talkers and 52 listeners (curve B). From Hollien *et al.*, 1998, 2000, 2001b.

TABLE VII. Summary table of the number of reversals found for the three primary factors of SFF, duration (rate) and nonfluencies. All values are in percent. Internal refers to reversals between any adjacent intoxication levels ($N=315$); overall refers to the sober to severely intoxicated contrasts ($N=105$).

Factor	Men	Women	Mean
SFF (Hz)			
Internal	35	33	34
Overall	5	19	11
Duration (sec.)			
Internal	28	29	28
Overall	21	12	17
Nonfluencies			
Internal	16	10	13
Overall	0	0	0
Means			
Internal	26	24	25
Overall	9	10	9

presented in two ways; first the values between any of the adjacent levels (internal) are contrasted and then the overall sober-intoxicated data are reported; the lack of a shift was counted as a reversal. First, it can be noted that the behavior of the great majority of the subjects was consistent with the various trends cited above, but nearly all experienced a reversal—especially an internal one—for SFF or speaking rate. However, the question remained: are these deviations scattered among all subjects or are there a few individuals who account for most of them. Assessment of the subject-by-subject performances demonstrated that just seven individuals (four males, three females) accounted for nearly half of the internal reversals and for *all* of the ''overall'' ones. Indeed, once their data were removed, the overall trends stabilized and were found to be much more robust. Thus, it appears that about one-fifth of any given population cannot be expected to exhibit the shifts which are predicted by this research. The reason that this subgroup differs from the main cohort will constitute the basis for further research.

VI. CONCLUSIONS

The following conclusions are drawn from the data generated by this project.

(1) It can be expected that most people's speaking fundamental frequency will rise as they become intoxicated. This parameter is a reasonably robust one and shifts should occur independent of type of speech.
(2) Speaking fundamental frequency variability may increase, if only slightly. This parameter is not considered to be a good predictor of the level of advancing intoxication.
(3) Increased utterance duration can be expected to correlate with increments in inebriation. Specifically, speaking rate will be slowed for most individuals and this relationship can be expected to be reasonably robust.
(4) Vocal intensity probably will not change *systematically* with advancing inebriation.
(5) Nonfluencies in speech will rise sharply with increase in intoxication. This parameter also appears to be the best predictor of intoxication *level*.
(6) Systematic differences are not predicted among the drinking level practices (mild, moderate, heavy) excepting, perhaps, that the suprasegmental degradation for heavy drinkers may be a little muted.
(7) It would be hazardous to apply the relationships found here to *all* talkers, primarily because about 20% of them will not systematically exhibit the cited behaviors.

Finally, an additional contribution made by this project results from the methodology developed. The use of sequential or continual increases in ethanol dosage coupled to rigorous subject selection, strict control of intoxication and close tracking of inebriation level should permit reasonably precise research to be conducted in this area.

ACKNOWLEDGMENTS

This research was supported by NIAAA grant AA-09377. The authors wish to thank Dr. Fulton Crews, Dr. Patricia Hollien, Allan Alderman, and Dr. Anders Lofqvist for their assistance with the project.

Andrews, M. L., Cox, W. M., and Smith, R. G. (**1977**). ''Effects of alcohol on the speech on non-alcoholics,'' Central States Speech J. **28**, 140–143.
Arbuckle, T. Y., Chaikelson, J., and Gold, D. P. (**1994**). ''Social drinking and cognitive function revisited: The role of intellectual endowment and psychological distress,'' J. Stud. Alcohol **55**, 352–361.
Bates, M. (**1989**). ''The effect of reported occasions of alcohol intoxication on two process involving the visual discrimination of movement,'' J. Stud. Alcohol **50**, 143–154.
Bauer, L. A., Schumock, G., Horn, J., and Opheim, K. (**1992**). ''Verpamil inhibits ethanol elimination and prolongs the perception of intoxication,'' Clin. Pharmacol. Ther. **52**, 6–10.
Behne, D. M., and Rivera, S. M. (**1990**). ''Effects of alcohol on speech: Acoustic analysis of spondees,'' Res. Speech Perception **16**, 263–291.
Behne, D. M., Rivera, S. M., and Pisoni, D. B. (**1991**). ''Effects of alcohol on speech: Durations of isolated words, sentences and passages,'' Res. Speech Percept. **17**, 285–301.
Cahalan, D., Cisin, I. H., and Crossley, H. M. (**1969**). ''American drinking practices: A national survey of drinking behavior and patterns,'' Monograph No. 6, Rutgers Center of Alcohol Studies, New Brunswick, N.J.
Cantarou, A., and Trumper, M. (**1975**). ''Water, sodium, chloride, potassium: physiological considerations,'' *Clinical Biochemistry* (W.B. Saunders, Philadelphia), pp. 339–367.
Chin, S. B., and Pisoni, D. B. (**1997**). *Alcohol and Speech* (Academic Press, San Diego).
Connors, G. J., and Maisto, S. A. (**1980**). ''Effects of alcohol, instructions and consumption rate on motor performance,'' J. Stud. Alcohol **41**, 509–517.
Cooney, O. M., McGuigan, K., Murphy, P., and Conroy, R. (**1998**). ''Acoustic analysis of the effects of alcohol on the human voice,'' J. Acoust. Soc. Am. **103**, 2895.
Dubowski, K. M. (**1985**). ''Absorption, distribution and elimination of alcohol: Highway safety aspects,'' J. Stud. Alcohol Suppl. **10**, 98–108.
Fairbanks, G. (**1960**). *Voice and Articulation Drillbook* (Harper and Row, New York).
Fisher, H. B., and Logemann, J. A. (**1971**). *The Fisher-Logemann Test of Articulatory Competence* (Houghton Mifflin, Boston).
Fletcher, S. G. (**1978**). *The Fletcher Time-By-Count Test of Diadochokinetic Syllable Rate* (C.C. Publications, Tigard, OR).
Gullberg, R. G. (**1992**). ''The elimination rate of mouth alcohol: Mathematical modeling and implications in breath alcohol analysis,'' J. Forensic Sci. **37**, 1363–1372.
Harding, P. M., and Field, P. H. (**1987**). ''Breathalizer accuracy in actual law enforcement practice,'' J. Forensic Sci. **32**, 1235–1240.

Hicks, J. W., Jr., and Hollien, H. (**1981**). The Reflection of Stress in Voice—1: Understanding the Basic Correlates, Proceedings of the Carnahan Conference on Crime Countermeasures, Lexington, KY, pp. 189–191.
Hill, J. C., and Toffolon, G. (**1990**). ''Effect of alcohol on sensory and sensorimotor visual functions,'' J. Stud. Alcohol **51**, 108–113.
Hindmarch, I., Kerr, J. S., and Sherwood, N. (**1991**). ''The effects of alcohol and other drugs on psychomotor performance and cognitive function,'' Alcohol Alcohol. **26**, 71–84.
Hollien, H. (**1990**). *Acoustics of Crime* (Plenum, New York).
Hollien, H. (**1993a**). Review of NTSB Reports, Re: Effects of Alcohol on Speech, Forensic Communication Assoc., Gainesville, FL, March (1990). Also accepted by Hon. B. Shortell in (Consolidated) vs Exxon *et al.*, Case No. A95-095 Civil, Superior Court, State of Alaska.
Hollien, H. (**1993b**). ''An oil spill, alcohol and the Captain,'' Forensic Sci. Int. **60**, 97–105.
Hollien, H. (**2001a**). *Forensic Voice Identification* (Academic Press, London).
Hollien, H., Liljegren, K., Martin, C. A., and DeJong, G. (**2001b**). ''Production of intoxication states in actors: Acoustic and temporal characteristics,'' J. Forensic Sci. **46**, 68–73.
Hollien, H., Hill, R., and Martin, C. A. (**2000**). ''Perceptual assessment of intoxication level,'' J. Acoust. Soc. Am. **107**, 2919.
Hollien, H., and Martin, C. A. (**1996**). ''Conducting research on the effects of intoxication on speech,'' Forensic Linguistics **3**, 107–129.
Hollien, H., Bishop, J., Huntley-Bahr, R., and Gelfer, M. P. (**1999a**). ''Near-field speech intelligibility in CBW masks,'' Mil. Med. **164**, 543–550.
Hollien, H., Liljegren, K., Martin, C. A., and DeJong, G. (**1999b**). Prediction of intoxication levels by speech analysis, in *Advances in Phonetics*, edited by A. Braun (Steiner Verlag, Stuttgart), Vol. 106, pp. 40–50.
Hollien, H., DeJong, G., and Martin, C. A. (**1998**). ''Production of intoxication states by actors: Perception by lay listeners,'' J. Forensic Sci. **43**, 1163–1172.
Hollien, H., Geison, L., and Hicks, Jr., J. W. (**1987**). ''Voice stress evaluators and lie detection,'' J. Forensic Sci. **32**, 405–418.
Johnson, K., Pisoni, D. B., and Bernacki, R. H. (**1990**). ''Do voice recordings reveal whether a person is intoxicated,'' Phonetica **47**, 215–237.
Jones, A. W. (**1993**). ''Pharmacokinetics of ethanol in saliva: Comparison with blood and breath alcohol profiles, subjective feeling of intoxication and diminished performance,'' Clin. Chem. **39**, 1837–1844.
Jones, A. W., and Jönsson, K. (**1994**). ''Food induced lowering of blood-ethanol profiles and increased rate of elimination immediately after a meal,'' J. Forensic Sci. **39**, 1084–1093.
Kent, R., Kent, J., and Rosenbeck, J. (**1987**). ''Maximum performance tests of speech production,'' J. Speech Hear Disord. **52**, 367–387.
Klingholz, F., Penning, R., and Liebhardt, E. (**1988**). ''Recognition of low-level alcohol intoxication from the speech signal,'' J. Acoust. Soc. Am. **84**, 929–935.
Künzel, H. J. (**1987**). Sprecherekennung: Grundzuge Forensischer Sprachverabeitung, Jeidelber, Kriminalistik-Verlag.
Künzel, H. J. (**1990**). Influence of alcohol on speech and language, Paper presented at the American Academy of Forensic Sciences, Cincinnati, Ohio, February.
Künzel, H. J., Braun, A., and Eysholdt, U. (**1992**). *Einfluss von Alcohol auf Sprache und Stimme* (Kriminalistik-Verlag, Heidelberg, Germany).
Lester, L., and Skousen, R. (**1974**). ''The phonology of drunkness,'' Papers from the Parasession on Natural Phonology, Linguistic Society of America, pp. 233–239.
Levine, J. M., Kramer, G. C., and Levine, E. N. (**1975**). ''Effects of alcohol on human performance; an integration of research findings based on an abilities classification,'' J. Appl. Psychol. **60**, 285–293.
Lovell, W. S. (**1972**). ''Breath tests for determining alcohol in the blood,'' Science **178**, 264–272.
Millar, K., Hammersley, R. H., and Finnigan, F. (**1992**). ''Reduction of alcohol-induced performance impairment by prior ingestion of food,'' Br. J. Psychol. **83**, 261–278.
Nagoshi, C. T., Noll, R. T., and Wood, M. D. (**1992**). ''Alcohol expectancies and behavioral and emotional responses to placebo vs. alcohol administration,'' Alcohol Clin. Exp. Res. **15**, 255–260.
Natale, M., Kanzler, M., Jaffe, J., and Jaffe, J. (**1980**). ''Acute effects of alcohol on defensive and primary-process language,'' Int. J. Addict. **15**, 1055–1067.
National Transportation and Safety Board (**1990a**). *Speech Examination Study* (NTSB Bureau of Technology, Washington, D.C.).
National Transportation and Safety Board (**1990b**). *Speech Examination Study Addendum* (NTSB Bureau of Technology, Washington, D.C.).
Netsell, R. (**1983**). ''Speech motor control: Theoretical issues with clinical impact,'' in *Clinical Dysarthria*, edited by W. Berry (College Hill Press, San Diego), pp. 1–19.
Nolan, J. F. (**1983**). *The Phonetic Basis of Speaker Recognition* (Cambridge U. P., Cambridge, UK).
Pisoni, D. B., and Martin, C. S. (**1989**). ''Effects of alcohol on the acoustic-phonetic properties of speech: Perceptual and acoustic analyzes,'' Alcohol. Clin. Exp. Res. **13**, 577–587.
Pisoni, D. B., Hathaway, S. N., and Yuchman, M. (**1985**). Effects of Alcohol on the Acoustic-Phonetic Properties of Speech, SRL Tech. Note 85-03. Quoted in Chin and Pisoni, *Alcohol and Speech* (Academic Press, New York, 1997).
Pokorny, A. D., Miller, B. A., and Kaplan, H. B. (**1972**). ''The BriefMAST: A shortened version of the Michigan alcoholism screening test,'' Am. J. Psychiatry **129**, 342–348.
Sasaki, H., Matsuzaki, Y., Nakagawa, T., and Arai, H. (**1995**). ''Cognitive function in rats with alcohol ingestion,'' Pharmacol. Biochem. Behav. **52**, 845–848.
Scherer, K. (**1981**). ''Non-linguistic vocal indicators of emotion and psychopathology,'' in *Emotions and Psychopathology*, edited by E. E. Izard (Plenum, New York).
Scherer, K. (**1995**). ''Expression of emotions in voice and music,'' J. Voice **9**, 249–260.
Sobelle, L., and Sobelle, M. (**1972**). ''Effects of alcohol on the speech of alcoholics,'' J. Speech Hear. Res. **15**, 861–868.
Sobelle, L., Sobelle, M., and Coleman, R. (**1982**). ''Alcohol-induced dysfluency in nonalcoholics,'' Folia Phoniatr. **34**, 316–323.
Steingass, H. P., Saitory, G., and Canavan, G. M. (**1994**). ''Chronic alcoholism and cognitive function,'' Personality, Individual Diffs. **17**, 97–109.
Stevens, K. N. (**1971**). ''Sources of inter- and intra-speaker variability in the acoustic properties of speech sounds,'' Proceedings of the Seventh International Congress on Phonetic Science, Montreal, pp. 206–232.
Streufert, S., Pogash, R., Roache, J., Gingrich, D., Landis, R., Severs, W., Londardi, L., and Kantner, A. (**1992**). ''Effects of alcohol intoxication on risk taking, strategy and error rate in visuo-motor performance,'' J. Appl. Psychol. **77**, 515–524.
Trojan, F., and Kryspin-Exner, K. (**1968**). ''The decay of articulation under the influence of alcohol and paraldehyde,'' Folia Phoniatr. **20**, 217–238.
Wallgren, H., and Barry, H. (**1970**). *Actions of Alcohol* (Elsevier, Amsterdam), Vols. 1 and 2.
Watanabe, H., Shin, T., Matsao, H., Okuno, F., Tsuji, T., Matsuoka, M., Fukaura, J., and Matsunaga, H. (**1994**). ''Studies on vocal fold injection and changes in pitch associated with alcohol intake,'' J. Voice **8**, 340–346.
Watkins, R. L., and Adler, E. V. (**1993**). ''The effect of food on alcohol absorption and elimination patterns,'' J. Forensic Sci. **38**, 285–291.
Westbury, J. R., and Dembrovski, J. (**1993**). Articulatory Kinematics of Normal Diadochokinetic Performance, Annual Bulletin Logopedics and Phonetic Res. Instit., Tokyo, pp. 13–36.
Zacchia, C., Pihl, R. O., Young, S. N., Ervin, I. (**1991**). ''Effect of sucrose consumption on alcohol induced impairment in male social drinkers,'' Psychopharmacology (Berlin) **105**, 49–56.

Surrogate analysis for detecting nonlinear dynamics in normal vowels

Isao Tokuda[a)]
Department of Computer Science and Systems Engineering, Muroran Institute of Technology, Muroran, Hokkaido 050-8585, Japan

Takaya Miyano
Department of Intelligent Machines and System Engineering, Hirosaki University, Hirosaki, Aomori 036-8561, Japan

Kazuyuki Aihara
Department of Mathematical Engineering and Information Physics, Faculty of Engineering, The University of Tokyo, Bunkyo-ku, Tokyo 113-8656, Japan
and CREST, JST, Honmachi, Kawaguchi, Saitama 332-0012, Japan

(Received 16 July 1999; revised 20 August 2001; accepted 28 August 2001)

Normal vowels are known to have irregularities in the pitch-to-pitch variation which is quite important for speech signals to be perceived as natural human sound. Such pitch-to-pitch variation of vowels is studied in the light of nonlinear dynamics. For the analysis, five normal vowels recorded from three male and two female subjects are exploited, where the vowel signals are shown to have normal levels of the pitch-to-pitch variation. First, by the false nearest-neighbor analysis, nonlinear dynamics of the vowels are shown to be well analyzed by using a relatively low-dimensional reconstructing dimension of $4 \leqslant d \leqslant 7$. Then, we further studied nonlinear dynamics of the vowels by spike-and-wave surrogate analysis. The results imply that there exists nonlinear dynamical correlation between one pitch-waveform pattern to another in the vowel signals. On the basis of the analysis results, applicability of the nonlinear prediction technique to vowel synthesis is discussed. [DOI: 10.1121/1.1413749]

PACS numbers: 43.70.Gr, 43.25.Rq [AL]

I. INTRODUCTION

In the studies of human speech, linear dynamical systems analysis, such as the power spectrum analysis and the linear predictive coding (LPC) model, is the most popular and standard methodology.[1–5] This is because acoustical characteristics of human speech are mainly due to the resonances of the vocal tract, which form the basic spectral structure of the speech signals.[1] In fact, linear dynamical systems analyses have been widely and successfully applied to speech analysis and synthesis. One example is the analysis of vowels which are known to be well characterized by their power spectral structures, especially by the locations of the several peak formant frequencies. Despite the successful applications of the linear systems analysis, human speech, strictly speaking, is a nonlinear dynamical phenomenon which involves nonlinear aerodynamic, biomechanical, physiological, and acoustic factors. In fact, a variety of vocal fold models are based on nonlinear modeling of the vocal fold physiology and nonlinear aerodynamics.[6–9] In speech synthesis, the nonlinear physiological models such as the two-mass model[6] and the glottal waveform models[10–12] are used for the excitation signals of LPC vocoders. Nonlinear dynamical information is also used implicitly in the standard speech coding schemes. For example, in the code-excited linear prediction (CELP) scheme,[13] a combination of code-vectors from codebooks is used to model periodic and aperiodic impulsive components of the excitation signals of LPC. These nonlinear techniques imply that some of the important qualities of speech are inherently characterized by nonlinear dynamics.

Despite the complicated vocal production mechanism, which is usually considered to be high-dimensional, the concept of dissipative nonlinear dynamics[14] implies a possibility that the complex vocal phenomena originate from deterministic nonlinear dynamics with only a small number of state variables. From this viewpoint, nonlinear dynamical system analysis[15,16] has been recently carried out for a variety of vocal phenomena.[17–33] For diagnosis of pathological voices, various nonlinear dynamics such as periodic, quasi-periodic, and chaotic dynamics have been analyzed[17–21] and in non-stationary infant cries possible bifurcation phenomena leading to chaos have been studied.[22] In fricative consonants chaotic dynamics has been discussed[23] and in normal phonation of vowels irregularity in pitch-to-pitch variation has been investigated in terms of low-dimensional nonlinear dynamics.[24–33]

Among these nonlinear speech studies, this article focuses on the nonlinear dynamics of vowels.[24–33] It has been known that in normal phonation of vowels cyclic changes in pitch amplitudes and pitch periods are observed.[34] By psychoacoustic experiments, it has been shown that this pitch-to-pitch variation is indispensable for speech signals to be perceived as natural human sound.[35–38] Since the naturalness of sound is an important factor for speech synthesis, the ir-

a)Electronic mail: tokuda@csse.muroran-it.ac.jp

regular property of the pitch-to-pitch variation of vowels is worthwhile investigating.

There have been several studies that considered the effect of pitch-to-pitch variation on the quality of synthesized vowels. It has been reported that the buzzerlike quality of the vowels synthesized by periodic excitation of LPC vocoders can be improved to some extent, if the standard deviations of the pitch amplitudes and pitch periods of the LPC excitation signals are optimized.[39–44] It has also been indicated that frequency characteristics of the sequences of the pitch periods and pitch amplitudes have strong influence on the voice quality and optimization of such frequency characteristics enhances the natural quality of the synthesized vowels.[36–38] If the original sequence of the pitch periods and pitch amplitudes obtained from real subjects are available, perceptually transparent speech can be synthesized by using standard speech coding schemes such as the code-excited linear prediction (CELP) scheme[13] and the multi-band excitation (MBE) scheme.[45] Such schemes, however, require a huge database or codebooks of pitch data for every voiced phonation of real speakers. They also provide no insight into the physiological mechanism that gives rise to the pitch-to-pitch variation of vowels, since they merely use a database of real pitch signals.

Compared to the conventional techniques, recently developed nonlinear prediction models for vowel synthesis are quite interesting. Townshend[24] and Banbrook *et al.*[25] used local linear function models, Sato *et al.*[26] and Tokuda *et al.*[27] used neural networks, Kubin[28] used polynomial function models, and Mann and McLaughlin[29] and Judd[30] used radial basis function models for the vowel synthesis. They reported that the irregular dynamical property of the pitch-to-pitch variation that contributes to natural vowel sounds is well reproduced by the nonlinear prediction models. Such nonlinear prediction models can provide speech synthesis techniques *possibly* simpler than the conventional ones in the sense that they are based on the function approximation techniques which do not require any huge database of pitch sequences. Although the conventional nonlinear prediction models that need optimization of many free parameters should be further refined for practical use, it is important to explore a new approach to vowel synthesis.

The studies of the nonlinear predictions imply that a dominant portion of the irregularity of vowels is due to low-dimensional possibly chaotic dynamics, because chaos is the only dynamics that deterministically gives rise to irregular behavior in nonlinear systems. In order to examine the plausibility of the nonlinear prediction models of vowels, it is important to study the irregular property in vowels from the viewpoint of nonlinear systems, especially deterministic chaos. In fact, there exist several studies that report chaotic dynamical properties in normal vowels. By fractal dimensional analysis with reliable dimension estimate technique,[32] noninteger fractal dimension lying between 1.0 and 3.0 was estimated for vowel signals. By the Wayland test,[33] deterministic nonlinearity was detected for normal vowels. Geometrical structure that resembles a typical chaotic orbit is observed by singular systems analysis of time-delay embedding of normal vowels.[25,27] By Lyapunov spectrum analysis, a positive Lyapunov exponent[27,31] or weakly positive but close to zero Lyapunov exponent[25] was computed for normal vowels.

Despite these intensive studies, it is still difficult to confirm chaotic dynamics in normal vowels, because reliable estimation of nonlinear dynamical quantities from short-term speech data requires delicate numerical computation.[46–48] It should also be noted, on the other hand, that analysis of very-long-term data can suffer from nonstationarity. Moreover, we have to be very careful in analyzing and discussing low-dimensional chaos in real-world systems, since noisy data can sometimes mimic chaotic behavior.[49–51] Rapp *et al.*[51] demonstrated that the Grassberger–Procaccia algorithm falsely detects low-dimensional chaotic dynamics in artificial data generated by a simple filtering of a purely random number sequence. Since this kind of spurious result may often take place in laboratory experiments, nonlinear systems analysis combined with additional techniques such as surrogate data techniques is recommended.[50,51]

The present article does not directly prove chaotic dynamical properties in vowels. Instead, we investigate strength of nonlinearity in the irregular dynamics of the pitch-to-pitch variation of vowels. Our approach is based upon the method of surrogate data.[52–54] The surrogate data analysis is a kind of statistical hypothesis testing which is used to detect nonlinear dynamical structure in time series data observed from an unknown dynamical system. We test a null-hypothesis that

''There is no nonlinear dynamical correlation between one pitch waveform pattern to another.''

According to the null-hypothesis, we generate sets of spike-and-wave surrogate data and compute nonlinear dynamical statistics of the original and surrogate data. By observing whether there is any significant difference between estimates of the original and surrogate data, the null-hypothesis is tested.

To our knowledge, a comprehensive analysis of the vowel signals based on the above surrogate method has not been reported. In Refs. 32 and 55, Fourier transformed (FT) surrogate analysis was carried out for testing nonlinearity in normal vowels. The FT surrogate analysis that is to test a linear *Gaussian* property of vowels is not really interesting, because vowels are in general not considered to be generated from linear *Gaussian* processes in speech research. Instead, we examine nonlinear dynamical correlation between the pitch waveforms of vowels by the spike-and-wave surrogate analysis. By showing that there exists nonlinear dynamics in the pitch-to-pitch variation of vowels, we discuss the plausibility of modeling the vowels by nonlinear prediction techniques. Possible application of the nonlinear analysis results to the physiological modeling of vowels is also discussed.

The present article is organized as follows. In Sec. II, details of the vowel signals studied in this article are provided. Pitch-to-pitch variation observed in the vowel signals is also evaluated. In Sec. III, false nearest-neighbor analysis is carried out to study how many dimensions are necessary for nonlinear analysis of the vowels. In Sec. IV, nonlinear dynamics of the vowels are examined by spike-and-wave surrogate analysis. The final section is devoted to conclu-

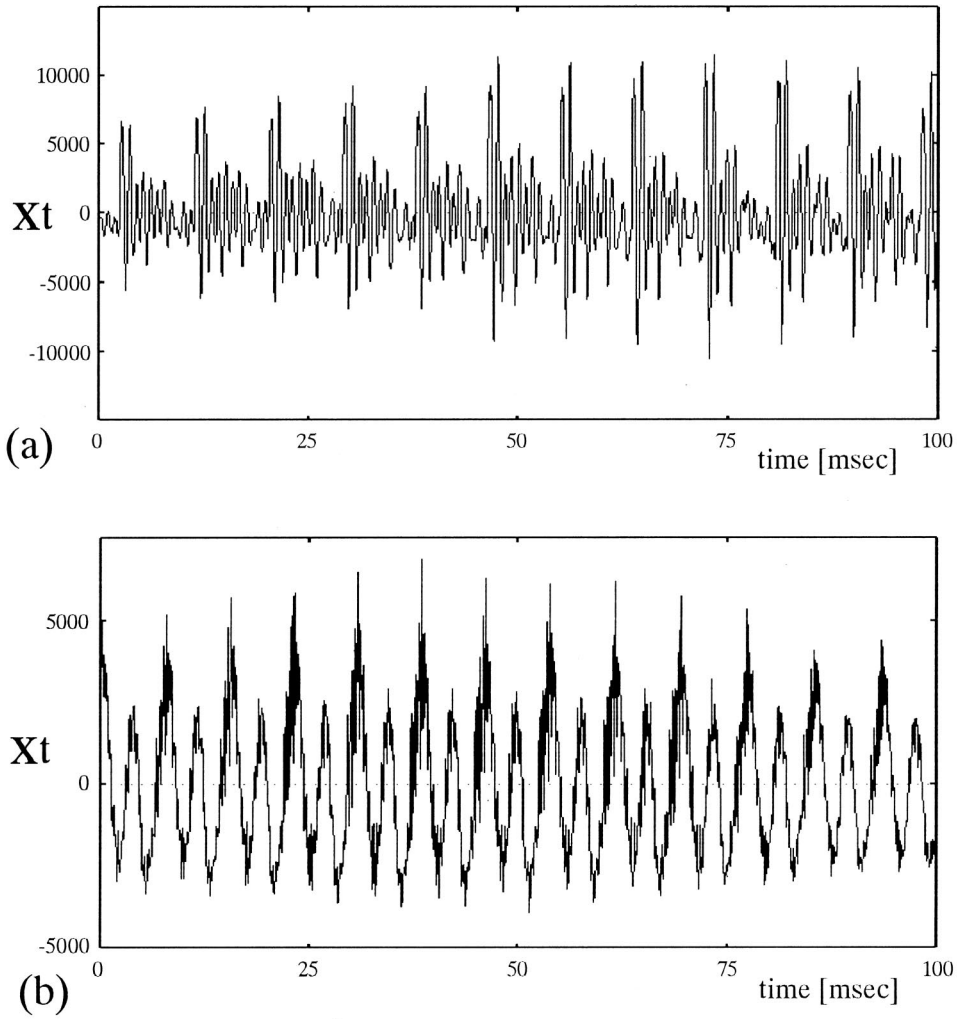

FIG. 1. (a) Speech signal $\{x_t : t = 1,2,...,2048\}$ of vowel /a/ (subject: mau). (b) Speech signal of vowel /i/ (subject: mau).

sions of our experiments and discussions on possible application of nonlinear dynamics to speech synthesis.

II. EXPERIMENTAL DATA

A. Speech data

For our analysis, speech signals of five vowels /a/, /i/, /u/, /e/, and /o/ recorded from five subjects are exploited. Each vowel is spoken only once by each subject. We analyze five vowels so that we can consider dependency of nonlinear dynamical characteristics of vowels on the vocal tract shape. If the vocal tract shape gives rise to strong constriction at voiced phonation, we may expect that nonlinearity of the vocal fold dynamics is weakened by a filtering effect of the vocal tract. We study this effect for five vowels. The subject group is composed of three male speakers (mau, mms, mmy) and five female speakers (fsu, fyn) with no laryngeal pathology. The speech data are in the standard ATR (Advanced Telecommunications Research Institute International) database which is accessible at http://www.ctr.atr.co.jp. The speech signals are low-pass filtered with a cut-off frequency of 8 kHz and digitized with a sampling rate of 20 kHz and with 16-bit resolution. The initial transient phase and the final decay phase are removed from all data and the almost stationary part of the data is extracted. As examples, speech signals denoted by $\{x_t \in \mathbf{R}: t = 1,2,...,N_{\text{data}}\}$ ($N_{\text{data}} = 2048$) are drawn for two vowels /a/ and /i/ (subject: mau) in Figs. 1(a) and (b).

B. Pitch-to-pitch variation

It is well known that cyclic changes in maximal peak amplitudes and pitch periods are observed in normal vowel signals.[34] Let us evaluate the level of this pitch-to-pitch variation in our speech data. First, maximum peak amplitudes and pitch periods are successively extracted from each vowel signal by using the peak-picking and zero-crossing method.[56–60] In our speech data, 15 to 35 pitch periods were extracted from each vowel signal. We call the sequences of the maximum peak amplitudes and the pitch periods amplitude sequence (AS) and period sequence (PS), respectively. Then, the standard deviation of the AS and PS is computed for each vowel signal. In order for normalization, the coefficient of variation (C.V.) is used as a measure for the size of fluctuations in AS and PS, where C.V. stands for the standard deviation of a sequence normalized by the mean.[61]

In Figs. 2(a) and (b), histograms of the mean and the standard deviation of pitch periods computed from our 25 vowel signals are respectively shown. The mean pitch period ranges from 3.5 to 9 ms and the standard deviation ranges from 0.06 to 0.48 ms. As is shown in Fig. 2(c), the C.V. of

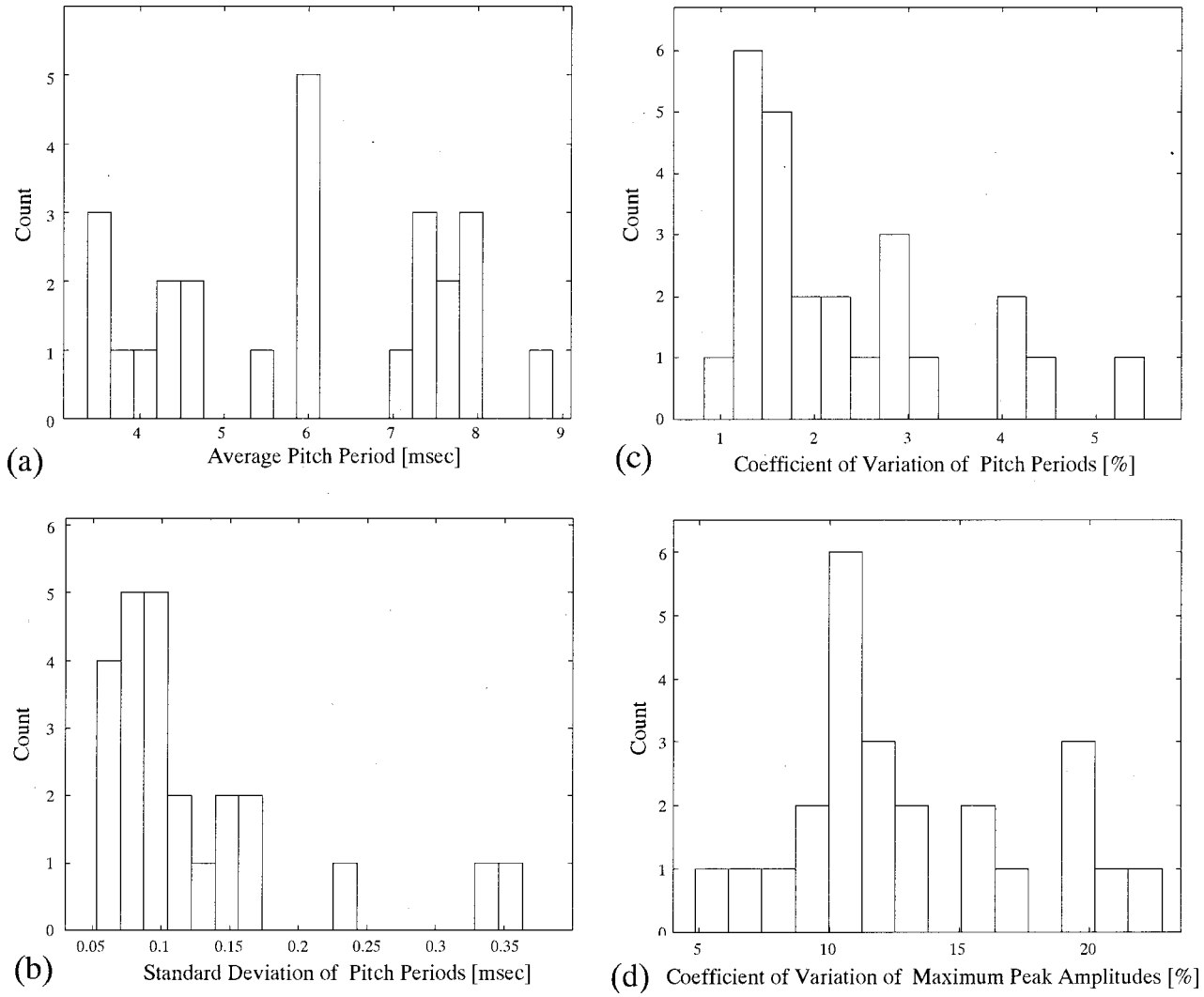

FIG. 2. (a) Distribution of the mean pitch period computed from 25 vowel signals. (b) Distribution of the standard deviation of pitch periods computed from 25 vowel signals. (c) Distribution of the coefficient of variation of pitch periods computed from 25 vowel signals. (d) Distribution of the coefficient of variation of maximum peak amplitudes computed from 25 vowels.

pitch periods ranges from 1% to 5.3% and its mode is located around 1.2%. The mode is within the normative range $1.05\pm0.40\%$ which was reported for normal voiced sounds.[62]

Figure 2(d) shows a C.V. of maximum peak amplitudes computed from the 25 vowels. The C.V. of maximum peak amplitudes ranges from 5% to 29% and its mode is located around 10.6%. The mode is very close to the normative range $6.68\pm3.03\%$ which was reported for normal voiced sounds.[62]

According to the evaluation of the cyclic changes in maximal peak amplitudes and pitch periods, we can observe a normal level of pitch-to-pitch variation in our speech data. In the following sections, we investigate irregular properties of this pitch-to-pitch variation from the view point of nonlinear dynamics.

III. MINIMUM EMBEDDING DIMENSION OF VOWELS

In nonlinear dynamical systems analysis,[15,16] it is in general supposed that an observed time series with a single variable is generated by deterministic nonlinear dynamics with a low-dimensional attractor. The first step for the nonlinear analysis of a single time series is to reconstruct a qualitatively similar dynamical trajectory to the original in a relatively low-dimensional delay-coordinate space as[63,64]

$$\mathbf{x}(t)=(x_t,x_{t-\tau},\ldots,x_{t-(d-1)\tau}), \tag{1}$$

where d and τ stand for the reconstruction dimension and the time lag, respectively. Figures 3(a) and (b) show examples of two vowel signals /a/ and /i/ (subject: mau) reconstructed in the delay-coordinate space. As is discussed in Ref. 27, dynamical behavior that resembles a Shil'nikov-type chaos and a two-dimensional torus are recognized in the three-dimensional space of Figs. 3(a) and (b), respectively.

The result of Sauer *et al.*[64] states that when the original dynamical system that generates time series has a corresponding attractor with a box-counting dimension of d_A, a topologically equivalent attractor can be prevalently reconstructed in the delay-coordinate space when $d>2d_A$. Although the mathematical result provides a sufficient topological condition for avoiding self-crossings of the trajectories in the delay-coordinate space, the natural ques-

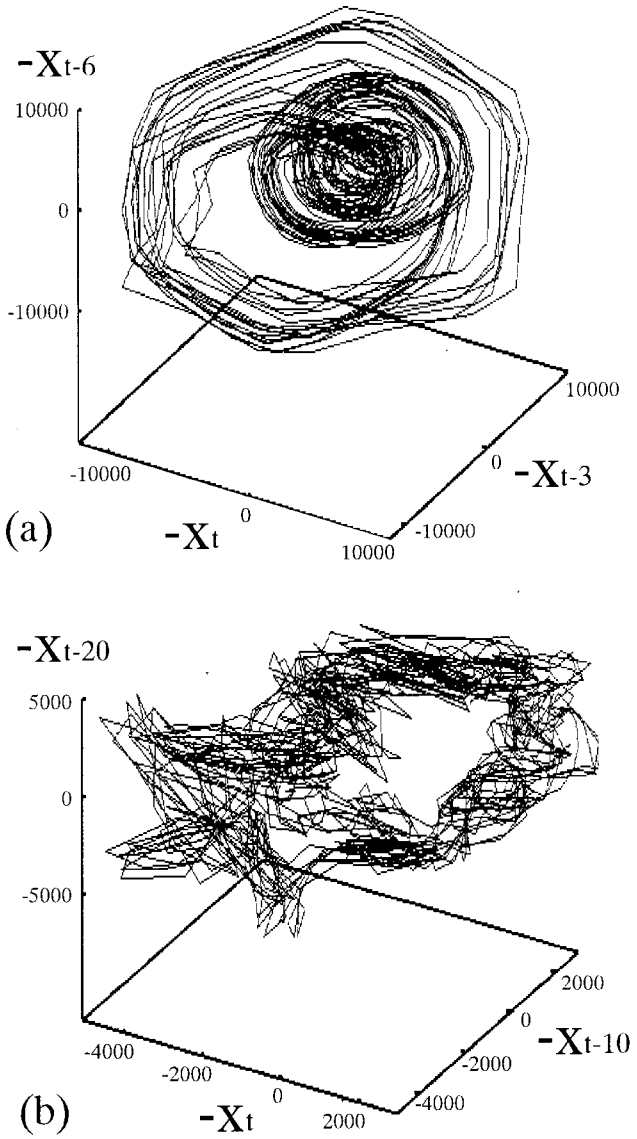

FIG. 3. (a) Reconstructed dynamics of the vowel /a/ of Fig. 1(a) in a three-dimensional delay-coordinate space (x_t, x_{t-3}, x_{t-6}). As is reported in Ref. 27, Shil'nikov-type dynamical structure can be recognized. (b) Reconstructed dynamics of the vowel /i/ of Fig. 1(b) in a three-dimensional delay-coordinate space $(x_t, x_{t-10}, x_{t-20})$. The dynamics resembles a quasi-periodic attractor.

tion is the following:

Given a time series from an unknown dynamical system, how can the minimum embedding dimension d_E be determined for reconstructing the original dynamics?

In order to determine the minimum embedding dimension d_E, let us analyze the speech data by the false nearest-neighbor (FNN) method.[65] The FNN method provides a practical computational algorithm for estimating the minimum embedding dimension d_E of a time series data. Due to the simplicity of the algorithm and ease of its implementation, the FNN analysis has been widely applied to various real-world data.[16]

The FNN algorithm determines the minimum embedding dimension d_E by focusing on a topological change in the reconstructed dynamics in delay-coordinate space. Suppose that a time series $\{x_t\}$ is reconstructed in delay-coordinate space by Eq. (1) with the reconstruction dimension d. For each data point $\mathbf{x}(t)$, denote its rth nearest neighbor by $\mathbf{x}(t_r)$. Then the square of the Euclidean distance between $\mathbf{x}(t)$ and $\mathbf{x}(t_r)$ is given by

$$R_d^2(t,r) = \|\mathbf{x}(t) - \mathbf{x}(t_r)\|^2 = \sum_{k=0}^{d-1} [x_{t-k\tau} - x_{t_r-k\tau}]^2. \tag{2}$$

Let us see a change in the distance R_d when the reconstruction dimension is increased as $d \to d+1$. The addition of the new $(d+1)$-th coordinate increases the distance between $\mathbf{x}(t)$ and $\mathbf{x}(t_r)$ by

$$R_{d+1}^2(t,r) = R_d^2(t,r) + [x_{t-d\tau} - x_{t_r-d\tau}]^2. \tag{3}$$

If the increase in the distance from $R_d(t)$ to $R_{d+1}(t)$ is significantly large as

$$\left[\frac{R_{d+1}^2(t,r) - R_d^2(t,r)}{R_d^2(t,r)}\right]^{1/2} > R_{\mathrm{tol}} \quad (R_{\mathrm{tol}}\text{: threshold value}), \tag{4}$$

then $\mathbf{x}(t_r)$ can be considered as a "false" nearest neighbor to $\mathbf{x}(t)$ caused possibly by the self-crossing of orbit in the d-dimensional reconstruction space. Hence the condition (4) provides a first criterion for false nearest neighbors.

There is a second criterion for false nearest neighbors. Since we deal with time series with finite data points, the trajectory distribution can be sparse in the reconstruction space and some nearest neighbors to $\mathbf{x}(t)$ might not be so close, i.e., $R_d(t) \approx R_A$ (R_A: an attractor size). If such distant nearest neighbors are "false" nearest neighbors, addition of a new $(d+1)$-th coordinate may stretch their distances by the attractor size and will result in $R_{d+1}(t) \approx 2R_A$. Hence, for such distant neighbors, the second criterion for false neighbors is given by

$$\frac{R_{d+1}(t)}{R_A} > 2, \tag{5}$$

where the attractor size R_A can be computed as

$$R_A^2 = \frac{1}{N_{\mathrm{data}} - (d-1)\tau} \sum_{t=1+(d-1)\tau}^{N_{\mathrm{data}}} \|\mathbf{x}(t) - \overline{\mathbf{x}}\|^2, \tag{6}$$

$$\overline{\mathbf{x}} = \frac{1}{N_{\mathrm{data}} - (d-1)\tau} \sum_{t=1+(d-1)\tau}^{N_{\mathrm{data}}} \mathbf{x}(t). \tag{7}$$

The "false" nearest neighbor is finally defined as the nearest neighbor that satisfies either of the first criterion (4) or the second criterion (5).

Figures 4(a) and (b) show results of the FNN analysis applied to two subject speakers mau and mms, where percentages of the false nearest neighbors of two vowels /a/ and /i/ are drawn simultaneously. The time lag is selected as $\tau = 3$ so that the window length of the delay-coordinates $w = (d-1)\tau$ is set to be nearly equal to the first zero-crossing point of the auto-correlation function when vowel /a/ (mau) is reconstructed in three-dimensional space. The threshold value is set as $R_{\mathrm{tol}} = 10$ and the reconstruction dimension is varied from $d = 1$ to $d = 7$. In this analysis, "true" or "false" of only the first nearest neighbor is considered, i.e., $r = 1$.

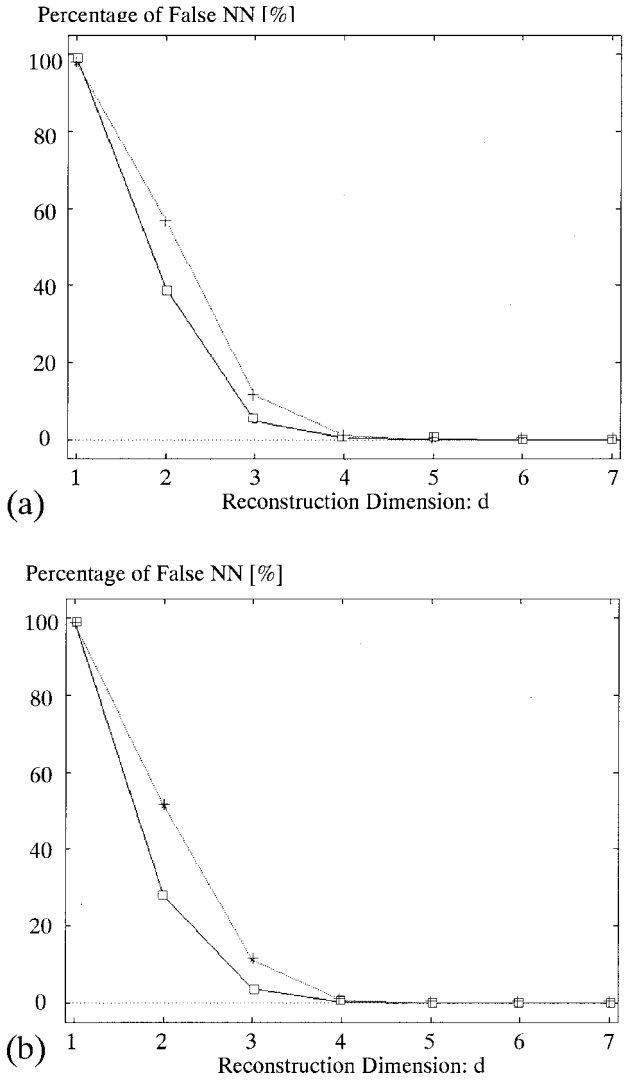

FIG. 4. Results of the FNN analysis applied to two subjects, (a) mau and (b) mms. In each figure, percentages of the false nearest neighbors of two vowels /a/ (solid line with squares) and /i/ (dotted line with crosses) are drawn simultaneously.

As the reconstruction dimension is increased from $d=1$, we see that the percentage of false nearest neighbors is decreased and becomes almost zero for the reconstruction dimension higher than $d=4$ for the two vowels. It is discussed in Ref. 65 that convergence to zero false-nearest-neighbor cannot be obtained in a noisy random data, since random data have practically infinite degrees of freedom. This implies that the speech signal of the two vowels can be characterized by relatively low-dimensional dynamics as $d \leqslant 7$ and the minimum embedding dimension would be $d_E=4$. For five vowels (/a/, /i/, /u/, /e/, /o/) and for five subjects (mau, mms, mmy, fsu, fyn), similar results have been obtained. Hence, the results of the FNN analysis do not seem to depend upon either the vowels or the subjects.

There are preceding studies of FNN analysis of vowels. Behrman[21] reported that six to eight (sometimes less) reconstruction dimensions are required for nonlinear analysis of normal vowels and Judd[30] reported that four dimensions are necessary to unfold the topological structure of a normal vowel. The present results basically agree with their results.

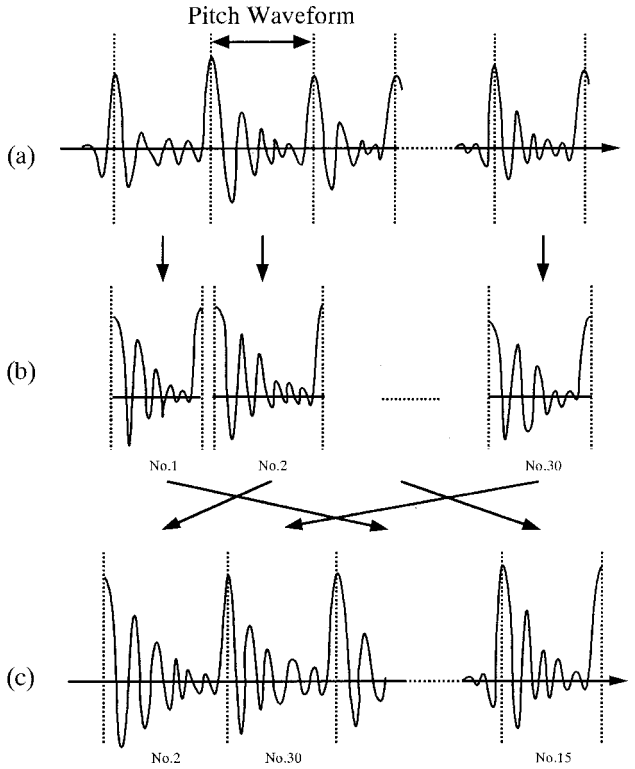

FIG. 5. Method of creating spike-and-wave surrogate data. (a), (b) Divide the original speech signal into pitch-waveform patterns by cutting the signal at maximal peak amplitudes. (c) Shuffle the pitch-waveforms and reconnect them with each other in random order.

IV. SURROGATE ANALYSIS

The FNN analysis of the previous section has shown that characteristic dynamics of the vowels can be reconstructed in a relatively low-dimensional delay-coordinate space of $4 \leqslant d \leqslant 7$. On the basis of the FNN analysis, let us further examine the nonlinear dynamical structure of the vowels by the method of surrogate data.[52–54]

The surrogate data analysis is a kind of statistical hypothesis testing which is to test a null-hypothesis H_0 that the speech signal is generated from a particular class of nondeterministic dynamical process. In accordance with the null-hypothesis H_0, sets of artificial time series, called *surrogate data*, which preserve some of the statistical properties of the original speech signal are created by a surrogate algorithm. Then a discriminating statistic T is computed for the original and the surrogate data. If the original discriminating statistic T_{origin} is significantly different from that of the surrogate data, the null-hypothesis H_0 can be rejected. The surrogate data have the property of "constrained realization,"[53] which is to randomize the original data by strictly preserving some of the original statistical properties. It is empirically known that the surrogate analysis is effective for statistical hypothesis testing when a *nonlinear* discriminating statistic T, whose distribution function is not well known, is utilized.

Among a variety of surrogate data analyses, spike-and-wave surrogate analysis is carried out in this study. The spike-and-wave surrogate analysis has been introduced by Theiler[54] for the analysis of epileptic EEG signals. The epileptic EEG signals are characterized by repeated occurrence of spike-and-wave patterns, where the variation of spike-and-

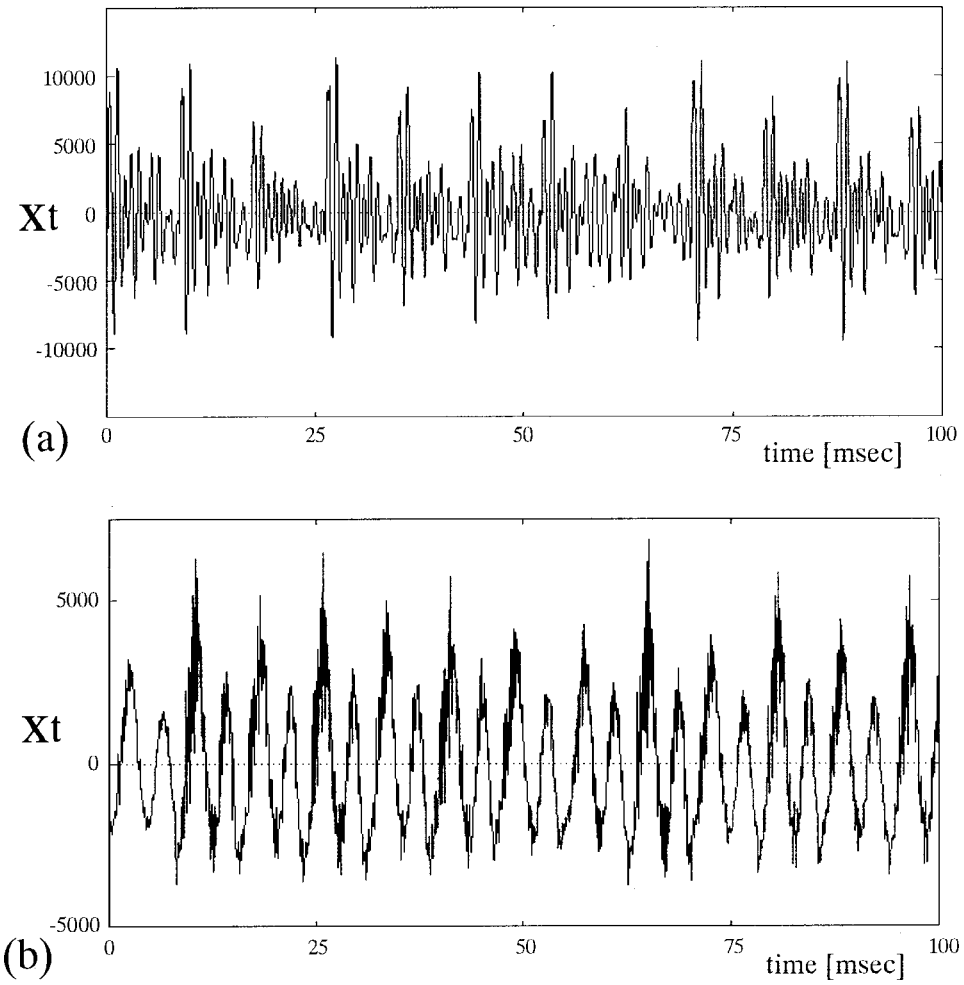

FIG. 6. (a) Spike-and-wave surrogate data made from the vowel signal /a/ of Fig. 1(a). (b) Spike-and-wave surrogate data made from the vowel signal /i/ of Fig. 1(b).

wave patterns had been considered as noisy components of limit cycle dynamics. By the surrogate analysis that examines nonlinear dynamical correlation between the spike-and-wave patterns, nonlinear dynamics that underlies the irregularity of the spike-and-wave patterns was detected in the epileptic EEG signals. In a similar manner, we study nonlinear dynamical correlation between pitch-waveform patterns in the vowel signals.

In the spike-and-wave surrogate analysis, we consider the following null-hypothesis:

H_0: "There is no nonlinear dynamical correlation from one pitch-waveform pattern to another."

A. Surrogate data

In the surrogate analysis, it is a necessary condition that the subject data are stationary. Stationarity means that statistical characteristics of time series do not change in time. Since speech production is inherently a nonstationary dynamical process, we have to be careful when applying the surrogate analysis to speech. Even in a single phonation of a vowel, it is known that vocal tract configuration slightly changes in time. In order to apply the surrogate analysis to stationary parts of the data, relatively short-term vowel signals ($\approx$100 ms) consisting of about 15 to 35 pitch waveforms are extracted.

Of course, there exists a drawback of using such short-term data for the surrogate analysis. Especially for computing a discriminating statistic, reliable estimation of the nonlinear dynamical quantity from short-term data is quite a difficult task.[46–48] In this sense, there is a limitation of analyzing speech signals by the surrogate method which needs to reliably estimate nonlinear dynamical quantities from short-term stationary data.

The spike-and-wave surrogate data can be generated as follows (see Fig. 5).

(1) Divide the original speech signal into pitch-waveforms by cutting the signal at the maximal peak amplitudes.
(2) Shuffle the pitch-waveforms and reconnect them with each other in random order.

By this surrogate shuffling, both histogram and pitch-waveform patterns of the original vowel signal are exactly preserved. For the statistical test, 39 sets of spike-and-wave surrogate data are created for each vowel. Figures 6(a) and (b) show spike-and-wave surrogate signals made from the original speech signals of Figs. 1(a) and (b), respectively. We see that the pitch-waveform structures of the original speech are preserved in the surrogate data.

In Figs. 7(a) and (b), the power spectra of the vowel signals /a/ and /i/ (subject: mau) are compared with those of their surrogate signals. In each figure, the bold line indicates the power spectrum of the original data, while the dotted lines indicate the power spectra of 39 sets of surrogate data. The power spectrum of the original data is covered with

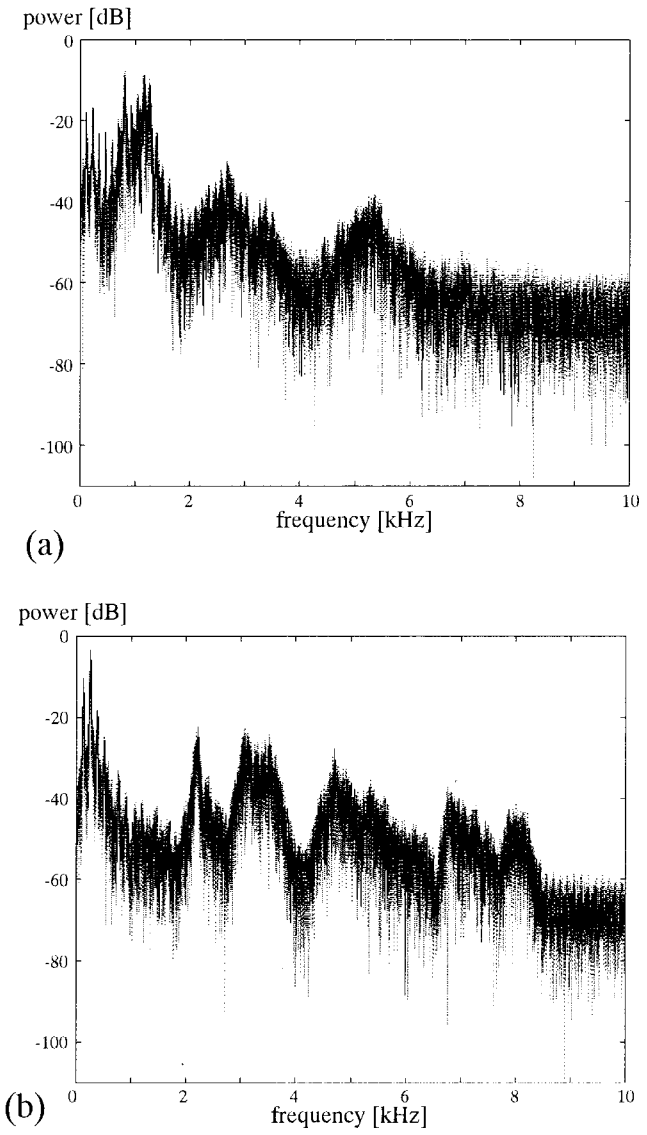

FIG. 7. (a) Power spectra of the original speech signal of Fig. 1(a) (bold line), and its spike-and-wave surrogate signals (dotted line). (b) Power spectra of the original speech signal of Fig. 1(b) (bold line), and its spike-and-wave surrogate signals (dotted line).

those of the surrogate data and hence the original data structure cannot be distinguished from the surrogate data. This implies that linear dynamical quantities such as the power spectrum cannot detect a difference between the original vowel and its spike-and-wave surrogates.

Ifukube *et al.*[35] studied the effect of pitch waveform fluctuations on the perception of natural vowels. They created a surrogate data from a vowel /a/ in a similar manner with the spike-and-wave method and carried out a listening test. Their psychoacoustic test reported that the surrogate data shuffling instantly destroyed natural perception of the vowel. This implies that the human auditory system is capable of perceiveing the naturalness of human sound in terms of the irregular dynamical structure of vowels. Presently, there is no way to quantify naturalness in terms of the irregular property of the vowels. If a nonlinear dynamical quantity can differentiate the original vowel signal from the surrogate data, such a nonlinear quantity might be a candidate for characterizing the naturalness of the vowels.

B. Wayland translation error

As a discriminating statistic T of the surrogate analysis, the Wayland translation error[66] is exploited.

The Wayland algorithm assumes that a time series $\{x_t\}$ is generated from a continuous nonlinear dynamical system and the reconstructed trajectory in the delay-coordinate space $\{\mathbf{x}(t):t=1+(d-1)\tau,..,N_{\text{data}}\}$ is described by a continuous mapping $f:R^d\rightarrow R^d$ as $\mathbf{x}(t+1)=f(\mathbf{x}(t))$. Since f is continuous, "nearby" data points, e.g., $\mathbf{x}(t)$ and $\mathbf{x}(s)$, are transformed to nearby states in T-step future, $\mathbf{x}(t+T)$ and $\mathbf{x}(s+T)$, in the delay coordinate space. With respect to the assumption of continuity in the reconstructed dynamics, the Wayland translation error e_{trans} can be calculated as follows.

For a fixed data point $\mathbf{x}(t_0)$, called a *translation center*, find its k-nearest neighbors $\mathbf{x}(t_1),\ldots,\mathbf{x}(t_k)$. Then, with respect to a *translation horizon* T, the translation vectors $\{\mathbf{v}_j=\mathbf{x}(t_j+T)-\mathbf{x}(t_j):j=0,...,k\}$ are computed. If the neighboring points $\mathbf{x}(t_1),\ldots,\mathbf{x}(t_k)$ are transformed to neighboring points $\mathbf{x}(t_1+T),\ldots,\mathbf{x}(t_k+T)$ in T-step future states, the translation vectors $\{\mathbf{v}_j\}$ are expected to point in similar directions. With respect to the diversity of the translation vectors, the translation error is calculated as

$$e_{\text{trans}}=\frac{1}{k+1}\sum_{j=0}^{k}\frac{\|\mathbf{v}_j-\overline{\mathbf{v}}\|^2}{\|\overline{\mathbf{v}}\|^2}\left(\overline{\mathbf{v}}=\frac{1}{k+1}\sum_{j=0}^{k}\mathbf{v}_j\right). \tag{8}$$

Figures 8(a) and (b) show the translation errors computed for speech signals of vowels /a/ and /i/ (subject: mau) and 39 sets of their surrogates. In each figure, error curves are drawn for the original speech data (solid line with circles) and for the surrogate data (solid lines with no circles). In order to reduce the statistical error for estimating the translation error of each time series, 20 sets of 301 translation centers $\mathbf{x}(t_0)$ are randomly chosen and the median of each set of translation errors is calculated. Then the average over the 20 medians is estimated as the translation error e_{trans}. The reconstruction dimension is varied as $d=2,...,15$ and other parameters are set to $\tau=10$, $k=4$, and $T=50$.

According to the numerical studies of the Wayland algorithm,[66] *Gaussian* white noise gives rise to a translation error of $e_{\text{trans}}\approx 1$ independently of d. Colored noise, on the other hand, exhibits a translation error which monotonically decreases to ~ 0.5 with increase in d due to the sustained autocorrelation.[67]

In Figs. 8(a) and (b), the original speech data give rise to translation error much less than 0.5, namely, $e_{\text{trans}}\ll 0.5$, with the minimum at $d\approx 11$ in case of (a) and $d\approx 8$ in case of (b). This implies that the vowel signals are described by neither *Gaussian* noise nor colored noise and that the qualitative dynamics of the vowel is well reconstructed with the dimension of $d\leqslant 11$. Moreover, the original data exhibit translation error curve which is distinctively lower than those of the 39 sets of the spike-and-wave surrogate data. In fact, for all five vowels (/a/, /i/, /u/, /e/, /o/) of the five subjects (mau, mms,

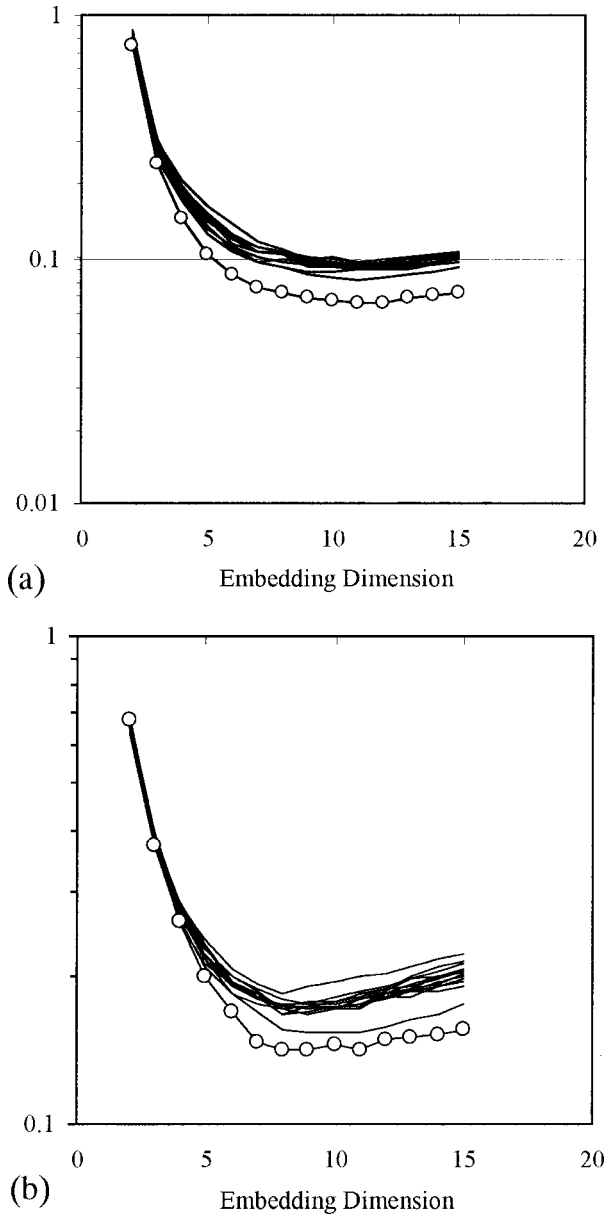

FIG. 8. (a) The translation error curve $e_{\text{trans}}(d=2,...,15)$ of the original vowel /a/ (subject: mau) (solid line with circles) and 39 sets of its spike-and-wave surrogates (solid lines with no circle). (b) The translation error curve of the original vowel /i/ (subject: mau) (solid line with circles) and 39 sets of its spike-and-wave surrogates (solid lines with no circle).

mmy, fsu, fyn), the translation errors of the original data are lower than those of the surrogate data. This means that for all vowel signals the spike-and-wave surrogate hypothesis is rejected with a level of $\alpha=0.05$ $(=\frac{2}{40})$. This is in general a strong rejection level for a statistical test and the results are independent of the vowels and the subjects. Therefore, we may conclude that there is nonlinear dynamical correlation between the pitch-waveforms of the vowel signals and such nonlinear dynamics has been destroyed by the spike-and-wave shuffling.

In several studies, the pitch-to-pitch variation of vowels is considered merely as noisy components of limit cycles.[17,20,23] If the pitch-to-pitch variation was generated from a purely stochastic random noise added to periodic cycles, statistical characteristics of the vowel signals may not have been changed by the surrogate shuffling so significantly. The present results therefore indicate that the pitch-to-pitch variation of vowels cannot be simply regarded as random noise added to limit cycles.

We note that the method of generating the spike-and-wave surrogate data is based on the extraction of pitch waveforms and their reconnection in a randomized order. By this shuffling, discontinuity can occur at the reconnected points of the surrogate data. This could have an influence on the numerical results of the surrogate analysis. In order to avoid such a problem, an algorithm can be improved by applying, e.g., a smoothing filter to the reconnection points. We consider, however, that this may not change our main results, since our results show strong rejection levels for all vowel signals.

V. CONCLUSIONS AND DISCUSSIONS

The dynamical structure and characteristics of normal vowels have been investigated by nonlinear systems analysis. By the false nearest-neighbor analysis, the minimum embedding dimension required for nonlinear analysis of vowels was estimated to be $d_E=4$. The analysis also revealed that the nonlinear dynamics of the vowels is well reconstructed and analyzed in relatively low-dimensional delay-coordinate spaces with $4\leqslant d\leqslant 10$. Then, nonlinear dynamics of the vowels were further studied by the spike-and-wave surrogate analysis which exploits Wayland translation error as the nonlinear discriminating statistic. On the basis of the surrogate analysis, we have shown a possibility that there exists nonlinear dynamical correlation between one pitch-waveform pattern to another in the vowel signals.

Let us consider the present results in the light of the LPC modeling of vowels. In speech synthesis, vowels are usually synthesized by LPC models excited by impulse trains. In the sense that the intervals of the spike trains correspond to the pitch periods of the vowel signals, the present surrogate test implies that the spike intervals for the LPC model should not be mutually independent, but they may have nonlinear dynamical correlation. In conventional speech coding techniques such as the CELP scheme, the impulse excitation signals are selected from codebooks of periodic and aperiodic spike signals. Such schemes are not always efficient in the sense that they require a huge database of pitch sequences. If the intervals of the spike trains have a nonlinear dynamical correlation, such spike trains can be modeled by nonlinear prediction models. The nonlinear prediction models can provide speech synthesis techniques *possibly* simpler than the conventional ones in the sense that they are based on function approximation techniques which do not require any pitch database. It is our future work to examine plausibility of modeling LPC excitation signals by nonlinear prediction models that reproduce irregular properties of vowels with natural human sound quality.

We finally note that one of the most important applications of nonlinear analysis of vowels is to aid the development of nonlinear models for voice production, which can clarify the physiological mechanism that gives rise to the pitch-to-pitch variation of vowels. It is, however, still difficult to develop such physiological models from the present

study, since the present nonlinear analysis is not directly related to voice physiological models. There are several works that attempted to relate nonlinear analysis results to voice physiological models. For example, Herzel *et al.* interpreted nonsynchronous chaotic dynamics of pathological voice in terms of nonsymmetric vocal fold vibrations.[68,69] A similar approach to interpret the pitch-to-pitch variation of vowels will be explored in a future study.

ACKNOWLEDGMENTS

This study was presented at the Second International Conference on Voice Physiology and Biomechanics in Berlin in March 1999. The authors express their special gratitudes to Dr. Anders Löfqvist and two anonymous reviewers for their careful and thoughtful comments on the original manuscript. They also thank Professor J. Kurths, Professor H. Herzel, and Professor A. I. Mees and Dr. K. Judd, Dr. T. Ikeguchi, Dr. S. McLaughlin, and Dr. N. Aoki for stimulating discussions and valuable comments on the present work. This research was partially supported by Grant-in-Aid for Scientific Research (No. 10750259) of Japanese ministry of education, science, sports and culture and by Special Coordination Funds for Promoting Science and Technology (SCF).

[1] G. Fant, *Acoustic Theory of Speech Production* (Mouton, Gravenhage, 1960).
[2] B. S. Atal and S. L. Hanauer, ''Speech analysis and synthesis by linear prediction of the speech wave,'' J. Acoust. Soc. Am. **50**, 637–655 (1971).
[3] J. D. Markel and A. H. Gray, *Linear Prediction of Speech* (Springer-Verlag, Berlin, 1976).
[4] D. H. Klatt and L. C. Klatt, ''Analysis, synthesis, and perception of voice quality variations among female and male talkers,'' J. Acoust. Soc. Am. **87**, 820–857 (1990).
[5] D. G. Childers and C. K. Lee, ''Vocal quality factors: Analysis, synthesis, and perception,'' J. Acoust. Soc. Am. **90**, 2394–2410 (1991).
[6] K. Ishizaka and J. L. Flanagan, ''Synthesis of voiced sounds from a two-mass model of the vocal cords,'' Bell Syst. Tech. J. **51(6)**, 1233–1268 (1972).
[7] I. R. Titze and D. T. Talkin, ''A theoretical study of the effects of various laryngeal configurations on the acoustics of phonation,'' J. Acoust. Soc. Am. **66**, 60–74 (1979).
[8] R. C. Scherer, I. R. Titze, and J. F. Curtis, ''Pressure-flow relationships in two models of the larynx having rectangular glottal shapes,'' J. Acoust. Soc. Am. **73**, 668–676 (1983).
[9] N. Miki, ''Recent progress of the acoustic theory of speech production process,'' J. Acoust. Soc. Jpn. **48**(1), 15–19 (1992).
[10] A. E. Rosenberg, ''Effect of glottal pulse shape on the quality of natural vowels,'' J. Acoust. Soc. Am. **49**, 583–590 (1971).
[11] G. Fant and Q. Lin, ''Frequency domain interpretation and derivation of glottal flow parameters,'' Speech Trans. Lab. Q. Prog. Stat. Rep. **2**(3), 1–21 (1988).
[12] H. Fujisaki and M. Ljungqvist, ''Proposal and evaluation of models for glottal source waveform,'' Proc. IEEE Int. Conf. Acoust., Speech, Signal Processing (1986), pp. 1605–1608.
[13] M. R. Schroeder and B. S. Atal, ''Code-excited linear prediction (CELP): High-quality speech at very low bit rates,'' Proc. IEEE Int. Conf. Acoust., Speech, Signal Processing, Tampa, FL (1985), pp. 937–940.
[14] G. Nicolis and I. Prigogine, *Self-Organization in Nonequilibrium Systems* (Wiley, New York, 1977).
[15] W. Lauterborn and U. Parlitz, ''Methods of chaos physics and their application to acoustics,'' J. Acoust. Soc. Am. **84**, 1975–1993 (1988).
[16] H. D. I. Abarbanel, R. Brown, J. J. Sidorowich, and L. S. Tsimring, ''The analysis of observed chaotic data in physical systems,'' Rev. Mod. Phys. **65**, 1331–1392 (1993).
[17] I. R. Titze, R. J. Baken, and H. Herzel, ''Evidence of chaos in vocal fold vibration,'' in *Vocal Fold Physiology*, edited by I. R. Titze (Singular, San Diego, 1993), pp. 143–188.
[18] H. Herzel, D. Berry, I. R. Titze, and M. Saleh, ''Analysis of vocal disorders with method from nonlinear dynamics,'' J. Speech Hear. Res. **37**, 1008–1019 (1994).
[19] M. Tigges, P. Mergel, H. Herzel, T. Wittenberg, and U. Eysholdt, ''Observation and modelling of glottal biphonation,'' Acustica **83**, 707–714 (1997).
[20] A. Behrman and R. J. Baken, ''Correlation dimension of electroglottographic data from healthy and pathologic subjects,'' J. Acoust. Soc. Am. **102**, 2371–2379 (1997).
[21] A. Behrman, ''Global and local dimensions of vocal dynamics,'' J. Acoust. Soc. Am. **105**, 432–443 (1999).
[22] W. Mende, H. Herzel, and I. R. Titze, ''Bifurcations and chaos in newborn cries,'' Phys. Lett. A **145**, 418–424 (1990).
[23] S. S. Narayanan and A. A. Alwan, ''A nonlinear dynamical systems analysis of fricative consonants,'' J. Acoust. Soc. Am. **97**, 2511–2524 (1995).
[24] B. Townshend, ''Nonlinear prediction of speech signals,'' in *Nonlinear Modeling and Forecasting*, edited by M. Casdagli and S. Eubank, SFI Studies in Sciences of Complexity (Addison–Wesley, Reading, MA, 1992), pp. 433–453.
[25] M. Banbrook, S. McLaughlin, and I. Mann, ''Speech characterization and synthesis by nonlinear methods,'' IEEE Trans. Speech Audio Process. **7(1)**, 1–17 (1999).
[26] M. Sato, K. Joe, and T. Hirahara, ''APOLONN brings us to the real world,'' Proc. Int. Joint Conf. Neural Networks **1**, 581–587 (1990).
[27] I. Tokuda, R. Tokunaga, and K. Aihara, ''A simple geometrical structure underlying speech signals of the Japanese vowel /a/,'' Int. J. Bifurcation Chaos Appl. Sci. Eng. **6**(1), 149–160 (1996).
[28] G. Kubin, ''Nonlinear processing of speech,'' in *Speech Coding and Synthesis*, edited by W. B. Kleijin and K. K. Paliwal (Elsevier Science, Amsterdam, 1995), pp. 557–610.
[29] I. Mann and S. McLaughlin, ''Nonlinear dynamical modelling for speech synthesis using radial basis functions,'' preprint (2000).
[30] K. Judd, ''Nonlinear modelling: Keep it simple, vary the embedding, and make sure the dynamics are right,'' presented at Newton Institute Workshop on Nonlinear Dynamics and Statistics, Cambridge, 21–25 September 1998.
[31] A. Kumar and S. K. Mullick, ''Nonlinear dynamical analysis of speech,'' J. Acoust. Soc. Am. **100**, 615–629 (1996).
[32] T. Ikeguchi and K. Aihara, ''Estimating correlation dimensions of biological time series with a reliable method,'' J. Int. Fuzzy Sys. **5(1)**, 33–52 (1997).
[33] T. Miyano, ''Are Japanese vowels chaotic?,'' Proc. 4th Int. Conf. Soft Computing (1996), Vol. 2, pp. 634–637.
[34] L. Dolanský and P. Tjernlund, ''On certain irregularities of voiced speech waveforms,'' IEEE Trans. Audio Electroacoust. **16**(1), 51–56 (1968).
[35] T. Ifukube, M. Hashiba, and J. Matsushima, ''A role of 'waveform fluctuation' on the naturality of vowels,'' J. Acoust. Soc. Jpn. **47**(12), 903–910 (1991).
[36] T. Kobayashi and H. Sekine, ''The role of fluctuations in fundamental period for natural speech synthesis,'' J. Acoust. Soc. Jpn. **47**(8), 539–544 (1991).
[37] O. Komuro and H. Kasuya, ''Characteristic of fundamental period variation and its modeling,'' J. Acoust. Soc. Jpn. **47**(12), 928–934 (1991).
[38] N. Aoki and T. Ifukube, ''Analysis and perception of spectral $1/f$ characteristics of amplitude and period fluctuations in normal sustained vowels,'' J. Acoust. Soc. Am. **106**, 423–433 (1999).
[39] R. W. Wendahl, ''Laryngeal analog synthesis of harsh voice quality,'' Folia Phoniatr. **15**, 241–250 (1963).
[40] R. W. Wendahl, ''Laryngeal analog synthesis of jitter and shimmer auditory parameters of harshness,'' Folia Phoniatr. **18**, 98–108 (1966).
[41] S. Hiki, K. Sugawara, and J. Oizumi, ''On the rapid fluctuation of voice pitch,'' J. Acoust. Soc. Jpn. **22**, 290–291 (1966).
[42] R. F. Coleman, ''Effect of median frequency levels upon the roughness of jittered stimuli,'' J. Speech Hear. Res. **12**, 330–336 (1969).
[43] R. F. Coleman, ''Effect of waveform changes upon roughness perception,'' Folia Phoniatr. **23**, 314–322 (1971).
[44] A. J. Rozsypal and B. F. Miller, ''Perception of jitter and shimmer in synthetic vowels,'' J. Phonetics **7**, 343–355 (1979).
[45] D. R. Griffin and J. E. Lim, ''Multiband excitation vocoder,'' IEEE Trans. Acoust., Speech, Signal Process. **36**(8), 1223–1235 (1988).
[46] J. Theiler, ''Spurious dimension from correlation algorithms applied to limited time-series data,'' Phys. Rev. A **34**(3), 2427–2432 (1986).

[47] L. A. Smith, ''Intrinsic limits of on dimension calculations,'' Phys. Lett. A **133**(6), 283–288 (1988).
[48] D. Ruelle, ''Deterministic chaos: Science and fiction,'' Proc. R. Soc. London, Ser. A **427**, 244–248 (1990).
[49] D. Ruelle, ''Where can one hope to profitably apply the ideas of chaos?'' Phys. Today **July**, 24–30 (1994).
[50] P. E. Rapp, ''Chaos in the neurosciences: cautionary tales from the frontier,'' Biologist **40**(2), 89–94 (1993).
[51] P. E. Rapp, A. M. Albano, T. I. Schmah, and L. A. Farwell, ''Filtered noise can mimic low-dimensional chaotic attractors,'' Phys. Rev. E **47**, 2289–2297 (1993).
[52] J. Theiler, S. Eubank, A. Longtin, B. Galdrikian, and J. D. Farmer, ''Testing for nonlinearity in time series: the method of surrogate data,'' Physica D **58**, 77–94 (1992).
[53] J. Theiler and D. Prichard, ''Constrained-realization Monte-Carlo method for hypothesis testing,'' Physica D **94**, 221–235 (1996).
[54] J. Theiler, ''On the evidence for low-dimensional chaos in an epileptic electroencephalogram,'' Phys. Lett. A **196**, 335–341 (1995).
[55] T. Miyano, A. Nagami, I. Tokuda, and K. Aihara, ''Detecting nonlinear determinism in voiced sounds of Japanese vowel /a/,'' Int. J. Bifurcation Chaos Appl. Sci. Eng. **10**(8), 1973–1979 (2000).
[56] H. Hollien, J. Michel, and E. T. Doherty, ''A method for analyzing vocal jitter in sustained phonation,'' J. Phonetics **1**, 85–91 (1973).
[57] Y. Horii, ''Some statistical characteristics of voice fundamental frequency,'' J. Speech Hear. Res. **18**, 192–201 (1975).
[58] Y. Horii, ''Fundamental frequency perturbation observed in sustained phonation,'' J. Speech Hear. Res. **22**, 5–19 (1979).
[59] I. R. Titze, Y. Horii, and R. C. Scherer, ''Some technical considerations in voice perturbation measurements,'' J. Speech Hear. Res. **30**, 252–260 (1987).
[60] I. R. Titze and H. Liang, ''Comparison of $F0$ extraction methods for high-precision voice perturbation measurements,'' J. Speech Hear. Res. **36**, 1120–1133 (1993).
[61] N. B. Pinto and I. R. Titze, ''Unification of perturbation measures in speech signals,'' J. Acoust. Soc. Am. **87**, 1278–1289 (1990).
[62] R. C. Scherer, V. J. Vail, and C. G. Guo, ''Required number of tokens to determine representative voice perturbation values,'' J. Speech Hear. Res. **38**, 1260–1269 (1995).
[63] F. Takens, ''Detecting strange attractors in turbulence,'' in *Lecture Notes in Math* (Springer, Berlin, 1981), Vol. 898, pp. 366–381.
[64] T. Sauer, J. A. York, and M. Casdagli, ''Embedology,'' J. Stat. Phys. **65**(3), 579–616 (1991).
[65] M. B. Kennel, R. Brown, and H. D. I. Abarbanel, ''Determining embedding dimension for phase-space reconstruction using a geometric construction,'' Phys. Rev. A **45**(6), 3403–3411 (1992).
[66] R. Wayland, D. Bromely, D. Pickett, and A. Passamante, ''Recognizing determinism in a time series,'' Phys. Rev. Lett. **70**(5), 580–582 (1993).
[67] T. Miyano, ''Time series analysis of complex dynamical behavior contaminated with observational noise,'' Int. J. Bifurcation Chaos Appl. Sci. Eng. **6**, 2031–2045 (1996).
[68] P. Mergel and H. Herzel, ''Modeling biphonation,'' Speech Commun. **22**, 141–154 (1997).
[69] I. Steinecke and H. Herzel, ''Bifurcations in an asymmetric vocal-fold model,'' J. Acoust. Soc. Am. **97**, 1874–1884 (1995).

A two-microphone dual delay-line approach for extraction of a speech sound in the presence of multiple interferers[a)]

Chen Liu,[b)] Bruce C. Wheeler, William D. O'Brien, Jr., Charissa R. Lansing, Robert C. Bilger, Douglas L. Jones, and Albert S. Feng[c)]

Beckman Institute for Advanced Science and Technology, University of Illinois at Urbana-Champaign, Urbana, Illinois 61801

(Received 28 June 2000; revised 14 June 2001; accepted 19 September 2001)

This paper describes algorithms for signal extraction for use as a front-end of telecommunication devices, speech recognition systems, as well as hearing aids that operate in noisy environments. The development was based on some independent, hypothesized theories of the computational mechanics of biological systems in which directional hearing is enabled mainly by binaural processing of interaural directional cues. Our system uses two microphones as input devices and a signal processing method based on the two input channels. The signal processing procedure comprises two major stages: (i) source localization, and (ii) cancellation of noise sources based on knowledge of the locations of all sound sources. The source localization, detailed in our previous paper [Liu *et al.*, J. Acoust. Soc. Am. **108**, 1888 (2000)], was based on a well-recognized biological architecture comprising a dual delay-line and a coincidence detection mechanism. This paper focuses on description of the noise cancellation stage. We designed a simple subtraction method which, when strategically employed over the dual delay-line structure in the broadband manner, can effectively cancel multiple interfering sound sources and consequently enhance the desired signal. We obtained an 8–10 dB enhancement for the desired speech in the situations of four talkers in the anechoic acoustic test (or 7–10 dB enhancement in the situations of six talkers in the computer simulation) when all the sounds were equally intense and temporally aligned. [DOI: 10.1121/1.1419090]

PACS numbers: 43.72.Ar, 43.72.Dv, 43.60.Bf [DOS]

I. INTRODUCTION

Selective hearing is a useful mechanism for extracting desired signals in complex acoustic environments such as a cocktail party. This so-called ''cocktail party'' effect has been studied psychophysically (Cherry, 1953; Blauert, 1983; Bregman, 1990; Bronkhorst and Plomp, 1992). The ability to hear in complex acoustic environments is largely attributed to the capacity to discern the spatial origins of sound sources. The neural circuitry and the underlying mechanisms for sound localization are fairly well established (Konishi *et al.*, 1988; Takahashi and Keller, 1994; Yin and Chan, 1990). Sound localization involves binaural processing of minute differences in time, intensity, and spectrum between the two ears. However, although we know the capacity of the auditory system to selectively attend to sounds originating from one source and suppress the other sounds in the ambiance, the underlying mechanisms for doing so are largely unknown. Therefore, designing an artificially intelligent system today to achieve selective hearing is still largely based on our relatively rich knowledge of the physical world (e.g., signal processing techniques) plus our limited knowledge of the biological world.

One of the prominent noise suppression concepts is the EC or equalization-and-cancellation scheme of Durlach (Durlach, 1960, 1972). It requires two inputs followed by a two-stage signal processing: (i) equalization that makes the noise components identical in both channels; and (ii) cancellation or subtraction of the noise components in one channel from those in the other channel. Actually most two-microphone-based noise cancellation techniques to date (e.g., Widrow *et al.*, 1975; Strube, 1981; Chabries *et al.*, 1982; Chazan *et al.*, 1988; Weiss, 1987; Peterson *et al.*, 1987) are essentially variants of the EC scheme and differ primarily in the procedures by which the filter parameters are adapted. Thus far, these have rendered satisfactory noise reduction only for situations in which there are one desired source and one noise source.

Our noise cancellation technique described herein also falls in this category. However, it is devised so as to cancel multiple noise sources more efficiently by capitalizing on the knowledge of the spatial directions of the sound sources in the environment. For the purpose of sound localization, we have designed a system (Liu *et al.*, 2000) based on a broadband ''dual delay-line'' structure and the coincidence detection principle of Jeffress (1948). Our noise cancellation technique also adopts the dual delay-line as the infrastructure.

So far the Jeffress model has been studied and various modifications have been developed to account for different psychological observations (see reviews in the book chapters by Colburn and Durlach, 1978; Colburn, 1996; and Stern and Trahiotis, 1995, 1997). It was only recently that the Jeffress model began to be considered for use in the extraction of

[a)]Portions of this paper were presented at the Hearing Aid Research & Development Conference, Bethesda, MD, September 1997.

[b)]Present address: Motorola Labs, 1141 Opus Place, Downers Grove, IL 60515.

[c)]Electronic mail: a-feng@uiuc.edu

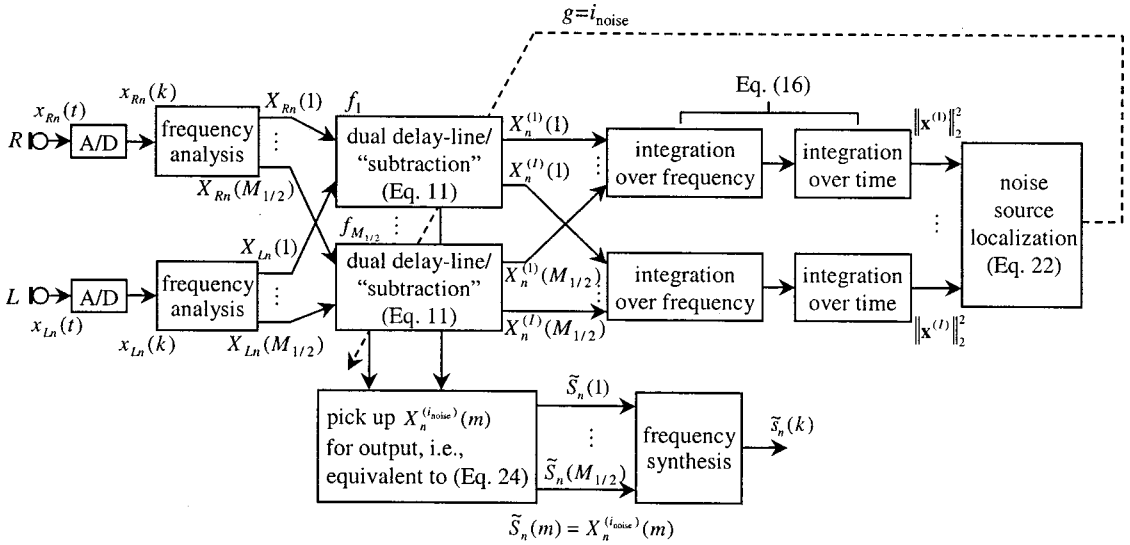

FIG. 1. The block diagram of System I for extraction of the desired source, whose location is known *a priori*, in the presence of one noise source whose location is estimated by the system.

speech in noise (e.g., Bodden, 1993; Banks, 1993). Since the model maps the acoustic space into a network, one appealing feature is the potential for detecting the number and the azimuths of sound sources present in the auditory space. This provides the mechanism by which the system can focus on, and extract the signal from, one desired source direction, while at the same time suppressing the sounds arising from the other directions. In his acoustic processor, Bodden (1993, 1996) basically took the Jeffress' coincidence sound localization models, as implemented by Lindemann (1986) and Gaik (1993), and added a time-variant Wiener filter for noise cancellation after sounds had been localized. However, since it is impossible to obtain an accurate estimate of the power density spectra of both the desired and noise signals, the result will always have residual noise and some cancellation and distortion of the desired signal.

The work described herein was motivated by the need to find a general solution for signal extraction in real world situations where there are multiple (>2) concurrent sound sources. Our signal extraction technique evolved from a subtraction procedure. Note that, interestingly, subtraction is also employed in the directional hearing mechanism with a pressure-gradient receiver (Feng and Shofner, 1981). Theoretically, a conventional noise cancellation system using a two-microphone array performs well when there are two sources but its performance degrades rapidly as the number of sources increases. To attack this problem, we developed a broadband noise cancellation strategy, making the two-microphone array subtraction approach more effective by taking advantage of the dual delay-line structure.

In this paper, we first introduce a subtraction method, which is the core of our noise cancellation technique. The subtraction procedure is then extended via the broadband dual delay-line structure for cancellation of multiple sources. In Sec. II A, we describe the subtraction procedure in the context of extracting a desired source at a known location in the presence of one interfering source at an arbitrary location. The subtraction operation is mathematically analyzed in Sec. II B. Section II C gives a beamforming interpretation of the subtraction method. In Sec. II D, the method is generalized to situations in which neither the location of the desired source nor that of the interference is known. Section III describes a strategy for extending the method to a system suitable for cancellation of multiple interfering sources. Section IV presents the experimental results and analysis. Discussion of several practical issues is given in Sec. V.

II. INTRODUCTION TO THE NEW CANCELLATION SCHEME

A. Cancellation algorithm based on the dual delay-line structure

In this section we will describe a new noise cancellation algorithm. It is fundamentally a subtraction operation applied on the two input signals. The signals are received by two microphones, which are paired with a fixed inter-microphone distance. The subtraction is conducted based on the infrastructure of the dual delay-line network in the frequency domain. A block diagram of the basic signal processing system (System I) is shown in Fig. 1. The two inputs, $x_{Ln}(t)$ and $x_{Rn}(t)$, are digitized, their digital versions being $x_{Ln}(k)$ and $x_{Rn}(k)$, respectively. Their spectra, $X_{Ln}(m)$ and $X_{Rn}(m)$, $m=1,\ldots,M$, are obtained through discrete Fourier transform (DFT). The subscripts L and R denote left and right channels, and n the frame index of the short-term Fourier analysis.

For clarity, we shall focus on the system description for an arbitrary frequency ω_m. For each frequency, the complex signals from the two channels are fed into a pair of delay-lines (Fig. 2), both of which are composed of I delay units with delay values τ_i $(i=1,\ldots,I)$ given by

$$\tau_i=\frac{\mathrm{ITD}_{\max}}{2}\sin\left(\frac{i-1}{I-1}\pi-\frac{\pi}{2}\right),\quad i=1,\ldots,I, \tag{1}$$

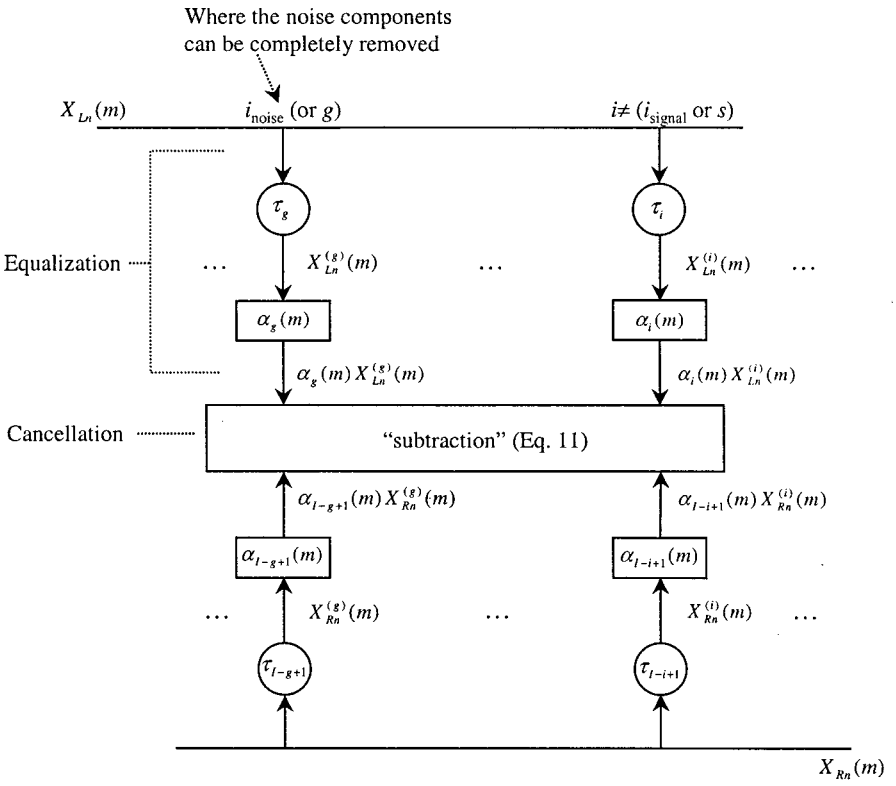

FIG. 2. The dual delay-line used as the basic structure in our system.

where $\mathrm{ITD}_{\max}=D/c$ is the maximum inter-microphone time difference, D is the inter-microphone distance, c is the speed of sound, and I is an odd number greater than 1. By using Eq. (1), it can be shown that the time delays are antisymmetric with respect to the midpoint $(I+1)/2$, i.e.,

$$\tau_{I-i+1}=-\tau_i, \quad i=1,\ldots,(I+2)/2-1. \tag{2}$$

It is noted that if there is no diffracting object between the two microphones, the horizontal plane can be uniformly divided into I sectors with the azimuth of each sector being

$$\theta_i=\frac{\pi}{2}-\frac{i-1}{I-1}\pi, \quad i=1,\ldots,I. \tag{3}$$

Therefore, the azimuths can be mapped one-to-one onto the corresponding positions in the delay line

$$\tau_i=-\frac{\mathrm{ITD}_{\max}}{2}\sin\,\theta_i, \quad i=1,\ldots,I. \tag{4}$$

Note that the resolution of the dual delay-lines representing the spatial azimuth is determined by the values of the time-delay units τ_i that have a time unit such as millisecond. As will be described in detail next, the delays are applied to the left and right input signals at each frequency in the frequency domain. Thus the dual delay-line works like rotating two separate phasors in the opposite directions in the complex plane [Eqs. (9) and (10)] until they are in phase, i.e., the so-called coincidence operation. The step size of the rotation, $\exp(-j\omega_m\tau_i)$, can be arbitrarily small in the frequency domain. Therefore, the azimuthal resolution of the dual delay-lines is not controlled by the sampling rate. Some other relevant discussions will be given in Sec. II C.

Figure 2 shows that the dual delay-line structure is similar to that adopted previously for sound localization (Liu *et al.*, 2000) except that a compensation element $\alpha_i(m)$ has been added following each delay unit. These elements, which compensate for differences in the intensity of noise at the two microphones, are functions of both azimuth and frequency. Appendix A derives the compensation values for the ideal case of point sources with distance-dependent amplitude decline, in a lossless medium. In practice, however, all the values of $\alpha_i(m)$ and τ_i $(i=1,\ldots,I)$ are to be adjusted empirically the same time when the system is being calibrated to compensate for asymmetries between the two microphones. The compensation factors remain fixed so long as the asymmetries are not changed. This fixed interaural intensity difference (IID) corresponding to each interaural time difference (ITD) mimics that observed in humans (Gaik, 1993). In the anechoic chamber tests reported below, the values of ITD units τ_i $(i=1,\ldots,I)$ were set uniformly while the values of IID $\alpha_i(m)$ $(i=1,\ldots,I)$ were determined empirically.

In this subsection let us suppose the direction of the desired source is known *a priori* and we use $i_{\mathrm{signal}}=s$ to denote the in-phase (coincident) position along the dual delay-line for the desired signal components. We use $i_{\mathrm{noise}}=g$ to denote the in-phase position for the noise signal components. Note that the position index along the dual delay-line is coincident with the index of the delay units in the left channel. After equalization, the in-phase desired signal components are identical in the left and right channels at $i_{\mathrm{signal}}=s$, which is assumed to be $S_n(m)=A_s\exp[j(\omega_m t+\phi_s)]$; likewise, the in-phase noise signal component is identical in the left and right channels at $i_{\mathrm{noise}}=g$, which is assumed to be $G_n(m)=A_g\exp[j(\omega_m t+\phi_g)]$, where ϕ_s and ϕ_g are the initial phases for signal and noise, respectively. Based on

these assumptions, the left and right channel input (microphone) signals are, respectively,

$$X_{Ln}(m)=\frac{1}{\alpha_s(m)}S_n(m)\exp(j\omega_m\tau_s)+\frac{1}{\alpha_g(m)}G_n(m)\exp(j\omega_m\tau_g) \quad (5)$$

and

$$X_{Rn}(m)=\frac{1}{\alpha_{I-s+1}(m)}S_n(m)\exp(j\omega_m\tau_{I-s+1})+\frac{1}{\alpha_{I-g+1}(m)}G_n(m)\exp(j\omega_m\tau_{I-g+1}). \quad (6)$$

Then, we can find the mathematical representation for the equalized signals $\alpha_i(m)X_{Ln}^{(i)}(m)$ for the left channel, and $\alpha_{I-i+1}(m)X_{Rn}^{(i)}(m)$ for the right channel at any arbitrary point i (except $i=s$), along the dual delay-line. They are

$$\alpha_i(m)X_{Ln}^{(i)}(m)=\frac{\alpha_i(m)}{\alpha_s(m)}S_n(m)\exp[j\omega_m(\tau_s-\tau_i)]+\frac{\alpha_i(m)}{\alpha_g(m)}G_n(m)\exp[j\omega_m(\tau_g-\tau_i)] \quad (7)$$

and

$$\alpha_{I-i+1}(m)X_{Rn}^{(i)}(m)=\frac{\alpha_{I-i+1}(m)}{\alpha_{I-s+1}(m)}S_n(m)\times\exp[j\omega_m(\tau_{I-s+1}-\tau_{I-i+1})]+\frac{\alpha_{I-i+1}(m)}{\alpha_{I-g+1}(m)}G_n(m)\times\exp[j\omega_m(\tau_{I-g+1}-\tau_{I-i+1})], \quad (8)$$

where

$$X_{Ln}^{(i)}(m)=X_{Ln}(m)\exp(-j\omega_m\tau_i) \quad (9)$$

and

$$X_{Rn}^{(i)}(m)=X_{Rn}(m)\exp(-j\omega_m\tau_{I-i+1}). \quad (10)$$

The subtraction step in the algorithm performs the following operation on each signal pair, $\alpha_i(m)X_{Ln}^{(i)}(m)$ and $\alpha_{I-i+1}(m)X_{Rn}^{(i)}(m)$, for $i=1,\ldots,I$, at any location along the delay line except the location where $i=s$:

$$X_n^{(i)}(m)=\frac{\alpha_i(m)X_{Ln}^{(i)}(m)-\alpha_{I-i+1}(m)X_{Rn}^{(i)}(m)}{[\alpha_i(m)/\alpha_s(m)]\exp[j\omega_m(\tau_s-\tau_i)]-[\alpha_{I-i+1}(m)/\alpha_{I-s+1}(m)]\exp[j\omega_m(\tau_{I-s+1}-\tau_{I-i+1})]}, \quad \text{for } i\neq s. \quad (11)$$

A caveat in using Eq. (11) is that if the value of the denominator is too small, a small positive constant ϵ is added to limit the magnitude of $X_n^{(i)}(m)$.

B. Physical meaning of the delay-line subtraction operation

To analyze the operation, Eq. (11) can be expressed in the following form via substitution of Eqs. (7) and (8):

$$X_n^{(i)}(m)=S_n(m)+G_n(m)v_{s,g}^{(i)}(m), \quad i\neq s, \quad (12)$$

where

$$v_{s,g}^{(i)}(m)=\frac{[\alpha_i(m)/\alpha_g(m)]\exp[j\omega_m(\tau_g-\tau_i)]-[\alpha_{I-i+1}(m)/\alpha_{I-g+1}(m)]\exp[j\omega_m(\tau_{I-g+1}-\tau_{I-i+1})]}{[\alpha_i(m)/\alpha_s(m)]\exp[j\omega_m(\tau_s-\tau_i)]-[\alpha_{I-i+1}(m)/\alpha_{I-s+1}(m)]\exp[j\omega_m(\tau_{I-s+1}-\tau_{I-i+1})]}, \quad i\neq s. \quad (13)$$

Equations (11) and (13) can be simplified when the antisymmetric relationship in Eq. (2) is used. Thus,

$$X_n^{(i)}(m)=\frac{\alpha_i(m)X_{Ln}^{(i)}(m)-\alpha_{I-i+1}(m)X_{Rn}^{(i)}(m)}{[\alpha_i(m)/\alpha_s(m)]\exp[j\omega_m(\tau_s-\tau_i)]-[\alpha_{I-i+1}(m)/\alpha_{I-s+1}(m)]\exp[-j\omega_m(\tau_s-\tau_i)]}, \quad \text{for } i\neq s, \quad (14)$$

and

$$v_{s,g}^{(i)}(m)=\frac{[\alpha_i(m)/\alpha_g(m)]\exp[j\omega_m(\tau_g-\tau_i)]-[\alpha_{I-i+1}(m)/\alpha_{I-g+1}(m)]\exp[-j\omega_m(\tau_g-\tau_i)]}{[\alpha_i(m)/\alpha_s(m)]\exp[j\omega_m(\tau_s-\tau_i)]-[\alpha_{I-i+1}(m)/\alpha_{I-s+1}(m)]\exp[-j\omega_m(\tau_s-\tau_i)]}, \quad i\neq s. \quad (15)$$

When ignoring the compensation factors $\alpha_i(m)$, an interesting observation of the subtraction [Eq. (11) or (14)] is that it computes the difference between each pair of taps at the ith location divided (shifted) by a factor that is determined only by the difference in time delay between that location and the location corresponding to the desired signal. Next we will show that Eq. (11) performed at the location i in the dual delay-line corresponding to the noise source will cancel the noise signal and provide an estimate of the desired signal. Moreover, the location can be found using an energy quantity.

A signal vector containing all the frequency components for the preceding N time frames is $\mathbf{x}^{(i)}=(X_1^{(i)}(1), X_1^{(i)}(2), \ldots, X_1^{(i)}(M), X_2^{(i)}(1), \ldots, X_2^{(i)}(M), \ldots, X_N^{(i)}(1), \ldots, X_N^{(i)}(M))^T$, $i=1, \ldots, I$, where T denotes vector transposition. The energy $E[\mathbf{x}^{(i)}]$ of vector $\mathbf{x}^{(i)}$ is

$$E[\mathbf{x}^{(i)}]=\|\mathbf{x}^{(i)}\|_2^2=\sum_{n=1}^{N}\sum_{m=1}^{M}|X_n^{(i)}(m)|^2 = \sum_{n=1}^{N}\sum_{m=1}^{M}|S_n(m)+G_n(m)v_{s,g}^{(i)}(m)|^2, \quad i=1, \ldots, I, \tag{16}$$

where the energy of the signal $X_n^{(i)}(m)$ is

$$E[X_n^{(i)}(m)]=|X_n^{(i)}(m)|^2=|S_n(m)+G_n(m)v_{s,g}^{(i)}(m)|^2. \tag{17}$$

To separate the complex signal into the desired signal and noise, we define the following vectors in the similar manner

$$\mathbf{s}=(S_1(1), S_1(2), \ldots, S_1(M), S_2(1), \ldots, S_2(M), \ldots, S_N(1), \ldots, S_N(M))^T,$$

and

$$\mathbf{g}^{(i)}=(G_1(1)v_{s,g}^{(i)}(1), G_1(2)v_{s,g}^{(i)}(2), \ldots, G_1(M)v_{s,g}^{(i)}(M), G_2(1)v_{s,g}^{(i)}(1), \ldots, G_2(M)v_{s,g}^{(i)}(M), \ldots, G_N(1)v_{s,g}^{(i)}(1), \ldots, G_N(M)v_{s,g}^{(i)}(M))^T,$$

where $i=1, \ldots, I$. The energy of $\mathbf{s}$ and $\mathbf{g}^{(i)}$ are, respectively,

$$E[\mathbf{s}]=\|\mathbf{s}\|_2^2=\sum_{n=1}^{N}\sum_{m=1}^{M}|S_n(m)|^2 \tag{18}$$

and

$$E[\mathbf{g}^{(i)}]=\|\mathbf{g}^{(i)}\|_2^2=\sum_{n=1}^{N}\sum_{m=1}^{M}|G_n(m)v_{s,g}^{(i)}(m)|^2, \quad i=1, \ldots, I. \tag{19}$$

In general, the desired signal and the noise signal are independent. Thus, vectors $\mathbf{s}$ and $\mathbf{g}^{(i)}$ are orthogonal. According to the Pythogoras Theorem, we would have the following relationship:

$$E[\mathbf{x}^{(i)}]=\|\mathbf{x}^{(i)}\|_2^2 = \|\mathbf{s}+\mathbf{g}^{(i)}\|_2^2 = \|\mathbf{s}\|_2^2+\|\mathbf{g}^{(i)}\|_2^2=E[\mathbf{s}]+E[\mathbf{g}^{(i)}], \quad i=1, \ldots, I. \tag{20}$$

Because $\|\mathbf{g}^{(i)}\|_2^2 \geqslant 0$,

$$E[\mathbf{x}^{(i)}]=\|\mathbf{x}^{(i)}\|_2^2 \geqslant \|\mathbf{s}\|_2^2=E[\mathbf{s}], \quad i=1, \ldots, I. \tag{21}$$

The equality in Eq. (21) is satisfied, or equivalently $\min E[\mathbf{x}^{(i)}]$ occurs, only when $E[\mathbf{g}^{(i)}]=\|\mathbf{g}^{(i)}\|_2^2=0$, which happens in either of the following two conditions:

(a) When $G_n(m)=0$, i.e., the noise source is silent. In this case, there is no need for doing localization of the noise source and noise cancellation.

(b) When $v_{s,g}^{(i)}(m)=0$, Eq. (15) indicates that this case corresponds to $i=g=i_{\text{noise}}$. Therefore, $E[\mathbf{x}^{(i)}]$ has its minimum at $i=g=i_{\text{noise}}$ and the minimum value, according to Eq. (21), is $E[\mathbf{s}]$. Thus,

$$E[\mathbf{s}]=E[\mathbf{x}^{(i_{\text{noise}})}]=\min_i E[\mathbf{x}^{(i)}]. \tag{22}$$

When $i=i_{\text{noise}}$, Eq. (12) provides

$$\tilde{S}_n(m)=X_n^{(i_{\text{noise}})}(m) = S_n(m)+G_n(m)v_{s,g}^{(i_{\text{noise}})}(m)=S_n(m). \tag{23}$$

In other words, in the presence of one desired source and one noise source, the subtraction operation [Eq. (11)] applied at the location $i=g(=i_{\text{noise}})$ in the dual delay-line structure can produce an accurate estimate of the desired signal. Namely,

$$X_n^{(g)}(m)=\frac{\alpha_g(m)X_{Ln}^{(g)}(m)-\alpha_{I-g+1}(m)X_{Rn}^{(g)}(m)}{[\alpha_g(m)/\alpha_s(m)]\exp[j\omega_m(\tau_s-\tau_g)]-[\alpha_{I-g+1}(m)/\alpha_{I-s+1}(m)]\exp[j\omega_m(\tau_{I-s+1}-\tau_{I-g+1})]}. \tag{24}$$

The above analysis with energy also suggests a simple method to estimate the location $g=i_{\text{noise}}$ of the noise source in the two-source situation where the direction of the desired source is known *a priori*. Specifically, localization of the noise source can be conducted by finding the location i_{noise} along the dual delay-line that produces the minimum value of $E[\mathbf{x}^{(i)}]$ [Eqs. (11), (16), and (22)]. Once the location i_{noise} is determined, the azimuth of the noise source is easily determined by using Eq. (3). The estimated noise location i_{noise} can be fed back to the dual delay-line for noise cancellation

and extraction of the desired signal using Eq. (24).

In Fig. 1, the blocks labeled ''Integration over Time'' and ''Integration over Frequency'' together calculate the energy $E[\mathbf{x}^{(i)}]$ defined in Eq. (16). The block labeled ''Noise Source Localization'' locates the minimum point of $E[\mathbf{x}^{(i)}]$, and then supplies this as the estimate of i_{noise} to the dual delay-line. Since all the components $X_n^{(i)}(m)$, $i=1,\ldots,I$, have been computed at the localization step, now we only need to pick up the appropriate component $X_n^{(i_{\text{noise}})}(m)$, i.e., $\tilde{S}_n(m)$; Eq. (24) does not need to be actually executed in this case. Note that all the frequency computations so far are conducted on the first half ($m=1,\ldots,M_{1/2}$) of the whole bandwidth. The block labeled ''Frequency Synthesis'' derives the second half ($m=M_{1/2}+1,\ldots,M$) by means of the symmetry property of the inverse discrete Fourier transform (IDFT) and then conducts the IDFT to generate the time-domain signal $\tilde{s}_n(k)$.

C. Beamforming interpretation of the delay-line subtraction operation

This system can be understood conceptually by an equivalent beamforming procedure. Equation (11) can be expressed in the following form:

$$X_n^{(i)}(m)=w_{Ln}^{(i)}(m)X_{Ln}^{(i)}(m)+w_{Rn}^{(i)}(m)X_{Rn}^{(i)}(m), \tag{25}$$

where $w_{Ln}^{(i)}(m)$ and $w_{Rn}^{(i)}(m)$ are beamforming weights. That is, for each location along the dual delay-line at each frequency, a specific nulling pattern is generated with the null pointed toward the direction corresponding to the delay-line location while the gain in the presumed target direction is kept unity. Figure 3(a) shows a broadband intelligibility-weighted beampattern (for definition, see Appendix B) for selected nulling directions at −80°, −60°, −40°, −20°, 20°, 40°, 60°, and 80° azimuth (labeled A through H, respectively) with the desired source at 0° azimuth. It can be seen that Eq. (11) actually positions a null in the direction of the noise source while keeping the broadband gain always unity in the direction of the desired source. Since each nulling pattern uses only 2 degrees of freedom, i.e., $w_{Ln}^{(i)}(m)$ and $w_{Rn}^{(i)}(m)$, to satisfy the two constraints (directions of null and unity-gain), the null patterns are fixed and there is no room to play optimization on the pattern shape. As will be presented in Sec. III, this study, by taking advantages of the dual delay-line network, the estimated source locations, as well as the broadband characteristics of dialog speech, sought to find an appropriate strategy [which is a nonlinear one as shown in Eq. (27)] to utilize the simple null patterns for target extraction among multiple interferers.

To extend the discussion on the azimuthal resolution of the dual delay-lines in Sec. II A, let us look at a distinguished feature of Eq. (11). In the numerator of Eq. (11), the signals in the two channels can be phase-shifted by any arbitrary (small) values in the frequency domain. However, the denominator eliminates the effect and thus $X_n^{(i)}(m)$ contains an intact component of the desired signal $S_n(m)$. Moreover, at the location $i=g=i_{\text{noise}}$ where the noise component is completely cancelled, only the desired signal is left in the result. If interpreted as a beamformer, Eq. (11) operated on the dual delay-line in the frequency domain enables a null steering precisely in any arbitrary direction regardless of the sampling rate.

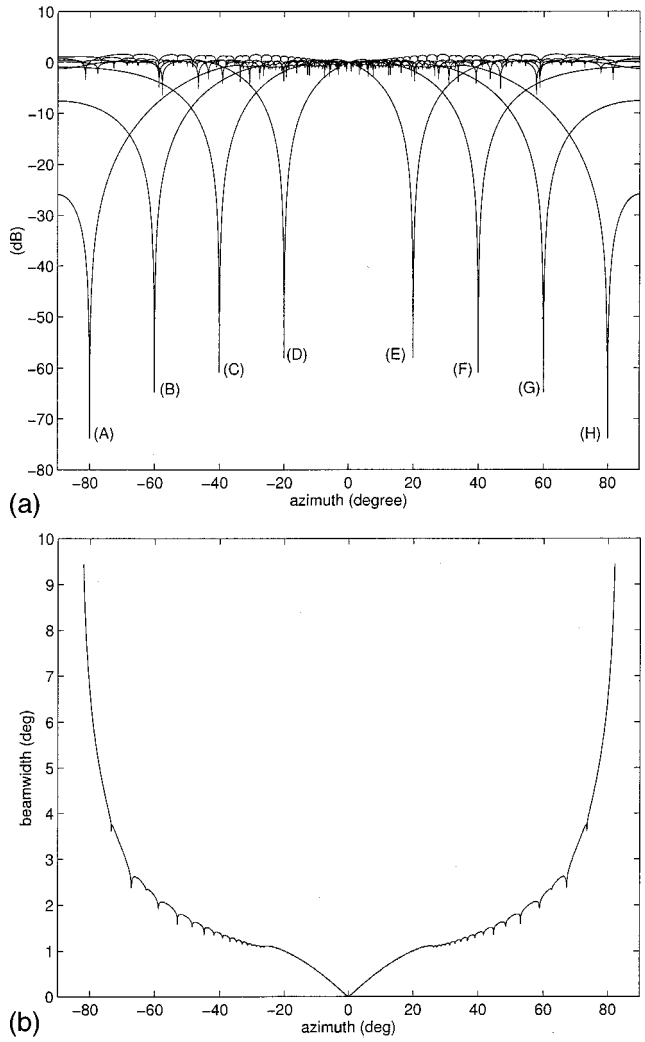

FIG. 3. (a) The intelligibility-weighted beampattern created by Eq. (11) for the cases where the desired source was always at 0° azimuth while the noise source was at −80° (A), −60° (B), −40° (C), −20° (D), 20° (E), 40° (F), 60° (G), and 80° (H) azimuth, respectively. The inter-microphone distance in this example was 144 mm. (b) The null-width of the intelligibility-weighted beampattern at −30 dB as a function of azimuth.

D. Extended application

The method suggested in the preceding subsection for localization and cancellation of the noise source is valid only when the direction of the desired source is known *a priori*. It cannot be directly applied in the situations where the direction of the desired source is also unknown. Therefore, we designed another system (System II in Fig. 4). The operation of this system is divided into two steps: it localizes both the desired source and noise source, and then selectively extracts the signal from the desired direction. The localization step employs an efficient localization method comprising dual delay-line coincidence detection followed by a nonlinear operation and then temporal and spectral integrations. The method was described in detail in a previous paper (Liu *et al.*, 2000) in which it was shown to accurately localize

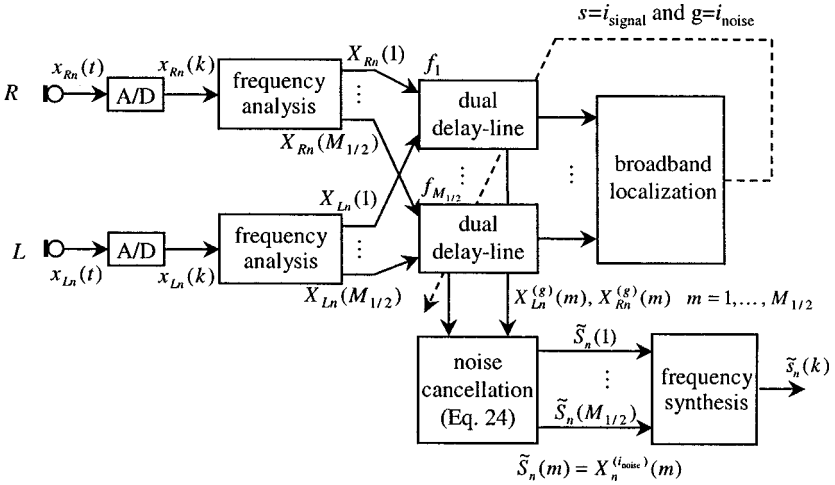

FIG. 4. The block diagram of System II for extraction of one desired source in the presence of a noise source when both source locations have to be estimated by the system. See Liu *et al.* (2000) for details about the block "Broadband Localization."

four talkers in an anechoic room and six talkers in computer simulation. Thus the localization block in Fig. 4 determines the in-phase positions, $i_{\text{signal}}=s$ and $i_{\text{noise}}=g$, of both the desired and noise sources along the dual delay-line, which were then used by the subtraction in Eq. (24) for extracting the desired signal $\tilde{S}_n(m)$. That is, except for the separate source localization step, System II employs the same noise cancellation method as described in the preceding subsection [Eq. (24)].

In comparison with System I, System II (without the assumption of direction of the desired source) is functionally more flexible. For example, in a situation with two talkers, there is no need to align the dual microphones physically toward one talker, and either talker can be taken as the desired one. The user can choose between the two sources at any time by using an electronic switch instead of changing the pointing direction of the microphones. Actually the microphones do not necessarily point to either of the sources.

We presented System I in the preceding subsection mainly for illustrating the mechanism of the dual delay-line subtraction [Eq. (11)] and shows its capacity for both noise-localization and desired-extraction. However, the operation in System I is computationally expensive because Eq. (11) must be applied to each tap in the dual delay-line for localization. Moreover, its use is limited to a two-talker (with the direction of the desired talker known *a priori*) situation. In comparison, the coincidence detection scheme for localization employed by System II is simpler in computation. What is more important is that, as we will show in the next section, System II can be further extended to situations with multiple interfering talkers.

Although our localization method worked quite well in a multiple-source environment, we normally observed relatively larger and more frequent localization errors for the lateral sources (Liu *et al.*, 2000). The robustness of the noise cancellation to localization errors can be roughly estimated by looking at the null-width of the nulls in Fig. 3(a). For example, the null-width evaluated at -30 dB is shown in Fig. 3(b). It shows that the width is wider when the direction of the null is farther away from the midline; that is, the noise cancellation method can tolerate bigger localization errors for lateral sources. Therefore, the greater localization errors for lateral sources do not degrade the system performance in terms of noise cancellation.

III. STRATEGY FOR BROADBAND MULTIPLE-SOURCE CANCELLATION

The greatest challenge associated with extension of the noise cancellation method from two-source situations to multiple-source (>2) situations is that a two-input system in theory can only effectively cancel the sound from *one* interfering source. This is due to the fact that only one null can be generated in the beampattern when using a two-microphone array. In the narrow-band situation, an apparent solution is to adaptively steer the null toward the most intense noise source at each moment. In the broadband situation, since the input signal is decomposed into its frequency components, one can formulate a separate one-null beampattern for each frequency. When there is one noise source as described in the preceding section, the nulls at all frequencies are steered in the same direction of the single noise source. However, when there are more than two sources, each frequency bin can be treated separately so that its beampattern null is adaptively steered at each moment toward the noise source that is emitting the most intense energy at that frequency, while maintaining unity gain toward the desired source. It is actually a dynamic application of the subtraction operation in Eq. (24). This noise cancellation strategy is based on the following rationale:

(a) Natural speech has many pauses and silent intervals, both of which usually occupy 60%–65% of the total time (Flanagan, 1972, p. 386). Therefore, when multiple talkers speak simultaneously, there are always a number of short temporal gaps present. The number of overlapping talkers at each moment is usually smaller than the total number of talkers.

(b) Even when multiple talkers speak at the same moment, different talkers likely dominate at different frequency bins at each moment due to the differences in articulation such as voicing and pitch. There are about ten phonemes per second in conversational speech, more than 60% of which are low-energy, high-frequency consonants, and less than 40% of which are high-

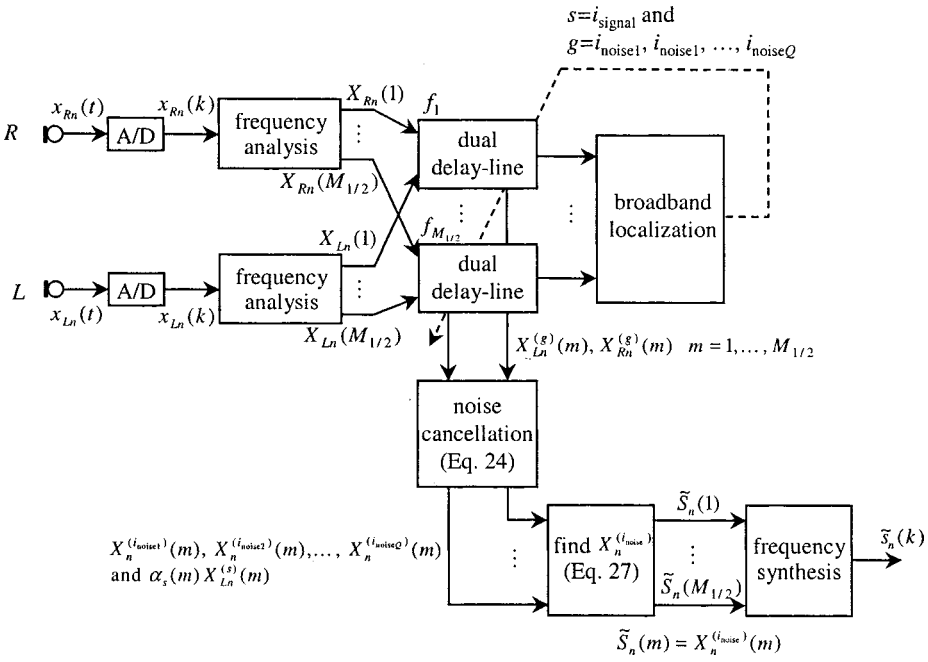

FIG. 5. The block diagram of System III for extraction of one desired source in the presence of more than one noise source when all the source locations have to be estimated by the system. See Liu *et al.* (2000) for details about the block "Broadband Localization."

energy, low-frequency vowels (Flanagan, 1972, p. 4). In the presence of multiple talkers, the talkers who are articulating the high-energy vowels are dominant in both the localization (Liu *et al.*, 2000) and cancellation [Eq. (27)] and hence more easily removed. On the other hand, due to the asymmetry of the filtering response of the human ear, the masking effect of low frequencies on high frequencies is much stronger than the reverse (Jeffress, 1970, p. 95). In other words, cancellation of a talker at his/her strongest frequency components, which are likely the major components of a vowel, may effectively cancel the masking effect of the talker.

To obtain the information about location of each source for the noise cancellation algorithm, the localization algorithm in Liu *et al.* (2000) is employed. Suppose there are Q noise sources with corresponding locations in the dual delay-line being $i_{\text{noise1}}, i_{\text{noise2}}, \ldots, i_{\text{noiseQ}}$. By applying Eq. (24), we obtain $X_n^{(i_{\text{noise1}})}(m), X_n^{(i_{\text{noise2}})}(m), \ldots, X_n^{(i_{\text{noiseQ}})}(m)$ for each frequency ω_m. If the localization is accurate, they all should include the component of the desired signal at frequency ω_m as well as components from interfering sources other than the one to be canceled. In order to determine the particular noise source to be canceled, the energies of $X_n^{(i_{\text{noise1}})}(m), X_n^{(i_{\text{noise2}})}(m), \ldots, X_n^{(i_{\text{noiseQ}})}(m)$ are calculated and compared. The minimum $X_n^{(i_{\text{noise}})}(m)$ is taken as output $\tilde{S}_n(m)$:

$$\tilde{S}_n(m)=X_n^{(i_{\text{noise}})}(m), \tag{26}$$

where $X_n^{(i_{\text{noise}})}(m)$ satisfies the following condition:

$$|X_n^{(i_{\text{noise}})}(m)|^2=\min\{|X_n^{(i_{\text{noise1}})}(m)|^2, |X_n^{(i_{\text{noise2}})}(m)|^2, \ldots, |X_n^{(i_{\text{noiseQ}})}(m)|^2, |\alpha_s(m)X_{Ln}^{(s)}(m)|^2\}. \tag{27}$$

By referring to the energy analysis in Sec. II B, it is easy to see that this strategy is logically consistent with Eq. (22). It is noted that, in Eq. (27), we also include the original signal $\alpha_s(m)X_{Ln}^{(s)}(m)$ for the following reason. The beampattern designed above sometimes may amplify other less intense noise sources. When the amount of noise amplification is larger than the amount of cancellation of the most intense noise source, it may be better to keep the input signal at that frequency at that moment unchanged. An extended system (System III in Fig. 5) was developed using System II (Fig. 4) as the foundation. In comparison with System II, it identifies multiple (>2) source directions and tentatively cancels each noise source; specifically it cancels the instantaneously most intense source on a frequency-by-frequency basis [Eq. (27)].

The cancellation step relies on the localization step to provide azimuth information for each source, which is usually a difficult task especially in the presence of multiple sources. However, as shown in our previous paper (Liu *et al.*, 2000), our localization system can satisfactorily localize four sources in an anechoic room and six sources in simulation, if not more. In addition, the cancellation step does not have rigid requirement that all the sources must be localized accurately. As a matter of fact, our strategy is to cancel the strongest noise component at each frequency bin—this is usually emitted from one of those momentarily relatively intense noise sources, which are easy to localize compared with other relatively less intense sources.

IV. EXPERIMENT

For the case of two talkers, once the locations of the talkers are determined, the sound from one talker can be removed by using System I or System II with essentially no residual noise while the estimated desired signal is distortionless. This was clearly supported in theory and also pre-

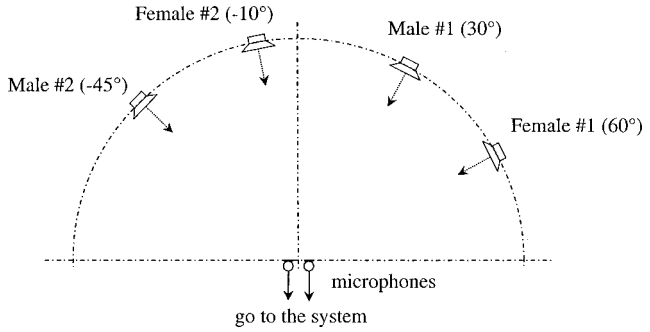

FIG. 6. Top view of the spatial configuration of one of our experimental setups. This experimental setup corresponds to test configuration #2 in Tables I and II.

viously demonstrated by Banks (1993). In this paper we present the results of four-talker experiments using the noise cancellation of System III.

The experiments employed a record-and-play procedure with four high-fidelity loudspeakers (ADS 200LC) and were conducted in an anechoic room and in a moderately quiet conference room with a reverberation time constant of approximately 400 ms. The speech materials consisted of spondaic words spoken by native speakers of American English; these were recorded in a sound studio at the Beckman Institute. All the speech recordings were equalized in average intensity and played through the loudspeakers. The words in each experimental condition were temporarily aligned, i.e., it was equivalent to all the talkers starting at the same time. The inter-microphone distance was 144 mm. All the loudspeakers were at a fixed equal distance of 1.0 m (unless otherwise stated) from the midpoint between the two microphones, and all the loudspeakers and microphones were at the same elevation ($\sim$1 m from the floor). Correspondingly, the compensation factors in Eq. (11) were determined for that distance.

The signals were low-pass filtered at 6 kHz and sampled at a 12.8-kHz rate with 16-bit quantization. In the short-term spectral analysis, a 20-ms segment of signal was weighted by a Hamming window, padded with zeros to 2048 points, and Fourier transformed with frequency resolution of about 6 Hz. Consecutive frames overlapped by 15 ms. The values of the time delay units τ_i ($i=1,\ldots,I$) were determined such that the dual delay-line has a uniform azimuthal resolution of 0.5° (i.e., $I=361$).

Two groups of talkers were used in our tests. Each group consisted of four different talkers speaking different spondaic words. Five tests were conducted for each group; each test adopted a different azimuthal arrangement of the sources, with the separation between adjacent sources ranging 10°–75°. Figure 6 illustrates one of the configurations. Each test consisted of four subtests in which each talker was taken in turn as the desired source with all the other talkers as the noise sources. The localization of the talkers was conducted using both the ''direct'' and ''stencil'' methods in Liu *et al.* (2000).

The system performance was evaluated using an objective intelligibility-weighted measure, whose concept was first proposed by Peterson (1989) and described in detail in Liu and Sideman (1996). Specifically, we used intelligibility-weighted signal cancellation, intelligibility-weighted noise cancellation, and net intelligibility-weighted gain (see Appendix B for definition).

As mentioned above, an array of tests was conducted with a number of variables such as different talkers, different spondaic words, different azimuthal arrangements, different localization methods, and different combinations of the variables. However, it is not necessary to present all our results since most of the variables, as they turned out to be, have no statistically significant effect on the final noise cancellation performance. Specifically, the experimental results showed no statistical difference due to talkers and words spoken. It also showed no significant effect from using the ''direct'' method versus the ''stencil'' method for source localization (Liu *et al.*, 2000). Therefore, we only present the results from Group #1 with the location information derived using the ''stencil'' method. As mentioned above, it contained five tests corresponding to five different spatial configurations. For each test, we present result from only one (arbitrarily chosen) of the four subtests since the location of the desired source has no obvious effect on noise cancellation. Table I shows typical results chosen from the anechoic chamber test

TABLE I. Experiment results attained from the anechoic room using System III. The results shown were derived from five tests (configurations) from Group #1 including two male speakers (M1 and M2) and two female speakers (F1 and F2). The spondaic word spoken by each talker is given in italic. The values in parentheses are cancellation of the desired sources in dB. Configuration test #2 is shown in Fig. 6.

	Intelligibility-weighted signal cancellation (dB)				Intelligibility-weighted noise cancellation (dB)	Net intelligibility-weighted gain (dB)
Test	M1 *"armchair"*	M2 *"playground"*	F1 *"pancake"*	F2 *"woodwork"*		
#1	−75°	0°	20°	75°		
	8.04	(0.15)	4.98	3.07	9.25	9.09
#2	30°	−45°	60°	−10°		
	8.34	4.71	4.12	(0.67)	8.38	7.71
#3	10°	−80°	−50°	45°		
	(0.55)	6.90	5.57	3.83	8.56	8.00
#4	−30°	15°	5°	−60°		
	10.53	2.07	(1.14)	6.35	8.27	7.13
#5	−25°	25°	−70°	80°		
	8.09	(0.34)	5.82	4.46	8.78	8.44

TABLE II. Same as Table I except that the recordings were made in a moderately quiet conference room with a 400 ms reverberation time [RT was derived using Schroeder's method; see J. Acoust. Soc. Am. **37**, 409–412 (1965)].

Test	Intelligibility-weighted signal cancellation (dB)				Intelligibility-weighted noise cancellation (dB)	Net intelligibility-weighted gain (dB)
	M1 *"armchair"*	M2 *"playground"*	F1 *"pancake"*	F2 *"woodwork"*		
#1	−75°	0°	20°	75°		
	4.82	(0.55)	4.07	2.06	6.73	6.18
#2	30°	−45°	60°	−10°		
	6.27	4.18	3.09	(0.58)	7.26	6.69
#3	10°	−80°	−50°	45°		
	(1.12)	3.85	2.91	2.71	5.75	4.63
#4	−30°	15°	5°	−60°		
	6.29	(0.85)	0.91	3.61	6.16	5.25
#5	−25°	25°	−70°	80°		
	5.70	(0.69)	4.28	2.92	6.97	6.29

while Table II the results from the conference room test. In the tables, the numbers in parentheses represent the degree of cancellation in dB of the desired source (which should ideally be 0 dB) and the other numbers represent the degree of noise cancellation for each noise source. Because we had separate recordings of speech signals from each talker, we applied the same processing both on the complex signal and synchronously on each signal corresponding to each talker as well. As such, we were able to tell the effect of processing on each signal involved. The next to the last column in the tables show the degree of cancellation for all the noise sources lumped together, while the last column gives the net intelligibility-weighted improvement (which considers both noise cancellation and loss in the desired signal). Our results from the anechoic room show that, in the intelligibility-weighted measure, the cancellation strategy was able to cancel each noise source by 3–11 dB, while the degradation in the desired source was very small (mostly smaller than 0.5 dB). The total noise cancellation was between 8 and 10 dB. For the conference room, the cancellation was roughly 2 dB less, indicating that the room reverberation degraded the system performance somewhat. In spite of the drop in system performance the system still produced a sizable gain in speech intelligibility.

In order to get an insight into the effect of the signal processing on each talker, we choose one subtest example (anechoic room; desired source: F1 at 60°; noise sources: M1 at 30°, M2 at −45°, and F2 at −10°). We display the signal waveform of each talker as well as the complex signal of all the four talkers, before [Fig. 7(A)] and after [Fig. 7(B)] the signal processing. Comparison of the two panels shows a great attenuation of the interfering talkers (M1, M2, and F2) while the desired signal (F1) is essentially not attenuated and the distortion of the desired talker is unperceivable. A moment-by-moment comparison shows that the momentarily strongest noise source was always reduced, indicating that the system adapted rapidly. The last trace in Fig. 7(B) is the system output, which turned out to be cleaner and closer to the desired speech [F1 in Fig. 7(A)] than the noisy unprocessed signal [the last trace in Fig. 7(A)].

In an informal listening experiment with normal hearing listeners, we found the unprocessed signal to be impossible to understand, even when the spatial cues were retained. After the processing, however, the extracted speech from a desired source was easily understandable.

Limited by our experimental facility, we only conducted on-site acoustic tests for four-talker situations. However, our computer simulation results for six-talker situations were quite similar. To avoid redundancy, we omit presentation of the details. Basically, we obtained a 7–10 dB enhancement in the intelligibility-weighted signal-to-noise ratio when there were six equally loud, temporally aligned speech sounds originating from six different sources.

V. DISCUSSION

There are three key differences between the algorithm proposed in this paper and conventional adaptive beamformers such as the Frost and Griffiths-Jim beamformers (Van Veen and Buckley, 1988), namely, (i) direct frequency-domain null steering, (ii) explicit source localization, and (iii) implicit utilization of dialogue characteristics. The frequency-domain null-steering algorithm described herein does rapid, independent steering of the beampattern at each frequency. Independent steering allows rapid steering of the single null at each frequency to the dominant interferer at that time and frequency. It provides a maximum potential to cancel intense components emitted from multiple interferers with only two inputs available. What distinguishes this method from other methods is that this independent steering can be implemented with no time delay when it is provided with instant localization information. When processing signals with strong, rapidly varying time-frequency structure such as speech, the net effect is to allow significant cancellation of several *simultaneous* interferers by exploiting differences in their instantaneous time-frequency structures. In contrast, slowly adapting time-domain algorithms such as the Frost (Frost, 1972) and Griffiths-Jim (Griffiths and Jim, 1982) beamformers are unable to track the nonstationary structure rapidly enough to achieve significant cancellation of more than a single interferer. This claim is clearly dem-

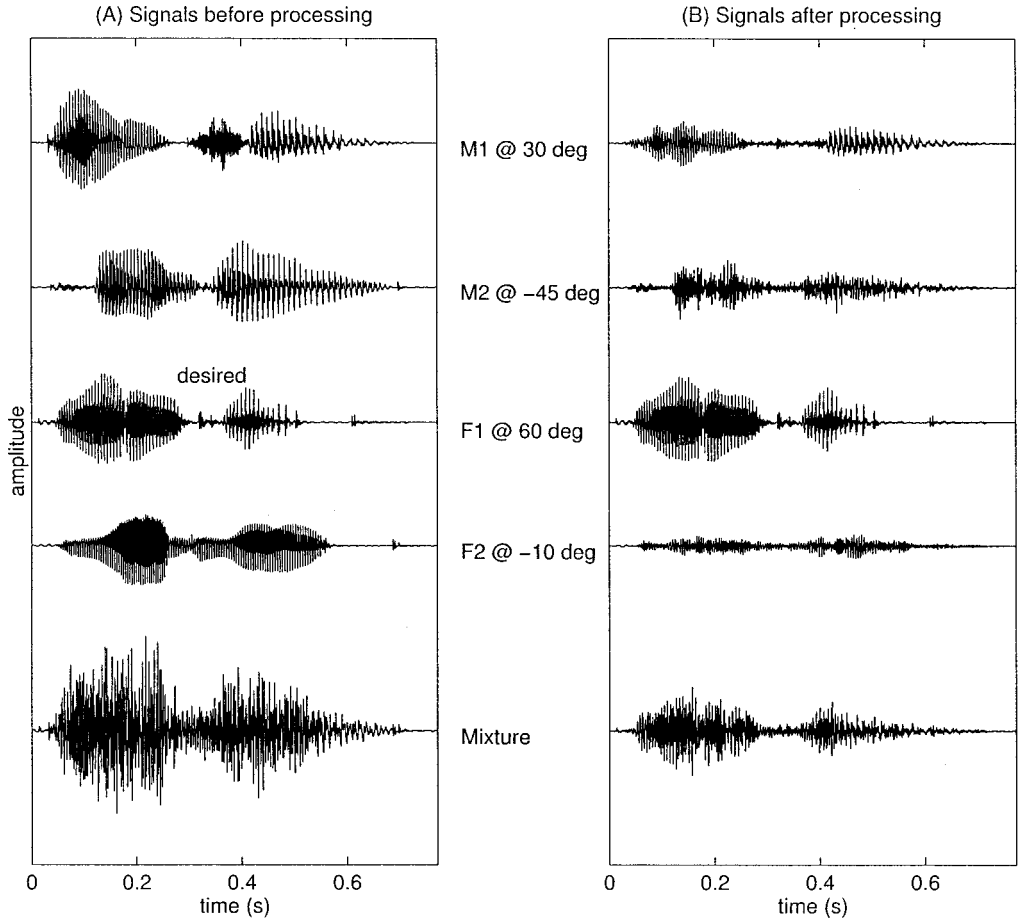

FIG. 7. The signal waveform of each talker as well as the complex signal of all the four talkers before (A) and after (B) the signal processing. See Fig. 6 for the test configuration.

onstrated in the results of comparison experiment presented in Yang *et al.* (2000) using complete sentences under a variety of signal-to-noise conditions.

The performance of this algorithm is comparable to the conventional beamformers for the case of a single interferer, but markedly better for cases involving more than one interferer. The comparisons conducted in Zheng *et al.* (2001) were made in computer simulation where up to four interferers were used at four different SNR settings (-6, -3, 0, $+3$ dB). In the presence of two or more interferers, the present method provided 6–7 dB of SNR gains, while the Frost beamformer and the Griffiths-Jim beamformer had SNR gains in the 2–5 dB range.

The second difference between the conventional beamformers and the proposed method is that the latter explicitly identifies the spatial directions of the target and interferers via a nonlinear, cross-frequency localization procedure (Liu *et al.*, 2000) and exploits this information to optimally steer the null pattern in each frequency bin. The localization is conducted on a frame-by-frame basis and the results are used immediately by the cancellation on the same frame. Therefore, as mentioned above, the adaptation time is virtually zero. This feature is especially important when processing signals with rapidly varying time-frequency structure such as speech. Explicit source localization also offers several other potential advantages, including the ability to steer toward a spatially moving target, better and more robust estimation of signal and interference locations from which to optimize the beam patterns, and the ability (not explored here) to perform additional useful tasks such as auditory scene characterization. The results in Zheng *et al.* (2001) suggest that these characteristics may indeed be advantageous in many situations (with different number of interferers, different spatial configurations, and different SNRs), particularly when the interferers are in close azimuthal proximity to the target.

The third, and most unique, difference is that our method takes full advantage of the characteristics and masking effect of human dialogue as detailed in Sec. III. That strategy makes it possible to utilize a limited resource (two inputs only) to obtain maximum speech intelligibility enhancement benefits such as effective cancellation of multiple interfering sources.

The improvement in signal quality reported in Tables I and II is encouraging but preliminary. The algorithm's performance in anechoic conditions (8–10 dB cancellation) is sufficient to justify further research, while the performance in the conference room (2 dB less cancellation) raises the question as to whether, when used in a real-time environment, the quality of the cancellation will degrade so as to no longer be useful. Practical computational limitations restricted the work reported here, although improvements have allowed off-line analysis over a wider range of materials (Zheng *et al.*, 2001). A related frequency domain beamformer (Lockwood *et al.*, 1999) has been implemented in

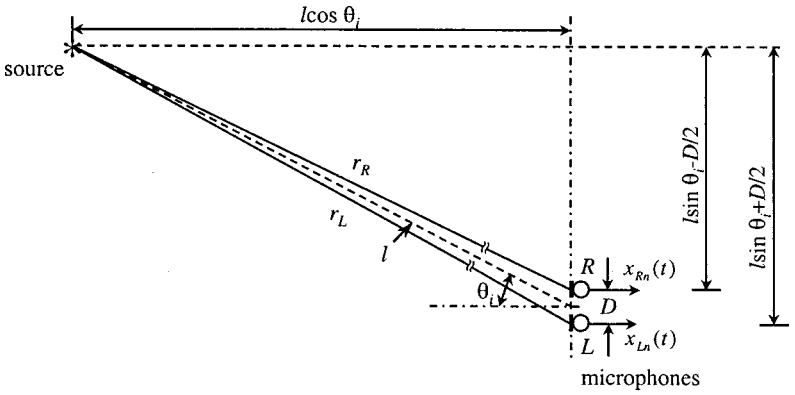

FIG. 8. Top view of the geometry of the source-microphone distance.

real-time (Elledge, 2000) with highly satisfying subjective sound improvement and quality (Larsen *et al.*, 2001). A real-time version of the present algorithm is in the process of implementation; it should permit subjective evaluations to determine whether the technique is viable for hearing aid and other applications.

One practical issue is that when the source to microphone distance is very short (e.g., 2 m or less), it is important to compensate for left–right differences in channel intensity; indeed preliminary tests indicated degradation of about 1 dB in the total net gain without compensation. However, for larger source-microphone distances (e.g., >2 m), the difference with and without compensation was insignificant.

VI. SUMMARY AND CONCLUSION

In this paper, we have presented the technique and experimental results that illustrate the performance of signal processing systems designed for effective extraction of a desired signal in the presence of multiple competing talkers. The signal processing technique is based on dual delay-line structure, a well-known biological network for binaural hearing. The entire system consists of two steps: localization of all sources and extraction of the desired source. Our anechoic chamber tests showed an 8–10 dB of speech enhancement in the presence of four equally loud, temporally aligned talkers; our computer simulation showed a 7–10 dB of speech enhancement in the presence of six equally loud, temporally aligned talkers. The system can localize all the sources present and allow the user to selectively extract any one of them, hence it is more flexible than assuming that the desired source is always straight ahead. It can be applied in many applications such as radar, sonar, communications, and robots.

It is noted that in the present study we focused on separating out a particular talker from all the other competing talkers, i.e., selective hearing. It is technically straightforward to convert the present system to a simulator that can capture the source to which the gaze of the listener is directed at any time instant. It is also possible to simply use multiple noise-cancellation components following the localization so as to extract each of the sources within the environment, i.e., to achieve separation of multiple signals.

The dual delay-line structure implies that the computation is highly parallel. That, and the repeated use of the Fourier transform, made it practical to implement the algorithm by means of VLSI for a fast, miniature device.

Our future work includes evaluation using formal tests in normal listening rooms with human subjects with real-time versions of the algorithm. We will also extend our algorithms to compensate for reverberant environments.

ACKNOWLEDGMENTS

This research was supported by grants from the Beckman Institute, UIUC and from the National Institute for Deafness and other Communication Disorders of the NIH (R21 DC 04870). The work was conducted when the first author (CL) was a Beckman Fellow. A number of people from the Beckman Institute generously donated their time to participate in the recording of speech materials used for our tests. Their generosity is acknowledged. We thank Dean Garstecki for permission to use the anechoic room at the Northwestern University. We also wish to thank the two anonymous reviewers for their constructive comments to an earlier version of the paper.

APPENDIX A: CALCULATION OF THE AMPLITUDE FACTORS

In this appendix we illustrate the calculation of the amplification factors $\alpha_i(m)$, which are used to compensate for differences in the amplitudes of signals arriving at the two microphones. In this example we model the sound source as a simple point source, ignore the absorption of energy by the media, and assume the amplitude variation is solely dependent on the differences in the distance from source to the microphones. In this case, the amplitude compensation is independent of frequency.

The amplitude of the received sound pressure $|\mathbf{p}|$ varies with the source–receiver distance r:

$$|\mathbf{p}| \propto \frac{1}{r} \tag{A1}$$

or

$$\frac{|\mathbf{p}_L|}{|\mathbf{p}_R|} = \frac{r_R}{r_L}, \tag{A2}$$

where $|\mathbf{p}_L|$ and $|\mathbf{p}_R|$ are the amplitude of sound pressures at the two microphones (Kinsler *et al.*, 1982, p. 168). According to the geometry in Fig. 8, the distances from the source

to the left and right microphones r_L and r_R are, respectively,

$$r_L = \sqrt{(l \sin \theta_i + D/2)^2 + (l \cos \theta_i)^2} = \sqrt{l^2 + lD \sin \theta_i + D^2/4} \quad \text{(A3)}$$

and

$$r_R = \sqrt{(l \sin \theta_i - D/2)^2 + (l \cos \theta_i)^2} = \sqrt{l^2 - lD \sin \theta_i + D^2/4}. \quad \text{(A4)}$$

For a pair of taps in the dual delay-line in Fig. 2, in order to equalize the signals at the tap outputs, the compensation factors $\alpha_i(m)$ and $\alpha_{I-i+1}(m)$ must satisfy the following condition:

$$|\mathbf{p}_L| \alpha_i(m) = |\mathbf{p}_R| \alpha_{I-i+1}(m). \quad \text{(A5)}$$

Substituting Eq. (A2) into Eq. (A5), the above condition becomes

$$\frac{r_L}{r_R} = \frac{\alpha_i(m)}{\alpha_{I-i+1}(m)}. \quad \text{(A6)}$$

We define the value of $\alpha_i(m)$ to be equal to

$$\alpha_i(m) = K\sqrt{l^2 + lD \sin \theta_i + D^2/4}, \quad \text{(A7)}$$

where K has unit of inverse length and is chosen for a convenient amplitude level. Applying the definition in Eq. (A7), the value of $\alpha_{I-i+1}(m)$ will be

$$\alpha_{I-i+1}(m) = K\sqrt{l^2 + lD \sin \theta_{I-i+1} + D^2/4} = K\sqrt{l^2 - lD \sin \theta_i + D^2/4}, \quad \text{(A8)}$$

where the relationship $\sin \theta_{I-i+1} = -\sin \theta_i$ can be obtained by substituting $I-i+1$ into i in Eq. (3). By substituting Eqs. (A7) and (A8) into Eq. (A6), one can verify that the values assigned to $\alpha_i(m)$ in Eq. (A7) satisfy the condition in Eq. (A6).

APPENDIX B: DEFINITION OF THE INTELLIGIBILITY-WEIGHTED MEASURE

For any signal s, the intelligibility-weighted measure $\Gamma(s)$ is calculated by (Link and Buckley, 1993)

$$\Gamma(s) = \int_{BW} W_{\mathrm{AI}}(f) 20 \log_{10} \mathrm{rms}_{1/3}(|S(f)|) df, \quad \text{(B1)}$$

where

$$W_{\mathrm{AI}}(f) = \frac{1/[1 + (f/1925)^2]}{\int_{BW} 1/[1 + (f/1925)^2] df}, \quad \text{(B2)}$$

$$\mathrm{rms}_{1/3}(|S(f)|) = \left[\frac{\int_{2^{-1/6}f}^{2^{1/6}f} |S(f')|^2 df'}{(2^{1/6} - 2^{-1/6}) f} \right]^{1/2} \quad \text{(B3)}$$

and BW denotes the frequency range. The system improvement in the intelligibility-weighted measure for the target signal T and interference I are, respectively,

$$\Delta\Gamma(T) = \Gamma(T_o) - \Gamma(T_i) \quad \text{(B4)}$$

and

$$\Delta\Gamma(I) = \Gamma(I_i) - \Gamma(I_o), \quad \text{(B5)}$$

where the subscripts i and o denote the input and output, respectively. The overall (or net) intelligibility-weighted gain, G_I, is the sum of the two measures, thus

$$G_I = \Delta\Gamma(T) + \Delta\Gamma(I). \quad \text{(B6)}$$

In our experiment, since we had separate recordings of the target and noise signals, i.e., T_i and I_i (the latter might include more than one interfering talker), we were able to apply the same processing framewise on either of them and obtain the results T_o and I_o, respectively. The framewise processing [Eq. (11)], however, was determined based on the target and noise signals mixed together as would be encountered in the real situation. It is noted that the spectrum $S(f)$ was computed based on the full-length signal, which in our case was a whole spondaic word. We used the full long-term spectrum, as opposed to a frame-by-frame spectrum, for two reasons: (1) It was consistent with the way the intelligibility-weighted measure was applied in other papers published in the area such that our results could be compared directly with earlier results; (2) Since our system has virtually no adaptation time (i.e., it almost always is successful in localizing the strongest interference within a few milliseconds), there is no advantage to computing with the short-term spectra.

Since the intelligibility-weighted measure was constructed as an estimate of the subjective improvement based on the objective calculation, it deliberately emphasized the low frequency domain according to the "critical-band" theory. However, because the low frequency domain is always the hardest to clean with the approaches using multi-microphone arrays of limited size, the intelligibility-weighted measure usually has a smaller value (~1 dB difference in our experiment) than the non-weighting counterpart, i.e., SNR. Nonetheless, this effect does not change the overall picture of the performance; especially the comparison of our system with others, as given in the paper, remains valid.

Similarly, if we denote the array beampattern as $E(f, \theta)$, where f is frequency and θ is the incident direction, the intelligibility-weighted beampattern, $\overline{E}(\theta)$, is defined by (Liu and Sideman, 1996)

$$\overline{E}(\theta) = \int_{BW} W_{\mathrm{AI}}(f) E(f, \theta) df. \quad \text{(B7)}$$

Banks, D. (**1993**). "Localization and separation of simultaneous voices with two microphones," IEE Proc. I **140**, 229–234.

Blauert, J. (**1983**). *Spatial Hearing: The Psychophysics of Human Sound Localization*, John S. Allen, translator (The MIT Press, Cambridge, MA).

Bodden, M. (**1993**). "Modeling human sound source localization and the cocktail-party-effect," Acta Acust. **1**, 43–55.

Bodden, M. (**1996**). "Auditory demonstration of a cocktail-party-processor," Acust. Acta Acust. **82**, 356–357.

Bregman, A. S. (**1990**). *Auditory Scene Analysis: The Perceptual Organization of Sound* (The MIT Press, Cambridge, MA).

Bronkhorst, A. W., and Plomp, R. (**1992**). "Effect of multiple speechlike maskers on binaural speech recognition in normal and impaired hearing," J. Acoust. Soc. Am. **92**, 3132–3139.

Chabries, D. M., Christiansen, R. W., Brey, R., and Robinette, M. (**1982**). "Application of the LMS adaptive filter to improve speech communication in the presence of noise," Proc. IEEE ICASSP, 148–151.

Chazan, D., Medan, Y., and Shvadron, U. (**1988**). ''Noise cancellation for hearing aids,'' IEEE Trans. Acoust., Speech, Signal Process. **36**, 1697–1705.
Cherry, E. C. (**1953**). ''Some experiments on the recognition of speech, with one and with two ears,'' J. Acoust. Soc. Am. **25**, 975–979.
Colburn, H. S., and Durlach, N. I. (**1978**). ''Models of binaural interaction,'' in *Handbook of Perception, IV: Hearing*, edited by E. C. Carterette and P. F. Morton (Academic, New York).
Colburn, H. S. (**1996**). ''Computational models of binaural processing,'' in *Auditory Computation*, edited by H. L. Hawkins, T. A. McMullen, A. N. Popper, and R. R. Fay (Springer, New York), pp. 332–400.
Durlach, N. I. (**1960**). ''Note on the equalization and cancellation theory of binaural masking level differences,'' J. Acoust. Soc. Am. **32**, 1075–1076.
Durlach, N. I. (**1972**). ''Binaural signal detection: Equalization and cancellation theory,'' in *Foundations of Modern Auditory Theory*, edited by V. T. Jerry (Academic, New York), pp. 369–462.
Elledge, M. E., Lockwood, M. E., Bilger, R. C., Feng, A. S., Jones, D. L., Lansing, C. R., O'Brien, W. D., and Wheeler, B. C. (**2000**). ''Real-time implementation of a frequency-domain beamformer on the TI C62X EVM,'' the 10th Ann. DSP Technol. Educ. Res. Conf., Houston, TX, August 2–4, 2000.
Feng, A. S., and Shofner, W. P. (**1981**). ''Peripheral basis of sound localization in anurans: Acoustic properties of the frog's ear,'' Hear. Res. **5**, 201–216.
Flanagan, J. L. (**1972**). *Speech Analysis, Synthesis and Perception* (Springer-Verlag, Berlin).
Frost, O. L. (**1972**). ''An algorithm for linearly constrained adaptive array processing,'' Proc. IEEE **60**, 926–935.
Gaik, W. (**1993**). ''Combined evaluation of interaural time and intensity differences: Psychoacoustic results and computer modeling,'' J. Acoust. Soc. Am. **94**, 98–110.
Griffiths, L. J., and Jim, C. W. (**1982**). ''An alternative approach to linearly constrained adaptive beamforming,'' IEEE Trans. Antennas Propag. **AP-30**, 27–34.
Jeffress, L. A. (**1948**). ''A place theory of sound localization,'' J. Comp. Physiol. Psychol. **41**, 35–39.
Jeffress, L. A. (**1970**). ''Masking,'' in *Foundations of Modern Auditory Theory*, edited by J. V. Tobias (Academic, New York), pp. 85–114.
Kinsler, L. E., Frey, A. R., Coppens, A. B., and Sanders, J. V. (**1982**). *Fundamentals of Acoustics* (Wiley, New York).
Konishi, M., Takahashi, T., Wagner, H., Sullivan, W. E., and Carr, C. E. (**1988**). ''Neurophysiological and anatomical substrates of sound localization in the owl,'' in *Auditory Function: Neurobiological Bases of Hearing*, edited by M. E. Gerald, W. E. Gall, and W. M. Cowan (Wiley, New York), pp. 721–745.
Larsen, J., Lockwood, M. E., Lansing, C. R., Bilger, R. C., O'Biren, W. D., Jones, D. L., Wheeler, B. C., and Feng, A. S. (**2001**). ''Performance of a frequency-based minimum variance beamforming algorithm for normal and hearing impaired listeners,'' J. Acoust. Soc. Am. **109**, 2494.
Lindemann, W. (**1986**). ''Extension of a binaural cross-correlation model by contralateral inhibition. I. Simulation of lateralization for stationary signals,'' J. Acoust. Soc. Am. **80**, 1608–1622.
Link, M. J., and Buckley, K. M. (**1993**). ''Prewhitening for intelligibility gain in hearing aid arrays,'' J. Acoust. Soc. Am. **93**, 2139–2145.
Liu, C., and Sideman, S. (**1996**). ''Simulation of fixed microphone arrays for directional hearing aids,'' J. Acoust. Soc. Am. **100**, 848–856.
Liu, C., Wheeler, B. C., O'Brien, Jr., W. D., Bilger, R. C., Lansing, C. R., and Feng, A. S. (**2000**). ''Localization of multiple sound sources with two microphones,'' J. Acoust. Soc. Am. **108**, 1888–1905.
Lockwood, M. E., Jones, D. L., Elledge, M. E., Bilger, R. C., Feng, A. S., Goueygou, M., Lansing, C. R., Liu, C., O'Brien, Jr., W. D., an Wheeler, B. C. (**1999**). ''A minimum variance frequency-domain algorithm for binaural hearing aid processing,'' J. Acoust. Soc. Am. **106**, 2278.
Peterson, P. M. (**1989**). ''Adaptive array processing for multiple microphone hearing aids,'' Ph.D. Dissertation, Dept. Elect. Eng. and Comp. Sci., MIT; Res. Lab. Elect. Tech. Rept. 541, MIT, Cambridge, MA.
Peterson, P. M., Durlach, N. I., Rabinowitz, W. M., and Zurek, P. M. (**1987**). ''Multimicrophone adaptive beamforming for interference reduction in hearing aids,'' J. Rehabil. Res. Dev. **24**, 103–110.
Stern, R. M., and Trahiotis, C. (**1995**). ''Models of binaural interaction,'' in *Hearing*, edited by B. C. J. Moore (Academic, San Diego), pp. 347–386.
Stern, R. M., and Trahiotis, C. (**1997**). ''Models of binaural perception,'' in *Binaural and Spatial Hearing in Real and Virtual Environments*, edited by R. H. Gilkey and T. R. Anderson (Lawrence Erlbaum Associates, Mahwah, NJ), pp. 499–532.
Strube, H. W. (**1981**). ''Separation of several speakers recorded by two microphones (cocktail-party processing),'' Signal Process. **3**, 355–364.
Takahashi, T. T., and Keller, C. H. (**1994**). ''Representation of multiple sound sources in the owl's auditory space map,'' J. Neurosci. **14**, 4780–4793.
Van Veen, B. D., and Buckley, K. M. (**1988**). ''Beamforming: a versatile approach to spatial filtering,'' IEEE ASSP Mag., April 1988, 4–24.
Weiss, M. (**1987**). ''Use of an adaptive noise canceler as an input preprocessor for a hearing aid,'' J. Rehabil. Res. Dev. **24**, 93–102.
Widrow, B., Glover, J. R., McCool, J. M., Kaunitz, J., Williams, C. S., Hearn, R. H., Zeidler, J. R., Dong, E., and Goodlin, R. C. (**1975**). ''Adaptive noise cancelling: Principles and applications,'' Proc. IEEE **63**, 1692–1716.
Yang, K. L., Lockwood, K. L., Elledge, M. E., and Jones, D. L. (**2000**). ''A comparison of beamforming algorithms for binaural acoustic processing,'' Proceedings of the 9th IEEE Digital Signal Processing Workshop, Hunt, TX, October 15–18, 2000.
Yin, T. C. T., and Chan, J. C. K. (**1990**). ''Interaural time sensitivity in medial superior olive of cat,'' J. Neurophysiol. **64**, 465–488.
Zheng, Y., Lockwood, M. E., Wheeler, B. C., Jones, D. L., Feng, A. S., O'Brien, W. D., Bilger, R. C., and Lansing, C. R. (**2001**). ''Comparison of binaural beamformers for speech extraction in complex auditory scenes,'' J. Acoust. Soc. Am. **109**, 2494.

Improvements in intelligibility of noisy reverberant speech using a binaural subband adaptive noise-cancellation processing scheme

Paul W. Shields and Douglas R. Campbell[a)]
Electronic Engineering and Physics Division, School of Information and Communications Technologies, University of Paisley, High Street, Paisley, Renfrewshire PA1 2BE, Scotland, United Kingdom

(Received 22 April 1999; revised 4 December 2000; accepted 24 August 2001)

This article reports on the performance of an adaptive subband noise cancellation scheme, which performs binaural preprocessing of speech signals for a hearing-aid application. The multi-microphone subband adaptive (MMSBA) signal processing scheme uses the least mean squares (LMS) algorithm in frequency-limited subbands. The use of subbands enables a diverse processing mechanism to be employed, splitting the two-channel wide-band signal into smaller frequency-limited subbands, which can be processed according to their individual signal characteristics. The frequency delimiting used a linear- or cochlear-spaced subband distribution. The effect of the processing scheme on speech intelligibility was assessed in a trial involving 15 hearing-impaired volunteers with moderate sensorineural hearing loss. The acoustic material consisted of speech and speech-shaped noise signals, generated using simulated and real-room acoustic environments, at signal-to-noise ratios (SNRs) in the range -6 to $+3$ dB. The results show that the MMSBA scheme delivered average speech intelligibility improvements of 11.5%, with a maximum of 37.25%, in noisy reverberant conditions. There was no significant reduction in mean speech intelligibility due to processing, in any of the test conditions. [DOI: 10.1121/1.1413750]

PACS numbers: 43.72.Ew, 43.71.Ky, 43.66.Ts [SPB]

I. INTRODUCTION

It is common for persons suffering from sensorineural hearing loss to experience considerable difficulty understanding speech in the presence of medium to high reverberation or background noise, particularly from competing speakers. The difficulties occur at SNRs around and below 6 dB, which cause few problems for normal-hearing listeners. Subjects with sensorineural hearing loss may require 5 to 15 dB greater SNR (Plomp, 1986), and aided subjects may exhibit a SRT (speech reception threshold; 50% correct recognition level) around 8 dB worse (Soede *et al.,* 1993) than normal-hearing subjects. This article reports on a test of the following experimental hypothesis: multi-microphone subband adaptive signal processing can improve speech intelligibility for listeners with sensorineural hearing loss operating in noisy reverberant conditions. The control condition is a linear hearing-aid response prescribed by the NAL fitting procedure of Byrne and Dillon (1986).

It is a criticism of much research into the enhancement of speech signals corrupted with noise and/or reverberation that emphasis is placed on measuring improvement of SNR or speech transmission index, rather than the quantitative improvement in terms of speech intelligibility (Ludvigsen *et al.,* 1993; Saunders and Kates, 1997). There are notable exceptions such as Soede *et al.* (1993), Hoffman *et al.* (1994), and smaller scale experiments by Kompis and Dillier (1994) and Vanden Berghe and Wouters (1998). The experimental conditions used and results obtained by these researchers are summarized in Table I, and a brief description of their work, and relevant others, follows for comparison with the work reported in this article.

Allen *et al.* (1977) tested a two-microphone signal-processing scheme that removed room reverberation from speech. The scheme operates in frequency-limited subbands using a ''cophase and add'' process that removes any delay that may exist between the two input signals in a given subband. The reconstructed wideband speech was reported to have reduced reverberation.

Schwander and Levitt (1987) and Weiss (1987) used wideband processing adaptive noise cancellation (ANC) schemes with one omnidirectional and one directional microphone. Weiss identified four of the main factors limiting performance of an adaptive noise canceller:

(1) the presence of noise at the primary input of the system that is not correlated with the noise at the reference input
(2) the presence of wanted speech in the reference system input
(3) the length of the adaptive filter, and
(4) filter adaptation time.

As a means of addressing factor 2 above, Greenberg and Zurek (1992) investigated a two-microphone Griffiths–Jim beamforming approach for a hearing-aid application. The scheme split the frequency range into a high- and a low-frequency band for processing. The results demonstrated a 20 to 25 dB SNR improvement in an anechoic environment, dropping to a few dB improvement in a moderately reverberant room.

a)Electronic mail: d.r.campbell@paisley.ac.uk

TABLE I. Summary of quoted speech intelligibility enhancement experiments.

	Researchers				
	Soede *et al.*	Hoffman *et al.*	Kompis and Dillier	Vanden Berghe and Wouters	Shields and Campbell
No. of normal hearing test subjects	30	10	9	2	10
No. of hearing-impaired test subjects	45	None	6	3	None
Test material	Dutch sentences	English words	German words	English words/ sentences	English sentences
Reverberation T_{60} time (s)	0.2	0 "living room" "conference room"	0.4	0.45	0, 0.35, 1.8 (simulated) 0.3 (real-room)
Noise type	Speech shaped	Cafeteria babble	Speech shaped	Speech shaped	Speech shaped
Noise orientation	Diffuse (8 speakers)	45 degrees off axis	45 degrees off axis	90 degrees off axis	135 degrees off axis
Initial SNR (dB)	Not stated	−6	−15 to −5	Not stated	−11 to −4
SNR improvement (dB)		1.4 to 22.7	Not Stated	Not measured	6 to 30
SRT improvement (dB)	7	2.2–26.1	Not Stated	4.6 (words) 5.6 (sentences)	Not measured
Normal-hearing intelligibility improvement (%)	Not measured	Not measured	Approx. 25	Not measured	17.6 (average across all T_{60})
Hearing-impaired intelligibility improvement (%)	Not measured	Not measured	Approx. 18	Not measured	Not measured

Soede *et al.* (1993) used a five-microphone array of endfire or broadside configuration in a "delay and sum" beamforming approach. The diffuse speech-shaped masking noise field was generated using eight loudspeakers in a sound-insulated room. The intelligibility testing was performed using 30 normal-hearing, and 45 hearing-impaired subjects using sentences presented in Dutch. The results from testing showed an improvement in SRT of 7 dB (standard deviation 1.9 dB) and 6.8 dB (standard deviation 2.1 dB), respectively, for the broadside and endfire configurations.

Hoffman *et al.* (1994) used three- and seven-microphone adaptive array configurations. The microphones were forward facing and evenly spaced between the listeners ears. Ten normal-hearing subjects were tested using eleven spondaic English words. Reverberation was included by means of computer simulation, with multi-talker babble as the masking source at an angle of 45 degrees to the forward-facing microphone array axis. The results showed SNR improvements ranging from 3.1 dB in "conference room" reverberation to 22.7 dB in anechoic conditions, with a corresponding improvement of 3.6 to 26.1 dB in SRT.

Kompis and Dillier (1994) used a combination of adaptive processing with two directional microphones situated above the ears. The experiments used a room with reverberation time $T_{60}=0.4$ s and a single speech-shaped noise source at 45 degrees to the sagittal plane. Nine normal-hearing and six hearing-impaired subjects were tested using a German minimal pair test. Results showed an improvement in intelligibility of approximately 25% for normal-hearing and 18% for hearing-impaired listeners, with standard deviations varying from 3.1% to 13.4%.

Vanden Berghe and Wouters (1998) examined a real-time adaptive noise cancellation (ANC) scheme using a two-microphone endfire system in a test room with a reverberation time of $T_{60}=0.45$ s. The speech source was either open set words or sentences, with a competing source of speech-shaped noise at 90 degrees. Two normal-hearing and three hearing-impaired subjects were tested, showing a 5.6-dB (standard deviation 1.0 dB) improvement in SRT for sentence speech material.

Shields and Campbell (1998) used the MMSBA (two-microphone) processing scheme described within this article. SNR improvements of up to 31dB in simulation and 6dB from real-room ($T_{60}=0.3$ s) recordings were reported using speech corrupted with speech-shaped noise. The increase in SNR was accompanied by a significant mean improvement in intelligibility of 17.6% (across all reverberation times) for

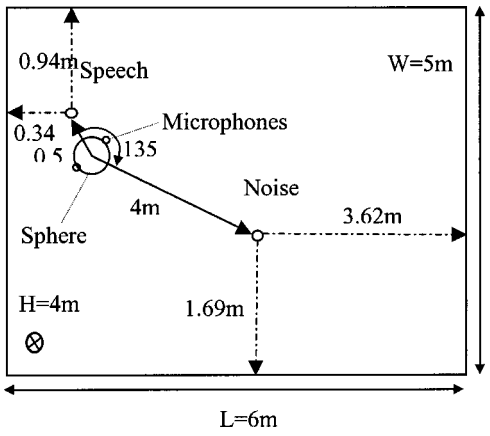

FIG. 1. Geometry for simulated room including speech and noise sources.

ten normal-hearing subjects tested under simulated and real-room conditions using 80 sentences presented in English. Unlike the scheme reported by Allen *et al.* MMSBA processing is aimed at reducing *both* reverberation and noise using an adaptive noise cancellation scheme. The schemes of Schwander and Levitt, and Weiss used one omnidirectional and one directional microphone in an attempt to compensate for factors 1 and 2 above, whereas MMSBA uses two omnidirectional microphones. In the form reported here it uses two inputs like that of Greenberg and Zurek, but not in the Griffiths–Jim beamforming configuration, although it can utilize that arrangement (Shields and Campbell, 1999). Similar to Allen *et al.* it divides the wideband input signals into a number of subbands but with frequency limits determined by a linear or cochlear distribution formula. Additionally, different processing schemes are used within the subbands dependent on the correlation between the noise components in these bands.

Since it would be unrealistic for a hearing aid application, the MMSBA processing scheme does not use the classical ANC configuration where a reference microphone is placed to estimate the noise component. Instead, when the noise correlation between the primary and reference inputs is high, the MMSBA scheme requires a voice activity detector (VAD) to restrict adaption to the ''noise only'' periods. In acoustic scenarios where the noise correlation is low and the speech correlation high, the wanted speech can be enhanced if it exhibits high correlation between the two channels.

Addressing factors 3 and 4 above, the use of multiple bands allows reduced-order filters in each band (Toner and Campbell, 1993) compared with wideband approaches. This significantly reduces the adaptation time and misadjustment noise of the ANC, and offers the possibility of significant parallelism in processing.

II. METHOD

A. Room acoustics and equipment orientation

Simulated room acoustics were used in an attempt to create a realistic, but easily controllable reverberant scenario in which persons suffering from sensorineural hearing loss would experience difficulty with speech intelligibility. The simulated room ($6\times5\times4$ m^3) of Fig. 1 contained a speech source at a distance of 0.5 m directly in front (0 degrees azimuth) of the input microphones (omnidirectional and placed at opposite points of a spherical simulated head of diameter 18 cm), and a masking source of speech-shaped noise at 135 degrees azimuth, at a distance of 4 m.

The acoustics were created by computer simulation of a rectangular room using a program based on the ''image method'' (Allen and Berkley, 1979) with the temporal improvements provided by Peterson (1986), and inclusion of head-related transfer functions as used by Culling *et al.* (1994). This provided acoustic transfer functions in the form of FIR filters, which modeled the impulse responses between a sound source (speech or noise) and the microphone positions, within an empty rectangular room, including the diffraction and attenuation effects of the simulated head. The simulation did not take into consideration the pinna or ear canal transfer functions; it also includes an assumption that the absorption or reflection coefficients of each surface are uniform and independent of angle of incidence. The absorption coefficients of all six surfaces were equal. The reverberation time chosen was $T_{60}=0.35$ s, which is representative of a typical domestic living room (Mackenzie, 1964). A room of similar dimensions to that of the simulated room above was used to make real-room recordings. Unlike the simulated room, furnishings were present in the form of tables and chairs, etc. These features were included to create as ''typical'' a living room situation as possible. The recordings were made using a KEMAR manikin, Knowles Model Number DB-4004, with Bruel and Kjaer Type 4134 microphones fixed within the ear canal using a Zwislocki occluded ear simulator, Knowles Model Number DB-1001. Thus, a form of simulated head was present in both simulated and real-room acoustic situations. The orientation of the speech and noise sources were as implemented for the simulation. The reverberation time (T_{60}) for the real room was established experimentally to be approximately 0.3 s.

Figure 2 shows the acoustic model from Fig. 1. Both speech, *S*, and noise, *N*, pass through their respective left and right acoustic FIR transfer functions, H_{11}, H_{12}, H_{21} and H_{22}, before forming the Primary, *P*, and reference, *R*, inputs to the MMSBA processing scheme. This illustrates the binaural speech and noise paths from their respective point sources to the input microphones of the system through the room acoustic transfer functions. This two-input approach could enable the system to exploit correlated and uncorrelated characteristics of the input signals, analogous to the binaural unmasking effect (Moncur and Dirks, 1967; Plomp, 1976). The binaural unmasking effect allows subjects listening binaurally to perform better, in speech intelligibility testing in noise, than subjects listening monaurally.

All signals were sampled at 20 kHz with 12-bit resolution. A FIR filter length of 2048 points for the simulated room acoustics, equivalent to 0.1 s, was established experimentally through visual inspection of impulse responses and subjective listening to be adequately representative of acoustic transfer functions with $T_{60}=0.35$ s. During this time reverberant energy had decayed by approximately 17 dB.

Using simulated room acoustics the speech and noise

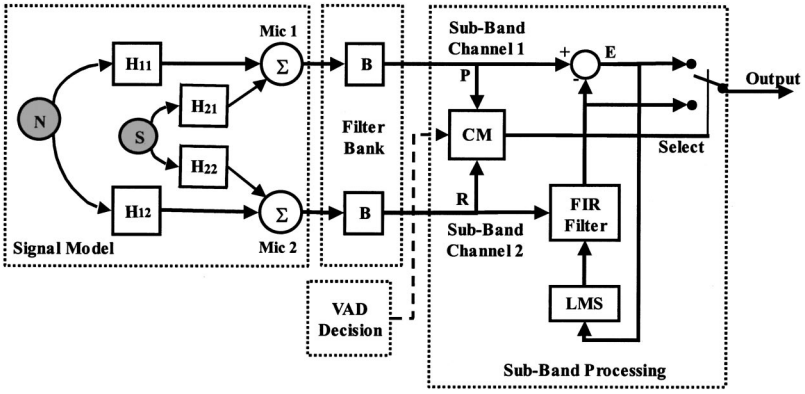

FIG. 2. Block diagram of acoustic model.

signals were convolved with their respective FIR acoustic transfer functions. In the real-room case the speech and the noise material were recorded separately. The convolved speech and noise material at the microphone was later combined using computer software to generate the various desired SNRs.

B. LMS Subband adaptive noise cancellation

The subband speech enhancement scheme implemented used an adaptive noise cancellation algorithm in frequency-limited subbands (Toner and Campbell, 1993). From Fig. 3 it can be seen that the inputs from the microphones, mic 1 and mic 2, are split into M contiguous subbands before processing using the subband processing (SBP) scheme, one band of which is shown in Fig. 2.

The MMSBA scheme can perform diverse subband adaptive processing, in which paired frequency bands from the two input microphones can be processed according to their individual properties. Three example conditions and processing techniques are listed here:

(1) Noise level below predetermined threshold; do not process subband, allow signal to pass unfiltered.
(2) Noise signals highly correlated between channels; when no speech is present in either channel, adapt the filter to minimize the noise signal, and then process with the ''frozen'' converged filter when speech is present. In this condition the adaptive filter estimates a transfer function describing the differential acoustic path experienced by the ''noise'' signal.

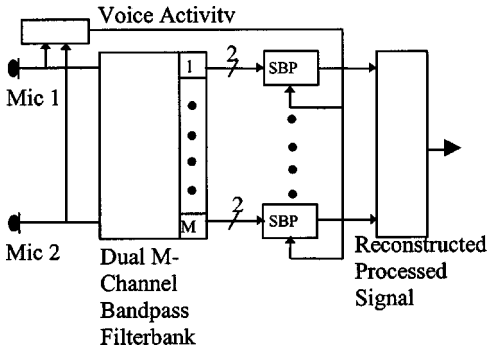

FIG. 3. Block diagram of MMSBA processing scheme.

(3) Noise signals uncorrelated between channels; sum all bands of this type and continuously adapt the filter, its output being used to estimate the speech signal.

In all the experiments presented in this article, a combination of conditions 2 and 3 were used for processing.

The correlation coefficient corr was estimated in each frame using

$$\text{corr}=\frac{\Sigma(p_i-\overline{p})(r_i-\overline{r})}{\sqrt{\{[\Sigma(p_i-\overline{p})^2][\Sigma(r_i-\overline{r})^2]\}}}, \tag{1}$$

where p and r are the primary and reference microphone inputs within a subband respectively. Signals were deemed to be uncorrelated if the correlation coefficient fell below the threshold value of corr=0.7. This resulted in condition 2 being implemented in the first 2, 4, or 8 subbands, respectively, for a linear 8, 16, or 32 subband decomposition, with the remaining subbands processed using condition 3.

The cochlear spacing function concentrates more subbands into the lower frequency region than linear spacing. When the subband distribution was cochlear spaced, applying the correlation condition above selected the first 5, 9, or 20 subbands for processing using condition 2, with remainder processed using condition 3.

The filter lengths used to model the differential transfer functions in each subband were chosen on a performance basis after pilot experiments. The filter length for subband processing using condition 2 was 512 taps. The remaining bands were processed using condition 3, with a filter length of 16 taps.

A voice activity detector (VAD) was assumed available and, although not a trivial problem, is a separate issue. Agaiby and Moir (1997) present an interesting VAD scheme that benefits from multiple microphones. The test signals all had a ''noise only'' period of duration 8000 samples (0.4 s) prior to the wanted speech. During all subsequent experiments, this period was used for adaptation in condition 2 above. The remaining 33 000 samples of each test signal contained speech plus noise, corresponding to the ''freeze'' period used with condition 2.

C. Subband decomposition

The use of subbands reduces the problem of identifying a single long-duration differential transfer function to that of

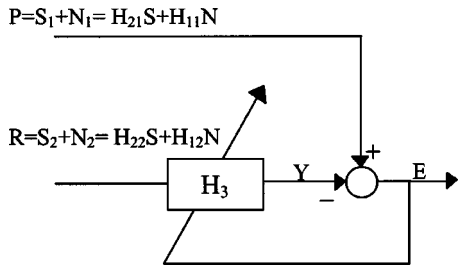

FIG. 4. LMS adaptive noise canceller.

identifying a set of less complex parallel filters. This approach improves the convergence of the adaptive algorithm while controlling the computational cost. For reasons of experimental flexibility, the subband decomposition process was performed by splitting the two input channels into frames of length 256 samples, then applying a 50% overlap add FFT scheme. The frequency bins were then separated into 8, 16, or 32 subbands with either linear or cochlear spacing prior to reconstructing the subband time domain signal. Using this approach, the error from decomposing the signal into frequency-limited subbands and synthesizing a wideband signal was found to be on the order of 0.001%.

When the input signals to the system include speech, the power distribution with frequency is nonuniform. Consideration of the adaptation performance of the LMS algorithm used suggests that it may be advantageous to distribute the subbands in such a way that the signal power is more uniformly distributed across the subbands than a simple linear spacing would provide. Spacing the subbands according to a ''cochlear'' distribution tends to prevent one subband dominating the overall convergence rate of the adaptive algorithm (Darlington and Campbell, 1996). The cochlear distribution function used to calculate the band edges for the 8, 16, and 32 subbands was based on that of Greenwood (1990),

$$F(x)=A(10^{ax}-k)\ \ \text{Hz}, \tag{2}$$

where $F(x)$ is the upper and lower cutoff frequency for each ''cochlear'' filter ($A=165$, $a=2.1$, $k=0.88$).

D. The subband processing scheme

In the classical noise cancellation configuration (Fig. 4) the desired speech signal is only present in the primary channel, i.e., $S_2=0$. The unwanted noise is assumed to be uncorrelated with the wanted speech signal, S_1, and highly correlated between the primary, N_1, and reference, N_2, channels. When the filter adapts to minimize the performance criterion the weights of the adaptive filter, H_3, will converge to a model of the differential acoustic transfer function between the two inputs, resulting in the filter output, Y, providing an estimate of the noise, N_1, in the primary channel. Therefore, the output, E, is an estimate of the speech signal S_1. The problem with this type of approach is that, in many practical situations, it is unlikely that the wanted speech signal will be present in only one channel, i.e., $S_2\neq 0$. One solution is to adapt the filter weights to minimize the noise when only noise signals, N_1 and N_2, are present. This could typically occur for a few tenths of a second during a gap in the speech signal. The filter weights H_3 can be frozen at the converged noise canceling values when speech is detected, forming a filter that preferentially suppresses the noise.

From Fig. 4, at the primary input

$$P=H_{21}S+H_{11}N. \tag{3}$$

At the reference input

$$R=H_{22}S+H_{12}N, \tag{4}$$

which implies

$$E=P-Y=(H_{21}-H_{22}H_3)S+(H_{11}-H_{12}H_3)N. \tag{5}$$

The classical stationary noise cancellation problem is to identify H_3 such that the power J_e of the error E is minimized,

$$J_e=\frac{1}{2\pi j}\oint_{|z|=1} EE^*z^{-1}\,dz. \tag{6}$$

Defining the noise spectral density Θ_{nn}, then, during a noise only period, $S=0$ and

$$J_e=\frac{1}{2\pi j}\oint_{|z|=1}(H_{11}-H_{12}H_3)\times\Theta_{nn}(H_{11}-H_{12}H_3)^*z^{-1}\,dz, \tag{7}$$

which is minimized in the least squares sense when

$$H_3=H_{11}(H_{12})^{-1}. \tag{8}$$

H_3 is now the transfer function that minimizes the noise appearing in E. Using H_3 as a fixed processing filter when speech and noise are present *ideally* yields

$$E=(H_{21}-H_{22}H_3)S,$$

and E is a noise-reduced filtered version of the speech signal.

In the experiment reported here, adaptive noise cancellation using the LMS algorithm was implemented in subbands. The step size μ of the LMS algorithm was calculated for each individual band dependent on the variance of the band-limited reference input signal, σ_b. The variance for each subband was calculated using the recursive estimate:

$$\sigma_b^2=\alpha\sigma_{i-1}^2+(1-\alpha)\sigma_i^2, \tag{9}$$

where $0<\alpha<1$ is a ''forgetting factor'' typically set at 0.95.

III. EXPERIMENTS: INTELLIGIBILITY TESTING

A. Apparatus

The hearing assessment workstation used to present the audio material to the hearing-impaired subjects was a replica of that used by the Institute of Hearing Research (IHR) at Nottingham University and the Glasgow Royal Infirmary. The hardware consisted of an IBM compatible PC with a dual output video card and a PC30AT 1/O card. The first video output was connected to a standard VGA monitor, visible only to the operator. The second output was connected to a touch screen for presentation of the test words and subject feedback. The PC30AT 1/O card was used to convert the unprocessed and processed, digitally stored, noisy reverberant speech files to analog before transmission through a

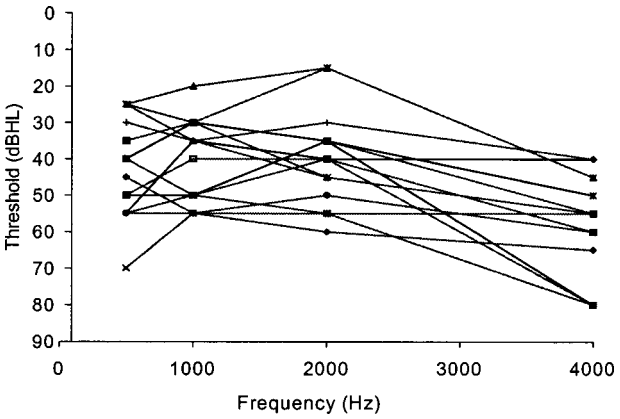

FIG. 5. Audiogram data for the 15 sensorineural hearing-impaired subjects.

Technics SH-8095 12-channel graphic equalizer to provide the necessary NAL frequency compensation (Byrne and Dillon, 1986) required for each subject's hearing loss. Finally, a Grason Stadler GSI 16 audiometer (acting as a precession attenuator and safety limiter) and TDH-50P headphones were used to deliver the monaural signal to each subject.

B. Subjects

Fifteen hearing-impaired subjects were assessed, nine males and six females, having a mean age of 64.3 years ranging from 41 to 77 years, with standard deviation 8.3 years. The hearing-impaired volunteers were asked for their cooperation while visiting the ENT departments at the Glasgow Royal Infirmary and Paisley Alexandra Hospitals. All the subjects were regular hearing aid users, diagnosed with sensorineural hearing loss. Figure 5 shows the audiogram data for the 15 subjects, whose hearing thresholds averaged over the audiometric test frequencies 500, 1000, 2000, and 4000 Hz were 44.9 dB HL, standard deviation 10.2 dB HL. Each subject was tested using one ear that normally wore a hearing aid. The hearing loss was symmetric for nine of the subjects; for the remaining six subjects with asymmetric hearing loss the subject's ear with greater hearing loss was selected for testing.

C. Stimuli

The FAAF test developed by Foster and Haggard (1979) uses common words from the English language in a four-alternative forced-choice format. It consists of 20 sets of four words (see Table II). The subjects were asked to identify each of the 80 keywords ''****'' presented audibly in a carrier sentence; ''*Can you hear* **** *clearly*?'' The options visually presented to the subjects on the touch screen differed by only one phoneme, e.g., TIN, BIN, PIN, and DIN. Nine sets vary the initial consonant, 11 the final consonant. The 80-word four-alternative approach yields a ''chance level'' score of 20. There is little or no practice effect due to the random presentation of the four words in column format on-screen (Foster and Haggard, 1987). The choice of simple words provides familiar material that is easy for a test subject to learn, even for moderate levels of literacy. One effect of the simplicity of the corpus is to reduce the variance in score due to an individual's verbal ability, which is advantageous when only a small number of subjects are available. The test has been adopted in the United Kingdom for research into hearing impairment. The masking noise source was speech shaped, matched to the long-term spectra of the 80 FAAF sentences.

TABLE II. FAAF Corpus: 80 key words used in intelligibility testing in four-alternative forced-choice format, delivered by carrier sentence ''Can you hear **** clearly.''

nan	din	wet	rib	dale
than	pin	bet	rick	nail
van	tin	get	rig	mail
man	bin	yet	rip	bail
some	rode	teen	port	veal
sud	rose	sheen	fought	seal
sun	robe	seen	thought	zeal
sub	rove	keen	taught	feel
ridge	milks	mash	lad	how
rich	milk	match	lands	high
rids	mick	mats	lads	ham
ritz	mix	mass	land	hang
coast	cab	cop	bag	bang
post	gab	cot	back	bag
boast	dab	cod	bat	bad
ghost	tab	cob	bad	ban

D. Experimental procedure

Ethical approval and informed consent procedures were followed. Subjects attended five visits to the University of Paisley to perform the listening tests. Each subject was paid a modest attendance allowance. Each visit lasted approximately 2 h, consisting of three 30-min sessions separated by a 5-min and 10-min interval. Audiometry was performed on subjects initially to record their audiogram, and subsequently to verify that there was no significant change in hearing level since the previous visit. All test signals were presented with NAL compensation. On the first visit each subject was given as many clean speech practice sentences (no noise or reverberation) as required to familiarize him or herself with the testing procedure. It has been demonstrated that there is little practice effect from exposure to the test material in this way (Foster and Haggard, 1987). During the familiarization period the most comfortable level (MCL) for listening was es-

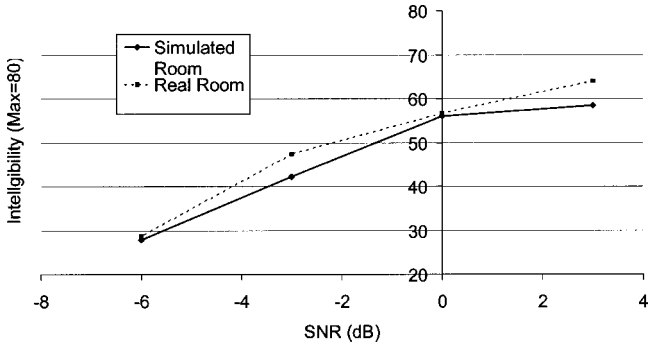

FIG. 6. Unprocessed speech intelligibility scores for simulated and real-room acoustics.

TABLE III. Paired *t*-test results from simulated versus real-room data.

Signal-to-noise ratio (dB)	*t*-test (*p* of null hypothesis) (two-tailed)	*p* (alternative hypothesis: acoustical conditions significantly different)	Significant at 95%?
3	0.014	0.986	Yes
0	0.697	0.303	No
−3	0.037	0.963	Yes
−6	0.563	0.437	No

tablished for each subject. The MCLs varied between 75 and 80 dB SPL, with a mean of 78 dB SPL. The use of subject's MCL is more representative of real-world hearing-aid use, whereby the subject has some control over individual listening level. The FAAF sentences were presented at SNRs of −6, −3, 0, and +3 dB, chosen to be representative of real-life ''difficult'' conditions and to elicit a significant number of errors.

The factors and levels were SNR (−6, −3, 0, and +3 dB), subband distribution (linear, cochlear), subband spacing (8, 16, and 32) and acoustic condition (simulated, real-room), with the comparison being between speech intelligibility scores before and after processing. The experiment was thus a four-factor repeated measures within-subjects design. The sequence of treatment presentation was performed in a Latin squares design to minimize any subject fatigue effects. During the test procedure no information related to the experimental factors in each test was given to the subject prior to listening to the test material, i.e., the tests were performed ''single blind.''

Additional scores were recorded at SNRs of +6 and +9 dB, but not all the above factors were manipulated. The results from these SNRs were separately analyzed and are kept separate in the following discussion, being referred to as the non-full factor observations.

IV. RESULTS AND STATISTICAL ANALYSIS

A. Comparison of simulated versus real-room acoustic intelligibility scores

In order to compare speech intelligibility from both simulated and real-room acoustics, the unprocessed scores from the real-room and simulated echoic rooms are plotted in Fig. 6. Table III presents results of an analysis using a paired *t*-test, after having verified the statistical normality of the data. The latter two columns show the probability (*p*) and significance of the simulated and real-room intelligibility scores being statistically separable from one another. When the SNR is 0 or −6 dB the null hypothesis is not rejected, but for the +3 and −3 dB case the simulated room scores are significantly different from the real-room condition.

TABLE IV. ANOVA using raw intelligibility score.

Factor	Degrees of Freedom	*F* ratio	Probability that factor NOT significant
SNR	3	418.72	0.000
Acoustics	1	1.04	0.307
Processing	1	256.54	0.000
Subject	14	64.58	0.000

TABLE V. ANOVA using difference in intelligibility score.

Factor	Degrees of freedom	*F* ratio	Probability that factor NOT significant
SNR	3	134.60	0.000
Acoustics	1	36.86	0.000
No. of subbands	2	1.05	0.351
Subband spacing	1	24.39	0.000
Subject	14	9.75	0.000

B. ANOVA of intelligibility scores

An analysis of variance (ANOVA) was performed on the intelligibility scores using both absolute recorded scores, and the difference in score ''processed minus unprocessed,'' with the results presented in Tables IV and V. The factor residuals were examined and shown to have a normal distribution with homogeneous variance, validating the assumptions of the ANOVA model. When analyzing the processing effect to determine the significance of the factors, ''number of subbands'' and ''subband spacing,'' the difference in score was used, since the unprocessed condition did not contain data on these factors. In Table IV the factor ''acoustics'' with the levels ''simulated'' or ''real-room'' is the only one that is not statistically significant. Table V shows ''number of subbands'' (8, 16, or 32) to be the only factor that is not statistically significant.

Examination of Figs. 7–10 suggests that there is no significant degradation of intelligibility due to processing when the SNR is at the higher levels, e.g., +3 dB. This is confirmed by the results of the one-tailed *t*-tests shown in Tables VI and VII. The three cases that are omitted from the tables all show a mean improvement in score. The limited examples with SNR of +6 or +9 dB, not included in Tables VI and VII, all had an increase in mean intelligibility score due to processing except one case, 32 linear subbands at +6 dB SNR in a simulated environment, which gave a decrement that was not statistically significant (*t*-test). This implies that there is no significant reduction in processed speech intelli-

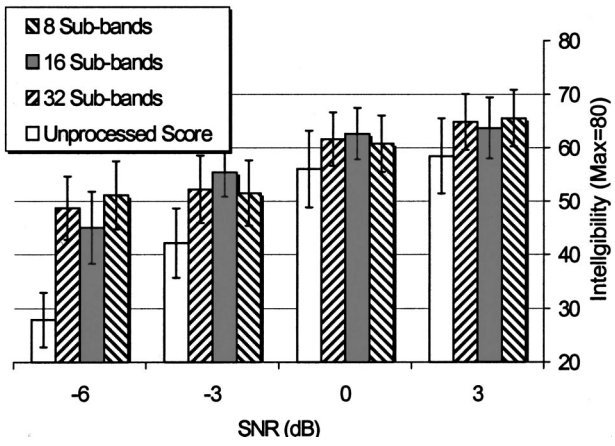

FIG. 7. Intelligibility scores for simulated room acoustics and linear spacing.

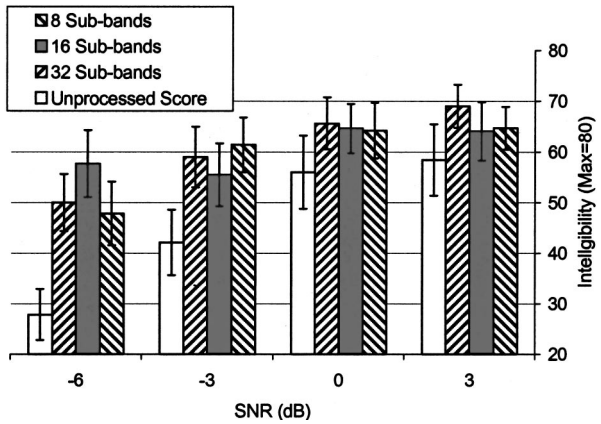

FIG. 8. Intelligibility scores for simulated room acoustics and cochlear spacing.

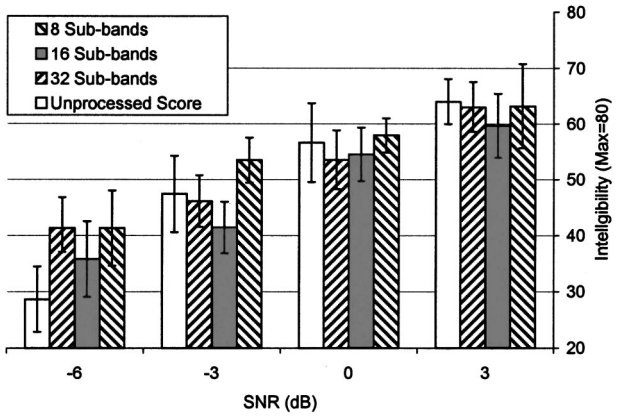

FIG. 9. Intelligibility scores for real-room acoustics and linear spacing.

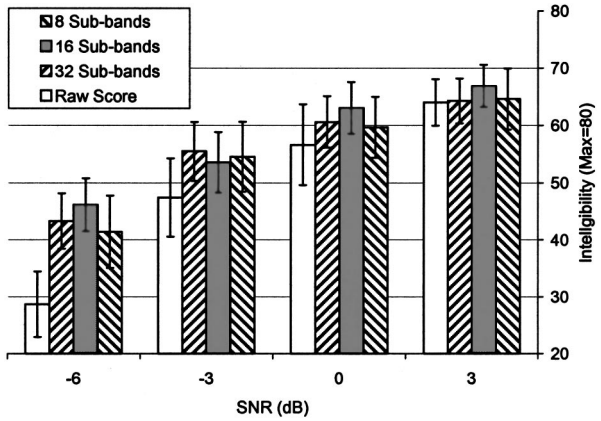

FIG. 10. Intelligibility scores for real-room acoustics and cochlear spacing.

gibility in cases where intelligibility scores for the hearing-impaired subjects are already high, which is an important feature for any hearing aid application.

At −6 and −3 dB SNR, where the unprocessed scores are initially low, Figs. 7–10 show many examples of a significant improvement in speech intelligibility at the 95% confidence level due to processing. This presents a consistent improvement due to processing using the MMSBA scheme. The observation is confirmed by the results from the ANOVA, Table IV, showing ''processing'' as a significant factor in the intelligibility scores.

In Figs. 7–10 the 95% confidence bars for the 8, 16, and 32 subband scores overlap strongly for all of the conditions, indicating weak significance of the factor ''number of subbands.'' This is confirmed in the ANOVA results of Table V where number of subbands did not appear as a significant factor.

Figures 11 and 12 present the intelligibility scores and 95% confidence intervals when processing the speech signals using the factor ''subband spacing,'' with the levels ''cochlear'' or ''linear'' in a simulated or real-room environments. Tables VIII and IX show the results of a paired *t*-test analysis applied to the mean intelligibility scores for ''linear'' versus ''cochlear'' spacing in the simulated and real-room cases.

The results in Tables VIII and IX fail to unequivocally establish the significance of the factor ''subband spacing.'' Seven out of 12 cases are statistically significant for the simulated room acoustics, with only three significant for the real-room case. However, the ANOVA results in Table V establish ''subband spacing'' as a significant factor.

C. SRT estimation

It was recognized that the 50% SRT could be estimated for simulated and real-room acoustic environments from the data presented in Figs. 13 and 14. These were plotted using average unprocessed and processed scores at all SNRs, with cochlear spacing across 8, 16, and 32 subbands. Cochlear spacing was chosen due to its small but consistent average improvement in intelligibility over linear spacing (Figs. 11 and 12). The improvement in SRT when projecting the processed score line back to provide a 50% correct score (40/80) using a second-order polynomial is approximately 3 dB using real-room acoustics, and 7 dB for simulated room acoustics.

TABLE VI. Paired *t*-test results from simulated data at 3 dB SNR.

Acoustics and subband spacing	*t*-test (*p* of null hypothesis) (one-tailed)	*p* (alternative hypothesis: intelligibility decrement due to processing)	Significant at 95%?
Linear/8 subbands	Processing	gave a mean score	improvement
Linear/16 subbands	0.233	0.767	No
Linear/32 subbands	0.139	0.861	No
Cochlear/8 subbands	0.087	0.913	No
Cochlear/16 subbands	0.186	0.814	No
Cochlear/32 subbands	Processing	gave a mean score	improvement

TABLE VII. Paired *t*-test results from real-room data at 3 dB SNR.

Acoustics and subband spacing	*t*-test (*p* of null hypothesis) (one-tailed)	*p* (alternative hypothesis: intelligibility decrement due to processing)	Significant at 95%?
Linear/8 subbands	0.287	0.713	No
Linear/16 subbands	0.177	0.823	No
Linear/32 subbands	0.440	0.560	No
Cochlear/8 subbands	0.311	0.689	No
Cochlear/16 subbands	Processing	gave a mean score	improvement
Cochlear/32 subbands	0.410	0.590	No

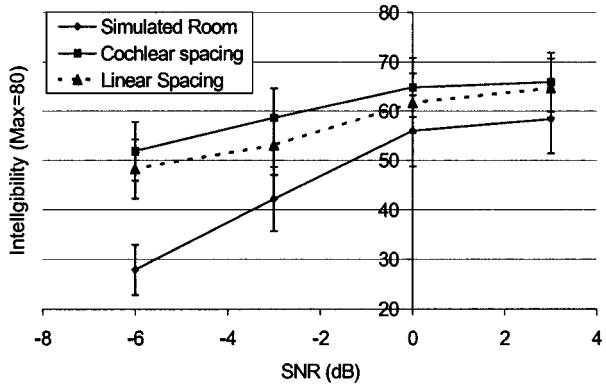

FIG. 11. Intelligibility scores grouped by subband spacing using simulated room acoustics.

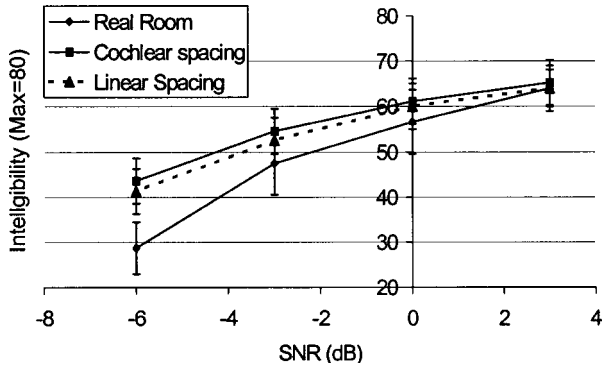

FIG. 12. Intelligibility scores grouped by subband spacing using real-room acoustics.

V. DISCUSSION

The average intelligibility improvement across all experimental conditions was 11.5%, with a maximum improvement in speech intelligibility of 37.3% using 16 ''cochlear-spaced'' subbands and data from simulated room acoustics (Fig. 8) and 21.8% using 16 ''cochlear-spaced'' subbands and data from real-room acoustics (Fig. 10). The ANOVA results in Table V reveal ''acoustics'' to be a significant factor, which supports this observed difference in maximum scores due to processing.

The inferred improvement in SRT lies between approximately 7 and 3 dB for simulated and real-room environments, respectively, as shown in Figs. 13 and 14. This improvement approaches the value of 8 dB, which Soede *et al.* (1993) suggested as the processing benefit required to enable hearing-impaired listeners to match the performance of normal-hearing listeners, and compares favorably to the 5.6 dB achieved by Vanden Berghe and Wouters (1998) and the 7 dB by Soede *et al.* (1993). It is interesting to note that monaural listening to the results of the binaural MMSBA processing of the real room data shows a SRT improvement comparable to that expected from true binaural listening in the real room. Table V shows the ''number of subbands'' used within the MMSBA processing scheme not to be a significant factor, and 8 subbands have been shown to provide a statistically significant speech intelligibility improvement. That the performance using 8 subbands cannot be distinguished from that of 16 or 32 subbands implies that there

TABLE VIII. Paired *t*-test comparison of intelligibility scores using simulated acoustics.

No. of subbands and SNR	*t*-test (*p* ofnull hypothesis) (two-tailed)	*p* (alternative hypothesis): linear spacing performing differently to cochlear spacing	Significant at the 95% level?
8 subbands/3 dB SNR	0.460	0.540	No
8 subbands/0 dB SNR	0.017	0.983	Yes
8 subbands/−3 dB SNR	0.000	1.000	Yes
8 subbands/−6 dB SNR	0.126	0.874	No
16 subbands/3 dB SNR	0.442	0.558	No
16 subbands/0 dB SNR	0.038	0.962	Yes
16 subbands/−3 dB SNR	0.959	0.041	No
16 subbands/−6 dB SNR	0.000	1.000	Yes
32 subbands/3 dB SNR	0.002	0.998	Yes
32 subbands/0 dB SNR	0.016	0.984	Yes
32 subbands/−3 dB SNR	0.000	1.000	Yes
32 subbands/−6 dB SNR	0.481	0.519	No

TABLE IX. Paired *t*-test comparison of intelligibility scores using real-room acoustics.

No. of subbands and SNR	*t*-test (*p* of null hypothesis) (two-tailed)	*p* (alternative hypothesis): linear spacing performing differently to cochlear spacing	Significant at the 95% level?
8 subbands/3 dB SNR	0.274	0.726	No
8 subbands/0 dB SNR	0.645	0.355	No
8 subbands/−3 dB SNR	0.291	0.709	No
8 subbands/−6 dB SNR	0.197	0.874	No
16 subbands/3 dB SNR	0.030	0.970	Yes
16 subbands/0 dB SNR	0.520	0.480	No
16 subbands/−3 dB SNR	0.013	0.987	Yes
16 subbands/−6 dB SNR	0.000	1.000	Yes
32 subbands/3 dB SNR	0.962	0.038	No
32 subbands/0 dB SNR	0.063	0.937	No
32 subbands/−3 dB SNR	0.281	0.719	No
32 subbands/−6 dB SNR	0.268	0.732	No

may be no need to increase the complexity of the processing scheme by implementing higher numbers of subbands. A question not addressed is, could less than 8 subbands still provide a useful performance increment? Shields and Campbell (1998) confirmed that when using data from a simulated anechoic room there was no advantage in adopting a multiband ANC approach over a single wideband ANC approach. They also reported that when using data from a real reverberant room a 16 subband MMSBA process provided an SNR improvement of around 6 dB whereas approximately 2.5 dB was obtained using a single wideband ANC approach. Thus the number of subbands required appears related to the complexity of the environmental acoustics, and it is likely that in less reverberant situations less than 8 subbands will be adequate; however, a generally useful hearing aid will need to cater for practically important worst case scenarios (e.g., large halls), either automatically or by user program selection.

Tables VI and VII confirm that processing did not significantly reduce intelligibility at +3 dB SNR (non-full factor examples at +6 and +9 dB also showed no significant decrement). This feature is obviously required in a practical device, to ensure that there are no unwanted deleterious effects due to processing when the SNR is such that there is little difficulty with unprocessed speech intelligibility.

The effect of subband spacing (Figs. 11 and 12 and Tables VIII and IX) suggests that a cochlear-spaced subband distribution gives consistently better intelligibility scores than a linear distribution. The ANOVA in Table V shows that overall the ''spacing'' factor is significant. However, this effect is not statistically significant in every case, as demonstrated by the mixed results of the paired *t*-tests shown in Tables VIII and IX. With cochlear spacing there are more bands being independently processed using ''adapt and freeze'' (condition 2). However, the actual bandwidth covered by these bands (2.02 kHz) was close to that of the corresponding linear case (2.5 kHz) for the 8- and 32-band cases. In the 16-band case with cochlear spacing ''adapt and freeze'' was selected over a bandwidth of 1.53 kHz while the linear case covered 2.5 kHz. This implies a degree of consistency in the operation of the correlation measure used to select bands and means that the ''adapt and freeze'' processing was operating over comparable frequency ranges for the linear and cochlear spaced cases. Using cochlear spacing applies the ''adapt and freeze'' processing in a more concentrated way in the lower frequency range. This tends to prevent the high-energy, low-frequency bands from dominating the convergence process of the adaptive filters, giving benefits from reduced adaptation time and misadjustment noise.

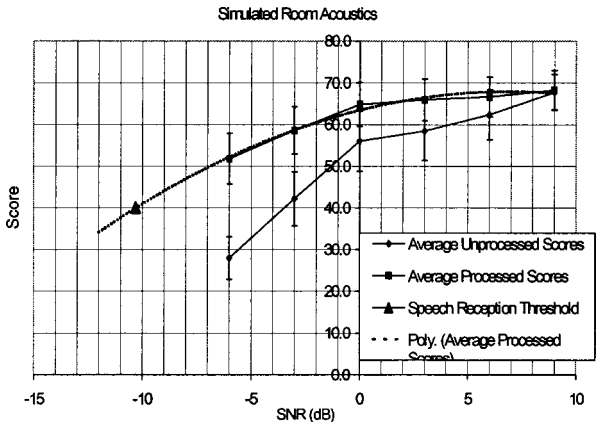

FIG. 13. SRT predictions for simulated room acoustics.

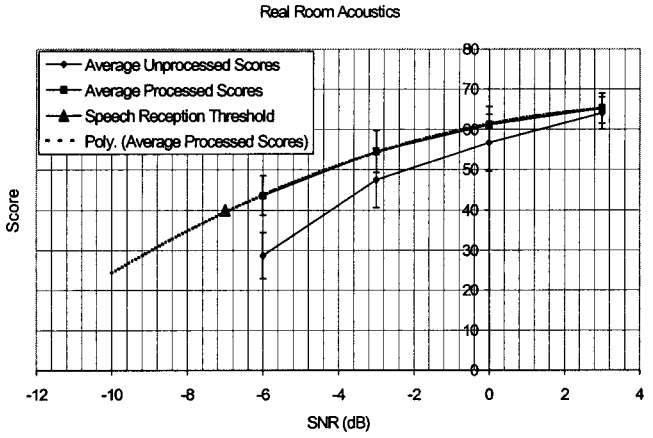

FIG. 14. SRT predictions for real-room acoustics.

The latter may be responsible for the marginally better performance using cochlear spacing.

The data in Table III show that for two out of four test conditions the ''image'' method produced intelligibility scores that are not statistically separable from those obtained using real-room acoustics; however, the factor ''room acoustics'' emerged as significant in the ANOVA results in Table V. An implication of these ANOVA results and the inconsistent results from the analysis shown in Table III is that while simulated room acoustics using the ''image'' method is useful for developing, and perhaps especially for rejecting candidate algorithms, one should not rely on such a relatively simple simulation to predict the benefit likely to be delivered by a processing scheme.

VI. CONCLUSION

The results presented in this article provide an evaluation of the potential for the MMSBA processing scheme to improve speech intelligibility for hearing-impaired listeners in the presence of noise and reverberation. In particular, we have the following.

(1) The MMSBA processing scheme has been shown to provide a statistically significant and practically useful speech intelligibility improvement in the presence of simulated or real-room reverberation and speech-shaped noise.
(2) The estimated SRT for hearing-impaired subjects in a noisy reverberant environment has been improved due to processing by approximately 7 dB, using both simulated and real-room acoustics.
(3) It has been demonstrated that processing using the MMSBA scheme has no significant detrimental effect on intelligibility at high SNR where unaided intelligibility scores are large.
(4) It appears that cochlear spacing may perform marginally better than linear spacing.
(5) A system with only 8 subbands (low computational complexity) can provide a statistically and practically significant intelligibility improvement.
(6) The experimental hypothesis that multi-microphone subband adaptive signal processing can improve speech intelligibility for listeners with sensorineural hearing loss operating in noisy reverberant conditions, when compared to their performance when using a standard linear hearing aid, is supported.

ACKNOWLEDGMENTS

The authors thank for their advice and support: J. Foster of the Institute of Hearing Research (IHR) at the University of Nottingham for assisting with the real-room recordings; Dr. J. Culling, then with the IHR at the University of Nottingham, for the modified room simulation software; and Professor S. Gatehouse of the IHR at Glasgow Royal Infirmary who supplied the speech material and subject contact. The commitment shown by the 15 subjects who participated in the experiments is gratefully acknowledged. This investigation was supported by the Scottish Office Department of Health Grant No. K/RED/4/237. D. R. Campbell was supported by a Leverhulme Trust Fellowship during the work reported in this article. The reviewing and editorial team is thanked for their constructive criticism.

Agaiby, H., and Moir, T. J. (**1997**). ''Knowing the wheat form the weeds in noisy speech,'' *ESCA Eurospeech 97*, Rhodes, Greece, pp. 1119–1122.
Allen, J. B., and Berkley, D. A. (**1979**). ''Image method for simulating small-room acoustics,'' J. Acoust. Soc. Am. **65**, 943–950.
Allen, J. B., Berkley, D. A., and Blauert, J. (**1977**). ''Multimicrophone signal-processing technique to remove room reverberation from speech signals,'' J. Acoust. Soc. Am. **62**, 912–915.
Byrne, D., and Dillion, H. (**1986**). ''The National Laboratories (NAL) new procedure for selecting the gain and frequency response of a hearing aid,'' Ear Hear. **7**, 257–264.
Culling, J. F., Summerfield, Q., and Marshall, D. H. (**1994**). ''Reverberation on the use of binaural cues and fundamental difference separating concurrent vowels,'' Speech Commun. **14**, 71–95.
Darlington, D. J., and Campbell, D. R. (**1996**). ''The effect of modified filter distribution on an adaptive, sub-band speech enhancement method,'' *IEEE Digital Signal Processing Workshop*, Leon, Norway, 1–4 September 1996.
Foster, J. R., and Haggard, M. P. (**1979**). ''FAAF—an efficient analytical test of speech perception,'' Proceedings of the Institute of Acoustics, pp. 9–12.
Foster, J. R., and Haggard, M. P. (**1987**). ''The four alternative auditory feature test (FAAF)—Linguistic and psychometric properties of the material with normative data in noise,'' Br. J. Audiol. **21**, 165–174.
Greenberg, J. E., and Zurek, P. M. (**1992**). ''Evaluation of an adaptive beamforming method for hearing aids,'' J. Acoust. Soc. Am. **91**, 1662–1676.
Greenwood, D. D. (**1990**). ''A cochlear frequency position-function for several species—29 years later,'' J. Acoust. Soc. Am. **87**, 2592–2605.
Hoffman, M. W., Trine, T. D., Buckley, K. M., and Van Tasell, D. J. (**1994**). ''Robust adaptive microphone array processing for hearing-aids: Realistic speech enhancement,'' J. Acoust. Soc. Am. **96**, 759–770.
Kompis, M., and Dillier, N. (**1994**). ''Noise reduction for hearing aids: Combining directional microphones with an adaptive beamformer,'' J. Acoust. Soc. Am. **96**, 1910–1913.
Ludvigsen, C., Elberling, C., and Keidser, G. (**1993**). ''Evaluation of a noise reduction method—Comparison between observed scores and scores predicted from STI,'' Scand. Audiol. Suppl. **38**, 50–55.
Mackenzie, G. W. (**1964**). *Acoustics* (Focal, London, England), Chap. 7, p. 142.
Moncur, J. P., and Dirks, D. (**1967**). ''Binaural and monaural peech intelligibility in reverberation,'' J. Speech Hear. Res. **10**, 186–195.
Peterson, P. M. (**1986**). ''Simulating the response of multiple microphones to a single acoustic source in a reverberant room,'' J. Acoust. Soc. Am. **80**, 1527–1529.
Plomp, R. (**1976**). ''Binaural and monaural speech intelligibility of connected discourse in reverberation as a function of azimuth of a single sound source (speech or noise),'' Acoustic **31**, 200–211.
Plomp, R. (**1986**). ''A signal to noise ratio model for speech reception threshold of the hearing impaired,'' J. Speech Hear. Res. **29**, 146–154.
Saunders, G. H., and Kates, J. M. (**1997**). ''Speech intelligibility enhancement using hearing-aid array processing,'' J. Acoust. Soc. Am. **102**, 1827–1837.
Schwander, T., and Levitt, H. (**1987**). ''Effect of two-microphone noise reduction on speech recognition by normal-hearing listeners,'' J. Rehabil. Res. Dev. **4**, 87–92.
Shields, P. W., and Campbell, D. R. (**1998**). ''Intelligibility improvements obtained by an enhancement method applied to speech corrupted by noise and reverberation,'' Speech Commun. **25**, 165–175.
Shields, P., and Campbell, D. R. (**1999**). ''Speech enhancement using a multi-microphone sub-band adaptive Griffith-Jim noise canceller,'' 6th Eurospeech, Budapest, Hungary, 5–10 September.
Soede, W., Berkhout, A. J., and Bilsen, F. (**1993**). ''Development of a directional hearing instrument based on array technology,'' J. Acoust. Soc. Am. **94**, 785–798.
Toner, E., and Campbell, D. R. (**1993**). ''Speech enhancement using subband intermittent adaptation,'' Speech Commun. **12**, 253–259.
Vanden Berghe, J., and Wouters, J. (**1998**). ''An adaptive noise canceller for hearing aids using two nearby microphones,'' J. Acoust. Soc. Am. **103**, 3621–3626.
Weiss, M. (**1987**). ''Use of an adaptive noise canceller as an input preprocessor for a hearing aid,'' J. Rehabil. Res. Dev. **4**, 93–102.

Ultrasonic properties of random media under uniaxial loading

M. F. Insana[a)]
Department of Biomedical Engineering, University of California, One Shields Avenue, Davis, California 95616

T. J. Hall
Department of Radiology, University of Kansas Medical Center, 3901 Rainbow Boulevard, Kansas City, Kansas 66160

P. Chaturvedi
Sprint PCS, 15405 College Boulevard, Lenexa, Kansas 66219

Ch. Kargel
Department of Biomedical Engineering, University of California, One Shields Avenue, Davis, California 95616

(Received 12 June 2000; accepted for publication 26 August 2001)

Acoustic properties of two types of soft tissue-like media were measured as a function of compressive strain. Samples were subjected to uniaxial strains up to 40% along the axis of the transducer beam. Measurements were analyzed to test a common assumption made when using pulse-echo waveforms to track motion in soft tissues—that local properties of wave propagation and scattering are invariant under deformation. Violations of this assumption have implications for elasticity imaging procedures and could provide new opportunities for identifying the sources of backscatter in biological media such as breast parenchyma. We measured speeds of sound, attenuation coefficients, and echo spectra in compressed phantoms containing randomly positioned scatterers either stiffer or softer than the surrounding gelatin. Only the echo spectra of gel media with soft scatterers varied significantly during compression. Centroids of the echo spectra were found to be shifted to higher frequencies in proportion to the applied strain up to 10%, and increased monotonically up to 40% at a rate depending on the scatterer size. Centroid measurements were accurately modeled by assuming incoherent scattering from oblate spheroids with an eccentricity that increases with strain. While spectral shifts can be accurately modeled, recovery of lost echo coherence does not seem possible. Consequently, spectral variance during compression may ultimately limit the amount of strain that can be applied between two data fields in heterogeneous media such as lipid-filled tissues. It also appears to partially explain why strain images often produce greater echo decorrelation in tissues than in commonly used graphite–gelatin test phantoms. [DOI: 10.1121/1.1414703]

PACS numbers: 43.80.Cs, 43.35.Bf [FD]

I. INTRODUCTION

The theory of acoustic wave propagation in heterogeneous media[1] can successfully explain many aspects of ultrasonic scattering measurements in soft biological tissues when essential material properties are known.[2] Except for blood, we know little about the exact anatomical microstructure that scatters ultrasound. We know that energy is redirected at spatial fluctuations in medium mass density ρ and bulk compressibility κ. Furthermore, compressibility fluctuations $\Delta\kappa=\kappa-\overline{\kappa}$ for collagen and elastin are often substantial[3] with respect to the spatial average $\overline{\kappa}$, whereas the corresponding density fluctuations, e.g., from lipid-filled structures, are less but significant: values for $\overline{\kappa}\Delta\rho/\rho\Delta\kappa$ have been measured in the range of 0 to 0.5 for blood, liver, and skeletal muscle.[4,5]

Coupling this information with mathematical analyses that link scatterer size to ultrasonic frequency spectra,[6,7] investigators have studied the inverse problem of identifying scattering structures[8] and thus are able to track *in vivo* changes in the microvascular diameter below the diffraction limit for diagnostic wavelengths.[9,10] Ultimately, similarities between matched ultrasonic and histological measurements are used to verify the sources of scattering based on size, number density, and collagen content. In this paper we describe another discriminating scattering feature that may be useful in defining scattering sources—changes in the centroid of the backscattered echo spectrum with the amount of applied strain.

The idea for this study originated during early elasticity imaging experiments designed to investigate relationships between large- and small-scale viscoelastic properties of tissue-like media.[11] It is essential that local acoustic properties be invariant under strain if we are to obtain accurate time delay estimates from echo correlation analysis. Specifically, the microscopic spatial distribution of tissue bulk moduli that dominates scattering properties in soft tissues must be uncorrelated with the macroscopic spatial distribution of tissue shear moduli that determines the appearance of strain

a)Electronic mail: mfinsana@ucdavis.edu

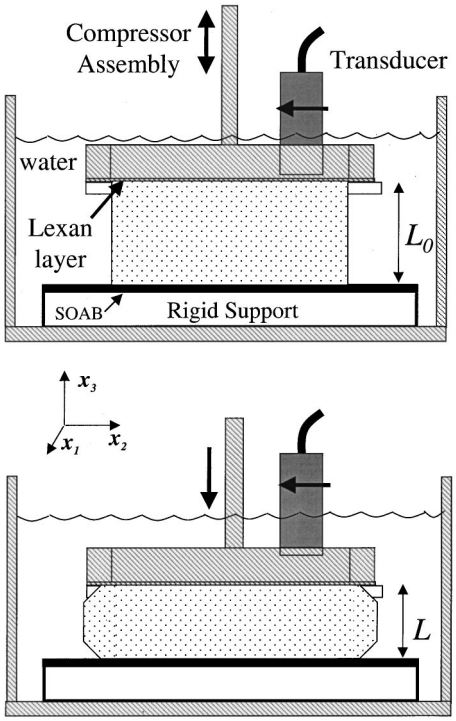

FIG. 1. The apparatus for measuring acoustic properties of cylindrical samples is illustrated (top). The force was applied downward against an immobile Lucite block by the Lexan layer deforming the sample (bottom). The sound-absorbing (SOAB) rubber was included during backscatter measurements and removed during speed and attenuation measurements. The transducer beam axis was oriented normal to and scanned parallel to the Lucite block surface through the Lexan.

images.[12] Only then can echo correlation provide a reliable method for tracking object motion.

In this paper we summarize a series of experiments involving two classes of materials originally developed by Madsen *et al.* as ultrasound phantoms.[13] Type I materials are glass-sphere-in-gelatin suspensions and type II materials are oil-droplet-in-gelatin dispersions. The diameter ranges of glass microspheres in the type I samples are either small (35–75 μm) or large (150–180 μm). All glass microspheres are randomly positioned and much stiffer than the surrounding gelatin. Type II materials contain oil spheres dispersed randomly throughout the gelatin. The mean oil sphere diameter varies in different samples between 20 and 400 μm. At room temperature, the oils are liquids, similar to the lipid at body temperature, and therefore much softer than the surrounding gelatin.

We measured speeds of sound, attenuation coefficients, and backscattered echo spectra for each sample up to 10 MHz and for applied uniaxial stresses producing strains up to 0.4. Samples were compressed in a plane normal to the top planar surface such that all points on the surface were displaced the same amount along $-x_3$ (Fig. 1). No attempt was made to match the acoustic properties of the gel samples to specific body tissues. Instead, we sought to produce samples with sound speed, attenuation, and backscatter features within the range of values reported for human soft tissues.[14] The results below indicate the reliability of echo tracking in a broad range of deformations for tissue-like media, and suggest a new method for identifying the anatomical sources of bioacoustic scattering.

TABLE I. Type I materials: Glass-in-gel suspensions.

Sample	Glass sphere diameter (μm)	Mass (g/l)	Sound speed at 2.5 MHz (m/s)	Atten. coefficient (dB/cm) at 2.5/5.0/7.5/10.0 MHz
1	35–75	33.3	1590	0.74/1.88/3.83/6.91
2	150–180	6.67	1575	0.47/1.10/1.67/2.71

II. MATERIALS AND METHODS

Type I Materials.[15] One-hundred twenty grams of animal hide gelatin (type A, 275 bloom, Fisher Scientific, Hampton, NH) were mixed into each liter of a 6% *n*-propanol-in-water solution at room temperature. The mixture was placed in a 29 mm Hg vacuum for a few minutes to remove gases. The beaker of dissolved, degassed gelatin was then heated at 45 °C in a water bath for about 90 min until it became translucent. The clear gelatin solution was removed from the heat, glass microspheres (Potters Industries, Inc., Valley Forge, PA) as specified in Table I were added and thoroughly mixed with a spoon, and the beaker was cooled to 30 °C while stirring. The liquid glass–gel mixture was poured into a cylindrical mold 7.5 cm in diameter and 2.5 cm in height, sealed, and rotated at 1 rpm overnight. Congealed samples were removed from the molds and stored at room temperature in a sealed container with a small amount of propanol–water solution to minimize desiccation. Samples 1 and 2 in Table I are type I. Samples A and B (see Sec. III) are also type I, but have no added scatterers.

Type II Materials.[13] More of the clear gelatin solution described above was heated in a water bath to 70 °C. Instead of glass microspheres, 250 ml of an oil were emulsified into each liter of liquid gelatin by vigorous mixing with a spoon. The different types of oils used in this study are listed in Table II. Care was taken to prevent introducing air while mixing. The emulsion was cooled to 30 °C before being poured into the cylindrical molds and rotated in room air overnight. After congealing and removal from its mold, an inspection microscope was used to measure the average di-

TABLE II. [a]Type II Materials: Oil[b]-in-gel dispersions.[c]

Sample	Oil type	Oil conc. (ml/l)	Sound speed (m/s) at 2.5 MHz	Atten. coefficient (dB/cm) at 2.5/5.0/7.5/10.0 MHz
3	corn	250	1557	1.18/3.69/6.90/10.78
4	motor	250	1556	0.87/3.68/7.56/11.79
5	peanut	250	1561	0.95/3.72/6.85/10.65
6	mineral	250	1567	0.87/2.86/5.03/7.47

[a]The acoustic properties listed in Tables I and II are for uncompressed samples. Averaging attenuation coefficients for samples 3–5 gives the following least-squares fit to a second-order polynomial between 0 and 10.0 MHz, where we include $\alpha(0)=0$ dB/cm: $\alpha_{3-5}(f)=-0.1253+0.3700f+0.0760f^2$. The fits for samples 1 and 2 yield, respectively, $\alpha_1(f)=-0.0034+0.0659f+0.0619f^2$, and $\alpha_2(f)=-0.1407+0.1925f+0.0087f^2$.

[b]The motor oil was SAE 10W30.

[c]Data from two corn-oil samples were obtained. The two samples are referred to as sample 3 and sample 3′ in the figures.

ameter of oil drops visible from the surface of the colloid, now a dispersion. Samples 3–6 in Table II are type II.

Strain. In the following, we report an engineering strain $\epsilon' = (L_0 - L)/L_0$ as that resulting from the compressive stress applied.[16] L_0 is the initial sample height along the compression axis, x_3 in Fig. 1, and L is the instantaneous height. If the stiffness of the sample is uniform throughout its volume, then ϵ' approximates the spatial derivative of displacement along x_3, i.e., $\epsilon' \simeq \partial u_3/\partial x_3$.

Strain for the finite displacements used in this study is defined in the Lagrangian frame as[17]

$$\epsilon_{33} = \frac{\partial u_3}{\partial x_3} + \frac{1}{2}\left[\left(\frac{\partial u_1}{\partial x_3}\right)^2 + \left(\frac{\partial u_2}{\partial x_3}\right)^2 + \left(\frac{\partial u_3}{\partial x_3}\right)^2\right]. \tag{1}$$

ϵ_{33} is the Lagrangian strain tensor that describes deformation of a unit volume along the x_3 axis. If the derivatives are small, then $\epsilon_{33} \simeq \partial u_3/\partial x_3$, the infinitesimal strain tensor, which is approximately ϵ' for homogeneous media. $\partial u_3/\partial x_3$ is not small in this study. Nevertheless, we use ϵ' to specify the strain for convenience. Readers can convert between Lagrangian and engineering strains using $\epsilon_{33} \simeq \epsilon'(1 + \epsilon'/2)$.

Measurement geometry has a large influence on steady-state deformation patterns in stressed samples, often more than material properties such as elastic modulus and Poisson's ratio ν. For these nearly incompressible media, parallel-plate compressor geometry, full-slip boundary conditions, and quasistatic measurement conditions, sample volume is conserved. We treat samples under these conditions as Hookean elastic solids,[17] so that $\epsilon_{11} = \epsilon_{22} = -\nu\epsilon_{33}$.

Acoustic measurements. Measurements were made in distilled/degassed water at room temperature (between 18.8 and 20.4±1 °C) with the apparatus diagrammed in Fig. 1. The transducers had one circular PZT element, 19 mm in diameter, that was focused at f/2.8 (videoscan immersion, Panametric, Waltham, MA). Two transducers with nominal frequencies 3 and 10 MHz were used in this study. Test samples were deformed by uniformly displacing the top surface of the sample downward a known amount ±4 μm. Applied forces were held several minutes before recording waveforms to minimize variability caused by viscous creep. With the possible exception of the mineral oil sample, each test sample contained a sufficient number of scatterers per resolution volume (>5–10) to be considered an incoherent scattering source.

A pulse-echo variation on the narrow-band-through-transmission substitution technique described by Madsen *et al.*[13] was used to measure sound speed and attenuation. Sinusoidal pressure bursts were transmitted through the sample and reflected at normal incidence at the surface of a 5-cm-thick Lucite block. The sound-absorbing (SOAB) layer shown in Fig. 1 was removed. The duration of the voltage burst that excited the transducer was adjusted between 10 and 20 cycles to avoid reverberations. The transducer–reflector distance remained unchanged during the experiment and was approximately equal to the radius of curvature of the spherically focused transducers. The compressive force was applied to the sample through a 1-mm thick Lexan layer that was rigidly attached to the compressor assembly. This layer may have flexed slightly during compression; a 1-mm flexure at $\epsilon' = 0.4$ corresponds to a −10% strain error for 25-mm-thick samples.

We recorded measurements of echo phase ϕ and amplitude A near the center of the voltage burst as viewed from a digital oscilloscope display. The phase was estimated from the time shift in a zero crossing near the center of the burst. $M = 10$ independent measurement pairs (A_m, ϕ_m), $1 \leqslant m \leqslant M$, were obtained after scanning the transducer at 2-mm lateral increments with the sample in place. Only five phase measurements were used to estimate sound speed while all ten were used to estimate attenuation. One reference measurement pair (A_0, ϕ_0) was recorded with the sample removed. Wave properties in the latter case are determined entirely by the distilled water, but, in both situations, the thin Lexan layer used to compress the sample remained in place.

The substitution technique involves an expression for the speed of sound in a sample, $c(\epsilon', T)$ (m/s), as a function of ϵ', measurement temperature T (°C), speed of sound in water[18] $c_0(T)$ (m/s), sample thickness $d(\epsilon')$ (m), and mean temporal phase shift introduced by placing the sample in the sound beam $\Delta\phi\,(\mathrm{s}) = (\Sigma_{m=1}^{M}\phi_m)/M - \phi_0$. Writing $\Delta\phi(\epsilon', T) = 2d(\epsilon')[1/c(\epsilon', T) - 1/c_0(T)]$ and rearranging terms, we find

$$c(\epsilon', T) = \frac{2d(\epsilon')c_0(T)}{2d(\epsilon') + c_0(T)\Delta\phi(\epsilon', T)}. \tag{2}$$

Attenuation coefficients, $\alpha(f, \epsilon', T)$, at frequency f (MHz) were found from the ratio of peak-to-peak burst amplitudes with $[A = (\Sigma_{m=1}^{M}A_m)/M]$ and without (A_0) the sample in place and sample thickness d via

$$\alpha(f, \epsilon', T) = \frac{10}{d(\epsilon')}\log_{10}\frac{A(f, \epsilon', T)}{A_0(f, T)}. \tag{3}$$

Castor oil was used as a standard sample to calibrate attenuation estimates.[13] Large-amplitude sinusoids were transmitted, yet the amplitude was not so large as to violate linearity and agreement (±3%) with published values for attenuation in castor oil: $0.834f^{5/3}$ (dB/cm) at 20 °C.[19]

Following measurements of sound speed and attenuation, echo spectra were recorded. We digitized 10.24 μs echo time series generated by the backscatter of broadband pulses within a sample. The transmitted pulse duration was approximately two cycles, producing a −6-dB bandwidth of 60% of the peak frequency for pulses reflected from a Lucite surface in water at 20 °C. A Panametrics (Waltham, MA) pulser–receiver Model 5052UA was used. M was increased to 25 waveforms, each digitized at 8 bits and 5×10^7 samples/s to give $N = 512$ points per waveform. Adjusting the transducer–sample distance, we placed the center of the time series at the radius of curvature of the transducer. A SOAB layer was used as shown in Fig. 1 to reduce reverberations.

The magnitude of the discrete Fourier transform $|G[k]|$, $0 \leqslant k \leqslant N/2 - 1$, was computed using a fast Fourier transform algorithm.[20] From the set of recorded time series, $g_{m\epsilon}[n]$, $0 \leqslant n \leqslant N - 1$, at each strain value ϵ', we estimated the mean frequency spectrum,

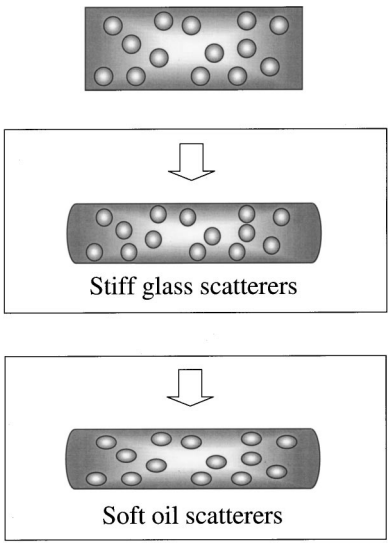

FIG. 2. An illustration of sample deformation. Stiff scatterers redistribute but do not deform during uniaxial compression. Soft spherical scatterers redistribute and deform into oblate spheroids during deformation. Scatterers are not to scale.

$$|G_\epsilon[k]| = \frac{1}{M}\sum_{m=1}^{M}\left|\sum_{n=0}^{N-1} g_{m\epsilon}[n]e^{-i2\pi kn/N}\right|. \tag{4}$$

The summation over M waveforms yields an approximation to an ensemble average.[21]

Echo spectra shown in Sec. III below describe a shift in the peak value of $|G_\epsilon[k]|$ with increasing ϵ'. We summarized changes in echo spectra by a scalar value obtained from estimates of the normalized first moment or spectral *centroid*,[22]

$$f_c(\epsilon') = \Delta f \frac{\Sigma_{k=0}^{N/2} k|G_\epsilon[k]|}{\Sigma_{k=0}^{N/2}|G_\epsilon[k]|}, \quad \Delta f = \frac{1}{NT}, \tag{5}$$

where T is the sampling interval, in this case 20 ns. The centroid indicates any monotonic weighting of spectral values, such as those expected for a change in the scattering function with ϵ'.

Statistical analysis. We state our confidence that acoustic parameters vary as a function of engineering strain ϵ' using the following analysis. The mean $\bar{y}$ and variance $\hat{\sigma}_y^2$ are sample moments of the (assumed) normally distributed parameter y, and are computed from M uncorrelated measurements. The expected value, $E\{y\}$, will fall within the interval[23]

$$\bar{y} - \frac{\hat{\sigma}_y t_{M-1;\gamma/2}}{\sqrt{M}} \leqslant E\{y\} \leqslant \bar{y} + \frac{\hat{\sigma}_y t_{M-1;\gamma/2}}{\sqrt{M}}, \tag{6}$$

with $100(1-\gamma)$ percent confidence. Setting $\gamma=0.01$, we find the 99% confidence interval. Values found outside of this interval are assumed to be from a different distribution. We used look-up tables[23] and experimental parameters to find the threshold value $t_{M-1;\gamma/2}$ that determines the probability $\Pr(t_{M-1} > t_{M-1;\gamma/2}) = \int_{t_{M-1;\gamma/2}}^{\infty} p(t)dt = \gamma/2$. t_{M-1} is the student t statistic; $t_{9;0.005}=3.250$ and $t_{4;0.005}=4.604$.

Intersample attenuation coefficients varied widely. Consequently, we normalized $\alpha(\epsilon')$ values relative to that at $\epsilon'=0$ to find $\beta(\epsilon')=\alpha(\epsilon')/\alpha_0$ for studying ϵ' dependences. Assuming the attenuation estimates at different values of ϵ' are independent and that the variance σ_α^2 is independent of ϵ', then the uncertainty in β is found by propagating errors according to[24]

$$\sigma_\beta = \left[\sigma_\alpha^2\left(\frac{\partial\beta}{\partial\alpha}\right)^2 + \sigma_{\alpha_0}^2\left(\frac{\partial\beta}{\alpha_0}\right)^2\right]^{1/2} = \frac{\sigma_\alpha}{\alpha_0}\sqrt{1+\beta^2}. \tag{7}$$

The error bars in Fig 4 are examples of σ_β.

Centroid predictions. It is reasonable to assume that soft scatterers in compressed samples will deform in the manner of the surrounding gelatin (Fig. 2). Changes in the ultrasonic echo spectrum may be predicted if we understand how the backscatter spectrum from oblate spherical oil droplets varies with eccentricity. Oils in type II samples are approximately spherical with radius r_0 before compression. After deformation into oblate spheroids, the minor axis will be $r_1=(1-\epsilon')r_0$ for $0\leqslant\epsilon'<1$. To conserve volume, the major axis must therefore be $r_2=r_0/\sqrt{(1-\epsilon')}$, so the eccentricity is $\sqrt{1-(r_1/r_2)^2}=\sqrt{1-(1-\epsilon')^3}$. Fortunately expressions that describe scattering from an acoustically soft oblate spheroid are available. See Appendix A for details.

We computed scatter fields from one oblate spheroid insonated with many plane waves at frequencies in the transducer bandwidth. Assuming that only incident waves are scattered (single-scatter Born approximation[1]) and that the scatter field at the receiving aperture is entirely incoherent, we integrated the exact numerical solution for the pressure field at frequency f, i.e., $p_f(\mathbf{x},t,\epsilon')$ from Appendix A. The integration is over the transducer aperture to find the net force at the surface.[25] The net force was multiplied by a Gaussian pulse-echo system response, $H(f)$ (Appendix B), computed for the same frequencies, and then integrated over frequency to give the echo signal samples $\tilde{g}_\epsilon[n]$. Taking the discrete Fourier transform and finding the magnitude, we arrive at the predicted echo spectrum, $|\tilde{G}_\epsilon[k]|$. Finally, the predicted spectral centroid, $\tilde{f}_c(\epsilon')$, was computed from Eq. (5), where $|\tilde{G}_\epsilon[k]|$ replaced $|G_\epsilon[k]|$.

III. RESULTS

Sound speed. Figure 3 shows that the speed of sound does not vary significantly over the range $0\leqslant\epsilon'\leqslant0.2$ for three oil-in-gel dispersion samples, all having scatterers more compressible than the background gelatin. Invariance was determined by finding that all the measurement points for a given sample fall within the 99% confidence interval ($\pm$6.9 m/s) about the mean value for that sample. Including data from type I media with stiff scatterers (not shown in Fig. 3), we determined the speeds of sound in each sample tested were independent of the applied strain, i.e., $c(\epsilon',T)=c(T)$.

Attenuation. Figure 4 shows the relative change in the attenuation coefficient for samples when $\epsilon'\leqslant0.2$. There is a slight increase with compression, e.g., the linear regression analysis gives $\beta(\epsilon')=\alpha(\epsilon')/\alpha_0=0.76\epsilon'+0.993$ at 2.5 MHz and $\beta(\epsilon')=0.25\epsilon'+0.991$ at 5.0 MHz. There is no physical reason for assuming a linear dependence, so these equations are just a convenience. One point at 2.5 MHz and one at 5 MHz fall outside the 99% confidence interval for stating that the expected value for β is one.

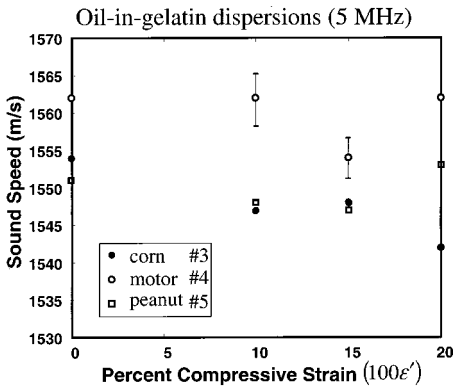

FIG. 3. Speeds of sound are plotted as a function of percent compression for oil-in-gel dispersions: ●, sample 3; ○, sample 4; and □, sample 5. Sample numbers are listed in Tables I and II. Error bars indicate ±one standard deviation.

The apparent increases in β with ϵ' in Fig. 4 could result from the changing geometry of the experiment rather than material properties of the sample. Because sound speeds are significantly higher in all samples ($1556\ \text{m/s} \leqslant c \leqslant 1590\ \text{m/s}$) than in the surrounding water (1483 m/s), it is possible that compression varies the degree of sound wave refraction and thus modifies the echo detected. We explored this possibility by constructing samples A and B. Both are type I materials and neither contained added scatterers. The only difference is

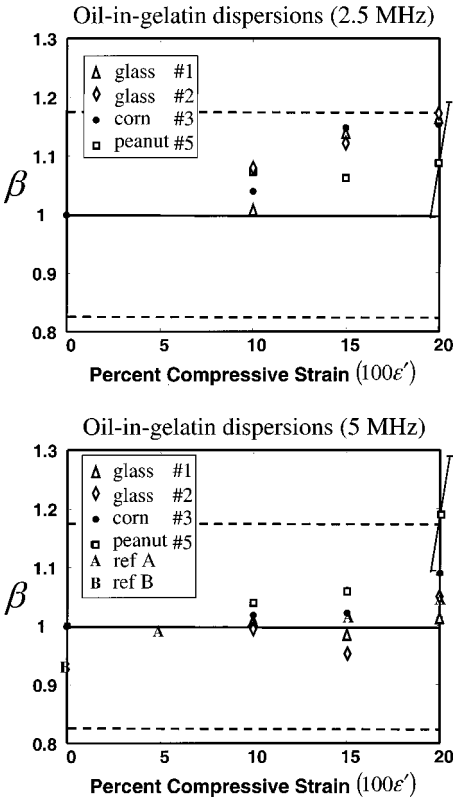

FIG. 4. Attenuation coefficients in dB/cm, normalized by the values at 0% compression, $\beta(\epsilon') = \alpha(\epsilon')/\alpha_0$, are plotted versus percent compression. (a) 2.5 MHz and (b) 5.0 MHz. △, sample 1; ◇, sample 2; ●, sample 3; and □, sample 5. Error bars indicate $\pm\sigma_\beta$. In (b), points labeled A and B refer to measurements on samples A and B, as discussed in Sec. III. The solid line is $\beta(\epsilon') = 1$ and the dashed lines define the 99% confidence interval that the expected value is unity.

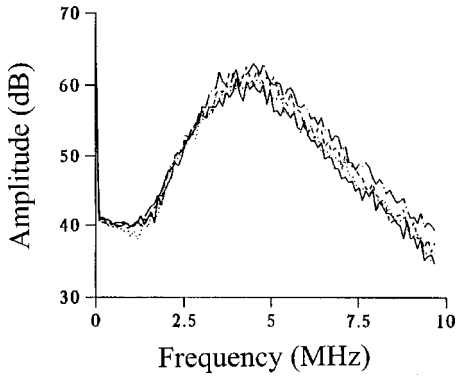

FIG. 5. Backscattered echo spectra via Eq. (4) are plotted for sample 3 at 0% (solid), 10% (dotted), 20% (dashed), and 30% (dot–dashed) compression.

that sample A is 2.5 cm thick while sample B is 2.0 cm thick (80% of A). We also eliminated the thin Lexan compression layer from the measurement and replaced it with a 2.5-cm thick agar plate having a speed of sound matched to distilled water at room temperature to avoid reverberation. The elastic modulus of the agar was approximately 500 times that of the gelatin sample and therefore did not deform significantly during sample compression.

The attenuation coefficients, Eq. (3), for uncompressed samples A and B at 5 MHz are α_A (5 MHz, 0, 22 °C) = 0.69 ± 0.12 dB/cm and α_B (5 MHz, 0, 22 °C) = 0.64 ± 0.16 dB/cm. $\beta(\epsilon')$ increases slightly with ϵ' for sample A, similar to the type I samples with scatterers [Fig. 4(b)], reaching a maximum at $\beta(0.2) = 1.043$. The experimental conditions for sample A compressed to $\epsilon' = 0.2$ and uncompressed sample B are identical, so the 7% attenuation difference, if significant, can only be due to the stress in sample A. The difference is not significant, however, because the lack of scatterers reduces the attenuation value and hence increases the relative uncertainty: $\beta_{B/A}(0) = \alpha_B(0)/\alpha_A(0) = 0.928 \pm 0.262$ (s.d.).

We conclude (a) that it is the varying measurement geometry and/or an absorption process in the stressed gelatin that produces a small increase in attenuation with ϵ', the former being most likely. (b) Surface reverberations and the magnitude of volumetric scattering do not affect β. (c) There is no significant difference in β for type I and II samples. Consequently, we set $\alpha(f, \epsilon', T) \simeq \alpha(f, T)$ for the purpose of spectral estimation. This decision is discussed further in Sec. III and Appendix B.

Backscatter. Figure 5 suggests an obvious change in the backscatter echo spectra with ϵ' for the corn oil sample. As this sample is compressed, the amplitudes of high-frequency spectral components are increased more than those at lower frequencies. This trend is more clearly visible in the measured centroid shifts plotted in Fig. 6; $\Delta f_c = f_c(\epsilon') - f_c(0)$, where $f_c(0)$ is the average value for all six uncompressed samples listed in Tables I and II. Note that $f_c(0)$ is determined primarily by the response of the ultrasound system for random scattering media, so it is not surprising that the centroids measured for each undeformed sample are similar. For $0 \leqslant \epsilon' \leqslant 0.3$, the centroid shifts measured for the two glass-in-gel samples were essentially zero. That is expected for stiff scatterers that are spatially reoriented but not individually

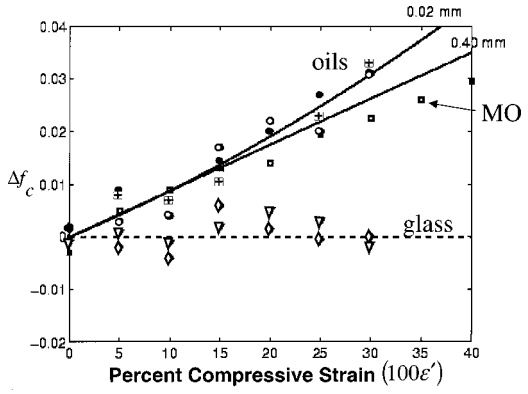

FIG. 6. Measured change in centroid values for stiff scatterers (◇, sample 1 and ▽, sample 2) and soft scatterers (●, sample 3; +, sample 3′; ○, sample 5; and □, sample 6). Measured values obtained via Eq. (5) were subtracted from the average value of all samples measured at 0% compression. Data from the mineral oil sample is marked MO. Solid curves are predicted centroid shifts for oil-droplet spheroidal scatterers with uncompressed diameters of 20 and 400 μm.

deformed—the scattering function is unchanged. The number density of scatterers remains constant with ϵ' because the gelatin volume is conserved under deformation. However, liquid oil scatterers, being softer than the gel, easily deform with the gelatin, which alters the scattering function. Since the centroid frequency increases, it appears that the change in oil drop shape results in increased scattering at higher frequencies.

Measured values of Δf_c for oil-in-gel samples are plotted as points along with predicted values, $\Delta \tilde{f}_c$, displayed as solid lines in Fig. 6. We see larger centroid shifts for smaller oil drops at higher compressions. We examined the surface of several oil-in-gel samples under an inspection microscope and found that the two corn oil and the peanut oil samples had the smallest mean oil-drop diameter, roughly 20 μm. The average diameter of mineral oil drops was much larger, roughly 400 μm. The oil-drop size appears to be determined by oil viscosity and mixing time. The agreement among measured and predicted values in Fig. 6 leads us to conclude that the deformation of scatterers softer than the background produces measurable and predictable changes in the *mean* echo spectrum not observed with scatterers much stiffer than the background.

Samples were found to fracture at $0.3<\epsilon'<0.4$. Therefore c, α measurements were limited to $\epsilon'<0.2$ to ensure sample integrity for scattering measurements. Echo spectra were acquired on each sample at 5% increments until fractures became evident.

IV. DISCUSSION

Scattering in most soft biological tissues is believed to be a small percentage of the total attenuation. Absorption mechanisms dominate propagational losses.[26] Based on more than a decade of experimentation with phantoms, our impressions are that scattering equals or exceeds absorptive losses in glass-in-gel samples with glass-sphere diameters greater than 20 μm, and absorption dominates attenuation in the oil-in-gel dispersion samples. However, measurements of total scattering cross sections are needed to make that determination, and those measurements have not been made. Given these observations, it is not surprising that the mean echo spectrum in compressed dispersions can change without significantly affecting attenuation. We did not correct the spectral estimates for the slight increase in attenuation with ϵ'. Had we applied the correction, the centroid shift Δf_c would be slightly larger and the difference between type I and II scatterers in Fig. 6 would be greater. Also, correcting echo spectra for $\beta(\epsilon')$ would yield an in increase Δf_c for type I materials, which seems likely. These effects are examined quantitatively in Appendix B.

The observed spectral variance suggests that echo waveforms from lipid-filled biological media, such as breast tissue, can decorrelate when strained. Figure 6 shows that Δf_c is proportional to ϵ' for compressions up to 10%. Greater than 10%, the magnitude of the centroid shift depends on scatterer diameter, increasing faster for smaller Rayleigh scatterers than larger Mie scatterers. This source of waveform decorrelation, which has not been discussed in the literature previously, could pose fundamental limitations for elasticity imaging of tissues with lipid-filled scattering sites.

We anticipated the effects of simple scaling strains on the frequency response of scattering from random *point* targets, and suggested a pulse-shaping method to mitigate waveform decorrelation.[11] Pulse shaping would be helpful for strain estimation in the glass-in-gel samples. However, the deformation of finite-size scatterers, as described in this report, further decorrelates echo waveforms in a manner that cannot be anticipated or compensated in an individual spectrum, e.g., that from a single time series. Scatterer deformation changes the scattering response and hence is an irreversible source of echo decorrelation. Strain imaging algorithms that work well in simulation or using phantom data, usually perform at a reduced level in tissues, in the sense that decorrelation noise is increased.[27]

Spectral variance poses problems for strain imaging but also offers opportunities to identify the sources of scattering in biological media. Measurements of Δf_c in breast tissues, for example, may be used to distinguish the relative contribution of scattering from collagen-filled (stiff) versus lipid-filled (soft) structures. If $\Delta f_c=0$, we can assume any lipid component to the tissue acts as a matrix media that contains scatterers but does not scatter sound significantly. Alternatively, if the centroid increases linearly with compression, then it is likely that soft, deformable scatterers play a significant role in echo formation.

V. CONCLUSIONS

The average sound speed, attenuation, and echo spectrum from random, tissue-like scattering media containing stiff spheres is unchanged by uniaxial compressions up to 40%. This finding verifies a fundamental assumption required for strain imaging using these media. However, the mean echo spectrum increases with compressive strain preferentially at high frequency and in a predictable manner for media containing deformable scatterers. Consequently, the use of ultrasonic echoes to track movement of lipid-filled scattering objects in the body will suffer additional waveform decorrelation in proportion to ϵ'. These effects were

observed in phantoms but have yet to be examined in biological tissues. Our results suggest caution in designing strain imaging techniques and new opportunities for identifying scattering sources in biological media.

ACKNOWLEDGMENTS

The valuable assistance of Birgit Trummer and Gernot Plevnik is gratefully acknowledged. This study was supported in part by National Institute of Health NIH Grant No. CA82497.

APPENDIX A

In this appendix we briefly summarize the scattering equation for the oblate spheroid described by Senior and Uslenghi,[28] which is applied in the last part of Sec. II.

An oblate spheroid is formed by rotating an ellipse about its minor axis. Plane sound waves at wavelength λ and temporal frequency f,

$$p_i = \exp[i2\pi(x_3/\lambda - ft)], \tag{A1}$$

are assumed to be incident on the spheroid. The minor spheroid axis, direction of wave propagation, and direction of the applied deformation force are all oriented along x_3 (Fig. 1). The time-independent form of the scattered pressure in the farfield of one acoustically soft spheroid (''soft'' means the pressure difference across the scatterer surface is zero) is

$$p_f = -2\sum_{n=0}^{\infty} \frac{i^n}{N_n(-iq)} \frac{R_n^{(1)}(-iq, i\xi_1)}{R_n^{(3)}(-iq, i\xi_1)} \times R_n^{(3)}(-iq, i\xi_1) S_n(-iq, -1) S_n(-iq, \eta). \tag{A2}$$

(ξ, η, ϕ) are spheroidal coordinates related to rectangular coordinates (x_1, x_2, x_3) via

$$x_1 = \frac{b}{2}\sqrt{(\xi^2+1)(1-\eta^2)}\cos\phi,$$
$$x_2 = \frac{b}{2}\sqrt{(\xi^2+1)(1-\eta^2)}\sin\phi, \quad x_3 = \frac{b}{2}\xi\eta, \tag{A3}$$

where $0 \leqslant \xi < \infty$, $-1 \leqslant \eta \leqslant 1$, and $0 \leqslant \phi < 2\pi$. ξ and η contours form sets of confocal ellipses and hyperbolas, respectively, that have been rotated about the minor axis, which is parallel to x_3. The surface $|\xi| = \xi_1$ (constant) defines the scatterer boundary with major axis length $b(\xi^2+1) = r_0/\sqrt{1-\epsilon'}$ and minor axis length $b|\xi| = (1-\epsilon')r_0$. The last two expressions give the relationship between engineering strain and scatterer geometry in elliptical coordinates. q is the product of the wave number, $2\pi/\lambda$, and half the elliptical interfocal distance, $b/2$.

The advantage of elliptical coordinates is that the wave equation becomes separable in terms of radial and angular solutions. $R_n^{(j)}(-ic', i\xi)$, $j = 1,2,3$ are radial spheroidal wave functions of the jth kind, and $S_n(-ic', \eta)$ are angular spheroidal wave functions, where n is a positive integer. [Note that plane waves incident along the minor axis means that the subscript integer m found for these wave functions in (Ref. 28) is zero. For example, $R_{mn}^{(j)}(-ic', i\xi)|_{m=0} \equiv R_n^{(j)}(-ic', i\xi)$.] These are the radial and angular ''solutions'' to the wave equation in spheroidal coordinates. $S_n(-ic', \eta)$ are found from expansions in associated Legendre functions of the first kind.[29] Similarly, $R_n^{(j)}(-ic', i\xi)$ are formed from sums of weighed spherical Bessel functions. $N_n(-ic')$ are functions of associated constants, including eigenvalues for the differential equation. These are formed using recurrence formulas and tables of constants given by Flammer.[29] The notation, derivations, and formulas coded in FORTRAN and MATLAB for our application are due to Flammer, although relations described by Lowan in Chap. 21 of Abramowitz and Stegun on spherical wavefunctions[30] were helpful. Readers wishing to do the same should be aware of differences in the coordinate systems used in these[28–31] and other references and a few typos, e.g., a missing minus sign in Eq. (3.1.7) in Ref. 29.

Tabulated values for functions and constants are given in several of the references cited above. These were used to determine the number of terms in the respective sums needed for convergence. Convergence was established when the computed values varied from the tabulated values less than 0.01%.

APPENDIX B

In this appendix we explore the magnitude of the effects of ultrasonic frequency-dependent attenuation on the spectral centroid and explains our model for echo formation.

Assume a linear, time-invariant imaging system that maps the acoustic impedance function for the object being scanned, $z(x)$ into an echo sample g_m via the convolution integral adapted from Maurice and Bertrand,[32]

$$g_m = \left[\int_{-\infty}^{\infty} dx\, h\left(t_m - \frac{2x}{c}\right) z''(x)\right] + n_m.$$

Acoustic impedance and its second derivative, $z'' = \partial^2 z/\partial x^2$, are generally functions of three spatial dimensions but for this purpose are simplified to one dimension x. Derivatives are taken along the direction of wave travel. n_m is a noise sample. $h(t)$ is the pulse-echo impulse response, having carrier frequency f_0 and pulse-length parameter σ_t, that we model for all time t assuming the Gaussian form,

$$h(t) = \frac{1}{\sqrt{2\pi}\sigma_t}\exp(-t^2/2\sigma_t^2)\sin(2\pi f_0 t). \tag{B1}$$

It is known that if you represent the object function $z(x)$ as a spatially uncorrelated Gaussian random variable, the expected frequency spectrum of the echo data is determined by the impulse response of the imaging system.[33] Furthermore, it has been shown that the echo amplitude from a Gaussian pulse undergoing Rayleigh scattering and exponential attenuation remains Gaussian, although the peak frequency and spectral width vary (see Appendix C in Ref. 34). Consequently, it is reasonable to represent the magnitude of the echo frequency response as

$$|H(f)| = \exp[-2\pi^2(f-f_0)^2\sigma_t^2], \quad f \geqslant 0 \tag{B2}$$

where $H(f)$ is the Fourier transform of $h(t)$. From Eq. (5), it can be shown that the centroid frequency for $|H(f)|$ is f_0.

Our concern is the change in spectral centroid from excess attenuation caused by sample compression. We model the effects of excess attenuation as a change in the frequency response of the measurement system,

$$|H(f,\epsilon')| = \exp[-2\pi^2(f-f_0)^2\sigma_t^2] \times \exp[-\mathcal{A}(f,\epsilon')], \quad f \geqslant 0. \tag{B3}$$

The excess attenuation, $\mathcal{A}(f,\epsilon')$, is found from the ratio of attenuation factors,

$$\exp[-\mathcal{A}(f,\epsilon')] = \frac{\exp[-2(\alpha L - \alpha_0 L_0)]}{\exp[-2\alpha_0(L-L_0)]} = \exp[-2L(\alpha-\alpha_0)],$$

where $\alpha \equiv \alpha(f,\epsilon') \geqslant \alpha_0 \equiv \alpha(f,0)$, and L_0, L are the sample thicknesses before and after compression producing strain ϵ'. Therefore

$$\mathcal{A}(f,\epsilon') = 2L(\alpha-\alpha_0) = 2\alpha_0 L_0(1-\epsilon')(\beta-1), \tag{B4}$$

where $\beta = \alpha/\alpha_0$ and $\epsilon' = (L_0 - L)/L_0$ were defined previously. If there is no excess attenuation, $\alpha = \alpha_0$ and $\mathcal{A}(f,\epsilon') = 0$.

We modeled the attenuation coefficient in Eq. (B4) as a quadratic function of frequency, $\alpha_0 = q_0 + q_1 f + q_2 f^2$; see Tables I and II. Defining the constants $C = 2L_0(1-\epsilon')(\beta-1)$, $C_1 = 1 + q_2 C/2\pi^2\sigma^2$, and combining the exponent of Eq. (B3) with Eq. (B4) and the quadratic attenuation model, we find

$$-2\pi^2\sigma_t^2\left(f^2 - 2ff_0 + f_0^2 + C\frac{q_0 + q_1 f + q_2 f^2}{2\pi^2\sigma_t^2}\right) = -2\pi^2\sigma_t^2 C_1\left[f^2 - \frac{2}{C_1}\left(f_0 - \frac{Cq_1}{4\pi^2\sigma^2}\right)f + \frac{f_0^2}{C_1} + \frac{Cq_0}{2\pi^2\sigma^2 C_1}\right]. \tag{B5}$$

Adding and subtracting the term

$$\frac{1}{C_1^2}\left(f_0 - \frac{Cq_1}{4\pi^2\sigma^2}\right)^2$$

from Eq. (B5) allows us to complete the square and find

$$-2\pi^2\sigma_t^2 C_1\left\{\left[f - \frac{1}{C_1}\left(f_0 - \frac{Cq_1}{4\pi^2\sigma_t^2}\right)\right]^2 - \frac{f_0^2}{C_1^2}(1-C_1)\right\} + \frac{C^2 q_1^2}{8\pi^2\sigma_t^2 C_1^2} - \left(Cq_0 + \frac{f_0 q_1 C}{C_1}\right). \tag{B6}$$

The effect of excess attenuation $\mathcal{A}(\epsilon')>0$ on the magnitude of the backscattered spectrum is given by terms that depend on frequency, viz., the first term in Eq. (B6). The spectral width is modified by the factor C_1 and the centroid is downshifted from f_0 by the amount

$$\frac{1}{C_1}\left(f_0 - \frac{Cq_1}{4\pi^2\sigma_t^2}\right) - f_0. \tag{B7}$$

Figure 4(a) shows $\beta_{\max} \simeq 1.17$ at $\epsilon' = 0.2$. In all cases $L_0 = 2.54$ cm. The coefficients q_0, q_1, and q_2 for the samples are listed in Tables I and II (in dB). For a Gaussian pulse at 2.5 MHz center frequency having a full-width-at-half-maximum value of two wavelengths, $\sigma_t = 1/\sqrt{2\ln 2} f_0 = 0.34\,\mu$s. With these values and Eq. (B7), the attenuation-compensated centroid shifts measured for the oil-in-gel samples would increase values in Fig. 6, at most, by 13 kHz at $\epsilon' = 0.2$. Corresponding values of Δf_c for the glass-in-gel samples would increase, at most, 6.5 kHz for sample 1 and 4.1 kHz for sample 2 if compensated for attenuation. Thus compensating for attenuation effects on the backscatter spectra would increase the relative differences between the measurements for type I and II samples shown in Fig. 6.

[1] A. Ishimaru, *Wave Propagation and Scattering in Random Media: Single Scattering and Transport Theory* (Academic, New York, 1978), Vol. I.
[2] R. C. Waag, IEEE Trans. Biomed. Eng. **31**, 884 (1984).
[3] S. Fields and F. Dunn, J. Acoust. Soc. Am. **54**, 809 (1973).
[4] D. K. Nassiri and C. R. Hill, J. Acoust. Soc. Am. **79**, 2048 (1986).
[5] R. C. Waag, D. Dalecki, and P. E. Christopher, J. Acoust. Soc. Am. **85**, 423 (1989).
[6] F. Lizzi, M. Ostromogilsky, E. Feleppa, M. Rorke, and M. Yaremko, IEEE Trans. Ultrason. Ferroelectr. Freq. Control **34**, 319 (1987).
[7] M. F. Insana and D. G. Brown, "Acoustic scattering theory applied to soft biological tissues," in *Ultrasonic Scattering in Biological Tissues*, edited by K. K. Shung and G. A. Thieme (CRC Press, Boca Raton, 1993), pp. 75–124.
[8] J. H. Rose, M. R. Kaufman, S. A. Wickline, C. S. Hall, and J. G. Miller, J. Acoust. Soc. Am. **97**, 656 (1995).
[9] D. J. Coleman, *et al.*, Eur. J. Ophthalmol. **5**, 96 (1995).
[10] M. F. Insana, J. G. Wood, T. J. Hall, G. G. Cox, and L. A. Harrison, Ultrasound Med. Biol. **21**, 1143 (1995).
[11] M. Bilgen and M. F. Insana, J. Acoust. Soc. Am. **99**, 3212 (1996).
[12] The bulk modulus $\mathcal{K}$ is traditionally defined from the pressure/volume ratio and describes how a medium changes volume when subjected to a force (Ref. 35). The shear modulus $\mathcal{G}$ is traditionally defined from the shear stress/shear strain ratio and describes how a medium changes shape when subjected to a force. In soft biological tissues $\mathcal{K} \gg \mathcal{G}$ so that the elastic modulus $= 9\mathcal{G}\mathcal{K}/(3\mathcal{K}+\mathcal{G}) \simeq 3\mathcal{G}$ and Poisson's ratio $= 3\mathcal{K} - 2\mathcal{G}/(6\mathcal{K}+2\mathcal{G}) \simeq 0.5$.
[13] E. L. Madsen, J. A. Zagzebski, and G. R. Frank, Ultrasound Med. Biol. **8**, 277 (1982).
[14] S. Goss, R. Johnston, and F. Dunn, J. Acoust. Soc. Am. **68**, 93 (1980).
[15] T. J. Hall, M. Bilgen, M. F. Insana, and T. A. Krouskop, IEEE Trans. Ultrason. Ferroelectr. Freq. Control **44**, 1355 (1997).
[16] Engineering strain is often defined as the negative of this quantity. Since we are most interested in compressive deformations, it is convenient to drop the minus sign.
[17] Y. C. Fung, *A First Course in Continuum Mechanics*, 3rd ed. (Prentice–Hall, Englewood Cliffs, NJ, 1994).
[18] M. Greenspan and C. E. Tschiegg, J. Acoust. Soc. Am. **31**, 75 (1959).
[19] F. Dunn, P. D. Edmonds, and W. J. Fry, "Absorption and dispersion of ultrasound in biological media," in *Biological Engineering* (McGraw-Hill, New York, 1969), pp. 214–215.
[20] A. V. Oppenheim, R. W. Schafer, and J. R. Buck, *Discrete-Time Signal Processing*, 2nd ed. (Prentice–Hall, Upper Saddle River, NJ, 1999).
[21] To avoid confusion, we note here that spectral estimates for single-trace time series do vary with compression. In fact, those changes have been used to estimate blood velocity (Ref. 36) and strain (Ref. 37). An ensemble average of time series yields an echo spectrum that depends only on the scattering and absorption coefficients of the random medium and the system response function. Because the system response does not change, variations in the average echo spectrum with compression are caused by changes in the medium properties.
[22] R. N. Bracewell, *The Fourier Transform and Its Applications*, 2nd ed. (McGraw-Hill, New York, 1978).
[23] J. Bendat and A. Piersol, *Random Data Analysis and Measurement Procedures*, 2nd ed. (Wiley, New York, 1986).
[24] P. R. Bevington, *Data Reduction and Error Analysis for the Physical Sciences* (McGraw-Hill, New York, 1969).
[25] M. F. Insana, R. F. Wagner, D. G. Brown, and T. J. Hall, J. Acoust. Soc. Am. **87**, 179 (1990).

[26] M. E. Lyons and K. J. Parker, IEEE Trans. Ultrason. Ferroelectr. Freq. Control **35**, 511 (1988).
[27] Y. Zhu, P. Chaturvedi, and M. F. Insana, Ultrason. Imaging **21**, 127 (1999).
[28] J. J. Bowman, T. B. A. Senior, and P. L. E. Uslenghi, *Electromagnetic and Acoustic Scattering by Simple Shapes* (North-Holland, Amsterdam, 1969), Chap. 13.
[29] C. Flammer, *Spheroidal Wave Functions* (Stanford University Press, Stanford, CA, 1957).
[30] A. N. Lowan, ''Spheroidal wave functions,'' in *Handbook of Mathematical Functions With Formulas, Graphs, and Mathematical Tables*, edited by M. Abramowitz and I. Stegun (Dover, New York, 1965).
[31] P. M. Morse and H. Feshbach, *Methods of Theoretical Physics* (McGraw-Hill, New York, 1953).
[32] R. L. Maurice and M. Bertrand, IEEE Trans. Med. Imaging **18**, 593 (1999).
[33] R. F. Wagner, S. W. Smith, J. M. Sandrick, and H. Lopez, IEEE Trans. Sonics Ultrason. **30**, 156 (1983).
[34] M. F. Insana, L. T. Cook, M. Bilgen, and P. Chaturvedi, J. Acoust. Soc. Am. **107**, 1421 (2000).
[35] N. W. Tschoegl, *The Phenomenological Theory of Linear Viscoelastic Behavior* (Springer-Verlag, Heidelberg, 1989).
[36] J. A. Jensen, *Estimation of Blood Velocities Using Ultrasound* (Cambridge University Press, New York, 1996).
[37] E. E. Konofagou, T. Varghese, J. Ophir, and S. K. Alam, Ultrasound Med. Biol. **25**, 1115 (1999).

A point process approach to assess the frequency dependence of ultrasound backscattering by aggregating red blood cells

David Savéry and Guy Cloutier[a)]
Laboratory of Biomedical Engineering, Clinical Research Institute of Montréal, 110 Avenue des Pins Ouest, Montréal, Québec H2W 1R7, Canada and Laboratory of Biorheology and Medical Ultrasonics, University of Montréal Hospital, Québec, Canada

(Received 29 December 2000; accepted for publication 9 September 2001)

To study the shear-thinning rheological behavior of blood, an acoustical measurement of the erythrocyte aggregation level can be obtained by analyzing the frequency dependence of ultrasonic backscattering from blood. However, the relation that exists among the variables describing the aggregation level and the backscattering coefficient needs to be better clarified. To achieve this purpose, a three-dimensional random model, the Neyman–Scott point process, is proposed to simulate red cell clustering in aggregative conditions at a low hematocrit ($H<5\%$). The frequency dependence of the backscattering coefficient of blood, in non-Rayleigh conditions, is analytically derived from the model, as a function of the size distribution of the aggregates and of their mass fractal dimension. Quantitative predictions of the backscatter increase due to red cell aggregation are given. The parametric model of backscatter enables two descriptive indices of red cell aggregation to be extracted from experimental data, the packing factor W and the size factor Δ. Previously published backscatter measurements from porcine whole blood at 4.5% hematocrit, in the frequency range of 3.5 MHz–12.5 MHz, are used to study the shear-rate dependence of these two indices.
 [DOI: 10.1121/1.1419092]

PACS numbers: 43.80.Cs, 43.80.Jz, 43.35.Bf [FD]

LIST OF SYMBOLS

a	mean radius of the red blood cells
B	a compact set of points
c	speed of sound
$\overline{C}$	relative impedance mismatch between red cells and plasma
D	mass fractal dimension
Δ	size factor
δ	Dirac δ-function
$E[A]$	mathematical expected value of a random variable A
f, f_0, f_i	frequencies
$f_X(\boldsymbol{x})$	probability density function of $\boldsymbol{X}$
Φ	eigenvectors matrix of the covariance matrix $E[\boldsymbol{X}^T\boldsymbol{X}]$
$g(\boldsymbol{r})$	pair-correlation function
H	hematocrit
I	identity matrix
I_{incident}	intensity of the incident pressure wave
j	$\sqrt{-1}$
$J(W,\Delta)$	quadratic error to minimize for nonlinear regression
$J_{\min}$	minimal value of $J(W,\Delta)$
$\boldsymbol{k}, \boldsymbol{k}_i$	incident wave vectors
$\chi(\boldsymbol{k})$	backscattering coefficient
κ_0	compressibility
l_{cor}	correlation length
λ	wavelength
M	total number of particles
m	number density
m_0	number density of the aggregates
$N(\boldsymbol{x})$	local microscopic density
$N_c, N_c(i)$	random numbers of particles per aggregate
n_c	mean number of particles per aggregate, $E[N_c]$
$d\Omega$	solid angle of observation relatively to the scattering volume
P	probability
dP	power of the backscattered wave in $d\Omega$
$\boldsymbol{q}$	scattering vector ($-2\boldsymbol{k}$ for backscattering)
$\boldsymbol{r}$	spatial position of the observer
ρ_0	mass density
$S(\boldsymbol{q})$	structure factor $=(1/M)\lvert\Sigma_i \exp(-j\boldsymbol{q}\cdot\boldsymbol{x}_i)\rvert^2$
Σ	diagonal matrix of the eigenvalues of the covariance matrix $E[\boldsymbol{X}^T\boldsymbol{X}]$
σ	standard deviation of $\boldsymbol{X}$ when $\boldsymbol{X}$ is isotropic
$\sigma_b(-2\boldsymbol{k})$	backscattering cross-section
σ_c	standard deviation of N_c, $\sigma_c^2=E[N_c^2]-E[N_c]^2$
A^T	transposition of a matrix A
V_s	volume of the particle
V_B	volume of the compact set B
dV	scattering volume
W	packing factor $=\lim_{\boldsymbol{q}\to 0} S(\boldsymbol{q})$
$X=\{\boldsymbol{x}_i\}_{i=1\ldots M}$	set of the random positions of the red blood cells
$\boldsymbol{X}$	random position of a red cell inside a centered aggregate
$\boldsymbol{X}_{il}$	position of the lth particle inside the ith aggregate
$\boldsymbol{x}$	position within the scattering volume

[a)]Electronic mail: guy.cloutier@umontreal.ca

$Y=\{\boldsymbol{Y}_i\}$	set of the random positions of the centers of aggregates
Z_p	acoustical impedance of the particle
Z_0	mean acoustical impedance
$Z_X(B)$	random number of particles of X falling into the compact set B

I. INTRODUCTION

Blood is a complex tissue to characterize by ultrasonic means because of its heterogeneous structure. Blood interacts with acoustic waves because of the presence of cells flowing in the plasma (99% are red cells) that scatter ultrasound nonisotropically. The high density of red cells (their volumic fraction reaches about 45%) and their ability to form reversible aggregates under the cumulative effects of chemical, physical and hydrodynamic interactions create intricate spatial structures that influence the scattering properties of blood.

Clinically, the purpose of blood characterization by ultrasound is to offer the possibility of investigating *in vitro* and *in vivo* the rheological attributes of blood. The viscoelasticity and the thixotropy of blood strongly depend on the formation and disruption of red blood cell aggregates and any disturbance in these mechanical parameters can alter the micro and macrocirculation by initiating stasis zones, enhancing thrombus formation, and favoring tissue ischemia.[1] It would consequently be relevant to assess *in vivo* the hemorheological disorders of patients and to take them into account in conventional cardiovascular risk profiles.[2]

Classical tissue characterization techniques consist of finding the frequency dependence of attenuation and backscatter properties of the material and using them as acoustical indicators of the underlying microstructure. This was proven useful to detect diseased tissues in several clinical applications. Infarcted myocardium,[3] atherosclerotic carotid arteries[4] or cirrhotic livers[5] were shown to have scattering properties that differ from their healthy counterparts. Spectral characterization of blood backscattering has already been performed experimentally[6–8] and has shown sensitivity to the microstructural packing state of the red blood cells.

Theoretical efforts have been made to elucidate the relation between the backscattering properties of blood, usually quantified by the value of the backscattering coefficient, and the frequency of the incident wave, the hematocrit, the flow condition (steady state or turbulent), or the red cell aggregation level.[9–13] Twersky[9] proposed a parameter called packing factor to describe the backscattering coefficient of a distribution of hard particles. The primary assumption of this theory is that the spatial scale of the inhomogeneities in acoustical impedance must be much smaller than the acoustical wavelength.

This approximation succeeds to explain the hematocrit dependence of the backscattering by nonaggregating suspensions of red cells but fails to predict the frequency dependence observed in experimental conditions when red cell aggregation is significant. As the packing factor is independent on the frequency, the backscattering coefficient is expected to increase linearly with the fourth power of the frequency[14] in the low frequency approximation. However Yuan and Shung,[6] Foster *et al.*,[7] and Van der Heiden *et al.*[8] observed that the frequency dependence of blood is lower when the flow rate is decreased, and thus when the aggregation is enhanced for frequencies as low as 3.5 MHz.

These results suggest that the theoretical understanding of blood scattering at higher frequencies is incomplete. We propose to generalize the packing factor theory for higher frequencies by introducing the frequency-dependent structure factor. It is intended to use it as a spectral signature of the aggregation process that is more relevant for ultrasonic characterization than a single measurement at a low frequency.

The purpose of this study was to predict the frequency dependence of the backscattering coefficient from blood characterized by different levels of red blood cell aggregation. It is hypothesized that the spatial pattern formed by the aggregates of red cells governs the backscattering strength of blood. Red cell positioning is modeled as a random spatial point-process and it is considered that red cell aggregation modifies the statistical parameters of this random phenomenon. The Neyman–Scott process (NSP) gives a random framework that is convenient for the analytical derivation of the backscattering coefficient. In this paper, the method used to theoretically predict the backscattering coefficient of a weak scattering suspension is described in Sec. II, then the NSP is introduced in Sec. III to model red cell aggregation and to derive the analytical expression of the backscattering properties of blood. In Sec. IV, results on the predicted effects of red cell aggregation on the backscattering coefficient are given, and the question of inferring descriptive aggregation parameters using experimental backscatter data is discussed.

II. SCATTERING BY A SUSPENSION OF WEAK SCATTERERS

A. Decomposition of the backscattering coefficient

The propagation of an acoustic wave into a linear medium depends on the spatial distribution of density $\rho_0(\boldsymbol{x})$ and compressibility $\kappa_0(\boldsymbol{x})$, where $\boldsymbol{x}$ represents the spatial position. When these spatial functions are precisely known, the wave equation can be theoretically solved once the source parameters are given, and conveys the relation between the pressure measured at the surface of the receiver and the various acoustic properties of the medium. In a heterogeneous medium like blood, it would be difficult to describe accurately the exact spatial distributions of density and compressibility. This is why the propagation medium is seen, in this article, as a realization of a random process which can be characterized by statistical mean parameters that depict its macroscopical properties. Measurement of the backscattering properties of a sample of this material should provide clues on the value of these mean parameters as shown in this section.

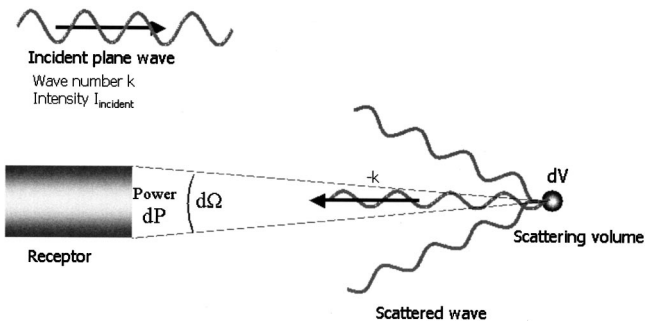

FIG. 1. Scattering experiments and symbols.

In this paper, we assume that an ideal backscattering experiment (Fig. 1) consists of the insonification of a material volume dV by a monochromatic pressure plane wave of intensity I_{incident} and by the measurement of the power dP of the backscattered wave into a small solid angle $d\Omega$. The result is expressed in normalized terms ($\text{m}^{-1}\,\text{sr}^{-1}$) by the differential backscattering coefficient. If the incident plane wave has a wave vector $\boldsymbol{k}$ ($|\boldsymbol{k}|=2\pi/\lambda$, λ being the wavelength), the (differential) backscattering coefficient $\chi(\boldsymbol{k})$ is defined by:

$$\chi(\boldsymbol{k})=\frac{dP}{I_{\text{incident}}d\Omega\, dV}. \tag{1}$$

The fluctuations in density and compressibility within blood are supposed small enough to hypothesize that the Born approximation is valid. We also assume that the medium dV is composed of $M=m\,dV$ identical spherical particles whose centers are positioned in $\{\boldsymbol{x}_i\}_{i=1\ldots M}$, m being the number density of the particles. The M particles are embedded in a homogeneous medium (like the plasma) with a mean characteristic acoustical impedance Z_0.

These hypotheses allow to write the backscattering coefficient in the known factorized form:[9]

$$\chi(\boldsymbol{k})=mS(-2\boldsymbol{k})\sigma_b(-2\boldsymbol{k}). \tag{2}$$

In Eq. (2) are introduced the structure factor $S(\boldsymbol{q})=(1/M)\left|\sum_{i=1}^{M}e^{-j\boldsymbol{q}\cdot\boldsymbol{x}_i}\right|^2$, function of the scattering vector $\boldsymbol{q}=-2\boldsymbol{k}$, and the backscattering cross-section of the individual scatterer $\sigma_b(-2\boldsymbol{k})$.

For weak scattering spherical particles of radius a and volume $V_s=\frac{4}{3}\pi a^3$, the backscattering cross-section is given by:[15]

$$\sigma_b(-2\boldsymbol{k})=\frac{1}{4\pi^2}V_s^2\overline{C}^2k^4\left(3\frac{\sin(2ka)-2ka\cos(2ka)}{(2ka)^3}\right)^2, \tag{3}$$

where $\overline{C}=(Z_p-Z_0)/Z_0$ is the small relative mismatch between Z_p, the particle impedance, and Z_0.

Equation (2) exhibits the expected result that the scattering strength of a tissue depends on the intrinsic acoustical properties of the scatterers, described by the backscattering cross-section $\sigma_b(-2\boldsymbol{k})$, and also on the spatial positioning of particles whose second order statistics are described by the structure factor $S(\boldsymbol{q})$. The aggregation phenomenon is supposed to only affect the structure factor, as red cell properties and hematocrit remain constant in the sample macroscopical volume.

B. Pair-correlation function of a point process and structure factor

The structure factor $S(\boldsymbol{q})$ can be influenced in a complex way by the hematocrit H, the geometric dimension of the particle and also by the physical factors governing the aggregation process. To theoretically estimate variations of the structure factor, the positioning of the scatterers in the medium is considered as a realization of a random point process, that obeys a random model with average parameters characterizing the aggregation level. Theoretically, a point distribution can be described by its microscopic density $N(\boldsymbol{x})$:

$$N(\boldsymbol{x})=\sum_{i=1}^{M}\delta(\boldsymbol{x}-\boldsymbol{x}_i), \tag{4}$$

where δ is the Dirac δ-function and $X=\{\boldsymbol{x}_i\}_{i=1\ldots M}$ are considered as random positions of the scatterers. Writing $\hat{N}(\boldsymbol{q})=\int N(\boldsymbol{x})e^{-j\boldsymbol{q}\cdot\boldsymbol{x}}d\boldsymbol{x}$ the Fourier transform of the microscopic density, the mean structure factor can be derived from the mean energy spectrum of $N(\boldsymbol{x})$ by:

$$S(\boldsymbol{q})=\frac{E[|\hat{N}(\boldsymbol{q})|^2]}{M}, \tag{5}$$

where $E[\,]$ represents the expected value of a random variable. The pair-correlation function

$$g(\boldsymbol{r})=\frac{P(\boldsymbol{x}\in X \text{ and } \boldsymbol{x}+\boldsymbol{r}\in X)}{P(\boldsymbol{x}\in X)P(\boldsymbol{x}+\boldsymbol{r}\in X)},$$

can be related to the structure factor. Writing $E[N(\boldsymbol{x})N(\boldsymbol{x}+\boldsymbol{r})]=m^2g(\boldsymbol{r})+m\,\delta(\boldsymbol{r})$, one derives[9] for $\boldsymbol{q}\neq\boldsymbol{0}$:

$$S(\boldsymbol{q})=1+m\int(g(\boldsymbol{r})-1)e^{-j\boldsymbol{q}\cdot\boldsymbol{r}}d\boldsymbol{r}. \tag{6}$$

This formula shows that variations of the pair-correlation function induced by changes in the spatial organization of the red cells will directly affect the structure factor and the scattering properties of blood.

C. Correlation length and corresponding scattering regimes

Depending on the relative values of the correlation length l_{cor}, defined by $|\boldsymbol{r}|>l_{\text{cor}}\Rightarrow g(\boldsymbol{r})=1$, and of the wavelength λ, two different aggregation regimes can be distinguished. This correlation length can be roughly seen as the diameter of the clusters present in the medium.

1. Rayleigh scattering

When $l_{\text{cor}}\ll\lambda$, we have the low frequency approximation that leads to the definition of the *packing factor W*, the zero-frequency limit of the structure factor. This happens when scatterers are aggregated in clusters much smaller than the wavelength. In this case,

$$\lim_{q\to 0}S(\boldsymbol{q})=W=1+m\int(g(\boldsymbol{r})-1)d\boldsymbol{r}, \tag{7}$$

and

$$\chi(\boldsymbol{k}) = mW\sigma_b(-2\boldsymbol{k}) \approx \frac{1}{4\pi^2} HWV_s \overline{C^2} k^4. \quad (8)$$

A medium with uncorrelated particles, corresponding to $l_{cor} \approx 0$ has thus a unit packing factor. A low hematocrit ($H < 5\%$) suspension of nonaggregating red blood cells can be approximated by such a model. The packing factor can be seen as a corrective factor that takes into account the correlations between positions of scatterers. The variations of the packing factor with the hematocrit, polydispersity and shape of hard particles have been theoretically studied by Twersky.[9,16] For nonaggregating particles, W tends toward 1 when the hematocrit H is low, and vanishes when H is close to 100%, because, in this case, heterogeneities giving birth to scattering no longer exist in the medium. The peak of low frequency backscattering, that arises when HW is maximal, occurs for $H_{max} \approx 13\%$ for nonaggregating spheres but can vary with the shape of the scatterers or with the polydispersity of the distribution.[16]

By definition, W does not depend on the frequency. This low frequency approximation can thus only consider the fourth power frequency dependence (k^4) of the backscattering coefficient in the Rayleigh scattering regime.

2. Non-Rayleigh scattering and aggregation

At least two situations can provoke the irrelevance of the low frequency approximation: either when the acoustical frequency is increased (to obtain a better spatial resolution) or when the aggregation level is so elevated that the correlation length l_{cor} becomes non-negligible compared to the wavelength. One can test the validity of these assumptions by estimating the frequency dependence of the backscattering coefficient, which should be proportional to k^4 under Rayleigh conditions.

Frequency dependencies of the backscattering coefficient of whole blood as low as $k^{1.3}$ (in the frequency range of 22–37 MHz,[8] at a shear rate under 1 s^{-1}) or $k^{0.4}$ (in the range 30–70 MHz,[7] at a shear rate of 0.16 s^{-1}) have been reported in the literature. This shows that the Rayleigh approximation is inappropriate to study scattering from aggregating red cells as a function of the frequency. A particular random spatial point process, the Neyman–Scott process (NSP), is proposed to predict the effect of aggregation on the backscatter data and to clarify the relation between the frequency and the backscattering coefficient.

III. MODELING OF RED CELL AGGREGATION BY THE NEYMAN–SCOTT PROCESS

A. Random point processes

We consider that the set of positions $X = \{\boldsymbol{x}_i\}_{i=1\ldots M}$ of the particle centers is the realization of a random spatial process, M being either constant or a random variable such as $E[M] = m\,dV$. To fully characterize a point process, one can specify[17] the random numbers $Z_X(B)$ of points falling into a compact set B included in dV. The process of aggregation is supposed locally stationary in the sample volume, which implies that the random variable $Z_X(B)$ depends only on the shape of B and not on the position of its center. The pair-correlation function can simply be seen as a second order property, when B is the pair of points $\{\boldsymbol{x}, \boldsymbol{x}+\boldsymbol{r}\}$:

$$g(\boldsymbol{r}) = \frac{P(\boldsymbol{x} \in X \text{ and } \boldsymbol{x}+\boldsymbol{r} \in X)}{P(\boldsymbol{x} \in X)^2}$$

$$= \frac{1 - 2P(Z_X(\{\boldsymbol{x}\}) = 0) + P(Z_X(\{\boldsymbol{x}, \boldsymbol{x}+\boldsymbol{r}\}) = 0)}{[1 - P(Z_X(\{\boldsymbol{x}\}) = 0)]^2}. \quad (9)$$

X is said to be a Poisson process with number density m when $Z_X(B)$ is a Poisson random variable with mean value mV_B, V_B being the volume of B. In this case, Eq. (9) with $P[Z_X(B) = 0] = e^{-mV_B}$ gives $g(\boldsymbol{r}) = 1$. No spatial structure exists in the Poisson point process as the correlation length is zero, and this is why a Poisson point process can be described as a complete random distribution. The evaluation of the structure factor gives, at all frequencies, $S(\boldsymbol{q}) = 1$. A stationary Poisson point process thus cannot be an appropriate model to simulate clusters of scatterers as encountered in certain red cell aggregation conditions.

B. The Neyman–Scott point process

The Neyman–Scott process is a random point process commonly used to model clusters of points. This random model efficiently described different statistical spatial data such as the positioning of trees in the forest,[18] the distribution of precious stones in soil[19] or the patterns of rainfall cells.[20]

The red cells are supposed to be grouped in clusters having random features obeying the same probability law. We intend to characterize aggregate morphology by a small number of geometrical quantities taken as aggregation indices. However, the relation between the different physical interactions involved in the aggregation process (hydrodynamics, depletion or bridging effects of the plasmatic macromolecules, electrostatic forces) and the microstructural factors defining the configurations of erythrocyte clusters will not be directly modeled, as we only want to geometrically describe the aggregation level.

The basis of a realization of an NSP lies on a Poisson process Y with a number density m_0. Each point $\boldsymbol{Y}_i$ is the center of the ith cluster surrounded by a random number $N_c(i)$ of points, sampled from a random variable N_c. To construct this cluster, $N_c(i)$ independent realizations $\{\boldsymbol{X}_{il}\}_{l=1\ldots N_c(i)}$ of a random vector $\boldsymbol{X}$ are generated, and the $N_c(i)$ points $\boldsymbol{Y}_i + \boldsymbol{X}_{il}$ compose the cluster. The microscopic density $N(\boldsymbol{x})$ can then be written as:

$$N(\boldsymbol{x}) = \sum_i \sum_{l=1}^{N_c(i)} \delta(\boldsymbol{x} - \boldsymbol{Y}_i - \boldsymbol{X}_{il}). \quad (10)$$

The parameters needed to fully describe the NSP are thus:

(1) the number density m_0 of the centers of clusters $\{\boldsymbol{Y}_i\}$,
(2) the discrete probability density function $P(N_c = n)$ of the random number N_c of points per cluster,
(3) the spatial probability density function $f_X(\boldsymbol{x})$ of the random vector $\boldsymbol{X}$ (with mean 0), that characterizes the cluster size.

The characteristic function and the two first moments of the discrete distribution $Z_{\mathrm{NSP}}(B)$ have already been computed[17] as a function of the moments of N_c ($n_c = E[N_c]$ and $\sigma_c^2 = \mathrm{Var}[N_c]$), of $f_X(\boldsymbol{x})$ and of the shape of B. The number density m equals $m_0 n_c$ and the pair-correlation function $g(\boldsymbol{r})$ can be determined and is given by:

$$g(\boldsymbol{r}) = 1 + \frac{1}{m}\left(\frac{\sigma_c^2}{n_c} + n_c - 1\right)\int f_X(\boldsymbol{x}) f_X(\boldsymbol{x}+\boldsymbol{r})\, d\boldsymbol{x}. \tag{11}$$

According to Eq. (6), the structure factor can also be derived by computing the Fourier transform of $g(\boldsymbol{r})-1$:

$$S(\boldsymbol{q}) = 1 + \left(\frac{\sigma_c^2}{n_c} + n_c - 1\right)\left|\int f_X(\boldsymbol{x}) e^{-j\boldsymbol{q}\cdot\boldsymbol{x}}\, d\boldsymbol{x}\right|^2. \tag{12}$$

C. Aggregation parameters

The random spatial probability density $f_X(\boldsymbol{x})$ physically characterizes the spatial dimension of the clusters by determining the dispersion of the red cells around the center of an aggregate. We consider here the simplest random vector distribution to model $f_X(\boldsymbol{x})$, i.e., the Gaussian model with zero mean and covariance matrix $E[\boldsymbol{X}^T\boldsymbol{X}] = \Phi^T\Sigma\Phi$. The diagonal matrix Σ represents the spatial standard deviations in the principal axes, and the orthogonal matrix Φ is the matrix of the unitary principal axes $\{\boldsymbol{e}_1, \boldsymbol{e}_2, \boldsymbol{e}_3\}$ of the clusters. An anisotropic shape of the clusters would result in different eigenvalues $\{\sigma_1^2 \geqslant \sigma_2^2 \geqslant \sigma_3^2\}$ of the covariance matrix $E[\boldsymbol{X}^T\boldsymbol{X}]$. On the contrary, if the clusters are isotropic, the covariance matrix takes a simple spherical form: $E[\boldsymbol{X}^T\boldsymbol{X}] = \sigma^2 I$, where I is the identity matrix.

The structure factor can then be analytically computed by using Eq. (12):

$$S(\boldsymbol{q}) = 1 + \left(\frac{\sigma_c^2}{n_c} + n_c - 1\right)\exp[-(\Phi\boldsymbol{q})^T\Sigma(\Phi\boldsymbol{q})]. \tag{13}$$

If the clusters are isotropic, the pair-correlation function and the structure factor have a simpler expression:

$$g(\boldsymbol{r}) = 1 + \frac{1}{4\pi^{3/2} m \sigma^3}\left(\frac{\sigma_c^2}{n_c} + n_c - 1\right)\exp[-2^{-3/2}|\boldsymbol{r}/\sigma|^2], \tag{14}$$

and

$$S(\boldsymbol{q}) = 1 + \left(\frac{\sigma_c^2}{n_c} + n_c - 1\right)\exp[-|\sigma\boldsymbol{q}|^2]. \tag{15}$$

To link the spatial standard deviation σ, related to the gyration radius of the clusters, to the first two moments $\{n_c, \sigma_c\}$ of N_c, a fractal-like behavior is assumed by writing:[21]

$$\sigma/a = (n_c - 1)^{1/D}. \tag{16}$$

The fractal dimension D morphologically characterizes the growth process of the aggregates. Linear aggregates as the rouleaux have a fractal dimension close to 1, whereas compact spherical aggregates have a greater fractal dimension close to 3. As an isotropic model was adopted in the current study, D is related to the packing compactness of the aggregates. The distance between particles of the same cluster tends to decrease when D increases.

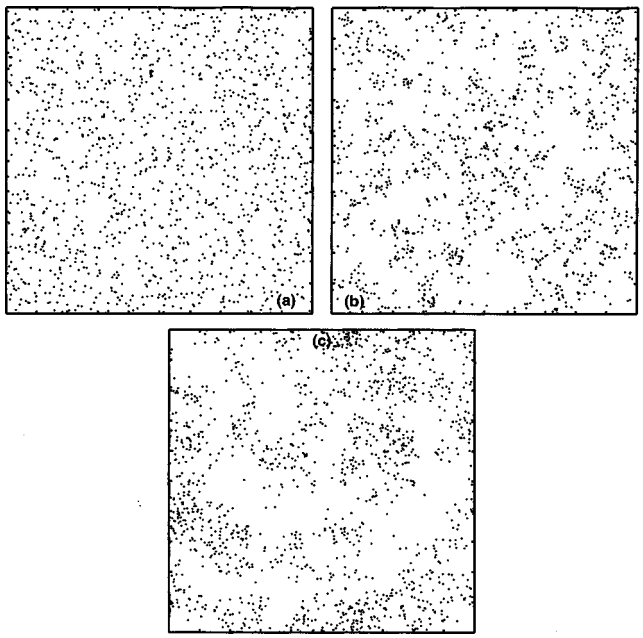

FIG. 2. 2D realizations of a Neyman–Scott model in a unit window. $H = 0.4$, $a = 0.01$, $D = 2$. N_c is uniformly taken between 1 and $2n_c - 1$, where (a) $n_c = 1$, (b) $n_c = 5$, (c) $n_c = 15$.

Combination of Eq. (15) and Eq. (16) yields the expression of the Gaussian isotropic structure factor:

$$S(\boldsymbol{q}) = 1 + (W-1)\exp\left(-\frac{|a\boldsymbol{q}|^2}{2\Delta^2}\right). \tag{17}$$

Two nondimensional aggregation parameters, W, the packing factor, and Δ, a size factor, contribute to $S(\boldsymbol{q})$:

(1) $W = n_c + (\sigma_c^2/n_c)$ increases when the number of cells per aggregate grows. W can be seen as an indicator of the size of aggregates in terms of *number* of cells per aggregate. W is the limit of the structure factor when the incident frequency tends toward zero.

(2) $\Delta = (1/\sqrt{2})(n_c - 1)^{-1/D} = a/(\sqrt{2}\sigma)$ decreases when the spatial dimension of the cluster increases. This index Δ is related to the *spatial* extent of the clusters and controls the rate of decrease of the structure factor between W and 1, when varying the incident frequency.

Figure 2 illustrates spatial patterns generated by the NSP. Three 2D realizations (2D simulations are here shown for convenience but all results presented in the rest of the paper are three-dimensional) are shown in a unit window with $H = 0.4$, $a = 0.01$, $D = 2$, and with N_c, taken as a random integer uniformly distributed between 1 and $2n_c - 1$, with $n_c = 1$, 5 and 15. Table I gives the packing factors and the size factors corresponding to these configurations.

D. Analytical formulation of the backscattering coefficient

By substituting Eqs. (17) and (3) into Eq. (2), and noting that $m = H/V_s$, one obtains the backscattering coefficient of

TABLE I. Values of the packing factor and of the size factor for the 2D simulations shown in Fig. 2. The fractal dimension is $D=2$.

n_c	W	Δ	σ/a
1	1	$+\infty$	0
5	6.3	0.35	2
15	19.7	0.19	3.7

a medium composed of weak scattering spherical particles with an arrangement described by an isotropic Gaussian Neyman–Scott model:

$$\chi^{\{W,\Delta\}}(k)=\frac{1}{3\pi a}H\overline{C^2}(ka)^4\left[3\,\frac{\sin 2ka-2ka\cos 2ka}{(2ka)^3}\right]^2 \times(1+(W-1)e^{-2(ka)^2/\Delta^2}). \quad (18)$$

IV. RESULTS AND DISCUSSION

Because of the variations of the structure factor with the packing factor W and the size factor Δ, the backscattering coefficient of blood varies with the morphology of the red cell aggregates. Depending on the range of frequencies studied, the sensitivity of the backscattering coefficient to changes in aggregation properties can also vary. The proposed model allows to evaluate both the effect of the aggregate size, quantified by the two first moments of the random number of cells per aggregate, n_c and σ_c, and the effect of the geometrical compactness of the aggregates, described by the mass fractal dimension D. In this section, the effect of these factors on the frequency dependence of the backscattering coefficient is studied, and an inversion method is proposed to infer aggregation level of porcine red blood cells from experimental backscatter data previously reported in the literature.[6]

A. Relation between the backscattering coefficient and the frequency

Figure 3 shows the relation between the backscattering coefficient of diluted porcine blood, computed by the model, and the incident frequency for varying sizes of aggregates ($D=2$, $\sigma_c/n_c=10\%$). The chosen hematocrit was $H=4.5\%$. The radius a of the red cells was 2.5 μm, and the relative impedance mismach was chosen at 0.11 by taking published values[22] of the compressibilities and densities of the porcine red cells and of the plasma. The speed of sound c was assumed to be 1540 m s^{-1}.

Several features should be noted, depending on the range of frequencies studied.

- At very low frequencies, the red cells in a single aggregate are concentrated in a domain much smaller than the acoustical wavelength and consequently scatter coherently without phase delay. The aggregates can then be considered as single Rayleigh scatterers with an effective volume WV_s. Since the central positions of the aggregates are spatially Poisson-distributed in the NSP (at this low hematocrit condition), the backscattered power is simply proportional to WV_s, and thus is sensitive to variations of the number of cells per aggregate. Furthermore, Rayleigh scattering implies that the backscattering coefficient increases proportionally with k^4, as observed in Fig. 3.
- At very high frequencies, red cells are separated by distances corresponding to many wavelengths. Phases between backscattered echoes are then uniformly distributed between 0 and 2π and the structure factor $S(\boldsymbol{q})$ becomes 1. The backscattered power is no longer sensitive to the aggregation process but only to the intrinsic properties of the red cells. Figure 3 shows that all curves asymptotically approach this aggregation-independent form. When the frequency reaches $1.37\times(c/2\pi a)=134$ MHz (corresponding to the maximal backscattering cross-section of the red

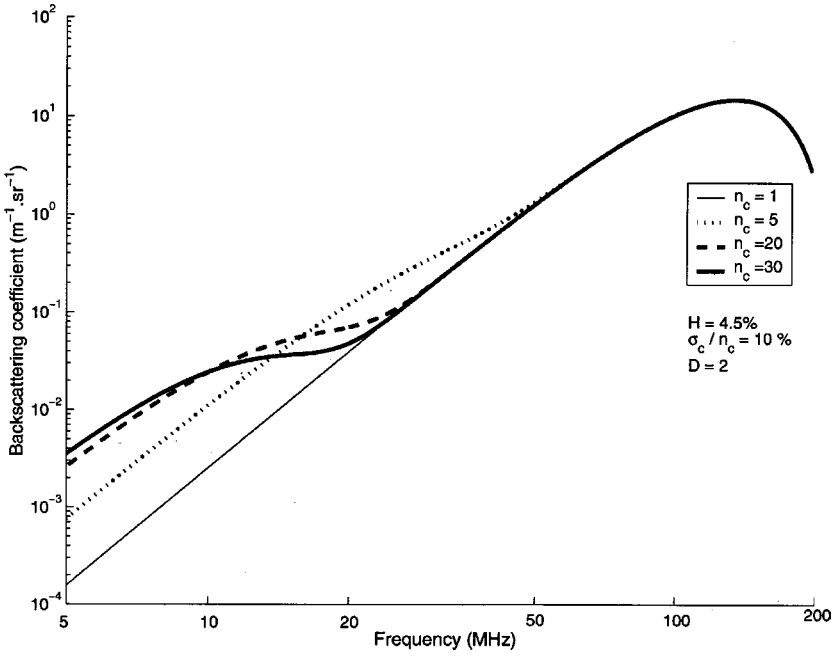

FIG. 3. The backscattering coefficient of porcine blood as a function of the frequency for different aggregation conditions as predicted by the Neyman–Scott modeling.

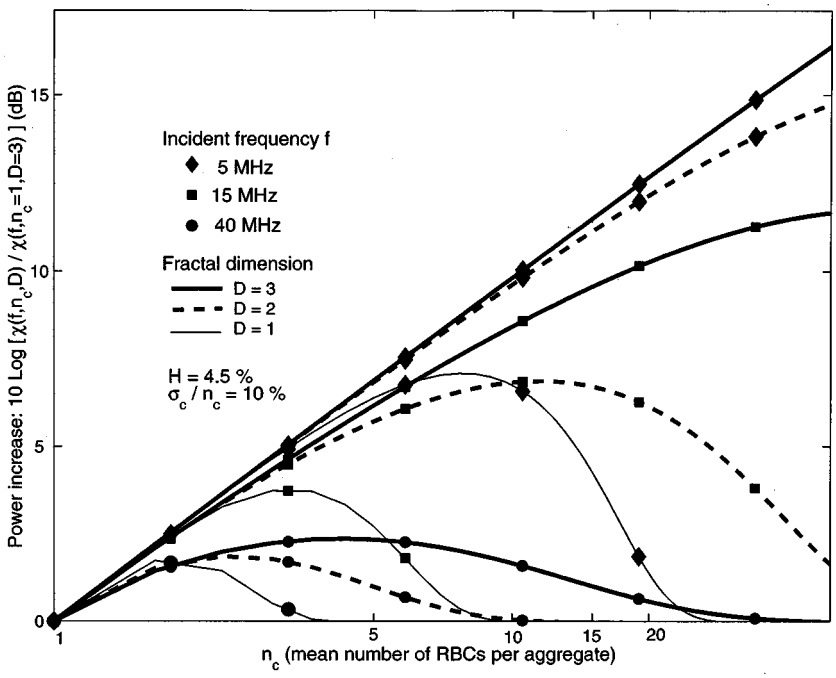

FIG. 4. The backscattered power increase due to the aggregation of red blood cells as predicted by the Neyman–Scott modeling, as a function of the mean number of cells per aggregate n_c, for different frequencies and fractal dimensions of aggregates. The hematocrit is fixed at $H=4.5\%$ and the polydispersity is characterized by $\sigma_c/n_c=10\%$. The reference power is the disaggregated state, when $n_c=1$ and $\sigma_c=0$.

cell), the backscattering coefficient has a maximal value and then further decreases because of the progressive cancellation of the echoes scattered by the spherical particles. This results from the fact that the wavelets backscattered by boundaries of the particles interfere when the dimensions of the particle are comparable to the wavelength.

- The intermediate frequency range between the two previous scattering regimes is characterized by a decrease of the spectral slope $\partial \log \chi(k)/\partial \log k$. When the gyration radius of the aggregates is elevated, the size factor Δ decreases. This transition then appears at lower frequencies and is more pronounced when the packing factor W has a high value. The experimental observation that the frequency dependence decreases in presence of red cell aggregates could be explained by this transitional scattering behavior: non-Rayleigh effects occur more markedly when aggregates are present.

B. Relation between the backscattering coefficient and the size of aggregates

Figure 4 shows the variations of the backscattering coefficient at three fixed frequencies (5 MHz, 15 MHz and 40 MHz) as a function of the mean number of cells per aggregate and fractal dimension D. A constant hematocrit $H=4.5\%$ and a polydispersity characterized by $\sigma_c/n_c=10\%$ were used for these computations. Results are presented in terms of the power increase (in dB) due to the aggregation in comparison with the disaggregated state [when $S(\boldsymbol{q})=1$].

The increase in backscattered power due to aggregation is conditioned both by the fractal dimension of the clusters and by the mean number of particles inside the aggregate.

When $n_c \ll (\lambda/a)^D$, the power increase is simply proportional to n_c: the suspension behaves as a collection of bigger particles with size σ that satisfies the Rayleigh hypothesis $\sigma \ll \lambda$. Combination of a compact growth of aggregates ($D \approx 3$) and of a low frequency insonification results in this type of scattering.

After this linear increase, the raise in power peaks and is controlled by the unphasing. The higher the frequency, the less pronounced is the relative increase of the backscatter due to aggregation.

A spatial growth of the aggregates, without variation of the number of cells per aggregate, would result in phase differences between echoes coming from the cells of the cluster and thus in a decrease of the backscattered power. On the other hand, an increase of the number of scatterers in the clusters, keeping the aggregate volume constant, increases the scattering strength of each aggregate. These reasons explain why an increase of n_c has two competitive effects: an increase of the power due to the compaction of the aggregate, and a decrease of the power due to the spatial dilation of the aggregates resulting in incoherent echoes.

Generally, for a fixed number of cells per clusters, the power increase is bigger when the clusters are compact, and thus when D is closer to 3. The effect of the fractal dimension is more pronounced when the aggregates are bigger.

As shown in Fig. 4, in aggregative conditions, a level of backscattering coefficient ambiguously corresponds to two different values of n_c. Moreover, the fact that two factors, W and Δ, characterize the NSP, shows that at least two measurements must be accomplished to estimate their values. This therefore suggests that a good characterization of the aggregation phenomenon requires measurements on a large band of frequencies rather than at a single frequency. The following subsection gives a method to extract morphological informations on the aggregates by performing measurements over a whole range of frequencies. This can be technically achieved by using either a broadband transducer that emits short pulses and by making a spectral analysis of the

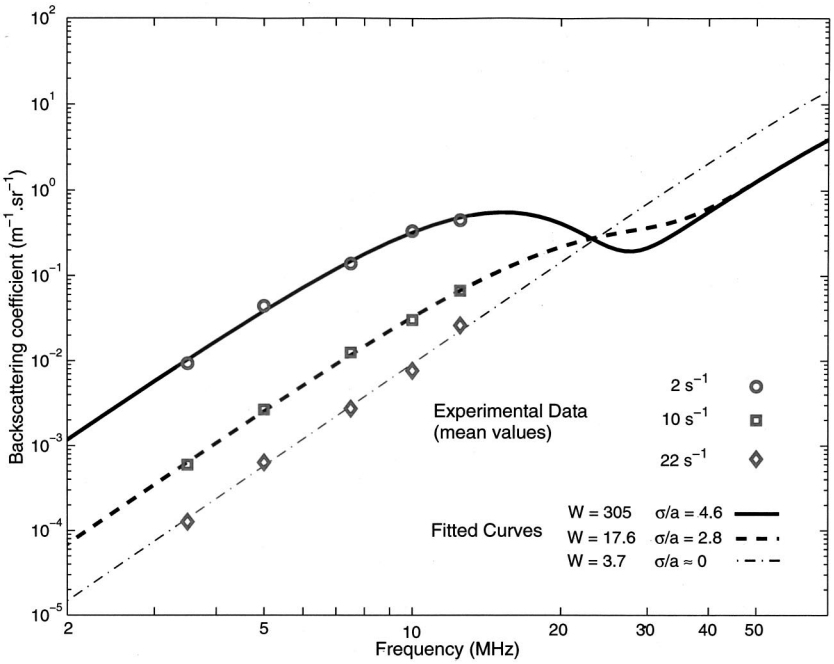

FIG. 5. Experimental backscatter data obtained by Yuan and Shung (Ref. 6) for porcine whole blood flowing at different shear rates, for a hematocrit $H=4.5\%$. Fitted curves are also shown with estimated values of W (packing factor) and σ/a (normalized radius of the aggregates).

backscattered signal, or by using several transducers with different central frequencies.

C. Extraction of structural information on the aggregation level from backscattering experiments

In Fig. 5, mean results of backscattering experiments obtained by Yuan and Shung[6] are presented for porcine whole blood, circulating in a laminar shear flow, at a low hematocrit $H=4.5\%$. The *in vitro* model, used by these authors, allowed to control the flow rate inside a cylindrical tube and consequently to modulate the aggregation level of the red cells by changing the mean shear rate. Five different transducers were used to study the frequency dependence of the backscattering coefficient. Mean backscattering coefficients measured for mean shear rates of 2 s^{-1}, 10 s^{-1} and 22 s^{-1} are shown (the plasmatic fibrinogen concentration, a protein that affects the level of aggregation, was kept constant at 210 mg/dl in the three experiments). As expected, at a fixed frequency, the backscattering coefficient decreased when the shear rate increased. The spectral slope is 4 at a shear rate of 22 s^{-1} and decreases with decreasing shear rate (a power law fitting between 3.5 MHz and 12.5 MHz gives a mean spectral slope of 3.7 for 10 s^{-1}, and 3 for 2 s^{-1}).

To assess the aggregation state of the red cells for these flowing conditions, a regression method was used to estimate the parameters W and Δ. The analytical expression of the structure factor obtained by the model was fitted to experimental structure factors derived from experimental measurements of backscattering coefficients.

Supposing that the experimental backscattering coefficients $\{\chi_i\}_{i=1\ldots M_f}$ were measured at M_f different frequencies $\{f_i\}_{i=1\ldots M_f}$, the corresponding experimental structure factors $\{S_i\}_{i=1\ldots M_f}$ can be computed by using Eq. (2). Noting $k_i=2\pi f_i/c$ the sequence of wave numbers, one obtains:

$$S_i=\frac{V_s\chi_i}{H\sigma_b(-2k_i)}$$

with

$$\sigma_b(-2k_i)=\frac{4a^2}{9}(k_ia)^4\overline{C^2}\left|3\frac{\sin 2k_ia-2k_ia\cos 2k_ia}{(2k_ia)^3}\right|^2. \tag{19}$$

If the blood sample is characterized by the structure factor W and the size factor Δ, the theoretical structure factors at the same frequencies should be given by Eq. (17):

$$S_i^{\text{theory}}=1+(W-1)\exp\left(-\frac{f_i^2}{2f_0^2}\Delta^{-2}\right), \tag{20}$$

with $f_0=c/4\pi a=49$ MHz for porcine red blood cells.

A nonlinear regression on the parameters $\{W,\Delta\}$ was performed by minimizing the mean quadratic error $J(W,\Delta)$ between the theoretical and the experimental values. It is a two variables optimization problem that consists in minimizing a least-square criterion:

$$J(W,\Delta)=\frac{1}{M_f}\sum_i (S_i-S_i^{\text{theory}})^2$$

$$=\frac{1}{M_f}\sum_i (S_i-1-(W-1)e^{-f_i^2/2f_0^2\Delta^{-2}})^2. \tag{21}$$

The Nelder–Mead simplex algorithm was used to solve this nonlinear regression problem. The estimates $\{\hat{W},\hat{\Delta}\}$ and the minimal value $J_{\min}=J(\hat{W},\hat{\Delta})$ correspond to the best prediction error $J_{\min}^{1/2}$. The resulting curves of the frequency dependence of the backscattering coefficient appear in Fig. 5.

Table II gives the numerical values of the aggregation parameters obtained by this fitting procedure. The aggregate spatial extent $\hat{\sigma}$ and the packing factor $\hat{W}$ are both decreasing

TABLE II. Estimated values of the aggregation parameters corresponding to experimental data obtained by Yuan and Shung (Ref. 6).

Shear rate (s^{-1})	$\hat{W}$	$\hat{\Delta}$	$\hat{\sigma}/a$	error $J_{\min}^{1/2}$
2	305	0.31	4.6	21
10	17.6	0.51	2.8	0.8
22	3.7	$+\infty$	0	0.5

with the shear rate. The hypothesis of the disruption of the clusters with an increase of the shear forces is compatible with this tendency.

To reconstitute the aggregate morphology, the three variables $\{n_c, \sigma_c, D\}$ are required, but the nonlinear regression only supplies two factors. In order to estimate the moments n_c and σ_c of N_c, the fractal dimension D is supposed to be known. The estimated mean number $\widehat{n_c}$ of red cells per aggregate and the polydispersity $\widehat{\sigma_c}$ are computed by using the two relations $\hat{W}=\widehat{n_c}+(\widehat{\sigma_c^2}/\widehat{n_c})$ and $\hat{\Delta}=(1/\sqrt{2})(\widehat{n_c}-1)^{-1/D}$. Table III gives the resulting values of $\widehat{n_c}$ and $\widehat{\sigma_c}$ for different fractal dimensions. Some fractal dimensions do not always allow the inversion of the relation, which shows that they may not be physically possible. For a shear rate of 10 s^{-1}, e.g., $\hat{\sigma}_c^2$ is found negative for $D=3$: the aggregates must have a lower fractal dimension than 3. For a high shear rate, the fractal dimension has a low impact because the size of the aggregates remains small.

Three-dimensional realizations of the NSP are generated to visually show the spatial organization of the red cell aggregates (Figs. 6, 7, 8). The random number of cells per aggregate (N_c) is supposed to follow a log-normal distribution[23] with the fitted variance and mean. The chosen hematocrit is still 4.5%. For these simulations, we hypothesized that at a shear rate of 2 s^{-1}, the clusters are more compact and thus have a fractal dimension close to 3, whereas that for a shear rate of 10 s^{-1}, D is smaller (simulation is generated for $D=2$). When the shear rate is 22 s^{-1}, the fractal dimension does not influence the structure because most of the aggregates are disrupted ($n_c \approx 1$).

D. Summary of the basic assumptions of the model, its strengths and limitations

In this study, blood is considered as a medium with weakly varying acoustical properties, as the mismatch between the red blood cell impedance and the plasmatic impedance is only 11%. This allows one to use the Born approximation to relate the frequency-dependent backscattering coefficient to the characteristics of the spatial distribution of acoustical impedance. It was hypothesized that the red blood cells, that create the fluctuations of impedance, are all similar in shape, and that their relative positioning in the scattering volume results from a stationary random process. The influence of the intrinsic physical properties of the red cells on the backscattering properties of blood is well described by the backscattering cross-section σ_b of a spherical particle in the range of classical imaging frequencies. The influence of

TABLE III. First moments (mean n_c and standard deviation σ_c) of the size histogram as a function of the mass fractal dimension D for the models fitted to the experimental data of Yuan and Shung (Ref. 6).

Shear rate (s^{-1})	$\widehat{n_c}$ $D=1$	$\widehat{\sigma_c}$ $D=1$	$\widehat{n_c}$ $D=2$	$\widehat{\sigma_c}$ $D=2$	$\widehat{n_c}$ $D=3$	$\widehat{\sigma_c}$ $D=3$
2	5.6	40.9	22.1	79	98.3	143
10	3.8	7.2	8.8	8.8	23	impossible
22	1	1.6	1	1.6	1	1.6

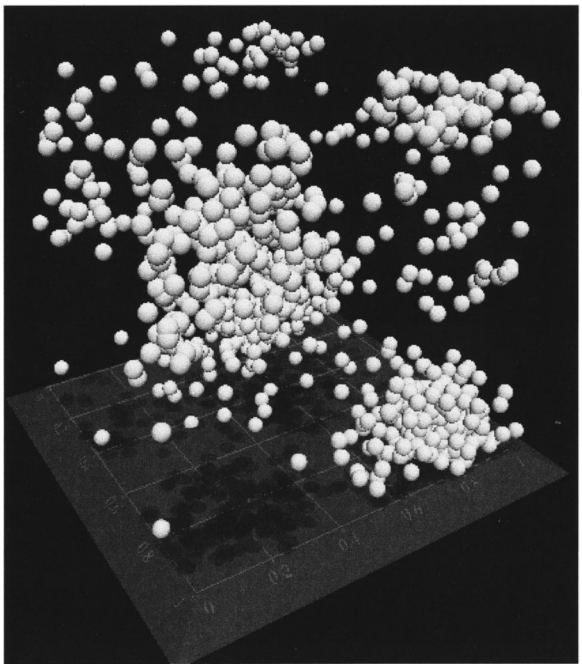

FIG. 6. A realization of the Neyman–Scott process for fitted parameters n_c, σ_c and σ, corresponding to experiments with blood flowing at a shear rate of 2 s^{-1} and a hematocrit $H=4.5\%$. The fractal dimension D is 3. The simulation was generated in a cube with dimensions of 150 μm.

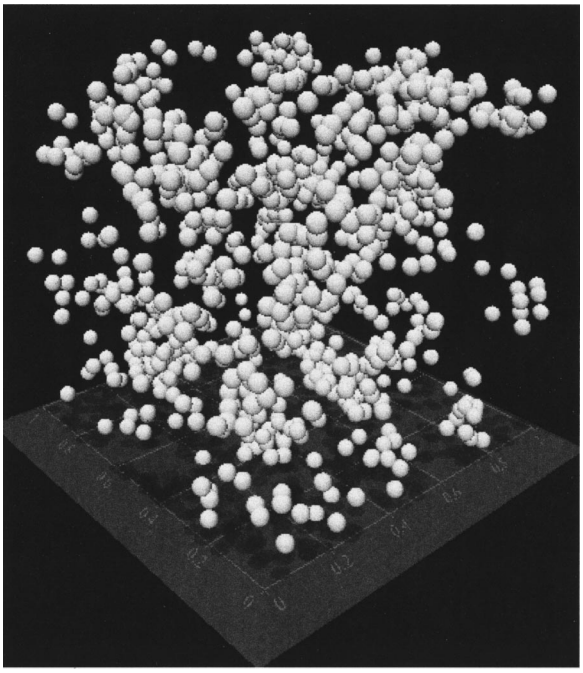

FIG. 7. A realization of the Neyman–Scott process for fitted parameters n_c, σ_c and σ, corresponding to experiments with blood flowing at a shear rate of 10 s^{-1} and a hematocrit $H=4.5\%$. The fractal dimension D is 2. The simulation was generated in a cube with dimensions of 150 μm.

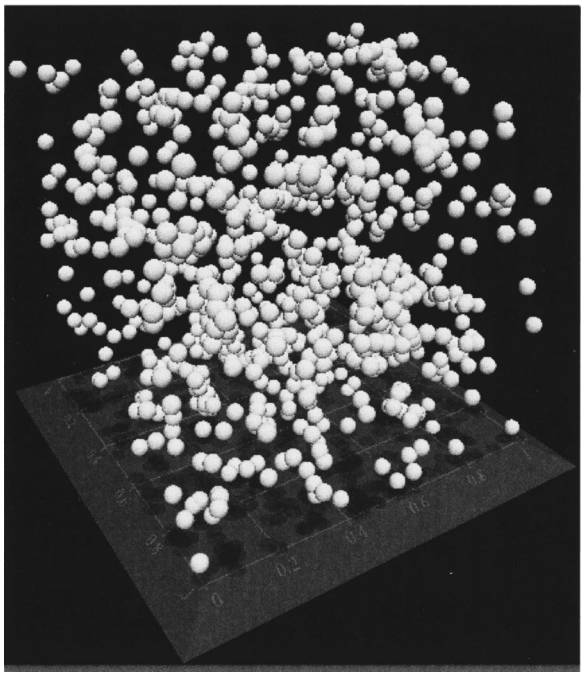

FIG. 8. A realization of the Neyman–Scott process for fitted parameters n_c, σ_c and σ, corresponding to experiments with blood flowing at a shear rate of 22 s^{-1} and a hematocrit $H=4.5\%$. The fractal dimension D is 1. The simulation was generated in a cube with dimensions of 150 μm.

the red cell aggregation level is investigated by modeling the spatial density $N(\boldsymbol{x})$ of the red cell positions by the Neyman–Scott point process. The complexity of modeling $N(\boldsymbol{x})$ in physiological conditions comes from two reasons. First, the high density of the red cells (about 5×10^6 mm^{-3}), representing a normal hematocrit around 45%, imposes important restrictions on the random positioning of the red cells because of their nonoverlapping. Second, the reversible aggregation process favors the creation of groups of red cells with varying morphologies. The NSP provides a statistical description of the aggregates by characterizing their number of cells and their spatial extent. The main advantage of the NSP is the fact that it allows the analytical computation of the Fourier spectrum of $N(\boldsymbol{x})$, which directly gives the frequency dependent structure factor. It gives a parametric model to the frequency dependence of backscatter experimental data, and provides meaningful morphological features of the aggregates ($\{W,\Delta\}$ or $\{n_c,\sigma_c\}$ when the fractal dimension D is known), that are more physically relevant for blood characterization than the absolute value of the backscattering coefficient or the spectral slope.

However, the simplicity of the NSP has a drawback: constraints imposed by the high hematocrit behavior are not taken into consideration. Equation (18) shows that the backscattering coefficient evolves linearly with the hematocrit when the medium is described by the NSP. But it is known, when the hematocrit is greater than a few percents, that the ultrasonic backscatter of blood tends to decrease. For nonaggregating red blood cells ($n_c=1$ and $\sigma_c=0$), the value of the packing factor predicted by the NSP is 1, whereas in this case W was shown[12,24] to be hematocrit-dependent [for spherical hard scatterers, the three-dimensional Percus–Yevick approximation yields $W\approx(1-H)^4/(1+2H)^2$]. This nonlinear relation between the hematocrit and the backscattering coefficient cannot be predicted by the NSP. Moreover, the NSP generates clusters of points that allows cells overlapping. When the medium is dense, this results in unrealistic realizations. Experimentally, the linear relationship between the backscattering coefficient and the hematocrit was shown valid[25] up to $H\approx5\%$. One can therefore consider that the NSP is appropriate to model red cell aggregate configurations for a hematocrit under 5%.

Despite these limitations, these results could be clinically valuable in hematological laboratories to study the erythrocyte aggregability for blood sample adjusted to a fixed low hematocrit. *In vitro* scattering measurements with diluted red cell suspensions can provide flow dependence of $\{W,\Delta\}$, and would characterize the intrinsic properties of red cells to aggregate. It may be of interest to note that optical microscopic observations[26] of red cell aggregates, already used in research laboratories, are also performed at these low hematocrits for adequate morphological measurements.

One fundamental interest of the Neyman–Scott model was to distinguish intrinsic effects of the aggregation level on the backscattering from the effect of hematocrit. Non-Rayleigh effects associated with the growth of the gyration radius of the aggregates were related to the frequency dependence of the backscattering coefficient. However, to apply inference techniques to blood characterization with more physiological hematocrits (around 45%) to predict physical parameters describing the aggregation process, spatial stochastic processes that can both describe dense and aggregative media will have to be studied for modeling red cell positioning. Unfortunately, more complex estimation techniques are required to characterize them because spectral properties of such random processes may not be analytically calculated.

V. CONCLUSION

Ultrasound backscattering properties of blood are dependent on the packing state of the red cells. It would be of interest to use this dependence to quantitatively measure the erythrocyte aggregation level by acoustical means. To reach this goal, a clear understanding of the relation existing between the variables describing the aggregation state and the backscatter data must be found. Most of the previous theoretical studies intended to clarify the hematocrit-dependence of the backscattering, or concerned low frequency backscattering by non-Rayleigh red cell aggregates. However, the influence of the aggregation level on the frequency dependence of the backscattering was not directly addressed whereas experimental results showed that at a low shear rate, aggregates of red cells cannot be considered as Rayleigh scatterers even at low frequencies.

To extend scattering theory to aggregating red cell suspensions, the spatial pattern due to the clustering was modeled by a random process. Considering that the erythrocyte positioning is the realization of a Neyman–Scott process, and using the Born approximation, the structure factor of a low hematocrit ($H<5\%$) but aggregative suspension of red blood cells was predicted analytically, as a function of the size distribution of the aggregates and of their mass fractal

dimension. This probabilist framework conveyed a parametric model to extract the average size of the clusters of red cells and its polydispersity from backscatter data, assuming that the mass fractal dimension is known. Experimental measurements on a 4.5% hematocrit porcine blood obtained by Yuan and Shung[6] were used to test the efficiency of the model. The disaggregation of the groups of red cells and the decrease of the polydispersity, both associated with an increase of the shear rate, could be determined by a regression technique.

The NSP represents a first step to the random modeling of the microstructural organization of red blood cells, that helps to understand the frequency dependence of the backscattering properties of blood due to aggregation. It must be emphasized that $S(\boldsymbol{q})$, the structure factor, is a crucial quantity to determine for blood characterization. It reflects the organization of the red cell network, equivalently to the pair correlation function. The zero-frequency limit of the structure factor, the packing factor W, is useful to describe low frequency scattering (Rayleigh scattering). However, low frequency measurements only give limited structural informations, as Bascom and Cobbold pointed out,[10] because the packing factor W does not uniquely define the pair correlation function as the structure factor does. A spatial random model, as the NSP, allows us to characterize the spectral variations of the structure factor of a low hematocrit suspension by a small number of variables. This kind of parametric approach reveals particularly useful when considering the experimental difficulties in reliably measuring backscattering coefficients of materials.[27] Substantial *a priori* knowledge of the frequency dependence is expected to compensate for the uncertainties of the measurements. The NSP highlighted two factors as the structure factor W and the size factor Δ, themselves related to meaningful geometrical properties of the red cell aggregates. For high hematocrits and aggregative suspensions, an appropriate model still remains to be found, to discriminate such significant factors and to use them as clinical indices of red cell aggregation.

ACKNOWLEDGMENTS

We wish to thank Isabelle Fontaine for many helpful discussions and for reviewing the manuscript. This work was supported by the following grants: Studentship from the ''Groupe de recherche en modélisation biomédicale'' of the Institute of Biomedical Engineering of the École Polytechnique and Université de Montréal; Scholarship from the ''Fonds de la recherche en santé du Québec;'' Grants from the Medical Research Council of Canada (# MOP-36467)—now the Canadian Institutes of Health Research—and the Heart and Stroke Foundation of Québec.

[1] G. D. O. Lowe, ''Agents lowering blood viscosity, including defibrinogenating agents,'' in *Cardiovascular Thrombosis: Thrombocardiology and Thromboneurology*, 2nd ed., edited by M. Verstraete, V. Fuster, and E. J. Topol (Lippincott-Raven, Philadelphia, 1998), Chap. 18, pp. 321–333.

[2] W. Koenig and E. Ernst, ''The possible role of hemorhelogy in atherothrombogenesis,'' Atherosclerosis (Berlin) **94**, 93–107 (1992).

[3] Z. Vered, G. A. Mohr, B. Barzilai, C. J. Gessler, S. A. Wickline, K. A. Wear, T. A. Shoup, A. N. Weiss, B. E. Sobel, and J. G. Miller, ''Ultrasound integrated backscatter tissue characterization of remote myocardial infarction in human subjects,'' J. Am. Coll. Cardiol. **13**, 84–91 (1989).

[4] S. Takiuchi, H. Rakugi, K. Honda, T. Masuyama, N. Hirata, H. Ito, K. Sugimoto, Y. Tanagitani, K. Moriguchi, A. Okamura, J. Higaki, and T. Ogihara, ''Quantitative ultrasonic tissue characterization can identify high-risk atherosclerotic alteration in human carotid arteries,'' Circulation **102**, 766–770 (2000).

[5] P. Stetson and G. Sommer, ''Ultrasonic characterization of tissues via backscatter frequency dependence,'' Ultrasound Med. Biol. **23**, 989–996 (1997).

[6] Y. W. Yuan and K. K. Shung, ''Ultrasonic backscatter from flowing whole blood: II. Dependence on frequency and fibrinogen concentration,'' J. Acoust. Soc. Am. **84**, 1195–1200 (1988).

[7] F. S. Foster, H. Obara, T. Bloomfield, L. K. Ryan, and G. R. Lockwood, ''Ultrasound backscatter from blood in the 30 to 70 MHz frequency range,'' IEEE Ultrasonics Symposium Proceedings 1599–1602 (1994).

[8] M. S. van der Heiden, M. G. de Kroon, N. Bom, and C. Borst, ''Ultrasound backscatter at 30 MHz from human blood: Influence of rouleau size affected by blood modification and shear rate,'' Ultrasound Med. Biol. **21**, 817–826 (1995).

[9] V. Twersky, ''Low frequency scattering by correlated distributions of randomly oriented particles,'' J. Acoust. Soc. Am. **81**, 1609–1614 (1987).

[10] P. A. Bascom and R. S. Cobbold, ''On a fractal packing approach for understanding ultrasonic backscattering from blood,'' J. Acoust. Soc. Am. **98**, 3040–3049 (1995).

[11] L. Y. Mo and R. S. Cobbold, ''A unified approach to modeling the backscattered Doppler ultrasound from blood,'' IEEE Trans. Biomed. Eng. **39**, 450–461 (1992).

[12] I. Fontaine, M. Bertrand, and G. Cloutier, ''A system-based approach to modeling the ultrasound signal backscattered by red blood cells,'' Biophys. J. **77**, 2387–2399 (1999).

[13] B. G. Teh and G. Cloutier, ''Modeling and analysis of ultrasound backscattering by spherical aggregates and rouleaux of red blood cells,'' IEEE Trans. Ultrason. Ferroelectr. Freq. Control **47**, 1025–1035 (2000).

[14] P. M. Morse and K. U. Ingard, *Theoretical Acoustics* (Princeton University Press, Princeton, NJ, 1986).

[15] M. F. Insana and D. G. Brown, ''Acoustic scattering theory applied to soft biological tissues,'' in *Ultrasonic Scattering in Biological Tissues*, edited by K. K. Shung and G. A. Thieme (CRC, Boca Raton, FL, 1993), Chap. 5, pp. 75–124.

[16] N. E. Berger, R. J. Lucas, and V. Twersky, ''Polydisperse scattering theory and comparisons with data for red blood cells,'' J. Acoust. Soc. Am. **89**, 1394–1401 (1991).

[17] J. Serra, *Image Analysis and Mathematical Morphology* (Academic, London, 1982).

[18] J. L. F. Batista and D. A. Maguire, ''Modeling the spatial structure of tropical forests,'' Forest Ecology & Management **110**, 293–314 (1998).

[19] J. Caers, ''A general family of counting distributions suitable for modeling cluster phenomena,'' Math. Geol. **28**, 601–624 (1996).

[20] B. Bacchi, R. Ranzi, and M. Borga, ''Statistical characterization of spatial patterns of rainfall cells in extratropical cyclones,'' J. Geophys. Res. [Atmos.] **101**, 26277–26286 (1996).

[21] M. Elimelech, J. Gregory, X. Jia, and R. A. Williams, *Particle Deposition & Aggregation. Measurement, Modeling and Simulation* (Butterworth-Heinemann, Woburn, MA, 1995).

[22] Y. W. Yuan and K. K. Shung, ''Ultrasonic backscatter from flowing whole blood: I. Dependence on shear rate and hematocrit,'' J. Acoust. Soc. Am. **84**, 52–58 (1988).

[23] K. W. Lee, ''Change of particle size distribution during Brownian coagulation,'' J. Colloid Interface Sci. **92**, 315–325 (1983).

[24] V. Twersky, ''Acoustic bulk parameters in distributions of pair-correlated scatterers,'' J. Acoust. Soc. Am. **64**, 1710–1719 (1978).

[25] L. Y. L. Mo, I. Y. Kuo, K. K. Shung, L. Ceresne, and R. S. C. Cobbold, ''Ultrasound scattering from blood with hematocrits up to 100%,'' IEEE Trans. Biomed. Eng. **41**, 91–95 (1994).

[26] S. Chen, B. Gavish, S. Zhang, Y. Mahler, and S. Yedgar, ''Monitoring of erythrocyte aggregate morphology under flow by computerized image analysis,'' Biorheology **32**, 487–496 (1995).

[27] E. L. Madsen, F. Dong, G. R. Frank, B. S. Garra, K. A. Wear, T. Wilson, J. A. Zagzebski, H. L. Miller, K. K. Shung, S. H. Wang, E. J. Feleppa, T. Liu, W. D. O'Brien, Jr., K. A. Topp, N. T. Sanghvi, A. V. Zaitsev, T. J. Hall, J. B. Fowlkes, O. D. Kripfgans, and J. G. Miller, ''Interlaboratory comparison of ultrasonic backscatter, attenuation, and speed measurements,'' J. Ultrasound Med. **18**, 615–631 (1999).

Differential degradation of antbird songs in a Neotropical rainforest: Adaptation to perch height?

Erwin Nemeth[a] and Hans Winkler
Konrad Lorenz Institute for Comparative Ethology, Austrian Academy of Sciences, A-1160 Wien, Austria

Torben Dabelsteen
Department of Animal Behaviour, Zoological Institute, University of Copenhagen, Tangensvej 16, DK-2200 Copenhagen, Denmark

(Received 10 April 2001; revised 12 September 2001; accepted 26 September 2001)

Habitat characteristics that affect transmission and degradation of acoustical signals should influence strongly the evolution of bird songs. In this study propagation properties of songs of five antbird species were measured in a rainforest in southern Venezuela. The investigated species (*Myrmothera campanisona, Thamnophilus aethiops, Thamnophilus amazonicus, Myrmotherula axillaris*, and *Herpsilochmus dorsimaculatus*) use different song post heights at all levels of the rainforest. Because there is a height-specific pattern in degradation, it is hypothesized that their songs are adapted to species-specific transmission paths. To test this assumption, transmission parameters (excess attenuation, signal-to-noise ratio, and blur ratio) were measured for the songs at five different heights and at three different distances. In three of the five species, the results indicate a strong influence of environmental conditions on the design of the vocalizations. Degradation was minimized by the concentration of the signal to a narrower frequency range, the usage of lower frequencies, or a slower time structure for the songs near the ground. The results are discussed in relation to acoustical models of sound propagation and physiology, and it is suggested that height-dependent degradation within a forest is an important selection pressure for transmissibility in avian communication. [DOI: 10.1121/1.1420385]

PACS numbers: 43.80.Ev, 43.80.Lb [WA]

I. INTRODUCTION

Several studies indicate that bird song frequencies (e.g., Jilka and Leisler, 1974; Morton, 1975; Nottebohm, 1975) or time features (e.g., Cosens and Falls, 1984; Sorjonen, 1983; Wiley, 1991; Badyaev and Leaf, 1997) are adapted to species-specific habitats. Wiley and Richard (1978) consider reverberations as a main factor for degradation of bird songs in forested habitats and hypothesize that temporal properties of songs of forest oscines have evolved to reduce the effects of reverberations. Comparisons of songs of species of open and closed habitats seemingly confirm this hypothesis, as songs of inhabitants of more open habitats have shorter repetition periods (Wiley, 1991; Badyaev and Leaf, 1997). The low-pitched, whistlelike bird songs in tropical rainforests, which inspired some of the first studies of the adaptation of bird vocalizations to habitat characteristics (e.g., Chappuis, 1971; Morton, 1975; Marten *et al.*, 1977), may thus counter the effect of reverberations.

In our study, we visited the tropics to examine more closely the propagation characteristics of bird songs at various heights in a rainforest. It is the first experimental and multi-species comparison of bird songs within a habitat type. Our main hypothesis is that the songs of our study species are adapted to different species-specific song post heights. Inside a forest, the acoustic environment changes as it ascends from the ground to the canopy. Whereas near the canopy, atmospheric turbulence can alter acoustical signals (Richards and Wiley, 1980), close to the ground, frequencies below 1 kHz are extremely attenuated (''ground effect,'' Embleton, 1996). Stem and leave sizes become smaller higher in the canopy, producing height-specific patterns of sound degradation.

But what does adaptation of bird songs mean in this context? Wiley and Richards (1982) point out that it is a simplified view to assume that long-range signals have evolved to be transmitted with the least alteration to the greatest distances possible. Such signals adapted to an optimal, not maximal, distance (Lemon *et al.*, 1981), and more degradation itself may be a desirable characteristic for some song elements if they are intended to reach only receivers nearby (e.g., mates, Dabelsteen *et al.*, 1993). Additionally, blurring of signals can be used by birds as a distance (''ranging'') and location cue (Richards, 1981), which may contribute an important, ''desired'' feature of bird vocalizations (Morton, 1982; McGregor and Krebs, 1984; Morton, 1986; Shy and Morton, 1986; Morton and Derrickson, 1996; Holland *et al.*, 2001). Conclusive evidence of the adaptation of a signal feature would, therefore, need information about the intended receivers (partners or neighbors or both), the intended transmission distances (home ranges, neighbor distances), and the location of the receivers. Here we test a simple ''maximization'' model (Morton, 1975; Lemon *et al.*, 1981). We adopt an operational, nonhistorical view of adaptation (see Reeve and Sherman, 1993) and consider a song of a single species as adapted to song post height if it shows a lower degradation of the signal compared to the same signal at other heights and relative to the overall pattern in degra-

[a]Electronic mail: e.nemeth@klivv.oeaw.ac.at

dation in other species. To test the adaptation of songs to singing post height, we recorded the songs of five sympatric antbird species, which sing in different heights of a neotropical rainforest. The species belong to the family of Thamnophilidae (Amazonian Antshrike *Thamnophilus amazonicus*, White-shouldered Antshrike *Th. aethiops*, White-flanked Antwren *Myrmotherula axillaris*, Spot-backed Antwren *Herpsilochmus dorsimaculatus*) and Formicariidae (Thrush-like Antpitta *Myrmothera campanisona*). These recordings were used to extract parts of the songs that were transmitted over different distances and at different heights to compare the degradation. Here, we use degradation as a general term (*sensu* Dabelsteen *et al.*, 1993; Holland *et al.*, 1998) that encompasses any changes of a signal during transmission. We measured three aspects: (*i*) excess attenuation (EA), that is, the attenuation that exceeds the predicted geometrical spreading, (*ii*) signal-to-noise ratio (SNR), and (*iii*) blurring, which describes the amount of change in amplitude and frequency modulations (Dabelsteen *et al.*, 1993).

II. METHODS

A. Study site

The study site, Surumoni (3° 10′ 27″ N, 65° 40′ 19″ W, 105 m a. s. l.), is named after a small blackwater tributary of the upper Orinoco and is situated 15 km west of the village of La Esmeralda in southern Venezuela. It consists of a primary forest area, which has not been cleared since historic time. A 40-m-high crane on 100-m-long rails allows access to a 1.7-ha area of the forest. Average canopy height is 20–25 m, with the highest tree reaching 34 m. The average stem diameter 1.5 m above ground (for stems$>$10 cm) is 19.8 cm with a maximum of 80 cm (Rainer and Horchler, unpublished data). Vegetation density was lowest in midstory, at approximately 10 to 15 m (Ellinger, in press).

The bird fauna is typical for the Amazonian lowlands, with 270 species having been identified at the crane location. Recordings of the test songs were made in November–December 1997. Experiments were done from 19 to 27 May 1998. During the transmission experiments, weather conditions were rather constant: mean (range) for temperature $=24.8\,^{\circ}$C (22.5 °C to 28.1 °C), mean humidity$=88.4\%$ (100% at the ground to 73% in the canopy), wind speed<0.5 m/s (J. Szarzynski, personal communication). Background noise in the range of 0–16 kHz varied during the day from 35 to 55 dB SPL. Insects within a frequency range from 3.15 to 12.5 kHz produced the main part of it (Ellinger, in press). As most of our birds use lower frequencies and insect activity was not so intense during our experiments, we had no insect masking of our test sounds.

B. Study birds and song post heights

The five antbird species were chosen because of their sympatric occurrence, their close phylogenetic relationship, and their different song post heights. In all these species, both males and females sing. Both sexes of all species reacted to playback of their conspecific song by approaching and singing. Whereas White-flanked Antwrens and Amazonian Antshrikes accompany mixed flocks regularly, all other species are described as more or less solitary (Ridgely and Tudor, 1994). The song post heights (at least 15 per species) were estimated in November–December 1997 from spontaneous singing birds, thus excluding reactions to playback tapes in the study area. Additional estimates of song post heights were made in November 1998.

C. Measurements of song characteristics

All frequency and time characteristics of the songs of the species were measured with Avisoft Sonagraph Pro. The accuracy of time and frequency measurements depended on the different window sizes and time settings of the sonagrams (Beecher, 1988). Maximums of 0.4 ms time and 5 Hz frequency resolutions were achieved. We used the following designations for the song characteristics: A song consists of elements, which are the simplest units of continuous sound, and pauses between the elements. The loudest frequency of a song or element is the frequency at which it has maximum energy as determined from a power spectrum.

D. Test sounds

Songs for transmission experiments were recorded 1.5 to 8 m from the birds without any obstacle between the microphone and the birds using a Sony Professional Walkman WM-DC6 or a Tascam DAP 1 DAT Recorder connected to an AKG CK 62 ULS condenser microphone (omnidirectional with linear frequency characteristic). They were digitized with a sampling rate of 44.1 kHz or transmitted digitally to a computer. It was not possible to use full songs for the propagation experiments, because they elicit strong acoustical reactions from the local birds that would superimpose on the experimental recordings. For each species, a representative part was selected, except in the White-shouldered Antshrike, where the song is dominated by the fundamental and the first overtone (see Fig. 2). Here the song was divided into a lower and higher frequency part, and two test sounds were used. All six elements were filtered using a linear phase FIR (finite impulse filter) of order 199 (test sound: center frequency kHz, frequency range kHz): Thrush-like Antpitta: 0.875, 0.775–0.975; lower frequency: 0.625, 0.425–0.825; White-shouldered Antshrike higher frequency: 1.275, 0.875–1.675; White-flanked Antwren: 1.950, 1.225–2.425; Amazonian Antshrike: 1.420, 0.68–2.68; Spot-backed Antwren: 1.420, 1.25–2.45. The test sounds consisted out of two to six elements with natural interelement pauses.

E. Transmission experiments

Five heights (0.15, 2, 6, 12.5, and 21 m) and three distances (17.5, 37, and 54.5 m) were chosen to represent song posts and receiver locations. Microphone and loudspeaker were mounted in the middle of a 40-cm-long beam orientated perpendicular to the transmission distance and were moved with strings to the designated heights (see Fig. 1). The choice of the distances was a compromise between several constraints: (*i*) the loudspeaker and microphone had to be moved freely without disturbance by branches or leaves to the selected heights, (*ii*) all microphone and speaker locations were within the study plot to allow fastening by using the crane,

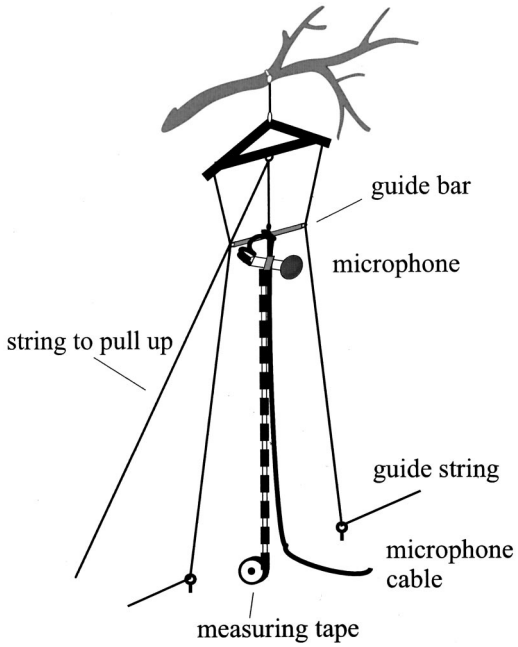

FIG. 1. Setup of the microphone for the transmission experiments. The microphone is rigidly connected to a guide bar, which can be moved by a string. The two guide strings are used to define the direction of the microphone. The same mechanism was used for the loudspeaker.

and (*iii*) all locations were as far as possible away (26 m) from the rails of the crane to minimize possible acoustical influences. In all positions microphone and loudspeaker were approximately aligned. However, we corrected for slight deviations from the perfect line by adjusting the orientation of the loudspeaker. Microphone and loudspeaker were always at the same height, which resulted in 15 different transmission paths. In the experiments, the order of transmission along different paths was randomly chosen. The whole sequence was repeated once. For analysis, we chose the recordings made during wind speeds below 0.5 m/s.

The test tape was transmitted from a Toshiba Satellite notebook with a 16-bit New Media WAVjammer sound card connected with a 30-m cable to a Sony SRS58 active loudspeaker. The notebook operated with 220 V from a generator 350 m away; a car battery powered the loudspeaker. The voltage of the battery was kept in a range of 12.7–12.9 V and provided a constant outcome of the loudspeaker. The propagation pattern of the loudspeaker was measured in an anechoic chamber and can be characterized as omnidirectional in all essentials. In the anechoic chamber we also estimated the frequency characteristics of the loudspeaker and determined how these influence the output level (SPL) of the test sounds. Then we corrected for the differences in SPL in the determination of the SNR values of the transmitted sounds. Thus, the test sounds are treated as if they had been emitted with the same SPL. For the recordings, an AKG CK 62 ULS condenser microphone with a PK12-48 microphone preamplifier was connected to a RENA MS1 microphone amplifier and to a Tascam DAP 1 DAT-recorder. The sampling frequency was 44.1 kHz.

Like the loudspeaker, the DAT recorder was calibrated to allow for estimation of sound pressure levels of the rerecorded test sounds. Before transmission, the test sounds were put into random order on a computer with intervals of 2 s to avoid forward masking and decrease the chance of interference by other bird sounds in the forest. The random order sequence was changed between each transmission experiment using the software Cool Edit Pro. In each experiment, this sequence was repeated eight times. We refer to the experimental recordings as the observation sounds, which are compared with non-degraded model sounds in the data analysis. The models were recorded with the same equipment in an anechoic room in the Technical Institute Vienna (TGM). The microphone was 1.7 m away from the loudspeaker to avoid near-field acoustic effects.

F. Data analysis

The observation sounds and the model sounds were transferred digitally to a computer. Of the eight repetitions in each experiment, the first four that were not superimposed by other sounds or fluctuating wind noise were selected. One second of undisturbed background noise was selected from the 2 s of ''silence'' before each observation sound. The element-specific filter settings for the test sounds were then applied respectively to models, observation sounds, and background noise periods.

The data analysis was based on the comparison of the filtered observation sounds with the respective model sounds [see Dabelsteen *et al.* (1993) for further details and Holland *et al.* (1998)]. Specifically, we used three measures of attenuation and degradation: (*i*) signal-to-noise ratio (SNR), (*ii*) excess attenuation (EA), which is the level of attenuation in excess to the 6 dB/dd predicted by spherical spreading, and (*iii*) a blur ratio, which expresses the distortion in amplitude and frequency patterns over time.

The SNR is calculated from the relation of the observation sound to the background noise. First, the energy of the noise component (En) of the observation is measured from the noise recordings immediately before each element. Then model and observation were aligned in time by maximizing the cross correlation between them to locate the exact beginning of the attenuated sound. In the aligned position, the energy of the observation sound (Ey) was determined and the SNR calculated: $\mathrm{SNR}=10\log[(\mathrm{Ey}-\mathrm{En})/\mathrm{En}]$. Note that the SNR ratio was corrected for the frequency-dependent output level of the loudspeaker.

The EA is derived from the relation of the amplitude functions (AFs) of model sound and observation sound. The AFs of the sounds are created by Hilbert transformation [for details, see Dabelsteen and Pedersen (1985)], and then AFs of model and observation are aligned by maximizing the cross correlation. In the aligned position, the energy of the observation was estimated by a factor k_{AF}, which is necessary to attenuate the model sound to the observation. Here k_{AF} was used to estimate the EA: $\mathrm{EA}=-20\log k_{\mathrm{AF}}-A$, where A is the attenuation caused by spherical spreading.

The energy of the difference signal ($\mathrm{Ex}_{\mathrm{AF}}$) between the k_{AF} attenuated model and the observation represents the blurring of the observed sound. The ratio of the energy of this difference signal to the energy of the observed sound ($\mathrm{Ex}_{\mathrm{AF}}/\mathrm{Ey}_{\mathrm{AF}}$) is the blur ratio.

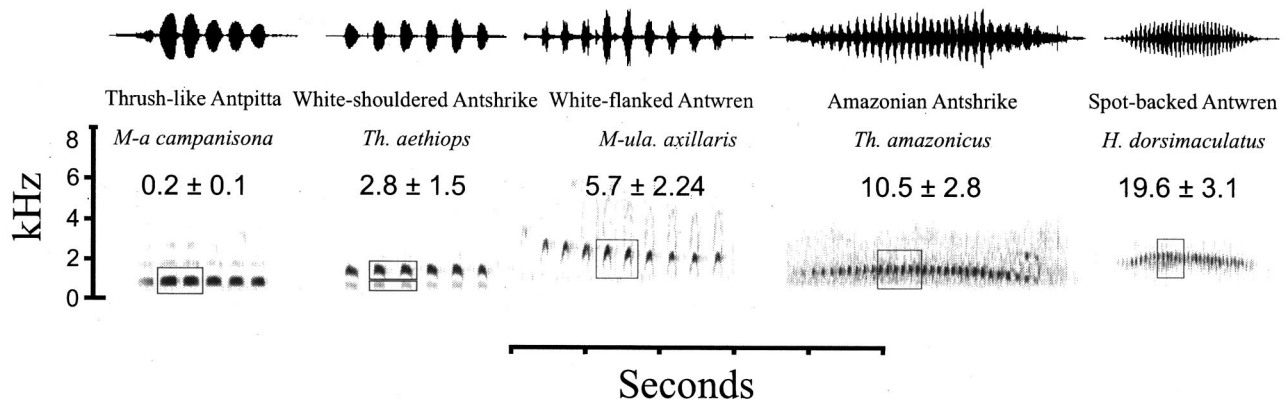

FIG. 2. Sonagrams with oscillograms of the songs of the five investigated species. Numbers are for the average song post heights with standard deviations, *n* exceeds at least 25 singing posts per species. Part of the songs, which were used for transmission experiments, are framed in the sonagrams. The overtones of the song of the Thrush-like Antpitta look quite intense at the figure, but actually they are 25 to 30 dB softer than the fundamental in this species.

G. Fixed time periods of song as experimental unit

An important question was to decide which unit of song we should use to compare the different species. As already mentioned, the strong reactions of conspecific individuals prohibited the transmission and measurement of whole songs. We first thought to compare elements between the species, but element length differs considerably among species, from 25 ms in the Spot-backed Antwren to 235 ms in the Thrush-like Antpitta, and preliminary measurements showed that this leads to an underestimation of blurring in the very short elements. Hence, we decided to standardize the different test sounds to the same time period, which was given by the shortest experimental song length of 290 ms. Thus, the attenuation and degradation measures for all species refer to the same amount of song time in each species. It includes also the measurement of interelement pauses, which is a deviation in the application of this method from former studies (Dabelsteen *et al.*, 1993; Holland *et al.*, 1998) and influences the blur ratio values. In this procedural change pauses are treated as part of the signal, and reverberations, which fall into the silent parts of our test sounds, are counted as blurring of the whole signal. This seems appropriate if we consider trills in bird songs: because the units of a trill have more or less the same frequency, single units can be masked by reverberations of the previous ones (''forward masking''), and the whole signal can become unidentifiable. The same condition applies to our study songs. All of them have simple elements with more or less overlapping frequency ranges and can be seen as trills with varying element and time structure (see Fig. 2). This approach assumes that the pause length influences the blur ratio values. If we look at pause times, which are shorter than the reverberation time (reverberation time is here defined as measurable duration of reverberations after one element). Longer pauses mean more reverberations, and a longer pause length increases the value of the blur ratio. In the case of our experimental sounds, we had a fixed absolute duration for all species-specific sounds. Here the ratio of total pause time to element time can determine the degradation values. A higher proportion of elements should lead to lower blur ratio values, whereas a larger amount of pause components tends to create larger values. Actually, we find this relationship in our test sounds. The experimental sounds of the White-flanked Antwren have the highest average blur ratio values and also the largest proportion of pauses (54%) on the whole song, whereas the sounds of the Thrush-like Antpitta had the lowest average blur ratio values with a proportion of pauses of 38% (see Sec. III). We could try to correct for this relationship, but the crucial question behind it is whether our measured values mirror the real situations in the perception mechanism of the birds. If they do, it means that reverberations during the song element are less disturbing in the perception than during the pauses. We think it can be true in our case of potential forward masking, when the reverberations are able to ''destroy'' the temporal pattern of the whole signal. If it applies, it is significant that our experimental sound pauses do not deviate from the real natural

TABLE I. Song characteristics, weight, and song post heights of the investigated species. Numbers are averages of measurements of at least eight songs per species; standard deviations are given in brackets.

Species	Song length (s)	Element length (ms)	Interelement pauses (ms)	Lowest frequency (kHz)	Highest frequency (kHz)	Loudest frequency (kHz)	Body mass (g)	Song post height (m)
Thrush-like Antpitta	2.06(±0.11)	214 (±19.8)	101 (±18.3)	0.846(±0.024)	0.898(±0.030)	0.875(±0.010)	47.0[a]	0.15(±0.08)
White-shouldered Antshrike	2.53(±0.67)	165 (±17.8)	172 (±16.4)	0.738(±0.055)	1.605(±0.065)	1.510(±0.045)	29.6[b]	2.8 (±1.50)
White-flanked Antwren	3.67(±0.4)	139 (±7.5)	165 (±16.1)	1.39 (±0.216)	4.556(±0.135)	2.03 (±0.057)	8.42[b]	5.5 (±2.25)
Amazonian Antshrike	2.4 (±0.17)	54.5(±9.3)	52.2(±11.6)	1.160(±0.120)	2.300(±0.11)	1.525(±0.035)	17.6[b]	10.5 (±2.80)
Spot-backed Antwren	1.59(±0.10)	24.3(±3.8)	23.7(±3.3)	1.150(±0.110)	2.464(±0.108)	2.04 (±0.060)	~11.0[c]	19.6 (±3.10)

[a]Dunning (1993).
[b]Preleuthner (personal communication, birds from the study area).
[c]Weight of near relative *Herpsilochmus rufimarginatus*, weight of Spot-backed Antwren is unknown.

patterns in the songs. Fortunately, this is not the case. If we compare the proportion of elements in whole songs and our test sounds, they are very similar ($r=0.97,\ p<0.01,\ n=5$).

H. Statistics

In all experiments, 6 different test sounds on 15 different transmission paths with 4 repetitions produced 360 observation sounds and 360 noise samples. In species with more than one test sound the average values were taken to represent the species. An exception is the White-shouldered Antshrike, where both the fundamental and the first harmonic formed a unit of analysis. The reason lies in the very different transmission properties of these two parts. Therefore, three-factor ANOVAs [6(species)×5(height)×3(distance)] with four repetitions were calculated with SNR, EA, and blur ratio as dependent variables. Only main and two-factor interaction effects were considered. A nonlinear multiple regression was used to model the different transmission variables as a function of height and distance. This was used to calculate the residuals of the species-specific sounds from the predicted value for all sounds. The respective regressions included distances between senders and receivers as well. Statistical calculations were conducted with SPSS, Statistica, and our own multiple regression programs.

III. RESULTS

A. Song structure and song post height

All songs (Fig. 2) are rather stereotypical sequences of simple elements. That of the White-shouldered Antshrike is an exception, with elements consisting of two harmonics. In this case, the fundamental frequency at 0.806 kHz was on average 6 dB weaker than the first overtone (measured in eight recordings at a distance of 4–6 m with a microphone height of 1.5 m and the bird 2 m above the ground). A striking relationship is the decreasing element length with height (Table I, Spearman rank-order correlation $r_s=1,\ p<0.001$). The only other significant relationship between song post and song features is the increase in loudest frequency with song post height (Spearman rank-order correlation $r_s=0.89,\ p<0.05$). Not surprisingly, body mass shows a significant positive correlation only with frequency measures, where heavier birds use lower frequencies, regardless of whether we consider the highest (Spearman rank-order correlation $r_s=-0.1,\ p<0.05$) or lowest frequencies of their songs (Spearman rank-order correlation $r_s=0.89,\ p<0.05$).

TABLE II. Factorial ANOVA table for background noise (3 distances×5 heights×6 species-specific filter settings); main and two-factor interaction effects. Distance (17.5, 37, and 54.5 m) and height (0.15, 2, 6, 12, and 21 m) refer to the distance between microphone and loudspeaker and their height above ground level.

Source of variation	d.f.	*F* ratio	*P*
Main effects			
Species	5	90.735	<0.000 01
Height	4	219.397	<0.000 01
Distance	2	417.804	<0.000 01
Two-factor interaction effects			
Species×Height	20	6.858	<0.000 01
Species×Distance	10	8.535	<0.000 01
Height×Distance	8	58.554	<0.000 01

TABLE III. Factorial ANOVA table for the signal-to-noise ratio, details like Table II.

Source of variation	d.f.	*F* ratio	*P*
Main effects			
Species	5	272.556	<0.000 01
Height	4	578.479	<0.000 01
Distance	2	1314.346	<0.000 01
Two-factor interaction effects			
Species×Height	20	40.711	<0.000 01
Species×Distance	10	6.571	<0.000 01
Height×Distance	8	27.531	<0.000 01

B. Transmission experiments

1. Variation in background noise

For the interpretation of the transmission variables (EA, SNR, and blur ratio), it is important to know how the background noise varied at the different recording locations. Background noise values are given as root mean square (rms) values and are determined within the width of the frequency filter for each test sound. Thus, it is equivalent to the noise within the frequency range of each test sound.

In the ANOVA, all main and first-order interaction effects were significant (Table II). Distance explained most of the variance, and of all the interactions the one between distance and height explained most. The strong effect of distance is explained by a lower ambient noise level at the 54.5-m distance. We attribute this difference to a different vegetation structure at this point, with a more open canopy and denser vegetation near the ground. At all distances, there was less background noise at the ground and a strong dependence on the species-specific frequency ranges.

2. Correlation between EA, SNR, and BLUR

The three different measures were strongly intercorrelated ($p<0.0001,\ n=358$). EA increased with decreasing SNR ($r=-0.732$). Blur ratio increased with EA ($r=0.742$) and decreased with increasing SNR ($r=-0.698$).

TABLE IV. Factorial ANOVA table for excess attenuation, details like Table II.

Source of variation	d.f.	*F* ratio	*P*
Main effects			
Species	5	649.66	<0.000 01
Height	4	12 681.74	<0.000 01
Distance	2	1005.79	<0.000 01
Two-factor interaction effects			
Species×Height	20	370.70	<0.000 01
Species×Distance	10	136.35	<0.000 01
Height×Distance	8	351.40	<0.000 01

TABLE V. Factorial ANOVA table for blur ratio, details like Table II.

Source of variation	d.f.	*F* ratio	*P*
Main effects			
Species	5	1648.394	<0.000 01
Height	4	2002.684	<0.000 01
Distance	2	752.816	<0.000 01
Two-factor interaction effects			
Species×Height	20	83.118	<0.000 01
Species×Distance	10	91.058	<0.000 01
Height×Distance	8	193.437	<0.000 01

3. Main and two-factor interaction effects

All three measures (SNR, EA, and blur ratio) had significant main and two-factor interaction effects (Tables III–V and Figs. 3–5), which explained in all degradation measures more than 98% of the total variance.

The SNR was most strongly influenced by distance, with 58% of the variance explained. The relative small decrease between 37 and 54.5 m may be explained by the already mentioned lower background noise level at the greatest distance (see previous subsection). Species differences explained 12% of total variance height explained 25%.

The effect of height explained 83% of the variance in the EA (Table IV). When the loudspeaker was moved from 0.15 to 2 m, the sound pressure level of the signals increased on average by more than 10 dB (Fig. 4). The species-specific test sounds and distance explained only 4.3% and 7% of the total variance.

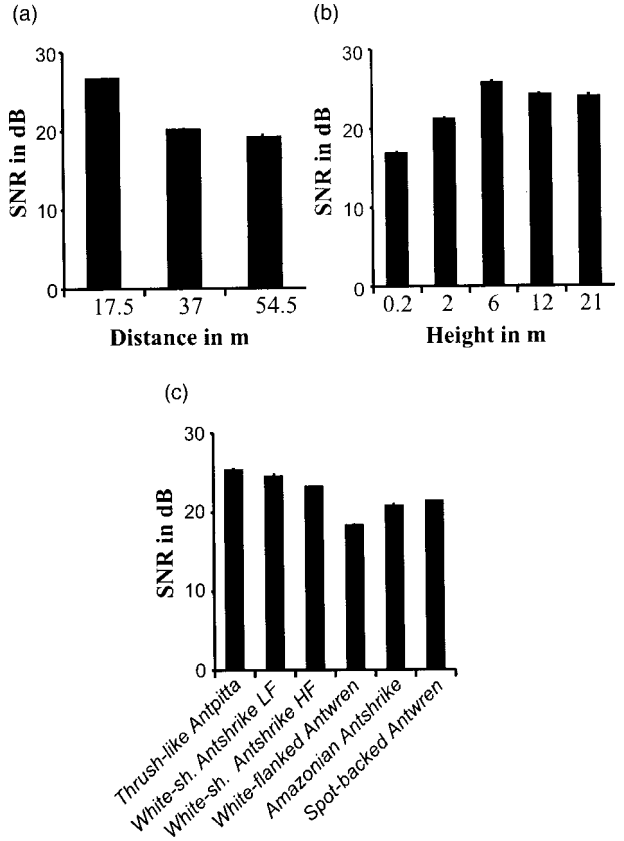

FIG. 3. Signal-to-noise ratio (means±s.e.), main effects of (a) transmission distance, (b) height of speaker and microphone, and (c) species sounds.

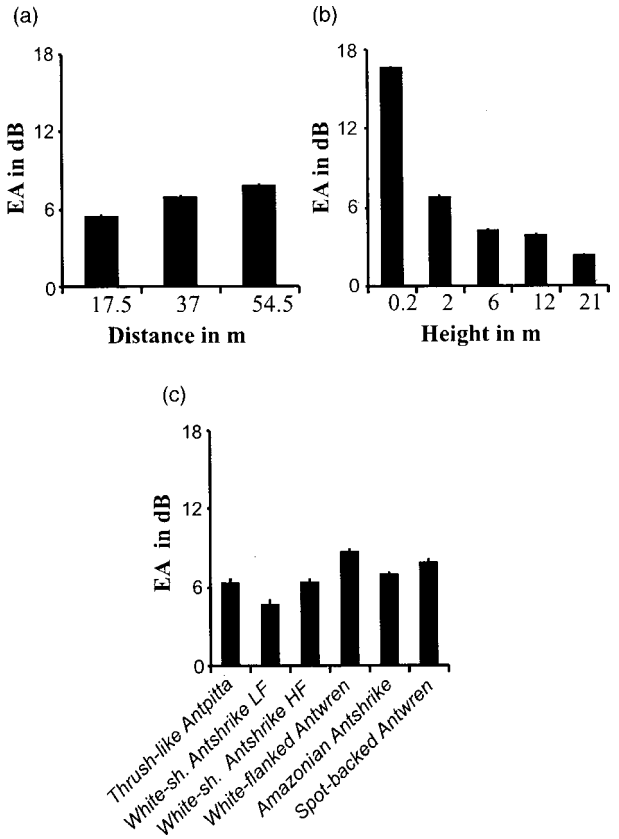

FIG. 4. Excess attenuation (means±s.e.), main effects of (a) transmission distance, (b) height of speaker and microphone, and (c) species sounds.

Height also explained most of the variance (42.5%) in the blur ratio. In contrast to what was found for EA and SNR distance was the factor that explained the lowest proportion (12.3%) of the variance for blur ratio. Species-specific test sounds explained here more than a third of the total variance (Table V, Fig. 5).

4. Influence of frequency and filter width of the test sounds

The highest SNR levels were found for elements with low-frequency ranges ($r_s=-0.92$, $p<0.01$, $n=6$), while excess attenuation increased with frequency of the test sounds (Spearman rank-order correlation $r_s=0.94$, $p<0.01$, $n=6$). Blur ratio also increased at higher frequencies (Spearman rank-order correlation $r_s=0.94$, $p>0.01$, $n=6$), but also related negatively to the filter-width (Spearman rank-order correlation $r_s=-0.82$, $p<0.05$, $n=6$) of the experimental sounds. The effect of frequency is most clearly demonstrated in the higher and lower harmonics of the White-shouldered Antshrike, which were treated separately because these elements differ only in frequency and frequency range (Figs. 2, 4, and 5).

5. Comparison of species and heights in absolute and relative levels of degradation

The means of the main effects of the species sounds were used to compare the absolute levels of degradation (Tables II–IV) in the different species. To investigate how each species-specific test sound deviated from the overall

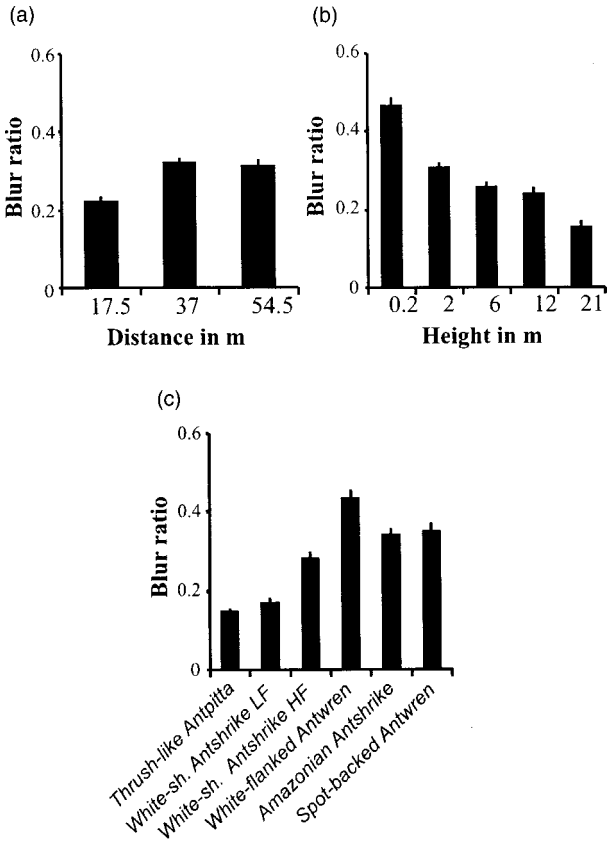

FIG. 5. Blur ratio (means±s.e.), main effects of (a) transmission distance, (b) height of speaker and microphone, and (c) species sounds.

pattern of degradation, we calculated for each degradation measure a regression on height and distance for all species together. From this we derived the species-specific residuals at different heights (Fig. 6). These residuals were used for two purposes. First, we compared the values of degradation at the species-specific song post with the values of the other species at this height. Second, we compared single species values at the experimental height closest to the song post height with the other heights. If degradation was minimized in one of our three measures at the species-specific song post, we expected there relative to other heights a minimum of EA or blur ratio or a maximum in SNR. Note that we took the residual values as main criterion for an adaptation to the song post height, since they are independent of the overall pattern of degradation.

(a) *Thrush-like Antpitta (song post height 0.15 m)*. Although the experimental song of the antpitta had, in all heights, a low excess attenuation on average (Fig. 4), we found the strongest attenuation of all species near the ground (Fig. 6). If we compare the residual values of the Antpitta test song at different heights, we find also the highest values at the ground. The SNR is the highest of all species at all heights, however, it has the lowest residual values close to the ground. The absolute blur ratio values are the lowest of all species, and the residuals have their minimum near the ground.

(b) *White-shouldered Antshrike (song post height 2.8 m)*. In this species, fundamental frequency and first overtone were tested separately. Close to the species-specific song post height at 2 m, the residuals of the fundamental showed a minimum in EA and blur ratio and a maximum in SNR. The minimum in the residuals of the first overtone was in all three degradation measures not close to the species-specific song post height. A *post hoc* comparison of degradation values showed that near the song post height at 2 m, the fundamental part of the test sound was at all distances and in all three measures significantly less degraded (Scheffé test, $p < 0.001$, $n = 59$).

(c) *White-flanked Antwren (song post height 5.5 m)*. The experimental song of the White-flanked Antwren had the highest degradation values in all three measures. In the residuals of its test sound the minima in blur ratio and EA or the maximum in SNR were not close to the song post height.

(d) *Amazonian Antshrike (song post height 10 m)*. The experimental song of the Amazonian Antshrike was more degraded according to all measures of degradation than the average test sounds. As in the White-flanked Antwren, we found no minima or maxima in the residuals of its test song near the species-specific song post height.

(e) *Spot-backed Antwren (song post height 19.6 m)*. The song of this canopy-living antbird had on average relatively high values of degradation (Figs. 3–5). In the canopy the experimental songs had, relative to the other species, the lowest attenuation values and the highest SNR values. In the comparison of the residuals of its test sound near the song post height to other heights, we found at the canopy less degradation in all three measures, but there was also near the ground a maximum in SNR and a minimum in EA (Fig. 6). Only in the blur ratio was there a clear minimum near the species-specific song post height.

IV. DISCUSSION

A. Overall patterns in degradation

At 54.5-m distance, the average excess attenuation values for our test sounds ranged from 18 dB at the ground to 1.3 dB at the canopy 21 m above the ground. The excess attenuation at the ground reached quite high values, with more than 20 dB in two species at 54.5 m in our study site. These values exceed the attenuation measured at 100 m in a mature rainforest with less vegetation on the ground and are more typical for sites with a denser understory (Marten *et al.*, 1977, Fig. 3). The quality and accuracy of our results was confirmed by separate measurements of excess attenuation in our study site (Ellinger, in press). Though white noise was transmitted and different equipment was used at similar transmission heights (0.45, 2.5, 6, 12.5, and 18 m), the estimated values were similar to our values [e.g., near the ground, where EA reached 20 dB at 53 m for 0.8 kHz (Ellinger, in press)].

Because the signal-to-noise ratio decreases when attenuation increases, it is not surprising that the SNR mirrors the results of EA at different heights and distances. As expected, we also found the largest SNR values in test sounds with the narrowest filter widths. The blur ratio decreased slightly at the greatest distance of 54.5 m. It probably can be attributed

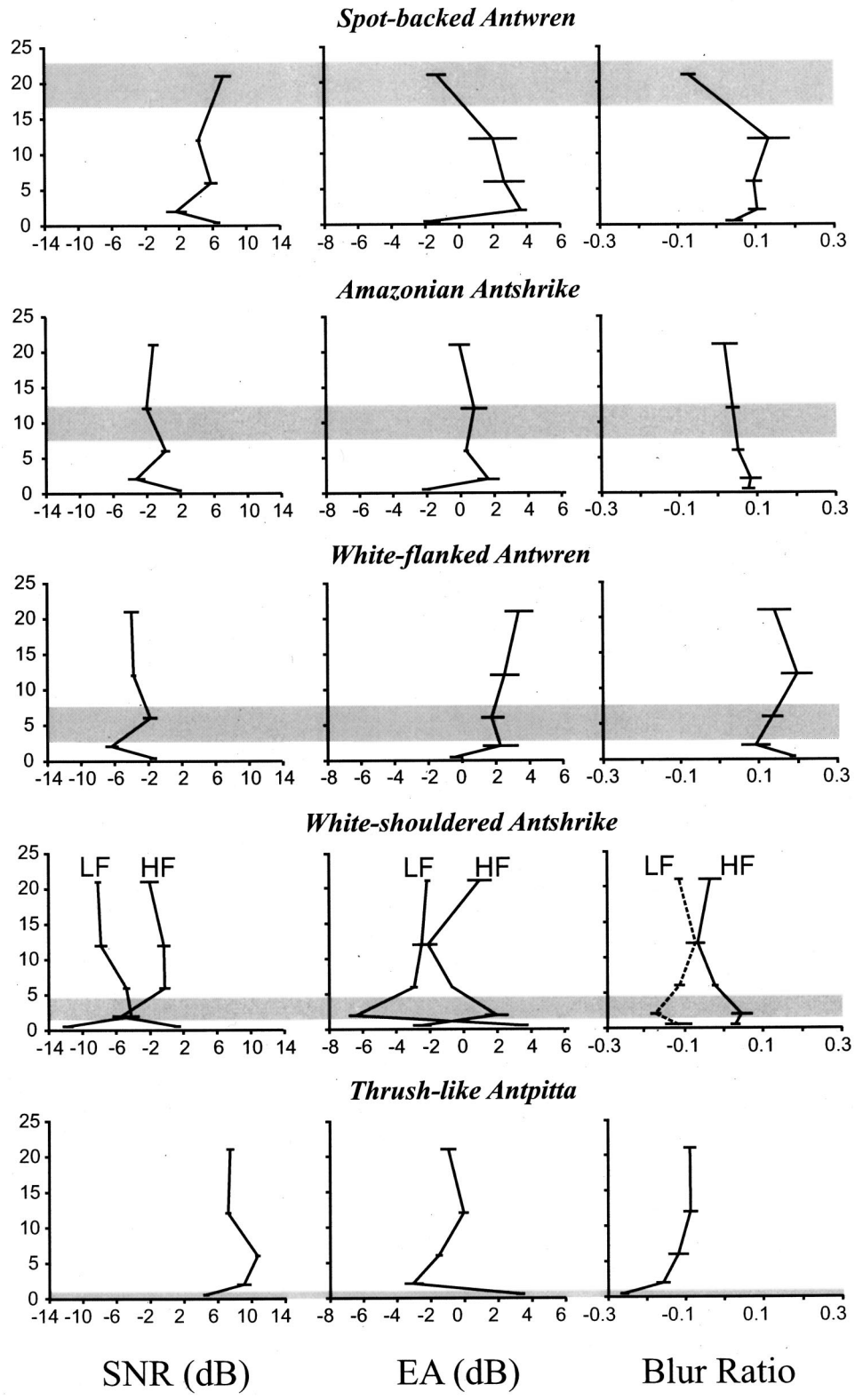

FIG. 6. Species-specific residuals of signal-to-noise ratio, excess attenuation, and blur ratio at different heights. The residuals are from a nonlinear regression. The gray areas mark the song post height (mean±s.e.). LF and HF means lower and higher frequency components of the song elements of the White-shouldered Antshrike.

to the different vegetation structure at this point. Also Dabelsteen *et al.* (1993) and Holland *et al.* (1998) found a decrease in blur ratio at larger distances. This suggests that the blur ratio is more dependent on the local environment near the receiver and that the change with distance is less regular than for EA or SNR (Dabelsteen *et al.*, 1993). Like EA and SNR, the blur ratio reached the highest values close to the ground.

B. Degradation close to the ground and the song of the Thrush-like Anpitta

Higher attenuation close to the ground is caused mainly by destructive interferences between direct and reflected waves (''ground effect'') and is a well-known feature of sound propagation outdoors (Embleton, 1996; Wempen, 1986). The simplest effects of the ground on sound fields are

due to transmission path length differences between direct and reflected waves, which results in phase differences between the two waves. The relative positions of the source and receiver determine which frequencies lose or gain energy due to phase differences. The physical characteristics of the ground and the distance between sender and receiver have a major impact on the attenuation as well (see Embleton, 1996). If the source is very close to the ground, as in our experimental height of 0.15 m, we have grazing incidence of sound waves. In this special case, destructive interference is not enough to explain the frequency-dependent attenuation near the ground. Rather, sound propagation can be described as being influenced by low-pass filtering: above a cutoff frequency, the direct sound waves are canceled out by the reflecting waves, whereas sounds below this frequency pass along the surface in full strength (see Wempen, 1986; Embleton, 1996). The cutoff frequency varies with the physical characteristics of the ground but is always lower than 1 kHz.

Wiley and Richards (1982) mentioned the case of grazing incidence in connection with ground-living antbirds and wondered how these species circumvent the extreme attenuation. At the beginning of our study, we hypothesized that the low-pitched song (average frequency of about 0.9 kHz) of the ground-living antpitta would be below the cutoff frequency and we would find less attenuation of this song near the ground. Actually the opposite was true: the test sound of the Thrush-like Antpitta showed the highest values in excess attenuation of all species close to the ground (Fig. 6). Because even the lower pitched test sound of the White-shouldered Antshrike (0.65 kHz) was heavily attenuated at the ground, it is likely that the cutoff frequency was lower than 600 Hz. The song of the antpitta has a very narrow frequency range, which caused a higher SNR in our results and compensated at least partly for the loss in energy by attenuation (Fig. 6).

The song elements are also longer than in the other species, and therefore could be easier to detect [temporal summation, Klump and Maier (1990), see Results ''Song characteristics and degradation'']. Since we do not know the exact sound pressure level of the real song, it is possible that the species compensates the higher loss in attenuation by louder singing. However, this does not explain why the species sings under these disadvantageous circumstances. Maybe extreme morphological and behavioral adaptations confine the species to the ground.

Though the antpitta test song attenuated extremely at the ground, it had there the lowest blur ratio values of all species and, in comparison to other heights, we find a minimum in the residuals to the overall degradation curve (Fig. 6). We think that lower absolute blur ratio in comparison to other species results partly from the simple structure of the signal, and partly in small proportion of the pause time to the total time of our test sound (see Sec. II G). The relative minimum in blur ratio at the ground in comparison to the residuals at other heights implies that the antpitta song has characteristics that resist the stronger degradation at the ground more than the other songs. One of the most striking features of the antpitta song is the long element with a simple amplitude structure and very slow amplitude modulations (see Fig. 2). In comparison to songs with faster amplitude changes, songs with slow amplitude modulations are less degraded by reverberations (Wiley and Richards, 1982). To explain the relatively low blurring of the antpitta song near the ground, we also have to presume that more reverberations occur close to the ground than higher up. Indeed, this condition was found at our study site by means of RT60 measurements (RT60 is a measure used in architectural acoustics; it is the time it takes a signal to decay 60 dB from it offset). At a distance of 53 m, the RT60 between 0.5 and 1 kHz was 2.3 s close to the ground (0.45 m), whereas at 16-m height, it was 1.4 s (Ellinger, in press).

C. Fundamental and first overtone in the White-shouldered Antshrike

The song of *Thamnophilus aethiops* (song post height 2 m) offers a special case with a song consisting of a fundamental frequency and a first harmonic. The lower frequency, which is uttered with 6 dB less energy, is less degraded than the first overtone near the species-specific song post height in all degradation measures. By 37 m, the fundamental frequency was louder than the first overtone. The low EA of the fundamental can be attributed to the lower frequency because, except close to the ground, lower frequencies attenuate less in all terrestrial environments (Embleton, 1996). The SNR increases with the decreasing EA and bandwidth of the fundamental. The lower blur ratio can probably also be attributed to the higher frequency-dependent attenuation of the first overtone. But why does this species not sing only or mainly at the fundamental frequency? A probable reason could be a physiological constraint; for example, the mass of the sound-producing structure determines the frequency, and in many birds this mass is dependent on body size (Bowman, 1979; Wallschläger, 1980; Ryan and Brenowitz, 1985). Overall, the fundamental of the song seems well adapted relative to the species-specific song post height (Fig. 6).

D. Degradation in the canopy and the time structure of the song of the Spot-backed Antwren

Among the remaining three species, only the results for the test song of the canopy-living Spot-backed Antwren indicate an adaptation to the species-specific song post height. Here we found relatively low blur ratio values at the 21-m transmission height, and there is also a tendency for better transmissibility in the canopy in the EA and SNR values (see Fig. 6). The song of the species consists of very short pauses and elements with a length of about 25 ms (Table I). In an experimental study of reverberations in a deciduous forest, Richards and Wiley (1980) found that birds should use trills with pauses longer than 20–50 ms to avoid masking of interelement pauses by reverberations. Our results concerning the blur ratio values, which include also the measurement of reverberations (see Sec. II), support this assumption in the Spot-backed Antwren: we found higher values of blur ratio relative to the average blur ratio of all species below the canopy (Fig. 6) and lower values above the canopy. Therefore we hypothesize that the antwren can use faster repetitive songs because of fewer reverberations in the canopy. Then it

is more appropriate to call the use of short pauses a release from constraints rather than an adaptation to forest acoustics.

Alternatively, the fast temporal structure of this song could be an adaptation to amplitude fluctuations caused by wind or atmospheric turbulence at the canopy (Wiley and Richards, 1982). Irregular fluctuations in amplitude can change the amplitude pattern of a signal if the modulation frequency of the signal is equal to or lower than the modulation frequency of the atmospheric fluctuations. We measured the influence of atmospheric turbulence in additional transmission experiments with pure tones (1, 2, 4, and 8 kHz) over 20 and 60 m in 2- and 21-m height (Nemeth and Winkler, unpublished data). We found a peak in amplitude variation at a modulation frequency of 0.2 Hz, but failed to detect significant amplitude modulations at higher frequencies. Thus, none of the songs of our investigated species can be influenced seriously by such a low modulation frequency, and we conclude that irregular amplitude fluctuations have no impact on the transmissibility of the investigated songs.

E. Song characteristics and height-dependent degradation

A striking feature in the songs of all our study birds is the strong negative correlation between length of elements and song post height (see Table I). One possible explanation of this relationship could be found in the height-dependent reverberation times. Reverberation time increases with decreasing height (Ellinger, in press), which could influence the structure of elements and pauses of the songs. As in the Spot-backed Antwren, the pauses are masked if they are shorter than the effective reverberation time, as the mentioned 20–50 ms (Richards and Wiley, 1980). Because reverberation decreases with height, long pauses at low heights would avoid degradation. On the element part of the song it would favor slow amplitude modulations close to the ground. Similarly, this would also explain the differential song structure of our study birds.

The strong correlation between song element length and song post height in our species may have an alternative explanation: because the degradation increases near the ground, the use of longer elements could improve the detection through a process called temporal summation. In effect, elements longer than the time over which sound energy is summed are easier to detect than shorter elements (Klump and Maier, 1990). Temporal summation seems to be widespread in birds (e.g., Dooling and Searcy, 1985) and is probably a general mechanism to enhance detection in unfavorable conditions (Klump, 1996).

V. CONCLUSIONS: A PANGLOSSIAN VIEW ON THE TRANSMISSIBILITY OF BIRD SONGS?

We have used the term adaptation to describe a state of being in relation to other states in the same environment. An adaptation to the singing post height was thus supposed whenever a test sound of our study species was less degraded at species-specific song post heights in any of our three degradation measures. So far, we based the discussion of our results solely on this rather particular notion. But, how reasonable are our assumptions? Can we speak about adaptation of the vocalizations to the environment and neglect other selection pressures for the design of acoustic signals?

Adaptation is an important, but ''slippery'' concept in biology (Reeve and Sherman, 1993) and to describe every trait of an organism as an optimal solution of evolution has been described as one of the most dangerous pitfalls of the ''Adaptionist Program'' (Gould and Lewontin, 1979). One accepts as final evidence for an adaptation if it can be shown that it results in a higher fitness in a given environment when compared to alternatives. Many studies on adaptation cannot deliver this proof and apply some indirect fitness criteria [''design performance'' (Krimbas, 1984)]. In our case better transmissibility of signals or the minimization of degradation serves as such a criterion. We are aware that there are other possible explanations for the design of vocalizations [e.g., sexual selection on the variability of song elements, see, e.g., Catchpole and Slater (1995)]. But, transmissibility is a prerequisite for all other selecting pressures affecting vocalizations (Wiley and Richards, 1982) and can itself be an important target of selection (Morton, 1986).

In our transmission experiments we found large height-dependent variability in the degradation values of our test sounds. Therefore we assume that within a rainforest the selective demands on acoustic communication are severe. In at least three of five species we found that our test songs degraded less at their species-specific song post heights in relation to those of the other species. These results indicate that songs are adapted to the transmissibility at different heights. The mechanisms by which degradation is minimized differ among species. This is possible because excess attenuation, SNR, and blurring of the signals can vary more or less independently from each other. Near the ground, the Thrush-like Antpitta compensates the loss through extreme attenuation by using relatively long elements in a narrow frequency range, thereby achieving a high SNR. The White-shouldered Antshrike produces an extremely low-pitched fundamental that surpasses the first overtone at longer range in all degradation measures, although it contains less energy and a worse SNR at the beginning. The canopy-living Spot-backed Antwren can afford to deliver trill elements at a high rate because there are less intense reverberations above the canopy to mask them. Released from this constraint, the bird can produce fast trills that may have other specific advantages in communication. In all three species songs were least blurred at their own song post height.

Song post height, in principle, is at the disposal of the singer. Thus a bird can choose a specific song post height because its song propagates there well. This, however, may be costly if foraging height and song post height differ greatly or if the bird is constrained otherwise in reaching and negotiating a certain stratum. To account for this aspect, we compared the singing post heights with species-specific foraging heights at the same study site (Preleuthner and Winkler, unpublished data) In four of our species the average foraging height is within the range of the measured singing post height (species, average foraging heights of both sexes, standard deviations, number of observations): Thrush-like Antpitta, 0.02 m, 0.17 m, $n=20$; White-shouldered Ant-

shrike, 1.91 m, 2.05 m, $n=42$; White-flanked Antwren, 4.8 m, 2.75 m, $n=235$; the Spot-backed Antwren was always found in the canopy ($n=13$), but here exact height measures are missing. The only exception is the Amazonian Antshrike, which foraged at an average height of 5 m (standard deviation$=3.4$ m, $n=42$) and sang at 10 m (see Table I). In this species we found no indication for an adaptations of the song to the song post height.

The comparison of foraging and song post heights points to a hidden implication of our experimental setup: we transmitted the experimental sounds only horizontally because we assumed that the receiver of the signal is at the same height. This seems to be correct in at least four of five species.

Another simplification of our experiments is the fact that all experimental songs were analyzed (see Sec. II) with the same sound pressure level. We do not know how much the SPL differs between the species, and this neglected feature could well be an important feature for better transmissibility. Also, the hearing threshold between the species could differ and influence the result. Again, a closer knowledge of the species-specific behavior would be desirable.

However, our results stress the importance of height-dependent degradation as selection pressure for avian communication and we think that future experiments will reveal more fine-tuned adaptations of avian vocalizations to the acoustic environment within a rainforest.

ACKNOWLEDGMENTS

We thank all those who were involved in the planning and execution of the study. Niki Goeth was indispensable in the field experiments. Simon Boel Pederson advised us in the use of his software program SIGPRO. Ole Næsby Larsen took part in the discussion and planning of the experiments. Heiko Weix supported us in technical questions at the beginning of the study. Dieter Hohenwarter and Alexander Niemczanowskie from the Institute of Technology in Vienna helped in the calibration of the equipment. Dieter Deutsch and Anton Noll from the Acoustic Research Institute of the Austrian Academy of Sciences enabled the digital transfer of data to the computer. Richard Wagner made a constructive review of an earlier draft of the article. We thank one anonymous reviewer, Sandra L. L. and Abbot S. Gaunt for useful comments. The study was funded by the Austrian Science Foundation, Project No. P11563-Bio.

Badyaev, A. V., and Leaf, E. S. (**1997**). ''Habitat Associations of Song Characteristics in *Phylloscopus* and *Hippolais Warblers*,'' Auk **114**, 40–46.

Beecher, M. D. (**1988**). ''Spectographic analysis of animal vocalizations: implications of the 'uncertainty principlé,' '' Bioacoustics **1**, 187–208.

Bowman, R. I. (**1979**). ''Adaptive morphology of song dialects in Darwin Finches,'' J. Ornith. **120**, 353–380.

Catchpole, C. K., and Slater, P. J. B. (**1995**). *Bird Song: Biological Themes and Variations* (Cambridge U. P., London), pp. 115–187.

Chappuis, C. (**1971**). ''Un exemple de l'influence du milieu sur les émissions vocales des oiseaux: Lévolution des chants en forêt équatoriale,'' Terre et Vie **2**, 183–202.

Cosens, S. E., and Falls, J. B. (**1984**). ''A comparison of sound propagation and song frequency in temporal marsh and grassland habitats,'' Behav. Ecol. Sociobiol. **15**, 161–170.

Dabelsteen, T., and Pedersen, S. P. (**1985**). ''A method for computerized modification of certain animal sounds for communication study purposes,'' Biol. Cybern. **52**, 399–404.

Dabelsteen, T., Larsen, O. N., and Pedersen, S. B. (**1993**). ''Habitat-induced degradation of sound signals: Quantifying the effects of communication sounds and bird location on blur ratio, excess attenuation, and signal-to-noise ratio in blackbird song,'' J. Acoust. Soc. Am. **93**, 2206–2220.

Dooling, R. J., and Searcy, M. H. (**1985**). ''Temporal integration of acoustic signals by the Budgerigar,'' J. Acoust. Soc. Am. **77**, 1917–1920.

Dunning, J. B. (**1993**). ''Body masses of birds of the world,'' in *CRC Handbook of Avian Body Masses*, edited by J. B. Dunning (CRC, London), pp. 3–332.

Ellinger, N. (**in press**). ''The acoustic characteristics of the lowland rainforest at the Suromoni study site,'' Bioacoustics.

Embleton, T. F. W. (**1996**). ''Tutorial on sound propagation outdoors,'' J. Acoust. Soc. Am. **100**, 31–48.

Gould, S. J., and Lewontin, R. C. (**1979**). ''The Spandrels of San Marco and the Panglossian Paradigm: A critique of the adaptionist programmme,'' Proc. R. Soc. London, Ser. B **205**, 581–598.

Holland, J., Dabelsteen, T., and Pedersen, S. B., (**1998**). ''Degradation of wren Troglodytes troglodytes song: Implication for information transfer and ranging,'' J. Acoust. Soc. Am. **103**, 2154–2166.

Holland, J., Dabelsteen, T., Bjern, C. P., and Perdersen, S. B. (**2001**). ''The location of ranging cues in wren song: evidence from calibrated interactive playback experiments,'' Behaviour **138**, 189–206.

Jilka, A., and Leisler, B. (**1974**). ''Die Einpassung dreier Rohrsängerarten (*Acrocephalus schoenobaenus, A. scirpaceus, A. arundinaceus*) in ihre Lebensräume in Bezug auf das Frequenzspektrum ihrer Reviergesänge,'' J. Ornith. **115**, 192–212.

Klump, G. M. (**1996**). ''Bird communication in the noisy world,'' in *Ecology and Evolution of Acoustic Communication in Birds*, edited by D. E. Kroodsma and E. H. Miller (Cornell U. P., Ithaca), pp 321–338.

Klump, G. M., and Maier, E. H. (**1990**). ''Temporal summation in the European starling (*Sturnus vulgaris*),'' J. Comp. Psychol. **104**, 94–100.

Krimbas, C. B. (**1984**). ''On adaptation, neo-Darwinian tautology, and population fitness,'' Evol. Biol. **17**, 1–57.

Lemon, R. E., Struger, J., Lechowicz, M. J., and Norman, R. F. (**1981**). ''Song features and singing heights of American warblers: Maximization or optimization of distance,'' J. Acoust. Soc. Am. **69**, 1169–1176.

Marten, K., Quine, D., and Marler, P. (**1977**). ''Sound transmission and its significance for animal vocalization II. Tropical forest habitats,'' Behav. Ecol. Sociobiol. **2**, 291–302.

McGregor, P. K., and Krebs, J. A. (**1984**). ''Sound degradation as distance cue in Great Tit (*Parus major*),'' Behav. Ecol. Sociobiol. **16**, 49–56.

Morton, E. S. (**1975**). ''Ecological sources of selection on avian sounds,'' Am. Nat. **109**, 17–43.

Morton, E. S. (**1982**). ''Grading, Discreteness, Redundancy and Motivation-Structural Rules,'' in *Acoustic Communication in Birds, Vol. 1*, edited by D. E. Kroodsma and E. H. Miller (Academic, Ithaca), pp. 183–210.

Morton, E. S. (**1986**). ''Prediction from the ranging hypothesis for the evolution of long distance signals in birds,'' Behaviour **99**, 65–86.

Morton, E. S., and Derrickson, K. C. (**1996**). ''Song ranging by the dusky antbird, *Cercomacra tyrannina*: ranging without song learning,'' Behav. Ecol. Sociobiol. **39**, 195–201.

Nottebohm, F. (**1975**). ''Continental patterns of song variability in *Zonotrichia capensis*: some possible ecological correlates,'' Am. Nat. **115**, 605–624.

Reeve, H. K., and Sherman, P. W. (**1993**). ''Adaptation and the goals of evolutionary research,'' Q. Rev. Biol. **68**, 1–32.

Richards, D. G. (**1981**). ''Estimation of distance of singing conspecifics by the Carolina wren,'' Auk **98**, 127–133.

Richards, D. G., and Wiley, R. H. (**1980**). ''Reverberations and amplitude fluctuations in the propagation of sound in a forest. Implications for animal communication,'' Am. Nat. **108**, 17–34.

Ridgely, R. S., and Tudor, G. (**1994**). *The Birds of South America. The Suboscine Passerines*, 2nd ed. (Oxford U. P., Oxford).

Ryan, M. J., and Brenowitz, E. A. (**1985**). ''The role of body size, phylogeny, and ambient noise in the evolution of bird song,'' Am. Nat. **126**, 87–100.

Shy, E., and Morton, E. S. (**1986**). ''Adaptation of amplitude structure of songs to propagation in field habitat in song sparrows,'' Ethology **72**, 177–184.

Sorjonen, J. (**1983**). ''Transmission of the two most characteristic phrases of the song of the thrush nightingale *Luscinia luscinia* in different environmental conditions,'' Orn. Scand. **14**, 278–282.
Wallschläger, D. (**1980**). ''Correlation of song frequency and body weight in passerine birds,'' Experientia **36**, 412.
Wempen, J. (**1986**). ''Outdoor sound propagation close to the ground,'' in *Sound Propagation in Forested Areas and Shelterbeds*, edited by M. J. M. Martens (Faculty of Sciences, Catholic University, Nijmegen, The Netherlands), pp. 83–106.
Wiley, R. H. (**1991**). ''Association of song properties with habitats for territorial oscine birds of eastern North America,'' Am. Nat. **138**, 973–993.
Wiley R. H., and Richards, D. G. (**1978**). ''Physical constraints on acoustic communication in the atmosphere: Implications for the evolution of animal vocalizations,'' Behav. Ecol. Sociobiol. **3**, 69–94.
Wiley, R. H., and Richards, D. G. (**1982**). ''Adaptations for acoustic communication in birds: sound transmission and signal detection,'' in *Acoustic Communication in Birds, Vol. 1*, edited by D. E. Kroodsma and E. H. Miller (Academic, Ithaca), pp. 131–181.

Fundamental precision limitations for measurements of frequency dependence of backscatter: Applications in tissue-mimicking phantoms and trabecular bone

Keith A. Wear[a)]
U.S. Food and Drug Administration, Center for Devices and Radiological Health, HFZ-142, 12720 Twinbrook Parkway, Rockville, Maryland 20852

(Received 18 April 2001; accepted for publication 1 September 2001)

Various models for ultrasonic scattering from trabecular bone have been proposed. They may be evaluated to a certain extent by comparison with experimental measurements. In order to appreciate limitations of these comparisons, it is important to understand measurement precision. In this article, an approach proposed by Lizzi and co-workers is adapted to model precision of estimates of frequency-dependent backscatter for scattering targets (such as trabecular bone) that contain many scatterers per resolution cell. This approach predicts uncertainties in backscatter due to the random nature of the interference of echoes from individual scatterers as they are summed at the receiver. The model is validated in experiments on a soft-tissue-mimicking phantom and on 24 human calcaneus samples interrogated *in vitro*. It is found that while random interference effects only partially explain measured variations in the magnitude of backscatter, they are virtually entirely responsible for observed variations in the frequency dependence (exponent of a power law fit) of backscatter. [DOI: 10.1121/1.1416907]

PACS numbers: 43.80.Ev [FD]

I. INTRODUCTION

Ultrasound techniques are recognized for effectiveness in osteoporosis detection (Glüer, 1997; Njeh *et al.*, 2000a). Calcaneal broadband ultrasonic attenuation (BUA) and speed of sound (SOS) are highly correlated with calcaneal bond mineral density (BMD) (Langton *et al.*, 1984; Rossman *et al.*, 1989; Tavakoli and Evans, 1991; Zagzebski *et al.*, 1991; Njeh *et al.*, 1996; Langton *et al.*, 1996; Bouxsein and Radloff, 1997; Laugier *et al.*, 1997; Chappard *et al.*, 1997; Nicholson *et al.*, 1998; Hans *et al.*, 1999; Trebacz and Natali, 1999; Njeh *et al.*, 2000b), which is in turn a useful indicator of osteoporotic fracture risk in the hip (Cummings *et al.*, 1993). BUA (sometimes in combination with SOS) has been demonstrated to be predictive of hip and other fractures in women in prospective (Hans *et al.*, 1996; Bauer *et al.*, 1997) and retrospective (Schott *et al.*, 1995; Turner *et al.*, 1995; Glüer *et al.*, 1996; Thompson *et al.*, 1998) studies. Bone sonometry is less expensive, faster, simpler, and more portable than its x-ray counterparts: dual-energy x-ray absorptiometry (DEXA) and quantitative computed tomography (QCT). In addition, ultrasound produces no ionizing radiation.

Scattering from bone has received less attention than attenuation and sound speed. The study of scattering is important, however, because it can elucidate mechanisms responsible for attenuation (the combined result of absorption and scattering). In addition, scattering measurements have shown some diagnostic promise in their own right in studies *in vitro* (Roberjot *et al.*, 1996; Wear and Armstrong, 2000; Hoffmeister *et al.*, 2000 and in press) and *in vivo* (Wear and Garra, 1997; Giat *et al.*, 1997; Wear and Garra, 1998). Backscatter is known to provide information regarding size, shape, number density, and elastic properties of scatterers (Faran, 1951; Morse and Ingard, 1986). In trabecular bone applications, trabeculae are likely candidates for scattering sites due to the high contrast in acoustic properties between mineralized trabeculae and marrow (Wear, 1999; Luo *et al.*, 1999). The diminished number and thicknesses of trabeculae with bone that are associated with increased fracture risk would be expected to reduce backscatter.

In a previous study, measurements of average frequency-dependent backscatter coefficient, $\eta(f)$, from human calcaneal trabecular samples closely obeyed a power law dependence on frequency, $\eta(f)=Af^n$ throughout the typical diagnostic range (300–700 kHz) with n having a value slightly greater than 3, close to the cubic dependence expected from cylindrically shaped scatterers (e.g., trabeculae) (Wear, 1999). A subsequent study reproduced this finding (Chaffai *et al.*, 2000). This result has implications with regard to the relative roles of scattering and absorption in determining attenuation in trabecular bone. Attenuation in the diagnostic range has been found in numerous studies to be approximately proportional to frequency to the first power. These two different coexisting frequency dependences could be consistent only if absorption is a larger component of attenuation than scattering. This result has been reinforced by studies of the anisotropy of backscatter and attenuation in trabecular bone (Wear, 2000).

Empirical estimates of the exponent (n) of the frequency dependence of backscatter coefficient have been demonstrated to be consistent with a model in which trabeculae correspond to cylinders that are long (longer than the beam width), thin (relative to the ultrasonic wavelength) and oriented approximately perpendicular to the ultrasound propagation direction (Wear, 1999). Measurements have also

a)Electronic mail: kaw@cdrh.fda.gov

exhibited compatibility with an autocorrelation model (Chaffai *et al.*, 2000). Another model in which scattering is assumed to be proportional to the mean fluctuation in sound speed in a random continuum has been proposed (Nicholson *et al.*, 2000). In contrast to the studies previously listed, this model predicts that commonly observed linear attenuation (in the diagnostic range of frequencies) can be explained by scattering. The random continuum model also predicts variations in acoustic parameters with porosity and scatterer size that are consistent with observations, including the reported nonlinear dependence of attenuation on porosity (Serpe and Rho, 1996).

Evaluation of models in relation to empirical findings requires knowledge of accuracy and precision of measurements. Lizzi *et al.* (1997) developed and validated a model for predicting precision of measurements of backscatter from liver and prostate. In the present article, the model of Lizzi and co-workers is adapted to bone. As with liver and prostate, ultrasonic echoes from trabecular bone may be modeled as superpositions of signals from unresolvable scatterers throughout the transducer resolution cell (defined by the pulse duration in one dimension and the beam cross section in the orthogonal dimensions). Like liver and prostate, trabecular bone contains many scatterers (trabeculae) per resolution cell. One modification of Lizzi's approach in the present article is to model scattering as a power law, $\eta(f)=Af^n$. Statistical and experimental methods along with results in tissue-mimicking phantoms and calcaneal samples are described next.

II. METHODS

A. Statistical methods

Power law fits to data may be obtained by performing least-squares linear fits to log transformed data. Formulas for variances in estimates of parameters from a least-squares linear fit (i.e., slope and intercept) may be found in many sources (e.g., Lindgren, 1958; Bevington and Robinson, 1992).

Lizzi *et al.* (1997) have presented an analysis of the statistical properties of estimates of the spectral slope (dB/MHz) and mid-band fit (dB) of the logarithm of the ratios of backscattered power spectra to calibration spectra (obtained from echoes reflected from a glass plate) versus frequency data. (Note that this is not a power law fit because the frequency data was NOT log transformed.) Lizzi *et al.* have provided analytic forms for the probability density function for log-transformed power spectral measurements for speckle targets commonly encountered in medical ultrasound in which there are many scatterers per resolution cell (Wagner *et al.*, 1983). This pdf is shown in Fig. 1.

Backscatter coefficients may be measured using a reference phantom method (Zagzebski *et al.*, 1993; Wear, 1999). A reference phantom with known frequency-dependent backscatter coefficient, $\eta_R(f)$, and attenuation coefficient, $\alpha_R(f)$, placed in the water tank at the same distance as for the bone samples is used. Power spectra from the bone samples, $I_B(f)$, and the phantom $I_R(f)$ are measured. The backscatter coefficient, $\eta_B(f)$, is then obtained from

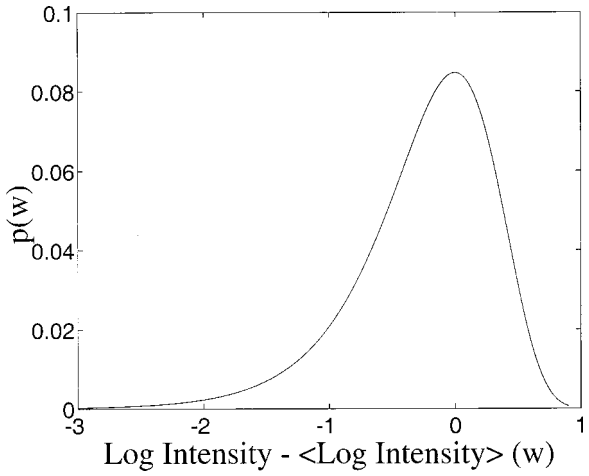

FIG. 1. Probability density function for spectral intensity from a speckle-target. Angular brackets ($\langle\,\rangle$) denote mean.

$$\eta_B(f)=\frac{1}{T^4}\frac{G[\alpha_B(f),l]}{G[\alpha_R(f),l]}\frac{I_B(f)}{I_R(f)}\eta_R(f), \tag{1}$$

where T is the amplitude temperature coefficient at the water/bone interface. Due to the high degree of porosity of the samples, T may be assumed to be one (Droin *et al.*, 1998). The function $G[\alpha(f),l]$ compensates for attenuation effects and is given by (O'Donnell and Miller, 1981)

$$G[\alpha(f),l]=\frac{4\alpha(f)l}{1-e^{-4\alpha(f)l}}, \tag{2}$$

where l is the gate length. The logarithm of the estimated backscatter coefficient is then

$$\log\,\eta_B(f)=\log I_B(f)-\log I_R(f)+\log G[\alpha_B(f),l] -\log G[\alpha_R(f),l]+\log\,\eta_R(f). \tag{3}$$

Assuming that the various measurements are uncorrelated with each other, the variance of the estimate of $\log\,\eta_B(f)$ is equal to the sum of the variances of the estimates of the five terms on the right side of Eq. (3) (Bevington and Robinson, 1992, Eq. 3.13). The backscattering and attenuation properties of the reference phantom are presumed to be known and have fixed values (zero variances). Therefore they do not contribute to the variance of the estimated log backscatter coefficient. Therefore,

$$\mathrm{Var}\{\log\,\hat{\eta}_B(f)\}=\mathrm{Var}\{\log\,\hat{I}_B(f)\}+\mathrm{Var}\{\log\hat{I}_R(f)\} +\mathrm{Var}\{\log\,\hat{G}[\alpha_B(f),l]\}, \tag{4}$$

where "Var" denotes "the variance of" and "$\hat{}$" denotes "the estimate of." Typically, the first term, $\mathrm{Var}\{\log\,\hat{I}_B(f)\}$, contributes the most to $\mathrm{Var}\{\log\,\hat{\eta}_B(f)\}$. The reasons for this are as follows. $I_R(f)$ is usually known to much greater precision than $I_B(f)$ (and therefore has far lower variance) since well-designed reference phantoms are relatively homogeneous and big enough to enable much spatial averaging for the measurement of reference backscattered spectra. (See Sec. II C.) The third term on the right side of Eq. (4) is due to variance in attenuation estimates. Attenuation in bone samples is typically measured with a through-transmission

method. Through-transmission signals have relatively high signal-to-noise ratios, and are not plagued by the random interference effects that characterize speckle backscatter. So, for practical purposes,

$$\mathrm{Var}\{\log \hat{\eta}_B(f)\} = \mathrm{Var}\{\log \hat{I}_B(f)\}. \tag{5}$$

The validity of Eq. (5) is tested experimentally in this article.

In this article, backscatter coefficient $\eta(f)$ is assumed to obey a power law dependence on frequency, f, so that $\eta(f) = Af^n$. A linear fit of the form, $y(x) = \log A + nx$ is performed where y is the logarithm of the backscatter coefficient, x is the logarithm of frequency, $\log A$ is the intercept, and n is the slope (or power law exponent for the non-log-transformed data). Note that, after log transformation, a constant value may be added or subtracted from each of the log frequency (x) data points so that the intercept corresponds to any particular frequency of interest (such as mid-band value or transducer center frequency) rather than zero frequency.

Bevington and Robinson give the following relations for the variances in estimates of linear-regression coefficients (Bevington and Robinson, 1992): $\sigma^2_{\log A} = (1/\Delta)\Sigma(x_i^2/\sigma_i^2)$ and $\sigma_n^2 = (1/\Delta)\Sigma(1/\sigma_i^2)$ where

$$\Delta = \sum \frac{1}{\sigma_i^2} \sum \frac{x_i^2}{\sigma_i^2} - \left(\sum \frac{x_i}{\sigma_i^2} \right)^2. \tag{6}$$

The variance of measurements of log spectral intensity (or log backscatter coefficient) at a frequency corresponding to x_i is denoted by σ_i^2. Conveniently, for speckle targets (as Lizzi *et al.* point out) σ_i is a constant equal to 0.56 (or 5.6 dB in the formulation of Lizzi *et al.*) for all frequencies in the usable band of the transducer. Interestingly, these results are applicable regardless of the frequency dependence of scattering. The power law exponent may be 3 (thin cylinders), 4 (small spheres) or any other physically realizable value.

B. Calcaneus samples

Twenty-four human (gender and age unknown) calcaneus samples were obtained. They were defatted using a trichloro-ethylene solution. Defatting was presumed not to significantly affect measurements since attenuation (Langton *et al.*, 1996; Alves *et al.*, 1996) and speed of sound (Alves *et al.*, 1996; Njeh and Langton, 1997) of defatted trabecular bone have been measured to be only slightly different from their counterparts with marrow left intact. The cortical lateral sides were sliced off, leaving two parallel surfaces with direct access to trabecular bone. The thicknesses of the samples varied from 14 to 21 mm. In order to remove air bubbles, the samples were vacuum degassed underwater in a desiccator. After vacuum, samples were allowed to thermally equilibrate to room temperature prior to ultrasonic interrogation. Ultrasonic measurements were performed in distilled water at room temperature. The temperature was measured for each experiment and ranged between 19.1 °C and 21.2 °C. The relative orientation between the ultrasound beam and the calcanea was the same as with *in vivo* measurements performed with commercial bone sonometers, in which sound propagates in the mediolateral (or lateromedial) direction.

C. Ultrasonic methods

A tissue-mimicking phantom (manufactured at the University of Wisconsin) was also scanned in order to validate the expressions for variance of estimates of magnitude and frequency dependence of backscatter. The phantom had an attenuation coefficient of 0.52 dB/cmMHz and a backscatter coefficient of $8.84\times10^{-6}\times f^{3.56}$ $\mathrm{cm}^{-1}\,\mathrm{Sr}^{-1}$.

A Panametrics (Waltham, MA) 5800 pulse/receiver was used. Samples were interrogated in a water tank using Panametrics broadband transducers with the following characteristics: 1-MHz center frequency, 1-in. diameter (d), 1.5-in. focal length (z) (for bone measurements) and 3.5 MHz, 0.75-in. diameter, 1.5-in. focal length (for phantom measurements). Received ultrasound signals were digitized (8 bit, 10 MHz) using a LeCroy (Chestnut Ridge, NY) 9310C Dual 400-MHz oscilloscope and stored on computer (via GPIB) for off-line analysis.

Radio-frequency (rf) echo signals from ten lines within the test phantom were acquired. (The transducer was translated laterally between successive acquisitions.) Twenty rf lines were acquired from a reference phantom. (Backscatter coefficients were computed from one test phantom rf line at a time using the average power spectrum, based on all 20 lines, from the reference phantom. This resulted in a 20:1 ratio of reference lines to test lines so that backscatter coefficient variance was dominated by the statistical properties of the test lines as discussed earlier.) Six rf lines were acquired from each bone sample (compared with 32 lines from the reference phantom).

The number of independent measurements available from each bone sample was limited by the ratio of the calcaneal surface area to the beam cross section. In the middle of the usable bandwidth (0.8 MHz, see Sec. II D), an estimate for the beam width [width of the main lobe of the Airy pattern (Goodman, 1968)] is $2.44\lambda Z/d = 7$ mm corresponding to a beam cross sectional area of 1.6 cm^2. This estimate tends to be conservative (low) since the beam diverges beyond the focal plane due to diffraction and the distorting effects of propagating through inhomogeneous tissue. Spectra were estimated from the squared modulus of the fast Fourier transform (FFT). A Hamming window was applied prior to taking the FFT.

Backscatter coefficients were measured using a reference phantom method (Zagzebski *et al.*, 1993; Wear, 1999) as discussed earlier. Attenuation measurements were required in order to compensate signals prior to backscatter coefficient estimation. Attenuation was measured using a standard through-transmission substitution method as previously described (Wear, 1999).

D. Data analysis

A central band of frequencies (corresponding to the usable bandwidth) from the frequency-dependent backscatter coefficient data was used for analysis. For the phantom data

acquired at 3.5 MHz, the band was 2.5 to 4.0 MHz. For the bone data acquired at 1.0 MHz, the band was 0.4 to 1.2 MHz. Over the selected band, the logarithm of the backscatter coefficient versus logarithm of frequency data were least-squares fit to a straight line. The slope of the fit (n) of the log transformed data corresponded to the exponent of the power law fit of backscatter coefficient, $\eta(f)=Af^n$. The parameters of the fit (A,n) were also used to estimate the logarithm of the backscatter coefficient at the transducer center frequency, $m=\log(Af_0^n)$ where f_0 was 3.5 MHz (phantom) or 1.0 MHz (bone).

For the phantom data, precision of estimates of log magnitude (m) and frequency dependence (n) as functions of gate length were investigated. Gate length (L) is determined by gate duration (T) according to $L=cT/2$ for reflection mode where c=speed of sound. Gate duration determines resolution in the frequency domain, $\Delta f=1/T$ for a rectangular window and $\Delta f=1.33/T$ for a Hamming window (Lizzi *et al.*, 1997). The frequency resolution determines the number of independent samples in the least-squares fit, $N=B/\Delta f$, where B is the analysis bandwidth.

Each of the ten rf lines acquired from the phantom was partitioned along its length into q equal segments for $q=1$, 2, 3, 4, 5, 6, 8, 10, and 12. This yielded nine data sets, each one containing $10q$ rf segments of length $1.8/q$ cm and duration $23.4/q$ μsc. Spectral and regression analysis were applied to yield estimates of m and n for each segment. The means (μ_m and μ_n) and the standard deviations (σ_m and σ_n) of m and n were computed for each segment length. The variances of the estimates of σ_m and σ_n were computed using the bootstrap method (Efron and Tibshirani, 1993). The bootstrap technique entails multiple resampling (with replacement) from the acquired data in order to generate a distribution of a parameter (such as σ_m and σ_n), from which statistics such as means and variances may be derived.

For the bone data, precision of estimates as function of analysis bandwidth was explored. The usable band of frequencies was 0.4 to 1.2 MHz. Using a lower limit of 0.4 MHz, the upper limit was varied from 0.5 to 1.2 MHz in increments of 0.1 MHz with spectral and regression analysis applied for each frequency band. As the bandwidth was increased, the number of independent samples used ($N=B/\Delta f$) also increased, thus reducing variabilities of estimated parameters.

III. RESULTS

The variation of σ_m (precision of estimate of log magnitude) with gate length for the phantom is shown in Fig. 2. Though the dependences on gate length are similar, the theory (solid line) tends to underestimate the observed variance (asterisks) somewhat. This is probably due to sources of variance not incorporated into the model, such as the two right-most terms in Eq. (4) and/or some degree of spatial inhomogeneity in the phantom.

The variation of σ_n (precision of estimate of frequency dependence) with gate length for the phantom is illustrated in Fig. 3). There is excellent agreement between theory (solid line) and experimental data (asterisks), somewhat better than

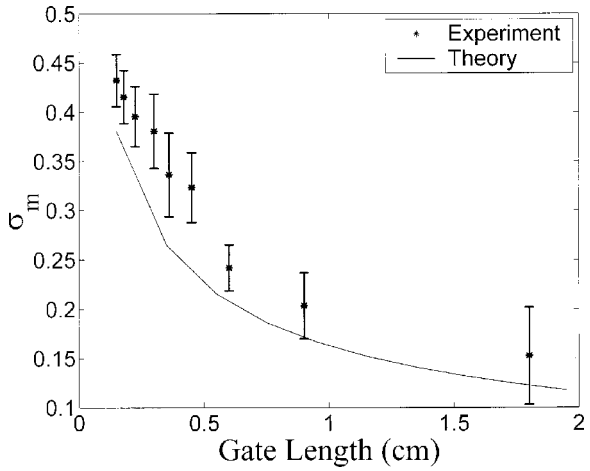

FIG. 2. Variation of σ_m with gate length for the phantom. Both theory (solid line) and experimental data (asterisks) are shown. Error bars denote standard deviations.

that seen in Fig. 2. This may be due to the fact that spatial variations in scatterer concentration would be expected to contribute additional variance in the magnitude of backscatter (Fig. 2) but not in the frequency dependence (Fig. 3). The frequency dependence of backscatter depends on scatterer size but not concentration provided that multiple scattering and coherent scattering are not big effects.

The variation of σ_m with upper frequency band limitation for the bone samples is depicted in Fig. 4. While the theory and experimental data exhibit similar dependences on the upper frequency limit for analysis, the theory tends to underestimate the observations. This could again be attributable to increased variance due to the two right-most terms in Eq. (4) and/or biological variations in scatterer (trabecular) concentration and size. This possibility will be explored in the next section.

The variation of σ_n with upper frequency band limitation for the bone samples is shown in Fig. 5. As with the phantom, there is excellent agreement between theory and experiment. In this case, virtually all of the observed vari-

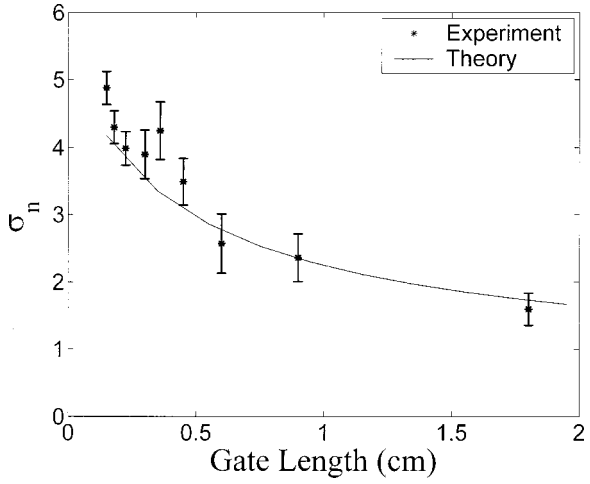

FIG. 3. Variation of σ_n with gate length for the phantom. Both theory (solid line) and experimental data (asterisks) are shown. Error bars denote standard deviations.

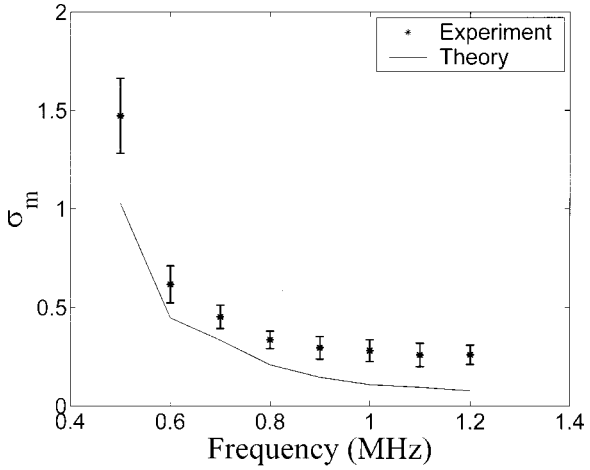

FIG. 4. Variation of σ_m with gate length for the bone samples. Both theory (solid line) and experimental data (asterisks) are shown. Error bars denote standard deviation.

ance is predicted by the fundamental precision limitation of the measurement method.

IV. DISCUSSION

The results previously presented suggest that the statistical considerations explored here are powerful for predicting virtually all observed variations in frequency dependence of backscatter. The statistical model tends to underestimate observed variations in magnitude of backscatter, however. Qualitatively, the coexistence of these two results can be explained in terms of scattering targets (e.g., phantom or trabecular bone) that have the following properties: (1) many scatterers per resolution cell, (2) scatterers with similar frequency dependence of differential scattering cross section (e.g., $n=3$ for thin cylinders, $n=4$ for small spheres, or any other physically realizable values for n), (3) scatterers potentially exhibiting a range of variation of differential scattering cross section magnitudes, and (4) spatial or biological variations in scatterer concentration. In this section, these ideas will be elaborated quantitatively.

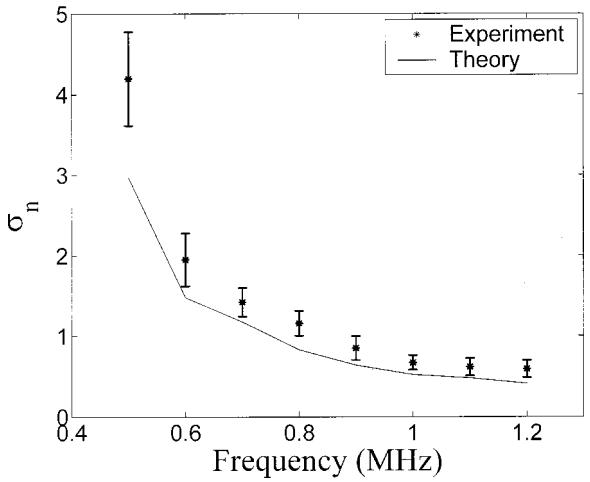

FIG. 5. Variation of σ_n with gate length for the bone samples shown in Fig. 4. Both theory (solid line) and experimental data (asterisks) are shown. Error bars denote standard deviations.

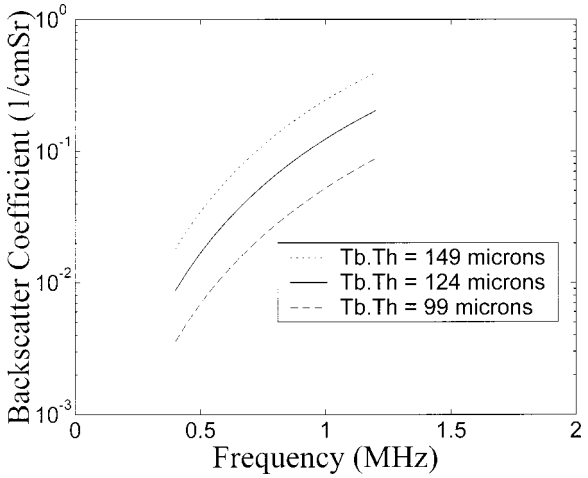

FIG. 6. Frequency-dependent backscatter coefficient for three different mean trabecular thicknesses (93, 127, and 161 microns). The three values correspond to the mean ± two standard deviations reported for human calcaneal trabecular thickness (Ulrich *et al.*, 1999).

In Fig. 6, predicted backscatter coefficients for three trabecular thicknesses (with constant scatterer concentration), as functions of frequency, assuming a cylinder scatterer model (Wear, 1999) are shown. The three values correspond to the mean±two standard deviation reported for human calcaneal trabecular thickness (Ulrich *et al.*, 1999). It may be seen that throughout this four standard deviation variation in trabecular thickness, the magnitude of backscatter coefficient varies considerably while the frequency dependence of backscatter remains roughly constant.

In Fig. 7, the variation of backscatter coefficient at 1.0 MHz with trabecular thickness over a range of trabecular thicknesses corresponding to the mean ± two standard deviations reported for human calcaneal trabecular thickness (Ulrich *et al.*, 1999) is illustrated. Over this range, the backscatter coefficient varies by about a factor of 5. A change of one standard deviation in trabecular thickness would correspond to a change of (log 5)/4=0.17 in log magnitude. An effect of this magnitude is sufficient to approximately ac-

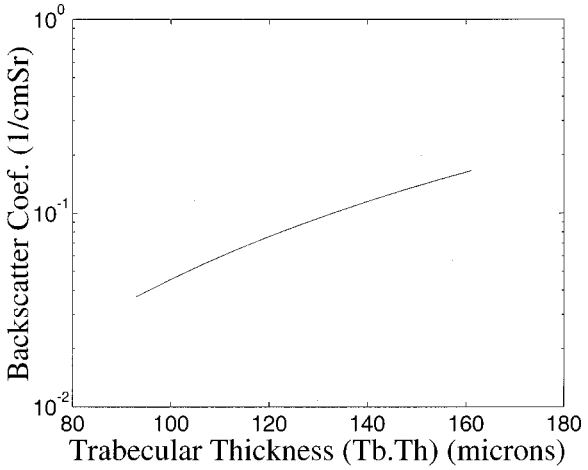

FIG. 7. Backscatter coefficient at 1.0 MHz as a function of trabecular thickness. The range of trabecular thicknesses shown corresponds to the mean ±two standard deviations reported for human calcaneal trabecular thickness (Ulrich *et al.*, 1999).

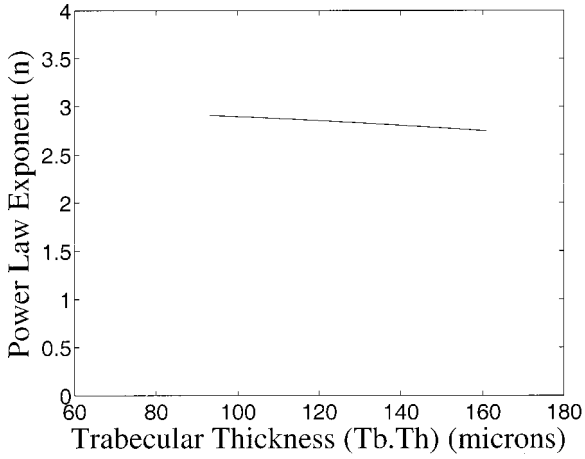

FIG. 8. Exponent of power law fit to frequency-dependent backscatter coefficient as a function of trabecular thickness. The range of trabecular thicknesses shown corresponds to the mean ± two standard deviations reported for human calcaneal trabecular thickness (Ulrich *et al.*, 1999).

count for the discrepancy between the statistically predicted and empirical variations shown in Fig. 4.

Moreover, variations in scatterer concentration may contribute to additional variations in backscatter coefficient. Measurements of means and standard deviations of mean trabecular spacing in human calcaneus have been reported to be 630 ± 110 μm (Hausler *et al.*, 1999) and 684 ± 109 μm (Ulrich *et al.*, 1999) corresponding to a coefficient of variation ($CV_{Tb.Sp}$) of 16% to 17%. This would lead to a coefficient of variation for scatterer concentration or backscatter coefficient, $CV_{conc}=(1+CV_{Tb.Sp})^{-2}-1=26\%-27\%$ or 0.13–14 variation in the logarithm of the backscatter coefficient.

In Fig. 8, the variation of n with trabecular thickness over a range of trabecular thicknesses corresponding to the mean±two standard deviations reported for human calcaneal trabecular thickness (Ulrich *et al.*, 1999) is shown. The variation is quite small, ranging from 2.91 (at 93 μm) to 2.75 (at 161 μm). This range corresponds roughly to a standard deviation of $0.16/4=0.04$ and is small relative to the precision of the measurement, predicted here to be 0.41 and measured to be 0.60 ± 0.08.

V. CONCLUSIONS

Several models to predict frequency dependence of backscatter from bone have been proposed. Some have been evaluated by direct comparison to experimental measurements. Knowledge of measurement precision is essential in order to understand the limitations of such comparison. In this article, a model to predict uncertainties in measurements of frequency-dependent backscatter in soft-tissue-mimicking phantoms and bone has been proposed and validated. This model predicts fluctuations in estimates of power law exponents (n) consistent with measured values. The primary source of this variability is random interference of echoes emanating from individual scatterers within resolution cells rather than biological variability.

Chaffai and co-workers (2000) reported measurements of n from individual human calcaneus samples ranging from 2.76 to 3.86. (In these experiments, as in the present article, a 1-MHz broadband transducer and an analysis range of 0.4 to 1.2 MHz were used.) They speculated that the extent of this range may be attributable to variations in microarchitecture but could alternatively be explained by precision limitations. The present article strongly supports the latter interpretation. The variabilities of estimates of n observed by Chaffai *et al.* and seen in Fig. 5 are almost entirely accounted for by precision limitations. Trabecular thicknesses, for example, may exhibit a wide range of biological variability but trabeculae are always narrow compared to typical ultrasonic wavelengths, resulting in a small range of true backscatter power law exponent (n) (see Fig. 8) relative to measurement precision.

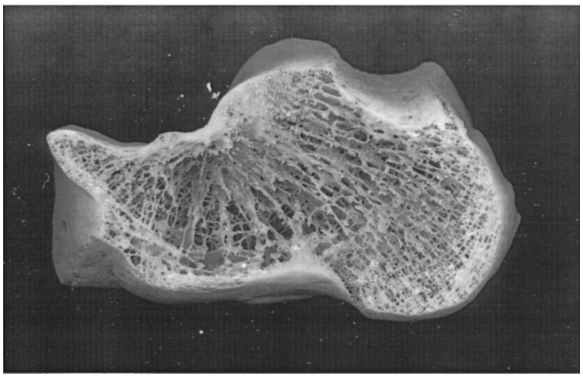

FIG. 9. Human calcaneus with lateral cortical plates sliced off.

Measured average values of power law exponent (n) in the low frequency range have been reported as 3.26 (Wear, 1999) and 3.38 (Chaffai *et al.*, 2000), which are a little higher than would be predicted by the cylinder model. Certainly, the cylinder model is only an approximation. The existence of platelike structures in addition to rodlike trabeculae complicates the situation. However, as seen in Fig. 9, it is not unreasonable to postulate that cylinderlike objects (trabeculae) contribute a substantial portion of the scattering. In addition, only those platelike structures oriented approximately perpendicular to the ultrasound propagation direction can measurably affect the frequency dependence of scattering. Finally, plates are comparatively rare in bones from older objects, upon which the data from the studies mentioned above are based.

Other models (Chaffai *et al.*, 2000; Nicholson *et al.*, 2000) are useful alternatives that also demonstrate some consistency with experimental results and have the advantage of not being as geometrically restrictive as the cylinder model. One advantage of the cylinder model compared with these, however, is that it is not restricted to scatterers (trabeculae) with small deviations in acoustic properties compared with the embedding medium (marrow) (Chaffai *et al.*, 2000; Ueda and Ozawa, 1985; Nicholson *et al.*, 2000; Sehgal and Greenleaf, 1984; Sehgal, 1993; Chivers, 1977). This assumption may be more appropriate for soft tissues than bone as the contrasts in density and sound speed between trabeculae and marrow are somewhat greater than those typically encountered in soft tissues (Duck, 1990, see Tables 4.1, 4.2, 4.3a, and 5.1). In addition, unlike the other models, the cylinder

model allows for the propagation within trabeculae of shear waves, which have been demonstrated to propagate in cortical bone (Grenoble *et al.*, 1972). Nevertheless, the various models for ultrasonic scattering from bone are useful in that they help explain certain observations. Given the complexity of the problem, it is not unexpected that all current models, including the cylinder model, are somewhat simplistic in some respect.

In addition to the precision limitations discussed in this article, the frequency-dependent backscatter measurement has accuracy limitations as well. As mentioned previously (Wear, 1999), the potential effects of coherent scattering, multiple scattering, small measurement volumes (often only a few wavelengths deep), ultrasonic beam distortion (due to propagation through an inhomogeneous medium, bone), and phase cancellation compromise accuracy. Given these numerous complicating factors, it may not be possible to ascertain at present whether the greater limitation to our understanding of ultrasonic scattering from bone is imperfect modeling or experimental uncertainty.

ACKNOWLEDGMENTS

The author is grateful for funding provided by the U.S. Food and Drug Administration Office of Women's Health. The author thanks Ernest Madsen, University of Wisconsin, and Timothy Hall, University of Kansas, for providing the test and reference phantoms used in this study. The author is also appreciative of the helpful suggestions of Sandy Stewart, Food and Drug Administration.

Alves, J. M., Ryaby, J. T., Kaufman, J. J., Magee, P. P., and Siffert, R. S. (**1996**). ''Influence of marrow on ultrasonic velocity and attenuation in bovine trabecular bone,'' Calcif. Tissue Int. **58**, 362–367.

Bauer, D. C., Gluer, C. C., Cauley, J. A., Vogt, T. M., Ensrud, K. E., Genant, H. K., and Black, D. M. (**1997**). ''Broadband ultrasound attenuation predicts fractures strongly and independently of densitometry in older women,'' Arch. Intern. Med. **157**, 629–634.

Bevington, P. R., and Robinson, D. K. (**1992**). *Data Reduction and Error Analysis for the Physical Sciences*, 2nd ed. (McGraw-Hill, New York), Chap. 6.

Bouxsein, M. L., and Radloff, S. E. (**1997**). ''Quantitative ultrasound of the calcaneus reflects the mechanical properties of calcaneal trabecular bone,'' J. Bone Miner. Res. **12**, 839–846.

Chaffai, S., Roberjot, V., Peyrin, F., Berger, G., and Laugier, P. (**2000**). ''Frequency dependence of ultrasonic backscattering in cancellous bone: Autocorrelation model and experimental results,'' J. Acoust. Soc. Am. **108**, 2403–2411.

Chappard, C., Laugier, P., Fournier, B., Roux, C., and Berger, G. (**1997**). ''Assessement of the relationship between broadband ultrasound attenuation and bone mineral density at the calcaneus using BUA Imaging and DXA,'' Osteoporosis Int. **7**, 316–322.

Chivers, R. C. (**1997**). ''The scattering of ultrasound by human tissues—some theoretical models,'' Ultrasound Med. Biol. **3**, 1–13, Appendix.

Cummings, S. R., Black, D. M., Nevitt, M. C., Browner, W., Cauley, J., Ensrud, K., Genant, H. K., Palermo, L., Scott, J., and Vogt, T. M. (**1993**). ''Bone density at various sites for prediction of hip fractures,'' Lancet **341**, 72–75.

Droin, P., Berger, G., and Laugier, P. (**1998**). ''Velocity dispersion of acoustic waves in cancellous bone,'' IEEE Trans. Ultrason. Ferroelectr. Fre.Control **45**, 581–592.

Duck, F. A. (**1990**). *Physical Properties of Tissues* (Academic, San Diego), Chaps. 4 and 5.

Efron, B., and Tibshirani, R. J. (**1993**). *An Introduction to the Bootstrap* (Chapman & Hall, New York).

Faran, J. J. (**1951**). ''Sound scattering by solid cylinders and spheres,'' J. Acoust. Soc. Am. **23**, 405–418.

Giat, P., Chappard, C., Roux, C. Laugier, P., and Berger, G. (**1997**). ''Preliminary clinical assessment of the backscatter coefficient in osteoporosis,'' in Proceedings 22nd International Symposium Ultrasonic Imaging and Tissue Char., Washington, D.C., 16 (Abstract).

Glüer, C., Cummings, S. R., Bauer, D. C., Stone, K., Pressman, A., Mathur, A., and Genant, H. K. (**1996**). ''Osteoporosis: Association of recent fractures with quantitative US findings,'' Radiology **199**, 725–732.

Glüer, C. C. (**1997**). ''Quantitative ultrasound techniques for the assessment of osteoporosis: expert agreement on current status,'' J. Bone Miner. Res. **12**, 1280–1288.

Goodman, J. W. (**1968**). *Introduction to Fourier Optics* (McGraw–Hill, New York).

Grenoble, D. E., Katz, J. L., Dunn, K. L., Gilmore, R. S., and Linga Murty, K. (**1972**). ''The elastic properties of hard tissues and apatites,'' J. Biomed. Mater. Res. **6**, 221–233.

Hans, D., Dargent-Molina, P., Schott, A. M., Sebert, J. L., Cormier, C., Kotzki, P. O., Delmas, P. D., Pouilles, J. M., Breart, G., and Meunier, P. J. (**1996**). ''Ultrasonographic heel measurements to predict hip fracture in elderly women: the EPIDOS prospective study,'' Lancet **348**, 511–514.

Hans, D., Wu, C., Njeh, C. F., Zhao, S., Augat, P., Newitt, D., Link, T., Lu, Y., Majumdar, S., and Genant, H. K. (**1999**). ''Ultrasound velocity of trabecular cubes reflects mainly bone density and elasticity,'' Calcif. Tissue Int. **64**, 18–23.

Hausler, K. D., Rich, P. A., Smith, P. C., and Barry, E. B. (**1999**). ''Relationships between static histomorphometry and ultrasound in the human calcaneus,'' Calcif. Tissue Int. **64**, 477–480.

Hoffmeister, B. K., Whitten, S. A., and Rho, J. Y. (**2000**). ''Low megahertz ultrasonic properties of bovine cancellous bone,'' Bone **26**, 635–642.

Hoffmeister, B. K., Whitten, S. A., Kaste, S. C., and Rho, J. Y. (**in press**). ''Effect of collagen and mineral content on the high frequency ultrasonic properties of human cancellous bone,'' Bone.

Langton, C. M., Palmer, S. B., and Porter, R. W. (**1984**). ''The measurement of broadband ultrasonic attenuation in cancellous bone,'' Eng. Med. **13**, 89–91.

Langton, C. M., Njeh, C. F., Hodgskinson, R., and Carrey, J. D. (**1996**). ''Prediction of Mechanical Properties of the Human Calcaneus by Broadband Ultrasonic Attenuation,'' Bone **18**, 495–503.

Laugier, P., Droin, P., Laval-Jeantet, A. M., and Berger, G. (**1997**). ''*In vitro* assessment of the relationship between acoustic properties and bone mass density of the calcaneus by comparison of ultrasound parametric imaging and quantitative computed tomography,'' Bone **20**, 157–165.

Lindgren, B. W. (**1958**). *Statistical Theory* (McGraw-Hill, New York), pp. 31–89 and 280–282.

Lizzi, F. L., Feleppa, E. J., Astor, M., and Kalisz, A. (**1997**). ''Statistics of ultrasonic spectral parameters for prostate and liver examinations,'' IEEE Trans. Ultrason. Ferroelectr. Freq. Control **44**, 935–942.

Luo, G., Kaufman, J. J., Chabrera, A., Bianco, B., Kinney, J. H., Haupt, D., Ryaby, J. T., and Siffert, R. S. (**1999**). ''Computational methods for ultrasonic bone assessment,'' Ultrasound Med. Biol. **25**, 823–830.

Morse, P. M., and Ingard, K. U. (**1968**). *Theoretical Acoustics* (Princeton University Press, Princeton, NJ).

Nicholson, P. H. F., Strelitzki, R., Cleveland, R. O., and Bouxsein, M. L. (**2000**). ''Scattering of ultrasound in cancellous bone: predictions from a theoretical model,'' J. Biomech. **33**, 503–506.

Nicholson, P. H. F., Muller, R., Lowet, G., Cheng, X. G., Hildebrand, T., Ruegsegger, P., Van Der Peere, G. J., Duqueker, J., and Boonen, S. (**1998**). ''Do quantitative ultrasound measurements reflect structure independently of density in human vertebral cancellous bone?'' Bone **23**, 425–431.

Njeh, F., and Langton, C. M. (**1997**). ''The effect of cortical endplates on ultrasound velocity through the calcaneus: an *in vitro* study,'' Br. J. Radiol. **70**, 504–510.

Njeh, C. F., Fuerst, T., Diessel, E., and Genant, H. K. (**2000a**). ''Is quantitative ultrasound dependent on bone structure? A reflection,'' Osteoporosis Int. **12**, 1–15.

Njeh, C. F., Hodgskinsson, R., Currey, J. D., and Langton, C. M. (**1996**). ''Orthogonal relationships between ultrasonic velocity and material properties of bovine calcellous bone,'' Med. Eng. Phys. **18**, 373–381.

Njeh, C. F., Hans, D., Li, J., Fan, B., Fuerst, T., He, Y. Q., Tsuda-futami, E., Lu, Y., Wu, C. Y., and Genant, H. K. (**2000b**). ''Comparison of six calcaneal quantitative ultrasound devices: precision and hip fracture discrimination,'' Osteoporosis Int. **11**, 1051–1062.

O'Donnell, M., and Miller, J. G. (**1981**). ''Quantitative broadband ultrasonic backscatter: An approach to nondestructive evaluation in acousticallly inhomogeneous materials,'' J. Appl. Phys. **52**, 1056–1065.

Roberjot, V., Laugier, P., Droin, P., Giat, P., and Berger, G. (**1996**). ''Measurement of integrated backscatter coefficient of trabecular bone,'' in Proceedings of the 1996 IEEE Ultrasonics Symposium, Vol. 2, pp. 1123–1126.

Rossman, P., Zagzebski, J., Mesina, C., Sorenson, J., and Mazess, R. (**1989**). ''Comparison of Speed of Sound and Ultrasound Attenuation in the Os Calcis to Bone Density of the Radius, Femur, and Lumbar Spine,'' Clin. Phys. Physiol. Meas. **10**, 353–360.

Schott, M., Weill-Engerer, S., Hans, D., Duboeuf, F., Delmas, P. D., and Meunier, P. J. (**1995**). ''Ultrasound discriminates patients with hip fracture equally well as dual energy X-ray absorptiometry and independently of bone mineral density,'' J. Bone Miner. Res. **10**, 243–249.

Sehgal, C. M. (**1993**). ''Quantitative relationship between tissue composition and scattering of ultrasound,'' J. Acoust. Soc. Am. **94**, 1944–1952.

Sehgal, C. M., and Greenleaf, J. F. (**1984**). ''Scattering of ultrasound by tissues,'' Ultrason. Imaging **6**, 60–80.

Serpe, L., and Rho, J. Y. (**1996**). ''The nonlinear transition period of broadband ultrasound attenuation as bone density varies,'' J. Biomech. **29**, 963–966.

Tavakoli, M. B., and Evans, J. A. (**1991**). ''Dependence of the velocity and attenuation of ultrasound in bone on the mineral content,'' Phys. Med. Biol. **36**, 1529–1537.

Thompson, P., Taylor, J., Fisher, A., and Oliver, R. (**1998**). ''Quantitative heel ultrasound in 3180 women between 45 and 75 years of age: compliance, normal ranges and relationship to fracture history,'' Osteoporosis Int. **8**, 211–214.

Trebacz, H., and Natali, A. (**1999**). ''Ultrasound velocity and attenuation in cancellous bone samples from lumbar vertebra and calcaneus,'' Osteoporosis Int. **9**, 99–105.

Turner, H., Peacock, M., Timmerman, L., Neal, J. M., and Johnston, Jr., C. C. (**1995**). ''Calcaneal ultrasonic measurements discriminate hip fracture independently of bone mass,'' Osteoporosis Int. **5**, 130–135.

Ueda, M., and Ozawa, Y. (**1985**). ''Spectral analysis of echoes for backscattering coefficient measurement,'' J. Acoust. Soc. Am. **77**, 38–47.

Ulrich, D., van Rietbergen, B., Laib, A., and Ruegsegger, P. (**1999**). ''The ability of three-dimensional structural indices to reflect mechanical aspects of trabecular bone,'' Bone **25**, 55–60.

Wagner, R. F., Smith, S. W., Sandrik, J. M., and Lopez, H. (**1983**). ''Statistics of speckle in ultrasound B-scans,'' IEEE Trans. Sonics Ultrason. **30**, 156–163.

Wear, K. A. (**1999**). ''Frequency dependence of ultrasonic backscatter from human trabecular bone: theory and experiment,'' J. Acoust. Soc. Am. **106**, 3659–3664.

Wear, K. A. (**2000**). ''Anisotropy of ultrasonic backscatter and attenuation from human calcaneus: Implications for relative roles of absorption and scattering in determining attenuation,'' J. Acoust. Soc. Am. **107**, 3474–3479.

Wear, K. A., and Armstrong, D. W. (**2000**). ''The relationship between ultrasonic backscatter and bone mineral density in human calcaneus,'' IEEE Trans. Ultrason. Ferroelectr. Freq. Control **47**, 777–780.

Wear, K. A., and Garra, B. S. (**1997**). ''Assessment of bone density using broadband ultrasonic backscatter,'' Proceedings of the 22nd International Symposium Ultrasonic Imaging and Tissue Char., Washington, D.C., 14 (abstract).

Wear, K. A., and Garra, B. S. (**1998**). ''Assessment of bone density using ultrasonic backscatter,'' Ultrasound Med. Biol. **24**, 689–695.

Zagzebski, J. A., Rossman, P. J., Mesina, C., Mazess, R. B., and Madsen, E. L. (**1991**). ''Ultrasound transmission measurements through the os calcis,'' Calcif. Tissue Int. **49**, 107–111.

Zagzebski, J. A., Yao, L. X., Boote, E. J., and Lu, Z. F. (**1993**). ''Quantitative Backscatter Imaging,'' in *Ultrasonic Scattering in Biological Tissues*, edited by K. K. Shung and G. A. Thieme (CRC, Boca Raton, FL, 1993).

Suppression of large intraluminal bubble expansion in shock wave lithotripsy without compromising stone comminution: Methodology and *in vitro* experiments

Pei Zhong[a] and Yufeng Zhou
Department of Mechanical Engineering and Materials Science, Duke University, Durham, North Carolina 27708

(Received 12 May 2001; accepted for publication 10 September 2001)

To reduce the potential of vascular injury without compromising the stone comminution capability of a Dornier HM-3 lithotripter, we have devised a method to suppress intraluminal bubble expansion via *in situ* pulse superposition. A thin shell ellipsoidal reflector insert was designed and fabricated to fit snugly into the original reflector of an HM-3 lithotripter. The inner surface of the reflector insert shares the same first focus with the original HM-3 reflector, but has its second focus located 5 mm proximal to the generator than that of the HM-3 reflector. With this modification, the original lithotripter shock wave is partitioned into a leading lithotripter pulse (peak positive pressure of 46 MPa and positive pulse duration of 1 μs at 24 kV) and an ensuing second compressive wave of 10 MPa peak pressure and 2 μs pulse duration, separated from each other by about 4 μs. Superposition of the two waves leads to a selective truncation of the trailing tensile component of the lithotripter shock wave, and consequently, a reduction in the maximum bubble expansion up to 41% compared to that produced by the original reflector. The pulse amplitude and -6 dB beam width of the leading lithotripter shock wave from the upgraded reflector at 24 kV are comparable to that produced by the original HM-3 reflector at 20 kV. At the lithotripter focus, while only about 30 shocks are needed to cause a rupture of a blood vessel phantom made of cellulose hollow fiber (i.d.$=$0.2 mm) using the original HM-3 reflector at 20 kV, no rupture could be produced after 200 shocks using the upgraded reflector at 24 kV. On the other hand, after 100 shocks the upgraded reflector at 24 kV can achieve a stone comminution efficiency of 22%, which is better than the 18% efficiency produced by the original reflector at 20 kV ($p=0.043$). All together, it has been shown *in vitro* that the upgraded reflector can produce satisfactory stone comminution while significantly reducing the potential for vessel rupture in shock wave lithotripsy.
[DOI: 10.1121/1.1416906]

PACS numbers: 43.80.Ev, 43.80.Gx, 43.25.Yw [FD]

I. INTRODUCTION

In the past two decades, shock wave lithotripsy (SWL) has been used routinely as an effective and safe treatment modality for the majority of stone patients.[1,2] However, clinical and animal studies have also demonstrated that SWL is accompanied by some forms of renal injury, such as hematuria, formation of diffuse hemorrhage and multiple hematomas within the renal parenchyma, perirenal fat, and subcapsular connective tissue, as well as kidney edema.[3,4] The injury is primarily vascular lesions, with extensive damage to the endothelial cells and rupture of capillaries and small blood vessels.[3,4] In young adult patients, the vascular injury associated with SWL only affects about 2% of their functional renal mass.[5] Therefore, most of these patients recover following the treatment without significant clinical consequences. There are, however, subgroups of patients who are at much higher risk for chronic injury following SWL. These include patients with solitary kidneys, pre-existing hypertension and, in particular, pediatric and elderly patients.[4] For these high-risk patients, the long-term adverse effect of SWL-induced tissue injury is a serious clinical concern and a topic of continued investigation.[6] It is therefore highly desirable to improve lithotripsy technology to minimize tissue injury in SWL.

To reduce the adverse effects of SWL, it is important to understand the mechanisms whereby the vascular injuries are produced. Most previous studies suggest that cavitation, the formation and subsequent expansion and collapse of gas/vapor bubbles in the acoustic field of a lithotripter, may play an important role in the vascular injury in SWL. In particular, shock wave–bubble interaction with resultant microjet formation has been implicated as a mechanism by which the perforation of a vessel wall, preferably in medium-to-large size blood vessels, could be produced.[3,7] However, asymmetric collapse of a bubble with resultant high-speed microjet formation may not be produced if the bubble size is small (for example, less than 0.5 mm in diameter in the acoustic field of a XL-1 lithotripter) due to reduced cross-section area for shock wave-bubble interaction.[7] Thus, for the majority of vascular injury in SWL, which is often observed in capillaries and small blood vessels, a different mechanism must be responsible. Based on results from animal studies and theoretical calculations of SWL-induced bubble dynamics in blood, we and others have proposed that the expansion of intraluminal bubbles in small blood vessels would be signifi-

[a]Electronic mail: pzhong@acpub.duke.edu

cantly constrained, and their subsequent collapse could be severely weakened.[8–11] Conversely, the large, rapid expansion of an intraluminal bubble could significantly dilate a vessel wall, which may lead to rupture if the resultant circumferential stress exceeds the tensile failure strength of the vessel.[9,10] This hypothesis was recently confirmed using vessel phantoms made of cellulose hollow fibers.[10,12] More importantly, it has been shown by both *in vitro* phantom[12,13] and *in vivo* animal studies[14] that if the large expansion of cavitation bubbles is suppressed by the inversion of a lithotripter waveform, the propensity for vascular injury can be greatly reduced. These observations provide an important clue for the reduction of vascular injury in SWL.

It should be noted that shear stresses generated by the scattering of a lithotripter shock wave (LSW) propagating in an inhomogeneous medium has also been postulated as a possible mechanism for vascular injury.[15] Others have suggested that shear stresses associated with the microstreaming produced by oscillating bubbles may cause cell lysis.[3,16] Although *in vitro* experiments have demonstrated that shear stress produced by shock front distortion in an inhomogeneous medium can cause damage to nitrocellulose membranes,[15] it is still unknown whether such a mechanism could lead to rupture of blood vessels *in vivo*. Further, the shear stress theory has difficulty explaining why minimal damage is produced in swine kidneys exposed to a clinical dose of inverted LSWs.[14]

Bubble dynamics in SWL is strongly influenced by the pressure waveform and pulse sequence.[17–19] Hence, it is possible that optimization of the waveform and sequence of LSWs may produce more desirable cavitation activity for better stone comminution and reduced tissue injury. In fact, recent studies have shown that stone comminution *in vitro* can be significantly improved by the forced (instead of inertial) collapse of cavitation bubbles near a target concretion.[10,20,21] Moreover, animal studies have demonstrated that suppression of bubble expansion by inversion of the LSW could substantially reduce vascular injury *in vivo*.[13,14] Unfortunately, the inversion of LSWs also diminishes stone comminution;[13,14] and thus, it cannot be used for lithotripsy. Overall, it is clear that further optimization of the pressure waveform, distribution, and sequence of the LSWs is needed in order to maximize stone comminution while minimizing tissue injury in SWL.

In this work, we developed a method to modify the pressure waveform of the LSW to suppress the large intraluminal bubble expansion in SWL without compromising stone comminution capability of a Dornier HM-3 lithotripter. This strategy is based on the idea that a weak compressive wave superimposing or immediately following the tensile component of a LSW can suppress the expansion of cavitation bubbles induced in a lithotripter field. While others have explored different approaches to modify the ellipsoidal reflector of a lithotripter, their aims were either to produce stronger shear stress in the target stone[22] or to concentrate cavitation near the lithotripter focus point.[19,23] In the following, we first describe the design concept and its theoretical confirmation. We then detail the experimental approach to alter the HM-3 reflector and the physical characterization to assess the influence of this modification on the lithotripter field, bubble expansion, stone comminution, and vessel rupture. It was found that the upgraded reflector could produce satisfactory stone comminution with greatly reduced potential for vascular injury.

II. DESIGN CONCEPT AND EXPERIMENTAL METHODS

A. Design concept and theoretical assessments

The expansion of cavitation bubbles in SWL is determined primarily by the tensile component of a LSW.[17,18] To suppress cavitation without compromising stone comminution capability of a lithotripter, it is possible conceptually to use a compressive wave either to cancel partially the tensile component of a LSW or to disturb sufficiently the radial expansion of the bubble. The feasibility of this *in situ* pulse superposition approach was assessed theoretically by assuming that a half-sinusoidal compressive wave of 1.5 μs pulse duration and 10–20 MPa peak pressure can be superimposed, at various interpulse delays (Δt), with a typical LSW produced by an HM-3 lithotripter (Fig. 1). The corresponding bubble dynamics in water were calculated using the Gilmore model implemented in a numerical code developed previously.[24] Gas diffusion was not considered since we are mainly interested in the expansion phase of the bubble dynamics.[12] For the original HM-3 pulse, the maximum bubble radius was predicted to be 1.1 mm. In comparison, superposition of the compressive wave with the HM-3 pulse was found to significantly reduce the maximum bubble expansion. With proper interpulse delay ($\Delta t = 3.0–6.5\ \mu$s), the maximum bubble radius was predicted to be in the range of 0.3–0.7 mm for a compressive wave with a peak pressure of 10–20 MPa, corresponding to a 36%–74% reduction in maximum bubble expansion.

As we have shown recently via high-speed photography, the initial expansion of a bubble induced in a small blood vessel phantom during SWL could be quickly stopped by the constraint of the vessel wall once bubble-vessel contact was established.[12] Presumably, the kinetic energy associated with the expanding bubble at the moment of the contact would be largely converted into the mechanical energy consumed by the circumferential dilation of the vessel wall, which eventually led to rupture. If the bubble were produced in a free field without constraint, the kinetic energy would be converted into the potential energy of the bubble at its maximum expansion.[12] Therefore, on a first order approximation, the energy absorbed by the vessel wall can be estimated by the difference in potential energy E_p between the bubble at the size of the vessel lumen and the bubble at its maximum expansion in a free field:

$$E_p = \int_{R_v}^{R_{\max}} P_0 4\pi R^2\, dR = \frac{4}{3}\pi (R_{\max}^3 - R_v^3) P_0, \tag{1}$$

where R is bubble radius, $R_{\max}$ is the bubble radius at maximum expansion, R_v is the radius of the vessel lumen, and P_0 is the ambient pressure of the surrounding liquid. For small blood vessels ($R_v < 0.1$ mm, and thus $R_v/R_{\max} < 0.01$ in a typical lithotripter field), E_p is proportional to $R_{\max}^3$. There-

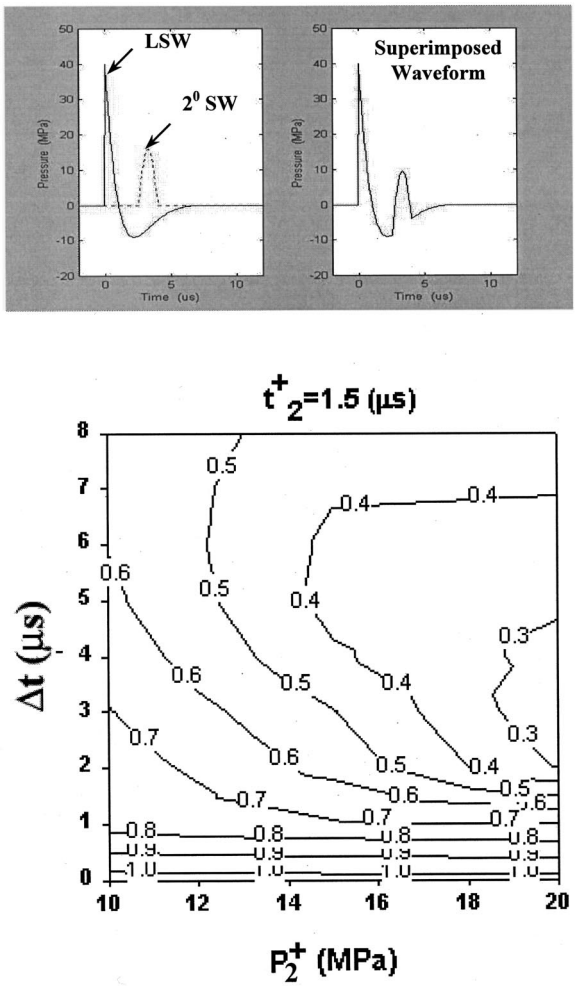

FIG. 1. The effect of *in situ* pulse superposition on the maximum bubble expansion in an HM-3 lithotripter field. The contour plot depicts the maximum bubble radius in mm calculated using the Gilmore model as a function of the peak pressure of the second wave (P_2^+) and the interpulse delay (Δt). The pulse duration of the second wave (t_2^+) is 1.5 μs. LSW: lithotripter shock wave, SW: shock wave.

fore, a small reduction in $R_{\max}$ (for example, 30%) could lead to a profound decrease in E_p ($\sim$66%) and, consequently, the propensity for vessel rupture. This is the physical basis for utilizing an *in situ* pulse superposition technique to reduce the potential of vascular injury in SWL.

B. Modification of the HM-3 reflector

To produce *in situ* pulse superposition, we devised a general strategy for the modification of electrohydraulic shock wave lithotripters. A thin shell ellipsoidal reflector insert (see Table I for its geometric parameters) was designed

TABLE I. The geometric parameters of the original HM-3 and the upgraded ellipsoidal reflectors. Note: a, b, c are the semimajor axis, semiminor axis, and half-focal length of the original HM-3 reflector and a', b', c' are the corresponding values for the upgraded reflector, respectively.

HM-3 reflector	Upgraded reflector
$a=138.1$ mm	$a'=132.5$ mm
$b=78.0$ mm	$b'=71.5$ mm
$c=114.0$ mm	$c'=111.5$ mm

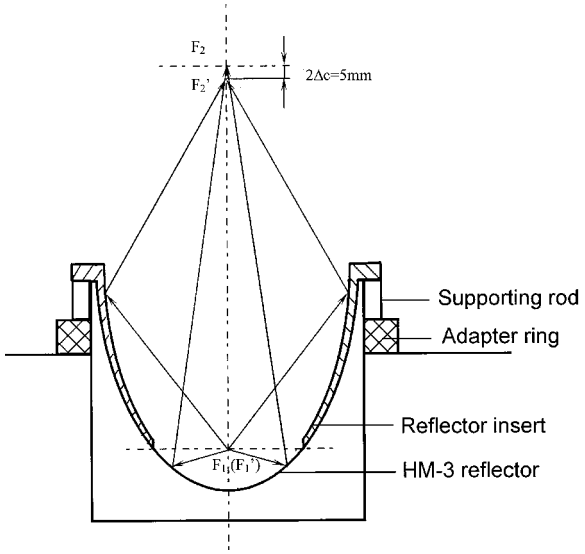

FIG. 2. A schematic diagram of the design and geometry of a reflector insert, in relation to the original HM-3 reflector.

and fabricated to fit snugly into the original reflector of an HM-3 lithotripter (Fig. 2). The inner surface of the reflector insert was designed to share the same first focus ($F_1'=F_1$), but with its second focus (F_2') located 5 mm proximal to the generator than that (F_2) of the original HM-3 reflector. Because the insert reflector covers a large portion of the original HM-3 reflector, it becomes the primary reflecting surface to form a leading LSW after each spark discharge at F_1. Wave reflection from the remaining uncovered bottom surface of the HM-3 reflector, on the other hand, produces a second shock wave. Due to the geometric differences between the insert and the HM-3 reflectors, this second shock wave is delayed from the leading LSW. The interpulse delay can be controlled by appropriate selection of the geometry of the ellipsoidal reflector insert. Considering that the distance between the geometric foci of the HM-3 and insert reflectors is $F_2-F_2'=2c-2c'=2\Delta c$, the interpulse delay Δt can be approximated by

$$\Delta t=\{2a-(2a'+2\Delta c)\}/C_0, \tag{2}$$

where a, b, c are the semimajor axis, semiminor axis, and half-focal length of the original HM-3 ellipsoidal reflector (with $a^2=b^2+c^2$), and a', b', c' are the corresponding values for the reflector insert, respectively, and C_0 is the sound speed in water. From Eq. (2) and Table I, the interpulse delay produced by the reflector insert is estimated to be about 4 μs.

The reflector insert was fabricated in eight segments, with each segment being able to be attached to the original HM-3 reflector via an adapter ring using position pins, screws, and supporting rods (Fig. 3). There are six small (40°) and two large (60°) segments, allowing some adjustments of the pressure amplitude and intensity of the two waves by altering the number of the reflector inserts used. Because the bottom surface of the original HM-3 reflector is used for the generation of the second shock wave, the effective reflecting surface for the leading LSW is significantly reduced. To compensate partially for this loss, the upper rim

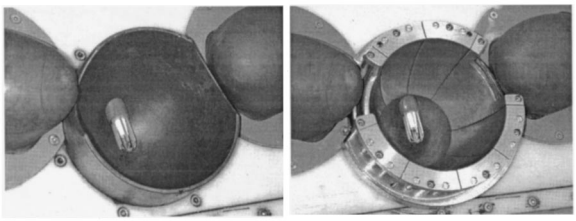

FIG. 3. Photographs showing (a) the original HM-3 reflector and (b) the upgraded reflector. The reflector insert was fabricated in eight segments, with each segment being able to be attached individually to the original HM-3 reflector via an adapter ring using position pins, screws, and supporting rods.

of the reflector insert was extended 10 mm above the aperture of the original HM-3 reflector. In this design, the effective solid angles of the upgraded reflector for the leading LSW and the second wave are 65° and 21.6°, respectively, compared to 61° for the original HM-3 reflector. In addition, by placing the geometric focus of the reflector insert 5-mm proximal to the generator than F_2, a higher peak positive pressure could actually be produced at F_2. This is because the maximum peak positive pressure in a lithotripter field is not produced exactly at the geometric focus of the reflector, but rather shifted about 5–10 mm away from the generator because of nonlinear propagation of the LSW.[25–27]

C. Physical characterization

1. Pressure waveform measurements

The pressure waveforms produced by the original and upgraded HM-3 lithotripter were measured using a hydrophone system with disposable PVDF membranes and a nominal bandwidth of 50 MHz (Sonic Industries, Hatboro, PA). To protect it from cavitation damage, the PVDF membrane was encapsulated in castor oil and recalibrated.[28] The hydrophone was attached to a three-axis translation stage, tilted at 14° angle from the horizontal plane to align normal to the shock wave axis of the HM-3 generator. Before the experiment, the sensing element of the hydrophone was aligned with F_2 under the guidance of the biplanar fluoroscopic imaging system of the HM-3 lithotripter. The alignment was accomplished by placing a pair of thin wires crossing each other right underneath the sensing element of the hydrophone. After the alignment, the thin wires were carefully removed before shock wave exposure. The hydrophone was scanned in 2.5-mm steps both along and transverse to the shock wave axis at F_2 to map the acoustic field of the lithotripter. Four measurements were made at each location, with the pressure wave forms registered on a digital oscilloscope (LeCroy 9314M, Chestnut Ridge, NY) operated at 100 MHz sampling rate.

2. Passive cavitation detection

To assess qualitatively the maximum bubble expansion in the acoustic field of the HM-3 lithotripter, a 1 MHz focused transducer (V392-SU, Panametrics, Waltham, MA) with a focal length of 101.6 mm and a −6 dB beam diameter of ~4 mm was used to measure the acoustic emission (AE) associated with bubble oscillations in water.[8] The focused transducer, attached to a three-axis translation stage, was first aligned perpendicularly to the lithotripter axis and confocally with F_2. It was then scanned along the lithotripter axis in 5-mm steps both prefocally and postfocally. Ten samples of AE signals were recorded at each position.

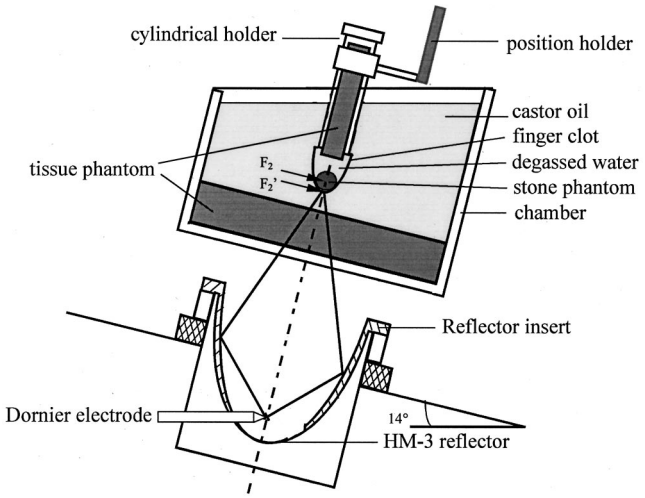

FIG. 4. Experimental setup for stone comminution tests in an HM-3 lithotripter. Tissue mimicking phantoms were used to simulate the effects of tissue attenuation on incident lithotripter shock waves.

D. Performance evaluation

1. Tissue mimicking phantom

To mimic the tissue environment *in vivo*, an acrylic testing chamber (25.4×25.4×15.2–21.6 cm, L×W×H) with a 115-μm thick polyester membrane at the bottom was placed above the HM-3 generator (see Fig. 4). The lithotripter focus, located on the central axis of the chamber, is about 50 mm from the bottom surface. A slab of tissue mimicking phantom (25.4×2.54 cm, Diameter×Thickness), prepared following the method described by Madsen and associates,[29] was placed at the bottom of the chamber, which was filled with castor oil. The sound speed and attenuation coefficient of the tissue phantom was determined by a through transmission technique to be 1550 m/s and 0.8 dB/cm/MHz, respectively, in the frequency range of 1.0–3.5 MHz. Pressure measurements using a PVDF membrane hydrophone revealed that the tissue phantom reduces the peak positive and peak negative pressure of the LSW by 23% and 7%, respectively, while almost doubling the rise time of the shock front (16.8 ns in water vs 29.4 ns with tissue mimicking phantom).[21] These results are similar to the variations in pressure waveforms measured *in vitro* versus *in vivo* in a swine kidney.[30]

2. Stone comminution

To mimic stone comminution in the renal pelvis, a special holder was fabricated using a rubber finger cot (30×20 mm, L×D) and a plastic cylinder (70×25 mm, L×D) (see Fig. 4). Spherical stone phantoms ($D=10$ mm) were made of plaster-of-Paris with a powder to water mixing ratio of 1.5 to 1.0 by weight, which has an acoustic impedance within the range reported for renal calculi.[31] The weight of each

phantom (in dry state) was measured. Before placing it into the holder, each stone phantom was immersed in degassed water for at least 10 minutes until no visible bubbles could be observed to come out from the phantom. A cylinder of tissue-mimicking material was also placed inside the holder above the stone phantom. Furthermore, the holder was connected to the hydraulic gantry of the HM-3 lithotripter so that the stone phantom could be positioned at F_2 under biplanar fluoroscopic imaging guidance. A total of 100 shocks were delivered to the stone phantom, using either the original or upgraded reflector at a pulse repetition rate of 1 Hz. After the shock wave exposure, all the fragments were carefully removed from the holder, spread out into a layer on paper, and let dry at room temperature for 24 hours. The dry fragments were then filtered through an ASTM standard sieve (W.S. Tyler No. 10) with 2-mm grid. The comminution efficiency was determined by the percentage of fragments less than 2 mm, which can be discharged spontaneously after clinical shock wave treatment.[32] Six samples were used under each test configuration.

3. Rupture of vessel phantoms

The propensity of vascular injury produced by the original and upgraded HM-3 lithotripter was evaluated using a vessel phantom made using a single cellulose hollow fiber of 0.2-mm inner diameter and a wall thickness of 8 μm (Spectrum, Gardena, CA).[12] Degassed water (O_2 concentration: <4 mg/L), seeded with 0.1% contrast agent Optison (Mallinckrodt Inc., St. Louis, MO) by volume serving as cavitation nuclei, was circulated by a peristaltic pump (Model 7619-50, Cole–Parmer, Vernon Hills, IL) at a flow rate of 217 mm/second in the hollow fiber. The use of contrast agents in the test fluid is to ensure that cavitation inside the vessel phantom can be produced consistently to facilitate the comparison of vessel rupture potential produced by the original and upgraded HM-3 lithotripter. The vessel phantom was immersed in a testing chamber filled with highly viscous castor oil to suppress cavitation activity outside the vessel phantom. In addition, a low pulse repetition rate (<0.1 Hz) of the LSWs was employed so that before each shock wave exposure any visible bubbles outside the vessel phantom could be removed. This approach was used to minimize the shear stress generated either by the scattering of LSW from bubbles trapped in castor oil or by simultaneous bubble expansion both inside and outside the hollow fiber.[10] Rupture of the vessel phantom could be easily identified since the circulating fluid (i.e., degassed water seeded with ultrasound contrast agents) would leak out, forming a liquid droplet in castor oil at the rupture site. At this point, the experiment was stopped and the number of shocks delivered was recorded. Before the next test (using a new vessel phantom), the castor oil containing the liquid droplet was aspirated out using a syringe and equal volume of fresh castor oils were replenished to the test chamber. If no rupture was observed after 200 shocks, the experiment was also terminated. A total of six samples were used under each test configuration, from which the mean value and standard deviation of the number of shocks needed to cause a rupture were determined.

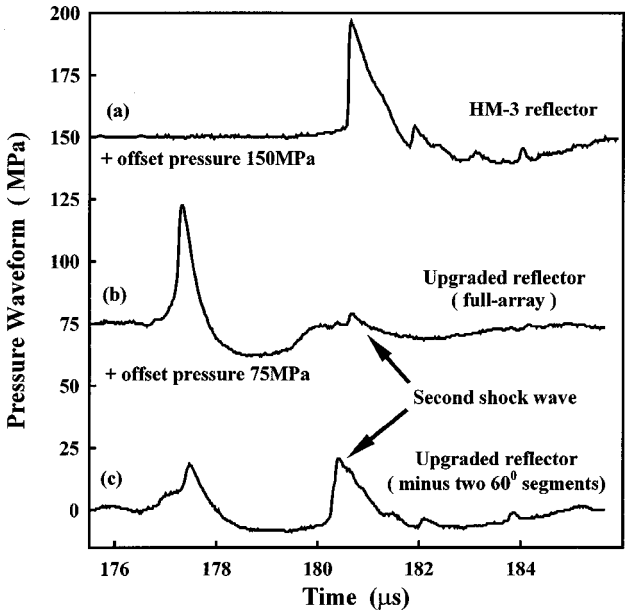

FIG. 5. Representative pressure wave forms of the lithotripter shock waves generated by using (a) the original HM-3 reflector, (b) the upgraded reflector (full-array), and (c) the upgraded reflector (without two 60° segments), all at an output voltage of 24 kV.

III. RESULTS

A. Physical characterization

1. Pressure wave forms and distribution

Figure 5 shows three representative pressure wave forms of the LSWs produced at F_2 by the original and upgraded reflectors at 24 kV. Using the original HM-3 reflector, a typical LSW was measured at 180.6 μs after the spark discharge [Fig. 5(a)], which was registered by a photodetector to provide a reliable time reference ($t=0$ s) of the event. This LSW consists of a leading compressive wave of ~ 1 μs pulse duration followed by a tensile component of ~ 4 μs, similar to the pressure wave forms measured in previous studies.[33,34] Due to the higher propagation speed of the LSW, its arrival time at F_2 is about 3 μs earlier than that estimated using the acoustic wave speed in water. In comparison, using the full-array reflector insert a LSW was measured at 176.8 μs, in consequence of the shorter major axis of the reflector insert [Fig. 5(b)]. In addition, a second pulse, largely compressive, was detected superimposing on the tensile tail of the leading LSW. On average, the peak-to-peak time delay between the leading LSW and the second wave is 3.8 μs, close to the estimated interpulse delay based on the geometric differences between the original and upgraded reflectors. Furthermore, it is interesting to note that when two large (60°) segments located opposite to each other were removed from the reflector insert, the leading LSW became weaker while the second wave grew stronger [Fig. 5(c)]. This result demonstrates the feasibility of altering the pressure waveform of the LSW by simply adjusting the geometry of the reflector insert. A comprehensive evaluation of this approach, however, is beyond the scope of this investigation. In the following, only the results from the full-array reflector insert are presented.

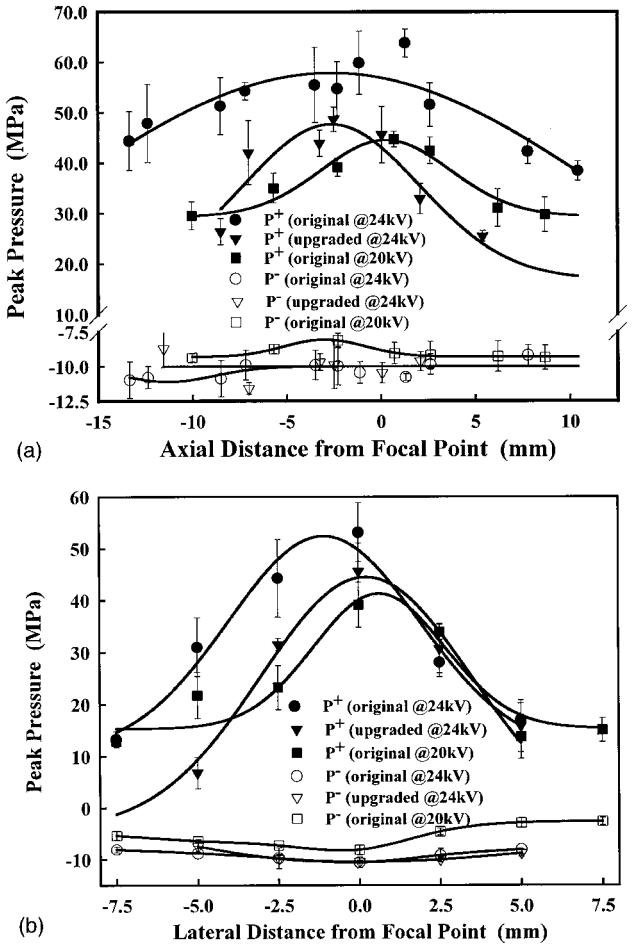

FIG. 6. Distribution of the peak pressure of the lithotripter shock waves (a) axial distribution and (b) transverse distribution, generated by using the original reflector at 20 and 24 kV, and the upgraded reflector at 24 kV.

The distributions of the peak positive (P^+) and peak negative (P^-) pressure of the LSWs generated by the original and upgraded reflectors, both along and transverse to the shock wave axis at F_2, are shown in Fig. 6. To highlight the general beam profile, the original data points from each reflector configuration were fitted with a Gaussian distribution curve using a commercial graphic program (SigmaPlot 5.0, SPSS, Chicago, IL). It can be seen that the beam profile produced by the upgraded reflector at 24 kV fits in between those produced by the original reflector at 20 and 24 kV. In general, P^+ from the upgraded reflector at 24 kV was found to be much closer to the value produced by the original reflector at 20 kV than at 24 kV. This is because the effective reflecting surface for the LSW in the upgraded reflector is significantly reduced compared to the original HM-3 reflector; therefore, it has to be compensated by increasing the output voltage of the lithotripter. At F_2, the mean values and standard deviations of P^+ for the original reflector at 20 and 24 kV are 44.7 ± 1.5 and 59.8 ± 6.3 MPa, respectively, while the corresponding value for the upgraded reflector at 24 kV is 45.6 ± 5.6 MPa. In comparison, the corresponding values for P^- are similar between the original and upgraded reflectors; they are -10.4 ± 0.78 and -10.5 ± 0.74 MPa for the original and upgraded reflector at 24 kV, and -9.1 ± 0.76 MPa for the original reflector at 20 kV, respectively. From the original data in Fig. 6(a), it can also be seen that the maximum P^+ was measured slightly beyond the geometric focus of each reflector ($z=0$ mm for the original and $z=-5$ mm for the upgraded). Yet, the maximum P^- was found to shift towards the shock wave generator. These characteristic shifts in the maximum of P^+ and P^- are presumably caused by the nonlinear propagation of the LSW.[25–27] Based on the distribution of P^+, the -6-dB transverse beam width at F_2 were determined to be 7.2 and 8.3 mm for the original reflector at 20 and 24 kV, respectively, and 7.2 mm for the upgraded reflector at 24 kV. These values are smaller than those reported previously;[33,34] and the reason for the discrepancy is unknown. Due to the limited data available, the -6-dB focal zone along the shock wave axis could not be determined.

Table II summarizes the pressure amplitudes and temporal parameters of the shock waves produced by the original and upgraded reflectors at F_2. One notable change in the temporal profile of the LSWs is that the rise time of the shock front produced by the upgraded reflector (221 ns) is much longer than that (27 ns) produced by the original reflector. This could be caused in part by a small misalignment between the different segments of the reflector insert; for instance, a misalignment of 0.15 mm would lead to a 100 ns delay in wave front arrival time. This problem, however, can be amended by fabricating the reflector insert as a single unit once the optimal geometry of the reflector is determined. Another notable change from the upgraded reflector is the significant reduction in the pulse duration of the tensile component of the LSW (t^-). At 24 kV, although P^- is comparable between the original and upgraded reflectors, t^- is reduced by about 48% using the reflector insert. This reduction in t^- should greatly lessen the expansion of cavitation bubbles induced by the LSW. At F_2, the P^+ for the second shock wave is estimated to be about 10.4 MPa using a wave

TABLE II. Peak pressure and temporal parameters of the shock waves produced by different reflector configurations. Beam width: -6 dB range of the peak positive pressure transverse to the lithotripter axis. t_r: Rise time of the shock front, measured from 10% to 90% of the peak positive pressure. t^+: Positive pulse duration, measured by the zero-crossing duration of the first positive cycle of the shock wave. t^-: Negative pulse duration, measured by the zero-crossing duration of the first negative cycle of the shock wave.

Reflector configuration	P^+ (MPa)	P^- (MPa)	Beam width (mm)	t_r (ns)	t^+ (μs)	t^- (μs)
Original HM-3 @ 24 kV	59.84 ± 6.29	-10.44 ± 0.78	8.3	27.3 ± 4.6	0.87 ± 0.06	3.93 ± 0.17
Upgraded @ 24 kV	45.57 ± 5.58	-10.46 ± 0.74	7.2	220.8 ± 96	1.06 ± 0.34	2.06 ± 0.28
Original HM-3 @ 20 kV	44.68 ± 1.54	-9.05 ± 0.76	7.2	27.0 ± 4.3	1.36 ± 0.17	4.90 ± 0.06

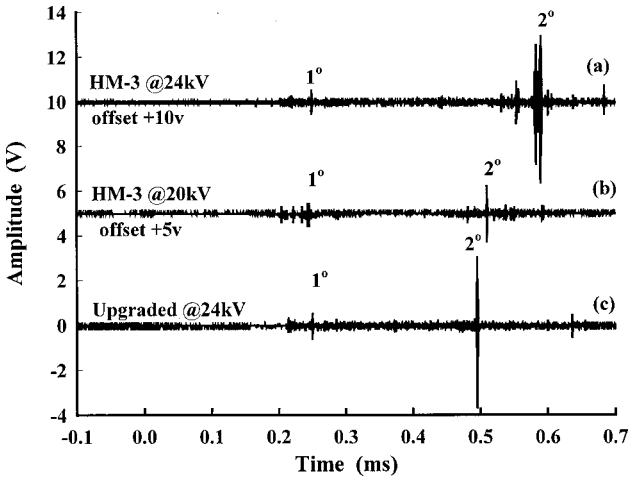

FIG. 7. Typical acoustic emission (AE) signals produced by using the original HM-3 reflector at (a) 24 kV and (b) 20 kV, and (c) the upgraded reflector at 24 kV. The collapse time of the bubble cluster is determined by the time delay between the peak pressure of the first (1°) and second (2°) AE bursts.

form subtraction method. As shown in Fig. 5, the pulse duration of the second shock wave is about 2 μs at F_2.

2. Acoustic emission

Figure 7 shows three typical acoustic emission (AE) signals associated with cavitation bubbles produced by the original and upgraded reflectors around the beam focus of the HM-3 lithotripter. Two distinct, temporally separated pressure bursts were detected in each AE trace. The first burst corresponds to the initial compression and ensuing expansion of cavitation nuclei by the incident LSW and the second one corresponds to the subsequent inertial collapse of the bubble cluster.[17,24,35] Previous studies have shown that the collapse time (t_C), defined by the time delay between the peaks in the first and second pressure bursts, correlates with the maximum expansion of the bubble cluster.[8,28,35] Using the 1 MHz focused hydrophone, the variation in t_C along the lithotripter axis was determined (Fig. 8). It was found that

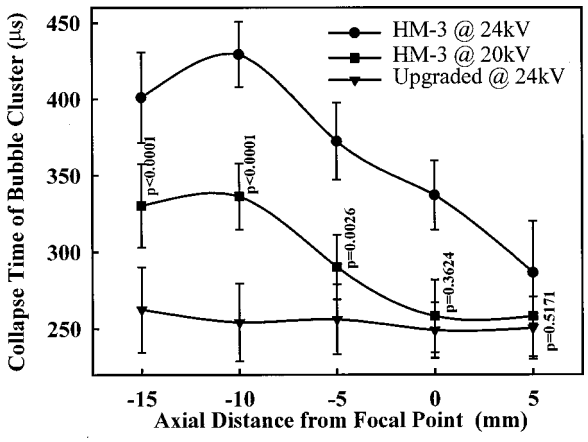

FIG. 8. Collapse time of the bubble clusters generated in water along the lithotripter axis by using the original HM-3 reflector at 20 and 24 kV, and the upgraded reflector at 24 kV. A student's *t*-test was performed to determine statistically significant differences ($p<0.05$) between the results produced by the original HM-3 reflector at 20 kV and that from the upgraded reflector at 24 kV for each axial location. The significant levels (p values) are shown in the figure.

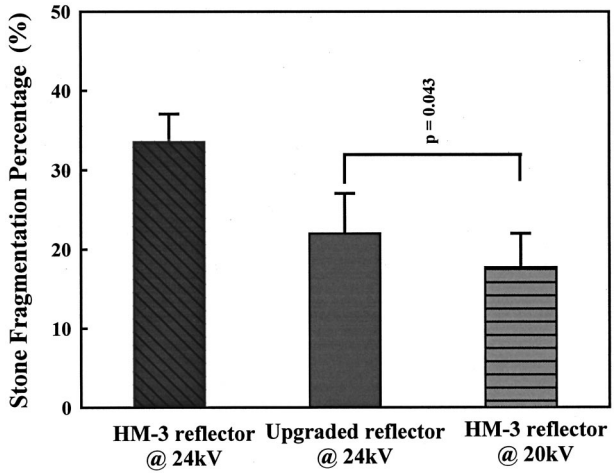

FIG. 9. Percentage of stone fragments less than 2 mm in size following 100 shocks produced by using the original HM-3 reflector at 20 and 24 kV, and the upgraded reflector at 24 kV. A student's *t*-test was performed to determine statistically significant differences ($p<0.05$) between the results produced by the original HM-3 reflector at 20 kV and that from the upgraded reflector at 24 kV. The significant levels (p values) are shown in the figure.

for the original HM-3 reflector the maximum t_C was produced profocally at $z=-10$ mm, which is consistent with the position of the maximum P^- for the LSWs (Fig. 6). In comparison, t_C from the upgraded reflector at 24 kV is generally smaller than that from the original reflector both at 20 and 24 kV. The largest differences were observed at $z=-10$ mm, with t_C being reduced from 334 and 429 μs for the original reflector at 20 and 24 kV to 254 μs for the upgraded reflector at 24 kV, corresponding to a 24% and 41% reduction, respectively. At F2, although the value of t_C was found to be slightly reduced from the original reflector at 20 kV to the upgraded reflector at 24 kV, the difference is not statistically significant ($p=0.3624$).

B. Stone comminution

Using the phantom system (see Fig. 4) designed to mimic stone comminution in the renal pelvis during SWL, the fragmentation efficiencies produced by the original and upgraded reflectors were evaluated. As shown in Fig. 9, 18% and 33% of the stone mass were reduced to fragments less than 2 mm following 100 shocks produced by the original lithotripter at 20 and 24 kV, respectively. Correspondingly, a fragmentation efficiency of 22% was achieved using the upgraded reflector at 24 kV. These results indicate that although stone fragmentation is reduced by about 33% using the upgraded reflector at 24 kV, it is still better than that produced by the original HM-3 reflector at 20 kV. Together with the results in Fig. 6, it is clear that increasing the output voltage of the lithotripter can compensate the reduction in pressure amplitude and fragmentation power due to the modification of the reflector.

C. Rupture of vessel phantoms

Using the original HM-3 reflector, rupture of the hollow fiber vessel phantoms was produced consistently along the shock wave axis around F_2 both at 20 and 24 kV (Fig. 10). The propensity for rupture was found to be higher prefocally

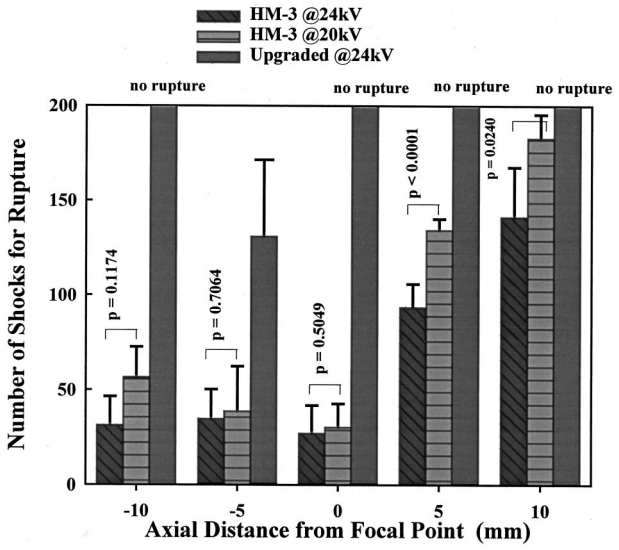

FIG. 10. The relationship between the number of shocks to cause a rupture of a cellulose hollow fiber (i.d.=0.2 mm) and its axial position in the lithotripter field ($n=6$). A student's *t*-test was performed for each location between the results of 20 kV and 24 kV using the original HM-3 reflector. The significant levels (p values) are shown in the figure.

($z=0--10$ mm) where less than 60 shocks were needed to cause a rupture than postfocally ($z=5-10$ mm) where 100 to 200 shocks were needed. Overall, the damage potential was found to increase with the output voltage of the lithotripter, especially along the beam axis where $z>5$ mm. These results are expected considering that P^- of the LSW increases with the output voltage of the lithotripter, and its maximum is reached around $z=-10$ mm. In contrast, using the upgraded reflector, no rupture of the vessel phantom could be observed even after 200 shocks. The only exception was at $z=-5$ mm where rupture was observed after 131 ± 41 shocks (mean$\pm$s.d.), which may correspond to the highest tensile pressure produced by the upgraded reflector [see Fig. 6(a)]. Nevertheless, this average number is still about three times of the number of shocks needed to cause a rupture using the original reflector (39 ± 24 at 20 kV and 35 ± 16 at 24 kV, respectively). All together, these results suggest that compared to the original HM-3 reflector, the upgraded reflector can produce satisfactory stone comminution with greatly reduced potential for vascular injury.

IV. DISCUSSION

To reduce the potential for vascular injury without compromising the stone comminution capability of a Dornier HM-3 lithotripter, we have devised a method to suppress intraluminal bubble expansion via *in situ* pulse superposition. This is achieved by a simple modification of the original ellipsoidal reflector to partition each shock wave generated by the spark discharge at F_1 into a leading LSW and an ensuing second compressive wave, separated from each other by about 4 μs. The superposition of the two waves leads to a selective truncation of the trailing tensile component of the LSW, and consequently, a reduction in bubble expansion. This strategy is based on our recent observation that the rapid, large intraluminal bubble expansion constitutes an important mechanism for the rupture of capillaries and small blood vessels in SWL.[12] In this study, we have shown *in vitro* that such a strategy can produce satisfactory stone comminution while significantly reducing the potential for vessel rupture. This improvement, if confirmed *in vivo*, could significantly reduce the adverse effects of lithotripsy, which will be particularly important for pediatric and elderly patients who are at much higher risk for SWL-induced chronic injury.[6]

Since the pulse duration of the second compressive wave is about 2 μs, it cannot completely neutralize the tensile component of the LSW ($\sim$4 μs). Therefore, the interpulse delay between the leading LSW and the second compressive wave could be critical in determining the effectiveness of using an *in situ* pulse superposition technique to suppress bubble expansion. Furthermore, as shown in Fig. 5 the size and geometry of the reflector insert can significantly influence the pressure amplitude and profile of the LSW, and thus affect the resultant bubble activity. In this work, we chose an interpulse delay of $\sim$4 μs based on theoretical evaluation of the maximum bubble expansion in response to a modified LSW (see Fig. 1) for proof of principle. Further optimization in the geometry and size of the reflector insert and in the interpulse delay is needed to improve the effectiveness of this approach (especially at $z=-5$ mm) while maintaining satisfactory stone comminution.

At the lithotripter focus, the measured t_C is similar between the values for the original reflector at 20 kV and that for the upgraded reflector at 24 kV (Fig. 8), but the potential for vessel rupture is quite different (Fig. 10). Our interpretation of these results is that although t_C correlates well with the maximum expansion of the bubble cluster, it does not provide any information about the rate and maximum dilation of the vessel wall by the expanding intraluminal bubbles, which are critical parameters in determining vessel rupture.[12] Moreover, when measured in a free field, the value of t_C could be affected by bubble aggregation along the lithotripter axis.[8,12] To gauge more accurately the potential for vessel rupture in a lithotripter field, techniques that can quantify the rate and maximum dilation of a vessel wall by intraluminal expansion of cavitation bubbles are needed.

It is important to note that although cavitation has long been speculated to play an important role both in stone comminution[36–38] and in tissue injury,[3,4] only recent studies have demonstrated that the underlying mechanisms by which cavitation contributes to stone comminution and to tissue injury are different.[12,39] It is therefore reasonable to suggest that selective manipulation of the bubble dynamics in SWL may enhance treatment efficiency while simultaneously reducing tissue injury. For example, it has been shown that the forced collapse of LSW-induced cavitation bubbles near a stone surface produced by a piezoelectric annular array generator that is retrofitted around a HM-3 reflector can significantly enhance the efficiency of stone comminution in SWL.[20,21] Combined with the *in situ* pulse superposition technique developed in this work, it may be possible to selectively intensify cavitation activity near the target stone for improved treatment efficiency while suppressing bubble ex-

pansion in adjacent renal tissues along the lithotripter axis to reduce the adverse effects of SWL.

ACKNOWLEDGMENTS

This work was supported in part by NIH through Grants Nos. RO1-DK52985, RO1-DK58266, and PO1-DK20543. We also acknowledge Dr. Songlin Zhu for his technical assistance in the calculations of bubble dynamics using the Gilmore model.

[1] C. Chaussy and G. J. Fuchs, ''Current state and future developments of noninvasive treatment of human urinary stones with extracorporeal shock wave lithotripsy,'' J. Urol. (Baltimore) **141**, 82–792 (1989).
[2] Ch. Renner and J. Rassweiler, ''Treatment of renal stones by extracorporeal shock wave lithotripsy,'' Nephron **81**, 71–81 (1999).
[3] M. Delius, ''Medical applications and bioeffects of extracorporeal shock waves,'' Shock Waves **4**, 55–72 (1994).
[4] A. P. Evan and J. A. McAteer ''Q-effects of shock wave lithotripsy,'' in *Kidney Stones: Medical and Surgical Management*, edited by F. L. Coe *et al.* (Lippincott–Raven, Philadelphia, PA, 1996), pp. 549–570.
[5] P. Blomgren, B. A. Connors, J. E. Lingeman, L. R. Willis, and A. P. Evan, ''Quantitation of shock wave lithotripsy-induced lesion in small and large pig kidneys,'' Anat. Rec. **249**, 341–348 (1997).
[6] A. P. Evan, L. R. Willis, J. E. Lingeman, and J. A. McAteer, ''Renal trauma and the risk of long-term complications in shock wave lithotripsy,'' Nephron **78**, 1–8 (1998).
[7] A. Philipp, M. Delius, C. Scheffczyk, A. Vogel, and W. Lauterborn, ''Interaction of lithotripter-generated shock waves in air bubbles,'' J. Acoust. Soc. Am. **93**, 2496–2509 (1993).
[8] P. Zhong, I. Cioanta, F. H. Cocks, and G. M. Preminger, ''Inertial cavitation and associated acoustic emission produced during electrohydraulic shock wave lithotripsy,'' J. Acoust. Soc. Am. **101**, 2940–2950 (1997).
[9] P. Zhong, I. Cioanta, S. L. Zhu, F. H. Cocks, and G. M. Preminger, ''Effects of tissue constraint on shock wave-induced bubble expansion in vivo,'' J. Acoust. Soc. Am. **104**, 3126–3129 (1998).
[10] P. Zhong, X. F. Xi, S. L. Zhu, F. H. Cocks, and G. M. Preminger, ''Recent developments in SWL physics research,'' J. Endourol **13**, 611–617 (1999).
[11] E. L. Carstensen, D. S. Campbell, D. Hoffman, S. Z. Child, and E. J. Aymebellegarda, ''Killing of *Drosophila* larvae by the fields of an electrohydraulic lithotripter,'' Ultrasound Med. Biol. **16**, 687–698 (1990).
[12] P. Zhong, Y. F. Zhou, and S. L. Zhu, ''Dynamics of bubble oscillation in constrained media and mechanisms of vessel rupture in SWL,'' Ultrasound Med. Biol. **27**, 119–134 (2001).
[13] D Cathignol, J. Tavakkoli, J. A. Birer, and A. Arefiev, ''Comparison between the effects of cavitation induced by two different pressure-time shock waveform pulses,'' IEEE Trans. Ultrason. Ferroelectr. Freq. Control **45**, 788–799 (1998).
[14] A. P. Evan, L. R. Willis, B. A. Connors, J. A. McAteer, J. E. Lingeman, R. O. Cleveland, M. R. Bailey, and L. A. Crum, ''Can SWL-induced cavitation and renal injury be separated from SWL-induced impairment of renal hemodynamics?'' J. Acoust. Soc. Am. **103**, 3037 (1998).
[15] D. Howard and B. Sturtevant, ''In vitro study of the mechanical effects of shock-wave lithotripsy,'' Ultrasound Med. Biol. **23**, 1107–1122 (1997).
[16] J. A. Rooney, ''Hemolysis near an ultrasonically pulsating gas bubble,'' Science **169**, 869–871 (1970).
[17] C. C. Church, ''A theoretical study of cavitation generated by an extracorporeal shock wave lithotripter,'' J. Acoust. Soc. Am. **86**, 215–227 (1989).
[18] Z. Ding and S. M. Gracewski, ''Response of constrained and unconstrained bubbles to lithotripter shock wave pulses,'' J. Acoust. Soc. Am. **96**, 3636–3644 (1994).
[19] M. R. Bailey, ''Control of acoustic cavitation with application to lithotripsy,'' Ph.D. Dissertation, University of Texas at Austin, 1997.
[20] X. F. Xi and P. Zhong, ''Improvement of stone fragmentation during shock wave lithotripsy using a combined EH/PEAA shock wave generator—In vitro experiments,'' Ultrasound Med. Biol. **26**, 457–467 (2000).
[21] X. F. Xi, ''Dynamic shock wave-inertial bubble interaction for improvement of shock wave lithotripsy,'' Ph.D. Dissertation, Duke University, 2000.
[22] F. E. Prieto and A. M. Loske, ''Bifocal reflector for electrohydraulic lithotripters,'' J. Endourol **13**, 65–75 (1999).
[23] D. L. Sokolov, M. R. Bailey, and L. A. Crum, ''Effect of dual-reflector lithotripter on stone fragmentation and cell damage,'' J. Acoust. Soc. Am. **108**, 2518 (2000).
[24] S. L. Zhu and P. Zhong, ''Shock wave-inertial microbubble interaction: A theoretical study based on the Gilmore formulation for bubble dynamics,'' J. Acoust. Soc. Am. **106**, 3024–3033 (1999).
[25] M. Mueller, ''Dornier-Lithotripter im Vergleich. Vermessung der Stoßellenfelder und Fragmentationswirkungen. (Comparison of Dornier lithotripters. Measurements of shock wave fields and fragmentation effectiveness),'' Biomed. Tech. **35**, 250–262 (1990).
[26] A. J. Coleman, M. Whitlock, T. Leighton, and J. E. Saunders, ''The spatial distribution of cavitation induced acoustic emission, sonoluminescence and cell lysis in the field of a shock wave lithotripter,'' Phys. Med. Biol. **38**, 1545–1560 (1993).
[27] M. A. Averkiou and R. O. Cleveland, ''Modeling of an electrohydraulic lithotripter with the KZK equation,'' J. Acoust. Soc. Am. **106**, 102–112 (1999).
[28] P. Zhong, H. F. Lin, X. F. Xi, S. L. Zhu, and E. S. Bhogte, ''Shock wave-inertial microbubble interaction: Methodology, physical characterization, and bioeffect study,'' J. Acoust. Soc. Am. **105**, 1997–2009 (1999).
[29] E. L. Madsen, J. A. Zagzebski, and G. R. Frank, ''Oil-in-geltine dispersions for use as ultrasonically tissue-mimicking materials,'' Ultrasound Med. Biol. **8**, 277–287 (1982).
[30] R. O. Cleveland, D. A. Lifshitz, B. A. Connors, A. P. Evan, L. R. Willis, and L. A. Crum, ''In vivo pressure measurements of lithotripsy shock waves in pigs,'' Ultrasound Med. Biol. **24**, 293–306 (1998).
[31] C. J. Chuong, P. Zhong, and G. M. Preminger, ''A comparison of stone damage caused by different modes of shock wave generation,'' J. Urol. (Baltimore) **148**, 200–205 (1992).
[32] *Extracorporeal Shock Wave Lithotripsy: New Aspects in the Treatment of Kidney Stone Disease*, edited by C. Chaussy (S. Karger, Basel, 1982).
[33] A. J. Coleman and J. E. Saunders, ''A survey of the acoustic output of commercial extracorporeal shock wave lithotripters,'' Ultrasound Med. Biol. **15**, 213–227 (1989).
[34] M. R. Bailey, D. T. Blackstock, R. O. Cleveland, and L. A. Crum, ''Comparison of electrohydraulic lithotripters with rigid and pressure-release ellipsoidal reflectors. I. Acoustic fields,'' J. Acoust. Soc. Am. **104**, 2517–2524 (1998).
[35] A. J. Coleman, M. J. Choi, and J. E. Saunders, ''Detection of acoustic emission from cavitation in tissue during clinical extracorporeal lithotripsy,'' Ultrasound Med. Biol. **22**, 1079–1087 (1996).
[36] A. J. Coleman, J. E. Saunders, L. A. Crum, and M. Dyson, ''Acoustic cavitation generated by an extracorporeal shockwave lithotripter,'' Ultrasound Med. Biol. **13**, 69–76 (1987).
[37] L. A. Crum, ''Cavitation microjets as a contributory mechanism for renal calculi disintegration in ESWL,'' J. Urol. (Baltimore) **140**, 1587–1590 (1988).
[38] P. Zhong, C. J. Chuong, and G. M. Preminger, ''Propagation of shock waves in elastic solids caused by the impact of cavitation microjets: Part II. application to extracorporeal shock wave lithotripsy,'' J. Acoust. Soc. Am. **94**, 29–36 (1993).
[39] M. Delius, ''Minimal static excess pressure minimises the effect of extracorporeal shock waves on cells and reduces it on gallstones,'' Ultrasound Med. Biol. **23**, 611–617 (1997).

Auditory display of knee-joint vibration signals

Sridhar Krishnan
Department of Electrical and Computer Engineering, Ryerson University, Toronto, Ontario M5B 2K3, Canada

Rangaraj M. Rangayyan[a)]
Department of Electrical and Computer Engineering and Department of Surgery, University of Calgary, Calgary, Alberta T2N 1N4, Canada

G. Douglas Bell and Cyril B. Frank
Department of Electrical and Computer Engineering, Department of Surgery, and Sport Medicine Centre, University of Calgary, Calgary, Alberta T2N 1N4, Canada

(Received 31 March 2000; accepted for publication 27 August 2001)

Sounds generated due to rubbing of knee-joint surfaces may lead to a potential tool for noninvasive assessment of articular cartilage degeneration. In the work reported in the present paper, an attempt is made to perform computer-assisted auscultation of knee joints by auditory display (AD) of vibration signals (also known as vibroarthrographic or VAG signals) emitted during active movement of the leg. Two types of AD methods are considered: audification and sonification. In audification, the VAG signals are scaled in time and frequency using a time-frequency distribution to facilitate aural analysis. In sonification, the instantaneous mean frequency and envelope of the VAG signals are derived and used to synthesize sounds that are expected to facilitate more accurate diagnosis than the original signals by improving their aural quality. Auditory classification experiments were performed by two orthopedic surgeons with 37 VAG signals including 19 normal and 18 abnormal cases. Sensitivity values (correct detection of abnormality) of 31%, 44%, and 83%, and overall classification accuracies of 53%, 40%, and 57% were obtained with the direct playback, audification, and sonification methods, respectively. The corresponding d' scores were estimated to be 1.10, -0.36, and 0.55. The high sensitivity of the sonification method indicates that the technique could lead to improved detection of knee-joint abnormalities; however, additional work is required to improve its specificity and achieve better overall performance. [DOI: 10.1121/1.1413995]

PACS numbers: 43.80.Qf, 43.80.Vj, 43.80.Jz [FD]

I. INTRODUCTION

Auscultation, the method of examining functions and conditions of physiological systems by listening to the sounds they produce, is one of the ancient modes of diagnosis. The first use of vibration or acoustic emission as a diagnostic aid for bone and joint disease is found in Laennec's treatise on auscultation (cited by Mollan *et al.*[1]). Laennec was able to diagnose fractures by auscultating crepitus caused by the moving broken ends of bone. Heuter, in 1885, used a myodermato-osteophone (a type of stethoscope) to localize loose bodies in human knee joints (see Mollan *et al.*[1]). In 1929, Walters reported on the auscultation of 1600 joints and detected certain sounds before symptoms become apparent;[2] he suggested that the sounds might provide early signs of arthritis.

After 1933, most of the works reported on knee-joint sounds have been on objective analysis of the sound or vibration signals (also known as vibroarthrographic or VAG signals) for noninvasive diagnosis of knee-joint pathology.[3–11] Although auscultation of knee joints using stethoscopes is occasionally practiced by clinicians, there is no published evidence of their diagnostic value. Also, no study has been reported on computer-aided auscultation of knee-joint sounds (except our preliminary reports related to the present paper.[12,13] This paper proposes methods for computer-aided auscultation of knee-joint sounds based on auditory display (AD) techniques.

The VAG data acquisition procedure is briefly described in Sec. II. An introduction to AD techniques is presented in Sec. III. In Sec. IV, the motivation for AD and auditory analysis of VAG signals is outlined. The proposed AD techniques are described in Sec. V. In Sec. VI, the performance of the proposed methods is evaluated with easily recognizable signals. Experimental results of auditory analysis of VAG signals are provided in Sec. VII. In Sec. VIII, the conclusions of the work are presented.

II. DATA ACQUISITION

Each subject sat on a rigid table in a relaxed position with the leg being tested freely suspended in air. An accelerometer (Dytran 3115a) was affixed on the skin surface at the mid-patella position of the knee joint by using double-sided adhesive tape. The VAG signal was recorded as the subject swung the leg over an approximate angle range of 135° $\rightarrow$0°$\rightarrow$135° in 4 s. Informed consent was obtained from

a)Author to whom correspondence should be addressed; electronic mail: ranga@enel.ucalgary.ca.

every subject. The experimental protocol has been approved by the Conjoint Health Research Ethics Board of the University of Calgary.

The VAG signals were prefiltered (10 Hz–1 kHz) and amplified before digitizing at a sampling rate of 2 kHz. Further details of data acquisition may be found in Krishnan *et al.*[9] The database used in the present study consists of 37 signals (19 normal and 18 abnormal). The abnormal signals were collected from symptomatic patients scheduled to undergo arthroscopy, and there was no restriction imposed on the type of pathology.

III. AUDITORY DISPLAY

AD may be defined as aural representation of a stream of data.[14] The field of AD is emerging, and has recently drawn attention in the areas of geophysics,[15] biomedical engineering,[16,17] speech signal analysis,[18] image analysis,[19–23] aids for the handicapped,[23–25] and computer graphics.[24] AD should be performed in such a manner as to take advantage of the psychoacoustics of the human ear. AD techniques may be broadly classified into two categories: audification and sonification.[14] The following sections give brief descriptions of the two types of AD techniques.

A. Audification

Audification is the direct transformation of a data stream to the auditory domain for the purposes of monitoring and analysis. Filters and signal processing techniques may be used to assist the user of the display in isolating certain events, but there are no sound-synthesizing elements involved. Audification has been applied to seismic signal analysis[15] for studying earthquakes, and to speech signal analysis[18,26] for speaker verification and identification purposes. Audification of the phonocardiogram[16] has been shown to assist cardiologists in studying the transient property of heart sounds and the more complex random property of heart murmurs. Audification of random-textured images has been explored for the analysis of magnetic resonance images of the brain.[19–22]

B. Sonification

In sonification, features extracted from the data are used to control a sound synthesizer. The sound signal generated does not bear a direct relationship to the original data. A simple example of a sonification technique is the mapping of parameters derived from a data stream to AD parameters such as pitch and loudness. Fitch and Kramer[17] performed sonification of physiological data and compared it with standard visual display. They observed that the subjects performed faster and accurate analysis with sonification of physiological data than with visual display. Sonification procedures have been proposed for aural analysis of images with ordered texture.[19–22]

IV. MOTIVATION FOR AD OF VAG

Prior to graphical recording and analysis of VAG signals, auscultation of knee joints was the only noninvasive method available to distinguish normal joints from degenerated joints. Significant success has been claimed by several researchers using the auscultation technique. However, classification of knee joints by auscultation is a highly subjective technique. Furthermore, a significant portion of the VAG signal energy lies below the threshold of auditory perception of the human ear in terms of frequency and/or intensity. The situation may be ameliorated by developing AD methods for computer-aided auscultation of knee-joint vibrations.[12,13] The main motivating factors in applying AD techniques to VAG are as follows.

(1) It has been established through objective signal analysis of VAG that sounds generated by abnormal knees are distinctive and different from those produced by normal knees.[3–11] Sounds of diagnostic value may be made prominent by applying suitable AD techniques to VAG.
(2) AD of VAG obtained by using vibration sensors may facilitate relatively noise-free and localized auditory analysis when compared to direct auditory analysis via auscultation with a stethoscope.
(3) AD of VAG can be combined with other objective signal analysis procedures to reach a reliable diagnostic decision in a multimedia setting.
(4) AD of VAG can be used to train health-care professionals, and may lead to the development of a teaching tool for learning auscultation of knee-joint sounds.

V. PROPOSED METHODS FOR AD OF VAG

The work described in this paper hypothesizes that auditory analysis of VAG data may aid an orthopedic surgeon or physician in making diagnostic inferences. In this section, both audification and sonification techniques for auditory analysis of VAG data are developed. This study is the first attempt to listen to knee sounds detected by vibration sensors.

A. Audification of VAG signals

It is evident from a review of auscultation of knee joints that significant diagnostic information can be deduced by listening to knee sounds through a stethoscope. Although a common stethoscope does not have better dynamic range of frequency response and sensitivity than those of vibration sensors, its ability to facilitate auscultation of important diagnostic events is well established. The audification of VAG signals was performed in two ways: (1) direct playback, and (2) audification via a time-frequency scaling method based on a signal decomposition technique using matching pursuit (MP).[27]

1. Direct playback

In direct playback, the digitized VAG signals were converted to the audio file (.au) format, and played at the sampling rate of 2 kHz using the ''audiotool'' program in an Ultrasparc (SUN microsystems) station. The signals were of 4 s duration, covering one complete cycle of leg swing. Direct playback of VAG signals was expected to provide more information than the sounds heard using a stethoscope due to better noise immunity, sensitivity, and low-frequency response of the accelerometer than the stethoscope.

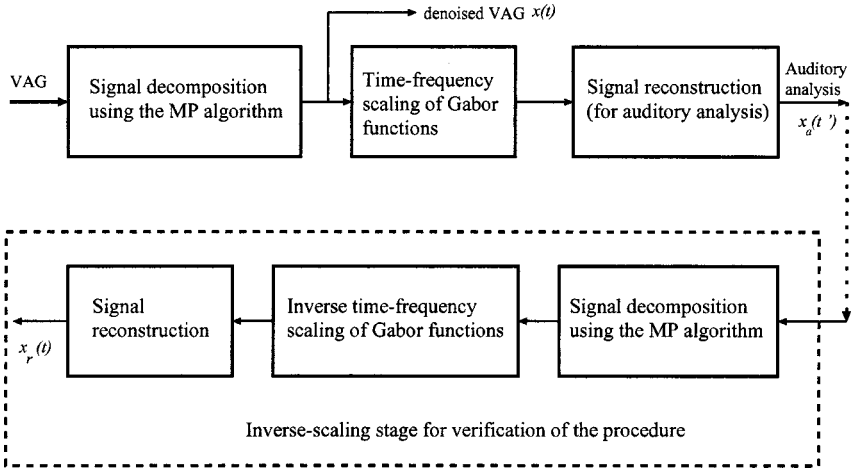

FIG. 1. Block diagram of the MP-based audification method.

2. MP-based audification

VAG signals lie at the lower end of the frequency spectrum (i.e., typically they have most of their energy between 0 and 200 Hz, after which the energy decreases rapidly), and audible sound is only a part of their total spectral content. The presence of background noise, muscle vibration artifacts, and the complex nature of the VAG signal make auscultation difficult. A technique that shifts the frequency spectrum of components of diagnostic relevance to a higher and more easily perceptible range may be useful. On the other hand, clicks of clinical interest are of very short duration, and direct auscultation or direct audification may not facilitate auditory analysis of the subtle characteristics of such transients. A method that scales transients to a longer duration could facilitate improved auscultation.

In this study, time-frequency (TF) scaling is performed using the method proposed by Zhang *et al.*[16] for heart sounds. The TF scaling is achieved by decomposing the signal into components with good time and frequency localization properties. One such method is the decomposition of the given signal based on the matching pursuit algorithm.[11,27] The MP algorithm decomposes the given signal into components by projecting it on an overcomplete collection of TF functions; these functions have a Gaussian form in both the time and frequency dimensions, and are known as Gabor functions. The TF functions generated as a result of the decomposition procedure are suitably time scaled and frequency scaled. The scaled TF functions are used in the synthesis stage to construct a TF-scaled signal.

Figure 1 shows the block diagram of the MP-based audification method. The original VAG signal is decomposed into TF functions by using the MP method as described in the Appendix. The MP decomposition process is stopped once the coherent structures of the signal are extracted.[28] At the decomposition stage, the MP algorithm provides the parameters a_n, s_n, p_n, f_n, and ϕ_n in Eqs. (A1) and (A2). By scaling t, s_n, and p_n, a time-scaled version of the signal can be obtained. Scaling f_n gives a frequency-scaled version of the signal. The scaling parameters can be varied suitably to obtain the desired perceptual, frequency, and temporal characteristics.

In joint TF scaling, the time (t) and the frequency (f_n) variables are transformed to new variables t' and f_n', respectively, by the scalar transformations

$$t' = \alpha t, \quad f_n' = \beta f_n, \tag{1}$$

where α and β are positive numbers. The use of $\alpha > 1$ expands the signal in time, and $\alpha < 1$ compresses the signal in time. On the other hand, $\beta > 1$ shifts the spectral bandwidth to a higher frequency range, and $\beta < 1$ shifts the spectral bandwidth to a lower frequency range. In the case of critically sampled signals, the following condition should be met:

$$f_s \geqslant 2\beta f_m, \tag{2}$$

where f_m is the maximum frequency component present in the signal, and f_s is the sampling rate. The condition in Eq. (2) avoids frequency aliasing in frequency-scaled versions of the signals.

In the present application, we are interested in playing VAG signals for a longer duration with frequency mapping to a ''comfortable'' audible band. The temporal properties of the signal are related to the time position p_n and the scale factor s_n. Therefore, in the time-scaling procedure, the temporal placement and the scale factors are transformed to p_n' and s_n', where $p_n' = \alpha p_n$ and $s_n' = \alpha s_n$. In the case of frequency scaling, the frequency variable f_n is transformed to $f_n' = \beta f_n$. The TF-scaled Gabor function is then given by

$$g_{\gamma_n'}(t) = \frac{1}{\sqrt{s_n'}} g\left(\frac{t - p_n'}{s_n'}\right) \exp[j(2\pi f_n' \alpha t + \phi_n)]$$

$$= \frac{1}{\sqrt{\alpha s_n}} g\left(\frac{t' - \alpha p_n}{\alpha s_n}\right) \exp[j(2\pi \beta f_n \alpha t + \phi_n)]. \tag{3}$$

MP reconstruction using the TF-scaled functions provides the desired TF-scaled signal $x_a(t')$, which may be expressed as

$$x_a(t') = \sum_{n=0}^{M-1} a_n g_{\gamma_n'}(t'), \tag{4}$$

where M is the total number of coherent TF structures provided by MP decomposition.

The inverse TF scaling part shown in Fig. 1 may be used to verify the scaling procedures. After TF scaling, the tem-

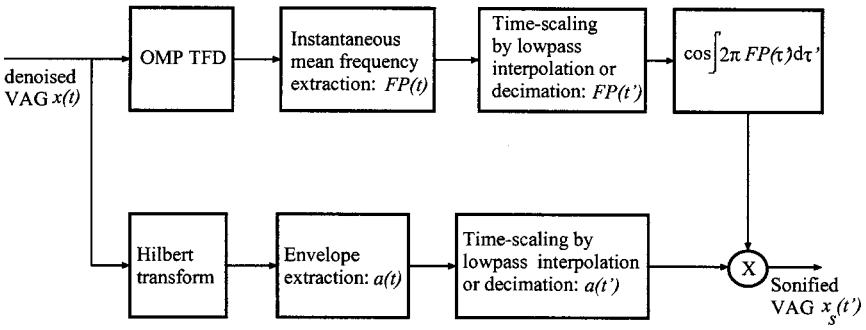

FIG. 2. Block diagram of the IMF-based sonification method.

poral and/or spectral properties of the signals are changed, and verification of the scaling process becomes difficult. Therefore, for evaluation of the scaling process, an inverse scaling procedure was also implemented, where the variables t' and f' are transformed back to t and f, by using the inverse scale parameters $1/\alpha$ and $1/\beta$, respectively. If there is no distortion caused by the scaling transformations and the MP decomposition procedures, the denoised signal $x(t)$ (see the Appendix) and the inverse-scaled signal $x_r(t)$ should be identical.

B. Sonification of VAG signals

It is known that VAG signals are multicomponent signals.[11] Hence, in TF scaling, shifting all of the components of a VAG signal to a different frequency band may not bring out the event of interest, and may obscure the features of diagnostic value. In an effort to facilitate AD of only the important characteristics of VAG signals, a sonification algorithm is proposed. A block diagram of the proposed sonification method is shown in Fig. 2.

The sonification algorithm involves amplitude modulation (AM) and frequency modulation (FM). The instantaneous mean frequency (IMF) of a signal is an important parameter in characterizing multicomponent, nonstationary signals such as VAG.[11,29] The IMF indicates how the mean frequency of a signal varies with time. The FM part of the sonified signal is obtained by frequency-modulating a sinusoidal waveform with the IMF of the VAG signal. The auditory characteristics of the FM part alone will be tonal, which could quickly cause boredom and fatigue. To obviate this problem, an AM part is obtained as the magnitude of the analytic version of the VAG signal. The AM part provides an envelope to the signal and frequency deviation (bandwidth) about the IMF. The IMF-based sonification algorithm is summarized as follows.

(1) Construct a positive time-frequency distribution (TFD)[11,30] of the signal. In this work, positive TFDs of VAG signals were constructed using the optimized matching pursuit algorithm.[11]

(2) Extract the IMF [frequency parameter $\mathrm{FP}(t)$] as the first central moment of the TFD along the frequency axis.

(3) Lowpass-interpolate the $\mathrm{FP}(t)$ waveform by the required time-scale factor, i.e., obtain $\mathrm{FP}(t')$, where $t'=\alpha t$.

(4) Take the Hilbert transform of the denoised VAG signal and form its analytic representation as

$$a(t)=x(t)+jH\{x(t)\}, \tag{5}$$

where $H\{\}$ is the Hilbert transform.

(5) Extract the envelope of the signal by taking the magnitude of $a(t)$, i.e.,

$$|a(t)|=\sqrt{x^2(t)+(H\{x(t)\})^2}. \tag{6}$$

(6) Lowpass-interpolate the envelope by the required time-scale factor; that is, obtain $a(t')$.

(7) Construct the sonified signal $x_s(t')$ by combining the envelope and the IMF components, i.e.,

$$x_s(t')=|a(t')|\cos\left(\int_{-\infty}^{t'} 2\pi \mathrm{FP}(\tau')d\tau'+\phi_0\right), \tag{7}$$

where ϕ_0 is an arbitrary phase constant. The derivative of the phase of $a(t)$ may be used to extract the IMF of the signal. Extensive research has been conducted on the extraction of the IMF of a signal via the phase of its analytic form.[31–34] However, it has been observed that the IMF extracted via the phase of the analytic signal often leads to paradoxical results such as the IMF taking negative and noninterpretable values.[32,34,35] The approach of using TFDs to extract the IMF provides an interpretable value that is always positive.[11,30]

The advantages of the IMF-based sonification method are as follows.

(1) It helps in auditory analysis of a multicomponent nonstationary signal in terms of its main features such as $\mathrm{FP}(t)$ and $a(t)$.
(2) $\mathrm{FP}(t)$ takes high values for transients and noise. However, by making use of the envelope (intensity) information, noise can be made less audible as compared to transients.
(3) If $\mathrm{FP}(t)$ is in the subaudible range, it can be shifted to the audible band by frequency scaling. Frequency scaling can be achieved by multiplying $\mathrm{FP}(t)$ by the required frequency scale factor β; that is, $\mathrm{FP}'(t)=\beta\,\mathrm{FP}(t)$.
(4) Integration of $\mathrm{FP}(t)$ ensures a continuous phase, and the method does not require any phase unwrapping.
(5) Integration of $\mathrm{FP}(t)$ makes the method insensitive to noisy $\mathrm{FP}(t)$ estimates.

The IMF-based method has the following limitations.

(1) If the duration of the envelope is significantly increased by interpolation (i.e., with $\alpha \gg 1$), the frequency spectrum of the envelope becomes narrower; this may introduce only a small deviation about the IMF.
(2) In the case of a noisy signal, FP(t) will have an almost uniform waveform, and does not provide much information unless the envelope can contribute some information. In the present study, this problem is overcome by processing denoised versions of the VAG signals.
(3) The method may not be applicable to information-rich signals such as speech: the formant structure of voiced speech cannot be adequately represented by the relatively simple IMF. For AD of signals with rich spectral information, audification may be the better choice.

VI. PERCEPTUAL EVALUATION

The performance of the MP-based audification algorithm and the IMF-based sonification algorithm was evaluated with signals of known characteristics. Two types of signals were considered: (1) a synthetic nonstationary signal, and (2) a speech signal.

The synthetic nonstationary signal is shown in Fig. 3(a). The synthetic signal has an almost-constant envelope [derived using Eq. (6)] as shown in Fig. 3(b). The FM law (IMF) of the signal is shown in Fig. 3(c). It is evident from the spectrogram shown in Fig. 3(d) that the signal is monocomponent in nature. The spectrograms of the audified and sonified versions of the synthetic signal shown in Figs. 3(e) and (f), respectively, clearly indicate the effects of a time-scaling operation with $\alpha = 2$. In the case of a monocomponent signal such as the one shown in the present example, the IMF of the signal matches the original frequency dynamics of the signal, and the IMF-based sonification method should provide superior performance when compared to the MP-based audification method.

The sounds were played back using the audiotool, and evaluated by a signal processing researcher with a background in classical music (R.M.R.). No information was provided about the scaling. R.M.R. was able to aurally identify the original, time-scaled, frequency-scaled, and time-frequency scaled versions of the synthetic signal.

The methods were also evaluated with an easily intelligible speech signal of the word ''greasy'' spoken by a female, shown in Fig. 4(a) (sampled at 8 kHz; source[27]). The speech signal has both voiced and unvoiced sounds. The envelope of the speech signal computed using Eq. (6) and the IMF computed from its positive TFD are shown in Figs. 4(b) and (c). The spectrogram of the speech signal is shown in Fig. 4(d). The voiced sounds possess formants in the spectrum whereas the fricative appears as wideband noise.[36] The MP-based audified speech signal's spectrogram, shown in Fig. 4(e), indicates the effects of frequency scaling with $\beta = 2$ and time scaling with $\alpha = 2$. In the case of the MP-based audification method, R.M.R. was able to differentiate between the time-scaled, frequency-scaled, and time-frequency-scaled versions of the speech signal. R.M.R. also noticed a continuous and distinct background sound that was referred to as a ''waterflow'' or gurgling sound; the waterflow sound was more evident with frequency scaling. The artifact could be due to the nonuniform envelope of the speech signal, which, when stretched in the time domain, might have become aurally dominant. In an attempt to overcome this artifact, a lowpass-filter-based envelope correction method was applied. The envelope correction method was able to reduce the waterflow sound, but the resultant sound had an artificial quality. It was decided not to perform envelope correction, and to recognize but ignore the waterflow sound in subsequent analysis with MP-based audification.

Auditory analysis of the result of application of the IMF-based sonification method to the ''greasy'' speech signal indicated that only a part of its intelligibility was retained. R.M.R. did not notice any waterflow artifact as with the MP-based audification method. The spectrogram of the IMF-based sonified signal is shown in Fig. 4(f). It can be observed that the IMF represents the main features of the different sounds in the speech signal. The spectrogram shown in Fig. 4(f) clearly indicates the envelope-IMF behavior of the sonified speech signal. The formant structure is, however, lost.

VII. AUDITORY ANALYSIS OF VAG SIGNALS

Auditory analysis of VAG signals was performed by two orthopedic surgeons (G.D.B. and C.B.F.) with significant experience in knee-joint auscultation and arthroscopy. The experiment was conducted in three stages: In the first stage, familiarization and training were provided through the results of application of the MP-based audification and IMF-based sonification methods to the ''greasy'' speech signal and four VAG signals (two normals and two abnormals). In the second stage, the methods were tested with the database of 37 VAG signals. In stage three, a post-test evaluation was performed with eight VAG signals.

A. First stage: Initial selection

The initial selection session (first stage) was conducted in order to determine if the MP-based audification and IMF-based sonification methods could provide enhanced diagnostic information. The initial selection stage was also used to determine the desired time-scale and frequency-scale factors. Prior to the initial selection experiment, G.D.B. was provided with auscultation and arthroscopic information about the subjects whose VAG signals were used. In the initial selection stage with VAG signals, seven versions of each signal were presented in the following order.

(1) The original signal without any scaling (direct playback at 2 kHz). The original signal was used as a reference to compare with the scaled versions.
(2) Time scaled by a factor of 2 using the MP-based audification method.
(3) Time scaled and frequency scaled by factors of 2 using the MP-based audification method.
(4) Time scaled by a factor of 2 using the IMF-based sonification method.

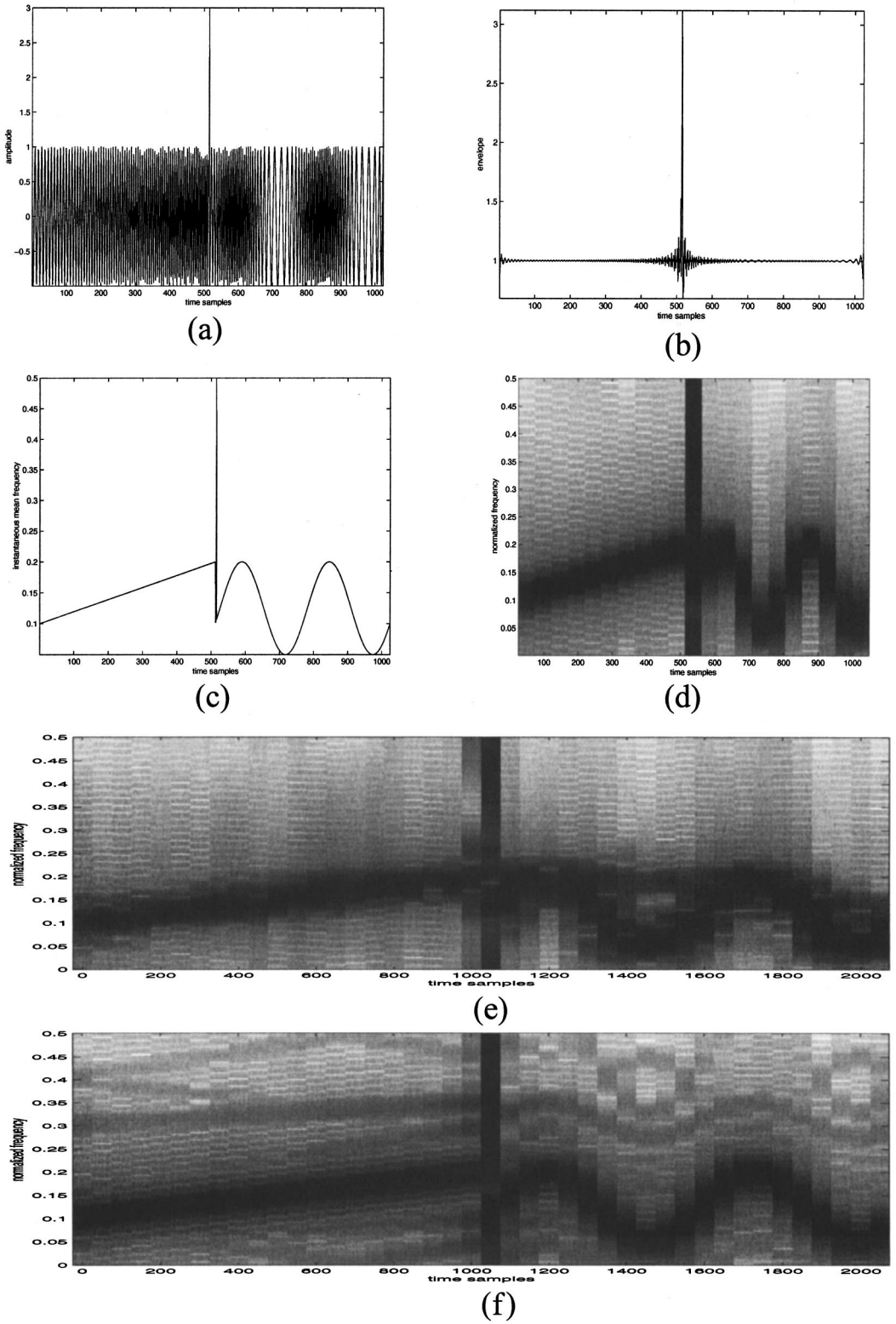

FIG. 3. (a) Synthetic signal consisting of a chirp, a transient, and a sinusoidal FM component. The time axis is shown in samples: The actual time in seconds depends upon the playback rate. (b) Envelope of the synthetic signal in (a). (c) Ideal instantaneous mean frequency of the synthetic signal in (a). (d) Spectrogram of the signal in (a). The frequency axis shows normalized frequency, with 0.5 representing half the sampling (playback) rate. (e) Spectrogram of the MP-based audified synthetic signal with a time-scale factor of 2. (f) Spectrogram of the IMF-based sonified synthetic signal with a time-scale factor of 2.

(5) Time scaled by a factor of 4 using the MP-based audification method.
(6) Time scaled by a factor of 4 and frequency-scaled by a factor of 2 using the MP-based audification method.
(7) Time scaled by a factor of 4 using the IMF-based sonification method.

G.D.B. was asked to comment on the diagnostic value and

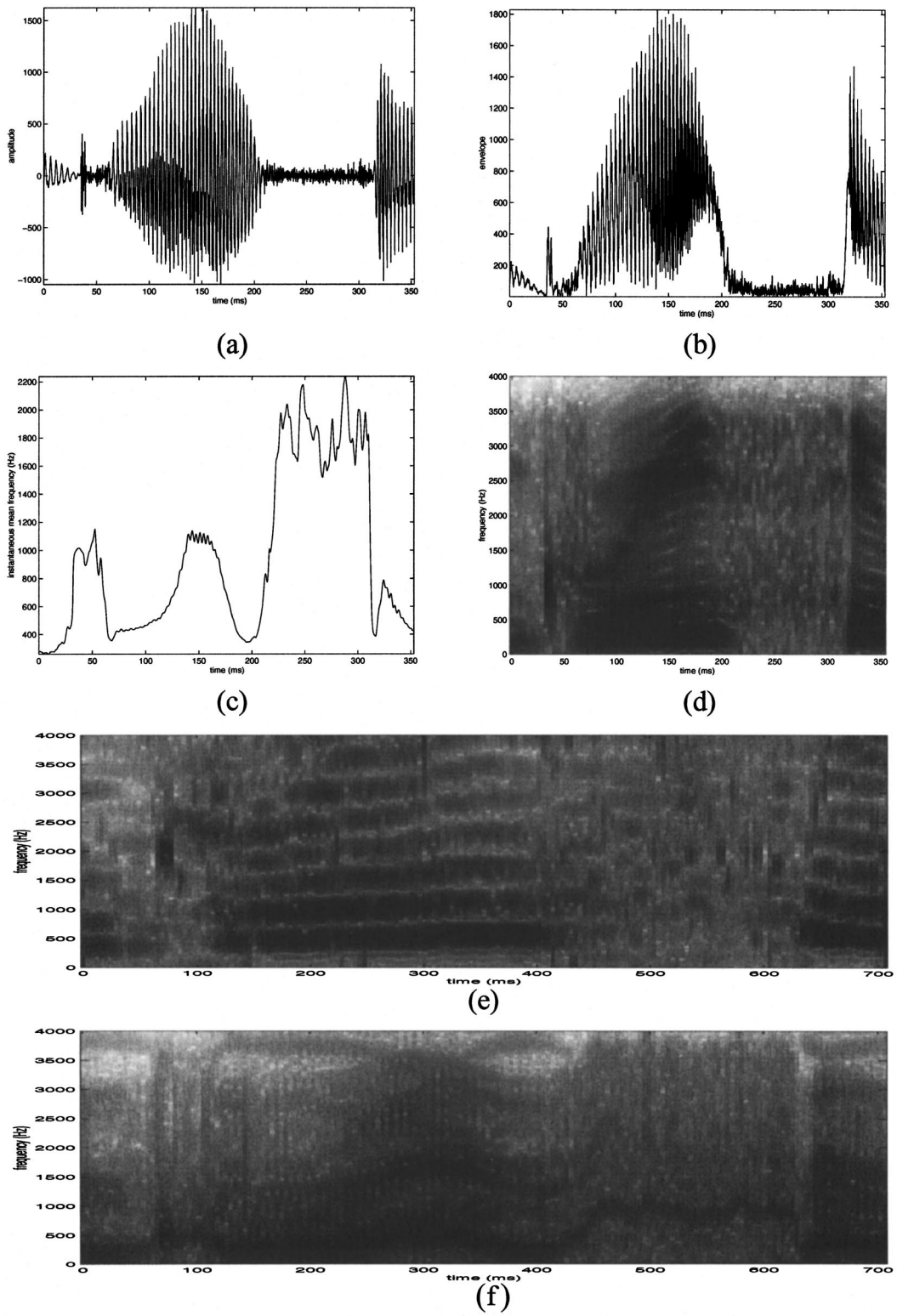

FIG. 4. (a) Speech signal of the word ''greasy'' spoken by a female. [Source-MP software (Ref. 27)]. (b) Envelope of the speech signal in (a) [(Ref. 27)]. (c) IMF of the speech signal in (b) estimated using its OMP TFD. (d) Spectrogram of the speech signal in (a). (e) Spectrogram of the MP-based audified version of the speech signal. A time factor of 2 and a frequency scale factor of 2 were used. (f) Spectrogram of the IMF-based sonified version of the speech signal in (a). A time-scale factor of 2 was used.

the quality of the scaled sounds. The following aural inferences were made by G.D.B.

(1) Direct playback of VAG data obtained via the vibration sensor results in sounds that are similar to those heard through a stethoscope placed at the mid-patella position.
(2) Time scaling helps in better appreciation of click and pop sounds.
(3) Time scaling by a factor of 4 results in sounds that are too long.
(4) Scaling does not preserve the exact aural nature of grind-

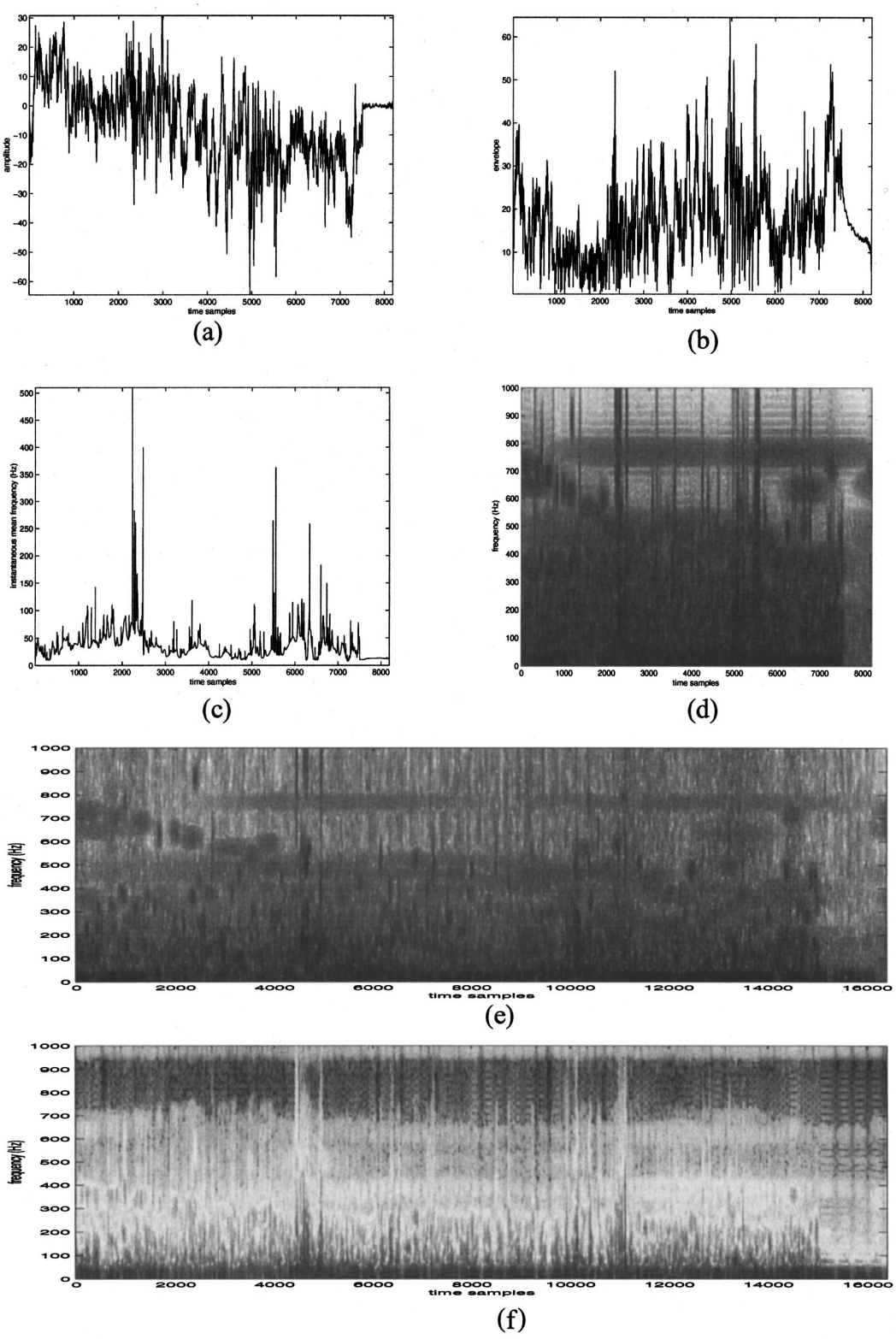

FIG. 5. (a) An abnormal VAG signal of a patient with chondromalacia patella grade II and III. The duration of the signal is 4 s, with the sampling rate being 2 kHz. (b) Envelope of the VAG signal in (a). (c) IMF of the VAG signal in (a) estimated using its TFD. (d) Spectrogram of the VAG signal in (a). (e) Spectrogram of the MP-based audified version of the VAG signal in (a). A time-scale factor of 2 was used. (f) Spectrogram of the IMF-based sonified version of the VAG signal in (a). A time-scale factor of 2 was used.

ing sounds. Time-scaling results in grinding sounds being converted into a series of discrete sounds.

(5) Frequency scaling does not provide appreciable information.

G.D.B. also noted the continuous waterflow background sound with the MP-based audified data. However, the sound being very distinctive, he agreed that it was very likely to be an artifact, and decided to ignore such sounds in further

analysis. Based on the initial selection session with four distinctive VAG signals, G.D.B. suggested two-times time-scaled MP-based audification and two-times time-scaled IMF-based sonification methods as suitable methods for diagnostic purposes with minimal training.

For the sake of illustration, plots of an abnormal VAG signal of a patient with chondromalacia patella grades II and III, and the processed versions of the signal are presented in Fig. 5. Figure 5(a) shows the original VAG signal; the spectrogram of the signal is shown in Fig. 5(d). The spectrograms and related entities of the audified and the sonified versions of the signal are shown in Figs. 5(b), (c), (e), and (f). The spectrogram of the processed versions clearly indicate the effects of time scaling when compared to the original spectrogram shown in Fig. 5(d). The envelope and the IMF of the signal are shown in Figs. 5(b) and (c), respectively. The spectrogram in Fig. 5(f) clearly illustrates the envelope-IMF behavior of the sonified signal.

B. Second stage: Test stage

From the initial evaluation, G.D.B. selected the two-times time-scaled MP-based audification method (henceforth to be called method B) and the two-times time-scaled IMF-based sonification method (method C) for the test (second) stage. The direct-playback sounds (method A) were also presented. The purpose of the classification experiment in the test stage was to determine the diagnostic improvement provided by the processed sounds given by methods B and C as compared to method A. G.D.B. and C.B.F. participated as evaluators of the test stage. The test stage included auditory classification experiments performed with the same database three times; twice by G.D.B. with a time gap of 45 days between the repeat experiments, and once by C.B.F. The details of the test stage are summarized in the following.

(1) The experiment was conducted with 37 VAG signals (19 normals and 18 abnormals). In total, 111 sounds (three sounds for each case corresponding to methods A, B, and C) were presented in random order. No two versions of the same signal were provided consecutively.
(2) The experiment was conducted in a quiet computer laboratory. The sounds were played at the rate of 2 kHz through the Ultrasparc audiotool, and were listened to using a pair of high-quality (Sennheiser HD 470) headphones.
(3) For each sound, the evaluators were asked to provide their diagnosis as normal, abnormal knee, or uncertain, and to note the nature of the sound heard as click, pop, grinding, silent, or uncertain. No information was provided about the patients, the nature of the signals, or the AD method used, and the evaluators did not look at the computer monitor when the sounds were being played. The sounds were replayed when requested, and intervals of 60–120 s were provided between sounds to prevent fatigue.

TABLE I. Schematic representation of a contingency table.

	Method II			
Method I	Normal	Uncertain	Abnormal	Total
Normal	$a(1)$	$b(2)$	$c(3)$	$R1$
Uncertain	$d(4)$	$e(5)$	$f(6)$	$R2$
Abnormal	$g(7)$	$h(8)$	$i(9)$	$R3$
Total	$C1$	$C2$	$C3$	$\cdots$

C. Objective evaluation of diagnostic efficiency

1. McNemar's test of symmetry

In order to evaluate the diagnostic efficiency of the AD methods, McNemar's test of symmetry[37,38] was applied. McNemar's test is based on contingency tables that compare the results of two methods. Contingency analysis uses two sets of tables in the present work, one for the abnormal signals and the other for normal signals, to compare two different analysis techniques. These two tables allow us to evaluate changes in both the ''sensitivity'' (chance of ''catching'' an abnormal knee, true-positive fraction, or percentage of hits) and ''specificity'' (correct labeling of a normal knee, or true-negative fraction) of diagnosis using a new technique. The rows of a table represent the outcomes of one method for reference (in the present study, method A), and the columns represent the outcomes of another method to be evaluated (method B or C). The entries in the table are counts that correspond to particular diagnostic categories, which in the present study are classification of the knee as normal, abnormal, or uncertain.

A schematic representation of a contingency table for McNemar's test for two methods labeled as I and II with three diagnostic categories is presented in Table I. A separate table is prepared for each original category: in the present study we have two contingency tables for each study, one for normal signals and the other for abnormal signals. (The ''uncertain'' category does not apply to the VAG signals in the databases.) The variables *a*, *b*, *c*, *d*, *e*, *f*, *g*, *h*, and *i* denote the counts in each cell, and the numbers in parentheses denote the cell number. $C1$, $C2$, and $C3$ denote the total numbers of

TABLE II. Contingency table for method B (MP-based audification) and method C (IMF-based sonification) vs method A (direct playback) for 18 abnormal signals. The entries are based on the auditory classification performed by G.D.B. and C.B.F. combined over three trials ($18\times3=54$ entries).

	Method B			Method C		
Method A	Normal	Uncertain	Abnormal	Normal	Uncertain	Abnormal
Normal	21	1	13	5	0	30
Uncertain	1	0	1	1	0	1
Abnormal	6	1	10	2	1	14

TABLE III. Sensitivity and specificity of methods A, B, and C (combined over three trials).

Methods	Sensitivity	Specificity	Overall accuracy
Method A	17/54 (31%)	42/57 (74%)	59/111 (53%)
Method B	24/54 (44%)	22/57 (39%)	46/111 (40%)
Method C	45/54 (83%)	18/57 (32%)	63/111 (57%)

counts in the corresponding columns, and $R1$, $R2$, and $R3$ denote the total numbers of counts in the corresponding rows.

Each cell in the contingency table represents a paired outcome: For example, in evaluating the diagnostic efficiency of method II versus method I, with abnormal signals as determined by arthroscopy, cell number 3 will contain the number of signals that G.D.B. or C.B.F. classified as normal by method I but abnormal by method II. The row totals $R1$, $R2$, and $R3$, and the column totals $C1$, $C2$, and $C3$ may be used to determine the sensitivity and specificity of the methods, where sensitivity is defined as the percentage of abnormals classified correctly, and specificity is defined as the number of normals classified correctly. For both the original categories, high values along the main diagonal indicate no significant change in diagnostic performance with method II when compared to method I.

2. Evaluation of sensitivity

In a contingency table for abnormal cases, a high value in the upper-right portion (cell number 3 in Table I) will indicate an improvement in diagnosis (higher sensitivity) with method II as compared to method I. Table II provides the cell counts for the contingency table for method B (MP-based audification) and method C (IMF-based sonification) versus method A (direct playback) for the original category of 18 abnormal signals. The entries are based on the combined scores of two experiments performed by G.D.B. and one experiment by C.B.F. ($18\times3=54$ entries). The high main-diagonal entries in the table for method B indicate that there is no significant improvement as compared to method A as per the evaluators' auditory classification of abnormal signals.

The contingency table for method C (IMF-based sonification) versus method A (direct playback) for the original category of abnormal signals shows a significant improvement with method C as compared to method A: 30 sounds that were called normal with method A were correctly classified as abnormal with method C. From Table II, the sensitivities of methods A, B, and C can be computed, which are listed in Table III.

3. Evaluation of specificity

In evaluating a contingency table for normal signals, method II will show a higher specificity than method I if a large value is found in cell number 7 (see Table I). Table IV provides the contingency table for methods B and C versus method A for the original category of 19 normal signals ($19\times3=57$ entries). Method B has performed worse than method A: The value of 22 in the upper-right-hand corner indicates that method B led to 22 sounds being called abnormal while they were correctly called normal with method A.

From the contingency table for method C versus method A for the original category of normal signals, it is seen that method C has performed worse than method A for normal signals. From Table IV, the specificity of methods A, B, and C can be computed, and are listed in Table III.

4. Comparative analysis of the methods

The sensitivity and specificity of the three methods based on the auditory classification provided by G.D.B. and C.B.F. are tabulated in Table III. In computing the sensitivity and specificity, the ''uncertain'' entries were not considered. For example, the sensitivity of method A was computed as $R3$/(total number of abnormal entries) from the table corresponding to the original category of abnormal signals, whereas the specificity was computed as $R1$/(total number of normal entries) from the table corresponding to the original category of normal signals. The sensitivity of method B or C is given as $C3$/(total number of abnormal entries) from the table for the original category of abnormal signals. The specificity of method B or C is given as $C1$/(total number of normal cases) from the table for the original category of normal signals.

Methods A and B have shown poor sensitivity of 31% and 44%, respectively, but the sensitivity has been substantially improved to 83% with method C. Methods B and C have both shown poor specificity as compared to method A. This indicates that the higher sensitivity of the methods with processed sounds has been gained at the expense of a decrease in specificity. The combined or overall accuracy of method C is not significantly higher than that of method A (see Table III). Regardless, the higher sensitivity may be valuable in a screening application.

McNemar's method can be used to perform detailed statistical analysis of improvement in performance based upon contingency tables as illustrated. The small number of cases in the present study result in low values in the tables that do not permit such analysis.

TABLE IV. Contingency table for methods B and C vs method A for 19 normal signals. The entries are based on the auditory classification performed by G.D.B. and C.B.F. combined over three trials ($19\times3=57$ entries).

	Method B			Method C		
Method A	Normal	Uncertain	Abnormal	Normal	Uncertain	Abnormal
Normal	19	1	22	18	3	21
Uncertain	0	0	1	0	0	1
Abnormal	3	1	10	0	0	14

TABLE V. Post-test evaluation of eight cases by G.D.B. Changes, if made in the third stage of post-test evaluation to the diagnosis made in the second stage, are indicated by the pairs with the → symbol. Legend: CMP—chondromalacia patella (the numbers I, II, III, and IV denote the different clinical grades), N—normal, Ab—abnormal, U—uncertain.

Case No.	Clinical or arthroscopic diagnosis	Auditory classification		
		Method A	Method B	Method C
1	CMP I and II (range 0°→135°), mixture of sounds (range 20°→0°)	N	N	Ab
2	CMP IV (range 0°→135°), grinding sound (range 80°→40°)	N	U	Ab
3	CMP III and IV (range 30°→120°), grinding sound (range 60°→0°)	Ab	Ab	Ab
4	Lateral mensical tear, no sound	N	N	Ab
5	Normal, no sound	N	N	Ab
6	Normal, no sound	N	U	N
7	Normal, grinding sound (50°→0°)	Ab→N	N	Ab→N
8	Normal, click (range 50°→55°)	N	N	N

5. Analysis of d' scores

Although not designed explicitly as a two-choice signal detection experiment (e.g., signal consistency in terms of equal numbers of ''noise'' and ''signal plus noise'' samples, and only ''yes'' or ''no'' responses), the departures from these guidelines in the present study are sufficiently modest to allow the estimation of observer sensitivity (d') in terms of signal detection theory for each of the three listening conditions. d' is defined as the normalized difference between the means of the probability density functions (PDFs) representing ''noise only'' and ''signal plus noise'' stimuli.[39] The normalization factor is the standard deviation of the PDFs (assumed to be equal for the two groups of stimuli). In the present context, the ''signal'' to be detected is an abnormality in a knee-joint sound; background artifacts and sounds related to normal knee-joint surfaces are considered to be ''noise'' that confounds the detectability of the abnormal knee-joint sounds. With the recognition that the experiments were conducted twice by one observer and only once by the other, d' scores were computed in two ways. In one method, the results of the second trial by G.D.B. were ignored, and the results of the first trial by G.D.B. and that of C.B.F. were averaged resulting in d' for methods A, B, and C of 1.19, −0.29, and 0.85, respectively. In the second approach, in order to derive results that could be compared with the sensitivity and specificity analyses described in the preceding sections, both trials of G.D.B. and the single trial of C.B.F. were averaged as though they were provided by three different observers. This approach resulted in d' scores for methods A, B, and C of 1.10, −0.36, and 0.55, respectively. The d' scores suggest trends similar to those shown by the sensitivity and specificity values. Method B (audification) fared poorer than what might be expected by chance, and was the least effective of the three methods. Method A (direct playback) was better than method C (sonification). The higher sensitivity of method C relative to that of method A that was reported in the preceding analysis was lost in the d' calculation due to poor specificity (i.e., a high false-alarm rate). Since no prior experience or response accuracy feedback was provided, it is possible that further training and familiarization could improve both the specificity and d' for sonification.

D. Third stage: Post-test evaluation

Eight VAG signals were selected to perform a post-test evaluation (third-stage) by G.D.B. While performing post-test evaluation, clinical information related to the signals, such as arthroscopy and auscultation reports obtained at the time of original data acquisition, were also provided to G.D.B. Table V shows the diagnosis provided by G.D.B. after listening to the sounds provided by methods A, B, and C. Changes, if made in the third stage of post-test evaluation to the diagnosis made in the second stage, are indicated by the pairs with the → symbol. Cases 1–4 correspond to abnormal knees, and cases 5–8 to normal knees.

The following inferences were made in the post-test evaluation:

(1) Clicks heard using method A were of low intensity.

(2) Grinding sounds were heard as a series of short clicks with methods A and B, but were continuous with method C. With case 3, method C provided a grinding-like sound that covered the full angular range of the pathology as noted during arthroscopy. (It is also worth noting that for case 1—an abnormal knee with low-grade chondromalacia patella—G.D.B. provided the correct classification only with method C.)

(3) G.D.B. correctly classified case 4, which is an abnormal but silent knee, only with method C. He indicated that the sonified signal generated by method C for case 4 had an ''up and down crescendo'' sound. It may be inferred from case 4 that the IMF-based sonification method has successfully provided an auditory display of the main discriminant features of the signal.

(4) In cases 5–8, G.D.B. was successful in correctly classifying the normal silent knees with method A. He noted that in the case of normal and silent knees, method C produces a continuous ''bubbling'' sound. Although G.D.B. could not provide the correct classification for the noisy nor-

mal knee (case 7) with methods A and C in the second stage, he changed his opinion to the correct category during the post-test evaluation stage. It was noted that the audified sound for case 7 had discrete low-intensity clicks with method B.

The subjective and objective findings of auditory analysis of VAG signals suggest that computer-aided auscultation of VAG signals could lead to a potential noninvasive tool for diagnosis of knee-joint cartilage pathology.

VIII. CONCLUSIONS

Novel methods for computer-aided auditory analysis of VAG signals based on audification and sonification techniques were proposed in this paper. The procedures incorporate advanced signal analysis techniques using adaptive time-frequency distributions, instantaneous mean frequency functions, and envelope detection based upon the Hilbert transform. The methods were tested on synthetic signals and speech signals before applying them to VAG signals. The original and the processed sounds were assessed by two orthopedic surgeons to classify them as belonging to normal or abnormal knees. The IMF-based sonification method has shown good potential in improving the sensitivity of auditory analysis of VAG signals. The method needs to be improved to obtain a gain in specificity as well.

The results obtained in the present pilot study on auditory analysis of VAG signals are preliminary. Studies with more cases, more observers, and detailed statistical analysis are required to establish the potential of the methods. Also, in future work, the ''waterflow'' artifact associated with the MP-based audification method has to be prevented or filtered successfully. The IMF-based sonification algorithm may find applications with other non-speech, multicomponent, nonstationary signals.

ACKNOWLEDGMENTS

We gratefully acknowledge support from the Alberta Heritage Foundation for Medical Research and the Natural Sciences and Engineering Research Council of Canada. We thank Dr. Donald W. Kline, Department of Psychology, University of Calgary, for assistance with d' analysis.

APPENDIX

Matching pursuit (MP)[27] is a signal decomposition algorithm that decomposes a given signal using basis functions that have excellent TF properties. The MP algorithm selects the decomposition vectors depending upon the signal's properties. The given signal $x(t)$ is projected onto a dictionary of TF functions obtained by scaling, translating, and modulating a window function $g(t)$:

$$x(t)=\sum_{n=0}^{\infty} a_n g_{\gamma_n}(t), \tag{A1}$$

where

$$g_{\gamma_n}(t)=\frac{1}{\sqrt{s_n}} g\left(\frac{t-p_n}{s_n}\right)\exp[j(2\pi f_n t+\phi_n)], \tag{A2}$$

and a_n are the expansion coefficients. The scale factor s_n is used to control the duration or width of the window function, and the parameter p_n controls temporal placement. $1/\sqrt{s_n}$ is a normalizing factor that restricts the norm of $g_{\gamma_n}(t)$ to 1. The parameters f_n and ϕ_n are the frequency and phase of the exponential function, respectively. γ_n represents the set of parameters (s_n, p_n, f_n, ϕ_n). In the present work, the window is a Gaussian function, i.e., $g(t)=2^{1/4}\exp(-\pi t^2)$; the TF functions are then called Gabor functions.

In practice, the algorithm works as follows. The signal is iteratively projected onto a Gabor function dictionary. The first projection decomposes the signal into two parts:

$$x(t)=\langle x, g_{\gamma_0}\rangle g_{\gamma_0}(t)+R^1 x(t), \tag{A3}$$

where $\langle x, g_{\gamma_0}\rangle$ denotes the inner product (projection) of $x(t)$ with the first TF function $g_{\gamma_0}(t)$. The term $R^1 x(t)$ is the residue after approximating $x(t)$ with $g_{\gamma_0}(t)$. This process is continued by projecting the residue onto the subsequent functions in the dictionary, and after M iterations

$$x(t)=\sum_{n=0}^{M-1} \langle R^n x, g_{\gamma_n}\rangle g_{\gamma_n}(t)+R^M x(t), \tag{A4}$$

with $R^0 x(t)=x(t)$. There are two ways of stopping the iterative process: one is to use a prespecified limiting number M of the TF functions, and the other is to check the energy of the residue $R^M x(t)$. A very high value of M and a zero value for the residual energy will decompose the signal completely at the expense of high computational complexity. In this work, decomposition is stopped after extracting the first M coherent structures of the signal, determined using a decay parameter[27]

$$\lambda(m)=\sqrt{1-\frac{\|R^m x\|^2}{\|R^{m-1}x\|^2}}, \tag{A5}$$

where $\|R^m x\|^2$ denotes the residual energy level at the mth iteration. The decomposition is continued until the decay parameter does not reduce any further. At this stage, the selected components represent the coherent structures and the residue represents the incoherent structures in the signal with respect to the dictionary. The residue may be assumed to be due to random noise, since it does not show any TF localization. The signal reconstructed using the M coherent structures extracted, i.e.,

$$x(t)=\sum_{n=0}^{M-1} \langle R^n x, g_{\gamma_n}\rangle g_{\gamma_n}(t), \tag{A6}$$

provides the MP-denoised version of the original signal.[11,28]

[1] R. A. B. Mollan, G. C. McCullagh, and R. I. Wilson, ''A critical appraisal of auscultation of human joints,'' Clin. Orthop. Relat. Res. **170**, 231–237 (1982).
[2] C. F. Walters, ''The value of joint auscultation,'' Lancet **1**, 920–921 (1929).
[3] M. L. Chu, I. A. Gradisar, and R. Mostardi, ''A noninvasive electroacoustical evaluation technique of cartilage damage in pathological knee joints,'' Med. Biol. Eng. Comput. **16**, 437–442 (1978).
[4] G. F. McCoy, J. D. McCrea, D. E. Beverland, W. G. Kernohan, and R. A. B. Mollan, ''Vibration arthrography as a diagnostic aid in disease of the knee,'' J. Bone Jt. Surg. **69**, 288–293 (1987).

[5] Y. Nagata, ''Joint-sounds in gonoarthrosis—clinical application of phonoarthrography for the knees,'' J. UOEH **10**, 47–58 (1988).
[6] S. Tavathia, R. M. Rangayyan, C. B. Frank, G. D. Bell, K. O. Ladly, and Y. T. Zhang, ''Analysis of knee vibration signals using linear prediction,'' IEEE Trans. Biomed. Eng. **39**, 959–970 (1992).
[7] N. P. Reddy, B. M. Rothschild, M. Mandal, V. Gupta, and S. Suryanarayanan, ''Noninvasive acceleration measurements to characterize knee arthritis and chondromalacia,'' Ann. Biomed. Eng. **23**, 78–84 (1995).
[8] Z. M. K. Moussavi, R. M. Rangayyan, G. D. Bell, C. B. Frank, K. O. Ladly, and Y. T. Zhang, ''Screening of vibroarthrographic signals via adaptive segmentation and linear prediction modeling,'' IEEE Trans. Biomed. Eng. **43**, 15–23 (1996).
[9] S. Krishnan, R. M. Rangayyan, G. D. Bell, C. B. Frank, and K. O. Ladly, ''Adaptive filtering, modelling, and classification of knee joint vibroarthrographic signals for non-invasive diagnosis of articular cartilage pathology,'' Med. Biol. Eng. Comput. **35**, 677–684 (1997).
[10] R. M. Rangayyan, S. Krishnan, G. D. Bell, C. B. Frank, and K. O. Ladly, ''Parametric representation and screening of knee joint vibroarthrographic signals,'' IEEE Trans. Biomed. Eng. **44**, 1068–1074 (1997).
[11] S. Krishnan, R. M. Rangayyan, G. D. Bell, and C. B. Frank, ''Adaptive time-frequency analysis of knee joint vibroarthrographic signals for noninvasive screening of articular cartilage pathology,'' IEEE Trans. Biomed. Eng. **47**, 773–783 (2000).
[12] R. M. Rangayyan, S. Krishnan, G. D. Bell, and C. B. Frank, ''Computer-aided auscultation of knee joint vibration signals,'' in Proceedings of the European Medical and Biological Engineering Conference, Vienna, Austria, November 1999, pp. 464–465.
[13] S. Krishnan, R. M. Rangayyan, G. D. Bell, and C. B. Frank, ''Sonification of knee-joint vibration signals,'' in CDROM Proceedings of World Congress on Medical Physics and Biomedical Engineering, Chicago, IL, July 2000.
[14] G. Kramer, ''An introduction to auditory display,'' in *Auditory Display: Sonification, Audification, and Auditory Interfaces*, edited by G. Kramer (Addison–Wesley, Reading, MA, 1994), pp. 1–77.
[15] C. Hayward, ''Listening to the Earth sing,'' in Ref. 14, pp. 369–404.
[16] X. Zhang, L.-G. Durand, L. Senhadji, H. C. Lee, and J.-L. Coatrieux. ''Analysis-synthesis of the phonocardiogram based on the matching pursuit method,'' IEEE Trans. Biomed. Eng. **45**, 962–971 (1998).
[17] W. T. Fitch and G. Kramer, ''Sonifying the body electric: Superiority of an auditory over a visual display in a complex, multivariate system,'' in Ref. 14, pp. 307–325.
[18] T. F. Quatieri, R. B. Dunn, and T. E. Hanna, ''A subband approach to time-scale expansion of complex acoustic signal,'' IEEE Trans. Speech Audio Process. **3**, 515–519 (1995).
[19] R. M. Rangayyan, A. C. G. Martins, and R. A. Ruschioni, ''Aural analysis of image texture via cepstral filtering and sonification,'' Proc. SPIE **2656**, 283–294 (1996).
[20] A. C. G. Martins, R. M. Rangayyan, L. A. Portela, E. Amaro Jr., and R. A. Ruschioni, ''Auditory display and sonification of textured images,'' in Proceedings of the Third International Conference on Auditory Display, Palo Alto, CA, 1996, pp. 9–11.
[21] A. C. G. Martins and R. M. Rangayyan, ''Experimental evaluation of auditory display and sonification of textured images,'' in Proceedings of the Fourth International Conference on Auditory Display, Palo Alto, CA, 1997, pp. 1–5.
[22] A. C. G. Martins, R. M. Rangayyan, and R. A. Ruschioni, ''Auditory display and sonification of texture in images,'' J. Electron. Imaging **10**, 690–705 (2001).
[23] P. Meijer, ''An experimental system for auditory image representation,'' IEEE Trans. Biomed. Eng. **39**, 112–121 (1992).
[24] D. L. Mansur, M. M. Blattner, and K. L. Joy, ''Sound graphs: A numerical data analysis method for the blind,'' J. Med. Systems **9**, 163–174 (1985).
[25] D. Lunney, R. C. Morrison, M. M. Cetera, R. V. Hartness, R. T. Mills, A. D. Salt, and D. C. Sowell, ''A microcomputer-based laboratory aid for visually impaired students,'' IEEE Micro. 19–31 (Aug. 1983).
[26] D. Malah, ''Time-domain algorithm for harmonic bandwidth reduction and time scaling of speech signals,'' IEEE Trans. Acoust., Speech, Signal Process. **27**, 121–133 (1979).
[27] S. G. Mallat and Z. Zhang, ''Matching pursuit with time-frequency dictionaries,'' IEEE Trans. Signal Process. **41**, 3397–3415 (1993).
[28] S. Krishnan and R. M. Rangayyan, ''Automatic denoising of knee joint vibration signals using adaptive time-frequency representations,'' Med. Biol. Eng. Comput. **38**, 2–8 (2000).
[29] S. Krishnan, ''Adaptive signal processing techniques for analysis of knee joint vibroarthrographic signals,'' Ph.D. dissertation, University of Calgary, Calgary, AB, Canada, June 1999.
[30] L. Cohen and T. Posch, ''Positive time-frequency distribution functions,'' IEEE Trans. Acoust., Speech, Signal Process. **33**, 31–38 (1985).
[31] D. Gabor, ''Theory of communication,'' Proc. IEE **93**, 429–457 (1946).
[32] B. Boashash, ''Estimating and interpreting the instantaneous frequency of a signal. 1. Fundamentals,'' Proc. IEEE **80**, 519–538 (1992).
[33] L. Cohen, ''Time-frequency distributions—A review,'' Proc. IEEE **77**, 941–981 (1989).
[34] P. J. Loughlin and B. Tracer, ''On the amplitude- and frequency-modulation decomposition of signals,'' J. Acoust. Soc. Am. **100**, 1594–1601 (1996).
[35] P. J. Loughlin, ''Comments on the interpretation of instantaneous frequency,'' IEEE Signal Process. Lett. **4**, 123–125 (1997).
[36] L. R. Rabiner and R. W. Schafer. *Digital Processing of Speech Signals* (Prentice–Hall, Englewood Cliffs, NJ, 1978).
[37] J. L. Fleiss, *Statistical Methods for Rates and Proportions*, 2nd ed. (Wiley, New York, 1981).
[38] J. H. Zar, *Biostatistical Analysis*, 2nd ed. (Prentice–Hall, Englewood Cliffs, NJ, 1984).
[39] J. A. Swets, W. P. Tanner Jr., and T. G. Birdsall, ''Decision processes in perception,'' in *Signal Detection and Recognition by Human Observers: Contemporary Readings*, edited by J. A. Swets (Wiley, New York, 1964), pp. 3–57.

Three-dimensional modeling of hearing in *Delphinus delphis*

James L. Aroyan[a)]
JRJ Simulation & Design, 338 Wilkes Circle, Santa Cruz, California 95060

(Received 30 October 2000; revised 17 June 2001; accepted 3 July 2001)

Physical modeling is a fertile approach to investigating sound emission and reception (hearing) in marine mammals. A method for simulation of hearing was developed combining three-dimensional acoustic propagation and extrapolation techniques with a novel approach to modeling the acoustic parameters of mammalian tissues. Models of the forehead and lower jaw tissues of the common dolphin, *Delphinus delphis*, were created in order to simulate the biosonar emission and hearing processes. This paper outlines the methods used in the hearing simulations and offers observations concerning the mechanisms of acoustic reception in this dolphin based on model results. These results include: (1) The left and right mandibular fat bodies were found to channel sound incident from forward directions to the left and right tympanic bulla and to create sharp maxima against the lateral surfaces of each respective bulla; (2) The soft tissues of the lower jaw improved the forward directivity of the simulated receptivity patterns; (3) A focal property of the lower-jaw pan bones appeared to contribute to the creation of distinct forward receptivity peaks for each ear; (4) The reception patterns contained features that may correspond to lateral hearing pathways. A ''fast'' lens mechanism is proposed to explain the focal contribution of the pan bones in this dolphin. Similar techniques may be used to study hearing in other marine mammals. [DOI: 10.1121/1.1401757]

PACS numbers: 43.80.Lb, 43.64.Tk, 02.70.Bf, 02.70.Pt [WA]

I. INTRODUCTION

The auditory systems of cetaceans differ significantly from those of terrestrial mammals. These differences include the absence of external pinnae, the reduction or absence of auricular cartilages and associated musculature, partial or complete occlusion of the meatal tube, a modified tympanic membrane, generally greater variation of basilar-membrane support and width within the cochlea, and increased auditory-nerve fiber diameters and ganglion cell counts (Fraser and Purves, 1960; Norris, 1968; Bullock *et al.*, 1968; McCormick *et al.*, 1970; Ridgway *et al.*, 1974; Fleischer, 1980; Ketten and Wartzok, 1990). In odontocete cetaceans (toothed whales including dolphins and porpoises), additional modifications have occurred in the tissues of the lower jaw and ear complexes that include an excavated and thinned posterior mandible, deposition of fatty tissues, and increased isolation of the tympano–periotic complex containing the middle and inner ears within an extracranial peribullar cavity (Norris, 1964, 1980; Norris and Harvey, 1974; Fleischer, 1980; Varanasi *et al.*, 1982; Morris, 1986; Ketten, 1994, 1998, 2000).

In odontocetes, it is thought that the lower jaw plays an important role in acoustic reception. Chemically distinct fats of lowered density and acoustic velocity fill the mandibular canals of odontocetes and extend back to the tympano–periotic complex.[1] Norris (1964) proposed that, among other pathways, sound may enter the head through the windows of fat that overlie the thinned pan bones of the mandible, propagate through the pan bones, and become guided or channeled back to the ear complexes by the fat bodies. Norris (1968, 1980) also speculated that the angular transmission properties of the pan bones might provide a mechanism for enhancing direction-dependent differences in the received sound field at each ear.

Several experiments with dolphins have confirmed the involvement of the lower jaw in hearing. Norris and Harvey (1974) measured a twofold increase in intensity within the lower-jaw tissues of *T. truncatus* as sound propagated from the anterior to the posterior portion of the right intramandibular fat body. Brill *et al.* (1988) found that a low acoustic attenuation hood placed over the lower jaw of an echolocating bottlenose dolphin had little impact on target discrimination performance, while a high attenuation hood resulted in a significantly lowered performance. Measurements of auditory-evoked potentials have elicited maximum responses for sources positioned over the lower jaw in dolphins (Bullock *et al.*, 1968; McCormick *et al.*, 1970). Although lower-jaw involvement in odontocete hearing now appears to be widely accepted, details of the reception pathways remain less clear. Experimental studies of sound propagation within cetacean head and ear tissues pose complex and difficult challenges for researchers attempting to clarify hearing mechanisms. Alternative approaches are therefore of interest.

The physical reception of sound at the ears of terrestrial mammals is often studied by moving an acoustic source about the head of the animal under anechoic conditions while measuring sound pressure inside the auditory meatus. Equivalent information is gained, however, by reversing the roles of source and receiver in such an experiment. The principle of acoustic reciprocity tells us that the same information would be obtained if we instead place a small source at each ear and then measure the sound field about the head. Fortunately, computers can now handle this task. Aroyan (1996) developed mammalian tissue modeling techniques

[a)]Electronic mail: jaroyan@cruzio.com

and methods for computing underwater sound fields emitted by source and tissue models. Hence, the physical reception of sound at the ears of marine mammals can be modeled.

This article describes the technique and results of simulations of sound propagation from the underwater environment to the ear complexes in the common dolphin, *Delphinus delphis*. A set of observations concerning the mechanisms of hearing in this dolphin is offered based on model results. Questions regarding propagation within the middle-and inner ears are not pursued here, although it is clear that detailed ear models could be embedded within overall head simulations of the type presented to address such questions. Single-frequency head-related transfer function (HRTF) filters for the common dolphin are derivable from the results of this study and could likewise be obtained for other marine mammals from similar studies.

II. MODEL OF THE DOLPHIN HEAD

A. Tissue density and velocity

An approximate technique was used to map the acoustic parameters of mammalian (including delphinid) soft tissues from x-ray CT attenuation data (Aroyan, 1996). This approach generates approximations of the density and velocity distributions within scanned delphinid tissues that agree well with reported measurements (Norris and Harvey, 1974). Because of its apparent simplicity, this technique may be of broad interest to researchers in tissue modeling.[2]

The base data for the current study was an x-ray CT scan of the head of a male (body length = 1.92 m) common dolphin, *Delphinus delphis* (identified as specimen D4 in Cranford *et al.*, 1996). Individual scans consisted of 320×320-pixel transverse images on a 1.5-mm square grid. The spacing between the scan planes varied from 5.0 mm over the rostrum, to 1.5 mm over the narial region, to 3.0 mm over the posterior cranium. For the hearing simulations reported here, the CT data were linearly interpolated along the body axis to planes uniformly spaced 3.0 mm apart to generate a 3.0-mm cubic grid. Figure 1(a) illustrates the skin isosurface of the interpolated tissue data (grid size 149×87×93). The current study assumed this data to be linearly related to x-ray attenuation in Hounsfield units (HU).

Tissue density was modeled using the linear mapping to image (HU) values shown in Fig. 2(a). This model is based on medical bone mineral and soft-tissue density scanning practices (Henson *et al.*, 1987; see the discussion in Aroyan, 1996). Three calibration points confirming this linear mapping were provided by the known density (0.90 g/cc) of the inner melon (Varanasi *et al.*, 1975), the known density (1.18 g/cc) of the Plexiglas specimen registration frame, and the maximum density (roughly 2.7 g/cc) of delphinid periotic bone (Lee *et al.*, 1996). Values below −138 HU were below all soft-tissue structures (except air sacs which were modeled separately). Since it was necessary to map air surrounding the scanned specimen to seawater, all points below −138 HU were mapped to the density of seawater (1.03 g/cc).

Tissue velocity information was obtained by combining the density mapping with a correlation discovered to exist between the density and velocity values reported in literature

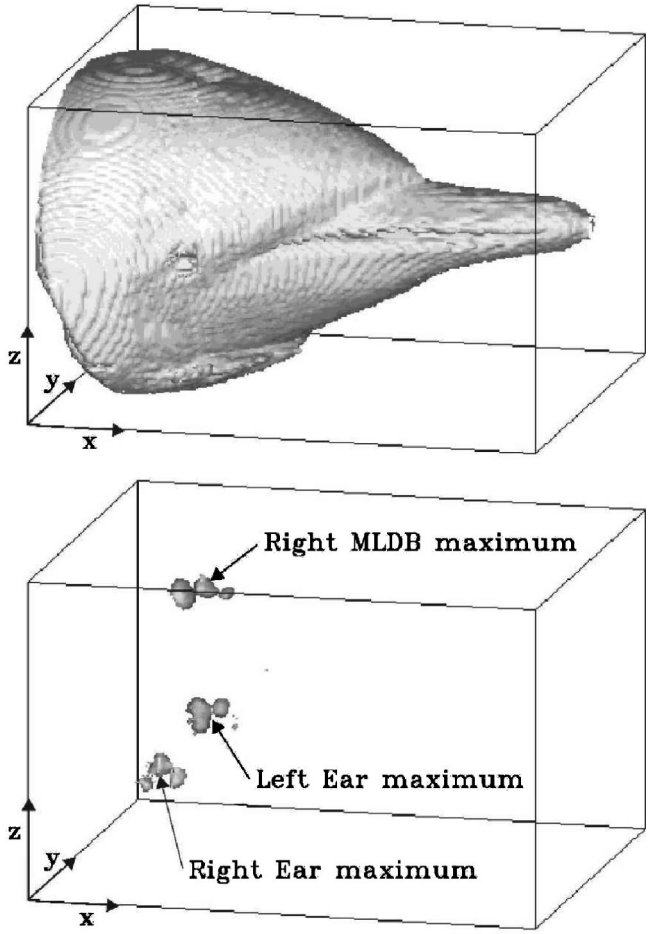

FIG. 1. (a) Visualization of the skin isosurface of the half-resolution full head model (model 3). The rectangular model volume has *x, y, z* side lengths of 44.7 cm, 26.1 cm, and 27.9 cm. (b) Illustration of an isosurface at 30% of the maximum total acoustic energy density W_{total} within the same tissue model volume (and perspective) when the model is ensonified by a 50-kHz sound beam from directly ahead. The locations of the three bright focal maxima that occur within the model are labeled.

sources for various normal fresh terrestrial mammalian soft tissues at 37 °C (Aroyan, 1996). Figure 2(b) plots density and velocity values and approximate ranges for several types of normal fresh terrestrial mammalian soft tissues and delphinid melon and lower-jaw lipids at 37 °C from literature sources (corrected for measurement temperature). The density and velocity error bars for the mammalian tissues in Fig. 2(b) correspond to 1-sigma deviations in reported values; the ranges for delphinid melon lipids correspond to the ranges reported to exist within layered melon tissues (Norris and Harvey, 1974; Varanasi *et al.*, 1975; Litchfield *et al.*, 1979). It is important to note that the velocity of fresh terrestrial mammalian soft tissues is linearly well-correlated with density in the range from normal fat to tendon. This correlation was recently confirmed to hold over the full range of human soft tissues (Mast, 2000), and has significant consequences for acoustic modeling of mammalian tissues and quantitative ultrasonic imaging.

The solid line in Fig. 2(b) indicates the mapping of soft-tissue velocity to density used in the current study. The unique delphinid melon and lower-jaw lipids were incorporated by adding an extension from normal fat down to the

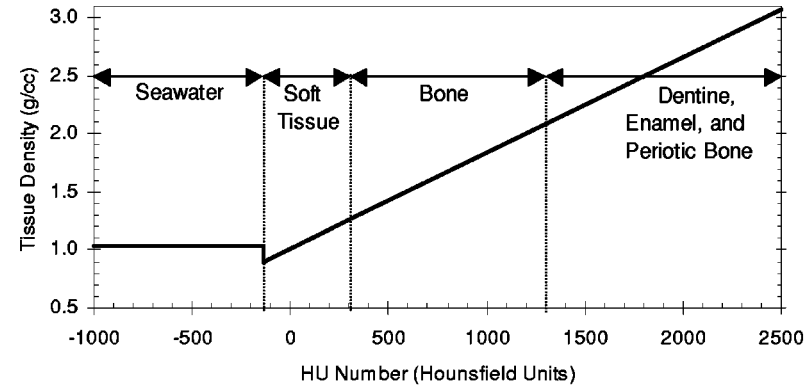

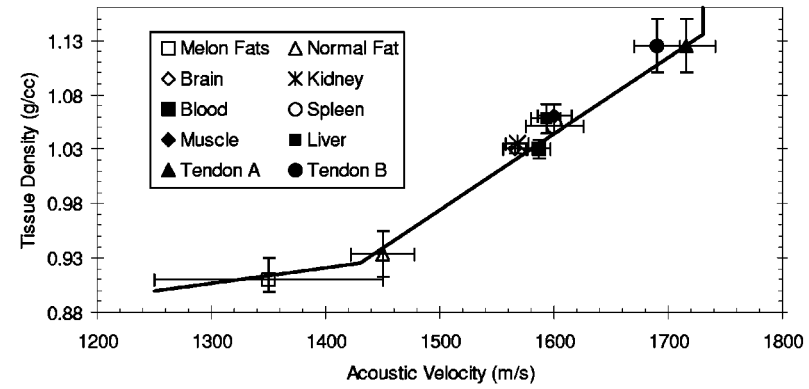

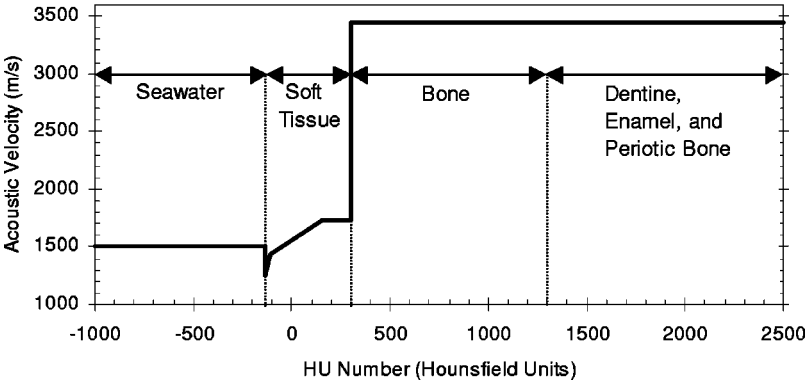

FIG. 2. (a) Plot of the linear mapping from CT values (in Hounsfield units) to tissue density used in the simulations. Tissue types corresponding to mapped CT ranges are indicated. (b) Plot of approximate values of ranges of density and velocity for several types of normal terrestrial mammalian soft tissues and delphinid melon lipids measured at 37 °C. TendonA refers to propagation perpendicular to the tendon fiber bundles. TendonB refers to propagation along the tendon fiber axis. The solid line indicates the piecewise linear mapping of density to velocity used in the simulations over the range of soft tissues. (c) Plot of the mapping from CT values (in Hounsfield units) to tissue velocity used in the simulations.

lower delphinid lipid density and velocity threshold. Given the magnitude of the variations in mammalian soft-tissue densities and velocities, a two-slope linear model was considered satisfactory for the series of simulations reported here. The acoustic phenomena of interest to this study result mainly from relatively short propagation paths (10 wavelengths or less) through fats, muscle, bone, and connective tissue of the lower head. Initial trials tested the effect of varying the piecewise-linear density-to-velocity mapping within limits of the error bars in Fig. 2(b). Because these variations did not produce significantly different emission patterns, tissue velocity was presumed to be modeled adequately by the solid line in Fig. 2(b).

Combining the linear HU-to-density mapping [Fig. 2(a)] with the empirical density-to-velocity mapping [Fig. 2(b)] determines velocity over the soft-tissue range. Figure 2(c) illustrates the HU-to-velocity mapping over the full HU scan range used in the current study. Note that the attenuation range below −138 HU (below all soft-tissue structures except air cavities) was assigned the velocity of seawater (1500 m/s), and that bone velocity for all voxels above the bone threshold at 300 HU was modeled as a constant 3450 m/s. Details of this mapping are discussed in Aroyan (1996) and Aroyan *et al.* (2000).[3]

B. Model of the ears

Definition of an appropriate model for the ears depends to some extent on assumptions regarding the function of the middle and inner ears. The densest portion of the periotic bone of each (left and right) inner ear served as the location of a small extended source (roughly 2 cc in volume) in the hearing receptivity simulations. This source location was chosen because it is assumed to be the cochlear site for each ear (Ketten and Wartzok, 1990). Such an approach assumes a picture of the hearing process in which the cochlea of the inner ears function as point receivers. It is possible that sound transduction in delphinids involves more complex

mechanisms, and alternative theories may suggest different receiver models. It should be emphasized that no attempt was made to resolve details of the propagation of sound from the surrounding bullae into the inner ears—this is clearly impossible without high-resolution ear models. Rather, the strategy adopted here was to utilize a low-resolution model of the tympanic and periotic bones with a constant velocity of 3450 m/s as an approximation for wavelengths of sound larger than the ear complexes. At 50 kHz, the wavelength of sound in bone is approximately 7 cm—roughly twice as large as the tympano–periotic complex in this dolphin. Precisely where one places the sources within the ear bones is therefore not of much consequence in the current simulations.[4]

C. Model of the air sinuses

A simple model of the peribullar cavities (surrounding much of the middle- and inner ears) and the pterygoid sinuses (extending laterally and anteriorly from the ear cavities) was used in the current study. Air sinuses were located in the *Delphinus* CT data by extracting coordinates with values below the soft-tissue threshold, and comparing the results with anatomical studies (Fraser and Purves, 1960). The full head models also included a model of the upper nasal air sacs used in the forehead emission simulations (Aroyan, 1996; Aroyan *et al.*, 2000). As in previously reported simulations (Aroyan, 1990; Aroyan *et al.*, 1992), air spaces were simulated as pressure-release surfaces by setting the pressure to zero inside the spaces. Note that this procedure eliminates any potential air–cavity resonance behavior. Although an urgently important topic for future studies, the question of whether (and under what conditions) air–cavity resonances may affect the hearing process in cetaceans is not pursued here.

III. METHODS

The following approach was used to investigate the hearing process in *D. delphis*. First, 3D acoustical models of the dolphin's head and lower jaw tissues were constructed from x-ray CT data. To provide an initial glimpse into the conduction pathways within the head, propagation of sound from forward directions into the tissue models was then simulated. Next, simulations of far-field emission patterns were conducted by placing sources at the ears in a variety of head models. By acoustic reciprocity, these emitted patterns are equivalent to the hearing receptivity patterns for those specific ear and tissue models. Hearing mechanisms were investigated by visualizing the patterns of sound propagation within the models and by examining the computed emission (receptivity) patterns.

A. Acoustic propagation method

Propagation in tissue models was simulated by numerical integration of the acoustic wave equation. In the current project, all tissues (including bone) were modeled as inhomogeneous fluids, and shear wave modes were ignored.[5] In

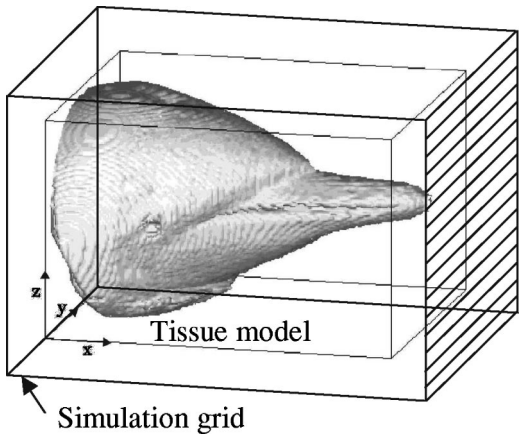

FIG. 3. Simulation grid layout. To visualize acoustic propagation patterns within the models, the front face of the grid (line filled) was used as a source to ensonify the tissue region. To simulate receptivity, the pressure and its normal derivative over a rectangular surface surrounding the ear–source and tissue models were input to an extrapolation program.

fluids of inhomogeneous density and velocity, the linearized wave equation for acoustic pressure p is (Pierce, 1981; Aroyan, 1990)

$$\frac{1}{c^2(\mathbf{x})}\frac{\partial^2 p}{\partial t^2}=\nabla^2 p-\frac{\nabla p\cdot\nabla\rho(\mathbf{x})}{\rho(\mathbf{x})}. \tag{1}$$

Both the sound speed c and density ρ are functions of position $\mathbf{x}$, while the acoustic pressure p is dependent on position and time, $p=p(\mathbf{x},t)$.

A finite-difference time-domain (FDTD) scheme was used to propagate the solution of Eq. (1) forward in time. This scheme was fourth order in the spatial derivatives of pressure, second order in the spatial derivatives of density, and second order in the time derivative of pressure (Aroyan, 1996; Aroyan *et al.*, 2000). Third-order (fourth-degree) Halpern and Trefethen absorbing boundary conditions were applied at the extreme grid edges to reduce reflections from grid boundaries (Aroyan, 1996).

Figure 3 illustrates the simulation grid layout with the tissue model region indicated. In the simulations used to visualize propagation patterns within the head and lower-jaw tissues, the front face of the grid served as a flat (cosine-windowed) source to ensonify the tissue region. In the hearing receptivity simulations, sources were placed within the models (inner ears) and emission patterns were computed as described below.

Several different quantities can be visualized to illustrate the patterns of sound propagation within tissue models. For example, one can visualize the total acoustic energy density W_{total} as the sum of the potential acoustic energy density $W_{\text{potential}}$ and the kinetic acoustic energy density W_{kinetic} (Pierce, 1981; Morse and Ingard, 1968)

$$W_{\text{total}}=W_{\text{potential}}+W_{\text{kinetic}}=\frac{1}{2\rho c^2}[\text{Re}(p)]^2+\frac{\rho}{2}|\text{Re}(\mathbf{u})|^2, \tag{2}$$

where the vector fluid velocity $\mathbf{u}=\nabla p/(i\omega\rho)$. Aroyan (1996) chose to visualize the potential energy density $W_{\text{potential}}$. In this article we visualize either the total or the potential acoustic energy density within the tissue models.

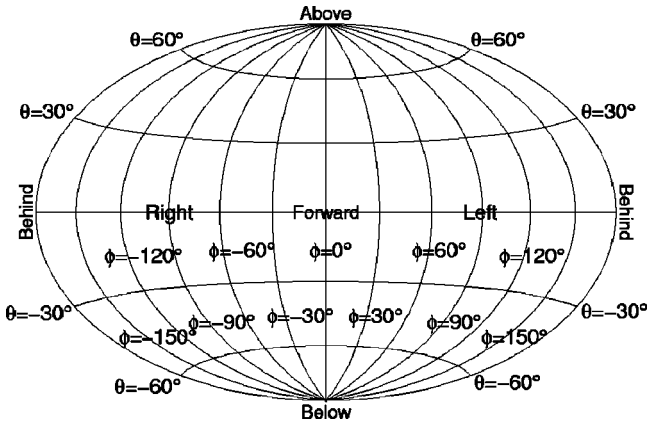

FIG. 4. Global mapping of reception direction angles θ and ϕ.

B. Acoustic extrapolation method

Computer memory limitations prohibit direct propagation of the acoustic fields emitted by the dolphin head models into the far field on 3D grids. A boundary element technique was used instead to obtain acoustic emission patterns. To compute the emission pattern of a source and tissue model, Fourier time transforms of the simulated pressure and its normal derivative over a surface immediately surrounding the tissue region of the grid were input to a far-field extrapolation routine. The transforms were interpolated with complex polynomials over boundary surface elements, allowing a high-order approximation to the extrapolation integral to be computed. The far-field surface integral and other details of this technique are provided in Aroyan (1996).

The receptivity (emission) patterns in this paper were computed for 7200 directions (3-deg increments in both latitude and longitude). The patterns are plotted using a global mapping of direction angles that is diagramed in Fig. 4. Note that vertical angle θ and horizontal angle ϕ are defined as follows: $(\theta,\phi)=(0°,0°)$ corresponds to forward of the receiver, (0°,90°) to left of the receiver, (90°,ϕ) to straight up from the receiver, etc.

IV. RESULTS OF THE SIMULATIONS

A. Visualization of focal locations within the head

To provide an overview of the acoustical properties of the head of the common dolphin, consider the result of ensonifying a full head model with a (cw) 50-kHz sound beam incident from directly forward of the animal. Figure 1(a) illustrates the skin isosurface of this full model that incorporated the skull, soft tissues, upper nasal air sacs, the peribullar cavities surrounding most of the inner ears, and the pterygoid sinuses. The full head model utilized the CT dataset mapped to a 3.0-mm cubic grid.

Figure 1(b) illustrates an isosurface at 30% of the maximum total acoustic energy density W_{total} [Eq. (2)] within the same model volume (and perspective) illustrated in Fig. 1(a). Significantly, three bright focal points occur within the model, each having a roughly funnel-shaped configuration of energy density leading up to it (more clearly visible as the isosurface level is lowered). A funnel occurs within the tissue of the forehead that narrows back to create a bright maximum just below the right monkey lips–dorsal bursae (MLDB) complex (Cranford *et al.*, 1996) within the soft tissue of the nasal complex. This clustering of focal points recurs within a small (roughly 1 cc) volume of the nasal passages over a range of ensonification directions for all frequencies tested and is quite robust with respect to tested variations of the density and velocity model mappings. Because dolphins emit biosonar pulses from their foreheads and rostrums, this focal characteristic of the upper head suggests localization of the biosonar source tissues within a small volume of the right side of the nasal passages. Further results concerning the biosonar emission system of the common dolphin are discussed in Aroyan *et al.* (2000).

Figure 1(b) also illustrates a pair of focal maxima (which narrow to point maxima as the isosurface level is increased) positioned along the anterolateral surfaces of the tympanic bulla of each respective (left and right) ear. It may be noted that the lower-jaw tissues appear to be focusing sound arriving from forward directions onto the ear complexes.

Below, we look more closely at the lower-jaw reception behavior suggested by Fig. 1(b). In order to separate out the effects of various tissue components, the results of hearing simulations using three different head models of the common dolphin will be compared. These models were constructed as follows. Model (1) included the skull, the ear bones, and a simplified upper nasal air sacs model (without peribullar cavities, without pterygoid sinuses, and without soft tissues). Model (2) included the skull, the ear bones, a simplified upper nasal air sacs model, the peribullar cavities, and the pterygoid sinuses (but *without* soft tissues or lower jaw fats). Model (3) included the complete skull, ear bones, air cavities, and soft-tissue model (with the lower-jaw fats). In all models, air spaces within the scanned tissues that were not part of the modeled air sinus and sac systems were effectively ''filled'' with seawater.

B. Visualization of propagation patterns within the lower jaw

We now examine in greater detail the lower-jaw region of the full head results. To provide visual orientation in subsequent figures, Fig. 5 provides three representations of the tissues within a lower portion of the full head model pictured in Fig. 1(a). Consider first the result of ensonifying (full) head model 2 with a 50-kHz sound beam incident from directly forward of the animal. Figures 6(a) and (b) illustrate an isosurface at 13% of the maximum potential energy density $W_{\text{potential}}$ visualized only within the lower head subvolume of Fig. 5 (viewed from the right side and from directly above). Strong reflections are seen in Fig. 6 from forward-facing portions of the rostrum and skull of model 2, with acoustic energy distributed broadly over the entire posterior and ventral skull and ear complexes. Distinct maxima do not appear near the ears.

A dramatic change occurs, however, when the soft tissues (including the lower-jaw fats) are added into the head model. Figure 7 illustrate an isosurface at 13% of the maxi-

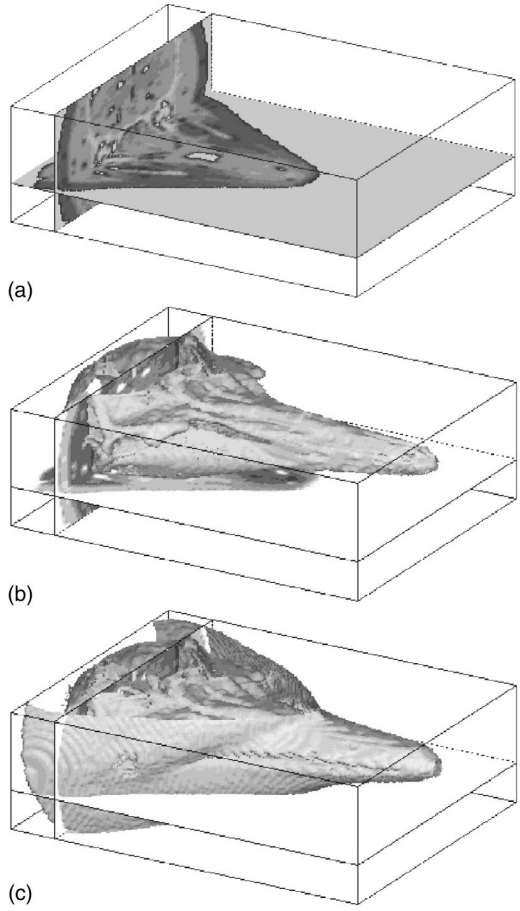

FIG. 5. (a) Tissues within the lower head subvolume illustrated by slice planes. In the horizontal slice, the lower-jaw fats are seen as slightly darker tissue surrounding the pan bones and extending back towards the middle–inner-ear complexes. Parts of the peribullar cavities can be seen around the left and right tympanic bullae (the white structures along the intersection of the two slice planes). (b) Same tissue slice planes with skull isosurface added. (c) Same tissue slice planes with skin and skull isosurfaces added.

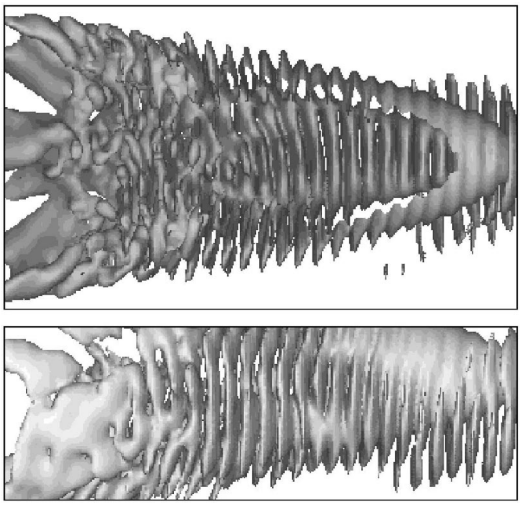

FIG. 6. Visualizations of an isosurface of acoustic energy density within the lower head tissue subvolume resulting from a 50-kHz ensonification of model #2 including the skull, the nasal air sacs, and the peribullar and pterygoid sinuses (but without soft tissue). Top diagram is a view of the lower head subvolume from above. Lower diagram is a view of the lower head subvolume from the right side.

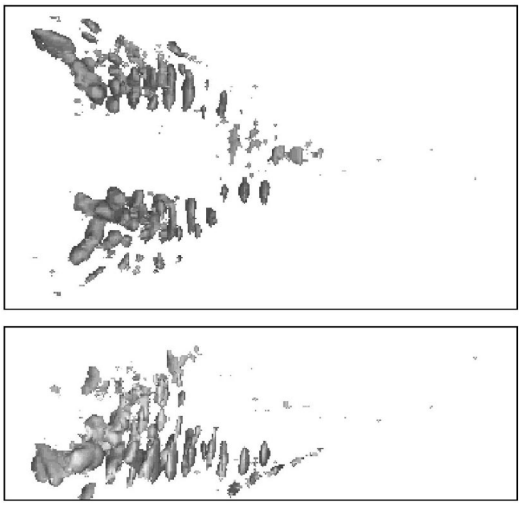

FIG. 7. Visualizations of an isosurface of acoustic energy density within the lower head tissue subvolume resulting from a 50-kHz ensonification of model #3 including the skull, the soft tissues, the nasal air sacs, and the peribullar and pterygoid sinuses. Top diagram is a view of the lower head subvolume from above. Lower diagram is a view of the lower head subvolume from the right side.

mum $W_{\text{potential}}$ visualized within the same lower head volume when model 3 was ensonified with a 50-kHz sound beam from the forward direction. The acoustic energy density now exhibits maxima immediately adjacent of both the left and right bullae [see also Fig. 1(b) at the 30% isosurface level]. Collimation or guiding appears as rough ''funnels'' of energy density passing through and below the pan bones and extending back to the region of the ear complexes. For this direction of return, the right funnel of maximum energy density touches the anterolateral region of the right tympanic bulla, while the left funnel culminates against the anterolateral region of the left tympanic bulla. Waveguiding behavior appears to be occurring within posterior portions of the intramandibular fat bodies, while both collecting and lensing appear to be occurring within anterior portions of the lateral-mandibular fat bodies. Similar maxima and focal structures were also observed in 12.5-, 25-, and 75-kHz simulations (not illustrated here). The intensification process is also evident from contours of energy density within horizontal sections of these data at the level of the ear complexes (Au *et al.*, 1998). These contours increase in roughly conical patterns that begin in the lateral-mandibular fat bodies, continue through (and below) the pan bones into the intramandibular fat bodies, and reach maximum apexes against the left and right bullae. Some incident energy also appears to be reflected laterally off of the pan bones and posterolaterally from the ear complexes themselves.

C. Individual left- and right-ear receptivity patterns

Sound propagation from far-field directions to the ears was simulated by reversing the problem and placing sources at the individual ears. The resulting far-field patterns are equivalent to the coupling between the far-field points (considered as sources) and the ear (considered as a receiver). It should be mentioned that truncation of the scanned specimen below the occipital condyle invalidates some rearward angu-

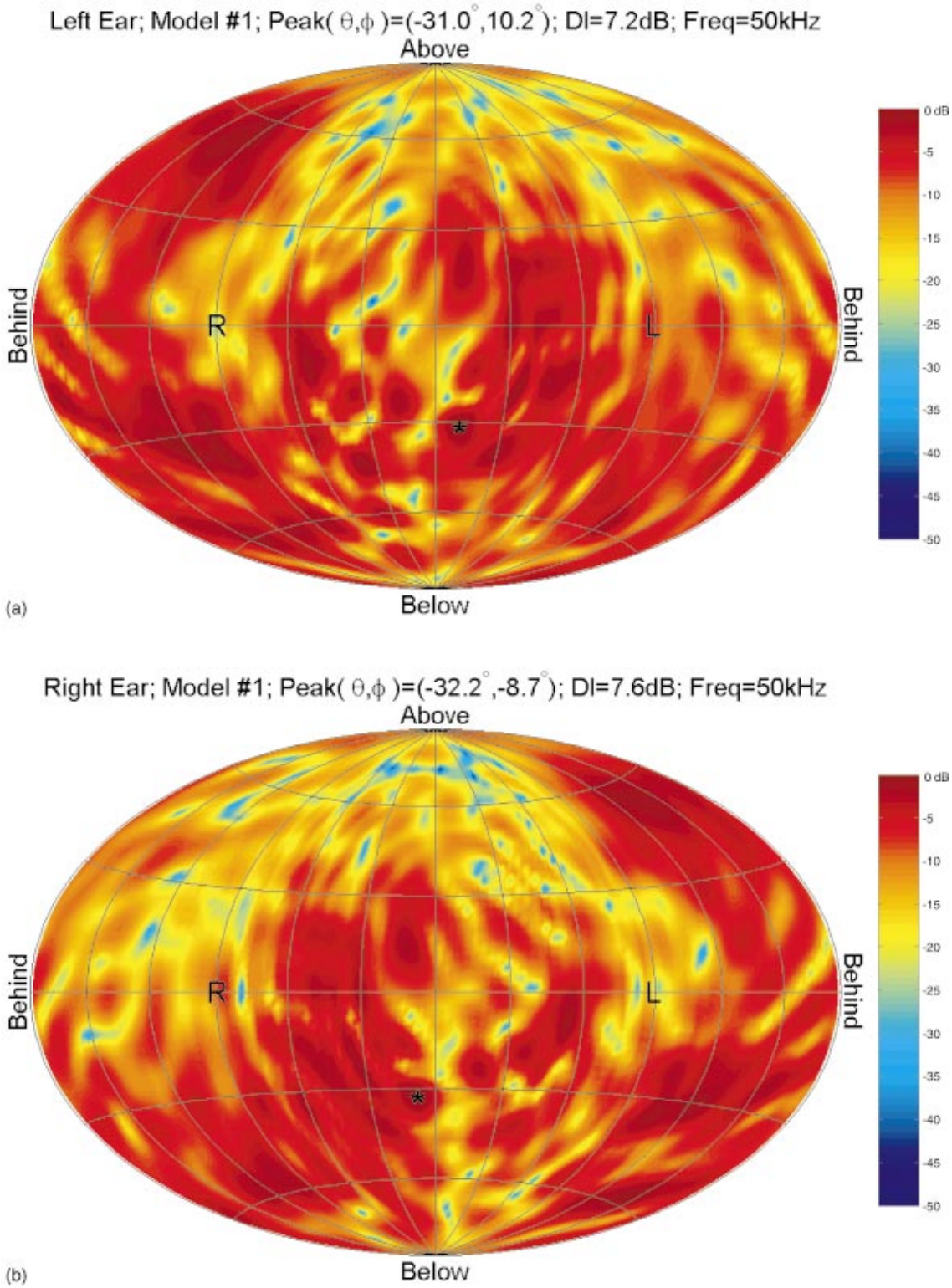

FIG. 8. Decibel maps of simulated far-field receptivity for 50-kHz sources at the inner ears of model #1 including only the skull and the nasal air sacs (without soft tissue and without the peribullar and pterygoid sinuses). (a) Source placed within LEFT inner ear. (b) Source placed within RIGHT inner ear.

lar simulation directions in head model 3 including soft tissues. The invalidated angular region for models 1 and 2 is smaller and caused only by absence of the remainder of the skeleton and air cavities posterior to the skull.

Consider first the receptivity patterns computed for head model 1. Recall that model 1 included the skull and nasal air sacs, but without soft tissues and without the peribullar cavities and pterygoid sinuses. Figure 8(a) illustrates the far-field distribution computed for a cw source of frequency 50 kHz placed within the periotic bone of the left ear. Likewise, Fig. 8(b) illustrates the far-field distribution for a 50-kHz source placed within the right ear. (Figure 4 explains the mapping of reception directions used in these plots.)

The left- and right-ear receptivity patterns in Fig. 8 have little directivity. Energy is spread over downward directions in a rather complex pattern, with an unexpected broad back-

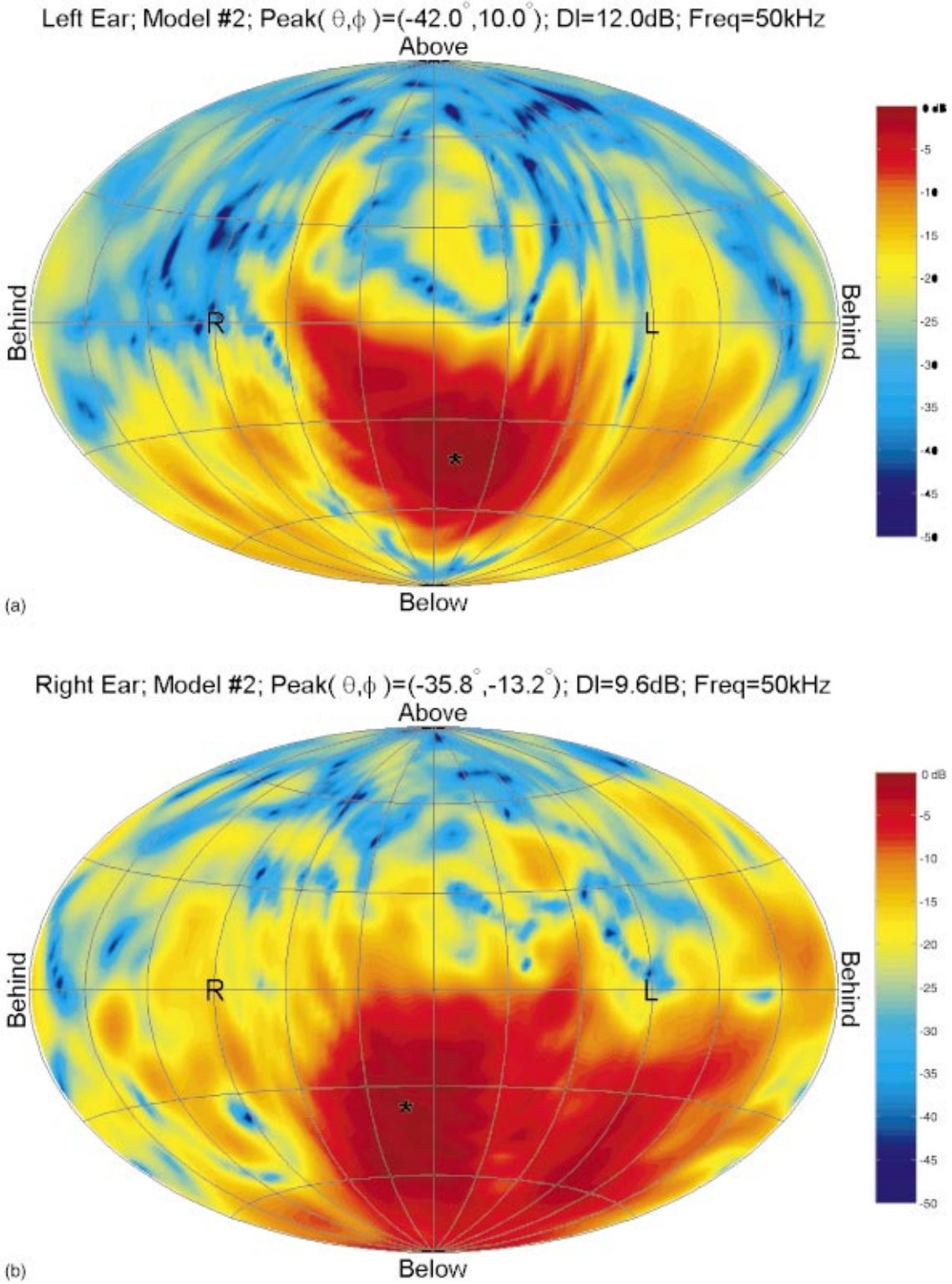

FIG. 9. Decibel maps of simulated far-field receptivity for 50-kHz sources at the inner ears of model #2 including the skull, the nasal air sacs, and the peribullar and pterygoid sinuses (but without soft tissue). (a) Source placed within LEFT inner ear. (b) Source placed within RIGHT inner ear.

ward and upward beam opposite the peribullar concavity of each ear. The sharp pattern peaks (indicated by asterisks) lie roughly 31° below the forward horizon, and occur on the same side as the respective ear. These individual pattern peaks appear to be caused by a previously unrecognized focal effect of sound propagating through the pan bones of the lower jaw. This focal effect will be discussed in the conclusions.

Consider next the effect of adding the peribullar cavities and pterygoid sinuses back into the model. Figure 9 illustrates the left- and right-ear receptivity patterns at 50 kHz for model 2 including the skull, nasal air sacs, peribullar cavities, and pterygoid sinuses, but still *without* soft tissues. Notable shifts have occurred in the patterns, which are now largely directed downward and forward. The peaks for the left and right ears lie quite low (42.0° and 35.8°, respec-

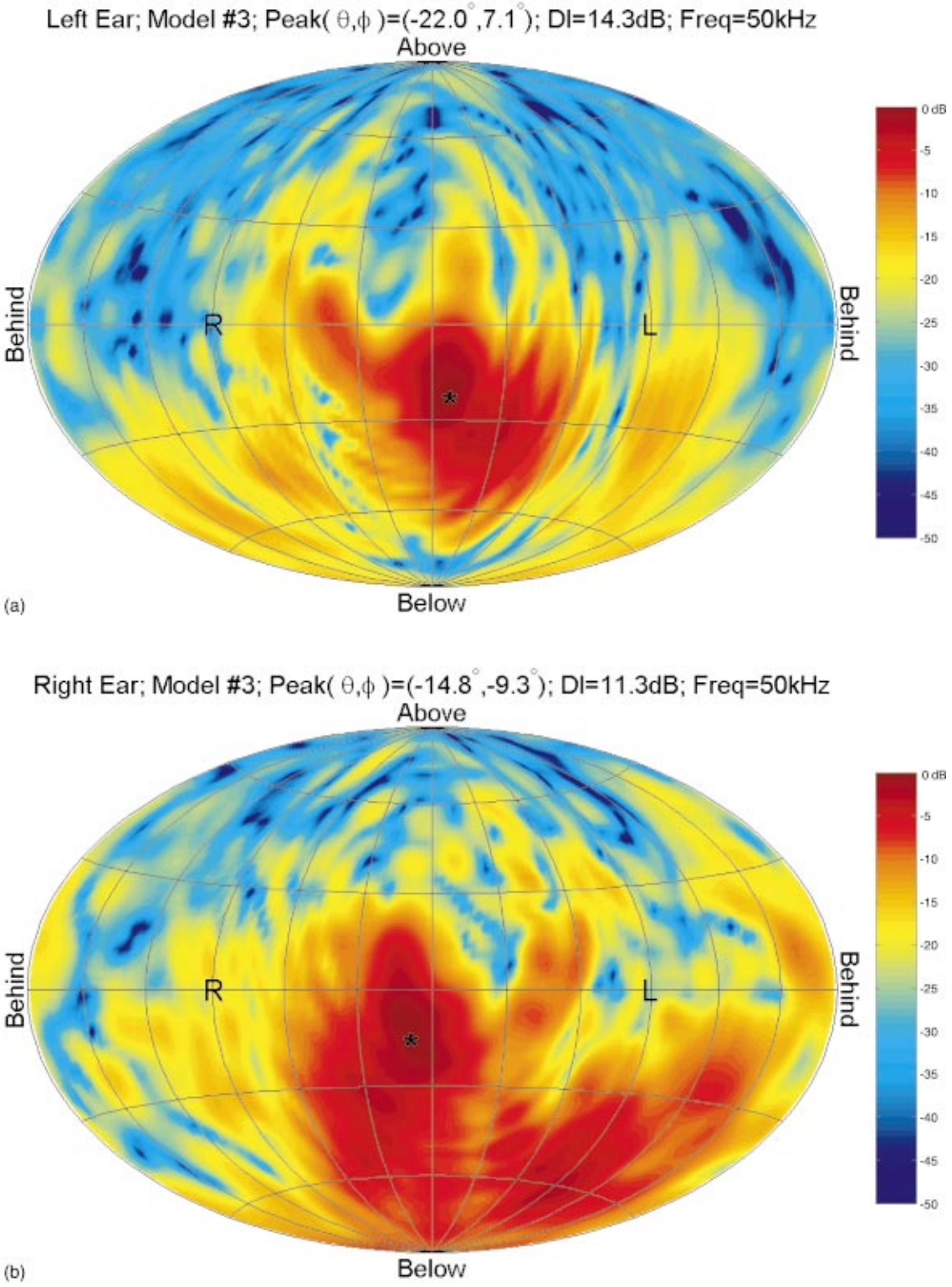

FIG. 10. Decibel maps of simulated far-field receptivity for 50-kHz sources at the inner ears of model #3 including the skull, soft tissue, nasal air sacs, and the peribullar and pterygoid sinuses. (a) Source placed within LEFT inner ear. (b) Source placed within RIGHT inner ear.

tively) below the forward horizon, and again occur on the same side as the ears themselves. In addition, several posterior and ventral lateral minor maxima may be noted.

Adding soft tissues (including the lower-jaw fat bodies) back into the model causes a further dramatic shift in the reception patterns. Figure 10 illustrates the left- and right-ear receptivity patterns at 50 kHz for model 3 containing the skull, soft tissues, nasal air sacs, peribullar and pterygoid sinuses. Note that the reception patterns have become enhanced in the forward direction, with the left- and right-ear peaks raised significantly (now 22.0° and 14.8°, respectively, below the forward horizon). This enhancement appears to be caused by the waveguiding and lensing behavior of the lower-jaw fat bundles. Note also that significant differences

in both elevation and azimuth exist between the left- and right-ear reception patterns. Again, several posterior and ventral lateral minor maxima are evident.

V. DISCUSSION OF RESULTS

The *D. delphis* hearing simulation results hold a rich set of potential implications. A series of observations based on model results is offered below. Possible refinements of the current methods as well as caveats for future applications are noted in conclusion.

As expected, a simple model of the peribullar and pterygoid sinuses was found to contribute significantly to the creation of mainly downward and forward reception patterns by insulating the ears from most other directions of incidence. Acoustic isolation of the tympano–periotic complexes from the skull is thought to be critical to maintaining interaural path differences for underwater sound localization (Dudok van Heel, 1962; Norris, 1968, 1980; Norris and Harvey, 1974; Fleischer, 1980; Oelschlager, 1986).

Directional variations were apparent in all computed receptivity patterns. Clear differences in both elevation and azimuth exist in the left versus right ear 50-kHz receptivity patterns (Fig. 10), and were also found in 12.5-, 25-, and 75-kHz patterns (not illustrated here). Most mammals utilize combinations of acoustical cues arising from intensity, phase, and frequency filtering of sound propagation to the ears to localize sound sources (Heffner and Heffner, 1992; Brown, 1994). Reception patterns that vary with horizontal and vertical angle, frequency, and distance are key to human hearing localization (Weinrich, 1984; Kuhn, 1987). Asymmetric elevation dependencies of the left- and right-ear reception patterns are known to exist in humans, cats, and barn owls (Brown, 1994). Figure 10(b) is in general agreement with the horizontal directional dependence measured experimentally by Norris and Harvey (1974) in mandibular fat near the right-ear complex of a bottlenose dolphin. Horizontal and vertical angular discrimination capabilities have been reported for the bottlenose dolphin (Renaud and Popper, 1975) and for the harbor porpoise (Popper, 1980) equal to or better than human discrimination (in air). The results of the current study suggest that both binaural (interaural intensity and phase) and monaural (frequency spectral) localization cues are available to provide horizontal and vertical directional cues to the ears of the common dolphin. Directional plots of interaural intensity and phase differences are derivable from simulated receptivity data.

Evidence was found of focal behavior resulting from sound propagation through the pan bones of the lower jaw. In order to explain this result, it is proposed that the thinner-at-the-center thickness profile (Norris, 1964, 1968) of the pan bones surrounded by low-velocity fat may act as a ''fast'' lens structure contributing to the creation of distinct forward peaks for each ear. Receptivity peaks on the same side as the ears themselves were obtained in simulated hearing patterns even for head models 1 and 2 (Figs. 8 and 9) in the absence of soft-tissue model components, showing the phenomenon to be distinct from the effect of the lower-jaw fat bodies. It is clear, however, that only an approximation to pan bone propagation can be obtained by simulation on a 3.0-mm cubic grid. As noted below, high-resolution elastic models of the mandible may be required to fully resolve acoustic propagation through the odontocete lower jaw. For this reason, the Appendix provides a supplementary analysis of the expected pan bone focal behavior for compressional waves given the pan bone geometry measured by Norris (1968). This simple analysis yields the same conclusion as the simulation result of a moderate-to-weak pan bone focal contribution to the creation of forward receptivity peaks for each ear.

The surprising differences between the acoustic energy distributions of Fig. 6 and Fig. 7 suggest that the soft tissues of the lower head markedly alter the patterns of sound propagation within the lower jaw. A dual focal structure in the lower jaw became apparent when soft tissues were added into the complete model (model #3). Sound incident below the jaw line from forward directions appears to enter the head of this dolphin in the region of the fat deposits forward of the pan bones, to propagate through (and below) the pan bones of the lower jaw, and to be guided by the left and right mandibular fat bodies back onto the left and right bullae. Isosurfaces of energy density indicate increases in acoustic intensity within the fat bodies of the lower jaw that reached maxima against the antero-lateral surfaces of the left- and right-ear complexes (Au *et al.*, 1998).

A significant fraction of the simulation energy reaching the ears in model #3, however, was found to propagate through portions of the fat bundles that extend below the mandible in *D. delphis*. This suggests that propagation along fatty pathways not passing directly through the pan bones may contribute to hearing from forward directions in this dolphin. Scans of several odontocetes reveal fats extending below the mandible and forward along each side of the lower jaw in addition to the intramandibular fats and the fats overlying the pan bones (Cranford *et al.*, 1996).[6]

The lower-jaw fats also had pronounced effects on the simulated receptivity patterns. Channeling and focusing by the lower-jaw fat bodies appear to enhance the forward receptivity of both left and right ears. Although they differ from measured response patterns, the trends in the simulation results are clear. At 12.5 kHz (results not illustrated), the left- and right-ear reception patterns were broadly distributed (average directivity index 6.2 dB), with vertical peak angles falling well below the horizon (average $-62.5°$), and horizontal peak angles well off the central axis (average 42.5° out from the same side as the respective ear). As frequency increased, the pattern peaks narrowed and rose in angle toward the forward horizon. At 75 kHz (results not illustrated), the left- and right-ear reception patterns were quite narrow (average directivity index 15.8 dB), with vertical peak angles closer to the horizon (average $-17.0°$), and horizontal peak angles approaching the central axis (average 16.2° on the same side as the respective ear). These results are consistent with the proposal that the lower-jaw fats act as forward-facing lenses and waveguides coupling a skull and air sacs (model #2) reception pattern directed more broadly downward and forward. High frequencies may be more strongly guided by the lower-jaw fats; indeed, the focal strength and steering effects of a 2D model of *D. delphis* melon tissue were found to increase with frequency (Aroyan, 1990;-

Aroyan *et al.*, 1992). The overall trend of vertical and horizontal peaks sharpening and converging into the forward direction with increasing frequency also appears consistent with the suggestion of Ketten (1998) that the anterior fat channels may be specialized for ultrasonic sonar signal conduction.

Striking differences, however, exist between the vertical peak angles of these simulated receptivity patterns and peak response angles measured for live animals. The patterns in Fig. 10 are peaked roughly 25–30° lower in vertical angle than the experimentally determined receive pattern of a bottlenose dolphin. Simulated vertical peak angles in *D. delphis* rise with frequency toward the forward horizon, but experimental response patterns for *T. truncatus* were found to be peaked between 5–10° in vertical angle for 30, 60, and 120 kHz (Au and Moore, 1984). Possible explanations for these angular discrepancies include the following:

(i) Real differences exist in the acoustic receptivity patterns of common and bottlenose dolphins.
(ii) The physical receptivity patterns of dolphins are not peaked in the forward direction for all frequencies, and auditory directional filtering is responsible for the forward response peaks measured in live bottlenose dolphins.
(iii) The inner ears may not function exclusively as point receivers as approximated by the model, and hearing response may depend in a complex fashion on sound-field distributions over the tympanic bullae or other structures.
(iv) Pan bone propagation may not be well-modeled by compressional wave algorithms.

It is appropriate here to comment only on the last of these possibilities. While the author believes the current simulations to be capable of resolving lower-jaw soft-tissue propagation up to 75 kHz (5.6 grid points per wavelength at the minimum tissue velocity), detailed studies of propagation through odontocete lower jaw bones may require high-resolution elastic modeling of the mandible.[7] Nevertheless, one might anticipate that elastic wave propagation behaviors involving shear modes are more likely to affect high-frequency results than low-frequency results—yet it is the angles of the low-frequency results that are most puzzling. The significance of the low vertical angles of the simulated reception patterns must be addressed by future research.

A final observation concerns features in the receptivity patterns that may correspond to subsidiary hearing pathways. Inferior and/or posterior lateral local maxima can be seen in Fig. 10 on the same sides as the respective ears, suggesting an increased sensitivity in lateral and inferior directions. Indeed, multiple subsidiary maxima can be identified including inferior and lateral maxima on the sides *opposite* each ear. Similar features can be identified in the receptivity patterns for model #3 at 75 kHz (not illustrated here). While these features appear to fade at 25 kHz and below (not illustrated here), the decibel differences between the sensitivity in lateral directions compared to the forward peak rapidly shrinks with decreasing frequency. Hence, even though no distinct lateral features are apparent at 12.5 kHz, the lateral sensitivity (for both ears) is only about 5 dB below the forward peak. Far-field receptivity is not equivalent to the sensitivity at the ears to sources moved over the head of a dolphin,[8] complicating comparison of simulated patterns with experimentally measured sensitivity distributions (Bullock *et al.*, 1968; McCormick *et al.*, 1970, 1980). Nevertheless, the simulation results appear in qualitative agreement with the response split reported in several studies for frequencies below 20 kHz between the sensitivity to sources at or near the external auditory meatus and sources placed over or near the mandible. This is especially true if energy loss caused by source spreading with distance from the ears is taken into account. Other features of Fig. 10 may correspond to additional pathways, including paths through melon fats of the upper head. Note, however, that soft-tissue channeling may not be the sole mechanism responsible for these subsidiary maxima. For example, lateral features are present in the receptivity patterns computed for model #2 (*without* soft tissues) at 50 kHz (Fig. 9), and are even recognizable in the patterns computed for model #1 (Fig. 8). This suggests that skull (and perhaps air sinus) reflections may be involved in creating lateral maxima. In particular, the locations of the ears within the peribullar concavities of the skull may help to create lateral and downward subsidiary maxima via reflection. It is conceivable that reflections from various skull, lower-jaw, and hyoid bone surfaces may help to provide frequency dependent directional cues, analogous to the cues created by the pinnae in humans. Clearly, further explorations are warranted.

In conclusion, the current investigation has yielded a new approach to simulation of hearing and a series of observations concerning the mechanisms of hearing in one delphinid cetacean. To the extent that the lower-jaw anatomy of the common dolphin is representative of other delphinids, it is reasonable to suggest that the lower jaws of other dolphins may also exhibit strongly directional reception. Indeed, all odontocetes may have evolved similar tissue-borne sound reception channels as an adaptation to a fully aquatic environment (Norris, 1964, 1968, 1980; Norris and Harvey, 1974; Fleischer, 1980; McCormick *et al.*, 1970, 1980; Ketten, 1994, 2000).

The core techniques used to investigate the hearing of *D. delphis* are applicable to a variety of marine mammals. Individual (or combined) right- and left-ear 3D receptivity patterns can be simulated and propagation pathways studied in other species with appropriate modifications of the methods discussed above. To this end, it is perhaps worth mentioning several potential refinements of the current methods and some caveats for future studies. Future applications could incorporate higher resolution scans,[9] scans retaining additional tissue posterior to the skull, and standard phantoms. Spiral x-ray CT techniques may be useful in resolving details of critical tissue interfaces. It should be emphasized that postmortem artifacts are always present to some extent, and careful inspection for artifacts is mandatory whenever a postmortem scan is used as the basis of living tissue models. The importance of using the freshest possible specimens and of minimizing gross-level tissue distortion is obvious. Much work remains in investigating and optimizing acoustic tissue

models based on x-ray CT data. Scanner beam energy and data postprocessing affect details of the acoustic parameter mappings. Mappings may be confirmed and/or supplemented with information from sampled measurements of tissue density and velocity. Participation by collaborating biologists in all aspects of model construction should be mandatory, and high-quality scan data should be made available to all researchers. Refined models of the peribullar and pterygoid sinuses incorporating resonances may permit exploration of mechanisms of interaction with the hearing process under varying conditions of diving and vascular infusion. A number of extensions are also possible from the standpoint of numerical propagation methods. If deemed important, tissue absorption can be incorporated into most propagation codes. Full elastic wave propagation codes are available, and may be useful for investigating thin-bone and inner-ear model propagation. Simulation of pulses rather than continuous wave propagation is also possible; in this case, k-space or pseudospectral propagation algorithms may prove optimal (Wojcik *et al.*, 1997; Mast *et al.*, 2001). Certain studies may benefit from switching to a finite-element spatial grid since it is possible to enforce grid fidelity to the geometry of critical tissue interfaces. Calculation of the acoustic intensity vector $[\mathrm{Re}(-p\mathbf{u})]$ within the tissue models may offer improved visualization of propagation pathways. It is also possible to integrate this vector over cross-sectional tissue areas to quantitatively compare the acoustic energy flux through various structures. This may, for example, be useful in quantifying degrees of waveguiding behavior. The extrapolation integral could be modified for calculation of near fields to obtain the receptivity patterns for nearby sources. As previously mentioned, simulations of the type presented in this paper can be extended to include dynamical models of the middle ears and perhaps also inner-ear models. All of the above possibilities represent exciting opportunities for future research.

ACKNOWLEDGMENTS

The author is indebted to the reviewers of this article, to Joel Kent (Elo TouchSystems, Inc., Fremont, CA), and to Darlene Ketten (Woods Hole Oceanographic Institution) for many insightful comments and suggestions. Thanks are due Ted Cranford for lending the author his CT dataset of a common dolphin, and for allowing visualization of these data in the author's dissertation and two resulting articles. Finally, the current study could not have been completed without the indirect but essential encouragement of Ken Norris (1924–1998). As one might guess, Ken was delighted with the results of this study: ''The jaw stuff, of course, warms my little geriatric heart.''

APPENDIX

This appendix offers an elementary analysis of the pan bone ''fast lens'' focal behavior. The pan bone ''window'' geometry is simplified in order to derive an order of magnitude estimate of focal distance based on the measurements of Norris (1968).

Consider sound propagation through a concave lens. A cylindrical pan bone geometry (oriented along the roughly cylindrical axis of the excavated posterior lower jaw) of radius r and acoustic velocity c_2 is assumed. The thickness is assumed to vary from h at the center to $h+\Delta h$ at the perimeter. Figure A1 diagrams the lens in cross section. Let the velocity of sound in the medium surrounding the lens be c_1. Concave lenses will focus if constructed of materials having sound speed higher than the surrounding medium ($c_2>c_1$). At some focal distance f from the lens, the center and edge rays may add in phase to create a focal point. Assuming lens thickness varies appropriately with radius, all on-axis rays will converge at this focal distance.

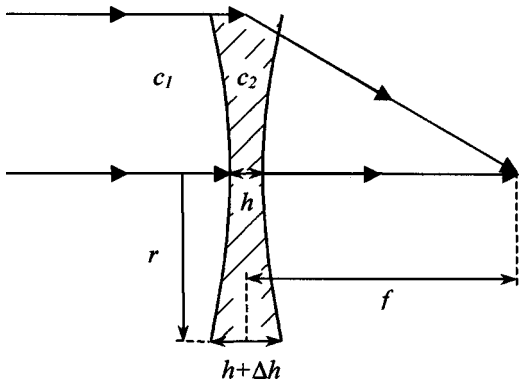

FIG. A1. Cross section of concave cylindrical lens (focusing when sound speed $c_2>c_1$).

For on-axis rays, the focal distance is easily estimated. If Δh is much smaller than radius r, the plane of the lens can be represented as a vertical line in cross section. For $\Delta h \ll r$, requiring the edge and center rays arrive at the focal distance f simultaneously leads to the following formula:

$$f=\frac{c_2^2 r^2-\Delta h^2(c_2-c_1)^2}{2\Delta h c_2(c_2-c_1)}\cong\frac{c_2 r^2}{2\Delta h(c_2-c_1)}. \tag{A1}$$

The effect of off-axis propagation on the focal length can be estimated by constructing an equivalent lens normal to the beam direction. Consider the two lenses shown in Fig. A2. These lenses will have the same focal length if the phase delay is the same for each ray. For simplicity, the case that $h=0$ is shown. Also, we assume the long focal length limit ($f\to\infty$) where beam deflection is negligible in the region of the lens. For parallel rays arriving at an angle θ with respect

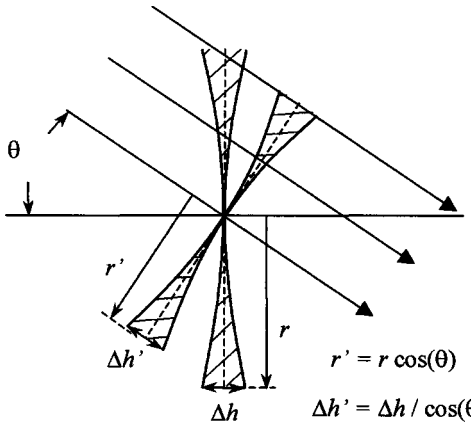

FIG. A2. Equivalent lens (in cross section) for off-axis propagation.

to the axis of the lens, the two lenses are equivalent if $r' = r\cos(\theta)$ and $\Delta h' = \Delta h/\cos(\theta)$. Because $f \propto r^2/\Delta h$, we obtain

$$f' = f\cos^2(\theta) \cong \frac{c_2 r^2 \cos^3(\theta)}{2\Delta h(c_2 - c_1)}, \tag{A2}$$

as an estimate of the modified focal length. Because f is reduced, the focusing power of the lens is increased for off-axis propagation.

Norris (1968) tabulated measurements of pan bone window dimensions and thickness variations for 11 different species of odontocetes. From these data, r is roughly estimated to vary between 2–5 cm, and Δh to be of order 1–2 mm. For compressional wave velocities c_1 and c_2, we estimate $c_1 = 1300$ m/s in the fats surrounding the pan bone, and $c_2 = 3500$ m/s in the compact homogeneous pan bone. Strictly speaking, angle θ corresponds to the angle of sound incidence on the pan bone within the surrounding fats. This angle will vary for different geometries of the water–skin–fat–bone interfaces and for different directions of reception. For sound incident from directly forward of the animal, $\theta = 28°$ is a rough estimate based on the skin surface angle information in Norris (1968) and application of Snell's law through the water–skin–fat interfaces. Because curvature is small over the central areas of the pan bones that were measured, curvature is ignored here.

The above assumptions yield estimates of f [using Eq. (A2)] that vary between 11 and 140 cm. In conjunction with soft-tissue channeling over a total propagation distance within the lower-jaw tissues of roughly 10–20 cm for sound paths passing through the pan bone in midsized delphinids, the pan bone could contribute a moderate-to-weak focusing effect.

[1]Morris (1986) provides a summary of research on the biochemical composition of these fats.

[2]Note that scanning and data treatment methods appropriate for other applications may differ from the methods used in the current investigation.

[3]Tissue absorption was deemed insignificant over the frequency range of interest to this study, and was not incorporated into the current tissue models.

[4]High-resolution middle-ear models (see, for example, Wada *et al.*, 1992) could be embedded within full head models to study detailed aspects of sound propagation within the ear complexes.

[5]Shear modes are heavily damped in soft tissues and thus are expected to have little effect on soft-tissue propagation. Acoustic propagation through the bones of the lower jaw, however, may require shear wave modes for complete solution.

[6]The morphology of these fat bodies deserves clarification along with their acoustic functionality. For example, in one species (*Kogia breviceps*), the fats lying below the lower jaw appear substantially larger in cross-sectional area than the intramandibular fats and the fats overlying the pan bones.

[7]Note, however, that the physical effect of increasing the thickness of a panel of bone-like material submerged in seawater from 1.5 to 3.0 mm lowers compressive sound power transmission at 50 kHz by less than 18 percent at normal incidence (Norris, 1968).

[8]Physical reception at the ears due to sources moved over the skin of the dolphin's head should be influenced by signal type, source directivity and distance from the ear complex, as well as the efficiency of tissue channeling. In-air measurements add the additional distortion of a highly reflective skin–air interface. The receptivity measured using this approach is not the transfer function between the skin surface and the individual ear complexes, nor is it the same thing as the far-field directional receptivity of the ears.

[9]The importance of improved resolution depends on both the properties of the tissues being modeled and the wavelengths simulated. Low-resolution models may be sufficient to model the lower frequency hearing ranges of most noncetacean marine mammal species.

Aroyan, J. L. (**1990**). "Numerical simulation of dolphin echolocation beam formation," M. S. thesis, University of California, Santa Cruz.

Aroyan, J. L. (**1996**). "Three-dimensional numerical simulation of biosonar signal emission and reception in the common dolphin," Ph.D. dissertation, University of California, Santa Cruz.

Aroyan, J. L., Cranford, T. W., Kent, J., and Norris, K. S. (**1992**). "Computer modeling of acoustic beam formation in *Delphinus delphis*," J. Acoust. Soc. Am. **92**, 2539–2545.

Aroyan, J. L., McDonald, M. A., Webb, S. C. Hildebrand, J. A., Clark, D., Laitman, J. T., and Reidenberg, J. S. (**2000**). "Acoustic Models of Sound Production and Propagation," in *Hearing by Whales and Dolphins*, edited by W. W. L Au, A. N. Popper, and R. R. Fay (Springer, New York), pp. 409–469.

Au, W. W. L., and Moore, P. W. B. (**1984**). "Receiving beam patterns and directivity indices of the Atlantic bottlenose dolphin," J. Acoust. Soc. Am. **75**, 255–262.

Au, W. W. L., Mohl, B., Nachtigall, P. E., Pawloski, J., and Aroyan, J. L. (**1998**). "Acoustic pathways of hearing in the bottlenose dolphin, *Tursiops truncatus*," J. Acoust. Soc. Am. **103**, 2908(A).

Brill, R. L., Sevenich, M. L., Sullivan, T. J., Sustman, J. D., and Witt, R. E. (**1988**). "Behavioral evidence for hearing through the lower jaw by an echolocating dolphin (*Tursiops truncatus*)," Marine Mammal Sci. **4**, 223–230.

Brown, C. H. (**1994**). "Sound Localization," in *Springer Handbook of Auditory Research: Comparative Hearing: Mammals*, edited by A. N. Popper (Springer, New York), pp. 57–96.

Bullock, T. H., Grinnell, A. D., Ikezono, E., Kameda, K., Katsuki, Y., Nomoto, M., Sato, O., Suga, N., and Yanagisawa, K. (**1968**). "Electrophysiological studies of central auditory mechanisms in cetaceans," J. Comp. Physiol. **59**, 117–156.

Cranford, T. W., Amundin, M., and Norris, K. S. (**1996**). "Functional morphology and homology in the odontocete nasal complex: Implications for sound generation," J. Morphol. **228**, 223–285.

Dudok van Heel, W. H. (**1962**). "Sound and Cetacea," Netherlands J. Sea Res. **1**, 407–507.

Fleischer, G. (**1980**). "Morphological adaptations of the sound conducting apparatus in echolocating mammals," in *Animal Sonar Systems*, edited by R. G. Busnel and J. R. Fish (Plenum, New York), pp. 895–898.

Fraser, F. C., and Purves, P. E. (**1960**). "Hearing in cetaceans: Evolution of the accessory air sacs and the structure and function of the outer and middle ear in recent cetaceans," Bull. British Mus. (Nat. Hist.), **7**, 1–140.

Heffner, R. S., and Heffner, H. E. (**1992**). "Evolution of sound localization in mammals," in *The Evolutionary Biology of Hearing*, edited by D. B. Webster, R. R. Fay, and A. N. Popper (Springer, New York), pp. 691–715.

Henson, P. W., Ackland, T., and Fox, R. A. (**1987**). "Tissue density measurement using CT scanning," Australas. Phys. Eng. Sci. Med. **10**, 162–166.

Ketten, D. R. (**1994**). "Functional analyses of whale ears: Adaptations for underwater hearing," IEEE Proc. Underwater Acoust. **1**, 264–270.

Ketten, D. R. (**1998**). "Dolphin and bat sonar: Convergence, divergence, or parallelism," 4th International Biosonar Conference 1:43.

Ketten, D. R. (**2000**). "Cetacean ears," in *Hearing by Whales and Dolphins*, edited by R. R. Fay, A. N. Popper, and W. W. L. Au (Springer, New York), pp. 43–108.

Ketten, D. R., and Wartzok, D. (**1990**). "Three-dimensional reconstructions of the dolphin ear," in *Sensory Abilities of Cetaceans: Laboratory and Field Evidence*, edited by J. A. Thomas and R. A. Kastelein (Plenum, New York), pp. 81–91.

Kuhn, G. F. (**1987**). "Physical acoustics and measurements pertaining to directional hearing," in *Directional Hearing*, edited by W. A. Yost and G. Gourevitch (Springer, New York), pp. 3–25.

Lee, S., Hanson, D. B., and Page, E. A. (**1996**). "Some acoustical properties of the otic bones of a fin whale," J. Acoust. Soc. Am. **99**, 2421–2427.

Litchfield, C., Karol, R., Mullen, M. E., Dilger, J. P., and Luthi, B. (**1979**). "Physical factors influencing refraction of the echolocative sound beam in Delphinid Cetaceans," Mar. Biol. (Berlin) **52**, 285–290.

Mast, T. D. (**2000**). "Empirical relationships between acoustic parameters in human soft tissues," ARLO **1**(2), 37–42.

Mast, T. D., Souriau, L. P., Liu, D.-L. D., Tabei, M., Nachman, A. I., and Waag, R. C. (**2001**). ''A *k*-space method for large-scale models of wave propagation in tissue,'' IEEE Trans. Ultrason. Ferroelectr. Freq. Control **48**, 341–354.

McCormick, J. G., Wever, E. G., Palin, J., and Ridgway, S. H. (**1970**). ''Sound conduction in the dolphin ear,'' J. Acoust. Soc. Am. **48**, 1418–1428.

McCormick, J. G., Wever, E. G., Ridgway, S. H., and Palin, J. (**1980**). ''Sound reception in the porpoise as it relates to echolocation,'' in *Animal Sonar Systems*, edited by R. G. Busnel and J. R. Fish (Plenum, New York), pp. 449–467.

Morris, R. (**1986**). ''The acoustic faculty of dolphins,'' in *Research on Dolphins*, edited by M. M. Bryden and R. Harrison (Clarendon, New York), pp. 369–399.

Morse, P. M., and Ingard K. U. (**1968**). *Theoretical Acoustics* (Princeton University Press, Princeton).

Norris, K. S. (**1964**). ''Some problems of echolocation in cetaceans,'' in *Marine Bio-acoustics*, edited by W. N. Tavolga (Pergamon, New York), Vol. 2, pp. 317–336.

Norris, K. S. (**1968**). ''The Evolution of Acoustic Mechanisms in Odontocete Cetaceans,'' in *Evolution and Environment*, edited by E. T. Drake (Yale University Press, New Haven), pp. 297–324.

Norris, K. S. (**1980**). ''Peripheral sound processing in odontocetes,'' in *Animal Sonar Systems*, edited by R. G. Busnel and J. R. Fish (Plenum, New York), pp. 495–509.

Norris, K. S., and Harvey, G. W. (**1974**). ''Sound transmission in the porpoise head,'' J. Acoust. Soc. Am. **56**, 659.

Oelschlager, H. A. (**1986**). ''Comparative morphology and evolution of the otic region in toothed whales (Cetacea: Mammalia),'' Am. J. Anat. **177**, 353–368.

Pierce, A. D. (**1981**). *Acoustics: An Introduction to its Physical Principles and Applications* (McGraw-Hill, New York).

Popper, A. N. (**1980**). ''Sound emission and detection by delphinids,'' in *Cetacean Behavior: Mechanisms and Functions*, edited by L. M. Herman (Wiley, New York), pp. 1–52.

Renaud, D. L., and Popper, A. N. (**1975**). ''Sound localization by the bottlenose porpoise *Tursiops truncatus*,'' J. Exp. Biol. **63**, 569–585.

Ridgway, S. H., McCormick, J. G., and Wever, E. G. (**1974**). ''Surgical approach to the dolphin's ear,'' J. Exp. Zool. **188**, 265–276.

Varanasi, U., Feldman, H. R., and Malins, D. C. (**1975**). ''Molecular basis for formation of lipid sound lens in echolocating cetaceans,'' Nature (London) **255**, 340–343.

Varanasi, U., Markey, D., and Malins, D. C. (**1982**). ''Role of isovaleroyl lipids in channeling of sound in the porpoise melon,'' Chem. Phys. Lipids **31**, 237–244.

Wada, H., Metoki, T., and Kobayashi, T. (**1992**). ''Analysis of dynamic behavior of human middle ear using a finite-element method,'' J. Acoust. Soc. Am. **92**, 3157–3168.

Weinrich, S. (**1984**). ''Sound field calculations around the human head,'' Tech. Rep. 37, The Acoustics Laboratory, Tech. Univ. of Denmark.

Wojcik, B., Fornberg, B., Waag, R. C., Carcione, L., Mould, J., Nikodym, L., and Driscoll, T. (**1997**). ''Pseudospectral methods for large-scale bioacoustic models,'' Proc. IEEE Ultrason. Symp., Vol. 2, pp. 1501–1506.

Numerical analysis of ultrasonic transmission and absorption of oblique plane waves through the human skull

Mark Hayner and Kullervo Hynynen[a)]
Brigham and Women's Hospital/Harvard Medical School, Boston, Massachusetts 02115

(Received 13 December 2000; accepted for publication 6 August 2001)

Ultrasonic transmission and absorption of oblique plane waves through the human skull are analyzed numerically for frequencies ranging from 1/2 to 1 MHz. These frequencies are optimum for noninvasive ultrasound therapy of brain disorders where numerical predictions of skull transmission are used to set the phase and amplitude of source elements in the phased array focusing system. The idealized model of the skull is a three-layer solid with ivory outer and inner layers and a middle marrow layer. Each layer is modeled as a flat, homogeneous, isotropic, linear solid with effective complex wave speeds to account for focused energy losses due to material damping and scattering. The model is used to predict the amplitude and phase of the transmitted wave and volumetric absorption. Results are reported for three different skull thicknesses: 3 mm, 6 mm, and 9 mm. Thickness resonances are observed in the transmitted wave for 3 mm skulls at all frequencies and for the 6 mm skulls below 0.75 MHz. Otherwise, the transmission is dominated by the direct wave. Skull phase errors due to shear waves are shown to minimally degrade the power at the focus for angles of incidence up to 20° from normal even for low material damping. The location of the peak volumetric absorption occurs either in the outer ivory or middle marrow layer and shown to vary due to wave interference. [DOI: 10.1121/1.1410964]

PACS numbers: 43.80.Sh, 43.80.Vj [FD]

I. INTRODUCTION

The feasibility of MRI guided, noninvasive, trans-skull, focused ultrasonic therapy for brain cancer and other disorders has been demonstrated both numerically[1] and experimentally.[2] A schematic of such a system is shown in Fig. 1. An array of source elements with spherical geometry directs ultrasonic energy at a common focus coincident with the tumor. Individual elements are properly phased so that waves add coherently at the focus. Due to the conversion of acoustic energy into heat, the temperature of the tumor increases producing a therapeutic effect.[3] The advantage of ultrasonic therapy is that it may be performed noninvasively without requiring the removal of portions of the skull.

There are two central problems with this type of therapy. The first is skull heating due to direct wave absorption and also due to wave scattering and subsequent absorption. In fact, as we will show here, the skull may absorb nearly all of the incident energy depending on the angle of incidence and its geometric and material properties. By using large solid angle sources (nearly hemi-spherical) to distribute the heat over the largest possible area of the skull, temperature elevations are kept to a minimum. Further improvements may be realized by shading the radiated power from each source element. An optimized system maximizes energy flow through all regions of the skull while maintaining skull temperatures below the maximum allowable value. To ensure that skull temperatures do not exceed an allowable value, a computer model is used to predict the temperature inside the skull based on the outer skull surface temperature, which is monitored during therapy.

The second central problem is phase shifting due to the propagation of focused energy through different regions of the skull (with different thicknesses) by dilational and shear waves. Clement *et al.*[2] demonstrated experimentally that by properly phasing the source elements coherent focused power can be maintained. For noninvasive therapy, the source elements phases are based entirely on computer model predictions of the skull phase shifts.

Wave transmission and absorption through the skull at normal incidence has been studied experimentally by Fry *et al.*,[4] Martin and McElhaney,[5] Smith *et al.*,[6] Goss *et al.*,[7] and Goldman and Hueter.[8] Martin and McElhaney and Fry conducted damping and dilational wave speed measurements on the individual skull layers. Fry compared experimental results with a three-layer numerical model for the skull with an inner and outer ivory layer and a middle marrow layer. The mean properties of the ivory and marrow layers measured by Fry are summarized in Table I. It was Fry who suggested that the optimum frequency range for trans-skull therapy is from $f=0.5$ MHz up to $f=1$ MHz with the lower limit dictated by resolution requirements and the upper by prohibitive absorption in the skull. Fry also showed that scattering from fat and blood inclusions within the bone marrow layer of the skull is significant. Fry's scattering model is based on that developed by Mason and McSkimin,[9] which is based on Rayleigh scattering from individual scatterers.

In this paper, we study wave transmission and absorption at oblique angles of incidence using an idealized numerical transmission model of the skull. Focused ultrasound from the source elements is incident on the skull at oblique angles because the shape of the skull is nonspherical. Previous numerical and experimental studies of skull transmission are limited to normal incidence thus completely ignoring the

a)Electronic mail: kullervo@bush.harvard.edu

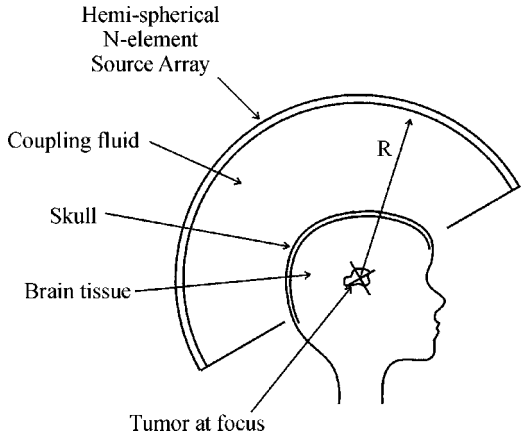

FIG. 1. Schematic of the wide area focused ultrasound system.

role of shear waves and also refraction of both the dilational and shear waves. Our transmission model is based on the full linear elastic equations for a solid and includes the effects of the shear wave as well as multiple reflections within the layered structure of the skull. Because no data on the shear wave speed and attenuation is available, we assume that, nominally, the shear wave speed is half the dilational wave speed and the shear loss factor is equal to the dilational loss factor.

II. TRANSMISSION MODEL

In this section, we describe the calculation of the transmission and absorption of harmonic plane waves through the skull at specified angles of incidence and frequency. For the frequency range considered here, the wavelengths of shear and dilational waves in the skull are roughly an order of magnitude greater than the minimum radius of curvature for a typical skull. On this basis, we assume that the equations of motion of the skull are those for horizontally layered media with no curvature. This assumption is much like modeling a thin cylindrical shell as a flat plate, which is known to be valid when the wavelength of compressional waves are smaller than the radius of curvature (see Junger and Feit, Fig. 7.7 Ref. 10). The angular distribution of incident energy, however, still depends on the skull geometry.

Another assumption is that the different thickness regions of the skull are isolated from one another and that the transmission and absorption can be calculated for each region separately. The thickness regions are isolated because the material damping in the skull is extremely high with loss factors exceeding 1/10. This high damping inhibits waves from reflecting off the surfaces of the skull layers and traveling laterally from one thickness region to another.

TABLE I. Nominal skull properties.

Layer	Outer ivory	Marrow	Inner ivory
Subscript index	3	4	5
Density (kg/m^3)	1900	1700	1900
Dilational speed (m/s)	2900	2500	2900
Shear speed (m/s)	1450	1250	1450
Loss factor, η (–)	0.1542	$0.12+0.12f^3$	0.1985

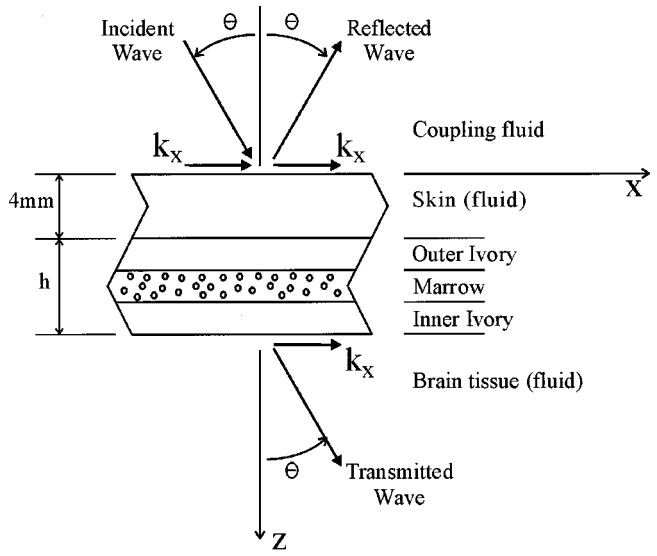

FIG. 2. Schematic of the skull cross-section.

A schematic of the skull cross-section is shown in Fig. 2. The skull is modeled as a six-layer system with the layers numbered from 1 to 6 proceeding from top to bottom. The incident wave propagates in the top coupling fluid layer through an outer skin layer and three layers of skull to the brain tissue. The coupling fluid and the brain tissue are modeled as semi-infinite fluids (water) with density $\rho_1=\rho_6=1000$ kg/m^3 and sound speed $c_1=c_6=1500$ m/s. The skin has thickness $h_2=4$ mm and is modeled as a fluid with density $\rho_2=1116$ kg/m^3, $c_2=1537$ m/s, and loss factor $\eta_2=0.0196$ (see Duck[11]). The layers of the skull are modeled as homogeneous isotropic solids with density ρ_j, dilational speed c_{dj}, dilational wave loss factor η_{dj}, shear speed c_{sj}, and shear wave loss factor η_{sj}, where $j=3,4,5$ corresponds to the outer ivory layer, the middle marrow layer, and the inner ivory layer, respectively. The total skull thickness is designated as h and throughout this paper we assume that the layers of the skull have equal thickness. This assumption is based on measurements by Fry, where the maximum deviation of the layer thickness from the mean layer thickness is within 12% for all six samples with total thickness h ranging from 2.80 mm to 6.10 mm. The assumed nominal properties of the skull are summarized in Table I. Losses are entered into the model by letting the wave speed,

$$c=c(1-i\eta/2). \tag{1}$$

For $\eta \ll 1$, this is consistent with the energy decay of a propagating wave proportional to

$$\exp(-\eta\omega x/c). \tag{2}$$

The densities, dilational wave speeds, and dilational wave loss factors are taken from Fry. The frequency dependent term in η_3 accounts for scattering in the marrow layer with f in megahertz. We assume that the shear speeds for each layer are half the value of the dilational wave speeds and the loss factors are the same. Unless otherwise specified these properties are used throughout this paper.

A brief description of the model is given here. The model is described in greater detail in the Appendix. In ad-

dition to material properties and layer thicknesses, the inputs to the model are frequency and angle of incidence. The outputs are the total phase shift of the transmitted wave across the skull and skin ϕ, the fraction of incident power transmitted TC, the fraction of incident power absorbed AC, and the normalized volumetric absorption α.

Transmission and absorption are calculated in a rectangular coordinate system $\{x,y,z\}$ using the wave-based Finite Element Method or WFEM.[12] WFEM is an essentially exact solution of the governing wave equations for the different media. The fluid layers are governed by a single wave equation. The solid layers of the skull are governed by one dilational wave equation and two shear wave equations.

To solve for ϕ, TC, AC, and α, the approach proceeds as follows. We consider the transmission of a plane wave propagating in the coupling fluid, incident at a given angle θ with the skull surface normal, and oscillating at a fixed frequency ω. Because of the assumed symmetry about the normal z axis, we may consider a wave with a y-axis wavenumber component $k_y=0$ without loss of generality. Due to trace-matching the x-axis components of wavenumber for all the layered media are equal to

$$k_x=\frac{\omega}{c}\sin(\theta), \tag{3}$$

which is the trace wavenumber of the incident wave. This reduces our three-dimensional (3-D) problem to a 1-D problem. We then find the 1-D WFEM stiffness matrix relating interface surface stresses to displacements for the skin and skull layers and then assemble them in a global stiffness matrix using conventional FEM procedures.[13] The WFEM stiffness matrices are formulated in terms of free waves propagating within the layer, which are essentially eigenvalue solutions of the wave equations at fixed ω, k_x, and k_y. The assembly of the global stiffness matrix assumes slip fluid–solid boundary conditions and welded solid–solid boundary conditions. We then solve for the incident, reflected, and transmitted wave amplitudes that satisfy the boundary conditions at the coupling fluid–skin interface and skull–brain tissue interface. If the incident wave has unit amplitude and zero phase at $x=y=z=0$ and we designate A_r as the reflected wave amplitude and A_t as the transmitted wave amplitude, then

$$\phi=\arctan\left(\frac{\mathrm{Im}(A_t)}{\mathrm{Re}(A_t)}\right) \text{ and } \quad AC=1-A_rA_r^*-A_tA_t^*, \tag{4}$$

where the latter relation must hold from the conservation of energy and the superscript * denotes the complex conjugate operation. The normalized volumetric absorption is defined as

$$\alpha=\frac{1}{\Pi_{z=0}}\frac{d\Pi}{dz}, \tag{5}$$

where Π is the z component of power flow at z and $z=0$ is the interface between the coupling fluid and the skin. The power flow is calculated in post-processing by first calculating the stresses and displacements through the thickness of each layer and then using

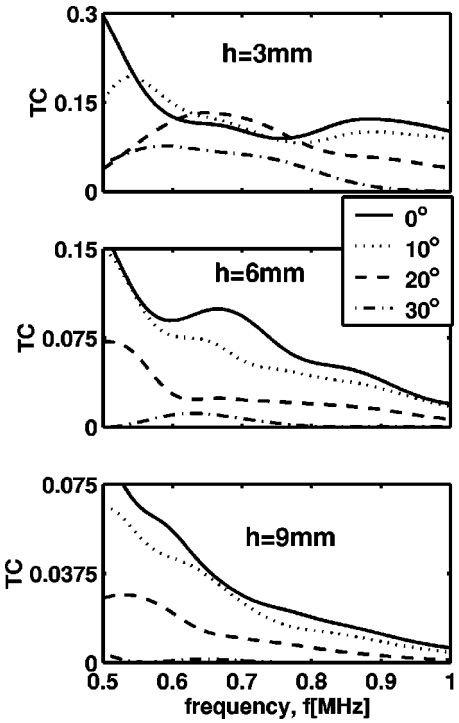

FIG. 3. Power transmission versus frequency.

$$\Pi(z)=-\tfrac{1}{2}\mathrm{Re}(\hat{\sigma}_{xz}(-i\omega\hat{u})^*+\hat{\sigma}_{yz}(-i\omega\hat{v})^* + \hat{\sigma}_{zz}(-i\omega\hat{w})^*), \tag{6}$$

$\hat{u}$, $\hat{v}$, and $\hat{w}$ are the displacements in the x, y, and z directions and $\hat{\sigma}_{xz}$, $\hat{\sigma}_{yz}$, and $\hat{\sigma}_{zz}$, are the surface stresses in the x, y, and z directions. The units for α are meter^{-1}.

III. RESULTS

The numerical results are presented here. We begin with what we will refer to as the nominal case where the properties are those given in Table I with each layer thickness assumed to be equal and the assumed shear speeds in the ivory and bone marrow layers that are half of their respective dilational speeds.

A. Transmission and absorption

The power transmission coefficients, TC, for the nominal case is plotted in Fig. 3 for the frequency range extending from $f=0.5$ MHz to 1 MHz. Transmission is plotted for three different total thicknesses of $h=3$, 6, and 9 mm representing thin, average, and thick regions of a typical adult skull. The transmission and absorption characteristics of skull regions thicker than 9 mm are similar to those for 9 mm. A skin layer of 4 mm thick is also present for all cases. In each of the three subplots there are four curves corresponding to angle of incidence $\theta=0°$, 10°, 20°, and 30°, where the $\theta=0°$ is normal incidence.

For the 9 mm thick skull, the transmission averaged over frequency and at $\theta=0°$, 10°, and 20° is roughly 2.3%. The transmission falls off nearly monotonically with both increased angle of incidence and frequency. This is due to the combination of high damping and thickness, when all but the

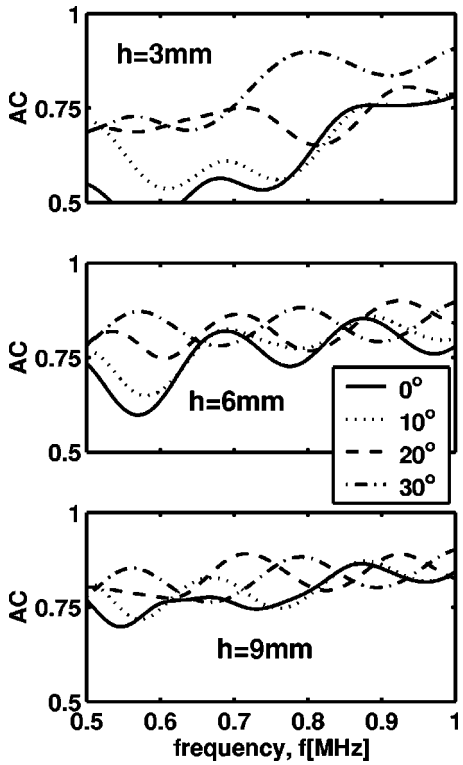

FIG. 4. Power absorption versus frequency.

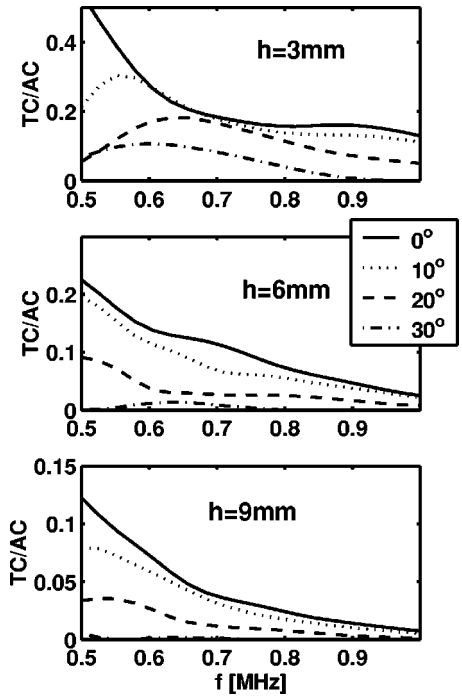

FIG. 5. Gain versus frequency.

direct dilational and shear waves are filtered out by attenuation. As shown in Eq. (2), the exponent of energy decay is proportional to the distance traveled and frequency when the loss factor is a constant. Waves at a higher angle of incidence decay more rapidly due to longer path lengths. There is little difference in the transmission between $\theta=0°$ and 10° indicating that there is little coupling into the shear wave. There is a significant drop (roughly 50%) in transmission between $\theta=10°$ and 20° and an even greater drop between $\theta=20°$ and 30°. Near $f=0.55$ MHz at 20°, a local peak in transmission is evident most likely due to a resonant skull response due to the constructive interference of dilational and shear waves. This is discussed in more detail below. The transmission at 30° is essentially zero.

For the 6 mm thick skull, the averaged transmission is roughly 5.2% or about twice that for the 9 mm skull. The transmission falls off monotonically with an increased angle of incidence but not with frequency. Pronounced local peaks in transmission are seen at $f=0.7$ MHz for $\theta=0°$ and also at $f=0.52$ MHz for $\theta=20°$ due a resonant skull response. There is a significant drop in TC of roughly 50% between $\theta=10°$ and 20°. Transmission at 30° is again nearly zero.

For the 3 mm thick skull, the averaged transmission is roughly 11% or about twice that for the 6 mm skull. Transmission peaks are more pronounced. The transmission is no longer monotonic with either angle or frequency. In fact, at $f=0.7$ MHz, the peak transmission occurs at $\theta=20°$.

The corresponding power absorption coefficients (ACs) are plotted in Fig. 4. Absorption tends to increase with frequency, thickness, and angle of incidence. Fluctuations in the absorption with frequency are due to constructive and destructive wave interference. These fluctuations are more pronounced than that seen in transmission. Fluctuations in AC decrease with increasing thickness but are still present in the 9 mm skull. The frequency averaged absorption coefficients at $\theta=0°$, 10°, and 20° for $h=3$, 6, and 9 mm are 66%, 78%, and 80%, respectively.

There are many strategies that may be employed to optimize the source array design so that the power at the focus is maximized for a given maximum allowable temperature elevation in the skull. One such strategy is to shade the source array such that the gain, defined as $G=TC/AC$, is equal at all points on the skull. The basic idea of such a strategy is to increase transmission through sections of the skull that have high transmission compared to absorption. This strategy would make sense only when the total absorption is proportional to the temperature rise. As shown in Fig. 5, the gain has much the same character as the transmission plotted in Fig. 3 but is generally smoother because peaks in transmission tend to be aligned with peaks in absorption. It is an open question whether this optimization strategy is best because the peak temperature may be more closely related to the local absorption coefficient α rather than the total absorption AC. A detailed thermal model of the skull is needed to answer this question.

The transmission and absorption may be viewed in terms of modes. For high attenuation this is usually not the preferred view but, as seen from the previous results, a mode viewpoint might be appropriate. To discuss the mode viewpoint, we present the AC and TC contour plots for the 6 mm skull in Fig. 6 and Fig. 7, respectively. Overlaid on both plots are the trajectories of the free *in-vacuo* through thickness modes of the skull. These are the loci of points in frequency-angle space ($f-\theta$ space) at which the response of the skull to normal forcing is infinite after damping is set to zero. Mathematically these loci correspond to f–θ pairs at which the

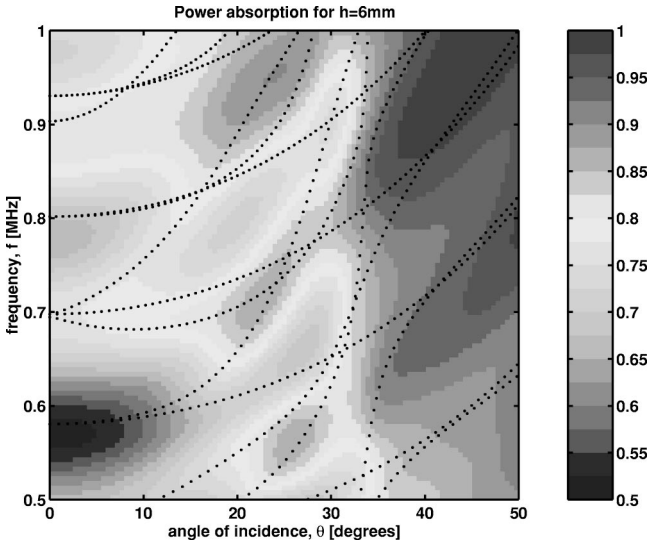

FIG. 6. Power absorption versus frequency and the angle of incidence for $h=6$ mm.

skull stiffness matrix calculated as described in the Appendix is singular. At these through-thickness resonances the impedance of the skull is low and controlled by damping and there is high absorption and possibly high transmission (if the absorption is not too high). The regions of high absorption and transmission are seen to follow the trajectories in $f-\theta$ space especially in regions where trajectories cross or are close to each other. High absorption and transmission is not seen everywhere along the trajectories because the coupling between the acoustic wave and the mode may be poor. At normal incidence, the modes are either pure dilational or pure shear modes, which are totally uncoupled from the fluid. For a homogeneous (single layer skull), the frequency spacing between modes at $\theta=0°$ is uniform but, as shown in the figure, this is not true for layered skulls. Another artifact of the layering is that the trajectories of the resonances may have negative slopes indicating that the off-normal resonance is lower than the normal resonance.

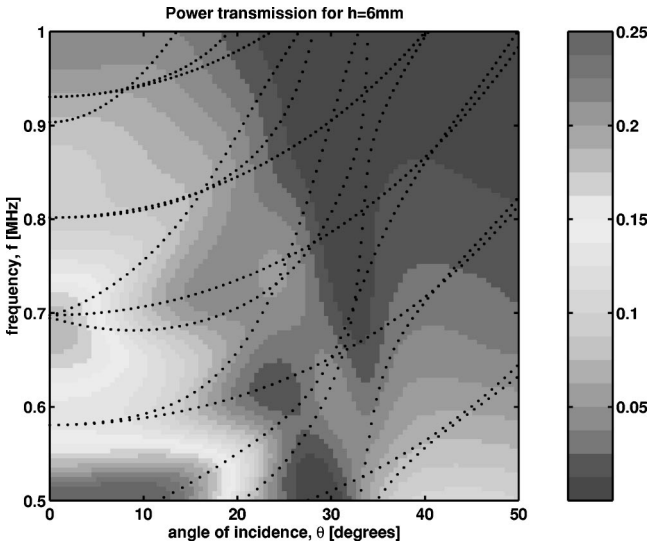

FIG. 7. Power transmission versus frequency and the angle of incidence for $h=6$ mm.

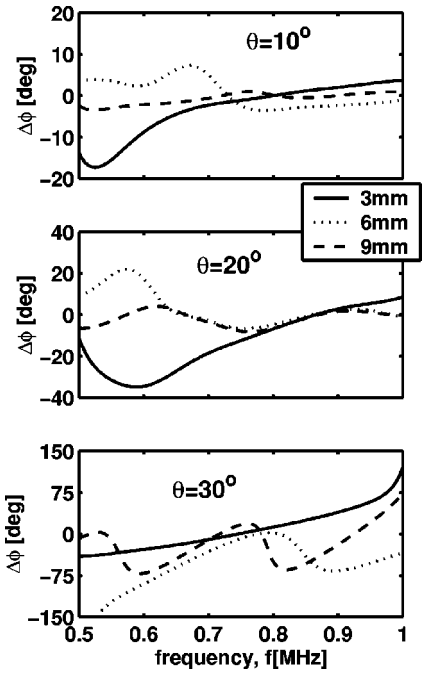

FIG. 8. Phase error $\Delta\phi$ versus frequency.

B. Phase error

For ultrasound therapy to work properly the phase of each element in the source array must be accurately set so that energy from the different source elements arrives at the focus and adds coherently. Phase shifts occur due to propagation through the coupling fluid, skull, and brain tissue. The phase shift due to the skull is the most difficult to predict for a number of reasons including conversion to and from shear waves excited at off-normal angles of incidence.

To demonstrate how the phase depends on the shear speeds in the ivory and marrow layers we run the model at a fixed θ and then run it again with the shear speeds set to zero. The phase error $\Delta\phi$ due to not including shear is then defined by the difference in the phase shifts predicted by the two runs. The results are plotted in Fig. 8 for thickness values of $h=3$, 6, and 9 mm at $\theta=10°$, 20°, and 30°. The error $\Delta\phi$ for $\theta=0°$ is, of course, zero. The results show that the phase error is limited to less than 20° at $\theta=10°$ and less than 40° at $\theta=20°$ for all three thicknesses with the highest phase error towards the lowest frequency. At $\theta=30°$, the maximum phase error approaches 150° for the 3 mm thickness towards 1 MHz, approaches 75° for the 9 mm thickness towards 1 MHz, and exceeds 150° for the 6 mm thickness towards 0.5 MHz.

To get a sense of how accurately the phase must be predicted, the power at the focus of an M element array with equal power radiated from each element may be approximated as

$$\Pi(M,\phi_{\max})=\lim_{N\to\infty}\frac{1}{M^2N}\sum_{n=1}^{N}\left|\sum_{m=1}^{M}\exp(+i\phi_{mn})\right|^2, \quad (7)$$

where the number of realizations N is taken as large, the phase of each source element realization ϕ_{mn} is assumed to fall randomly within the range $-\phi_{\max}<\phi_{mn}<+\phi_{\max}$, and Π

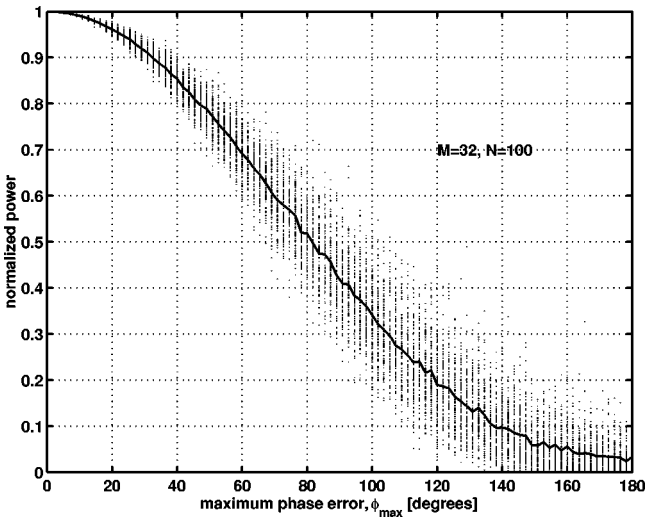

FIG. 9. Normalized power versus the maximum phase error, $\phi_{\max}$.

is normalized such that the $\Pi(M,0)=1$. Using $M=32$ and $N=100$, the power at the focus versus $\phi_{\max}$ is plotted in Fig. 9 (along with each realization). Assuming $\phi_{\max}=40°$, which is the worst case $\Delta\phi$ at $\theta=10°$ and 20°, the reduction in power is less than 20%. Assuming $\phi_{\max}=75°$, which is a typical value for $\Delta\phi$ at $\theta=30°$, the reduction in power is about 50%.

C. Volumetric absorption, α

While the total absorption is an important quantity, it may or may not be directly proportional to the temperature rise in the skull depending on the spatial distribution of energy absorption and how that energy is removed by some combination of conduction, perfusion, and convection. In fact, it may be that the temperature is proportional to the local energy dissipation or the total dissipation within an individual skull layer.

To see how energy is locally dissipated in the skull, we plot the volumetric absorption versus the thickness coordinate z in Fig. 10 for the three skull thicknesses and at 0.5 and

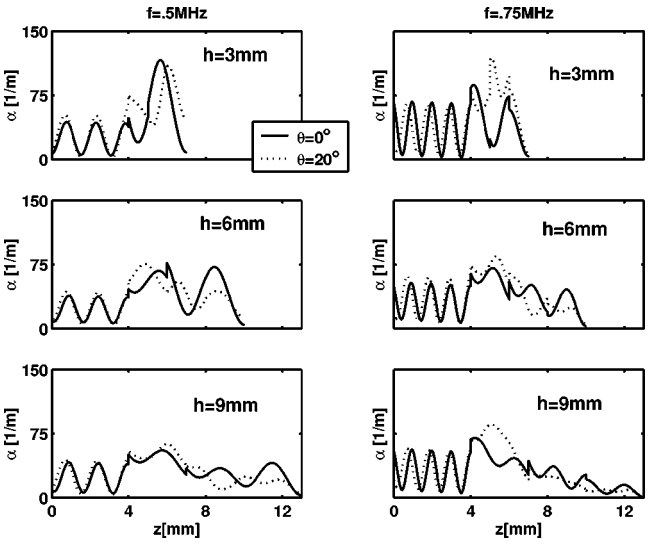

FIG. 10. Volumetric absorption versus the z-coordinate position.

TABLE II. Low ivory loss factor.

Layer	Outer ivory	Marrow	Inner ivory
Subscript index	3	4	5
Low ivory loss factor, η (–)	0.1542/3	$2(0.12+0.12f^3)$	0.1985/3

0.75 MHz and at $\theta=0°$ and 20°. In calculating these results, we assume that the angular distribution of incident power normal to the skull surface falls off slowly as $\cos\theta$. We also assume that scattered energy is immediately converted into heat, which is an idealization of a complicated process involving initial scattering, absorption due to material damping, rescattering due to neighboring inclusions, reflection, and transmission from layer interfaces. We expect that most of the scattered energy is locally dissipated because material damping is so high.

The peaks and valleys shown in Fig. 10 clearly show that wave interference is an important factor in determining how energy is distributed through the skull. Moreover, the distribution is a function of angle of incidence most likely due to shear wave excitation. The thinner the skull, the higher the maximum volumetric absorption. For instance, $\alpha=115/m$ in the 3 mm skull at $f=0.5$ MHz, $\theta=0°$, and $z=5.65$ mm, which is more than double $\alpha=53/m$ in the 9 mm skull at $f=0.5$ MHz, $\theta=0°$, and $z=5.77$ mm. For the 9 mm skull, the maximum occurs in the outer ivory layer (between 4 mm and 7 mm) at both frequencies. For the 6 mm skull, the maximum also occurs in the outer ivory layer (between 4 mm and 6 mm) at both frequencies. For the 3 mm skull, the maximum occurs in the middle marrow layer (between 5 mm and 6 mm) at both frequencies. In all cases, the exact location of the maximum is a function of both frequency and θ.

D. Low ivory damping

Fry's own reflection loss measurements (see Fry's Fig. 4 for skull sample No. 6) indicate that the ivory loss factors are substantially lower than the values reported elsewhere in the same paper. It is interesting that in Fry's transmission model the ivory loss factor is set to $\eta=0.01$. To see how a lower ivory loss factor alters the results, we re-run our model using the values specified in Table II. These values are based on our own calibration with Fry's Fig. 4 results for transmission and reflection at normal incidence. Note that the marrow loss factor is doubled to match the transmission results. Shear and dilational wave loss factors are again assumed to be equal.

Using the low ivory and high marrow loss factors given in Table II, TC, $\Delta\phi$, and α are recalculated. As shown in Fig. 11, the TC for the low ivory loss factors are somewhat higher than for the nominal results but not much changed in character. As shown in Fig. 12, the phase error for $\theta=10°$ and 20° is also somewhat higher but also not much changed in character. The phase error for $\theta=30°$ is again high but with a completely different frequency dependence. As shown in Fig. 13, however, the volumetric absorption is completely altered. Nearly all the energy is absorbed in the marrow layer for all three thicknesses and at both frequencies. The maximum absorption occurs towards the outer surface for the 6

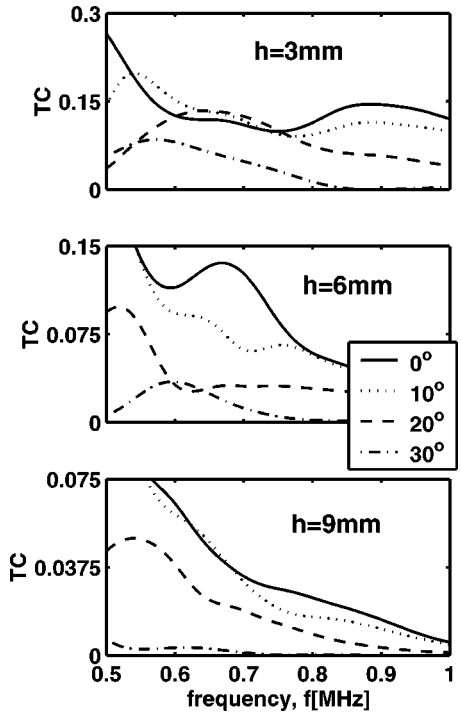

FIG. 11. Power transmission versus frequency for low ivory damping.

mm and 9 mm skull at both frequencies but is variable for the 3 mm skull depending both on θ and frequency.

E. Variation in Poisson's ratio

For the nominal case, we assumed that the shear speeds of the ivory and the marrow layers are half their respective dilational speeds, that is, $c_s = c_d/2$ corresponding to a Poisson's ration $\nu = 0.33$. To see how the results are sensitive to this assumption, we recalculate TC and $\Delta\phi$ using low shear speeds set to $c_s = c_d/4$ corresponding to a Poisson's ratio of about $\nu = 0.45$ and high shear speeds set to $c_s = c_d/1.56$ corresponding to a Poisson's ratio of about $\nu = 0.15$. All other properties are set to the nominal values given in Table I.

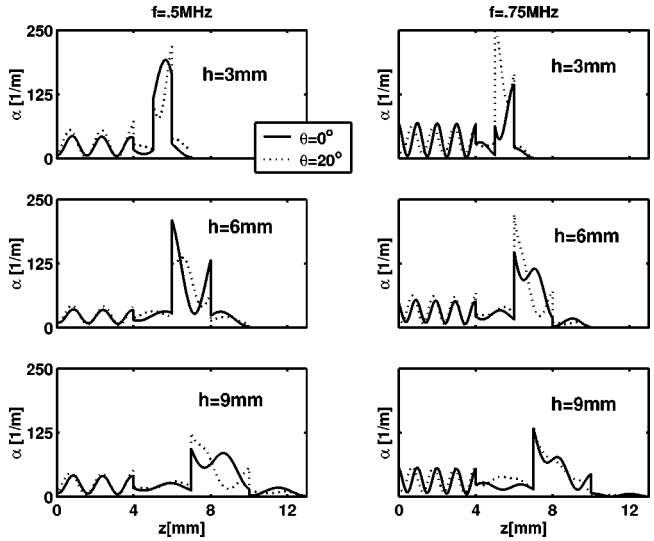

FIG. 13. Volumetric absorption versus the z-coordinate position for low ivory damping.

The transmission for low shear, plotted in Fig. 14, may be compared to Fig. 3. Above 0.75 MHz, there is very little difference in the transmission. There are significant differences in transmission particularly for the 3 mm skull at 0.5 MHz, where the transmission is nearly doubled for $\theta = 10°$ and nearly tripled for $\theta = 20°$. These results indicate that for nominal to low shear speeds the shear wave only plays a significant role at the lower frequencies and for the thinner skulls. The transmission for high shear, plotted in Fig. 15,

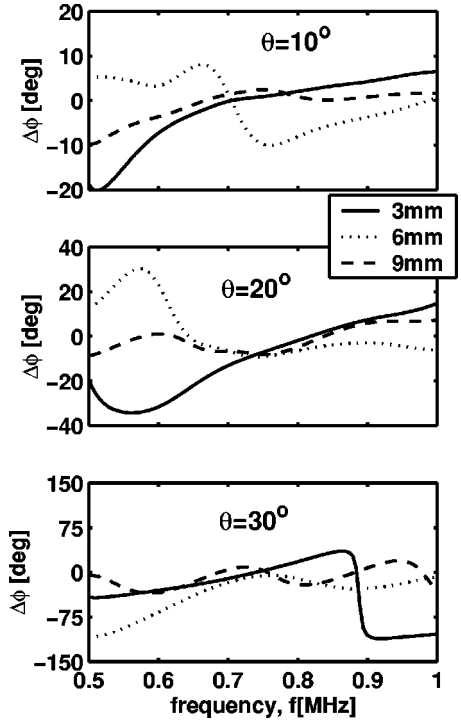

FIG. 12. Phase error $\Delta\phi$ versus frequency for low ivory damping.

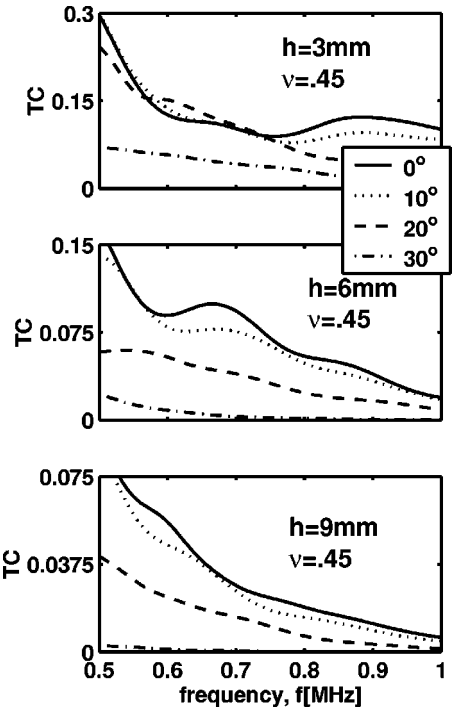

FIG. 14. Power transmission versus frequency for low shear speed.

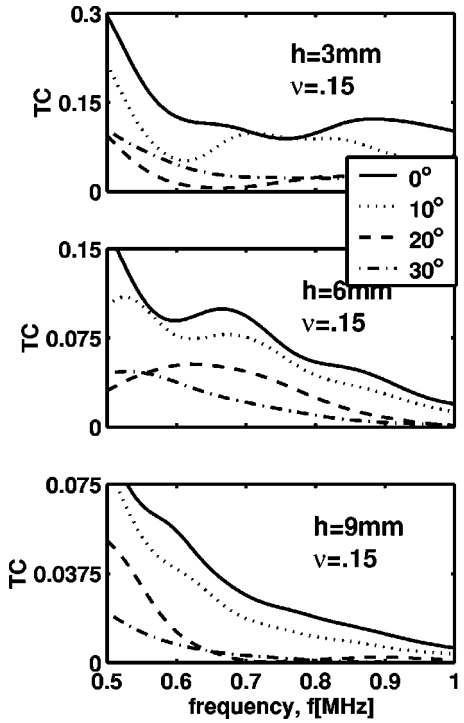

FIG. 15. Power transmission versus frequency for high shear speed.

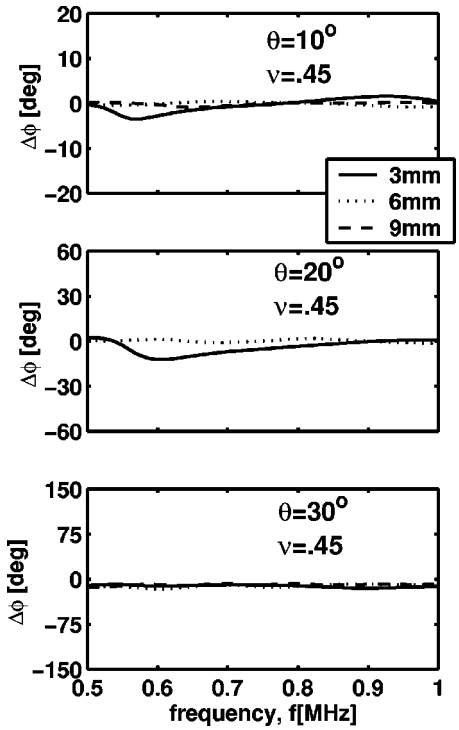

FIG. 16. Phase error $\Delta\phi$ (degrees) versus frequency for low shear speed.

may also be compared to Fig. 3. For high shear speeds the transmission is quite different particularly for the 3 mm and 6 mm skulls at $\theta=10°$ and $\theta=20°$. For $h=3$ mm, the transmission at $\theta=10°$ and $f=0.6$ MHz is 2.7 times less than at the nominal value of shear speed. For $h=3$ mm, the transmission at $\theta=20°$ and $f=0.66$ MHz is 2.2 times less than at the nominal value of shear speed and the frequency averaged value is 3.8 times lower. Also, for $h=6$ mm and $f=0.5$ MHz, the transmission at $\theta=10°$ is 1.5 times less and at $\theta=20°$ is 2.3 times less.

The phase error for the low shear speed as plotted in Fig. 16 is nearly negligible error at all frequencies, all skull thicknesses, and all angles of incidence. The phase error for the high shear speed as plotted in Fig. 17 has about the same maximum error when compared with the nominal case at $\theta=10°$ but an increased maximum $\Delta\phi$ of up to 60° at $\theta=20°$. The phase error at $\theta=30°$ is prohibitively high in light of Fig. 9.

IV. CONCLUDING REMARKS

We have examined the transmission and volumetric absorption characteristics through various representative skull thicknesses versus frequency and angle of incidence. Key assumptions included are the following: flat skull layers with equal thickness and with shear speeds equal to half the dilational speeds. We believe that the flat layer assumption is quite good. In addition to the arguments above to support this assumption, we also modeled the transmission using equations for a cylindrical solid but found essentially no difference in the results for any orientation of the cylinder axis with respect to the incident wave. We also emphasize that the equal thickness assumption is based on measurement and does not make the numerical modeling any easier. The formulation as presented in the appendix is general and each layer may have a different thickness. The only skull thickness measurement by Fry that does not come close to the equal layer thickness is the 9.5 mm parietal bone section, which has a marrow layer thickness equal to four times the outer ivory layer thickness. Transmission through skull sections this thick are given by the direct wave transmission and

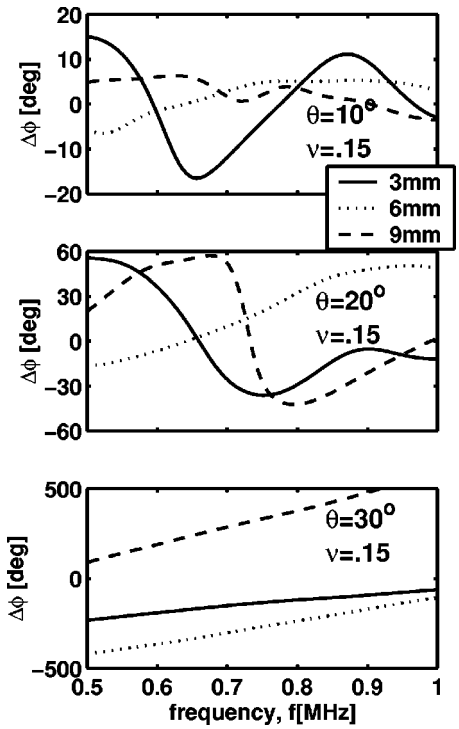

FIG. 17. Phase error $\Delta\phi$ (degrees) versus frequency for high shear speed.

the only difference in transmission is due to differences in the damping between the marrow and the ivory.

There are no measurements on skull shear speeds and our assumption that $c_s = c_d/2$ or $\nu = 0.3$ is based on a typical value for a solid. We have bracketed the problem by examining high and low shear speed values. The transmission calculation is shown to be sensitive to shear speed particularly for the thin skull section. The amplitude shading of source array may be optimized only when the transmission is accurately known. Measurements are needed to fix this property. The numerical model presented is numerically efficient so that layer shear speeds may be backed out of measured data. We should note that it is also possible that the marrow shear speed is a different fraction of the dilational speed than in the ivory layer.

The $\Delta\phi$ defined above is the phase error that would be incurred if the shear waves in the skull are ignored but having otherwise perfect knowledge of the skull layer densities, thicknesses, and dilational wave speeds. This of course is not true, particularly for the dilational wave speeds, which can only be inferred after MRI or CT measurements. Additional phase errors are incurred because the underlying assumptions of our model (flat and parallel surfaces, homogeneous materials) are also not perfectly valid. In light of this, there is some benefit to be gained by including shear effects in phase predictions especially for source arrays that operate at the lower frequencies between 0.5 and 0.75 MHz.

The low ivory damping results demonstrate that energy dissipation is sensitive to the loss factors in the ivory and marrow layers and that both reflection and transmission measurements are necessary to fix their values. We suggest that Fry's results are contradictory and more measurements are needed to resolve this issue. If it turns out that the ivory layer damping is indeed low then the scattering of both dilational and shear waves in the marrow layer becomes much more important.

It is clear that a detailed analysis of how energy is removed from an individual's skull would be valuable and is a recommended topic for further study. A good first step in that direction would be to consider a simple 1-D thermal model. Such a model requires knowledge of the skull and source array geometries from which the angular distribution of incident energy due to all source elements at a particular thickness region on the skull surface may be estimated from a simple (forward) ray theory. Once this is known, the volumetric absorption may be calculated as described in this paper, integrated over the angle of incidence, and then applied as input to the thermal model. The thermal model would include conduction through the skull and outer skin layer and convection into the coupling fluid. Such a model would tend to overpredict the temperature rise because it ignores lateral conduction and perfusion. The advantage of a simple 1-D thermal model is that it is numerically efficient and could be used to provide initial optimization of a source array with amplitude shading. We speculate that the temperature rise in thick sections of the skull may be so high that source elements directed at these sections should be turned off. We also speculate that a high percentage of the total transmission will be through the thin sections of the skull, which have the highest transmission levels and are nearer to the coupling fluid, which acts as heat sink. From the results presented above, the transmission through the thinner skull sections of skull show a high sensitivity to angle of incidence and frequency, especially at the lower frequencies, suggesting that source arrays with large numbers of elements and amplitude shading would be highly beneficial.

ACKNOWLEDGMENTS

This research was supported by NCI Grant No. CA76550 and TxSonics Inc. of Haifa, Israel.

APPENDIX: NUMERICAL MODEL OF ACOUSTIC TRANSMISSION AND ABSORPTION THROUGH THE SKULL

The governing equations for an elastic solid[14] and details of the numerical model of the skull are given here. The numerical model is used to calculate transmission and absorption of harmonic plane waves through the skull as a function of frequency and angle of incidence. The method implemented is the wave-based finite element method (WFEM), which was used by Kausel and Roesset[12] to study the response of seismic waves in layered soils. The WFEM method is closely related to the Direct Global Matrix (DGM) method proposed by Schmidt and Jensen.[15]

1. Governing equations

Here we present the homogeneous governing equations for an elastic solid oriented in the rectangular coordinate system $\{x,y,z\}$. The equations apply to any of the three layers of the skull. It is not necessary to consider the nonhomogeneous equations because external forcing is applied through the boundary conditions at the interfaces between the layers.

The solid has density ρ and Lame′ parameters λ and μ. The motions at a particular point are given by the displacement,

$$\mathbf{u} = \{u,v,w\}^T, \tag{A1}$$

where the components of the displacement act in the positive $\{x,y,z\}$ coordinate directions, respectively. Material damping is included by allowing λ and μ to be complex.

The governing equations for an elastic solid are given by the strain-displacement relations, the constitutive relation, and the momentum equations. The strains are related to the displacements by

$$\boldsymbol{\varepsilon} = \mathbf{M}\mathbf{u}, \tag{A2}$$

where

$$\boldsymbol{\varepsilon} = \{\varepsilon_{xx}, \varepsilon_{yy}, \varepsilon_{zz}, \gamma_{xy}, \gamma_{xz}, \gamma_{yz}\}^T, \tag{A3}$$

and the differential operator matrix,

$$\mathbf{M}=\begin{bmatrix} (\ )_{,x} & 0 & 0 \\ 0 & (\ )_{,y} & 0 \\ 0 & 0 & (\ )_{,z} \\ (\ )_{,y} & (\ )_{,x} & 0 \\ (\ )_{,z} & 0 & (\ )_{,x} \\ 0 & (\ )_{,z} & (\ )_{,y} \end{bmatrix}. \tag{A4}$$

The stresses are related to the strains by the constitutive relation

$$\boldsymbol{\sigma}=\mathbf{C}\boldsymbol{\varepsilon}, \tag{A5}$$

where

$$\boldsymbol{\sigma}=\{\sigma_{xx},\sigma_{yy},\sigma_{zz},\sigma_{xy},\sigma_{xz},\sigma_{yz}\}^T \tag{A6}$$

and

$$\mathbf{C}=\begin{bmatrix} \lambda+2\mu & \lambda & \lambda & 0 & 0 & 0 \\ \lambda & \lambda+2\mu & \lambda & 0 & 0 & 0 \\ \lambda & \lambda & \lambda+2\mu & 0 & 0 & 0 \\ 0 & 0 & 0 & \mu & 0 & 0 \\ 0 & 0 & 0 & 0 & \mu & 0 \\ 0 & 0 & 0 & 0 & 0 & \mu \end{bmatrix}. \tag{A7}$$

The homogeneous momentum equations are

$$\mathbf{N}\boldsymbol{\sigma}=\rho\mathbf{u}_{,tt}, \tag{A8}$$

where the differential operator matrix,

$$\mathbf{N}=\begin{bmatrix} (\ )_{,x} & 0 & 0 & (\ )_{,y} & (\ )_{,z} & 0 \\ 0 & (\ )_{,y} & 0 & (\ )_{,x} & 0 & (\ )_{,z} \\ 0 & 0 & (\ )_{,z} & 0 & (\ )_{,x} & (\ )_{,y} \end{bmatrix}. \tag{A9}$$

It may be shown that the momentum equations for an elastic solid may be expressed in terms of three wave equations given by

$$\begin{bmatrix} c_d^2 & 0 & 0 \\ 0 & c_s^2 & 0 \\ 0 & 0 & c_s^2 \end{bmatrix}\nabla^2\boldsymbol{\phi}=\boldsymbol{\phi}_{,tt}, \tag{A10}$$

where

$$\boldsymbol{\phi}=\{\phi,\psi,\chi\}^T, \tag{A11}$$

the dilational wave speed is related to the Lame′ constants by

$$c_d^2=\frac{\lambda+2\mu}{\rho}, \tag{A12}$$

and the shear speed is related to the Lame′ constants by

$$c_s^2=\frac{\mu}{\rho}. \tag{A13}$$

The potential functions ϕ, ψ, and χ represent a dilational wave and two shear waves, respectively. The dimensions of ϕ and ψ are length squared and the dimensions of χ are length cubed.

The displacements are related to the potential functions by

$$\mathbf{u}=\mathbf{P}\boldsymbol{\phi}, \tag{A14}$$

where the differential operator matrix,

$$\mathbf{P}=\begin{bmatrix} (\ )_{,x} & (\ )_{,y} & (\ )_{,xz} \\ (\ )_{,y} & -(\ )_{,x} & (\ )_{,yz} \\ (\ )_{,z} & 0 & -(\ )_{,xx}-(\ )_{,yy} \end{bmatrix}. \tag{A15}$$

Note that when $(\ )_{,y}=0$, the ϕ and χ waves are excited only by u and w displacements (but not v) and the ψ wave is excited only by v displacements (but not u and w).

2. Transformed equations

For steady-state transmission problems, it is convenient to solve for the equations of the previous section by transforming them into the x and y wavenumber domains and the frequency domain. The solution to the transformed problem is then given by two matrix relations relating wave amplitudes to displacements and also wave amplitudes to stresses.

The transform is defined by the triple Fourier transform pair,

$$\begin{aligned} u=&\frac{1}{(2\pi)^3}\int_{k_y=-\infty}^{\infty}\int_{k_x=-\infty}^{\infty}\int_{\omega=-\infty}^{\infty}\hat{u}\exp(+ik_x x) \\ &\times\exp(+ik_y y)\exp(-i\omega t)d\omega\ dk_x\ dk_y \\ \Leftrightarrow\hat{u}=&\int_{y=-\infty}^{\infty}\int_{x=-\infty}^{\infty}\int_{t=-\infty}^{\infty}u\exp(-ik_x x) \\ &\times\exp(-ik_y y)\exp(+i\omega t)dt\ dx\ dy, \end{aligned} \tag{A16}$$

where ω is radial frequency, k_x is the wavenumber component in the x direction, and k_y is the wavenumber component in the y direction.

The transform of Eq. (A10) is

$$(k_x^2+k_y^2-(\ )_{,zz})\hat{\boldsymbol{\phi}}=\begin{bmatrix} k_d^2 & 0 & 0 \\ 0 & k_s^2 & 0 \\ 0 & 0 & k_s^2 \end{bmatrix}\hat{\boldsymbol{\phi}}, \tag{A17}$$

where

$$k_d=\frac{\omega}{c_d}\quad\text{and}\quad k_s=\frac{\omega}{c_s} \tag{A18}$$

are the material wavenumbers for the dilational wave and the two shear waves.

The solution to Eq. (A17) is

$$\hat{\boldsymbol{\phi}}=\boldsymbol{\Lambda}^+\mathbf{A}^+ +\boldsymbol{\Lambda}^-\mathbf{A}^-, \tag{A19}$$

where

$$\mathbf{A}^{\pm}=\{A^{\pm},B^{\pm},C^{\pm}\}, \tag{A20}$$

$$\boldsymbol{\Lambda}^+=\begin{bmatrix} \exp(+ih_z z) & 0 & 0 \\ 0 & \exp(+ik_z z) & 0 \\ 0 & 0 & \exp(+ik_z z) \end{bmatrix},$$

$$\mathbf{\Lambda}^- = \exp(+ih_z h) \times \begin{bmatrix} \exp(-ih_z z) & 0 & 0 \\ 0 & \exp(-ik_z z) & 0 \\ 0 & 0 & \exp(-ik_z z) \end{bmatrix}, \tag{A21}$$

and

$$h_z = \sqrt{k_d^2 - k_x^2 - k_y^2} \quad \text{and} \quad k_z = \sqrt{k_s^2 - k_x^2 - k_y^2}. \tag{A22}$$

Our convention is to eliminate the ambiguity introduced by the square root function by taking the value of h_z and k_z that are either on the positive real axis or in the upper half complex h_z and k_z wavenumber planes. In this way, the waves with amplitudes $\mathbf{A}^+$ propagate energy in the positive z direction and the waves with amplitudes $\mathbf{A}^-$ propagate energy in the negative z direction.

By transforming Eq. (A14) and using Eq. (A19), we can write the displacements as

$$\hat{\mathbf{u}} = \{\hat{u}, \hat{v}, \hat{w}\}^T = \mathbf{d}^+ \mathbf{\Lambda}^+ \mathbf{A}^+ + \mathbf{d}^- \mathbf{\Lambda}^- \mathbf{A}^-, \tag{A23}$$

where

$$\mathbf{d}^{\pm} = \begin{bmatrix} ik_x & ik_y & \mp k_x k_z \\ ik_y & -ik_x & \mp k_y k_z \\ \pm ih_z & 0 & (k_x^2 + k_y^2) \end{bmatrix}. \tag{A24}$$

Using Eq. (A5), we can also write the surface stresses at z equal to a constant as

$$\hat{\boldsymbol{\sigma}}_z = \{\hat{\sigma}_{xz}, \hat{\sigma}_{yz}, \hat{\sigma}_{zz}\}^T = \mathbf{c}^+ \mathbf{\Lambda}^+ \mathbf{A}^+ + \mathbf{c}^- \mathbf{\Lambda}^- \mathbf{A}^-, \tag{A25}$$

where

$$\mathbf{c}^{\pm} = \begin{bmatrix} \mp 2\mu k_x h_z & \mp \mu k_y k_z & i\mu k_x (k_x^2 + k_y^2 - k_z^2) \\ \mp 2\mu k_y h_z & \pm \mu k_x k_z & i\mu k_y (k_x^2 + k_y^2 - k_z^2) \\ -\lambda(k_x^2 + k_y^2) - (\lambda + 2\mu) h_z^2 & 0 & \pm i2\mu k_z (k_x^2 + k_y^2) \end{bmatrix}. \tag{A26}$$

Equation (A23) and Eq. (A25) may also be used for a fluid with zero shear after redefining

$$\mathbf{d}^{\pm} = \begin{bmatrix} ik_x & 0 & 0 \\ ik_y & 0 & 0 \\ \pm ih_z & 0 & 0 \end{bmatrix} \tag{A27}$$

and

$$\mathbf{c}^{\pm} = \begin{bmatrix} 0 & 0 & 0 \\ 0 & 0 & 0 \\ -\rho\omega^2 & 0 & 0 \end{bmatrix}. \tag{A28}$$

3. Transmission and absorption

In the previous section, we established the relationship between wave amplitudes, displacements, and stresses for both an individual solid or fluid layer. In this section, we show how to calculate acoustic transmission and absorption for the skull modeled by the six-layer system shown in a Cartesian coordinate system $\{x,y,z\}$ in Fig. 2. The system layers are numbered from 1 to 6 proceeding from top to bottom. The layers are separated by 5 interfaces numbered from 1 to 5 proceeding from top to bottom. The top layer represents the coupling fluid between the source and the skull. The coupling fluid carries the incident and reflected waves. The bottom layer represents the brain tissue and carries the transmitted wave. The remaining layers represent the outer skin and the ivory and marrow skull layers. The brain tissue and the skin layer are modeled as fluids and all three skull layers are modeled as solids. All layers are flat and infinitely extended in the x and y directions. The top and bottom layers are semi-infinite in z.

It is convenient to define local coordinates systems for each layer. All local coordinate systems are simple translations of the global coordinate system (the one shown in Fig. 2) along the global z axis. The origins of the local coordinate systems for layer 1 and 6 are located at $z=0$ and $z=h$. The origins for the remaining layers are located at the top interface defining that particular layer. When necessary, we will refer to individual layer variables with a superscript in braces. For example, the third layer defined by interface 3 and 4 has thickness $h^{(3)}$ with interface 3 located at $z^{(3)}=0$ and interface 4 located at $z^{(3)}=h^{(3)}$.

The incident wave is assumed to be oscillating at fixed frequency ω and incident at such an angle that the x and y components of the trace wavenumber are

$$k_x = \omega \sin(\theta)/c, \tag{A29}$$

and $k_y=0$. There is no loss of generality in assuming $k_y=0$ because the fluid and solid layers are isotropic and homogeneous, which makes the problem symmetric about the z coordinate.

Our goal is to calculate the reflection coefficient,

$$A_r = \frac{(A^-)^{(1)}}{(A^+)^{(1)}}, \tag{A30}$$

the transmission coefficient,

$$A_t = \frac{(A^+)^{(6)}}{(A^+)^{(1)}}, \tag{A31}$$

the power transmission coefficient,

$$TC = A_t A_t^*, \tag{A32}$$

and the power absorption coefficient,

$$AC = 1 - A_r A_r^* - A_t A_t^* . \tag{A33}$$

To solve for A_r, A_t, TC, and AC, we must know the wave amplitudes in layer 1 and 6 as a function of the incident wave amplitude. Without loss of generality, we may set the incident wave amplitude to unity. To solve for $(A^-)^{(1)}$ and $(A^+)^{(6)}$, we must solve for the wave amplitudes in all of the individual layers. There are 22 unknown wave amplitudes: the reflected wave amplitude in layer 1, the two amplitudes in fluid layer 2, the 6 wave amplitudes in each of layers 3, 4, and 5, and the transmitted wave amplitude in layer 6. The 22 equations needed to solve for the 22 wave amplitudes are given by specifying the boundary conditions at the interfaces. At interfaces 1, 2, and 5, there is continuity of normal displacement, which is satisfied by setting

$$\hat{w}^{(1)}|_{z^{(1)}=0} = \hat{w}^{(2)}|_{z^{(2)}=0}, \quad \hat{w}^{(2)}|_{z^{(2)}=h^{(2)}} = \hat{w}^{(3)}|_{z^{(3)}=0},$$

and

$$\hat{w}^{(5)}|_{z^{(5)}=h^{(5)}} = \hat{w}^{(6)}|_{z^{(6)}=0}. \tag{A34}$$

At interfaces 1, 2, and 5, there is continuity of normal stress, which is satisfied by setting

$$\hat{\sigma}_{zz}^{(1)}|_{z^{(1)}=0} = \hat{\sigma}_{zz}^{(2)}|_{z^{(2)}=0}, \quad \hat{\sigma}_{zz}^{(2)}|_{z^{(2)}=h^{(2)}} = \hat{\sigma}_{zz}^{(3)}|_{z^{(3)}=0},$$

and

$$\hat{\sigma}_{zz}^{(5)}|_{z^{(5)}=h^{(5)}} = \hat{\sigma}_{zz}{}^{(6)}|_{z^{(6)}=0}. \tag{A35}$$

At interfaces 2 and 5, there is zero shear stress on the solid layers, which is satisfied by setting

$$\begin{aligned} &\hat{\sigma}_{xz}^{(3)}|_{z^{(3)}=0} = 0, \quad \hat{\sigma}_{yz}^{(3)}|_{z^{(3)}=0} = 0, \\ &\hat{\sigma}_{xz}^{(5)}|_{z^{(5)}=h^{(5)}} = 0, \quad \hat{\sigma}_{yz}^{(5)}|_{z^{(5)}=h^{(5)}} = 0. \end{aligned} \tag{A36}$$

At interfaces 3 and 4, there is continuity of displacement, which is satisfied by setting

$$\hat{\mathbf{u}}^{(3)}|_{z^{(3)}=h^{(3)}} = \hat{\mathbf{u}}^{(4)}|_{z^{(4)}=0} \quad \text{and} \quad \hat{\mathbf{u}}^{(4)}|_{z^{(4)}=h^{(4)}} = \hat{\mathbf{u}}^{(5)}|_{z^{(5)}=0}. \tag{A37}$$

At interfaces 3 and 4, there is continuity of stress, which is satisfied by setting

$$\hat{\boldsymbol{\sigma}}_z^{(3)}|_{z^{(3)}=h^{(3)}} = \hat{\boldsymbol{\sigma}}_z^{(4)}|_{z^{(4)}=0} \quad \text{and} \quad \hat{\boldsymbol{\sigma}}_z^{(4)}|_{z^{(4)}=h^{(4)}} = \hat{\boldsymbol{\sigma}}_z^{(5)}|_{z^{(5)}=0}. \tag{A38}$$

From here, there are two methods for finding the wave amplitudes. One method is to use Eq. (A23) and Eq. (A25) to express Eq. (A34) through Eq. (A38) in terms of the unknown wave amplitudes. Terms in Eq. (A34) and Eq. (A35) that are proportional to $(A^-)^{(1)} = 1$ are source or forcing terms. All the unknown wave amplitudes are then calculated simultaneously by inverting a global 22 by 22 matrix. This approach of expressing the boundary conditions in terms of the wave amplitudes and inverting a global matrix is the DGM method described by Schmidt and Jensen.[15]

The alternative method, which produces identical results to within machine error, is the WFEM method described by Kausel and Roesset.[12] This approach differs only in the order in which various quantities (stresses, displacements, wave amplitudes) are determined. In this approach the layer stiffness matrices, which relate the displacements at layer interfaces to stresses at layer interfaces, are first calculated for all but the top layer. A global stiffness matrix is then assembled from the layer stiffness matrices. The forcing due to the incident wave is applied to the global stiffness matrix to solve for all the interface displacements. Once these are determined the wave amplitudes are found through Eq. (A23).

[1] J. Sun and K. Hynynen, "The potential of transskull ultrasound therapy and surgery using the maximum available skull surface area," J. Acoust. Soc. Am. **105**, 2519–2527 (1999).

[2] G. Clement, J. White, and K. Hynynen, "Investigation of a large-area phased array for focused ultrasound surgery through the skull," Phys. Med. Biol. **45**, 1071–1083 (2000).

[3] K. Hynynen, "Focused ultrasound surgery guided by MRI," Sci. Med. **3**, 62–71 (1996).

[4] F. J. Fry and J. E. Barger, "Acoustical properties of the human skull," J. Acoust. Soc. Am. **63**, 1576–1590 (1978).

[5] B. Martin and J. McElhaney, "The acoustic properties of human skull bone," J. Biomed. Mater. Res. **5**, 325–333 (1971).

[6] S. Smith, D. Phillips, O. von Ramm, and F. Thurstone, "Real time b-mode echo-encephalography," Ultrasound Med. Biol. **2**, 373–381 (1976).

[7] S. Goss, L. Frizzell, and F. Dunn, "Ultrasonic absorption and attenuation in mammalian tissues," Ultrasound Med. Biol. **5**, 181–186 (1979).

[8] D. Goldman and T. Hueter, "Tabular Data of the velocity and absorption of high frequency sound in mammalian tissues," J. Acoust. Soc. Am. **28**, 468–470 (1967).

[9] W. P. Mason and H. J. McSkimin, "Attenuation and scattering of high frequency sound waves in metals and glasses," J. Acoust. Soc. Am. **19**, 464–473 (1947).

[10] M. Junger and D. Feit, *Sound, Structures, and Their Interaction*, 2nd ed. (MIT Press, Cambridge, MA, 1972).

[11] F. Duck, *Physical Properties of Tissue* (Academic, London, England, 1990).

[12] E. Kausel and J. Roesset, "Stiffness matrices for layered soils," Bull. Seismol. Soc. Am. **71**, 1743–1761 (1981).

[13] K. J. Bathe, *Finite Element Procedures in Engineering Analysis* (Prentice–Hall, Englewood Cliffs, NJ, 1982).

[14] J. D. Achenbach, *Wave Propagation in Elastic Solids* (North-Holland and Elsevier, New York, 1975).

[15] H. Schmidt and F. Jensen, "A full wave solution for propagation in multilayered viscoelastic media with application to Gaussian beam reflection at fluid–solid interfaces," J. Acoust. Soc. Am. **77**, 813–825 (1985).